NORTH ATLANTIC TREATY ORGANISATION

RESEARCH AND TECHNOLOGY ORGANISATION

BP 25, 7 RUE ANCELLE, F-92201 NEUILLY-SUR-SEINE CEDEX, FRANCE

RTO MEETING PROCEEDINGS 79(I)

Ageing Mechanisms and Control
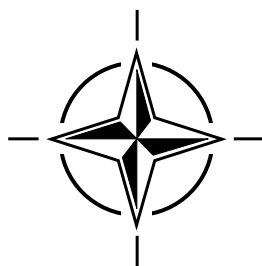(Les mécanismes vieillissants et le contrôle)

Symposium Part A – Developments in Computational Aero- and Hydro-Acoustics
(Symposium Partie A – Développements dans le domaine de l'aéroacoustique et l'hydroacoustique numériques)

Symposium Part B – Monitoring and Management of Gas Turbine Fleets for Extended Life and Reduced Costs
(Symposium Partie B – Le suivi et la gestion des turbomoteurs en vue du prolongement de leur durée de vie et de la diminution des coûts)

Papers presented at the RTO Applied Vehicle Technology Panel (AVT) Symposium held in Manchester, United Kingdom, 8-11 October 2001.

Published February 2003

Distribution and Availability on Back Cover

This page has been deliberately left blank

_____

Page intentionnellement blanche

NORTH ATLANTIC TREATY ORGANISATION

RESEARCH AND TECHNOLOGY ORGANISATION

BP 25, 7 RUE ANCELLE, F-92201 NEUILLY-SUR-SEINE CEDEX, FRANCE

RTO MEETING PROCEEDINGS 79(I)

Ageing Mechanisms and Control
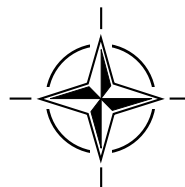(Les mécanismes vieillissants et le contrôle)

Symposium Part A – Developments in Computational Aero- and Hydro-Acoustics
(Symposium Partie A – Développements dans le domaine de l'aéroacoustique et l'hydroacoustique numériques)

Symposium Part B – Monitoring and Management of Gas Turbine Fleets for Extended Life and Reduced Costs
(Symposium Partie B – Le suivi et la gestion des turbomoteurs en vue du prolongement de leur durée de vie et de la diminution des coûts)

Papers presented at the RTO Applied Vehicle Technology Panel (AVT) Symposium held in Manchester, United Kingdom, 8-11 October 2001.

The Research and Technology Organisation (RTO) of NATO

RTO is the single focus in NATO for Defence Research and Technology activities. Its mission is to conduct and promote cooperative research and information exchange. The objective is to support the development and effective use of national defence research and technology and to meet the military needs of the Alliance, to maintain a technological lead, and to provide advice to NATO and national decision makers. The RTO performs its mission with the support of an extensive network of national experts. It also ensures effective coordination with other NATO bodies involved in R&T activities.

RTO reports both to the Military Committee of NATO and to the Conference of National Armament Directors. It comprises a Research and Technology Board (RTB) as the highest level of national representation and the Research and Technology Agency (RTA), a dedicated staff with its headquarters in Neuilly, near Paris, France. In order to facilitate contacts with the military users and other NATO activities, a small part of the RTA staff is located in NATO Headquarters in Brussels. The Brussels staff also coordinates RTO's cooperation with nations in Middle and Eastern Europe, to which RTO attaches particular importance especially as working together in the field of research is one of the more promising areas of initial cooperation.

The total spectrum of R&T activities is covered by the following 7 bodies:

- AVT   Applied Vehicle Technology Panel
- HFM   Human Factors and Medicine Panel
- IST   Information Systems Technology Panel
- NMSG   NATO Modelling and Simulation Group
- SAS   Studies, Analysis and Simulation Panel
- SCI   Systems Concepts and Integration Panel
- SET   Sensors and Electronics Technology Panel

These bodies are made up of national representatives as well as generally recognised 'world class' scientists. They also provide a communication link to military users and other NATO bodies. RTO's scientific and technological work is carried out by Technical Teams, created for specific activities and with a specific duration. Such Technical Teams can organise workshops, symposia, field trials, lecture series and training courses. An important function of these Technical Teams is to ensure the continuity of the expert networks.

RTO builds upon earlier cooperation in defence research and technology as set-up under the Advisory Group for Aerospace Research and Development (AGARD) and the Defence Research Group (DRG). AGARD and the DRG share common roots in that they were both established at the initiative of Dr Theodore von Kármán, a leading aerospace scientist, who early on recognised the importance of scientific support for the Allied Armed Forces. RTO is capitalising on these common roots in order to provide the Alliance and the NATO nations with a strong scientific and technological basis that will guarantee a solid base for the future.

Ageing Mechanisms and Control

Symposium Part A – Developments in Computational Aero- and Hydro-Acoustics

(RTO MP-079(I) / AVT-074)

Executive Summary

Computational aero- and hydro-acoustics is a relatively new and rapidly expanding technical discipline with a large potential for (more) accurate prediction of the acoustic characteristics of air and sea vehicles.

The acoustic characteristics of air and sea vehicles are of increasing importance for war-time as well as peace-time operations. Examples are:

– The acoustic signature of sea and air vehicles in military operations in war-time.

– Acoustic fatigue loads and their consequences for the structural integrity of air vehicles.

– Effects of inboard noise levels and the near-field acoustic environment on the effective and efficient operation of the vehicle and its systems (human factors).

– Community noise of air vehicles during peace-time operation.

The (accurate) modelling and prediction of the acoustic characteristics of (military) vehicles is therefore of increasing importance for the design as well as the operation of such vehicles and, hence, highly relevant for the NATO community.

The objective of the symposium was to create an opportunity for exchange of information on recent and current developments in computational acoustics between specialists in aero-acoustics and hydro-acoustics from the member states of NATO for the benefit of identifying the most successful and promising approaches for the prediction of noise characteristics of air and sea vehicles.

The intended program of the symposium was set-up for 32 'ordinary' paper presentations and 3 invited speakers.

However, as a consequence of the events of the 11th of September in the USA, many authors and other intended attendees, from the US in particular, were not permitted or did not want to travel. This resulted in the situation that 11 out of the 32 'ordinary' papers were not presented (requiring significant ad-hoc adaptation of the program) and that the average number of attendees (estimated about 40) was substantially smaller than expected.

Among the remaining 21 papers there were many good ones, in particular from France and Germany.

Excellent presentations were given by the invited speakers: Prof. Tam from Florida State University (US), Dr Blake from the USNavy and Dr Castelo Branco from Portugal. The presentation by the latter, on 'Low Frequency Noise: A Major Risk Factor in Military Operations' triggered a lot of discussion and it was suggested that the paper should be disseminated on a broad scale within the NATO community.

In the closing session of the symposium an extraordinary well prepared Technical Evaluation was presented by Dr Philip Morris of Pennsylvania State University. This was followed by a lively general discussion among the symposium attendees.

The general feeling among (most of) the attendees was that the objective of the symposium was well met; this in spite of the extraordinary circumstances resulting from the 11th of September.

Les mécanismes vieillissants et le contrôle

Symposium Partie A – Développements dans le domaine de l'aéroacoustique et l'hydroacoustique numériques

(RTO MP-079(I) / AVT-074)

Synthèse

L'aéroacoustique et l'hydroacoustique numériques sont des disciplines techniques relativement nouvelles, en plein essor, susceptibles de fournir des prévisions précises des caractéristiques acoustiques des véhicules aériens et maritimes. Celles ci sont d'une importance croissante pour les opérations de guerre comme pour les activités en temps de paix. Il s'agit par exemple :

– De la signature acoustique des véhicules aériens et maritimes lors d'opérations militaires de guerre.

– Des charges en fatigue acoustique et leurs conséquences pour l'intégrité structurale des véhicules aériens.

– Des effets des niveaux du bruit intérieur, ainsi que de ceux de l'environnement acoustique du champ proche sur l'exploitation effective et efficace du véhicule et de ses systèmes (facteurs humains).

– Du bruit provoqué en ville par des aéronefs lors d'opérations en temps de paix.

La modélisation et la prévision (précises) des caractéristiques des véhicules militaires sont par conséquent d'une importance croissante pour la conception et l'exploitation de tels véhicules. Ces activités présentent donc un grand intérêt pour les pays membres de l'OTAN.

L'objectif du symposium était de donner l'occasion aux spécialistes de l'aéroacoustique et de l'hydroacoustique des pays membres de l'OTAN d'échanger des informations sur les développements récents et actuels en acoustique numérique. Il devait permettre ainsi d'identifier les approches les plus prometteuses et les plus réussies de la prévision des caractéristiques acoustiques des véhicules aériens et maritimes.

Le programme initial du symposium avait été établi sur la base de 32 communications écrites « normales » et 3 conférenciers invités.

Cependant, en raison des événements du 11 septembre 2001 aux Etats-Unis, de nombreux auteurs et participants annoncés, en particulier des Etats-Unis, n'ont pas été autorisés à se déplacer ou n'ont pas souhaité participer. Sur les 32 communications normalement prévues 11 n'ont pas pu être présentées et la participation moyenne a été beaucoup moins forte que prévue. La majorité des 21 communications restantes a été cependant de bonne qualité, notamment les contributions de la France et de l'Allemagne.

D'excellentes présentations ont été faites par les conférenciers invités : Le Prof. Tam de Florida State University (US), le Dr. Blake de l'US Navy et le Dr. Castelo Branco du Portugal. La présentation de ce dernier, sur « Le bruit de fréquence basse : facteur de risque majeur » a provoqué de nombreuses discussions et il a été proposé de procéder à une diffusion plus large de cette communication au sein de l'OTAN.

Lors de la séance de clôture, le Dr. Philip Morris de la Pennsylvania State University a fait une excellente évaluation technique qui a donné lieu à une discussion animée.

La plupart des participants ont considéré que les objectifs du symposium avaient été atteints, malgré les circonstances extraordinaires résultant des événements du 11 septembre.

Ageing Mechanisms and Control

Symposium Part B – Monitoring and Management of Gas Turbine Fleets for Extended Life and Reduced Costs

(RTO MP-079(I) / AVT-075)

Executive Summary

Financial constraints on NATO nations have made it imperative to retain weapon systems for longer periods than originally planned and to operate those retained systems in ways not envisioned by the designers. Technologies that extend the useful lives of weapon systems and their components are of strong benefit to the NATO nations. Part B of the fall symposium clearly identified a number of methodologies in use and being developed to allow the safe extension of life for gas turbines used in weapon systems.

Two excellent keynotes on experience obtained from marine gas turbine operations of the UK Royal Navy and on the USAF experiences with aircraft gas turbines set the scene. They specifically addressed the reduction of turn round time without a companion reduction in the level of operational support and the use of RCM-based support plans, illustrated with benefits obtained on the C-5 fleet.

The twenty four papers from seven NATO nations including an invited paper from Australia were provided by Original Equipment Manufacturers (7), government Research and Technology Organisations (7), operators (6), independent Research and Technology Organisations (3), and independent manufacturers (1). Three of the originally planned papers were withdrawn but three additional papers were obtained in a timely manner to restore the stream to its planned level. The audience represented the spectrum of NATO.

The main categories were covered: maintenance and logistics practices, general design practices, usage data and mission analysis, and life determination methodologies. These categories provided material of interest to, respectively, the fleet manager, the equipment designer, the fleet operators, and the technical specialists responsible for fundamental technologies.

All sessions were well attended and produced much spirited attendee discussion with the presenters and with other attendees. A consensus view emerged that full fleet monitoring is optimal for understanding fleet life. Further, limitations in existing data bases with regard to both content and ability to support appropriate data manipulation were identified as a significant concern. The existence of design conservatism (demonstrated by aging systems which have exceeded their planned lives) illustrated the need for more research into the failure mechanisms such as crack growth in order to identify and safely use the remaining life in fielded systems.

This stream of the symposium originated in the work of the former PEP WG28, now AVT-017, documented in RTO-TR-28, "Recommended Practices for Monitoring Gas Turbine Engine Life Consumption", April, 2000. It is recommended that significant research be continued/undertaken in crack propagation and that a symposium on life cycle cost modeling be considered. Further, a specialist's meeting is recommended for the topic of non-destructive testing and residual stress determination. Finally, continued emphasis should be placed on methods whereby databases of materials and usage/damage can be developed and shared.

Les mécanismes vieillissants et le contrôle

Symposium Partie B – Le suivi et la gestion des turbomoteurs en vue du prolongement de leur durée de vie et de la diminution des coûts

(RTO MP-079(I) / AVT-075)

Synthèse

Les contraintes financières que subissent aujourd'hui les pays membres de l'OTAN entraînent un maintien en service de systèmes d'armes bien au-delà des délais initialement prévus et une exploitation de ces systèmes dans des conditions non envisagées par les concepteurs. Toutes les technologies ayant une incidence sur l'augmentation de la durée de vie utile des systèmes d'armes et de leurs composants présentent donc un intérêt certain pour les pays membres de l'OTAN. La partie B du symposium d'automne a clairement identifié un certain nombre de méthodologies qui permettent de prolonger, en toute sécurité, la durée de vie des turbomoteurs équipant les systèmes d'armes; certaines sont déjà en application et d'autres en cours de développement.

La réunion a commencé par deux excellents discours thématiques sur l'expérience acquise dans l'exploitation des turbomoteurs embarqués par la Royal Navy (GB), ainsi que sur l'expérience de l'USAF en matière de turbomoteurs avionnés. En particulier, ont été abordés la réduction des délais de mise en œuvre sans réduction associée du niveau du soutien opérationnel, ainsi que la mise en œuvre de plans d'entretien à coût réduit (RCM), avec des exemples de gains obtenus dans le cas de la flotte C-5.

Vingt-quatre communications ont été présentées par 7 pays membres de l'OTAN, et une communication a été présentée par l'Australie sur invitation. La répartition des conférenciers par secteur d'activité était la suivante : Fabricants de matériels de base (7); organisations gouvernementales de recherche et technologie (7); utilisateurs (6); organisations indépendantes de recherche et technologie (3) et fabricants indépendants (1). Trois communications initialement prévues ont dû être annulées mais trois communications supplémentaires ont été obtenues en temps utile rétablissant ainsi le programme à son niveau initial. L'assistance était représentative de l'ensemble des pays membres de l'OTAN.

Les principaux domaines couverts furent : les pratiques en matière de maintenance et de logistique; les processus généraux de conception; les relevés d'usure et l'analyse de la mission; ainsi que les méthodologies de détermination du cycle de vie. Ces sujets ont fourni des textes intéressants pour les gestionnaires de flottes aériennes, les concepteurs d'équipements, les exploitants et les spécialistes techniques responsables des technologies fondamentales.

Toutes les sessions ont accueilli de nombreux participants et ont vu des discussions animées entre l'assistance et les conférenciers. Il a été unanimement reconnu que la maîtrise du cycle de vie d'une flotte passe par le suivi de l'intégralité des appareils. En outre, les limitations des bases de données existantes en ce qui concerne aussi bien leur contenu que leur capacité à manipuler les données appropriées ont été identifiées comme un sujet de préoccupation majeur. L'existence d'une tendance conservatrice au niveau de la conception (attestée par la permanence de systèmes vieillissants qui ont dépassé leurs cycles de vie prévus) a fait ressortir le besoin d'entreprendre des travaux de recherche supplémentaires sur les mécanismes de défaillance, tels que la propagation des fissures, afin de pouvoir définir et exploiter en toute sécurité la durée de vie restante des systèmes en service.

Les communications présentées lors de cette partie du symposium ont pour origine les travaux de l'ancien groupe de travail PEP WG28, désormais connu sous le nom d'AVT-017, publiés sous la référence : RTO-TR-28 « Pratiques recommandées pour le contrôle du vieillissement des turbomoteurs » en avril 2000. Il y a lieu de poursuivre ou entreprendre des travaux de recherche d'envergure sur la propagation des fissures et d'envisager l'organisation d'un symposium sur la modélisation des coûts globaux de possession. De plus, une réunion de spécialistes pourrait être organisée sur le thème des essais non destructifs et sur la détermination des tensions résiduelles. Enfin, il faut continuer de privilégier les méthodes permettant le développement et le partage de bases de données sur les matériaux et sur la corrélation entre utilisation et détérioration.

Programme Committee

Symposium Part A – Developments in Computational Aero- and Hydro-Acoustics

Chairman
Prof. Ir. Joop Slooff
National Aerospace Laboratory/ NLR
Anthony Fokkerweg 2
1059 CM Amsterdam
The Netherlands
em: jwslooff@nlr.nl

BELGIUM
Prof. C. Hirsch
Vrije Universiteit Brussel
Dienst Stromingsmechanica
Pleinlaan, 2
B-1050 Brussel
em: hirsch@stro10.vub.ac.be

CANADA
Dr. D.G. Zimcik
National Research Council Canada
IAR
Ottawa, Ontario, K1A 0R6
em: david.zimcik@nrc.ca

FRANCE
Mr. G. Elias
ONERA
29, ave de la Division Leclerc
BP 72, 92322 Chatillon Cedex
em: elias@onera.fr

GERMANY
Dr. J. Delfs
Institute of Design Aerodynamics
DLR
Postfach 3267
18022 Braunschweig
em: jan.delfs@dlr.de

Dr. M. Hoenlinger
Krauss Maffei-Wegmann GmbH & Co. KG
Krauss Maffei Str. 11
80997 Muenchen
em: michael.hoenlinger@kmweg.de

GREECE
Prof. S. Tsangaris
National Technical University of Athens
Dept. of Mechanical Engineering
P.O. Box 64070
15710 Zografu, Athens
em:sgt@fluid.mech.ntua.gr

ITALY
Prof. M. Gennaretti
Dipartimento di Ingegneria Meccanica e
Industriale
Universita Roma Tre
via della Vasca Navale 79
00146 Roma
em: m.genneretti@uniroma3.it

PORTUGAL
Prof. A. Suleman
Instituto Superior Technico
Departmento de Engenharia Mecanica
avenida Rovisco Pais
1096 Lisboa Codex
em: suleman@alfa.ist.utl.pt

SPAIN
Mr. J.M. Riola Rodriguez
El Pardo Model Basin
El Pardo
E-28048 Madrid
em: riola@cehipar.es

TURKEY
Prof. Dr. C. Ciray
Aeronautical Eng. Department
Middle East Technical University
Inonu Bulvari PK06531
Ankara
em: cciray@metu.edu.tr

UNITED KINGDOM
Mr. R. Cottington
Assistant Director, Air Transport
DERA Pyestock
Farnborough, Hants, GU14 0LS
em: rvcottington@qinetiQ.com

Mr. D. Lovell
Air Vehicle Studies
F9, 401 Building, DERA
Pyestock, Farnborough, Hants GU14 0LX
em: dalovell@qinetiQ.com

UNITED STATES
Dr. R. R. Antcliff
Aerospace Vehicle Systems Technology
Program
Office, Mail Stop 113, 11 Langley Boulevard
NASA Langley Research Centre
Hampton, VA 23681-2199
em: r.r.antcliff@larc.nasa.gov

Dr. R. S. Christiansen
Associate Director for Plans, Code X
Dryden Flight Research Centre
Edwards, CA 93523
em: richard.christiansen@drfc.nasa.gov

Dr. D. Paul
Air Force Research Laboratory
2130 8th St. Suite
Wright Patterson AFB
OH 45433-7652
em: donald.paul@va.afrl.af.mil

Dr. L.P. Purtell
Mechanics and Energy Conversion Division
Code 333 - Office of Naval Research
800 North Quincy Street
Arlington, VA 22217-5660
em: purtelp@onr.navy.mil

Contents

Reference

SYMPOSIUM ON AGEING MECHANISMS AND CONTROL
PART A – DEVELOPMENT IN COMPUTATIONAL AERO- AND HYDRO-ACOUSTICS

SESSION I.1: PROPULSION & POWER NOISE: PROPELLERS

Paper 1 withdrawn

SESSION II.2: FLUID FLOW NOISE: CAVITIES

SESSION III: NOISE PROPAGATION

SESSION IV: STRUCTURAL RESPONSE AND ACOUSTIC LOADS SUPPRESSION

Programme Committee

Symposium Part B – Monitoring and Management of Gas Turbine Fleets for Extended Life and Reduced Costs

Chairman
Mr. G. Lazalier
Sverdrup Technology Inc.
AEDC Group, MS-9109
Arnold AFB, Tennessee 37389, USA
em: glen.lazalier@arnold.af.mil

BELGIUM
Prof. C. Hirsch
Vrije Unviersiteit Brussel
Dienst Stromingsmechanica
Pleinlaan, 2
B-1050 Brussels
em: hirsch@stro10.vub.ac.be

Prof. Dr. Vantomme
Royal Military Academy (RMA)
Department of Civil Engineering
avenue de la Renaissance, 30
B-1000 Brussels
em: jvt@cobo.rma.ac.be

CANADA
Mr. D. Rudnitski
Structures, Materials
    and Propulsion Laboratory
Institute for Aerospace Research
1500 Montreal Road, Building M-7
National Research Council of Canada
Ottawa, Ontario K1A 0R6
em: don.rudnitski@nrc.ca

DENMARK
Mr. E. Dannenberg
Danish Defence Research Establishment
Ryvangs Alle 1, P.O. Box 2715
DK-2100 Copenhagen
em: ed@ddre.dk

FRANCE
Mr. P. Donguy
SNECMA
2, Boulevard General Martial Valin
75724 Paris Cedex 15
em: paul.donguy@snecma.fr

GERMANY
Dr. M. Albers
MTU Motoren- und Turbinen-Union (MTM)
Muenchen GmbH
Dachauer Strasse 665
80995 Muenchen
em: martin.albers@muc.mtu.de

Prof. Dr. D. Hennecke
Fachgebiet Gasturbinen und Flugantriebe
Darmstadt University of Technology
Petersenstrasse 30
64287 Darmstadt
em: hennecke@gfa.tu-darmstadt.de

GREECE
Prof. Dr. P. Kotsiopoulos
Hellenic Air Force Academy
Dekelia, Attiki
em: petkot@central.ntua.gr

Dr. K. Mathioudakis
Technical University of Athens
Dept. of Mechanical Engineering
P.O. Box 64069, 157 10 Athens
em: kmathiou@central.ntua.gr

Prof. S. Paipetis
School of Engineering
Dept. of Mechanical Engineering
University of Patras, 26100 Patras
em: paipetis@mech.upatras.gr

ITALY
Prof. L. DeLuca
Departimento di Energetica
Politecnico di Milano
Piazza Leonardo da Vinci 32
20133 Milano
em: fivbd@tin.it

THE NETHERLANDS
Mr. W.P.J. Visser
NLR
Anthony Fokkerweg 2
1059 Amsterdam
em: wvisser@nlr.nl

NORWAY
Mr. I. Sollien
Norwegian Defence Research Establishment
(FFI)
P.O. Box 25
NO-2027 Kjeller
em: ivar.sollien@ffi.no

POLAND
Dr. R. Szczepanik
Air Force Institute of Technology
01-494 Warsaw
M. Box 69
str.Ksiecia Boleslawa 6
em: ryszard@afit.polbox.pl

PORTUGAL
Maj. P. A. Costa
Laboratorio de Aeronautica
Academia da Forca Aerea
Granja do Marques
2710 Sintra
em: mop13967@mail.telepac.pt

Lt. Col. M. de Matos G. Chambel
CLAFA/DMA
avenida de Forca Aerea
2720 Alfragide
Fax: 351 121 4716361

TURKEY
Prof. O.C. Eralp
Middle East Technical University
Mechanical Engineering Dept.
Inonu Bulvari, 06531 Ankara
em: ceralp@metu.edu.tr

UNITED KINGDOM
Mr. R. Cottington
Assistant Director, Air Transport
DERA Pyestock
Farnborough, Hants, UK GU14 0LS
em rvcottington@QinetiQ.com

Contents

Publications of the RTO
Applied Vehicle Technology Panel

MEETING PROCEEDINGS (MP)

**Advanced Flow Management: Symposium Part A – Vortex Flows and High Angle of Attack for Military Vehicles /
Part B – Heat Transfer and Cooling in Propulsion and Power Systems**
MP-069(I), February 2003

Low Cost Composite Structures / Cost Effective Application of Titanium Alloys in Military Platforms
MP-069(II), February 2003

**Ageing Mechanisms and Control: Symposium Part A – Developments in Computational Aero- and Hydro-Acoustics /
Part B – Monitoring and Management of Gas Turbine Fleets for Extended Life and Reduced Costs**
MP-079(I), February 2003

Ageing Mechanisms and Control: Specialists' Meeting on Life Management Techniques for Ageing Air Vehicles
MP-079(II), February 2003

Unmanned Vehicles (UV) for Aerial, Ground and Naval Military Operations
MP-052, January 2002

**Active Control Technology for Enhanced Performance Operational Capabilities of Military Aircraft,
Land Vehicles and Sea Vehicles**
MP-051, June 2001

Design for Low Cost Operation and Support
MP-37, September 2000

Gas Turbine Operation and Technology for Land, Sea and Air Propulsion and Power Systems (Unclassified)
MP-34, September 2000

Aerodynamic Design and Optimization of Flight Vehicles in a Concurrent Multi-Disciplinary Environment
MP-35, June 2000

Structural Aspects of Flexible Aircraft Control
MP-36, May 2000

New Metallic Materials for the Structure of Aging Aircraft
MP-25, April 2000

Small Rocket Motors and Gas Generators for Land, Sea and Air Launched Weapons Systems
MP-23, April 2000

Application of Damage Tolerance Principles for Improved Airworthiness of Rotorcraft
MP-24, January 2000

Gas Turbine Engine Combustion, Emissions and Alternative Fuels
MP-14, June 1999

Fatigue in the Presence of Corrosion
MP-18, March 1999

Qualification of Life Extension Schemes for Engine Components
MP-17, March 1999

Fluid Dynamics Problems of Vehicles Operation Near or in the Air-Sea Interface
MP-15, February 1999

Design Principles and Methods for Aircraft Gas Turbine Engines
MP-8, February 1999

Airframe Inspection Reliability under Field/Depot Conditions
MP-10, November 1998

Intelligent Processing of High Performance Materials
MP-9, November 1998

Exploitation of Structural Loads/Health Data for Reduced Cycle Costs
MP-7, November 1998

EDUCATIONAL NOTES (EN)

Active Control of Engine Dynamics
EN-020, November 2002

Supercavitating Flows
EN-010, January 2002

Aging Aircraft Fleets: Structural and Other Subsystem Aspects
EN-015, March 2001

Aging Engines, Avionics, Subsystems and Helicopters
EN-14, October 2000

Measurement Techniques for High Enthalpy and Plasma Flows
EN-8, April 2000

Development and Operation of UAVs for Military and Civil Applications
EN-9, April 2000

Planar Optical Measurements Methods for Gas Turbine Engine Life
EN-6, September 1999

High Order Methods for Computational Physics, Published jointly with Springer-Verlag, Germany
EN-5, March 1999

Fluid Dynamics Research on Supersonic Aircraft
EN-4, November 1998

Integrated Multidisciplinary Design of High Pressure Multistage Compressor Systems
EN-1, September 1998

TECHNICAL REPORTS (TR)

Performance Prediction and Simulation of Gas Turbine Engine Operation
TR-044, April 2002

Evaluation of Methods for Solid Propellant Burning Rate Measurements
TR-043, February 2002

Design Loads for Future Aircraft
TR-045, February 2002

Ice Accretion Simulation Evaluation Test
TR-038, November 2001

NATO East-West Workshop on Magnetic Materials for Power Applications
TR-031, August 2001

Verification and Validation Data for Computational Unsteady Aerodynamics
TR-26, October 2000

Recommended Practices for Monitoring Gas Turbine Engine Life Consumption
TR-28, April 2000

A Feasibility Study of Collaborative Multi-facility Windtunnel Testing for CFD Validation
TR-27, December 1999

This page has been deliberately left blank

_____

Page intentionnellement blanche

Technical Evaluation Report

Philip J. Morris
Boeing/A. D. Welliver Professor of Aerospace Engineering
Penn State University
University Park, PA 16802, USA

INTRODUCTION

In the past five to ten years computational aero- and hydro-acoustics (CAA and CHA) have emerged as fields with tremendous potential for physical understanding and prediction of the noise generated by unsteady flows. Many of these advances have been due to the extraordinary increases in computational power that have occurred. In addition, new algorithms, specifically designed for acoustics problems, have been developed.

The NATO/AVT Symposium, held in the Manchester Town Hall, on October 8-11, 2001, provided an opportunity for the assessment of the most promising approaches for the prediction of noise from air and sea vehicles. The program committee, chaired by Prof. Ir. Joop Slooff of the National Aerospace Laboratory/NLR, recognized that the acoustic characteristics of both air and sea vehicles are important in both wartime as well as peacetime operations. In particular, they noted the following four areas of importance:

- "Acoustic fatigue loads and their consequences for structural integrity are important factors in the design and operation of vehicles, air vehicles in particular.
- The acoustic signature of sea and air vehicles is of great importance for military operations in wartime.
- For air vehicles the contribution to community noise during peacetime operations is of growing concern.
- For sea and air as well as land vehicles the inboard noise level and, for air vehicles, the near field acoustic environment is important for the effective and efficient operation of the vehicle and its systems."

The papers presented at the Symposium all contributed in some way to one or more components of the theme. The papers were grouped into sessions focused in the following areas:

- Propulsion and Power Noise
- Fluid Flow Noise
- Noise Propagation
- Structural Response and Acoustic Loads Suppression.
  In addition, there were three invited lectures:
- An overview of CAA by Professor Christopher K. W. Tam, Florida State University, USA
- A description of emerging computational tools by Dr. William Blake, U. S. Navy, USA
- A discussion of physiological and psychological effects of low frequency noise by Dr. N. A. A. Castelbranco, Center for Human Performance, Portugal.

The Symposium schedule originally included 29 technical presentations and 3 invited lectures. Prior to the meeting 11 papers were withdrawn or the authors failed to attend. Some of this significant reduction in the number of presented papers was clearly due to the tragic events of September 11, 2001 that put constraints on travel: particularly for government employees or military personnel. However, not all the withdrawals could be obviously blamed on these events and this was very disappointing for the Symposium organizers. In any event, the quality and relevance of the remaining papers provided a sound basis for discussions and conclusions.

In this evaluation it is not intended to provide a detailed summary of the presentations or questions and responses, though some comments are made on each paper presented at the Symposium. Rather, an emphasis will be placed on those areas where further progress is necessary or where particular advances have been made. The evaluation begins with a review of the invited lectures. This is followed by a discussion of the presentations grouped by the first three technical areas listed above. There were no presentations in the last area: Structural Response and Acoustic Loads. An attempt is made to identify areas in need of study that were not addressed directly in the Symposium. Finally, some suggestions are made for future research directions.

INVITED LECTURES

Appropriately, Christopher K. W. Tam of Florida State University delivered the first invited lecture. He has developed specialized algorithms that minimize dissipation and dispersion. He has also provided several non-reflecting boundary conditions for zero flow, uniform flow and nonuniform flow at outflow boundaries. All these techniques are widely used in the CAA community. The techniques were outlined and the rationale behind their development was explained. An example that demonstrated the use of these methods was given in the form of the simulation of jet screech. In this study, Tam used a multi-size-mesh, multi-time-step strategy to reduce computation time. The Cartesian grid in the vicinity of the jet nozzle was very fine and coarser grids, by a factor of two, extended out to the far field. The grid size of the coarsest grid was 2^n times coarser than the finest mesh. In this way the time steps for each region may be synchronized and only the finest grid used the smallest time step. In addition, the Navier Stokes equations were used on the finest grid domains near the jet flow. The Euler equations were used in the coarser domains. No problem was encountered at the interface between the two regions. The agreement between experiment and simulation in terms of modal content, frequencies and absolute levels was impressive.

Even though the simulation considered a three-dimensional phenomenon, a quasi three-dimensional approach was used with only 5 azimuthal modes being considered. Though this is appropriate for the very organized resonant phenomenon under consideration, it avoids the computational complexity associated with truly three-dimensional, broadband, unsteady phenomena. The true broadband component of the measured noise was not resolved and any suggestion of broadband behavior was due to the finite time sampling.

In response to questions concerning the use of high-order schemes in shock-containing flows, Tam noted that he used a selective artificial damping scheme to eliminate high wavenumber components and that the method was not akin to a TVD scheme. Tam also noted that he used the artificial damping throughout the computational domain. Also, with the use of a multi-size- mesh, multi-time-step strategy there was no need for a non-uniform grid. This technique required the least CPU time for the problem under consideration. However, this would not be the case for problems with a more complex geometry. A question was raised as to whether the use of the use of the k-ε turbulence model might cause the loss of physical significance. Tam replied that the turbulence model simulated the cumulative effects of the small-scale turbulence. Since the wavelengths of the large-scale instabilities are so much greater than the fine scale turbulence, the scale disparity allows the neglect of the effect of each individual fine scale eddy. Only their cumulative effect needs to be modeled.

William Blake described various computational and experimental methods that are under development for the prediction of fan or propulsor noise with a particular emphasis on low Mach number or hydrodynamic applications. The tools are in a modular form with different aspects of the problem being treated separately. For example, LES or DNS may be used to describe the details of the flow field near the blade. For engineering purposes, on complex geometries, a combination of RANS and embedded LES methods are used. The fluid loading and noise sources may be described in terms of a surface dipole for acoustically compact sources. Blake argued that the essential difference between aeroacoustic and hydroacoustic applications is the lack of quadrupole source mechanisms. In addition, bubbly flows and cavitation are also not present in aeroacoustic applications. Examples were given for several applications. In the case of the response of rotors to inlet turbulence it was shown how an inversion of the predicted noise, based on simple strip theory, could be used to extract information on the incoming turbulence. Cascade effects and rotor/stator interaction were also described. The distortion of wakes by a swirling

flow, which is important in the determination of the interaction of the wake with a downstream stator, was discussed. It was noted that the stability of the wake flows follow Rayleigh's criterion for rotating flows. In addition, Blake indicated that full three-dimensional effects were under investigation. Finally, various approaches to the prediction of trailing edge noise were described. Blake stressed the importance of the use of a combination of computational methods when near term engineering applications are under study. He also emphasized the importance of experimental verification of each step in the development of prediction schemes. In response to questions concerning the universality of the predicted inflow turbulence spectrum, Blake indicated that there could be significant differences between different applications and geometries.

Dr. Nuno A. A. Castelo Branco of the Center for Human performance, Alverca, Portugal, delivered the final invited lecture. The topic of his lecture, the risk factors associated with exposure to low frequency noise (LFN), was not central to the Symposium theme of computational methods. However, the presentation provided an enlightening and sobering introduction to the damaging physiological and psychological consequences of exposure to LFN. It was explained how repeated exposure can result in decreased capacity for cognitive functions, the sudden onset of respiratory problems, and mood alterations. These effects are not captured in the usual psychoacoustic metrics, as they cannot be heard: being at frequencies below that of human hearing. However, exposure can result in physiological changes such as thickening of the pericardium and cardiovascular thickening. Dr. Castelo Branco was asked what regulations were under consideration to protect military personnel or civilians from the effects of LFN. He responded that no changes to current legislation were planned or underway with two exceptions: Puerto Rico and Mozambique. In the former case a January 2001 law limits the emission of LFN and in Mozambique preparations for a new law include LFN. He noted that permissible exposure levels for LFN, the necessary recovery times for each type of exposure period and dose-response data are unknown. These are necessary for human exposure legislation. Individual susceptibility indicators are under study in Dr. Castelo Branco's group: but as yet, there is insufficient data. Dr. Castelo Branco's lecture provided a startling exposure of the attendees to the importance of another aspect of aeroacoustics that appears to have been almost overlooked.

Propulsion and Power Noise

The first papers in this area focused on fan noise and its prediction. Yin and Delfs described calculations of the noise radiated by ducted and unducted fans. The fan was represented by spatially distributed rotating dipoles. They used a multi-domain strategy similar to that discussed by Tam. Their predictions showed that in the absence of flow the ducted fan radiated no noise as the modes were cut off. In the presence of flow, a mode generated by the fan was cut on according to theory and this was shown by the numerical solution. In addition, the inclusion of a shear flow outside the uniform parallel stream representing the parallel duct flow was shown to change the radiated noise directivity: presumably due to refraction. It was surprising that the shear layer only seemed to generate an instability wave when excited by the transient sound radiation. One might expect a thin shear layer to support a wide range of unstable frequencies. It would be easy to check using a parallel flow stability analysis whether this is the case. Also, it would be instructive to include the shear layer generated by the duct boundary layer in the calculations. In response to questions the authors indicated that swirling flow could be included in the calculations and that the imposed shear was only external to the duct wall.

Wilson submitted a paper that introduced a different perspective to the analysis of numerical simulations. Faced with the likelihood that discrete boundary conditions for internal flows are imperfect, a method was presented to extract the "real" acoustics from numerical reflections. This is an intriguing approach that may be very helpful when a traditional CFD code is being used to analyze aeroacoustic behavior. The paper indicated the conditions and regions where the wave-splitting technique would fail to work. These include the fan exit region owing to the presence of swirl and lined ducts. Also, the method does not work well near the cut-on/cut-off boundary. To some extent, the paper begs the question as to whether the technique could not be employed to improve the existing nonreflecting boundary conditions.

de la Calzada, Quintana and Burgos described the application of a traditional nonlinear CFD code for the simulation of acoustic propagation. Few details of the code were provided. In addition, the examples did not make use of standard benchmark problems that would have allowed a better assessment

of the accuracy of the method. The importance of nonreflecting boundary conditions and grid resolution were highlighted. The paper raises the interesting question of the balance between the use of an existing and well-tested (for CFD purposes) code for acoustics problems and the development of a specialized high order code. In the long term, the latter choice is likely to be appropriate: but in the short term, especially if complex geometries are to be analyzed, the continued use of a low-order accurate existing codes with a very refined grid may be the logical choice. The authors emphasized this point in response to questions. It was their intention to minimize the number of different codes used in the simulation of unsteady aero-thermal behavior of turbine stages and they were concentrating on only having one code. They also argued that the typical acoustic wavelengths considered were already much longer than the typical scale of the viscous regions in the flow. Thus a fine mesh was already necessary to resolve the viscous effects. Of course, this is balanced by the need for additional grid points in potential flow regions. In terms of execution time the authors indicated that the nonlinear code took only twice as long as the linear code: the nonlinear code requiring one day to run the flat plate cases presented in the paper.

Huttl, Kahl, Kennepohl and Heinig described the use of a linearized Euler solver for the study of acoustic propagation and the interaction of sound waves with a cascade. The code used a finite-volume discretization and a three-step Runge-Kutta time integration. The authors demonstrated the effect of propagation angle relative to coordinate directions on a very skewed Cartesian grid. The details of the boundary conditions were not provided. Though, in answer to questions, it appears that the boundary conditions were prescribed on the basis the analytical solution. This would seem to overspecify the problem. The authors gave some criteria for accuracy in amplitude and phase for plane waves. It is not clear how this would help for broadband acoustic phenomena with significant variations in propagation angle. The authors' comparisons with an analytic solution for sound propagation through a cascade of plates were impressive though the boundary conditions were again unspecified. Though this is a good starting point, the performance of the code for realistic blade geometries and loading and broadband disturbances is unknown.

Djaffar, Alexandre and Hany described a fan noise generation and propagation code developed by Pratt & Whitney Canada. An important component of this work was the integration of a CFD solver for the fan pressure distribution and its coupling with an acoustic radiation code. The numerical method was based on a spectral element technique and the grid generation was achieved with a CAD based approach. The test cases considered were sufficiently realistic to indicate the potential for CAA methods to make a real contribution in the near term to fan aeroacoustic design.

Jayatunga, Kroeff, Carrotte, McGuirk and Petersen authored the one paper in the area of Power Systems. This was a combined experimental and computational study of the flow and noise in the diffuser of an industrial gas turbine engine. A steady RANS CFD calculation and experiments were used to identify the gross features of the flow and the potential noise producing regions. Once the diffuser was identified as a primary noise source, a geometrically simplified model was examined using LES. On the basis of preliminary results from the LES the acoustic analogy was used to predict the radiated noise power. The source was modeled as a ring of dipoles. However, since the LES provides the wavenumber/frequency characteristics of the wall pressure fluctuations, (once a long enough time sample has been obtained), this information could be used to describe the noise source.

In the area of Jet Noise, Page, McGuirk, Behrouzi and Hossain described a combined experimental computational study. As in the previous paper the averaged flow properties were determined by a RANS CFD solution. The information on turbulent kinetic energy and length and time scales were then used in a "four source model" for the noise from a coaxial jet. The agreement between the CFD and experiments was reasonable in the early stages of the jet development though it deteriorated further downstream. This could have been associated with experimental errors in seeding the ambient flow. No noise predictions were provided. In response to questions the authors argued that RANS CFD would be more effective than LES or Detached Eddy Simulation (DES) for jets with complex exit geometries. However, it is difficult to see how the inherently isotropic k-ε turbulence model could capture the subtle mixing effects of serrations or chevrons. Also, the authors indicated that they were not yet modifying the "four source model" on the basis of the CFD but were determining the equivalent coplanar exit conditions presently required by the model.

Harper-Bourne described his prediction scheme for the near-field noise of combat aircraft. This paper could have fallen into the category of Acoustic Loads, as it dealt with both hydrodynamic and acoustic loads in the jet near field. Prediction models for both the jet mixing noise and shock-associated noise were presented. The predictions were based on the Lighthill acoustic analogy with the turbulent source statistics described in a fixed reference frame. Predictions of both Sound Pressure Level (SPL) and spatial coherence of the near field were made. The agreement between the predictions and measurements was quite good: though the method is semi-empirical and uses some of the measured data within the prediction scheme. However, it did show the effectiveness of the acoustic analogy formulation - even in the jet near field. In response to questions the author indicated that the assumptions about the form of the source cross correlations do affect the convective amplification factors. Details are contained in the AIAA paper (AIAA 99-1838) referenced in the written version of the paper.

Bogey, Bailly and Juvé presented an impressive LES study of a Mach 0.9 jet. The agreement achieved between predictions and experiment for both the flow and noise properties and available experiments was excellent. The authors chose a relatively low Reynolds in order to be able to capture as many turbulent scales as possible within the framework of the LES. They also described their interrogation of the instantaneous flow and noise fields to identify regions of apparent strong noise production. They concluded that the flow properties at the end of the potential core correlated well with the largest excursions in the acoustic pressure signal at small angles to the jet downstream axis. It appears that the frequency of the noise radiation is set by the fundamental stability properties of the jet flow: but that the breakdown of the large turbulent structures at the end of the potential core scatters energy into the low wavenumbers required for noise radiation. The highest resolved frequency, approximately a Strouhal number of unity, was set by the grid resolution in the near and mid acoustic fields where the linearized Euler equations were used to propagate the sound. The frequency resolution in the flow field was higher and a broader frequency range of the radiated noise could be predicted.

FLUID FLOW NOISE

In the area of shear layers and vortex shedding/interaction, Michael Howe presented the first paper. This paper described a methodology for the determination of the Green's function in the presence of either stationary or vibrating boundaries. The technique used the Kirchhoff vectors for the body in the definition of the compact Green's function. The Kirchhoff vector components are the velocity potentials of incompressible flow past the body having unit speed in the component direction at a large distance from the body. I had not encountered the use of these vectors before and they appear to be a powerful analytic tool. Several cases were examined including a source in the vicinity of a surface irregularity, sound from a vortex interacting with a sphere, parallel blade vortex interactions, edge noise, and a projectile entering a duct. This last case, that could represent a high-speed train entering a tunnel with an entry hood, gave impressive agreement with experiment. In every case the unsteady flow was deterministic. In the last case of the projectile entering the duct the noise contribution from the vortex sheets shed from the discontinuities in the duct cross section were small. Thus, although these solutions serve as excellent benchmark cases to validate CAA codes, it is not clear that the paper represents either CAA or CHA (at least as far as I understand their definition).

Golanski, Fortune and Lamballais presented a low Mach number DNS of a temporally evolving shear layer. They compared this low Mach number approximation with a full DNS and showed good agreement. The purpose of the study was to examine noise scaling for nonisothermal turbulent shear flows. For an isothermal shear they showed that the scaling with Mach number could be deduced from Lighthill's acoustic analogy assuming a "quadrupole" source. However, for the nonisothermal case the scaling was better approximated by assuming that the nonisentropic, "dipole" source term was dominant. This has implications for source modeling in heated turbulent flows. However, the results are only formally valid at very low Mach number, which may be of limited practical importance.

Lummer, Grogger and Delfs described the use of mean flow fields calculated using a steady RANS CFD code in CAA simulations. The paper was focused on the development of efficient and accurate interpolation methods to map the RANS flow field onto a CAA grid. The largest errors were observed where the CFD grid had kinks or was very coarse: but in the latter case these are regions where the mean flow gradients are small. An example of the solution of the linearized Euler equations was

provided for the interaction of an acoustic pulse with an airfoil. This paper provided an example of the numerical algorithms that must be carefully developed when the acoustics of nonuniform men flows are examined. It is also possible to converge the mean flow to a steady state on the CAA grid prior to the introduction of unsteadiness. Local time stepping and multigrid methods are useful in this approach. In response to questions the author agreed that the mass and momentum balances for the interpolated mean flow on the CAA grid were not checked. However, the linearized Euler equations were solved in non-conservative form so artificial fluxes will always be present. It was assumed that the modeling error in the RANS calculation was at least one order of magnitude larger than that introduced by interpolation.

Ewert, Meinke and Schröder described several formulations of hybrid CFD/CAA methods. These included a compressible extension of the viscous/acoustic splitting technique of Hardin and Pope, the linearized Euler equations with momentum sources, and the "acoustic perturbation equations." The last represent an attempt to separate acoustic and non-acoustic sources within the framework of an acoustic analogy. An example problem of the noise radiated by a cylinder in a laminar flow at low Reynolds number was given. The general methodologies all depended on a separate compressible CFD solution for the flow field and the use of linearized Euler equations for sound propagation. Since the compressible near field solution is available, the radiated noise could presumably also be obtained using an acoustic analogy, wave extrapolation method such as the Ffowcs Williams Hawkings equation.

Manoha, Delahay, Redonnet, Ben Kheli, Guillen, Sagaut and Mary described a similar set of approaches. Here, the near field flow solution was extended to the far field using either the Ffowcs Williams Hawkings acoustic analogy, applied on the surface, a Kirchhoff integral method or the discretized Euler equations. The porous surface Ffowcs Williams Hawkings integral method (also referred to as a wave extrapolation method) was not used. This might have improved the matching between the extrapolated solution and the direct computation as evidenced by the discontinuity observed when the Kirchhoff integral method was used. The authors applied their numerical approach to the noise radiated by a lifting airfoil. The focus was on the noise generated and scattered near the trailing edge. In results not given in the written version of the paper they showed how upstream and downstream propagating waves in the airfoil boundary layer could be distinguished using the wavenumber frequency transform of the LES solution. This indicated that some scattering occurred at the leading edge as well. This is a very effective way of interpreting the unsteady data.

Two papers were presented in the area of cavity noise. The first, by Soemarwoto and Kok used two different sets of equations to describe the flow. The first was based on a RANS solution with the k-ω turbulence model throughout the entire domain. The second only applied this model in the boundary layer regions. The Euler equations were used in the reminder of the domain. This choice was made as the RANS solution was too diffusive for the separated shear layer flow and suppressed the broadband behavior. Also, the apparent resonant third and fourth resonant modes were found to be harmonics of the lower modes and did not conform to Rossiter's formula. The results were stated to show good agreement with experiment for the amplitude of the resonant modes when the latter model was used. The effect of a ramp at the cavity trailing edge was shown to suppress the resonant feedback effects. The authors indicated that the flow/acoustic code was fully coupled with a structural dynamics code for aeroelastic calculations. They also stated that the discretization errors of their code had been assessed separately. Also, they argued that the initial conditions played no role in the results as sufficient time had been allowed for transients to exit the computational domain before sampling was performed. The authors also responded that a Detached Eddy Simulation was under consideration to overcome the diffusive nature of the RANS model.

Gloerfelt, Bailly and Juvé described a two-dimensional DNS of a cavity with length to depth ratio of 2. They used their simulation to evaluate different methods to extrapolate the near flow field solution to the far field. In particular the porous Ffowcs Williams Hawkings acoustic analogy was considered. Examples where the volume integral was included or omitted were given. The porous Ffowcs Williams Hawkings acoustic analogy method was compared with a Kirchhoff method for different integration surfaces above the cavity. Since the additional nonlinear terms given by the former method are small in the case considered, there was little difference between the two wave extrapolation techniques. There was a difference in the radiated noise field when only the surface integral was included in the acoustic analogy. This was because the volume term contained significant information on the noise sources.

However, it is more expensive to implement (even in two-dimensions). The authors concluded that for the problem under investigation the wave extrapolation methods provided the most efficient method for obtaining the radiated noise field.

NOISE PROPAGATION

The technical presentations concluded with two presentations on noise propagation. Kirkup described several applications of the Boundary Element Method (BEM). He noted that for both exterior and interior acoustic problems in uniform media the BEM has considerable advantages over either Finite Element or Finite Difference methods. This is because the problem may be transformed into a surface integral form. Examples were given of applications of the method and a suite of Fortran routines available to potential users were introduced. The author noted that the method was very efficient for sound propagation in uniform media (calculations taking only seconds or minutes on a modern PC) but was unable to describe propagation in nonuniform media. The order of accuracy depended on the elements used. The examples given by the author used piecewise constant elements as these are the simplest and most efficient to implement.

Blom, Hagmeijer and Védy described the development of the Discontinuous Galerkin (DG) method for the solution of the linearized Euler equations. This method has the advantage that it can be high-order accurate on an unstructured grid with only local dependencies. This makes the method efficient for parallel implementation. The authors gave an example of the use of their three-dimensional code in the solution of a two-dimensional sound propagation benchmark problem. They also provided some information on the parallel performance of the method. A grid dependence study was performed to assess the convergence of the scheme. They noted that a formal order of accuracy had only been established for a one-dimensional problem on a uniform grid. The authors also indicated that, for structured grids, finite difference methods would be more efficient: however, the DG method is more suitable for unstructured grid calculations.

SUMMARY AND CONCLUSIONS

The technical presentations at the Symposium showed how far computational methods for the prediction of noise from unsteady flow have advanced in only a few years. However, the papers also indicated that considerable progress is still to be made. Perhaps the clearest distinction between the different approaches that were presented was between methods that focused on the understanding of the physics of sound generation and radiation and those that attempted to solve problems of immediate practical importance. The distinguishing characteristic between these two classes mostly lay in the complexity of the geometry considered. For the most part, methods that have been developed and applied successfully to CAA problems have been based on high-order accurate algorithms. Methods developed for problems involving complex geometries have typically been low-order accurate. The exceptions to this are spectral element methods, such as those described by Djaffar *et al.* that inherently involve the use of structured grids, and the Discontinuous Galerkin method. The latter may be applied on unstructured grids but suffers computational costs when high-order basis functions are used for the nonlinear Euler or Navier-Stokes equations. Thus, it would appear that the directions for future work will involve:

- Detailed studies of fundamental aeroacoustic phenomena for simple geometric cases, and
- Hybrid schemes, where a detailed near field flow solution is coupled with an acoustic analogy or wave extrapolation method to obtain the radiated noise.

In the latter case, a trade must be made between the order of accuracy of the method, with the resulting decrease in the grid resolution requirements, and the applicability of the method to problems with complex geometry. In addition, the availability of existing unsteady flow solvers must be considered, especially if the aeroacoustic calculations are part of a larger suite of programs that might include aerodynamic performance and aeroelastic behavior. The compatibility of the codes is certainly an issue.

In terms of algorithmic development, a basic set of CAA algorithms is now available. Further development may be necessary for strong shock-containing flows: but the example given by Tam for the screech simulation suggests that this is not a problem if selective artificial damping is used. A caveat would be that this example did not involve the interaction of a broad range of turbulent scales with the

shocks. Thus, it would appear that the door is open for attacks on problems that are generated by "real world" geometries. This is where further algorithmic development appears to be needed. If a reliance on low-order, traditional unsteady CFD methods, with a very fine grid, is to be avoided, then much remains to be done to develop *efficient* high-order schemes for complex geometries. Until such methods appear, complex geometric aeroacoustic problems will continue to only be amenable to detailed flow field simulations, with low-order schemes on a very fine grid, coupled with extrapolation methods for the radiated noise.

Though the field of CAA has much to accomplish, the high-order methods that have been developed so far hold tremendous potential for applications in other areas of fluid dynamics. It should be recognized that these methods are a considerable improvement over traditional CFD methods for unsteady flow problems. Thus, applications to problems in areas such as transition, turbulence simulation, thermoacoustics, nonlinear wave propagation, to name but a few, are ripe for attack by the CAA community.

As a final comment, it is interesting to note that none of the papers addressed the issue of noise reduction. At the same time as we gain an increased understanding of the physics of noise generation, our focus should be on how this information could be used to reduce noise. That is at least as great a challenge as the "simple" simulation or prediction of noise generation and radiation.

Reference # of Paper: Technical Evaluation Report
Discusser's Name: Dr. Bastiaan Oskam
Author's Name: Prof. Philip Morris
Question:

     You concluded that there is no need for new algorithms. How about shock noise due to shock/turbulence interaction? Do we not need higher-order accurate algorithms that can also represent shock waves without spurious oscillations?

Answer:

     The point I was trying to make was that there are many high-order accurate algorithms now available for wave propagation on structured grids. Further effort in this area would appear to be a waste of effort. In addition, the results presented by Professor Tam indicated that a careful combination of high-order methods and artificial damping do result in the accurate simulation of shock-containing flows. However, in that area, I would agree that the broadband interaction problem has yet to be tackled and I would withhold any conclusions until that problem is attempted. The main point I was trying to make was that a great deal of effort should be expended to develop robust and efficient methods for aeroacoustic problems on unstructured. Then CAA can be applied to geometries of practical interest.

This page has been deliberately left blank

———————

Page intentionnellement blanche

Marine Use of Gas Turbines

Keynote Address

M. Botley
Ship Support Agency
Room 123 J Block
MOD, Foxhill, Bath
BA15 5AB
United Kingdom

Ladies, Gentlemen

Firstly, I would like to thank the Applied Vehicle Technology Panel organising committee of this symposium for the opportunity of addressing you this morning. I am very conscious of the fact that such a symposium attracts many leading scientists, engineers and academics in the fields that are the subject matter of the event. In such company, and recognising the content of some of the papers due to be presented over the next 4 days, it would be foolish of me to attempt to discuss the technical detail and challenges associated with the process of extending engine life. However, I am the Head of the Group within the United Kingdom Ministry of Defence that is responsible for in-service support of marine propulsion equipments and I feel that I have some credibility in discussing the use of marine gas turbines, the strategic issues that impact on their in-service support and the environment within which they operate. This environment will be a familiar one to many here - one that demands high standards of reliability and availability whilst at the same time being subject to substantial pressures to drive down the overall cost of ownership of these expensive equipments. There are, of course, many elements that contribute to the life cycle costs, some of which I will touch on this morning and others that will be the subject of presentations later in the seminar.

This invitation offers me the opportunity of giving you a short insight into how the Royal Navy has developed marine gas turbines over the last 50 years and how their use has been developed up to the present day including a comparison of the requirements of marine and aero gas turbine engines.   I will discuss some of the characteristics of the marine support environment and the strategy adopted by the Royal Navy to take marine propulsion forward into the 21st century.

In order to set the scene, I would like to spend just a few minutes summarising how the Royal Navy arrived at where we are today with every modern major surface warship powered by gas turbine engines.

The middle of the 19th century saw a significant move away from combined sail and steam propulsion of warships to wholly mechanically propelled vessels driven by steam powered reciprocating engines. However, at the dawn of the new century a new technology burst upon the scene. Queen Victoria's Royal Navy fleet review in 1897 saw a steam turbine driven yacht – TURBINA – demonstrate unmatchable performance before the astonished Naval Authorities of the day who had shown little

interest in the technology before that time. It marked the start of a new era of steam turbine powered ships that was to last well into the second half of the 20th century. Steam turbines were introduced into service remarkably quickly which is in marked contrast to the next marine propulsion revolution – gas turbine propulsion.

The first experimental marine gas turbine went to sea in 1947 and the world's first warship to rely entirely on gas turbine propulsive power was HMS Grey Goose, which was commissioned in 1953. Impressive though the engine was, it was large and very complex and sophisticated for its time being intercooled and recuperated. It was realised that what was needed was a ship propulsion arrangement using a simple cycle solution which had good space and weight characteristics and reasonable lower ship speed efficiency. This could be achieved either by running sided engines or using cruise diesels. I have to say here that I recognise that the diesel engine was also developed, with significant strides made between the two world wars and this generic equipment to this day plays a major role in the propulsion of many of the navies and merchant marine vessels around the world. But of course, it is not the subject of this seminar and I will say no more on diesel engine development today. Gas turbines were used as boost engines along side steam propulsion plant in two classes of vessel introduced into service during that period. Tribal Class Frigates and County Class destroyers. Both used Metropolitan Vickers G6 engines.

In those early days, marine engineers and naval architects were convinced that it would be quite impractical to use lightweight, relatively flimsy aircraft derivative engines. Fortunately, such engines were being introduced into smaller craft such as Motor Torpedo Boats. It was realised that the substantial benefit of building on the investments incurred by aero engine designers in engines that had been subject to substantial development resulted in engines that were compact, reliable, offered high powers and relatively good efficiencies. Today's lightweight, aero derivative gas turbines are used universally in all types of warship from small, fast craft to large carriers.

The next major milestone was the introduction of the aero-based twin spool marine Olympus. First run in Germany on a test bed in 1963 it eventually went to sea in two Finnish corvettes some six months before a prototype propulsion package in the Frigate HMS Exmouth. This had a single Olympus engine and two Proteus cruise engines. These were well proven in smaller craft and in advance of the Tyne engine, which was not yet available. It was this trials ship that finally convinced the United Kingdom to rely on gas turbines as the main propulsion for all future warships.

As an aside, it is interesting to note that the United States with its greater financial and technical resources started a programme of investigating and developing marine gas turbines in 1940. They conducted exhaustive trials and experiments but it was not until 1966, more than a quarter of a century later, that they put their first gas turbine to sea and not until 1975, with the appearance of the SPRUANCE Class destroyer that they first used gas turbines in a major Warship.

Olympus engines went on to power vessels ranging from frigates to carriers and are still found in numbers today. Subsequent engines used by the Royal Navy, and all of which are in use today are the Tyne – used extensively as a cruise engine and the Spey

– another twin spool, simple cycle aero derivative that started test bed running in 1960, went into aero service in 1964 and was first used in warships in the marine version some 15 years later as a boost engine.

So what are we looking for in a marine gas turbine plant?

Naturally it has to be affordable – this is not just the initial purchase but the substantial post procurement support costs.

It has to be minimum weight and space. This is not of course just the propulsion plant. For example, tankage to achieve a desired ship range will clearly vary with propulsion efficiency.

We are looking for the availability of high powers relative to merchant standards. However, the equipment must be capable of long periods at part load since very little time is actually spent at full power. Naturally therefore, part load efficiency is also very important.

Since it is fitted into a warship, it must be capable of operating in an action environment withstanding underwater explosions, blast and action damage.

It must be capable of operating in a salt laden environment, in high sea states and across a wide temperature range.

The system must be flexible enough to allow fast starting, rapid manoeuvring, good endurance and continuous operation at low powers.

It needs high availability with minimum requirement for onboard maintenance.

And to complete the package it should be low noise with a low smoke and Infra red signature.

These requirements are dealt with by providing a fully integrated package drawing on the inherent performance and characteristics of the gas turbine, careful   combinations of machinery and the application of supporting ship design features such as shock mounting and integrated intakes and exhausts.

So just how does the marine gas turbine differ from its aero parentage?

When compared to the marine gas turbine engine the military combat aircraft engine is a very much higher rated machine aimed at maximizing the thrust-to-weight ratio. This is achieved through higher pressure ratios and temperatures. For example, modern combat aircraft engine turbine entry temperatures are approaching 2000^0C as opposed to that of the marine Spey which is around 750^0C. As a consequence, overhaul lives of aircraft engines are measured in hundreds of hours as opposed to, for example, 9000 hours for the marine Spey. Hence factors of an order of magnitude are typical.

Due to the differences in usage profile, or throttle modulation, the consumption of component lives governed by low cycle fatigue is again very much greater in a combat engine. It can typically be as much as 50 times higher than for the marine gas turbine.

And, again, reflecting the rating, the levels of reliability for a combat engine tend to be lower than an engine operating in a military marine environment although airworthiness requirements clearly mandate that safety is paramount.

The marine gas turbine has its unique logistic and engineering support problems in that ships often operate many thousands of miles away from "base" for periods of 6 months or more.

The through life support costs of a combat engine can represent up to 40% of the total aircraft platform requirement. This is huge compared with that for a marine gas turbine.

And finally, the marine gas turbine is only one element, albeit an important one, within an overall propulsion system and needs to be considered as such in support terms unlike the fixed wing equivalent.

Because of the continuous demand to optimise performance and reduce costs over the past 30 years we have seen substantial improvements in marine gas turbines with extensions in time between overhauls, major increases in availability and reliability and significant improvements in specific fuel consumption across the power range.

I would now like to turn to the support environment within which we manage the gas turbines of the Royal Navy. In fact the Warship Support Agency provides overarching in service gas turbine support and cooperation through two Memoranda of Understanding involving 4 European nations, 21 years of collaboration and over 3 million shared running hours. The membership of the Olympus and Tyne Memoranda of Understanding, in place since 1980, comprises the United Kingdom, Netherlands, France and Belgium. The Memoranda of Understanding for the Spey was signed in 1989 between the United Kingdom and the Netherlands.

In 1998 the United Kingdom conducted a Strategic Defence Review. It was a foreign policy led initiative to reassess Britain's security interests and defence needs and consider how the roles, missions and capabilities of our Armed Forces and supporting structure should be adjusted to meet the new global strategic realities.

It was needed for four main reasons; UK defence projects were consistently showing time and cost overruns; Defence equipment was becoming increasingly complex and diverse demanding more flexible and shorter acquisition procedures; the threats were less predictable, and recent events certainly highlight this. This demands that new technology needs to be deployed quicker; and finally, defence industry was restructuring demanding that we review our relationship with them.

Ministers agreed that changes were necessary and the strategic defence review government white paper and supporting documents set out the rationale for change and made a number of important recommendations including the setting up of the Defence Logistics Organisation which joined together the three separate logistics support organisations, the Naval Support Command, the Quartermaster General and RAF Logistics Command together with elements of the Assistant Chief of the Defence Staff all under the Chief of Defence Logistics, currently General Sir Sam Cowens.

Now I could bore you all with considerable detail on the Defence Logistics Organisation mission statement, vision, values and so on. You will be relieved to know that I have no intention of doing so. However, it would be remiss of me in the context of this topic not to describe their strategic goal which is to reduce output costs by 20% within 5 years whilst ensuring that the organisation continues to deliver, and where appropriate improve, outputs. This was necessary in order to create the financial headroom to modernise the equipment of the United Kingdom armed forces and to deliver such dramatic reductions in such a short time without crude cuts there was clearly a need to change the way we do business in order to make step changes in performance. It is this emphasis on driving down costs that is central to the strategy and is what I will major on for the remainder of this address.

So what steps have we taken and how are we achieving a change in which we do business. One of the first steps, and arguably one of the most influential was the formation of Integrated Project Teams. I reside in the Warship Support Agency that is an organisation that is responsible for almost every aspect of Fleet support, including material support. It covers everything from running the Naval bases to direct support to the front line. The bringing together of all the elements of warship support is fundamental to achieving the efficiencies being sought by the defence logistics organisation.

The IPTs are at the very core of the Warship Support organisation being directly responsible for the day-to-day support management of the platforms and equipments, in my case propulsion equipment, and are directly accountable to the Chief Executive. As an IPT leader, I am thus empowered to conduct business with a team that has a full range of competencies – technical, commodity management, commercial and contracts and finance. We have been encouraged to challenge accepted practice and seek novel solutions to problems. Clearly, one must be careful to ensure that such solutions are not be at the expense of introducing larger corporate inefficiencies and this is monitored closely. And naturally, when changes introduce clear benefits, IPTs are encouraged to share these new practices with other IPTs.

So what has all this got to do with gas turbines? By way of an example, if one goes back to the organisation as it existed before the Defence Review, one could observe two quite separate organisations responsible for on the one hand technical support, development and post design services and on the other an organisation responsible for the supply of spares and consumables and the repair of equipment returned from the front line. Both groups had separate line management chains and they were housed at geographically separated locations. Now, of course there was communication between the two but there is an enormous difference between this structure and one where both

groups are fully collocated and working within the same management group. Not only were communications improved almost beyond recognition but also the much greater understanding of one group by another led to immediate and direct efficiencies and allowed reassessment of working practices and procedures to be conducted much more effectively.

We saw recognition by those responsible for post design work of poor subcomponent reliability that had been masked by routine and regular provision of stores. In house technical expertise was injected into equipment overhaul lines for the first time and we saw logisticians getting early advice on equipment changes which prevented wasted provisioning of obsolete spares. Whilst individually trivial, in total, an organisational shift which reaped and continues to reap substantial benefits and efficiencies.

Another initiative that we have pursued in our aim to drive down the cost of ownership of gas turbines is to study the overhaul of repairable stock or rotables. A team of specialist headquarters staff, together with IPT members – both logisticians and technical, together with storage and transport organisations and industry looked at the total repair loop process. Studies undertaken in the IPT to date in one equipment area have identified significant benefits by improvements in the return and storage system, forecasting and contractor turn round times. In this case, in consultation with the contactor, and at no additional cost to MoD we have reduced average overhaul turn round times by as much as 85%. Of course these sorts of figures will not always be possible but it illustrates that the potential is there. In cost terms one might expect to reduce the overall cost of support in this area by the order of 20%.

Another major initiative was to drive down the volume and value of our stock holdings. Because we have moved away from the management of finances in cash terms alone and moved to Resource Accounting, costs that were never seriously considered before become significant. Interest on capital and the cost of maintenance of capital assets emphasised the need to drive down stock whilst not significantly increasing risk to the front line or the overhaul process. Experience has shown that these reductions can be very significant and I expect reductions of 30 % or more. In the case of the Marine Propulsion IPT these figures are by no means trivial.

The last area that I should like to cover which has made good progress since the formation of Integrated Project Teams is the changing relationship with industry. There is little doubt that we have seen a number of major changes, individually not particularly revolutionary in themselves, but in the climate of change that we now inhabit transform our business relationship. The cornerstone of achieving best value for money in the Ministry of Defence remains competition. But having been through a competition in the equipment area we are seeing a number of changes including much longer term contracts incentivised to deliver continuous improvement through the life of the contract; movement towards prime contracts and, in our case, more comprehensive support arrangements with power by the hour close to reality in some areas of the business. Partnering arrangements have also been pursued trying to change the culture and relationship, developing an environment of openness and trust.

Other areas where significant improvements have been evident are performance monitoring, customer focused business agreements removal of duplication and exchange of information to learn from other areas good practice. Time today does not permit more detail in these areas.

Finally I would just like to say a few words regarding the future of gas turbines in the Royal Navy. One of the trends in recent years in the United Kingdom has been to move towards a prime-contacting environment for the procurement of new equipments.   We were concerned that in the marine engineering field such an environment risked development stagnation. There were essentially three reasons for this; the timescales for significant development of new technology were incompatible with platform programmes and the pace of industry led marine engineering development was deemed likely to be too slow; significant departures from known technology represented a degree of risk that future prime contractors were unlikely to be prepared to carry and, unlike most weapons fits, it is very difficult if not impossible to make fundamental changes in the propulsion equipment through the life of the platform such that incremental change is generally not possible. Because of this a marine engineering strategy paper was produced which discussed the best approach to improved propulsion system s for the Royal Navy's future warships due to enter service in the early part of this century. In order to break out of development stagnation it was recommended that some development work was sensible in order to de risk new technologies to the point where a prime contractor would be prepared to take responsibility without an unacceptable risk premium. The paper confirmed that to reduce manpower and running costs Integrated Full Electric Propulsion should be adopted, as should complex cycle gas turbine alternators as an alternative to diesel power generators. The paper was endorsed at board level and confirmed an earlier MoD decision to establish an Electric Ship Programme. Studies indicated that the optimum fit was for three classes of prime mover equipment including high power (21MW), medium power (6-8MW) and anchor load units (1-2MW). Whilst the principle focus was on complex cycle gas turbines, it did not rule out other prime mover options. We are currently looking at a candidate, which meets the requirements of the lowest power option. However, a strong candidate for the high power option was always going to be WR21 Intercooled Recuperated gas turbine the design and development of which began at the behest of the United States Navy on a joint US/UK basis in 1991 with Northrop Grumman as prime contractor and Rolls Royce supplying the RB211 based gas generator and power turbine. This engine is currently undergoing production testing and will first see service in the United Kingdom Type 45 destroyer later this decade. Whether it will see service in the United States in the foreseeable future remains to be seen.

I hope that I have gone some way to setting the scene that we in the United Kingdom marine gas turbine business find ourselves in. The considerable emphasis on cost reduction and continuous improvement is entirely in keeping with the environment that we are faced with.

I for one look forward to an interesting and stimulating seminar and I trust that you will all find the next three days rewarding.

Ladies and gentlemen, thank you for your patience.

This page has been deliberately left blank

_____

Page intentionnellement blanche

Extending Aircraft Engine Lives

Otha B. Davenport
ASC/LP
2145 Monahan Way
Bldg. 28
Wright Patterson AFB, Oh
45433-7017
USA

Ladies and Gentlemen,

It gives me great pleasure to appear before you today. I am honored to be the keynote speaker and the topic of extended engine life is extremely important to many of our military and civilian aircraft today. I have been fortunate to have a career where I have found myself working both beginning of new high technology developments of aircraft and aircraft engines to the older or even ancient "Keep them Flying" type programs. The advanced technology development programs always seem to be endowed with plenty of money and the charisma of new technology while the aging programs continually struggle to obtain the necessary support to insert new life in to systems to provide safe and reliable operations.

When I was a young man, I didn't think much about aging. Now that I am older, wiser and much more mature, I have decided that I would like to set some life goals. One of my goals is to live a viable life to the age of 100 which is an age many people are living today due to new medical technology and improved lifestyles from a century ago. My other goal is to score my age or better in golf. Now, when I was thirty, shooting my age in golf seemed an impossibility, and I still haven't seen any of the young pros like Tiger Woods shooting a round of golf where they score anything better than twice their age. However, if I reach 80, I will have a better chance of scoring my age than I do today. As you can see, these two goals are compatible – golf scores of 80 or better when I am 80, providing even more margin as I get closer to a hundred.

Our aging Gas turbine engines also have two goals – one is to achieve a service life greater than the design service life and the other is to reliably and safely perform the mission. Let's consider some o f the aspects of extending

engine life that must be considered to maintain and upgrade our engine fleets to provide capable systems for longer times.

A Plan – The first item of business is to accomplish our planning to provide for the aging engine upgrades, maintenance and fixes. We have developed plans called " Engine Life Management Plan" for all of our fielded engines. The plan incorporates information relative to the engine design, the fielded usage, the technical criteria to keep the engines operational, and planned fixes and upgrades. The plan is updated on approximately a two-year cycle. The plan provides us with the information necessary to manage the program. It does not prevent surprises and believe me we get our share of surprises, but the plan helps provide the guidance and control for the program. The gas turbine plan is much like the human life plan where we spend a big portion of health care expenditures during the infant period and an even bigger expenditure, as we grow older. As an infant, there are many health costs associated with the birth of a new baby --- hospital, doctor, nurse, shots, and early infant disease. As we mature and age the health care systems take a small, but consistent share of our earnings; however, as we become senior citizens we expend a great amount of the health care monies for a few more good years. I checked some information and the Federal Interagency Forum on Aging Statistics, which indicated that an 85-year-old would have health care expenditures 2.8 times more than a 65-Year-old person would. Gas turbine engines are similar; the cost to bring a new engine into the system is high at the beginning and aging engines are like aging people. How many of you have budgeted for maintenance cost increases of approximately 300% for engines in the last 20 percent of their life? If we want gas turbines to work effectively, we need to be prepared to expend the necessary monies for parts, assemblies, and upgrades to provide safe and reliable operation.

I would like to talk about some of my favorite items for a development engine and how we must reshape your thinking for a fielded engine. We look at engine development as having several key areas, which include the performance, operability, and structural life aspects of the engine. We drive our technologists to provide the maximum performance possible in order to give the warfighter the greatest advantage in operations and tactics. There truly is no second place in combat. Once the warfighter receives their system and discovers the best way to use the system, we must maintain the engines to provide the expected capabilities.

Fielded engine performance and thrust must be maintained. We might think that we could increase engine life at the expense of performance and that a

slight decrease in turbine temperature may provide longer life engines. We must discard this idea as it is important to maintain the engine performance for our warfighters because the way you train is the way you fight! By the same token, the operability considerations give unrestricted throttle movements, stall free operation at high levels of air distortion, and starting of the engine must be maintained throughout the life of the program. This is a key consideration for older engines since the key control components may no longer be manufactured and technology may have evolved to higher levels permitting advanced retrofitable digital controls, but not the capability to maintain current systems. Finally, we come to the structural life of the engine, the item that really limits how long we can keep a fielded engine operating. Our engine designs are normally developed to a fixed scenario – a set of missions to include training, normal operation, and combat. When the operators obtain a weapon system, a new set of operational missions are developed based on tactics, capabilities, and needs. They may use engine structural life at a greater rate than originally anticipated for the program, thus necessitating the need for many new parts, component improvement programs, and repair techniques. This is the issue for engine life and durability in fielded engines. A successful weapon system may have a planned fielded life that is extended and then extended again. We have systems in the USAF that have had long lives, yet have plans which keep them in our inventory for another 10 to 20 even forty years. One system will at retirement, have covered over 60% of the total time for powered flight. These programs require safe and reliable operation for the planned system life expectancy. How do we do this!!! Let me provide you some thoughts in this area.

Sometimes it is necessary to redesign an engine or series of components and sometimes is only necessary to review the processes involved in the maintenance scenario. We are in the process of revitalizing Reliability Centered Maintenance (RCM) in our engines. We started out several years ago looking at the reliability of the engine for the C-5 airlift aircraft.   After an in depth review of the maintenance processes, we came to the conclusion that we had to modify our fix-fly-fail-fix maintenance and pay more attention to the maintenance program. We examined a lot of data and discovered that each of our heavy maintenance overhauls produced engines with Time On Wing lives significantly lower than our expectations. We talked to our commercial counterparts, examined our data in detail, reviewed the engine build criteria, and tried a pilot test on our aircraft at Luke and Cannon AFB. The results soon became convincing and we are now implementing Reliability Centered Maintenance for all of our engines

throughout the world. Here are some of our findings. We have increased our engine time on wing by two or three fold for some of our front line fighter aircraft and as a result we are avoiding costly unscheduled engine shop visits. Our flight line, intermediate level, and depot level personnel have all become familiar with the results and through our training program have become advocates of RCM. The improvements have come about as a result of realizing that our maintenance processes and practices directly impact our operations. RCM has become a great success story.

Build Standards and Workscope Planning are important keys to the Reliability Centered Maintenance improvements we have seen. In some cases, an engine coming in for overhaul may include modules with real useful life, but not for the engine that is to be rebuilt to the build standards. In this case a module with some life may be shuttled to another engine in order to align module time for the engine. We may then put an engine back into the field with a limited life as well as one with nearly full life, thus maximizing our utilization while minimizing our overall costs.   In every case like this, a working group of engineers, maintainers, and logisticians is needed. They must be fully cognizant of the engine type being overhauled as well as the individual engine serial numbers.

We must monitor and trend our engine usage during operational service. We need to know how the fielded engines are being utilized in order to adequately perform service inspections, maintenance and overhaul. The usage monitoring area is one where I believe technology may have a great impact in the next few years. Computer and information technology schemes will enhance the manner in which we gather, maintain and analyze data. The prognostics aspects of inspections can be greatly enhanced by new equipment in the hands of our trained mechanics. This is an area we need to exploit in order to extend the lives of our fielded aircraft engines.

New technologies are extremely difficult to introduce into fielded engine systems due to the up front design development, and kit costs that must be absorbed by the system. However, many technologies will have a profound impact on the engine operation and life that will return the initial investment many times. These technologies need to be thoroughly understood prior to commitment. Examples include the revision of an engine control system to utilize digital control technologies or a new blade or disk embodying advanced material manufacturing, or design technologies.

Many times we find ourselves in a quandary as a result of fielded engine failures. Failure analysis techniques have to be continually updated and improved to provide the best capabilities to assure we have properly diagnosed the problems and provided the proper solution for the fielded engine community. An example is the trend towards more HCF failures in newer engines and analytical tools to understand these problems.

When you look at an engine you can see that it is made up of many parts and assemblies; some are large and some are small and some are more critical than others. Small parts may cause large problems. Many times we have concentrated on the critical large parts in an engine to provide extended life and small parts begin to fail in a manner that caused larger failure modes. One of the things we do not want to overlook are the small critical parts that individually or collectively may result in catastrophic failure. These parts may also be made of alloys that are not always available and create unwarranted schedule delays if we do not understand their nature. I personally have had a bolt or two that I would have liked to seen redesigned from the beginning.

Material developments may be key to enhancing the life of fielded engines. When we find we have some materials in an engine that limit the life and a problem develops, we start looking for material alternates or newly developed materials. These materials may provide relief to a short-term issue or may provide parts than enhance the fielded engine life. An increase in the Turbine Inlet Temperature of 50 degrees may cut the life of a turbine blade in half.

Repair capabilities for blades, disks, seals, and key engine components such as fuel controls may either enhance our overhaul capabilities or grind thing to a halt. We are continually looking for better materials and repair techniques to keep our fielded engine fleet operating at minimal costs. In one instance we have our research laboratories working on the repair of a new technology combustor and at the same time supporting the Air Logistics Centers in the repair of fielded engine combustors. We work hard to bring the technology producers together with the technology consumers.

Commercial airline engines also have aging engines and the desire to have an engine stay on wing for a longer time prior to overhaul. Recently (Jan 01) the US FAA issued an Advisory Circular with new criteria for engine rotating parts. The AC describes the acceptable means for showing compliance applicable to the design and life management of high energy

rotating parts of aircraft gas turbine engines. The AC includes both a life management plan and damage tolerance analysis for rotating parts.

Lastly, I would like to say a few words about High Cycle Fatigue and engine durability. The engine life cycle has many challenges. We have had operability problems with inlet distortion in the 60s and 70s that we have learned to deal with. We had engine structural integrity problems we had to deal with in the 70s and 80s and we have been dealing with High Cycle Fatigue issues throughout the 1990s. We have expended large sums of money to understand the High Cycle Fatigue problems that have impacted some of our front line engines and have developed new analytical tools to understand the phenomena and put in place new design mechanisms for new parts and engines. We feel that we now somewhat understand the HCF issues and need to move on to extending the life of our engines with improved durability initiatives. We must consider durability early in our research and development programs; and build engines that will last for the long expected field service usage lives. I believe the durability issues of the early years of the 21st century will enable us to continue to extend the lives of current operational engines and provide improved engines for the modern air warfighter.

The challenge we have today is to keep the aircraft flying with reliable, safe, high performance engines.

Thank You, If you have any questions I will be pleased to provide a response.

Computational Aeroacoustics: An Overview

Christopher K.W. Tam
Department of Mathematics, Florida State University
Tallahassee, FL 32306–4510, USA

Abstract

An overview of recent advances in computational aeroacoustics (CAA) is presented. CAA algorithms must not be dispersive and dissipative. It should propagate waves supported by the Euler equations with the correct group velocities. Computation domains are inevitably finite in size. To avoid the reflection of acoustic and other outgoing waves at the boundaries of the computation domain, it is required that special boundary conditions be imposed at the boundary region. These boundary conditions either absorb all the outgoing waves without reflection or allow the waves to exit smoothly. High-order schemes, invariably, supports spurious short waves. These spurious waves tend to pollute the numerical solution. They must be selectively damped or filtered out. All these issues and relevant computation methods are briefly reviewed. Jet screech tones are known to have caused structural fatigue in military combat aircrafts. Numerical simulation of the jet screech phenomenon is presented as an example of a successful application of CAA.

1. Introduction

Aeroacoustic problems are by nature very different from standard aerodynamics and fluid mechanics problems. Before discussing how to solve aeroacoustics problems numerically or simulate them computationally, an approach generally referred to as Computational Aeroacoustics (CAA), it is important to recognize and to have a good understanding of these differences. These differences pose a number of major challenges to CAA. A few of the important computational challenges are listed below.

a. Aeroacoustics problems, by definition, are time dependent, whereas aerodynamics and fluid mechanics problems are generally time independent or involve only low frequency unsteadiness.

b. Aeroacoustics problems typically involve frequency range that spreads over a wide bandwidth. Numerical resolution of the high frequency waves becomes a formidable obstacle to accurate numerical simulation.

c. Acoustic waves usually have small amplitudes. They are very small compared to the mean flow. Oftentimes, the sound intensity is five to six orders smaller. To compute sound waves accurately, a numerical scheme must have extremely low numerical noise.

d. In most aeroacoustics problems, interest is in the sound waves radiating to the far field. This requires a solution that is uniformly valid from the source region all the way to the measurement point at many acoustic wavelengths away. Because of the long propagation distance, computational aeroacoustics schemes must have minimal numerical dispersion and dissipation. Also, it should propagate the waves at the correct wave speeds and is isotropic irrespective of the orientation of the computation mesh.

e. In general, flow disturbances in aerodynamics or fluid mechanics problems tend to decay exponentially fast away from a body or their source of generation. Acoustic waves, on the other hand, decay very slowly and actually reach the boundaries of a finite computation domain. To avoid the reflection of outgoing sound waves back into the computation domain, radiation boundary conditions must be imposed at the artificial exterior boundaries to assist the waves to exit smoothly. For standard computation fluid dynamics (CFD) problems, such boundary conditions are usually not required.

f. Aeroacoustics problems are archtypical examples of multiple-scales problems. The length scale of the acoustic source is usually very different from the acoustic wave length. That is, the length scale of the source region and that of the acoustic far field region can be vastly different. Computational aeroacoustic methods must be designed to deal with problems with greatly different length scales in different parts of the computational domain,

It must be acknowledged that CFD has been very successful in solving fluid and aerodynamics problems. CFD methods are generally designed for computing time independent solutions. Because of the tremendous success of CFD, it is tempting to use these methods to solve aeroacoustics problems as well. In the past, there have been a number of attempts to do just that. However, the results have proven to be quite discouraging. For example, Hsi and Perie tried to use a commercial CFD code "RADIOSS" to solve sound scattering problems. Their effort was published in the proceedings of the Second CAA Workshop on Benchmark Problems (NASA CP3352, June 1997, edited by C.K.W. Tam and J.C. Hardin). The results were disastrous. The computed results were highly dispersive and differed significantly from the exact solutions.

As elaborated above, it should be clear that the nature of aeroacoustics problems are substantially different from those of traditional fluid dynamics and aerodynamics problems. To be able to compute or simulate aeroacoustics problems accurately and efficiently, standard CFD schemes, designed for applications to fluid problems, are generally not adequate. For this reason, there is a need for an independent development of CAA. This was what happened in the last ten years. During this period, great advances have been made both in the development of CAA methodology and in their applications to real world problems.

To simulate an aeroacoustic phenomenon or problem numerically, the computation algorithm must consist of three basic elements. They are:

(i) A time marching computation scheme.

(ii) An artificial selective damping algorithm or filtering procedure.

(iii) A set of radiation/outflow numerical treatments for use at the boundaries of the computation domain.

A good quality time marching scheme is basic to any computation effort. Artificial selective damping or a filtering procedure is essential to eliminating spurious numerical waves that could contaminate the computed solution. Also such damping terms can often help to suppress numerical instabilities at the boundaries of the computation domain or at surfaces of discontinuities such as mesh-size-change interfaces. Numerical boundary treatments serve two basic purposes. First, they are to allow outgoing waves to leave the computation domain with little reflection. Second, they are to reproduce all the effects of the outside world on the computation domain. For instance, if there is incoming acoustic and vorticity wave or there is an inflow, they are to be generated by the numerical boundary conditions.

2. Spatial Discretization in Wavenumber Space

In this section, we consider how to form finite difference approximations to the partial derivatives of spatial coordinates. The standard approach of truncated Taylor series assumes that the mesh size goes to zero; i.e., $\Delta x \rightarrow 0$, in formulating finite difference approximation. In real applications, Δx is never equal to zero. Therefore, we will investigate how well we can approximate $\partial/\partial x$ by a finite difference quotient with a finite Δx. The treatment below follows the work of Tam and Webb[1] and Tam[2]

Suppose we use a $(2N+1)$ point stencil to approximate $\partial/\partial x$; i.e.,

$$\left(\frac{\partial f}{\partial x}\right)_{\ell} \cong \frac{1}{\Delta x}\sum_{j=-N}^{N}a_j f_{\ell+j}. \tag{2.1}$$

At our disposal are the coefficients a_j; $j=-N$ to N. We will now choose these coefficients such that the Fourier Transform of the right side of (2.1) is a good approximation of that of the left side, for arbitrary function f. Fourier Transform is defined only for functions of a continuous variable. Let's first generalize

(2.1) to all points along the *x*-axis. The generalized form of (2.1), applicable to any set of points at Δx apart, is

$$\left(\frac{\partial f}{\partial x}\right)(x) \cong \frac{1}{\Delta x}\sum_{-N}^{N}a_j f(x+j\Delta x). \tag{2.2}$$

(2.1) is a special case of (2.2). By setting $x = \ell\,\Delta x$ in (2.2), (2.1) is recovered.

The Fourier Transform of a function $F(x)$ and its inverse are related by

$$\tilde{F}(\alpha) = \frac{1}{2\pi}\int_{-\infty}^{\infty}F(x)e^{-i\alpha x}dx, \quad F(x) = \int_{-\infty}^{\infty}\tilde{F}(\alpha)e^{i\alpha x}d\alpha. \tag{2.3}$$

Now by applying Fourier Transform to (2.2) and making use of the Derivative and Shifting Theorems, it is found

$$i\alpha\tilde{f} \cong \frac{1}{\Delta x}\left[\sum_{j=-N}^{N}a_j e^{ij\alpha\Delta x}\right]\tilde{f} = i\overline{\alpha}\tilde{f} \tag{2.4}$$

where

$$\overline{\alpha} = \frac{-i}{\Delta x}\sum_{j=-N}^{N}a_j e^{ij\alpha\Delta x}. \tag{2.5}$$

Clearly, $\overline{\alpha}$ is the effective wave number of the finite difference scheme. $\overline{\alpha}\,\Delta x$ is a periodic function of $\alpha\Delta x$ with a period of 2π. To assure that the Fourier transform of the finite difference scheme is a good approximation of that of the partial derivative over the band of wavenumber $\eta \le \alpha\Delta x \le \eta$, it is required that a_j be chosen to minimize the integrated error, E, over this wavenumber range, where,

$$E = \int_{-\eta}^{\eta}\left|\alpha\Delta x - \overline{\alpha}\Delta x\right|^2 d(\alpha\Delta x). \tag{2.6}$$

For $\overline{\alpha}$ to be real, the coefficients a_j must be antisymmetric; i.e.,

$$a_0 = 0, \qquad a_{-j} = -a_j \tag{2.7}$$

The conditions for E to be a minimum are,

$$\frac{\partial E}{\partial a_j} = 0, \qquad j = 1,2,\ldots,N. \tag{2.8}$$

(2.8) provides N equations for the N coefficients a_j, $j=1,2,\ldots,N$.

For a 7-point stencil ($N=3$) there are three coefficients. It is possible to require (2.2) to be accurate to $O(\Delta x^4)$ by Taylor series expansion. This leaves one free parameter for optimization. By setting $\eta=1.1$, it is easy to find,

$$a_0 = 0.0, \qquad\qquad a_1 = -a_{-1} = 0.77088238051822552,$$

$$a_2 = -a_{-2} = -0.166705904414580469, \quad a_3 = -a_3 = 0.02084314277031176.$$

The choice of $\eta=1.1$ turns out to provide an overall best group velocity approximation[2].

The relationship between $\overline{\alpha}\,\Delta x$ and $\alpha\Delta x$ over the interval 0 to π for the optimized 7-point stencil is shown graphically in Figure 1. For $\alpha\Delta x$ up to about 1.2, the curve is nearly the same as the straight line $\overline{\alpha}\,\Delta x = \alpha\Delta x$. Thus, the finite difference scheme can provide reasonable approximation to $\alpha\Delta x<1.2$ or $\lambda>5.2\Delta x$ where λ is the wavelength. For $\alpha\Delta x$ greater than 2, the $\overline{\alpha}(\alpha)$ curve deviates increasingly from the straight-line relationship. Thus, the wave propagation characteristics of the short waves of the finite difference scheme are very different from those of the partial differential equations. Figure 1 also shows the $\overline{\alpha}\,\Delta x$ versus $\alpha\Delta x$ relations for the standard 6th-order, 4th-order and 2nd-order central difference schemes. Their resolved bandwidth is narrower. In other words, more mesh points per wavelength is needed for propagating a wave accurately.
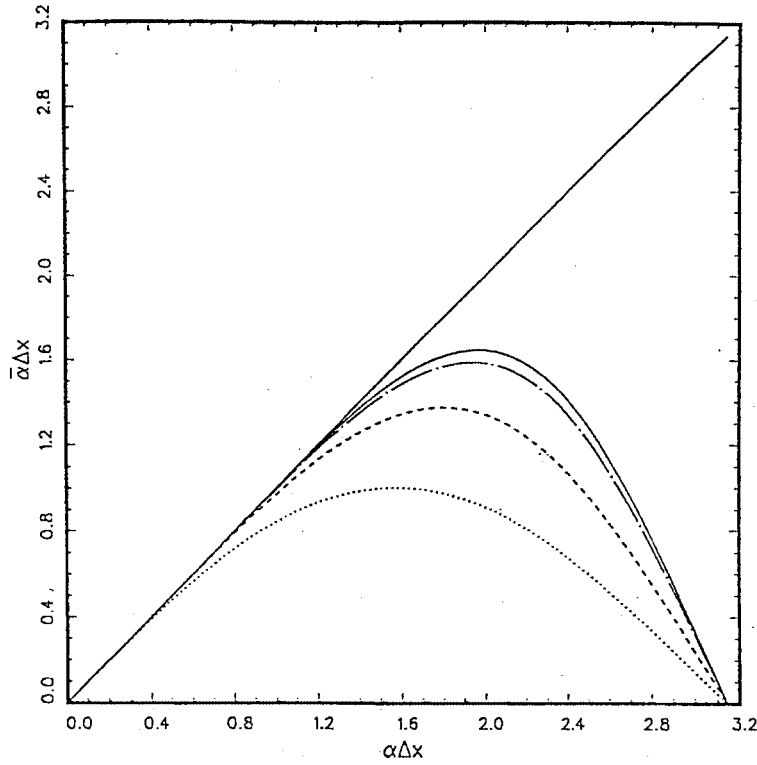
Figure 1. $\bar{a}\,\Delta x$ versus $\alpha\Delta x$. ————— optimized 4th-order scheme, —·—·—· standard 6th-order scheme, — — — — — standard 4th-order scheme. ·········· standard 2nd-order scheme.

Example. Let us consider the initial value problem of the one-dimensional convective wave equation. We will use dimensionless variables with Δx as the length scale, $\Delta x/c$ ($c=$ sound speed) as the time scale. The mathematical problem is:

$$\frac{\partial u}{\partial t} + \frac{\partial u}{\partial x} = 0, \qquad -\infty < x < \infty \tag{2.9}$$

$$t = 0, \qquad .\ u = f(x) \tag{2.10}$$

The exact solution is

$$u = f(x - t).$$

In other words, the solution consists of the initial disturbance propagating to the right at a dimensionless speed of 1, without any distortion of the waveform. Let us consider the initial disturbance in the form of a Gaussian function,

$$f(x) = 0.5\ \exp\left[-\ell n2\left(\frac{x}{3}\right)^2\right]. \tag{2.11}$$

On using a $(2N+1)$-point stencil finite difference approximation to $\partial/\partial x$ of (2.9), the original initial value problem is converted to the following system of ordinary differential equations

$$\frac{du_\ell}{dt} + \sum_{j=-N}^{N} a_j u_{\ell+j} = 0, \qquad \ell = \text{integer} \tag{2.12}$$

$$t = 0, \qquad u_\ell = f(\ell). \tag{2.13}$$

For the Gaussian pulse, the initial condition is,

$$t = 0, \qquad u_\ell = 0.5\ \exp\left[-\ell n2\left(\frac{\ell}{3}\right)^2\right]. \tag{2.14}$$

The system of ordinary differential equations (2.12) and initial condition (2.14) can be integrated in time numerically using the Runge-Kutta or a multi-step method. The solution using the standard 2nd-order (N=1), 4th-order (N=2), 6th-order (N=3) and the optimized 7-point scheme (N=3, η=1.1) at t=400 are shown in Figure 2. The exact solution in the form of a Gaussian pulse is shown as the dotted curves. The second-order solution is in the form of a wave train. There is no resemblance to the exact solution. The numerical solution is totally dispersed. The 4th-order solution is better. The 6th-order scheme is even better. But there are still some dispersed waves trailing behind the main pulse. The optimized scheme gives a very acceptable numerical result.
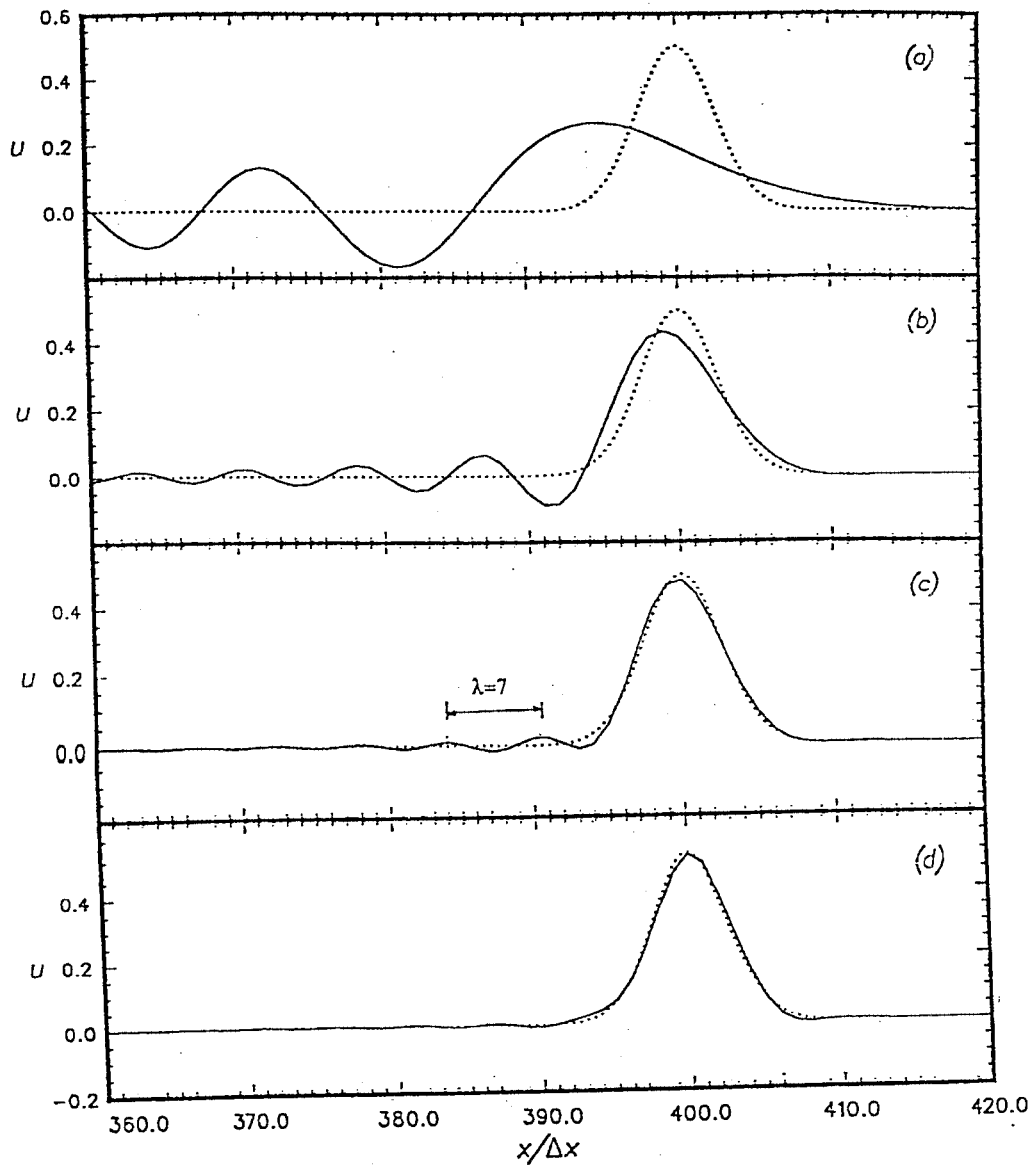

Figure 2. comparison between computed and exact solutions of the simple one-dimensional wave equation. (a) 2nd-order central difference scheme. (b) 4th-order central difference scheme. (c) 6th-order central difference scheme. (d) DRP scheme (7-point stencil).
——————numerical solution; $\cdots\cdots\cdots$ exact solution.

3. Time Discretization

There are two types of explicit time-marching schemes. They are:

(1) Single-step scheme; e.g., Runge-Kutta method.

(2) Multi-step scheme; e.g., Adams-Bashford method.

Both types of methods are discussed in standard textbooks. Here we will only discuss the optimized multi-step method. One important advantage of multi-step method is that it can be used in a multi-size-mesh multi-time-step algorithm[2]. Such an algorithm is very efficient and nearly optimal in computation time.

Suppose $\mathbf{u}(t)$ is the unknown vector. The time axis is divided into a uniform grid with time step Δt. We will assume that the values of $\mathbf{u}$ and $d\mathbf{u}/dt$ are known at time level $n, n–1, n–2, n–3$. (Note: In CAA, $d\mathbf{u}/dt$ is given by the governing equations of motion.) To advance to the next time level, Tam and Webb[1] use the following 4-level finite difference approximation

$$\mathbf{u}^{(n+1)} = \mathbf{u}^{(n)} + \Delta t \sum_{j=0}^{3} b_j \left(\frac{\partial \mathbf{u}}{\partial t} \right)^{(n-j)}. \tag{3.1}$$

The last term on the right side of (3.1) may be regarded as a weighted average of the time derivatives at the last 4 mesh points. There are four constants, namely, b_0, b_1, b_2 and b_3. They can be determined by optimization through the use of Laplace transform. Tam and Webb suggested the following numerical values.

$$\begin{aligned} b_0 &= 2.3025580888, \quad b_1 = -2.4910075998, \\ b_2 &= 1.5743409332, \quad b_3 = -0.3858914222. \end{aligned} \tag{3.2}$$

4. Radiation and Outflow Boundary Conditions

Many interesting acoustic problems are exterior problems. To simulate this class of problems it is necessary to impose radiation and outflow boundary conditions at the boundaries of the finite computation domain. To ensure that the computed solutions are of high quality these boundary conditions must be sufficiently transparent to the outgoing disturbances so that they exit the computation domain without significant reflections. As is well known, the linearized Euler equations can support three types of waves. Thus, in general, the outgoing disturbances would contain a combination of acoustic, entropy and vorticity waves each having a distinct wave propagation characteristic. Here a set of radiation and outflow boundary conditions compatible with the optimized high-order scheme is developed starting with the asymptotic solution. A review on numerical boundary condition can be found in Ref. [4].

Consider the exterior problem involving a uniform flow of velocity u_0 in the x-direction and sound speed a_0 past some arbitrary acoustic, vorticity and entropy sources as shown in Figure 3. It will be assumed that the boundaries of the computation domain are quite far from the sources. At boundaries where there are only outgoing acoustic waves the solution is given by the following asymptotic solution,

$$\begin{bmatrix} \rho \\ u \\ v \\ p \end{bmatrix} \equiv \begin{bmatrix} \rho_a \\ u_a \\ v_a \\ p_a \end{bmatrix} = \frac{F\left(\dfrac{r}{V(\theta)} - t, \theta \right)}{r^{\frac{1}{2}}} \begin{bmatrix} \dfrac{1}{a_0^2} \\ \dfrac{\hat{u}(\theta)}{\rho_0 a_0} \\ \dfrac{\hat{v}(\theta)}{\rho_0 a_0} \\ 1 \end{bmatrix} + O\left(r^{\frac{-3}{2}} \right) \tag{4.1}$$

where $V(\theta)=a_0[M\cos\theta +(1-M^2\sin^2\theta)^{1/2}]$. The subscript 'a' in (ρ_a,u_a,v_a,p_a) above indicates that the disturbances are associated with the acoustic waves alone. By taking the time t and r derivatives of (4.1) it is straightforward to find that for arbitrary function F of the acoustic disturbances satisfy the following equations.

$$\left(\frac{1}{V(\theta)}\frac{\partial}{\partial t}+\frac{\partial}{\partial r}+\frac{1}{2r}\right)\begin{bmatrix}\rho\\u\\v\\p\end{bmatrix}=0+O\left(r^{\frac{-5}{2}}\right). \tag{4.2}$$

Equation (4.2) provides a set of radiation boundary conditions.
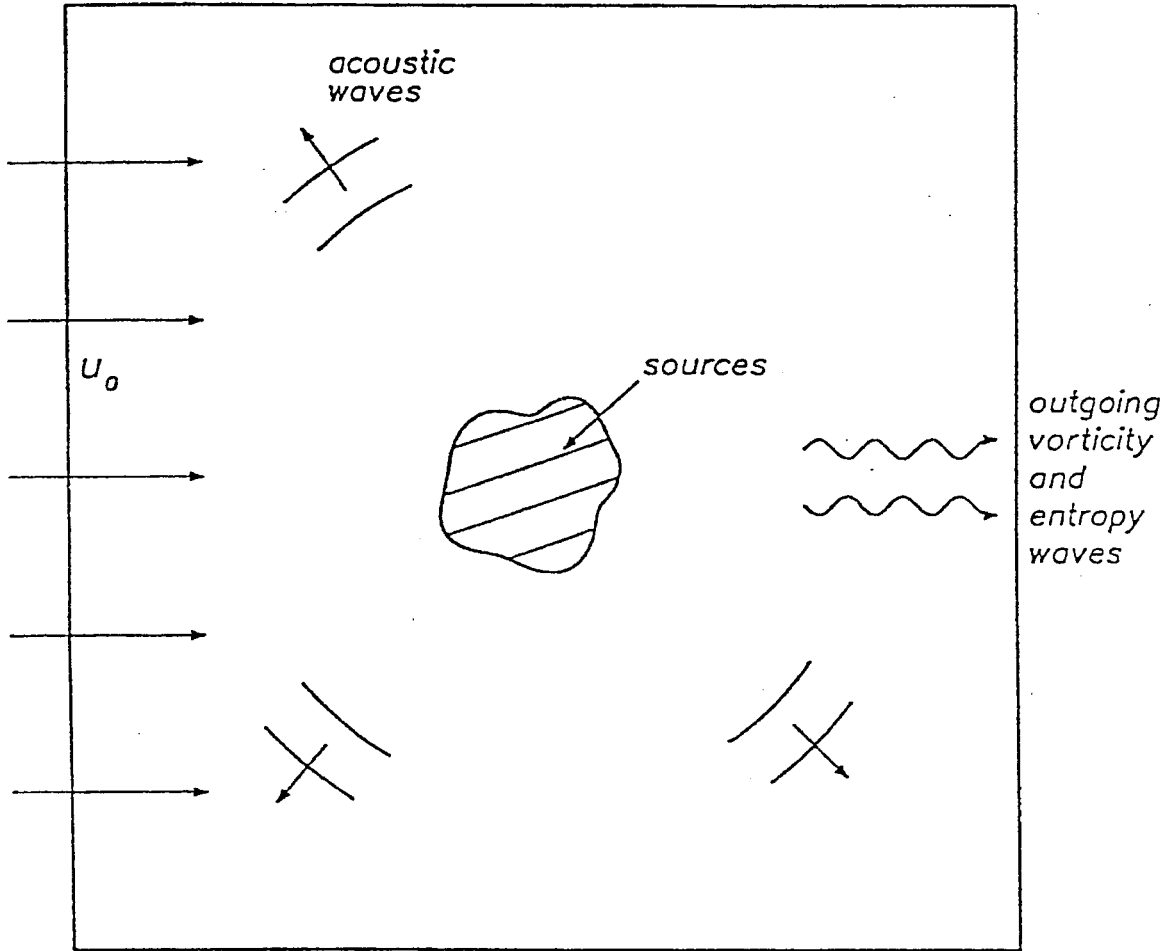
Figure 3. Acoustic, vorticity and entropy wave sources in a uniform flow.

At the outflow region, the outgoing disturbances, in general, consist of a combination of acoustic, entropy and vorticity waves. The asymptotic solutions for the density, velocity and pressure fluctuations are given by

$$\begin{bmatrix}\rho\\u\\v\\p\end{bmatrix}=\begin{bmatrix}\chi(x-u_0t,y)+\rho_a\\\dfrac{\partial\psi}{\partial y}(x-u_0t,y)+u_a\\-\dfrac{\partial\psi}{\partial x}(x-u_0t,y)+v_a\\p_a\end{bmatrix}+.... \tag{4.3}$$

where the explicit form of (ρ_a, u_a, v_a, p_a) may be found in (4.1). The functions χ, ψ and F are entirely arbitrary. These functions can be eliminated by combinations of derivatives. In this way, the following outflow boundary conditions can be derived.

$$\frac{\partial \rho}{\partial t} + u_0 \frac{\partial \rho}{\partial x} = \frac{1}{a_0^2}\left(\frac{\partial p}{\partial t} + u_0 \frac{\partial p}{\partial x} \right)$$

$$\frac{\partial u}{\partial t} + u_0 \frac{\partial u}{\partial x} = -\frac{1}{\rho_0} \frac{\partial p}{\partial x}$$

$$\frac{\partial v}{\partial t} + u_0 \frac{\partial v}{\partial x} = -\frac{1}{\rho_0} \frac{\partial p}{\partial y}$$

$$\frac{1}{V(\theta)} \frac{\partial p}{\partial t} + \cos\theta \frac{\partial p}{\partial x} + \sin\theta \frac{\partial p}{\partial y} + \frac{p}{2r} = 0$$

(4.4)

5. Artificial Selective Damping

Numerical waves of wavenumber α for which $\overline{\alpha}(\alpha)$ is not nearly equal to α (see figure 1) will not propagate with the correct wave speed. For waves on the right side of the maximum of the $\overline{\alpha}$ versus α curve of figure 1, the wave speed is negative (because $d\overline{\alpha}/d\alpha$ is negative) or opposite to the correct wave propagation direction. These are the spurious waves of the computation scheme[5]. They must be removed from the computation if a high quality numerical solution is desired. A way to do this is to apply artificial selective damping to the discretized equations. Suppose we add a damping term, $D(x)$, to the right side of the momentum equation of the linearized Euler equations in one dimension

$$\frac{\partial u}{\partial t} + \frac{1}{\rho_0} \frac{\partial p}{\partial x} = D(x).$$

(5.1)

Let us discretize the spatial derivative using the 7-point optimized stencil.

$$\frac{du_\ell}{dt} + \frac{1}{\rho_0 \Delta x} \sum_{j=-3}^{3} a_j p_{\ell+j} = -\frac{\nu}{(\Delta x)^2} \sum_{j=-3}^{3} d_j u_{\ell+j}.$$

(5.2)

In (5.2) it is assumed that D_ℓ is proportional to the values of u_ℓ within the stencil and d_j be the weight coefficients and ν is the artificial kinematic viscosity. $\nu/(\Delta x)^2$ has the dimension of $(\text{time})^{-1}$, so that d_j's are pure numbers. Now we wish to choose d_j's so that the artificial damping would be concentrated mainly on the high wavenumber or short waves.

The Fourier transform of the generalized continuous form of (5.2) is,

$$\frac{d\tilde{u}}{dt} + \ldots = -\frac{\nu}{(\Delta x)^2} \tilde{D}(\alpha \Delta x) \tilde{u}.$$

(5.3)

where

$$\tilde{D}(\alpha \Delta x) = \sum_{j=-3}^{3} d_j e^{ij\alpha \Delta x}.$$

(5.4)

On ignoring the terms not shown in (5.3), the solution is

$$\tilde{u} \sim e^{-\frac{\nu}{(\Delta x)^2} \tilde{D}(\alpha \Delta x)t}.$$

(5.5)

Since $\tilde{D}(\alpha \Delta x)$ depends on the wavenumber, the damping will vary with wavenumber. For our need, we like $\tilde{D}$ to be zero or small for small $\alpha \Delta x$ but large for large $\alpha \Delta x$. This can be done by choosing d_j

appropriately. Tam, Webb and Dong[5] suggested that $\tilde{D}$ should be a positive even function of $\alpha\Delta x$. They used a Gaussian function as a template to determine d_j's. Their analysis gives the following values.

$$d_0 = 0.3276986608$$

$$d_1 = d_{-1} = -0.235718815$$

$$d_2 = d_{-2} = 0.0861506696$$

$$d_3 = d_{-3} = -0.0142811847$$

A plot of $\tilde{D}$ versus $\alpha\Delta x$ for this choice is shown in Figure 4. Figure 4 indicates that the grid-to-grid oscillations with $\alpha\Delta x=\pi$ or wavelength equal to 2 mesh spacings is most heavily damped. On the other hand, $\alpha\Delta x=0$ and the low wavenumber waves are hardly damped at all. Experience has shown that the adoption of artificial selective damping in a computation scheme can effectively eliminate all spurious short waves in the numerical solution.
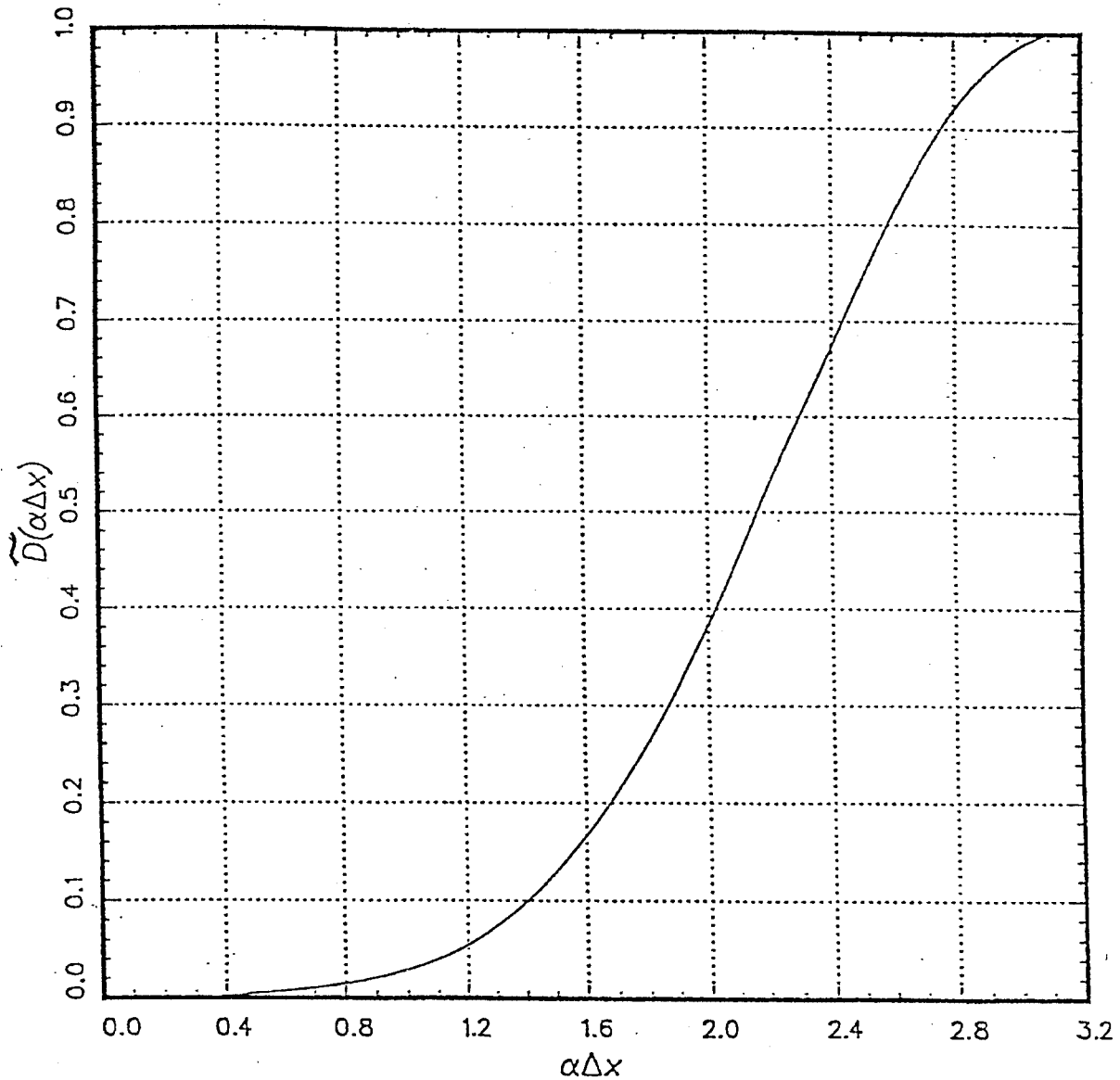

Figure 4. $\tilde{D}(\alpha\Delta x)$ versus $\alpha\Delta x$ (damping curve). $\sigma = 0.3\pi$, 7-point stencil.

6. Numerical Simulation of the Jet Screech Phenomenon

It had been reported[6–9] that structural fatigue damages sustained by the B1-A, B2-B and the F15 aircrafts were most likely the result of dynamic loading contributed by screech tones. The screech phenomenon is known to occur when a supersonic jet is imperfectly expanded. It is driven by a feedback loop. The tones are discrete frequency sound. They are generated by the interaction of downstream propagating instability waves of the jet flow and the shock cells inside the jet plume.

Experimentally, screech tones from choked jets are found to belong to four distinct modes. The A_1 and A_2 modes are axisymmetric modes with slightly different frequencies. The B and C modes are flapping modes. Their frequencies also differ only slightly. In the literature, there are semi-empirical formulas designed to predict the screech frequencies. However, these formulas are unable to predict individually the frequencies of the A_1 and A_2 modes nor the frequencies of the B and C modes. They give only a single approximate frequency for the axisymmetric modes and a single frequency for the flapping modes. The feedback loop of the screech tones is highly nonlinear. As a result, there is no tone intensity prediction formula available at the present time; not even a totally empirical one.

To provide numerical prediction of the screech frequencies and intensities as well as to better understand the physics of the problem, Shen and Tam[10–12] performed numerical simulations of the screech phenomenon. For marching the solution in time, they used the multi-size-mesh multi-time-step Dispersion-Relation-Preserving scheme. This is an improved and extended version of the optimized scheme discussed in Sections 2 and 3. Artificial selective damping was included both for the elimination of spurious short waves as well as for shock capturing purpose. In their work, a nonlinearized form of the outflow boundary conditions was used. Flow entrainment was also included in their radiation boundary condition. To simulate the effect of fine scale turbulence, the k–ε turbulence model was employed. Screech is driven by a self-excited feedback loop. Hence no external excitation is needed. In the computer simulation of Shen and Tam, the computation started from zero initial condition. In other words, the jet was turned on at time zero. After the transient disturbances had exited the computation domain, the computation locked itself onto a screech mode (sometime on two coexisting modes) automatically, exactly as in a physical experiment.

Shen and Tam[10–12] reported that their numerical simulation not only reproduced the screech frequencies of the four modes correctly but also the tone intensities were accurately given by the computed solution. Experimentally, it is observed that as the Mach number of the jet increases, at certain jet Mach numbers, there is an abrupt switch of the screech mode. This is referred to as the staging phenomenon. In the numerical simulations of Shen and Tam, the staging phenomenon was reproduced. In addition, they studied the effect of jet temperature and nozzle lip thickness on tone frequencies and intensities. Their computed results matched well with those measured experimentally[13]. Figures 5 and 6 show comparisons between the screech tone wavelengths and intensities measured from the numerical simulations of Shen and Tam[12] and the physical experiments of Ponton and Seiner[13]. As can be seen, the CAA simulations are in excellent agreement with experimental measurements over the entire range of Mach number investigated.

7. Conclusion

In this paper, computational challenges for the solution of aeroacoustics problems are discussed. To meet these challenges, specially designed high-order CAA computation schemes are developed. In addition to time marching schemes, impressive advances have also been made on numerical boundary treatment as well as on how to eliminate spurious numerical waves. As an example to illustrate the usefulness and effectiveness of these newly developed CAA methods, results of the numerical simulation of screech tones from under-expanded supersonic jets are briefly discussed. It appears that CAA has now emerged from just a novel computation method to become a powerful practical tool. CAA will undoubtedly have an enormous impact on the solution and investigation of practical aeroacoustics problems in the years to come.
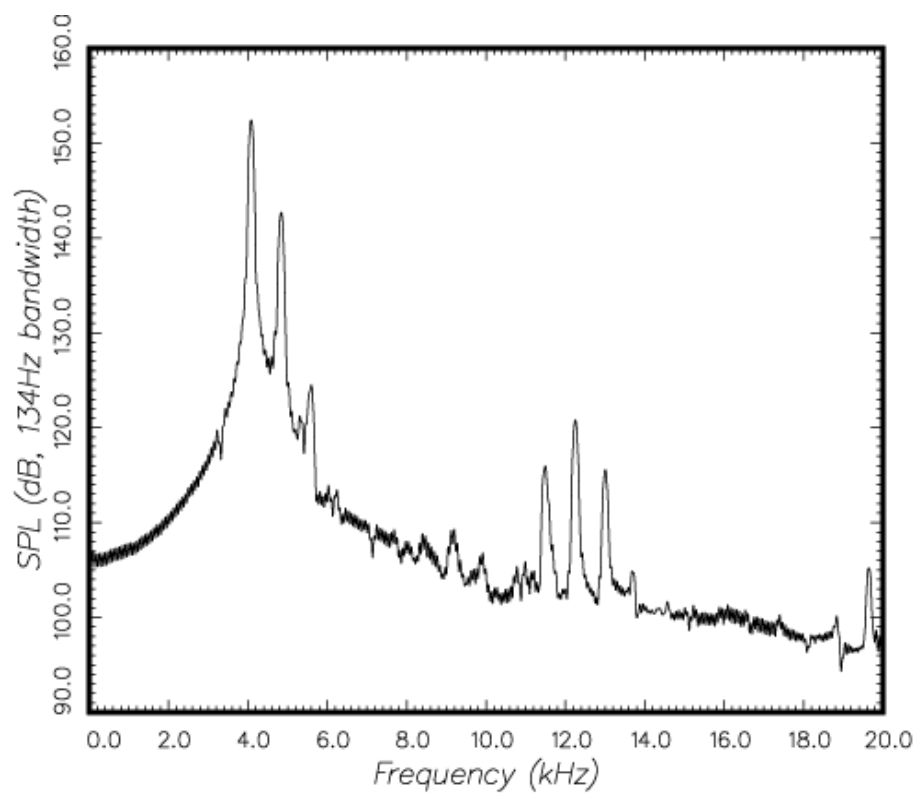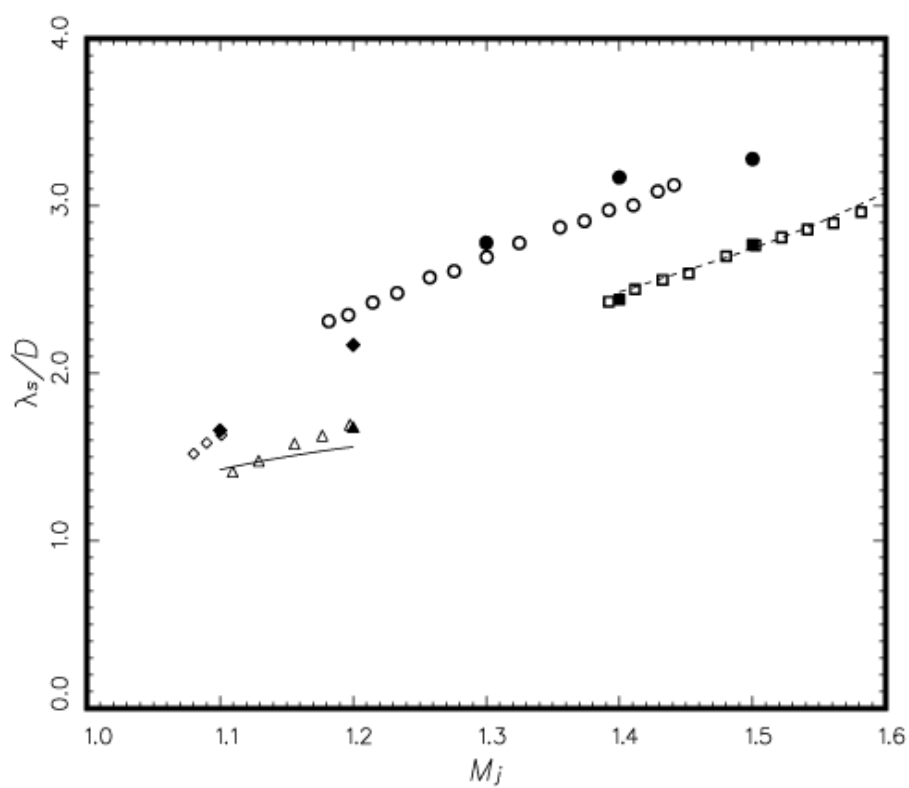
Figure 5.

Figure 6.

Acknowledgments

References

1. Tam, C.K.W. and Webb, J.C. Dispersion-Relation-Preserving finite difference schemes for computational acoustics. *Journal of Computational Physics*, **107**, 262–281, 1993.

2. Tam, C.K.W. Computational Aeroacoustics: Issues and Methods. *AIAA Journal*, **33**, 1788–1796, 1995.

3. Tam, C.K.W. and Kurbatskii, K.A. Multi-size-mesh multi-time-step Dispersion-Relation-Preserving scheme for multiple scales aeroacoustics problems, to appear in the *International Journal of Computational Fluid Dynamics*, 2002.

4. Tam, C.K.W. Advances in numerical boundary conditions for computational aeroacoustics. *Journal of Computational Acoustics*, **6**, 377–402, 1998.

5. Tam, C.K.W., Webb, J.C. and Dong, Z. A study of the short wave components in computational acoustics. *Journal Computational Acoustics*, **1**, 1–30, 1993.

6. Seiner, J.M., Manning, J.C. and Ponton, M.K. Dynamic pressure loads associated with twin supersonic plume resonance. AIAA Paper 85-0533, 1985.

7. Seiner, J.M., Manning, J.C. and Ponton, M.K. Model and full scale study of twin supersonic plume resonance. AIAA Paper 87-0244, 1987.

8. Shaw, L.L., Otto, C.J., Banaszak, D.L. and Plzak, G.A. F-15 8.33% model internozzle dynamic pressure environment. AFWAL-TM-86-198-FIBG, May 1986.

9. Berndt, D.E. Dynamic pressure fluctuations in the internozzle region of a twin jet nacells. Society of Automotive Engineers, Warrendale, PA, SAE-841540, Oct. 1984.

10. Shen, H. and Tam, C.K.W. Numerical simulation of the generation of axisymmetric mode jet screech tones. *AIAA Journal*, **36**, 1801–1807, 1998.

11. Shen, H. and Tam, C.K.W. Effects of jet temperature and nozzle lip thickness on screech tones, *AIAA Journal*, **38**, 762–767, 2000.

12. Shen, H. and Tam, C.K.W. Three-dimensional numerical simulation of the jet screech phenomenon. AIAA Paper 2001-0820, 2001.

13. Ponton, M.K. and Seiner, J.M. The effects of nozzle exit lip thickness on plume resonance, *Journal of Sound and Vibration*, **154**, 531–549, 1992.

Reference # of Paper: Invited Lecture #1
Discusser's Name: Dr. Brian J. Tester
Author's Name: Prof. C. K. W. Tam
Question:
     The numerical simulations show energy over a broad range of frequencies. Is the broadband energy meaningful and, if so, what noise generation mechanisms does it represent?
Answer:
     Because the computation took a long time to carry out the simulation was not as long as I would like. The relatively short simulation time causes the half-widths of the screech tones in the computed noise spectra to be broader than they should be. For this reason, one should not take the broadband part of the spectra too seriously.

Discusser's Name: Prof. Dr. Rolf Radespiel
Author's Name: Prof. C. K. W. Tam
Question:
     By using a turbulence model in the acoustic simulation one changes the nature of the unsteady problem to be solved. Haw can you be sure not to lose relevant physical information by introducing a turbulence model?
Answer:
     In the numerical simulation, a k-ε turbulence model was used to simulate the effect of the fine-scale turbulence. This is justified because of scale separation. The wavelengths of the instability waves in the jet flow are much larger than the scale of the fine-scale turbulence. This length scale disparity permits one to ignore the individual eddy motions of the fine-scale turbulence. Only the collective effect of the fine-scale turbulence on the large-scale motion is considered.

Discusser's Name: Dr. Mahmood Khalid
Author's Name: Prof. C. K. W. Tam
Question:
     Did you have any difficulties with computational instabilities at the interface between the Euler and Navier-Stokes domains? Did you apply the selective artificial damping technique uniformly across the entire computational field?
Answer:
     No, I have never encountered computational instabilities at the interface between Euler and Navier-Stokes regions. In the numerical simulation of jet screech, background artificial selective damping was incorporated in the computation in each computational subdomain.

This page has been deliberately left blank

_____

Page intentionnellement blanche

Simulation of Open- and Ducted-Rotor Noise Using CAA-Multidomain Method

Jianping Yin, Jan W. Delfs
DLR, Institut fuer Aerodynamik und Stroemungstechnik, Technische Akustik
Lilienthalplatz 7, 38108 Braunschweig, Germany
e-mail: Jianping.yin@dlr.de

Abstract

The sound field generated by an open rotor and that radiated by the same rotor placed inside a semi-infinite duct is simulated using a Computational Aeroacoustic (CAA) multi-domain method. The linearized Euler equations in cylindrical coordinates are used as governing equations in solving this problem. Both Tam's radiation and PML boundary conditions are used. Comparisons of results by using the two different far-field boundary conditions will be given. A multi-domain Cartesian grid system is used so that the number of grid points can be kept as a minimum. A combination of DRP and a specially optimized cell-centered high order differencing scheme is implemented in the area of two Cartesian grid interfaces. The effect of mean flow including a shear layer on the noise radiation off the ducted rotor is studied.

1. Introduction

The prediction of open or ducted rotor noise as shown in Fig.(1) is a challenging problem as there are large difference in scales between the noise source near the rotor and the sound field. The most commonly used methods for this type of problem are integral methods based on both FW-H and Kirchhoff formulations[1,2]. These approaches to compute noise radiation from rotors in the subsonic flow regime are split into two steps. In a first step, the near-field aerodynamics and acoustics close to the source, or on the surface when using FW-H with impenetrable surface, are computed using an aerodynamics code. This then serves as input to the integral method which computes the acoustic pressure at any desired observer location in the far-field. For the computation of acoustic propagation over large distances without dissipation, these hybrid methods are much more computationally efficient than CFD methods, but they suffer from the limitation that acoustic waves are assumed to propagate through a medium which is largely at rest or at most in uniform motion relatively to the observer.

In the present paper, the sound field generated by an open and ducted rotor is simulated using Computational Aeroacoustics (CAA). The CAA method [3] has the advantage over a CFD method in accurately predicting small amplitude acoustic fluctuations and their correct propagation to the far field even in non-uniform flow. The linearized Euler Equations (LEE) are used as governing equations in solving this problem. The problems considered are taken from the third CAA benchmark problems workshop[4]. In this benchmark problem, a rotor is simplified as distribution of a rotating force acting on the fluid. In the far-field area of the computation domain as well as the duct inflow in the ducted rotor case, both Tam's radiation and Perfect Matched Layer (PML)[5] boundary conditions are used. Comparisons of results by using the two different far-field boundary conditions will be given. Because of the disparity between the length scales in the source region and the acoustic wavelengths, a multi-domain Cartesian grid system is used in which local resolution enhancement is achieved by stepping the grid size of neighboring Cartesian grid blocks by factors of two so that the number of grid points can be kept as a minimum. In the area of two Cartesian grid interfaces, a combination of Tam & Webb's DRP and a specially optimized cell-centered high order differencing scheme is implemented [6,7].

The report is structured as follows. The governing equations, numerical schemes, boundary conditions and multi-domain method are discussed at first. The noise radiation from open and ducted rotor with subsonic and supersonic rotational speeds are studied. Some of the results are compared with the

analytical solutions. In order to demonstrate the effect of mean flow on the noise radiation off the ducted rotor, a mean flow is introduced including a shear layer, separating the ambient medium from the jet flow exiting out of the duct.

2. Governing Equations

The basic set of equations for the present analysis are the three dimensional LEE with a non-uniform mean flow in cylindrical coordinates. Under the assumption that the perturbations are small, LEE can be obtained by splitting the flow variables of the Euler equations into the mean and perturbation terms. The linear perturbation field represents acoustic, vorticity and entropy waves. The linearized perturbation equations or LEE about the mean flow in cylindrical coordinates then have the following forms :

$$\frac{\partial \rho'}{\partial t} + \bar{u}\frac{\partial \rho'}{\partial x} + \bar{v}\frac{\partial \rho'}{\partial r} + \frac{\bar{w}}{r}\frac{\partial \rho'}{\partial \theta} + \bar{\rho}(\frac{\partial u'}{\partial x} + \frac{\partial v'}{\partial r} + \frac{\partial w'}{r\partial \theta} + \frac{v'}{r}) + \frac{\rho'\bar{v}}{r} =$$

$$-\bar{u}_x\rho' - \bar{\rho}_x u' - \bar{u}_r\rho' - \bar{\rho}_r v' - \bar{w}_\theta \frac{\rho'}{r} - \bar{\rho}_\theta \frac{w'}{r}$$

$$\frac{\partial u'}{\partial t} + \bar{u}\frac{\partial u'}{\partial x} + \bar{v}\frac{\partial u'}{\partial r} + \frac{\bar{w}}{r}\frac{\partial u'}{\partial \theta} + \frac{1}{\bar{\rho}}\frac{\partial p'}{\partial x} = -\bar{u}_x u' - \bar{u}_r v' - \bar{u}_\theta \frac{w'}{r} + \frac{\bar{p}_x}{\bar{\rho}^2}\rho' + F_x(x,r,\theta)$$

$$\frac{\partial v'}{\partial t} + \bar{u}\frac{\partial v'}{\partial x} + \bar{v}\frac{\partial v'}{\partial r} + \frac{\bar{w}}{r}\frac{\partial v'}{\partial \theta} - \frac{2\bar{w}w'}{r} + \frac{1}{\bar{\rho}}\frac{\partial p'}{\partial r} =$$

$$-\bar{v}_x u' - \bar{v}_r v' - \bar{v}_\theta \frac{w'}{r} + \frac{\bar{p}_r}{\bar{\rho}^2}\rho' + F_r(x,r,\theta)$$

$$\frac{\partial w'}{\partial t} + \bar{u}\frac{\partial w'}{\partial x} + \bar{v}\frac{\partial w'}{\partial r} + \frac{\bar{w}}{r}\frac{\partial w'}{\partial \theta} + \frac{(\bar{w}v' + \bar{v}w')}{r} + \frac{1}{\bar{\rho}r}\frac{\partial p'}{\partial \theta} =$$

$$-\bar{w}_x u' - \bar{w}_r v' - \bar{w}_\theta \frac{w'}{r} + \frac{\bar{p}_\theta}{\bar{\rho}^2 r}\rho' + F_\theta(x,r,\theta)$$

$$\frac{\partial p'}{\partial t} + \bar{u}\frac{\partial p'}{\partial x} + \bar{v}\frac{\partial p'}{\partial r} + \frac{\bar{w}}{r}\frac{\partial p'}{\partial \theta} + \frac{\gamma}{r}(\bar{p}v' + \bar{v}p') + \gamma\bar{p}(\frac{\partial u'}{\partial x} + \frac{\partial v'}{\partial r} + \frac{1}{r}\frac{\partial w'}{\partial \theta}) =$$

$$-\bar{p}_x u' - \bar{p}_r v' - \bar{p}_\theta \frac{w'}{r} - \gamma(\bar{u}_x + \bar{v}_r + \frac{\bar{w}_\theta}{r})p' \qquad (1)$$

In which u', v' and w' are the axial (x), radial (r) and azimuth (θ) velocity perturbation components respectively. ρ' and p' are the density and the pressure respectively. $\bar{u}, \bar{v}, \bar{w}, \bar{p}$ and $\bar{\rho}$ are the corresponding mean values, and the subscripts x, r and θ denote their partial derivatives. The (F_x, F_r, F_θ) denote the components of the source term. All quantities are written in non-dimensionalized form with respect to length scale b (radius of the blade), velocity scale c (sound speed), time scale b/c, density scale ρ_0 (ambient density), and pressure scale $\rho_0 c^2$.

When a parallel mean flow condition ($\bar{u} \neq 0$, $\bar{v} = \bar{w} = 0$ and $\bar{\rho} = \gamma\bar{p} = 1$) is introduced, the Eq.(1) can be simplified as

$$\frac{\partial u'}{\partial t} + \bar{u}\frac{\partial u'}{\partial x} + \frac{\partial p'}{\partial x} = -\bar{u}_r v' + F_x(x,r,\theta)$$

$$\frac{\partial v'}{\partial t} + \bar{u}\frac{\partial v'}{\partial x} + \frac{\partial p'}{\partial r} = F_r(x,r,\theta)$$

$$\frac{\partial w'}{\partial t} + \bar{u}\frac{\partial w'}{\partial x} + \frac{1}{r}\frac{\partial p'}{\partial \theta} = F_\theta(x,r,\theta)$$

$$\frac{\partial p'}{\partial t} + \bar{u}\frac{\partial p'}{\partial x} + \frac{v'}{r} + (\frac{\partial u'}{\partial x} + \frac{\partial v'}{\partial r} + \frac{1}{r}\frac{\partial w'}{\partial \theta}) = 0$$

$$(2)$$

Since for the parallel mean flow there is no coupling of the velocity and pressure perturbation with the density, the density equation contained in Eq.(1) is neglected in Eq.(2).

To simplify the problems while keeping the main physics, the rotor is replaced by a distribution of rotating body forces. The components of body force or the source terms (F_x, F_r, F_θ) in Eq.(1) and Eq.(2) are given from the third CAA benchmark problems workshop as follows,

$$
\begin{bmatrix} F_x(x,r,\theta,t) \\ F_r(x,r,\theta,t) \\ F_\theta(x,r,\theta,t) \end{bmatrix} = \mathrm{Re} \left\{ \begin{bmatrix} \tilde{F}_x(x,r) \\ 0 \\ \tilde{F}_\theta(x,r) \end{bmatrix} e^{im(\theta-\Omega t)} \right\}
\tag{3}
$$

where $\mathrm{Re}\{\ \}$ is the real part and $(\tilde{F}_x, \tilde{F}_\theta)$ denotes the body force distribution in r and x. In addition, the m is the number of rotor blades and Ω is the angular velocity of the rotor. Therefore, the frequency of the radiated sound is $m\Omega$.

The actual rotor noise is a 3-D problem, but by factoring out the azimuthal dependence with

$$
\begin{bmatrix} u'(x,r,\theta,t) \\ v'(x,r,\theta,t) \\ w'(x,r,\theta,t) \\ p'(x,r,\theta,t) \end{bmatrix} = \mathrm{Re} \left\{ \begin{bmatrix} \tilde{u}(x,r,t) \\ \tilde{v}(x,r,t) \\ \tilde{w}(x,r,t) \\ \tilde{p}(x,r,t) \end{bmatrix} e^{im\theta} \right\}
\tag{4}
$$

the problem can be reduced to a 2-D problem. Then the governing equations for $(\tilde{u}, \tilde{v}, \tilde{w}, \tilde{p})$ can be obtained by inserting Eq.(3) and Eq.(4) into Eq.(2),

$$
\begin{aligned}
&\frac{\partial \tilde{u}}{\partial t} + \bar{u}\frac{\partial \tilde{u}}{\partial x} + \frac{\partial \tilde{p}}{\partial x} = -\bar{u}_r \tilde{v} + \tilde{F}_x(x,r)e^{-im\Omega t} \\
&\frac{\partial \tilde{v}}{\partial t} + \bar{u}\frac{\partial \tilde{v}}{\partial x} + \frac{\partial \tilde{p}}{\partial r} = 0 \\
&\frac{\partial \tilde{w}}{\partial t} + \bar{u}\frac{\partial \tilde{w}}{\partial x} + \frac{im}{r}\tilde{p} = \tilde{F}_\theta(x,r)e^{-im\Omega t} \\
&\frac{\partial \tilde{p}}{\partial t} + \bar{u}\frac{\partial \tilde{p}}{\partial x} + \frac{\tilde{v}}{r} + (\frac{\partial \tilde{u}}{\partial x} + \frac{\partial \tilde{v}}{\partial r} + \frac{im}{r}\tilde{w}) = 0
\end{aligned}
\tag{5}
$$

The Eq.(5) will be used to solve open and ducted rotor problems. The solutions to the Eq.(5) can be directly discretized in x and r for Cartesian grids and a given parallel mean flow. The DRP finite difference scheme[8] and the artificial selective damping [9] are used for the spatial discretization.

2. Boundary Conditions

Due to the limitation of a finite computational domain, numerical outer boundary conditions are needed for the acoustic simulation. At the outer boundary of the computational domain, two types of non-reflecting boundary conditions are implemented. These are asymptotic radiation and outflow boundary conditions as well as PML[5] conditions. The details of the radiation and outflow boundary conditions developed by Tam and Dong were given in ref.[10]. In the case of ducted rotor, the solid wall boundary condition must be satisfied at the surface of the duct wall. In addition, along the axis of the cylindrical coordinates; i.e., $r = 0$, a special set of equations are used.

2.1 PML Boundary Conditions

The asymptotic radiation and outflow boundary conditions developed in ref.[10] can only be used for weakly non-uniform flow. Its use for the flow with strong shear layer across the far-field boundary area is not suitable. PML conditions are implemented as an absorbing boundary condition. One advantage of using PML is that PML can be easily implemented for non-uniform mean flow. The PML technique has proved to be effective and easy to implement. For the open and ducted rotor problems, the PML equations used in the PML domain are derived by splitting the variables of the governing equations (5) :

$$\frac{\partial \tilde{u}_1}{\partial t} + \sigma_x \tilde{u}_1 = -\bar{u}\frac{\partial \tilde{u}}{\partial x} - \frac{\partial \tilde{p}}{\partial x}$$

$$\frac{\partial \tilde{u}_2}{\partial t} + \sigma_r \tilde{u}_2 = -\bar{u}_r \tilde{v}$$

$$\frac{\partial \tilde{v}_1}{\partial t} + \sigma_x \tilde{v}_1 = -\bar{u}\frac{\partial \tilde{v}}{\partial x}$$

$$\frac{\partial \tilde{v}_2}{\partial t} + \sigma_r \tilde{v}_2 = -\frac{\partial \tilde{p}}{\partial r}$$

$$\frac{\partial \tilde{w}_1}{\partial t} + \sigma_x \tilde{w}_1 = -\bar{u}\frac{\partial \tilde{w}}{\partial x}$$

$$\frac{\partial \tilde{w}_2}{\partial t} + \sigma_r \tilde{w}_2 = -\frac{im}{r}\tilde{p}$$

$$\frac{\partial \tilde{p}_1}{\partial t} + \sigma_x \tilde{p}_1 = -\bar{u}\frac{\partial \tilde{p}}{\partial x} - \frac{\partial \tilde{u}}{\partial x}$$

$$\frac{\partial \tilde{p}_2}{\partial t} + \sigma_r \tilde{p}_2 = -\frac{\tilde{v}}{r} - \frac{\partial \tilde{v}}{\partial r} - \frac{im}{r}\tilde{w}$$

(6)

where $\tilde{u} = \tilde{u}_1 + \tilde{u}_2$, $\tilde{v} = \tilde{v}_1 + \tilde{v}_2$, $\tilde{w} = \tilde{w}_1 + \tilde{w}_2$ and $\tilde{p} = \tilde{p}_1 + \tilde{p}_2$. The absorption coefficients σ_x and σ_r are varied gradually in the PML domain. As shown in Fig.(3a) and Fig.(8a) the PML domains used for the open and the ducted rotor case, σ_x is set zero at the right and left PML domains and σ_r is zero at the top PML domain. At the corner regions, both coefficients are nonzero. In the present paper, the following form has been used for the variation of σ_x or σ_r within the PML domains:

$$\sigma = \sigma_{max}(1.0 - e^{-(d/D)^2})$$

(7)

in which D is the width of the PML domain, d is the distance from its interface with the interior domain and σ_{max} is the maximum value of σ, which is dependent on grid size.

2.2 Solid Wall Boundary Condition

For the ducted rotor, on the surface of the duct wall, the fundamental physical requirement is the non-penetration boundary condition:

$$\vec{v} \bullet \vec{n} = 0 \ \ or \ \ \tilde{u}n_x + \tilde{v}n_r + \tilde{w}n_\theta = 0$$

(8)

where $\vec{n}$ is the unit normal on the wall and can be written as $\vec{n} = (n_x, n_r, n_\theta) = (0, \ 1, \ 0)$ for a plane wall. Then Eq.(8) becomes

$$\tilde{v} = 0$$

(9)

By taking the dot product of the momentum equations of Eq.(5) with $\vec{n}$ for the plane wall, the Eq.(8) is equivalent to :

$$\frac{\partial \tilde{p}}{\partial r} = 0$$

(10)

In the case of the ducted rotor, both Eq.(9) and (10) are used on the wall surface. For the flat wall, Eq.(9) can be easily implemented. To satisfy Eq.(10), the numerical treatment in conjunction with high-order finite difference schemes derived by Tam and Dong [9] is implemented. In this method, ghost values of pressure are chosen so that Eq.(10) can be satisfied on each boundary condition enforcement point.

2.2 Conditions at the Centerline $r = 0$

As $r \rightarrow 0$, Eq.(5) has a numerical singularity and cannot be used directly. Since for $m \neq 0$ on the centerline $r = 0$, $\tilde{v} = \tilde{w} = \tilde{p} = 0$, the singularity terms in Eq.(5) may be replaced by partial derivative terms using L'Hospital's Rule, which are

$$\frac{\tilde{v}}{r} = \frac{\partial \tilde{v}}{\partial r}, \quad \frac{\tilde{w}}{r} = \frac{\partial \tilde{w}}{\partial r}, \quad \frac{\tilde{p}}{r} = \frac{\partial \tilde{p}}{\partial r} \tag{11}$$

at $r = 0$.

3. Multi-Domain Grid Design

Because of the disparity between the length scales in the source region and the acoustic wavelengths, a multi-domain Cartesian grid system is used. The computation domain is divided into several sub-domains enclosed by rectangular solid lines as shown in Fig.(2a) for an open rotor computation. For clarity, only part of the outside domain is given in Fig.(2a). The highest resolution is used in the area closest to the rotor blade or the source region respectively. When moving away from source region to the acoustic field, the grid size is stepped up by factors of two from inner to outer sub-domains. In principle, an overlapping grid technique for the use of high resolution schemes [11] can be used in the interface area. To make the computation more efficient, a special interface treatment between Cartesian grids was used. Since the grid spacing in adjacent Cartesian areas differs by a factor of 2, it is not difficult to form a 7 points DRP stencil at every point in region A with mesh size Δx or Δr and every point in region B (mesh size $\Delta x / 2$ or $\Delta r / 2$) except for points in the interface region, which is within a distance of three points from the interface in region B as shown in Fig.(2b). In the interface region, when grid lines on two grids coincide with each other, a cell-centered symmetric stencil with optimized coefficients is used, such as the point marked 'cc' in Fig.(2b). The stencil used at 'cc' can be written in the form

$$\left(\frac{\partial f}{\partial x} \right)_{cc} = \frac{1}{\Delta x} \sum_{j=-3}^{3} a_j f_j \tag{12}$$

The optimized stencil coefficients are

$$a_{-3} = -a_3 = \text{-0.0046875}$$
$$a_{-2} = -a_2 = 0.0651041666667$$
$$a_{-1} = -a_1 = \text{-1.171875}, \quad a_0 = 0.0$$

For the points on the non-coincidence lines, function values on several 'hanging' points marked as 'h' in Fig.(2b) are required. The values on these 'hanging' points are explicitly obtained by a two dimensional Lagrange interpolation. The interface treatments used here have been validated in ref.[6,7] on the basis of CAA Benchmark problems.

4. Artificial Selective Damping (ASD)

The ASD terms are added in the right hand side of the discretized finite difference equations in order to eliminate spurious short waves and improve numerical stability. In the interface regions among Cartesian grids, the irregularities are created by using different grid size and stencil. These irregularities are also very efficient in generating short spurious numerical waves. For the field points where the cell-centered

symmetric stencil Eq.(12) is used, a damping stencil with the same configurations was derived. The optimized stencil coefficients of the damping operator are

$$d_{-3} = d_3 = \text{-0.01092915}, \quad d_{-2} = d_2 = 0.06004774$$
$$d_{-1} = d_1 = \text{-0.2991186}, \quad d_0 = 0.5$$

In addition, for the grid points located at the centerline $r = 0$, the imposition of stronger ASD is required since there is a change of governing equations which may result in the generation of spurious short waves.

5. Numerical Simulations and Discussions

Numerical results on noise radiation from the open and ducted rotor will be discussed in the following sections. Because the variables $(\tilde{u}, \tilde{v}, \tilde{w}, \tilde{p})$ used in the governing equations are complex, the results presented are taken from Eq.(4) for zero azimuth angle $\theta = 0$. The directivity, $D(\phi)$, of the radiated sound is defined as

$$D(\phi) = R^2 \overline{p'^2(R, \phi, \theta, t)} \tag{13}$$

Where $\overline{}$ is the time average. The definition of R and ϕ is given in Fig.(1) for the open rotor. For the ducted rotor, R is measured from the open end of the duct.

5.1 Open Rotor

The sound generated by an open rotor is simulated. Following body force distributions $(\tilde{F}_x, \tilde{F}_\theta)$ are used to simulate the impact of the rotor blades on the surrounding air[4].

$$\tilde{F}_\theta(x, r) = \begin{cases} F(x) r J_m(\alpha_{mN} r) & r \le 1 \\ 0 & r > 1 \end{cases}$$
$$\tilde{F}_x(x, r) = \begin{cases} F(x) J_m(\alpha_{mN} r) & r \le 1 \\ 0 & r > 1 \end{cases} \tag{14}$$
$$F(x) = \exp\left\{ -(\ln 2)(x/h_w)^2 \right\}, \quad h_w = 0.1$$

where $J_m(\ )$ is the m th-order Bessel function, α_{mN} is the Nth root of $J'_m(\alpha_{mN}) = 0$ and h_w is the half-width of the Gaussion-like forcing function. For a B blade rotor, the body force is spaced in $\dfrac{2\pi}{B}$ radians apart and spins with rotor rotational speed Ω. The m is chosen as the number of the rotor blades B. The choice of the Bessel functions in Eq.(14) has no other significance than making the analytical solution simple. The 8-blade rotor ($B = 8$) is involved in the computation. α_{mN} is chosen as $\alpha_{8,1} = 9.64742$ in which $N = 1$ so that the force in the radial direction corresponds to a mono-peak function. In ducted rotor, N has the meaning of the radial mode number.

The whole computational domain is $x \times r = [-17, \ 17] \times [0, \ 17]$. The problem is symmetric about the x-axis. Thus only the solution in the upper half $x - r$ plane needs to be computed. The symmetric condition is applied for $(\tilde{u}, \tilde{w}, \tilde{p})$ and the anti-symmetric condition is applied for $\tilde{v}$. The choice of the grid size depends on the acoustic wave length and h_w. In general, 4 grid points are necessary to resolve the half-width of the forcing function and the minimum of 8 grid points per wave length has to be used in the far-field.

Two rotational speeds are used, one with subsonic tip speed $\Omega = 0.85$ and the other with supersonic tip speed $\Omega = 1.15$. The grid sizes of the smallest domain are $\Delta x_s = 0.025$ for $\Omega = 0.85$ and $\Delta x_s = 0.02$ for $\Omega = 1.15$ respectively. The time advancing scheme used throughout the paper is the classical 4 stage Runge-Kutta scheme with a time step $\Delta t = 0.005$ if there is no other specification. In the open rotor computation, the mean flow $\bar{u}(r) = 0$ is assumed. The width of the PML domain is chosen as to contain 10 grid points.

Fig.(3) shows a snapshot of the acoustic pressure contours and the details of the multi-domain grid system for the open rotor with subsonic tip speed. The rectangular box in the plots is the interface between two Cartesian domains. The results show most of the acoustic radiation is concentrated in the direction around the plane of rotation. The results in zoom scale in Fig.(3b) also demonstrate that the contour lines go through grid interfaces very smoothly without any noticeable reflection. Fig.(4) gives the directivity at $R = 15.0$ obtained computationally in comparison with the exact solution [4] for $\Omega = 0.85$. There is good agreement between the numerical simulation and the analytical solution although the latter was obtained with the assumption of $R \rightarrow \infty$. To compare the effect of different far-field boundary conditions, the result with Tam's asymptotic far-field boundary condition is also presented in the figure. Only little difference was found. In addition, the comparison on the directivity for different rotational speed in Fig.(5) shows that, as expected, the radiation from the rotor with the supersonic tip speed is stronger.

5.2 Ducted Rotor

For the ducted rotor, the governing equations Eq.(5) are again used together with solid wall boundary conditions on both sides of the duct wall. In general, the effect of the duct wall will force the acoustic disturbance to be continuously reflected back and thereby cause cancellations and reinforcements. From the standard modal analysis of duct acoustic theory, the in-duct pressure for a cylinder duct can be expressed as superposition of various rotational modes,

$$p(r,\theta,x,t) = \sum_m \sum_{N=0}^{\infty} A_{mN} J_m(K_{mN}r)\exp[im(\theta - \Omega_m t) + iK_x x] \tag{15}$$

where m and N are the circumferential and the radial mode numbers respectively. In general, K_{mN} is called the radial wave number and can be obtained by satisfying the wall boundary condition. For a hard walled duct, K_{mN} is the N th root of $J'_m(K_{mN}) = 0$. Ω_m is the rotational speed of the m's mode. When the body force felt by the B-blade rotor is steady (as in the present paper), the rotational speed of all modes is equal to Ω and the circumferential mode number m can only be chosen as $m = \mu B$, ($\mu = 1,2,3,\dots$), therefore only the acoustic signal with frequency $f_\mu = \dfrac{\mu B \Omega}{2\pi} = \mu f_1$, is generated. f_1 is called rotor blade passing frequency (BPF).

From Eq.(15) it is known that whether an acoustic mode can be propagated along the duct (x) or not depends on the axial wave number K_x. For cylindrical ducts with uniform mean flow at a Mach number $M = \bar{u}$, K_x is obtained by

$$K_x = \frac{-KM + \sqrt{K^2 - K^2_{mN}(1 - M^2)}}{1 - M^2} \tag{16}$$

where $K = \mu B \Omega$ is the non-dimensional wave number of the acoustic disturbance. The modes with real K_x are the propagating modes and called cut-on modes. The modes with non-zero imaginary part of K_x are exponentially decaying in amplitude along the duct and therefore called cut-off modes.

From Eq.(16), it can be derived that the acoustic wave with BPF and its high harmonics f_μ can be propagated through the duct only if the rotational speed Ω satisfies,

$$\Omega > \frac{K_{mN}}{m}\sqrt{1-M^2} \tag{17}$$

where the right hand side of Eq.(17) is called <u>cut-off rotational speed</u> Ω_c in the present paper.

For the ducted rotor with the same body force function as Eq.(14), the Eq.(15) can be simplified since the given body force function can only excite one rotational mode,

$$p(r,\theta,x,t) = J_m(K_{mN}r)\exp\left[im(\theta-\Omega t)+iK_x x\right] \tag{18}$$

where $K_{mN} = \alpha_{mN}$ and $m = B$ as well as $N = 1$ as specified.

5.2.1 Effect of Uniform Mean Flow on Noise Radiation from Open End of Duct

In the ducted rotor case, the same body force function Eq.(14) as for the open rotor is used. An infinitely thin duct wall is placed at $r = 1.0$ along $-4.1 \leq x \leq 8.0$. PML conditions are implemented on the left side of the duct to simulate an infinite length of the duct. Symmetry about the x-axis is assumed. The size of the computational domain is $[-4.1,\ 16.5]\times[0,\ 8]$.

For the case without considering any mean flow or $M = 0$, Ω_c is equal to 1.206 according to Eq.(17) when setting $m = B = 8$, $N = 1$, and $K_{mN} = \alpha_{mN} = \alpha_{8,1} = 9.64742$ as in the open rotor case. The two rotational speeds Ω used in the open rotor case are all smaller than $\Omega_c = 1.206$ so that all the acoustic disturbances are cut-off or evanescent. This can be seen as well by looking at the time history outside the duct. <u>Fig.(6)</u> gives the pressure time history sensed at $R = 6.0$ and $\phi = 52°$ for $\Omega = 1.15$. R is measured from the center of the duct end located at $(x,r) = (8.0,\ 0.0)$. It shows that the intensity of sound radiation decreases very quickly after the initial transient state. Thus there is no sound radiation out of the open end of the duct even for slightly supersonic tip Mach number. This also proves that the environment around an acoustic source plays an important role in noise propagation.

From Eq.(17), it can be seen that, Ω_c will be reduced if mean flow is involved. Therefore, with changing the mean flow Mach number, the condition for Ω to either represent a propagational or non-propagational signal will also be changed. For example, for the case $M = 0.5$ inside and outside of the duct, Ω_c reduces to 1.044 so that the noise generated by the rotor with $\Omega = 1.15$ will radiate from the open end of the duct. The pressure time history for the ducted rotor with $\Omega = 1.15$ under uniform mean flow $M = 0.5$ is given in <u>Fig.(7)</u> at the same position as in <u>Fig.(6)</u>. The results indicate that a time periodic state has been reached after the initial transient state due to sound radiation from the duct end. <u>Fig.(8)</u> shows the pressure contour at $t = 40$ and its enlarged plot close to the grid interface. The results prove again the numerical treatment is successful. It should be mentioned that since the pressure disturbance propagates in the duct on a helical path, the pressure contour given in <u>Fig.(8)</u> is only a cut in the three dimensional spiral pattern. Due to the mean flow convection effect, the spinning mode will propagate much faster in downstream direction of the rotor than upstream of the rotor. The difference of the length scale upstream and downstream of the rotor, as shown in <u>Fig.(8)</u> demonstrates the mean flow convection effect.

5.2.2 Effect of Shear Layer on Noise Radiation

In previous section, it was demonstrated that the effect of a mean flow in the duct may cause the propagation of acoustic modes which are cut-off for vanishing mean flow. Furthermore, when there are gradients in the mean flow typically due to the shear layer between the ambient medium and the jet flow

emanating from the duct, instability waves may be generated by acoustic excitation. Finally, the propagation of the acoustic waves through the shear layer will change the acoustic directivity pattern.

In order to show the main effect of the presence of such a shear layer an analytical shear flow was introduced separating the flow field in $r \leq 1$ from the ambient medium. The parallel mean velocity profile is,

$$\bar{u}(r) = \begin{cases} M_\infty + (M - M_\infty) \exp\left\{-(\ln 2)(\dfrac{r-b}{h_w})^2\right\} & r > b \\ M & h \geq r \geq 0 \end{cases} \tag{16}$$

where the mean flow is uniform inside $r \leq 1$ with $M = 0.5$. The Gaussian distributed function is used to describe the variation of the shear flow. The half width of this function is $h_w = 0.25$. The other parameters are $b = 1.0$ and $M_\infty = 0.0$. The computation domain as well as the grid arrangement is the same as in Fig.(8). PML equations of Eq.(6) are again used. It should be mentioned that the shear layer chosen here is for the purpose of demonstrating the effect of the shear layer on noise propagation and not to show the excitation of the instability wave. No instability mode is indeed excited under the considered signal frequency.

Fig.(9) shows the instant pressure contour at two different times. Apart from the acoustic waves radiated from open duct end, depicted in Fig.(9a) a hydro-dynamical instability in form of a wave packet is observed inside the shear layer. The instability is convected out of the computation domain at later times as shown in Fig.(9b). Therefore these instability waves are believed to be excited purely by the multi-frequency transients occurring when the force Eq.(14) is turned on at $t = 0$. This demonstrates that the considered shear flow is stable for the acoustic excitation from the open duct end at $\Omega = 1.15$. The comparison of the directivity at $R = 6.0$ for uniform and shear layer mean flow is given in Fig.(10) which shows that the radiation pattern has been shifted upstream after passing through the shear layer.

6. Summary

The noise radiation from an open and ducted rotor is simulated using a CAA multi-domain method. The results for the ducted rotor show that there is no sound radiation out of the open end of the duct when the rotational speed of the ducted rotor is below the cut-off rotational speed. The sound field generated by an open and ducted rotor can be extremely different because the presence of the duct wall will cause cancellations and reinforcements of both propagating and reflecting waves. The effect of mean flow in the duct may cause the propagation of the acoustic modes which are cut-off for no flow. The validations using benchmark problems for the open rotor case also show that the presented method has good accuracy in terms of the schemes and the boundary conditions used.

7. Reference

1. Ffowcs Wiliams, J., Hawkings, D.: Sound Generation by Turbulence and Surfaces in Arbitrary Motion, Phil. Trans. Roy. Soc. A264, 1969.
2. Brentner, K. S.; Farassat, F.: Helicopter Noise Prediction: The Current Status and Future Direction, DGLR/AIAA 14th Aeroacoustics Conference, Aachen, Germany, 1992.
3. Tam, C.K.W.: Computation Aeroacoustics: Issues and Methods, AIAA J. Vol. 33, pp.1788-1796, Oct. 1995.
4. Third Computational Aeroacoustics (CAA) Workshop on Benchmark Problems, NASA CP 2000-209790, Edited by Milo, D. Dahl, August, 2000.
5. Hu, F. Q. : On Perfectly Matched Layer as An Absorbing Boundary Condition, AIAA 96-1664, 1996.
6. Delfs, J., Yin, J. "CAA-Simulation of Aeroacoustic Sources on Overlapped grids". Second Aeroacoustic Workshop SWING, Braunschweig (de), 06.-07.10.2000, DLR, (2000)

7. Yin, J. and Delfs, J.W. Sound Generation from Gust-Airfoil Interaction using CAA-Chimera Method. AIAA Paper 2001-2136, 7th AIAA/CEAS Aeroacoustics Conference 2001.

8. Tam, C.K.W. and Webb, J.C. "Dispersion Relation Preserving Finite Difference Schemes for Computational Acoustics", J. Comp. Phys.,107,262-281,1993.

9. Tam, C.K.W. and Dong, Z. "Wall Boundary Conditions for High-order Finite Difference Schemes in Computational Aeroacoustics", Theoretical and Computational Fluid Dynamics, 6, 303-322,1994.

10.Tam, C.K.W. and Dong, Z. "Radiation and Outflow Boundary Conditions for Direct Computation of Acoustic and Flow Disturbances in a Nonuniform Mean Flow", CEAS/AIAA Paper 95-007,June 1995.

11.Delfs, J. W. "An overlapping grid technique for the use of high resolution schemes of computational aeroacoustics at complex geometries". AIAA Paper 2001-2199, 7th AIAA/CEAS Aeroacoustics Conference 2001.
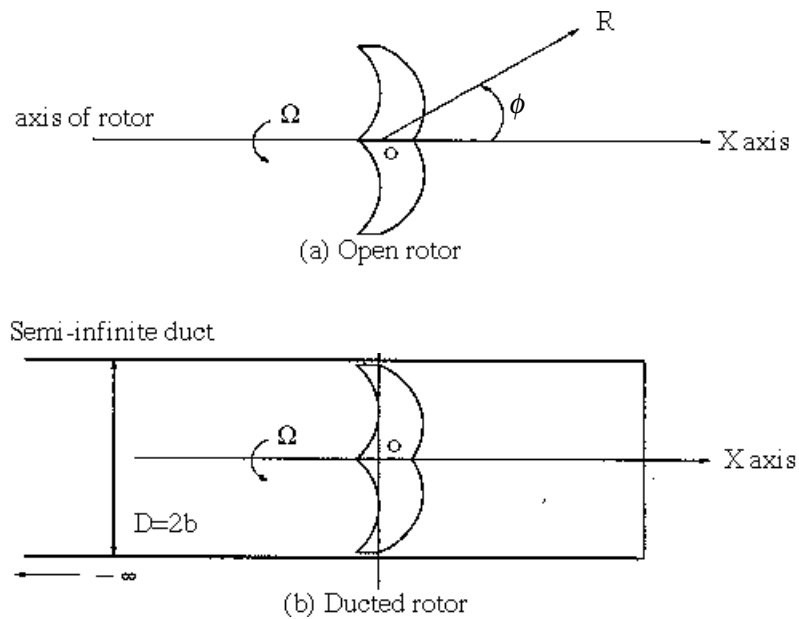
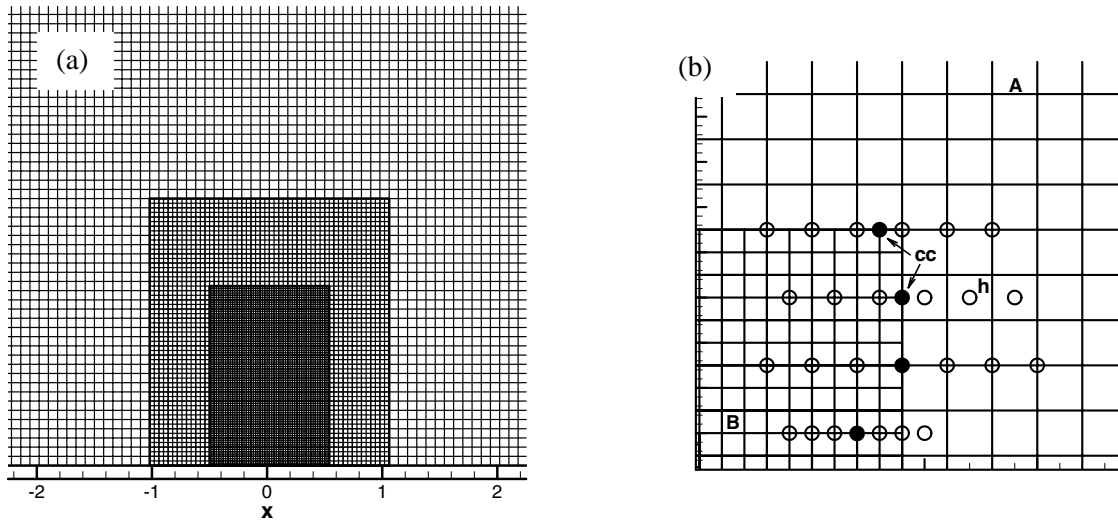**Fig. 1** A sketch of the open and ducted rotor problems

Fig. 2 (a) Multi-domain grid system used for the open rotor computation

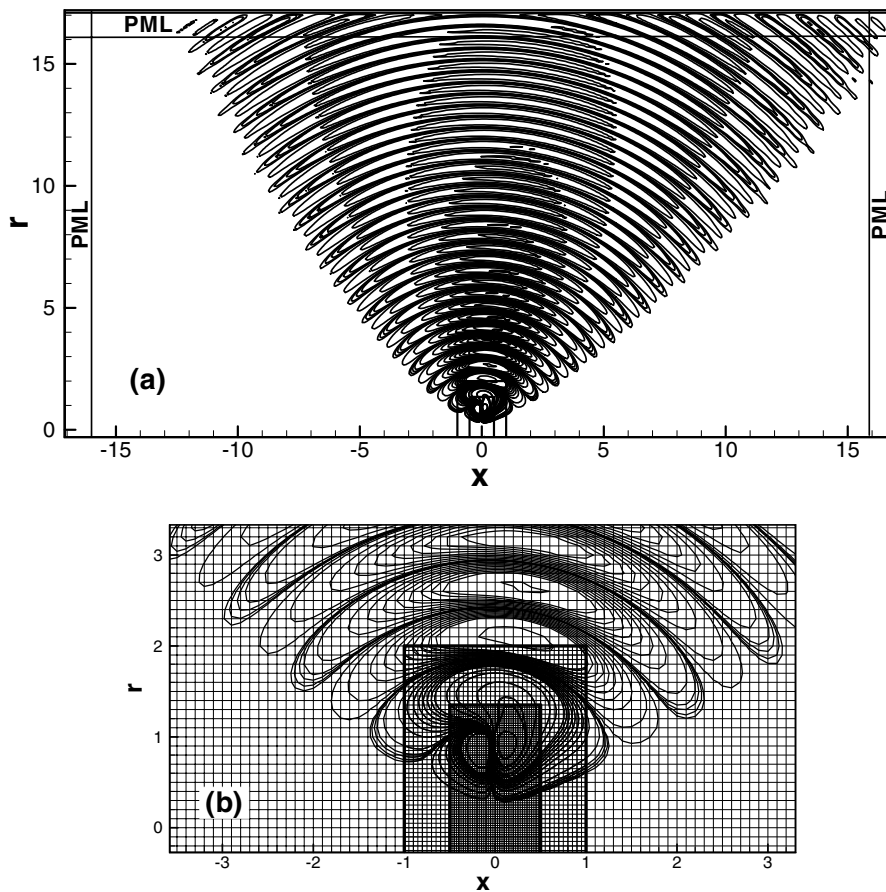(b) Special interface treatment between Cartesian grids

Fig. 3 (a) Acoustic pressure contour for the open rotor with $\Omega = 0.85$

(b) A zoom view from (a) in the area close to the rotor

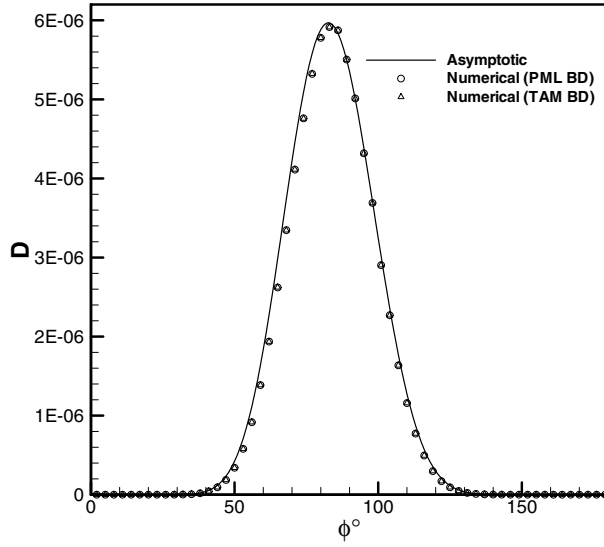**Fig. 4** Comparison of the numerically obtained directivity at $R = 15.0$ and the exact solution [4] for $\Omega = 0.85$ with two different far-field (PML and TAM) boundary conditions (BD)
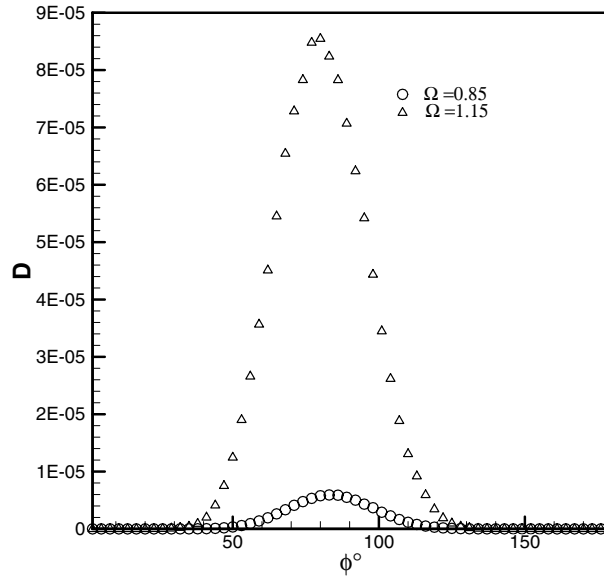
Fig. 5 Comparison of the directivity for different rotational speeds
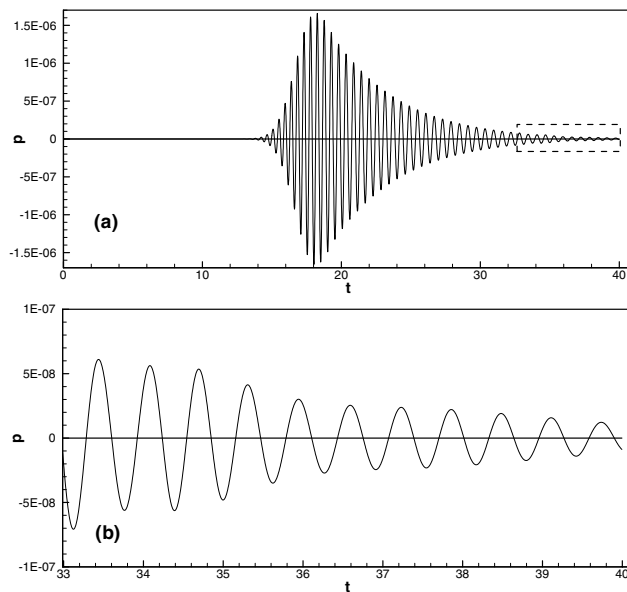
Fig. 6 (a) Pressure time history sensed at $R = 6.0$ and $\Phi = 52°$ for $\Omega = 1.15$ (b) Zoom-view of the box in (a); ducted rotor case with M = 0.0.
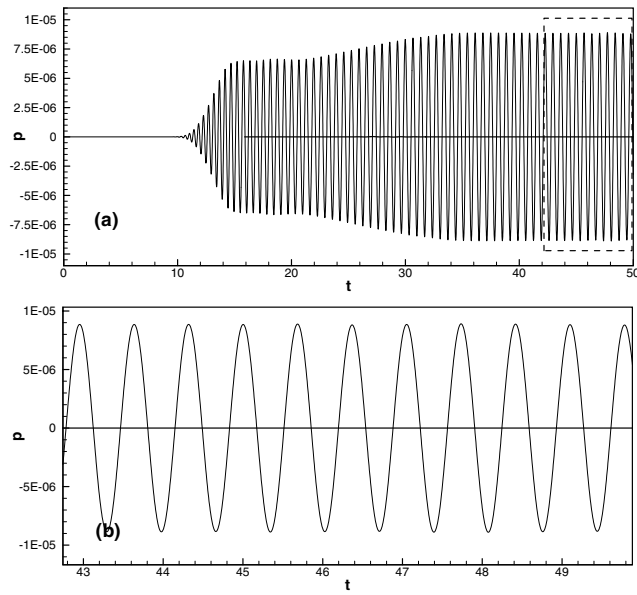
Fig. 7 (a) Pressure time history sensed at $r = 6.0$ and $\Phi = 52°$ for $\Omega = 1.15$ (b) Zoom-view of the box in (a); ducted rotor case with $M = 0.5$.
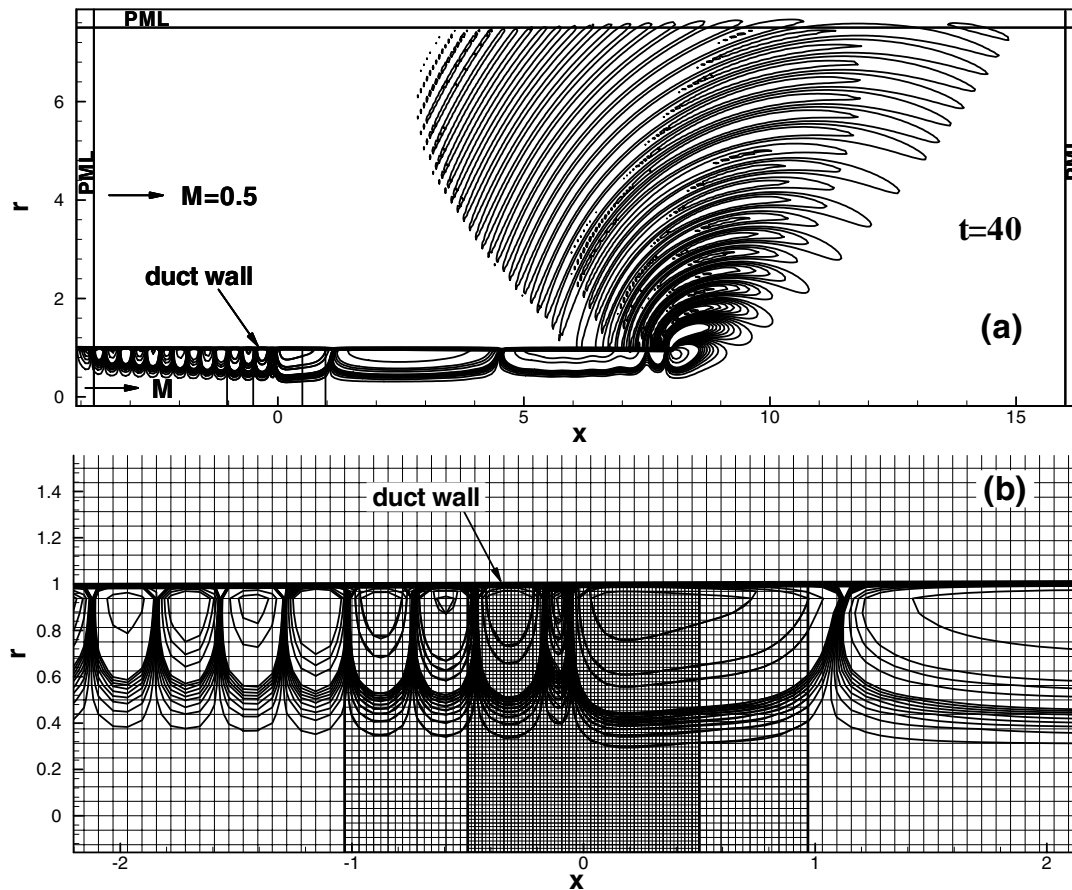
Fig. 8 Pressure contour at $t = 40$. and its enlarged plot close to grid interface; ducted rotor case with $M = 0.5$ and $\Omega = 1.15$
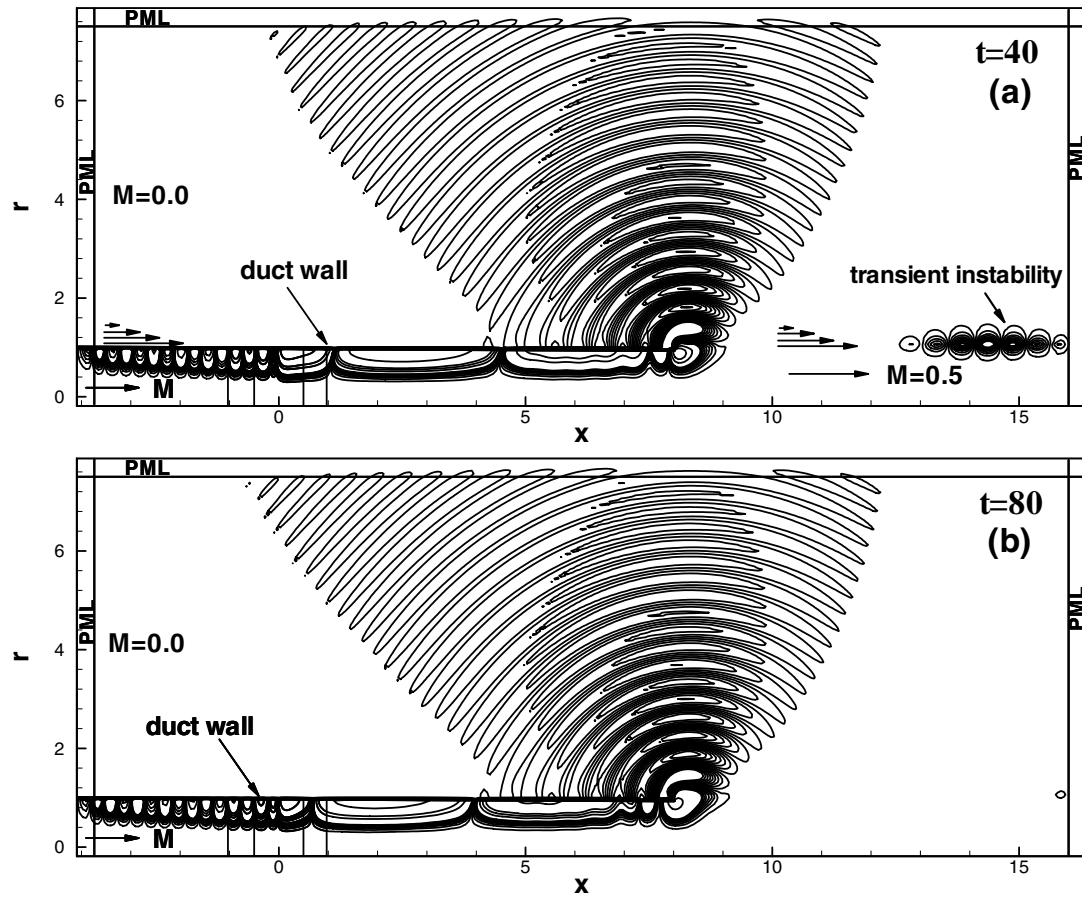
Fig. 9 Pressure contour at two different times; ducted rotor case with a given shear flow and $\Omega = 1.15$
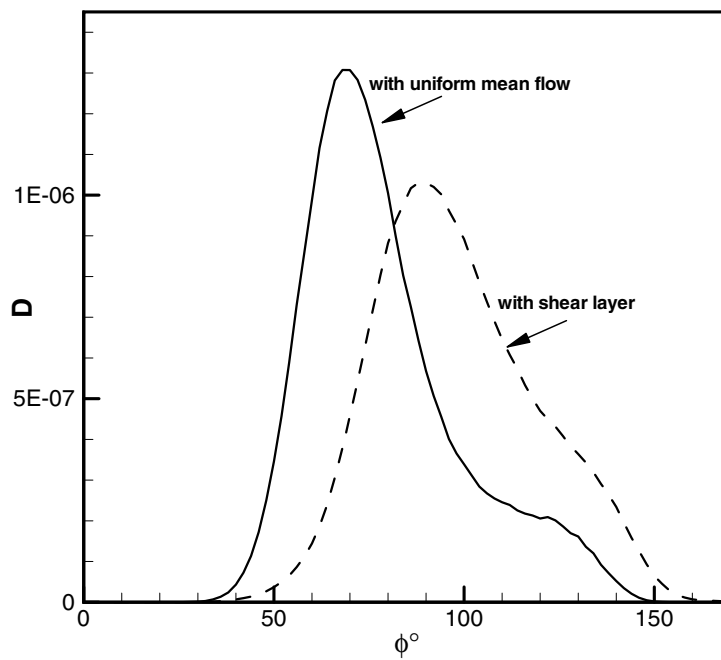
Fig. 10 Comparison of noise radiation directivity at $R = 6.0$ for uniform mean flow and mean flow with shear layer

Reference # of Paper: 2
Discusser's Name: Mr. Jose M. Riola Rodriguez
Author's Name: Dr. Jianping Yin
Question:
Do you think this model is applicable to swirling flows or only in axial flows?
Answer:
Yes. The method itself is not limited to axial flows.

Discusser's Name: Dr. Brian J. Tester
Author's Name: Dr. Yianping Yin
Question:
Is the free shear layer of the jet being modeled as well as the shear layer on the outside of the duct?
Answer:
No. The shear layer separating the jet and the ambient medium is modeled by an analytical, parallel flow profile. This profile is only imposed on the outside of the duct wall.

This page has been deliberately left blank

_____

Page intentionnellement blanche

A Method for Deriving Tone Noise Information from CFD Calculations on the Aeroengine Fan Stage

A.G. Wilson
Rolls-Royce plc
ML 81
P.O. Box 31, Moor Lane
Derby, DE24 8BJ
United Kingdom

Abstract

A wavesplitting procedure is proposed by which noise information can be derived from CFD calculations on the aeroengine fan stage. Noise propagation in the ducted regions is compared with well-understood linear behaviour in parallel wall ducts. Deviations from this behaviour are used to highlight important features of the flow solution. These include genuine flow features such as non-linear acoustic interaction as well as dissipation and boundary condition errors deriving from the numerical solution of the equations. Properly applied, the method provides quantitative noise source amplitudes, accounting for (modest) reflections from the boundaries of the CFD domain. At the same time confidence can be gained that the CFD results are accurate for the wavelengths and frequencies being analysed, and that the CFD domain sufficiently covers the region of interest.
Examples are given of how the method can be applied to steady and unsteady CFD calculations. Limitations of the method are also discussed.

Introduction

Wavesplitting (decomposition of a flow field into upstream and downstream travelling eigenmodes) is widely used in CFD boundary conditions to determine the direction in which information is travelling, and hence to prevent spurious reflections at the boundaries of the domain. Tyler and Sofrin (1961) first derived the acoustic modes for uniform axial flow in cylindrical and annular ducts. This formulation has been widely and successfully applied to boundary conditions: Giles, for example, used the modes with varying levels of approximation to produce 1D and 2D non-reflecting conditions (Giles 1990, Saxer and Giles 1993). Other authors have proposed a complete 3D formulation. The method has, however, clear limitations. Ducts are not in general parallel annulus. Flow is generally non-uniform radially. Amplitudes (particularly with regard to rotor alone tones) are so high that the acoustic perturbations behave non-linearly (Morfey and Fisher 1970). Moreover, in addition to these physical features, CFD solutions have their own characteristics: smoothing, grid and boundary conditions all affect the noise prediction process. Rowley and Colonius (1998) developed numerically non-reflecting boundary conditions by calculating linear modes using the true mean flow profile and included in their analysis the discretisation of the particular CFD code being used.

In this paper a wavesplitting method is developed for use *inside* the computational domain, as an aid to deriving tone noise information from the CFD solution. As with the boundary conditions, a decision has to be made as to the complexity required. 1D and 2D analyses are insufficient for the general case. Instead a 3D uniform axial flow method based on Tyler and Sofrin modes is adopted. This has many advantages over more complex methods:

- The modes can be calculated quickly using standard Bessel functions.
- The modes are orthogonal, making decomposition easier and faster.
- The behaviour of the Tyler and Sofrin modes is well understood.
- The resulting wavesplitting routines are general across all CFD codes.

Two methods are given for splitting the flow field at a given axial plane into Tyler and Sofrin modes, depending on whether or not vortical as well as acoustic waves are present in the flow. The output of each method is a number representing amplitude and phase for the upstream and downstream travelling acoustic waves at each circumferential and radial harmonic.

Tyler and Sofrin modes propagate either at constant amplitude (cut-on waves) or with log amplitude varying linearly with axial distance (cut-off waves). In both cases the phase varies linearly with distance. The axial wavenumber, representing the rate of change of amplitude and phase, can be calculated analytically from the circumferential wavenumber, the wave frequency and the (axial) Mach number of the mean flow (appendix 1). Because the Tyler and Sofrin modes do not agree exactly with either the physical or the CFD calculated modes (for the reasons outlined above), the behaviour of the calculated wave amplitude varies from this 'ideal'. By plotting log amplitude and phase against axial distance it is possible to isolate these regions, and hence to direct further work at establishing whether the cause of the discrepancy is physical (eg non-linearity, hade angle, non-uniform mean flow) or numerical (eg dissipation error, reflections from the boundaries). This has proved an essential step in obtaining reliable noise information, and the examples below show how the analysis might proceed from the basic method to derive quantitative estimates of source noise.

Example 1: Steady CFD, Boundary Conditions, Non-linear effects

Before describing the mechanics of the method it is useful to consider an example to illustrate the progression of thought. Fig 1 shows the result of a steady CFD calculation of a research fan blade at rig scale, aimed at predicting fan-forward rotor alone noise. The pressure has been Fourier transformed circumferentially to decompose it into the harmonics of blade passing frequency that would be detected by a stationary microphone at the outer wall. The signal amplitude at the first blade passing harmonic is plotted on a log scale (in fact, as Sound Pressure Level, SPL[1]) against distance upstream of the fan tip leading edge. The large oscillations in amplitude are known from measurements to be false.
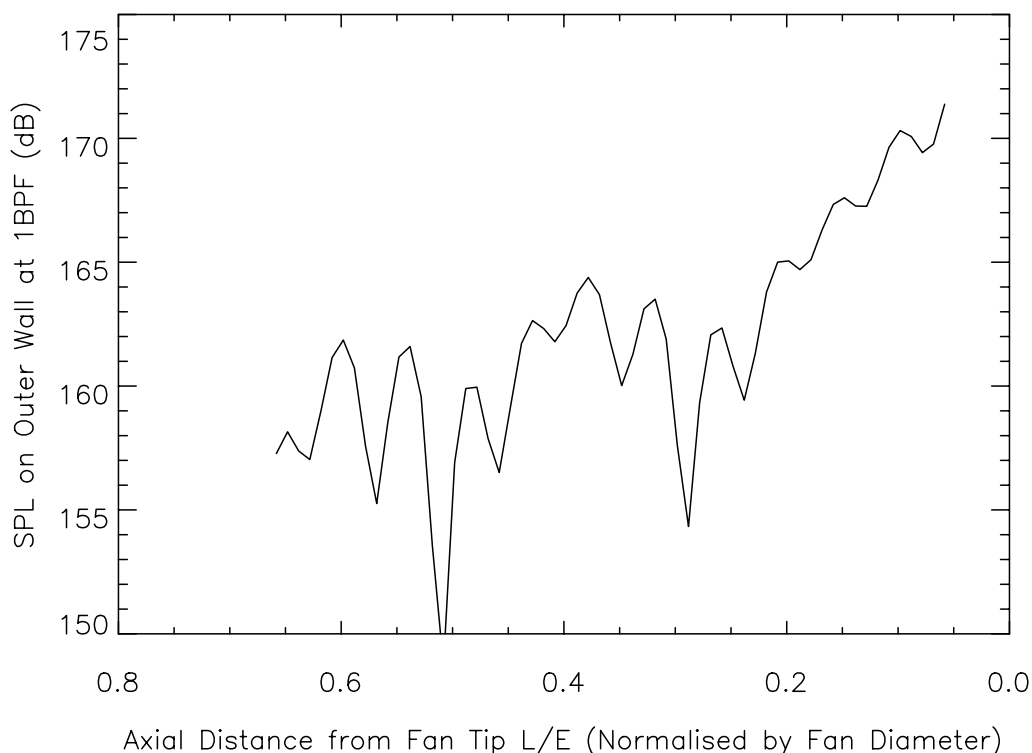

Figure 1. Steady CFD Solution for Fan Rotor Alone Noise; SPL on Outer Wall

---

[1] Sound Pressure Level (SPL) is defined in the usual way as $20\log_{10}(\text{Prms}/\ 2.10^{-5}\text{Pa})$

The starting strength close to the fan is known to be roughly correct, but the signal (if genuine) is contaminated by oscillations in the solution, making it hard to quantify the noise produced. Two lengthscales can be distinguished; a short wavelength oscillation with about eleven peaks over the axial domain, and a longer wavelength oscillation with troughs at x=0.5 and x=0.3.

The first step in the analysis procedure is to split the pressure signal into Bessel-Fourier harmonics. It will be seen later that over the majority of the domain the first radial harmonic dominates the signal at the outer wall. This harmonic is shown as the long dashes in fig 2, compared to the outer wall values from fig 1. The longer lengthscale oscillation has disappeared, leaving a smoothly varying version of the shorter wavelength disturbance. Thus the longer wavelength disturbance was due to interference at the outer wall between different radial harmonics.
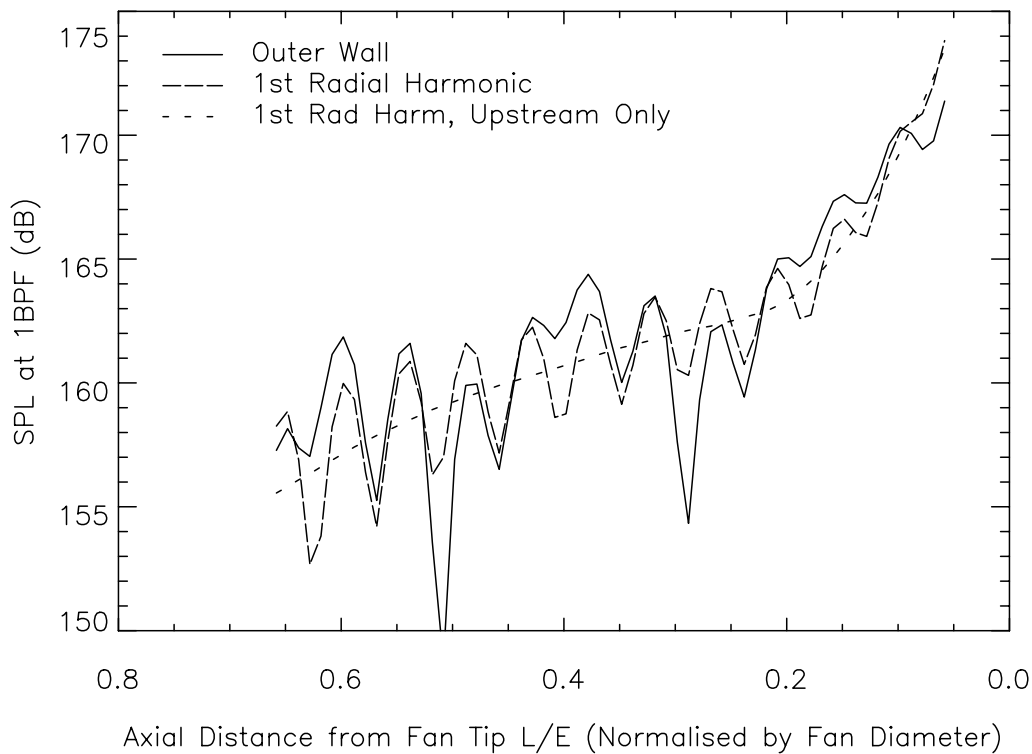
Figure 2. Steady CFD for Rotor Alone Noise, Bessel-Fourier Decomposition and Wavesplitting

In some cases this level of analysis is sufficient. The radial harmonic breakdown along the duct gives a great deal of information about both the source amplitude and the accuracy of the code, as will be discussed later. In this case, however, a further step is necessary to isolate the cause of the short wavelength oscillations. The periodic nature of the oscillations suggests some form of standing wave, and this particular case was run with 1D non-reflecting boundary conditions at the inlet boundary, which are known to be poor for the wavelengths and frequencies of interest.

By decomposing the axial velocity also into Bessel-Fourier harmonics the pressure variation represented by the long dashes in fig 2 can be split into forward and backward travelling components. The short dashes in that figure represent the upstream travelling component. The result is a smooth line, demonstrating that the oscillations observed at the outer wall are indeed due to the presence of a downstream wave reflected from the inlet boundary.
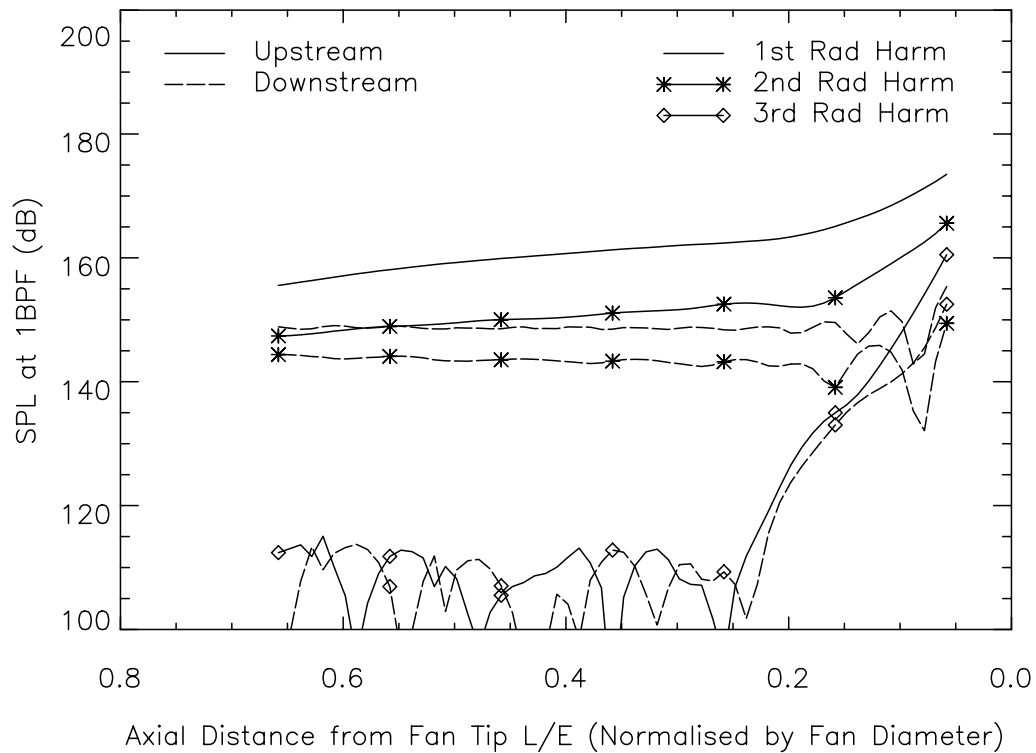
Figure 3. Steady CFD for Rotor Alone Noise: First Three Radial Harmonics of Upstream and Downstream Waves

Figure 3 shows upstream and downstream wave components of the noise for the first three radial harmonics at the first blade passing frequency. The third harmonic is cut-off and will be discussed later. The first two harmonics are cut-on, and Tyler and Sofrin's linear method would predict propagation at constant amplitude. The upstream waves, however, decay considerably, especially in the vicinity of the fan. Fig 4 shows the first radial harmonic, compared with Morfey and Fisher's 1D non-linear decay theory (Morfey and Fisher 1970). The agreement is not expected to be exact, given the assumptions implicit in the 1D calculation. However, the relatively close agreement near the fan suggests that the decay is in the main genuine and due to non-linear effects. The less good agreement further from the fan is thought to be due to the increasingly coarse grid away from the fan, which has the effect of attenuating the higher circumferential harmonics.

Figure 4. Steady CFD for Rotor Alone Noise, Comparison of First Radial Harmonic with Morfey-Fisher 1D Non-linear Decay Theory

The downstream travelling waves (dashed lines in fig 3) are lower amplitude and are less affected by non-linear decay. Hence they travel at more nearly constant amplitude over the majority of the domain. The high ratio of reflected to incident amplitude at the inlet to the domain confirms that the boundary conditions are indeed behaving poorly. The upstream wave amplitude, however, allows a quantitative noise estimate to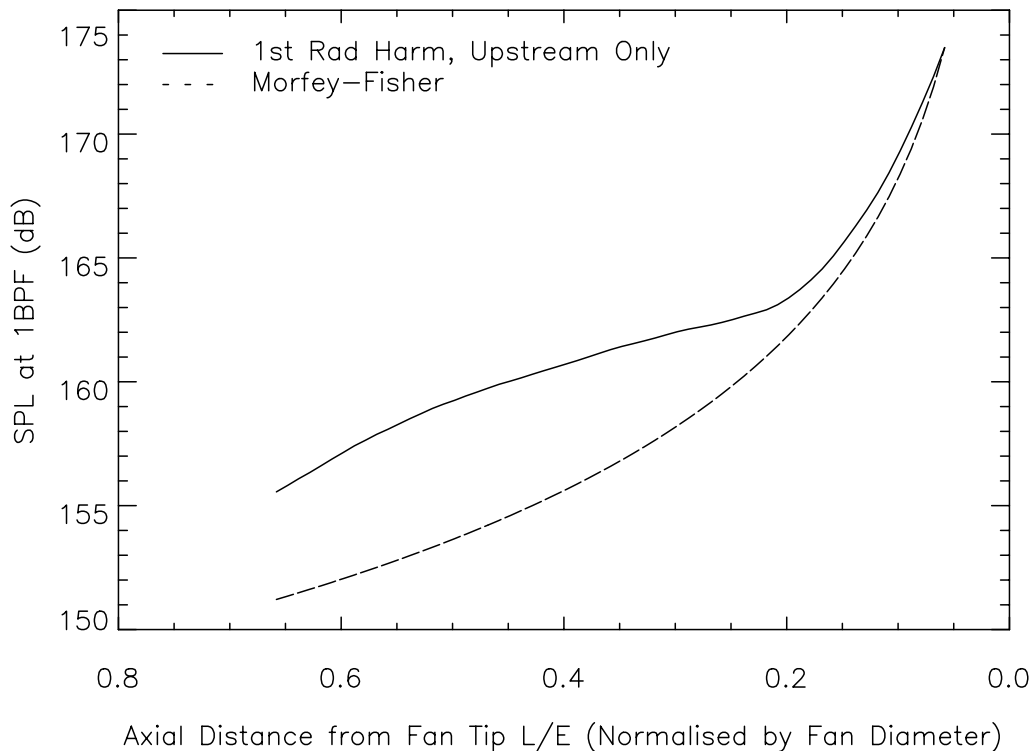 be obtained without contamination from these reflected waves, provided that the response of the fan to the downstream waves can be ignored. In this particular case the non-linear decay is sufficient to mask any minor changes in source amplitude, and the result is unlikely to be affected by the presence of the reflected waves.

The oscillations in amplitude of the reflected waves near the fan leading edge are a result of the assumptions in the mathematics of the wavesplitting. The relationship between pressure and velocity as calculated by the CFD code are slightly different to the analytic values, due to discretisation effects and the assumptions inherent in the analysis. Hence there is a limit to the extent to which upstream and downstream waves can be discriminated. This can be a particular problem near the cut-off boundary, as explained under example 2. The results in figure 3 show that upstream and downstream waves of this type can be discriminated to within 15-20dB of the higher signal amplitude.

The third harmonic shown in figure 3 is cut-off, and decays rapidly with axial distance to a 'floor' level of around 110dB. This floor level is set by 'leakage' between radial harmonics. The actual propagating modes in the calculation are not pure Bessel-Fourier harmonics, both because of discretisation effects and because the mean flow is not uniform. Hence the Bessel-Fourier breakdown in the wavesplitting process calculates some content at all radial harmonics even if only one mode is present. Nonetheless, the discrimination between radial modes (over 40dB from the first harmonic amplitude to the 'floor' level in fig 3) is more than sufficient for most purposes.

The reason for the poor discrimination between upstream and downstream waves near the domain exit at this third harmonic is not known. Typically (away from the cut-off point itself) reasonable discrimination is obtained for both cut-on and cut-off waves.

Figure 5 shows the amplitude of the upstream component of the third harmonic compares well with the exponential decay predicted in Tyler and Sofrin's theory.
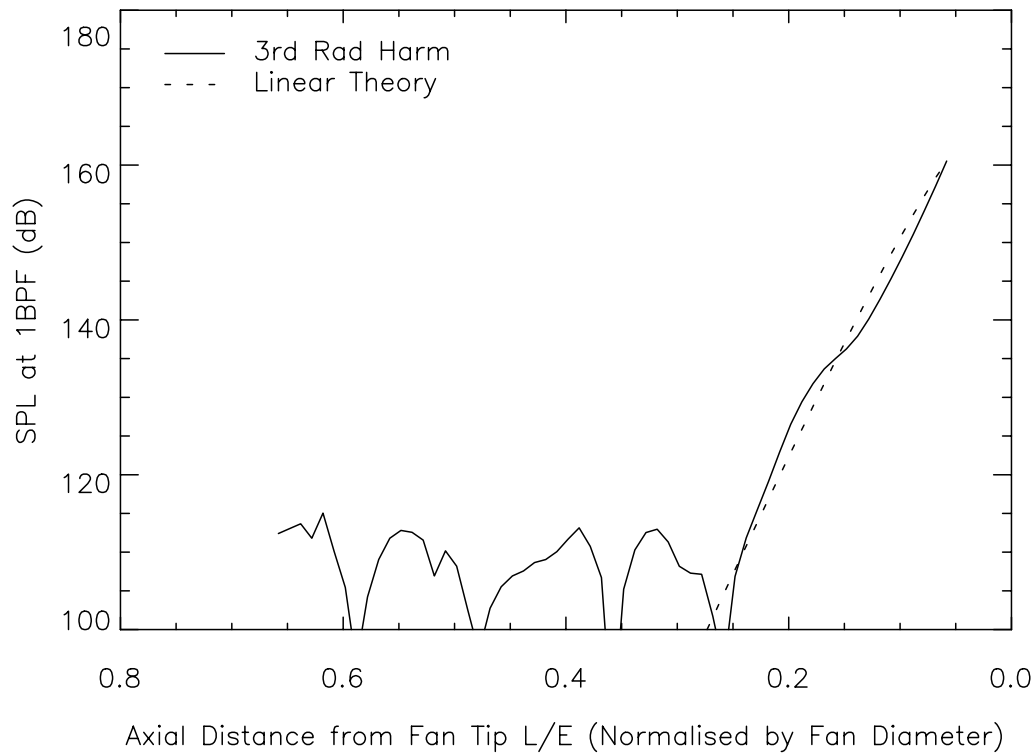
Figure 5. Steady CFD for Rotor Alone Noise, Comparison of Third Radial Harmonic Upstream Travelling Wave with Linear Theory

The noise output of the fan can only be estimated in the region where the mesh is sufficiently fine. In this case, the noise output (fig 3) is 163dB SPL in the first radial harmonic, 152dB in the second, and negligible output in the third and higher harmonics, all at a position 0.2 diameters upstream of the fan. Note that this figure could not easily have been obtained from either the wall pressure or the harmonic breakdown of pressure alone (fig 2).

Figure 4 suggests that there is still significant non-linear behaviour upstream of the 0.2m point. Depending on the use to which the data is to be put, it may be important to contain the non-linear behaviour within the CFD domain. In this case a second CFD calculation would be required with increased mesh density in the upstream region.

To summarise, in this first example the wavesplitting method has been used

- to demonstrate that the observed oscillations in pressure are due to reflections from the inlet boundary and interference between radial harmonics,
- to match the behaviour of the CFD solution to expectation and hence to give confidence in the solution,
- to gauge the significance of non-linear effects, and
- to obtain a quantitative measure of the fan-forward rotor alone noise in the presence of significant reflections from the upstream plane.

Method

The post-processing required for the wavesplitting method can be broken down into the following steps:

1. Fourier transform in time (non-linear unsteady CFD codes only).
2. Interpolate onto axial planes.
3. Decompose into Bessel-Fourier harmonics.
4. Calculate linear propagation parameters at each axial plane based on average mean flow.
5. Use linear theory to split Bessel-Fourier harmonics into upstream and downstream components.

It can be useful, in comparing the relative strengths of the radial harmonics, to add a sixth step:

6. Calculate acoustic energy flux for upstream and downstream components.

In linear theory with uniform axial mean flow and parallel annulus ducts (Tyler and Sofrin 1961), cut-on modes propagate with uniform amplitude and cut-off modes with exponential decay. Both types propagate with phase varying linearly with axial distance. The decay rates and axial wavenumber are calculated at step 4, and so by plotting amplitude on a log scale (eg as SPL) and phase on a linear scale, it is easy to compare the modal behaviour with theory. Variations from linear behaviour can then be easily identified and subjected to further analysis, as demonstrated in the examples above and below.

Step 1. Fourier transform in time.

Both the theoretical linear calculations and the wavesplitting require data at fixed position and fixed frequency. In steady CFD calculations on rotor blades the frequency is fixed by the circumferential harmonic (that is, a first blade passing harmonic in the circumferential direction will be heard at first blade passing frequency by a stationary observer). In linear unsteady calculations the frequency is fixed in the frame of reference of the CFD domain, and again the frequency in the stationary domain can be easily calculated for a given circumferential harmonic. In non-linear calculations a Fourier transform in time is required first to obtain data at a given frequency. Such a transform is easily calculated given a periodic converged solution.

Step 2. Interpolate onto axial planes.

Some care is required in this step, particularly in the presence of shocks, where a simple linear interpolation can lead to shock smoothing. In cases with structured or semi-structured grids, greater accuracy can sometimes be obtained by applying a circumferential FFT first (that is, to bring the first part of step 3 forward), and then to interpolate axially for amplitude and phase at a given plane.

Step 3. Decompose into Bessel-Fourier harmonics.

This process consists of a Fourier transform circumferentially, followed by a Bessel function decomposition in the radial direction. The latter is aided by the orthogonality condition (appendix 1). The choice of flow variables to be decomposed depends on the type of wavesplitting technique to be employed, as described under step 5.

Step 4. Calculate linear propagation parameters at each axial plane based on average mean flow.

The linear propagation parameters (axial wavenumbers for upstream and downstream propagating waves) are calculated for each circumferential and radial harmonic, based on a duct with parallel annulus walls and uniform axial mean flow (appendix 1). Given the approximations of the method a simply calculated Mach number based on area average axial velocity and temperature (or equivalent) at each axial plane is sufficient to define the equivalent mean flow.

Step 5. Use linear theory to split Bessel-Fourier harmonics into upstream and downstream components.

This step is not always necessary. In particular if the boundary conditions in the CFD calculation are known to be genuinely non-reflective, and the duct in which the analysis is being performed is fairly uniform, then the noise can be assumed to be travelling in a single direction only, and the pressure information alone is sufficient. In many cases, however, the effect of the boundary conditions and duct geometry is not known at acoustic wavelengths and frequencies, and this step is required.

Two methods of performing the wavesplit are detailed in appendix 1. The first, simpler method uses just the pressure and the axial velocity from the CFD solution, and is based on the assumption of irrotational flow (that is in total, not just irrotational mean flow). This is often a good approximation in the inlet duct. It is unlikely to be sufficient in the OGV exit duct, or in other calculations where vortical waves are prominent in the flow solution. Boundary conditions too (even if termed non-reflective) can introduce vorticity at the inlet plane.

The second method is still based on the assumption of uniform axial mean flow, but allows for vortical waves in the solution. This method is more complex, using the divergence of the flowfield to remove the effects of vorticity.

Step 6. Calculate acoustic energy flux for upstream and downstream components.

Usually the most useful quantitative output from the analysis method is the noise amplitude (SPL) in the different circumferential and radial harmonics. Sometimes, however, it is useful to compare the noise generated in the different harmonics, or to combine the results into a single figure. Tester (1972) gives a formula (reproduced in appendix 1) for acoustic energy flux based on the same uniform axial flow and parallel duct assumptions as the theoretical calculations in step 4 and the irrotationality assumption of the first method in step 5. The calculation can be applied directly to the interpolated flow variables at each axial plane at step 2, but it can also be applied to the upstream and downstream components of the individual circumferential and radial harmonics. Under the given assumptions these behave independently for cut-on modes (that is, the total energy flux is the sum of the constituents). For cut-off modes energy is

transported by combinations of upstream and downstream propagating waves, and thus the calculation has to be performed prior to the wavesplit.

By summing the energy flux over all the modes in one direction only (upstream or downstream), it is possible to calculate an overall source level in the cut-on modes disregarding any waves reflected from the boundary of the CFD domain.

Example 2: Unsteady CFD, Boundary Conditions, Dissipation Errors

This example comes from an investigation into non-reflective boundary conditions. Two separate 3D unsteady linear calculations were performed in a parallel annulus duct with two types of boundary condition at the inlet (Giles type 1D and 2D non-reflecting, Giles 1990, Saxer and Giles 1993). A uniform rectangular grid was used, with 61 points axially and 41 points circumferentially and radially, representative of a short section of the inlet duct for a typical aeroengine fan at rig-scale (Outer diameter around 0.43m). The base flow for the linear calculation was set to be uniform axial flow, again representative of a fan inlet duct at transonic conditions. In each case a 26-lobed upstream travelling acoustic wave was input at the outflow boundary, and the output analysed using the method described in the previous section.

Figure 6 shows some of the results from the calculation with 1D non-reflecting boundary conditions. The input wave had constant amplitude radially. This implies content at all radial harmonics, and so it is unsurprising that the wall amplitude (solid line in Figure 6) varies considerably along the length of the duct. The total amplitude of the first radial harmonic (dashed line) also varies, due to reflections from the inlet boundary. When the wavesplitting process is applied using the static pressure and axial velocity (dotted line), the long lengthscale oscillations are removed, but more oscillations are present at a shorter lengthscale.

The oscillations in wave amplitude are the result of vorticity introduced by the boundary conditions at the inlet boundary. The reflected vortical waves interfere with the axial velocity field, preventing an accurate analysis of the acoustic waves. This effect can be removed by applying the wavesplit method using static pressure and the divergence of the velocity field (see appendix 1). The result of this analysis is shown as the dash-dot line in Figure 6. All oscillations have been removed, leaving a uniformly decaying amplitude from which a quantitative estimate can be made of the dissipation error inherent in the numerical calculation (15dB per duct diameter). Similar calculations could be performed using the phase of individual waves to determine the propagation phase error.
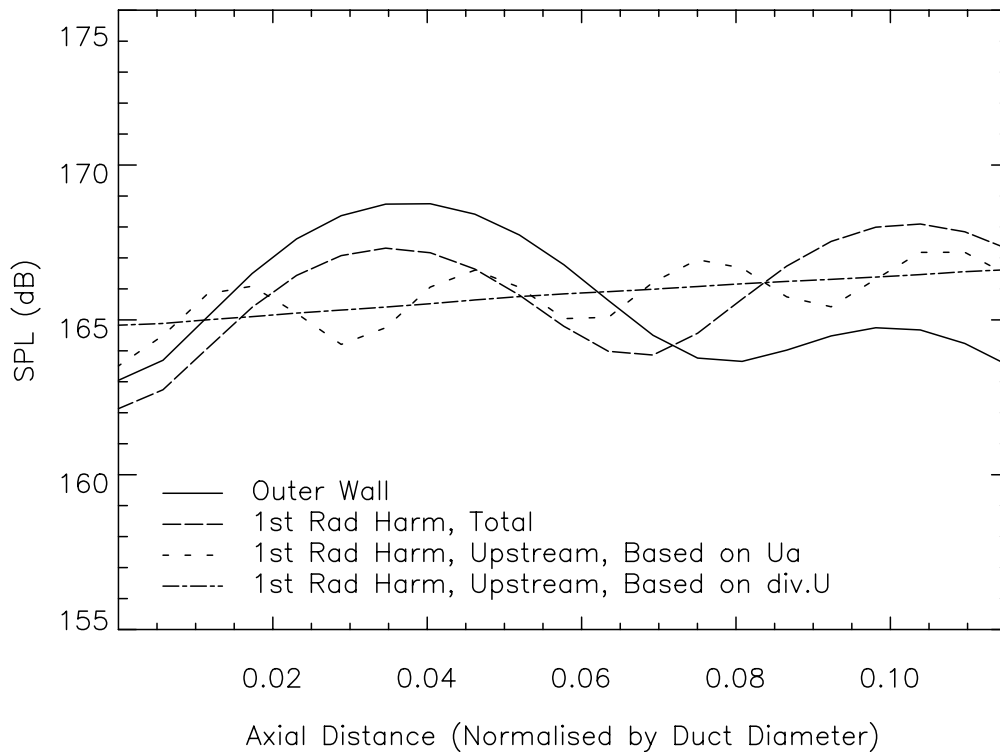

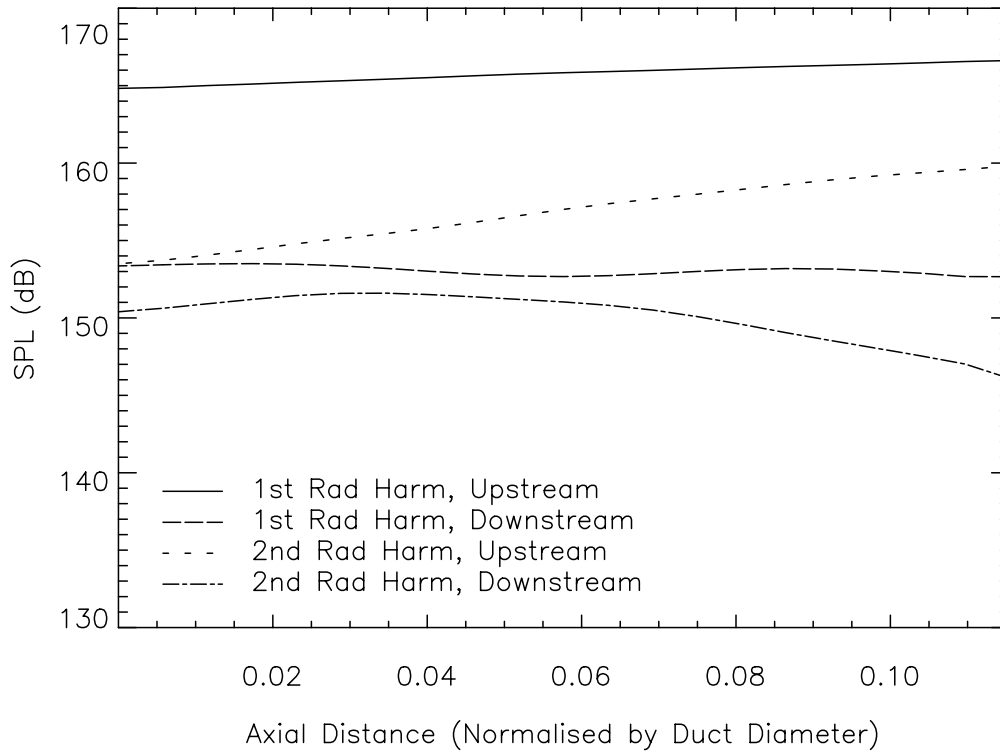**Figure 6. Unsteady CFD, Wavesplit Based on Ua and div.U**

Figure 7. Unsteady CFD: Upstream and Downstream Waves

Full results from the wavesplitting procedure at the first and second radial harmonics are presented in Figure 7. The second harmonic is very close to cut-off (cut-off ratio 1.01), and illustrates some of the difficulties commonly encountered close to the cut-on/cut-off boundary. The upstream wave shows an exceptionally fast rate of decay with axial distance, and the downstream wave in particular shows significant non-linear behaviour, in that the (log) amplitude varies non-linearly with axial distance.

Because information in near cut-off modes travels slowly along the duct there is more time for genuine non-linear and viscous phenomena to affect noise propagation between axial planes. The present calculations, however, were performed with an inviscid linear code, and so neither of these factors can explain the high decay rate of the upstream wave. The decay here is a result of the numerical smoothing applied in the CFD code.

In a CFD calculation smoothing is balanced by the rate at which the wave information travels upstream. Hence waves near cut-off tend to be heavily attenuated. The principle can illustrated using a simplistic 2D wave equation solved analytically with second order smoothing on the pressure term. Using the nomenclature defined in the appendix,

$$\frac{\partial \mathbf{u}}{\partial t} = -c\nabla p$$

$$\frac{\partial p}{\partial t} = -c\nabla.\mathbf{u} + \varepsilon\nabla^2 p$$

The level of smoothing ε is assumed to be small and fixed independently of the frequencies and wavelengths present in the solution. For a cut-on upstream plane wave at a given frequency ω it is possible to show (with some algebra) that to first order in ε the axial wavenumber of the smoothed wave is

$$\lambda = \hat{\lambda} + i\varepsilon\omega^2 / 2c^2 u_{\text{inf}}$$

where $u_{\text{inf}} = -c^2\hat{\lambda}/\omega$ is the rate at which information travels upstream, and $\hat{\lambda}$ is the axial wavenumber in the absence of smoothing. Thus the rate of decay with axial distance (determined by the imaginary part of the axial wavenumber) is $\varepsilon\omega^2 / 2c^2 u_{\text{inf}}$. Hence waves near the cut-off boundary ($u_{\text{inf}} \to 0$) are heavily attenuated.

In addition to the greater non-linear and smoothing effects, the wavesplitting process itself is liable to errors close to the cut-on/cut-off boundary. At this boundary the upstream and downstream linear waves

coalesce. In theory this could give large numerical errors in the wavesplitting solution (mathematically, f^{us} and f^{ds} get very close in equations 18, 19 of the appendix)[2]. In practice this is rarely a problem: even with a cut-off ratio of 1.01 there is sufficient discrimination to prevent large numerical errors.

Of much greater significance is the fact that the discrepancies between the CFD calculated modes and the analytical modes grow large near the cut-on/cut-off boundary. In the analytic axial mean flow formulation the axial wavenumber λ becomes very sensitive to flow conditions, and in particular to the cut-off ratio $\xi = \omega/c\mu\left(1 - U^2\right)$. Indeed, it can be seen from equation 7 of the appendix that at the boundary itself the derivative of λ with respect to ξ becomes infinite. It is unsurprising therefore that the analytic modes and those calculated by CFD (with non-uniform mean flow, smoothing and discretisation errors) can be very different near the boundary.

The following graph illustrates the problems that can occur near the cut-off boundary. The simple case is taken of a 2D wave equation solved using analytic derivatives in time and axially (x direction), but a simple central difference numerical derivative in the y direction. Forty points per wavelength were used, which is usually sufficient to give reasonable wave propagation. An exact modal solution to the numerical problem was calculated for a range of frequencies, to which the wavesplitting technique was applied. The graph shows the amplitude of the forward and reverse waves calculated by the method for points close to the cut-off boundary. As expected, the errors grow large close to the boundary, and very close to the boundary the calculated waves in both directions can be much larger in amplitude than the genuine wave. Note, though, that the errors are highly concentrated in the region of the boundary: away from this point (towards either cut-on or cut-off) the errors are small and the wavesplitting technique is successful.
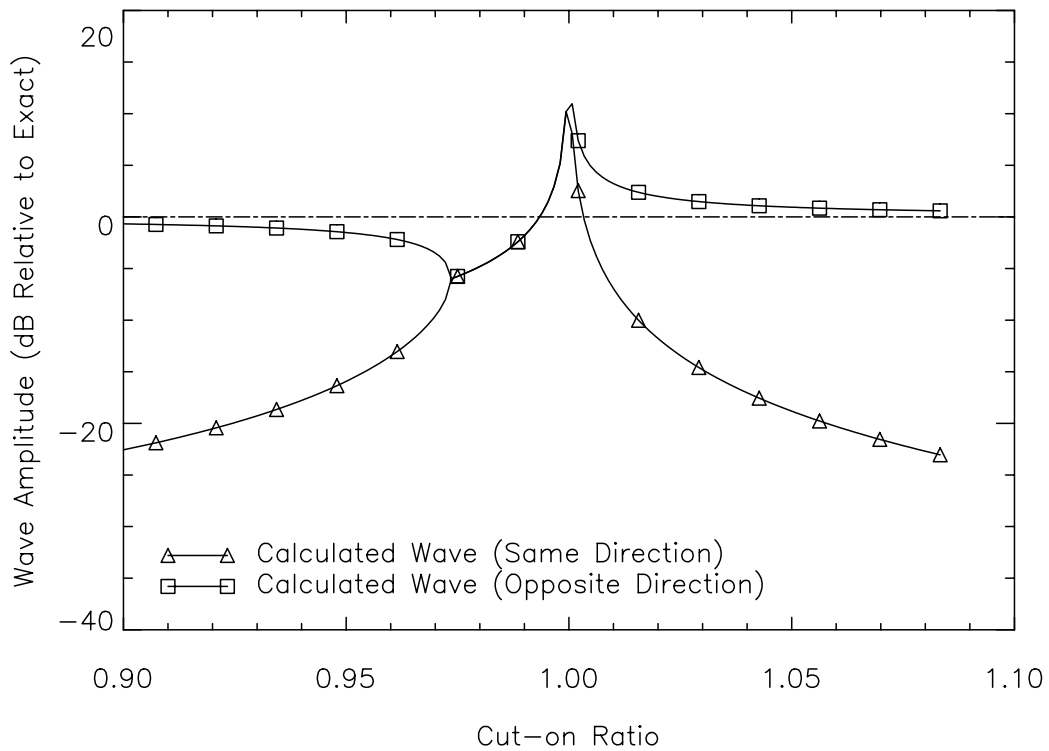
Figure 8. Errors in Wavesplitting Method Close to the Cut-Off Boundary

---

[2] With the second wavesplitting method, based on pressure and the divergence of the velocity, numerical errors could also cause a problem in regions of low or zero mean flow. This is because, although the axial wavenumbers of the upstream and downstream waves remain discrete with decreasing mean flow, the wavesplitting parameters f^{us} and f^{ds} (equation 22 of the appendix) become identical.

Returning to the CFD example, Figure 9 shows the results of the wavesplitting analysis for the 1D and 2D non-reflective boundary conditions. The 1D boundary conditions give a reflected wave with amplitude 11.5dB lower than the incident. The second radial harmonic, however, shows a reflection only 3dB lower than the incident (accepting the errors discussed above in the wavesplitting for this harmonic). Care has to be applied here, in that boundary conditions can scatter an incident wave at one radial harmonic into reflected waves at other harmonics. However, a more detailed analysis of the 1D non-reflective boundary conditions used in this case has shown that the downstream wave at the second radial harmonic is indeed a reflection of the same harmonic, rather than a scattered reflection from the first harmonic. The 2D non-reflective boundary conditions give a reflection of the first harmonic 30dB lower than the incident. This level is close to the level at which forward and backward waves can be discriminated, hence the oscillation with axial distance. The second harmonic is reflected at a level 4dB lower than the incident. A more detailed analysis of the boundary conditions has shown that this value would be 7.6dB without scattering from the higher amplitude first radial harmonic.

In both cases the high reflection coefficients for the second harmonic mirror the difficulty in wavesplitting close to the cut-off boundary.
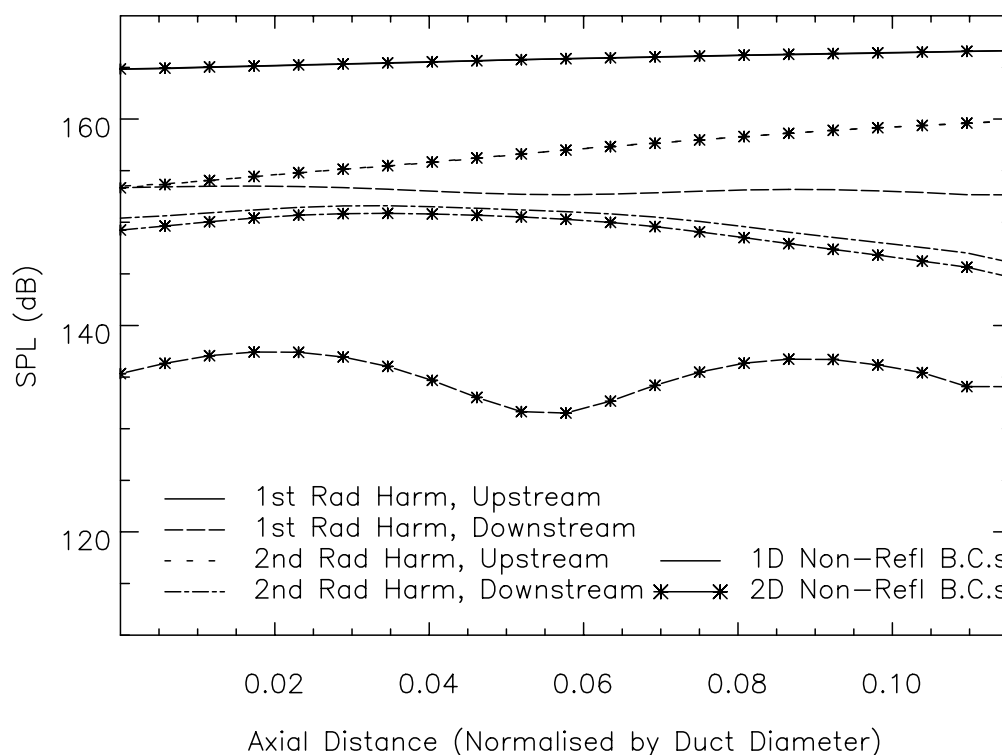
Figure 9. Unsteady CFD: Comparison of 1D and 2D Boundary Conditions

Further Example

The wavesplitting method has been applied to a flat plate wake/vane interaction case (Wilson 2001). In that work the method was also extended to provide fully 3D non-reflecting boundary conditions at inflow and exit.

Limitations

The major limitations of the analysis procedure have been identified as follows:

1) The method as it stands is unsuitable for use in regions where the propagating modes are known to differ strongly from Tyler and Sofrin modes. Examples are:
   a) Fan exit, where the high degree of swirl significantly affects the propagating modes.
   b) Lined ducts (although the method can still be applied in any hardwall regions upstream and downstream of the liner).
2) The method gives poor results close to the cut-on/cut-off boundary (as discussed under example 2).

3) The wavesplitting method based on pressure and axial velocity is limited to regions of irrotational flow. This can be a good approximation in the fan inlet region, subject to the boundary conditions at the inlet plane producing negligible vorticity. This limitation can be overcome by using the second wavesplitting method, based on pressure and the divergence of the velocity.

Summary

A procedure has been developed for deriving tone noise information from CFD solutions in the fan stage. A wavesplitting method is used at a number of axial locations upstream of the fan to derive upstream and downstream wave information from the CFD calculated flowfield. The development of these waves with axial distance is then compared to well-understood linear behaviour.

The method is equally applicable to the bypass duct downstream of the outlet guide vane (where, like the inlet, the mean flow is approximately axial). Application to other areas is subject to the limitations outlined in the previous section.

Examples have been given of how the method can be used

- to identify regions of non-linear behaviour
- to identify and eliminate the effect of modest spurious reflections at the domain boundaries
- to identify and eliminate the effect of modest vortical waves present in the solution
- to quantify numerical dissipation errors

and hence

- to quantify tone noise generation.

References

Giles MB, 1990, *Non-Reflecting Boundary Conditions for Euler Equation Calculations*, AIAA Journal, Vol 28, No. 12, pp 2050-2058

Cantrell RH, and Hart RW, 1964, *Interaction between Sound and Flow in Acoustic Cavities: Mass, Momentum and Energy Considerations*, J.A.S.A. Vol 36, No. 4, pp697-706

Morfey CL and Fisher MJ, 1970, *Shock-Wave Radiation from a Supersonic Ducted Rotor*, J. Roy. Aeron. Soc., vol 74, pp579-585

Rowley CW and Colonius T, 1998, *Numerically Nonreflecting Boundary Conditions for Multidimensional Aeroacoustic Computations*, AIAA 98-2220, presented at 4th AIAA/CEAS Aeroacoustics Conference, Toulouse, June 2-4

Saxer AP, and Giles MB, 1993, *Quasi-Three-Dimensional Nonreflecting Boundary Conditions for Euler Equations Calculations*, Journal of Propulsion and Power, March-April (No. 2), pp263-271

Tester BJ, 1972, *Sound Attenuation in Lined Ducts Containing Subsonic Mean Flows*, PhD Thesis, Univ. Southampton,

Tyler JM and Sofrin TG, 1962, *Axial Flow Compressor Noise Studies*, Trans S.A.E., Vol 70, pp309-332

Wilson AG, 2001, *Application of CFD to Wake/Aerofoil Interaction Noise – A Flat Plate Validation Case*, AIAA-2001-2135, presented at 7th AIAA/CEAS Aeroacoustics Conference, Maastricht, 28-30 May

Appendix 1 – Mathematics of Wavesplitting Technique

Nomenclature

U	Mean flow speed (assumed axial) normalised by speed of sound
$\bar{p}$	Mean flow pressure
$\bar{\rho}$	Mean flow density
c	Speed of sound based on mean flow pressure and density
u	Perturbation velocity normalised by speed of sound
p	Perturbation pressure, normalised by $\gamma\bar{p}$
γ	Ratio of specific heats (assumed constant)

Wave Solutions of the Euler Equations in Parallel Annulus Ducts

The linearised Euler equations for a perfect gas with constant ratio of specific heats and uniform mean flow in the *x* direction can be expressed as

$$\frac{1}{c}\frac{\partial \mathbf{u}}{\partial t} + U\frac{\partial \mathbf{u}}{\partial x} = -\nabla p \tag{1}$$

$$\frac{1}{c}\frac{\partial \rho}{\partial t} + U\frac{\partial \rho}{\partial x} = -\nabla.\mathbf{u} \tag{2}$$

Together with the equation of state and the energy equation this represents five equations in five unknowns. The wave solutions (that is, solutions for the flow variables that preserve their shape axially) are well known, and correspond to two acoustic waves, two vorticity waves and a single entropy wave.

For a parallel wall annular duct the acoustic waves can be written as

$$\mathbf{u} = \nabla\phi \tag{3}$$

$$\phi = ip/(\omega/c - U\lambda) \tag{4}$$

where $p = p_{m.k.\omega} \exp i(\omega t - \lambda x - m\theta)B_m^k(r)$ (5)

and $B_m^k(r)$ is a combination of the J- and Y-type Bessel functions:

$$B_m^k(r) = aJ_m\left(\mu_m^k r\right) + bY_m\left(\mu_m^k r\right), \tag{6}$$

where *a*, *b* and μ_m^k are chosen to satisfy the boundary condition $\mathbf{u}_r = \dfrac{\partial \phi}{\partial r} = 0$ on both the inner and outer

walls. If no routine is available to give these functions, a method is outlined later which requires only evaluation of the individual Bessel functions.

For each circumferential harmonic *m* and radial harmonic *k* there are two possible axial wavenumbers λ defined by

$$\lambda = \frac{-U\,\omega/c \pm \sqrt{(\omega/c)^2 - \mu_m^{k\,2}\left(1 - U^2\right)}}{1 - U^2} \tag{7}$$

λ is either real or complex depending on the sign of the term under the square root. It is convenient to consider the two cases separately:

Cut-on waves (λ real)

It can be seen from equation 5 that if λ is real, then the wave propagates axially at constant amplitude and varying phase. For forward subsonic mean flow $0 < U < 1$, the negative root in equation 7 corresponds to an upstream travelling wave, whilst the positive root corresponds to a downstream wave. Note that with mean flow $U > 0$ it is possible for λ to remain negative even for the downstream travelling wave. In this

case the wavefront is angled in the same direction as the upstream wave and indeed appears to move upstream. The group velocity, however, defining the direction in which information is transported, is still downstream, as is the transport of energy.

Cut-off waves (λ complex)

If λ is complex, then the wave decays exponentially in the direction of propagation. For forward subsonic mean flow $0 < U < 1$, the root of equation 7 with positive imaginary part represents an upstream wave decaying with upstream distance, and the root with negative imaginary part represents a downstream wave decaying with downstream distance. The phase variation is fixed by the first term in equation 7, which is independent of m and k. Hence all cut-off waves have the same 'spiral angle' (that is, the same rate of change of phase with axial distance).

In each case, the two roots of equation 7 correspond to one upstream and one downstream wave. Entropy and vorticity waves make no contribution to the pressure, and so at a given frequency ω, circumferential mode m and radial harmonic k, the entire unsteady pressure field can be written as the sum of the contributions from the two acoustic waves:

$$p = \left[p^{us}(x) + p^{ds}(x)\right] \exp i(\omega t - m\theta)B_m^k(r), \text{ where} \tag{8}$$

$$p^{us} = cst.\exp\left(-i\lambda^{us}x\right)$$
$$p^{ds} = cst.\exp\left(-i\lambda^{ds}x\right) \tag{9, 10}$$

Thus if p^{us} and p^{ds} are known at any single axial plane, then their (theoretical) values can be calculated at any other plane. Two methods are given below for splitting the unsteady pressure into its upstream and downstream components, depending on whether or not the flow can be assumed irrotational.

Wavesplitting in Irrotational Flow

The velocity and pressure perturbations of individual acoustic waves are linked by equations 3 and 4. Entropy waves, furthermore, make no contribution to either pressure or velocity. Hence for each harmonic (ω, m, k) the axial velocity can be derived from the upstream and downstream components of pressure (equ 8) as follows:

$$u_x = \left[u_x^{us}(x) + u_x^{ds}(x)\right] \exp i(\omega t - m\theta)B_m^k(r), \text{ where} \tag{11}$$

$$u_x^{us} = f^{us}p^{us}$$
$$u_x^{ds} = f^{ds}p^{ds}$$
$$f^{us} = \lambda^{us}/\left(\omega/c - U\lambda^{us}\right)$$
$$f^{ds} = \lambda^{ds}/\left(\omega/c - U\lambda^{ds}\right) \tag{12, 13, 14, 15}$$

Of more interest is the inverse process, whereby the upstream and downstream components can be determined from the static pressure and axial velocity. If at a given axial plane and these two variables are decomposed into Bessel-Fourier harmonics, with coefficients p', u', then

$$p' = p^{us} + p^{ds}$$
$$u_x' = u_x^{us} + u_x^{ds} = f^{us}p^{us} + f^{ds}p^{ds} \tag{16, 17}$$

Hence

$$p^{us} = \left(f^{ds}p' - u_x'\right)/\left(f^{ds} - f^{us}\right)$$
$$p^{ds} = \left(f^{us}p' - u_x'\right)/\left(f^{us} - f^{ds}\right) \tag{18, 19}$$

Wavesplitting in the Presence of Vortical Waves

In the presence of vortical waves the previous wavesplitting method fails, because the axial velocity is no longer a function of the acoustic waves alone. Hence another method is presented here, based on pressure and the divergence of the velocity field ($\nabla \cdot \mathbf{u}$). Note that this method too is based on the assumption of a uniform axial mean flow. Thus, whilst small amounts of vorticity can be handled using this method, it is not suitable for highly vortical flows such as those found between an aeroengine fan rotor and outlet guide vane.

The divergence of the velocity for acoustic waves can be calculated from the two pressure coefficients (equs 9, 10) using equ 4;

$$
\begin{aligned}
\nabla \cdot \mathbf{u}^{us} &= \nabla^2 \phi^{us} \\
&= -\left(\lambda^{us\,2} + \mu_m^{k\,2}\right)\phi^{us} \\
&= -\left(\lambda^{us\,2} + \mu_m^{k\,2}\right)ip^{us}\big/\left(\omega/c - U\lambda^{us}\right) \\
&= f^{us} p^{us}
\end{aligned}
\tag{20}
$$

where $f^{us} = -i\left(\lambda^{us\,2} + \mu_m^{k\,2}\right)\big/\left(\omega/c - U\lambda^{us}\right).$ $\qquad$ (21)

With some manipulation, this can be reduced to

$$
f^{us} = -i\left(\omega/c - U\lambda^{us}\right),
\tag{22}
$$

and similarly for the downstream waves.

Both $\nabla \cdot \mathbf{u}$ and p are identically zero for vorticity and entropy waves. Hence the upstream and downstream components can be obtained from $\nabla \cdot \mathbf{u}$ and p in an identical manner to the irrotational case (equs 16 to 19), but with $\nabla \cdot \mathbf{u}$ instead of u_x, and the new definitions of f^{us}, f^{ds}.

$\nabla \cdot \mathbf{u}$ can be calculated directly from the CFD solution using a simple difference sum. A refinement is to use the flow equations (1, 2) to remove the axial derivative of the velocity, such that the wavesplit can be performed using only data from a single axial plane. The following analysis is for isentropic flow, although the result also holds in the presence of entropy waves.

For isentropic flow, given the normalisation used, the continuity equation (2) can be expressed in terms of pressure:

$$
\frac{1}{c}\frac{\partial p}{\partial t} + U\frac{\partial p}{\partial x} = -\nabla.\mathbf{u} = -\overset{2D}{\nabla}.\mathbf{u} - \frac{\partial u_x}{\partial x},
\tag{23}
$$

where $\overset{2D}{\nabla}.\mathbf{u} = \frac{1}{r}\frac{\partial(ru_r)}{\partial r} + \frac{1}{r}\frac{\partial u_\theta}{\partial \theta}.$ $\qquad$ (24)

But from the axial component of the momentum equation (1),

$$
\frac{\partial p}{\partial x} = -\frac{1}{c}\frac{\partial u_x}{\partial t} - U\frac{\partial u_x}{\partial x}
\tag{25}
$$

Substituting this into equ 23, and applying a transform in the time direction $\dfrac{\partial}{\partial t} \rightarrow iw,$

$$\frac{iw}{c}p + U\left(-\frac{iw}{c}u_x - U\frac{\partial u_x}{\partial x}\right) = -\overset{2D}{\nabla}.\mathbf{u} - \frac{\partial u_x}{\partial x}$$

$$\Rightarrow \frac{\partial u_x}{\partial x} = -\left(\overset{2D}{\nabla}.\mathbf{u} + \frac{iw}{c}(p - Uu_x)\right)\Big/(1 - U^2) \tag{26}$$

$$\Rightarrow \nabla.\mathbf{u} = \overset{2D}{\nabla}.\mathbf{u} + \frac{\partial u_x}{\partial x} = -\left(U^2\overset{2D}{\nabla}.\mathbf{u} + \frac{iw}{c}(p - Uu_x)\right)\Big/(1 - U^2)$$

Thus to calculate $\nabla \cdot \mathbf{u}$ from data at a single axial location, it is necessary only to calculate the radial and circumferential derivatives in equ 24 and to substitute the result together with values for p and u_x into the equation above. Note that the circumferential derivative is trivial, as the data has previously been Fourier transformed. In the radial direction a simple finite difference method is often sufficient.

The use of a simple finite difference sum and the inclusion of the analytic flow equations do make the method somewhat approximate. Nonetheless, provided the vortical waves are of similar amplitude to the acoustic waves (or smaller) it is effective in isolating the acoustic component, as illustrated by example 2 of the main paper.

Acoustic Energy Flux

Tester (1972) gives an equation for modal energy flux with uniform axial mean flow (based on that of Cantrell and Hart, 1964). In the current nomenclature, at any given frequency,

$$I_{xmk} = \frac{\overline{\rho}c^3 B_{mk}^2}{2}\mathrm{Re}\left\{p_{mk}u_{mk}^* + M_x p_{mk}p_{mk}^* + M_x^2 p_{mk}u_{mk}^* + u_{mk}u_{mk}^* M_x\right\} \tag{27}$$

where p_{mk} and u_{mk} represent coefficients of pressure and axial velocity at a single circumferential (m) and radial (k) harmonic at the given frequency. The term

$$B_{mk}^2 = \int B_m^k(r)^2.2\pi r\mathrm{d}r \tag{28}$$

has been added to integrate the energy flux over the area of the duct (note that $B_{mk}^2 = \int B_m^k(r)^2.2\pi r\mathrm{d}r$ is purely real in this equation).

If the (m,k) mode is cut-on, then the upstream and downstream travelling waves are orthogonal with respect to the above equation. That is, the total energy flux in the mode is the sum of that calculated from just the upstream and downstream travelling components. If the mode is cut-off, then the upstream and downstream travelling waves interact to give energy flux, and the calculation has to be performed prior to the wavesplit.

Given the orthogonality of the radial harmonics, the total acoustic energy flux in a given circumferential harmonic m can also be calculated by integrating the radial profiles directly:

$$I_{xm} = \frac{\overline{\rho}c^3}{2}\int\mathrm{Re}\left\{p_m u_m^* + M_x p_m p_m^* + M_x^2 p_m u_m^* + u_m u_m^* M_x\right\}2\pi r\mathrm{d}r \tag{29}$$

where p_m and u_m now represent radial profiles of pressure and axial velocity components at the mth circumferential harmonic. Provided that a single value of M_x is used (rather than a radial profile) the result is equal to the sum of equ 27 over all radial harmonics k.

Calculation of $B_m^k(r)$

If no routine is available to give these functions, a method is outlined here which requires only values of the Bessel functions themselves and a method of hunting for zeros.

The boundary conditions require

$$\frac{\partial B_m^k}{\partial r} = a\mu_m^k J_m'\left(\mu_m^k r\right) + b\mu_m^k Y_m'\left(\mu_m^k r\right) = 0 \ \text{ at } \ r = r_1, r_2$$

$$\Rightarrow \quad aJ_m'\left(\mu_m^k r_1\right) + bY_m'\left(\mu_m^k r_1\right) = 0$$
$$aJ_m'\left(\mu_m^k r_2\right) + bY_m'\left(\mu_m^k r_2\right) = 0$$

(30, 31, 32)

This only has non-zero solutions for *a, b* if

$$J_m'\left(\mu_m^k r_1\right) Y_m'\left(\mu_m^k r_2\right) = Y_m'\left(\mu_m^k r_1\right) J_m'\left(\mu_m^k r_2\right).$$

(33)

Using the recurrence relationships

$$2J_m'(z) = J_{m-1}(z) - J_{m+1}(z) \ \text{ and } \ 2Y_m'(z) = Y_{m-1}(z) - Y_{m+1}(z)$$

(34, 35)

this equation can be rewritten

$$\left(J_{m-1}\left(\mu_m^k r_1\right) - J_{m+1}\left(\mu_m^k r_1\right)\right)\left(Y_{m-1}\left(\mu_m^k r_2\right) - Y_{m+1}\left(\mu_m^k r_2\right)\right) -$$
$$\left(Y_{m-1}\left(\mu_m^k r_1\right) - Y_{m+1}\left(\mu_m^k r_1\right)\right)\left(J_{m-1}\left(\mu_m^k r_2\right) - J_{m+1}\left(\mu_m^k r_2\right)\right) = 0$$

(36)

Viewing this as a function of μ_m^k, the values that are able to satisfy the boundary conditions can thus be found by hunting for zeros. The ratio *b/a* can be found by applying the boundary condition (30) at either the inner or the outer wall. The amplitude and phase of the remaining constant (*a* or *b*) is arbitrary. A convenient practical choice is to set the value at the outer wall to unity, $B_m^k(r_{ow}) = 1$. In this way, the coefficient of the pressure represents the value that would be measured by a microphone at the outer wall in the absence of other radial harmonics.

This page has been deliberately left blank

_____

Page intentionnellement blanche

Investigation on the Capability of a Non Linear CFD Code to Simulate Wave Propagation

Pedro de la Calzada
Pablo Quintana
Manuel Antonio Burgos
ITP, S.A.
Parque Empresarial Fernando
avenida Castilla 2
Edificio Japon
E-28830 San Fernando de Henares, Madrid
Spain

Abstract

The potential wave propagation is described by defining the driving parameters of the propagation characteristics. Then a parametric study with a non linear code is performed in order to define the mesh refinement needed to obtain a sufficient accuracy in the predictions of inflow and outflow perturbation propagation. The results are compared with a linear version of the code as well as with a linear code for flat plate response showing the good behaviour of the non linear code. As additional test cases, the behaviour of the code for simulating the response o a cascade of flat plates to potential disturbances is investigated. Results from the different linear and non linear codes are also compared. Different cases are investigated including one with large resonances, which is shown to be the most difficult case to be predicted, in special the resonance peaks as well as the trailing edge region regarding the wave phase behaviour.

1 Introduction

The principal aircraft and engine manufacturers in Europe are facing increasing pressure to reduce aircraft noise levels. Regarding the noise from engines, low pressure turbine (LPT) noise is becoming more important due to the decrease of jet noise with the high by pass ratio cycles and lower noise from the advanced design fans and negative scarfed intake angles. In a LPT, the interaction of unsteady flow with the turbine blading produces fluctuating forces along the blades and results in unwanted effects such as noise and forced vibration. Such excitations are mainly generated at multiples of the blade passing frequency and arise from a variety of sources. The two principal types of such interaction are usually referred to as potential flow and wake interaction. The former is associated with unsteady pressure variations generated by the upstream and downstream rows and could be of serious concern when the axial spacing between neighbouring blade rows are small or flow Mach numbers or excitation frequencies are high. The wake interaction is due to vortical perturbations generated by wakes convected from the viscous flow on upstream rows.

Trying to understand the generation of noise by the mechanisms above presented, simulation of unsteady aerodynamics with linear and nonlinear CFD codes is an ongoing activity within the turbomachinery industry. However, the accurate resolution of the unsteady aerodynamics and acoustics on low pressure turbines remains a formidable computational problem. This is due mainly to the spatial resolution required to accurately simulate the incoming waves (potential and vortical fluctuations) and the radiated cut-off and cut-on waves, even in the case that only the 2D problem is considered. Traditionally linear codes have been used in the simulation of unsteady flows in turbomachinery. This approach allows the use of relatively coarse meshes and they need less computational effort when compared with non linear Euler solvers. However they assume that perturbations are small when compared with steady variables and they need to solve a new set of equations for the unsteady variables. This approach has been taken by many authors ([1] and [2] among others).

A different approach is taken at ITP, where a non linear unstructured Navier Stokes solver is intended to be used for resolution of both the steady and unsteady aerodynamics and acoustics, that will allow the use

of only one code to solve both problems coupled. This seems to be the current approach taken by some other authors to simulate wake-boundary layer interaction [3] and to simulate potential interaction [4].

For this investigation an in-house code, with the non linear MU^2S^2T and linear MU^2S^2TL versions is used. An extensive investigation on the different parameters involved in the propagation of waves is being carried out with the objective to assess the mesh resolution requirement and the capability of the solver to accurately simulate wave propagation and unsteady response of blade rows.

The results will be presented in an step by step approach, from the different parameters involved in noise propagation to the comparison with analytical linear solution of a flat plate response to incoming disturbances.

2 Theoretical background of the wave propagation

The equation governing the unsteady velocity potential for small deviations for an uniform, isentropic and irrotational mean flow has the following expression.

$$\frac{\partial^2 \Phi}{\partial t^2} - 2 \cdot \frac{M}{c} \cdot \frac{\partial^2 \Phi}{\partial x \partial y} + (1 - M^2) \frac{\partial^2 \Phi}{\partial x^2} + \frac{\partial^2 \Phi}{\partial y^2} = 0 \ (1)$$

that has expression of the type

$$\Phi = \sum \sum A_{n,j} e^{i(\omega_n t + k_{yj} y + k_{xn,j} x)} \ (2)$$

as solution.

For turbomachinery kind of flow fields, the temporal and circumferential eigenvalues are

$$\omega_n = n\Omega \ (3)$$

$$k_{yj} = \frac{2\pi j}{\lambda_y} \ (4)$$

and a expression for the axial wave number

$$k_{x_{n,j}} = \frac{M_x(k_{yj}M_y + \frac{\omega}{c}) \pm \sqrt{(k_{yj}M_y + \frac{\omega}{c}) - k_y(1 - M_x^2)}}{1 - M_x^2} \ (5)$$

From (5), the resonance frequency can be defined as

$$\omega_r = \frac{ck_{yj}(1 - M^2)}{\sqrt{M_y \pm (1 - M_x^2)}} \ (6)$$

defining the cut-off ratio as

$$\xi = \frac{\omega}{\omega_r} \ (7)$$

Ratios higher that unity give, according to (5), the so call cut-on waves (waves propagating with constant amplitude), while ratios lower than unity give cut-off waves (exponentially decaying waves in axial direction).

For cut-on waves, the wavelength in axial direction can be defined

$$\lambda_x = \frac{2\pi}{k_{x_{n,j}}} \ (8)$$

for a propagation wave number

$$k = \frac{2\pi}{\sqrt{\lambda_x^2 + \lambda_y^2}} \quad (\,9\,)$$

3 Wave propagation simulation with CFD

From the expressions derived above, it can be easily seen that the physical characteristics of the propagation of a potential wave depends on the following parameters.

$$\Phi = f(U_x, U_y, \rho, T, R_g, \gamma, \mu, \omega, \lambda_y) \quad (\,10\,)$$

Where ψ stands for any unsteady fluid variable.

That involves longitudes, time, mass, temperature and angular quantities. If the speed of sound c, Rg, the wave length λ_y and the density ρ are taken for nondimensionalization, the problem is reduced to

$$\Phi = f(M_x, M_y, \xi, \mathrm{Re}) \quad (\,11\,)$$

Mx and My are mach number in x and y direction, ξ is the cut-off ratio, or the ratio of axial to circumferential wavelength (that involves also the Mach numbers, but gives the axial propagation characteristics), and Re states for the Reynolds number based in the wavelength λ_y.

If the propagation is to be simulated with a CFD code, parameters implicit to the code will be also relevant to the problem. These parameters have to do with the time and space discretization as well as the scheme used for the stabilization of the system of equations.

$$\Phi = f(M_x, M_y, \xi, \mathrm{Re}, CFL, \sigma 2, \sigma 4) \quad (\,12\,)$$

Other set of characteristics in the simulation of the wave propagation are the parameters depending on the definition of the mesh employed for the computation, typically Ny cells in y direction and Nx cells in axial direction. For wave propagation, is of interest to define n_y and n_x as the points per circumferential and axial wavelength respectively.

$$\Phi = f(M_x, M_y, \xi, \mathrm{Re}, CFL, \sigma 2, \sigma 4, n_x, n_y) \quad (\,13\,)$$

In real turbomachinery problems, potential and vortical wakes perturbations are present. As this paper is focused on potential disturbances, that are not affected by definition by the Reynolds number, no analysis on this parameter will be done here. Regarding the effect of the artificial viscosity parameters included in the code for stabilization, namely σ2 and σ4, their effect will not be investigated since has been already investigated on the same code by Corral et al. [6] . Nevertheless some conclusions of their work will be used and commented here. The only effect of the CFL number on wave propagation is computing time and no further results on the simulation will be presented here.

Therefore the parametric investigation will cover the dependence of the results on the following parameters:

$$\Phi = f(M_x, M_y, \xi, n_x, n_y) \quad (\,14\,)$$

In addition, studies on the effect of the quasi-structured versus fully unstructured meshes has been performed. For this analysis, quasi-structured meshes composed of quadrilateral cells with one preferred diagonal direction have been used.

In the Figure 1, the results for a potential perturbation imposed in the outlet, with a ξ ratio of 5.0, M=0.4 are displayed. Due to the high propagation angle of the wave, the simulation presents a low number of

points per axial wavelength and the results present a deficient prediction of the cut-on wave (the mesh has 80 points in circumferential direction and approximately 10 points per axial wavelength). Furthermore the Figure 1 shows that there is some effect of the chosen diagonal direction on the damping of the propagating wave.
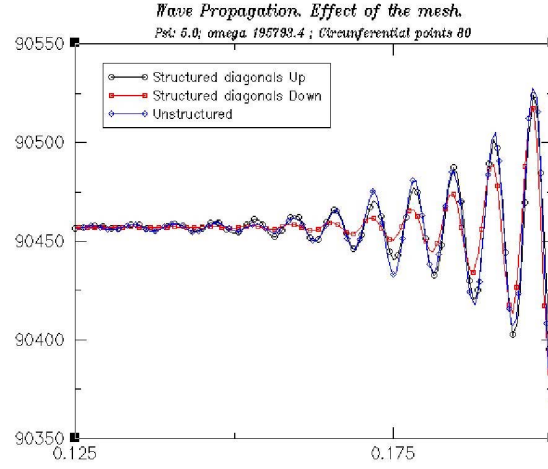

Figure 1: *Effect of the mesh. ξ: 5.0, ω:195793.4 rad/sec, outlet perturbation*

In turbomachinery noise, several circumferential modes are usually propagated, and therefore the effect of a preferred diagonal direction would have a different effect on each mode, hence worsening the accuracy of the simulation for some of the modes. In order to avoid that, the use of fully unstructured meshes is recommended, trying to minimise the numerical dissipation of the propagation waves due to cell structure.

All the computations shown in this study have been performed using the scalar dissipation model. Therefore limiting the test cases to a range on Mach number of 0.3<M<0.7. However when having very low or high subsonic Mach numbers the matricial dissipation model should be used, that has been already shown by to significantly improve the simulation of propagation of entropy and pressure waves which are more damped when using a more classical scalar model.

One of the critical features involved in the simulation of wave propagation with CFD is the numerical boundary conditions implemented. As recognised by other authors [1], the 1D unsteady non reflecting boundary conditions (UNRBC) are insufficient for an accurate simulation of propagating waves in short domains, and therefore more elaborated boundary conditions are needed. In this investigation, the 1D and 2D UNRBC by Giles [7] have been implemented and their influence on the wave propagation is shown.
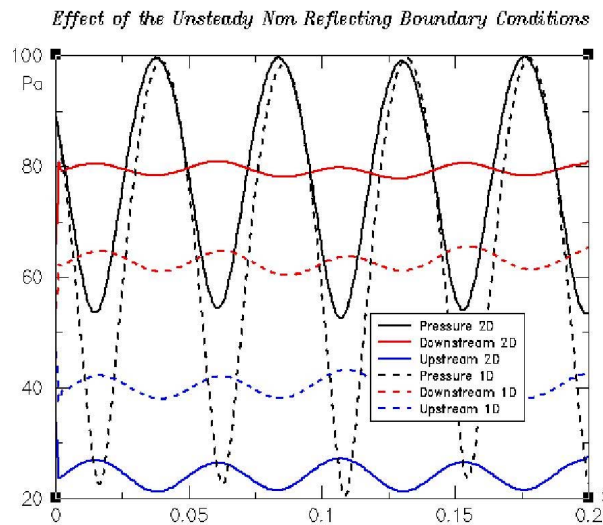

Figure 2: *Effect of UNRBC with ξ: 1.1, M: 0.4*

Figure 2 shows that in the case of the 1D non reflecting boundary conditions, the reflection can be up to 60 % of the downstream wave, giving a constructive interference and a pressure field with peak to mean values close to 50 % higher. In all the analysis presented hereafter, 2D non reflecting boundary conditions will be used.

The effect of the cut-off ratio ξ has been investigated through the simulation of different cut-off and cut-on waves. To avoid crossed effects with the mesh definition, all the simulations have been carried out with the same mesh.

For the postprocessing, the wave splitting technique proposed by Wilson [8], has been implemented, which allows to investigate in detail the behaviour of downstream and upstream waves, by means of eigenvalues and eigenfunctions.

Figure 3 shows results of some simulations of waves with ξ=0.7, 1.1, 3.0 and 5.0 imposed both in the inlet an in the outlet, with ny=80 points and Nx constant to 320 points
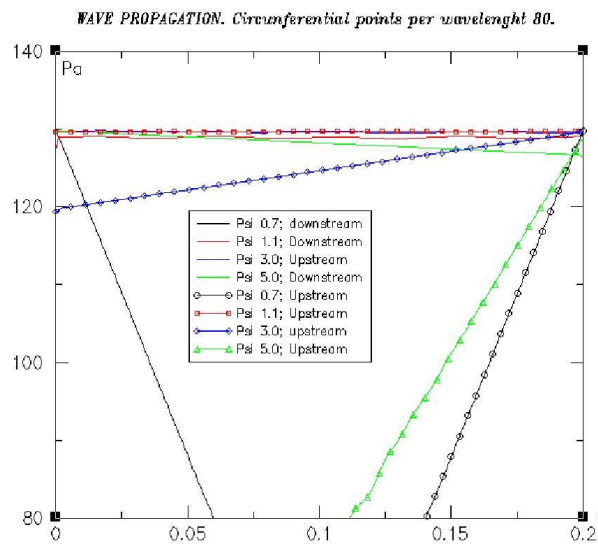

Figure 3: *Wave propagation for ξ: 0.7, 1.1, 3.0, 5.0 and ny: 80 points. Nx: 320 points*

As it can be seen, the waves with frequency ratios of 0.7, 1.1 and 3.0 are in general well simulated, with an small axial decay. A cut-off wave as the one with ratio 0.7 is also well simulated, with a linear decay of 0.5237 dB/m for downstream propagating waves and 0.5127 dB/m for upstream propagating waves (versus a theoretical decay of 0.5315 dB/m). Nevertheless, the waves with ξ ratio of 5.0 present deficient prediction. All the simulations have the same circumferential wavelength and number of points per circumferential wavelength n_y but different frequency to have the desired cut-off ratio. This change in frequency changes the propagation characteristics of the wave and therefore a lower number of point per axial wavelength are available as the cut-off ratio increases (for inlet perturbation).

ξ ratio	1.1	3.0	5.0
Points per axial wavelength n_x	3569	40	22.5

Table 1 *Points per axial wavelength for ξ =0.7, 1.1, 3.0, 5.0 with Nx=320 points*

Looking at Table 1 and Figure 3 it is shown that the accuracy of the simulation decreases with the number of points per axial wavelength, n_x.

In addition, this accuracy of the wave propagation prediction shown above decreases if a coarser mesh is used for the simulation, with different worsening depending on the ξ ratio (due to the different propagation angles and the resulting number of points per wavelength). This last effect is clearly seen in Figure 4, which shows the results of upstream and downstream running waves for inlet and outlet perturbations with ξ=3.0, n_y=20, 40 and 80 points per wavelength, and N_x/N_y=1.0

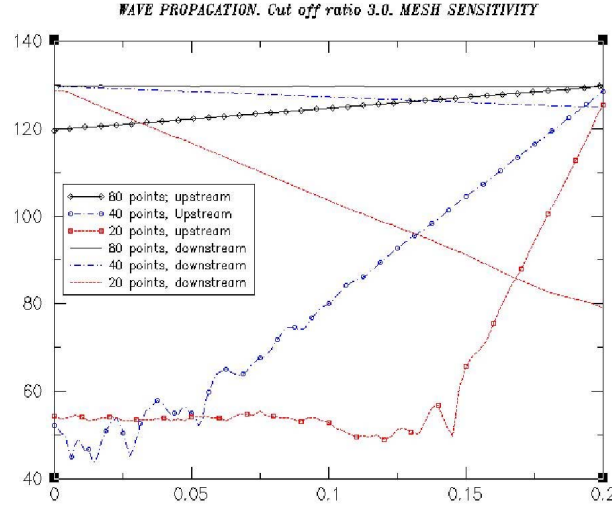WAVE PROPAGATION. Cut off ratio 3.0. MESH SENSITIVITY

Figure 4: *Mesh sensitivity in the simulation of the propagation of a 3.0 cut off ratio wave*

The figures shown above illustrate how the numerical results of the wave propagation depend strongly on both the number of points per axial and circumferential wavelength. In an effort to unify the effects of n_y and n_x, Wilson [9] proposed the analysis of wave propagation by means of an average points per wavelength

$$n_{av} = \frac{n_x n_y}{\sqrt{n_x^2 + n_y^2}} \quad (15)$$

parameter that weights the least defined direction.

The analysis of all the simulations computed shows that the dB decay per wavelength depends strongly on the average points per wavelength, in a correlation close to the 3rd order between the error and the points per wavelength. Taking 0.050 dB decay per wavelength as threshold for acceptable accuracy, at least 40 average points are required for the accurate simulation of propagation waves. From this average points per wavelength needed, it raises as the final conclusion that at least 50 points per wavelength in circumferential and axial directions are required for acceptable accuracy.

The effect of the mach numbers in the range 0.3<M<0.7 can be included in the above mentioned analysis, as the damping suffered by a wave (either upstream or downstream potential wave as well as vorticity waves) traversing the physical domain is moderated. In this case, the effect of the mach number will be a change in the axial propagation characteristics of the wave, that can be covered with the mesh analysis performed above.

However, when Mach number is higher than 0.7, demonstrated that upstream potential fields are highly damped due to the slow propagation velocity of such waves. In such a case, the previous accuracy analysis is not valid. In order to overcome this damping, matricial viscosity was implemented in the code, to reduce damping of the upstream running waves. If this matricial viscosity is used, then the accuracy analysis shown before is also valid for high mach numbers. Results of these simulations with the MU^2S^2T code can be found in [6].

4 Flat plate response

After analysing the characteristic parameters of the wave propagation when simulated with CFD codes, the next step is the interaction of a propagating wave with an isolated profile.

Before going into detail of the CFD results, an analysis of the parameters involved in the problem is performed.

The physical characteristics of a flat plate response to unsteady perturbations depend on the following variables

$$\Phi = f(l, t, d, \lambda_y, U_x, U_y, \omega, \rho, T, R_g, \gamma, \mu) \quad (16)$$

that involves longitudes, time, mass and temperature. Taking the pitch distance between blade rows d, the flow velocity U, the speed of sound and Rg for non dimensionalization, the following parameters are found.

$$\Phi = f(\frac{l}{d}, \frac{t}{d}, \frac{\lambda_y}{d}, M_x, M_y, St, \text{Re}) \quad (17)$$

where St stand for the Strouhal number $St = \dfrac{f \cdot l}{U}$

Tyler and Sofrin first studied the interaction between blade rows [10], showing that ratio of the wavelength to the passage pitch can only take certain values depending on the blade and vane number.

The theory presented in section 2 can be extended to rotor-stator interaction, if the span of the blade rows is small compared with the hub radius, which is an standard approximation in turbomachinery. In this case, the curvature of the duct passage is small, and therefore circumferential direction can be assumed to be the y direction, with

$$y = R \cdot \theta$$
$$k_{yj} = m_j \theta \quad (18)$$

Any unsteady variable take the following form

$$\Phi = \sum \sum A_{n,j} e^{i(\omega_n t + m_j \theta)} \quad (19)$$

The wave field in the stator frame must be invariant when θis increased the angular pitch of the stator Δ=2π /V and t is increased by Δ/Ω, due to the unsteady swirling perturbations with angular velocity Ω .

This forces the mode number, m, to be

$$m = kV - nB \quad (20)$$

In the stator frame of reference, the response should be circumferentialy periodic with period Δ=2π /V. Imposing that in (19), gives the following expression for the interblade phase angle (IPA).

$$\sigma = -\frac{2\pi B}{V} = -\frac{2\pi d}{\lambda_y} \quad (21)$$

Taking this into account, expression (17) takes the following form

$$\Phi = f(\frac{l}{d}, \frac{t}{d}, \sigma, M_x, M_y, St, \text{Re}) \quad (22)$$

As done in section 3, the Reynolds number will not be taken into account as the study will be limited to potential disturbances.

Within the different profile characteristics, the flat plates present the advantage that a semi-analytical solution of the unsteady response can be obtained with the approach presented by Whitehead [5] by means of a linearized solution of the fluid equations (LINSUB). Therefore, this study will make use of this results, and the effect of the profile $\frac{t}{d}$ thickness to the pitch length will be left for further studies.

The effect of the Strouhal number has a quite clear physical sense, meaning the ratio between the characteristic time of the unsteadyness, in this case $\dfrac{1}{f}$ of the incoming wave, and the characteristic time for the fluid to travel along the length of the plate. Results from LINSUB showing this effect on the plate response are shown in Figure 5.
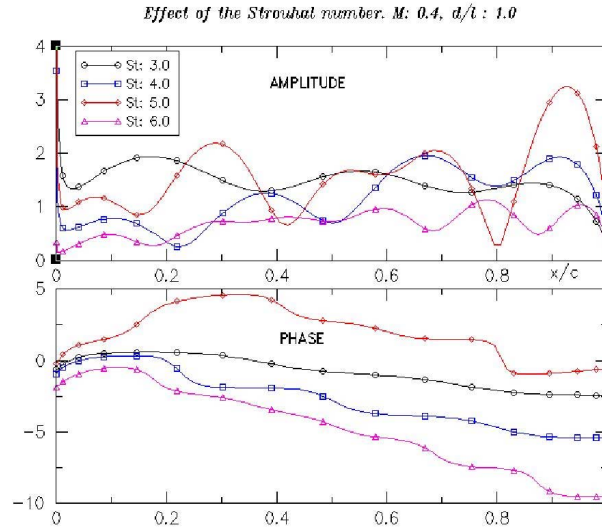

Figure 5: *Effect of the Strouhal number St on a flat plate*

The number of peaks in the flat plate is approximately equal to the Strouhal number, reflecting that the flow changes St times before leaving the flat plate channel.

However, for low or high mach numbers, this characteristic is distorted due to the compressibility/incompressibility effects. Figure 6 illustrate this effect for perturbations with St=5.0 and IPA 270 degrees.
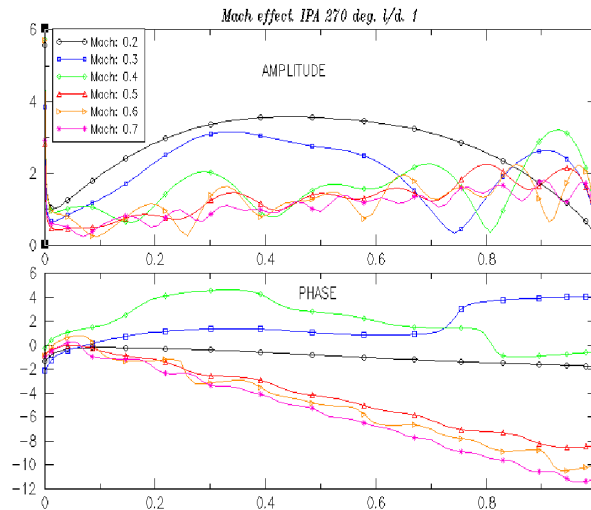

Figure 6: *Effect of the Mach number on a flat plate response*

The response of the plate at high mach numbers presents more peaks but the peak to mean level of the response is lower, while the opposite behaviour takes place at low mach numbers. This is thought to be due to compressibility effects damping the response while making easier the transmission of pressure waves at high mach numbers.

In (21) was shown that the IPA depends on the number of blades and vanes of the stage. Additionally the IPA also reflects the ratio of the circumferential wavelength of the incoming disturbance to the

distance between the flat plates. The effect of this ratio is shown in Figure 7, for the case of a wave with ξ=3.0, and a flat plate cascade of d/l =1 and a Strouhal number of 6.836
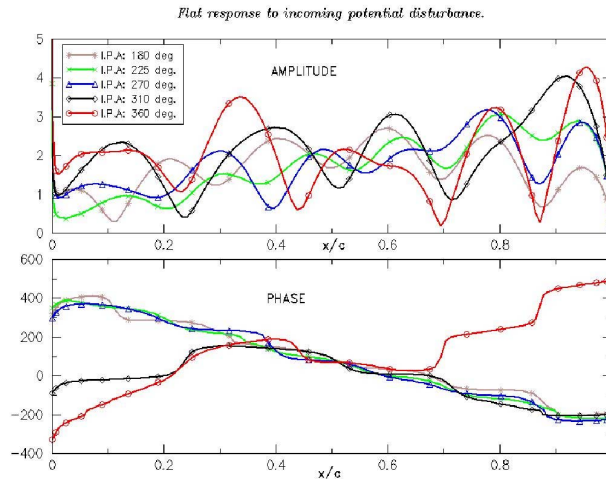

Figure 7: *Flat plate response for different interblade phase angles*

As previously explained, with M=0.4 the amplitude modulation along the blade row presents six peaks for all the interblade phase angle analysed. Nevertheless, as the interblade phase angle of the wave is increased, the peak to mean value of the amplitude modulation increases, to a maximum at 360 degrees. If the phase profile is analysed, it can be seen that the phase modulation is similar in all the cases studied but in the case of 360 degrees, for which a different trend is obtained.

According to Woodley & Peake [11] [12], when unsteady excitations interact with a blade row (either vorticity waves convected due to wakes or downstream-propagating pressure waves) at high frequencies, resonance on the blade row can take place giving a large amplitude response. This kind of behaviour is known as Parker-mode-type resonance, and according to [11] [12], the resonance appears only under certain combination of parameters (Mean flow Mach number, stagger angle, frequency, and blade and vane number).

To test the capability of the codes to simulate the response of the flat plate, a circumferential mode 30 resulting from the interaction of 90 rotating blades with 60 staggered flat plates was computed. The mean flow mach number of 0.4 giving a ξ ratio of 3.0 with and interblade phase angle of 180 degrees. The Strouhal number is set to 6.836 and the pitch to chord ratio to 1.0. In order to ensure a good propagation characteristics, the results from the initial investigation are used to set the grid definition upstream and downstream of the wave.
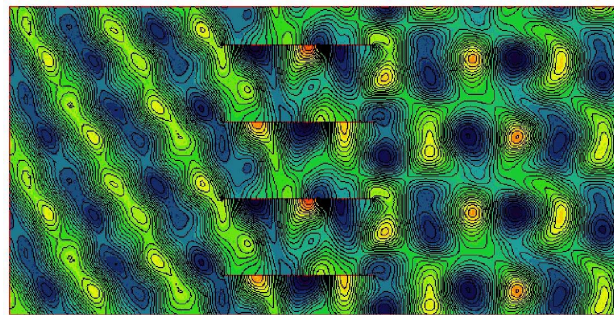

Figure 8: *Pressure field for a 60 plates configuration with I.P.A 180 º, M=0.4, d/l=1.0 and St=8.636*

In Figure 8 the resulting flow field is shown. The wave propagates with an angle close to 75º, impinging in the flat plate. The wave keeps on propagating in the channel between plates and is radiated downstream of the row where multiple interaction between modes gives the complex pattern of the figure.
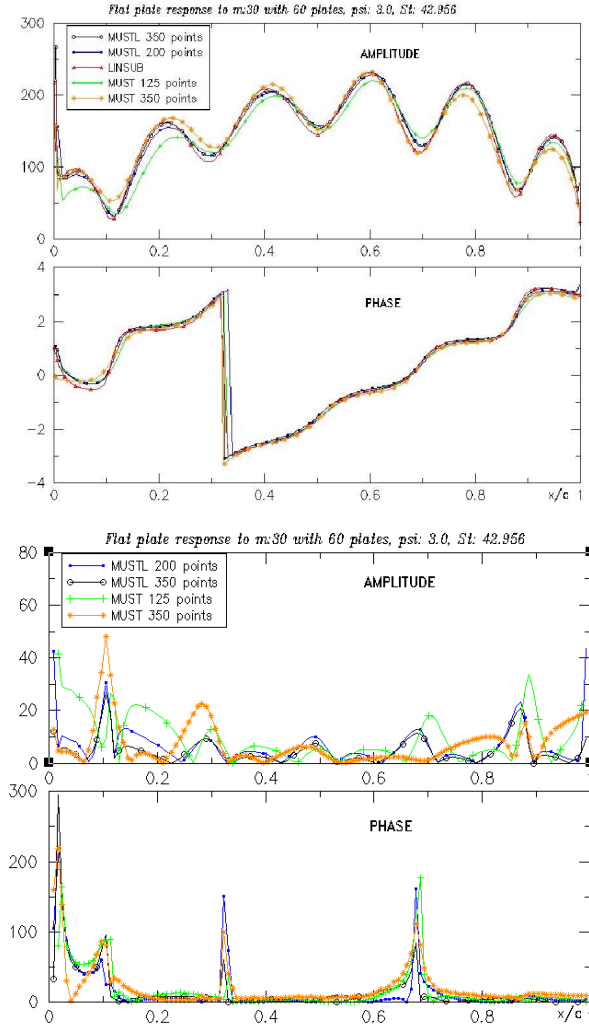
Figure 9: *Flat plate response for incoming disturbance with interblade phase angle 180 degrees. Top: Actual Values. Bottom: Percentage Relative Error*

The results of the flat plate response are shown in Figure 9.

The top graphic shows how the interaction between the flat plates and the wave is well simulated by both the linear and non linear version of the MU^{2}S^{2}T code. The six peaks resulting on the response are reproduced by all the computations, and good agreement with the phase is achieved. The greater differences take place close to the leading edge, probably due to the difficulties on the numerical modelization of the leading edge. Test cases with lower Strouhal numbers have shown lower effects of the boundaries on the plate response. In this case, due to the large Strouhal number, the flat plate response presents high complexity, making the influence of the leading edge significant. In the rest of the plate length, differences are below 10 % of the values predicted by LINSUB, with lower values as the mesh definition is refined. In Figure 9 is also reflected the higher accuracy of the linear with respect to the non-linear version of the code for the same number of points in the flat plate. Table 2 displays the mean error values for the amplitude and phase profiles with respect to the LINSUB value

CASE	Points per Peak	Mean Percentage Error	
		Amplitude	Phase
MUSTL 200 points	33	6.3 %	11.5 %
MUSTL 350 points	58	4.6 %	12.0 %
MUST 125 points	20.8	9.8 %	20.9 %
MUST 350 points	58	7.3 %	17.2 %

Table 2: *Mean relative error values of MUST codes with respect of LINSUB as function of the points in the flat plate. Interblade Phase Angle 180 deg*

A more complex test case arises from the same perturbation with an interface blade angle of 360 degrees, as presented in Figure 7. In this case, the resonance makes the peak to mean response amplitude larger, while keeping the number of peaks constant with respect to the test case previously shown.

An interblade phase angle of 360º comes from a circumferential mode -30 resulting from the interaction of a 90 blade configuration with 90 flat plates. The Mach number 0.4, with Strouhal number of 6.836 and d/c=1.0 are kept as in the previous test case.
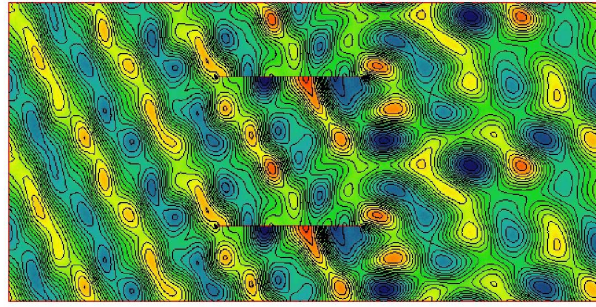

Figure 10: *Pressure field for a 90 plates configuration with I.P.A 360, M: 0.4, d/l: 1.0 and St: 8.636*

Figure 10 presents the resulting flow obtained. As in the previous test case, the potential wave impinges in the flat plate row with an angle close to 75 degrees. Due to the higher pitch distance between flat plates, the reflection pattern in the channel in between the plates is simpler than in the 180º IPA, with the travelling wave pattern still visible. Radiation downstream of the flat plate row gives a complex field of interactions.
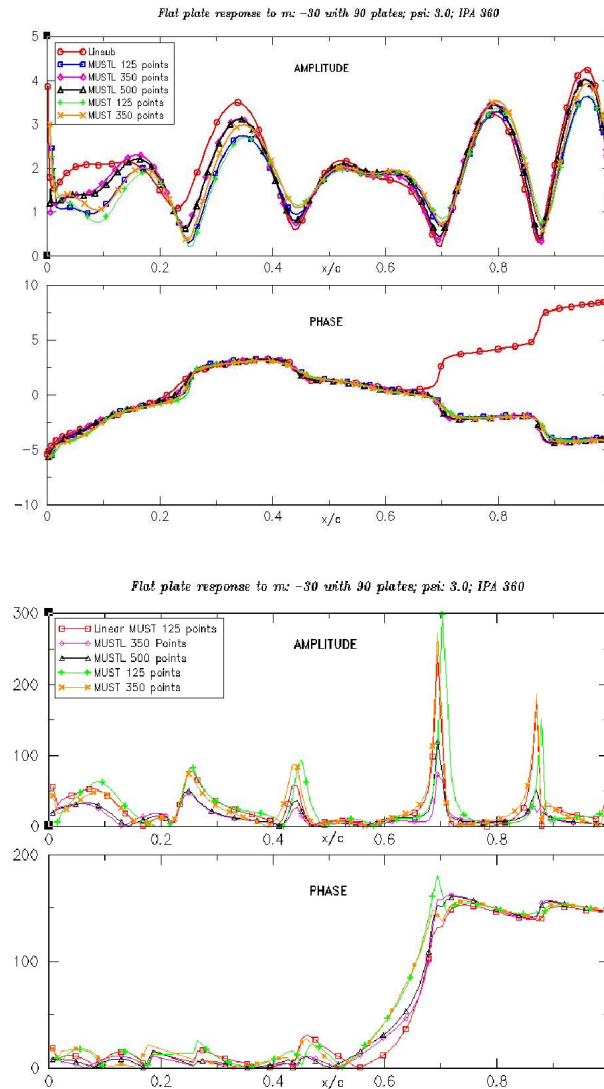

Figure 11*: Flat plate response for incoming disturbance with interblade phase angle 360 degrees.Top: Actual Values. Bottom: Percentage Relative Error*

The Figure 11 shows the flat plate response compared with the results from LINSUB for the linear and the non linear codes.

The top graphic shows how the interaction between the flat plates and the wave is well simulated by both the linear and non linear version of the MU^2S^2T code, accurately predicting the six peaks of the amplitude response. The differences reported in the area close to the leading edge also appear in all these simulations. Nevertheless, the correct peak to mean value is not reached with none of the simulations, not even with a finer mesh of 500 points in the flat plate.

The phase profile presents great differences in the area of the trailing edge, where none of the simulations is capable to reproduce the results obtained with LINSUB. The change in the trend of the phase variation is a phenomena observed already in other simulations, but that effect was removed with mesh refinement. Nevertheless, in this test case, most likely due to the high complexity of the plate response, the mesh refinement did not help to any improvement on the predictions accuracy.

The relative errors with respect to the LINSUB simulation clearly show how the differences along the plate are low (in the order of 20-25 %), except in the local maxima and minima of the amplitude response, where the relative error presents much larger peaks.

Table 3 displays the mean error values for the amplitude and phase profiles with respect to the LINSUB value

CASE	Points per Peak	Mean Percentage Error	
		Amplitude	Phase
MUSTL 150 points	25	26.2 %	59.8 %
MUSTL 350 points	58	13.9 %	59.1 %
MUSTL 500 points	83	15.5 %	60.1 %
MUST 150 points	25	28.4 %	66.3 %
MUST 350 points	58	26.8 %	65.4 %

Table 3 : *Mean relative error values of MUST codes with respect of LINSUB as function of the points in the flat plate. Interblade Phase Angle 180 deg.*

It can be seen how in both the linear and non linear versions of the MU^2S^2T code, the relative error decreases when the mesh is refined from 150 to 350 points. Surprisingly, when a very refined mesh with 500 points is employed, a worsening in the solution is found.

In all the simulations both amplitude and phase differences respect to LINSUB predictions are thought to be due to leading and trailing edge simulations. The plate edges effects on the plate response have been pointed out in [11] [12] to play an important role in the resonance behavior of cascades systems.

5 Conclusions

The basic principles of the wave propagation and flat plate interactions simulation have been shown.

It has been demonstrated that both cut-on and cut-off waves can be simulated with CFD codes. In order to ensure a correct modelization of the problem, fully unstructured grids with 2D non reflecting boundary conditions are recommended, since they have shown to have a major impact on the accuracy of the unsteady flow simulation. The main parameter of the accurate wave propagation simulation is the number of points per wavelength, both in circumferential and in axial direction. It has been shown that the effect of Mach number, flow angle, frequency and circumferential mode can be accurately predicted defining sufficient grid points per circumferential and axial wavelength. In case of high Mach numbers, this definition could be not enough to give the desired accuracy, and matricial viscosity should be used.

In the case of unsteady response of flat plates, the driving parameters have been shown. For the range of Mach numbers characteristic of low pressure turbines, the number of amplitude peaks can be determined with the Strouhal number. The amplitude of such response have be shown to be dependent on the interblade phase angle of the wave. Nevertheless, 60 points per response peak have been shown to give a sufficiently accurate response for all the interblade phase angles.

The behaviour of a non linear unstructured Navier Stokes solver for simulating wave propagation and transmission through a flat plate cascade have been studied and the results have been shown to reproduce the same level of accuracy than the linear version of the code (but with some more mesh refinement needed). The necessity of the implementation of 2D UNRBC for minimize the reflections of the wave has also been demonstrated.

6 Acknowledgements

7 Nomenclature

c: Speed of Sound, m/s

d: Pitch distance, m

k: Wave number

$k_{n,j}$: Axial eigenvalue, axial wave number, m^{-1}

k_{yj}: Circumferential eigenvalue, circumferential wave number, m^{-1}

m: Circumferential mode

n: Time harmonic

n_x: Number of points per axial wavelength.

n_y: Number of points per circumferential wavelength.

n_{av}: Average points per wavelength.

l: Profile length, m

t: Profile thickness, m

B: Blade number

CFL: Courant Friedrichs Lewy parameter

M: Mach number

N_x: Number of points in axial direction

N_y: Number of points in circumferential direction

R: Radius, m

Re: Reynolds Number

Rg: Gas constant

St: Strouhal number

T: Temperature, K

U: Mean flow velocity, m/s

V: Vane number

MU^2S^2T: Multirow Unsteady Unstructured Specific Solver for Turbomachinery

ω: Angular frequency, rad/s

ω_r: Resonance frequency, rad/s

λ_x: Axial wavelength, m

λ_y: Circumferential wavelength, m

σ: Interface Blade Angle (IPA), deg

ξ: Cut-off ratio

ρ: Density, kg/m^3

γ: Gas Constant

μ: Viscosity coefficient

$\sigma_2\sigma_4$: Artificial viscosity coefficients

Ω: Shaft rotational speed, rad/s

Ψ: Unsteady variable

Δ: Angular pitch, deg.

References

[1] A. G. Wilson. *Application of CFD to Wake/Aerofoil Interaction Noise- A Flat Plate Validation Case*. AIAA 2001-2135. May 2001.

[2] F. Kennepohl, G.Kahl, K. Heinig. *Turbine Blade/Vane Interaction Noise: Calculation with a 3D Time-Linearised Euler Method*. AIAA-2001-2152. May 2001.

[3] B. Lakshminarayana, A. Chernobrovkin, D. Ristic. *Unsteady Viscous Flow Causing Rotor-Stator Interaction in Turbines. Journal of Propulsion and Power*. Vol. 16, No, September-October 2000.

[4] G.A.Gerolymos, D. Vinteler, R. Haugeard, G. Tsanga, I. Vallet. *On the Computation of Unsteady Turbomachinery Flows. Part 2- Rotor/Stator Interaction using Euler Equations*. AGARD CP-571. May 1995.

[5] D.S. Whitehead. *Classical Two Dimensional Methods. Manual on Aeroelasticity in Axial Flow Turbomachines*, AGARD-AG-298, Vol. 1, Chap. III, 1987

[6] R. Corral, M.A. Burgos, A. Garcia. *Influence of the Artificial dissipation Model on the Propagation of Acoustic and Entropy Waves*. 45th ASME Gas Turbine and Aeroengine Congress. 8-11 May 2000

[7] M. B. Giles. *Nonreflecting Boundary Conditions for Euler Equation Calculations*. AIAA Journal, Vol. 28. No. 12, pp 2050-2058

[8] A. Wilson. *A method for Deriving Tone Noise Information from CFD Calculations on the Aeroengine Fan Stage*. To appear. 2000

[9] A.Wilson. *TurboNoiseCFD Deliverable 1.6: Review of Generic Studies*. 15 April 2001

[10] J.M. Tyler, T.G. Sofrin. *Axial Flow Compressor Noise Studies*. SAE Transactions, Vol 70, pp 309-332, 1962

[11] B.M.Woodley, N. Peake. *Resonant acoustic frequencies of a tandem cascade. Part 1. Zero relative motion*. J. Fluid Mech, Vol 393, pp 215-240, 1999

[12] B.M.Woodley, N. Peake. *Resonant acoustic frequencies of a tandem cascade. Part 2. Rotating Blade Rows*. J. Fluid Mech, Vol 393, pp 241-256, 1999

Reference # of Paper: 4
Discusser's Name: Dr. Jan Delfs
Author's Name: Mr. Pedro de la Calzada Mazeres
Question:
      What is the reason not to use a CAA approach such as that described by Professor Tam?
Answer:
      We are primarily interested in the prediction of the tonal noise due to stator-rotor interaction in turbines. For that, we need to solve first for the aerodynamics in order to accurately simulate the effect of both the potential field and the vortical wake convection. Our intention is to reduce the number of codes used in the simulation of the unsteady aero thermal behavior of turbine stages. Therefore we are concentrating our efforts to have only one code with the necessary features implemented to predict the unsteady and steady flow fields. We have updated our CFD code for the steady aero-thermal field in turbines and we want to keep this experience and improve the base code further. Therefore we are working on the code in the direction of CAA by improving the boundary conditions and the artificial viscous damping.
      Additionally, the modes and frequencies in which we are interested have long wavelengths on the order of the pitch in the circumferential direction. Thus, the mesh refinement needed to resolve the viscous boundary layer and wakes is probably finer than that needed to resolve the acoustics. So, we are happy to solve for the unsteady behavior with the same mesh and code we use for the steady aero-thermal field.

Discusser's Name: Mr. Jose M. Riola Rodriguez
Author's Name: Mr. Pedro de la Calzada Mazeres
Question:
      How long does the nonlinear code take to run compared to the linear version?
Answer:
      We have found a factor of two between the two codes. In order to have an idea of the total time needed for the flat plate cases presented here: for a mesh with around 20,000 nodes, the linear version runs overnight and the nonlinear version needs a full day.

This page has been deliberately left blank

_____

Page intentionnellement blanche

Resolution Requirements for the Numerical Computation of Tonal Noise in Compressors and Turbines of Aeroengines

T. Hüttl[1], G. Kahl, F. Kennepohl and K. Heinig
MTU Aero Engines GmbH
Dachauer Strasse 665
D-80995 München, Germany

Abstract

The time linearized Euler method Lin3D is applied to two sets of test cases. 2D wave propagation test cases in homogeneous flow are used to quantify numerical dissipation and dispersion of the discretization scheme. The minimum number of mesh diagonals between two wave fronts has been found to be an appropriate measure of the resolution of a wave. Correlations have been found that characterize the dissipation and dispersion behavior of the code and therefore the resolution requirements for a given flow simulation. The transmission and reflection of plane sound waves incident upon a single cascade of finite plates has also been calculated with Lin3D and compared with an analytical method of Koch [5]. The computed ratios of transmitted or reflected to incident pressure wave amplitude agree well with the analytical solution, even for scattered modes.

1. Introduction

The noise produced by jet engines has become one of the major concerns in today's pollution- and noise-conscious society. The jet-exhaust noise has been reduced significantly with the increasing by-pass ratios of modern turbofan engines. But now, the pure tonal noise, produced by rotor-stator interaction in compressors and turbines can become a dominant source of engine noise. Together with the noise generation and radiation, the sound transmission through blade rows in axial-flow turbomachines is also of great importance. Various calculation methods ranging from analytic methods for simplified flow and geometry, over empirical methods based on correlations calibrated by experimental data, to the wide range of numerical methods have been established within the aeroacoustic design process of turbomachines.

In this paper, we focus on a numerical calculation method, based on the time linearized Euler equations. This CFD code Lin3D developed at MTU is already used for aeroelastic design of aeroengine compressors and turbines. It may also be applied to the aeroacoustic design of these engine components. In contrast with analytical methods a more realistic description of blade and duct geometry is possible. Compared with Navier-Stokes methods, the computational requirements of Lin3D are much smaller. Before applying a code to a new kind of problems, its requirements and weaknesses have to be studied. It is the aim of the present study to investigate the resolution requirements of Lin3D for aeroacoustic computations.

First, the wave propagation in homogeneous flow has been computed in order to quantify the effect of numerical dissipation and dispersion on the solution. Then, the problem of the transmission of a sound wave through a blade row has been solved where the accuracy of the code can be benchmarked with an analytical method.

---

[1] Author for correspondence:
Dr. Thomas Hüttl, MTU Aero Engines GmbH, Abt. TPAI,
Dachauer Strasse 665, D-80995 München, Germany
Tel.: +49-(0)89-14 89-68 36 ; Fax: +49-(0)89-14 89-95242 ; Email: Thomas@Huettl.de

2. Numerical Method

The CFD code Lin3D is a time-linearized Euler method for 3D cascade flows [2,3,4]. The unsteady flow is assumed to be a small harmonic perturbation of the non-linear steady flow, so that the steady flow problem is decoupled from the unsteady problem. As long as the wave amplitudes remain moderate, the higher order terms in the governing equations derived under this assumption can be neglected and the describing unsteady flow equations become linear. The small-disturbance Euler equations are transformed into the frequency domain, so that the results are given as amplitudes and phases of the flow variables in the whole (3D) computational domain.

The base flow for the time linearized Euler code has been prescribed analytically for the investigations discussed here, but it can be the result of a steady 3D Euler computation, as well. Lin3D is restricted to small disturbances of the mean, inviscid, steady flow and its applicability is limited to cases with (predominantly) attached flow. The code is based on the linearization of the steady Euler method described in [1] and is an extension of the code described in [2,4].

Lin3D uses a Finite-Volume scheme with a 3-step Runge-Kutta time integration method. A structured H-type mesh with node centered variable arrangement is required to describe the geometry of the flow domain.

Lin3D has proven to be sufficient for most cases concerned with turbines. It is a fast and robust tool routinely used in the design process to assess flutter stability and forced response of compressor and turbine bladings. It features deforming meshes, non-reflecting boundary conditions, arbitrary eigenmodes (including chordwise bending), forced-response calculations for generalized forces due to up- and downstream disturbances and the possibility of calculation of acoustic modes. Lin3D runs on a wide variety of platforms ranging from workstations to multiprocessor vector supercomputers, with the option of parallel computing to speed up the turnaround times.

3. Wave propagation in homogeneous flow

3.1 Computational domain and setup

The accuracy of the code for wave propagation in homogeneous 2D flow has been tested for numerous upstream and downstream propagating waves. For each single test case the same equidistant mesh has been used, where the vector of the homogeneous mean flow is parallel to the mesh lines, see Figure 3.1. Physical and geometrical parameters of the cases are listed in Table 3.1. In order to realize a plane 2D flow with the 3D code in cylindrical coordinates, a small ratio of channel height ($r_{tip} - r_{hub} = 0.2m$) to tip radius ($r_{tip} = 300m$) has been chosen and discretized by 4 mesh cells.

Table 3.1: Physical and geometrical parameters of 2D wave propagation calculations.

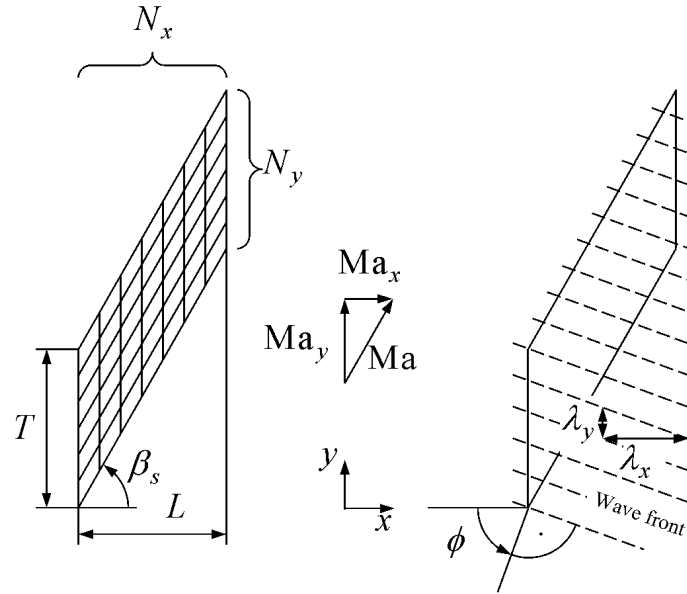| $L = 1.5m$	$N_x = 60$	$p_s = 85.15 kPa$
$T = 1.0m$	$N_y = 40$	$\text{Ma} = 0.5$
$\beta_s = 60°$	$a = 332.0 \dfrac{m}{s}$	$T_s = 274.3K$

Figure 3.1: Flow domain of 2D wave propagation calculations (without blades).

Two parameters are varied, the circular frequency ω and the incidence angle ϕ of the pressure wave:

$$\omega_A = 0.25\frac{\pi a}{T}, \; \omega_B = \frac{\pi a}{T}, \; \omega_C = 4\frac{\pi a}{T}, \; \omega_D = 16\frac{\pi a}{T}$$

$$\phi = 0°,15°,30°,45°,\ldots,345° \qquad (\text{not: } 90°,270°).$$

For upstream traveling waves ($90° < \phi < 270°$) the boundary conditions for a pressure perturbation have to be specified at the outlet plane; for downstream traveling waves ($0° \le \phi < 90°$ and $270° < \phi < 360°$) at the inlet plane. All waves are sinusoidal in the y-direction. The amplitudes are sufficiently small, so that non-linear effects can be neglected (peak to mean pressure variation of 0.1% of the static pressure).
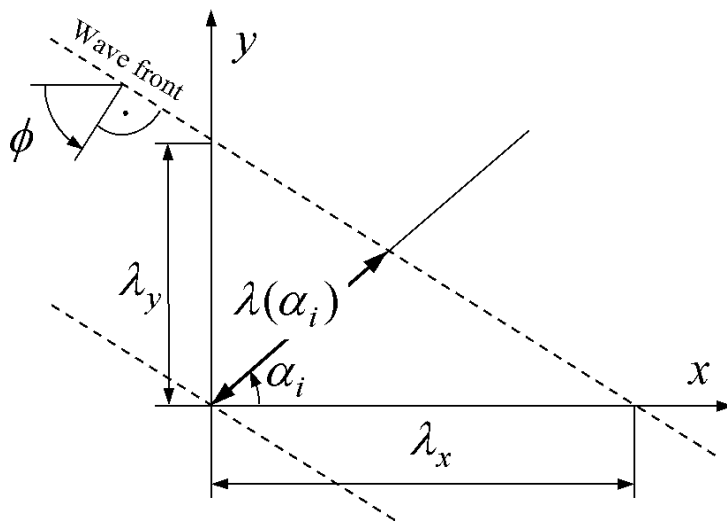
3.2 Resolution of the waves

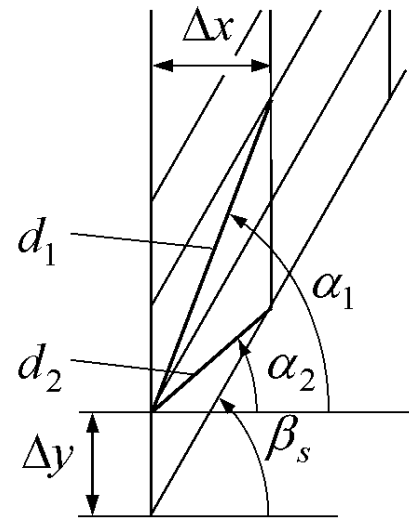**Figure 3.2:** Geometry of 2D waves.

Figure 3.3: H-type mesh geometry.

Although mean flow, flow domain, number of mesh points N_x, N_y and wave number

$$k = \frac{\omega}{a}$$

are chosen to be identical for constant ω, the resolution of the waves is not equal for the simulation, as it depends on the incident angle ϕ. However, the wave lengths λ also depend on ϕ for flow at $Ma \neq 0$. A characteristic quantity for the resolution R in discrete domains is the minimum number of mesh cell diagonals between two wavefronts:

$$R = \min\left(\frac{\lambda(\alpha_1)}{d_1}; \frac{\lambda(\alpha_2)}{d_2}\right) \quad .$$

$\lambda(\alpha_i)$ is the distance between two wavefronts along a line under an angle of α_i to the horizontal axis, see Figure 3.2.

$$\lambda(\alpha_i) = \frac{\lambda_x}{\cos\alpha_i + \tan\phi\sin\alpha_i} \quad .$$

λ_x can be obtained from

$$\lambda_x = \frac{2\pi c_x}{\omega} \quad , \quad \text{using} \quad c_x = a\,Ma\cos\beta_s + \frac{a}{\cos\phi} + a\,Ma\sin\beta_s\tan\phi \quad .$$

Two diagonals d_1 and d_2 exist in a structured H-type mesh (Figure 3.3). Their lengths and their angles α_1, α_2 are defined by

$$d_1 = \sqrt{\Delta x^2 + (\Delta x\tan\beta_s + \Delta y)^2} \quad , \quad \tan\alpha_1 = \tan\beta_s + \frac{\Delta y}{\Delta x} \quad ,$$

$$d_2 = \sqrt{\Delta x^2 + (\Delta x\tan\beta_s - \Delta y)^2} \quad , \quad \tan\alpha_2 = \tan\beta_s - \frac{\Delta y}{\Delta x} \quad , \text{ with } \Delta x = \frac{L}{N_x}, \Delta y = \frac{L}{N_y} \quad .$$
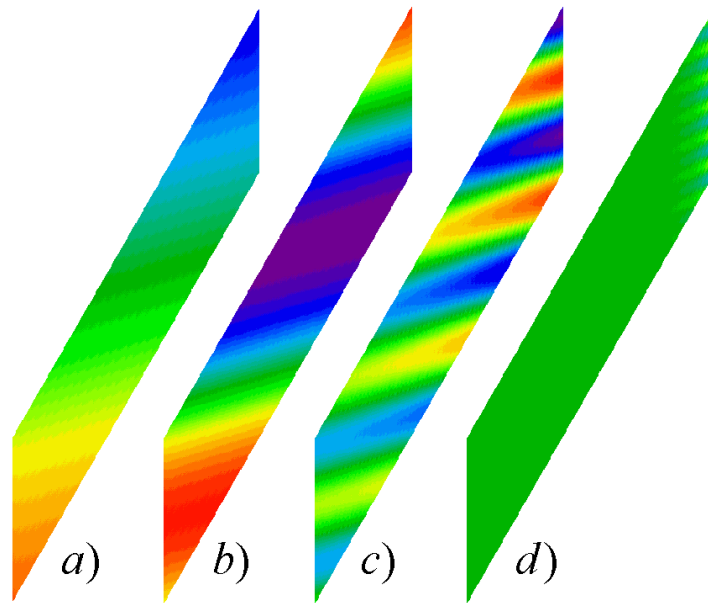
3.3 Results

Figure 3.4: Unsteady pressure for four wave propagation test cases with the same incident angle $\phi = 105°$ and different circular frequency ω: a) ω_A, b) ω_B, c) ω_C, d) ω_D.
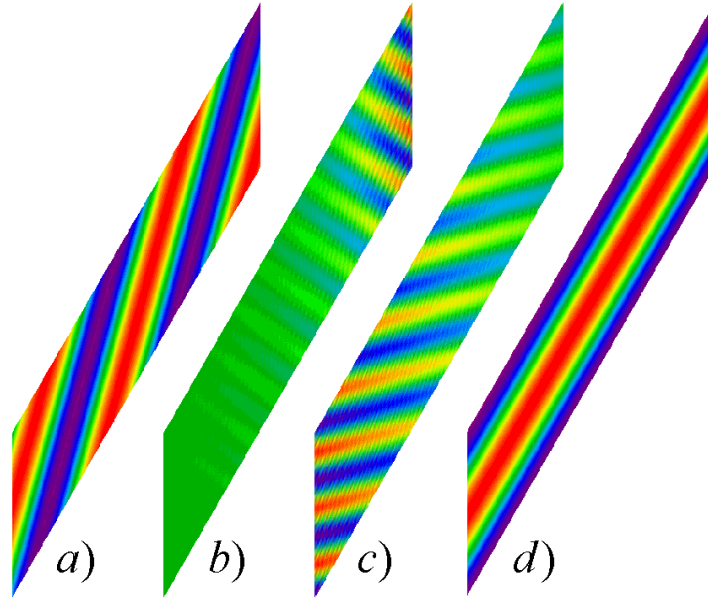
Figure 3.5: Unsteady pressure for four wave propagation test cases with the same circular frequency ω_C and different incident angle ϕ: a) $\phi = 165°$, b) $\phi = 225°$, c) $\phi = 285°$, d) $\phi = 330°$.

A first impression of the wave propagation in a 2D flow field is given in Figures 3.4 and 3.5. Figure 3.4 demonstrates that the damping of the waves increases for higher ω (smaller k, lower R). In Table 3.2, the values of the resolution R for four cases with the same circular frequency ω_C, plotted in Figure 3.5, are listed. This Figure shows that the damping depends on the resolution R, which is a function of the incident angle ϕ of the wave.

The purpose of the wave propagation test cases is to analyze, how strong numerical dissipation and numerical dispersion can affect the flow solution. Numerical dissipation and dispersion are unwelcome side effects of a discrete solution method and depend on the discretization scheme of the code. Numerical dissipation leads to the exponential decrease of the wave amplitudes $A(x)$ in (horizontal) propagation direction and can be quantified by the decay rate Dec

$$Dec = -20 \cdot \log_{10}\left(\frac{A(x + \Delta x)}{A(x)} \right) \qquad \text{for a downstream propagating wave}$$

$$Dec = -20 \cdot \log_{10}\left(\frac{A(x - \Delta x)}{A(x)} \right) \qquad \text{for an upstream propagating wave}$$

Numerical dispersion leads to an incorrect propagation velocity of a wave or to a change in its propagation direction. Dispersion can be quantified by the phase change error Pce, the difference between analytical $P_a(x)$ and numerical phase $P_n(x)$ change

$$Pce = \left| \left(P_n(x + \Delta x) - P_n(x) \right) - \left(P_a(x + \Delta x) - P_a(x) \right) \right|$$

Table 3.2: Resolution of the pressure waves of the four test cases in Figure 3.5.

Case	a	b	c	d
Incident angle	$\phi = 165°$	$\phi = 225°$	$\phi = 285°$	$\phi = 330°$
Resolution	$R = 22.4$	$R = 3.92$	$R = 5.43$	$R = 40.0$

Figure 3.6: Decay rate *Dec* (left) and phase change error *Pce* (right) of the wave propagation test cases drawn over the resolution R: $\triangle$ ω_A, $\diamondsuit$ ω_B, $\square$ ω_C, $\bigcirc$ ω_D, lines: $Dec_{lq} = 9.2 \cdot R^{-2.5}$ or $Pce_{lq} = 1.1 \cdot R^{-2.1}$.

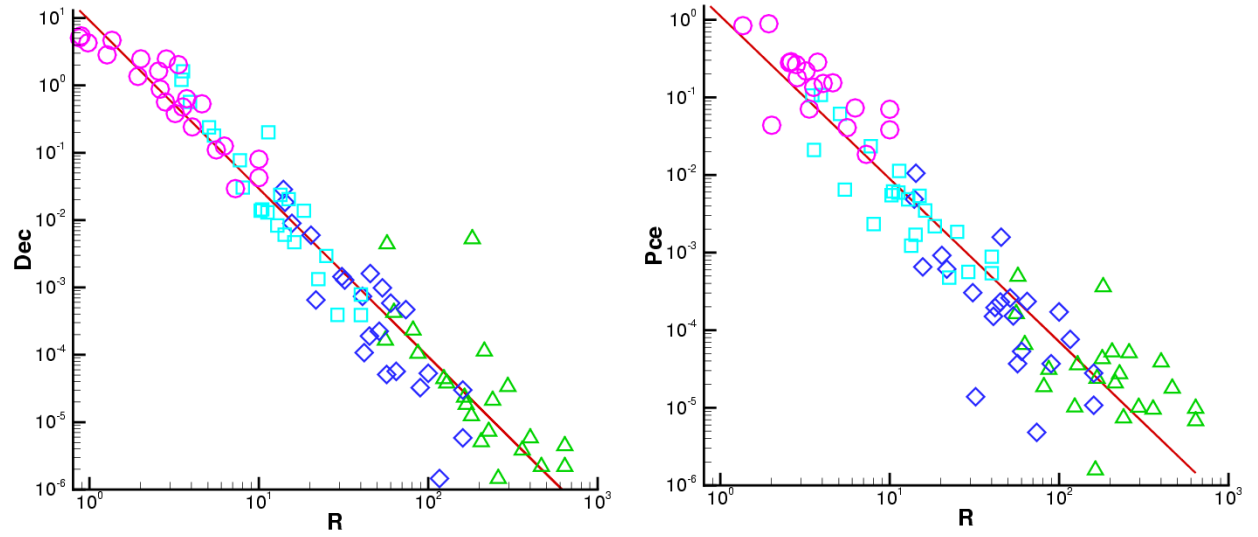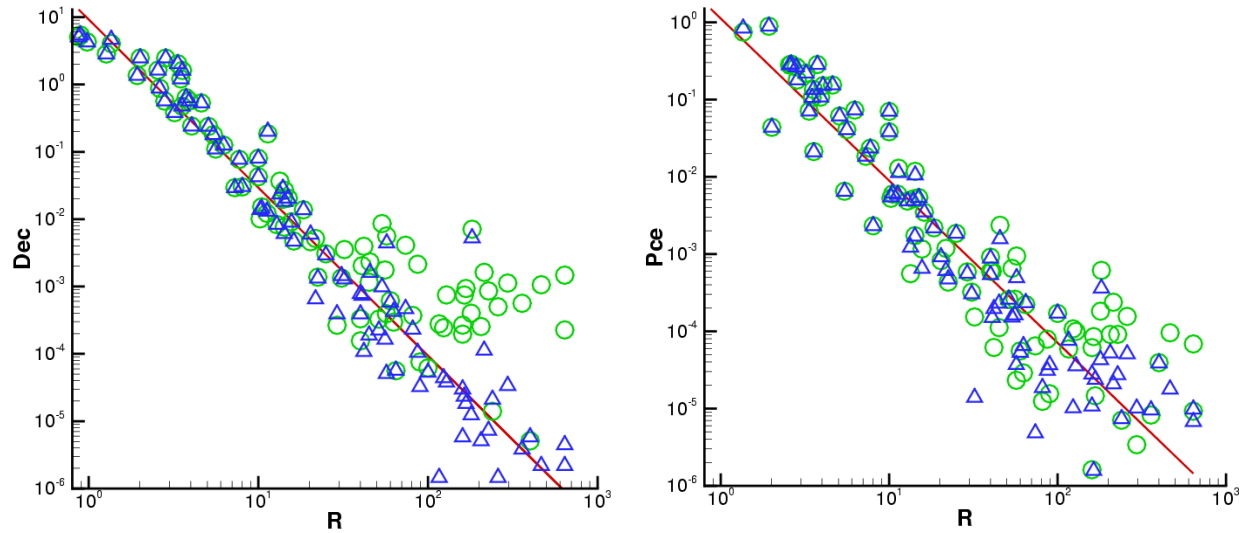**Figure 3.7:** Decay rate *Dec* (left) and phase change error *Pce* (right) of the wave propagation test cases drawn over the resolution R for two different convergence criteria: $\triangle$ low convergence criterium ($\mathrm{Res}_\rho = 5 \cdot 10^{-7}$), $\bigcirc$ high convergence criterium ($\mathrm{Res}_\rho = 5 \cdot 10^{-5}$), lines: $Dec_{lq} = 9.2 \cdot R^{-2.5}$ or $Pce_{lq} = 1.1 \cdot R^{-2.1}$.

In Figures 3.6 and 3.7, the decay rates and the phase change errors of the wave propagation test cases are drawn over the resolution R (section 3.2). Obviously, *Dec* and *Pce* are both correlated with R: With decreasing R, the decay rate and the phase change error and therefore numerical dissipation and dispersion increase.

When analysing *Dec* and *Pce* for different ω, it is not astonishing, that cases with higher frequency ω (smaller k) are worse resolved. Nevertheless, the symbol clouds for constant ω overlap with other distributions, because the incident wave angle ϕ has a remarkable effect on the resolution. Values of R for constant ω can even differ by one order of magnitude.

Using logarithmic scales on both axes, most of the plotted values are close to a straight line ($y = a \cdot R^b$). The parameters a, b can be obtained by the least squares method:

$$Dec_{lq} = 9.2 \cdot R^{-2.5}$$
$$Pce_{lq} = 1.1 \cdot R^{-2.1}$$

From linear theory for a 2nd order CFD code on a uniform mesh it is expected, that a 3rd order relationship exists between the decay rate and the resolution [6] and a 2nd oder relationship between the phase change error and the resolution. Better agreement with the 3rd order decay is achieved, if only cases B,C and D are used for the least squares fit ($Dec_{lq} = 14.9 \cdot R^{-2.8}$). The results of cases A might be influenced by the convergence criterion (density residual Res_ρ) of the code. This is demonstrated in Figure 3.7, where simulations with good convergence criterion are compared with simulations with worse convergence criterion: For higher R, the values of Dec and Pce deviate significantly from the least squares fit of the good convergence criterion. For a smaller (better) convergence criterion the cases with lower R are almost uninfluenced, but the values of Dec and Pce for higher R come closer to the correlation function.

Dec and Pce represent the accuracy of the calculation of a wave within the size of one mesh cell Δx. They define minimum requirements for the resolution of a pressure wave. As an example: if the decrease of the pressure amplitude by 1dB (0.1dB) due to numerical dissipation after 200 mesh cells Δx is assumed to be acceptable, we obtain $Dec = 5 \cdot 10^{-3}$ $\left(5 \cdot 10^{-4}\right)$ and need a resolution of the wave of $R = 20$ (50).

4. Interaction of plane waves with flat plates
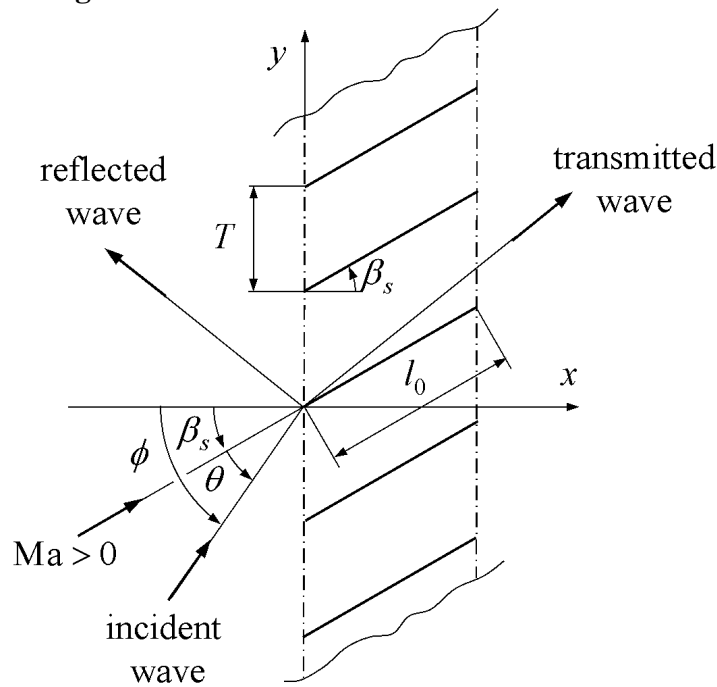
4.1 Geometry and settings

Figure 4.1: Geometry of the flat plate test cases.

In this section, the transmission and reflection of plane sound waves incident upon a single cascade of finite plates is studied. This problem, including scattering, has been solved by Koch [5] by means of the finite Wiener-Hopf technique. These analytical results will be used for comparison with computations using Lin3D.

A single cascade of parallel flat plates of length $l_0 = 1m$, staggered at an angle $\beta_s = 60°$ and at zero angle of attack, is considered and is shown in Figure 4.1. ϕ and $\theta = \phi - \beta_s$ are two different definitions of the angle of the incident wave. For the computation, the regions in front of the cascade, L_f, and behind it, L_b, both have an axial extension of $L_f = L_b = 0.5m$. Two circular frequencies have been studied: $\omega_A = 0.25\pi a \frac{1}{T}$ as a sub-resonant example and $\omega_B = \pi a \frac{1}{T}$ as a super-resonant example, where scattered modes appear. Only cut-on modes are considered. For other physical, geometrical and numerical parameters, the same values have been chosen as for the wave propagation test cases in section 3.
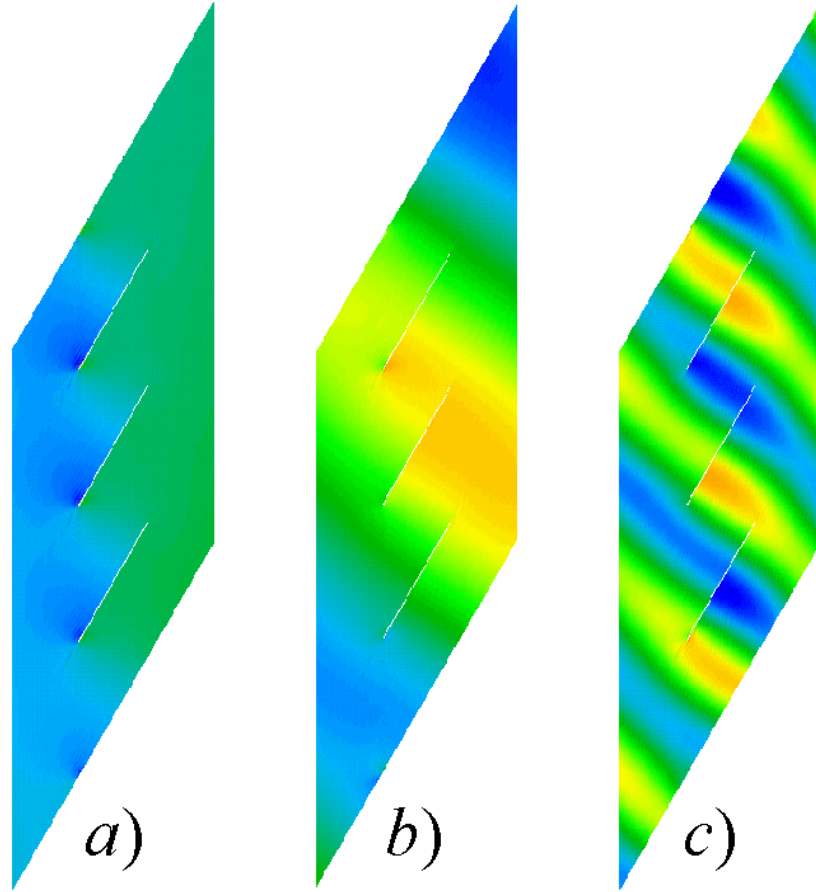

Figure 4.2: Unsteady pressure for three flat plate test cases: a) ω_A, $\phi = 345°$, b) ω_A, $\phi = 225°$, c) ω_B, $\phi = 225°$.

4.2 Sub-resonant test cases

The incident waves interact with the blades, when passing through a blade row. If the blades are perpendicular to the wave front, the wave is completely transmitted. For blades that are parallel to wave fronts, the waves are almost completely reflected (Close to this point, full reflection appears for a certain angle depending on the Mach number). In general, the incident acoustic

wave is partially reflected and partially transmitted through the blade row. For the sub-resonant test case, where mode scattering does not appear, two snap-shots of the pressure field are shown in Figures 4.2 a) and b).

For six representative cases, some parameters can be found in Table 4.1. Beside the incident wave angles ϕ, θ, the wave numbers k, k_x, k_y and the wave lengths λ, λ_x, λ_y are listed:

$$k = \frac{\omega}{a}, \ k_x = \frac{\omega}{c_x}, \ k_y = k_x \tan\phi, \ \lambda = \sqrt{\frac{\lambda_x^2 \lambda_y^2}{\lambda_x^2 + \lambda_y^2}}, \ \lambda_x = \frac{2\pi}{k_x}, \ \lambda_y = \frac{2\pi}{k_y}$$

Waves with a cut-off ratio $|\xi| > 1$ are cut-on (propagating waves), while waves are cut-off (exponentially decaying) for $|\xi| < 1$.

Table 4.1: Parameters of some of the sub-resonant flat plate test cases.

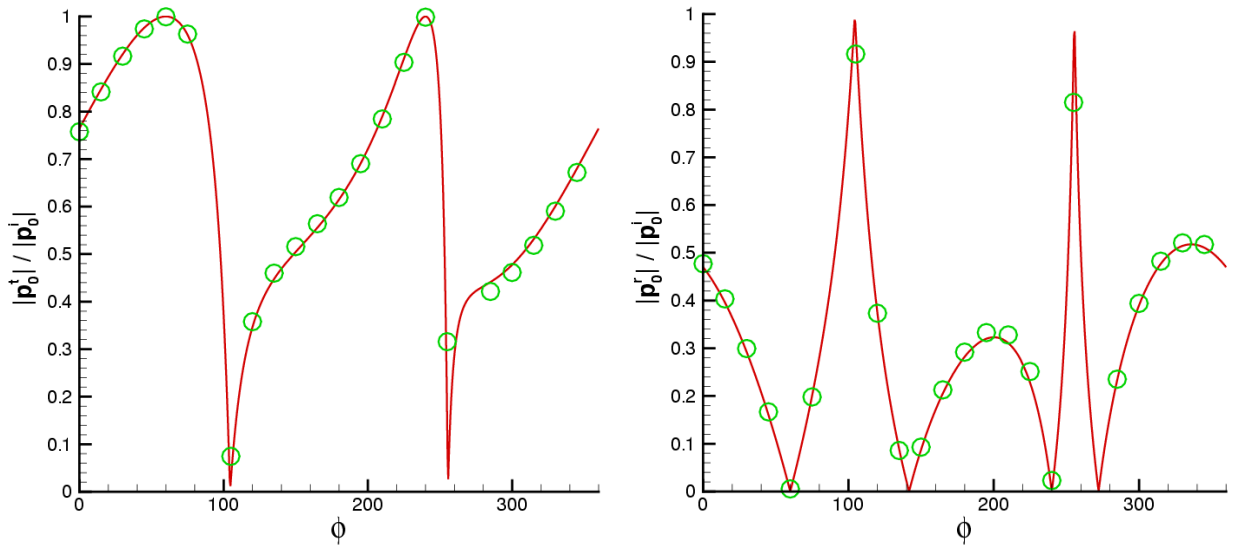| θ	ϕ	k	k_x	k_y	λ	λ_x	λ_y	ξ	$\left|p_0^t\right|/\left|p_0^i\right|$	$\left|p_0^r\right|/\left|p_0^i\right|$
75°	135°	0.785	-0.492	0.492	9.035	-12.778	12.778	1.140	0.4477	0.0885
120°	180°	0.785	-1.047	0.000	6.000	-6.000	∞	∞	0.6147	0.2820
165°	225°	0.785	-1.074	-1.074	4.137	-5.850	-5.850	1.366	0.9108	0.2284
255°	315°	0.785	0.638	-0.638	6.965	9.850	-9.850	2.300	0.5313	0.4769
300°	360°	0.785	0.628	0.000	10.00	10.000	∞	∞	0.7641	0.4700
345°	45°	0.785	0.374	0.374	11.86	16.778	16.778	1.497	0.9763	0.1606

Figure 4.3: Variation of transmitted (left) and reflected pressures (right) with incidence angle for the sub-resonant cases: Lines: analytical solution [5], ⭕ Lin3D.

The cut-off ratio ξ is also shown in Table 4.1:

$$\xi = \begin{cases} \dfrac{1}{\mathrm{Ma}_y + \sqrt{1 - \mathrm{Ma}_x^2}} \dfrac{k}{k_y} & k_y > 0 \\[3ex] \dfrac{1}{\mathrm{Ma}_y - \sqrt{1 - \mathrm{Ma}_x^2}} \dfrac{k}{k_y} & k_y < 0 \end{cases}$$

Furthermore, the (analytic) ratios of transmitted p_0^t or reflected p_0^r wave amplitudes to the amplitudes of the incident pressure wave p_0^i are listed for the six cases in Table 4.1.

The variations of these ratios $\left|p_0^t\right|/\left|p_0^i\right|$ and $\left|p_0^r\right|/\left|p_0^i\right|$ with incidence angle ϕ are drawn in Figure 4.3. A maximum transmission ratio $\left|p_0^t\right|/\left|p_0^i\right|=1$ is obtained for the two wave directions, where the upstream or downstream wave fronts are perpendicular to the blades ($\phi = 60°, 240°$). These maxima are correlated with minima of the reflection ratio $\left|p_0^r\right|/\left|p_0^i\right|=0$. Analytical and numerical results agree well with each other within the whole range of ϕ.

4.3 Super-resonant test cases

Scattered pressure waves ($m \neq 0$) are generated, when a pressure wave interacts with a cascade. For some of the cases with higher circular frequency $\omega_B = \pi a \frac{1}{T}$ scattered modes can be cut-on:

$$m = -1 \quad \text{is cuton for} \quad 10° < \phi < 174°$$
$$m = 1 \quad \text{is cuton for} \quad 223° < \phi < 294°$$

Therefore the cases with this frequency are called super-resonant. A snap-shot of the pressure field of one super-resonant case is shown in Figure 4.2 c). The variation of the ratios $\left|p_m^t\right|/\left|p_m^i\right|$, $\left|p_m^r\right|/\left|p_m^i\right|$ with incidence angle ϕ is drawn in Figure 4.4. Here again, analytical and numerical results agree well with each other within the whole range of ϕ.

5. Summary

The application of the time-linearized Euler method Lin3D to 2D wave propagation problems in homogeneous flow shows the dependency of numerical errors with the mesh resolution. For skewed meshes, the minimum number of mesh diagonals between two wave fronts is an appropriate measure for the mesh resolution. Numerical errors of the discretization scheme in form of numerical dissipation and numerical dispersion increase for increasing frequency at constant mesh. For constant frequency, the resolution of a wave depends on the angle of the incident wave and varies within one order of magnitude. The angle of the incident wave has therefore a significant effect on numerical errors. Correlations, calibrated with the simulations, can be used further to check the mesh size before performing simulations with Lin3D.

In a second study, the transmission and reflection of plane sound waves incident upon a single cascade of finite plates has been calculated with Lin3D. Computed results have been compared with an analytical method of Koch [5]. It has been looked at sub-resonant test cases and at super-resonant cases, where cut-on scattered modes appear. The computed ratios of transmitted or reflected to incident pressure wave amplitude agree well with the analytical solution. Even the ratios for scattered modes can be predicted accurately with Lin3D.

As a next step, the simulation of more realistic test cases with finite blade thickness, or 3D flow is envisaged.
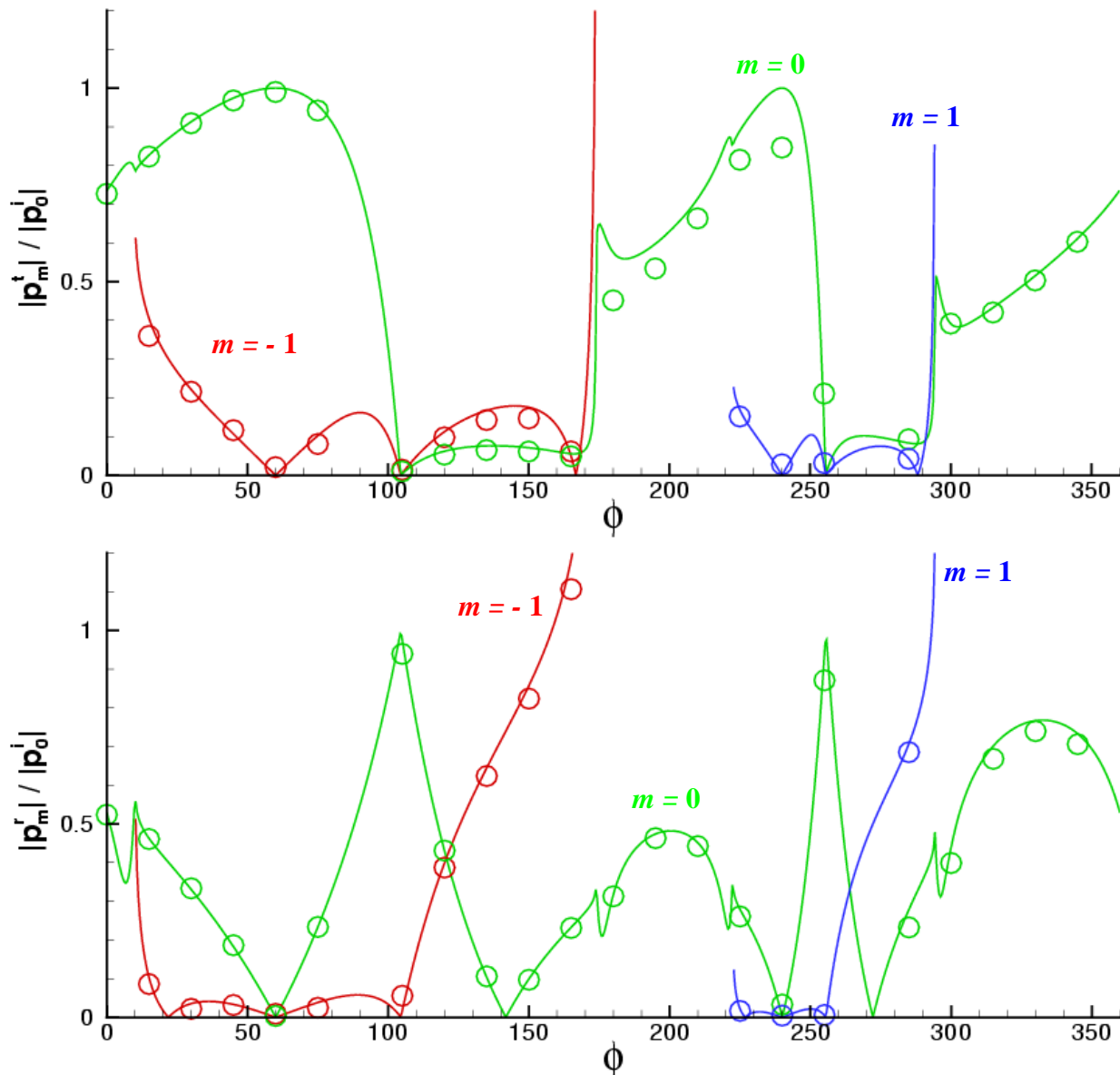
Figure 4.4: Variation of transmitted (top) and reflected pressures (bottom) with incidence angle for the super-resonant cases: Lines: analytical solution [5], ○ Lin3D.

6. Acknowledgement

7. References

[1] Happel, H.-W. and Stubert, B.: Computation of Transonic 3D Cascade Flow and Comparison with Experiments, *AGARD-CP-437*, 1988.

[2] Kahl, G.: Application of the Time Linearized Euler Method to Flutter and Forced Response Problems, *ASME-95-GT-123*, 1995.

[3] Kahl, G. and Klose, A.: Time Linearized Euler Calculations for Unsteady Quasi-3D Cascade Flows, *6th Symp. on Unsteady Aerodynamics and Aeroelasticity in Turbomachines and Propellers*, Notre Dame, IN, Sept. 15-19, 1991.

[4] Kahl, G. and Klose, A.: Computation of Time Linearized Transonic Flow in Oscillating Cascades, *Int. Gas Turbine and Aeroengine Congress and Exposition*, Cincinnati, Ohio - May 24-27, *ASME-93-GT-269*, 1993.

[5] Koch, W.: "On the Transmission of Sound Waves through a Blade Row", Journal of Sound and Vibration, 18 (1) pp. 111-128 (1971).

[6] Wilson AG, 2000, *A Method for Deriving Tone Noise Information from CFD Calculations on the Aeroengine Fan Stage*, to be submitted for presentation at the NATO RTO-AVT Symposium on Developments in Computational Aero- and Hydro-Acoustics, Manchester, UK, 8-11 October 2001.

Fan Tone Generation and Radiation System

Djaffar Ait-Ali-Yahia, Alexandre Jay and Hany Moustapha
E-Mails: Djaffar.Ait-Ali-Yahia@pwc.ca, Alexandre.Jay@pwc.ca and Hany.Moustapha@pwc.ca
Pratt & Whitney Canada, Department of Acoustics and Installations
1000 Marie-Victorin (01PA4), Longueuil, Quebec, Canada J4G 1A1

1. INTRODUCTION

Designing modern turbofan engines with higher bypass ratios is significantly limited by increasingly restrictive airport noise regulations. Independent of takeoff, cruise or landing operations, the fan rotor-stator interactions remain as one of the major engine sources of noise. Therefore, interest in understanding, modeling and eventually reducing this noise has increased the need for advanced Computational Aero-Acoustics (CAA) codes to serve as a primary tool in the fan design process.

Two years ago, Pratt & Whitney Canada (PWC) initiated a research effort to develop a fan tone generation and radiation system. As displayed in figure 1, this system integrates three in-house computational tools: a CFD fan analysis code such as NS3D, a CAA linear and nonlinear radiation codes, and a fan tone generation module which serves as a link between these CFD and CAA codes.

NS3D is a PWC proprietary code which solves the 3D Navier-Stokes equations for turbomachinery and external flow problems by using an SUPG finite element method on structured and unstructured grids. The development and the validation of this code was already dealt with in reference [1] and here will be mainly used to perform 3D unsteady rotor-stator analyses of fan stages. Therefore, the present paper focuses on the development of a noise generation module which computes the incident fan tone modes, as well as on the validation of the PWC CAA codes that serve in the propagation of the noise sources to the far-field.

Both axisymmetric, nonlinear and linear CAA codes [2,3] were developed for noise radiation from aircraft engines and, more specifically, for fan tone radiation computations. The nonlinear in-house codes, based on the Euler equations with a multidomain spectral method in space and an explicit 2N-storage Runge-Kutta in time, were first developed to achieve a more complete modelling of sound propagation phenomena. However, for typical industrial applications with high frequency incoming spinning modes, the nonlinear code is still demanding in terms of computer resources and it is limited to axisymmetric incident modes.

An intermediate approach has been developed by Eversman [4] that uses a linear modelling of sound propagation in which the mean-flow computation is decoupled from the acoustic field prediction. The methodology involves the solution in an axisymmetric frame of an incompressible potential equation for the mean-flow field and a linearized potential equation in the frequency domain for the acoustic field. Both equations are numerically discretized by a Galerkin finite element method with a direct solution of the resulting linear system of equations.

Although this approach is attractive for fan noise design purposes, it may eventually become prohibitive for acoustic modes with high frequencies. In fact, an accurate prediction of noise propagation with quadratic isoparametric elements requires a fine mesh spacing, with at least six to seven elements (equivalent to between 13 to 15 points) per wavelength. The demand on computer resources is further increased by the use of direct matrix solvers.

In the present paper, a fan tone generation procedure which is based on a high accurate spectral method is presented. The linear acoustic model [4] is also revisited with several numerical and implementation improvements. Finally, several relevant benchmarks are included to demonstrate the efficiency and the accuracy of the current fan tone system.
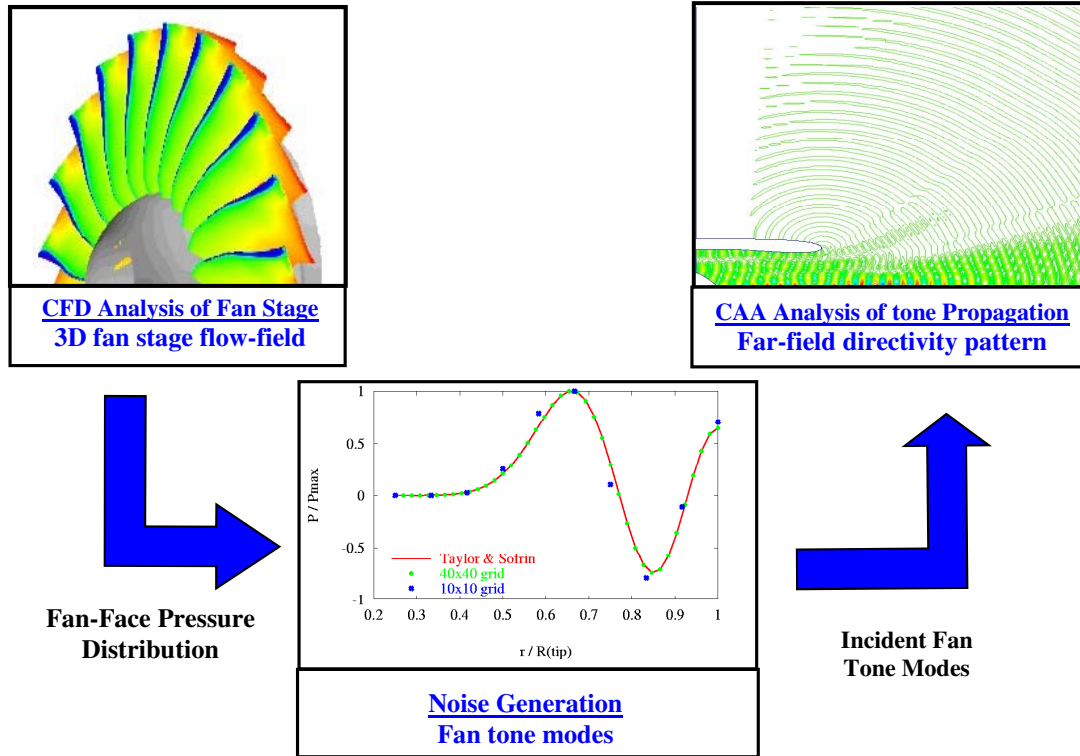

CFD Analysis of Fan Stage
3D fan stage flow-field

CAA Analysis of tone Propagation
Far-field directivity pattern

Fan-Face Pressure
Distribution

Incident Fan
Tone Modes

Noise Generation
Fan tone modes

Figure 1. Fan Tone Generation and Radiation System

2. FAN TONE GENERATION

2.1 Methodology

For an infinite annular duct, the general pressure solution for wave propagation in the positive z direction associated with a source located in the plane $z = 0$ is given by

$$p(r,\theta',z,t) = \sum_{n=1}^{+\infty} \sum_{m=-\infty}^{+\infty} \sum_{\mu=0}^{+\infty} P_{m\mu}^{n}\, E_{m}^{n}(\kappa_{m\mu}r)\, \exp[i(m\theta' - k_{m\mu}^{n}z - nB\,\Omega\,t)] \qquad (1)$$

where (r, θ', z) are the cylindrical coordinates in an absolute frame of reference, t is the time variable, n is the index of harmonic of BPF, m is the circumferential mode order, μ is the radial mode order, $P_{m\mu}^{n}$ is the pressure amplitude for the mode (m, μ) and harmonics n. In general $P_{m\mu}^{n}$ has a complex value.

E_m is the radial characteristic function or eigenfunction, and $\kappa_{m\mu}$ is the radial eigenvalue. Both these variables are computed by solving an eigenvalue problem subject to a Neumann boundary condition at the inner and outer duct walls. The variable $k_{m\mu}$ represents the axial wave number, which if real, corresponds to a propagating or a cut-on mode and, if complex, describes exponential decay or a cut-off mode.

The angular velocity, ω, of mode m is given by $\omega = n\, B\, \Omega / m$, where B represents the blade count and Ω is the shaft rotation frequency. Spinning modes can be generated by rotor-stator interactions or by a rotor alone. In both cases, the circumferential mode order m can only take some discrete values that are dictated by $m = nB + jV$, where B and V are the blade and vane counts, and j is any positive or negative integer.

FAN STAGE UNSTEADY ANALYSIS

3D Fan Flow Field

↓

SOLUTION POST-PROCESING

2D Pressure Distribution at Fan Face

↓

EIGENVALUE PROBLEM SOLVER

Radial Eigenvalues and Eigenfunctions

↓

FOURIER DECOMPOSITION

Amplitude of BPF Harmonics

↓

HANKEL DECOMPOSITION
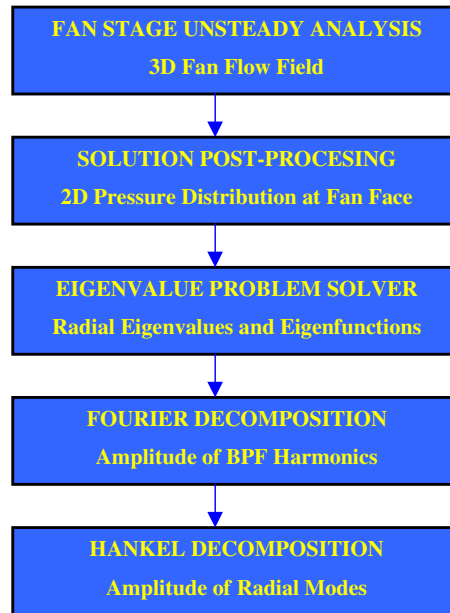
Amplitude of Radial Modes

Figure 2. Numerical algorithm of pressure modal expansion for a single harmonic

The numerical algorithm for fan tone generation is summarized in figure 2. Starting from a fan stage solution that could be provided by a CFD analysis code, the pressure field is interpolated into a reference plane which corresponds to the starting boundary (inlet boundary) for the acoustic calculations. This plane covers the blade passage area and is meshed with a 2D polar, uniform grid. The location of this reference plane as well as the size of its grid have a significant impact on the accuracy of predicted noise levels and therefore special care should be taken in their definitions. In general, the reference plane must be sufficiently far from the hydrodynamic field of the rotor blade, where large, non-propagation pressure variations caused by large fluid velocities in the vicinity of the blades may be present. Concerning the grid size, sufficient points should be used in the circumferential and radial directions in order to resolve the high frequencies as well as high radial modes contributions. The optimal number of points in both the circumferential and radial directions will be suggested in the validation section.

Once the acoustic pressure distribution is known on the reference plane, an FFT (Fast Fourier Transform) algorithm is used to compute the contribution of each circumferential mode m. The radial eigenvalue and eigenfunctions are then evaluated by solving a Bessel equation. The Bessel equation is discretized using a

Galerkin spectral element method and the resulting algebraic system of equations is solved by an iterative CG method. It should be noted that the eigenvalue problem depends solely on the circumferential index, m, and the hub to tip ratio, σ. The last step involves the calculation of mode amplitudes $P_{m\mu}$ by performing a Hankel expansion. The evaluation of integrals is carried out numerically using a spectral interpolation within each element.

2.2 Validation

In order to validate the proposed modeling and the accuracy of its numerical implementation, a fan stage with 16 blades and 32 vanes was considered. A pressure distribution made of a uniform mean-flow and the superposition of the first four radial modes ($m=16, \mu=0$-3) is assumed on the reference plane.

Assuming that only the circumferential mode $m= 16$ (corresponding to the first harmonics and $j= -1$) can propagate, the acoustic pressure takes the following analytical form

$$p(r,\theta) = \sum_{\mu=0}^{3} P_{m\mu} \left[J_m(\kappa_{m\mu}r) + Q_{m\mu}Y_m(\kappa_{m\mu}r) \right] \exp(im\theta) \qquad \text{with } m = 16 \qquad (2)$$

where the constants are defined in Table 1.

μ	$\kappa_{m\mu}$	$Q_{m\mu}$	$P_{m\mu}$
0	18.063	0.000	0.600
1	23.264	0.000	0.300
2	27.347	0.000	0.200
3	31.111	0.000	0.100

Table 1. Definition of pressure expansion constants.

The iso-contours of this non-dimensional pressure distribution is displayed in figure 3-(left) while the acoustic contribution is illustrated in figure 3-(right). The reference plane is chosen at an axial position where the hub to tip ratio $\sigma= 0.25$. This plane was meshed with different densities to investigate the grid dependency. The present validation work includes a coarse grid with 10x10 points, a medium grid with 20x20 points and a fine grid with 40x40 points per blade passage.
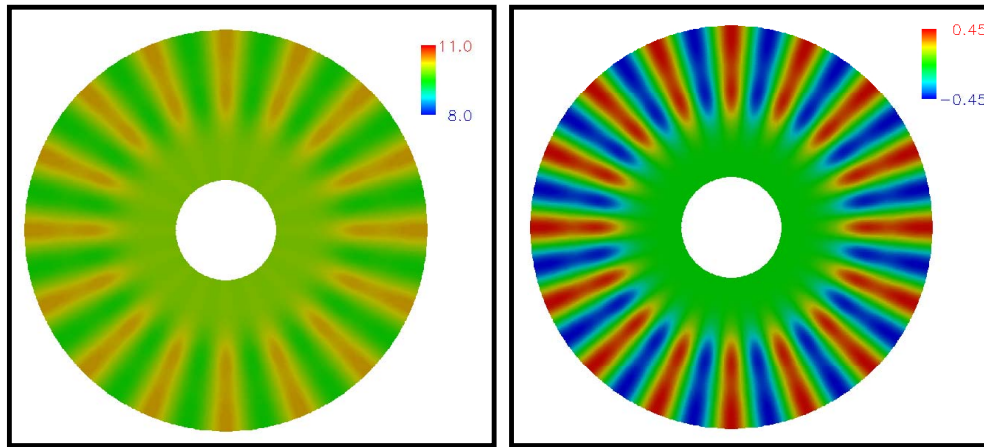
Figure 3. Iso-contours of non-dimensional pressure distribution (left) and its acoustic component (right).

Table 2 displays a comparison between the computed eigenvalues and, Tyler and Sofrin results [5]. It is observed that the predictions become less accurate as the radial index increases. It is also noticed that the grid with 10x10 points gives a 5% relative error for the highest considered radial mode while the use of a finer grid with 40x40 points lowers this error to 0.5%.

Radial Mode	Computed $\kappa_{m\mu}$			Tyler & Sofrin [5]
	10x10 points	20x20 points	40x40 points	
0	18.1102	18.0742	18.0659	18.063
1	23.5700	23.3366	23.2816	23.264
2	28.1608	27.5464	27.3954	27.347
3	32.6645	31.5100	31.2086	31.111

Table 2. Comparison between computed $\kappa_{m\mu}$ with Taylor & Sofrin results [5].

The computed eigenfunctions are compared against Sofrin & Taylor results [5] for different grid density in figure 4. It is clear that the grid with 10x10 points is not capable of resolving the shape of high radial modes such as μ= 2 or 3. On the other hand, the finest grid with 40x40 points leads to accurate description of all considered radial eigenfunctions.
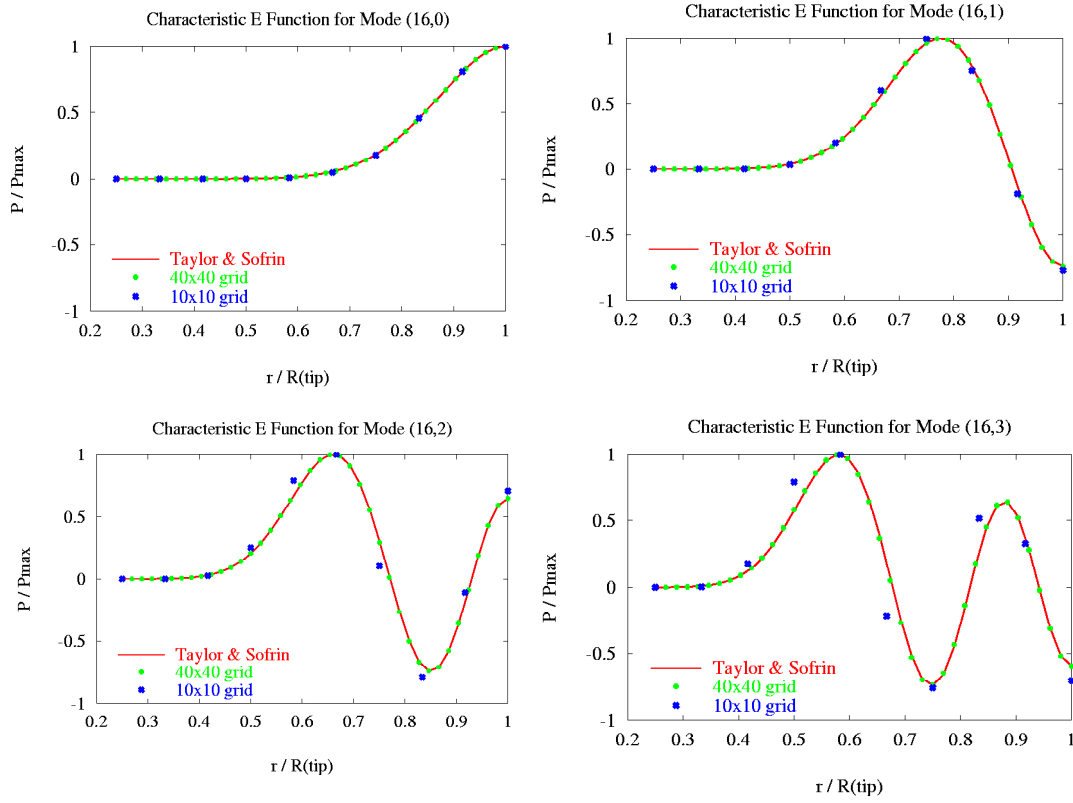
Figure 4. Characteristic E Functions (radial eigenfunction):
Comparison of predictions vs Tyler & Sofrin results for different grid densities

The FFT of the acoustic pressure distribution in the circumferential direction yields to Fourier coefficients $\hat{P}_m$ at each grid radial station. The histogram displayed in figure 5 shows that magnitude of Fourier coefficients $\left|\hat{P}_m\right|$ are only different from zero for the circumferential mode m=16, which is consistent with the assumed acoustic pressure given by the equation (2).
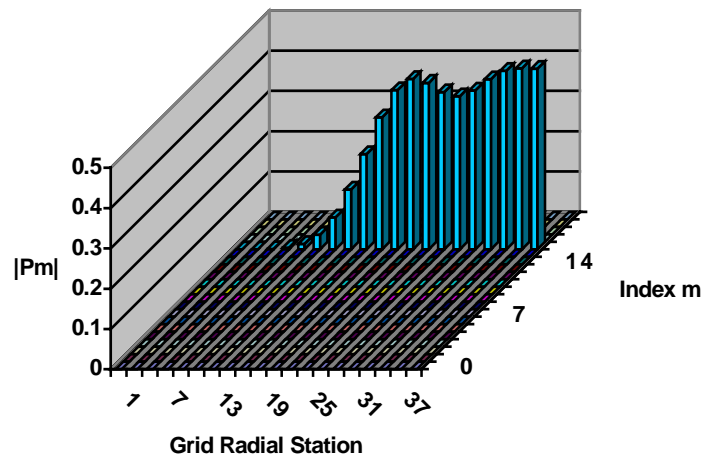

Figure 5. Fourier expansion of the pressure distribution on the finest grid.

Using these Fourier coefficients $\hat{P}_m$, a Hankel decomposition is performed in the radial direction to compute the contribution of each radial mode. The comparison of computed amplitudes $|P_{m\mu}|$ against the exact values given by Table 1 is presented in figure 6. It can be seen that the coarse grid with 10x10 points predicted poorly the amplitude of higher radial modes while the finer grid with 40x40 points allows better match to the exact values.
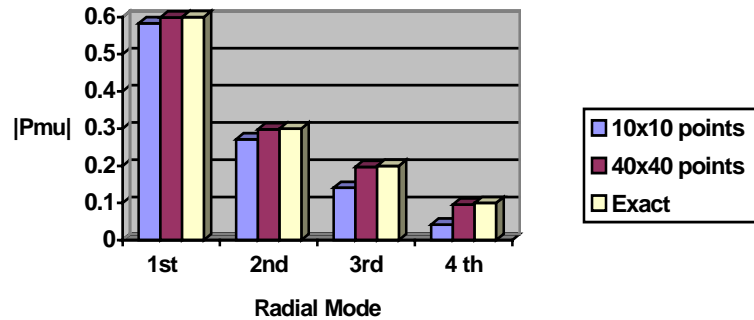

Figure 6. Comparison of computed amplitudes against exact values.

3. FAN TONE PROPAGATION

3.1 Methodology

The present methodology presents several numerical and implementation improvements to the linear acoustic model [4]. The mean-flow modelling is upgraded to the full potential equation. This is expected to improve predictions of the radiated sound field because the refraction effects, which occur mainly in the region of the inlet aperture, are accounted for. Spectral elements are used for space discretization, which brings down the number of necessary points per wavelength to between four and five for a sufficiently large number of Gauss-Chebyshev-Lobatto (GCL) points per element. The treatment of radiation boundary is drastically improved through a damping layer which better preserves phase information in the computational domain. The resulting algebraic systems of equations can be solved either by direct or iterative solvers, which are optimized on distributed memory machines through the use of the PETSc (Portable, Extensible Toolkit for Scientific Computations) library [6].

Finally, GCL grids are systematically generated using a CAD based approach [7] embedded within the aeroacoustic code. These grids may also be dynamically adapted by varying the number of GCL points per element as a function of blade passing frequency to yield the minimum number of points per wavelength needed to guarantee a certain level of accuracy.

3.2 Validation

A/ *Radiation from a Semi-Infinite Cylinder*

The acoustic solver is first tested on a sound radiation problem with no mean-flow from a semi-infinite cylinder of zero wall thickness, as displayed in figure 7. This test case is chosen due to the availability of an exact analytical solution.
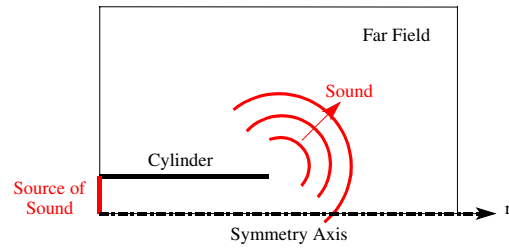
Figure 7. **Semi-infinite cylinder:** definition of sound radiation problem.

The radiation of the plane wave (0,0) and the first radial (0,1) modes are considered in the axisymmetric case, m=0, and with a reduced frequency of *10.3*. The domain was partitioned into 162 elements and the number of GCL points was varied between 6 and 8. This corresponds to a number of points per wavelength, N_λ=5.
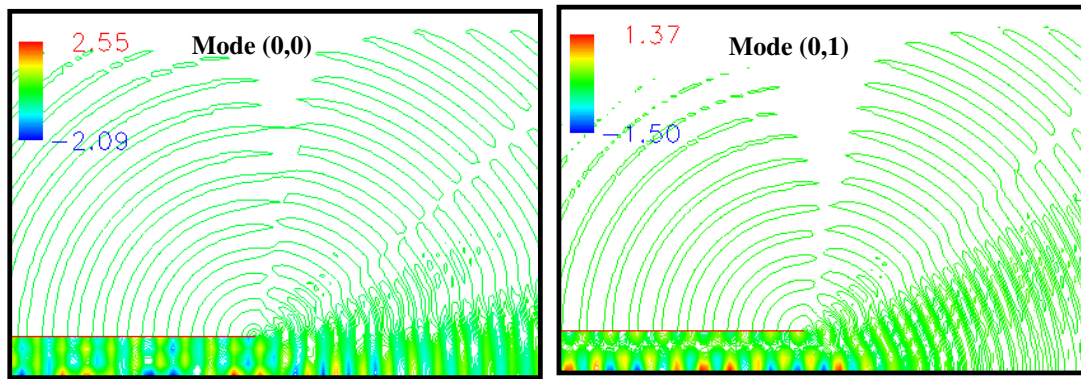

Figure 8. **Semi-infinite cylinder:** Contours of the real part of the acoustic pressure.

Once the complex acoustic pressure variable (real part is displayed in figure 8) is deduced from the acoustic potential, the amplitude of the acoustic pressure is computed by taking the module of the complex variable. The display of the amplitude of the acoustic pressure in figure 9 shows the existence of three main lobes.
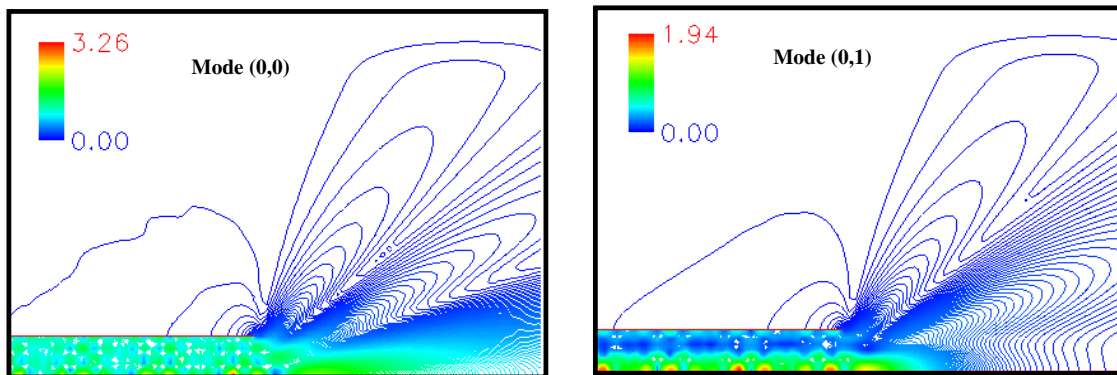

Figure 9. **Semi-infinite cylinder:** Contours of the amplitude of the acoustic pressure.

Figure 10 compares the computed sound pressure level (SPL) directivity in the far field against the analytical solution for radiation from a plane circular piston, vibrating in the same mode, as obtained by Tyler and Sofrin [5]. The agreement between the computation and the analytical result is excellent except at very high angles. This is expected since at these angles the influence of the walls, which the analytical solution does not account for, is more important.
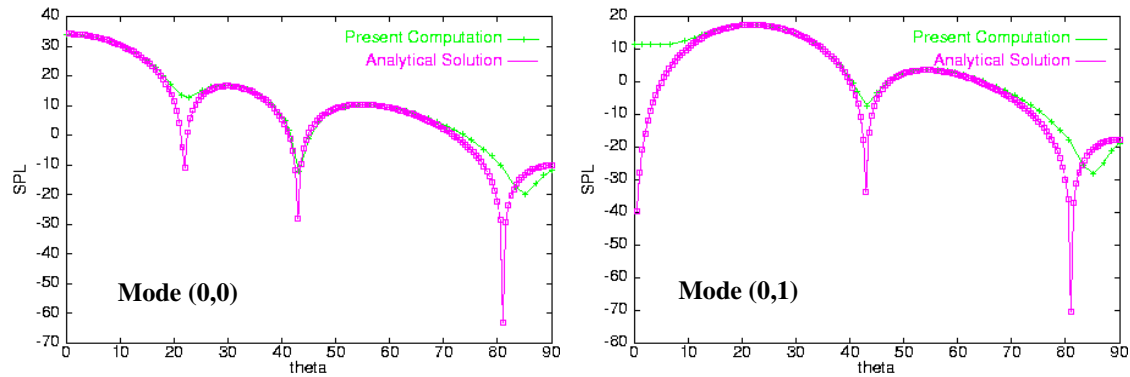

Figure 10. **Semi-infinite cylinder:** SPL directivity patterns.

B/   *Fan Tone Radiation from the PW545 Inlet*

The propagation code is also tested on the PW545 turbofan inlet with no mean-flow for the incoming spinning modes: BPF (0,0) and BPF (0,1). The angular speed is set to 12,000 *rpm* leading to a BPF of $3800Hz$ and a reduced frequency of 24.4.

Far field directivity patterns which are computed by linear and nonlinear analyses are compared in figure 11. Overall, a good agreement is observed between the linear and nonlinear predictions. This was expected since nonlinear effects were minimized in by considering a no mean-flow case and small acoustic amplitudes.
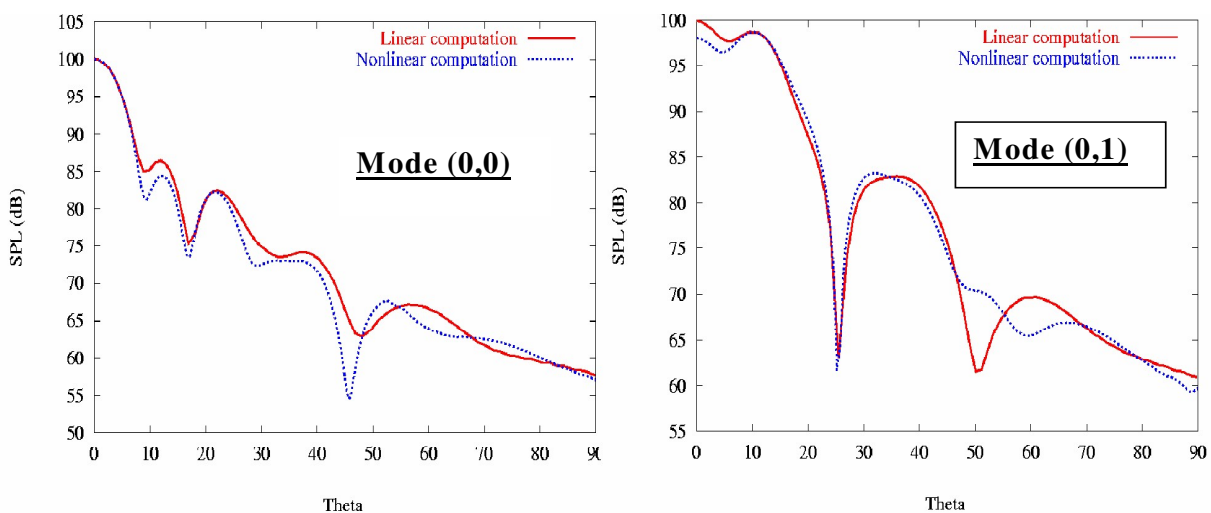

Figure 11. **PW545 inlet:** Far field directivity patterns using linear and nonlinear models.

The nonlinear acoustic solver was time marched until $t=30$ in order to achieve a periodic solution, necessitating around 11,000 iterations. This required 2 hours on four R10000 CPUs of an SGI Origin 2000 computer. On the other hand, the present linear acoustic solver required a single iteration or 7 minutes on a single R10000 CPU.

The effect of the mean-flow on the fan noise radiation is studied for the BPF (0,1) mode. The mean-flow is first computed for the far-field Mach number of 0.2 and a mass flow rate of 30kg/s and then an acoustic calculation is performed for the first radial mode with a nondimensional acoustic source amplitude of 0.01.
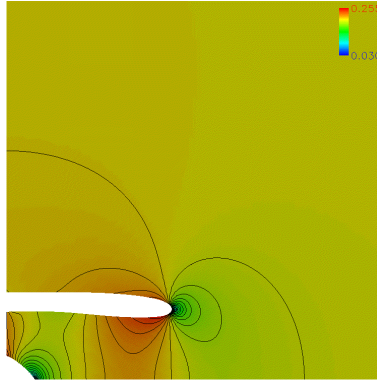
Figure 12. **PW545 inlet:** Mach number contours of the mean-flow.

The mean-flow solution is displayed in figure 12 as Mach number contours. A maximum Mach number of 0.26 is reached at the throat. The resulting radiation directivity pattern is compared with the corresponding no forward flight (i.e. no mean-flow) case in figure 13. This plot shows a reduction of 10 dB in the principal lobe.

Figure 13. **PW545 inlet:** effect of forward flight speed on the directivity pattern.

C/ *Fan Tone Radiation from the JT15D Inlet*

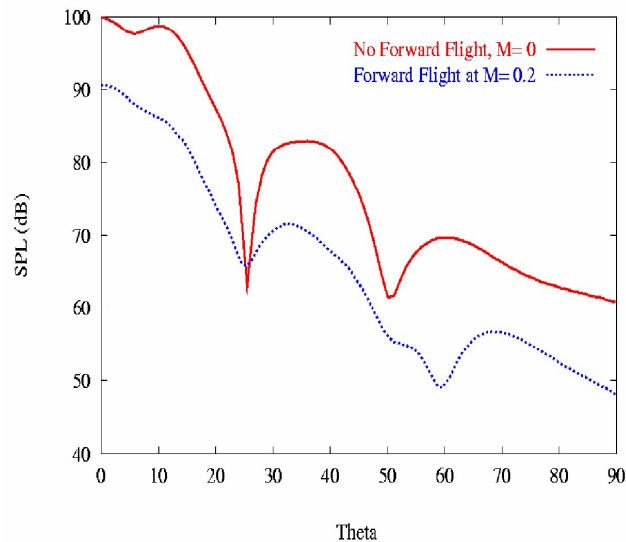In-flight measurements of the noise radiated from a modified JT15D-1 inlet have been presented by Preisser *et al* in reference [8]. The JT15D-1 is a small turbofan engine with 28 fan blades. An array of 41 small diameter rods have been installed on the casing of the nacelle, such that their interactions with the 28 fan blades generate modes with a circumferential order of 13 turning at BPF.
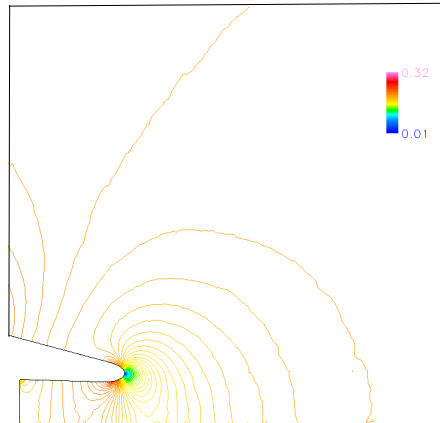
Figure 14. **JT15D inlet at 8010 RPM:** Mach number contours of the mean-flow.

In the considered case, only the mode (13,0) is above cut-off. Boundary conditions have been specified in terms of the mass flow rate at the fan face, set to 16.6 *kg/s*, and the far field Mach number of 0.204. The contours of the mean-flow Mach number are illustrated in figure 14. SPL contours, displayed in figure 15, look smooth and free of numerical reflections that could be generated by the far field boundary. This figure also shows the existence of a major lobe at an angle of 55 degrees with a maximum SPL of 170 *dB*.

Figure 15. **JT15D inlet at 8010 RPM:** SPL contours.

The computed directivity is compared with the experimental data in figure 16. We observe that the predicted directivity radiates at a slightly larger angle than the measured one.

Figure 16. **JT15D inlet at 8010 RPM:** SPL directivity.
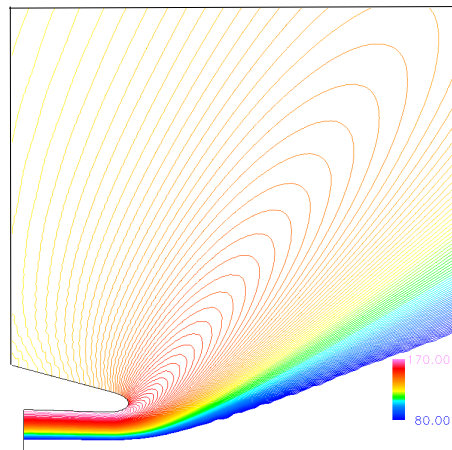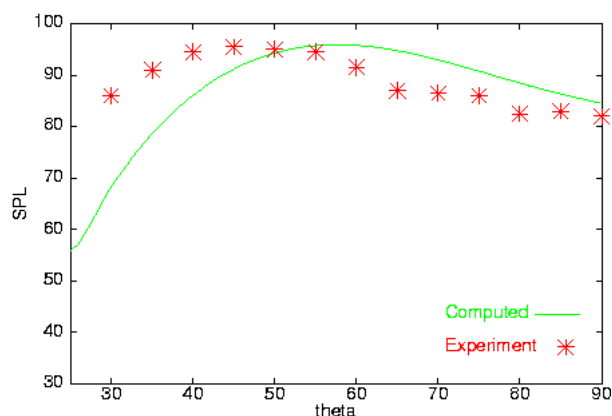
4. CONCLUSIONS

A fan tone generation and radiation system was presented. A computational module for fan tone generation has been developed and validated to serve as a link between any CFD fan analysis code and the in-house CAA radiation codes. The fan tone propagation codes were also validated on several generic and industrial benchmarks. These test cases demonstrate the potential of the present system for becoming an effective tool in performing a wide range of parametric studies for fan acoustic design.

5. REFERENCES

1. Tam, A., Ait-Ali-Yahia, D., Robichaud, M.P., Moore, M., Habashi, W.G., "Anisotropic Mesh Adaptation for 3D Flows on Structured and Unstructured Grids", Journal of Computer Methods in Applied Mechanics and Engineering, vol. 189, PP. 1205-1230, 2000.
2. Stanescu, D., Ait-Ali-Yahia, D., Habashi, W.G. and Robichaud, M., "Multidomain Spectral Computations of Sound Radiation from Ducted Fans", AIAA Journal, Vol. 37, No. 3, 1999, pp. 296-302.
3. Stanescu, D., Ait-Ali-Yahia, D., Habashi, W.G. and Robichaud, M.P., "Galerkin Spectral Element Method for Fan tone Radiation Computations", 6 th AIAA/CAES Aeroacoustics Conference, AIAA 2000-1912, June 12-14, 2000, Lahaina, Hawaii, USA.
4. Roy, I.D., Eversman, W., and Meyer, H.D., "Improved Finite Element Modeling of the Turbofan Engine Inlet Radiation Problem", NASA Report, Contract NAS3-25952, April 1993.
5. J.M. Tyler and T.G. Sofrin, "Axial Flow Compressor Noise Studies", SAE Transactions, Vol. 70, pp. 309-332.
6. Balay, S., Gropp, W.D., McInnes, L.C., and Smith, B.F., "PETSc User Manual", ANL-95/11, Revision 2.0.24, Argonne National Laboratory, 1999.
7. D. Ait-Ali-Yahia, D. Stanescu, M. Robichaud and W.G. Habashi, "Spectral Element Grid Generation and Nonlinear Computations for Noise Radiation from Aircraft Engines", AIAA Paper 99-1832, May 1999, Seattle, WA, USA.
8. Preisser, J.S., Silcox, R.J., Eversman, W., and Parrett, A.V., ``A Flight Study of Tone Radiation Patterns Generated by Inlet Rods in a Small Turbofan Engine", AIAA Paper 84-0499, Jan. 9-12, 1984, Reno, Nevada.

Computational Aero-Acoustic Studies of an Exhaust Diffuser

C. Jayatunga, G. Kroeff, J.F. Carrotte, J.J. McGuirk, B.A.T. Petersson
Department of Aeronautical and Automotive Engineering
Loughborough University
Loughborough LE11 3TU, UK

ABSTRACT.

The present paper describes work underway to develop a computational approach that can adequately simulate both the aerodynamic and acoustic behaviour of a typical exhaust diffuser/volute combination, such as are commonly used in industrial gas turbines for power generation use. An experimental rig was constructed to obtain a detailed understanding of the flow and acoustic properties of the system, and to provide guidance for computational modelling. Two different approaches are described for analysis of this system. The first uses CFD predictions carried out with a time-averaged RANS-based approach and a statistical turbulence model. Examples of the flow-field from this approach are presented. The second approach uses Large Eddy Simulation CFD, on a simplified geometry chosen on the basis of the experimental evidence, to provide information on the unsteady flow behaviour. This information is analysed and used to specify parameters for an acoustic analogy model. The acoustic model is also a simplified representation of the dominant noise source constructed from an experimentally derived viewpoint. The model is based on a ring of dipoles simulating the fluctuating pressure field associated with the unsteady vortex shedding/growth/merging process in the shear layer emerging from the diffuser exit. Spectral analysis of the unsteady velocity field provided by the LES calculation is used to determine amplitude, frequency dependence and phase relationships in the acoustic model. The basis of the model is described and sample outputs from both LES and acoustic model components are used to illustrate its performance.

INTRODUCTION.

Industrial gas turbines for electrical power generation are designed and supplied to the customer with an exhaust system that carries out a silencing function as well as providing for disposal of the exhaust gases into the surrounding atmosphere. The additional cost of the silencer can contribute significantly to the overall machine cost. This is particularly so if low frequency noise has to be removed. The design of the exhaust system must also comply with minimum ground footprint and packaging constraints, which usually require the exhaust flow to be turned from a horizontal flow path into the vertical to feed the silencer/exhaust stack. To reduce aerodynamic flow losses, which affect system efficiency, the annular duct downstream of the power turbine is connected to an annular diffuser/volute combination. An example of a typical geometry of such a system is shown in Figure 1. A short parallel-sectioned annular duct (formed between the machine outer casing and the central casing around the power transfer shaft) passes the flow to an annular diffuser. This is shown in Fig. 1 containing two rows of struts for structural purposes and with a scarfed exit to aid flow turning. The flow is then dumped into a volute, which directs the flow vertically into a rectangular cross-section duct feeding a downstream-located silencer. The flow characteristics associated with this geometry are strongly 3D and complex, containing recirculations, highly turbulent flow and possibly unsteady flow such as shedding from vanes and struts which are contained within the flow path. Currently, the interaction of these various flow features is poorly understood. The aerodynamic behaviour contributes to the overall system total pressure loss, but also acts as the origin of noise sources to create the range of frequencies that have subsequently to be silenced. Design optimisation methods, which can consider trade-offs between aerodynamic and acoustic aspects, are not currently available, leading to expensive testing at full-scale before an acceptable design is finalised.

Although the aerodynamic and acoustic behaviour of such components is extremely important in design optimisation of overall system performance, this seems to have received little attention to date. Compared with the extensive literature on the design of the diffuser systems elsewhere in the machine (e.g. in the main combustor [1] and [2]), exhaust diffusers have not been much studied. In terms of aerodynamic behaviour (loss reduction), evidence that the design is not straightforward was provided by the work of [3], where investigations of the need to install splitters in a short, wide-angle exhaust diffuser were reported. However, since this work was specifically aimed at performance of a particular existing engine design, little information of fundamental value emerged. On the acoustic front, some workers [4] have studied

Figure 1 Typical diffuser and volute geometry

noise generation due to vortex shedding from structural members (struts) in the flow path. It was shown that, since the struts were optimised for base-load operation, at lower operating power levels, where significant levels of swirl exit from the power turbine, large flow incidence angles on the struts lead to unsteady wakes and increased noise levels. Once again, however, no systematic understanding of the acoustic characteristics of general industrial gas-turbine exhaust diffusers evolved.

Fundamental acoustic studies of simple conical diffusers have been published ([5], [6], [7]). These authors have reported that separation in the diffuser is both a strong sound source in its own right, but also that the characteristics of the separation zone can be influenced by the acoustic properties of the duct system upstream and downstream of the diffuser. This implies for the present configuration, where the diffuser exit flow exhausts into a large volute box (see Fig. 1), that the jet shear layers created at diffuser discharge, the impingement of the jet on the volute back wall, and perhaps also the recirculation regions in the volute itself caused by flow turning, may all exert an influence on the acoustic behaviour.

In terms of aero-acoustic modelling, early work, trying to simulate the near-field processes that lead to jet noise, focussed on the vortex shedding process in the early-time period of jet shear layers. An example of this category of work is provided by [8]; a potential flow model for jet discharge was extended to allow for periodically shed ring vortices within the jet shear layer. The model was relatively successful in representing the mixing processes of the turbulent jet and also captured the correct spectral distribution of far-field noise. More recently, interest in terms of simulating jet noise (and other types of noise) has focused on development of Computational Aero-Acoustic (CAA) approaches. Two examples of some relevance to the present work may be found in [9] and [10]. The first has used the problem of turbulent boundary layer trailing edge noise to assess the current capabilities of CAA for this noise problem. The particular CAA approach adopted was based on a combination of: (i) Large Eddy Simulation (LES) CFD to capture the acoustic sources, and (ii) an acoustic analogy model based on the Lighthill formulation [11] to capture the propagation to the far-field. Predictions of far-field noise spectra were quite successful, but the authors pointed out the large computational cost of the LES calculation, even for this very simple geometry. In attempting to minimise the cost by choosing a solution domain as small as possible, the estimations of spanwise
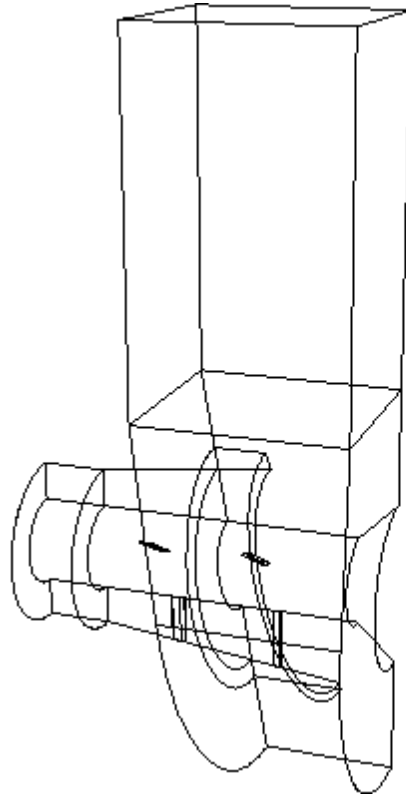
coherence of the noise deduced from the calculations showed that a wider computational domain should have been used, and this affected the accuracy of the predictions at the low frequency end. The CAA analysis reported in [10] was applied to a flow problem similar to one component of the present geometry. It considered a jet emerging from a circular duct into a larger space, although the discharged jet was still contained within a long circular duct of several times the jet diameter (this geometry has relevance to the human vocal tract if the initial jet diameter is considered to vary with time). Efforts were again made to minimise the computational costs, this time by considering only two-dimensional axi-symmetric flow. The emphasis of the work was placed on the demonstration of the ability of the high-order numerical techniques used to resolve the acoustic field. This was confirmed by the excellent agreement between the far-field acoustic pressure in the duct extracted directly from the CFD and results obtained from the same problem using the Fowcs-Williams and Hawkings version [12] of the acoustic analogy. Interestingly, the main noise source associated with a jet entering a larger space from a duct was found, by analysis of the directly computed acoustic signal, to be identified with a dipole source due to the unsteady forces exerted on the duct wall.

It is clear from the above that a complete understanding of the acoustic properties of flow inside the geometry shown in Fig. 1 will be difficult to achieve, and an adequate simulation model may have to take into account many factors. Accordingly, the methodology adopted in the present work was based around first conducting an experimental investigation of a scale model of the system under study to provide a clearer picture of it's important aerodynamic and acoustic details. This approach mirrors that described in [13] for an aero-engine exhaust system. This work focussed on identification of the 'extra' noise sources that are known to exist in aero-engine exhausts in addition to the basic jet noise. It is noteworthy that, once again, similar to the findings of [10], dipole sources were found to dominate, this time associated with fluctuating pressures on the turbine outlet struts, with the source strength varying with the level of flow swirl. This study seemed to have several similarities with the present problem. An experimental facility was therefore designed and built and both flowfield and acoustic measurements undertaken, as described below. Based upon the findings of the experimental investigation, computational approaches for both steady (i.e. time-averaged) and unsteady flow and acoustic fields were selected and applied, and illustrative samples of these are also provided here.

EXPERIMENTAL INVESTIGATION.

Test Facility.

Figure 2 shows the essential details of the test facility constructed. This contains all important features of the exhaust diffuser problem described above. The rig was constructed from Perspex and represents the flow path from power turbine exit through to silencer inlet. Air is supplied to the rig via a centrifugal fan. To isolate the fan noise from the acoustic measurements being made, the fan was located within an acoustically lined enclosure isolated from the plenum chamber that fed the test rig
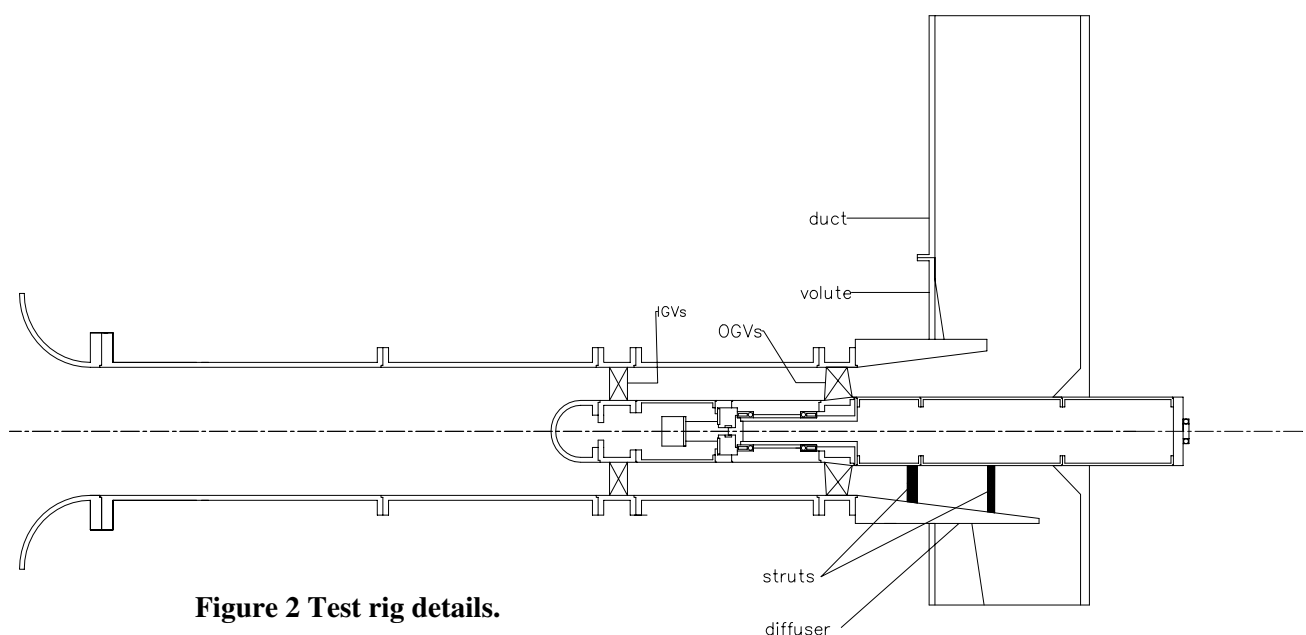

Figure 2 Test rig details.

via a bell-mouth, as shown in Fig. 2. Similar arrangements applied to the air exhausted from the rig into the test facility room. The rig incorporated all components downstream of the power turbine, i.e. a set of OGVs, a scarfed annular diffuser containing two rows of struts, and an exhaust volute. Inlet conditions to the exhaust system, simulating different power settings of the engine, were provided by 3 different sets of IGVs; these set the correct swirl level in the approach flow for 30%, 70% and 100% power conditions. The test rig was built in a modular fashion so that different components could be run in isolation or in (almost) any combination, i.e. with/without OGVs, with/without diffuser, with/without volute box, etc.

Aerodynamic Instrumentation and Measurements.
Measurements of the flowfield were made using five-hole pressure probes; measuring stations corresponded to OGV inlet, several planes within the diffuser and also within the volute. Radial traverses and also complete area traverses could be conducted (e.g. over a complete OGV blade passage to capture OGV wake behaviour). The instrumentation and motorised traverse gear were located within the centre shaft, part of which could rotate for accurate circumferential positioning. Space does not allow here a full survey of the data gathered, but Fig. 3 indicates a sample of the aerodynamic measurements taken. This shows three profiles of the time-mean axial velocity circumferentially averaged over the OGV blade pitch, for each level of inlet swirl. Flow conditions presented to the diffuser vary substantially with inlet swirl. At the 30% power condition, the incidence onto the OGV blades is high enough to cause separation near the blade tip. This is not the case for the 70% and 100% conditions, although at 70% there is still a region of low total pressure near the outer casing. As the flow passes down the diffuser, these inlet condition differences grow and the pitch-averaged profiles show a hub-biased shape at the low power conditions. It is likely that the diffuser is also separated over at least part of the circumference for the worst set of inflow conditions. In terms of the acoustic behaviour that will accompany these flow conditions, it is clear from the survey presented in the last section that diffuser separation will generate noise. The jet from the diffuser exit will also generate noise and the exit velocity profile in the jet is likely to be important; Fig. 3 shows that the profile shape at diffuser exit varies significantly, in particular the peak value of the axial velocity in the jet.
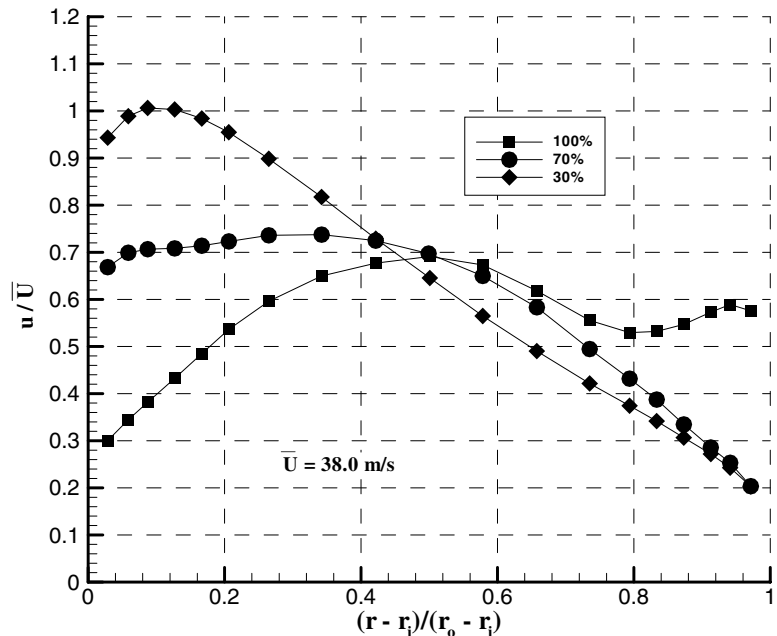

Figure 3 Circumferentially-averaged axial velocity profiles near diffuser exit.

Acoustic Instrumentation and Measurements.
Sound pressure measurements were taken with a 0.5 inch B&K microphone connected via pre-amplifiers to a Hewlett-Packard analyser; a foam windscreen was placed around the microphone to minimise interference from wind generated noise. The sound power for each configuration tested was obtained by averaging the sound pressure measurements taken at several fixed positions in the lab according to the relationship recommended in [**14**]. Before any measurements were taken, the acoustical properties of the lab containing the test facility were investigated by measuring its reverberation time and calculating the Schroeder frequency. These results showed that a quasi--diffuse sound field was present in the frequency range of interest and the Schroeder frequency was evaluated as 140 Hz. Since some frequencies of interest are below this level a large number of measurement points were used to obtain averages to guarantee the integrity of the results. Finally, background noise

measurements were taken to ensure that the background sound power levels were always at least 15dB below the measurements taken with the rig running.

The opportunity provided by the modular nature of the experimental facility was used to take acoustic measurements with various combinations of components present to identify whether the flow through/around particular components could be identified as a dominant aero-acoustic source, or whether that component could be viewed as acoustically unimportant. Fig. 4, for example, shows sound power level (SWL) measurements with and without the volute box present; all other components (IGVs, OGVs, struts, centre shaft, scarfed diffuser) were present and the data shown is for the 100% power level and an inlet Mach number of 0.08. There are several features of this spectrum which are characteristic of the system under study here. Firstly, the linear fall-off in SWL as frequency increases is expected if there is any jet-like contribution to the noise. The measurements
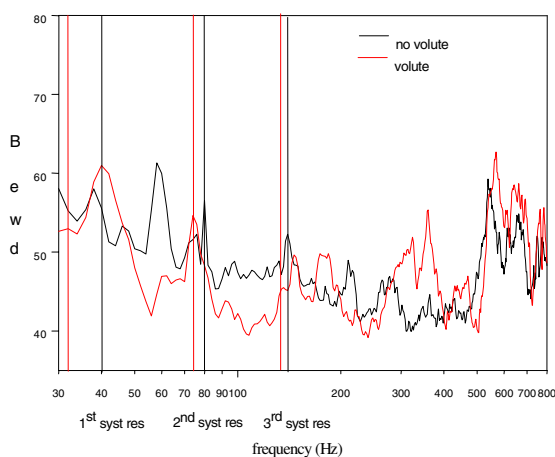
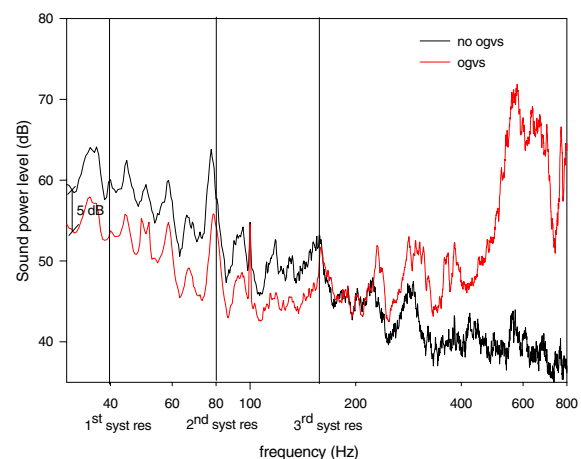**Figure 4 Sound power measurements with/without volute.**

Figure 5 Sound power measurements with/without OGVs.

should also decrease at low frequency below a peak noise level expected from simple jet noise data to be at a Strouhal number of order 1. This would occur at a frequency of around 50Hz in the present measurements, however, the limited size and non-anechoic nature of the room in which the data were taken mean that this low frequency fall-off cannot be detected. Secondly, various duct modes are excited by the aerodynamic behaviour of the system. The first three plane wave harmonics are indicated in Fig. 4 (they differ slightly for with/without volute cases as the duct length changes), and peaks in the spectrum are clearly visible close to these frequencies. It is likely that the unsteady flow processes inside the diffuser, particularly if it separates, and in the near field of the jet shear layer at diffuser exit are the causes of the excitation. Finally, above around 200HZ, higher order modes of the duct system are cut on. Since the acoustic behaviour of the upstream duct system in the model experiment will be different from the engine geometry, these higher order modes are not of great interest, and most attention has been placed on the lower frequency portion of the SWL measurements. This is in any case the difficult portion to silence in the practical application. It can be seen that the presence of the volute in fact reduces the sound level. The likely explanation here is that the back pressure provided by the volute stabilises the flow in the diffuser as is often observed in main combustor pre-diffusers. These data therefore imply that the volute itself is not a fundamental noise source, in spite of the impingement processes and internal recirculations it contains. Figure 5 shows a similar story for the OGVs. In the absence of any OGVs the SWL data at low frequencies increase by around 5dB and the higher order modes are cut-off. This indicates, again consistent with observations made in combustor pre-diffusers, that the enhanced turbulence created in the OGV wakes has a beneficial effect on the diffuser flow. The higher order modes are identified as being connected with the blade-to-blade circumferential dimensions and are not present when the OGVs are removed. Once again however, the characteristic acoustic signature at the low frequency end is unchanged by the presence/absence of OGV blades and these may therefore also be discounted as a primary noise source; they are only influential in as far as they affect the diffuser flow.

Figure 6 confirms that the IGVs also exert very little dominant effect on the noise characteristics. With both IGVs and OGVs present there is a level increase of around 3dB in the frequency range of interest, presumably because of either interaction noise or diffuser flow influences. Once more, however, we can conclude that the IGV presence/absence is not fundamental to determining the low frequency noise characteristics.
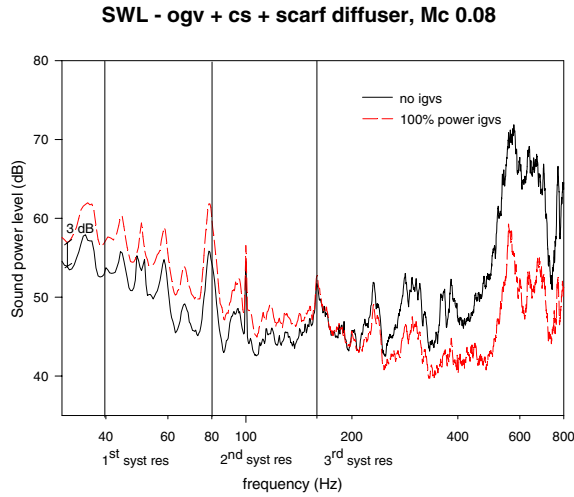
SWL - ogv + cs + scarf diffuser, Mc 0.08

SWL - 100% power igvs + cs + ogvs + scarf diffuser

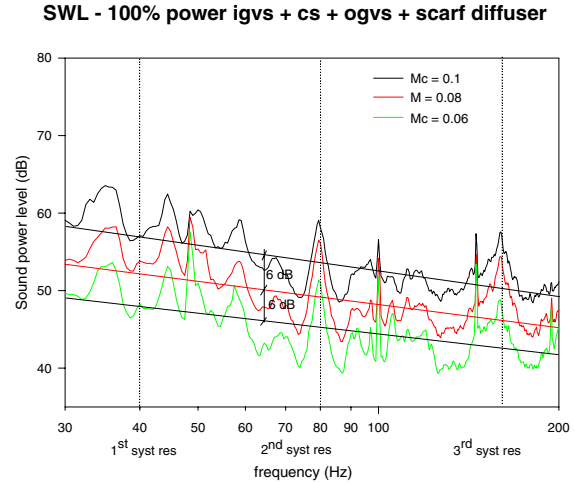**Figure 6 SWL data with/without IGVs.**

Figure 7 SWL data at varying Mach No.

The data in Figure 7 is the most illuminating of all. The configuration here contains all components except the volute box. The data were taken for varying flow rates, and three different inlet Mach numbers are indicated. Clearly at higher Mach numbers, as one would expect, the noise increases although again the overall characteristics remain unchanged. Of significance is the increment in dB level shown by the 'trend line' fitted to the data. A change in Mach number by +/- 0.02 leads to a change in noise level by +/- 6dB. This behaviour is exactly reproduced by a $(vel)^6$ relationship. This provides strong evidence that the dominant noise source is dipole-like. This is exactly the same as the findings in [**10**] and [**13**], where, in both cases, a jet emerging from a duct into a larger space lead to a fluctuating pressure field on the solid surfaces of the jet-containing duct close to its exit, which then provided the dominant dipole source for noise radiation to the far-field. This finding has an important message for computational modelling. The acoustic measurements also imply that, perhaps in contrast to original expectations, neither separation from the blades or strut surfaces (singly or via interaction), nor separation/impingement processes in the volute, are of significance as dominant noise sources. This means that all these complications can be ignored in terms of acoustic modelling and emphasis should be placed on capturing the unsteady pressure field near the diffuser exit, which in all probability is strongly coupled to the unsteady vortex shedding in the emerging jet shear layer.

COMPUTATIONAL INVESTIGATION.

Time-averaged CFD – RANS Modelling.
If the full geometrical complexity of the system under consideration needs to be considered in any flowfield simulations, then it is clear that at present this can only practically be achieved by solving for the time-averaged flow using the Reynolds-Averaged-Navier-Stokes (RANS) formulation of the equations of motion and a statistical model of turbulence. The evidence from the experimental acoustics investigation implies that some simplifications are possible, but for aerodynamic assessment and accurate loss prediction, all system components are likely to need consideration. The approach adopted here is based on the methodology used previously in combustor aerodynamic simulations where complex geometry is also an important factor. Details of the code used and examples of its use are given in [**15**], only a brief description is provided here. The numerical methodology is based on a multi-block, cell-centred, finite-volume, and implicit solution of the RANS equations, using the standard high-Reynolds number k-ε model. For treatment of complex shaped domains, the Cartesian forms of the equations are transformed into a general 3D non-orthogonal curvilinear system and a structured grid was generated to fit the geometry using an elliptic pde method.

Two examples of the predictions obtained for the diffuser/volute combination are given in Figs. 8 and 9. The inlet conditions for this calculation were taken from the experimental measurements, since it is known, as commented above, that accurate aerodynamic predictions of diffuser performance require the OGV wakes and associated turbulence generation to be taken into account. Fig. 8 shows the mixing out of the vane wakes as they pass down the diffuser; their behaviour influences the level of pressure recovery achieved by the diffuser and the accompanying level of loss. As can be seen in Fig. 8, The interaction between the vane wakes and the adverse pressure gradient in the diffuser determine
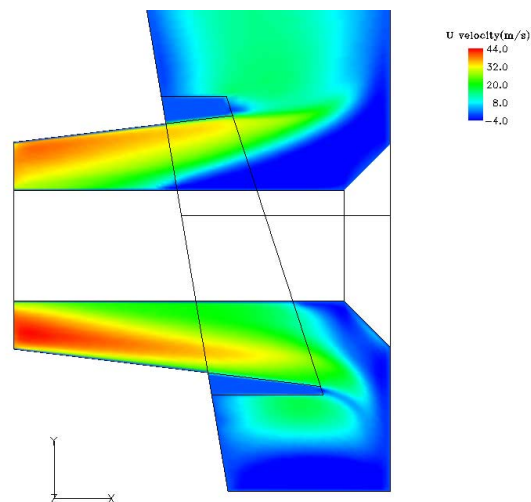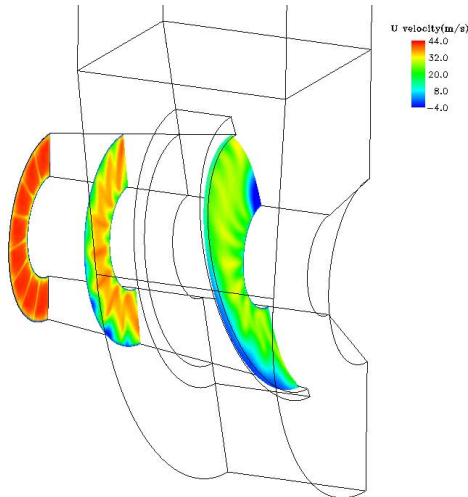

Figure 8 OGV wake mixing inside diffuser.   **Figure 9 Axial velocity contours at diffuser exit.**

any regions of separation present, and this calculation implies that there is separation inside the current diffuser, initially on the outer wall, but eventually at diffuser exit on the upper part of the central shaft. Fig. 9 shows a close-up view of this. If this steady state calculation is an accurate representation of events at diffuser exit then it is clear that the unsteady nature of the separation and the emerging jet will dominate the unsteady pressure field on the diffuser walls, which is believed to be the primary dipole-like noise source.

Unsteady CFD – LES Modelling.
It is clear that no information about the unsteady flow and pressure field can be deduced from the above CFD approach. For this, following the work of [**9**], the Large Eddy Simulation (LES) methodology has been selected for use. Since the acoustic measurements have shown that many features of the geometry do not significantly influence the primary noise characteristics, a simplified geometry has been chosen for the LES study. Initially only the annular diffuser and the annular jet, which emerges at diffuser exit into a larger space, have been considered. An unscarfed, plane-ended diffuser has been calculated in the first instance since it was much easier to generate a high quality orthogonal mesh for this geometry. The LES methodology is fully described in [**16**] and only indicative results of the predictions are presented here. In the first instance, only a simple eddy viscosity based Smagorinski sub-grid-scale model has been used for the non-resolved eddies. Fig. 10

shows an instantaneous snapshot of the axial velocity contours. It is very clear to see that the LES calculation has now captured the fluctuating eddy structure associated with the jet shear layers in a way that no RANS prediction can. The jet spreads as it penetrates into the enclosure outside of the diffuser and the air in this enclosure is recirculated
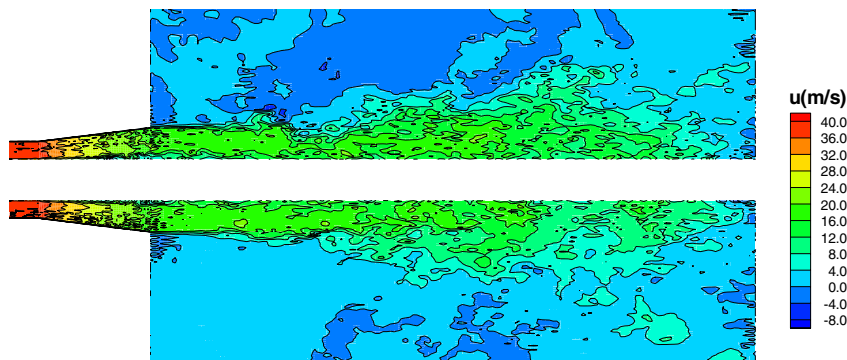

Figure 10 LES prediction of instantaneous velocity.

and entrained into the jet. Clearly a single snapshot cannot capture the unsteady flow features adequately. Fig.11 is therefore provided to indicate the time history of velocity at just one selected point, chosen to be at the exit plane and near the outer diffuser wall in the upper half of Fig. 10. The range of frequencies present in the time history is very clear, caused by the range of eddy sizes resolved by the grid used in the LES calculation. This range of fluctuating motions may also visualised by performing a spectral analysis of time histories, as shown in Fig. 12 for both velocity and pressure at the selected point. The velocity spectrum indicates a range of frequencies from around 10 to 1 kHz, with most energy in the O(100Hz) range.
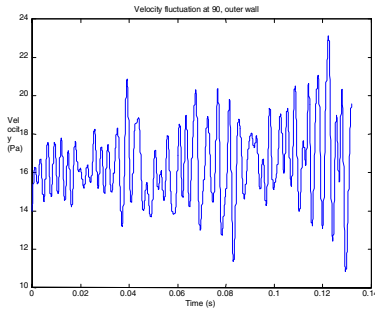

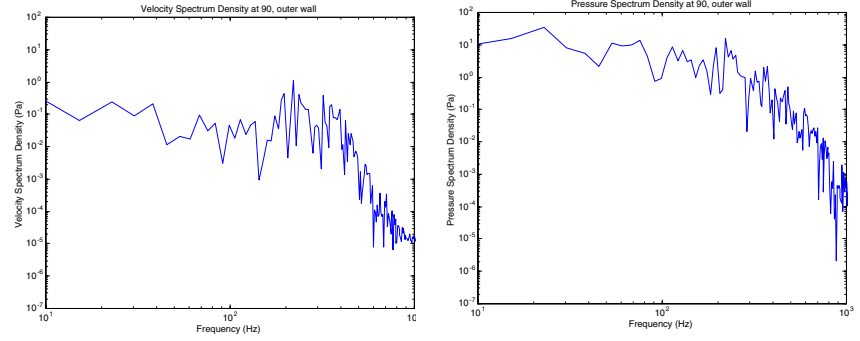**Figure 11 Time history of velocity from LES predictions.**

Figure 12 Spectral analysis of pressure and velocity t ime histories.

There is some evidence of a separate peak at 200Hz although the sample length is not quite long enough to confirm this absolutely. The pressure spectrum shows that the unsteady pressure on the duct wall is captured by the LES approach. This time-dependant information is of course precisely the information that can form the route to linking the aerodynamic and acoustic problems. Although the above analysis has not been carried out for exactly the geometric system under study, it is believed the calculations are representative and are sufficient to illustrate how this information may be used to feed into an acoustic model of the system.

Sound Field – Acoustic Modelling.
The unsteady results of the LES calculation could be used to drive a Lighthill-equation acoustic analogy model to simulate the sound propagation to the far field, as shown by [**10**]. However, the dominance of the dipole characteristic indicated in the acoustic measurements, and the identification of this with the unsteady pressure field on the diffuser duct wall, has encouraged a simpler approach to acoustic modelling to be attempted initially. A single dipole ring located at diffuser exit is postulated to represent the primary acoustic sources adequately. The parameters of the ring (number and distribution of dipoles, strength and phase relationships between individual dipoles in the ring) may all be varied, but the present investigation has concentrated on demonstrating the typical output of a simple dipole ring model, driven via information deduced from the LES predictions. The dipole ring is modelled as a sum of N discrete radially directed dipoles on a circle of radius r_0 centred on the geometric centre of the annular diffuser exit, and equally spaced from each other around the ring. For the present calculation r_0 has been taken as the diffuser outer radius. The acoustic pressure at some point in the far field for the nth individual dipole is given by:

$$p_n\left(\underline{r},k,t\right) = \mathrm{Re}\left(\hat{p}_n\left(\underline{r},k\right)e^{-i\omega t}\right)$$

Where $\underline{r}$ represents the vector between the dipole and the far field point and k is wave number (k=ω/c). The complex amplitude of the acoustic pressure is:

$$\hat{p}_n\left(\underline{r},k\right) = -k^2\hat{D}_n\left(k\right)\frac{\rho c}{4\pi\,|\,\underline{r}\,|}\cos\phi_n\left(1+\frac{i}{k\,|\,\underline{r}\,|}\right)e^{ik|\underline{r}|}$$

ρ and c are fluid density and sound speed respectively, $\hat{D}_n$ is the complex dipole source strength (volume velocity), which has a frequency dependent amplitude and phase, both of which are to be specified via LES information, the angle ϕ_n is the angle between the nth dipole and the vector to the

far field point. The acoustic pressure and velocity at any far field point due to the presence of all N dipoles in the ring are given by:

$$\hat{p}_{ff}\left(\underline{r},k\right)=\sum_{n=1}^{N}\hat{p}_{n} \qquad \hat{v}_{ff}\left(\underline{r},k\right)=\frac{1}{i\rho kc}grad\left(\hat{p}_{ff}\right)$$

and the sound intensity at any far field point may be calculated from:

$$I\left(\underline{r},k\right)=\frac{1}{2}\left(\hat{p}_{ff}.\hat{v}_{ff}^{*}+\hat{p}_{ff}^{*}.\hat{v}_{ff}\right)$$

Where an asterisk indicates a complex conjugate. In the example shown below, 8 dipoles have been considered and at each one the frequency dependent amplitude and phase information have been obtained by analysing the LES predictions at the corresponding point at diffuser exit. The Fourier transform of the velocity time history at each point yields the information needed to specify $\hat{D}_n$, the source strength is calculated using this velocity information and allocating a fraction of the dipole ring area to each dipole.

Fig. 13 shows a sound intensity plot for around a circle of radius 2m and centred on the axis of the dipole ring (approximately the location of the SWL measurements reported earlier). The plot is for a frequency of 83Hz, but the strong dipole-like character is present over a range of frequencies. At present the reason for the orientation of the dipole is unclear. Finally, the far field acoustic pressures produced by the dipole ring may be analysed to produce a sound pressure level plot; this is shown in Fig. 14 for a point on the 2m radius and above the top of the diffuser. This spectrum shows a peak at between 200 and 300 Hz which is where the velocity spectrum from the LES indicated a possible peak, but further analysis of the acoustic model predictions are required to confirm this.
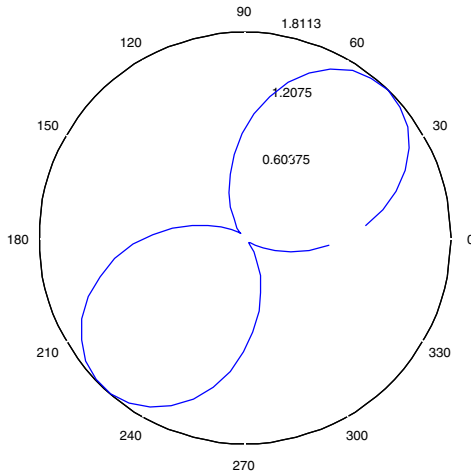
Figure 13 Sound Intensity plot deduced from acoustic model.
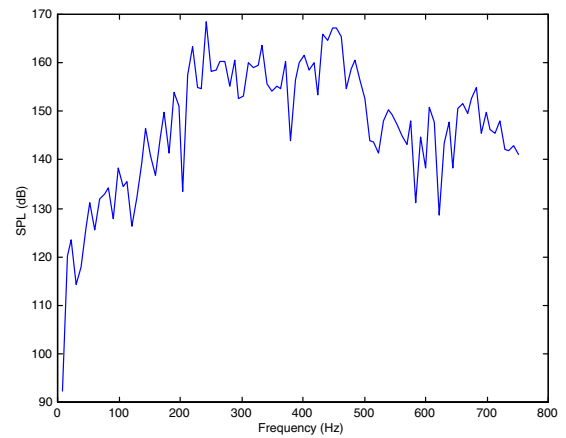
Figure 14 SPL level deduced from acoustic model.

SUMMARY/CONCLUSIONS.

This paper has summarised work carried out to construct a computational aero-acoustic model of a diffuser and volute combination relevant to industrial exhaust systems. The complex nature of the aerodynamic behaviour of this system and the many possible acoustic sources encouraged an initial experimental investigation to characterise the flowfield and eliminate some of the possible noise sources. This lead to a belief that any acoustic model should concentrate on the unsteady aerodynamic processes of possible diffuser separation and on vortex shedding/jet shear layer phenomena at diffuser exit. A RANS-based CFD calculation of the complete geometry showed that separation was predicted in the vicinity of the centre shaft, but this modelling approach allowed no information to be obtained on the unsteady flowfield. An LES calculation in a simplified geometry was then carried out. This methodology shows significant promise for providing the unsteady information so important for predicting the acoustic behaviour. To indicate how the LES-deduced unsteady flow information might

be used, a simplified acoustic model was constructed based on the assumption of a ring of dipoles simulating the important aerodynamic processes at diffuser exit. Frequency dependent amplitude and phase information for each dipole in the ring were deduced from the LES results. Illustrative examples of sound intensity and sound power level spectra were provided to indicate how this model could be used to provide such information. This approach is viewed as worthy of future study based on the present results.

REFERENCES.

[1]   D Zhou, T Wang, W R Ryan, "Cold flow computations for the diffuser-combustor section of an industrial gas-turbine", ASME paper 96-GT-513, 41st Int. Gas Turbine and Aeroengine Congress, Birmingham, UK, 1996.

[2]   A K Agrawal, J S Kaput, T Yang, "Flow interactions in the combustor-diffuser system of industrial gas-turbines", ASME paper 96-GT-454, 41st Int. Gas Turbine and Aeroengine Congress, Birmingham, UK, 1996.

[3]   H Harris, I Pineiro, T Norris, "A performance evaluation of a three splitter diffuser and a vaneless diffuser installed on the power turbine exhaust of a TF40B gas turbine", 43rd Int. Gas turbine and Aeroengine Congress, Stockholm, Sweden, 1998.

[4]   T F Fric, R Villarreal, R O Auer, M L James, D Ozgur, T K Stanley, "Vortes shedding from struts in an annular exhaust diffuser", ASME paper 96-GT-XXX 41st Int. Gas Turbine and Aeroengine Congress, Birmingham, UK, 1996.

[5]   A H M Kwang, A P Dowling, "Unsteady flow in diffusers", ASME Jnl. of Fluids Eng. Vol. 116, pp 842-847, 1994.

[6]   K R Fehse, W Neise, "Low frequency sound generated by flow separation in a diffuser", Eur. Jnl. Of Mechs-B-Fluids, Vol. 19, pp 637-652, 2000.

[7]   L van Lier, S Dequard, A Hirschberg, J Gorter, "Aero-acoustics of diffusers: an experimental study of typical industrial diffusers at Reynolds numbers $0(10^5)$", Jnl. of Acoustical Soc. Of America , Vol. 109, pp 108-115, 2001.

[8]   P O A L Davies, J C Hardin, A V J Edwards, J P Mason, "A potential flow model for calculation of jet noise", Prog. In Astronautics and Aeronautics, Vol. 43, pp 91-106, 1975.

[9]   M Wang, P Moin, "Computation of trailing-edge flow and noise using Large Eddy Simulation", AIAA Jnl., Vol. 38, pp 2201-2209, 2000.

[10]   W Zhou, S M Frankel, L Mongeau, "Computational aero-acoustics of an axi-symmetric jet in a variable area duct", AIAA paper 01-2788, 31st AIAA Dynamics Conference, Anaheim, USA, June, 2001.

[11]   M J Lighthill, "On sound generated aerodynamically", Proc. Roy. Soc., Vol. 211, pp564-587, 1952.

[12]   J E Fowcs-Williams and D L Hawkings, "Sound generation by turbulence and surfaces in arbitrary motion", Proc. Roy. Soc., Vol. 264, pp321-342, 1969.

[13]   W D Bryce and R C K Stevens, "An investigation of the noise from a scale model of an engine exhaust system", AIAA Paper 75-459, AIAA 2nd Aero-Acoustics Conference, Hampton, VA, USA, 1975.

[14]   J R Hassall and K Zaveri, "Acoustic Noise Measurements", Bruel and Kjaer Publication, 1988.

[15]   J J McGuirk and A Spencer, "Coupled and uncoupled CFD prediction of the characteristics of jets from combustor air admission ports", ASME Jnl. Of Engineering for Gas Turbines and Power, Vol. 123, pp 327 – 332, 2001.

[16]   G Tang, Z Yang, J J McGuirk, "LES predictions of aerodynamic phenomena in LPP combustors", ASME paper 2001-GT-465, 46th Int. Gas Turbine and Aeroengine Congress, New Orleans, LA, USA, June 2001

A CFD Coupled Acoustics Approach for the Prediction of Coaxial Jet Noise

G.J. Page, J.J. McGuirk, P. Behrouzi, M. Hossain
Department of Aeronautical and Automotive Engineering
Loughborough University
Loughborough, Leics. LE11 3TU, UK

M.J. Fisher
ISVR, University of Southampton
Highfield, Hants. SO17 1BJ, UK

SUMMARY

Prediction of jet noise is important for civil aircraft. Some CAA methodologies predict the full unsteady flow field of a jet in order to ascertain the far-field noise. The approach adopted here is to utilise CFD to obtain steady state information using a turbulence model and hence to provide inputs to a semi-empirical noise model, herein after referred to as the four source model. Predictions of a coaxial jet in comparison to laser measurements show that the CFD methodology can reproduce the experimental velocity field mixing and turbulence intensities. This leads to confidence that the CFD model can predict the influence of geometrical changes (such as nozzle area ratio) on the mean and turbulence field and so increase the validity of the four source model. Predictions of two geometries with differing area ratios showed that peak turbulence intensities are increased in the smaller area ratio, but this can be accounted for by the use of a 'fully mixed' velocity in a four source model for jet acoustics. Predictions of a three-quarter cowl geometry were used to determine the equivalent parallel coaxial jet found immediately downstream of the bullet. This was achieved by integrating the areas and mass flows in the primary and secondary streams at the nozzle exits and downstream of the bullet. It is found that a velocity ratio of 0.7 and area ratio of 2.6 at the nozzle exit planes can be considered equivalent to a velocity ratio of 0.5 and area ratio 5 in the parallel flow downstream of the bullet. Input of such information from a RANS CFD prediction may be a relatively simple method for extending the applicability of the four source model.

1 INTRODUCTION

Jet noise is an important component of the noise emission of civil aircraft. Even for high bypass ratio engines, jet noise is the most prominent source at the full power take off condition. For low to medium bypass ratio engines, internal mixing of the core and bypass streams using a forced mixer offers significant jet noise reductions. At high bypass ratios, however, the noise benefit of internal mixing is small due to both the high flow area ratio and the high velocity ratio. In addition, a long bypass cowl has significant weight and drag penalty.

As a result of the above, nozzle designs are actively being sought which might result in significant jet noise reductions for high bypass ratio, separate jet exhaust configurations. A novel approach by which this might be achieved is to modify the complex coaxial jet flow development downstream of the nozzles, either by geometric or acoustic means. Recent model-scale exhaust tests involving fairly subtle changes to the nozzle profile have met with considerable success. By serrating the basically conical nozzle exit profiles, substantial jet noise reductions have been measured under both static and flight-simulation conditions [1]. In order to exploit the benefits of this type of nozzle design, an understanding of the flow and resultant noise production is required.

The most general methodology for the prediction of far-field jet noise is to compute the near-field unsteady flow-field using a DNS or LES technique in conjunction with an acoustic analogy. Initial work

has concentrated on application to supersonic jets[2,3,4]; more recently subsonic jets have also been computed [5] with some success. Whilst this approach could be used for coaxial jets with serrated nozzles, many current LES methods would be unable to handle the complex geometric features and the large computer run times would make it infeasible for any design application. An alternative approach is to use CFD to predict the steady flow-field using a Reynolds Averaged Navier-Stokes (RANS) method with an appropriate turbulence model, and to use the predicted mean velocity and turbulence properties as inputs to an appropriate jet noise model [6,7] in order to predict the far-field. This type of approach has been used for coaxial jets with promising results[8]. Methods which attempt to resolve all (in DNS) or at least part (in LES) of the unsteady acoustic pressure within the flow field calculation may properly be considered as time-domain Computational Aeroacoustics (CAA). The approach of references [6,7,8] which only extract statistically averaged information from a steady state flow calculation for input to an acoustic model are here referred to as CFD Coupled Acoustics (CCA).

As an alternative to using an acoustic analogy basis for the noise model, a semi-empirical approach to jet noise modelling can be created by using a database of experimental jet noise measurements. These are used in combination with simple flow parameters extracted from experimental observations of mean flow and turbulence in coaxial jets; the best example of this approach is the 'four source model' [9,10]. Inherent in this type of approach are assumptions regarding parameters such as mean velocity and turbulence intensity profiles in the jet mixing layers and so changes in noise due to geometric changes in the nozzle design which affect the turbulence properties in the mixing layers of the jet cannot be easily predicted. The aim of the present work is to examine the benefit of adopting the CCA approach in order to improve the generality of the four source model. This will be done by using a RANS-based CFD prediction as a flow model for coaxial jets and extracting from these predictions the parameters required by the four source model (e.g. effective jet definition and turbulence intensity). This should make the four source model capable of extension to any configuration for which CFD analysis is possible.

Firstly, comparisons are shown between experiment and CFD for a coaxial, co-planar, nozzle representative of that used in the measurements of Ko and Kwan [11] in order to confirm the accuracy of the RANS-CFD approach adopted here, in particular the turbulence model. CFD predictions are then shown for a similar co-planar configuration with differing area ratios to show how this affects peak turbulence intensity and location. A three-quarter cowl geometry is also predicted in order to confirm how this affects turbulence levels and to establish a firm basis for translation of real nozzle exit conditions into an equivalent co-planar nozzle.

2   METHODOLOGY

2.1 Experimental
Experimental measurements were carried out in a water-tunnel facility designed specifically for near-field jet mixing problems [12]. The working section was 1.125m long, 0.37m wide and 0.3m high and was made of perspex to allow ample optical access. The primary and secondary flows have separate circuits with flow rates monitored by rotameters. It is also possible to provide a co-flowing stream outside of the jet nozzles to simulate a flight stream. Turbulence management units are provided in both jet flows in order to give a uniform profile with as low turbulence level as possible at the exit from the nozzle system. The tertiary flow is also used to create a very low velocity co-flow in order to stabilize the flow in the downstream mixing region.

An LDV system is used to provide mean velocity and turbulence data. This consisted of a single channel forward-scatter fringe-mode velocimeter with a Helium-Neon laser operating at a nominal power of 10mW. Naturally occurring particles within the water supply were found to be sufficient to produce a high data rate with no additional artificial seeding. Typical sampling rates were 1kHz and mean velocities were produced from a minimum of 25,000 samples. Bragg cell frequency shifting was incorporated into the system to provide sensitivity to flow direction and allow high turbulence intensities to be captured. Signal processing was carried out using a TSI IFA 550 frequency processor (as described in [13]). No corrections were made for sampling bias as errors were minimised by use of high data rates compared to typical velocity fluctuation frequencies, as suggested by Erdmann and Tropea [14].

2.2 Computational

The CFD methodology employed in the current work solves the time-dependent, mass-weighted and ensemble-averaged conservation equations for mass, momentum and total energy. The governing equations are discretized using a finite volume technique on a structured curvilinear multiblock mesh, using collocated variables. A segregated approach is used; each equation is discretized in the form of a scalar implicit equation with linearized coefficients. The pressure-correction technique is used to couple the velocity and pressure fields, and is implemented in such a manner to work efficiently for both incompressible and compressible flows [15].

The cell face flux is discretized using a basic first order upwind scheme for the convective flux (based upon the cell face normal velocity), and central differencing is used for all other terms. Higher order discretization schemes are implemented as a deferred correction to the first order upwinding of the convective part using a general upwind-biased MUSCL type scheme.

The standard k-ε turbulence model is used together with wall functions on the nozzle walls [16].

3   RESULTS

3.1 Calibration of Co-planar coaxial nozzle

The four source model [9] used the experimental data of Ko and Kwan [11] to justify that the peak turbulence intensity in the interaction region of a coaxial jet configuration should be 10% of the primary jet velocity, rather than the standard single jet turbulence level of 15%. The aim of the experimental measurements and initial CFD predictions in this work was to confirm the correctness of this assumption, and to validate the CFD model so that it can then be used to assess the influence of geometry changes on mean and turbulent quantities.

The geometry chosen for the experimental study is representative of that used by Ko and Kwan in that an identical secondary to primary area ratio (β) of 2.7 was used, whilst the contraction ratios, lip thicknesses, etc. were all somewhat different due to design considerations (see Fig. 1). The Reynolds number based upon primary diameter (D_i) and bulk average primary velocity is 80,000. The small geometrical differences were considered as having a negligible effect on the measured jet mixing. Figure 2 shows the various jet mixing and potential core regions which characterise coaxial jets. It is clear that the present experimental results are in good agreement with the Ko and Kwan study.
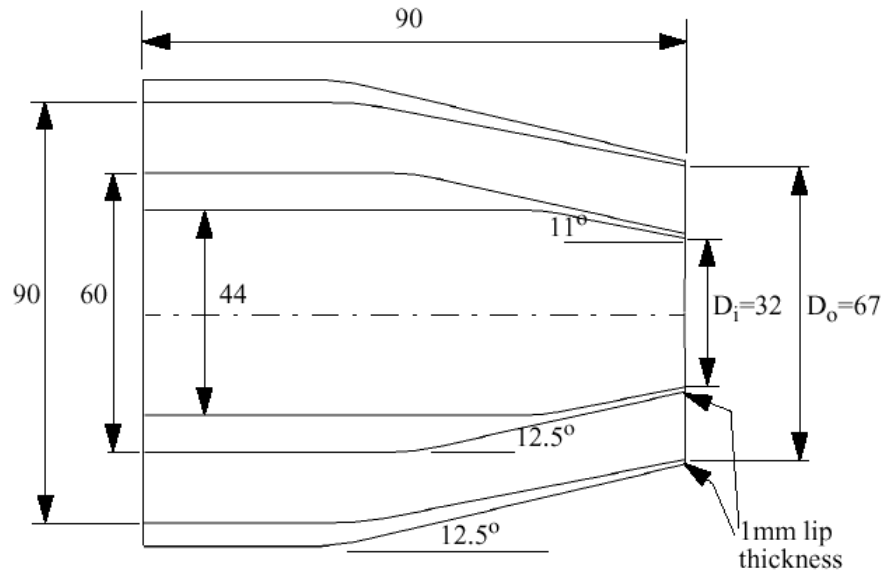
Figure 1. Co-planar, coaxial geometry
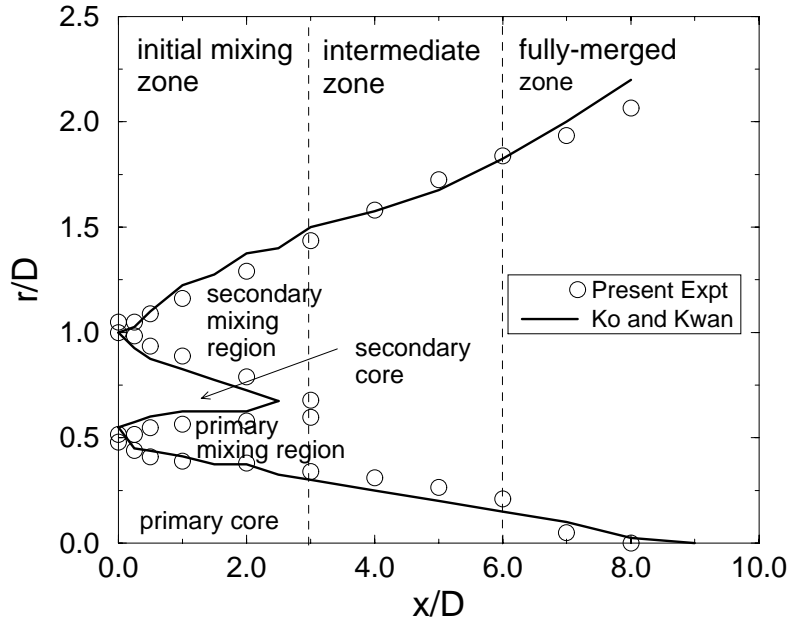
Figure 2. Coaxial jet regions

The CFD predictions used a two-dimensional axisymmetric configuration, with a downstream length of $30D_i$ as shown in Fig. 3. The grid contained four blocks with a total of approximately 10,000 grid points. This was a result of a grid refinement study and if the same grid density was used in a true three-dimensional topology would result in reasonable numbers of points. Since the experimental setup could not measure turbulence intensities and velocity profiles upstream of the nozzle, plug profiles were chosen for velocity and a sensitivity study was carried out on inlet turbulence intensity and length scale in order to achieve a reasonable match with mean and rms streamwise velocity at the first available measurement station (x/D_i=0.25), the final values used were a turbulence intensity of 3% (based on primary velocity) and a length scale of $0.5D_i$ for both the primary and secondary flows. The co-flowing stream was set at very low velocity (less than 2% of primary velocity) and itself had low turbulence levels.
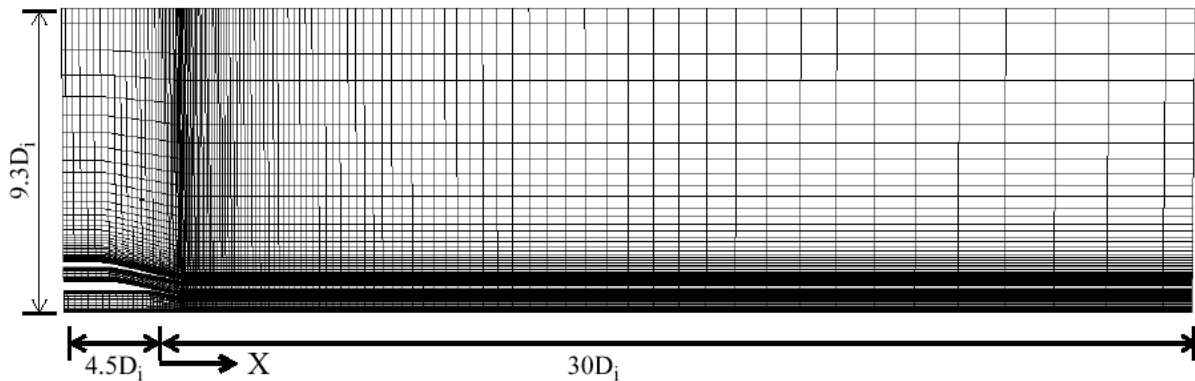
Figure 3. CFD domain and grid

Figure 4a) shows contours of axial velocity for the CFD predictions. The shear layer between the primary and secondary flow has merged into the outer shear layer by 7 primary diameters downstream, and the primary potential core length is around 12 primary nozzle diameters. The flow rates set in the experiment were such that using the geometric exit area the primary velocity should be $2.5ms^{-1}$, however, the nozzle exit angle combined with the presence of the secondary stream causes the primary stream tube to continue contracting downstream of the exit plane giving an actual primary jet core velocity of almost $3ms^{-1}$. As will be seen later, this is consistent with the experimental data. Contours of turbulence intensity for the CFD predictions are shown in Fig. 4b). To be consistent with the data presentation of Ko and Kwan, this is computed from the streamwise normal stress normalised by the geometric jet primary velocity. The last downstream location in the data presented by Ko and Kwan is at 8 primary diameters where the peak turbulence intensity is around 12%, the CFD predictions also show a 12% intensity at this location but the turbulence energy is *still increasing downstream* and the overall maximum is actually 16% at 17 primary diameters.
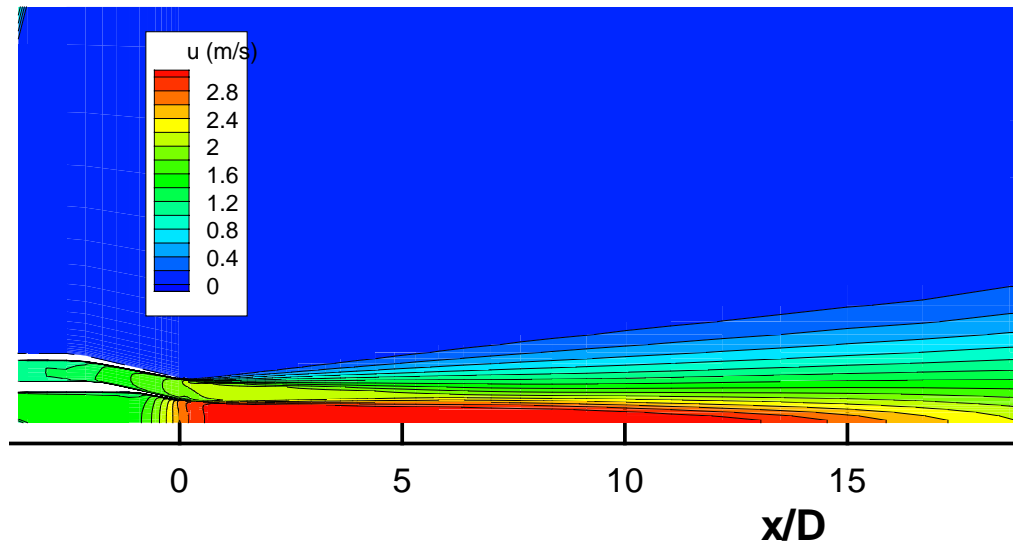
a) **axial velocity**
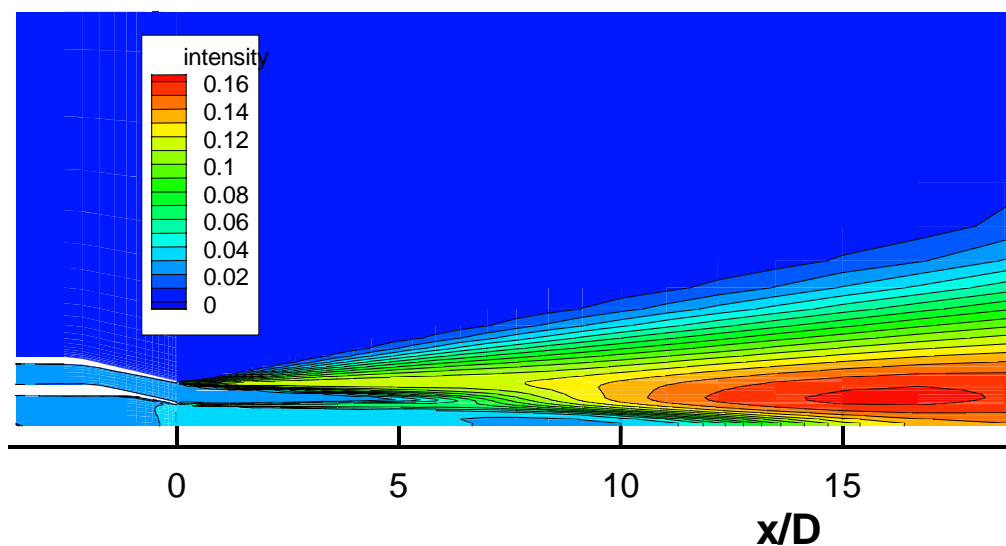
b) **turbulence intensity**

Figure 4. CFD prediction of calibration geometry

Comparisons of axial velocity for CFD and experiment are shown in Fig. 5, excellent agreement is observed at all axial stations. The only noticeable discrepancy is that the CFD shows a slightly 'flatter' primary velocity profile, this is to be expected since the upstream boundary conditions use a flat profile whereas the experiment has a complex feed system. Clearly this could be easily be improved by only small alterations to the upstream boundary condition profile. A comparison of turbulence intensity profiles is shown in Fig. 6. At the first location, the peak in the primary/secondary shear layer is underpredicted, but this is to be expected as the grid has only one node to resolve the peak at this station. Between 1 and 3 primary diameters downstream very good agreement is observed for both the primary/secondary shear layer peak and the primary core turbulent fluctuations. The secondary shear layer peak is underpredicted by a few % up to 3 primary diameters. At the 5 and 7 primary diameter stations the agreement is poorer with the experiment showing unexpectedly high fluctuations of around 18%. Also, it is noticeable that the experimental profiles are not smooth. Further investigation confirmed that the experimental data was taken without the presence of a co-flowing stream and low frequency unsteadiness was occurring as the jet flow spread into the experimental domain. Recent measurements have shown that this tends to increase the measured 'turbulence' levels of the furthest downstream stations by about 2%.
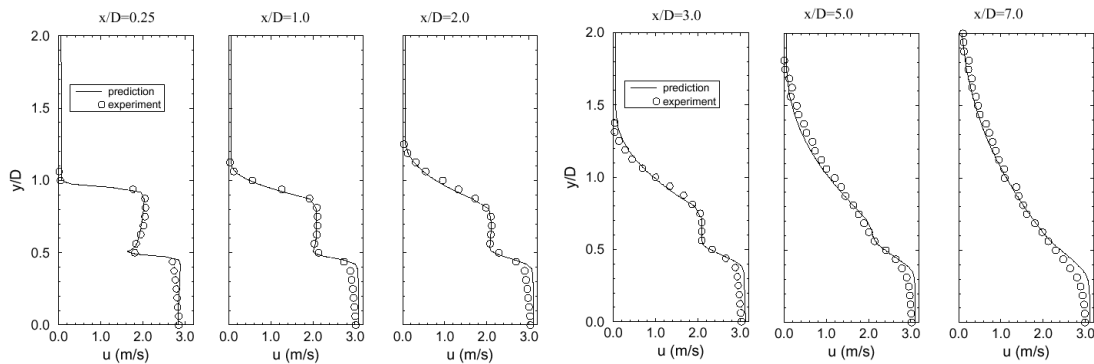
Figure 5. Mean velocity comparison, calibration geometry
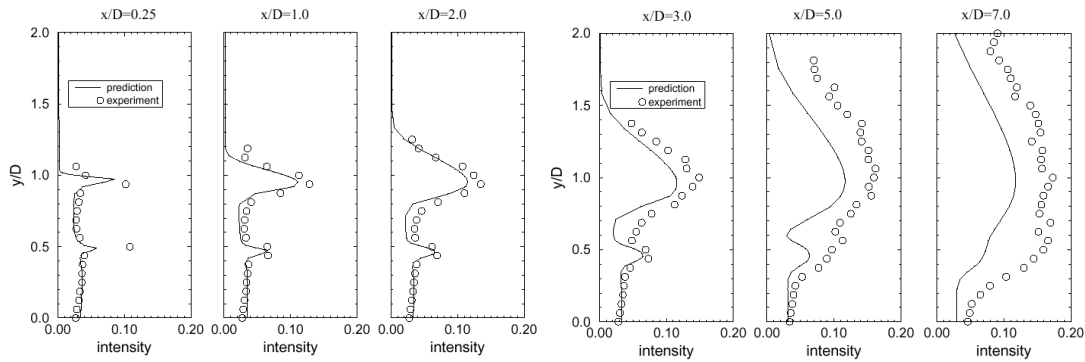
Figure 6. Turbulence intensity comparison, calibration geometry

This exercise shows that the RANS-CFD methodology is capable of highly accurate velocity predictions and good turbulence predictions. Both experiment and CFD confirm that the Ko and Kwan data is reasonable for the interaction region up to 7 primary diameters, but the value of 10% intensity used in the interaction region of the four source model is at the lower bound of that found in all three data sets. The steady increase in turbulence intensity up to a peak of 16% near the end of the potential core shows that the interaction region defined in the four source model cannot be characterised by a single level of turbulence intensity. All turbulence intensity data have been defined by the primary velocity at the geometric exit, but the acceleration downstream means that the actual primary core velocity is actually 20% higher - if this were used as the reference velocity for turbulence then the CFD and experimental values quoted in this section should be factored by 0.8 in order to compare to the Ko and Kwan values. The issue of an 'effective parallel' coaxial jet is investigated further in Section 3.3.

3.2 Influence of area ratio

The four source model is calibrated using experimental data for an area ratio of 2.7, and when applied to area ratios more typical of modern turbofan engines requires adjustments in order to match experimental noise spectra. By computing the flow for two differing area ratios we can observe how the mean and turbulent quantities change and so provide a more physical justification to factors introduced into the noise model.

The geometry used in Section 3.1 causes ambiguities in that the primary flow continues to accelerate downstream of the nozzle exit. The geometry used here aims to avoid this problem by using shallower convergence angles (5° inner and 7° outer) together with a small 20mm parallel extension and has also been used in experimental noise tests. The predictions also use a longer upstream development region and upstream turbulence boundary conditions have been altered to 1% intensity (based upon primary velocity) and a length scale of 0.1 primary diameters - this was to reflect the conditions expected in the noise test facility. The Reynolds number based upon primary velocity and diameter was 500,000.

Two cases have been calculated corresponding to area ratios (β) of 2 and 4, both with a velocity ratio (λ) of 0.7. Contours of turbulence intensity (normalised by primary jet velocity) are shown in Fig. 7. The β=2 case has a shorter potential core together with a region of peak turbulence that is further upstream and of a higher magnitude. The magnitudes of turbulence intensity are more clearly seen in Fig. 8 which shows the variation along axial lines aligned with the primary and secondary nozzle lips. The primary lip line shows that the turbulence intensity in the fully mixed zone is around 1.5% higher for an area ratio of 2 as compared to 4. In the initial region, turbulence intensity is essentially identical for both area ratios gradually reducing from 7% until the secondary and primary shear layers begin to merge (at 5 and 9 primary diameters respectively) when the intensity rapidly increases. The secondary lip line (Fig. 8b) also shows little difference in the initial region with a fairly constant intensity of 9.5% until the shear layers begin to merge.
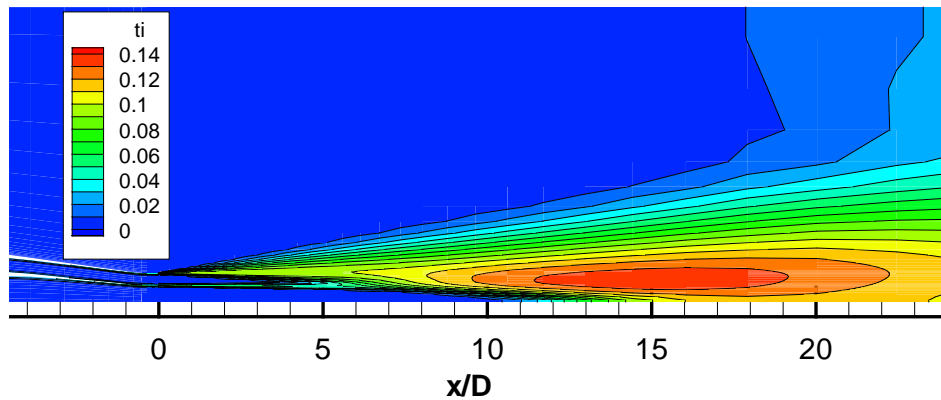
a) area ratio 2
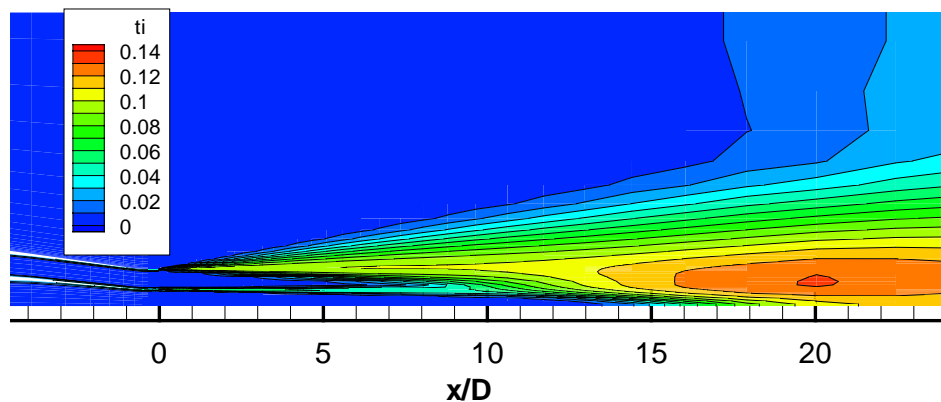
b) area ratio 4

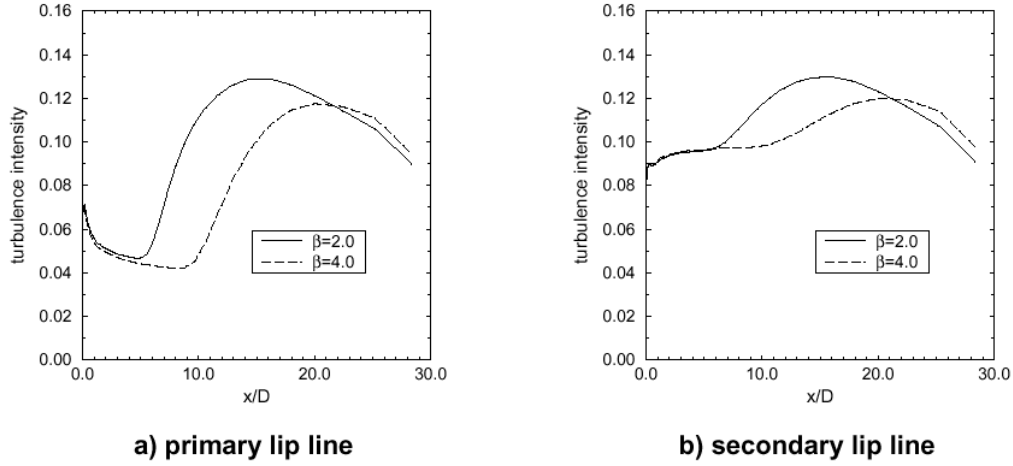**Figure 7. Influence of area ratio on turbulence intensity**

a) primary lip line **b) secondary lip line**

Figure 8. Turbulence intensity along nozzle lip lines

The four source model in the fully mixed region uses an equivalent 'fully mixed' velocity based upon conservation of mass and momentum, this is related to the primary velocity by

$$V_m = V_i \frac{(1 + \lambda^2 \beta)}{(1 + \lambda \beta)} \tag{1}$$

this gives for $\beta=2$, $V_m=0.825V_i$ and $\beta=4$, $V_m=0.779V_i$, so that V_m for $\beta=4$ is 0.94 of V_m for $\beta=2$. If we expect that the turbulent fluctuations should scale with the fully mixed velocity, then the peak turbulence intensities should also be in this ratio, which is indeed found to be the case. This confirms that although area ratio does influence peak turbulence intensity in the fully mixed region, this can be modelled by scaling with the fully mixed velocity.

3.3 Co-planar equivalent of three-quarter length nozzle

As was shown in Section 3.1, a convergent coaxial nozzle can create accelerations in the flow downstream of the geometric nozzle exit plane. This causes difficulties with the four source model as its basis is a parallel coaxial flow with a specified primary velocity and velocity ratio. In addition, many high bypass ratio turbofan engines do not have a full length cowl (as this leads to a weight penalty), the nozzle exits are no longer co-planar and there is also the presence of the bullet. Consequently the primary and secondary flows undergo acceleration, deceleration and curvature before reaching a parallel flow which may be considered as the input to the four source model. In this section we have computed the flow in a geometry with a three quarter length cowl and integrated the flow at various stations in order to deduce equivalent jet velocity and area ratios.

Predictions were carried out in a similar manner to the earlier calculations and resolved the downstream mixing region even though this was not of immediate interest. The calculations are incompressible so that variations in density can be ignored (a more complete study would recompute this flow with the correct nozzle pressure ratios and temperatures). At the nozzle geometric exits, the nominal velocity ratio was 0.7 and the area ratio was 2.6, the co-flowing stream velocity was set at 1% of the primary velocity. Figure 9 shows contours of velocity magnitude (normalised by the primary jet exit velocity) and velocity vectors. The flow has been integrated at the three stations in order to deduce equivalent areas and velocities. The boundary between the secondary flow and the freestream (which was 0.01 of the primary) was taken as the location where

$$u = u_c + 0.05(u_o - u_c) \tag{2}$$

and the boundary between the primary and secondary as the location where

$$u = u_0 + 0.5(u_i - u_0) \tag{3}$$

and subscripts *i, o, c* refer to primary, secondary and co-flow respectively.
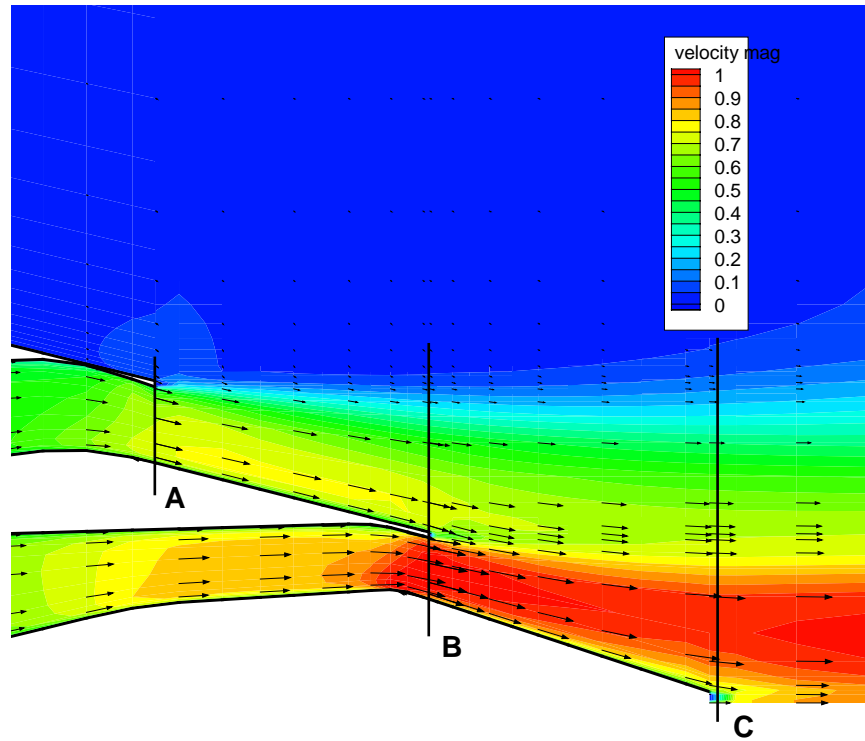
Figure 9. Three quarter length cowl velocity field

The results of the integration are given in Table 1. These show that by the primary exit plane (B), the secondary average velocity has reduced significantly, increased its mass flow due to entrainment and increased its effective area. From primary exit (B) to bullet (C) only a small deceleration is observed in both streams. The consequence is that the nominal $\lambda=0.7$, $\beta=2.6$ exit conditions are equivalent to a $\lambda=0.5$ and $\beta=5$ parallel coaxial flow immediately downstream of the nozzle. Caution should be expressed concerning the absolute accuracy of these figures as it was found that the secondary average velocity was sensitive to the location of the outer integral limit and the use of the 0.05 factor in Eq. (2) may not be the most appropriate choice.

Table 1: Integrated mean velocity and areas for three-quarter cowl

station	A	B	C
primary average velocity	-	1.0	0.97
secondary average velocity	0.7	0.49	0.45
normalised secondary mass flow	1.0	1.31	1.43
effective velocity ratio (λ)	(0.7)	0.49	0.46
effective area ratio (β)	(2.6)	4.6	5.3

4   CONCLUSIONS

Steady state Reynolds-averaged CFD predictions can be of use in providing mean flow and turbulence information for acoustic models.

When applied to coaxial jets, it is found that a CFD prediction with a k-ε turbulence gives good agreement with experimental LDV measurements for both mean velocity and turbulence intensity. The CFD

methodology can then be used with confidence to assess the influence of geometric changes to nozzle design on the mean and turbulent field and hence the change in the jet noise spectra.

Computation of two coaxial jet problems with differing area ratio showed that the peak turbulence intensity is greater for the lower area ratio, but the four source model use of an equivalent 'fully mixed' velocity will correctly reproduce this effect.

Many practical turbofan have three quarter length cowls and the two streams undergo curvature and flow acceleration and deceleration before a parallel coaxial flow is achieved. A CFD prediction of this geometry showed that a velocity ratio of 0.7 and area ratio 2.6 based upon the actual nozzle exits will be similar to a parallel coaxial jet with a velocity ratio of 0.5 and an area ratio of 5.

5   ACKNOWLEDGEMENTS

6   REFERENCES

1 Mead, C.J., Private Communication on recent work at DERA (Pyestock), 1998.

2 Mankbadi, R.R., Hayer, M.E. and Povinelli, L.A., 'Structure of Supersonic Jet Flow and Its Radiated Sound,' *AIAA Journal*, Vol. 32, no. 5, May 1994, pp897-905.

3 Mitchell, B.E., Lele, S.K and Moin, P., 'Direct Computation of Mach Wave Radiation in an Axisymmetric Supersonic Jet,' *AIAA Journal*, Vol. 35, no. 10, October 1997, pp1574-80.

4 Mankbadi, R.R., Hixon, R., Shih, S.-H. and Povinelli, L.A., 'Use of Linearized Euler Equations for Supersonic Jet Noise Prediction,' *AIAA Journal*, Vol. 36, no. 2, February 1998, pp140-47.

5 Zhao, W., Frankel, S.H. and Mongeau, L., 'Large Eddy Simulations of Sound Radiation from Subsonic Turbulent Jets,' *AIAA Journal*, Vol. 39, no. 8, August 2001, pp1469-1477.

6 Tam, C.K.W. and Auriault, L. 'Jet Mixing Noise from Fine-Scale Turbulence,' *AIAA Journal*, Vol. 37, no. 2, Feb. 1999, pp145-153.

7 Tam, C.K.W., Pastouchenko, N. and Auriault, L., 'Effects of Forward Flight on Jet Mixing Noise from Fine-Scale Turbulence,' *AIAA Journal*, Vol. 39, no. 7, July 2001, pp1261-1269.

8 Bechara, W., Lafon, P., Bailly, C. and Candel, S.M., 'Application of a k-ε Turbulence Model to the Prediction of Noise for Simple and Coaxial free jets,' *Journal of the Acoustical Society of America*, Vol. 97, no. 6, June 1995, pp3518-31.

9 Fisher, M.J., Preston, G.A. and Bryce, W.D., 'A Modelling of the Noise from Simple Coaxial Jets, Part I: with Unheated Primary Flow,' *Journal of Sound and Vibration*, Vol. 209, 1998, pp385-403.

10 Fisher, M.J., Preston, G.A. and Mead, C.J., 'A Modelling of the Noise from Simple Coaxial Jets, Part I: with Heated Primary Flow,' *Journal of Sound and Vibration*, Vol. 209, 1998, pp405-417.

11 Ko, N.W.M and Kwan, A.S.H, 'The Initial Region of Subsonic Co-axial Jets,' *Journal of Fluid Mechanics*, Vol. 73, 1976.

12 Behrouzi, P. and McGuirk, J.J., 'Experimental Studies of Tab Geometry Effects on Mixing Enhancement of an Axisymmetric Jet,' *JSME International Journal, Series B*, Vol. 41, 1998, pp908-917.

13 Jenson, L. and Menon, R.K., 'Evaluation Tests for LDV Signal Processors,' 3rd International Conference on Laser Anemometry Advances and Applications, Swansea, Wales, 1989.

14 Erdmann, J.C. and Tropea, C.D., 'Turbulence-Induced Statistical Bias in Laser Anemometry,' Proc. of 7th Biennial Symposium on Turbulence, Missouri-Roll, USA, 1981.

15 Page, G.J., Zhao, H., McGuirk, J.J., "A parallel multi-block Reynolds-averaged-Navier-Stokes method for propulsion installation applications", 12th Int. Symp. on Air Breathing Engines, Melbourne, Australia, Vol.1, 1991, pp. 864-876.

16 Launder, B.E. and Spalding, D.B. "The numerical computation of turbulent flows" *Comp.Methods in Applied Mech. and Eng*., 3, 1974, pp. 269-289.

Reference # of Paper: 10
Discusser's Name: Dr. David J. Moorhouse
Author's Name: Dr. G. J. Page
Question:
        At the end of your presentation you were commenting on actual engine parameters as opposed to an ideal experiment. Please comment on your confidence in the application of these methods to an actual full-scale engine.
Answer:
        While the absolute accuracy of the CFD prediction of a complete engine may be limited, we are providing a better approximation to the four-source model and so the noise predictions should be more accurate.

Discusser's Name: Prof. Ir. Joop Slooff
Author's Name: Dr. G. J. Page
Question:
        Did I understand correctly that until now you did not use the RANS data to refine the four-source model: but rather, to more precisely establish the proper values of parameters in the existing four source model?
Answer:
        Initially we are using the CFD predictions to adjust parameters of the existing model. We then intend to refine the four-source model based on the CFD and LDV results.

Predicting the Jet Near-Field Noise of Combat Aircraft

M. Harper-Bourne
QinetiQ, Farnborough, Hampshire
GU14 0LX, UK

Abstract

QinetiQ (previously DERA) is currently undertaking on behalf of the UK MOD an integrated programme of applied research to develop improved prediction methods for acoustic fatigue assessment on next generation combat aircraft. This paper describes ongoing work to develop practical methods of predicting the near-field noise of the high-speed exhausts of military jet engines, for use at an engineeering level. The study encompasses both jet mixing noise and broadband shock noise for single and twin jets and is focussed on predicting the intensity, spectra and spatial coherence of jet noise at the airframe, using a semi-empirical basis that marries aeroacoustic theory with source location data. The background to the development of the method through small scale heated model noise tests in the QinetiQ Noise Test Facility is described, followed by validation through near-field noise tests conducted in the QinetiQ GLEN sea-level engine test facility on a Rolls-Royce Spey turbojet engine.

1.   Introduction

Advances in the propulsion and airframe technology of combat aircraft have highlighted deficiencies in current knowledge of acoustic fatigue prediction (Ref. 1). These prevail in three areas. Firstly, in the pursuit of increased combat efficiency higher specific thrust engines are being developed producing higher levels of jet noise, further reducing the fatigue life of airframe and systems. Secondly, novel airframe and propulsion configurations are being adopted (e.g. JSF) that demand more advanced tools for the prediction of acoustic loading. Finally, new strategic requirements such as stealth, ASTOVL, supermanouverability and supercruise are resulting in the adoption of novel materials and lighter constructional techniques that must withstand the escalating jet noise environment. In combat, relatively small cracks in an aircraft's RAM could make it and its aircrew fatally vulnerable to attack by BVR missiles, for example.

The present paper reports ongoing research, being undertaken by QinetiQ for the UK MOD, to model the forcing functions of jet exhaust near-field noise (Fig. 1) essential to structural assessment, inparticular prediction of the exposure to the jet noise field in terms of overall level, spectral content and spatial coherence. The research is encompassing the primary noise sources of military turbojet exhausts, namely, jet mixing noise, Mach wave radiation and shock noise. A semi-empirical approach to modelling the noise sources has been adopted in order to provide practical engineering design aid tools within realistic time scales. The methodology combines classical aeroacoustic theory with measured source location data, enabling the noise field close to the jet to be defined spatially. The underlying source data is measured on (typically) $1/12^{th}$ scale heated air jets (single and twin). The developed methods are being validated against full scale engine near-field noise measurements, an example of which is presented.

2.   Near-field Research Programme

In general, use of sub-scale test data in aeroacoustics is well proven and has obvious cost benefits over full-scale engine tests, which can be reserved for model validation. For this work, the QinetiQ Noise Test Facility (NTF) at Pyestock, which is a unique world class noise measurement facility specifically designed for jet exhaust noise research, is being used. The facility permits the anechoic testing at model scale hot, high velocity, conditions representative of combat aircraft, with forward flight simulation if required. The need for a hot testing capability in jet noise research cannot be overemphasised as temperature determines the relative balance of the different noise sources present in the exhaust of a turbojet engine. In addition, model scale anechoic testing permits the individual components of jet noise to be studied, which would be impractical in engine tests. This flexibility provides scope for a more fundamental understanding of the noise mechanisms and the possibility of developing methods for the amelioration of jet noise.

The fundamental mechanisms of military jet engine noise, if not fully understood are at least well known (Ref. 2). In addition to the primary jet noise sources of Fig 1, it is intended that the jet noise modelling should address all of the features listed on Fig. 2, which includes relevant configuration and operational aspects. Of the noise sources, shock screech, which is a common feature at model scale, is rarely observed at full scale but may be relevant to the modelling of missile exhausts.

Generated within the engine, core noise needs to be identified and quantified directly from engine exhaust measurements. In the near-field it is also necessary to consider the hydrodynamic perturbations of the turbulent eddies in the exhaust (Fig. 3),which can be done at model scale. The hydrodynamic field does not propagate as sound but needs to be considered, along with the acoustic elements, when considering the nozzle structure, or when the exhaust is close to, or scrubbing, the airframe such as with buried 'stealthy' type propulsion nozzle systems. For the interaction of noise with the airframe, a proprietary boundary element method (Ref. 3) is proposed for use with the free field models of the current work.

$\mathbf{p}(\hat{\zeta}, \mathbf{t})$ Intensity and spectrum

$$C(\hat{z}, \hat{\zeta}, \tau) = \overline{\mathbf{p}(\hat{z}, \mathbf{t}).\mathbf{p}(\hat{\zeta}, \mathbf{t} + \tau)}$$

Spatial coherence and cross-spectrum

Mach Wave Radiation

Shock Noise

Mixing Noise

Free-jet simulation used in conjunction with acoustic FE/BE methods e.g. Comet for input to structural analysis
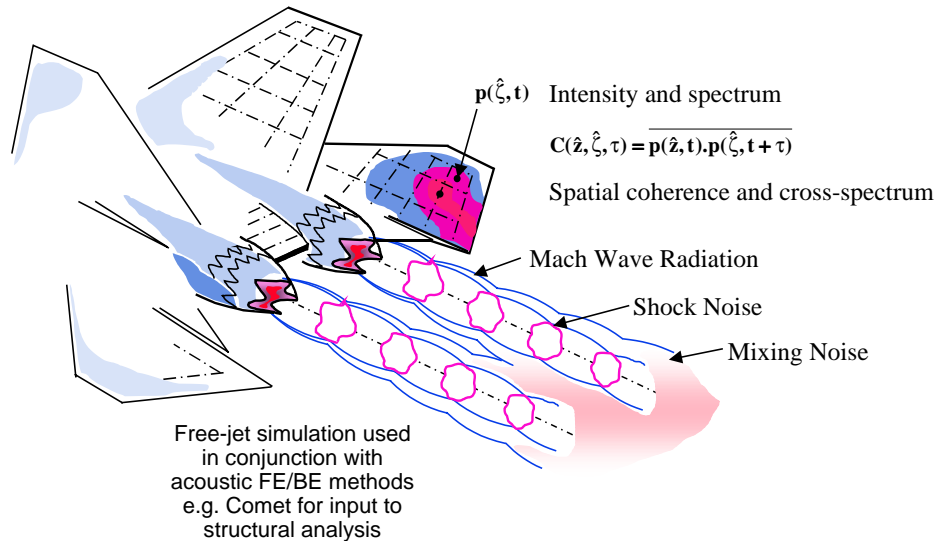
Fig.1 Combat Aircraft Jet Noise Sources

The fact that a jet flow is a spatially distributed noise source has significant implications when predicting jet near-field noise. The spatial extent of the sources along the jet and their frequency dependence can be determined using an acoustic imaging technique such as Polar Correlation (Refs. 4 and 5) illustrated in Fig. 4. This sound field analysis technique was developed originally to provide a source location capability for use on full scale engines for Rolls-Royce.

Mixing Noise
Eddy Mach Wave
Shock Noise
Screech
Hydrodynamic
Core Noise

Single Jet
Twin Jet
Thrust Vectoring
LO / Stealth
ASTOVL

Reheat
Altitude / Mach No
Ground Effect

'Jet noise sources'

'Propulsion configurations'

'Operational'
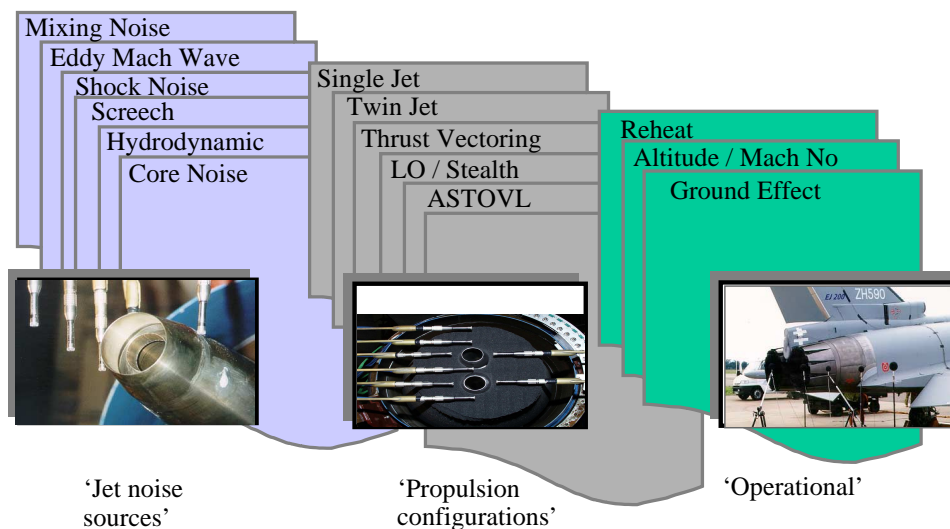
Fig.2 Near-Field Noise Research Programme

However, Polar Correlation is relatively expensive and time consuming and in order to provide a simple low cost source location capability for basic research at model scale, a wide angle (1.3m diameter) elliptic

mirror has been developed (Fig. 5a). Sound at the outer focal point is collected by the mirror and focussed onto a microphone (Fig. 5b) at the inner focal point. A motorised three-axis traverse allows the source distributions within a jet to be readily surveyed and sources separated by as little as one wavelength can be resolved.

Conical Nozzle

X =6.4D, Y = 4.2D, K=27dB, Nozzle Diameter = 36 mm

U_j/a_o	OASPL
1.228,	145.7 dB
1.134,	142.3 dB
1.057,	138.3 dB
0.996,	132.5 dB
0.825,	124.3 dB
0.575,	112 dB
0.407,	103.6 dB
0.28,	93 dB
0.15,	85 dB

Shock noise

Mixing noise

Hydrodynamic

SPL (dB)

Frequency (Hz)

Fig.3 Near-Field 1/3rd Oct. Spectra for 36mm Model Jet

Fig.4 Polar Correlation

Typical results for an underexpanded convergent nozzle are presented in Fig. 6, which clearly shows the peaks indicating the presence of the shock cells. These measu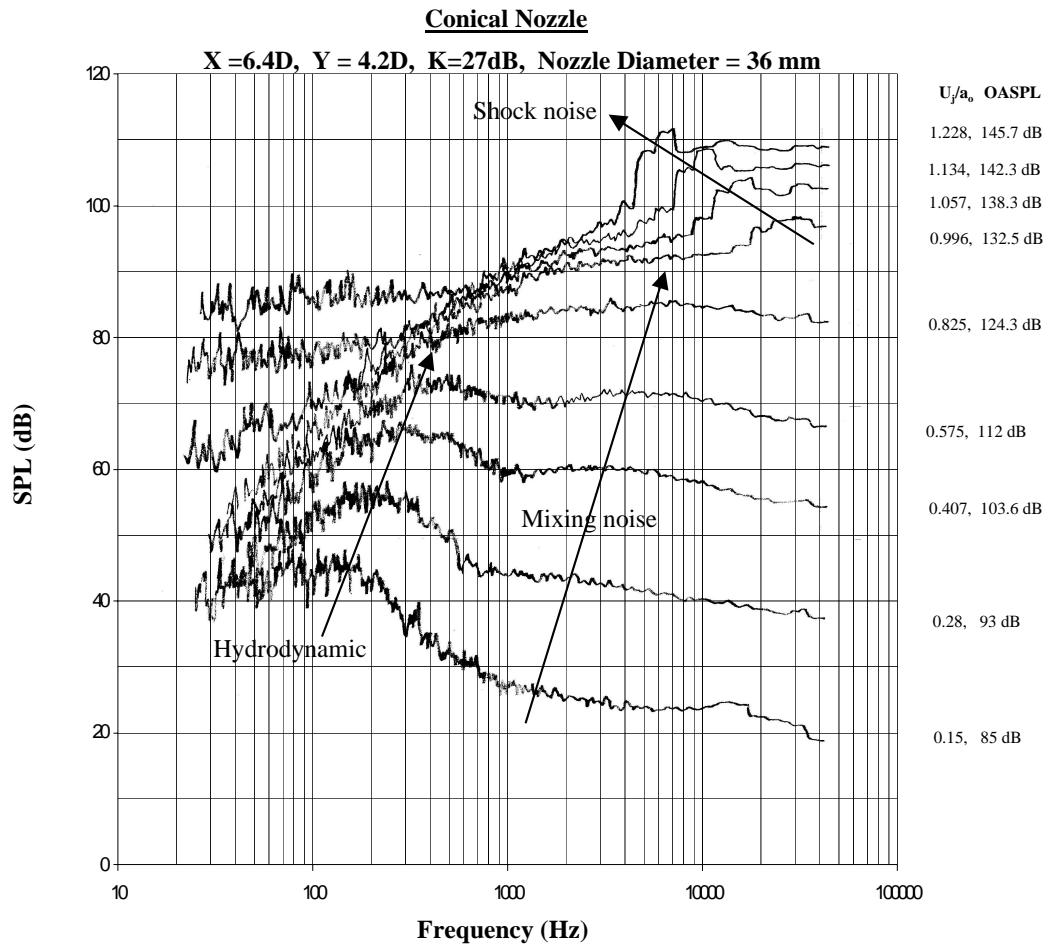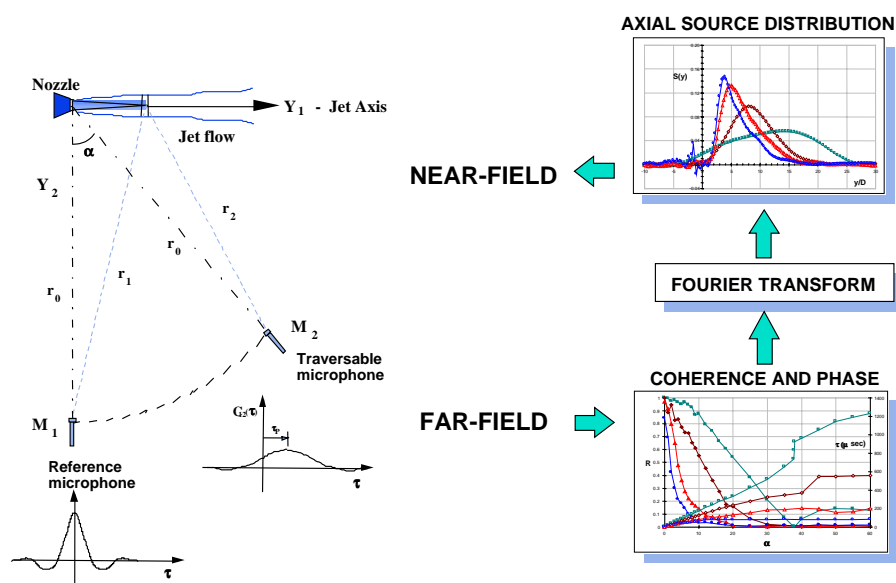rements have also helped confirm fundamental aspects of the shock noise model such as the discrete or concentrated form of the individual shock noise sources
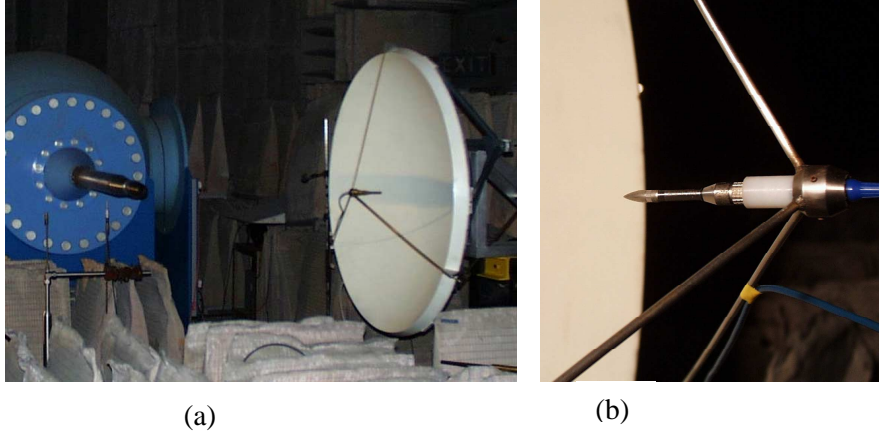

(a)   (b)

Fig.5 NTF Acoustic Mirror

3. Near-Field Modelling

3.1 Jet Mixing Noise

Lighthill's quadrupole theory of jet mixing noise (Ref. 6), yields for the far-field acoustic pressure

$$p(\hat{x}, t) = \frac{1}{4\pi a_0^2} \int_{\hat{y}} \ddot{T}_{rr}(\hat{y}, t - r/a_0) \frac{dV}{r} \tag{1}$$

where $T_{rr} = \rho U_r^2 + \{p - a_0 \rho\}$ is the Proudman form of the Lighthill quadrupole stress, i.e resolved in the direction of the observer (Fig. 7). In Ref. 7 it is shown that the near-field of a quadrupole element has the general form:

$$p \propto \frac{[\ddot{T}]}{a_0^2 r} + \frac{3[\dot{T}]}{a_0 r^2} + \frac{3[T]}{r^3} \tag{2}$$

The second and third terms in eqn. 2 are non-conservative and relate to the hydrodynamic component identified in Fig 3, while the first term is responsible for the near-field acoustic component. It therefore follows that eqn. 1 is also valid for the near-field acoustic pressure of a jet flow, as well as the far-field. For the high speed jet flows considered in the present work the term $\{p - a_0 \rho\}$, responsible for entropy noise (Ref. 8), is assumed negligible and ignored here.

Starting with the power spectral density of the acoustic near-field, in Ref. 9 a generic form is derived for the self noise of a jet using two-point space-time turbulence correlation measurements in eqn. 1. This exercise, undertaken in a fixed frame of reference, yields the following for the power spectral density (psd) of the mixing noise at point $\hat{z}$ (microphone M1) in Fig. 7:

$$G_1(\omega) = \frac{1}{\left(4\pi a_0^2\right)^2} \int_{y_1} S_r(y_1, \theta, \omega) \frac{dy_1}{r_1^2} \tag{3}$$

S_r is the source strength per unit slice of jet at the axial station y_1 for the radian frequency $\omega (= 2\pi f)$ in the direction of field point $\hat{z}$ and is given by

$$S_r(y_1, \omega, \theta) = G_{90}(\omega).D_p(y_1, \theta, \omega).C_A(y_1, s_d).S(y_1, \omega).D^2 \tag{4}$$

where: $G_{90}(\omega)$ is the far-field psd perpendicular to the jet axis, normalized to a radius of one nozzle diameter. $D_p(y_1, \theta, \omega)$ is the inherent directivity of the quadrupoles constituting the jet mixing noise sources, θ being the local angle to the jet axis of observation point $\hat{z}$ relative to the jet slice. $C_A(y_1, s_d)$ defines convective amplification (determined in a fixed frame of reference) resulting from the axial convection of the turbulent eddies within the jet shear layer and s_d is the Doppler shifted axial decay Strouhal number of the turbulence.

$S(y_1, \omega)$ is the normalized source strength density 90^0 to the jet axis, derived from source location measurements such as Polar Correlation or the acoustic mirror and is defined:

$$\int_0^\infty S(y_1, \omega) dy_1 = 1 \tag{5}$$

In Ref. 9, the lateral decay scales associated with self noise are shown to be acoustically compact and this permits the three dimensional form of eqn. 1 to be reduced to the axial line integral of eqn. 2. In Ref. 10, the one-dimensional form of eqn. 3 is shown to be acceptable providing $r_1 \geq D$ (stations closer than 1D are likely to incur errors exceeding 1dB).

For convective amplification, the fixed frame analysis of measured filtered turbulence space-time-correlations of Ref. 9 yields: $C_A(y_1, s_d) = \dfrac{1}{[1 + s_d^2]^m}$ where $s_d = \dfrac{\omega L_1}{U_c}[1 - M_c \cos\theta]$ and typically m=1.5

The quantity $\omega L_1 / U_c$ is the local longitudinal turbulence decay Strouhal number (L_1 being the axial separation at which $R(\eta_{l_1}, \omega) = 1/e$). Each spatial source distribution has a dominant characteristic value determined by the jet Strouhal number $\omega D / U_j$. Note for s_d large, the convective amplification tends to three powers of the Doppler factor. Also, at the Mach angle $s_d = 0$, and the convective amplification factor is equal to unity (rather than the infinity of Lighthill's original analysis).
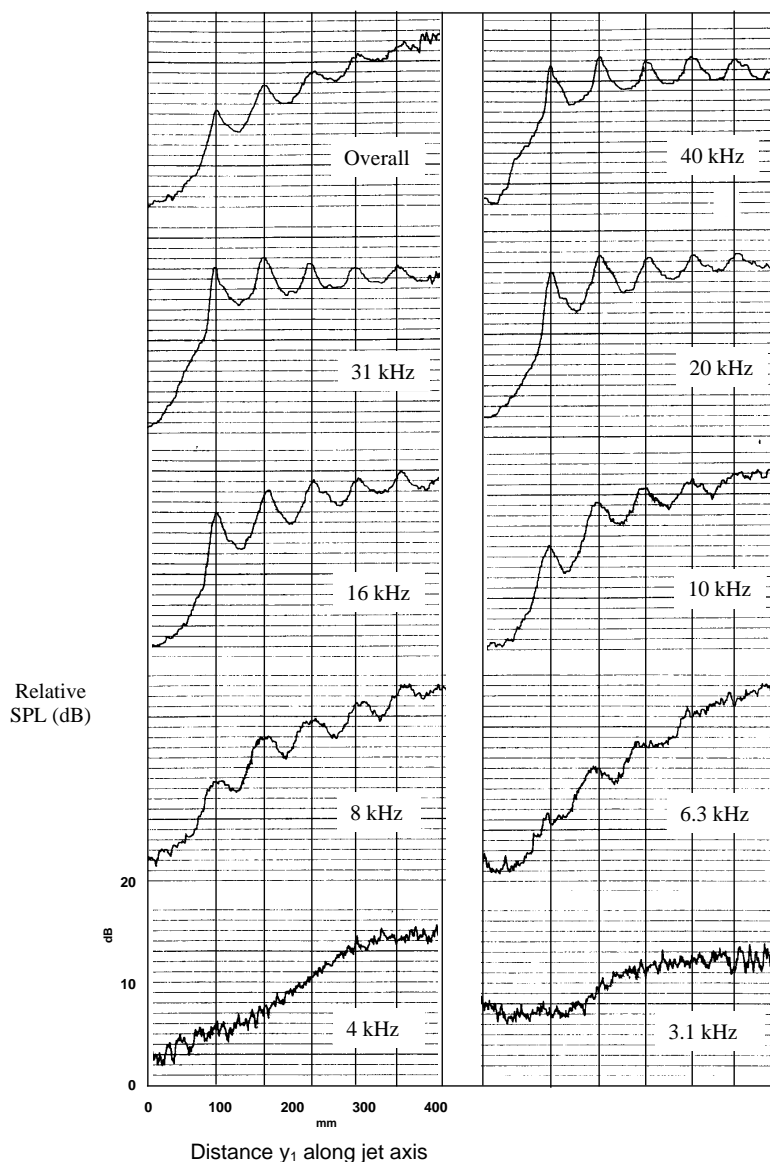

Fig.6 Mirror Axial Traverse, Underexpanded Jet, PR=3.7, 46 mm Conical Nozzle
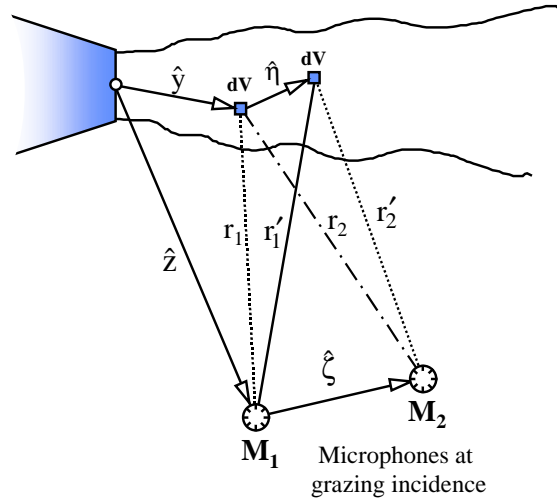
Fig.7 Co-ordinate System for Near-Field Analysis of Jet Mixing Noise

Typical source distributions for a range of jet Strouhal number are shown in Fig. 8 for a round convergent jet of velocity ratio $U_j / a_0 = 0.8$. These are shown as comprising two components educed from Polar Correlation measurements, one for the mixing region of the jet (red curve) and one for the fully developed downstream region (blue curve). The component curves take the form:

$$S_m(y_1, \omega) = W_m / [6Y_m] \cdot [y_1 / Y_m]^3 \cdot e^{-y_1 / Y_m} \quad \text{and} \quad S_{fd}(y_1, \omega) = 2.W_{fd} / Y_{fd} \cdot [y_1 / Y_{fd}]^3 \cdot e^{-[y_1 / Y_{fd}]^2}$$

where $Y_m = Y_{pm} / 3. D$, $Y_{fd} = Y_{pfd} . D . [2/3]^{0.5}$ and $S(y_1, \omega) = S_m(y_1, \omega) + S_{fd}(y_1 \omega)$. The quantities W and Y_p define the peak of each distribution and are functions of the jet Strouhal number $St = fD / U_j$

The effect of increasing Mach number M_j is to produce some stretching of the distributions. Where nozzle geometry, or some form of flow excitation, generates enhanced mixing, the distributions are likely to be shortened. Such an effect is described in Ref 10 for twin jets where a strong 'organ pipe' tone existed within the jet pipe at the Mach number under test. The result was increased broadband mixing noise whilst apparently shortening the source distributions by 50%.
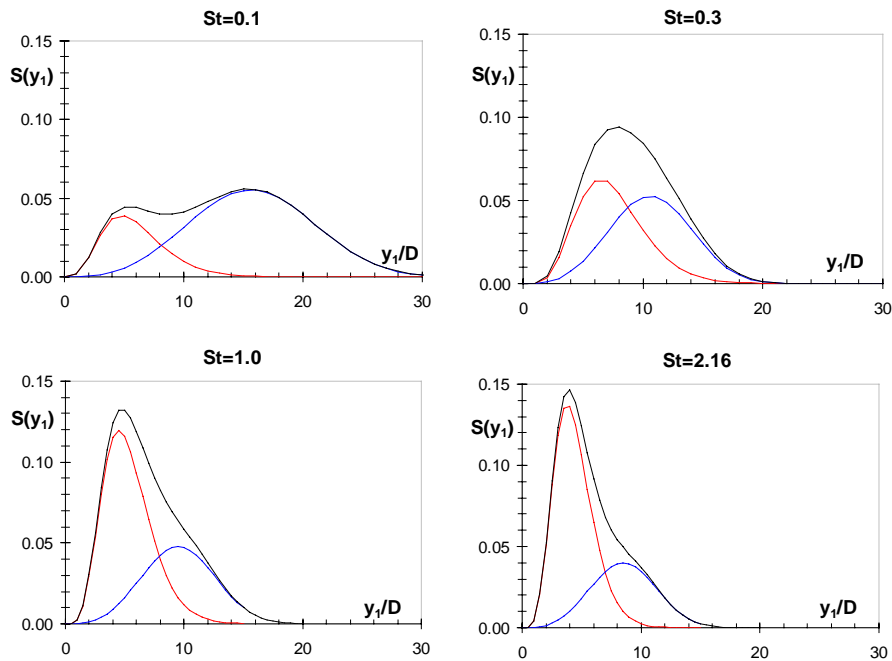

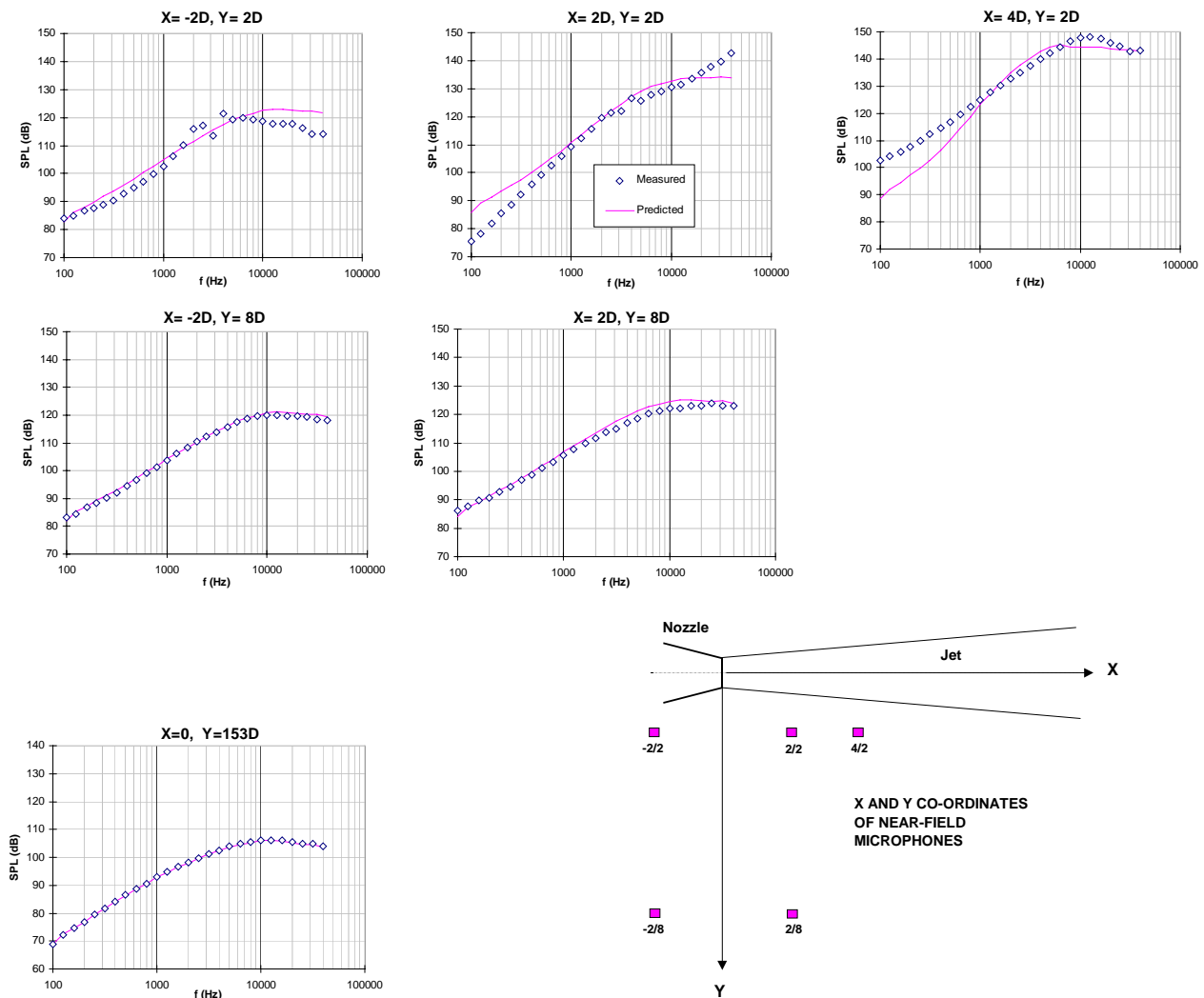*Fig.8 Generic Axial Distributions of Jet Mixing Noise*

Fig.9 Mixing Noise Predictions (M$_j$=1.5, T=885K, D=39mm Con-di Nozzle)

Using the generic maths model of eqns. 3 and 4, the near-field noise for any given jet size, combination of jets, jet velocity etc. can be predicted. In the case of multiple jets, Ref. 10 has revealed the need to incorporate the effects of jet shielding caused by refraction effects. However, this generally affects downstream stations away from the airframe.

Typical predictions using the model are compared with 1/3rd octave noise spectral measurements in Fig. 9 for a heated fully expanded M1.5 jet, for three inner near-field stations (Y=2D), two outer near-field stations (Y=8D) and a farfield station (Y=150D, $\theta = 90^0$). Since the method uses the far-field 90^0 noise spectrum for input, the good agreement obtained for this latter station (bottom left hand plot) simply verifies that the method is functioning correctly. Excellent agreement is also obtained for the outer nearfield positions (Y=8D) demonstrating that the objectives of the model are being met . At the inner near-field locations (Y=2D) some discrepancies are apparent between the measured and predicted spectra. However, the general agreement is still substantially good given that the predicted values are absolute and have not been adjusted empirically. At the downstream near-field station (X=4D), the discrepancy at low frequencies is probably due, at least in part, to the hydrodynamic field, which the results of Fig. 3 suggest would be relatively strong at this microphone location.

At stations close to the jet the assumption of grazing incidence, which is used to correct the microphone free field frequency response above 4kHz, could be an area for error since the sound waves are far from planar here. However, an area that is more likely to benefit from refinement concerns the possible axial variation of inherent directivity and longitudinal decay length scale (controlling convective amplification), which although treated as functions of Strouhal number are currently taken to be constant along the jet.

In the above test, the eddy convection speed is supersonic. However, at the Mach angle the model generates a radiation efficiency of unity and the Mach wave radiation is simply treated as jet mixing noise

within the model. In summary, Lighthill's classical theory, analysed in a frame of reference fixed relative to the nozzle, appears to provide a robust semi-empirical basis for predicting the near-field of jet mixing noise.

3.2 Shock Associated Noise

To compute the near-field of this jet noise component the phased linear array model of Ref. 11 is used. The model assumes that the shock noise is generated locally at the shock turbulence interaction sites formed at the end of each shock cell where a shock intersects the shear layer. The quasi-regular shock cell structure of an under-expanded supersonic jet is represented as shown in Fig 10, with the distance (L) between each source equal to the shock cell spacing, which reduces along the jet. The mirror measurements (Fig. 6) lend considerable credance to this discrete source structure. An important feature of the model is that adjacent sources are assumed to be correlated by convection of the turbulence, which retains some of its identity on passing from one shock to the next and sets the relative phase. This has two effects, firstly the characteristic frequency of shock noise, $f_p = U_c / \{L.[1 - M_c . \cos\theta]\}$ (Ref 11), reduces with increasing pressure ratio (Fig. 3) as a result of the shock cells lengthening and secondly, it exhibits a Doppler shift due to eddy convection. In Ref 11 a universal prediction scheme is derived, with the average shock spectrum and coherence (between adjacent cells) quantified through an analysis of far-field noise spectra. The overall intensity is shown to be a function of the Prandtl-Glauert factor β rather than jet velocity U_j, which controls jet mixing noise. This semi-empirical model of shock noise was adopted by the SAE as a standard prediction technique for aircraft engine noise (Ref. 12). Since the the work of Ref.11, studies have been undertaken to advance the physical understanding of shock noise (Ref. 13). However, for the acoustic analogy of the present work, the simple array model of Ref. 11 is considered adaquate.

With the shock noise source activity apparently concentrated at or close to those points where the shocks intersect the shear layer, for a round jet we may reasonably model the shock sources as annular regions of radius approximately equal to that of the nozzle as shown in Fig. 10a. Presuming that the azimuthal length scale of the source activity is similar to that of the turbulence then, as with jet mixing noise, for $r \geq D$ the equivalent point source array of Fig. 10b may be used to model the near-field of shock noise. Ignoring refraction etc caused by the flow, each source is assumed to be omnidirational and to have the relative strength indicated in Fig. 11a.
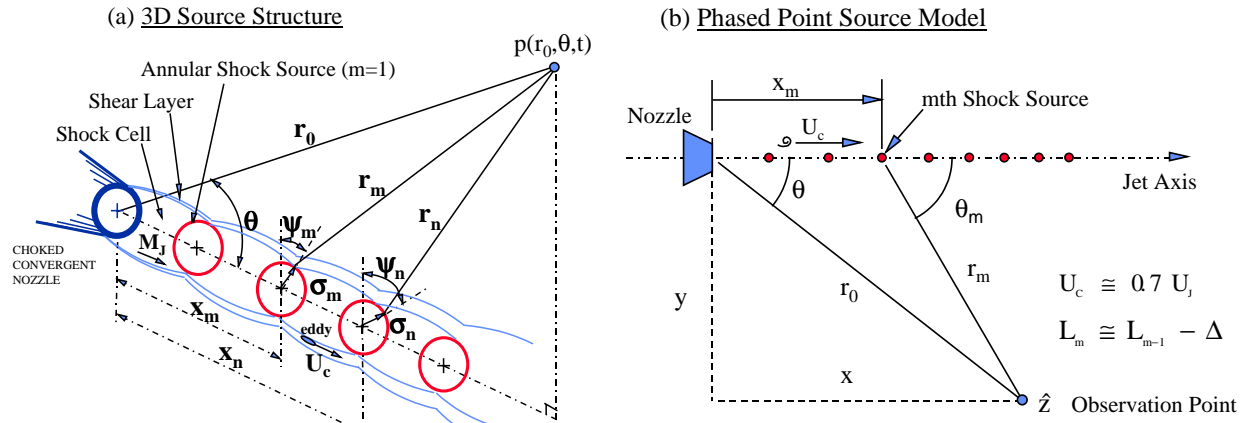
Fig.10 Shock Noise Source Model

Measurements confirm that the length of the first cell is given by Pack's formula (Ref. 11): $L_1 = 1.31 D\beta$ where $\beta = \sqrt{M_j^2 - 1}$ is the Prandtl-Glauert factor (M_J being the fully expanded Mach number inside a cell - a function of pressure ratio only) and D is the nozzle exit diameter. In practice, losses across the shocks and the effect of jet mixing take their toll and the shock cells reduce in length in an approximately linear fashion along the jet to yield for the mth cell: $L_m = L_1 - [m-1].\Delta L$ where $\Delta L = \delta.L_1$ and $\delta \approx 0.06$ (the latter depends on the degree of screech present as this can have a significant effect on the jet mixing rate and also the number N of active shock sources). In the flight case, the shock cells lengthen.

For the static model of Fig. 10b, the acoustic pressure at any field point $\hat{z}$ is simply:

$$p(\hat{z}, t) = \sum_{m=1}^{m=N} \frac{F_m(x_m, t - \frac{r_m}{a_0})}{r_m} \tag{6}$$

where F_m, the equivalent acoustic monopole source fluctuation for the mth shock, is evaluated at the appropriate retarded time and N is the number of shock sources. In the absence of screech, N is typically eight for an underexpanded jet issuing from a convergent nozzle. To determine the power spectral density of the shock noise we Fourier transform the auto-correlation of eqn.6, which we express in the form:

$$A_p(\hat{z}, \tau) = \sum_{m=1}^{N} \frac{1}{r_m} \sum_{n=1}^{N} \frac{\overline{F_m(x_m, t - \frac{r_m}{a_0}) F_n(x_n, t + \tau - \frac{r_n}{a_0})}}{r_n} \tag{7}$$

to subsequently obtain: $$G_p(\hat{z}, \omega) = \sum_{m=1}^{N} \sum_{n=1}^{N} \frac{G_{mn}(\omega)}{r_m r_n} e^{j\omega\left[\frac{r_m - r_n}{a_0} - \tau_{mn}(\omega)\right]} \tag{8}$$

where $G_{mn}(\omega) = \left|\tilde{G}_{mn}(\omega)\right| = R_{mn}(\omega).\{G_{mm}(\omega).G_{nn}(\omega)\}^{\frac{1}{2}}$, G_{mm} being the psd of the mth source and R_{mn} the coherence of sources m and n, which by definition must lie in the range 0 to 1.0 (for m = n, R is of course equal to unity for all ω). The terms for which $m \neq n$ cause interference effects in the spectrum, with constructive interference producing the Doppler shifted peak f_p mentioned previously.

Eddy convection generates the phase delay $\tau_{mn}(\omega) = \frac{x_n - x_m}{U_c(\omega)}$ where for a static jet the eddy phase speed is $U_c(\omega) = \kappa_c(\omega).U_j$ while for the flight case, $U_c = U_a + \kappa_c(\omega).\{U_j - U_a\}$. The convection factor $\kappa_c(\omega)$ varies slowly with frequency about the group convection value (Fig. 11b), which is about 0.72.

Since there is little data on how R_{mn} varies with m and n, the average for the whole jet, derived in Ref. 11 (as a function of frequency), is currently used in the model. Denoting the average coherence between adjacent shocks by C_1 and assuming Gaussian decay, the correlation coefficient may be written: $R_{mn}(\omega) = \{C_1(\omega)\}^{i^2}$ where $i = |n - m|$.

When completed, the acoustic mirror study (Fig. 6) should provide detailed data on the strength of individual shocks as a function of frequency. In the mean time, the overall shock strength data of Fig. 11a, which was obtained by placing an acoustic shield next to the jet, is used. For this we define a normalised relative source strength S_m so that $G_{mm}(\omega) = S_m.\frac{G_0(1, \omega)}{N}$ and $\sum_{m=1}^{m=N} S_m = 1$

where $G_0(1, \omega)/N$ is the average shock source strength (for r=1 metre) and $G_0(1, \omega) = r_0^2 G_0(r_0, \omega)$.

The overall intensity of shock associated noise is given by $I = \frac{\overline{p}^2}{p_0^2} = K\left(\frac{D}{r_0}\right)^2 g(\beta) \tag{9}$

For $\beta < 1.1$, $g(\beta) = \beta^4$ while for $\beta > 1.1$, the appearance of a Mach disc in the first cell results in a reduced dependence with $g(\beta) \approx \beta^{2.5}$.

The interference terms in eqn. 8 contribute little to the overall sound level and in order to satisfy eqn. 9, it can be shown that the source spectral density must be of the form:

$$G_0(r_0, \omega) = K_0.\left(\frac{D}{r_0}\right)^2.\frac{D}{a_0}.\beta.g(\beta).H_0(\sigma) \tag{10}$$

The function H_0 can be regarded as the universal source spectrum of shock noise. Its apparent dependence solely on pressure ratio rather than say jet velocity is recognised here by assuming H_0 to be a unique function of a Helmholtz number $\sigma = fL/a_0$ rather than Strouhal number $St_{cell} = fL/U_c$. In fact, whilst the interference effects are velocity dependent through the peak frequency f_{p90} and the Doppler factor, there is no evidence that the characteristic frequency of individual shock waves is velocity dependent.

The universal generic parameters, H_0 and C_1, as originally evaluated in Ref. 11 for unheated round jets, are presented, slightly modified, in fig.11b. These average data were obtained through a least squares fit of eqn. 8 to the measured far-field variation with polar angle θ of the sound spectral density (corrected to remove mixing noise).
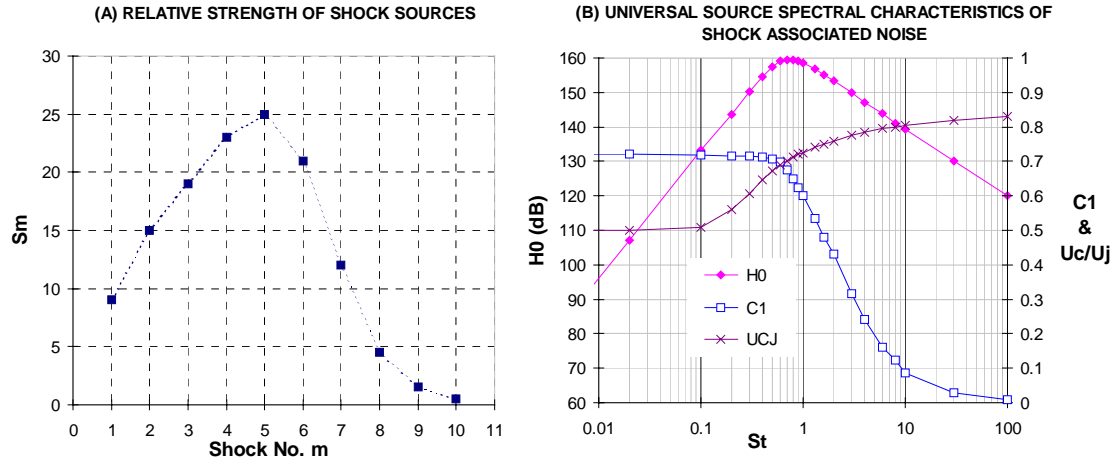
Fig.11 Shock Noise Model Data
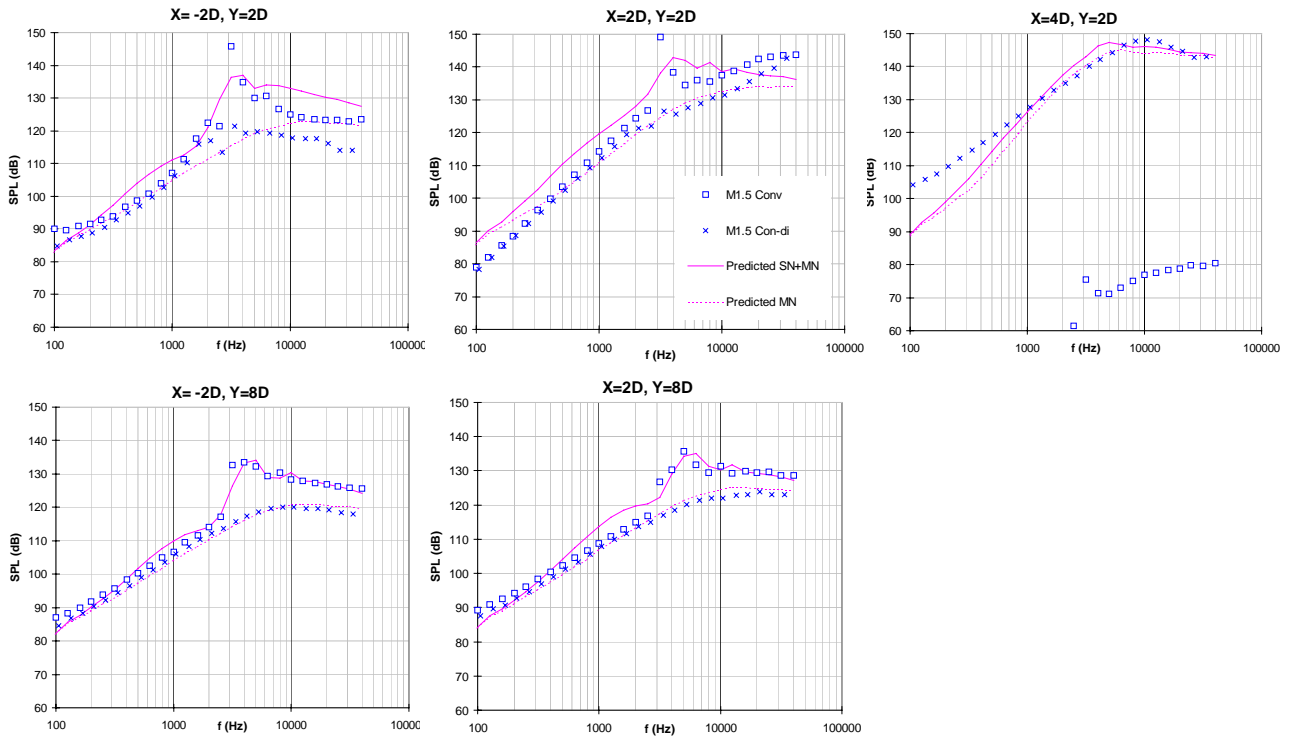
Fig.12 Shock Noise Predictions (M_j=1.5, T=885K, D=46mm Conical Nozzle)

The shock noise model is compared with measured near-field 1/3rd-octave spectra in Fig.12. For this test, which was also conducted in the NTF, the 39mm con-di nozzle was replaced with a convergent 46mm nozzle, and the five microphones were repositioned to retain the same X/D and Y/D values (Note that the downstream microphone malfunctioned in this test). Unfortunately, strong screech, which could affect the fidelity of the model, is visible in the data at the inner stations. Notwithstanding this, the degree of agreement between prediction and measurement is similar to that obtained for the mixing noise in Fig. 9. At the outer near-field stations reasonably good agreement is again obtained, while at the inner stations, discrepancies are once more in evidence. These should hopefully be rectified when more accurate information on the shock source strength as a function of frequency is available from the results of the acoustic mirror traverses referred to previously.

3.3 Spatial Coherence

The methodology used in deriving the jet noise near-field spectra has also been applied to predict the spatial coherence of the near-field noise. Knowledge of the spatial coherence is required in the correct assessment of airframe modal response.

The spatial coherence and phase for any two points $\hat{z}$ and $\hat{z}+\hat{\zeta}$ in the noise field (Fig. 7) is obtained from the cross-power spectral density of the acoustic signals at the points, which we can determine from the Fourier transform of the cross-correlation of the signals, namely;

$$C_{12}(\tau) = \underset{T\to\infty}{Lt}\ \frac{1}{T}\int_0^T p_1(t).p_2(t+\tau)dt \quad\text{and}\quad \tilde{P}_{12}(\omega) = \frac{1}{2\pi}\int_{-\infty}^{\infty}C_{12}(\tau).e^{-j\omega\tau}d\tau \qquad (11)$$

where τ is a time delay superimposed between the signals, C_{12} is the cross-correlation function and $\tilde{P}_{12}$ the (complex) cross-power spectral density (cpsd), which is conveniently expressed in terms of its modulus and phase:
$$\tilde{P}_{12}(\omega) = \left|\tilde{P}_{12}\right|\angle\tilde{P}_{12} = \sqrt{G_1(\omega).G_2(\omega)}.R_{12}(\omega).e^{j\omega\tau_p(\omega)}$$

R_{12} is the coherence of the two signals and τ_p the phase delay time. Typically, τ_p is a weak function of the frequency with a nominal value corresponding to the time delay at which the correlation function $C_{12}(\tau)$ peaks.

For jet mixing noise, inserting eqn.1 for the microphone signals in eqn. 11 and performing the Fourier transform we obtain, after some rearrangement, for the cross-power spectral density:

$$\tilde{P}_{12}(\omega) = G_{90}(\omega).\int_{y_1}D_{P_{12}}(y_1,\omega).C_{A_{12}}(y_1,\omega).S_0(y_1,\omega).e^{-jK[r_1-r_2]}\frac{dy_1}{r_1r_2} \qquad (12)$$

The principle difference between this result and the power spectral density of eqn. 3, is the presence of a diffraction exponential within the integral, involving the product of the wavenumber K of the sound and the path difference $r_1 - r_2$. A similar result is obtained for shock noise when the integral is then replaced by a double summation and the source strength is modified accordingly for S_m.
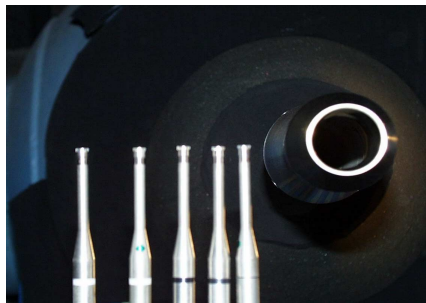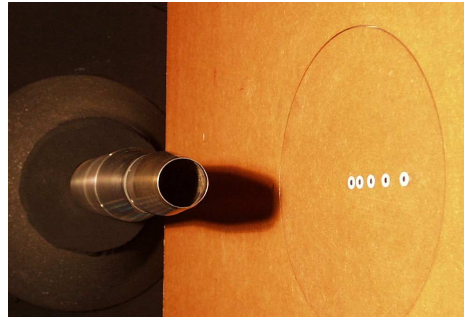
(a) Free Field Set-up   *(b) Semi-Free Field Set-up*

Figure 13. Model Scale Near-Field Jet Noise Tests on NTF Ground Rig

For a line source, such as jet mixing noise, which is spatially distributed relative to the wavelength of the sound, the diffraction exponential in eqn. 12 has a dispersive effect resulting in the decay of the coherence with increasing microphone separation. A single discrete source, shorter than say a quarter of a wavelength, would be acoustically compact and yield coherence $R_{12} \approx 1$ regardless of microphone separation. For multiple discrete sources separated spatially on a wavelength scale, such as shock noise, the coherence behaves in a complex manner comprising multiple peaks, not dissimilar to an optical diffraction pattern for a series of pin holes. In any event, the distributed nature of the sources has a significant effect on the coherence.

Finally, as with eqn.3, the factors D_p and C_A in eqn. 12 relate to the effect of inherent directivity and convective amplification but for two microphones in this instance. With the above exceptions, eqn. 12 is evaluated in exactly the same manner as eqn. 3, using the same generic source distribution data.
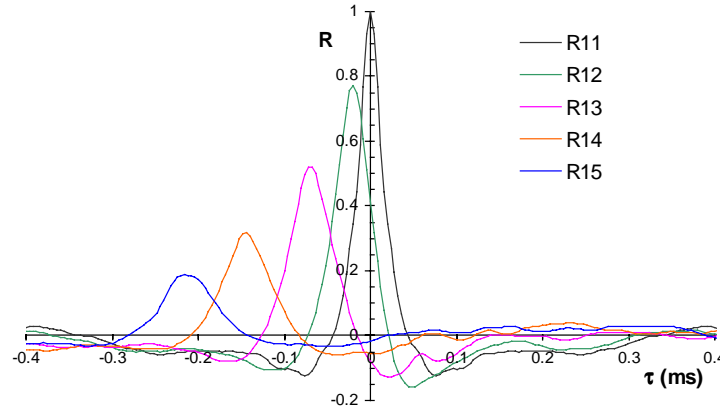

Figure 14. Near-Field Cross-Correlations for Model Scale Jet in the NTF

Model Scale Tests

   To investigate near-field spatial coherence, a 2D long linear array of five (6.3mm B&K) microphones was employed (Fig. 13a), with relative spacing between microphones increased progressively along the array to compensate for the lower rate of decay of correlation of the low frequency components of jet mixing noise. Similar tests were also made for a semi-free field environment (Fig 13b) using a large rigid board adjacent to the jet with flush mounted microphones.

   The microphone signals were acquired digitally using a sampling rate of 250Khz and appropriate anti-aliasing filters, for subsequent analysis off-line using software written in IDL (Interactive Data Language).
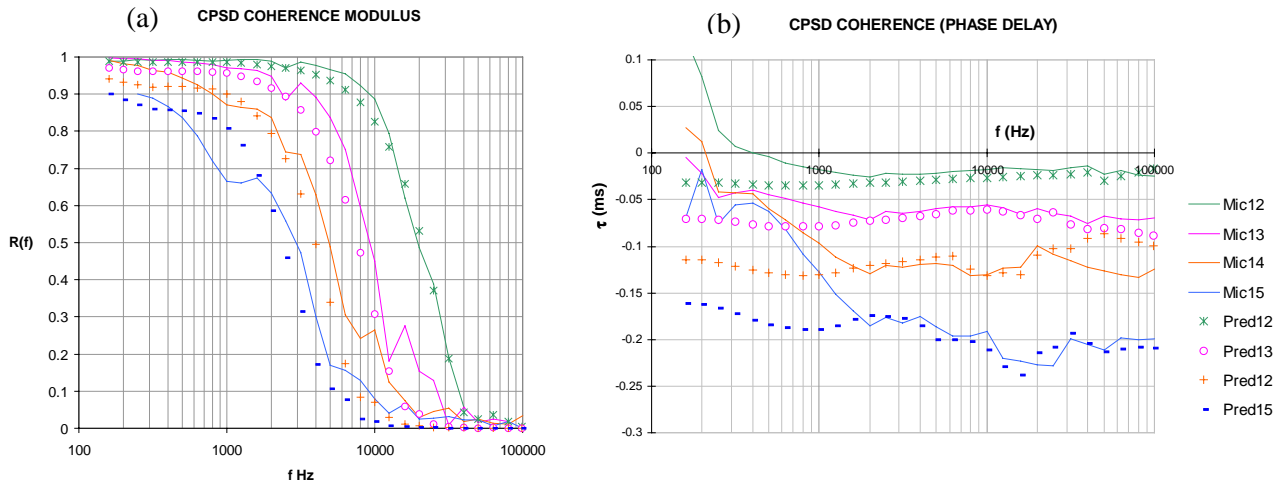
Figure 15 Model Scale Coherence and Phase Measurements Compared with Predictions

   Typical cross-correlations at M0.9, for a free-field set-up are shown in Fig. 14. For this the array was parallel to the jet axis and offset 3.5D. Microphone 1 was aligned with the nozzle exit and the array arranged downstream. The signals of the downstream microphones have been delayed relative to microphone 1. It is seen that the correlations not only decay with increasing microphone separation but that peak correlation occurs at increasingly negative time delay, indicating that the sound is coming from a spatially extended noise source whose centroid is downstream of the array. These observations are in keeping with those expected of mixing noise radiated by the turbulent shear layer of the jet.

   The coherence and phase for this test, determined in 1/3rd octave bands, is presented in Fig. 15 where they are compared with the predicted values obtained using eqn. 12. Referring to the coherence (Fig 15a), it will be seen that in general the predictions show good agreement with the measurements. As expected for a pure jet mixing noise source, the level of coherence reduces with increasing separation of the microphones and

also decreases with increasing frequency. At frequencies above about 50kHz (model scale) the correlation is virtually zero for all microphone separations. At this frequency the wavelength of the sound is around 7mm or 15% of nozzle diameter and the separation between microphones 1 and 2 was 15mm i.e. about two wavelengths at this frequency.

Turning to the phase information (Fig 15b), it will be seen that the agreement between measurement and theory is quite good above 2kHz where most of the energy resides, while below this frequency there is a growing discrepancy with reducing frequency, which is almost certainly due to the presence of the hydrodynamic near-field. In terms of phase angle, the error is quite small here being about 20 degrees at most, which is unlikely to be significant in airframe structural analysis.

Engine Tests

To provide data for initial validation of the near-field models applied to full scale engine applications, noise tests were conducted on a Spey turbojet engine in the QinetiQ GLEN sea-level engine test bed at Pyestock. Whilst far from ideal acoustically, the facility (used for engine controls development and validation) provided an important opportunity to obtain near-field noise measurements on a military turbojet engine for preliminary confirmation of the maths models at full scale.
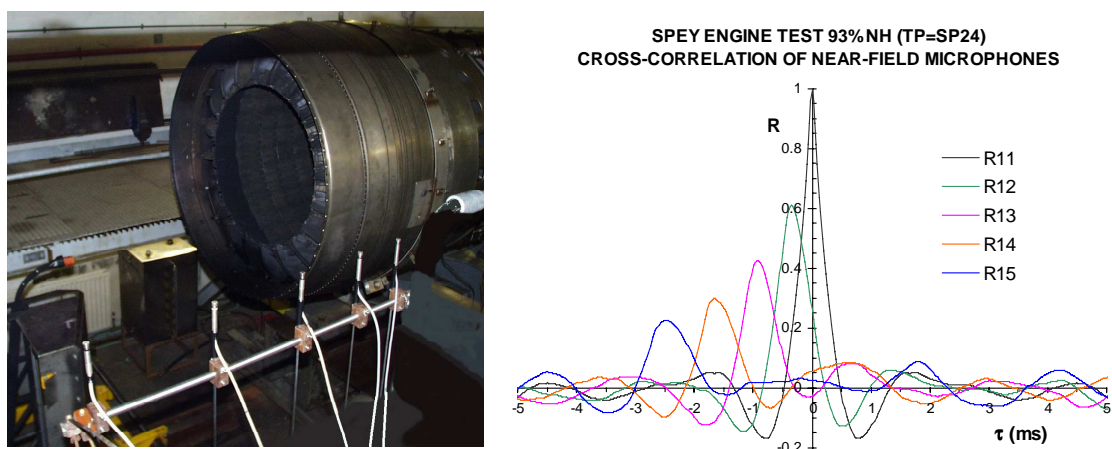
Figure 16   Noise Tests on Spey Engine in QinetiQ GLEN Sea-Level Test Facility
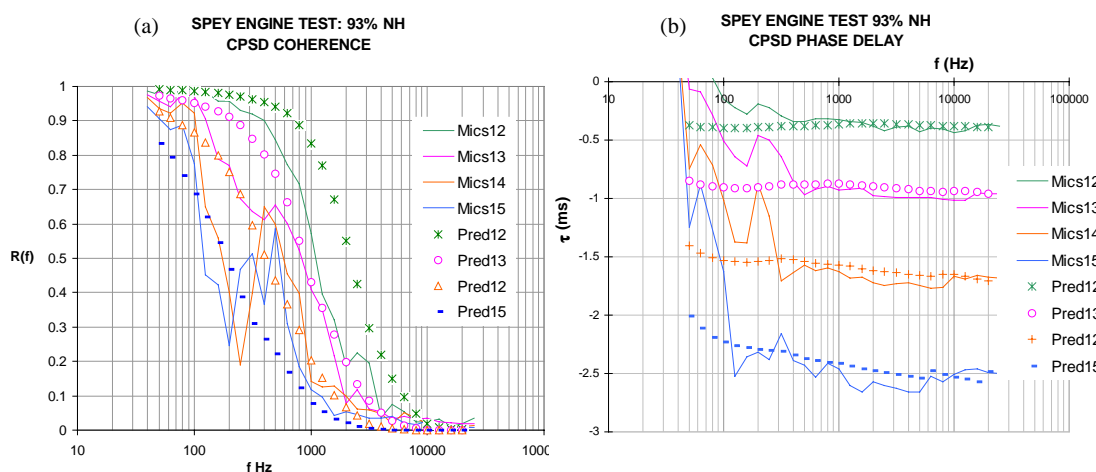
Figure 17. Engine Coherence Data

A scaled up version of the linear microphone array used in the model scale tests was employed but offset from the engine axis by only 1.4D to minimise the effect of reflections. A set of typical cross-correlations for the five microphone array is shown in Fig.16 for the engine run at $93\%N_H$. The associated coherence and phase measurements are presented in Fig 17 along with predictions made using the maths model, eqn 12 above. An exhaust diffuser duct (not visible in the photograph of Fig.16) was located 3 diameters downstream of the nozzle exit plane. Significant flow entrainment by the jet exhaust in the diffuser would be expected to result in stretching of the source distributions, which could account for the measured coherence

decaying more rapidly with frequency than predicted in Fig. 17a. The close proximity of the diffuser to the engine would have resulted in shielding of the downstream jet noise sourceses from the microphone array, which combined with the hydrodynamic field would account for the discrepancies in the phase below 300Hz in Fig. 17b. In summary, the measured overall trends in the engine test appear to be predicted well by the maths model with the discrepancies between the two largely attributable to the test environment. Although not ideal, the tests have nevertheless served a useful basis for initial validation of the near-field maths models on a full scale application, permitting their further development and refinement.

Concluding Remarks

A semi-empirical basis for predicting the spectral intensity and spatial coherence of the jet noise field adjacent to the supersonic exhausts of turbojets has been described. The methodology adopted marries the acoustic analogy with source location measurements and encompasses both jet mixing noise and broadband shock noise. It has been tested on both model scale heated supersonic jets and through engine measurements. Excellent agreement is being obtained between prediction and measurement for outer near-field stations of the jet. At stations very close to the jet, the overall levels are replicated well by the models but further work is required to refine the fidelity for these stations, notably at the higher frequencies. Extension of the models to include the hydrodynamic field is planned, to improve prediction at low frequencies close to the jet.

Acknowledgements

References

1. P D GREEN, 'Current and Future Problems in Structural Acoustic Fatigue'
   AGARD-CP-549, Impact of Acoustic Loads on Aircraft Structures, May 1994.

2. R A PINKER, 'A Brief Review of the Source Noise Technology Applicable to Fixed-Wing Military Aircraft', AGARD-CP-512, Combat Aircraft Noise, October 1991.

3. COMET/Acoustics: Computational Mechanics Tool, Automated Analysis Corporation

4. M HARPER-BOURNE, 'Radial Distribution of Jet Noise Sources Using Far-Field Microphones', AIAA Paper 98-2357, Toulouse, June 1998.

5. M J FISHER, M HARPER-BOURNE AND S A L GLEGG, 'Jet Noise Source Location: the Polar Correlation Technique', Journal of Sound and Vibration, vol. 51, 1977.

6. M J LIGHTHILL, 'Jet Noise', AGARD Specialists' Meeting on "The Mechanism of Noise Generation in Turbulent Flow", Rep 448, 1963.

7. S E WRIGHT, 'An Advanced Course in Noise and Vibration', Institute of Sound and Vibration Research, University of Southampton, Chapter 1, Theory of Sources, Sept 1972

8. C L MORFEY, 'Amplification of Aerodynamic Noise by Convected Flow Inhomogeneities', Journal of Sound and Vibration., vol 31, 1973.

9. M HARPER-BOURNE, 'Jet Near-Field Noise Prediction', AIAA Paper 99-1838, Seattle, May 1999.

10. M HARPER-BOURNE, 'Twin Jet Near-Field Noise Prediction', AIAA Paper 2000-1838, Moui, September 1999.

11. M HARPER-BOURNE and M J FISHER, 'The Noise from Shock Waves in Supersonic Jets.', AGARD-CP-131, Noise Mechanisms, September 1973.

12. 'Gas Turbine Jet Exhaust Noise Prediction', SAE Aerospace Recommended Practice ARP876 Rev D. 1994.

13. TAM C.K.W., 'Supersoinc Jet Noise', Annual Review of Fluid Mechanics, vol 27, 1995.

List of symbols

a_0	Ambient speed of sound
ASTOVL	Advanced Short Take Off and Vertical Landing
B&K	Bruel and Kjaer
BEM	Boundary Element Method
BVR	Beyond visible range
C_A	Eddy convection factor

Con-Di	Convergent-divergent nozzle
D	Nozzle diameter (mm)
D_p	Source inherent directivity
f	Frequency (Hz)
FE	Finite element
G	Power spectral density
GLEN	Ground Level ENgine (test facility)
Hz	Cycles per second
IDL	Ineractive Data Language
K	Wavenumber ($= 2\pi / \lambda$)
L_1	Eddy axial decay length scale (mm)
λ	Wave length of sound
M_c	Eddy convection Mach number
M_j	Jet Mach number
N_H	High speed shaft relative speed
NTF	QinetiQ Pyestock anechoic Noise Test Facility
p	Acoustic pressure
P	Cross-spectral Density
PR	Pressure Ratio (Total pressure/ambient pressure)
RAM	Radar Absorbent Material
r	Sound propagation distance (m)
R	Coherence modulus
S	Source strength
s_d	Doppler shifted Strouhal number ($= \omega L_1 / U_c$)
SPL	Sound Pressure Level
t	Time (s)
T	Signal averaging time (s)
τ	Time delay (ms)
τ_p	Phase delay time (ms)
θ	Angle to jet axis
U_c	Eddy convection velocity (m/s)
ω	Radian frequency ($= 2\pi f$)
x	Far-field co-ordinate (m)
y	Source co-ordinate (m)
z	Near-field co-ordinate (m)

This page has been deliberately left blank

_____

Page intentionnellement blanche

Flow Field and Sound Radiation of a Mach 0.9 Jet Computed by LES

Christophe Bogey, Christophe Bailly and Daniel Juvé
Laboratoire de Mécanique des Fluides et d'Acoustique
Ecole Centrale de Lyon & UMR CNRS 5509
BP 163, 69131 Ecully Cedex, France

1. Introduction

Spectacular improvements in jet noise prediction have been performed in the last decade, due to the progress in numerical simulations. Noting that hybrid approaches based on acoustic analogies present difficulties related to the modelling of source terms and to the formulation of a wave operator accounting for acoustic-flow interactions, methods for computing the sound directly from the resolution of the unsteady compressible Navier-Stokes equations have been developed. The objective of this approach is to determine both the flow field and the acoustic waves in the same calculation. In this way, the computed sound field is *a priori* exact because no acoustic model is used. It will also permit to investigate the sound generation mechanisms since all flow and acoustic quantities are provided by the computation. However, serious numerical issues[1] must be taken into account in this direct acoustic approach, owing to the great disparity of levels and length scales between the flow and the acoustic field. To overcome these difficulties, numerical techniques specific to Computational AeroAcoustics (CAA), suited to the behaviour of acoustic waves, have been proposed, such as non dispersive and non dissipative numerical schemes, or non-reflective boundary conditions. To make direct aeroacoustic calculations, the challenge is then to combine these CAA techniques with one of the methods used to solve the Navier-Stokes equations.

The three classical approaches commonly used to solve these flow equations have thus been experimented for aeroacoustic simulations: Direct Numerical Simulations (DNS) consisting in computing all turbulent scales, Large Eddy Simulations (LES) where only larger scales are calculated whereas the effects of unresolved ones are modelized via a subgrid scale model, and the unsteady Reynolds Averaged Navier-Stokes equations (RANS) using turbulence closures. Among the first three-dimensional applications performed in the last five years, we can put forward the DNS of Freund *et al.*[2,3] of the noise radiated by supersonic and subsonic circular jets, the LES of Morris *et al.*[4] of the radiation of a supersonic rectangular jet, and the study of screech tones generation in a round jet using unsteady RANS by Shen & Tam.[5]

The use of LES is important because it can theoretically be applied to high Reynolds number flows unlike DNS which is restricted to very low Reynolds number flows. Therefore, in the present study, a Large Eddy Simulation of a three-dimensional circular jet with a Mach number of 0.9 and a Reynolds number of 65000 is performed, carrying on earlier preliminary works.[6] The motivation is to show the feasibility of the the direct computation by LES of the sound generated by a subsonic flow. For this, CAA numerical methods are used in the simulation. The validation of the computation is then carried out by comparing systematically both flow properties and the radiated sound field with experimental data.

This paper is organized as follows. Numerical procedure, characteristics of the jet and parameters of the simulation are presented in section 2. The flow development is briefly shown in section 3, by studying the mean flow and the turbulent intensities. The radiated acoustic field is then investigated in section 4. Finally, concluding remarks are given in section 5.

2. Numerical simulation

2.1 Numerical procedure

The full three-dimensional Navier-Stokes equations written in a conservative form are solved. The numerical algorithm is low-dispersive and low-dissipative to compute directly the sound waves with accuracy, and has been successfully used in an earlier study on a two-dimensional mixing layer.[6] It combines the Dispersion-Relation-Preserving (DRP) finite-difference scheme of Tam & Webb[7] for space discretization with a four-step Runge-Kutta scheme for time integration. A selective damping[1] is also applied to filter out numerical oscillations, typically grid-to-grid waves, which are not computed properly by the algorithm, and to ensure numerical stability. The mesh is Cartesian and non uniform, to use different discretizations in the flow field and in the acoustic far-field.

The resolution of the full Navier-Stokes equations without modelling, by Direct Numerical Simulations (DNS), requires the calculation of all turbulent scales and is intrinsically restricted to low Reynolds number flows. To simulate flows at higher Reynolds number, Large Eddy Simulation (LES) can be performed by computing only the larger scales and by taking into account the effects of unresolved ones through a subgrid scale model. In the present study, a turbulent viscosity is classically implemented to provide the dissipation of the unresolved scales. Various models have been developed to give an evaluation of the turbulent viscosity from the resolved scales. To keep the problem as simple as possible for aerodynamics, we choose the Smagorinsky model.[8]

2.2 Boundary Conditions

In acoustic simulations, boundary conditions must minimize the magnitude of acoustic waves reflected when fluctuations leave out the computational domain. In this study, a formulation[9] derived from the behaviour of sound waves in the acoustic far-field is used. It is the extension of Tam & Dong[10] conditions for a three-dimensional geometry. Two conditions are applied: a

radiation condition for the inflow and for the lateral boundaries of the computational domain where only acoustic fluctuations propagates, and an outflow condition for the outflow where vortical and entropic disturbances are also convected by the flow.

The efficiency of the boundary conditions has been estimated using test cases.[11] The exit of vortical structures generates low-amplitude spurious waves, which are however not negligible with respect to the physical sound field characterized by very small amplitudes. Therefore a sponge zone is implemented in the outflow direction to dissipate flow fluctuations before they reach the outflow boundary, and also to filter out possible reflected waves. It is based on the combination of grid stretching with an artificial damping.[6]

2.3 Flow Parameters

The inflow longitudinal velocity $u(r)$ of the jet is given by the following hyperbolic-tangent profile

$$u(r) = \frac{U_j}{2} + \frac{U_j}{2} \tanh\left(\frac{r_0 - r}{2\delta_\theta}\right)$$

where U_j is the inflow centerline velocity, δ_θ the initial momentum thickness of the shear layer, and r_0 the jet radius. The fluid surrounding the jet is initially at rest.

The jet Mach number is $M_j = 0.9$. This choice is justified by the amount of experimental studies available in the literature, providing both aerodynamic results,[12] and acoustic results.[13–15] This Mach number implies also a high convection speed of turbulent structures, which reduces computation time. We can notice that the first simulation of a subsonic jet to determine directly its radiated field, a DNS carried out by Freund,[3] involves a Mach number 0.9, Reynolds number 3600 jet. In the present simulation, the jet Reynolds number is $Re_D = U_j \times D/\nu = 65000$. It is higher than Reynolds numbers reachable by DNS, but still lower than values of practical interest. The ratio between the initial jet radius and the initial momentum thickness of the shear layer δ_θ/r_0 is also an important parameter, because the laminar-turbulent transition depends on it. In this study, $\delta_\theta/r_0 = 0.05$, and the development of vortical structures in the shear zones is possible.

Finally, to obtain the natural flow development, the jet is forced by adding random velocity fluctuations into the inflow. These fluctuations are solenoïdal to minimize the generation of spurious acoustic waves by the excitation. They are introduced only in the shear layers, which are the unstable region of the jet. In these shear zones, turbulent intensities generated by the forcing are around 3%, which is similar to intensities measured near jet nozzle exits.

2.4 Numerical specifications

The computational domain, discretized by a grid of $255 \times 187 \times 127$ points, is defined by $0 \leq x/r_0 \leq 30$, $-5 \leq y/r_0 \leq 25$ and $-5 \leq z/r_0 \leq 5$ in the three coordinate directions. Radially, points are clustered in the jet with 26 points in the radius. The mesh spacing is minimum around $r = r_0$ with $\Delta_0 = \delta_\theta/1.6$, and increases outside the jet to reach $\Delta y_{max} = 0.4r_0$ in far-field. In the flow direction, the mesh spacing is constant up to $x = 20r_0$, with $\Delta x = 3\Delta_0$. Then, meshes are

stretched, to obtain $\Delta x_{max} = 0.54 r_0$, to form a sponge zone. An artificial damping is moreover applied in this zone, in the flow region only. In this way, the physical part of the computational domain extends up to $x = 20 r_0$ for the flow field, and up to $x = 30 r_0$ for the acoustic field.

The time step is given by $\Delta t = 0.7 \Delta_0 / c_0$. The simulation runs for 30000 iterations, the calculation of statistical means being performed only after 5000 iterations. Consequently, the simulation time corresponds to $22 \times Lx/c_0$, where $Lx = 30 r_0$. The computation is 15 hours long on a Nec SX-5, with a CPU time of 0.3μs per grid point and per iteration. More details of the simulation can be found in earlier papers.[9,11]

3. Flow Field

3.1 Flow Development

Figure 1 displays the vorticity fields provided by the simulation. The longitudinal vorticity field ω_{xy} shows that, initially, vortical structures are generated and grow in the shear layers. The shear zones of the jet interact around $x \simeq 10 r_0$, indicating the end of the potential core, which is consistent with experimental observations.[12] A developed turbulence is found downstream, illustrated by the transverse vorticity field ω_{yz}, and characterized by a typical three-dimensional mixing. Finally, flow fluctuations are dissipated by the sponge zone for $x > 20 r_0$.
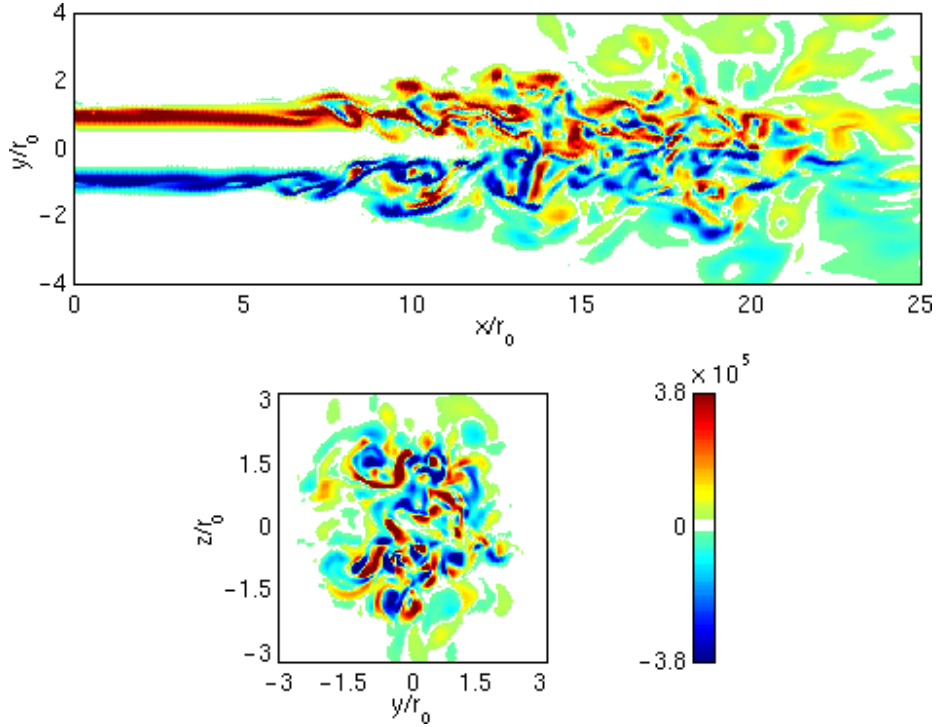

Figure 1: Snapshots of the vorticity field. Upper picture, ω_{xy} in the $x - y$ plane at $z = 0$; bottom picture, ω_{yz} in the $y - z$ plane at $x = 12 r_0$. Levels are given in s^{-1}.

3.2 Mean Flow Properties

The characteristics of the jet mean flow calculated from the simulation are presented in Figures 2. First, Figure 2(a) displays the longitudinal evolution of the inverse of the mean centerline velocity normalized by the inflow velocity U_j. Its value is 1 in the potential core, and grows linearly afterwards so that we can write $U_c/U_j = B \times D/(x - x_0)$ where $x_0 = 0$ is the virtual origin, and $B = 5.5$. This value is consistent with measurements of Wygnanski & Fiedler,[16] Panchapakesan & Lumley[17] and Hussein et al.,[18] as well as DNS result of Boersma et al.,[19] reported in Table 1.

Re_D	B	A	Reference
8.6×10^4	5.4	0.086	Wygnanski* et al.[16]
1.1×10^4	6.1	0.096	Panchapakesan* et al.[17]
9.5×10^4	5.8	0.094	Hussein* et al.[18]
2.4×10^3	5.9	0.095	Boersma** et al.[19]
6.5×10^4	5.5	0.096	Present simulation

Table 1: Mean flow parameters obtained from experiments*, DNS**, and present simulation.

Second, Figure 2(b) presents the longitudinal evolution of the jet half-width $\delta_{1/2}$ normalized with the radius r_0. Its value is fairly 1 up for $x < 6r_0$ where no large vortical structure is visible. Afterwards, in the turbulent region, the jet spreads linearly as $\delta_{1/2} = A \times (x - x_0)$ where $A = 0.096$, that is in agreement with data of Table 1.

Third, Figure 2(c) shows the longitudinal evolution of the flow rate. It grows regularly, indicating that the entrainment of the surrounding fluid occurs from the inflow of the computational domain. As deduced from the x^{-1} decay of the centerline velocity and from the linear spreading, a linear growth is found after the potential core, as $Q/Q_0 = C \times (x - x_0)/D$ where Q_0 is the initial flow rate and $C = 0.32$. This corresponds exactly to the measurement of Ricou & Spalding.[20]

Finally, radial profiles of the mean longitudinal velocity normalized by the centerline velocity U_c are plotted in Figure 2(d) as function of the nondimensional coordinate $y/(x - x_0)$, for five locations between $x = 15r_0$ and $x = 20r_0$. The spreading rate A is the half-width of the profiles which are superimposed. This confirms the self-similarity in the turbulent jet suggested by the previous longitudinal evolutions.

3.3 Turbulent Intensities

Intensities of flow perturbations in the jet are investigated. They are calculated in the $x - y$ plane at $z = 0$ using velocity fluctuations u', v' et w' and normalized with the local mean centerline longitudinal velocity U_c. They are given by the following expressions: $\sigma_{uu} = \sqrt{\overline{u'^2}}/U_c$, $\sigma_{vv} = \sqrt{\overline{v'^2}}/U_c$, $\sigma_{ww} = \sqrt{\overline{w'^2}}/U_c$, and $\sigma_{uv} = \sqrt{|\overline{u'v'}|}/U_c$.

Radial profiles of the turbulent intensities are shown in Figures 3 for five locations between $x = 15r_0$ and $x = 20r_0$, as function of the nondimensional coordinate $y/(x - x_0)$. Profiles are well superimposed, that is in agreement with the self-similarity in a fully turbulent jet. The mean
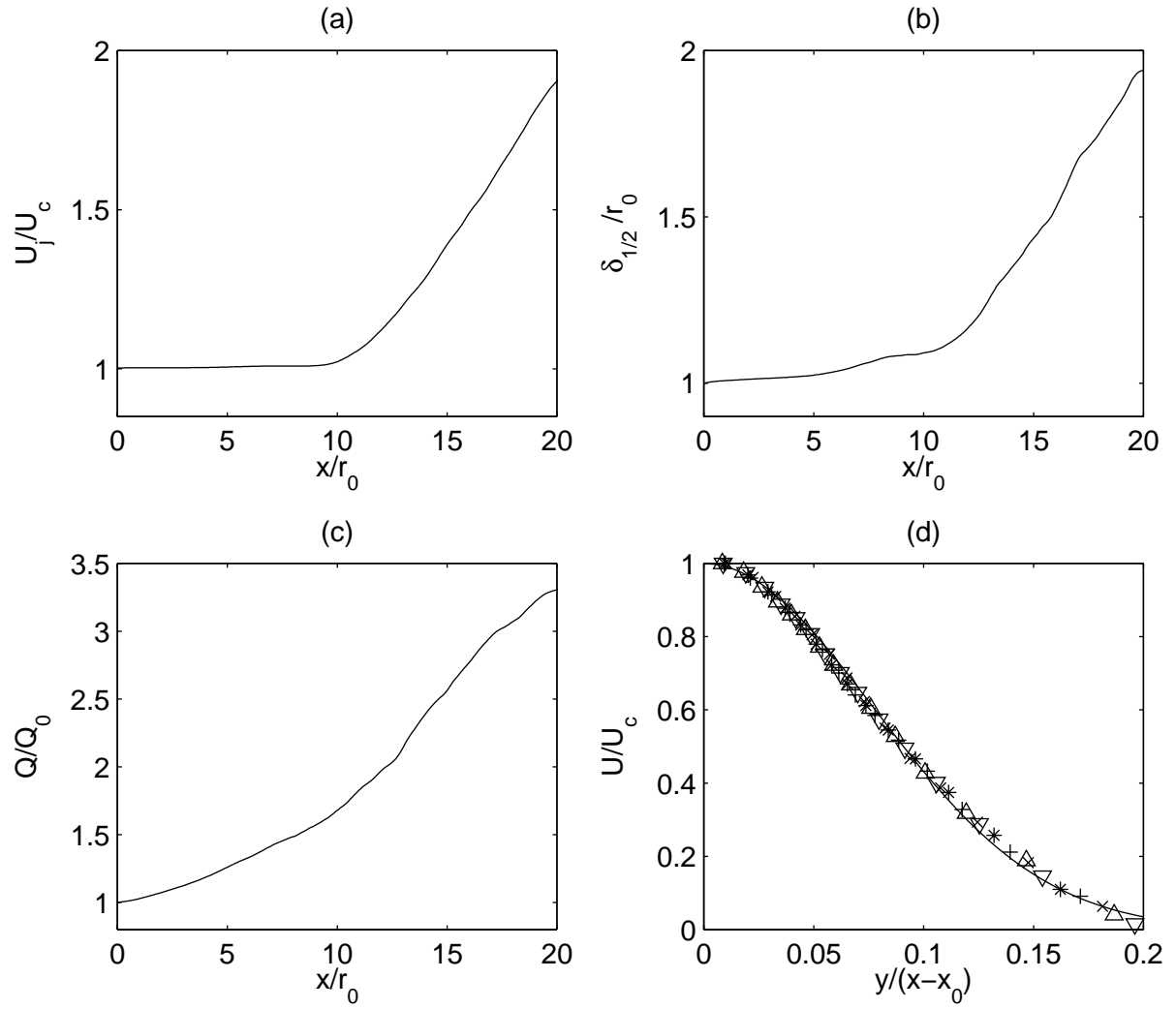
Figure 2: Longitudinal evolution of: (a), the inverse of the mean centerline velocity normalized with the inflow velocity U_j/U_c; (b), the half-width of the jet normalized with the jet radius δ_{12}/r_0; (c), the mean flow rate normalized with the inflow rate Q/Q_0. (d), Radial profiles of the mean longitudinal velocity normalized by the local centerline velocity U/U_c: $\times$, at $x = 15.8r_0$; $+$, at $x = 16.8r_0$; $*$, at $x = 17.7r_0$; $\triangledown$, at $x = 18.6r_0$; $\triangle$, at $x = 19.6r_0$. ———— , approximation with a Gaussian profile.

profiles calculated between $x = 15r_0$ and $x = 20r_0$ are also plotted as solid lines. They are very close to measurements, and stand between two experimental profiles provided by Panchapakesan & Lumley[17] and by Hussein $et\ al.$[18] respectively.
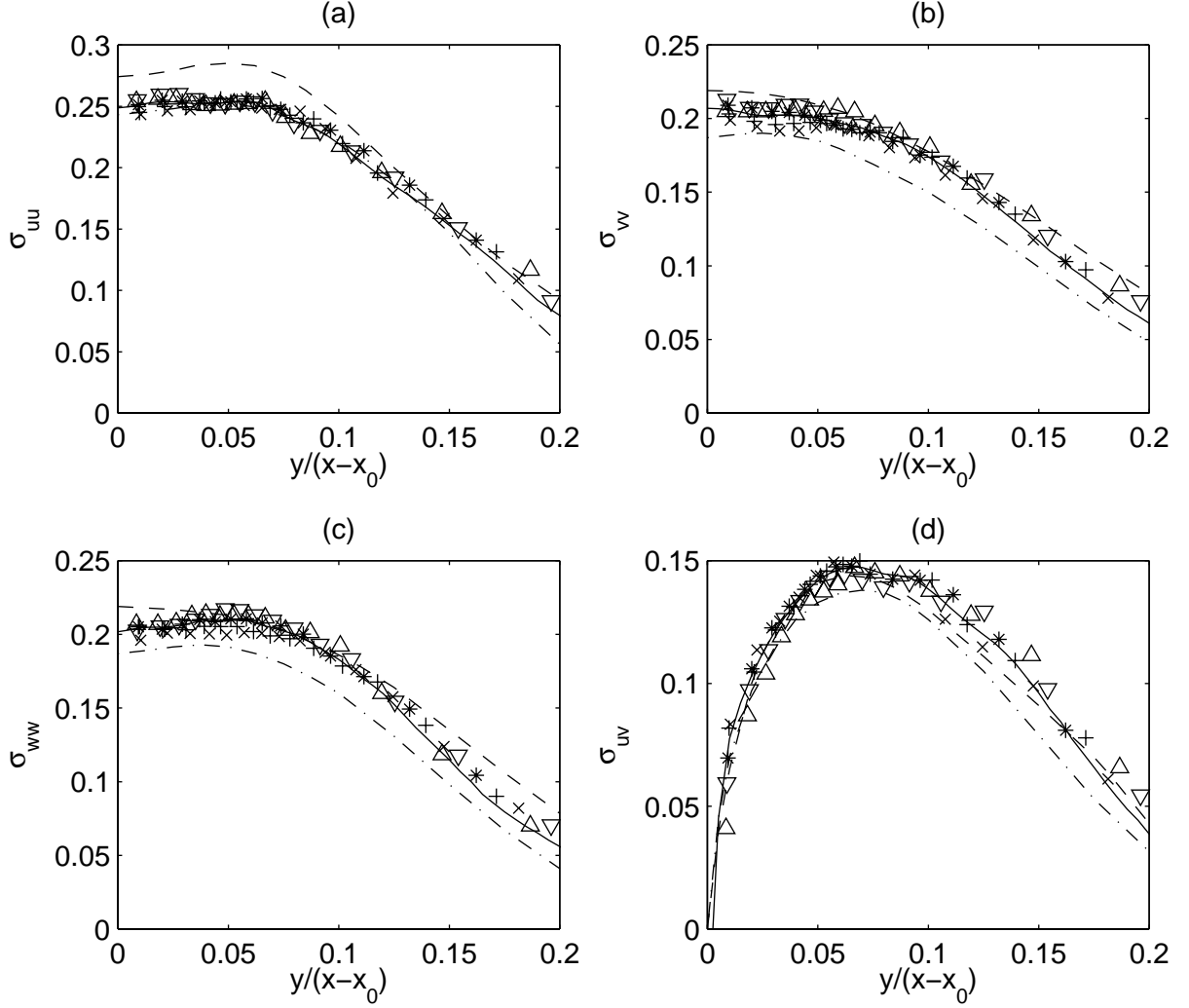
Figure 3: Radial profiles of the turbulent intensities: (a), σ_{uu}; (b), σ_{vv}; (c), σ_{ww}. $\times$, at $x = 15.8r_0$; $+$, at $x = 16.8r_0$; $*$, at $x = 17.7r_0$; $\triangledown$, at $x = 18.6r_0$; $\triangle$, at $x = 19.6r_0$. ———— , mean profiles calculated from $x = 15r_0$ to $x = 20r_0$; — · — · , experimental profiles obtained by Panchapakesan & Lumley[17]; — — — , experimental profiles obtained by Hussein, Capp & George.[18]

4. Sound Radiation

4.1 Dilatation field

Figure 4 displays the dilatation field $\Theta = \nabla.\mathbf{u}$ provided directly by the simulation. Outside the flow region where the mean flow is negligible, dilatation is proportional to the time derivative of the acoustic pressure via the relation $\Theta = -(1/\rho_0 c_0^2)\ \partial p/\partial t$.

Figure 4: Snapshot of the dilatation field $\Theta = \nabla.\mathbf{u}$ in the acoustic region, and of the vorticity field ω_{xy} in the aerodynamic region, in the $x - y$ plane at $z = 0$. The dilatation color scale is defined for levels from -90 à 90 s^{-1}, the vorticity scale is the same as in Figure 1.

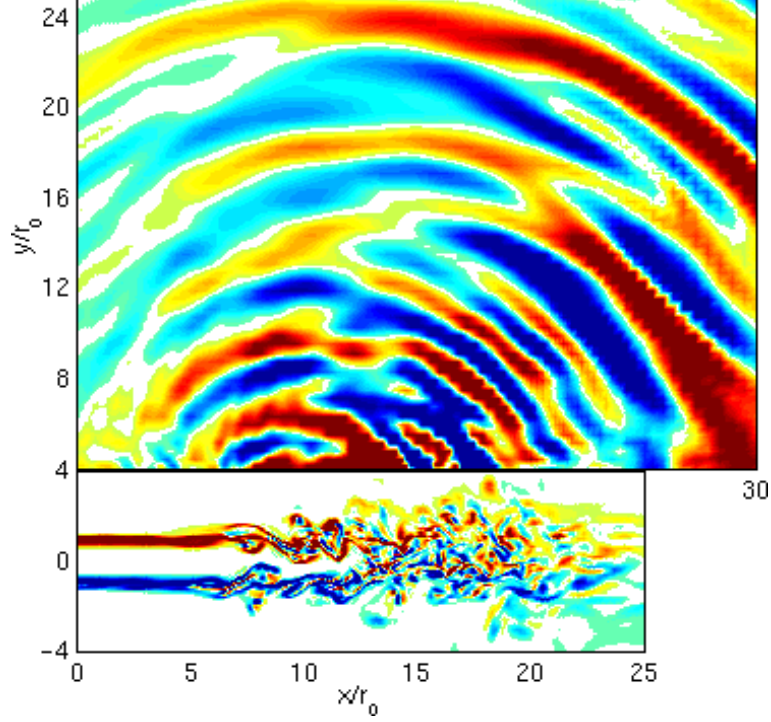This figure demonstrates that the dilatation field is not contaminated by spurious waves generated by the inflow excitation or reflected by the boundary conditions. Moreover, wave fronts are mainly coming from an origin located around $x \simeq 10r_0$, in the region where the mixing layers are merging, showing that predominant sound sources are located in the vicinity of the end of the potential core. This agrees both with the results of the recent DNS performed by Freund[3] and with the measurements of Chu & Kaplan[21] and Juvé et al.[22] using various source localization techniques. The computed radiated field is also more pronounced in the downstream direction according to experimental directivities.

4.2 Pressure field spectra

To characterize the computed acoustic field, sound pressure spectra are calculated in far field. They are transposed at a distance of $60r_0$ from the inflow using the r^{-1} decay of acoustic waves

from the sound sources located at $x = 10r_0$ to the recording points.

Figures 5(a) and (b) show the spectra found for angles of 30º and of 90º from the jet axis for Strouhal numbers $St > 0.15$. Levels are more than 10 dB higher for $\theta = 30$º than for $\theta = 90$º. Shapes are also different: for $\theta = 30$º, the spectrum is dominated by low frequency components with a peak found around $St \simeq 0.2$, whereas for $\theta = 90$º, the spectrum is larger with a preferred band of $0.2 < St < 0.5$ and a peak evaluated around $St \simeq 0.3$. This behaviour corresponds to experimental results,[14,22] and the classical interpretation is that, at low angles, the noise is mainly generated by the large scales, whereas at higher angles the fine-scale turbulence is responsible for a great part of the noise.
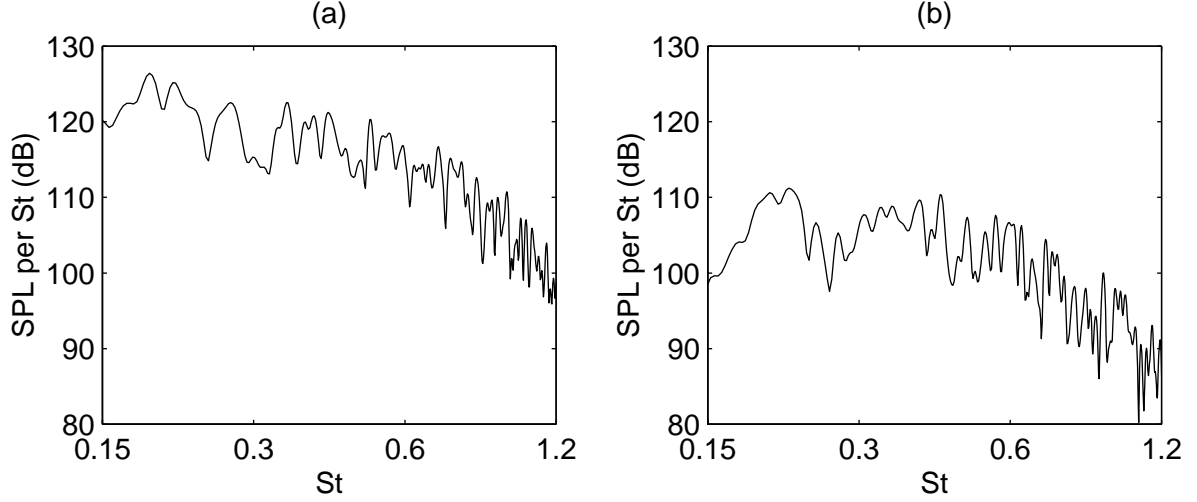
Figure 5: Sound pressure level as function of Strouhal number $St = fD/U_j$, at $60r_0$ from the jet nozzle, for an angle of: (a), $\theta = 30$º; (b), $\theta = 90$º.

4.3 Sound pressure level

The pressure spectra are now integrated from the Strouhal number $St = 0.15$ to provide the sound directivity. Figure 6 shows the computed sound pressure levels, with experimental data obtained by Mollo-Christensen $et\ al.$,[13] Lush,[14] and Stromberg $et\ al.$[15] for jets with similar Mach numbers but various Reynolds numbers

The agreement between calculated and measured sound levels is very good for all observation angles. As expected, the acoustic level reaches a peak around an angle of $\theta = 30$º. By considering the similarities between the noise radiated by jets with very different Reynolds numbers from 3600 up to 5.4×10^5, the sound sources associated to the large scales seem to be relatively independent of the Reynolds number. Moreover, at high observation angles, the result of the simulation stands between the measurements which are relatively scattered. This behaviour can be associated to a Reynolds number effect, because the fine-scale turbulence is much less developed at low Reynolds numbers.

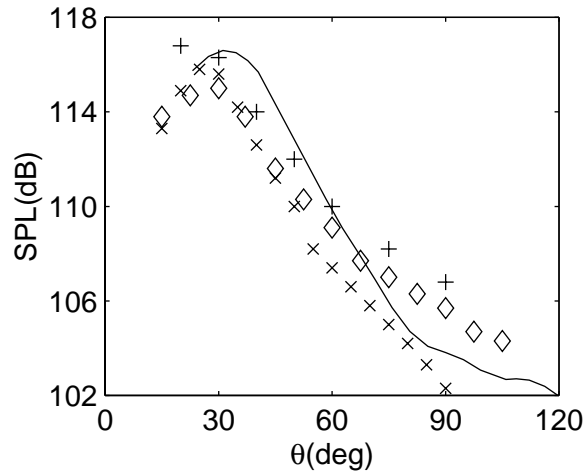Figure 6: Sound pressure level as function of angle θ measured from the jet axis, at $60r_0$ from the jet nozzle. Experimental data by: $+$, Mollo-Christensen *et al.*[13] ($M_j = 0.9$, $Re_D = 5.4 \times 10^5$); $\diamond$, Lush[14] ($M_j = 0.88$, $Re_D = 5 \times 10^5$); $\times$, Stromberg *et al.*[15] ($M_j = 0.9$, $Re_D = 3600$).

5. Conclusion

Results of a Large Eddy Simulation of a circular jet with a Mach number of 0.9 and a Reynolds number of 65000, carried out to compute directly the radiated sound field, has been presented. Both the flow field and the sound field computed have been investigated and compared systematically to experimental data available in the literature. Flow properties, namely flow development, mean flow parameters and turbulent intensities, are in very good agreement with measurements. The sound field provided by LES compares also successfully with experimental results in terms of directivity, spectra and levels. Sound sources in the jet are moreover found around the end of the potential core, as shown experimentally.

This study shows the feasibility of the direct calculation of the acoustic field generated by subsonic flows using LES. The excellent concordance with measurements supports that aerodynamic and acoustic mechanisms are well accounted for by the simulation. In that way, further works would have to investigate the generation mechanisms of jet noise.

Acknowledgments

References

[1] Tam, C.K.W., 1995, Computational aeroacoustics: issues and methods, *AIAA Journal*, **33**(10), 1788-1796.

[2]Freund, J.B., Lele, S.K. & Moin, P., 1998, Direct simulation of a Mach 1.92 jet and its sound field, AIAA Paper 98-2291.

[3]Freund, J.B., 1999, Acoustic sources in a turbulent jet: a direct numerical simulation study, AIAA Paper 99-1858.

[4]Morris, P.J., Long, L.N. & Scheidegger, T.E., 1999, Parallel computations of high speed jet noise, AIAA Paper 99-1873.

[5]Shen, H. & Tam, C.K.W., 1998, Numerical simulation of the generation of the axisymmetric mode jet screech tones, *AIAA Journal*, **36**(10), 1801-1807.

[6]Bogey, C., Bailly, C. & Juvé, D., 2000, Numerical simulation of the sound generated by vortex pairing in a mixing layer, *AIAA Journal*, **38**(12), 2210-2218.

[7]Tam, C.K.W. & Webb, J.C., 1993, Dispersion-relation-preserving finite difference schemes for computational acoustics, *J. Comput. Phys.*, **107**, 262-281.

[8]Smagorinsky, J.S., 1963, General circulation experiments with the primitive equations: I. the basic experiment, *Mon. Weath. Rev.*, **91**, 99-163.

[9]Bogey, C., Bailly, C. & Juvé, D., 2000, Computation of the sound radiated by a 3-D jet using Large Eddy Simulation, AIAA Paper 2000-2009.

[10]Tam, C.K.W. & Dong, Z., 1996, Radiation and outflow boundary conditions for direct computation of acoustic and flow disturbances in a nonuniform mean flow, *J. Comput. Acous.*, **4**(2), 175-201.

[11]Bogey, C., 2000, Calcul direct du bruit aérodynamique et validation de modèles acoustiques hybrides, Ph. D. Thesis of Ecole Centrale de Lyon, No. 2000-11.

[12]Lau, J.C., Morris, P.J. & Fisher, M.J., 1979, Measurements in subsonic and supersonic free jets using a laser velocimeter, *J. Fluid Mech.*, **93**(1), 1-27.

[13]Mollo-Christensen, E., Kolpin, M.A. & Martucelli, J.R., 1964, Experiments on jet flows and jet noise far-field spectra and directivity patterns, *J. Fluid Mech.*, **18**, 285-301.

[14]Lush, P.A., 1971, Measurements of subsonic jet noise and comparison with theory, *J. Fluid Mech.*, **46**(3), 477-500.

[15]Stromberg, J.L., McLaughlin, D.K. & Troutt, T.R., 1980, Flow field and acoustic properties of a Mach number 0.9 jet at a low Reynolds number, *J. Sound Vib.*, **72**(2), 159-176.

[16]Wygnanski, I. & Fiedler, H., 1969, Some measurements in the self-preserving jet, *J. Fluid Mech.*, **38**(3), 577-612.

[17]Panchapakesan, N.R. & Lumley, J.L., 1993, Turbulence measurements in axisymmetric jets of air and helium. Part I. Air jet. *J. Fluid Mech.*, **246**, 197-223.

[18]Hussein, H.J., Capp, S.P. & George, W.K., 1994, Velocity measurements in a high-Reynolds-number, momentum-conserving, axisymmetric, turbulent jet, *J. Fluid Mech.*, **258**, 31-75.

[19] BOERSMA, B.J., BRETHOUWER, G. & NIEUWSTADT, F.T.M., 1998, A numerical investigation on the effect of the inflow conditions on a self-similar region of a round jet, *Phys. Fluids*, **10**(4), 899-909.

[20] RICOU, F.P. & SPALDING, D.B., 1961, Measurements of entrainment by axisymmetrical turbulent jets, *J. Fluid Mech.*, **11**, 21-32.

[21] CHU, W.T. & KAPLAN, R.E., 1976, Use of a spherical concave reflector for jet-noise-source distribution diagnosis, *J. Acoust. Soc. Am.*, **59**(6), 1268-1277.

[22] JUVÉ, D., SUNYACH, M. & COMTE-BELLOT, G., 1980, Intermittency of the noise emission in subsonic cold jets, *J. Sound Vib.*, **71**(3), 319-332.

Emerging Computational Tools for Flow Acoustics

William K. Blake
Commander
Carderock Division
Naval Surface Warfare Center
Code 7051
9500 MacArthur Boulevard
West Bethesda, MD 20817-5700
United States

Abstract.

This lecture is a survey of multiple on-going efforts in the United States, largely sponsored by the Office Of Naval Research, that are devoted to the development of prediction methods for flow-generated sound. This research is meant to develop methods that are useful in future engineering applications that could involve complex three-dimensional geometries, high Reynolds number fluid mechanics, flow-induced vibration, and finite Mach number. This paper will focus specifically on development of tools for the calculation of forcing functions and on efforts to systematically validate them in anechoic wind tunnels. The slides that are discussed herein form a complete description of work as currently undertaken at the David Taylor Model Basin of NSWC-CD and its collegiate organizations.

1.0 Introduction.

As currently configured we are focussing on flow dipoles and flow-induced vibration. These methods are being integrated into a prediction system that evaluates the flow, the flow-induced forces on the surfaces, the vibration, and the sound from both flow dipoles and vibration. By necessity, the physics of such problems is multi-faceted and it is useful to develop the prediction system as a modular tool with component algorithms all interconnected by an object-oriented central integration node that imports, interconnects and exports the relevant flow-structural-and acoustic behavior parameters of interest. This tool is necessarily modular with computational components that are newly developed or "borrowed" from other applications. "Other applications" include the use and extension of some methods also being developed under joint NASA and ONR funding. Of many developmental challenges, one of the larger challenges is the definition of flow excitation pressures that either drive a structure or constitute the dipole sources. This lecture will focus on that aspect of our development. Specifically, the essential differences and common areas of aeroacoustics and hydroacoustics will be discussed. The common areas relate to the definition of flow-generated fluctuating pressures on the surfaces; we will discuss these as both narrow band and broadband sources. We will pay particular attention to the experimental verification of components that predict forcing functions. Examples will be given of aeroacoustic measurements of rotor – stator interaction dynamics in compressor elements, and the dipole sound generated by the trailing edges of lifting surfaces. See Slide 2.

Slide 3 is a partial list of the many organizations and co-investgators that have been contributing to the project as well as to this paper over the last three or four years. As identified in Slide 4, the potential application of the methods that are discussed in this lecture is rather broad. Nearly all the work that is reported in this lecture has been funded by a variety of programs that are or have been overseen by Dr. L. Patrick Purtell of ONR.

As currently modelled in the prediction methods that we will be discussing, the physics of flow induced sound is linearized. This means that flow-acoustic and structural acoustic instabilities are not included in the models. Sources are the result of linearly – driven fluid – structure systems in which the flow sources are unaffected by adjacent surface motion or near – field fluid pressures. Strictly acoustic interactions are included in the form of effects of mean flow convection and structural-acoustic fluid loading impedances. Thus, as listed in Slide 5, the modelling can be modularized, as we will discuss, under the assumptions listed in Slide 6. One of the most important assumptions is that of low-enough Mach number that acoustic loading of the flow sources does not occur. This allows us to use incompressible modelling of the flow, while still considering the complexities of three dimensionality and possible flow – driven surface motion.

2.0 Overview Of The Components Of The Prediction Approach For Low Mach Number.

Slides 7 through 10 provide an outline of the way we have structured the approach to modelling dipole sound from flow–driven surfaces that may be rigid or elastic. If we were to base our approach on the potential benefits of space-time accurate modelling of turbulent flow over rigid surfaces, as made possible with Direct Numerical Simulation (DNS) or Large Eddy Simulation (LES), then we would determine the blocked flow sources and surface pressures that are developed by the flow-surface interaction. The results of such computations would then be used in a pre-processor to the acoustic, or vibro-acoustic, calculation of the vibration or sound. This process is illustrated in Slide 7 which also lists some practical limitations to using it as a general engineering tool. The method has been used by the Stanford group (Moin, Wang) to model trailing edge dipoles and turbulent boundary wall pressure at low wave numbers (Chang, Piomelli). The trailing edge modelling is being verified with detailed flow-acoustic measurement programs at University of Notre Dame (Mueller) and U. Michigan (Ceccio).

For engineering application, we currently need approaches that require less computationally-intensive methods than LES and DNS and that provide shorter "turnaround" time. These approaches are built on steady flow Reynolds Averaged Navier Stokes (RANS) solutions, hybridized RANS-Statistical methods or RANS-embedded LES techniques, and 2-dimensional and 3-dimensional Euler methods. We will return to specifics in the flow modelling in later slides, so that we can continue discussion of the overall approach here. As shown in Slide 8, once the surface geometry is defined, the RANS-based prediction can provide models of flow-excitation surface pressure that are based on turbulent kinetic energy and mean velocity profiles (by methods to described later). If needed, the turbulence integral scale can also be derived from the calculation. With a Green's function, or simple transfer function, that is based on a description of blocked sources or surface pressures, we can calculated the sound from the rigid body. If the surface is acoustically compact, this function can be as simple as a calculation of the

net dipole force and the well-known relationship for the acoustic dipole. It may also be more complex for extended non compact surfaces or cascades of turbomachinery blades. This would be an approach one would use for the areoacoustics of compressor blades, for example.

The approach that can be used for flow – induced vibration and resulting sound is analogous, as shown in Slide 9. The acoustic functions for sound from rigid bodies are replaced by a Finite Element Model-based approach that develops the sound field as a modal expansion using *invacuo* modes as basis functions. The mode shapes are numerically convolved with the values of blocked pressure. These values are modelled as correlation functions for the flow statistics, that are based on computation, analytical regressions, and models extracted from bodies of experimental data. Often, these descriptions can be as simple as an algebraic step that involves the use of spatial correlation areas and spatial correlation lengths. This is especially the case when wave lengths of vibration and sound are longer than the spatial scales of the flow –induced drivering pressures. Slide 10 brings the aeroacoustic ("direct dipole") sound and the vibration-induced sound together as a superposition of sources.

The common areas of hydro- and aero-acoustics thus involve low Mach number flow dipoles and the definition of forcing functions that describe the magnitudes and spatial scales of surface pressures, as shown in Slide 11. What makes hydroacoustics and aeroacoustics differ is the lack of quadrupole source mechanisms in hyderoacoustics and the general unimportance of vibration and vibration sound in aeroacoustics. Of course, two phase flow noise involving bubbly media and cavitation are also absent in aeroacoustics. The remainder of the lecture will discuss the common areas: the forcing function modelling and verification of predictions, see Slide 11.

3.0 Example Area 1. Rotor- Stator Sound And Interaction Flows Of Turbo-Machinery.

3.1 Response Of Rotors To Inlet Turbulence: Utility Of Simple Strip Theory At Low Mach Number.

Slides 14 through 22 address the verification of prediction models for turbulence ingestion noise. In this work the anechoic wind tunnel at the Hessert Center of the University of Notre Dame under the direction of T. Mueller is being used to produce sound from propellers downstream of rectangular grids, see Slide 19. Strip theory is used to calculate the turbulence induced broadband forcing spectrum. The key element of this modelling is the description of the turbulence spectrum which is nearly homogeneous, see and Wojno et al (2001). Slide 20 shows calculated frequency-dependent radial and tangential correlation lengths of the grid-generated gust. These functions were obtained by integrating the Liepmann spectrum (Slide 16) with coordinate stretching that accounts approximately for slight anisotropy in the radial and tangential directions at the inlet plane of the propeller.

The Slide suggests that about 2 to 3 dB uncertainty may be caused by slight anisotropy alone. Slides 21 and 22 show that the strip theory, the Liepmann spectrum for the turbulence, and measured coefficients for the turbulence wave number spectra

provide excellent agreement with measured spectra of sound. The broad humps in the spectra (near 600 Hz for the 10 blade propeller and near 250 Hz and 500 Hz for the 4 blade propeller) are due to blade-blade correlation of the flow - induced forces. This correlation is due to tangential correlation lengths of the inflow turbulence which are at least on the order of the spacing of the blades. This point shall be discussed further below. Slide 23 compares a strip theory of Blake(1986) with that of Martinez (1996). The latter best applies when the radial correlation length of the turbulence is comparable to, or larger than, the length of the blades (here satisfied at low frequencies) and the number of blades is large. Blake's theory is applicable best when the radial correlation length is smaller than the span of the blades (here satisfied at moderate frequencies), but with an arbitrary number of blades.

One of the focus areas in the recent work is in the development of inversion methods (see Minniti et al (1986))by which we measure the time-dependent pressure response of blades to turbulence to infer the spectrum and correlation lengths of the inflow turbulence. Such approaches are particularly important for applications where the blades may be instrumented and direct flow measurement is not possible. The method is noninvasive and allows the *insitu* rotor dynamics to tailor the flow. Slides 24 through 27 present results of validating the inversion trechnique in the grid-generated propeller response. In this method, the propeller is instrumented with arrays of pressure sensors that respond to the gust – driven surface pressures on the blades. The sensors are arranged along the chord at a fixed span location and along the span the leading edge near (i.e. at a fixed percentage of local chord) in a "Tee" pattern. Linear airfoil theory is used for inversion; Sears' function for broadband turbulence ingestion and Filotas' function for periodic coherent gusts induced by the time – mean wakes. Slide 25 shows a comparison of the spectrum of the grid-generated turbulence that was developed in the rig that is illustrated in Slide 19. The turbulence wave number spectra are normalized on the mean velocity as a function of the convective wave number normalized on mesh spacing. Three measurements are shown: an average of spectra measured at points by a fixed hot wire anemometer probe, a spectrum measured in the rotation frame by a probe fixed to a blade of the propeller, ant a spectrum that was obtained by inversion of the surface pressure. The inflow had a small-magnitude distortion in the mean velocity that had a time-mean spatial pattern. This component was sensed by both the spinning anemometer and by the inverted surface pressures on the rotating blades and would show up in the spectrum as tones at blade passage frequency; these have not been plotted in Slide 25.

In order to measure the resultant coherent rotor response, a pressure sensor is installed on each blade at the same relative spanwise and chordwise location. The summed pressure at that radius is proportional to and represents the thrust loading, as thrust per unit span, at that radius. The ratio of the spectral density of summed pressure on all B blades to the average of the spectral densities of pressures at all locations on the individual blades is going to be B to B^2 depending on whether or not the gusts at the blades are fully uncorrelated or fully correlated, respectively. We call this ratio the "Array Gain" of the blade row to turbulent inflow because of its analogy to the array gain of signal processing of acoustical arrays in non-isotropic noise fields. In Slide 26, the propeller had 4 blades so the "Array Gain" should be between 4 and 16; the spectrum shown to the right shows that the turbulent flow "Array Gain" is 4 to 8 while the response to tones generated by the steady time-mean inhomogeneities in the inflow approaches 16. The frequencies of these maxima are determined by the blade spacing and the resultant relative velocity of the blades. Thus the peaks are centered just to the right of the blade

passage frequency by a ratio U_s/U_θ. The equation on the slide shows how, to first order, the approximate value of the *tangential* correlation length of the incomming turbulence can be extracted from the "Array Gain". The *radial* (or spanwise) correlation length can be extracted from the coherence that is measured between the summed surface pressure and the far field sound. This is illustrated in Slide 27 which shows the redial correlation length of the inflow turbulence as a function of convective wave number normalized on mesh spacing. The correlation length is normalized on the mesh spacing. To compare Slides 20 and 27 we take note of the fact that $\Lambda/M = \frac{1}{4}$ for the grid that was used. This note taken, we see that the radial correlation lengths aerodynamically measured agree well with that inferred from the coherence between the surface and far field pressures.

The results of these studies show that the use of strip theory at low Mach number gives excellent agreement with the measured response of propellers to turbulence. Blade to blade correlation of the forced response provides enhancements to the spectra of dipole sound. The center frequencies of these peaks are just to the right of the blade passage frequency as determined by the blade spacing and the aerodynamic pitch of the blades. This is because the encounter velocity of the blades with the turbulence is the resultant of the axial and rotational velocity. The results also verify the utility of the inverse technique for measuring the inflow distortions, the turbulence spectrum, and the correlation lengths. In this regard, the inverse method with instrumented blades behaves as a dynamic "probe" whose calibtration factor is the gust response function for the blades. The method can be used to obtain inflow profile surveys in cases that do not premit the installation of invasive probes of Laser probes. To first order the classical Liepmann spectrum provides an adequate "fit" to measured wave number spectrum of the grid-generated turbulence, as expected.

3.2 Cascade Effects And The Influence Of Finite Mach Number On Turbulence Ingestion Noise.

The cascade effects on the response of blade rows to inflow distortions are of interest at low frequencies and moderate Mach number. Two linearized cascade codes are being integrated into our prediction tool: "LINC" and "CASGUST". Both of these codes are being developed at the University of Notre Dame by H.Atassi, see e.g. Abdelhamid and Attassi (2000). They are frequency-domain Euler models for compressible flow and they provide lift response to a specified upstream gust that is defined in three dimensional wave number space. LINC is written for an infinite cascade of unloaded flat blades of vanishing thickness. CASGUST is a compressible flow model of an infinite cascade of blades with arbitrary loading and thickness. Slide 30 shows some integral equations that express the utilization of either of these codes as kernel functions, $C(\mathbf{k})$, that provide the spectrum of lift per unit span. One of the spectral models of the inlet gust is the Liepmann spectrum of Slide 16. Figure 31 provides contour maps of $|C(\mathbf{k})|^2$ for each of these codes for a cascade of NACA0012 airfolils at zero mean load and 45° stagger. Both wavenumbers k_1 and k_2 are normalized on half-chord. Superimposed on the contour maps are lines for the various orders of resonances that satisfy the equation

$$k_2 C/2 = \frac{C/S}{2\cos\gamma}\left[2\pi \cdot n - (k_1 C/2)\cdot\left[\tan\gamma \pm \left(\frac{2S\sin\gamma}{C}\right)\cdot\left(\frac{M}{\sqrt{1-M^2}}\right)\right]\right]$$

where M is Mach number, C is chord, S is the nose to nose slant distance along the stagger line, γ is the stagger angle, k_1 and k_2 are the streamwise and stream-normal wavenumbers, respectively, and n is the harmonic order of the interblade phase angle.

At the intersections of these lines the contours show relative maxima which are caused by reinforcements of upward and downward propagating waves. These represent non-propagating acoustic "modes". Slide 32 shows that these regions of acoustic coincidence are also responsible for slight "humps" in the strip theory spectrum of turbulence-induced lift fluctuations. Slide 33 shows that as Mach number is decreased the value of k_1 for coincidence increases, Slide 34 illustrates the associated effect on the spectrum of turbulence-induced lift fluctuations. The "humps" in the spectra shown in Slides 32 and 34 are analogous to those shown in the experimental data of Slides 21 through 23, but not due to the same phenomena. A careful examination of Slide 33 will disclose a series of peaks (dots) in the contours. Note especially those for the LINC calculation. Those dots are singularities that are associated with the inter-blade resonances and they represent the "Array Gain" of infinite values of the infinite cascade that are the result of the coherent summation of lifts on an infinite array of blades. Thus in a cascade of a *finite* number of blades at *finite* Mach number we expect the peaks that are caused by the blade to blade correlation. However, because of the pair of resonance conditions we expect this broadening to be increased over a wider frequency range, but the levels not to be increased. As indicated in Slide 33, as Mach number decreases the two conditions converge to one line at vanishing Mach number.

3.3 Flow Into And Sound Caused By A Stator Behind An Upstream Rotor.

Slides 35 through 40 examine the response of a downstream stator to the wakes of the blades of an upstream rotor. The interaction is due to the time mean wake defects and turbulent flow that is shed. The general experimental setup has already been discussed, here we note the additional strut that represents a two-blade stator. Propellers with 4, 10, and 20 blades were used. Slide 36 gives the general picture of the results, see Lynch (2001), for a complete discussion. The top view on the left is the map of rms turbulence level that is measured downstream of the rotor and at the location of the leading edge of the stator, but without the stator installed. The spectrum of turbulence that is generated by the grid upstream of the rotor is given by the black line. The light blue spectrum is that of the total turbulence in the rotor wake averaged over circumference and including both the blade wakes and the grid-generated turbulence that is passed through the propeller. The spectrum in red is the spectrum of the turbulence the blade wakes only, averaged over the circumference. The spectrum generated by the blade wakes was measured behind the propeller without the grid. The dark blue spectrum is the spectrum of the grid-generated turbulence that is obtained by subtracting the component due to blade wakes from the total circumferentially-averaged spectrum. The illustration on the right simply illustrates the color coding. Careful examination of the data will disclose that the integral scale of the turbulence has been reduced by the action of the propeller. The approximate values of the turbulence integral scale that have been extracted from the spectra are tabulated in Slide 37.

Slide 38 provides a study of the sound that is radiated by the stator alone. Two cases are shown: one without the turbulence-generating grid, the other with the

turbulence-generating grid. Without the grid, in the so-called "clean" flow, the spectrum is characterized with a vortex-shedding sound, the remaining part of the spectrum is nominally dominated by the facility background. When the grid is installed, the sound levels are increased for frequencies above approximately 400 Hz. The inflow turbulence creates disorder in the vortex shedding so that the vortex shedding peak is reduced in level and broadened. The dark curve with diamond symbols is the sound level that is calculated with a strip theory (see Blake(1986)) and the measured spectrum of the turbulence. Slide 39 shows that the turbulence created by the rotor blade wakes elevates the broadband spectrum for frequencies above 1000 Hz. Slide 36 shows that this is to be expected in this frequency range. The blade tones are due to the interaction of convected mean wakes into the stator. The broadband and narrow band character of the spectrum can be predicted from the measured flow. Finally, Slide 40 shows the stator-generated sound, the rotor-generated sound (the calculation of which was previously discussed with Slide 21), and the measured composite spectrum.

3.4 Distortion Of Convected Vortical Wakes By Swirl.

In turbo-machinery the mean swirl of the mean flow downstream of a rotor causes a relative growth of the vortical wakes that are shed from the stators, see e.g. El-Hadidi et al. (2000). The governing parameter for the evolution of the wake distortions is the radial gradient of the swirl velocity expressed in the dimensionless form of the Rayleigh stability parameter that is defined at the top of Slide 42. The analysis constitutes the solution of eigenfunctions for a linearized Euler equation for the convected modes of the flow. For moderate Mach numbers, say order 0.3, both pressure and vortical disturbances are solutions to the equations of motion; for low Mach numbers the convected vorticity modes are the only relevant solutions since their wave numbers are well-removed from the aclustic wave numbers of the acoustic modes. Thus here we devote our attention to the convected vorticity modes. These wake-driven modes are convected into the downstream stator row and cause blade passage tones that are analogous to those shown previously in Slide 40. The initial conditions are imposed on the problem in the form of a unit-amplitude axial velocity distortion that can be expanded into circumferential harmonics, see Slide 42. Slide 43 shows profiles of axial and radial velocity components along the radius and at a sequence of axial stations downstream of the rotor in a cylindrical duct. For linearly "stable" convection the mean swirl velocity increases with radius and the growing axial velocity fluctuations grow for a time, but stabilize to a constant value that is somewhat larger than the initial condition. Relatively "unstable" convection occurs when the mean swirl velocity decreases with radius. The convected axial velocity fluctuations continue to grow with distance downstream of the rotor.

This theory is being validated in a measurement program at the Johns Hopkins University under the direction of J. Katz. Slide 44 illustrates the type of data that is being collected using particle image velocimetry. A specially designed test rig was designed by co-workers H.Atassi (UND) and Y.T.Lee (NSWCCD) in order to provide both positive and negative stability parameters. The blades are made of plexiglass and the fluid is a concentrated solution of Sodium Iodide in water to provide an ingeneous method of rendering the blades invisible to the green light Laser. This allows a mapping of the fluid dynamics without shadowing by the blades. The objective is to measure the convected

wake harmonics and compare with the predicted values. The measurements will include both mean and turbulent velocities.

3.5 Three Dimensional Effects In Gust Response Of Blade Rows.

In a new direction, we are examining the effects of spanwise variability in three dimensional cascades. Slide 45 is shown the spanwise variation of calculated lift coefficient due to a circumferential harmonic of order m=15 of a transverse gust that is incident on an 8 blade stator. The value of k_2 is m/r and narrowly varies between m/r_t and m/r_h in this problem of coherent gust incidence. Two cases are shown; the left hand side applies to a frequency that is below the cylindrical duct cut-on frequency, that on the right applied to a frequency that is just above the cut-on frequency for plane-wave propagation. In both cases the blades are of zero thickness and unloaded. The strip theory using LINC predicts a duct cut-on mode even when it is not predicted by the three dimensional theory. Above the cut-on frequency of the duct, LINC predicts a second order cut-on mode while the linear three dimensional theory predicts a first order plane wave mode. Outside the near-singularity at cut-on of acoustic duct modes the strip theory gives a good simulation of the three dimensional solution. At very low Mach number, then, we expect that the strip theory as implemented in the preceding Slides will continue to provide suitable solutions.

4.0 Example Area 2: Dipole Sound Of Trailing Edges.

The project is addressing the sound from trailing edges at two levels of computational sophistication. The first approach is a hybrid method that uses steady flow Reynolds Averaged Navier Stokes solutions to calculate the time mean flow everywhere in the domain of interest. Such solutions are now commonly obtained at the Reynolds Numbers and geometric complexity of many engineering applications. They provide turbulent kinetic energy, time mean turbulence dissipation, mean velocity profiles, and surface pressures. Statistical models of the turbulent sources are then used to model surface pressures and analytic functions are used to use these spectra to calculate the trailing edge sound, see Blake, Lee, Zawadzki (1998).

Slides 47 and 48 outline the overall conditions and analytics of the method. The challenge is to use the RANS solutions to develop the surface pressure spectrum and correlation scales that are identified in the Slide 48. We currently use the model of pressure fluctuations that involves the mean shear turbulence interaction (MST) sources in the turbulent boundary layer. A recent large eddy simulation (Chang, Piomelli, Blake(1999)) suggests that the turbulence-turbulence (TT) interaction pressures are proportional to the mean shear turbulence (MST) interaction pressures. THus, calculation of the total spectrum may be based on the calculation of the MST component with a small multicative constant correction. In the RANS-Statistical approach, the modelling of fluctuating wall pressure is as sketched in Slides 49 through 52. In essence, RANS solutions are used for the local time mean turbulence intensity and mean shear across the boundary layer on the three dimensional surface. Analytical functions with empirical coefficients are used to express the local statistics of the pressure sources. These functions are used for the wave number spectrum of vertical component turbulent velocity fluctuations, the length scale for those spectra, and a function that describes the turbulent velocity correlation in at different wall-normal coordinates. Examples of these

are shown in Slides 53 and 54. This modelling was first tested to cakculate a locally homogeneous wall pressure field statistics in the plane of the surface. Slide 55 illustrates how well the modelling accounts for pressure fluctuations beneath a turbulent boundary layer on a flat plate. Slide 56 shows that the calculated sound level that is obtained with these spectra and with the equations on Slide 48 agrees well with measurements.

In a related study that is being conducted at the Center for Turbulence research at the Stanford University, Large Eddy Simulation is being used to calculate the sound from trailing edge flow. Slides 57 and 58 respectively give maps of the turbulent Reynolds stresses in the vicinity of the edge and a series of wall pressure spectra. The calculated wall pressure spectra are compared with measured values in Slide 58. Slide 59 shows the calculated spectrum of far field sound compared with measurements made on a similar airfoil in the Anechoic Flow Facility at NSWCCD in the mid 1970's (See Gershfeld, Blake, Kniseley (1988)). Several limitations prevail regarding the comparisons shown here between calculation and measurement. There were no flow measurements with which to define the boundary conditions for the simulation which could only examine the turbulence in a control volume situated near the edge. Time mean surface pressures were not measured at enough locations on the experimental airfoil to determine the mean lift on the surface. Radiated sound measurements did not accompany the flow measurements. Thus a combined computation and verification measurement program is being undertaken on a new lifting surface in a combined program at NSWCCD, the Stanford University, the University of Notre Dame, and the University of Michigan. Two dynamically-similar flow models will be examined experimentally and computationally in air and in water. LES, and RANS-Statistical model predictions will be made of the wall pressure statustics, flow induced dipole sound, and surface vibration. All calculations will be consistent in the flow-source modelling that is used. Measurements will include mean and turbulent flow, surface pressures in air and water, flow induced vibration in water, and flow induced trailing edge sound in air. As facility constraints permit, details of acoustic source physics will be obtained with which to test the flow modelling. In essence, this program will test the complete computational framework that is laid out in Slides 5 through 11.

We anticipate that these are the first steps in developing and verifying the prediction of edge-related flow dipoles using some mix of RANS Statistical method and LES-based acoustic predictions. We are just beginning to consider ways of modelling the flow dipoles of tip flow (see Slide 60), flaps, and lift augmentation flows.

5.0 Conclusion.

With the development of modern computational resources, we are having considerable success in calculating the flow-induced sound and flow-induced vibration in many engineering applications. The focus presented here has been on the prediction of flow-induced forcing functions for aeroacoustic dipoles and flow-excited vibration. The latter is of interest in hydrodynamic applications. While computations that are based on LES and Direct Numerical Simulation are possible for some idealized and special-purpose applications, hybrid methods are being developed for near term engineering applications.

Experimental verification of each step in the prediction process has been and is being given major consideration. Systematic verification that involves the use of signal processing techniques, substitution experiments, and special – purpose models are all being integrated in an program of development of prediction techniques.

6.0 References.

Abdelhamid, Y.A. and Atassi, H.M., "Effects Of Blade Shape And Loading On The Acoustic Radiation Of A Cascade". Paper 2000-2093-CP, 6th AIAA/CEAS Areoacoustics Conference, Lahana, Hawaii, June 2000.

Blake,W.K. Mechanics of Flow Induced Sound and Vibration, Academic Press, 1986.

Blake, W.K., Lee, Y.T., Zawadzki, I. "Evolving Design Tools For Predicting Aeroacoustics of Rotating Machinery", ASME Fluids Engineering Division Summer Meeting, Wasjhington, D.C., 1998.

Chang, P.A., Piomelli, U., Blake, W.K., "Relationship Between Wall Pressure and Velocity-Field Sources", Physics of Fluids, 11, pp 3434-3448,1999.

El-Hadidi, B. and Atassi, H.M., "Sound Generation and Scattering From Radial Vanes in Uniform Flow", 7th International Conference of Fluid Dynamics and Propulsion, Sharm El-Sheikh, Sini, Egypt, December,2001.

El-Hadidi, B. Atassi, H.M., Envia, E., Podboy, G. "Evolution of Rotor Wake in Swirling Flow". AIAA-2000-1991.

Gershfeld, J., Blake, W.K., Kniseley, C.W., "Trailing Edge Flows And Aerodynamic Sound", AIAA Thermophysics, Plasmaphysics, and Lasers Conference, San Antonio, Yx, 1988.

Lynch, Denis, An Experimental Investigation of the Unsteady Pressure of a Stator Located Downstream of a Propeller Ingesting Broadband Turbulence. Ph.D Thesis, Department of Aerospace and Mechanical Engineering, University of Notre Dame, 2001.

Martinez, R. "Asymptotic Theory of Broadband Rotor Thrust, Part 1. Manipulations of Flow Probabilities for a High Number of Blades; Part 2. Analysis of the Right Frequency Shift of the Maximum Response", J. App. Mechanics. 63, 136-148, 1996.

Minniti, R.J., Blake, W.K., Mueller, T.J., "Inferring Propeller Inflow and Radiation From Near-Field Response, Part 1: Analytic Development; Part 2: Empirical Application", AIAA Journal, 39, pp 1030 – 1046, 2001.

Wojno, J., Mueller, T.J., Blake, W.K., "Turbulence Ingestion Noise. Part 1: Experimental Characterization of Grid-Generated Turbulence; Part 2: Rotor Aeroacoustic Response to Grid-Generated Turbulence", AIAA Journal, Accepted for publication, 2001.

FLOW-STRUCTURE INTERACTION NOISE
AT LOW MACH NUMBERS

M. S. Howe
Boston University, College of Engineering
110 Cummington Street, Boston MA 02215

SUMMARY

The method of compact Green's functions is described for calculating the sound produced by low Mach number turbulence interacting with a surface and by surfaces in relative motion. The method is very powerful and can supply analytical predictions of complex fluid-structure interaction noise, and can also be used to make acoustic predictions by 'postprocessing' data obtained from a numerical simulation of a hydrodynamic interaction. The theory is illustrated by cases of sound production by a vortex interacting with a sphere, by the linear and nonlinear theories of parallel vortex-airfoil interaction noise, the trailing edge noise produced by an airfoil of finite thickness and of arbitrary chord, and by the compression wave generated when a projectile is fired into a long duct.

1. EQUATION OF VORTEX SOUND

Lighthill's acoustic analogy [1] can be recast to emphasize the importance of vorticity ($\boldsymbol{\omega}$) and entropy fluctuations as sources of sound by taking the *total enthalpy* B to be the fundamental acoustic variable [2, 3]. Lighthill identified the Reynolds stress as the principal acoustic source in homentropic flow. In that case

$$B = \int \frac{dp}{\rho} + \frac{1}{2}v^2,$$

where ρ is fluid density, $p \equiv p(\rho)$ the pressure, and $\mathbf{v}$ denotes velocity, and Lighthill's equation becomes

$$\left(\frac{D}{Dt}\left(\frac{1}{c^2}\frac{D}{Dt}\right) - \frac{1}{\rho}\nabla \cdot (\rho\nabla)\right) B = \frac{1}{\rho}\mathrm{div}(\rho\boldsymbol{\omega} \wedge \mathbf{v}), \tag{1.1}$$

where c is the local speed of sound.

In the irrotational acoustic far field Crocco's form of the momentum equation $\partial\mathbf{v}/\partial t = -\nabla B$ implies that $B = -\partial\varphi/\partial t$, where $\varphi(\mathbf{x}, t)$ is the velocity potential that determines the whole motion in the irrotational regions of the fluid. B is therefore *constant* in steady irrotational flow, and at large distances from the sources perturbations in B represent outgoing sound waves. If the mean flow is at rest in the far field, the acoustic pressure $p = \rho_o B \equiv -\rho_o\partial\varphi/\partial t$.

At low Mach numbers M local mean values of ρ and c differ from their uniform respective values ρ_o and c_o by terms of relative order M^2. The vortex sound equation (1.1) can then be simplified (a) by taking $c = c_o$ and $\rho = \rho_o$, and (b) by neglecting nonlinear effects of propagation and the scattering of sound by the vorticity. The production of sound is then governed by

$$\left(\frac{1}{c_o^2}\frac{\partial^2}{\partial t^2} - \nabla^2 \right) B = \mathrm{div}(\boldsymbol{\omega} \wedge \mathbf{v}), \tag{1.2}$$

where in the acoustic field

$$p(\mathbf{x}, t) \approx \rho_o B(\mathbf{x}, t). \tag{1.3}$$

2. VORTEX-SURFACE INTERACTION NOISE

Consider the solution of (1.2) in the presence of solid boundaries S that are either stationary or vibrating at small amplitude. Introduce a Green's function $G(\mathbf{x}, \mathbf{y}, t - \tau)$ that satisfies

$$\left(\frac{1}{c_o^2} \frac{\partial^2}{\partial \tau^2} - \frac{\partial^2}{\partial y_j^2} \right) G = \delta(\mathbf{x} - \mathbf{y}) \delta(t - \tau), \quad G = 0 \text{ for } \tau > t, \tag{2.1}$$

and has vanishing normal derivatives $\partial G / \partial x_n$, $\partial G / \partial y_n$ respectively for $\mathbf{x}$ and $\mathbf{y}$ on S. Then Green's theorem [3 - 5] supplies the solution of (1.2) in the form

$$B(\mathbf{x}, t) \approx - \int (\boldsymbol{\omega} \wedge \mathbf{v})(\mathbf{y}, \tau) \cdot \frac{\partial G}{\partial \mathbf{y}}(\mathbf{x}, \mathbf{y}, t - \tau) d^3\mathbf{y} d\tau + \nu \oint_S \boldsymbol{\omega}(\mathbf{y}, \tau) \wedge \frac{\partial G}{\partial \mathbf{y}}(\mathbf{x}, \mathbf{y}, t - \tau) \cdot d\mathbf{S}(\mathbf{y}) d\tau$$

$$+ \oint_S G(\mathbf{x}, \mathbf{y}, t - \tau) \frac{\partial v_j}{\partial \tau}(\mathbf{y}, \tau) dS_j(\mathbf{y}) d\tau, \tag{2.2}$$

provided frictional effects on S are effectively the same as for incompressible flow, where ν is the kinematic viscosity, and the vector surface element $d\mathbf{S}$ is directed into the fluid. The first integral describes the production of sound by convecting vorticity. Green's function takes account of the influence of the body on the efficiency of sound production by this source. The second, surface integral represents the sound produced by frictional forces on the body; it can be neglected in most applications at high Reynolds numbers. The final term is the contribution from normal velocity fluctuations on S.

Therefore, at large Reynolds number and for a non-vibrating surface, the pressure in the acoustic far field is given by

$$p(\mathbf{x}, t) = -\rho_o \int_V (\boldsymbol{\omega} \wedge \mathbf{v})(\mathbf{y}, \tau) \cdot \frac{\partial G}{\partial \mathbf{y}}(\mathbf{x}, \mathbf{y}, t - \tau) d^3\mathbf{y} d\tau. \tag{2.3}$$

The integral includes contributions from the direct radiation by quadrupole sources within the fluid (with intensity $\propto \rho_o v^3 M^5$ per unit volume [1]) and also from dipole sources on S. For a body with surface irregularities comparable in size to the turbulence length scale (when the irregularity is acoustically *compact*) the dipole intensity $\propto \rho_o v^3 M^3$; for turbulence near the leading or trailing edge of an airfoil of *non-compact* chord the intensity typically scales like $\rho_o v^3 M^2$. Thus at low Mach numbers, compact surface irregularities (or a compact foreign body) and edges of non-compact bodies are usually the dominant sources of flow generated sound. We shall consider these cases separately and demonstrate how detailed acoustic predictions can be made for complex interactions in terms of the appropriate *compact* approximation for the Green's function G.

3. COMPACT BODIES AND COMPACT SURFACE IRREGULARITIES

3.1 Compact bodies and cylindrical bodies of compact cross-section The leading order dipole radiation is calculated by approximating G in (2.3) by the *compact* Green's function [2, 3]

$$G(\mathbf{x}, \mathbf{y}, t - \tau) = \frac{1}{4\pi |\mathbf{X} - \mathbf{Y}|} \delta\left(t - \tau - \frac{|\mathbf{X} - \mathbf{Y}|}{c_o} \right) \tag{3.1}$$

$$\begin{aligned} \mathbf{X} &= \mathbf{x} - \boldsymbol{\varphi}^*(\mathbf{x}) \\ \mathbf{Y} &= \mathbf{y} - \boldsymbol{\varphi}^*(\mathbf{y}) \end{aligned} \Bigg\} \text{ Kirchhoff vectors for the body,}$$

2

where the vector components $X_j(\mathbf{x})$ and $Y_j(\mathbf{y})$ are the velocity potentials of incompressible flow past the body having unit speed in the j-direction at large distances from the body; φ_j^* is the velocity potential of the incompressible flow that would be produced by rigid body motion of S at unit speed in the j-direction. For a cylindrical body of *compact cross-section* parallel to the x_3-direction, we take

$$X_3 = x_3, \quad Y_3 = y_3.$$

The approximation (3.1) represents the solution of (2.1) correct to dipole order provided either $\mathbf{x}$ or $\mathbf{y}$ (or both) lie in the acoustic far field of S, in the limit in which the acoustic wavelength $\lambda \gg \ell \sim$ the length scale of S (Figure 1). Special cases referenced in the illustrations given below are listed in Table 1:

Standard special cases

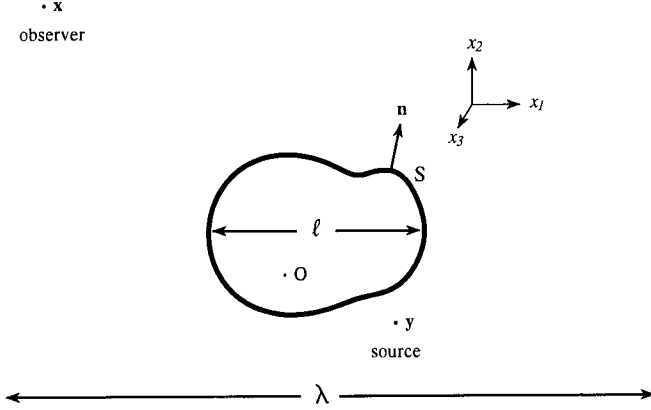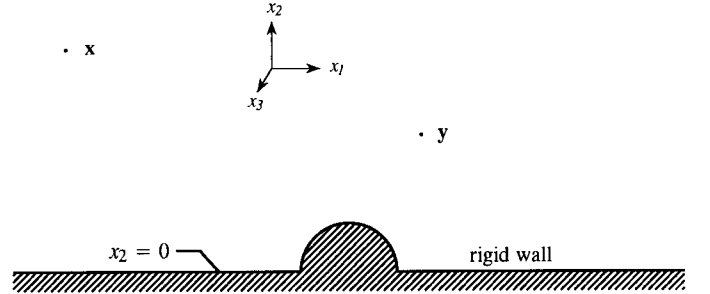| body	X_1	X_2	X_3
sphere of radius a center at origin	$x_1\left(1 + \frac{a^3}{2|\mathbf{x}|^3}\right)$	$x_2\left(1 + \frac{a^3}{2|\mathbf{x}|^3}\right)$	$x_3\left(1 + \frac{a^3}{2|\mathbf{x}|^3}\right)$
circular cylinder of radius a coaxial with the x_3-axis	$x_1\left(1 + \frac{a^2}{x_1^2+x_2^2}\right)$	$x_2\left(1 + \frac{a^2}{x_1^2+x_2^2}\right)$	x_3
strip airfoil $-a < x_1 < a, \ x_2 = 0, \ -\infty < x_3 < \infty$	x_1	$\mathrm{Re}(-i\sqrt{z^2 - a^2})$ $z = x_1 + ix_2$	x_3

Table 1

Figure 1

Figure 2

3.2 Surface irregularity This case involves turbulence sources adjacent to a surface that is *locally plane* on the scale of the acoustic wavelength except for the presence of one or more acoustically compact surface irregularities (Figure 2). The Green's function incorporates 'images' of all dipole sources 'in' the wall, such that the net *normal* dipole strength vanishes identically. If the wall coincides with $x_2 = 0$, with fluid in $x_2 > 0$, then

$$G(\mathbf{x}, \mathbf{y}, t - \tau) = \frac{1}{4\pi|\mathbf{X} - \mathbf{Y}|}\delta\left(t - \tau - \frac{|\mathbf{X} - \mathbf{Y}|}{c_o}\right) + \frac{1}{4\pi|\bar{\mathbf{X}} - \mathbf{Y}|}\delta\left(t - \tau - \frac{|\bar{\mathbf{X}} - \mathbf{Y}|}{c_o}\right), \qquad (3.2)$$

3

where

$$Y_1 = y_1 - \varphi_1^*(\mathbf{y}), \quad Y_2 = y_2, \quad Y_3 = y_3 - \varphi_3^*(\mathbf{y}) \left.\begin{array}{c}\\\\\\\\\end{array}\right\}$$

$$X_1 = x_1 - \varphi_1^*(\mathbf{x}), \quad X_2 = x_2, \quad X_3 = x_3 - \varphi_3^*(\mathbf{x})$$

(3.3)

and $\bar{\mathbf{X}} = (X_1, -X_2, X_3)$. The case of a two-dimensional surface irregularity (projection or cavity) uniform in, say, the x_3-direction is obtained by setting $Y_3 = y_3$, $X_3 = x_3$.

3.3. Radiation from a stationary compact body: vortex interacting with a sphere To evaluate (2.3) take the coordinate origin within S and consider an observer at $\mathbf{x}$ in the acoustic far field ($|\mathbf{x}| \to \infty$). Expand the compact Green's function G to first (*dipole*) order in the retarded time $\mathbf{x} \cdot \mathbf{Y}/c_o|\mathbf{x}|$:

$$G(\mathbf{x}, \mathbf{y}, t - \tau) = \frac{1}{4\pi|\mathbf{X} - \mathbf{Y}|}\delta\left(t - \tau - \frac{|\mathbf{X} - \mathbf{Y}|}{c_o}\right)$$

$$\approx \frac{1}{4\pi|\mathbf{x}|}\delta\left(t - \tau - \frac{|\mathbf{x}|}{c_o}\right) + \frac{x_j Y_j}{4\pi c_o|\mathbf{x}|^2}\delta'\left(t - \tau - \frac{|\mathbf{x}|}{c_o}\right), \qquad (3.4)$$

where the prime denotes differentiation with respect to t. The first δ-function is independent of $\mathbf{y}$ and makes no contribution to (2.3), which becomes

$$p(\mathbf{x}, t) \approx \frac{-\rho_o x_j}{4\pi c_o|\mathbf{x}|^2}\frac{\partial}{\partial t}\int(\boldsymbol{\omega} \wedge \mathbf{v})\left(\mathbf{y}, t - \frac{|\mathbf{x}|}{c_o}\right) \cdot \nabla Y_j(\mathbf{y})d^3\mathbf{y}, \quad |\mathbf{x}| \to \infty. \qquad (3.5)$$

The integral represents the retarded dipole strength produced by normal stresses on S. Indeed, the component F_j of the unsteady force exerted by the body on the fluid is given (for incompressible flow) by [3]

$$F_j = -\rho_o\int\boldsymbol{\omega} \wedge \mathbf{v} \cdot \nabla Y_j d^3\mathbf{y} - \eta\oint_S \nabla Y_j \cdot \boldsymbol{\omega} \wedge d\mathbf{S}, \quad \eta = \rho_o\nu, \qquad (3.6)$$

where the second, *frictional* component of force can be discarded at very large Reynolds numbers.

To illustrate the procedure consider the sound produced when a line vortex of strength Γ convects past a fixed, rigid sphere. Let the sphere have radius a with center at the coordinate origin, and let the vortex be initially far upstream of the sphere and parallel to the x_3-axis at a distance h above the plane of symmetry $x_2 = 0$ (Figure 3). There is a mean *irrotational* flow in the x_1-direction at speed U, which at sufficiently low Mach number ($M = U/c_o$) is given by

$$\mathbf{U} = U\nabla X_1(\mathbf{x}), \qquad (3.7)$$

where $X_1(\mathbf{x})$ is given in the first row of Table 1. The vortex is convected towards the sphere by the mean flow and deformed as it passes around the sphere; more distant parts of the vortex (at $|x_3| \gg a$) are unaffected and remain parallel to the x_3-direction. Figure 3 illustrates the distorted vortex at several values of $T = Ut/a$, when $h/a = 0.2$ and when the self-induced motion of the vortex is neglected.

When surface viscous effects and vortex shedding are ignored, the sound generated during the interaction is given by (3.5) in which $\boldsymbol{\omega}$ is approximated by the vorticity of the distorted line vortex. There is no contribution from unsteady 'drag' ($j = 1$) because $\mathbf{v} = U\nabla Y_1$ and $\boldsymbol{\omega} \wedge \nabla Y_1 \cdot \nabla Y_1 \equiv \mathbf{0}$. Similarly, there can be no net 'side-force' on the sphere because of the symmetric shape of the
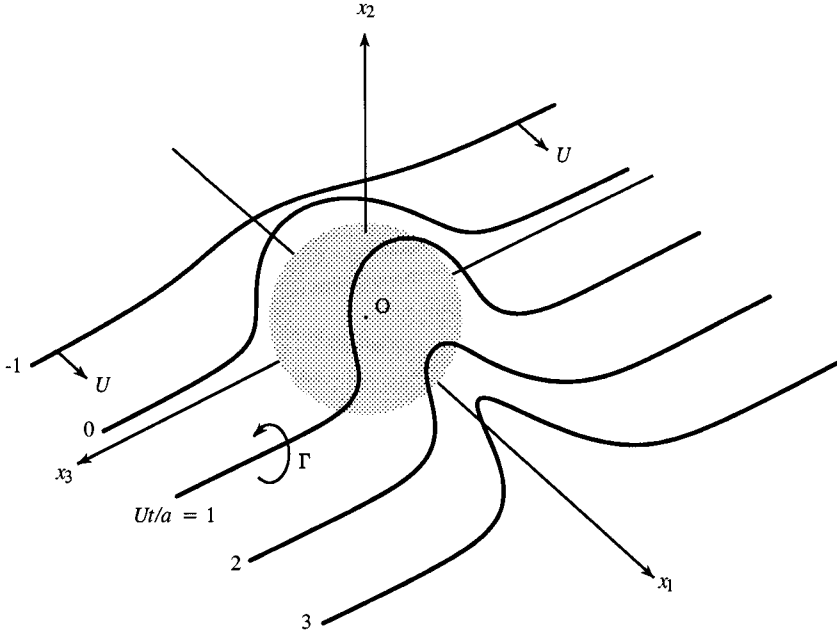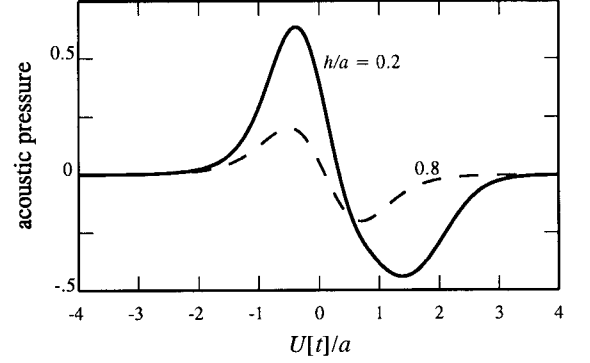
4

Figure 3

Figure 4

deformed vortex, and therefore there will be no contribution from $j = 3$. The sound is accordingly produced by a dipole orientated in the x_2-direction; i.e. the interaction produces an unsteady 'lift' in this direction which is responsible for the sound, and which can therefore be cast in the form

$$p(\mathbf{x}, t) \approx \frac{-\rho_o U \cos \Theta}{4\pi c_o |\mathbf{x}|} \frac{\partial}{\partial t} \int (\boldsymbol{\omega} \cdot \nabla Y_1 \wedge \nabla Y_2) \left(\mathbf{y}, t - \frac{|\mathbf{x}|}{c_o}\right) d^3 \mathbf{y}, \quad |\mathbf{x}| \to \infty, \qquad (3.8)$$

where $\Theta = \cos^{-1}(x_2/|\mathbf{x}|)$ is the angle between the observer direction $\mathbf{x}$ and the x_2-axis.

Typical plots of the nondimensional pressure

$$\frac{p(\mathbf{x}, t)}{\rho_o \Gamma U M \cos \Theta / 4\pi |\mathbf{x}|}$$

are shown plotted against $U[t]/a$ in Figure 4 for two values of h/a; they illustrate how the sound level decreases as the initial standoff distance h of the vortex increases.

In this calculation the unsteady interaction has been evaluated in a linearized approximation, when the unsteady drag is predicted to vanish. Thus, if the sphere is 'stuck' to a plane wall in the presence of a turbulent flow, the present approximation would yield no 'dipole' sound, since only the drag and side force can then make a finite dipole contribution because (from (3.2))

$$G(\mathbf{x}, \mathbf{y}, t - \tau) \approx \frac{1}{2\pi |\mathbf{x}|} \delta \left(t - \tau - \frac{|\mathbf{x}|}{c_o}\right) + \frac{x_1 Y_1 + x_3 Y_3}{2\pi c_o |\mathbf{x}|^2} \delta' \left(t - \tau - \frac{|\mathbf{x}|}{c_o}\right). \qquad (3.9)$$

3.4. Parallel blade-vortex interactions The same method of solution in terms of the compact Green's function is applicable to airfoils of compact chord and arbitrary span, but it is sufficient here to give explicit results when the span is compact.
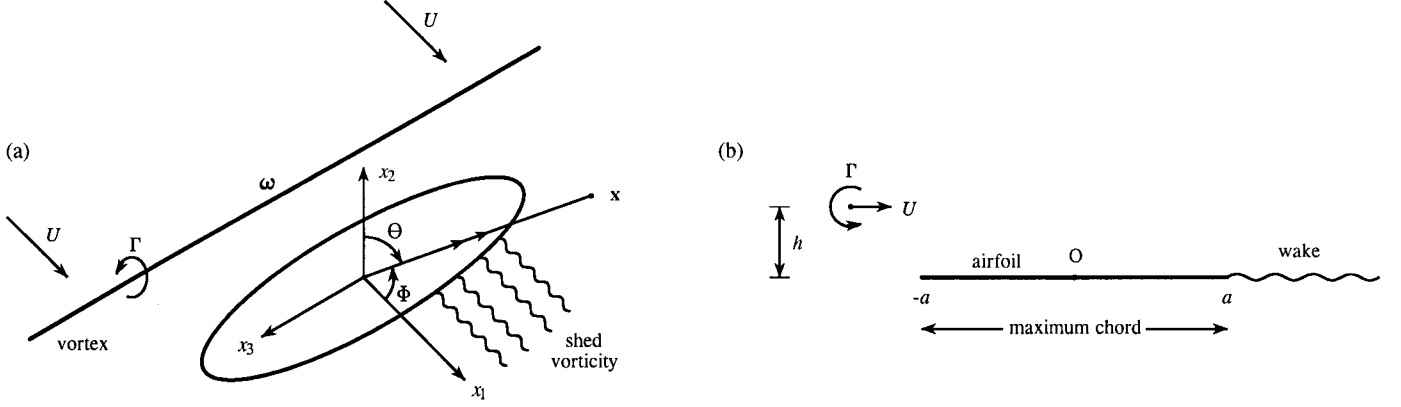
5

Figure 5

Consider a planar airfoil of rectangular or elliptic planform, orientated as illustrated in Figure 5 at zero angle of attack to a mean flow at speed U in the x_1-direction. A spanwise line vortex of strength Γ is swept past the airfoil at an initial standoff distance h above the airfoil, as indicated in the side view. For an airfoil of compact chord the acoustic pressure produced by the interaction is given by equation (3.5) where, for an airfoil of span L (between $-\frac{1}{2}L < x_3 < \frac{1}{2}L$),

$$
Y_1 = y_1, \qquad Y_2 = \begin{cases} \mathrm{Re}\!\left(-i\sqrt{z^2 - \hat{a}(y_3)^2}\right), & |y_3| < \frac{1}{2}L \\ y_2, & |y_3| > \frac{1}{2}L \end{cases}, \qquad Y_3 = y_3, \quad z = y_1 + iy_2,
$$

where $2\hat{a}(y_3)$ is the airfoil chord at the spanwise location y_3. For the rectangular airfoil $\hat{a}(y_3) \equiv a =$ constant; for the elliptic airfoil we set

$$
\frac{\hat{a}(y_3)}{a} = \sqrt{1 - \frac{4y_3^2}{L^2}}, \quad |y_3| < \frac{1}{2}L. \tag{3.10}
$$

Vorticity will be shed into the wake of the airfoil in accordance with the Kutta condition. This smooths out conditions at the trailing edge, so that sound is generated primarily by the interaction of the vortex with the leading edge. This is accounted for by removing the trailing edge singularity of the Green's function, by modifying the x_2-component of $\mathbf{Y}$ as follows:

$$
Y_2 = \mathrm{Re}\!\left(\sqrt{2\hat{a}(y_3)}\sqrt{z + \hat{a}(y_3)}\right), \quad |y_3| < \frac{1}{2}L. \tag{3.11}
$$

In the linearized approximation $\mathbf{v} = (U, 0, 0)$ in (3.5), and the line vortex remains rectilinear; the radiation is produced entirely by the lift dipole. If the vortex crosses the midchord of the airfoil at time $t = 0$, (3.5) yields

$$
\frac{p(\mathbf{x}, t)}{\rho_o \Gamma U M \cos\Theta (L/|\mathbf{x}|)/4\pi a} \approx -\frac{1}{2^{\frac{3}{2}}} \int_{-\frac{1}{2}}^{\frac{1}{2}} \mathrm{Im}\left(\frac{\sqrt{\frac{\hat{a}}{a}}}{\left(\frac{U[t]}{a} + \frac{\hat{a}}{a} + i\frac{h}{a}\right)^{\frac{3}{2}}} \right) d\hat{y}_3, \qquad M = \frac{U}{c_o}, \tag{3.12}
$$

6

where $\hat{y}_3 = y_3/L$. For a rectangular airfoil the right hand side evaluates to

$$-\frac{1}{2^{\frac{3}{2}}}\mathrm{Im}\left(\frac{1}{\left(\frac{U[t]}{a}+1+i\frac{h}{a}\right)^{\frac{3}{2}}}\right).$$

The acoustic pressure signatures (the left hand side of (3.12)) for the rectangular and elliptic airfoils are plotted in Figure 6 for a vortex standoff distance $h/a = 0.2$. For the rectangular airfoil, the peak amplitude is larger and the width of the acoustic pulse is narrower than for the elliptic airfoil, where the interaction of the leading edge with the vortex occurs over a longer time period.
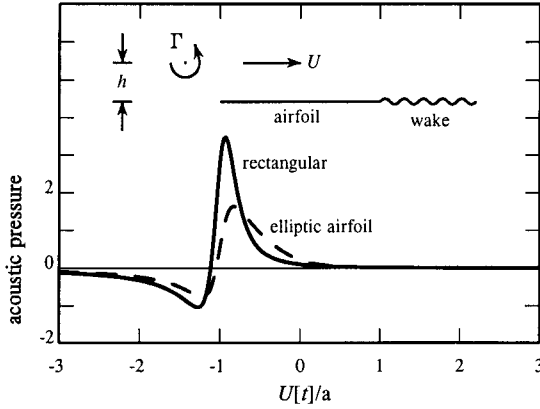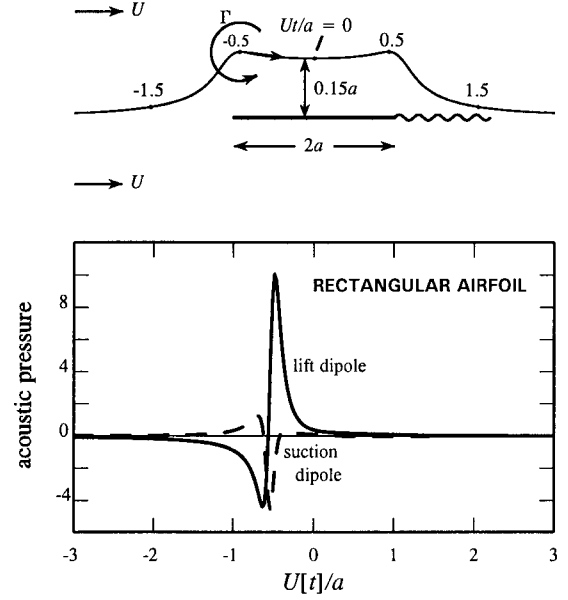

Figure 6

Figure 7

When the $h = 0$ 'image' vorticity in the airfoil prevents the vortex from impinging on the leading edge, and causes the trajectory to be locally deflected above the airfoil (for $\Gamma > 0$). For a rectangular airfoil this case can be treated by assuming that the section of the vortex within the span $-\frac{1}{2}L < x_3 < \frac{1}{2}L$ follows a path that is approximately the same as for locally two-dimensional flow, and by neglecting small contributions from the ends of the airfoil. There are now two distinct dipole components of the sound: that discussed above (p_2, say) associated with the unsteady lift, and a second smaller component (p_1) produced by the unsteady 'suction' force' at the leading edge. The corresponding nondimensional pressures

$$\frac{p_1(\mathbf{x},t)}{\rho_o\Gamma U M\cos\Phi(L/|\mathbf{x}|)/4\pi a}, \qquad \frac{p_2(\mathbf{x},t)}{\rho_o\Gamma U M\cos\Theta(L/|\mathbf{x}|)/4\pi a}$$

are plotted in Figure 7 for a velocity ratio $\Gamma/4\pi aU = 0.2$. The upper part of the figure shows the path followed by those sections of the vortex inboard of the airfoil tips.

7

4. NONCOMPACT BODIES

4.1 Edge noise Our discussion will be framed in terms of the canonical, parallel-sided airfoil shape illustrated schematically in Figure 8, which has chord ℓ and uniform thickness h, and a rounded nose. Take the origin O at a convenient point near the trailing edge such that the 'upper' and 'lower' planar surfaces of the airfoil are at $x_2 = \pm\frac{1}{2}h$, the x_1-axis is in the direction of the mean flow, and x_3 is parallel to the airfoil span (out of the plane of the paper in Figure 8a).

When these conditions are satisfied the far field acoustic pressure fluctuations $p(\mathbf{x}, \omega)e^{-i\omega t}$ of frequency ω produced by the interaction of the turbulence with the airfoil are given by the following form of (3.5)

$$p(\mathbf{x}, \omega) = \rho_0 \int \frac{\partial G}{\partial \mathbf{y}}(\mathbf{x}, \mathbf{y}, \omega) \cdot \left(\boldsymbol{\omega} \wedge \mathbf{v}\right)(\mathbf{y}, \omega) d^3\mathbf{y}, \tag{4.1}$$

where $G(\mathbf{x}, \mathbf{y}, \omega)$ is the *time harmonic* Green's function, which satisfies $G(\mathbf{x}, \mathbf{y}, t - \tau) = \frac{-1}{2\pi} \int_{-\infty}^{\infty} G(\mathbf{x}, \mathbf{y}, \omega)e^{-i\omega(t-\tau)}d\omega$.
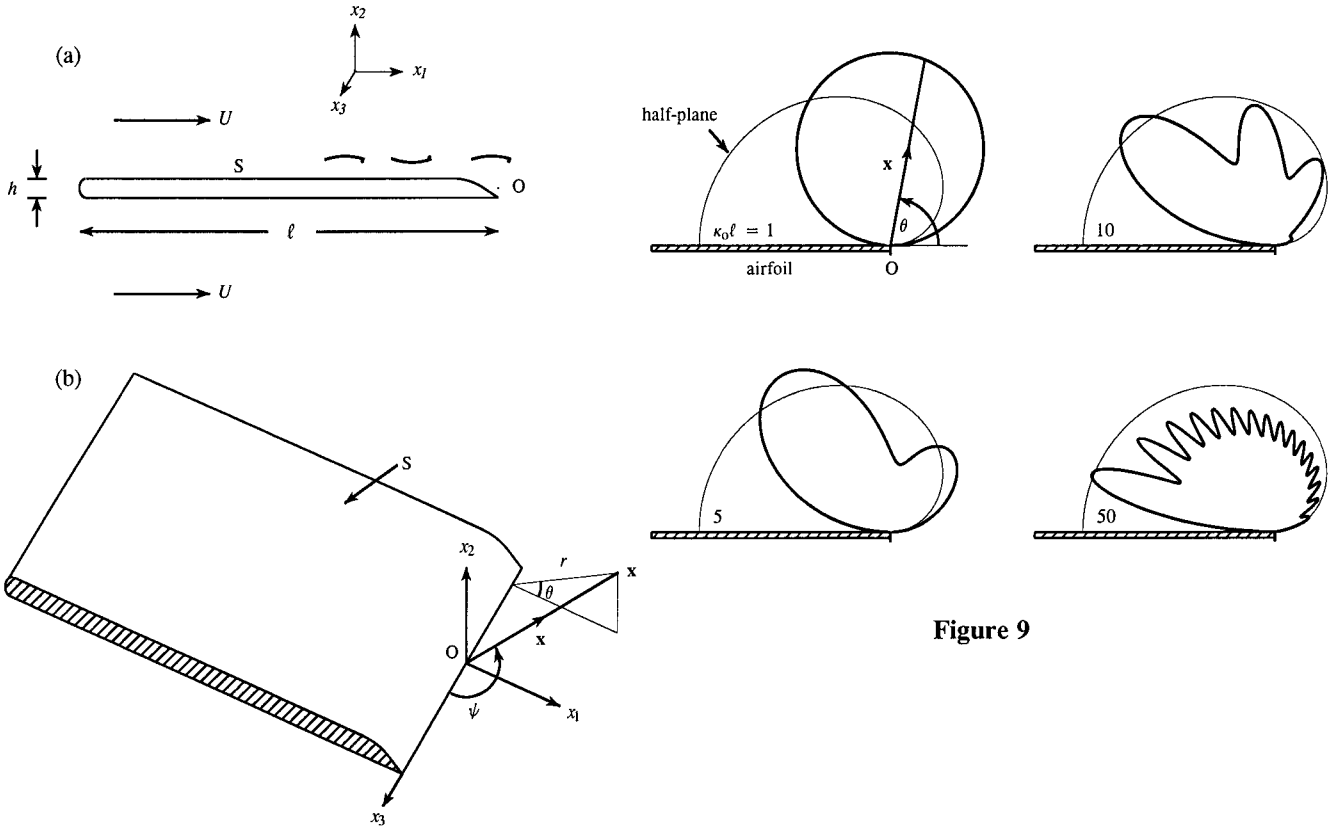

Figure 8

Figure 9

At low Mach numbers the trailing edge noise is dominated by contributions to (4.1) from the neighborhood of the edge. The wavelength of the sound $\sim \delta/M$, where δ is a length that characterizes the eddy size near the edge, and may in practice be of the order of the boundary layer thickness or the airfoil thickness h. In either case the acoustic wavelength greatly exceeds h when $M \ll 1$, which implies that the turbulence responsible for the edge noise is always very

8

much closer than an acoustic wavelength from the edge. Then the nondimensional source distance $\kappa_o\sqrt{y_1^2 + y_2^2} \sim \sqrt{y_1^2 + y_2^2}/$acoustic wavelength $\ll 1$, where $\kappa_o = \omega/c_o$ is the acoustic wavenumber. When the observation point $\mathbf{x}$ is in the acoustic far field and $\mathbf{y}$ is within the source region, Green's function can be expanded in terms of this small parameter. When the airfoil chord ℓ is noncompact $(\kappa_o\ell \gg 1)$, the first nontrivial term in this expansion yields

$$G(\mathbf{x},\mathbf{y},\omega) \approx \frac{-\sqrt{\kappa_o}\sin^{\frac{1}{2}}\psi\sin\left(\frac{\theta}{2}\right)\varphi^*(\mathbf{y})e^{i\kappa_o|\mathbf{x}-y_3\mathbf{i}_3|}}{\pi\sqrt{2\pi i}|\mathbf{x}-y_3\mathbf{i}_3|}, \quad \kappa_o\ell \to \infty, \quad \kappa_o\sqrt{y_1^2 + y_2^2} \ll 1. \qquad (4.2)$$

where $\mathbf{i}_3$ is a unit vector parallel to the airfoil span (in the positive x_3-direction). If $r = \sqrt{x_1^2 + x_2^2}$ denotes the observer distance from the edge of the airfoil ($\sim$ the x_3-axis), then (r,θ) are the polar coordinates of the observer position relative to a plane $x_3 = $ constant, i.e. $(x_1, x_2) = r(\cos\theta, \sin\theta)$; $\psi = \sin^{-1}(r/|\mathbf{x}|)$ is the angle between the observer direction $\mathbf{x}$ and the edge (see Figure 8b). The function $\varphi^*(\mathbf{y}) \equiv \varphi^*(y_1, y_2)$ of the source position $\mathbf{y}$ is the velocity potential of ideal, incompressible flow around the edge (in the anticlockwise direction), and therefore depends on the geometrical shape of the edge. At source distances $\sqrt{y_1^2 + y_2^2}$ from the edge that are large compared to the airfoil thickness h but small compared to the chord ℓ, $\varphi^*(\mathbf{y})$ must tend to the following expression for the potential of flow around a rigid *half-plane*:

$$\varphi^*(\mathbf{y}) \to \sqrt{r'}\sin(\theta'/2), \quad h \ll r' \ll \ell, \quad \text{where } (y_1, y_2) = r'(\cos\theta', \sin\theta'). \qquad (4.3)$$

In applications where the wavelength is not necessarily small compared to the chord ℓ the representation (4.2) is modified in its dependence on frequency and on the directivity, but the edge potential function $\varphi^*(\mathbf{y})$ is unchanged. This is illustrated in Figure 9 [6] for $\psi = 90°$ and $\kappa_o\ell = 1, 5, 10$ and 50. The heavy curves are polar plots of the *linear* pressure amplitude (normalized to the same maximum value); in each case the light curve corresponds to the $\sin\left(\frac{\theta}{2}\right)$ directionality for $\kappa_o\ell = \infty$. At the lowest frequency shown in Figure 9 ($\kappa_o\ell = 1$) the radiation peaks in directions normal to the airfoil, and the directivity coincides with that for a *dipole* source orientated in the x_2-direction (as for the compact chord airfoil of §3.4). Multiple lobes develop as the frequency increases, and the directivity tends in an oscillatory manner towards that for the semi-infinite airfoil. In all cases there are radiation nulls in the directions $\theta = 0°$ and $180°$, respectively downstream and upstream of the airfoil.

The above argument implies that the influence of finite chord on the trailing edge noise frequency spectrum does not depend on the edge geometry. In Figure 10 we compare the predicted edge noise spectra for a semi-infinite airfoil with that for an airfoil of finite chord ℓ for two different radiation directions, and for the following parameter values that are typical of model scale tests conducted in air and in associated numerical simulations [7 - 13]

$$\frac{\ell}{\delta_*} \approx 78, \quad M = 0.09, \qquad (4.4)$$

where δ_* is the boundary layer displacement thickness in the vicinity of the trailing edge. Significant departures from the half-plane prediction occur for $\omega\delta_*/U < 0.4$; in particular spectral levels are much reduced at frequencies below that of the spectral peak, which is shifted to higher frequencies.
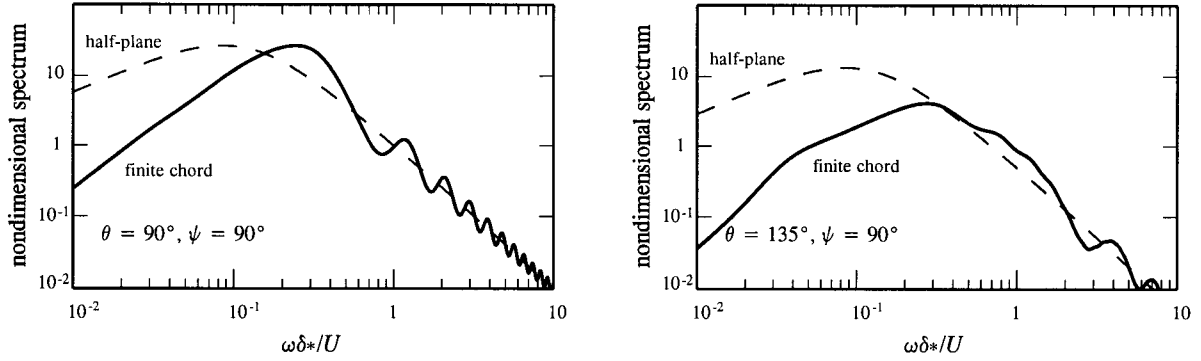
9

Figure 10

4.2 Projectile entering a duct

The overall pressure rise across the compression wave produced ahead of a bullet shaped body projected into a long, but finite duct of cross-sectional area $\mathcal{A} = \pi R^2$ fitted with a long, cylindrical entrance 'hood' of length ℓ_h and cross-section $\mathcal{A}_h = \pi R_h^2$ (Figure 11) is given approximately by [14]

$$\Delta p = \frac{\rho_0 U^2}{(1 - M^2)} \frac{\mathcal{A}_o}{\mathcal{A}} \left(1 + \frac{\mathcal{A}_o}{\mathcal{A}}\right), \tag{4.5}$$

where U and $\mathcal{A}_o$ respectively denote the projection speed and the cross-sectional area of the body, and $M = U/c_o$.

When the blockage $\mathcal{A}_o/\mathcal{A}$ is small and the projection Mach number M does not exceed about 0.4, the initial form of the compression wave can be calculated from the following modified form of (1.2):

$$\left(\frac{1}{c_o^2} \frac{\partial^2}{\partial t^2} - \nabla^2\right) B = \frac{U}{(1 - M^2)} \left(1 + \frac{\mathcal{A}_o}{\mathcal{A}}\right) \frac{\partial}{\partial t} \left(\frac{\partial \mathcal{A}_T}{\partial x_1}(x_1 + Ut)\delta(x_2)\delta(x_3)\right) + \operatorname{div}(\boldsymbol{\omega} \wedge \mathbf{v}), \tag{4.6}$$

The new source term is a slender body representation of the body, which is assumed to travel along the axis of the duct (the negative x_1-axis), where $\mathcal{A}_T(s)$ is the body cross-sectional area at distance s *from the tip of the nose*, which is taken to cross the entrance plane of the hood at time $t = 0$.

The characteristic wavelength of the sound produced when the body interacts with the duct entrance is sufficiently large ($\sim R_h/M$) that only plane waves can propagate into the duct. The corresponding compact Green's function for an observer at $\mathbf{x}$ deep inside the duct then has the form

$$G(\mathbf{x}, \mathbf{y}; t - \tau) =$$

$$\frac{c_o \mathcal{T}_J}{2\mathcal{A}_h} \sum_{n=0}^{\infty} \mathcal{R}_E^n \mathcal{R}_J^n \left\{ H\left([t] - \tau - \frac{(2n\ell + \varphi^*(\mathbf{y}))}{c_o}\right) + \mathcal{R}_E H\left([t] - \tau - \frac{(2n\ell - \varphi^*(\mathbf{y}))}{c_o}\right)\right\}$$

$$x_1 \to -\infty, \tag{4.7}$$

where $[t] = t + (x_1 - \ell')/c_o$ is the retarded time ($\ell' \approx 0.61 R_h$ being the 'end correction' of the hood entrance [15]). The velocity potential $\varphi^*(\mathbf{x})$ represents an irrotational, incompressible flow *out of*

10

the hood from $x_1 = -\infty$, normalized such that

$$\varphi^*(\mathbf{x}) \quad \sim \quad x_1 - \ell' \quad \text{when} \quad |x_1| \gg R_h \quad \text{within the hood,}$$

$$\sim \quad \frac{-\mathcal{A}_h}{4\pi|\mathbf{x}|} \quad \text{when} \quad |\mathbf{x}| \gg R_h \quad \text{outside the hood.} \tag{4.8}$$

Also,

$$\mathcal{R}_\mathrm{E} = -1, \quad \mathcal{R}_\mathrm{J} = \frac{\mathcal{A}_h - \mathcal{A}}{\mathcal{A}_h + \mathcal{A}}, \quad \mathcal{T}_\mathrm{J} = \frac{2\mathcal{A}_h}{\mathcal{A}_h + \mathcal{A}}. \tag{4.9}$$

$\mathcal{R}_\mathrm{E}$ is the reflection coefficient for long sound waves at the open end; $\mathcal{R}_\mathrm{J}$ is the reflection coefficient at the junction of the hood and uniform duct for reflection *back into* the hood; and $\mathcal{T}_\mathrm{J}$ is the transmission coefficient for transmission from the hood into the duct. Formula (4.7) is uniformly valid for source positions $\mathbf{y}$ lying within the hood and the neighborhood of its ends.
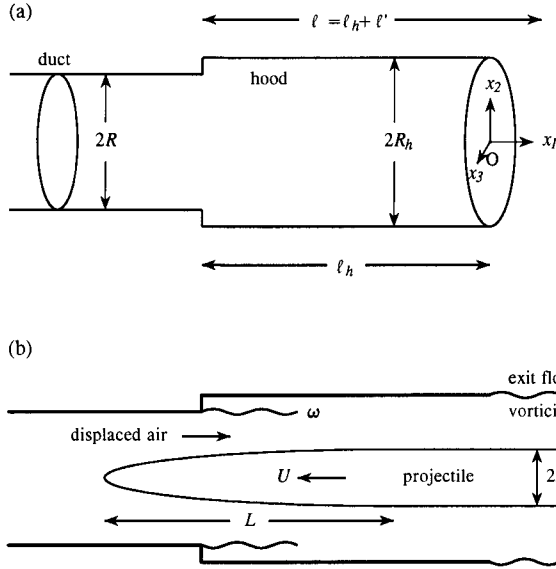

Figure 11

Figure 12

To understand the terms in the brace brackets of (4.7), consider the case where the source point $\mathbf{y}$ lies in the body of the hood. For $n = 0$ the first Heaviside function represents the front of the disturbance radiated into the duct; the second is the contribution from the wavefront that initially propagates towards the hood entrance, where it is reflected with reflection coefficient $\mathcal{R}_\mathrm{E} = -1$ and subsequently transmitted into the duct; the amplitude of each of these 'direct' waves is *increased* on transmission through the junction into the duct because the transmission coefficient $\mathcal{T}_\mathrm{J} > 1$. The terms in $n \geq 1$ represent contributions arriving at later times, after the transmission into the duct of those components of the direct waves that have suffered n reflections from both ends of the hood; the amplitude decreases by a factor $\mathcal{R}_\mathrm{J} < 1$ on each reflection back into the hood from the junction with the duct, so that the higher order modes rapidly decrease in amplitude.

The amplitude and profile of the sound wave radiated from the far end of the duct when the compression wave arrives is proportional to the compression wave pressure 'gradient' $\partial p/\partial t$
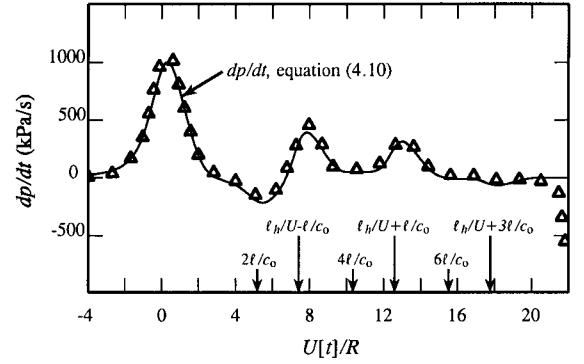
11

incident on the exit. The *linear theory* prediction of $\partial p/\partial t$ is given by the solution of (4.6) in terms of the Green's function (4.7). In a long duct it would also be necessary to account for nonlinear steepening of the compression wave; the solution of (4.6) should therefore be regarded as providing the *initial conditions* for such a nonlinear calculation.

The principal source of the compression wave is the monopole representing displacement of fluid by the nose of the projectile and a dipole generated by the drag produced by the pressure rise over the nose, both of which are accounted for by the first term on the right of (4.6) [14]. The vortex source represents secondary effects of separation on the body, on the duct walls, and in the shear layers of the 'exit' flows from the hood mouth and through the junction from the duct into the hood, of the fluid displaced by the entering projectile. The contribution from the monopole and dipole can be written

$$\frac{\partial p}{\partial t} = \frac{\rho_0 U^3}{(1 - M^2)} \left(1 + \frac{\mathcal{A}_o}{\mathcal{A}}\right) \iint_{-\infty}^{\infty} \frac{\partial \mathcal{A}_{\mathrm{T}}}{\partial y_1}(y_1 + U\tau)\frac{\partial^2 G}{\partial y_1^2}(\mathbf{x}, y_1, 0, 0; t - \tau)dy_1 d\tau. \tag{4.10}$$

Figure 12 illustrates a comparison of this solution with an experiment in air using a 7 m long horizontal, unflanged, circular cylindrical duct made of hard vinyl chloride, with inner radius $R = 5\,\mathrm{cm}$. An axisymmetric body is projected into the duct, guided by a 5 mm diameter taut steel wire extending along the duct axis. Pressure measurements are made using a wall-mounted transducer 1.5 m from the hood entrance. The hood consists of a circular cylindrical, vinyl chloride pipe of inner radius $R_h = 6.25\,\mathrm{cm}$; therefore $\mathcal{A}_h/\mathcal{A} \equiv R_h^2/R^2 = 1.5625$. A 10 cm collar at one end of the hood facilitates an airtight and smooth mating with the duct. When in place the hood has an overall length of 60.3 cm, and a 'working length' of $\ell_h = 50\,\mathrm{cm}$.

The projectile had an ellipsoidal nose profile obtained by rotating the curve $y = h\sqrt{(x/L)(2 - x/L)}$, $0 < x < L$ about the x-axis, so that

$$\frac{\mathcal{A}_T(x)}{\mathcal{A}_o} = \begin{cases} \frac{x}{L}\left(2 - \frac{x}{L}\right), & 0 < x < L, \\ 1, & x > L, \end{cases} \quad \text{where} \quad h = 2.235\,\mathrm{cm} \quad L = 11.18\,\mathrm{cm}, \tag{4.11}$$

and $\mathcal{A}_o = \pi h^2$. The model had overall length equal to 124.3 cm, and fore-aft symmetry with equal nose and tail profiles

The solid curve in Figure 12 is the prediction of equations (4.7), (4.10) for $U = 294\,\mathrm{kph}$ ($M = 0.24$), plotted as a function of the non-dimensional retarded time $U[t]/R$, where the nose of the projectile crosses the entrance plane of the hood at $t = 0$. The open triangles are observed values of the pressure gradient measured in the duct at a distance of 1.5 m from the entrance plane of the hood. The agreement between theory and experiment is excellent; the wavy nature of the pressure gradient profile is caused by interference between waves multiply reflected (temporarily trapped) within the hood before transmission into the duct. The theory based on (4.7) is seen to capture this interference perfectly.

12

REFERENCES

1. M. J. Lighthill 1952 On sound generated aerodynamically. Part I: General theory. *Proc. Roy. Soc. Lond.* **A211**, 564 - 587.

2. M. S. Howe 1975 Contributions to the theory of aerodynamic sound, with application to excess jet noise and the theory of the flute. *J. Fluid Mech.* **71**, 625 - 673.

3. M. S. Howe 1998 *Acoustics of Fluid-Structure Interactions*, Cambridge University Press.

4. L. D. Landau and E. M. Lifshitz 1987 *Fluid Mechanics* (Second edition). Oxford: Pergamon.

5. D. G. Crighton, A. P. Dowling, J. E. Ffowcs Williams, M. Heckl and F. G. Leppington 1992 *Modern Methods in Analytical Acoustics (Lecture Notes)*. Springer-Verlag: London.

6. M. S. Howe 2001 Edge-source acoustic Green's function for an airfoil of arbitrary chord, with application to trailing edge noise. *Q. J. Mech. and Appl. Math.* **54**, 139 - 155.

7. W. K. Blake 1986 *Mechanics of flow-induced sound and vibration*, Vol. 2: *Complex flow-structure interactions.* New York: Academic Press.

8. J. Gershfeld, W. K. Blake and C. W. Knisely 1988 *AIAA Paper* 88-3826-CP Trailing edge flow and aerodynamic sound.

9. W. K. Blake and J. L. Gershfeld 1989 in *Lecture Notes in Engineering* 46 (Ed. M. Gad-el-Hak). Frontiers in Experimental Fluid Mechanics: The aeroacoustics of trailing edges.

10. T. F. Brooks, D. S. Pope and M. A. Marcolini 1989 *National Aeronautics and Space Administration Reference Publication No. 1218.* Airfoil self-noise and prediction.

11. M. Wang 1997 *Annual Research Briefs* 37 - 49, (Center for Turbulence Research, Stanford University). Progress in large-eddy simulation of trailing-edge turbulence and aeroacoustics.

12. M. Wang 1998 *Annual Research Briefs* 91 -106, (Center for Turbulence Research, Stanford University). Computation of trailing-edge noise at low mach number using LES and acoustic analogy.

13. M. Wang and P. Moin 1999 Submitted to *AIAA J.* Computation of trailing-edge noise using large-eddy simulation.

14. M. S. Howe, M. Iida, T. Fukuda and T. Maeda 2000 Theoretical and experimental investigation of the compression wave generated by a train entering a tunnel with a flared portal *J. Fluid Mech.* **425**, 111 - 132.

15. Lord Rayleigh 1926 *The Theory of Sound*, Volume 2. London: Macmillan.

This page has been deliberately left blank

Page intentionnellement blanche

Prediction of Noise Radiated by a Non-Isothermal Mixing Layer Using a Low Mach Number Approximation

F. Golanski, V. Fortuné and E. Lamballais
Laboratoire d'Études Aérodynamiques
Bâtiment H
40, avenue du recteur Pineau
86022 POITIERS CEDEX, France

Abstract

The ability of an acoustic analogy to predict the sound radiated by a transitional mixing layer is evaluated by means of Direct Numerical Simulation results. The specific case of low Mach number flows with density variations is investigated. We consider the strategy where the acoustic source information is based on numerical results where the sound waves has been removed in order to limit the global computational cost of the prediction. It is shown that the low Mach number approximation coupled to the acoustic analogy can lead to very accurate predictions for the radiated sound if the acoustic sources in Lighthill's equation are taken into account carefully. The scaling laws of the acoustic intensity deduced from a repeated use of the Lighthill's analogy on a wide range of Mach numbers suggest a new interpretation about the experimental observations on the sound emission from hot and cold jets.

1 Introduction

A better control of the noise radiated by turbulence is required in many industrial applications. The improvement of sound prediction tools needs to study the sound generation and propagation, the main goal of the aeroacoustics. The far field sound can be predicted with the aid of a computer, with mainly two different numerical strategies. The first one consists in the explicit computation of the sound on a very large computational domain by solving the compressible Navier-Stokes equations in the context of the Direct Numerical Simulation (DNS). The direct access of the far acoustic field offered by this approach is clearly very attractive, but the direct sound calculation is still too expensive and problematic (boundary condition treatment) for turbulent flows in non-academic geometry. A second point is that for low Mach number applications, even for very simple flows, the computational cost is dramatically increased due to the numerical difficulties to consider simultaneously the turbulent fluctuations and the very fast and low amplitude acoustic phenomena. Hence, in our knowledge, no direct sound computation results using DNS at low Mach number are available in computational aeroacoustics except for very simple flow geometry [15, 7, 8]. An alternative method of far-field sound prediction is to use an acoustic analogy coupled to a near-field calculation (in the acoustic source zone) using DNS or Large Eddy Simulation (LES). In such an hybrid method, since simulation of the flow is necessary only in the region where the source terms are significant, the computational cost requirement is strongly decreased. The use of acoustic analogy in this context has been validated in previous studies [3, 7, 2, 15, 9, 8] by comparison between direct sound computation and its estimation by solving the Lighthill's equation. A crucial question in the use of acoustic analogy concerns the accuracy requirement for the acoustic source computation. Hence, a crude approximation of the acoustic sources can lead to wrong sound predictions. The more straightforward method to compute the near-field including acoustic sources is to solve directly the compressible Navier-Stokes equations at the Mach number of the flow under study. However, for low Mach number applications, even if the computational domain is limited to the active source region, such a compressible DNS/LES remains very expensive. In order to avoid this drawback, a second opportunity is to perform a DNS/LES based on governing equations where the sound waves are removed. The most common use is to consider the incompressible Navier-Stokes equations for isothermal flows, but an equivalent removal of sound waves can be obtained for non-isothermal applications in solving the low Mach number approximate
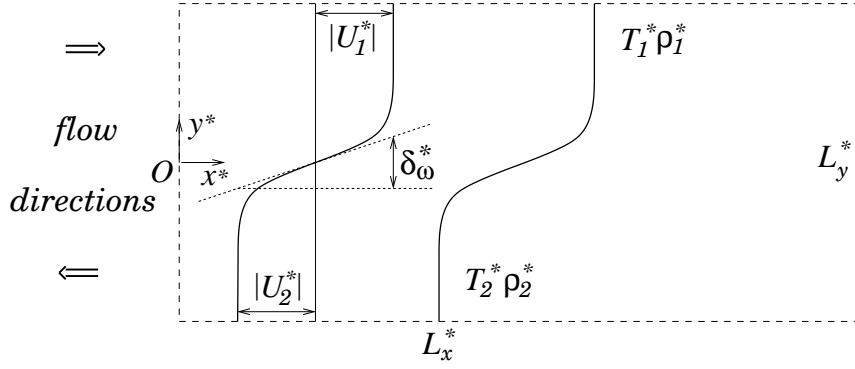
Figure 1: The temporal mixing layer flow configuration.

Navier-Stokes equations. Since the sound is removed from such DNS/LES results, it must be restored in the region of interest using the acoustic analogy. In this paper, we want to evaluate this strategy of sound removal/restoration in the context of a transitional non-isothermal flow. We first concentrate our attention on the acoustic source computation and their treatment in the acoustic analogy stage. Finally, scaling laws of acoustic intensity with the Mach number are discussed by varying the Mach number in the frame of the acoustic analogy.

2   Flow configuration

In this work, we consider the temporal development of a two-dimensional mixing layer between two streams of velocity, temperature and density noted respectively (U_1^*, T_1^*, ρ_1^*) and (U_2^*, T_2^*, ρ_2^*) in a rectangular domain of dimensions $L_x^* \times L_y^*$ (see figure 1 for more details about the flow and domain geometries). Note that throughout this paper, dimensional quantities are indicated by a superscript $*$. The flow is assumed to be periodic in the streamwise direction x^* while free-slip boundary conditions are imposed at $y^* = \pm L_y^*/2$. The initial pressure p^* is assumed to be constant. The initial mean velocity field is given by the following hyperbolic-tangent profile

$$\langle u^* \rangle (y^*) = \frac{U_1^* + U_2^*}{2} + \frac{U_1^* - U_2^*}{2} \tanh \left(\frac{2y^*}{\delta_\omega^*} \right) \tag{1}$$

where δ_ω^* is the initial vorticity thickness while the operator $\langle . \rangle$ indicates an average over the streamwise direction x^*. U_1^* and U_2^* are determined in order to verify the condition $U_c^* = 0$ where U_c^* is the convection velocity of the large scale structures [1] with

$$U_c^* = \frac{\sqrt{T_1^*} U_2^* + \sqrt{T_2^*} U_1^*}{\sqrt{T_1^*} + \sqrt{T_2^*}} \tag{2}$$

The initial temperature is deduced using the Crocco-Buseman relation

$$\begin{aligned}
T^*(y^*) &= \frac{1}{2c_p^*} \left[-\langle u^* \rangle^2 (y^*) - U_1^* U_2^* + \langle u^* \rangle (y^*)(U_1^* + U_2^*) \right] \\
&+ (T_1^* - T_2^*) \frac{\langle u^* \rangle (y^*)}{U_1^* - U_2^*} + \frac{T_2^* U_1^* - T_1^* U_2^*}{U_1^* - U_2^*}
\end{aligned} \tag{3}$$

In order to destabilize the flow, an incompressible disturbance field $(\tilde{u}^*, \tilde{v}^*)$ is added to the mean velocity. The vertical velocity perturbation is composed of a fundamental and two sub-harmonic disturbances such as

$$\tilde{v}^*(x^*, y^*) = A^* e^{-\sigma \left(\frac{y^*}{\delta_\omega^*} \right)^2} \left[\cos \left(\frac{8\pi}{L_x^*} x^* \right) + \frac{1}{8} \cos \left(\frac{4\pi}{L_x^*} x^* \right) + \frac{1}{16} \cos \left(\frac{2\pi}{L_x^*} x^* \right) \right] \tag{4}$$

with $A^* = 0.025 \, (U_1^* - U_2^*)$, and $\sigma = 0.05$. Since this set of initial conditions corresponds exactly to the one used in [7], a detailed comparison with one simulation referenced in this previous study will be given in the section 7.

3 Conservation laws

We consider a perfect gas flow governed by the following equations written in nondimensional form

$$\frac{\partial \rho}{\partial t} + \frac{\partial \rho u_i}{\partial x_i} = 0 \tag{5}$$

$$\frac{\partial \rho u_i}{\partial t} + \frac{\partial \rho u_i u_j}{\partial x_j} = -\frac{\partial p}{\partial x_i} + \frac{1}{Re}\frac{\partial \tau_{ij}}{\partial x_j} \tag{6}$$

$$\frac{\partial E}{\partial t} + \frac{\partial (p+E)u_j}{\partial x_j} = \frac{1}{Re}\frac{\partial u_i \tau_{ij}}{\partial x_j} + \frac{1}{M^2 RePr(\gamma - 1)}\frac{\partial^2 T}{\partial x_j^2} \tag{7}$$

$$p = \frac{\rho T}{\gamma M^2} \tag{8}$$

in a Cartesian coordinates $x_i = (x, y, z)$ where $u_i = (u, v, w)$ are the velocity components, p and ρ being respectively the pressure and density fields. All variables are nondimensionalized using δ_ω^* as reference length, $U_1^* - U_2^*$ as reference velocity, ρ_2^* as reference density and T_2^* as reference temperature. Here, $\gamma = c_p^*/c_v^*$ is the ratio of specific heats while the universal gas constant is noted $r^* = c_p^* + c_v^*$. The three fundamental nondimensional parameters are the Reynolds number $Re = \rho_2^*(U_1^* - U_2^*)\delta_\omega^*/\mu^*$, the Prandtl number $Pr = \mu^* c_p^*/k^*$ and the Mach number $M = (U_1^* - U_2^*)/\sqrt{\gamma r^* T_2^*}$, where both the dynamic viscosity μ^* and the thermal conductivity k^* are assumed to be constant. The viscous stress tensor is given by

$$\tau_{ij} = \frac{\partial u_i}{\partial x_j} + \frac{\partial u_j}{\partial x_i} - \frac{2}{3}\frac{\partial u_k}{\partial x_k}\delta_{ij} \tag{9}$$

while the total energy per unit volume is expressed by

$$E = \frac{p}{\gamma - 1} + \frac{1}{2}\rho\, u_i u_i. \tag{10}$$

These equations, usually refereed as the compressible Navier-Stokes equations, allow to describe the motion of a perfect gas in a wide range of Mach numbers by considering simultaneously the vortical, entropic and acoustic motions and their eventual coupling.

4 Low Mach number approximation

In many applications, the flow occurs at low speeds. If the fluid velocity is everywhere small compared to the sound speed, it can be clearly an advantage to exploit this feature in order to derive a set of equations easier to solve numerically. The main gain of such approach concerns the computational cost which can be strongly decreased in assuming that the Mach number M is low. More precisely, when the full compressible Navier-Stokes equations are considered, the presence of acoustic waves in the flow impose the use of very small time steps due to the numerical stability of explicit method through the CFL condition. Hence, if the same physical domain and spatial resolution are used, the computational cost of a compressible DNS is in first approximation proportional to M^{-1}. For very low Mach number flows, such a scaling of the computational cost is clearly a drawback, while being mainly conditioned by acoustic phenomena of negligible effects on the flow dynamics. In order to avoid this limitation, it is then very attractive to consider a simplified problem where the acoustic modes are decoupled from the vorticity and entropy modes. The set of equations governing the vorticity and entropy modes can be established by applying a low Mach number approximation to equations (5)−(8). Formally, these simplified equations are derived in introducing a small parameter

$$\varepsilon = \gamma M^2 \tag{11}$$

which is used to expand ρ, u_i and T as

$$\rho = \rho^{(0)} + \varepsilon \rho^{(1)} + \dots \tag{12}$$

$$u_i = u_i^{(0)} + \varepsilon u_i^{(1)} + \dots \tag{13}$$

$$T = T^{(0)} + \varepsilon T^{(1)} + \dots \tag{14}$$

while the state law (8) impose an expansion for p such as

$$p = \frac{p^{(0)}}{\varepsilon} + p^{(1)} + \dots \tag{15}$$

Note that in (15), $p^{(0)}$ and $p^{(1)}$ can be interpreted as nondimensional pressures using respectively $\rho_2^* r^* T_2^*$ and $\rho_2^*(U_2^* - U_1^*)$, so that $p^{(0)}$ is currently called the thermodynamic pressure while $p^{(1)}$ is refereed as the dynamic pressure. Substituting the expansions (12)−(15) into equations (5)−(8) leads to the following system at the lowest order in ε (see [14, 4] for more details)

$$\frac{\partial \rho^{(0)}}{\partial t} + \frac{\partial \rho^{(0)} u_i^{(0)}}{\partial x_i} = 0 \tag{16}$$

$$\frac{\partial p^{(0)}}{\partial x_i} = 0 \tag{17}$$

$$\rho^{(0)} \frac{\partial u_j^{(0)}}{\partial x_j} = \frac{1}{RePrT^{(0)}} \frac{\partial^2 T^{(0)}}{\partial x_j^2} \tag{18}$$

$$p^{(0)} = \rho^{(0)} T^{(0)} \tag{19}$$

Since we consider here an open physical domain, the spatially uniform thermodynamic pressure $p^{(0)}$ is also assumed to be constant in time and fixed to its value at the boundaries $y = \pm L_y/2$ with $p^{(0)} = 1$. In order to close the problem, an additional equation describing the velocity field $u_i^{(0)}$ must be obtained by considering the equation (6) at the zero-order in ε which yields the equation

$$\frac{\partial \rho^{(0)} u_i^{(0)}}{\partial t} + \frac{\partial \rho^{(0)} u_i^{(0)} u_j^{(0)}}{x_j} = -\frac{\partial p^{(1)}}{\partial x_i} + \frac{\partial \tau_{ij}^{(0)}}{\partial x_j} \tag{20}$$

The equations (16), (18), (19) and (20) form a closed system corresponding to a simplification of the Navier-Stokes equations in the frame of the low Mach number approximation. It is important to emphasize that these equations are only asymptotically valid for vanishing Mach number flows, but without any hypothesis about the density variations in space or during the time. Naturally, the assumption $\rho^{(0)} = $ const leads to the conventional incompressible Navier-Stokes equations

$$\frac{\partial u_i^{(0)}}{\partial t} + \frac{\partial u_i^{(0)} u_j^{(0)}}{\partial x_j} = -\frac{\partial P}{\partial x_i} + \frac{1}{Re} \frac{\partial^2 u_i^{(0)}}{\partial x_i^2} \tag{21}$$

$$\frac{\partial u_i^{(0)}}{\partial x_i} = 0 \tag{22}$$

with $P = p^{(1)}/\rho^{(0)}$. An important feature of the low Mach number approximation is that acoustic waves are removed from the derived equations [14]. Hence, this approximation can be viewed as an acoustic filtering procedure which is intrinsic to the derived equations. For low Mach number applications, such a removal of sound waves preserves the flow dynamics in allowing the use of large time step in simulations. In exchange, the ability offered by compressible Navier-Stokes equations to give directly acoustic predictions is loss.

5 Acoustic analogy

5.1 Lighthill's equation

Starting with the equations (5) and (6), the Lighthill's approach [13] consists in deriving a simplified wave equation for ρ such as

$$\frac{\partial^2 \rho}{\partial t^2} - c_\infty^2 \frac{\partial^2 \rho}{\partial x_i^2} = \frac{\partial^2 T_{ij}}{\partial x_i \partial x_j} \tag{23}$$

where the Lighthill's tensor

$$T_{ij} = \underbrace{\rho u_i u_j}_{\text{term 1}} + \underbrace{\left(p - c_\infty^2 \rho\right) \delta_{ij}}_{\text{term 2}} - \underbrace{\frac{1}{Re} \tau_{ij}}_{\text{term 3}} \tag{24}$$

is decomposed here into three terms which are interpreted as the "sources" of the sound waves. The value of c_∞ is the expected nondimensional sound speed in the region where the acoustic waves are considered. Assuming that the source terms are known, the resolution of equation (23) yields a prediction of the acoustic waves corresponding to a given distribution of T_{ij}. Moreover, due to the simplicity of the propagation operator in the left hand side of equation (23), the solution can be expressed analytically with the aid of the Green function formalism. Note that such an approach, refereed as the acoustic analogy, can give reliable information about the sound only in the regions where $T_{ij} \approx 0$, typically in the far acoustic field zone (see [13] for more details).

5.2 Source term treatment

The treatment of the source terms is the key element in the quality of the sound prediction given by the acoustic analogy. For free shear flows, the viscous term 3 can be neglected, even for the low Reynolds number cases considered here [8]. Consequently, this term will no longer be considered in this paper. The term 2 is also frequently omitted by invoking a compensating effect between the pressure and density fluctuations leading to a quasi-constant value for $p - c_\infty^2 \rho$. In fact, such a behaviour can be justified only for isothermal flows where the effects of heat conduction are negligible. More precisely, this last assumption implies that the flow evolution is isentropic with

$$\frac{d\rho}{dt} = \frac{1}{c^2} \frac{dp}{dt} \tag{25}$$

where c is a nondimensional local sound speed with $c^2 = T/M^2$. If in addition the flow evolution is quasi-isothermal, it is reasonable to assume that $c \approx c_\infty$ in the isentropic relation (25) which takes then the simplified form

$$\frac{d}{dt}\left(p - c_\infty^2 \rho\right) \approx 0 \tag{26}$$

Assuming that pressure and temperature fields are simultaneously uniform at one instant, it can be deduced from this last equation that the relation $p - c_\infty^2 \rho \approx \text{const}$ is verified at each time everywhere in the flow. Consequently, in previous works using acoustic analogy, the attention was concentrated mainly on the term 1 assumed to be the dominant contribution in T_{ij}. Naturally, the assumption $c \approx c_\infty$ is not valid in a non-isothermal case and term 2 can no longer be omitted. In a previous work [8], the importance of this term was demonstrated for a non-isothermal flow by analysing DNS results including the direct computation of sound. In the same study, the very small effects of the term 2 on sound emission were also confirmed for an isothermal flow in agreement with the considerations mentioned above.

5.3 Lighthill's equation and low Mach number approximation

In this work, we are interested in the use of an acoustic analogy for low Mach number flows. For isothermal flows, the common use is to determine T_{ij} from an incompressible DNS solving the equations (21),(22) by considering only the term 1 in (24) with $T_{ij} \approx \rho^{(0)} u_i^{(0)} u_j^{(0)}$. The knowledge of T_{ij} allows then to solve in a second step the equation (23) by choosing a relevant value for c_∞. The natural choice is $c_\infty = \sqrt{T/M^2}$ where T and M are respectively the nondimensional temperature and Mach number corresponding to the flow that is under study. In this work, we propose to generalize such an approach to the case of non-isothermal flows (with large density variations) by using the formalism of the low Mach number approximation. For such a purpose, it is worth to substitute the expansions $(12)-(15)$ into the definition (24) in order to evaluate a priori the contribution of each flow variable to the lowest orders in ε. Before doing this, it is important to express the value of c_∞ as a function of the flow parameters with

$$c_\infty^2 = \frac{T_\infty}{M^2} \tag{27}$$

$$= \frac{\gamma T_\infty}{\varepsilon} \tag{28}$$

where T_∞ is the nondimensional constant temperature where the sound is predicted. Thus, the expansion of T_{ij} truncated to zero-order in ε yields the following expression

$$T_{ij} = \underbrace{\rho^{(0)} u_i^{(0)} u_j^{(0)}}_{\text{term 1}} + \underbrace{\underbrace{\frac{1}{\varepsilon} \left(p^{(0)} - \gamma T_\infty \rho^{(0)} \right) \delta_{ij}}_{\text{term 2a}} + \underbrace{\left(p^{(1)} - \gamma T_\infty \rho^{(1)} \right) \delta_{ij}}_{\text{term 2b}}}_{\text{term 2}} + \dots \tag{29}$$

This relation suggests clearly how results obtained in the frame of the low Mach number approximation must be used in order to estimate T_{ij}. Thus, it can be observed that only the terms 1 and 2a can be deduced from such results due to the presence of $\rho^{(1)}$ in term 2b which is not considered in equations (16),(18),(19) and (20). The non-isothermal character of the flow can however be partially taken into account through the inhomogeneities of $\rho^{(0)}$ in term 2a. An important remark is that the term 2a is the lowest order term in ε. Consequently, it can be expected that this term become dominant for very low Mach number flows even if the density variations $\rho^{(0)}$ are moderate. The contribution of the terms 2a and 2b can be studied *a priori* by considering the relation (25) at the two lowest orders in ε. Thus, it is easy to show that isentropic condition implies

$$\frac{d\rho^{(0)}}{dt} = 0 \tag{30}$$

for the terms in ε^{-1} and

$$\frac{d}{dt} \left(p^{(1)} - \gamma T^{(0)} \rho^{(1)} \right) = 0 \tag{31}$$

at zero-order. In the isothermal case where $\rho^{(0)}$ and $T^{(0)}$ are strictly constant (contrary to the compressible variables ρ and T which conserve small variations), the term 2a automatically vanishes while the condition (31) with $T^{(0)} = T_\infty$ shows that the term 2b is conserved following the motion. All these points will be discussed using the results presented in the next sections.

To summarize, the present strategy of acoustic prediction in the frame of low Mach number approximation consists first in the resolution of equations (16), (18), (19) and (20) by assuming $\varepsilon \to 0$ followed by the application of acoustic analogy by considering a finite value for ε in equations (28), (23) and (29), ε being fixed in regards to the real Mach number of the application. Naturally, the validity range of ε has an upper limit which is conditioned by the quality of the assumption that compressibility effects on the real flow dynamics can be neglected.

5.4 Formulation of Lighthill's equation in temporal configuration

The present use of a periodic condition in the streamwise direction allows to consider a simplified flow configuration where the far acoustic field is easily accessible. Hence, due to the unlimited extent of the acoustic source in the x-direction, there is no far field in this direction and the acoustic wave propagation occurs mainly in the y-direction. More precisely, using the average operator $\langle . \rangle = (1/L_x) \int_0^{L_x} (.) dx$, it is possible to show that outside the active region of the flow, the mean part $\langle \phi \rangle$ of any flow variable ϕ travels with the local speed of sound c_∞ as a non-decaying plane wave, formally

$$\langle \phi \rangle = \langle \phi \rangle (y - c_\infty t), \tag{32}$$

while the disturbance $\phi' = \langle \phi \rangle - \phi$ suffers a $1/\sqrt{y}$ decay [11]. Note that the relation (32) can be verified even if the disturbance ϕ' is not negligible. Consequently, it can be stated that the far acoustic field is only composed of plane acoustic waves which are accessible by considering the mean quantities $\langle \phi \rangle$ at a distance $|y|$ from the shear zone where the condition (32) is verified. In practice, previous works [11, 7] have shown that this critical distance is moderate. For the present study, the mean acoustic quantities are predicted at the location $y = -30$, at a distance from the mixing layer center which is considered to be large enough to verify the condition (32) and consequently to have access to the far-field data.

Denoting the acoustic density as the density deviation from its ambient value in the prediction region, it is easy to express a specific formulation of Lighthill's equation verified by the corresponding mean quantity $\langle \rho - \rho_\infty \rangle$

$$\frac{\partial^2}{\partial t^2} \langle \rho - \rho_\infty \rangle - c_\infty^2 \frac{\partial^2}{\partial y^2} \langle \rho - \rho_\infty \rangle = \frac{\partial^2}{\partial y^2} \langle T_{yy} \rangle \tag{33}$$

with

$$\langle T_{yy}\rangle = \underbrace{\langle \rho v^2\rangle}_{\langle T_{yy}\rangle_1} + \underbrace{\langle p - c_\infty^2 \rho\rangle}_{\langle T_{yy}\rangle_2} \tag{34}$$

where the viscous term is omitted for clarity. In this paper, we will consider only this simplified form of the Lighthill's equation where only the knowledge of contributions on mean Lighthill's tensor component $\langle T_{yy}\rangle$ is required. Using the Green's function formalism and after some analytical developments [6], the solution to equation (33) can be written as

$$\langle \rho - \rho_\infty\rangle(y,t) = \underbrace{\frac{1}{2c_\infty^2}\int_{-\infty}^{+\infty}\frac{\partial}{\partial y'}\langle T_{yy}\rangle_1\left(y',t-\frac{|y-y'|}{c_\infty}\right)dy'}_{\langle \rho - \rho_\infty\rangle_1}$$

$$+ \underbrace{\frac{1}{2c_\infty^2}\int_{-\infty}^{+\infty}\frac{\partial}{\partial y'}\langle T_{yy}\rangle_2\left(y',t-\frac{|y-y'|}{c_\infty}\right)dy' + \frac{1}{2}(\rho_1+\rho_2)-\rho_\infty}_{\langle \rho - \rho_\infty\rangle_2} \tag{35}$$

where $\langle \rho - \rho_\infty\rangle_1$ and $\langle \rho - \rho_\infty\rangle_2$ are the contributions of the source terms $\langle T_{yy}\rangle_1$ and $\langle T_{yy}\rangle_2$ on the solution. The constant factor $\frac{1}{2}(\rho_1+\rho_2)-\rho_\infty$ in (35) is due to boundary terms at $y=\pm\infty$ associated to mean density gradient across the mixing layer (see [6] for more details). By convention, this factor is included in $\langle \rho - \rho_\infty\rangle_2$ in order to bring together the specific non-isothermal contributions. Finally, note that the spatial integration required in the solution (35) was numerically performed in this study by neglecting the contribution of the source terms outside of the y-range of the computational domain $[-L_y/2, +L_y/2]$.

6 Numerical methodology

The evolution equations numerically solved are

$$\frac{\partial \rho^{(0)}}{\partial t} = F_\rho \tag{36}$$

$$\frac{\partial \rho^{(0)}u_i^{(0)}}{\partial t} = -\frac{\partial p^{(1)}}{\partial x_i} + F_{u_i} \tag{37}$$

with

$$F_\rho = -u_j^{(0)}\frac{\partial \rho^{(0)}}{\partial x_j} - \frac{1}{RePrT^{(0)}}\frac{\partial^2 T^{(0)}}{\partial x_j^2} \tag{38}$$

$$F_{u_i} = \frac{\partial}{\partial x_j}\left(\tau_{ij}^{(0)} - \rho^{(0)}u_i^{(0)}u_j^{(0)}\right) \tag{39}$$

Note that in this work, following the technique proposed by [14], we solve a specific form of the density equation (36) which is a combination of the equations (16) and (19). The equations (36) and (37) are integrated in time using a Runge-Kutta scheme except for the pressure term in (37) which requires a specific treatment. More precisely, the discrete integration of these equations on a sub-time step from t_k to t_{k+1} gives

$$\frac{\left(\rho^{(0)}\right)^{k+1}-\left(\rho^{(0)}\right)^k}{\Delta t} = \alpha_k F_\rho^k + \beta_k F_\rho^{k-1} \tag{40}$$

$$\frac{\left(\rho^{(0)}u_i^{(0)}\right)^{k+1}-\left(\rho^{(0)}u_i^{(0)}\right)^k}{\Delta t} = -\frac{\partial \tilde{p}^{(1)}}{\partial x_i} + \alpha_k F_{u_i}^k + \beta_k F_{u_i}^{k-1} \tag{41}$$

with

$$\tilde{p}^{(1)} = \frac{1}{\Delta t}\int_{t_k}^{t_{k+1}} p^{(1)}dt \tag{42}$$

7

The present Runge-Kutta scheme having four sub-time step, we have $k = 1, 2, 3, 4$ with $t_1 = t_n$ and $t_5 = t_{n+1}$, $\Delta t = t_{n+1} - t_n$ being the full time step. The coefficients α_k and β_k are chosen to satisfy a fourth-order accuracy in time. Since $\tilde{p}^{(1)}$ is not known *a priori*, the equation (41) is fractioned into two steps

$$\frac{\left(\rho^{(0)} u_i^{(0)}\right)^\star - \left(\rho^{(0)} u_i^{(0)}\right)^k}{\Delta t} = \alpha_k F_{u_i}^k + \beta_k F_{u_i}^{k-1} \tag{43}$$

$$\frac{\left(\rho^{(0)} u_i^{(0)}\right)^{k+1} - \left(\rho^{(0)} u_i^{(0)}\right)^\star}{\Delta t} = -\frac{\partial \tilde{p}^{(1)}}{\partial x_i} \tag{44}$$

Taking the divergence of (44) and using the continuity equation (16), we can obtain a Poisson equation for $\tilde{p}^{(1)}$

$$\frac{\partial^2 \tilde{p}^{(1)}}{\partial x_i \partial x_i} = \frac{1}{\Delta t} \left(\frac{\partial}{\partial x_i} \left(\rho^{(0)} u_i^{(0)}\right)^\star - \frac{\partial}{\partial x_i} \left(\rho^{(0)} u_i^{(0)}\right)^{k+1} \right) \tag{45}$$

$$= \frac{1}{\Delta t} \left(\frac{\partial}{\partial x_i} \left(\rho^{(0)} u_i^{(0)}\right)^\star + \left(\frac{\partial \rho^{(0)}}{\partial t}\right)^{k+1} \right) \tag{46}$$

The computation of the density time derivative on the right hand side of the equation (46) can be performed using various explicit or implicit approximations [4]. In preliminary calculations, we tested several low- and high-order temporal schemes and we found that the somewhat crude approximation deduced from equation (36)

$$\left(\frac{\partial \rho^{(0)}}{\partial t}\right)^{k+1} = F_\rho^k + O(\Delta t) \tag{47}$$

is the more stable one, allowing the use of large time step while giving reliable results (see following sections).

For spatial discretization, all the spatial derivatives in equations (38),(39) and (46) are computed with the aid of centered compact finite difference schemes of sixth-order accuracy [10]. The computational grid is regular in a non-staggered configuration.

7 Results

7.1 Simulation parameters

The size of the computational domain $(L_x, L_y) = (30.7, 60)$, the ratio of densities $\rho_2/\rho_1 = 2$ and the fundamental parameters ($Re = 400$, $Pr = 0.75$) correspond exactly to a computational configuration referenced in the compressible study [7], as well as the number of grid points in the x-direction with $n_x = 256$. Contrary to this previous work, we do not use here a stretched grid in the y-direction. Since we want to ensure a comparable precision of present results with respect to the data of [7], the resolution in the y-direction was chosen in order to correspond to the resolution used in [7] near $y = 0$ (where the concentration of grid points is maximal) with $\Delta y = 0.12$ which leads to the choice $n_y = 501$. Finally, note that the isothermal case was also considered but will not be presented in details in this paper because all conclusions given in the following about the agreement between present results and previous data of [7] are preserved when $\rho_2/\rho_1 = 1$. Isothermal results will only be shortly considered in the section 7.4 in order to distinguish the isothermal and non-isothermal acoustic emission in terms of scaling laws.

7.2 Instantaneous field analysis

The validity of an acoustic prediction in the frame of low Mach number approximation is naturally conditioned by the validity of the assumption that compressibility effects are negligible on the flow dynamics. In order to verify this hypothesis, visualizations of vorticity and density fields are shown on figures (2) and (3) where present data $\omega_z^{(0)}$ and $\rho^{(0)}$ are compared with their compressible counterpart

ω_z and ρ obtained by [7] at $M = 0.2$. Only the near fields are presented, in the region where source terms are *a priori* significant. The five instants presented allow to observe the formation of four Kelvin-Helmoltz vortices ($t = 24$) followed by two successive pairings ($t = 64$ and $t = 152$). This sequence of transition events is in qualitative agreement with previous DNS results [12]. The remarkable agreement obtained at each time between present results and the compressible data of [7] can be considered as a convincing validation of the numerical methodology used here. It confirms also that at least up to $M = 0.2$, the compressibility do not play a significant part in the flow evolution. Note that the generation of counter-rotating vorticity, an important feature of the transition mechanisms in non-isothermal mixing layers, is very well recovered here, confirming the ability of our numerical code to describe accurately the variable density effects. Since the near fields seem to be well computed, it is reasonable to hope that present data can be used to deduce the correct source terms leading to an accurate prediction of sound. This question will be addressed in the next section.
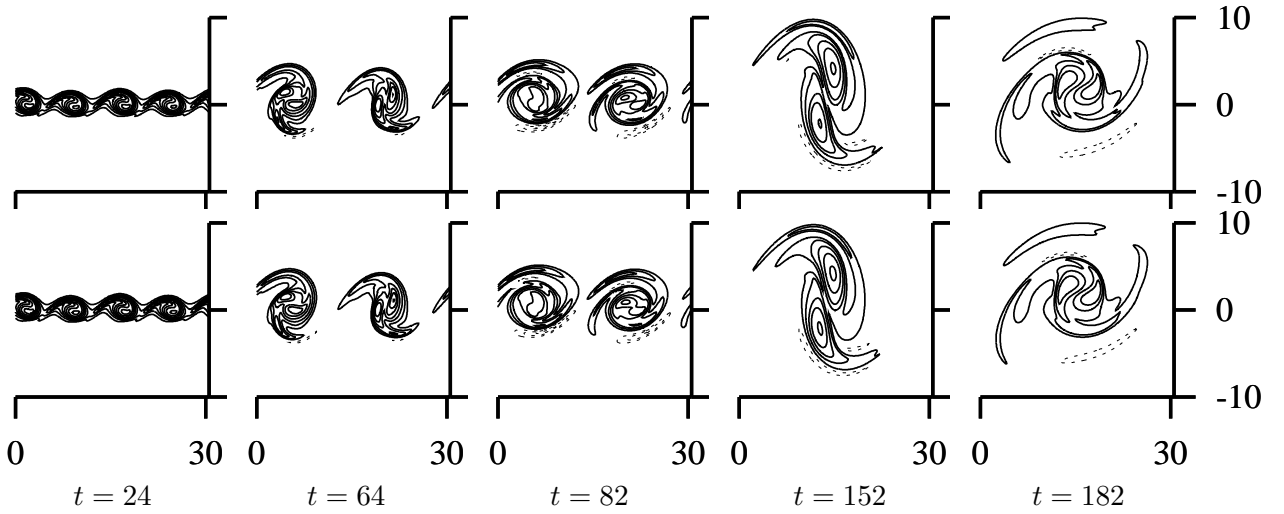
Figure 2: Comparison of vorticity isocontours obtained from present low Mach number approximate DNS ($\omega_z^{(0)}$, bottom) and from a compressible DNS of [7] at $M = 0.2$ (ω_z, top). The contour lines are plotted at intervals of ± 0.01, the dashed lines indicate positive contours (counter-rotating vorticity).
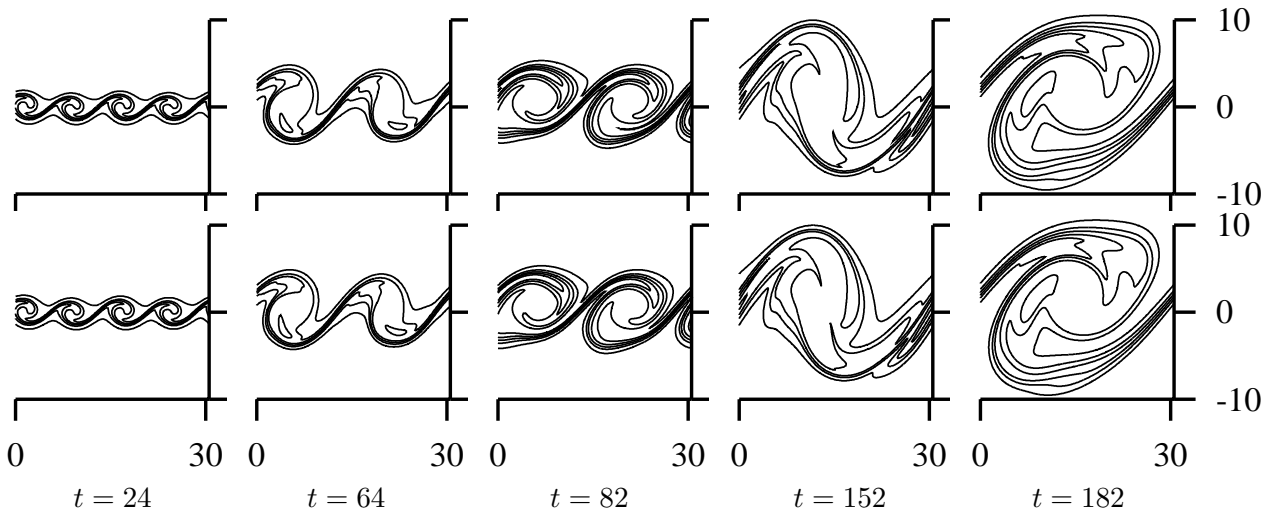
Figure 3: Comparison of density isocontours obtained from present low Mach number approximate DNS ($\rho(0)$, bottom) and from a compressible DNS of [7] at $M = 0.2$ (ρ, top). The contour lines are plotted at intervals of 0.1 from 0.5 to 1.

7.3 Source term analysis

Using the Lighthill's analogy in its temporal formulation for a similar mixing layer, a remarkable agreement was found by [7] between the direct computed sound and its estimation from the solution (35). However, it was emphasized in this study that such an agreement was possible in non-isothermal cases only when the temperature inhomogeneities were taken into account accurately in the two source terms $\langle T_{yy} \rangle_1$ and $\langle T_{yy} \rangle_2$ in (35). Note that since these previous results are fully compressible, the determination of the Lighthill's tensor was obvious. For present results, the compressible component of the motion being not computed, the situation is more delicate. Hence, it is clear that a simple substitution of ρ by $\rho^{(0)}$, u_i by $u_i^{(0)}$ and p by $p^{(1)}$ in the definition (24) of T_{ij} do not lead to a relevant prediction of sound. This point has already been mentioned in the section 5.3 where the development (29) of T_{ij} in ε shows that for the term 2, at zero-order in ε, $p^{(1)}$ is linked to $\rho^{(1)}$ instead of $\rho^{(0)}$, the contribution of $\rho^{(0)}$ being "amplified" by a factor $1/\varepsilon$ compared to the other contributions.

Since $\rho^{(1)}$ is not computed in present low Mach number approximate DNS, we propose here to neglect the term 2b in the approximation (29) of T_{ij}. Note that this assumption can not be justified using a simple argument about the low value of the Mach number because the order in ε of term 2b is the same than for the term 1. The solution obtained from (35) using this assumption is however shown on figure 4 where the time evolution of the mean acoustic density $\langle \rho - \rho_2 \rangle$ at $y = -L_y/2$ is plotted. At this location, the ambient quantities are $\rho_\infty = \rho_2$, $c_\infty = c_2$ and $T_\infty = T_2$. The time scale is shifted by $t_d = t - L_y/(2c_2)$, this correction corresponding to the time necessary for a wave to travel from $y = 0$ to $y = -L_y/2$ at the local sound speed $c_2 = \sqrt{T_2}/M$. On the same figure, the separated contributions of term 1 and term 2 are shown as well. The corresponding estimations of $\langle \rho - \rho_2 \rangle$ using the fully compressible data already performed by [7] at $M = 0.2$ are also given for comparison. Physically, the time variation of the acoustic density $\langle \rho - \rho_2 \rangle$ is due to the sound emission from the shear layer. More precisely, it has been shown by [7] that mainly three acoustic waves are generated during the transition of a 2D temporal mixing layer, each sound emission being consecutively generated by the roll-up and the two successive pairings of the large scale structures. It was also found by the same authors that the second pairing was the noisiest event of the transition in the 2D case. Despite the present approximations on T_{ij}, it is worth to observe that a good agreement is found between the present prediction of acoustic data and their compressible counterpart of [7]. Small though it is, the main difference between these data concerns the term 2. This behaviour is probably related to the lack of the term 2b in the Lighthill's tensor T_{ij} but could also be attributed to a weak Mach number effect on the flow dynamics (to our knowledge, no compressible data about this flow are available for $M < 0.2$). As a first conclusion, we consider here that the low Mach number approximation coupled to the Lighthill's analogy can give a good prediction of the sound radiated by the present non-isothermal flow with a computational cost considerably reduced compared to the fully compressible case. It is interesting to note that when compressible data are used as source terms, the acoustic analogy prediction is valid only for the Mach number considered in the DNS. A prediction at a different Mach number needs to perform again the simulation even if the change of Mach number has very weak effects on the dynamics. The advantage of the low Mach number approximation is that only one simulation is necessary to compute the source terms from which it is possible to deduce acoustic predictions for various Mach numbers. This attractive feature will be exploited in the next section in order to establish numerically the scaling laws followed by the acoustic wave intensities.

7.4 Scaling laws deduced from acoustic analogy

A common method to evaluate the sound level is to consider the acoustic intensity I_{ac} at a given location in the far-field region. In present temporal configuration, this quantity corresponds to the product of the mean acoustic velocity and pressure $I_{ac} = \langle p - p_2 \rangle \langle v \rangle$ evaluated at $y = -L_y/2$. In the acoustic far field, using the assumption that the plane wave propagation in the y-direction is well described by the linearized Euler equations, it is easy to show that the temporal variation of I_{ac} is directly related to the temporal variation of the acoustic density $\langle \rho - \rho_2 \rangle$ with $I_{ac} = -c_2^3 \langle \rho - \rho_2 \rangle^2 / \rho_2$. Note that this relation, very well verified by [7, 6], allows to deduce I_{ac} from the only knowledge of $\langle \rho - \rho_2 \rangle$. In order to study the dependance of I_{ac} with the Mach number, it is interesting to perform an acoustic analogy for a wide range of Mach numbers using the same source terms deduced from the
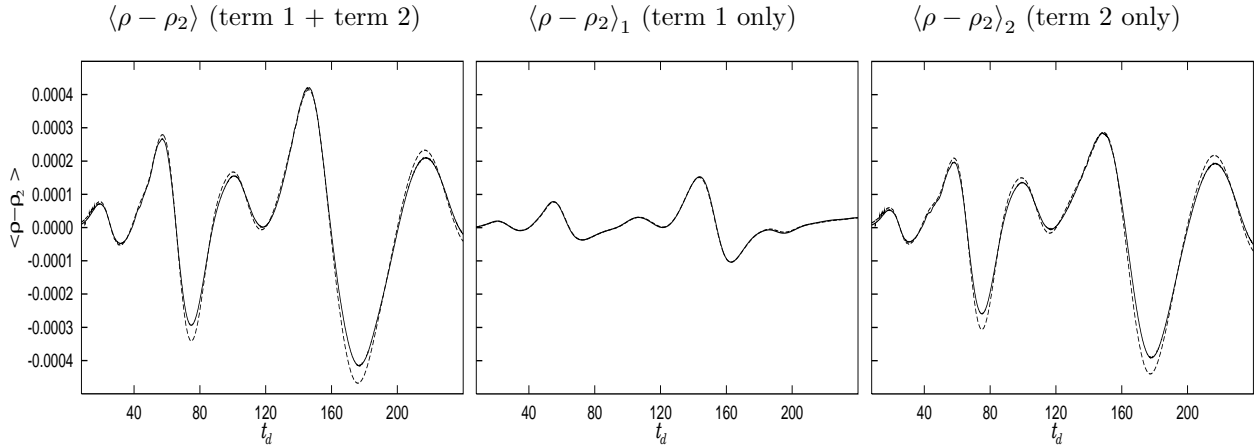
Figure 4: Time evolution of the acoustic density predicted from acoustic analogy applied to compressible DNS results [8] (- - - - -) and to present Mach number approximate results (——).

simulation presented previously. This procedure has been followed in solving 41 times the equation (33) for Mach numbers reparted on the interval $[0.0001, 0.75]$ with a logarithmic distribution. For each given Mach number, the maximum of $|I_{ac}|$ has been determined from the time history of I_{ac} and reported to a diagram $(|I_{ac}|_{\max}, M)$ which is presented on figure 5. The corresponding data deduced from the direct computation of [7] at three different Mach numbers are also given for comparison. Note that for this figure, the acoustic intensity data are nondimensionalized using the local quantities ρ_2 and c_2 (instead of $U_1 - U_2$) in accordance with the common use. Naturally, the excellent agreement of present acoustic predictions with the data of [7] can be observed again on this figure where the isothermal case is also presented. For this last case where $\rho_2/\rho_1 = 1$, the scaling of the maximum acoustic intensity is very well defined over the total range of the Mach number considered with $|I_{ac}|_{\max} \propto \rho_2 c_2^3 M^6$. A simple dimensional analysis of the solution (35), assuming the far field relation $\partial/\partial y \approx (1/c_2)\partial/\partial t$ and $T_{ij} = \rho^{(0)} u_i^{(0)} u_j^{(0)}$ allows to find easily this scaling without the accurate computation of the exact source term 1.

In the non-isothermal case, the situation is clearly less simple. Since the balance between the terms 1 and 2a depends on the Mach number, a dimensional analysis can not lead to a single exponent for the scaling of the acoustic intensity. This view is confirmed by the observation of the figure 5 where the acoustic intensity for $\rho_2/\rho_1 = 2$ shows a more sophisticated scaling. For very low Mach numbers, the scaling exponent of the acoustic intensity with the Mach number is around 2. Such a behaviour can be predicted *a priori* in assuming that the Lighthill's tensor can be approximated by $T_{ij} \approx (1/\varepsilon)(p^{(0)} - \gamma T_\infty \rho^{(0)})\delta_{ij}$ which leads to $|I_{ac}|_{\max} \propto \rho_2 c_2^3 M^2$. Naturally, the approximation of T_{ij} is valid only if $\varepsilon \ll 1$, that is for very low Mach number. For $M > 0.05$, the explicit solving of (33) shows a clear change in the scaling of I_{ac}, with the approximate scaling law $|I_{ac}|_{\max} \propto \rho_2 c_2^3 M^4$ in the range $0.02 < M < 0.2$. For $M > 0.2$, a new change of scaling occurs, but no well defined power law can be identified. Note that for $M > 0.5$, the compressible effects on the flow dynamics become nonnegligible, and present acoustic predictions can not be considered as physically valid. Nevertheless, acoustic results are considered here up to $M = 0.75$ in order to better identify the change in the scaling of I_{ac}.

A last comment about the figure 5 concerns the comparison between the isothermal and nonisothermal cases. It is interesting to note that the two different scalings of I_{ac} in isothermal and non-isothermal cases can give a qualitative interpretation of the experimental observations on the sound emissions from cold and hot jets [5]. Hence, for low Mach number, the source of the sound can be essentially attributed to the term 2 and consequently the non-isothermal case is clearly the noisiest one, in agreement with experimental trends for hot and cold jets. However, due to the large value of the scaling exponent in the isothermal case, the increase of the Mach number can lead to a situation where the sound level is stronger in the isothermal case. In cold and hot jet experiments, such an inversion was found to occur around the critical value $M \approx 0.7$. In present results, the corresponding critical value is $M \approx 0.6$, which is outside of the validity range of Mach numbers. Despite this reservation, it is
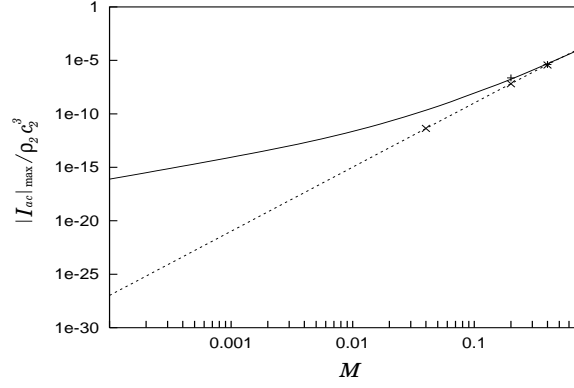
Figure 5: Maximum acoustic intensity versus the Mach number M. Isothermal case $\rho_2/\rho_1 = 1$: present results - - - -, direct computed results of [7] $\times$. Non-isothermal case $\rho_2/\rho_1 = 2$: present results ——, direct computed results of [7] $+$.

worth to observe that this inversion, resulting from a combination between the temperature and Mach number effects, can be understood without the presence of any compressible effects on turbulence, the compressibility being totally missing in present acoustic sources.

References

[1] D. W. Bogdanoff. Compressibility effects in turbulent shear layers. *AIAA Journal*, **21(6)**:926–927, 1983.

[2] T. Colonius and J. B. Freund. Application of Lighthill's equation to a Mach 1.92 turbulent jet. *AIAA Journal*, **38(2)**:368–370, 2000.

[3] T. Colonius, S. K. Lele, and P. Moin. Sound generation in a mixing layer. *J. Fluid Mech.*, **330**:375–409, 1997.

[4] A. W. Cook and J. J. Riley. Direct numerical simulation of a turbulent reactive plume on a parallel computer. *J. Comp. Phys.*, **129**:263–283, 1996.

[5] M. J. Fisher, P. A. Lush, and M. Harper Bourne. Jet noise. *J. Sound Vib.*, **28(3)**:563–585, 1973.

[6] V. Fortuné. *Étude par simulation numérique directe du rayonnement acoustique de couches de mélange isothermes et anisothermes*. PhD thesis, Université de Poitiers, 2000.

[7] V. Fortuné, E. Lamballais, and Y. Gervais. Étude par simulation directe temporelle des effets de la température sur l'émission acoustique des couches de mélange. *C. R. Acad. Sci.*, 328:693–700, 2000.

[8] V. Fortuné, E. Lamballais, and Y. Gervais. Study of temperature effects on radiated noise from mixing layers using DNS. In *7th AIAA/CEAS Aeroacoustics Conference, submitted to AIAA Journal*, Maastricht, The Netherlands, 2001.

[9] J. Freund. Noise sources in a low-Reynolds-number turbulent jet at Mach 0.9. *J. Fluid Mech.*, **438**:277–305, 2001.

[10] S. K. Lele. Compact finite difference schemes with spectral-like resolution. *J. Comp. Phys.*, **103**:16–42, 1992.

[11] S. K. Lele and C. M. Ho. Acoustic radiation from temporally evolving free shear layers. Technical report, Stanford University, 1994.

[12] M. Lesieur, C. Staquet, P. Le Roy, and P. Comte. The mixing layer and its coherence examined from the point of view of two-dimensional turbulence. *J. Fluid Mech.*, **192**:511, 1988.

[13] M. J. Lighthill. On sound generated aerodynamically I. General theory. *Proc. Roy. Soc. A*, **211**:564–587, 1952.

[14] P. A. McMurtry, W. H. Jou, J. J. Riley, and R. W. Metcalfe. Direct numerical simulations of a reacting mixing layer with chemical heat release. *AIAA Journal*, **24**(6):962–970, 1986.

[15] J. Whitmire and S. Sarkar. Validation of acoustic-analogy predictions for sound radiated by turbulence. *Phys. Fluids*, **12(2)**:381–391, 2000.

Using RANS Mean Flow Fields in Numerical Aeroacoustics Simulations (CAA)

M. Lummer, H.A. Grogger, J.W. Delfs
Deutsches Zentrum für Luft- u. Raumfahrt (DLR)
Institut für Aerodynamik und Strömungstechnik
Postfach 3267
D-38022 Braunschweig
Germany

Abstract

One way to perform CAA simulations is to split the flow field in a steady mean flow and turbulent and acoustic fluctuations. The small acoustic fluctuations can then be calculated from linearized Euler equations (LEE). The mean flow can be supplied by the solution of the Reynolds averaged Navier-Stokes (RANS) equations. Since different numerical requirements exist for the numerical grids of RANS and LEE simulations, an interpolation procedure between RANS and LEE grids is necessary. The following paper presents an interpolation procedure between different structured multi-block grids and its application to RANS/CAA simulations of a generic wing section.

1.   Introduction

The most accurate way to calculate the generation and propagation of sound in flows is the solution of the unsteady conservation laws of mass, momentum, and energy. Since this direct numerical simulation is even for simple flows an extremely expensive task, a lot of approximative methods have been proposed in order to attack real world problems. One of them is the splitting of the flow field in mean flow and turbulent and acoustic fluctuations. The mean flow is approximated by a solution of the Reynolds averaged equations (RANS), the turbulent fluctuations e.g. by an SNGR model (Stochastic Noise Generation and Radiation) [2,3,4,7], and the acoustic fluctuations by the solution of the linearized Euler equations (LEE). This approach is utilized in the german SWING project (Simulation of Wing-flow Noise Generation), which shall provide a general computer code for the calculation of airframe noise, especially that generated by high lift devices.

Using this RANS-LEE approach, it is generally necessary to use different grids for both calculations. The reason for this are the different numerical requirements in both cases. E.g. the RANS calculations need very fine grids in the boundary layers of the body, whereas the LEE require a sufficient fine resolution in the farfield of the body. Therefore the RANS solution has to be provided on the CAA grid by means of interpolation. The present paper discusses this transfer of RANS data into the CAA perturbation code in view of robustness, accuracy as well as the numerical implications on CAA simulations of airframe noise.

This article is structured as follows. First a brief overview of RANS calculations of a generic wing section will be given. Then the CAA grid and the interpolation procedure between the RANS grid and the CAA grid will be considered. Finally some results of CAA calculations with a Navier-Stokes and Euler mean flow will be presented.

2.   The RANS Calculations

As generic example, the viscous flow around a wing section of an airfoil representative for those at modern civil aircraft was calculated. The flow solver was the DLR FLOWer code [1,8,9], which solves the compressible Navier-Stokes equations on a grid consisting of topologically rectangular blocks (structured multi-block grid). The

free stream Mach number was $Ma = 0.2$, the Reynolds number $Re = 1.6 \times 10^6$ and angle of attack of $a = 7°$. As turbulence model, the k-w model of Wilcox was used.

2.1 The RANS Grid

The RANS grid consists of 12 blocks with a total of about 86000 grid points, cf. Fig.1. The topologically complicated structure of the grid stems from the fact that with the same topology also a wing section with deployed Fowler flap has to be calculated (as part of a future 3d simulation). It can be seen that a typical RANS grid becomes very coarse in the far field region. Any calculation of wave propagation would break down there.
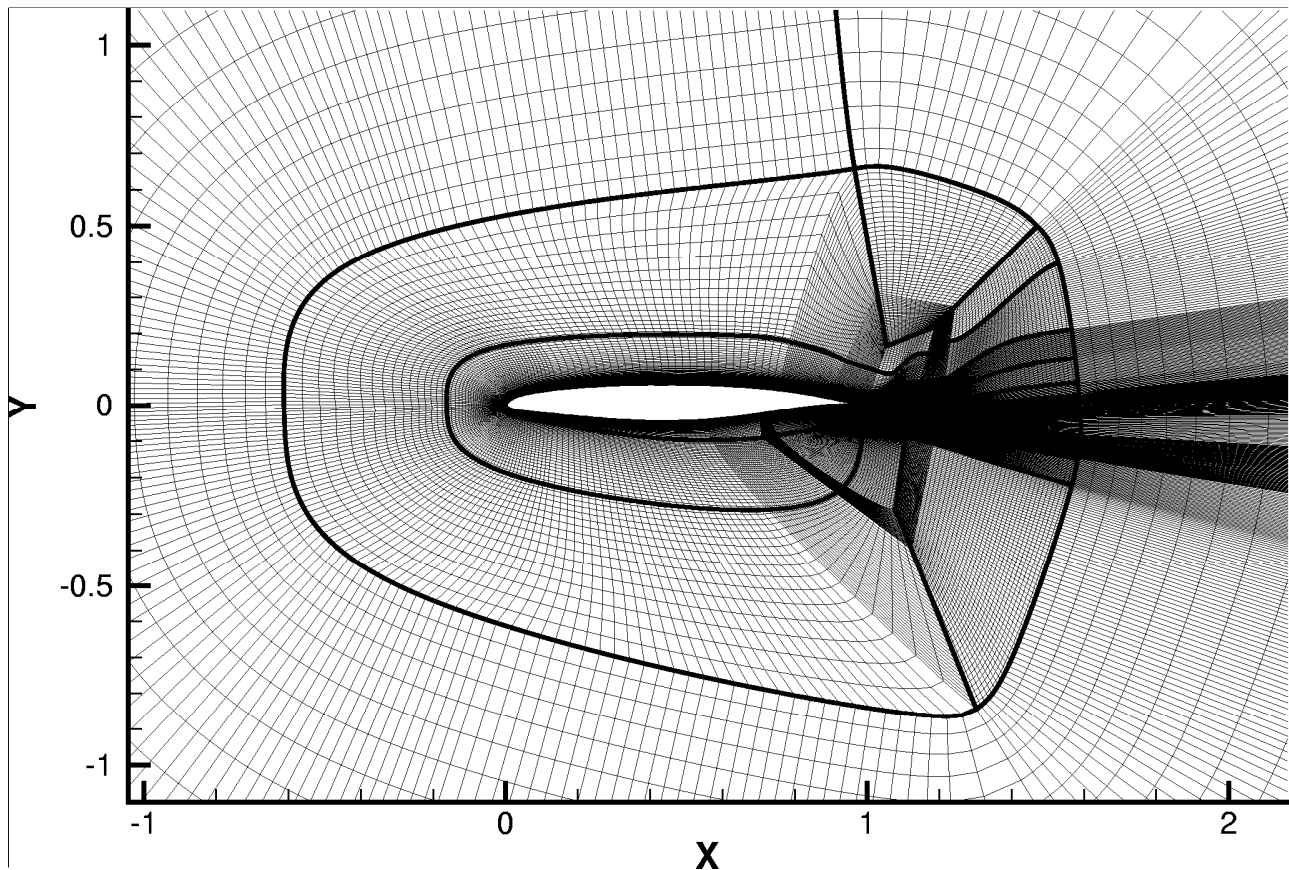
Fig. 1 The RANS grid(detail). (Thick lines are block boundaries)

2.2 The Mean Flow Field

The mean flow field around a wing section at high angle of attack has a strong pressure minimum at the nose of the profile, cf. Fig.3, which corresponds to high local velocities and gradients of the flow variables. The maximum Mach number at the nose is about $Ma = 0.45$ in contrast to a free stream mach number of 0.2. The thin boundary layer requests a small grid spacing there. In the present case the distance of the first grid line from the surface was 1×10^{-5} of the chord length. The examined wing section has a blunt trailing edge with a thickness of about 0.33% of the chord length. This finite trailing edge requests a considerable amount of fine tuning of the grid in order to achieve sufficient convergence of the RANS solution. Besides problems with the turbulence models there, the main reason for this difficulty is the complex grid topology in the wake of the profile. For comparison purposes also an Euler calculation was performed which needed a different grid not shown here.
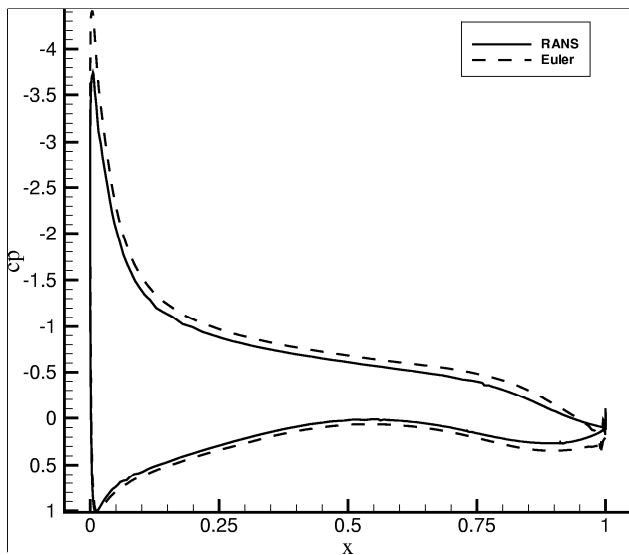
Fig. 2 The pressure distribution of the mean flow

3. Interpolation between RANS- and CAA-Grid

3.1 The CAA Grid

The CAA grid in the present example consists of 2 blocks with a total of about 18000 grid points, cf. Fig.3. The boundary layers of the profile were resolved by approximately 10 grid points with a minimum grid spacing of $5 \cdot 10^{-6}$ at the nose of the profile. This results in an allowable time step of the CAA calculation of the same magnitude. The minimum grid spacing at the nose is about the half of the spacing of the RANS grid there. This small spacing was chosen mainly in order to resolve possible small unsteady flow structures. It should be remarked however that the progression of the grid spacing at the nose is larger than the progression choosen in the RANS grid. The gridspacing in the far field was chosen such that one retains enough resolution of the evanescent sound waves and is therefore significantly smaller than in the RANS grid.
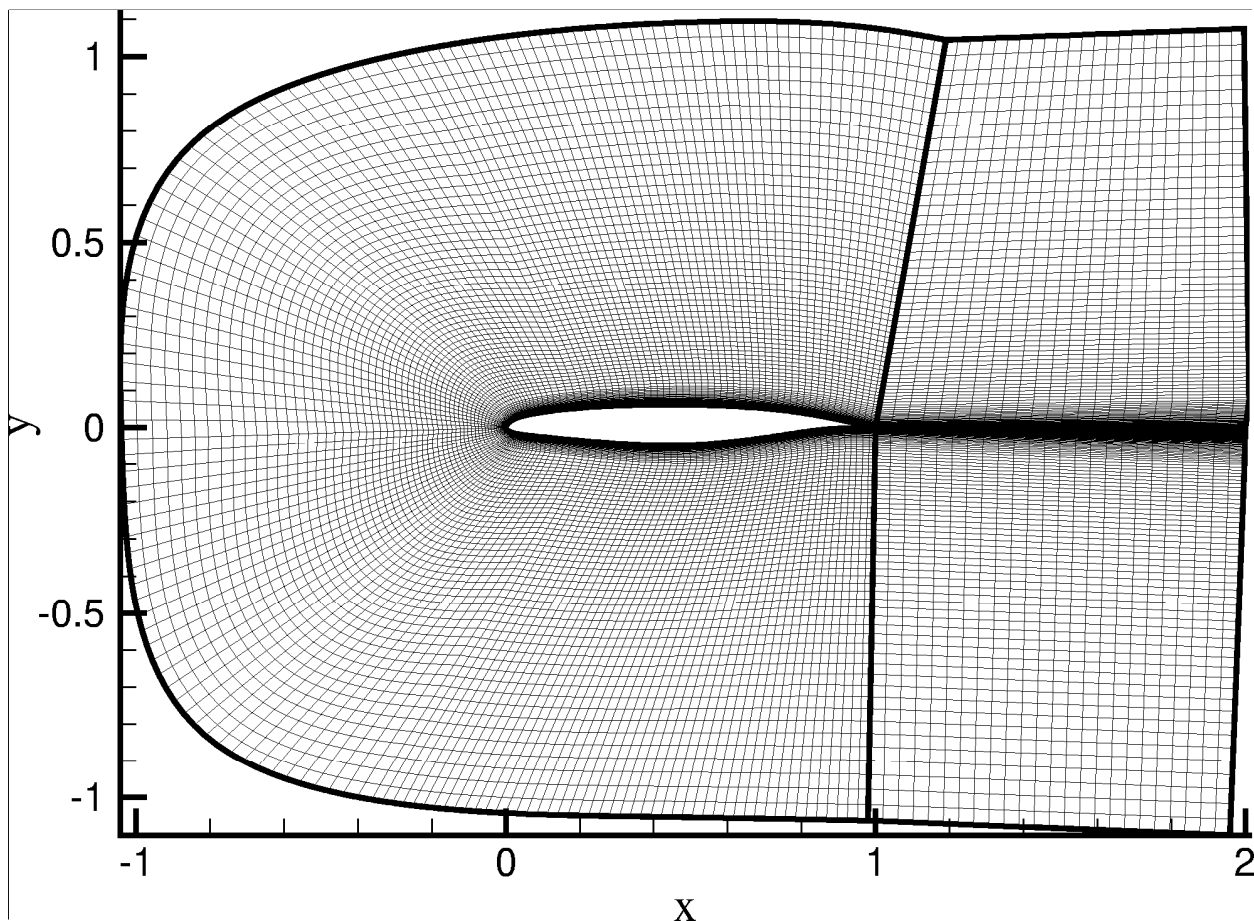
Fig. 3 The CAA grid (2 blocks. Thick lines are block boundaries.)

It should be noted as well, that a considerable coarsening (factor 20) of the CAA-grid normal to the boundary layer close to the surface will still allow for an adequate representation of essential features of the physics. As will be seen later, this is a consequence of the fact that the presence of boundary layers has only a small influence on the scattering problem considered.

3.2   The Interpolation Procedure

The interpolation procedure between the RANS grid and the CAA grid is complicated by two circumstances. First, the two grids can be located almost arbitrary in 3d space (The only restriction is, that the CAA grid has to be enclosed by the RANS grid). This results in an expensive search for appropriate initial conditions for the iterative determination of the parameters of a point of the CAA grid. The second issue is the very fact that in complicated 3d calculations, one has to search some million CAA points in some million RANS cells. This poses great demands upon the speed of the algorithm. Therefore an easy to evaluate, local polynomial approximation was chosen for the representation of the grid functions.

3.2.1   The Interpolating Polynomial

The RANS solver FLOWer developed at DLR utilizes a general curvilinear multi-block structure. Every block of the grid consists of the $n_1 \times n_2 \times n_3$ points

$$\mathbf{x}(i,j,k) = \begin{pmatrix} x_{ijk} \\ y_{ijk} \\ z_{ijk} \end{pmatrix} \quad , \quad 0 < i < n_1 - 1 \quad , \quad 0 < j < n_2 - 1 \quad , \quad 0 < k < n_3 - 1$$

Every flow variable in the FLOWer code is defined at these grid nodes. It is convenient to consider the grid coordinates and every other function defined on the block as function of the grid indices. I.e., we introduce parameters (ξ, η, ζ), in such a way that e.g.

$$\mathbf{x}(i,j,k) = \mathbf{x}(\xi = i, \eta = j, \zeta = k)$$

In the following, the symbol f stands for any variable that is defined at the grid nodes. The interpolation problem can now be formulated as follows

1. Choose an appropriate representation of a function $f(\xi, \eta, \zeta)$ on the block.
2. Determine for a given point $\mathbf{y}$ inside the block the values (ξ, η, ζ) from the vector equation $\mathbf{y} = \mathbf{x}(\xi, \eta, \zeta)$.

Since one has to interpolate a vast amount of points (up to some millions in 3d calculations), one needs a fast interpolation method with acceptable accuracy. This leads to a polynomial interpolation of the function f on every cell of the block. Therefore, we consider now a cell $i \leq \xi \leq i+1$, $j \leq \eta \leq j+1$, $k \leq \zeta \leq k+1$ of the block and introduce local coordinates $u = \xi - i$, $v = \eta - j$, $w = \zeta - k$ in this cell. The interpolation problem now boils down to a polynomial interpolation of a function on a unit cell $0 \leq u \leq 1, 0 \leq v \leq 1, 0 \leq w \leq 1$, where the function values (and perhaps appropriate derivates of the function) are given at the corners of this unit cell. The most simple interpolation is the linear one

$$f(u,v,w) = a_{000} + a_{100}u + a_{010}v + a_{001}w + a_{110}uv + a_{101}uw + a_{011}vw + a_{111}uvw$$

The eight coefficients $a_{000}, \ldots, a_{111}$ can be determined by the eight function values $f^{000} = f(0,0,0), \ldots, f^{111} = f(1,1,1)$ at the corners of the cell. Unfortunately the accuracy of this interpolation is quite poor. An improvement however can be achieved using a higher order polynomial. In this case one needs additional information from the neighboring cells or from derivatives at the corners of the cell in order to determine the higher number of coefficients. In order to construct a local approximation the second approach was choosen,

using appropriate values for the 2nd derivatives of f. It was convenient to consider the following polynomial up to third order in u, v and w as interpolating function

$$f(u,v,w) = a_{000} + a_{111}uvw + \begin{pmatrix} a_{110} \\ a_{011} \\ a_{101} \end{pmatrix}^T \begin{pmatrix} uv \\ vw \\ uw \end{pmatrix} + \begin{pmatrix} a_{100} \\ a_{010} \\ a_{001} \end{pmatrix}^T \begin{pmatrix} u \\ v \\ w \end{pmatrix} + \begin{pmatrix} a_{200} \\ a_{020} \\ a_{002} \end{pmatrix}^T \begin{pmatrix} u^2 \\ v^2 \\ w^2 \end{pmatrix} + \begin{pmatrix} a_{210} \\ a_{201} \\ a_{120} \\ a_{021} \\ a_{012} \\ a_{102} \end{pmatrix}^T \begin{pmatrix} u^2v \\ u^2w \\ uv^2 \\ v^2w \\ vw^2 \\ uw^2 \end{pmatrix} + $$

$$+ \begin{pmatrix} a_{211} \\ a_{121} \\ a_{112} \end{pmatrix}^T \begin{pmatrix} u^2vw \\ uv^2w \\ uvw^2 \end{pmatrix} + \begin{pmatrix} a_{300} \\ a_{030} \\ a_{003} \end{pmatrix}^T \begin{pmatrix} u^3 \\ v^3 \\ w^3 \end{pmatrix} + \begin{pmatrix} a_{310} \\ a_{301} \\ a_{130} \\ a_{031} \\ a_{013} \\ a_{103} \end{pmatrix}^T \begin{pmatrix} u^3v \\ u^3w \\ uv^3 \\ v^3w \\ vw^3 \\ uw^3 \end{pmatrix} + \begin{pmatrix} a_{311} \\ a_{131} \\ a_{113} \end{pmatrix}^T \begin{pmatrix} u^3vw \\ uv^3w \\ uvw^3 \end{pmatrix}$$

Now one has to determine the 32 coefficients $a_{000}, a_{100}, \ldots, a_{113}$. Eight equations are provided by the function values at the corners of the cell. Another 24 have to be determined from appropriate derivatives at the corners. Since only the function values are provided by the RANS calculation, one has to determine sufficiently accurate approximations of the derivatives at the grid points numerically. One way to do this is a (one-dimensional) cubic spline interpolation of the function along every grid line [11]. A cubic spline has continuous derivatives up to second order and therefore values for the second derivatives f_{uu}, f_{vv} and f_{ww} at the grid points can easily be obtained. An inspection of the second derivatives of the interpolating polynomial

$$f_{uu} = 2a_{200} + 6a_{300}u + 2a_{210}v + 2a_{201}w + 6a_{310}uv + 6a_{301}uw + 2a_{211}vw + 6a_{311}uvw$$

$$f_{vv} = 2a_{020} + 2a_{120}u + 6a_{030}v + 2a_{021}w + 6a_{130}uv + 2a_{121}uw + 6a_{031}vw + 6a_{131}uvw$$

$$f_{ww} = 2a_{002} + 2a_{102}u + 2a_{021}v + 6a_{003}w + 2a_{112}uv + 6a_{103}uw + 6a_{013}vw + 6a_{113}uvw$$

yields that the coefficients can be calculated successively from the following recursively solvable linear systems (Zero entries are marked with (.))

$$\begin{pmatrix} 2 & . & . & . & . & . & . & . \\ 2 & 6 & . & . & . & . & . & . \\ 2 & . & 2 & . & . & . & . & . \\ 2 & . & . & 2 & . & . & . & . \\ 2 & 6 & 2 & . & 6 & . & . & . \\ 2 & 6 & . & 2 & . & 6 & . & . \\ 2 & . & 2 & 2 & . & . & 2 & . \\ 2 & 6 & 2 & 2 & 6 & 6 & 2 & 6 \end{pmatrix} \begin{pmatrix} a_{200} \\ a_{300} \\ a_{210} \\ a_{201} \\ a_{310} \\ a_{301} \\ a_{211} \\ a_{311} \end{pmatrix} = \begin{pmatrix} f_{uu}^{000} \\ f_{uu}^{100} \\ f_{uu}^{010} \\ f_{uu}^{001} \\ f_{uu}^{110} \\ f_{uu}^{101} \\ f_{uu}^{011} \\ f_{uu}^{111} \end{pmatrix}, \quad \begin{pmatrix} 2 & . & . & . & . & . & . & . \\ 2 & 2 & . & . & . & . & . & . \\ 2 & . & 6 & . & . & . & . & . \\ 2 & . & . & 2 & . & . & . & . \\ 2 & 2 & 6 & . & 6 & . & . & . \\ 2 & 2 & . & 2 & . & 2 & . & . \\ 2 & . & 6 & 2 & . & . & 6 & . \\ 2 & 2 & 6 & 2 & 6 & 2 & 6 & 6 \end{pmatrix} \begin{pmatrix} a_{020} \\ a_{120} \\ a_{030} \\ a_{021} \\ a_{130} \\ a_{121} \\ a_{031} \\ a_{131} \end{pmatrix} = \begin{pmatrix} f_{vv}^{000} \\ f_{vv}^{100} \\ f_{vv}^{010} \\ f_{vv}^{001} \\ f_{vv}^{110} \\ f_{vv}^{101} \\ f_{vv}^{011} \\ f_{vv}^{111} \end{pmatrix}$$

$$
\begin{pmatrix}
2 & \cdot & \cdot & \cdot & \cdot & \cdot & \cdot & \cdot \\
2 & 2 & \cdot & \cdot & \cdot & \cdot & \cdot & \cdot \\
2 & \cdot & 2 & \cdot & \cdot & \cdot & \cdot & \cdot \\
2 & \cdot & \cdot & 6 & \cdot & \cdot & \cdot & \cdot \\
2 & 2 & 2 & \cdot & 2 & \cdot & \cdot & \cdot \\
2 & 2 & \cdot & 6 & \cdot & 6 & \cdot & \cdot \\
2 & \cdot & 2 & 6 & \cdot & \cdot & 6 & \cdot \\
2 & 2 & 2 & 6 & 2 & 6 & 6 & 6
\end{pmatrix}
\begin{pmatrix}
a_{002} \\ a_{102} \\ a_{012} \\ a_{003} \\ a_{112} \\ a_{103} \\ a_{013} \\ a_{113}
\end{pmatrix}
=
\begin{pmatrix}
f_{ww}^{000} \\ f_{ww}^{100} \\ f_{ww}^{010} \\ f_{ww}^{001} \\ f_{ww}^{110} \\ f_{ww}^{101} \\ f_{ww}^{011} \\ f_{ww}^{111}
\end{pmatrix}
,
\begin{pmatrix}
1 & \cdot & \cdot & \cdot & \cdot & \cdot & \cdot & \cdot \\
1 & 1 & \cdot & \cdot & \cdot & \cdot & \cdot & \cdot \\
1 & \cdot & 1 & \cdot & \cdot & \cdot & \cdot & \cdot \\
1 & \cdot & \cdot & 1 & \cdot & \cdot & \cdot & \cdot \\
1 & 1 & 1 & \cdot & 1 & \cdot & \cdot & \cdot \\
1 & 1 & \cdot & 1 & \cdot & 1 & \cdot & \cdot \\
1 & \cdot & 1 & 1 & \cdot & \cdot & 1 & \cdot \\
1 & 1 & 1 & 1 & 1 & 1 & 1 & 1
\end{pmatrix}
\begin{pmatrix}
a_{000} \\ a_{100} \\ a_{010} \\ a_{001} \\ a_{110} \\ a_{101} \\ a_{011} \\ a_{111}
\end{pmatrix}
=
\begin{pmatrix}
f^{000} \\ f^{100} - a_{200} - a_{300} \\ f^{010} - a_{020} - a_{030} \\ f^{001} - a_{002} - a_{003} \\ f^{110} - \cdots \\ f^{101} - \cdots \\ f^{011} - \cdots \\ f^{111} - \cdots
\end{pmatrix}.
$$

3.2.2   Calculation of the Parameters

Once an interpolating polynomial can be constructed for any function $f(\xi,\eta,\zeta)$, the main problem of the grid to grid interpolation can be tackled, i.e. the determination of the parameter values (ξ,η,ζ) for an arbitrary point $\mathbf{y}$ inside the RANS grid. This can be split into two parts
1. Find the appropriate block of the RANS grid and some initial conditions for the parameter values.
2. Solve the (nonlinear) vector equation $\mathbf{y} = \mathbf{x}(\xi,\eta,\zeta)$ for (ξ,η,ζ) using the polynomial approximation above for every component function of $\mathbf{x}$.

The crucial point in this algorithm is to provide appropriate initial conditions for the parameters. First, $\mathbf{y}$ is checked against the bounding box of a block. If $\mathbf{y}$ is inside the bounding box, initial conditions are searched in every cell of the block. In order to do this, $\mathbf{x}(\xi,\eta,\zeta)$ is approximated on every cell by a linear function. Initial values for (ξ,η,ζ) can than be found by solution of a simple system of linear equations. This procedure works for most of the cells of the RANS grid. If however the faces of a cell have strong curvature and/or if the the aspect ratio of the cells takes very large values this procedure can fail. This can happen especially with cells in the boundary layer at the nose of the profile. Then, a second pass is started which uses the parameter of successfully found neighboring points as initial values. If initial conditions are found, a Newton iteration is performed in order to solve $\mathbf{y} = \mathbf{x}(\xi,\eta,\zeta)$, which uses the full polynomial approximation of $\mathbf{x}$.

3.2.3   Treatment of Wall Points

Points at walls can be treated differently from interior ones, since a wall point in the CAA grid has to be one in the RANS grid representation of the wall too. Therefore, the search for initial conditions can be performed only over the surfaces of the RANS blocks. The difficulty which arises is that a wall point lies at a surface of a RANS block and the Newton iteration for the determination of the parameter values may run outside the block which deteriorates the convergence of the procedure. Now, however, one parameter value is known from the wall condition and consequently the search can be performed inside the face of the block (and not in the volume of the wall cell). In this case, the determining vector equation $\mathbf{y} = \mathbf{x}(\xi,\eta,\zeta)$ has to be replaced by a set of two equations, since we are searching two parameter values only. If, for example, $\zeta = const.$ denotes the coordinate of a wall, ξ,η are determined such that the difference vector $\mathbf{y} - \mathbf{x}(\xi,\eta)$ is perpendicular to both surface tangent vectors $\dfrac{\partial \mathbf{x}(\xi,\eta)}{\partial \xi}$ and $\dfrac{\partial \mathbf{x}(\xi,\eta)}{\partial \eta}$. This is equivalent to the condition that $\left| \mathbf{y} - \mathbf{x}(\xi,\eta) \right|$ is minimum. This approach also solves the problem encountered when small differences between the wall surfaces of both grids exist, originating from slightly different spline approximations in both cases.

3.2.4   Accuracy of the Interpolation

In order to check the accuracy of the interpolation, the test function $f(x, y) = x^2 + y^2$ was interpolated from the RANS grid onto the CAA grid. The relative error $(f^{CAA} - f^{RANS})/\max(f^{CAA})$ is below 10^{-4} in regions where strong mean flow gradients are expected, cf. Fig.4. This has proved to be sufficient for the intended purpose. The error displays characteristic extrema where large jumps in gridspacing on the RANS grid occur or the grid lines have some kinks which increase the error in the spline approximations. It should however be noted that far away from the body the RANS solution has almost no gradients anymore and in the vicinity of the body the gridspacing is very small. This also alleviates accuracy problems of the interpolation.
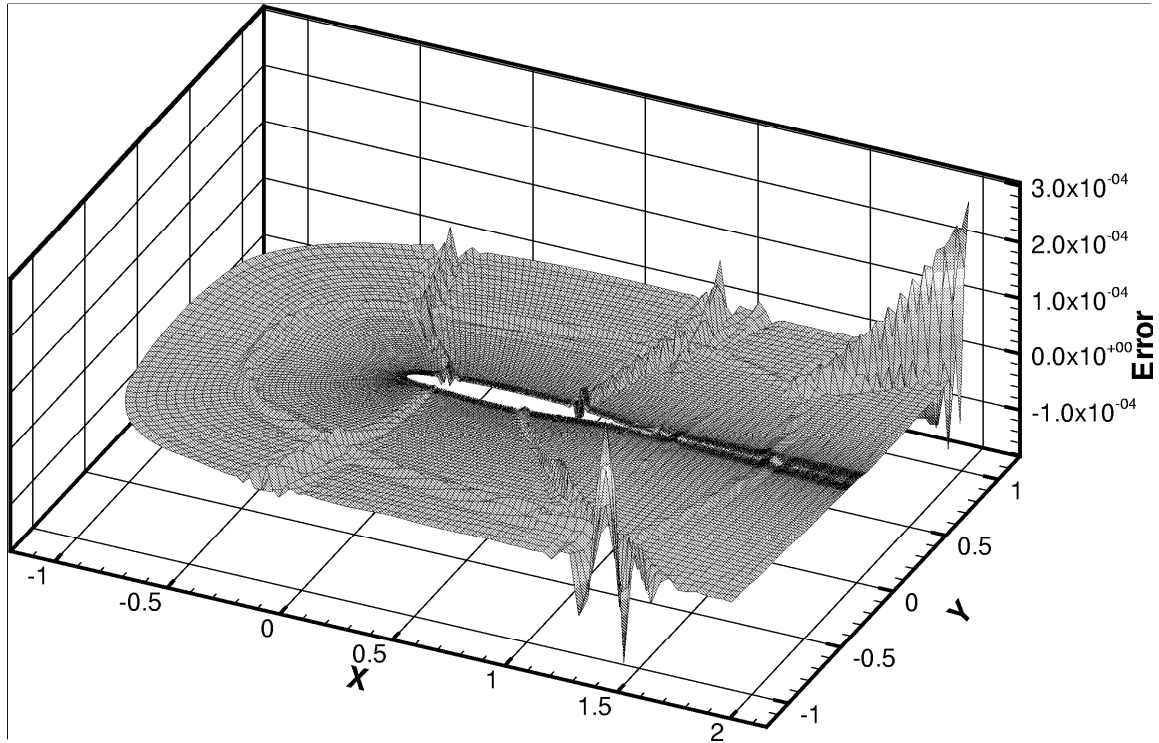
Fig. 4 The relative interpolation error on the CAA grid

4.   The CAA Calculations

For the solution of the linearized Euler equations the code PIANO was used, which is currently under development at DLR [5,6]. The LEE solved read in symbolical notation

$$\frac{\partial r}{\partial t} + \mathbf{v}_0 \cdot \tilde{\nabla} r + \mathbf{v} \cdot \tilde{\nabla} r_0 + r_0 \tilde{\nabla} \cdot \mathbf{v} + r \tilde{\nabla} \cdot \mathbf{v}_0 = 0$$

$$r_0 \frac{\partial \mathbf{v}}{\partial t} + r_0 \mathbf{v}_0 \cdot \tilde{\nabla} \mathbf{v} + r_0 \mathbf{v} \cdot \tilde{\nabla} \mathbf{v}_0 + r \mathbf{v}_0 \cdot \tilde{\nabla} \mathbf{v}_0 = -\tilde{\nabla} p$$

$$\frac{\partial p}{\partial t} + \mathbf{v}_0 \cdot \tilde{\nabla} p + \mathbf{v} \cdot \tilde{\nabla} p_0 + g p_0 \tilde{\nabla} \cdot \mathbf{v} + g p \tilde{\nabla} \cdot \mathbf{v}_0 = 0$$

Here r and p are the density and pressure disturbance and $\mathbf{v}$ is the vector of the disturbance velocity. The quantities with index 0 are the mean flow values. The equations were brought into dimensionless form with a reference length L, a reference density $r_\ast$ and a reference velocity $a_\ast$ which was choosen to be the velocity of sound far away from the body. These equations are solved on a structured multi-block grid, like the one used in the FLOWer code. The spatial derivatives are approximated by the usual 4th order DRP-stencils [14] and time

integration is done by the standard 4th order Runge-Kutta procedure. Inflow and outflow boundary conditions were used according to [14].

4.1 Filtering

Since the utilized DRP-Schemes have no dissipation, an efficient removal of spurious waves, i.e. waves which can not be resolved on the numerical grid, is necessary. The usual way to do this is to use artificial selective damping [13]. This approach is quite expensive, since additional terms have to be calculated in the differential equations. A more convenient way is to apply periodically during the calculation suitable digital filters on the fields [12,15]. In PIANO, symmetric 6th and 8th order filters are implemented. In the present study, the filters were used every hundred time steps. The 6th ($N = 3$) and 8th ($N = 4$) order filter are defined as [12]

$$\overline{\psi}_i = a_0\psi_i + \sum_{j=1}^{N} a_j(\psi_{i+j} + \psi_{i-j})$$

$$N = 3 \quad : \quad a_0 = 0.6875 \quad , \quad a_1 = 0.46875 \quad , \quad a_2 = -0.1875 \quad , \quad a_3 = 0.03125$$

$$N = 4 \quad : \quad a_0 = 0.7265625 \quad , \quad a_1 = 0.4375 \quad , \quad a_2 = -0.21875 \quad , \quad a_3 = 0.0625$$

$$\quad , \quad a_4 = -0.0078125$$

where $\overline{\psi}_i$ denotes the filtered quantity and ψ the unfiltered one. This filter is applied in the computational (ξ, η, ζ)-space in the several space dimensions subsequently. No filtering was used in the first N layers normal to a wall.

4.2 Smoothing Normal to Walls

During the calculations it has been observed that very strong gradients of the flow variables develop in the immediate vicinity of walls, especially at the leading edge of the wing section, which lead to numerical instability. Examination of the calculational results revealed that gridpoint fluctuations of the density normal to the wall are the driving force for those instabilities. Therefore, an ad hoc procedure was applied in order to smooth out those gridpoint fluctuations, which we call `diagonal smoothing`. If j denotes the direction normal to the wall and $j = 0$ the position of the wall, the diagonal smoothing procedure for a flow quantity is defined as

$$\overline{\psi_{i,j}} = a_0\psi_{i,j} + \sum_{k=1}^{N} a_k(\psi_{i-k,j+k} + \psi_{i+k,j+k}) \quad , \quad j = 0,1,...,N-1$$

The coefficients a_j are the same as for the filters above. The value of $N = 3$ was used in connection with 6th order filtering and $N = 4$ with 8th order filtering. This smoothing procedure was not applied normal to the trailing edge face. In the results presented, all flow quantities were smoothed, although in some calculations it would have been sufficient to smooth the density alone.

It should be emphasized however, that up to now no mathematical justification can be given for this kind of smoothing. This is a problem that clearly requests further investigations in the future.

4.3 Pressure Pulse Hitting the Leading Edge

A common benchmark problem for CAA codes is the scattering of a pressure pulse hitting the leading edge of a wing section. Fig.5 shows the scattering of a pressure pulse located at $x = -0.35, y = 0$ at time at $T = 0$ in front of the profile for the RANS mean flow and 8th order filtering. It can be seen, that the wave front travels slightly faster above the upper side of the profile due to the higher velocities of the mean flow there. The most remarkable phenomenon, which was not observed in scattering investigations using an Euler mean flow, is however the strong generation of vorticity in the boundary layer at the nose of the profile. This vorticity is convected by the mean flow along the upper surface of the profile. Fig.6 shows the contour plot of the v-velocity component and the local direction of the velocity field by means of momentary streamlines of the disturbance velocity. Fig. 7 shows the corresponding quantities for an Euler mean flow field, where almost no vorticity is generated in the vicinity of the body.
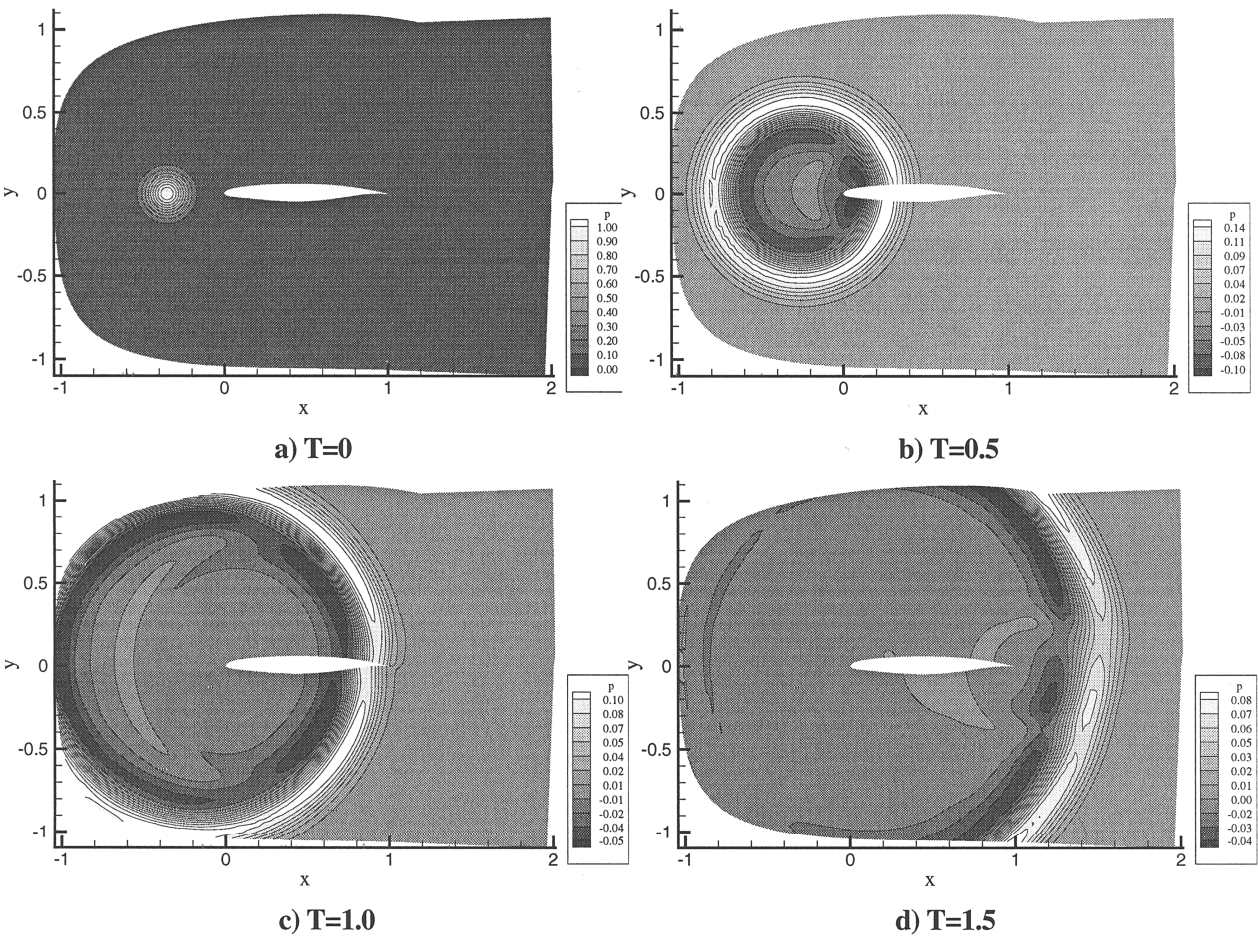
a) T=0 b) T=0.5

c) T=1.0 d) T=1.5
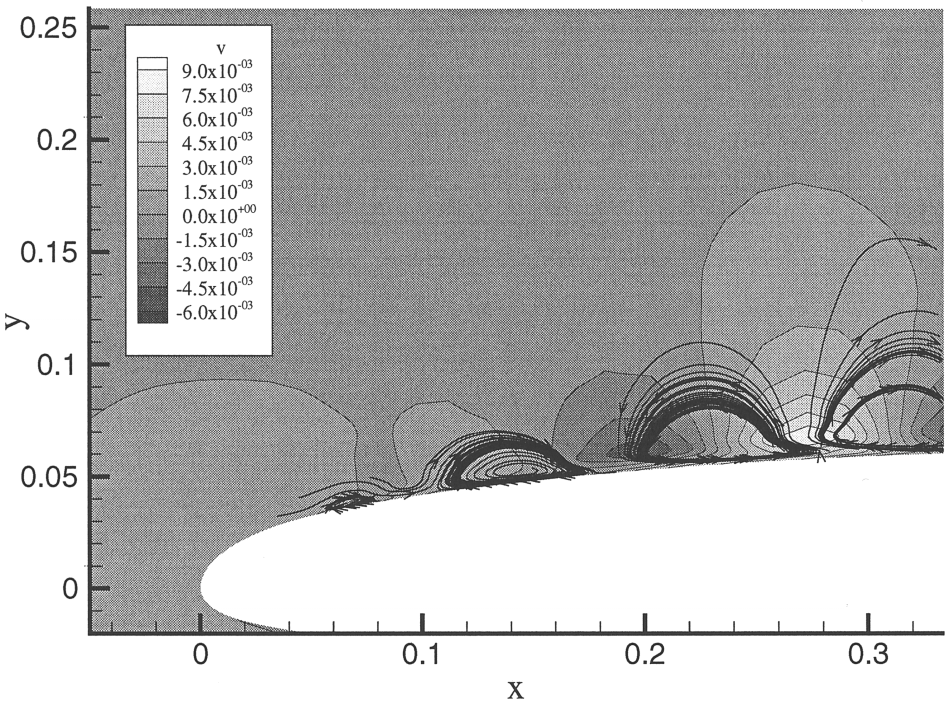
Fig.5 Scattering of a Pressure Pulse (RANS mean flow)

Fig.6 T=1.5, RANS mean flow: v-velocity field with streamlines of the disturbance velocity
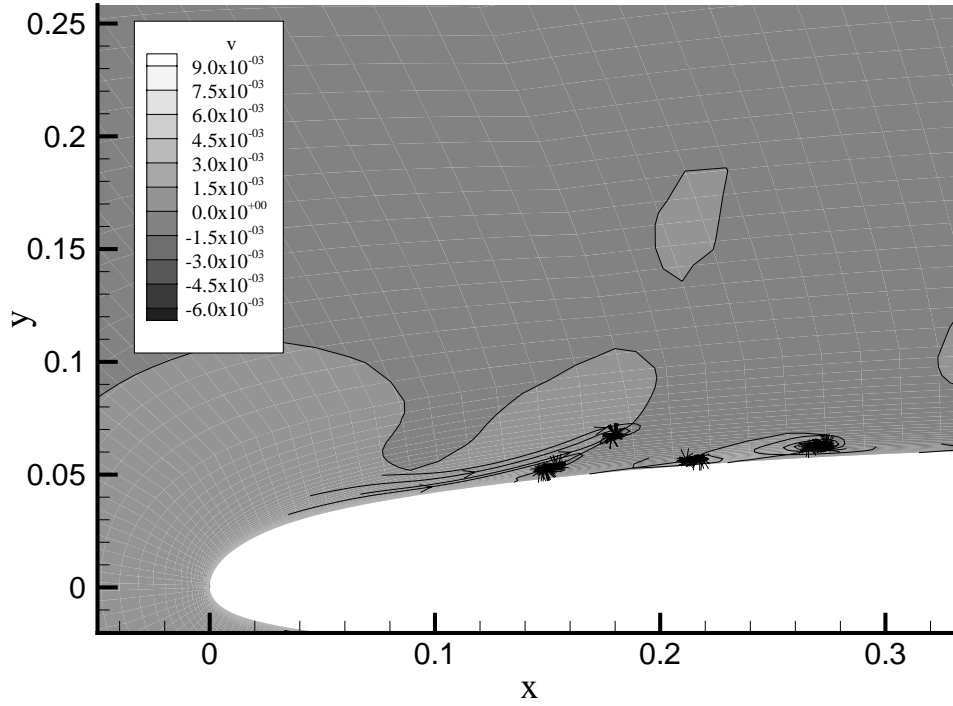
Fig. 7 T=1.5, Euler mean flow: v-velocity field with streamlines of the disturbance velocity

A physical explanation for this strong generation of disturbance vorticity in regions where the mean flow field has vorticity maxima too can be given if one considers the compressible vorticity transport equation:

$$\frac{D\boldsymbol{\omega}}{Dt} = -\boldsymbol{\omega}\nabla\mathbf{v} + (\boldsymbol{\omega}\cdot\nabla)\mathbf{v} + \frac{\nabla\rho\times\nabla p}{\rho^2}$$

After linearization the first term on the right hand side gives a term consisting of the product of the vorticity of the mean flow and the divergence of the disturbance velocity. Since the mean flow vorticity takes huge values in the boundary layer this results in a strong source term for the disturbance vorticity if the pressure wave arrives. Similar vortex structures have been found by Manoha et al. [10] performing a large eddy simulation of the flowfield around a NACA 0012 airfoil.
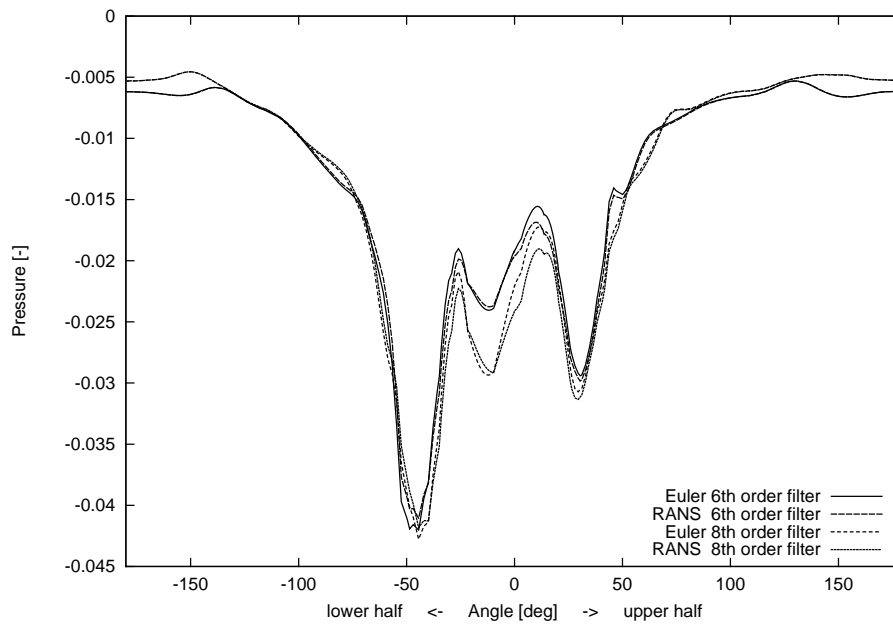
Fig. 8 T=1.5, Pressure on a circle around the profile for different mean flow fields and filters

In order to compare the influence of the different mean flow fields and two different filters, for T=1.5 the pressure on a circle (origin (0.5,0.0), radius 0.8) around the profile was plotted, cf. Fig.8. The angle 0° corresponds to the downstream direction.

It can be seen that the difference between the 6th and the 8th order filters is much larger than the difference between RANS- and Euler mean flow. As one would expect, one recognizes that the pressure profile for the 8th order filter has sharper gradients than that of the 6th order filter. The largest difference between the two filters occurs near the trailing edge of the profile (domain near angle 0°), which becomes clear if on considers that there the sharpest gradients in the disturbance flow field develop. The very small difference between the pressures of the RANS and Euler mean flow fields indicates that almost no sound is generated by the vortex structures mentioned above and that the influence of mean flow field wall boundary layers can be neclected in the scattering problem considered.

5.   Conclusions

For the solution of the linearized Euler equations with a RANS mean flow field the RANS grid can normally not be used. Therefore an interpolation procedure for the mean flow field between curvilinear structured multi-block RANS- and CAA-grids was suggested, which is based on a higher order polynomial approximation of the grid variables on each cell. The coefficients of the polynomial are determined from the function values and its 2nd derivatives at the corners of the cell. The 2nd derivatives are determined by one dimensional cubic spline interpolation along the gridlines. Of crucial importance is the provision of suitable initial conditions for the iterative determination of the the parameter values of the grid functions.

The interpolation procedure was applied on the scattering problem of a pressure pulse hitting the leading edge of a wing section at an angle of attack of $\alpha = 7°$. Remarkable is the strong production of vorticity in the nose region of the profile. This vorticity is transported by the mean flow along the upper surface of the profile, but obviously does not produce sound waves, as shows the comparison with calculations using an Euler mean flow. In the scattering problem considered, the differences in the pressure fields of the RANS and Euler mean flow cases are very small. The difference between 6th and 8th order filtering are most pronounced in the wake of the profile, where sharp gradients evolve which were more intensely smoothed by the 6th order filter.

An open problem that remains is the strong mathematical justification of the diagonal smoothing procedure, which had to be applied in immediate vicinity of solid walls, in order to stabilize the calculations.

6.   References

[1] Aumann, P.; Barnewitz, H.; Schwarten, H.; Becker, H.; Heinrich, R.; Roll, B.; Galle, M.; Kroll, N.; Gerold, T.; Schwamborn, D.; Franke, M.: "MEGAFLOW: Parallel complete aircraft CFD", Parallel Computing, vol. 27, no. 4, pp. 415-440, 2001.

[2] Bailly, C.; Juvé, D.: "A stochastic approach to compute subsonic noise using linearized Euler's equations", AIAA-paper 99-1872, American Institute of Aeronautics and Astronautics, 1999.

[3] Bailly, C.; Lafon, P.; Candel,S.: "A stochastic approach to compute noise generation and radiation of free turbulent flows", in 1st AIAA/CEAS Aeroacoustics Conference, 1995.

[4] Bailly,C.; Lafon, P.; Candel, S.: "Computation of noise generation and propagation for free and confined turbulent flows", in 2nd AIAA/CEAS Aeroacoustics Conference, 1996.

[5] Grogger, H.A.; Delfs, J.W.; Lauke, T.G.; Lummer, M.; Yin, J.: "Simulation of leading edge noise of airfoils using CAA based on body fitted grids", presented at the International Congress of Acoustics and Vibration ICAV7, Garmisch, Germany, submitted to International Journal of Acoustics and Vibration

[6] Grogger, H.A.; Lummer, M.; Lauke,Th.: "Simulation of the Interaction of a Three Dimensional Vortex with airfoils using CAA", AIAA-Paper No. 2001-2137, (2001)

[7] Kalitzin, N.; Wilde, A.: "Application of the stochastic noise generation and radiation model to trailing edge noise", in Aeroacoustic Workshop in connection with the German research project SWING - Proceedings (P. Költzsch and N. Kalitzin, eds.), (Dresden), TU Dresden, 1999

[8] Kroll, N.; Rossow, C.-C.; Becker, K.; Thiele, F.: "MEGAFLOW - a numerical flow simulation system", ICAS-Paper 98-2.7.4, 1998.

[9] Kroll, N.; Rossow, C.-C.; Becker, K.; Thiele, F.: "The MEGAFLOW project", Aerospace Science and Technology, vol. 4, no. 4, pp. 223-237, 2000.

[10] Manoha, E.; Delahay, C.; Redonnet, S.; Ben Khelil, S.; Guillen, P.; Sagaut, P.; Mary, I.: "Numerical prediction of the unsteady flow and radiated noise from a 3D lifting airfoil", NATO RTO-AVT Symposium on Aging mechanisms and Control, Part A – Development in Computational Aero- and Hydro-Acoustics, Manchester, UK, 8-11 Oct. 2001.

[11] Press, W.H.; Flannery, B.P.; Teukolksky, S.A.; Vetterling, W.T.: "Numerical Recipes", Cambridge: Cambridge University Press, 1986.

[12] Shang, J.S.: "High-order compact-difference schemes for time-dependent maxwell equations", Journal of Computational Physics, vol. 153, pp. 312-333, 1999.

[13] Tam, C.K.W.; Webb, J.C.; Dong, Z.: "A study of the short wave components in computational acoustics", Journal of Computational Acoustics, vol. 1, pp. 1-30, (1993)

[14] Tam, C.K.W.; Webb, J.C.; "Dispersion-Relation-Preserving Finite Difference Schemes for Computational Aeroacoustics", Journal of Computational Physics, vol. 107, pp. 262-281, (1993)

[15] Vasilyev, O.V.; Lund, T.S.; Moin, P.: "A general class of commutative Filters for LES in complex geometries", Journal of Computational Physics, vol. 146, pp. 82-104, 1998.

Reference # of Paper: 16
Discusser's Name: Prof. J. J. McGuirk
Author's Name: Dr. Markus Lummer
Question:

   The RANS solution is converged in the sense that mass and momentum balances on the RAND cells. Do you check that after interpolation the interpolated mean flow satisfies mass and momentum balance on the CAA grid? If not, the linearized Euler equations you solve in a discretized sense may contain artificial diffusive fluxes other than zero on their right hand sides.

Answer:

   The balance of the interpolated fluxes is not checked. Since the linearized Euler equations are solved in nonconservative form, artificial fluxes are always present on the right hand side: but are assumed to be small. We assume that the modeling error in the RANS calculations is at least one order of magnitude larger than possible errors introduced by the interpolation.

This page has been deliberately left blank

————————————

Page intentionnellement blanche

Computation of Aeroacoustic Sound Via Hybrid CFD/CAA-Methods

R. Ewert[1], M. Meinke[2], W. Schröder[3]
Aerodynamisches Institut
RWTH Aachen, Wüllnerstraße zw. 5 und 7
52062 Aachen, Germany

[1] Research Scientist, e-mail: roland@aia.rwth-aachen.de
[2] Senior Scientist, e-mail: matthias@aia.rwth-aachen.de
[3] Professor, Dept. Mechanical Engineering, e-mail: office@aia.rwth-aachen.de

Different formulations for a two step CFD/CAA approach are investigated. The acoustic field is simulated using linearized perturbation equations which are excited by sources determined from the unsteady compressible near field flow. The sound generated by a cylinder in laminar flow at Mach number M=0.3 and Reynolds number Re=200 is used as a test problem. It is examined whether the viscous/acoustic splitting method of Shen et al., which is based on a simulation of the incompressible flow field, can be adapted to a compressible base flow simulation. It is found that excessive artificial vorticity is generated in the wake of the cylinder due to the excitation of hydrodynamic instabilities. A new set of governing acoustic perturbation equations (APE) is proposed, which includes sources determined from a compressible flow simulation. As shown for the test problem, the occurrence of vorticity is prevented completely since the source solely excites acoustic modes in the APE.

1 Introduction

The future goal of this research is the development of computational tools to simulate turbulence related noise. The hybrid approach investigated in this paper predicts the acoustic field using a two step procedure. To motivate this approach we briefly consider the noise generated by the turbulent flow in the vicinity of a flat plate, fig. 1. In the first step, the unsteady compressible flow field in the vicinity of the sharp trailing edge is simulated via a large eddy simulation (LES) [3,8]. Fig. 1 shows a sketch of the computational domain used for the LES. Due to the large disparity in acoustic and hydrodynamic length scales, whose ratio scales inversely proportional to the Mach number, as well as energy levels [9], the demands concerning grid resolution, grid size, boundary conditions, and time steps differ for fluid and acoustic simulations. The larger acoustic length scale allows to use coarser grids for a pure acoustic simulation. Therefore, the acoustic field is computed with linearized perturbation equations in a second step using sources determined from the unsteady compressible flow field. The integration domain of the acoustic computation contains the whole plate. Hence, it allows to recognize diffraction at the leading edge and the prediction of directivities. This paper focuses on a comparison of different perturbation equations and source formulations. The laminar flow over a cylinder at a Mach *M=0.3* and a Reynolds number *Re=200* is considered as a test problem for this analysis. First, a direct numerical simulation is conducted that provides a reference solution. Subsequently, several source term formulations are applied to the cylinder flow. The results of the computation of the acoustic field are juxtaposed to evidence the characteristics of the various approaches.

2   Numerical Method

2.1 Discretization of the linearized perturbation equations

The aeroacoustic computations are based on linearized perturbation equations, which can be written including a source term S for a non-uniform flow in Cartesian coordinates (x_1, x_2)

$$\frac{\partial \mathbf{U}}{\partial t} + \mathbf{A}_i \frac{\partial \mathbf{U}}{\partial x_i} + \mathbf{B} \cdot \mathbf{U} = \mathbf{S}, \tag{1}$$

where U is the vector of the primitive variables of the perturbation quantities. Einstein's summation convention is to be applied to the products with equal indices. To use body fitted grids the governing equations are transformed to generalized curvilinear coordinates (ξ_1, ξ_2)

$$\frac{\partial \mathbf{U}}{\partial t} + \hat{\mathbf{A}}_i \frac{\partial \mathbf{U}}{\partial \xi_i} + \mathbf{B} \cdot \mathbf{U} = \mathbf{S} \qquad \text{with} \qquad \hat{\mathbf{A}}_i = \mathbf{A}_j \frac{\partial \xi_i}{\partial x_j}. \tag{2}$$

For the spatial discretization of eq. (2) the fourth-order dispersion relation preserving (DRP) scheme of Tam and Webb [10] is used. This scheme is designed such that for a wide range of wavenumbers the dispersion relations of the numerical scheme matches the physical dispersion relations. A first derivative with respect to a curvilinear direction ξ_1 is calculated for a quantity $f_{l,m}$ at mesh point l,m with a seven point stencil via

$$\left(\frac{\partial f}{\partial \xi_i} \right)_{l,m} = \sum_{j=-3}^{3} a_j f_{l+j,m.}$$

Appropriate coefficients a_j of the DRP-scheme minimize the difference between the physical and numerical dispersion relation over a chosen range of wavelengths and frequencies. In order to achieve fourth-order accuracy six of the coefficient are determined by constraints following from a Taylor series expansion around point l,m, while the one remaining can be used to minimize the dispersive error. The DRP-scheme yields a resolution of about 5.4 points per wavelength (PPW), while a central difference scheme of second order yields the same resolution limit with 20 PPW, therefore for 3D-applications the number of points can be reduced approximatly two orders of magnitude, compared to mainstream CFD spatial discretization methods.

Close to boundaries one-sided stencils are used. The integration in time is carried out with the fourth-order alternating two-step low dissipation and low dispersion Runge-Kutta scheme (LDDRK 5-6) proposed by Hu [11]. To suppress spurious high frequency waves artificial selective damping (ASD) according to Tam and Dong [13] has been used. The ASD is given as an additional source term $S_{l,m}$ in eq. (1) by

$$\mathbf{S}_{l,m} = -\frac{1}{\Delta_{\xi_1} \operatorname{Re}_\Delta} \sum_{j=-3}^{3} d_j \mathbf{U}_{l+j,m}^n - \frac{1}{\Delta_{\xi_2} \operatorname{Re}_\Delta} \sum_{j=-3}^{3} d_i \mathbf{U}_{l,m+i}^n, \; \Delta_{\xi_i} = \sqrt{\left(\frac{\partial x_1}{\partial \xi_i}\right)^2 + \left(\frac{\partial x_2}{\partial \xi_i}\right)^2},$$

where Re_Δ is the mesh Reynolds numer. The coordinates x_i are nondimensionalized with a reference length. The scaling of the damping with the grid size is chosen such that the magnitude of the mesh Reynolds number is nearly constant for a homogeneous damping effect on a mesh with variable cell size. A constant background value of the mesh Reynolds number with a typical value of $1/\operatorname{Re}_\Delta = 0.05$ and a slight increase close to boundaries is used. The damping term provides a wavenumber dependent damping such that long waves with scaled wavenumbers ≤ 1 are nearly unaffected.

3   Governing acoustic equations

3.1 Viscous/Acoustic Splitting Methods

The first formulation examined in this paper is based on the viscous/acoustic splitting technique first proposed by Hardin and Pope [14,15] later modified by Shen and Sorensen [16,17].Using Cartesian tensor notations the governing acoustic equations read

$$\frac{\partial \rho'}{\partial t} + \frac{\partial f_i}{\partial x_i} = 0,$$

$$\frac{\partial f_i}{\partial t} + \frac{\partial}{\partial x_j}\left[f_i\left(U_j + u'_j \right) + \rho_\infty U_i u'_j + p'\delta_{ij} \right] = 0, \qquad (3)$$

$$\frac{\partial p'}{\partial t} - c^2 \frac{\partial \rho'}{\partial t} = -\frac{\partial P}{\partial t}$$

with $f_i = \rho u'_i + \rho' U_i$. In these equations the flow variables are decomposed into incompressible and compressible primed perturbation variables

$$u_i = U_i + u'_i, \quad p = P + p', \quad \rho = \rho_\infty + \rho'.$$

The equations (3) are derived by introducing the decomposition of the flow variables into the Navier-Stokes and the continuity equation and by subtracting the governing equations for incompressible flow. Furthermore, the difference between compressible and incompressible viscous terms is neglected. As explained in section 3.3 the perturbation variables describe besides acoustic quantities also vorticity fluctuations due to mean/acoustic interaction. Furthermore, the difference between compressible and incompressible viscous terms is neglected. The perturbation quantities describe acoustic as well as non-acoustic unsteady and steady quantities, which determine the difference between the compressible and incompressible solutions. The third equation in (3) follows from the second law of thermodynamics. The local time derivative is used in combination with the constraint that the initial values of p', ρ' and entropy S satisfy the second law of thermodynamics. It is assumed that the time variation of the entropy can be dropped if vortex sound is considered. The unsteady incompressible velocity U_i and pressure P follow from an incompressible flow simulation. The time derivative of the incompressible pressure in eqn. (3) is the major source term for the acoustic equations. Even when the entropy is dropped in the pressure equation the relation between pressure and density is not isentropic due to the non-vanishing right-hand side. Therefore, Hardin and Pope used a further decomposition of the density into $\rho' = \rho'' + \rho_1$, where the double primed density denotes the isentropic density fluctuation related to the single primed pressure and ρ_1 is a compressible density correction caused by the incompressible pressure fluctuations. By introducing the additional density decomposition into (3), the formulation presented by Hardin et al. [15] is obtained, where additional source terms containing ρ_1 occur on the right-hand side of the continuity and momentum equation, and the continuity equation becomes a governing equation for the isentropic density perturbation. Since this component can be directly computed from the pressure via $p' = c^2 \rho''$ it is computationally simpler to drop the additional density decomposition.

To associate the formulation of Shen et al. with the problem of sources determined from a compressible flow simulation, first the system (3) is linearized over the time averaged incompressible flow simulation and then using the governing incompressible equations is rewritten in primitive variables

$$\frac{\partial \rho'}{\partial t} + \frac{\partial}{\partial x_k}\left(\rho' \overline{U}_k + \rho_\infty u'_k \right) = 0$$

$$\frac{\partial u'_i}{\partial t} + \overline{U}_k \frac{\partial u'_i}{\partial x_k} + \left(u'_k + \frac{\rho'}{\rho_\infty}\overline{U}_k \right)\frac{\partial \overline{U}_i}{\partial x_k} + \frac{1}{\rho_\infty}\frac{\partial p'}{\partial x_i} = 0 \qquad (4)$$

$$\frac{\partial p'}{\partial t} - \overline{c}^2 \frac{\partial \rho'}{\partial t} = -\frac{\partial P}{\partial t}.$$

For the computations the time averaged mean flow of the compressible flow simulation is used instead of the incompressible mean flow quantities since their difference is $O(M^2)$ small for low Mach numbers. If the source term of the pressure equation in (4) is computed directly from the pressure of the compressible flow

simulation, the acoustic equations are excited by the acoustic pressure fluctuations contained in the compressible solution. Due to the fact that their magnitude does not decay sufficiently fast with increasing distance to the cylinder they have a strong influence on the pressure levels computed via (4). It will be checked whether a spatial Gaussian filtering of the source in eqn. (10) is sufficient to separate the important near field hydrodynamic pressure fluctuations from the artificial far field ones. This issue will be addressed in the section results and discussion.

3.2 LEE with momentum sources

The second formulation is based on the source term formulation proposed by Bailly et al. [1]. The governing equations are the linearized Euler equations (LEE) which are linearized over the time averaged compressible flow solution. The equation written in primitive variables read

$$\frac{\partial \rho'}{\partial t} + \frac{\partial}{\partial x_k}\left(\rho'\overline{u}_k + \overline{\rho}u'_k\right) = 0$$

$$\frac{\partial u'_i}{\partial t} + \overline{u}_k \frac{\partial u'_i}{\partial x_k} + \frac{1}{\overline{\rho}}\frac{\partial p}{\partial x_i} + H_i = S_i \qquad (5)$$

$$\frac{\partial p'}{\partial t} + \frac{\partial}{\partial x_k}\left(p'\overline{u}_k + \gamma\overline{p}u'_k\right) + H_p = 0.$$

The terms H_i and H_p depend linearly on the perturbation quantities, where the proportionality factors are prescribed from mean flow quantities and gradients, respectively. Thus, depending on the sign of the coefficients these terms can cause an unstable growth. These expressions are neglected by Bailly et al. [1] in order to suppress the occurrence of shear layer instabilities. Variables with a bar denote time averaged quantities. The source term of the momentum equations was determined by the major non-linear contribution, i.e.,

$$S_i = -u'_k \frac{\partial u'_i}{\partial x_k} + \overline{u'_k \frac{\partial u'_i}{\partial x_k}} \; . \qquad (6)$$

The source term excites acoustic as well as vorticity components in the LEE such that the grid resolution has to be fine enough to properly resolve the vorticity components. Thus, the advantage of reduced grid resolution allowed for the simulation of pure acoustic modes is lost. The source (6) has been used with a no-slip wall boundary condition to prevent the occurence of unphysical high velocities in the vicinity of the wall.

3.3 Acoustic perturbation equations (APE)

The third formulation is based on the following acoustic perturbation equations (APE) [2]

$$\frac{\partial \rho'}{\partial t} + \frac{\partial f_i}{\partial x_i} = 0,$$

$$\frac{\partial f_i}{\partial t} + \frac{\partial}{\partial x_j}\left[f_i\left(U_j + u_j^a\right) + \rho_\infty U_i u_j^a + p^a \delta_{ij}\right] = \rho_\infty D_I\left(\omega, u_j^a\right) + \rho_\infty D_{II}\left(\rho', p, \underline{\tau}\right) + \rho' D_{III}\left(U_j, \underline{\tau}\right) \quad (7)$$

$$\frac{\partial p^a}{\partial t} - c^2 \frac{\partial \rho'}{\partial t} = -\frac{\partial}{\partial t}\left(\rho_\infty \Phi\right) + \frac{\gamma p}{c_p}\frac{\partial S}{\partial t}$$

where $f_i = \rho u_i^a + \rho' U_i$. It is derived from the continuity and the Navier-Stokes equations without introducing any simplifications and follows from a decomposition of a general source vector of the linearized Euler equations into acoustic and non-acoustic contributions in Fourier-/Laplace transform space. This source term filtering [4] is valid under the constraint of using a uniform mean flow field in the LEE. An extension to non-uniform flow is possible similarly to the derivation of higher acoustic analogies from Lighthill's acoustic analogy. The extension of Lighthill's acoustic analogy to a precursor of Lilley's equation

by transferring convection terms from the source to the wave operator side was discussed by Ribner [7]. In a second step the velocities have to be substituted using the momentum equation in order to get a scalar wave equation. As shown in [2] convection effects can be taken into account in the perturbation equations by shifting convection terms to the left-hand side, too. Due to the fact that rather a system of equations is solved for all acoustic quantities than a scalar wave equation for one variable, the second step of substitution is not necessary. The system (7) is the result of that analysis. As a formal finding of the source term filtering the velocities are decomposed into irrotational acoustic variables u_i^a and unsteady solenoidal base flow velocities U_i, i.e.,

$$u_i = U_i + u_i^a .$$

The solenoidal velocity is computed from the vorticity $\omega = \partial u_2/\partial x_1 - \partial u_1/\partial x_2$ of the compressible flow simulation by solving the Poisson problem

$$U_1 = \frac{\partial \Psi}{\partial x_2}, \quad U_2 = -\frac{\partial \Psi}{\partial x_1}, \quad \frac{\partial^2 \Psi}{\partial x_1^2} + \frac{\partial^2 \Psi}{\partial x_2^2} = -\omega .$$

One major source term of the system (7) is given by the term $\partial/\partial t(\rho_\infty \Phi)$, where $\rho_\infty \Phi$ matches in the limit of $M \to 0$ the incompressible pressure P, as shown in [2]. Neglecting the compressible viscous terms this quantity follows from the solution of

$$\frac{\partial^2 \Phi}{\partial x_1^2} + \frac{\partial^2 \Phi}{\partial x_2^2} = 2\left(\frac{\partial^2 \Psi}{\partial x_1^2} \frac{\partial^2 \Psi}{\partial x_2^2} - \left(\frac{\partial^2 \Psi}{\partial x_1 \partial x_2} \right)^2 \right), \tag{8}$$

which corresponds to the pressure poisson equation of an incompressible flow solver. From the source term filtering it follows that the pressure is identified as acoustic variable. In general, one would expect a decomposition of the pressure into an acoustic and a non-acoustic part called *pseudo sound pressure*. Note that the d'Alembert operator of the wave equation for the pressure as variable contains as a steady state limit the Laplacian operator and the related Lighthill equation changes in this limit into a Poisson equation for the pressure. Thus, it also contains the hydrodynamic near field. Due to the properties of $\rho_\infty \Phi$, however, this quantity is interpreted as pseudo sound pressure and the pressure is decomposed accordingly into

$$p = \rho_\infty \Phi + p^a ,$$

see also fig. 15. The primed perturbation density in (7) follows from the density decomposition

$$\rho = \rho_\infty + \rho' .$$

In general, it also describes non-acoustic quantities. The terms D_I, D_{II}, D_{III} on the left-hand side of the momentum equation are vorticity sinks, which cancel the vorticity generated due to acoustic/mean interaction on the left-hand side. In the limit $M \to 0$ the eqs. (7) match the formulation of Shen et al. (3) under the same assumption that entropy fluctuations can be neglected if low Mach number vortex sound is considered. The remaining differences are the vorticity sinks on the right-hand side of (7). Since the incompressible flow simulation does not contain the vorticity due to acoustic/mean interaction the missing sink terms allow the occurrence of this vorticity contribution as part of the acoustic computation. As these vorticity components occur in principle in the compressible base flow simulation, the additional sink terms are necessary to prevent the double computation of the discussed vorticity components.

The formulations used for the computations are obtained by introducing additional simplifications into the eqs. (7). The future goal is to use the method to predict turbulence related noise, where the unsteady base flow motion is mainly related to turbulent fluctuations. Neglecting the turbulent scattering of acoustic waves it seems to be acceptable to use a time averaged base flow field. Furthermore, for small acoustic fluctuations the non-linear terms can be dropped. Each vorticity sink term suppresses the vorticity generated by a related term on the left-hand side of (7). By simultaneously dropping the relevant left- and right-hand side terms, the generation of vorticity by the perturbation equations is prevented completely paying the price of neglecting

the acoustic source contribution of the left-hand side terms, too, which can be assumed to have a small influence. From this procedure the equations used for the computations read

$$\frac{\partial \rho'}{\partial t} + \frac{\partial}{\partial x_k}\left(\rho' \overline{U}_k + \rho_\infty u_k^a\right) = 0$$

$$\frac{\partial u_i^a}{\partial t} + \frac{\partial}{\partial x_i}\left(\overline{U}_k u_k^a\right) + \frac{1}{\rho_\infty}\frac{\partial p^a}{\partial x_i} = 0 \tag{9}$$

$$\frac{\partial p^a}{\partial t} - c_\infty^2 \frac{\partial \rho'}{\partial t} = -\frac{\partial}{\partial t}\left(\rho_\infty \Phi\right).$$

4   Results and Discussion

The flow around a circular cylinder at Mach number *M=0.3* and Reynolds number *Re=200* was used as test problem to compare different formulations of perturbation equations. The direct simulation of the compressible flow was carried out using an AUSM scheme for spatial discretization. The O-grid had a radial extension of *r/d=80* cylinder diameters and a resolution of *657 x 513* grid points in the radial and circumferential direction, respectively. Fig. 2 shows the perturbation pressure obtained from the CFD simulation by subtracting the time averaged pressure field.

The acoustic computations were performed on an O-grid with *257 x 161* grid points. The pressure derivative was computed from the CFD solution using second-order central differences. One time period of the vortex shedding, non-dimensionalized with the cylinder diameter *d* and the far field sonic speed was *T=17.0*. The time period was split into 43 source time levels and during the acoustic simulation the time dependent source was computed by linearly interpolating between two adjacent source data time levels. The details of the test cases considered are given in table 1.

	Definition
Case A	Source term $-\partial p/\partial t$ from CFD, perturbation equations (4), kinematic solid wall BC
Case B	$-\langle \partial p/\partial t \rangle$, spatial filtering with $\sigma = 5.0$, perturbation equations (9), kinematic solid wall BC
Case C	$-\langle \partial p/\partial t \rangle$, spatial filtering with $\sigma = 20.0$, perturbation equations (9), kinematic s. wall BC
Case D	Source $-\partial\left(\rho_\infty \Phi\right)/\partial t$ (eqn. (8)), perturbation equations (9), kinematic solid wall BC
Case E	Source term (6), perturbation equations (5), H_i and H_p dropped, no-slip solid wall BC
Case F	Source term (6), perturbation equations (5), no-slip solid wall BC

Table 1: Descriptions of computational cases

Fig. 3 shows the computed perturbation pressure field at time level *T=200* using eqs. (4) and the pressure derivative from the compressible flow simulation (case A, table 1). Compared with fig. 2 it is obvious that the acoustic pressure levels are overpredicted by a factor of about three. Furthermore, the structure of the vortex street is visible in fig. 3 indicating that vorticity is generated through the acoustic simulation. Fig. 7 shows the vorticity for this case. Compared with the magnitudes of the CFD solution, fig. 6, the vorticity magnitude is unphysically high. Fig. 9 presents the pressure signal for case A in a receiving point *r/d=40* above the cylinder, indicating that the solution becomes unstable for *T>200*. The only source of vorticity is due to acoustic/mean interaction and this magnitude was presumed to be clearly smaller than the magnitude of the overall vorticity from the CFD solution. Obviously in conjunction with the gradients of the base flow instabilities are excited.

To prevent the occurrence of vorticity in the simulation at all the APE formulation has been used for the cases B, C, and D. For the cases B and C the source has been approximated by spatially filtering the time derivative of the pressure to circumvent the excitation of spurious acoustic signals due to the acoustic signals

contained in the compressible flow simulation. A Gaussian filter kernel was used to separate the important near field hydrodynamic sources from the far-field acoustic signals, i.e.

$$\frac{\partial}{\partial t}\left(\rho_\infty \Phi\right) \approx \left\langle \frac{\partial p}{\partial t} \right\rangle = \frac{\partial p}{\partial t} \exp\left(-\frac{(r-r_0)^2}{\sigma^2}\right). \tag{10}$$

Fig. 8 shows the magnitude of the vorticity obtained for case B. It is clearly visible that no vorticity occurs in the acoustic simulation but a small amount due to the boundary condition is visible in the vicinity of the cylinder. No vortex structures in the wake of the cylinder appear for cases B and C, figs. 4 and 5, respectively. Case C was computed using a large filter width of $\sigma = 20.0$ in (10). Fig. 5 shows that the acoustic pressure is still about three times too large. For a small filter width $\sigma = 5.0$ the magnitude of the acoustic pressure and the lobes tilted in the flow direction agree fairly well with the CFD solution. Nevertheless, in the CFD solution in fig. 2 a modulation of the pressure waves is evident in the upper and lower area downstream the cylinder. As indicated by the direct simulation of Hatakeyama [6] for the cylinder problem using a high order compact finite difference scheme, according to the cases B and C no secondary lobes do occur. Thus, it is fair to assume that the low order scheme used for the direct simulation might fail to resolve the acoustic field properly. Fig. 10 depicts the perturbation pressure of the CFD simulation along the intersection line $X=0$ for different time levels T during one period of vortex shedding. A modulation of the pressure distribution is visible such that no common envelope can be identified in the figure. Furthermore, the decay of the pressure is smaller than $\propto r^{-1/2}$, pointing out the difficulties to resolve the acoustic field with common CFD tools.

Fig. 11 shows results of the various formulations described in table 1 for the decay of the pressure amplitudes. The curve related to case E is computed using the system (5) without the terms H_i and H_p. It is clear from fig. 11 that the acoustic pressure levels are underpredicted. Using the term H_i and H_p, case F, a large increase of the vorticity magnitudes in the computational solution is observed and the acoustic pressure levels are overpredicted. The result of case B and case D are computed applying the APE formulation. Case D is computed with the source according to eqn. (8), therefore the generation of spurious acoustic/acoustic signals is completely prevented. Case B is computed using a small filter width. The magnitudes of the pressure amplitudes are slightly smaller for case D, indicating that even with small spatial filter width used in case B still spurious acoustic signals are excited. The magnitudes of the pressure amplitudes of case B and D seem to be reasonable, compared with fig. 10. The directivity computed for the first harmonic frequency for case B is shown in fig. 12. Due to the mean flow the two lobes are tilted in the upstream direction. The result is compared with an analytical result for a 2D dipole in constant mean flow according to Guo [5]. The direction of the highest pressure amplitude follows to be $\theta \approx \pm 115^o$, which agrees fairly well with the computational result. Fig. 13 shows the decay of the effective pressure value for case B. In agreement with the asymptotic behavior of the 2D Green function, the pressure level decay is proportional to the power of –1/2.
Fig. 14 shows a contour plot of the pressure field for case D. Pressure levels as well as directivity agree quantitatively with the CFD solution in fig. 2.

5   Conclusion

Different formulations for a hybrid two step CFD/CAA approach have been investigated. As a 2D test case a laminar flow over a cylinder at Mach number 0.3 and Reynolds number 200 has been used. It was found that small vorticity sources due to acoustic/mean flow interaction in conjunction with a non-uniform mean flow are sufficient to generate excessive artificial vorticity in the acoustic solution. The generation of vorticity during the acoustic simulation can be successfully prevented when acoustic sources are used that solely excite acoustic modes in the governing equations. The evaluation of sources based on pressure derivatives from a compressible flow simulation yields large errors in the computed acoustic pressure levels due to the excitation of acoustic signals from acoustic signals contained in the CFD solution. The amplitude of the CAA computed acoustic signals could be reduced to a meaningful level if the acoustic source was spatially filtered in the vicinity of the cylinder to separate the essential hydrodynamic near field from the acoustic far field. An acoustic source has been computed using the vorticity of the compressible flow simulation. The occurrence of acoustic/acoustic generated spurious signals is suppressed completely. Applying this source the pressure magnitudes, the directivity of the computed sound field, and the decay of the pressure with increasing distance to the cylinder are reasonable.
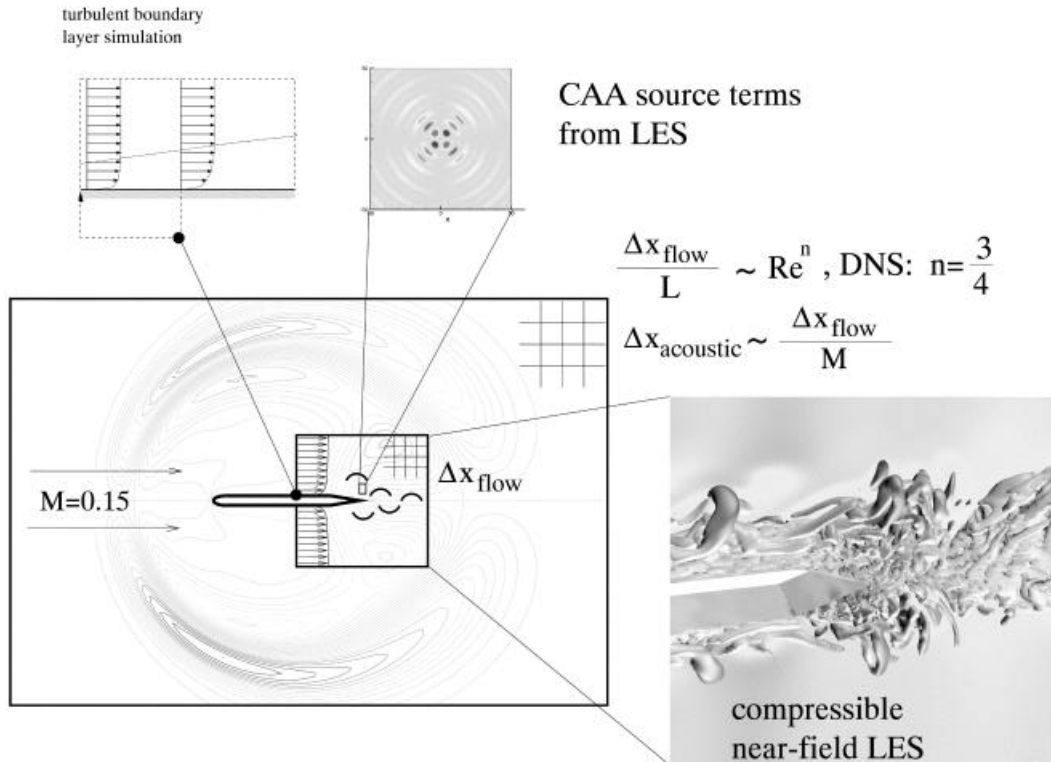
6 Figures

Fig. 1: Sketch of the computational domains to compute trailing edge noise with the hybrid approach; the CFD simulation resolves the vicinity of the trailing edge whereas the computational aeroacoustics (CAA) domain includes the whole airfoil section due to the less stringent demands concerning grid resolution thereby allowing to recognize scattering at the leading edge and the prediction of directivities
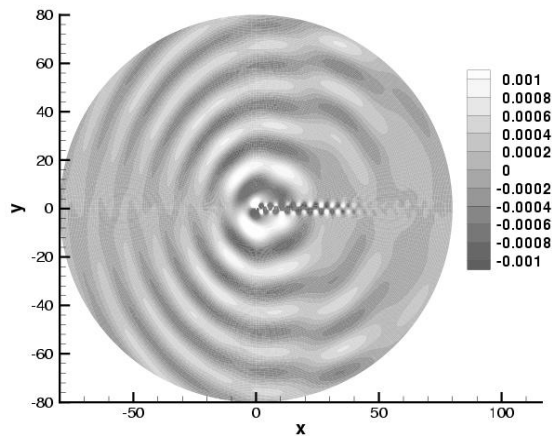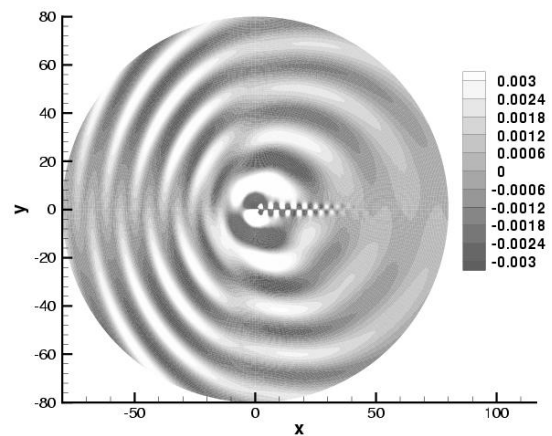

Fig 2: Perturbation pressure from the unsteady CFD simulation

Fig. 3: Pressure from the CAA solution at time level T=200, Case A, tab. 1
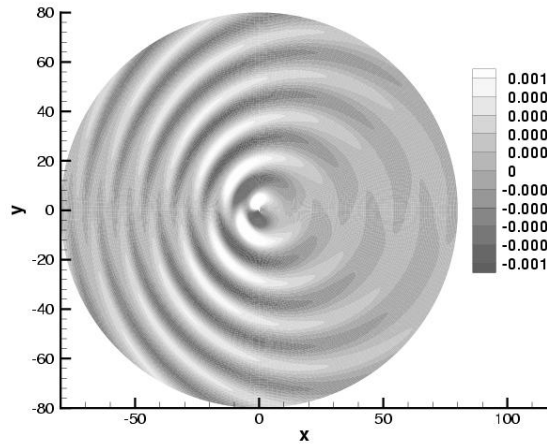
Fig. 4: Pressure from the CAA solution at time level *T=200,* Case B, tab. 1
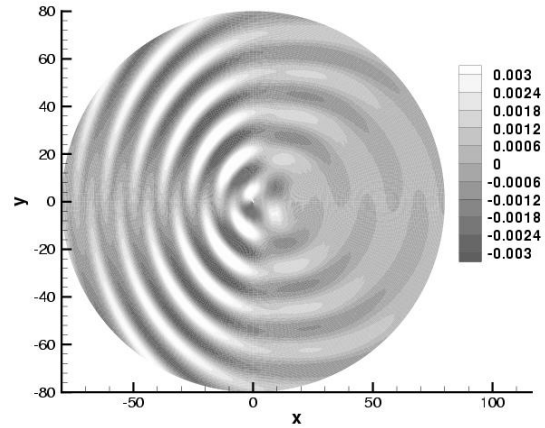
Fig. 5: Pressure from the CAA solution at time level *T=200,* Case C, tab. 1
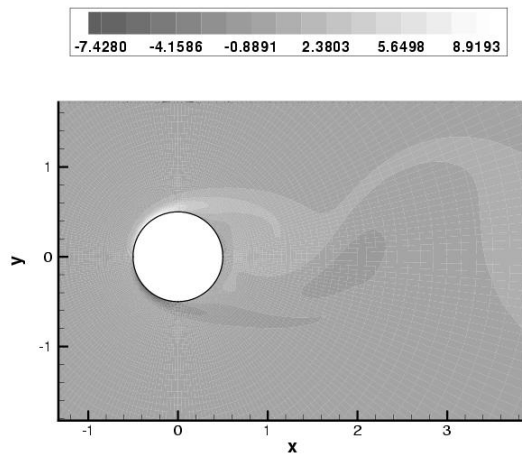
Fig. 6: Snapshot of the vorticity levels of the CFD solution
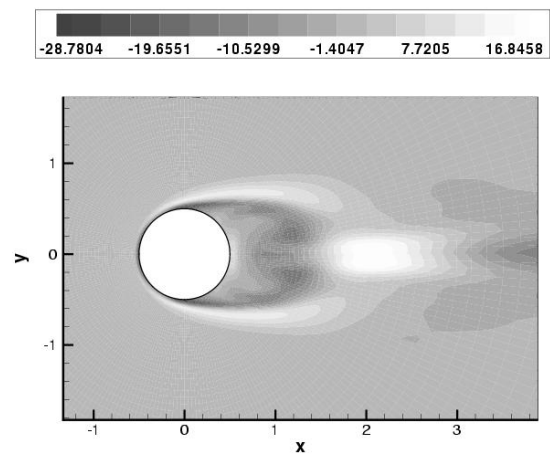
Fig. 7: Vorticity at time level T=200, CÁA Solution Case A
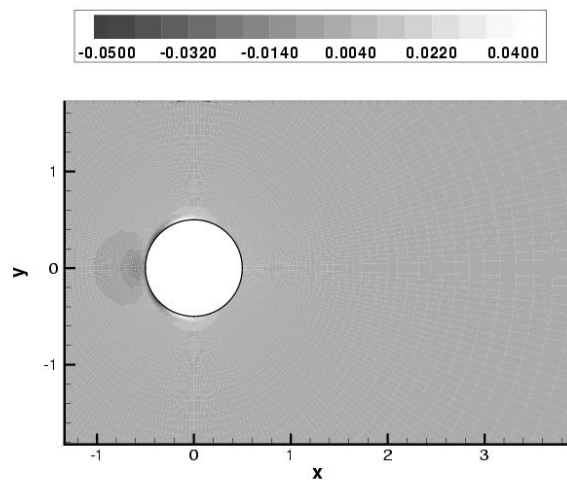
Fig. 8: Vorticity at time level T=200, CAA solution Case B
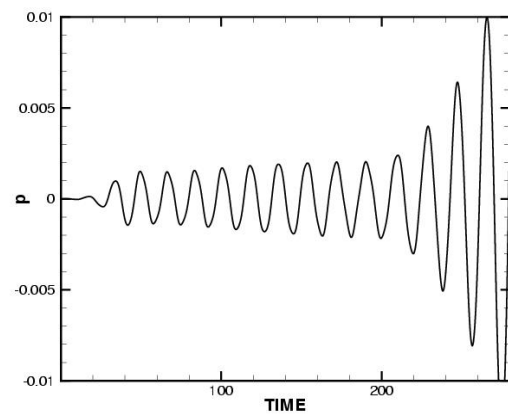
Fig. 9: Unstable pressure signal for a point at r/d=40 above the cylinder, Case A
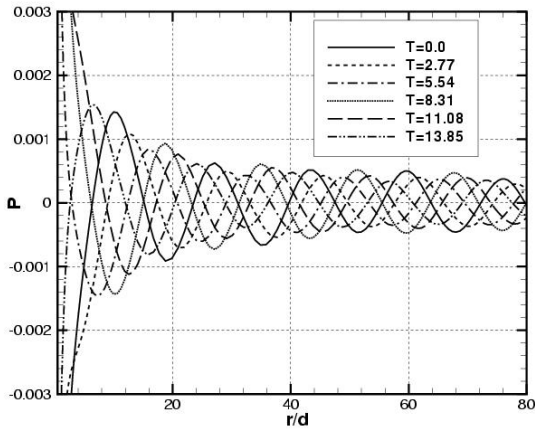
Fig. 10: Perturbation pressure from the unsteady CFD solution along line X=0
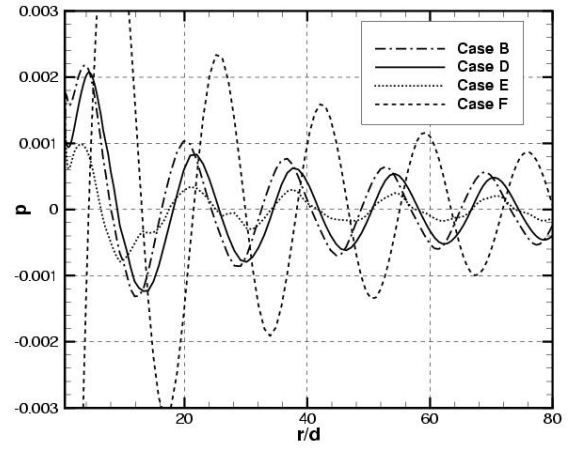
Fig. 11: Perturbation pressure on the intersection line X=0, CAA solutions
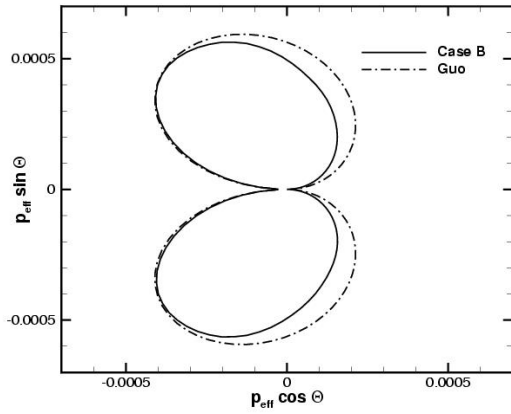
Fig. 12: Directivity for the first harmonic frequency
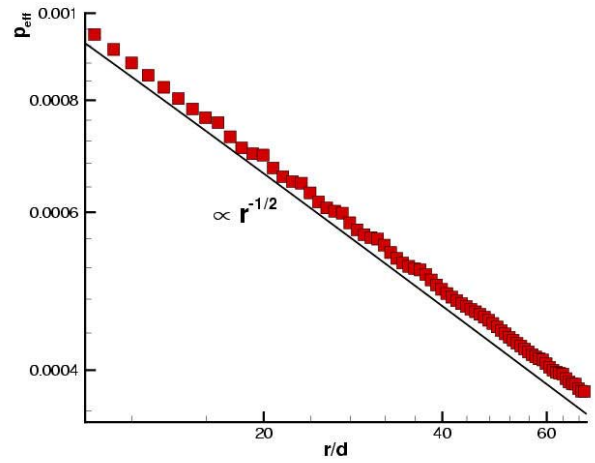
Fig. 13: Decay of the sound pressure perpendicular to the mean flow direction, Case B
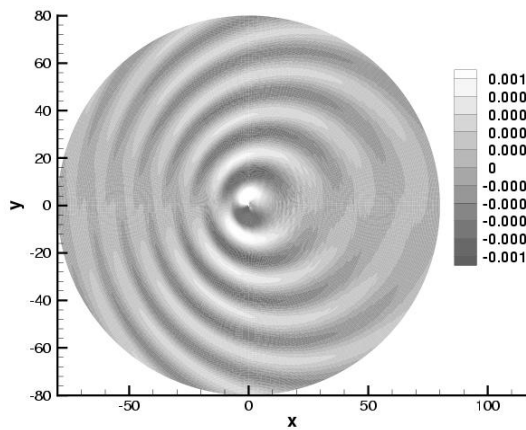
Fig. 14: Pressure from the CAA solution, source term $-\rho_\infty \partial\Phi/\partial t$, eqn. (8) (Case D)
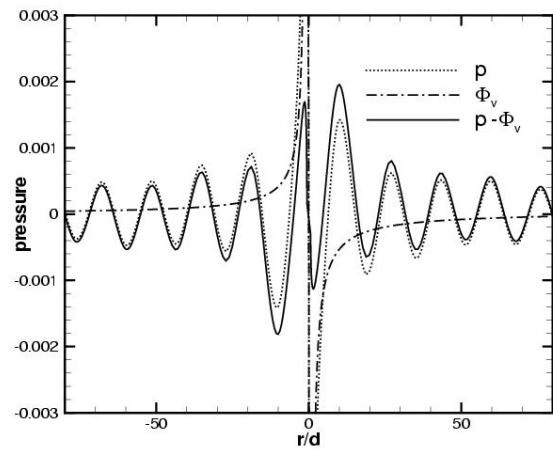
Fig. 15: Decomposition of the pressure with the pseudo sound pressure $\rho_\infty \Phi$ for a line X=0

Acknowledgments

References

[1] C. Bailly, C. Bogey, and D. Juve. Computation of the flow noise using source terms in linearized Euler´s equations. 2000. AIAA Paper 2000-2047.

[2] R. Ewert, M. Meinke, W. Schröder. Comparison of Source Term Formulations for a Hybrid CFD/CAA Method. AIAA Paper 2001-2200, 2001.

[3] R. Ewert, W. El-Askary, M. Meinke, W. Schröder. Computation of turbulence related noise on the basis of large-eddy simulation. In H. Koerner, W. Delfs, editors, *Second Aeroacoustic Workshop*, 2001.

[4] R. Ewert, M. Meinke, W. Schröder. Aeroacoustic source terms for the linearized Euler equations. AIAA Paper 2000-2046, 2000.

[5] Y. P. Guo. Application of the Ffowcs Williams/Hawkings equation to two dimensional problems. J.Fluid Mech. 403, pp 201-221, 2000.

[6] N. Hatakeyama, H. Hosoy, O. Inoue. DNS of Sound generated by Cylinder Wakes. Computational Fluid Dynamics 2000. N. Satofuka (Ed.). Springer 2001.

[7] H. S. Ribner. Perspectives on jet noise. AIAA Paper 81-0428. 1981.

[8] W. Schröder, M. Meinke, R. Ewert, W.A. El-Askary. LES of a turbulent flow around a sharp trailing edge. Proc. Workshop on Direct and Large Eddy Simulation IV, July 18-21, 2001, Kluwer Academic Publishers.

[9] S. Sarkar, M.Y. Hussaini. Computation of the acoustic radiation from bounded homogeneous flows. In J.C. Hardin, M.Y. Hussaini, editors, *Computational Aeroacoustics*, pages 335-349. Springer, 1993.

[10] C. Tam, J. Webb. Dispersion-relation-preserving finite difference schemes for computational acoustics. J. Comput. Phys., 107, pp. 262-281, 1993.

[11] F. Q. Hu, M.Y. Hussaini, J.L. Manthey. Low-dissipation and low-dispersion Runge-Kutta schemes for computational acoustics. J. Comput. Phys. 124, pp 177-191, 1996.

[12] C. Tam , Z. Dong. Wall boundary condition for high-order finite-difference schemes in computational aeroacoustics. Theoretical and Computational Fluid Dynamics Vol. 6, No. 6, pp 303-322, 1994.

[13] C. Tam , Z. Dong. A study of the short wave components in computational acoustics. Journal of Comput. Acoustics, Vol. 1, No. 1, pp 1-30, 1993.

[14] J.C. Hardin, D.S. Pope. Sound generation by flow over a two-dimensiona l cavity. AIAA Journal 33/6, pp 407-412, 1995.

[15] J.C. Hardin, D.S. Pope. An acoustic/viscous splitting technique for computational aeroacoustics. Theoret. Comput. Fluid Dynamics 6, pp. 323-340, 1994.

[16] W.Z. Shen, J.N. Sorensen. Aeroacoustic modelling of low-speed flows. Theoret. Comput. Fluid Dynamics 13, pp. 271-289, 1999.

[17] W.Z. Shen, J.N. Sorensen. Comment on the aeroacoustic formulation of Hardin and Pope. AIAA Journal 37, pp. 141-143, 1999.

This page has been deliberately left blank

_____

Page intentionnellement blanche

Numerical Prediction of the Unsteady Flow and Radiated Noise from a 3D Lifting Airfoil

E. Manoha, S. Redonnet, C. Delahay
P. Sagaut, I. Mary
Department of Computational Fluid Dynamics
and Aeroacoustics
ONERA, BP 72, 92322 Châtillon, France
eric.manoha@onera.fr

S. Ben Khelil, P. Guillen
Department of Applied Aerodynamics
ONERA, BP 72, 92322 Châtillon, France
eric.manoha@onera.fr

ABSTRACT

The numerical prediction of the aerodynamic noise radiated by an isolated airfoil is performed using a Computational AeroAcoustics (CAA) method. This hybrid method combines (i) a simulation of the nearfield unsteady flow and (ii) an acoustic method to estimate the noise radiated in the far field. This process is applied to a symmetrical NACA0012 airfoil with a constant section and a blunted trailing edge (TE), at a Mach number of 0.205 and an angle-of-attack of 5°. The Reynolds number based on the airfoil chord is 2.86 millions. The computational domain has a spanwise extent representing 3.3 % of the chord.

The nearfield unsteady flow around the airfoil is computed via a compressible three-dimensional Large Eddy Simulation (LES). This flow exhibits a superimposed pressure fluctuation field which presents the qualitative and quantitative features of the TE noise generated by the acoustic scattering of (i) the turbulent boundary layers convected on both airfoil sides (broad-band noise) and (ii) the alternated vortex shedding generated by the TE bluntness (narrow band component). Due to the strong stretching of the LES computational grid, which acts as an acoustic low-pass frequency filter, this acoustic field cannot radiate farther than a half-chord from the body.

Consequently, the LES must be relayed by an acoustic propagation method to correctly simulate the farfield noise. The most readily available methods are integral techniques which only need data on a control surface or in a control volume. A former estimation is performed via the Kirchhoff integration of pressure data on a control surface enclosing the airfoil and its wake. The position of this surface is subjected to a careful parametric study. Since very large spanwise integral lengh scales are observed on this surface, the acoustic field is assumed two-dimensional there, leading to interesting qualitative results but overestimated noise levels. On the other hand, wall pressure spanwise integral lengh scales reasonably match experimental values, suggesting to use the Ffowcs Williams-Hawkings integration of wall pressure data. This method provides farfield noise levels which agrees well with experimental data.

Both methods assume that the mean flow is uniform outside the control surface, which slightly distorts the solution since the actual flow is non-homogeneous. In order to avoid such distorsion, one can resort to a numerical method based on discretized linearized Euler equations (LEE) in which the total field is splitted into a mean flow and a pertubation field. The E3P code (Propagation of small perturbations using Euler equations) is currently developed for that purpose. The present paper shows its application to several complex acoustic scattering problems, then it shows how this code could be coupled to LES calculation on a two-dimensional interface.

NOTATIONS

a_0	:	sound celerity in the fluid at rest,
Δ	:	characteristic length scale,
$\overline{F_j}$	:	inviscid fluxes,
$\overline{F_j^v}$	:	viscous fluxes,
f_{θ_0}	:	selective function $f_{\theta_0}(\theta)$,
Φ	:	wavenumber-frequency spectrum $\Phi(k,\omega)$,
H	:	trailing edge thickness,
k	:	wavenumber,
κ	:	local instantaneous fluid thermal conductivity,
κ_0	:	thermal conductivity of the fluid at rest,
K_c	:	small scale kinetic energy,
λ_a	:	Acoustic wavelength $\lambda_a = \omega/c_o$,
M_0	:	flow Mach number $M_0 = U_0/a_0$, $M_0^2 = U_0^2/\gamma R T_0$,
μ	:	local instantaneous dynamic fluid viscosity,
μ_0	:	dynamic viscosity of the fluid at rest,
μ_t	:	turbulent dynamic viscosity,
$\vec{n}$	:	unit vector normal to S, oriented towards outside,
ω	:	frequency,
p	:	local instantaneous pressure in the flow,
p_0	:	pressure of the fluid at rest,
p'	:	pressure fluctuation, identified with acoustic pressure in the far field $p' = p - p_0$,
$\overline{Q_c}$	:	conservative flow variable,
ρ	:	local instantaneous density in the flow,
ρ_0	:	density of the fluid at rest,
ρ'	:	density fluctuation in the flow $\rho' = \rho - \rho_0$,
P_r	:	Prandtl number $P_r = \mu_0 C_p/\kappa_0$
R_e	:	Reynolds number $R_e = \rho_0 U_0 C/\mu_0$,
S_{ij}	:	filtered shear stress tensor $S_{ij}(\tilde{u})$,
S	:	Kirchhoff integration surface,
TE	:	trailing edge,

TBL　:　turbulent boundary layer,

$\vec{X}$　:　observer location in the airfoil framework,

$\vec{Y}$　:　source location in the airfoil framework,

t　:　reception time,

τ　:　emission time,

T　:　local instantaneous fluid temperature,

T_0　:　temperature of the fluid at rest,

$\vec{u}$　:　local instantaneous fluid velocity,

U_0　:　upstream flow velocity,

U_e　:　local mean flow velocity outside the boundary layer.

INTRODUCTION

The aerodynamic noise generated by the high lift devices - HLD, slats and flaps - of large airliners is an important contributor to the total radiated airframe noise, especially in approach configuration. It is widely admitted that this noise source will have to be reduced for the next generation of aircraft to meet the incoming strengthened noise regulations in the vicinity of airports. This goal will be reached by the design of new HLD concepts incorporating specific noise reduction devices. Although experiment will still play an important role in the design of such devices, it is thought that significant results will be obtained, with lower costs and shorter delays, from the numerical simulation, particularly considering the spectacular continuing progress of Computational AeroAcoustics (CAA) applications.

At the present time, the problem of the numerical simulation of HLD noise is still beyond the capabilities of complete Direct Numerical Simulation (DNS). It is most likely that, in the next future, only hybrid methods, in which the nearfield turbulent flow and the farfield noise are computed separately, will be able to solve complex aeroacoustic problems involving HLD.

Several Computational Fluid Dynamics (CFD) techniques are used in CAA hybrid methods. The less computationally expensive methods are based on steady Reynolds-Averaged Navier-Stokes (RANS) computations, in conjonction with stochastic models of the wavenumber-frequency spectrum of the turbulence [1]. RANS methods are also used to compute unsteady flows around airfoils for aeroacoustic predictions [2,3], but Large Eddy Simulation (LES) is often considered as one of the most promising method in the context of CAA applied to HLD noise [4,5,6].

On the other hand, a large panel of acoustic techniques, with various complexity and capabilities, can be used for the prediction of farfield noise. The most practical formulations belong to the family of integral methods such as (i) acoustic analogies, including Lighthill's analogy [5,7] and the Ffowcs Williams-Hawkings (FW-H) equation [2,3,8], (ii) the Boundary Element Method (BEM) [9] and (iii) the Kirchhoff integration method.

Most integral methods assume that, beyond a given distance from the noise sources and body surfaces, the sound propagates in a medium at rest, or moving with uniform velocity. This assumption may become a strong limitation, especially when the radiated noise results from a surface integration on a control surface which is located near solid walls where velocity gradients are significant. In that case, only the discretized LEE, the equations governing the acoustic propagation, may account for the propagation in non-homogeneous flows. Although Euler

equations have been widely used in CFD applications in the past, this know-how is of little help for acoustic simulation, since higher order schemes are needed to ensure numerical accuracy and low dispersion of acoustic waves [10]. At the present time hybrid CAA methods combining unsteady CFD and discretized LEE have only been applied to free field flows like jets and mixing layers, for which cartesian grids make computations particularly convenient. Their application to realistic geometries including airfoils needs curvilinear grids [11,12] on which the use of high order finite difference schemes is not straightforward.

First CAA studies at ONERA focused on trailing edge (TE) noise of isolated airfoils, a basic aeroacoustic mechanism which is present in complex HLD geometries. In an former study [5], only the uncompressible unsteady flow at the vicinity of the TE was simulated via LES, which was valid since aeroacoustic sources of such an airfoil are known to be concentrated in this region. For this purpose, the TE was modelled by a thick flat plate with an imposed mean velocity profile of a realistic boundary layer on each side. This simplification was also governed by the capabilities of PEGASE, the used LES code which only handled cartesian meshes. Then the radiated noise was obtained using the formulation Ffowcs Williams-Hall [13] based on Lighthill's acoustic analogy and the acoustic Green's function of an infinite half-plane (an approach that has been recently followed by Wang [6]). Despite encouraging results, this exploratory study presented two major weaknesses since (i) the exact airfoil shape was not correctly taken into account in the mechanism of acoustic diffraction of quadrupolar sources and, (ii) the flow simulation did not comprise the whole airfoil.

In a more recent study [9], point (i) was addressed by the use of an innovative acoustic method, also based on Lighthill's acoustic analogy, but associated to a Boundary Element Method to compute the exact acoustic Green's function of the studied airfoil. The method was restricted to cylindrical infinite surfaces with constant sections, for which the determination of the 3D acoustic Green's function is narrowed to a much simpler 2D problem and to acoustic radiation in far field. The application of this method to more realistic airfoil shapes (a NACA 0012 symmetrical profile and a high lift wing section with slat and flap), but with non-realistic unsteady flows, showed that, as long as the unsteady three-dimensional flow is known in the vicinity of a scattering surface of any shape, the resulting radiated noise can be predicted. Consequently, this method is particularly attractive when the turbulent flow is computed, for example by using LES, in a domain which covers only a small fraction of the whole rigid surface.

The present paper addresses point (ii), the objective being to perform an acoustic prediction based on the LES of the unsteady flow around a 3D lifting airfoil with a blunted TE.

The paper is organized as follows. The first part of the paper is devoted to the unsteady flow simulation via LES. The theoretical background of LES and its implementation in an in-house industrial CFD software are described. Then the airfoil geometry and the computational grid are presented, as well as the numerical procedure and storage method. A few basic aerodynamic results are given at the end of this part.

In the second part, the pressure field computed via LES near the airfoil is analyzed in details. It exhibits the qualitative and quantitative features of an acoustic field noise, generated by the acoustic scattering at the airfoil TE of (i) the turbulent boundary layers convected on both sides (broad-band noise) and (ii) the alternated vortex shedding generated by the TE bluntness (narrow band component). It is shown that, due to the strong

stretching of the LES computational grid, which acts as an acoustic low-pass frequency filter, this acoustic field cannot radiate farther than a half-chord from the body. Consequently, the LES must be relayed by an acoustic propagation method to correctly simulate the farfield noise. The most readily available methods are integral techniques which only need data on a control surface or in a control volume.

The third part of the paper presents a noise estimation performed via the Kirchhoff integration of pressure data on a control surface enclosing the airfoil and its wake. The position of this surface is subjected to a careful parametric study. Since very large spanwise integral lengh scales are found on this surface, the acoustic field is assumed two-dimensional there, leading to interesting qualitative results but overestimated farfield noise levels.

On the other hand, wall pressure spanwise integral lengh scales reasonably match experimental values, which suggested to use a Ffowcs Williams-Hawkings integration of wall pressure data. This application is presented in the fourth part of the paper. This method provides farfield noise levels which agrees well with experimental data.

However, both integral methods assume that the mean flow is uniform outside the control surface, which may distort the solution if the actual flow is non-homogeneous. In order to avoid such distorsion, one has to resort to a method based on discretized LEE in which the total field is splitted into a mean flow and a pertubation field. The E3P code (Propagation of small perturbations using Euler equations) is currently developed for that purpose. The fifth part of the paper shows its application to several complex acoustic scattering problems, then it shows how this code could be coupled to LES calculation on a two-dimensional interface.

LARGE EDDY SIMULATION

Code implementation

The LES method described below has been implemented in the FLU3M solver, an industrial CFD software which has been developed at ONERA for several years. This solver is based on the discretization of the compressible Navier-Stokes equations on multi-block structured meshes by a finite volume technique. A second order accurate implicit temporal integration is achieved thanks to an approximate Newton method. General informations about this solver are available in refs. [13,14].

Governing equations

Filtered Navier-Stokes equations

A dimensionless form of the Navier-Stokes equations is retained, which means that, in equations (1) to (8), the local instantaneous velocity $\vec{u}$, temperature T, density ρ, abscissa $\vec{x}$, dynamic viscosity μ and thermal conductivity κ are normalised respectively by U_0, T_0, ρ_0, C, μ_0 and κ_0.

The three-dimensional unsteady filtered Navier-Stokes equations are used for a viscous compressible Newtonian fluid. Any flow variable ϕ can be written as $\phi = \bar{\phi} + \phi'$, where $\bar{\phi}$ represents the large scale part of the variable and ϕ' its small

scale part. The filtering operator, classicaly defined as a convolution product on the computational domain [16], is assumed to commute with time and spatial derivatives. Moreover it is convenient for the clarity of the equations to introduce the Favre filtering $\tilde{\phi} = \overline{\rho\phi}/\bar{\rho}$. In conservative form, the filtered Navier-Stokes equations can be expressed in three-dimensional Cartesian coordinates (x_1, x_2, x_3) as :

$$\frac{\partial \overline{Q}_c}{\partial t} + \frac{\partial \overline{F}_j}{\partial x_i} - \frac{1}{R_e}\frac{\partial \overline{F}_j^{\,v}}{\partial x_i} = 0 \qquad (1)$$

where $\overline{Q}_c$, $\overline{F}_j$ and (assuming some approximations [17] and using Boussinesq eddy viscosity hypothesis) $\overline{F}_j^{\,v}$ are defined by :

$$\overline{Q}_c = \begin{pmatrix} \bar{\rho} \\ \bar{\rho}\tilde{u}_1 \\ \bar{\rho}\tilde{u}_2 \\ \bar{\rho}\tilde{u}_3 \\ \overline{\rho E} \end{pmatrix} \quad \overline{F}_j = \begin{pmatrix} \bar{\rho}\tilde{u}_j \\ \bar{\rho}\tilde{u}_1\tilde{u}_j + \delta_{1j}\bar{p} \\ \bar{\rho}\tilde{u}_2\tilde{u}_j + \delta_{2j}\bar{p} \\ \bar{\rho}\tilde{u}_3\tilde{u}_j + \delta_{3j}\bar{p} \\ (\overline{\rho E} + \bar{p})\tilde{u}_j \end{pmatrix} \quad \overline{F}_j^{\,v} = \begin{pmatrix} 0 \\ \bar{\sigma}_{1j} \\ \bar{\sigma}_{2j} \\ \bar{\sigma}_{3j} \\ \bar{\sigma}_{kj}\tilde{u}_k + \bar{q}_j \end{pmatrix} \quad (2)$$

where

$$\overline{\rho E} = \frac{\bar{p}}{\gamma - 1} + \frac{1}{2}\bar{\rho}\tilde{u}_j\tilde{u}_j \qquad (3)$$

$$\bar{\sigma}_{ij} = \left(\mu(\tilde{T}) + \mu_t\right)\left(\frac{\partial \tilde{u}_i}{\partial x_j} + \frac{\partial \tilde{u}_j}{\partial x_i} - \frac{2}{3}\delta_{ij}\frac{\partial \tilde{u}_k}{\partial x_k}\right) \qquad (4)$$

$$\bar{q}_j = \frac{\left(\mu(\tilde{T}) + \mu_t\right)}{P_r}\frac{\partial \tilde{T}}{\partial x_j} \qquad (5)$$

where the eddy viscosity μ_t must be expressed by a subgrid scale model. These equations are supplemented with the filtered equation of state :

$$\bar{p} = \frac{\bar{\rho}\tilde{T}}{\gamma M_0^2} \qquad (6)$$

Subgrid scale modelling

Selective mixed scale model

The selective mixed scale model, developed by Sagaut and Lenormand, has been retained, because it realizes a good compromise between accuracy, stability and computational cost [17,18]. More particularly, the use of a selective function allows to handle transitional flows [19], which is one of the keypoint of the present application.

The eddy viscosity is given by the non-linear combination :

$$\mu_t = \bar{\rho}f_{\theta_0}(\theta)C_m\Delta\sqrt{0.5 S_{ij}(\tilde{u})S_{ij}(\tilde{u})}\sqrt{K_c} \qquad (7)$$

of the filtered shear stress tensor $S_{ij}(\tilde{u})$, a characteristic length scale Δ (given by the cell volume of the mesh), the small scale kinetic energy $K_c = \sqrt{0.5(\tilde{u}_i')(\tilde{u}_i')}$, a constant parameter $C_m = 0.06$ (derived in reference [16]) and the selective function :

$$f_{\theta_0}(\theta) = \begin{cases} 1 & if\ \theta > \theta_0 = 10° \\ \tan^4(\theta/2)\big/\tan^4(\theta_0/2) & otherwise \end{cases} \qquad (8)$$

where θ is the angle between instantaneous and filtered vorticity. The test field $(\tilde{u}_i')$ is extracted from the resolved field $(\tilde{u}_i') = \tilde{u}_i - \overline{\tilde{u}_i}$, employing an averaging test filter denoted by : $\overline{\tilde{u}}_i = 0.25\tilde{u}_{i-1} + 0.5\tilde{u}_i + 0.25\tilde{u}_{i+1}$.

Numerical method

The Navier-Stokes equations are discretized using a cell-centered finite volume technique and structured multi-block meshes. The viscous fluxes are discretized by a second-order accurate centered scheme. For efficiency reason, an implicit time integration is employed to deal with the very small grid size encountered near the wall. Indeed the large disparity between the acoustic wave speed and the advection velocity at low Mach number renders explicit time integration unefficient. This is due to the fact that numerical stability considerations impose small time steps on the acoustic waves, while the physics is mainly driven by the solenoidal part of the flow, whose time scale, being associated to advection, is larger. Then a three-level backward differentiation formula is used to approximate the temporal derivative of $\overline{Q_c}$ leading to second-order accuracy. An approximate Newton method is employed to solve the non-linear problem. At each iteration of this inner process, the inversion of the linear system relies on Lower-Upper Symmetric Gauss-Seidel (LU-SGS) implicit method, originally proposed in reference [20]. More details about these numerical points are available in references [21,22].

Usually LES requires high-order centered scheme for the Euler fluxes discretization (with spectral-like resolution) in order to minimize dispersive and dissipative numerical errors. However such schemes cannot be applied easily in complex geometry. Indeed, most of aerodynamic codes able to deal with such a geometry are based on finite-volume technique in order to handle degenerated cell. Thus getting high-order method becomes very time consuming due to high-order quadrature needed to compute the fluxes along the cell boundaries. As several works (see [23] for instance) have shown that LES can be carried out with low-order centered scheme in case of sufficient mesh resolution, only second-order accurate scheme is employed in this study. But a special effort has been carried out to minimize the intrinsic dissipation of the scheme.

Thus the second order accurate hybrid upwind/centered discretisation, developped in [21], has been used in this study to achieve a good compromise between robustness and accuracy. The key point of the scheme is the use of a sensor, which allows to introduce locally some numerical dissipation when a numerical wiggle is detected on one of the primitive variables. Therefore, the effect of the SGS model is not affected by the numerical dissipation as long as odd-even decoupling is not detected in the flow solution.

Geometry, computational grid and numerical procedure

A two-dimensional (constant section in the spanwise direction) NACA 0012 airfoil with a $C = 0.6096$ m chord and a blunted TE of thickness $H = 2.5$ mm (0,4 % of the chord) has been retained for this study, with reference to the airfoil noise experiment conducted at NASA in 1980 by Brooks and Hodgson [24]. In this experiment, the airfoil had a span $S = 0.46$ m (or 75 % of the chord), whereas in the present simulation, the LES computational domain has a spanwise extent representing only 3.3 % of the chord.
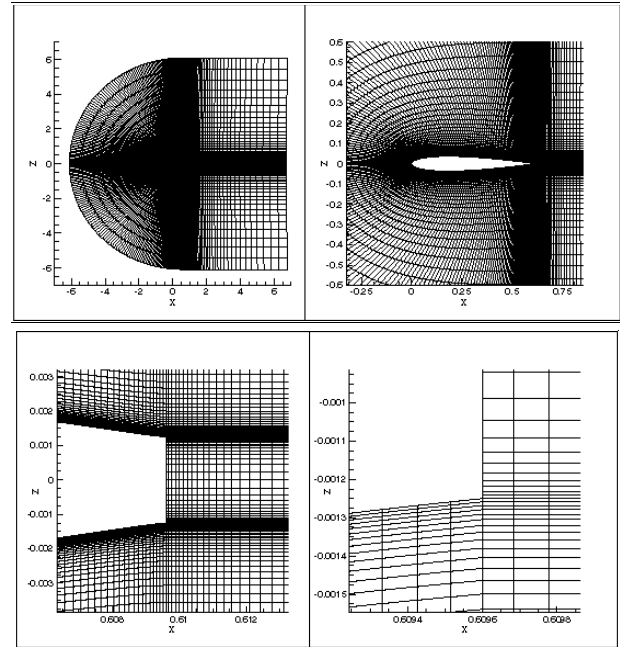
Figure 1 : Computational grid.

The upstream flow velocity is 69.45 m/s (maximal velocity in [24]), the Mach number is 0.205 and the Reynolds number based on upstream velocity and chord is 2.86 millions. The airfoil angle-of-attack with respect to the flow direction is 5°.

The 3D curvilinear computational grid is obtained by replication in the spanwise direction (y) of a 2D curvilinear structured grid made of two domains. Domain #1 is located upstream the TE (C-shape), with 309 points along the airfoil body and 97 points in the radial direction. Domain #2 is located downstream the TE, with 227 points in the (z) direction (including 35 points on the TE bluntness) and 103 points in the (x) direction. In order to minimize the influence of boundary conditions, a large computational domain is used. As shown in Figure 1, this 2D grid extents nearly 10 chords above and below the profil, as well as upstream and downstream. Regions in the vicinity of solid walls are highly refined. The whole mesh is made of 1.76 million points.

The horizontal plane $z = 0$ is a plane of symmetry. In any (x, z) plane, the smallest cells are located at the TE corners, with dimensions (in wall units) $\Delta z^+ = 1.5$ in the direction normal to the wall and $\Delta x^+ = 15$ along the chord. From the corners, the grid is streched in the streamwise direction (x) with a stretching coefficient equal to 1.06 (upstream) and 1.09 (downstream). In the (z) direction, the stretching coefficients are equal to 1.23 towards the $z = 0$ plane and 1.12 towards the grid periphery.

This 2D grid is replicated 32 times in the spanwise direction (y), with a constant step $\Delta y = 10^{-3} C$.

The mesh resolution is close to that of Weber and Ducros [22] who have shown that such resolution is sufficient to obtain reasonable results for such flows.

A no-slip condition is applied at the airfoil surface and a periodic conditon is imposed in the spanwise direction. Non-reflecting characteristic boundary conditions are applied for the far field. Moreover, a steady RANS computation using Baldwin-Lomax models provides an initial flow solution. In order to ensure the time-accuracy of the results, the physical time step is taken equal to 0.5 μs, meaning a sampling frequency of 2 MHz. An initial phase of 100,000 time steps was achieved, then the useful computation was performed over 130,000 time

steps with a total duration of 65 ms, representing the convection of the flow over 7.5 airfoil chords. The requirements of acoustic computations led to a storage of one time sample every 100, meaning a storage sampling of 20 kHz, with a useful frequency band of 10 kHz. The total computation cost was 360 CPU hours on a NEC-SX5 computer.
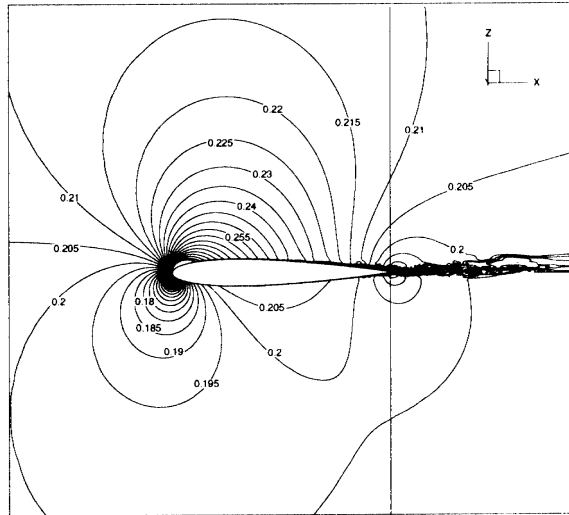

*Figure 2 : Contours of instantaneous
Mach number isovalues.*

Aerodynamic results

Figure 2 displays contours of instantaneous Mach number isovalues, showing the development of the TBLs and the wake. The transition between laminar and turbulent flows occurs at $x/C = 0.15$ on the succion side and at $x/C = 0.9$ on the pressure side. Mean velocity profiles near the TE were obtained by time-averaging instantaneous data. The integration of these velocity profiles provided TBL momentum thicknesses of $\delta_1 \approx 0.8$ mm on the pressure side and $\delta_1 \approx 1.5$ mm on the succion side. Brooks and Hodgson's [24] measurement on a similar airfoil was slightly higher ($\delta_1 \approx 3.9$ mm), which could be explained by the roughness strips of carbon random they used to artificially trip the boundary layer at x/C = 0.15.
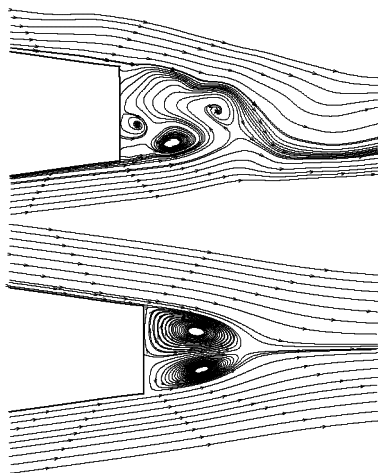
*Figure 3 : Flow streamlines at the trailing edge, instantaneous
(above) and time-averaged (below).*

It is though that the excessive slenderness of the computed TBL may be also explained by an unsufficient grid refinement in the chord direction x near the walls in the transition region. However, it will be shown in the next part that the computed flow presents general qualitative and quantitative features which makes it suitable for aeroacoustic applications.

Figure 3 shows details of the instantaneous (above) and time-averaged (below) flow streamlines around the blunted trailing edge. Time-averaged results have been favourably compared with the results of the mean flow computed separately using a RANS code.

UNSTEADY PRESSURE FIELD ANALYSIS

Surface pressure fluctuations

Time histories

Figure 4 (above) shows time histories of the wall pressure fluctuations near the TE at symmetrical points located on the pressure and succion sides. This plot exhibits a time period of 2 ms, meaning a dominant mechanism at a frequency near 5 kHz, and a clear phase opposition between both sides. This opposition is confirmed by the cross-spectrum phase between boths signals shown on Figure 4 (bottom). These features are typical of a mechanism of alternated vortex shedding at the TE.

Power spectral densities

Figure 5 shows the evolution along the chord (from the leading edge up to the TE) of the wall pressure power spectral density (0-10 kHz) on the succion side (above) and the pressure side (below). Spectra are characterized, on both airfoil sides, by a narrowband component emerging out of a wideband continuum.

Located near 4.7 kHz, the narrowband bump is due to the vortex shedding mechanism. It is perceived on the whole chord length with identical levels on both airfoil sides. It will be shown later that this component corresponds to acoustic waves generated at the TE and propagating in the upstream direction.
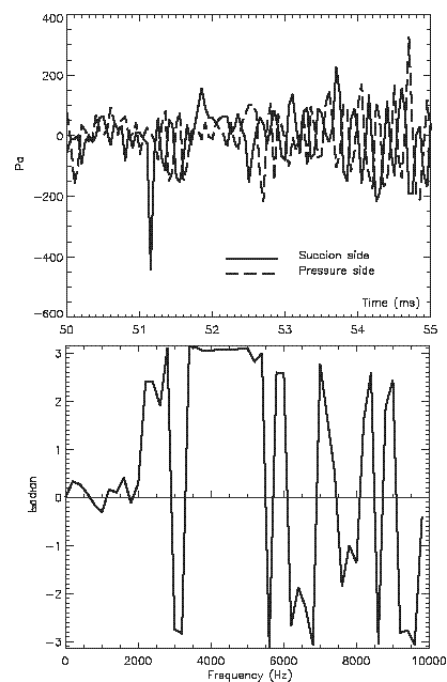
*Figure 4 : Wall pressure fluctuations
on pressure and succion sides near the TE.
Above : time histories. Below : cross-spectrum phase.*
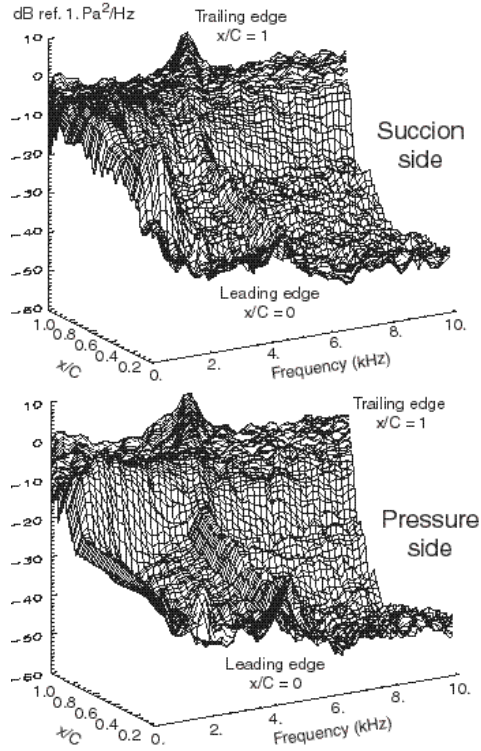
Figure 5 : Evolution of the wall pressure PSD along the chord.

The wideband continuum is generated by the convected turbulent boundary layers. Since the airfoil has a positive 5° angle-of-attack, the laminar-to-turbulent transition occurs at 15% of the chord on the suction side, and at 90% of the chord on the pressure side. From this transition point towards the TE, the boundary layer thickness grows, enriching spectra with higher frequency components. Notice that, on both airfoil sides, the vortex shedding component emerges from the continuum near the TE ($x/C > 0.98$), then is masked by the nearfield boundary layer, and finally emerges again at $x/C < 0.85$.
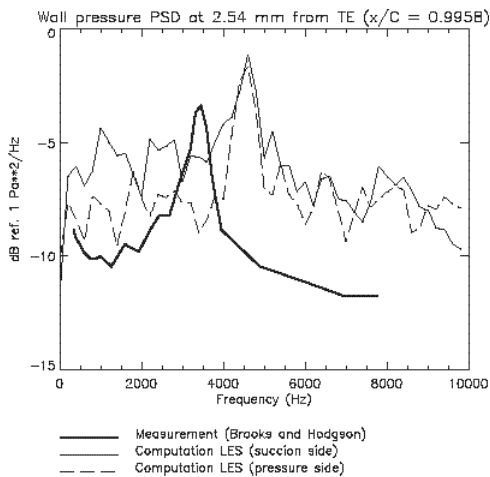
Figure 6 : Wall pressure PSD near the TE. Comparison of simulation (both airfoil sides) and experiment [24].

Comparison to experimental data

In their airfoil noise experiment (performed with same velocity, tripped TBL, but zero incidence) [24], Brooks and Hodgson measured surface pressure with arrays of pinhole sensors of diameter 0.34 mm. The closest distance between sensors and the TE was at 2.54 mm. Figure 6 compares the spectrum measured by this sensor with simulated data computed

data at the same position ($x/C = 0.9958$). The comparison is qualitatively satisfying : same narrowband component emerging by ≈ 7 dB from a wideband continuum. However, the quantitative comparison shows that predicted levels are overestimated by nearly 3 dB, and that the predicted vortex shedding frequency (4.7 kHz) is also overestimated (3.5 kHz in the experiment). Since this frequency is governed by a Strouhal number based on the wake thickness (sum of the TE thickness and TBL displacement thicknesses), this overestimation may be partly explained by the excessive slenderness of the computed turbulent boundary layer (TBL) with respect to the experimental one. However this cannot be solely explained by the absence of transition triggering in the simulation.

Wavenumber-frequency spectra

The spectral densities presented above are single-point data which do not provide any information on the propagative features of the wall pressure field. This information can be revealed by processing a discretized space-time Fourier transform of any function $p(x,t)$, providing the so-called wavenumber-frequency spectrum $\Phi(k,\omega)$. For example, a mono-dimensional wave with frequency ω_0 and velocity V_0 propagating in the x direction, say $p(x,t) = e^{i\omega_0 (t - x/V_0)}$, will appear in the (k,ω) domain as a Delta-function centered at $k = \omega_0/V_0$ and $\omega = \omega_0$. With the same process, a white noise propagating at celerity c_0 in the x direction will appear as a ridge along the $k = \omega/a_0$ line, or along the $k = -\omega/a_0$ line if the sound travels in the opposite (-x) direction.
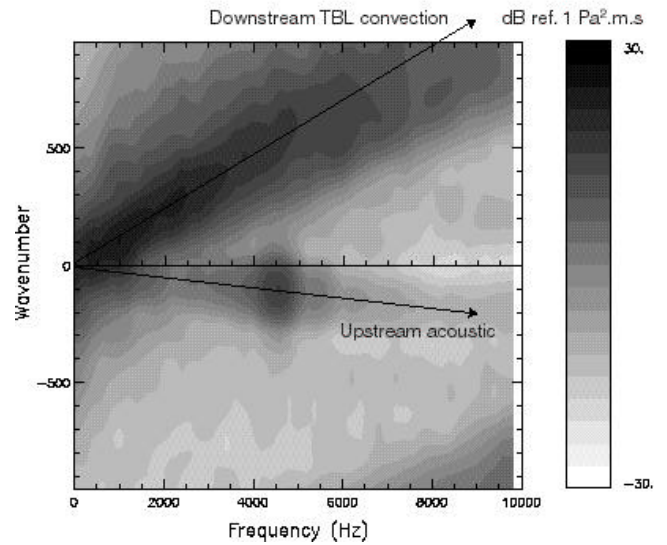
Figure 7 : Wavenumber-frequency spectrum of wall presssure fluctuations on the airfoil suction side at x/C = 0.9.

Figure 7 presents the results of this process applied to the wall pressure field computed via LES on the airfoil pressure side near the TE at $x/C = 0.9$. The wavenumber domain extent $[-\pi/\Delta x, \pi/\Delta x]$ depends on the local space sampling Δx of the pressure field, or the size of the grid cells. A wideband "convective ridge" can be observed along the $k = \omega/U_c$ line, generated by the convection, in the flow direction, of eddies inside the TBL at an average velocity U_c slightly inferior to the local mean flow velocity U_e. Another wideband component can

be observed along the $k = -\omega/(a_0 - U_e)$ corresponding to an acoustic propagation in the direction opposite to the flow, with a peak at 4.7 kHz, the vortex shedding frequency.
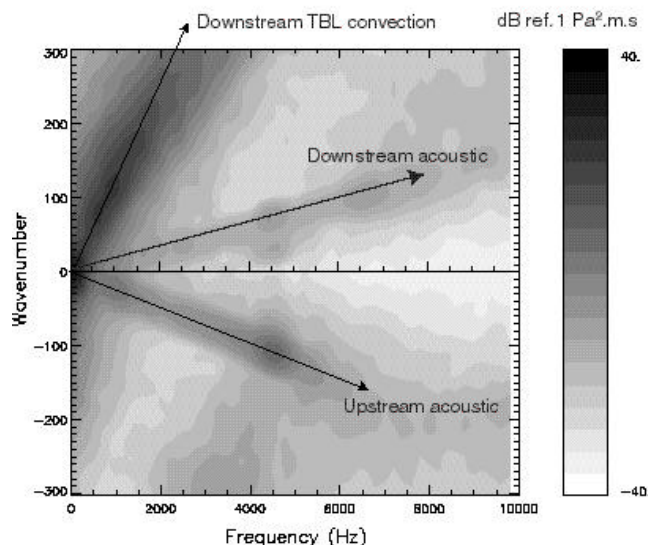
Figure 8 : Same as Figure 7 but x/C = 0.5.

Figure 8 presents the same results obtained at mid chord (*x/C* = 0.5). The convective ridge and the upstream acoustic component are again present. One interesting result is a new component $k = \omega/(a_0 + U_e)$ which corresponds to acoustic waves (also with a peak at 4.7 kHz) propagating in the flow direction (downstream), which may be generated by the diffraction, at the airfoil leading edge, of the acoustic waves propagating upstream.

Flow pressure fluctuations

Instantaneous maps of pressure fluctuations

The existence of a sound field generated at the TE, strongly suggested by the surface pressure results above, is confirmed on Figure 9 which shows instantaneous isovalues of the pressure fluctuations inside the flow. At every point of the LES grid, pressure fluctuations are computed by substracting the time-averaged pressure to the instantaneous pressure. The color table is adapted to the low values of the acoustic fluctuations (± 6 Pa) although there are much larger pressure fluctuations (up to ± 500 Pa) in the TBL and in the wake. Concentric waves are clearly observed near the TE, with a wavelength corresponding to the vortex shedding frequency 4.7 kHz which, as shown before, dominates the source spectrum by a few decibels. An animation was generated from 300 identical maps plotted for successive time steps ($\Delta t = 5.10^{-5}$ s) allowing to simultaneously visualize, with their respective celerity, the acoustic radiation in the fluid and the turbulence convection along the airfoil chord.
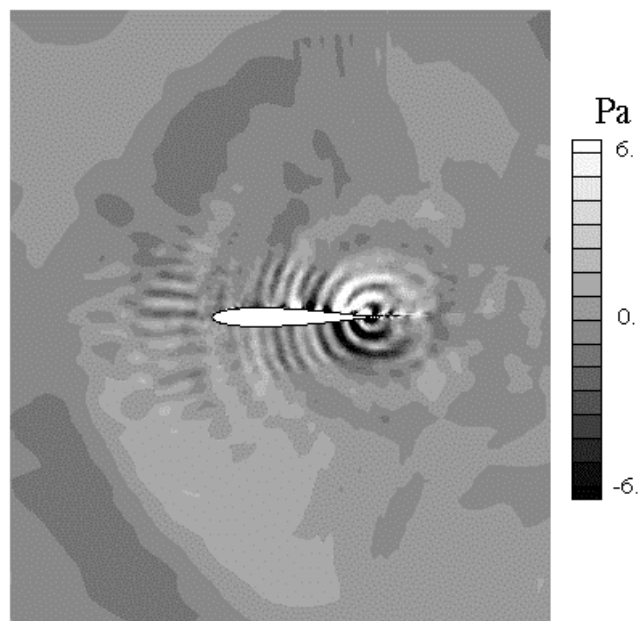
Figure 9 : Instantaneous isovalues of pressure fluctuations obtained from LES data.
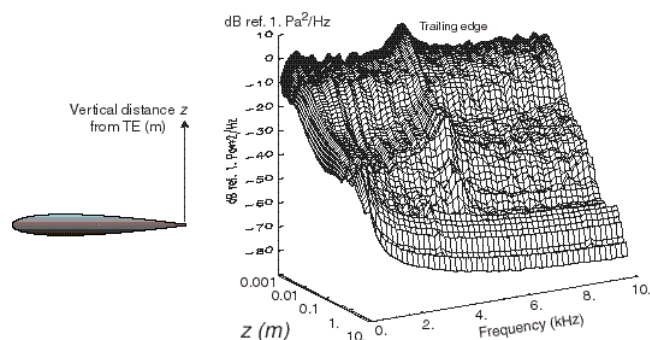
Figure 10 : Evolution of the wall pressure spectra along the vertical grid line x = C (starting from the TE upper corner) with respect to the vertical distance z.

Low-pass filtering by the CFD grid

It is interesting to notice that the wave pattern corresponding to the vortex shedding noise vanishes at a half-chord from the airfoil, when, at the same time, larger wavelength are observed much farther. This is explained by the radial stretching of the grid LES which acts on the noise field as a low-pass filter. It is known that the propagation of an acoustic wave will not be correctly simulated if it is discretized by using less than 4 or 6 cells by wavelength.

To illustrate this, Figure 10 shows the evolution of the wall pressure spectra along the vertical grid line *x* = *C* (starting from the TE upper corner) with respect to the distance from the TE (in logarithmic scale). This plot clearly shows that low frequency waves propagate much farther than high frequency waves.

Figure 11 shows the same information for several frequency bandwidths in which spectra are integrated. Each frequency bandwidth shows similar behaviour : (i) at short distance from the TE, spectra are dominated by high-level turbulence ; (ii) then there exists a domain where the pressure fluctuations decrease as $z^{-1/2}$, which is typical of a two-dimensional acoustic field ; (iii) beyond a cut-off distance the levels vanish. It was

checked that, for any frequency bandwidth, this cut-off distance corresponds to a grid location where cells become larger that a quarter acoustic wavelength.
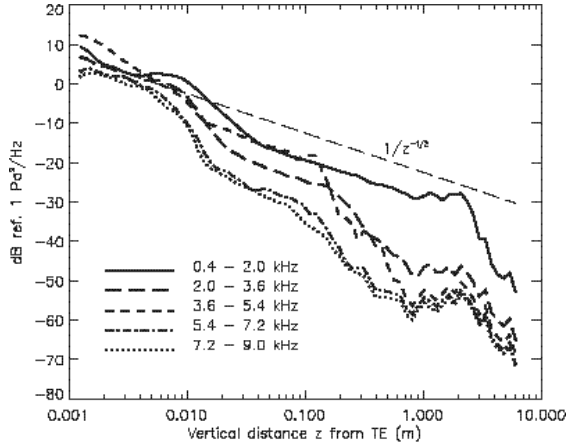
Figure 11 : Same information as in Figure 10, presented in integrated frequency bandwidths
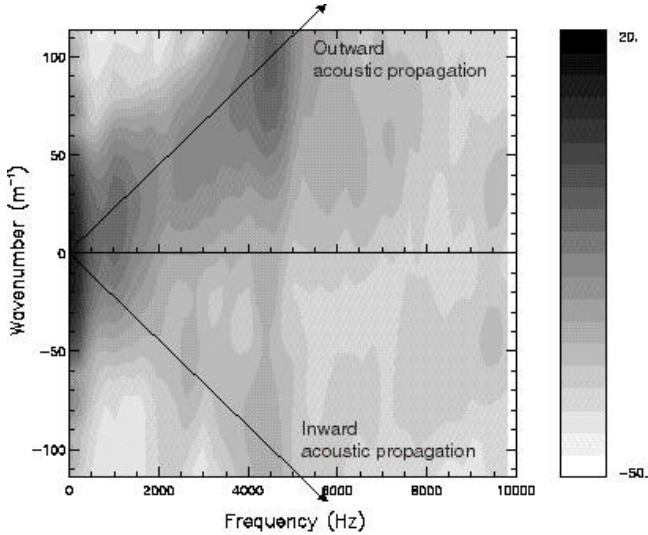

Figure 12 : Same information as in Figures 10 and 11, but presented through a wavenumber-frequency spectrum .

Figure 12 shows a wavenumber frequency spectrum computed from the LES pressure fluctuations field along the same vertical line $x = C$. The ridge located along the "acoustic line" $k = \omega/a_0$ clearly demonstrates the radiative acoustic nature of this pressure field with, again, a peak of power at the vortex shedding frequency 4.7 kHz. A much weaker component is also visible on the line $k = -\omega/a_0$ correponding to waves propagating towards the TE, but this peak lays more than 25 dB below the radiative component and may even not be physical with regards to the resolution of the process.

Spanwise coherences

Inside the TBL and the wake, turbulent structures or eddies are convected at low velocities $(< U_e)$ which means that typical spanwise lengh scales may be smaller than the spanwise extent of the LES domain, and correctly simulated. To illustrate this, Figure 13 shows the spanwise evolution of the coherence

$\gamma^2(\Delta y, f)$ of the surface pressure field near the TE in several frequency bandwidths. $\gamma^2(\Delta y, f)$ is defined as :

$$\gamma^2(\Delta y, f) = \frac{\left|S_{pp}(0, \Delta y, f)\right|^2}{\left|S_p(0, f)\right|\left|S_p(\Delta y, f)\right|} \qquad (9)$$

where $S_p(y, f)$ denotes the surface pressure spectrum at the spanwise position y and $S_{pp}(y_1, y_2, f)$ denotes the surface pressure cross spectrum between spanwise positions y_1 and y_2. The coherence rapidly vanishes at any frequency bandwidth, meaning that integral length scales are smaller than the spanwise extent of the LES domain. It can be seen that the largest length scales correspond to the vortex shedding frequency, a mechanism which significantly correlated in the spanwise direction. It should be noted that these spanwise coherences provide wall pressure spanwise integral length scales which are favorably compared to experimental values measured by Brooks and Hodgson on their NACA0012 airfoil [24].
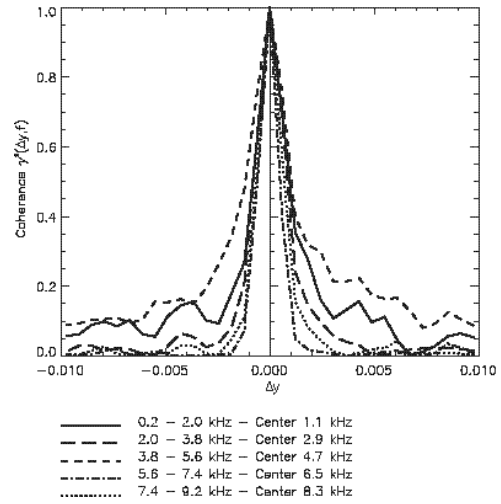
Figure 13 : Spanwise evolution of the coherence of the surface pressure field on the succion side near the TE (x/C = 0.9958). Integrated frequency bandwidths.

Figure 14 shows spanwise coherence of the pressure field above the TE on the grid line $j_0 = 54$ located at distance $z_0 = 37.9$ mm from the TE, where pressure fluctuations are expected to be mostly acoustic : as explained below, this particular grid line will be chosen for the generation of the integration surface used in the Kirchhoff prediction. Figure 14 shows that typical length scales seem to be much longer than the spanwise extent of the LES grid, especially at low frequency and the frequency of vortex shedding.

In other words, the very nearfield turbulent flow is expected to be strongly three-dimensional, whereas the acoustic field simulated at some distance of the airfoil looks two-dimensional. This result will have significant consequences in the process of spanwise replication of LES data.
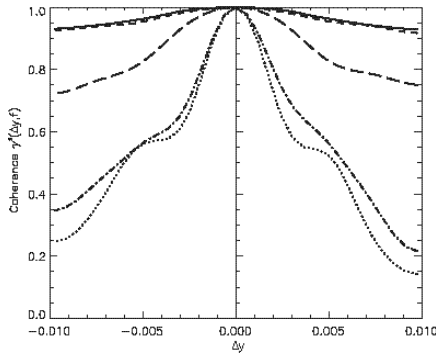
Figure 14 : Spanwise evolution of the coherence of the pressure field above the TE on the grid line $j_0 = 54$ at x/C= 1. Same integrated frequency bandwidths as Figure 14.

KIRCHHOFF ACOUSTIC PREDICTION

Introduction

The preceding results show that the compressible LES has the capacity of simulating the generation of the aeroacoustic mechanism of TE noise, including both aerodynamic sources and local radiated field. Unfortunately, due the strong grid stretching, this acoustic field rapidly collapses at rather short distance from the airfoil. As a consequence of the last part, it makes sense to find a surface, enclosing the airfoil, close enough to the body to ensure that the simulated acoustic field has not been low-pass filtered by the grid, or at least still contains the low-frequency bandwidth that we are interested in. Moreover, if this surface can be proved free of any vorticity convected by the flow, it is a perfect candidate for the application of a Kirchhoff integration.

Formulation

A 3D Kirchhoff formulation is implemented in the KIM (Kirchhoff Integration Method) code which was developed at ONERA for helicopter rotor noise prediction [25] and jet noise prediction [26]. This code provides the noise radiated by any three-dimensional surface in a flow with uniform velocity U_0 in the direction X_1, given the density (or pressure, assuming isentropy or $p' = c_0^2 \rho'$) and its normal gradient along this surface.

The formulation is [27] :

$$\rho'(\vec{X},t) = \iint f_K(\vec{X},\vec{Y},\tau) \frac{1}{4\pi d} \delta\left(t - \tau + \frac{D_{XY}}{c_0}\right) dS d\tau \qquad (10)$$

in which D_{XY} is the distance, corrected from convection effects, between the source point $\vec{Y}$, located on the integration surface, and the observer point $\vec{X}$ (both defined in a reference framework in which the surface S is at rest) :

$$\begin{cases} D_{XY} = \dfrac{d - M_0(X_1 - Y_1)}{\beta^2} \\ d = \sqrt{(1 - \beta^2)\delta_{1i} + \beta^2(X_i - Y_i)^2} \end{cases} \qquad (11)$$

$f_K(\vec{X},\vec{Y},\tau)$ is given by :

$$f_K(\vec{X},\vec{Y},\tau) = \frac{\rho'}{d^2}(1 - M_0^2)\vec{n}.(\vec{X} - \vec{Y}) + M_0^2 n_1 \frac{\partial \rho'}{\partial Y_1} - \frac{\partial \rho'}{\partial n}$$

$$+ \frac{1}{c_0}\left[M_0 n_1 + \frac{\vec{n}.(\vec{X} - \vec{Y})}{d}\right]\frac{\partial \rho'}{\partial \tau} \qquad (12)$$

This formulation assumes that the pressure field on S satisfies the convected wave equation :

$$\left(\frac{D^2}{D\tau^2} - a_0^2 \Delta\right)\rho' = 0 \text{ with } \frac{D}{D\tau} = \frac{\partial}{\partial \tau} + U_0 \frac{\partial}{\partial X_1}, \qquad (13)$$

which governs the propagation of acoustic waves in a medium with uniform velocity U_0 in the direction X_1.

Space-time discretization

The space-time discretization of the Kirchhoff integration on a given closed control surface assumes that temporal fluctuations of fluid pressure are time-sampled (with time step Δt and duration $N\Delta t$) at any cell (with maximal dimension $\Delta \sigma$) of a 2-layer (with maximal normal separation Δn between both layers) surface grid. If λ_a and $T_a = \lambda_a/c_0$ denote the acoustic wavelength and period, the crucial parameters of the process are $\Delta \sigma / \lambda_a$, $\Delta n/\lambda_a$ and $\Delta t/T_a$. These parameters were carefully adjusted on the basis of a parametric study (that can be found in the Annex of Ref. [24]) which was performed before to achieve actual Kirchhoff integration.

Construction of the control surface

Figure 15 shows how the integration surface is constructed from one given C-shaped grid line surrounding the airfoil in domain #1, extended in domain #2 by the two corresponding horizontal grid lines. These horizontal lines are stopped at nearly one third-chord from the TE, where acoustic levels are very low and grid cells become much larger than the acoustic wavelength.
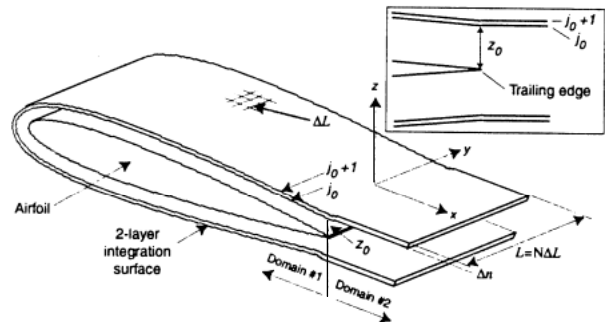

Figure 15 : Kirchhoff integration : construction of the control surface.

Then the three-dimensional surface is obtained by N replications in the spanwise direction along the desired span extent $L = N\Delta L$. In the present application, with reference to Brooks and Hodgson's experiment [24], the airfoil's span was taken equal to $L = 0.46$ m or 0.75C. N was fixed to $N = 92$ according to a parametric study presented in the Annex of Ref. [24].

It should be noted that the final 3D surface is not closed, neither at its two lateral sides (their contribution to the noise radiated in the z direction is neglectible) nor at its downstream

extremity (which contains very low acoustic levels and may be crossed by undamped vorticity convected in the wake).

The LES 3D grid has a spanwise extent limited to 3.3 % of the airfoil chord, so the LES data have to be extrapolated in the spanwise direction. The 2D behaviour of the simulated acoustic field, especially confirmed by the spanwise coherences presented on Figure 14, suggest to simply replicate, along the whole span L, the 2D field computed at $y = 0$.

Finally the critical design parameter of the integration surface is the index j_0 of the grid line surrounding the airfoil, which varies from $j_0 = 1$ on the airfoil, to $j_0 = 97$ at the grid border. Once this parameter is chosen, the normal separation Δn is directly related to j_0, as grid lines of indexes j_0 and $j_0 + 1$ are used to compute the pressure normal gradients.

z_0	j_0
5 mm	35
13.8 mm	45
24 mm	50
37.9 mm	54
42.6 mm	55
60.3 mm	58
136.9 mm	65
247 mm	70
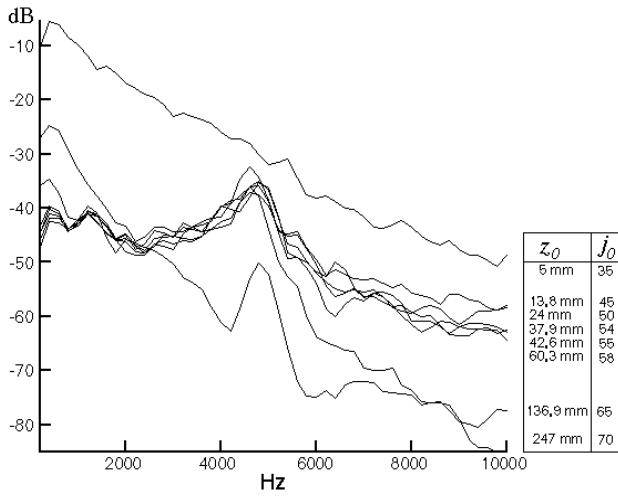
Figure 16 : Parametric study of the position of the Kirchhoff integration surface S (parameters : index j_0 of the used grid line, and normal distance z_0 to the airfoil TE). Noise radiated at $z_0 = 2C$ above the trailing edge.

Figure 16 shows the influence of j_0 on the power spectral density of the noise radiated at $z = 2C$ above the trailing edge, computed by the Kirchhoff integration. It should be noted that all other parameters were adjusted to final values deduced from the parametric studies described in the Annex.

On each presented spectrum, the index j_0 and the distance of the grid line from the airfoil are mentioned. This plot shows that a family of intermediate grid lines provide very similar spectra, which is a good indication of a region where the pressure field is mostly acoustic. The spectra computed from the grid lines nearest to the airfoil are obviously contaminated by intense vorticity convected in the TBL and the wake. On the other hand, spectra computed from farther grid lines are progressively attenuated in the high frequency band, which is another confirmation of the low-pass filtering generated by the grid stretching. The grid line $j_0 = 54$ located at the distance $z_0 = 37.9$ mm from the airfoil was finally chosen for the Kirchhoff computations. The normal distance between lines 54 and 55 is $\Delta n = 4.7$ mm.

Results

Instantaneous pressure distributions

The Kirchhoff integration method offers the conveniency of easily computing the noise at any location outside the control surface. If the available computing resources are sufficient, the

noise can be computed at thousands of locations to build instantaneous maps or time-animated pressure distributions.
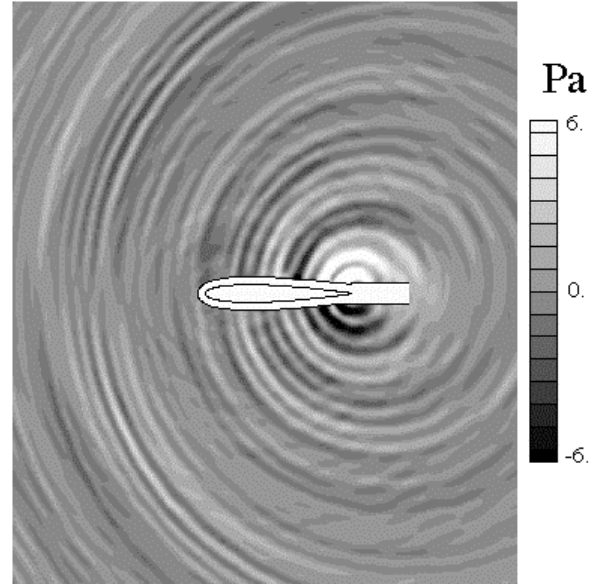
Figure 17 : Noise contours computed via the Kirchhoff method outside the integration surface.
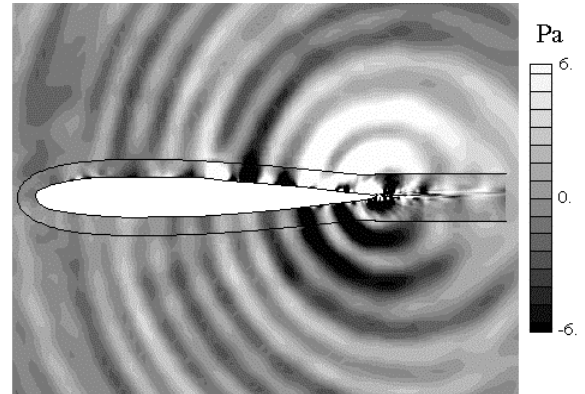
Figure 18: Pressure contours inside (LES) and outside (Kirchhoff) the integration surface

Figure 17 shows such a map computed on a two-dimensional cartesian grid of regular space step $\Delta x = \Delta y = 1.2$ cm which extends two chords around the airfoil. It is interesting to compare this Kirchhoff noise field to the similar result of Figure 9, which was obtained from the LES pressure fluctuation field. Both figures are using the same colour scale, showing how the acoustic field is rapidly filtered and eliminated from the LES data.

Figure 18 provides a closer view of the control surface region, in order to evaluate the continuity between the pressure fields inside and outside the surface. Inside the surface, the pressure field is directly deduced from the LES data as in Figure 9. Outside the surface, the pressure is computed via a Kirchhoff integration as in Figure 17.

Farfield noise

Figure 16 shows noise spectra computed from various Kirchhoff surfaces (including the surface based on the grid line $j_0 = 54$ $z_0 = 37.9$ mm which was finally chosen) at $z = 2C$. This specific position was chosen because it corresponds to the

location of a microphone in the Brooks and Hodgson's experiment [24]. The PSD measured by this microphone is presented on Figure 20 (dashed line). The noise predicted via the Kirchhoff integration overestimates the measured data by more than 15 dB. This overestimation may have several reasons acting together. Firstly, it is important to distinguish the nearfield unsteady CFD and the farfield noise prediction : it has been seen that wall pressure fluctuations already overestimated measured values by 3 to 5 dB, which means that the overprediction by the acoustic prediction may be closer to 10 dB.

Secondly, the spanwise replication of the central pressure field assumes that the acoustic field on the control surface is perfectly correlated (or fully two-dimensional) in the spanwise direction. This assumption was considered in accordance with the spanwise coherences shown on Figure 14. However, it is almost certain that these coherences are artificially overestimated due to the small extent of the LES computational domain (in a similar approach based on the Ffowcs Williams and Hall's TE noise theory applied to incompressible LES, Wang [6] showed that the radiated noise computed from CFD data replicated in the spanwise direction is very sensitive to the spanwise coherence of these data).

FFOWCS WILLIAMS-HAWKINGS INTEGRATION

Formulation

Since wall pressure spanwise coherences (Figure 13) and fluctuation levels (Figure 6) were found to match experimental data, a second noise prediction was achieved using the Ffowcs Williams-Hawkings (FW-H) method (dipole surface term only).

A 3D FW-H formulation is implemented in the FIM (FW-H Integration Method) code which was developed at ONERA for helicopter rotor noise prediction. This code provides the noise radiated by any three-dimensional surface in a flow with uniform velocity U_0 in the direction X_1, given the data ρ, p and ρu_i along this surface. The formulation is[29] :

$$\tilde{p}\left(\vec{X},t\right) = c_0^2 \iint f_{FWK}\left(\vec{X},\vec{Y},\tau\right)\frac{1}{4\pi d}\delta\left(t-\tau+\frac{D_{XY}}{c_0}\right)dSd\tau \quad (14)$$

where D_{XY} and d are defined in (11) and :

$$f_{FWK}\left(\vec{X},\vec{Y},\tau\right) = \frac{1}{\beta^2}\frac{\partial}{\partial\tau}\left\{\frac{1}{c_0^2}\left[\begin{array}{c}\frac{\beta^2}{d}\bar{A}.\left(\vec{X}-\vec{Y}\right)+\\\frac{M_0^2}{d}A_1\left(X_1-Y_1\right)-MA_1\end{array}\right]+B\left[1-\frac{M_0}{d}\left(X_1-Y_1\right)\right]\right\}$$
$$+\frac{1}{d^2}\left[\beta^2\bar{A}.\left(\vec{X}-\vec{Y}\right)+\left(M_0^2A_1-U_0B\right)\left(X_1-Y_1\right)\right]$$
$$(15)$$

and
$$\left\{\begin{array}{l}A_i = \frac{1}{c_0^2}\left[\tilde{p}n_i + \rho u_i\left(u_n-v_n\right)\right]\\B = \frac{1}{c_0^2}\left[\rho_0 v_n + \rho\left(u_n-v_n\right)\right]\\v_n = -U_0n_1\end{array}\right. \quad (16)$$

and all other notations are identical as in the Kirchhoff formulation. It should be noted that this formulation is not complete since it ignores the volume integration term : when the surface is taken at the airfoil wall, the volume outside the surface obviously contains a distribution of quadrupoles, but it is assumed that this term can be neglected (this assumption has been verified in aeroacoustic mechanisms involving solid walls, such as helicopter rotor noise or propeller noise).

Application

The application of the above formulation to the present case relies on the comparison of :

- the spanwise integral length scale of wall pressure fluctuations computed by LES : $\Lambda_y < 3$ mm,
- the spanwise extent of the LES computational domain : $S_{LES} \approx 20$ mm or 3,3 % of the chord,
- the spanwise extent of the real airfoil used in the experiment [24]: $S_{EXP} \approx 0,46$ m.

In a first step, the FIM code is used to compute the DSP $\Phi_{LES}(\omega)$ of the noise radiated by a narrow airfoil of span S_{LES}. This is done by using a surface located at the airfoil wall and integrating the data computed via LES on all the 33 planes of the 3D LES domain. It is then assumed that the real airfoil of span S_{EXP} is made of S_{EXP}/S_{LES} narrow airfoils located side-by-side. Since $\Lambda_y < S_{LES}$, any couple of these narrow airfoils behave as fully decorrelated sources and an estimation of the DSP $\Phi_{EXP}(\omega)$ of the noise radiated by the real airfoil of span S_{EXP} is given by :

$$\Phi_{EXP}(\omega) = \frac{S_{EXP}}{S_{LES}}\Phi_{LES}(\omega) \quad (17)$$

Results

Figure 20 shows the noise spectrum estimated via this numerical procedure at $z = 2C$ above the TE. It is compared, without correction or normalisation, to the experimental data obtained by Brooks and Hodgson at the same position.

It is interesting to notice that experiment and simulation differ in the same way (frequency shift and amplitude difference) as wall pressure spectra shown on Figure 6, which may confirm the validity of the acoustic method.
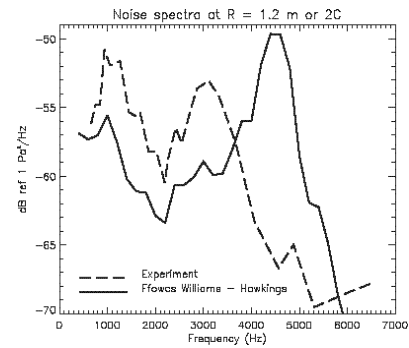

Figure 20 : Power spectral density of the noise radiated at z = 2C above the TE. Comparaison of computed (solid line) and measured (dashed line) data [24].

Directivity diagrams

Figure 21 shows a diagram obtained by computing (with both Kirchhoff and FW-H methods) the noise radiated on equally spaced points located on a circle of radius $r = 1.2$ m (or 2C) centered on the airfoil TE. The directivity is compared to the theoretical directivity of the noise emitted by turbulence

passing the trailing edge of an infinite half-plane. It is also compared to experimental values given by Brooks and Hodgson [24].
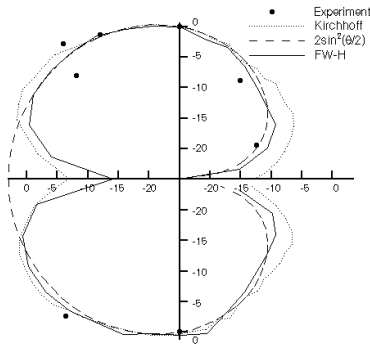

Figure 21 : Directivity diagram of radiated noise on a circle of radius 2C centered on the TE. Comparison of computed data (Kirchhoff and Ffowcs Williams Hawkings methods) with half-plane TE noise and experimental data [24].

LINEARIZED EULER EQUATIONS

The need

Going back to the pressure contours shown on Figure 18 obtained via the Kirchhoff integration, it is interesting to follow the acoustic waves emitted at the TE and propagating in the upstream direction, especially along the pressure side chord on which the TBL is only visible near the TE. At the vicinity of the TE, these waves are rather continuous in both LES and Kirchhoff pressure fields. When they have traveled along more than a half chord, it becomes clear that waves in the LES domain (inside the surface) are slightly slower than their counterpart propagating in the Kirchhoff domain outside the surface. To explain this, one must remember that the Kirchhoff method assumes that the flow outside the controle surface has a uniform velocity U_0, whereas the mean flow simulated via LES inside the control surface present local velocities U_e that may be significantly larger than U_0, especially on the succion side of a lifting airfoil. This last result underlines what is probably the most critical limitation of integral methods such as the Kirchhoff integration : outside a given surface or volume, they do not take into account the inhomogeneities of the mean flow.

This limitation fully justifies the development of a complementary tool based on the discretization of LEE, which have the ability to account for local mean velocity gradients. However, since the application of such methods may become very computationally consuming, especially in complex 3D cases, it should be strictly limited to the regions where strong velocity gradients make it really necessary. In the present problem, such region could be reasonably limited to a domain extending one chord away from the airfoil. Outside this new control surface, the mean flow can be considered as rather uniform and the Kirchhoff method can be applied to provide accurate prediction of the sound at much larger distance from the airfoil.

The E3P code

The E3P code (Propagation via Euler Equations under a Small Perturbation Hypothesis) based on discretized LEE is currently developped at ONERA for this purpose [12]. The formulation is based on the splitting of the total field in a mean flow and a perturbation field. The equations are discretized in conservative form and can be either linearized (only first terms are kept) or not (all linear and non-linear terms are used). Cartesian or curvilinear 2D/3D (monodomain) structured grids can be used. In the space domain, the discretization uses high order finite differente explicit or implicit schemes. In the time domain, multi-steps schemes (Adams-Bashford or Runge-Kutta) are used. Specific boundary conditions are implemented for solid surfaces, non-reflexive border, periodicity or data injection. Non-uniform mean flows are taken into account. The next part shows several configurations of acoustic scattering problems solved with this code. The last paragraph explains how this code could be coupled with unsteady CFD computations.

Acoustic scattering using E3P

Figure 22 shows the free-field radiation of an acoustic harmonic Gaussian source in a steady uniform flow at Mach 0.5, computed on a 200×200 weavy grid and compared with the analytic solution.
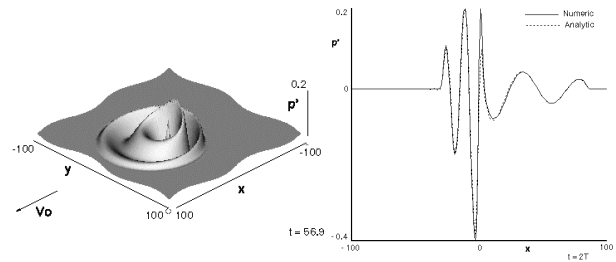

Figure 22 : Radiation of a harmonic Gaussian source in a uniform flow $M = 0.5$. E3P, weavy grid 200×200, compared with analytic solution.

Figure 23 shows the acoustic scattering of a harmonic source on a rigid circular cylinder of radius a in a fluid at rest. The RMS pressure field (amplitude and phase) along a circle of radius $2a$ is compared with results obtained with a Boundary Element Method (BEM). Figure 24 shows the same configuration, but with a non uniform (potential) mean flow around the cylinder. Figure 25 shows the acoustic scattering of a harmonic source on a rigid elliptic cylinder.

Figure 26 shows the acoustic scattering of a harmonic source on a rigid Joukowski airfoil in a potential mean flow. Figure 27 displays three-dimensional computation of the acoustic scattering of a harmonic source on a 3D rigid circular cylinder, again and with a potential mean flow.
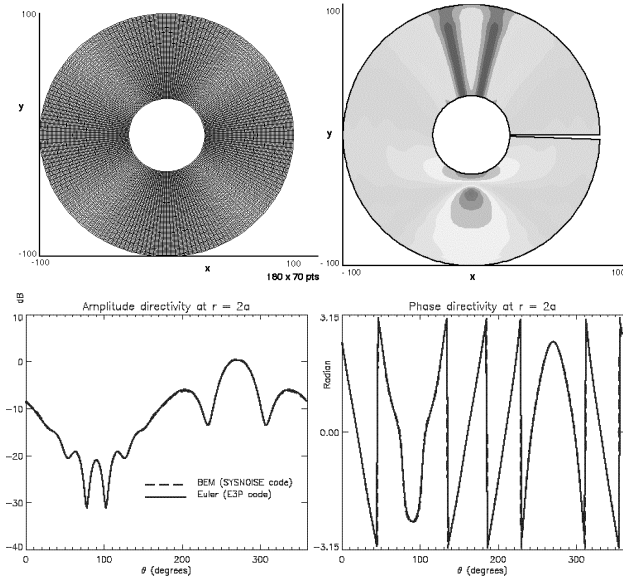
Figure 23 : Acoustic scattering of an harmonic source on a rigid circular cylinder (M = 0) of radius a. Cylindrical grid. RMS pressure field. Comparison of RMS pressure (amplitude and phase) at radius 2a with Boundary Element Method (BEM).
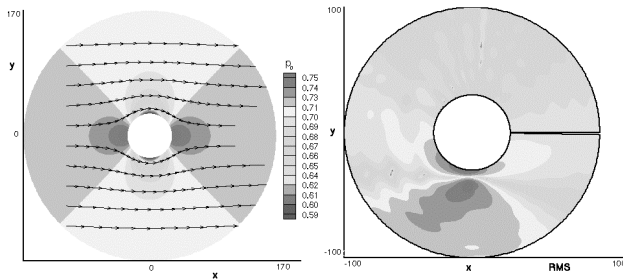

Figure 24 : Acoustic scattering of an harmonic source on a rigid circular cylinder with potential non-uniform mean flow (M = 0.3). RMS pressure field.
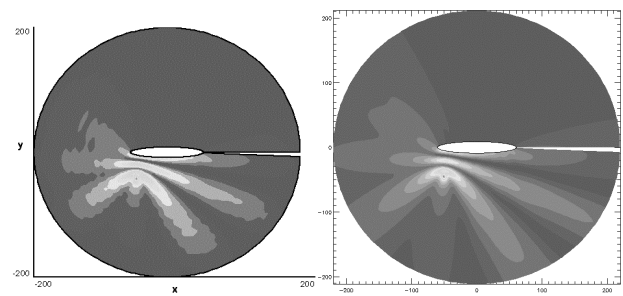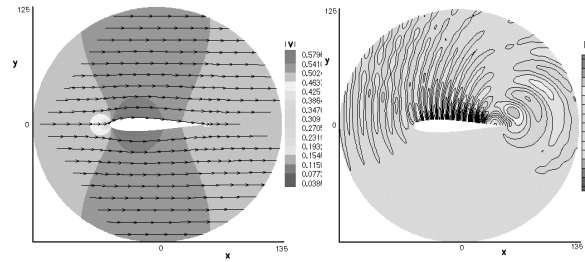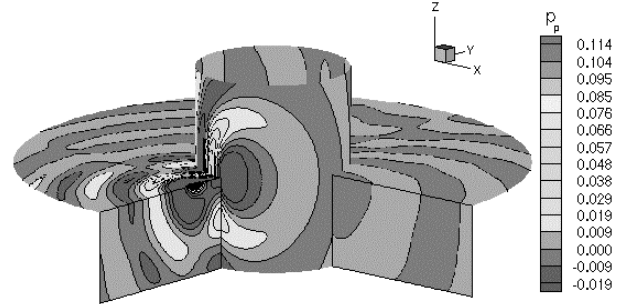

Figure 25 : Acoustic scattering of an harmonic source on a rigid elliptic cylinder (M = 0). Comparison of amplitude RMS pressure field (LHS)) with BEM results (RHS).

Figure 26 : Acoustic scattering of an harmonic source on a rigid Joukowski airfoil with potential non-uniform mean flow (M = 0.3). RMS pressure field.

Figure 27 : Acoustic scattering of an harmonic source on a rigid 3D circular cylinder with potential non-uniform mean flow (M = 0.3). RMS pressure field.

Toward coupling LEE with LES

The coupling of local unsteady CFD with discretized LEE is a complex problem. Up to now, most applications were based on the formulation of volume distribution of aeroacoustic sources constructed from the CFD results and used as right-hand-side source terms in Euler equations.

In the present application, it was shown that compressible LES is able to simulate the generation and local propagation of noise. This result suggests that LES could be coupled with the noise E3P code using a surface interface similar to the Kirchhoff control surface. This basic principle requires that a perturbation field can be injected at one border of a LEE domain, a functionality which, in a first step, was tested by injecting an acoustic field radiated by an harmonic source located outside the LEE domain.

Figure 28 shows such validation in the case of a a cylindrical grid. The (virtual) monopole is located inside the inner border of the domain, and its (analytical) field is injected on this inner border. The acoustic field computed in the LEE domain is favorably compared with the analytical field.
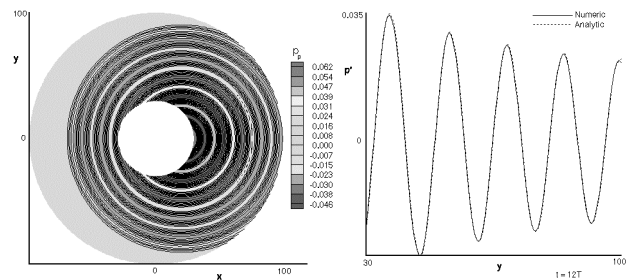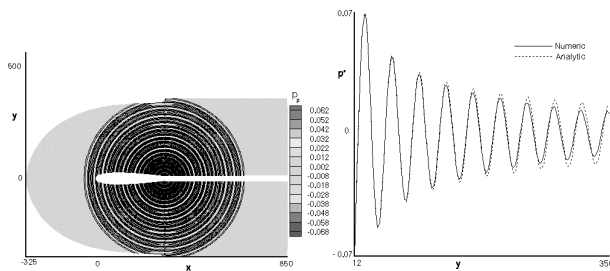

Figure 28 : Injection, at the inner border of a cylindrical grid, of the acoustic field radiated by a (virtual) monopole located inside the inner border. Comparison with the analytical field.

On Figure 29 the same analytical acoustic field is injected at the inner border of a grid which was derived from the LES grid shown on Figure 1. Again, the pressure field computed in the LEE domain is favourably compared with the abanlytical direct propagation. The next step will consist in injecting LES data at the same inner border.

It is believed that the next significant results of CAA applied to airfoil noise predictions will be obtained via the combination of (i) unsteady CFD (LES) for the nearfield flow, (ii) the linearized Euler equations for intermediate acoustic sound field and (iii) an integral method (Kirchhoff, Ffowcs Williams-Hawkings) for the prediction of the far field noise.

Figure 29 : Injection, at the inner border of a CFD grid, of the acoustic field radiated by a (virtual) monopole located inside this inner border. Comparison with the analytical field.

CONCLUSIONS

The unsteady flow past an isolated NACA0012 airfoil with a constant section and a blunted TE is computed via compressible LES. Detailed analysis of the results shows that the unsteady flow is accompanied by an acoustic field generated by the acoustic scattering of (i) the turbulent boundary layers convected on both airfoil sides (broadband noise) and (ii) the alternated vortex shedding generated by the TE bluntness (narrow band component). A close examination of surface pressure fluctuations near the TE shows that spanwise integral length scales are probably smaller than the computational domain extent in that direction, although the latter only represents 3.3 % of the chord. Surface pressure spectra are compared with published experimental data obtained on the same airfoil geometry. The computed vortex shedding frequency is slightly higher than the measured one, which can be explained by an underestimation of the TBL thicknesses. Predicted levels also slightly overestimate measured levels. Due to the strong stretching of the LES computational grid, which acts as an acoustic low-pass frequency filter, this acoustic field cannot radiate farther than a half-chord from the body.

In a second step, the LES has been relayed by an acoustic propagation method to simulate the farfield noise. For this purpose, two different integral methods have been used, a Kirchhoff integration and a Ffowcs Williams-Hawkings integration.

The Kirchhoff control surface is constructed via the spanwise development of a grid line surrounding the airfoil. This method necessitates a careful study of several critical parameters such as the position of the control integration surface enclosing the airfoil and its wake, the spanwise replication step, the distance between the two layers of the surface (for correct computation of pressure normal gradients) and the time step, all parameters being normalized by the acoustic wave length or

time period. Since the acoustic field generated at the TE shows strong two-dimensional characteristics, the pressure field on the integration surface is simply obtained by replicating the LES data in the spanwise direction. Predicted farfield noise spectra are compared with published experimental data obtained in an anechoic facility with the same airfoil geometry (but much larger span). Predicted levels overestimate experimental spectra, which is most probably due to the assumption that the acoustic field is fully correlated along the spanwise extent of the integration surface, which is obviously only true at very low frequencies and in the frequency domain of the vortex shedding.

In a second step, the Ffowcs Williams-Hawkings method was used along with wall pressure data which provided spanwise correlations matching experimental values. In this case, the far field noise spectrum is obtained in two steps. In a first step, the noise radiated by an narrow airfoil is obtained by integrating wall pressure data in the whole LES computation domain. Then the noise radiated by an airfoil with realistic span is obtained by summing decorrelated contributions of several identical narrow airfoils lying side-by-side. Final results favorably agree with experimental measurement.

Finally, close examination of acoustic waves propagating (i) in the LES pressure field inside the controle surface and (ii) in the Kirchhoff pressure field outside the surface, clearly shows the influence of the uniform-flow assumption which is implicit in most integral methods. This strongly justifies the use of a novel acoustic method based on the discretized LEE. This method is currently under development. Several solutions of acoustic scattering problems were solved with this code and are presented. Then it is shown how this tool could be combined with nearfield LES on the basis of a 2D interface. It is believed that this combination will soon bring significant progress in the field of the numerical prediction of airframe noise.

ACKNOWLEDGEMENTS

BIBLIOGRAPHY

1. Kalizin N. and Kalitzin G. *"Influence of Turbulent Models on SNGR Sound Predictions of Flow over Trailing Edge of a Flat Plate"*, AIAA Paper No. 2000-1982, 6th AIAA-CEAS Aeroacoustics Conference, Lahaina (Hawaii), 12-14 June, 2000.

2. Singer B.A., Brentner K.S., Lockard D.P. and Lilley G.M. *"Simulation of Acoustic Scattering from a Trailing Edge"*, AIAA Paper 99-0231, 37th Aerospace Sciences Meeting and Exhibit, Reno (NV), Jan. 12-15, 1999.

3. Singer B.A., Lockard D.P., Brentner K.S. *"Computational Aeroacoustic Analysis of Slat Trailing-Edge Flow"*, AIAA Journal, Vol. 38, No. 9, pp. 1558-1564, September, 2000.

4. Spyropoulos E.T. and Holmes B.S. *"Computation of the airframe noise of a wing-flap configuration"*, AIAA Paper 99-1801, 5th CEAS/AIAA Aeroacoustics Conference, Seattle, USA, 10-12 May, 1999.

5. Manoha E., Troff B. and Sagaut P. *"Trailing Edge Noise Prediction using Large Eddy Simulation and Acoustic Analogy"*, AIAA Journal, Vol. 38, No. 4, pp. 575-583, April (also AIAA Paper 98-1066), 2000.

6. Wang M. and Moin P. *"Computation of Trailing-Edge Flow and Noise Using Large-Eddy Simulation"*, AIAA Journal, Vol. 38, No. 12, pp. 2201-2209, December, 2000.

7. Lighthill M.J. *"On sound generated aerodynamically. I. General theory II. Turbulence as a source of sound"*, Proc. Roy. Soc. Lond., Vol. A 211, pp. 564-587, 1952. Vol. A 222, pp. 1-32, 1952.

8. Ffowcs Williams J.E. and Hawkings D.L. *"Sound generation by turbulence and surfaces in arbitrary motion"*, Phil. Trans. Royal Soc., Vol. A 264, pp. 321-342, 1969.

9. Manoha E., Elias G., Troff B. and Sagaut P. *"Towards the Use of Boundary Element Method in Computational Aeroacoustics"*, AIAA Paper 99-1980, 5th CEAS/AIAA Aeroacoustics Conference, Seattle, USA, 10-12 May, 1999.

10. Tam C.K.W. and Webb, J.C. *"Dispersion-Relation-Preserving Finite Difference Schemes for Computational Acoustics"*, Journal of Computational Physics, Vol. 107, pp. 262-281, 1993.

11. Grogger H.A., Delfs J.W., Lauke T.G., Lummer M. and Yin J. *"Simulation of leading-edge noise of airfoils using CAA based on body-fitted grids"*, 7th International Congress on Sound and Vibration, Garmisch-Partenkirchen, Germany, 4-7 July, 2000.

12. Redonnet S., Manoha, E. and Sagaut P. *"Numerical Simulation of Propagation of Small Perturbations interacting with Flows and Solid Bodies"*, AIAA Paper n° 2001-2223, 7th CEAS/AIAA Aeroacoustics Conference, Maastricht, The Netherlands, 28-30 May, 2001.

13. Ffowcs Williams J.E. and Hall L.H. *"Aerodynamic sound generation by turbulent flow in the vicinity of a scattering half plane"*, Journal of Fluid Mechanics, Vol. 40, pp. 657-670, 1970.

14. Péchier M. *"Prévisions numériques de l'effet Magnus pour des configurations de munitions"*, Thèse de l'Université de Poitiers, 1999.

15. Péchier M., Guillen P. and gayzac R. *"Magnus Effect over Finned Projectiles"*, J. of Aircraft and Rockets, 2001.

16. Sagaut P. *"Large Eddy Simulatiosn of incompressible flows. An introduction"*, Springer-Verlag, 2001.

17. Lenormand E., Sagaut P. and Ta Phuoc L. *"Large Eddy Simulations of Subsonic and Supersonic Channel Flow at Moderate Reynolds Number"*, Int. J. Numer. Meth. Fluids, Vol. 32, pp. 369-406, 2000.

18. Lenormand E., Sagaut P., Ta Phuoc L. and Comte P. *"Subgrid-Scale Models for Large Eddy Simulations of Compressible Wall Bounded Flows"*, AIAA Journal, Vol. 38, pp. 1340-1350, 2000.

19. David E. *"Modélisation des écoulements compressibles et hypersoniques : une approche instationnaire"*, Thèse de l'Institut National Polytechnique de Grenoble, 1999.

20. Yoon S. and Jameson A. *"An LU-SSOR Scheme for the Euler and navier-Stokes Equation"*, AIAA-Paper n° 87-600, 1987.

21. Mary I. and Sagaut P. *"Large Eddy Simulation of Flow around a high lift airfoil"*, AIAA Paper 2001-2559, 15th CFD Conference, Anaheim (Ca), 11-14 June, 2001.

22. Weber C. and Ducros, F. *"Large-Eddy and Reynolds-Averaged Navier-Stokes Simulation of Turbulent Flow over an airfoil"*, Int. J. CFD, Vol. 13, pp. 327-355, 2000.

23. Wu X., Jacobs R., Hunt J. and Durbin P. *"Simulation of Boundary layer Transition Induced by Periodically Passing Wake"*, J. Fluid Mech., Vol. 398, pp. 109-153,, 1999.

24. Brooks T.F. and Hodgson T.H. *"Prediction and comparison of trailing edge noise using measured surface pressures"*, Journal of Sound and Vibration, Vol. 78 (1), pp. 69-117, 1981.

25. Rahier G., Prieur, J. *"An Efficient Kirchhoff Integration Method for Rotor Noise Prediction Starting Indifferently from Subsonically or Supersonically Rotating Meshes"*, 53rd Annual Forum of the American Helicopter Society, Virginia Beach, VA, April-May, 1997.

26. Seror C., Sagaut P., Rahier G. *"Prévision du bruit de jet de l'ATSF : simulation aéroacoustique d'un jet supersonique à section rectangulaire"*, RTS ONERA n° 12/4418 DSNA/Y, Février 2000.

27. Prieur J. and Rahier, G.,. *"Comparison of Ffowcs Williams-Hawkings and Kirchhoff Rotor Noise Calculations"*, 4th AIAA/CEAS Joint Aeroacoustics Conference, Toulouse, Juin, 1998.

28. Manoha E., Delahay C., Ben Khelil S., Guillen P., Sagaut P. and Mary Y.*"Numerical prediction of the unsteady flow and radiated noise from a 3D lifting airfoil"*, AIAA Paper 2001-2133, 7th CEAS/AIAA Aeroacoustics Conference, Maastricht, The Netherlands, 28-30 May, 2001.

29. Ffowcs Williams J.E. and Hawkings D.L. *"Sound generation by turbulence and surfaces in arbitrary motion"* Phil. Trans. Royal Soc., Vol. A 264, pp. 321-342, 1969.

30. Manoha E., Delahay C., Redonnet S., Sagaut P., Mary I., Ben Khelil S. and Guillen P., *"The Numerical Prediction of Airfoil Trailing Edge Noise"*, 17th International Congress on Acoustics, Roma (IT), 3-7 September, 2001

This page has been deliberately left blank

_____

Page intentionnellement blanche

Computations of Three-Dimensional Unsteady Supersonic Cavity Flow to Study the Effect of Different Downstream Geometries

B.I. Soemarwoto and J.C. Kok
National Aerospace Laboratory NLR
Anthony Fokkerweg 2, 1059 CM Amsterdam
The Netherlands
soemarwt@nlr.nl, jkok@nlr.nl

Abstract

Computations of three-dimensional unsteady supersonic cavity flow are performed for a free-stream Mach number of 1.2. Two cavity geometries are considered: (i) a simple rectangular cavity of length-to-depth (L/D) and length-to-width (L/W) ratios of 4.5, and (ii) a cavity with a 45° ramp attached to the downstream wall of the simple rectangular cavity. Two flow models for computing the cavity flowfield are assessed: (a) the Reynolds-Averaged Navier-Stokes (RANS) equations with a k-ω turbulence model for the whole flow-field, and (b) a combination of an inviscid flow model using the Euler equations for the domain outside the boundary layer and the RANS model for the boundary layer. The structures of the flowfields resulting from the different models are observed. The effect of the different downstream geometries is assessed.

INTRODUCTION

The aeroacoustic environment arising from the three-dimensional supersonic flowfield around cavities is closely related with aeroacoustic loads on aircraft components, for example when weapon bays are open at supersonic speeds. The aeroacoustic environment can be separated into the broad-band noise representing pressure fluctuations typically produced by the turbulence, and the narrow-band discrete tones due to resonance involving finite-amplitude self-sustained pressure oscillations inside the cavity. Cavity geometries are characterized by the length-to-depth (L/D) ratio that determines the flowfields to be either closed, open or transitional (intermediate). Closed cavity flowfields are typically associated with shallow cavities ($L/D > 13$) producing broad-band noise. In this type of flow, the shear layer hits the bottom of the cavity, forming two recirculating regions inside the cavity under the shear layer. Open cavity flowfields are typically associated with deep cavities ($L/D < 10$) producing broad-band noise accompanied by distinct narrow-band discrete tones. This type of flow consists of internal and external regions separated by the shear layer spanning along the cavity opening, where the internal region contains a large recirculating flow. An intermediate value of $10 < L/D < 13$ is associated with transitional cavity flowfields.

Numerous prior experimental [1]-[4] and numerical [5]-[15] investigations have been performed. For example, methods based on the Euler equations [5],[15], laminar Navier-Stokes equations [13], Reynolds-Averaged Navier-Stokes (RANS) equations with algebraic [6],[7],[10] and two-equation [8],[9],[12] turbulence models, LES [11],[15], and DNS [14] have been applied. Unfortunately, the results from this large variation of flow models do not seem to lead to a definite conclusion as to which flow modelling is most suitable for simulating three-dimensional cavity flowfields. Although LES and DNS methods undoubtly have the highest potentials for capturing the complete physics, they require prohibitively high computational resources, especially when three-dimensional configurations and high Reynolds numbers are involved. For a routine use, such as for evaluating effects of different cavity geometries, RANS and Euler methods should be assessed for their applicability.

In the present investigation, an open cavity flowfield is considered with $L/D = 4.5$. Time-accurate computations of the three-dimensional supersonic flow over a cavity at a Mach number of $M = 1.2$ and a Reynolds number of $Re = 4.5 \cdot 10^6$ are performed using the NLR CFD system ENFLOW [16],[18]. This CFD system employs multi-block structured grids to simulate three-dimensional flows, where a different flow model may be defined in each block. Two approaches for modelling the cavity flowfield are taken. The first approach is to apply the RANS equations with a k-ω turbulence model for the whole flow domain of the cavity configuration. In the second approach, an inviscid flow model using the Euler equations is applied in

combination with the RANS equations and the k-ω turbulence model for the boundary layer regions over the solid surfaces including those of the cavity walls.

Shear layer instabilities have been found to play an important role in the formation of the self-sustained oscillations, while alternating impingements of the shear layer on the downstream edge of the wall appear to influence the amplitude of the oscillations. The shear layer impingements can be altered through modifying the geometry of the downstream edge. The frequency spectra of the sound pressure level, and in turn the aeroacoustic loads, can therefore be influenced by the geometry of the downstream edge.

The flowfields around a simple rectangular cavity and around a cavity of the same L/D ratio with a 45° solid ramp attached on the downstream edge will be computed. Results from the two different flow models will be discussed, and effects of the downstream edge geometries will be identified.

MODELLING OF THE FLOW

The two cavity geometries, a simple rectangular cavity and a cavity with a 45° ramp shown in Figure 2, are adopted from the WICS model [2]. The flow is assumed symmetrical with respect to the X-Z plane at the centreline of the cavity. The geometry is represented by a half model consisting of two parts: the cavity and a flat plate surrounding the cavity opening. The solid surfaces consist of the flat plate and the cavity walls.

Figure 1 gives an impression of the block topology used for both cavity geometries. The flow domain is decomposed into 13 blocks. A layer of blocks (blue) is constructed over the solid surfaces to represent the boundary layer regions. This layer is connected to the far-field boundaries by another layer of larger blocks (green). A block (red) is introduced upstream of the flat plate where the flow is treated as inviscid. This block allows the flow to enter the domain as a uniform flow, and to stagnate at the leading edge of the flat plate where the boundary layer starts. Downstream of the flat plate, another block (yellow) with an inviscid flow is placed connecting the cavity flowfield with the far-field outflow boundary.

Within each block a structured grid is generated. Inside the blocks associated with the boundary layer, a finer distribution of the grid points is applied towards the solid surface in order to adequately resolve the turbulent boundary layer. Outside these blocks, the computational grids are constructed to be approximately uniform and isotropic. The computational grids on the solid surfaces and those on the symmetry planes are shown in Figure 2 and Figure 3, respectively. The domain inside the cavity is represented by 262144 grid cells, of which 192x32x16 grid cells fill the domain inside the cavity but outside the boundary layers. The whole flow domain contains a total of 655360 grid cells.

Adiabatic no-slip boundary conditions are applied for all solid surfaces. Symmetry conditions are enforced on the X-Z plane at $Y = 0$ coinciding with the cavity centreline. On the horizontal surface upstream of the flat plate, a slip (zero normal velocity) condition is applied. This surface ensures that the flow enters the domain as a uniform flow and the boundary layer starts at the leading edge of the flat plate. Laminar boundary layers are assumed to cover up to 5% of the length measured from the flat plate leading edge to the cavity, downstream of which the boundary layers are assumed to be fully turbulent. On the side boundary, opposite to the symmetry plane, flow variables are enforced to have a zero gradient. Characteristics-based boundary conditions are applied on the far-field boundaries.

Two approaches in modelling the flow are considered. In the first approach, all blocks (green and blue) inside and around the cavity contain a viscous, turbulent flow governed by the RANS equations with a k-ω turbulence model. In the second approach, an inviscid flow governed by the Euler equations is applied to the green blocks, while the same RANS model is used inside the boundary layer blocks (blue).

The k-ω turbulence model [17] used in the computations employs a new set of diffusion coefficients to resolve the free-stream dependency problem of the original Wilcox k-ω model. Also, in the turbulence model a τ formulation for ω is implemented [18], where $\tau = 1/\omega$ is treated as a dependent variable instead of ω. This formulation avoids the problem of the singular behaviour of ω at solid walls.

For any instant of time, the cavity flowfield contains vortical flow structures. It is well known that for vortical flows the standard k-ω turbulence model is too diffusive to capture flow details near vortex cores. To cope with this problem, a parameter representing the ratio between the magnitude of the strain-rate tensor and the magnitude of vorticity is introduced to detect vortex cores. This parameter is used to increase the production term of the ω-equation, giving an effect of increasing the dissipation of the turbulence kinetic energy and of the eddy viscosity. This modification for vortical flow computations, which has been successfully applied to vortex dominated flows around delta wings [19], is also used in the present investigation.

The continuous equations are discretized in space using a cell-centred finite-volume scheme. Jameson-type second-order and fourth-order diffusion terms are introduced to capture shock waves and to prevent odd-even decoupling, respectively. Matrix coefficients are used for the artificial diffusion terms. These coef-

ficients have shown to be less diffusive than the standard scalar coefficients. The so-called dual-time stepping scheme is applied for the time integration of the unsteady equations which is second-order accurate.

RESULTS AND DISCUSSION

Simple rectangular cavity

For the simple rectangular cavity, computations are performed for a Mach number $M = 1.2$ and a Reynolds number $Re = 4.5 \cdot 10^6$. Rossiter's formula [1] is considered for estimating the cavity resonance frequencies:

$$f = \frac{V_\infty}{L} \frac{m - \gamma}{\dfrac{1}{\Phi_d} + \dfrac{a_\infty}{a_t} M_\infty}, \tag{1}$$

where $\gamma = 0.28$ and $\Phi_d = 0.57$ are used for $L/H = 4.5$. Index $m = 1,2,\ldots$ refers to the resonance mode, while a_∞ and a_t are the speeds of sound based on the free-stream total temperature and free-stream static temperature, respectively. The second resonance mode typically has a distinctive peak in the frequency spectrum, which is estimated by the above equation to be equal to 502 Hz. A sampling rate of about 10000 samples per second is selected in order to adequately resolve the second mode frequency by about 20 data points. This sampling rate defines the time step:

$$\Delta t = 0.0812 \, t_c, \tag{2}$$

where the characteristic time t_c is the time required by the flow to traverse the length of the cavity. The data from the experiment [1] provides

$$t_c = \frac{L}{V_\infty} = 1.2305 \cdot 10^{-3} \text{ s}. \tag{3}$$

After the starting transients have decayed, a sample size of $N = 1024$ time steps is produced from the time-accurate unsteady flow computations. The unsteady static pressure is observed at a grid point corresponding to the experimental pressure transducer K16 which is located on the bottom of the cavity at a distance of $0.015L$ from the aft wall.

Figure 4 presents the unsteady static pressure fluctuations and the frequency spectra. The Sound Pressure Level (SPL) in the frequency spectra is defined as:

$$\text{SPL} = 180 + 20 \log\left(\frac{p}{p_{\text{ref}}}\right) \text{dB}, \tag{4}$$

where $p_{\text{ref}} = 2.90075$ psi is the standard reference pressure.

The RANS model results in almost purely periodical fluctuations, in contrast with those obtained from the Euler with boundary layer model. The maximum amplitudes of the RANS model are significantly lower than those of the other model. The RANS model produces a distinct resonance at 518 Hz (peak B). This frequency matches the second mode at 518 Hz measured in the experiment. There is also a close agreement in the magnitude which is within the range of 2 dB. It is not clear whether Peak A at 205 Hz corresponds to the experimental value of the first mode at 225 Hz, because its magnitude is much lower (20 dB less) than that of the experimental value. Peaks C and D are precisely the multiples of 518 Hz (1037 Hz and 1555 Hz, respectively), and therefore should not be associated with the higher modes.

The Euler with boundary layer model produces two distinct peaks (numbered 1 and 2) at 215 Hz and 509 Hz. These frequencies are reasonably close to the experimental values, 225 Hz and 518 Hz, of the first and second modes. The third and higher modes occur in the experiment at 830 Hz and 1025 Hz, respectively. Peaks 3 and 4 appear at 812 Hz and 1008 Hz, though not distinctively, and have amplitudes that are in the range of 2 dB from the experimental values. The amplitude of the first (second) peak is within 2 dB (5 dB) difference from that of the first (second) mode's amplitude of the experiment.

Figures 5 and 6 present the instantaneous flow patterns produced by the RANS model which belong to a cycle between two consecutive minimum values of the static pressure at the grid point observed. The total pressure loss contours in Figure 5 show wave-like oscillating shear layers associated with vortices travelling inside the cavity. The cycle appears to consist of the following sequence: (1) an upward deflection of the

shear layer that leads to a fluid spill leaving the cavity, while a vortex has been formed downstream of the leading edge, (2-3) as the vortex moves downstream and gets stronger, the shear layer moves downward and its end impinges on the edge of the aft wall, (4-5) a compression wave (Figure 6) is formed in the aft wall region, (6) the downward movement of the shear layer induces fluid to enter the cavity and the pressure at the wall reaches a maximum, (7) the shear layer moves upward, (8-9) the vortex approaches the aft wall region while a new vortex is being formed near the leading edge, and (10) the process repeats itself. Figures 7 and 8 present the results obtained using the Euler with boundary layer model. Although the above sequence can still be identified, non-periodic oscillations are clearly indicated, in agreement with a larger number of frequency components resolved. The Euler boundary layer model results also show a more complex flow with eddies.

The overall sound pressure levels (OASPL) along the centreline of the cavity are also compared, where

$$OASPL = 180 + 20 \log \left(\frac{p_{rms}}{p_{ref}} \right) dB , \qquad (5)$$

with the root-mean-square of the static pressure given by

$$p_{rms} = \sqrt{\frac{1}{N} \sum (p_{ave} - p)^2} . \qquad (6)$$

Figure 9 shows a same tendency produced by both flow models. The experimental values are obtained from the data presented in Ref. [7]. The full RANS model agrees well with the experiment, except in locations around the cavity mid-point. More discrepancies are observed for the results of the Euler with boundary layer model, especially in the downstream half of the cavity.

Cavity with ramp

The same computational procedure, with the same sampling rate of about 10000 per second, is also used for the cavity with ramp. The modification of the trailing edge geometry for this case shows to have a large impact on the cavity flowfield. The RANS model resulted in a steady flow, where the shear layer completely divided the flow into two domains inside and outside of the cavity.

The effect of the trailing edge geometry on the unsteady cavity flowfield can still be observed from the computations using the Euler with boundary layer model. Figure 10 shows the pressure fluctuations and the corresponding frequency spectra. The amplitudes of the pressure fluctuations are significantly smaller than those of the simple rectangular cavity (Figure 4). This indicates that the compression waves become much weaker by the ramp effects. The total pressure loss contours in Figure 11 show completely different flow patterns from those of the simple rectangular cavity, especially in the way the shear layer impinges on the aft wall as shown in pictures 2-5. Also, it can be observed in pictures 7-9 of Figure 12 that the propagation of the compression waves is partly deflected following the orientation of the ramp. The first and second resonance modes are increased by about 30 Hz and 38 Hz, respectively. A shorter effective distance between the upstream and downstream walls may be responsible for this increase in frequency. The amplitude of the first mode is decreased by about 5 dB, while that of the second mode is only slightly decreased. The higher modes are less identifiable, and possibly have significantly lower amplitudes.

The effect of the trailing geometries on the OASPL can be observed in Figure 13. The ramp has an effect of reducing the sound pressure level along the cavity centreline, except in a small region near the beginning of the ramp where the sound pressure level is slightly increased. Larger reductions are observed on the upstream wall and in the upstream part of the cavity.

CONCLUSIONS

Three-dimensional computations of supersonic flow around two cavities of $L/D = 4.5$ with different trailing edge geometries have been performed. Two flow models have been considered for the computations.

For the simple rectangular cavity, using the RANS equations with the k-ω turbulence model, we have been able to capture the frequency and magnitude of the second resonance mode, which agrees quite well with the measured values. Using the Euler model, in combination with modelling of the boundary layers using the RANS equations and the k-ω turbulence model, we have been able to capture the frequencies and amplitudes of the first four modes in reasonable agreement with the experimental values. With regard to the

overall sound pressure level (OASPL) along the centreline of the cavity, the RANS model has been shown to produce a closer agreement with the experimental values, whereas the Euler with boundary layer model shows overpredictions in particular in locations downstream the cavity mid-point.

For the cavity with 45° ramp at the trailing edge, the RANS with k-ω model seems to be too dissipative to produce a self-sustained oscillation. The effect of the ramp has been assessed using the results from the Euler with boundary layer model. The ramp evidently reduces the amplitude of the pressure fluctuations. It is observed that the resonance modes have been increased slightly, while their amplitudes have been reduced.

The results clearly indicate that the RANS model is applicable only to limited cases of unsteady cavity flowfields. There seems to be a threshold, which is related to the physics of the unsteadiness, that separates unsteady solutions from steady solutions of the RANS equations. When an unsteady solution is obtained, however, the RANS model gives an accurate prediction of the resolved modes in terms of frequencies, amplitudes and OASPL. The Euler model in combination with RANS model for the boundary layer shows to be applicable to a large class of cavity flowfields, but it produces less accuracies especially in terms of OASPL. Finally, the best perpective for both an accurate simulation and a large class of cavity flowfields, at feasible computational costs, may be given by a hybrid LES model (replacing the Euler model) in combination with the RANS model for the boundary layer.

REFERENCES

[1]   R.C. Bauer and R.E. Dix. *Engineering Model of Unsteady Flow in a Cavity*. AEDC-TR-91-17, 1991.

[2]   R.E. Dix. Cavity aeroacoustics. Calspan Corporation/AEDC Operations.

[3]   Kung-Ming Chung. A study of transonic rectangular cavity of varying dimensions. *AIAA Paper 99-1909*, 1999.

[4]   M.A. Kegerise and E.F. Spina. An experimental investigation of flow-induced cavity oscillations. *AIAA Paper 99-3705*, 1999.

[5]   C.J. Borland. Numerical prediction of the unsteady flowfield in an open cavity. *AIAA Paper 77-673*, 1977.

[6]   D.P. Rizzetta. Numerical simulation of supersonic flow over a three-dimensional cavity. *AIAA Journal*, 26(7), 1988.

[7]   N.E. Suhs. Unsteady flow computations for a three-dimensional cavity with and without an acoustic suppression device. *AIAA Paper 93-3402*, 1993.

[8]   S.H. Shih, A. Hamed, and J.J. Yeuan. Unsteady supersonic cavity flow simulations using coupled k-ε and Navier-Stokes equations. *AIAA Journal*, 32(10), 1994.

[9]   X. Zhang. Compressible cavity flow oscillation due to shear layer instabilities and pressure feedback. *AIAA Journal*, 33(8):1404--1411, 1995.

[10] C.J. Tam, P.D. Orkwis, and P.J. Disimile. Algebraic turbulence model simulations of supersonic open-cavity flow physics. *AIAA Journal*, 34(11):2255--2260, 1996.

[11] N. Sinha, S.M. Dash, and N. Chidambaram. A perspective on the simulation of cavity aeroacoustics. *AIAA Paper 98-0286*, 1998.

[12] X. Zhang, A. Rona, and J.A. Edwards. The effect of trailing edge geometry on cavity flow oscillation driven by a supersonic shear layer. *The aeronautical journal*, pages 129--136, March 1998.

[13] P.D. Orkwis, B. Sekar, S. Chakravarthy, and O. Peroomian. Comparison of three Navier-Stokes equation solvers for supersonic open cavity simulations. *AIAA Journal*, 36(5), 1998.

[14] T. Colonius, A.J. Basu, and C.W. Rowley. Numerical investigation of the flow past a cavity. *AIAA Paper 99-1912*, 1999.

[15] B.R. Smith, J.K. Jordan, E.E. Bender, S.N. Rizk, and L.L. Shaw. Computational simulation of active control of cavity acoustics. *AIAA Paper 2000-1927*, 2000.

[16] J.W. Boerstoel, A. Kassies, J.C. Kok, and S.P. Spekreijse. *ENFLOW, A full-functionality system of CFD codes for industrial Euler/Navier-Stokes Flow Computations*. NLR TP 96286 (presented at the 2nd Int. Symp. on Aeron. Science and Tech., Jakarta, 1996).

[17] J.C. Kok. Resolving the dependence on freestream values for the k-ω turbulence model. *AIAA Journal,* 38(7), pp. 1292–1294, 2000.

[18] J.C. Kok and S.P. Spekreijse. *Efficient and accurate implementation of the k-ω turbulence model in the NLR multi-block Navier-Stokes system*. NLR TP-2000-144 (presented at ECCOMAS 2000, Barcelona, Spain, 11-14 September, 2000).

[19] F.J. Brandsma, J.C. Kok, H.S. Dol, A. Elsenaar. *Leading edge vortex flow computations and comparison with DNW-HST wind tunnel data*. RTO/AVT Vortex Flow Symposium, Norway, 2001.
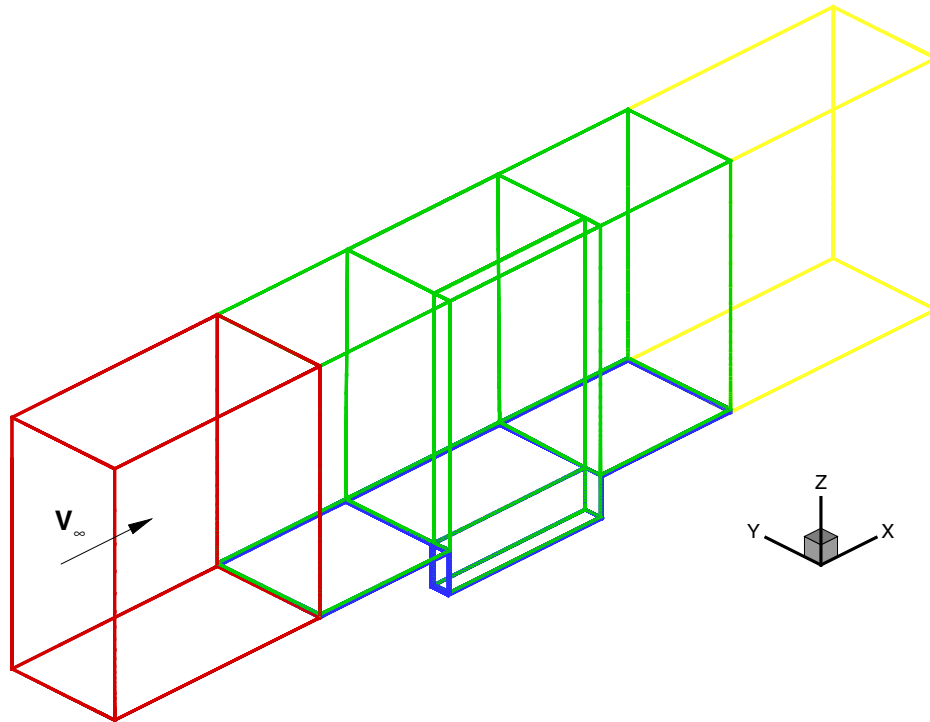
Figure 1 Flow domain modelling of the cavity flowfield.

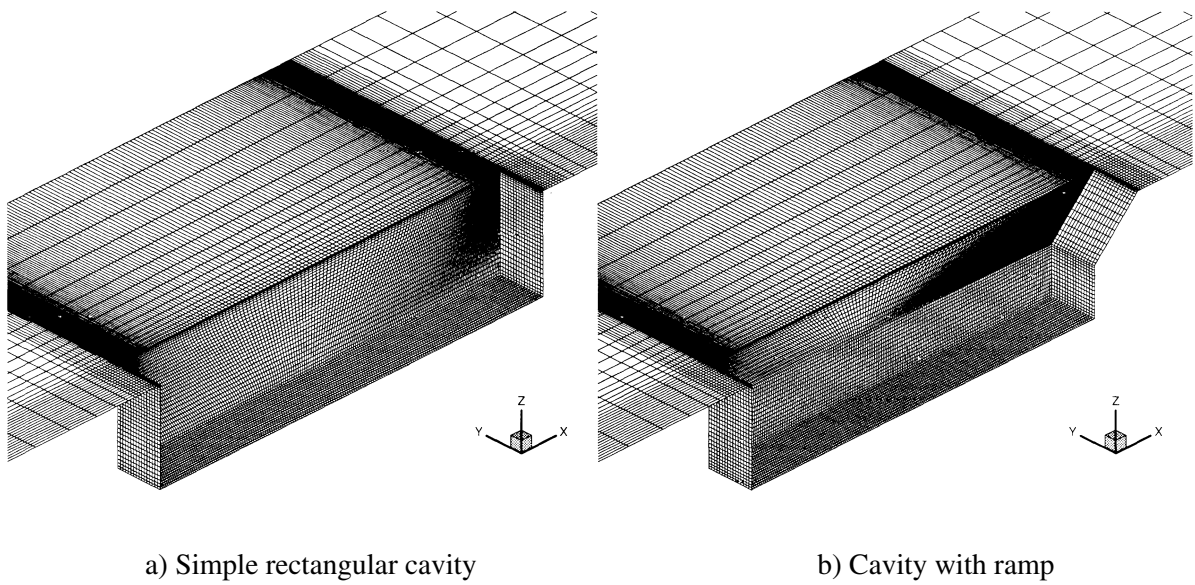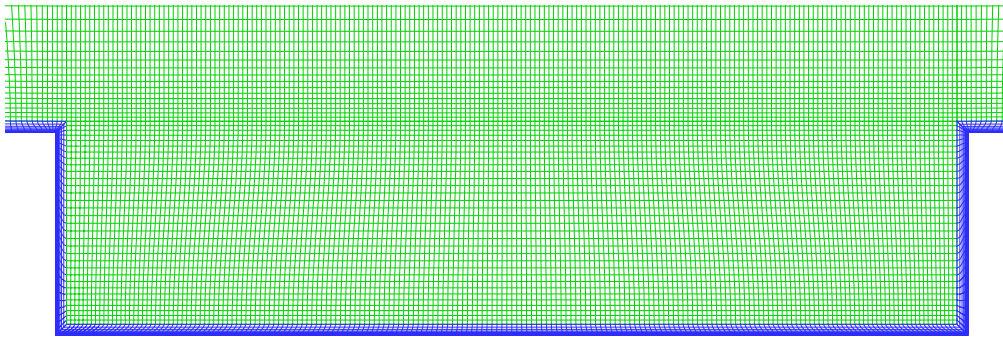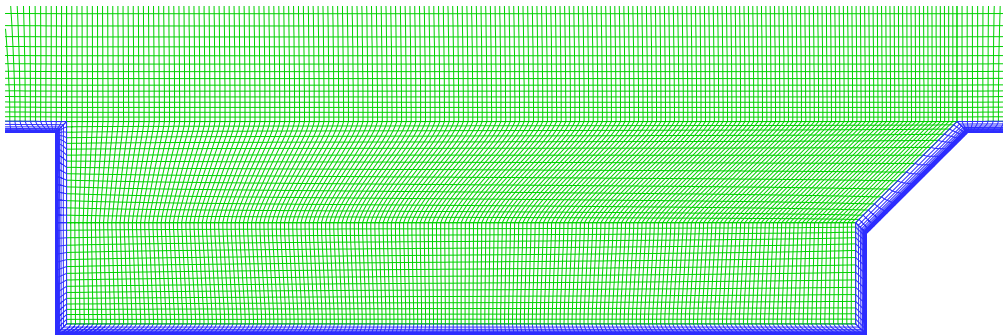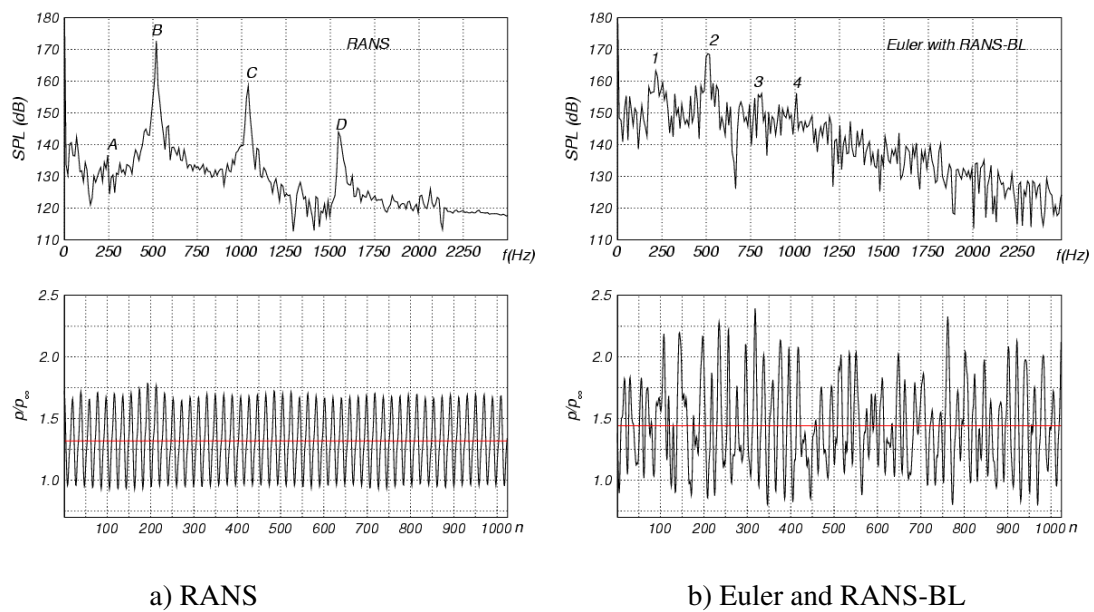a) Simple rectangular cavity

b) Cavity with ramp

Figure 2 Computational grids on the solid surfaces.

a) Simple rectangular cavity

b) Cavity with ramp

Figure 3 Computational grids on the symmetry planes.

a) RANS

b) Euler and RANS-BL

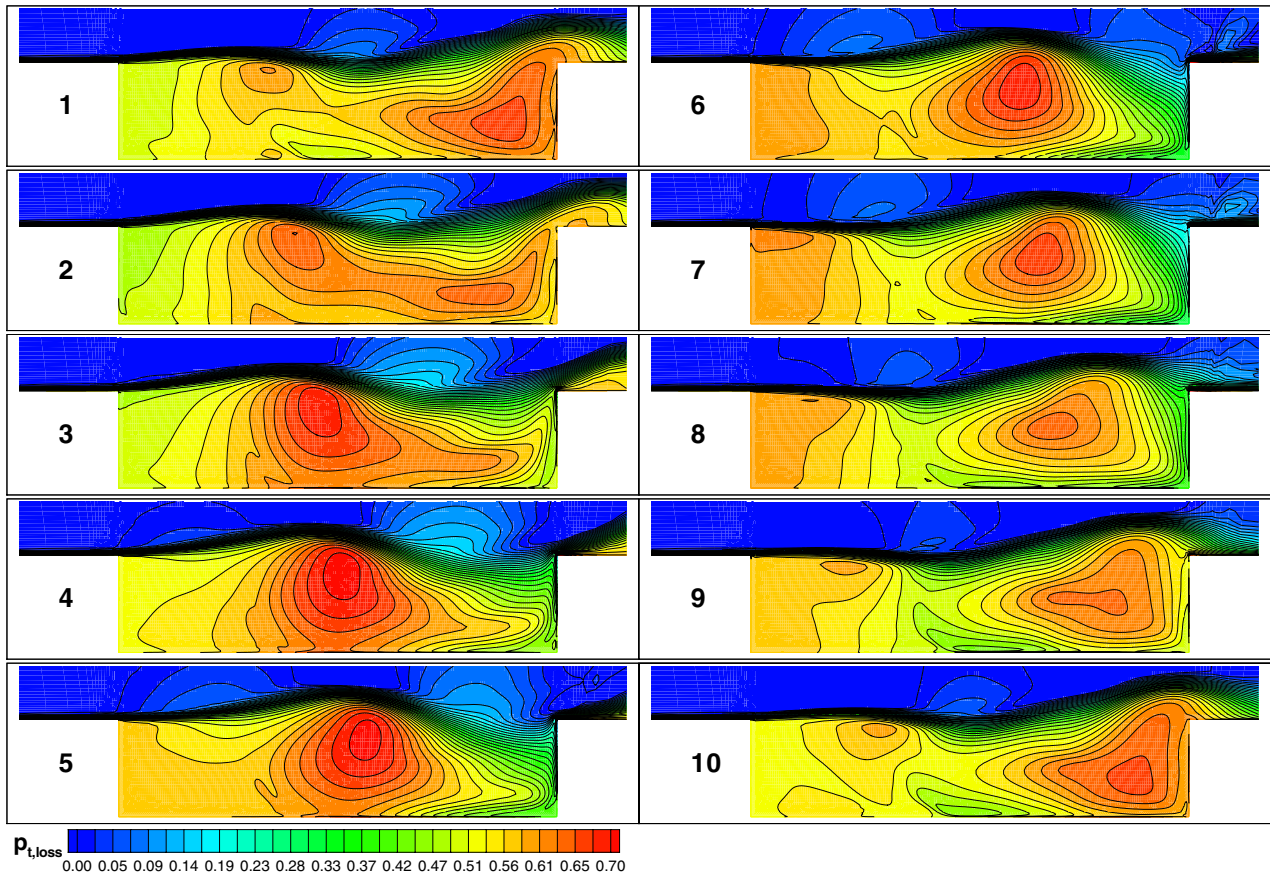**Figure 4 Unsteady pressure fluctuations and frequency spectra of the simple rectangular cavity flowfield.**

Figure 5 Instantaneous total pressure loss contours produced by the RANS model.
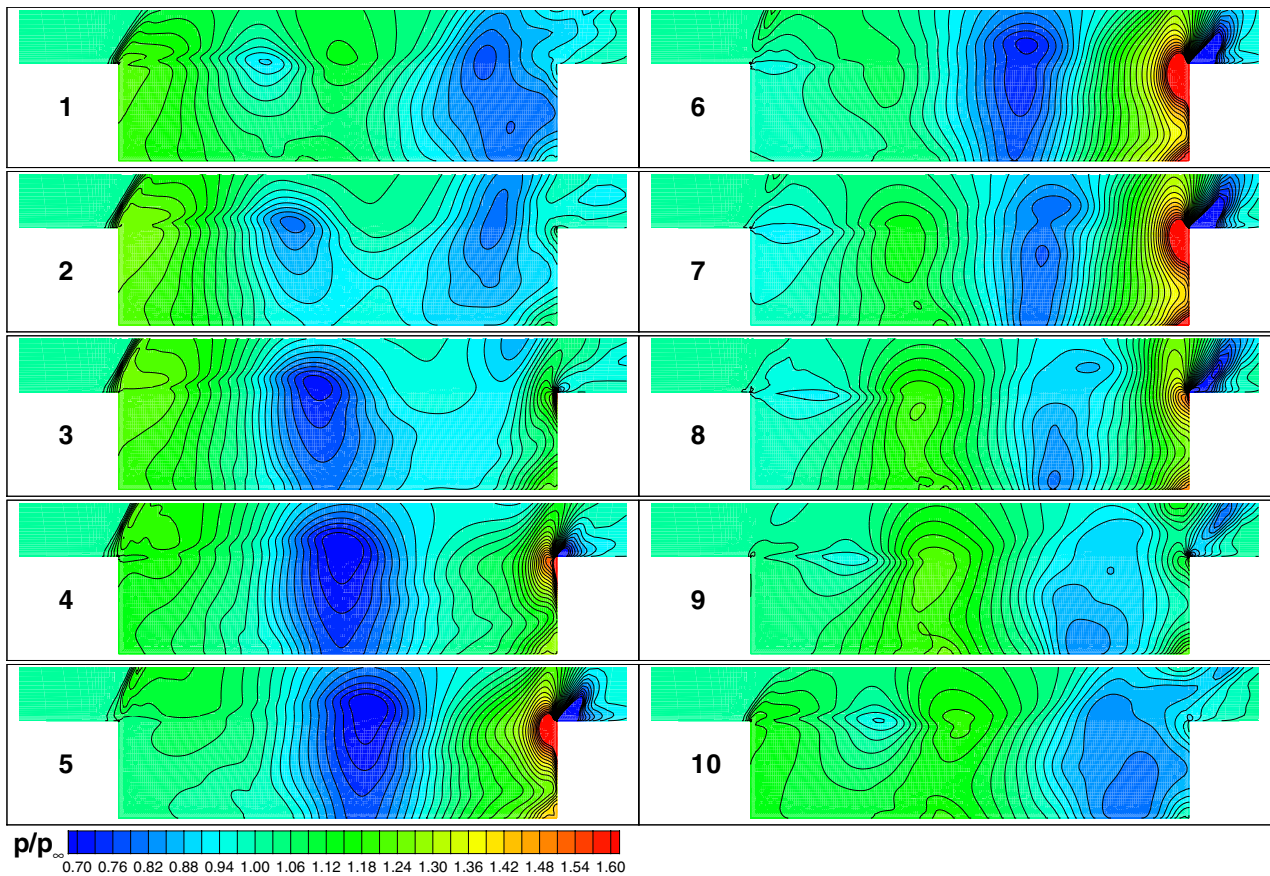
Figure 6 Instantaneous static pressure contours produced by the RANS model.
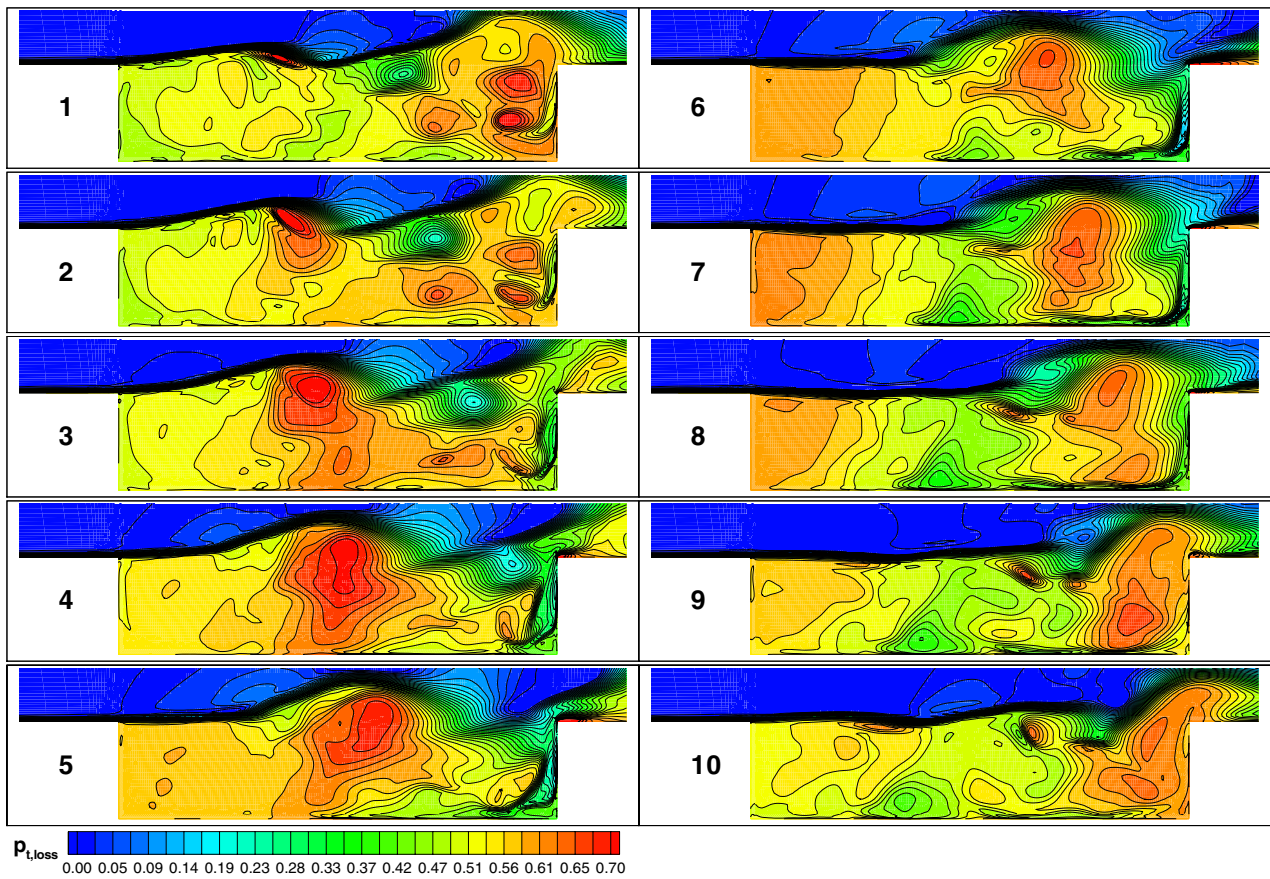
Figure 7 Instantaneous total pressure loss contours produced by the Euler with boundary layer model.
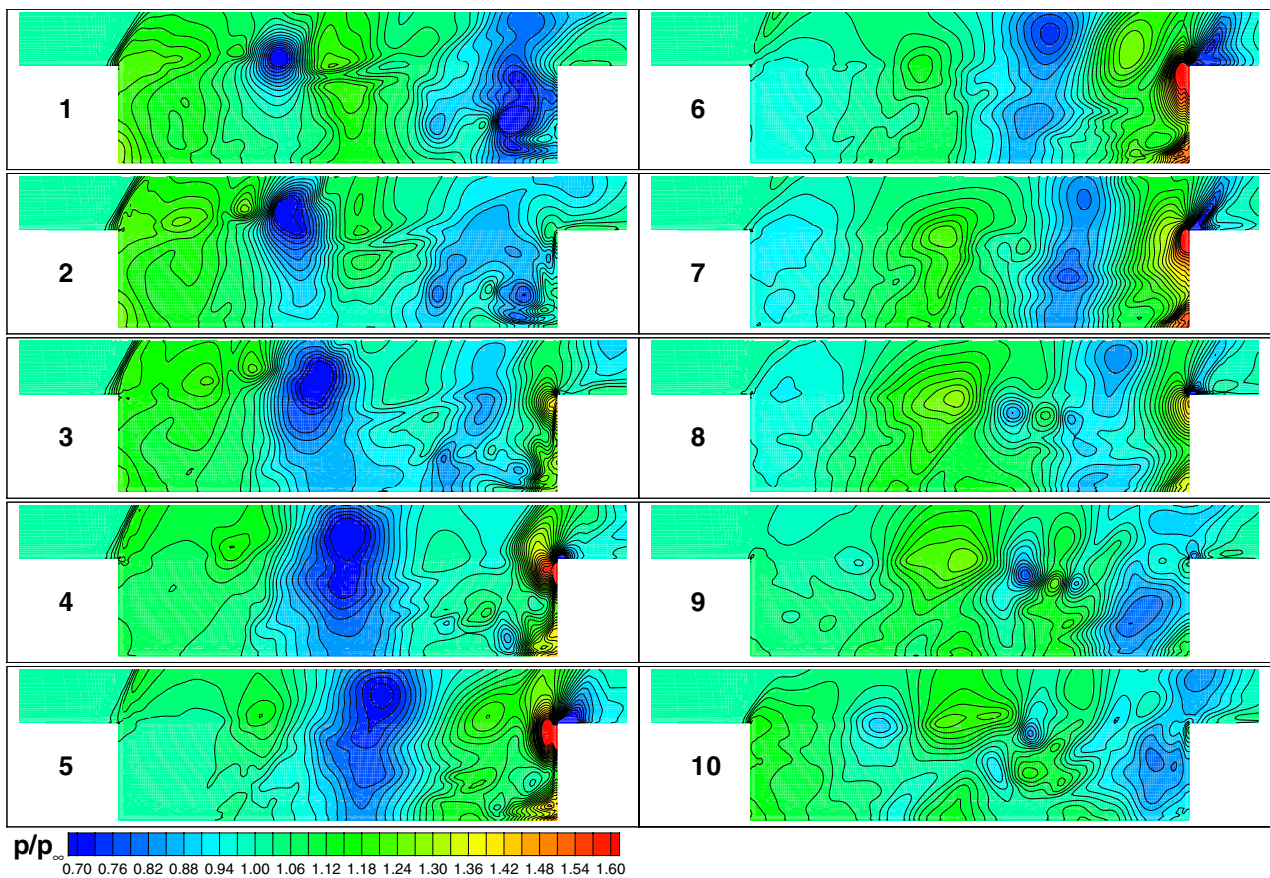
Figure 8 Instantaneous static pressure contours produced by the Euler with boundary layer model.
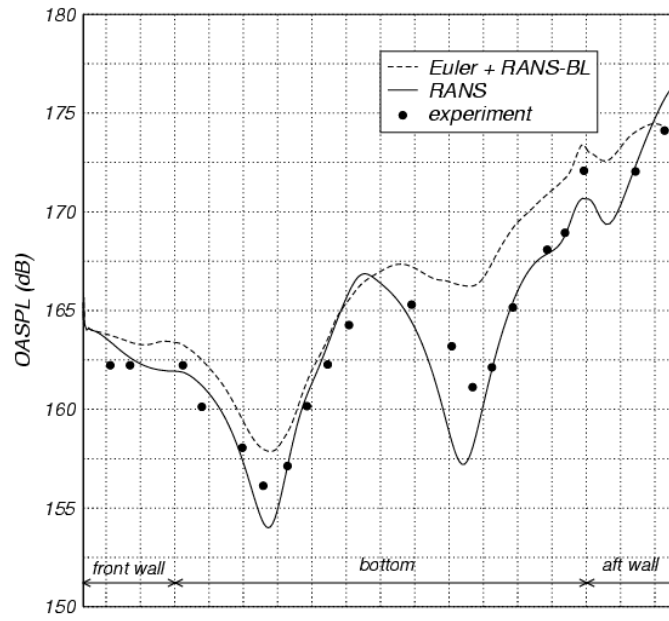
Figure 9 Overall sound pressure level (OASPL) along the centreline of the simple rectangular cavity (the experimental values are obtained from the data presented in Ref. [7]).
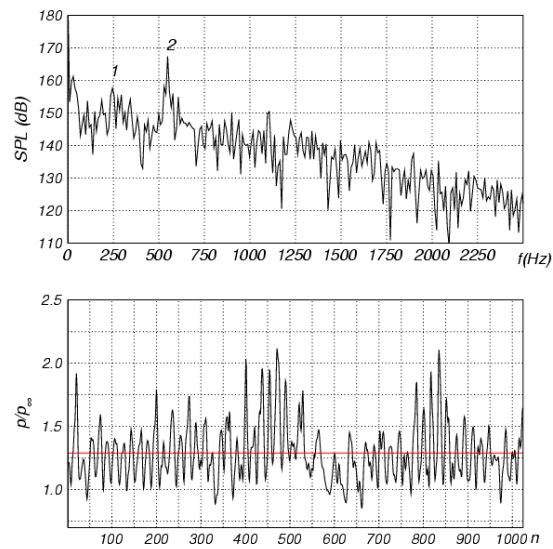
Figure 10 Unsteady pressure fluctuations and frequency spectra of the cavity with ramp.
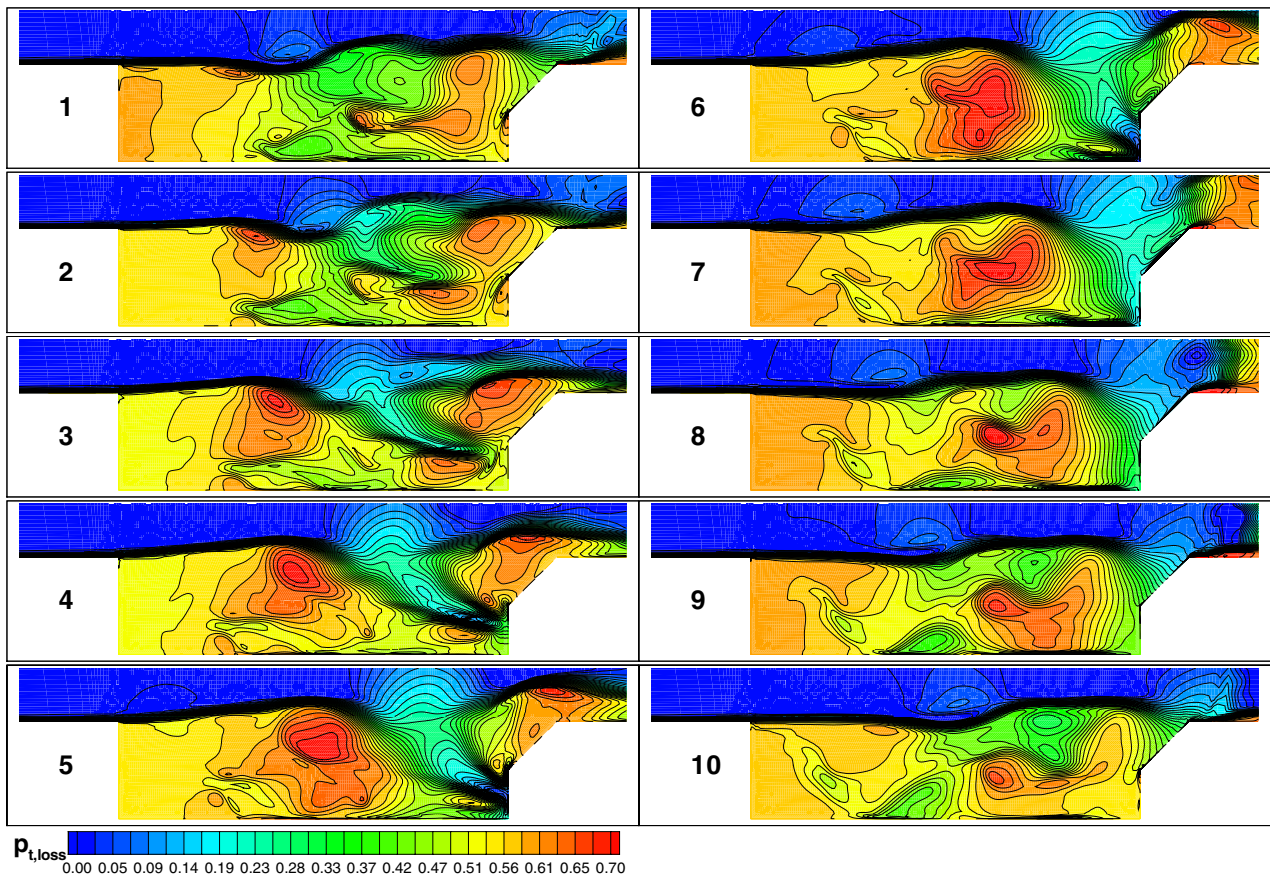
Figure 11 Instantaneous total pressure loss contours produced by the Euler with boundary layer model.
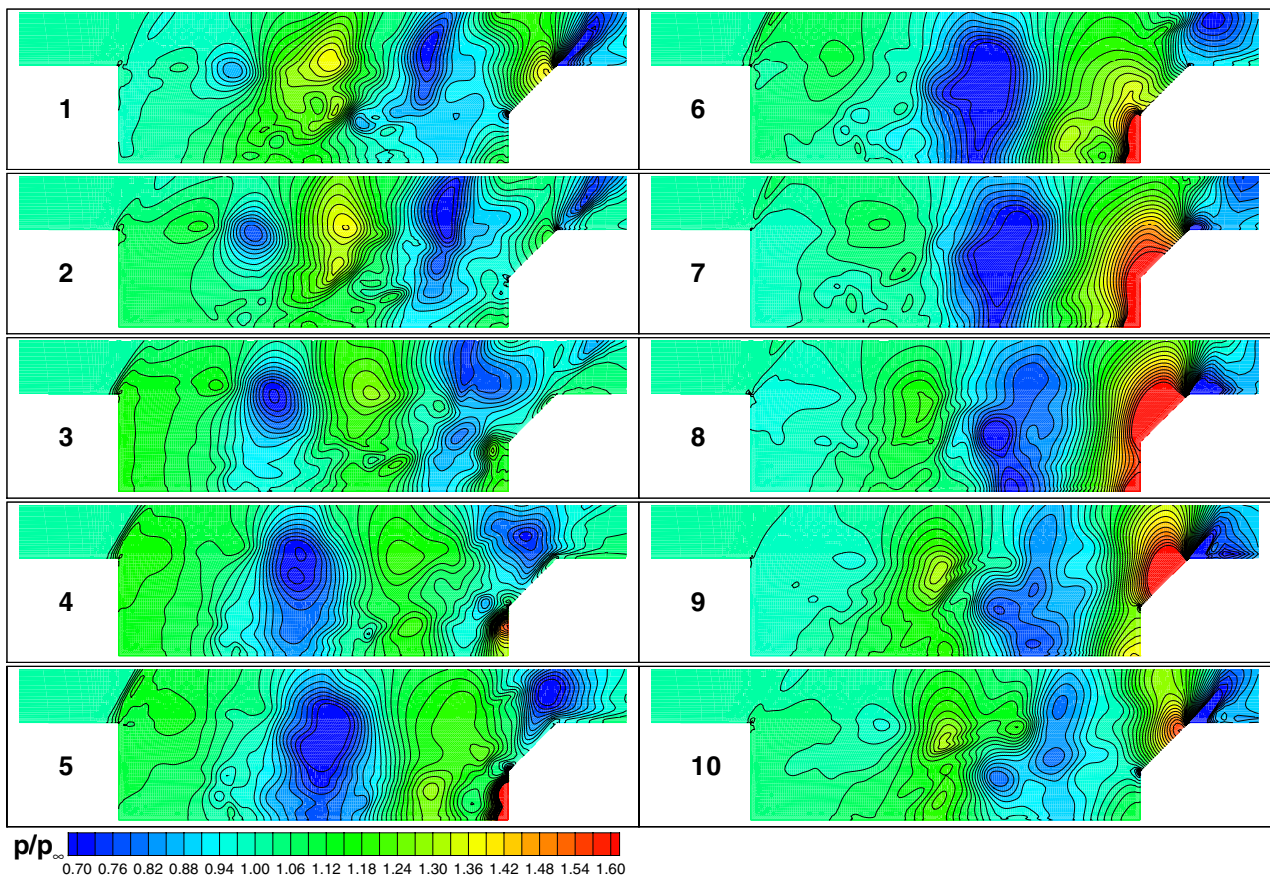
Figure 12 Instantaneous static pressure contours produced by the Euler with boundary layer model.
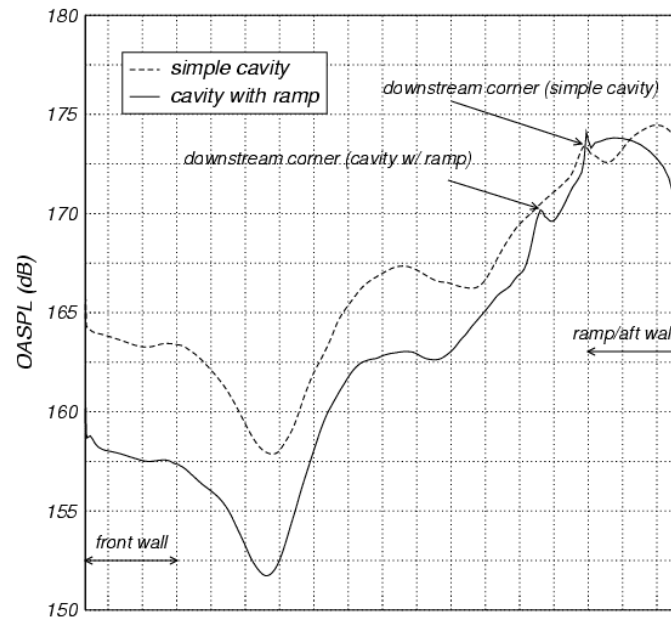
Figure 13 Effect of the trailing edge geometries to the overall sound pressure level.

Reference # of Paper: 21
Discusser's Name: Dr. Jan Delfs
Author's Name: Dr. Ir. B. I. Soemarwoto
Question:

      The RANS simulation shows periodic behavior while Rossiter's formula predicts resonant frequencies that are not harmonics of each other. So, the cavity oscillations occur in a quasi-periodic fashion rather than as a periodic phenomenon. Does your solution depend on the initial conditions for the excitation of different modes?

Answer:

      It is not expected that the solutions depend on the initial conditions. The solutions presented in the paper have been obtained after any transient effects have appeared to decay.

Discusser's Name: Prof. Dr. Rolf Radespiel
Author's Name: Dr. Ir. B. I. Soemarwoto
Question:

      Did you investigate the role that numerical discretization errors, such as dispersion and dissipation, play in your solutions?

Answer:

      No specific investigation has been made with respect to the numerical discretization errors. The sampling rate for the time step size covers 20 data points for the resolved mode and is represented spatially by 16 grid points.

Discusser's Name: Prof. Philip Morris
Author's Name: Dr. Ir. B. I. Soemarwoto
Question:

      Did you consider the use of the Detached Eddy Simulation (DES)? Could you give more details of the aeroelastic coupling? What do you plan to do? Is it a full coupling of the fluid and structure?

Answer:

      The use of DES is consistent with the conclusions presented in the paper. The aeroelastic simulation has a full coupling of the fluid (ENFLOW) and structure (NASTRAN).

This page has been deliberately left blank

_____

Page intentionnellement blanche

Direct Calculation of Cavity Noise
and Validation of Acoustic Analogies

Xavier Gloerfelt, Christophe Bailly and Daniel Juvé

Laboratoire de Mécanique des Fluides et d'Acoustique
Ecole Centrale de Lyon & UMR CNRS 5509
BP 163, 69131 Ecully cedex, France.

1. Introduction

Flow-induced cavity noise is a harmful noise source in many applications.[1] A complex nonlinear phenomenon is responsible for the intense self-sustained oscillations observed in experiments. However, the pysics is difficult to model analytically. The tonal Strouhal numbers are well approximated by Rossiter's formula[2] for a wide range of configurations but this simple semi-empirical analysis is not able to indicate the main oscillation mode neither its amplitude. Moreover, it is now generally recognized that noise generation mechanism can be dependent on the incoming boundary layer, the geometric properties of the cavity, the Mach number of the mean flow, and many other parameters. To predict detailed assessments of noise generation in complex cases, direct evaluation from fluid mechanics equations through DNS or LES with CAA tools represents the most thorough technique currently available. Nevertheless, the storage requirement and computation time make simulations of both the flow and acoustic fields difficult for realistic applications.

An alternative approach for computing the cavity noise consists of a two step calculation: nonlinear generation of sound and linear sound propagation. Once sources have been identified, with CFD or CAA calculations, there are several techniques to calculate the resulting radiated field. In this work, we propose to study numerical issues of three integral formulations: the Ffowcs Williams and Hawkings (FW-H) analogy which extends Lighthill's theory to account for solid boundaries and two Wave Extrapolation Methods (WEM) from a control surface, the Kirchhoff and porous FW-H methods. All these integral formulations have similar analytical insights based on Green's function formalism and suffer from the limitation of the observer in a uniform flow. The linear wave equation is assumed valid outside the source region, so that nonlinear propagation of acoustic waves is also not described.

In the first part of this paper, we shall present the direct computation of Navier-Stokes equations for a two-dimensional rectangular cavity with aspect ratio of 2, matching one configuration of Karamcheti's experiments.[3] In the second part, the far-field noise, associated with sources computed from the previous DNS, is obtained using the three integral formulations. Each method shall

1

be described and the results shall be compared with those of direct acoustic simulation taken as a reference.

2. Direct computation of cavity noise

2.1 Introduction

Despite the amount of numerical studies published on cavity flows, few deal with radiated noise. Initial attemps have been made in supersonic cases, where acoustic field is dominated by shock waves radiation. These CFD computations of compressible cavity flows used the two dimensional unsteady RANS (Reynolds Averaged Navier-Stokes) equations with a turbulence model.[4,5] The first computations of acoustic radiation from a cavity with a subsonic grazing flow have been carried out recently by Colonius *et al.*,[6] and Shieh & Morris[7] using 2-D Direct Numerical Simulation (DNS) at a Reynolds number based on cavity depth $Re_D \simeq 5000$. To investigate higher Reynolds numbers ($Re_D \simeq 2 \times 10^5$), Shieh & Morris[8] applied CAA tools to solve unsteady RANS with a turbulence model: the one equation Spalart-Allmaras turbulence model and Detached Eddy Simulation have been implemented.

In the present work, the tested configuration is a 2-D rectangular cavity with $L/D = 2$, where $L = 5.18$ mm is the cavity length and $D = 2.54$ mm is its depth. The incoming flow is a laminar boundary layer with a Mach number M= 0.7 and a thickness $\delta \approx 0.2D$. The Reynolds number chosen is $Re_D = 41000$ in order to match Karamcheti's experiment.[3] The latter studied the acoustic radiation from two-dimensional rectangular cavities cut into a flat surface at low Reynolds numbers. The acoustic fields were investigated by means of Schlieren observations, interferometry, and hot-wire anemometer. In our simulation, the freestream air temperature T_∞ is 298.15 K and the static pressure p_∞ is taken as 1 atm. The relatively thick incoming boundary layer ensures the shear layer mode of oscillations.[9] The choice of a high subsonic speed is interesting because the frequency increases slightly with Mach number and the cavity is no more compact relatively to the acoustic wavelength. Moreover, the test case is more relevant for integral methods because mean flow effects on sound propagation are important.

2.2 Numerical procedure

A Direct Numerical Simulation (no turbulence model) of the 2-D compressible Navier-Stokes equations is performed. These governing equations are discretized with a fourth order, seven-point stencil, DRP differencing operator spatially, and are advanced in time with the use of an explicit 4th order Runge-Kutta scheme.[9,10] Nonreflecting conditions are implemented to avoid spurious reflections which can superpose to physical waves. To this end, the radiation boundary conditions of Tam and Dong,[11] using a polar asymptotic solution of the linearized Euler equations in the acoustic far-field, are applied to the inflow and upper boundaries. At the outflow, we combine the outflow boundary conditions of Tam and Dong, where the asymptotic solution is modified to allow

the exit of vortical and entropic disturbances, with a sponge zone to dissipate vortical structures in the region where the shear layer leaves the computational domain. This sponge zone uses grid stretching and progressive additional damping terms.[10] Along the solid walls, the nonslip condition applies. The wall temperature T_w is calculated using the adiabatic condition. We keep centered differencing at the wall to ensure sufficient robustness using ghost points.

The computational mesh is built up from nonuniform Cartesian grid with 147×161 points inside the cavity and 501×440 outside, highly clustered near the walls. The minimum step size corresponds to $\Delta y_{min}^+ = 0.8$ in order to resolve the viscous sublayer. The computational domain extends over $8.5D$ vertically and $12D$ horizontally to include a portion of the radiated field. The upstream and downstream boundaries are sufficiently far away from the cavity to avoid possible self-forcing. The initial condition is a polynomial expression of the laminar Blasius boundary layer profile with no forcing terms. Owing to the strong anisotropic computational mesh, we have a very stiff discretized system. For explicit time marching schemes, an extremely small time step has to be used in order to satisfy the stability CFL criterion: $\Delta t = 0.7 \times \Delta y_{min}/c_\infty = 6.06 \times 10^{-9}$ s. A selective damping, with a mesh Reynolds number of $R_S = 4.5$, has to be introduced in order to filter out non physical short waves resulting from the use of finite differences and/or treatment of boundary conditions. It is applied a second time near the walls. The computation is 4 hours long on a Nec SX-5.

2.3 Results and discussion

a)   b)
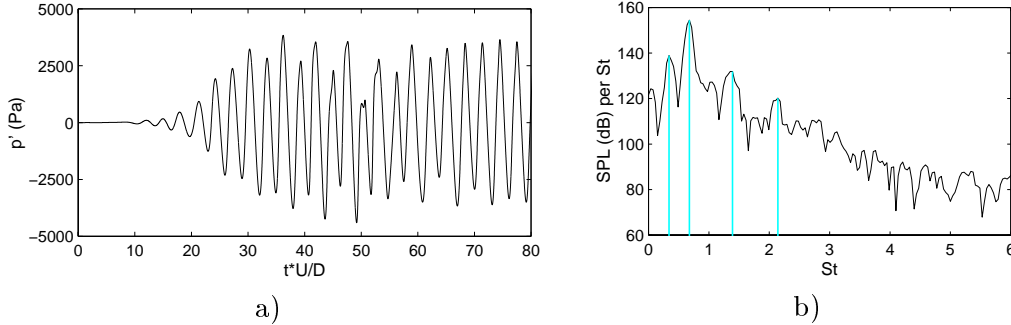
Figure 1: a) Pressure history versus time, and b) Spectrum of pressure fluctuations versus the Strouhal number St= fL/U_∞, at $x/D = -0.04$ and $y/D = 2D$.

Figure 1a gives a monitored pressure history in the near-field acoustic region. The flow reaches a self-sustained oscillatory state after a time of about $25D/U_\infty$ but is still irregular until $65D/U_\infty$. This transient time corresponds with the time needed by the recirculating flow to get installed in the cavity. The associated sound pressure level spectrum is depicted in figure 1b, and displays one principal peak at St= 0.68. Several secondary peaks are noticeable and represent harmonics or subharmonics of the fundamental mode f_0. The experimental Strouhal number of oscillations is St= 0.71. This error of 5% on the predicted frequency can be explained by the different incoming

3

flow parameters or by the neglected 3-D effects.

A snapshot of vorticity depicted in figure 2a shows the presence of two vortical structures convected in the shear layer and impinging periodically the downstream edge of the cavity at the frequency f_0. The induced compression waves travel upstream and excite the shear layer at the separation point near the leading edge, sustaining the oscillation process. The Rossiter semi-empirical formula[2] provides St$= 0.71$ for this configuration with always two vortices in the shear layer.

A Schlieren visualization, corresponding with vertical gradients of density, shows the structure of the radiated field in figure 2b. Two wave patterns are visible for the positive gradients (dark), which interfer during propagation. Their strong upstream directivity is characteristic of high speed convection by the free stream. These radiations are in qualitatively good agreement with the Schlieren picture taken from Karamcheti's experiment. From finite-frange interferometry, Karamcheti[3] estimated an overall pressure level of about 160 dB at a distance of around three cavity depths. The spectrum of figure 1b indicates a level of 156 dB at $2.9D$.
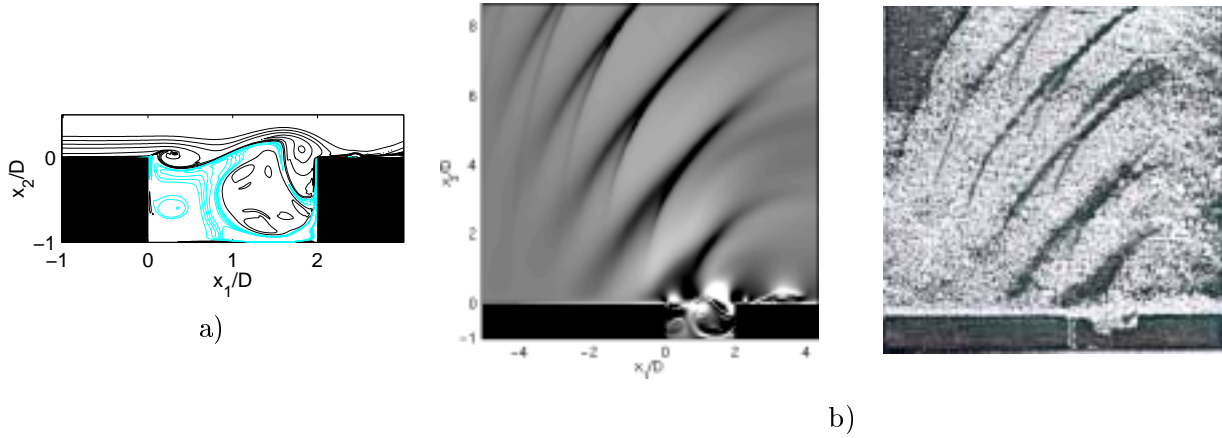
Figure 2: a) Snapshot of vorticity contours (16 contours between $\omega D/U_\infty = -10.5$ and 1.36: (———) negative contours, (———) positive contours). b) Schlieren pictures corresponding to transversal derivative of the density: present simulation on the left, Karamcheti's experiment[3] on the right.

3. Validation of integral methods

Integral methods rest upon two principal physical backgrounds: first, the acoustic analogy which split the computational domain in an aerodynamic region, where source terms responsible for noise generation are built up, and an acoustic region governed by a linear wave equation; second, the wave extrapolations which allow the evaluation of the far-field once some quantities are known on a control surface.

Recent advances in integral methods were essentially developed for the reduction of helicopter rotor noise[12] and have been recently applied for the prediction of jet noise.[13,14] Zhang, Rona, and Lilley[5] have used Curle's spatial formulation to obtain far-field spectra of cavity noise.

3.1 Acoustic analogy

The acoustic analogy was proposed by Lighthill[15] and was extended by Ffowcs Williams and Hawkings[16] to include the effects of solid surfaces in arbitrary motion. The FW-H equation is an exact rearrangement of the continuity equation and Navier-Stokes equations into the form of an inhomogeneous wave equation with two surface source terms and a volume source term. An integral solution can thus be obtained by convoluting the wave equation with the free-space Green function.

A serious restriction is that the observation region is assumed at rest. It is difficult to extend the propagation operator to include more complex flows. Only the case of a uniform flow is satisfactorily treated. Ffowcs Williams and Hawkings proposed the use of a Lagrangian coordinate transform assuming the surface is moving in a fluid at rest. Goldstein[17] preferred to take the convection effects in the wave equation. In the same manner, in the case of a motion with constant velocity $\mathbf{U}_\infty = (U_1, 0)$, the application of the Galilean transformation from the observer position $(\tilde{\mathbf{x}}, t)$, moving at $-\mathbf{U}_\infty$ to the fixed location $(\mathbf{x}, t)$, defined by:

$$x_i = \tilde{x}_i + U_i t,$$

leads to the convected FW-H equation[18]:

$$\left(\frac{\partial^2}{\partial t^2} + U_i U_j \frac{\partial^2}{\partial x_i x_j} + 2U_i \frac{\partial^2}{\partial x_i t} - c_\infty^2 \frac{\partial^2}{\partial x_i^2} \right) \left(H(f) c_\infty^2 \rho'(\mathbf{x}, \omega) \right)$$

$$= \frac{\partial^2}{\partial x_i \partial x_j} \left(\tilde{T}_{ij}(\mathbf{x}, \omega) H(f) \right) - \frac{\partial}{\partial x_i} \left(\tilde{F}_i(\mathbf{x}, \omega) \delta(f) \right) + \frac{\partial}{\partial t} \left(\tilde{Q}(\mathbf{x}, \omega) \delta(f) \right) \tag{1}$$

where the modified source terms including convection can be written as:

$$\tilde{T}_{ij} = \rho(u_i - U_i)(u_j - U_j) + \left[p - c_\infty^2 \rho' \right] \delta_{ij} - \tau_{ij} \tag{2}$$

$$\tilde{F}_i = \left[\rho_\infty U_i U_j + p \delta_{ij} - \tau_{ij} \right] \frac{\partial f}{\partial x_j} \tag{3}$$

$$\tilde{Q} = \left[-\rho_\infty U_j \right] \frac{\partial f}{\partial x_j} \tag{4}$$

H is the Heaviside function and the function $f = 0$ defines the surface Σ outside of which the density field is calculated. f is scaled so that $\partial f / \partial x_j = n_j$, the j-component of the unit normal vector pointing toward the observer domain $(f > 0)$. For a rigid body, we have simplified the surface source terms using the impenetrability condition $\mathbf{u}.\mathbf{n} = 0$.

For bidimensional geometries, it is more convenient to resolve this equation in the spectral-domain.[18] The frequency-domain formulation avoids the evaluation of the retarded time, which can be a critical point. The gain over the time-domain applications is enhanced in 2-D because of the weaker properties of the Heaviside function which replaces the Dirac function. Whereas the Dirac leads to a retarded time expression removing the temporal integration, the Heaviside function can

only change the upper limit of the integration to a finite value, the lower limit remaining infinite. The spectral formulation removes this time constraint by solving FW-H equation harmonically. With application of the Fourier transform:

$$\mathcal{F}\left[\phi(\mathbf{x},t)\right] = \phi(\mathbf{x},\omega) = \int_{-\infty}^{\infty} \phi(\mathbf{x},t)e^{-i\omega t}\,dt \tag{5}$$

equation (1) becomes

$$\left(\frac{\partial^2}{\partial x_i^2} + k^2 - 2iM_ik\frac{\partial}{\partial x_i} - M_iM_j\frac{\partial^2}{\partial x_i\partial x_j}\right)\left(H(f)c_\infty^2\rho'(\mathbf{x},\omega)\right)$$
$$= -\frac{\partial^2}{\partial x_i\partial x_j}\left(\tilde{T}_{ij}(\mathbf{x},\omega)H(f)\right) + \frac{\partial}{\partial x_i}\left(\tilde{F}_i(\mathbf{x},\omega)\delta(f)\right) - i\omega\tilde{Q}(\mathbf{x},\omega)\delta(f) \tag{6}$$

where $\mathrm{M}_i = U_i/c_\infty$. A Green function for this inhomogeneous convected wave equation is obtained from a Prandtl-Glauert transformation of the 2-D free-space Green's fonction in the frequency domain:

$$G(\mathbf{x}\mid\mathbf{y},\omega) = \frac{i}{4\beta}e^{i(\mathrm{M}k(x_1-y_1)/\beta^2)}H_0^{(2)}\left(\frac{k}{\beta^2}r_\beta\right) \tag{7}$$

where $r_\beta = \sqrt{(x_1-y_1)^2 + \beta^2(x_2-y_2)^2}$, $H_0^{(2)}$ is the Hankel function of the second kind and order zero, and $\beta = \sqrt{1-\mathrm{M}^2}$ is the Prandtl-Glauert factor, $\mathrm{M} < 1$. The integral solution of equation (6) is then given by:

$$H(f)p'(\mathbf{x},\omega) = -\int_{f=0}\tilde{F}_i(\mathbf{y},\omega)\frac{\partial G(\mathbf{x}\mid\mathbf{y})}{\partial y_i}\,d\Sigma - \int_{f=0}i\omega\tilde{Q}(\mathbf{y},\omega)G(\mathbf{x}\mid\mathbf{y})\,d\Sigma$$
$$-\iint_{f>0}\tilde{T}_{ij}(\mathbf{y},\omega)\frac{\partial^2 G(\mathbf{x}\mid\mathbf{y})}{\partial y_i\partial y_j}\,d\mathbf{y} \tag{8}$$

In 2-D, the volume integral is restricted to the surface including the aerodynamic sources T_{ij} and the surface integrals are calculated on the solid lines which represent rigid boundaries. We applied the spatial derivatives on the Green function to avoid the evaluation of derivatives of aerodynamic quantities. It is formally equivalent to the transformation in temporal derivatives as performed by di Francescantonio[19] or Farassat and Myers.[20]

3.2 Wave extrapolation methods

This kind of methods permits one to solve linear wave propagation problem once some flow quantities are given on a closed fictitious surface surrounding all the sources. The most famous one is the Kirchhoff method which makes a parallel with electromagnetism by using Kirchhoff's formula, published in 1883. The use of the FW-H equation for a permeable surface can provide an alternative extrapolation method as noted in the original Ffowcs Williams and Hawkings paper.[16] This method has been recently implemented by di Francescantonio.[19] At nearly the same time, Brentner and Farassat[21] demonstrated the relationship between the FW-H equation and the Kirchhoff equation for moving surfaces. The FW-H and Kirchhoff formulations solve the same physical problem, the differences between the two writings being due to some choices made in the derivation process.

The main advantage of wave extrapolation methods with respect to acoustic analogy approaches is that only surface integrals have to be evaluated because all non linear quadrupolar sources are enclosed in the control surface. The problem is thus reduced by one dimension, which is particularly interesting in a numerical point of view.

The convected Kirchhoff method

For a moving medium, the acoustic pressure at an arbitrary point $\mathbf{x}$ and time t is related to the distribution γ of sources within V and the distribution of the pressure and its derivative on the boundary of V by the generalized Green's formula.[17] For a 2-D configuration, it can be written as:

$$H(f)p'(\mathbf{x},t) = \int_{-\infty}^{\infty} \iint_{V(f>0)} \gamma(\mathbf{y},\tau) G(\mathbf{x},t|\mathbf{y},\tau)\, d\mathbf{y} d\tau$$

$$+ \int_{-\infty}^{\infty} \int_{\Sigma(f=0)} \left\{ G\frac{\partial p}{\partial y_i} - p\frac{\partial G}{\partial y_i} \right\} n_i\, d\Sigma(\mathbf{y}) d\tau + \frac{U_1}{c_\infty^2} \int_{-\infty}^{\infty} \int_{\Sigma(f=0)} \left\{ p\frac{DG}{D\tau} - G\frac{Dp}{D\tau} \right\} n_1\, d\Sigma(\mathbf{y}) d\tau$$

where D/Dt is the time rate of change seen by an observer moving along with the mean flow. Expressing the Green's function in the frequency-domain (7) and assuming all the quadrupolar source γ are included in Σ, we obtain:

$$H(f)p'(\mathbf{x},\omega) = \frac{i\beta}{4} \int_{f=0} \left\{ \frac{\partial p(\mathbf{y},\omega)}{\partial n_\beta} H_0^{(2)}\left(\frac{k}{\beta^2} r_\beta\right) + \frac{k}{\beta^2} p(\mathbf{y},\omega) \left[\frac{\partial r_\beta}{\partial n_\beta} H_1^{(2)}\left(\frac{k}{\beta^2} r_\beta\right) \right. \right.$$

$$\left. \left. - i\mathrm{M}\frac{\partial y_1}{\partial n_\beta} H_0^{(2)}\left(\frac{k}{\beta^2} r_\beta\right) \right] \times \exp\left(i\frac{\mathrm{M}k(x_1 - y_1)}{\beta^2} \right) \right\} d\Sigma_\beta \qquad (9)$$

where n_β and $d\Sigma_\beta$ are the Prandtl-Glauert transforms of n and $d\Sigma$. This is the bidimensional Kirchhoff formulation for a uniformly moving medium in the frequency-domain.

The Ffowcs Williams and Hawkings WEM

This method is sometimes called the porous FW-H method because it coincides with the application of the FW-H analogy on a fictitious porous surface. The analytical developments are the same that those of the FW-H analogy but the impenetrability condition is no more required, and, on the contrary, one has to allow a fluid flow across Σ. For a two-dimensional problem with uniform subsonic motion, the FW-H WEM is given by equation (8) without the volume integral:

$$H(f)p'(\mathbf{x},\omega) = -\int_{f=0} \tilde{F}_i(\mathbf{y},\omega)\frac{\partial G(\mathbf{x}\mid\mathbf{y})}{\partial y_i}\, d\Sigma - \int_{f=0} i\omega\tilde{Q}(\mathbf{y},\omega) G(\mathbf{x}\mid\mathbf{y})\, d\Sigma \qquad (10)$$

with the two source terms:

$$\tilde{F}_i = [\rho(u_i - 2U_i)u_j + \rho_\infty U_i U_j + p\delta_{ij} - \tau_{ij}]\frac{\partial f}{\partial x_j} \qquad (11)$$

$$\tilde{Q} = [\rho u_j - \rho_\infty U_j]\frac{\partial f}{\partial x_j} \qquad (12)$$

7

3.3 Numerical implementation

From an algorithmic point of view, there is almost no difference between the three integral approaches considered here. The first step is the recording of the aerodynamic quantities during one period of the DNS computation. The acoustic time step is 40 times the DNS time step corresponding to 131 points per period. In the convected Kirchhoff method, the pressure distribution and its normal derivative over the three lines L_1, L_2, and L_3 spanning the longitudinal direction are needed to perform the surface integration. The normal derivative $\partial p/\partial y_2$ is not directly available from the near field solution and is here calculated with the DRP scheme. The variables (u_1, u_2, p, ρ) are recorded on the same three fictitious lines for the FW-H WEM, and on the walls of the cavity and the surface around it for the FW-H analogy application as reported in figure 3.
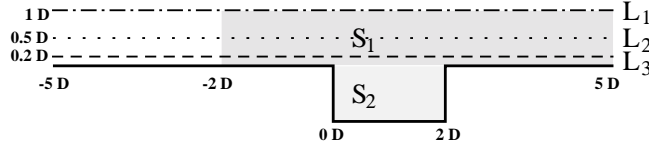
Figure 3: Schematic of the different line and surface sources for evaluation of integral formulations.

The source terms are calculated and transformed in the frequency-domain using the Fourier transform defined by (5). The integrals are then evaluated for each point of an acoustic meshgrid. This regular cartesian grid of 176×184 points covers a area of $(-5D; 5D) \times (-1D; 8D)$, corresponding with the main part of acoustic domain of DNS. Endly, an inverse Fourier transform is used to recover the acoustic signal in time-domain.

3.4 Results and discussions

In the Kirchhoff method, the results of the integration of (9) over L_1, L_2, and L_3 are depicted in figure 4. Same results are obtained for the extrapolation using the permeable form of the FW-H equation. The pressure fields from integration over L_1, L_2, and L_3 with source terms defined by (11), and (12), and with M= 0.7 in the observer domain are compared in figure 5. All the computed far-fields are consistent with that of DNS depicted in figure 6b, even when the control surface is located in the near-field region. The contour plots are only little sharper when the surface is farther from sources because more nonlinear effects are included in the control surface. In this configuration, the additional nonlinear terms appearing in the surface integrals of FW-H WEM but missing in the Kirchhoff formulation as noted by Brentner and Farassat[21] do not play a significant role and do not lead to the drastic differences observed in some previous comparisons when the control surface is too close to the sources.[21,22] Like di Francescantonio[19] or Prieur and Rahier,[23] we notice a similar behaviour of the two extrapolation methods. The advantage of porous FW-H method is only the fact that it uses directly the quantities computed by direct simulation without the need of further numerical process.
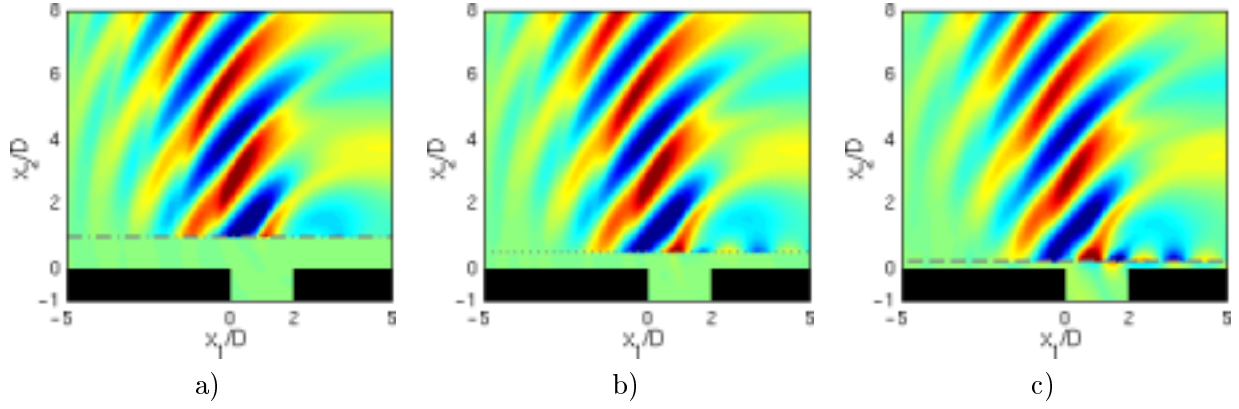
Figure 4: Pressure field calculated at the same time by a) Kirchhoff's method from L_1, b) Kirchhoff's method from L_2, c) Kirchhoff's method from L_3.
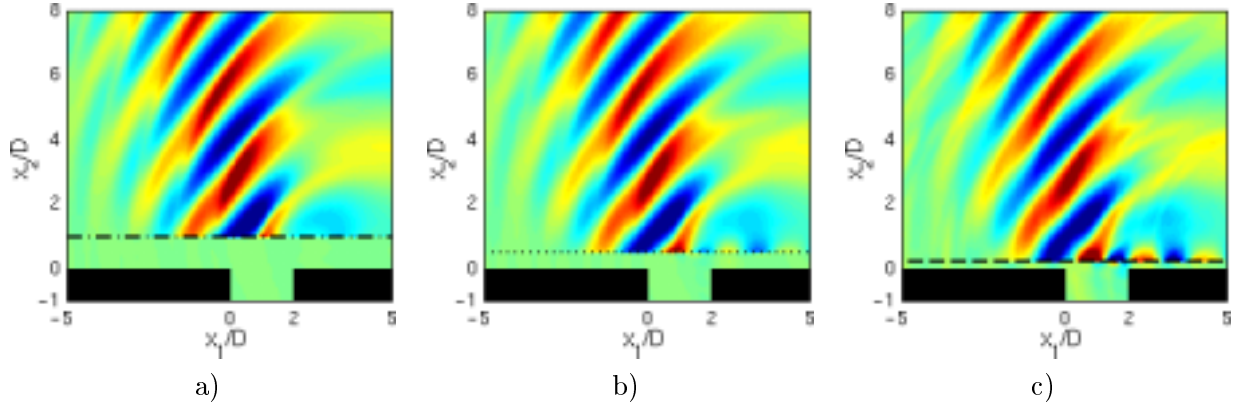

Figure 5: Pressure field calculated at the same time by a) FW-H WEM from L_1, b) FW-H WEM from L_2, c) FW-H WEM from L_3.

When we apply FW-H analogy, the surface integrals are evaluated on the physical rigid walls of the cavity and the volume integration is performed over the two surfaces S_1 and S_2 depicted in figure 3. The evaluation of volume integrals of T_{ij} are sensible to truncature effets, especially in the streamwise direction where the source terms decrease slowly. It is due to the presence of advected vortices, ejected from the cavity during the clipping process, in the reattached boundary layer on the downstream wall. By summing the volume and surface contributions (fig. 6a), we reconstruct the total sound field in reasonably good agreement with the DNS reference solution of figure 6b. A quantitative comparison with the other methods is provided by the pressure profiles and far-field directivity of figure 7. The results of the two WEM are similar and in fairly agreement with the DNS reference solution whereas more differences can be seen for the acoustic analogy profile. The main discrepancies for the directivity occur near the small angles θ (i.e. in the downstream direction) where the volume integration is abruptly cut by the end of the computational domain at $x_1 = 5D$, leading to truncature errors.

9

a)   b)
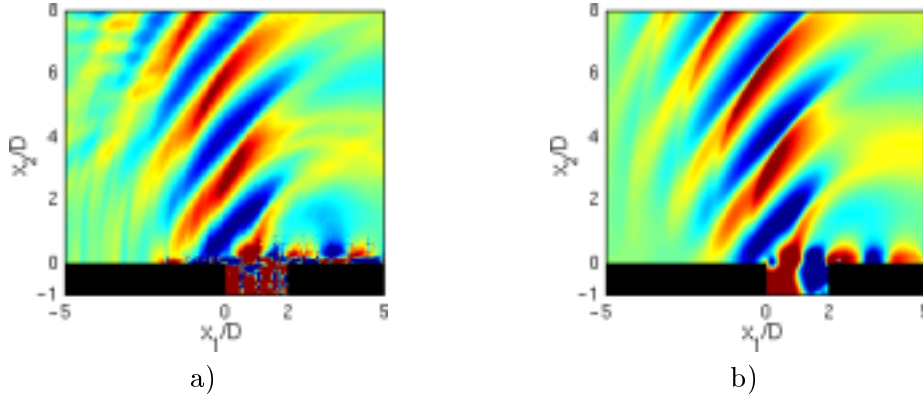
Figure 6: Pressure field calculated at the same time by a) FW-H analogy (surface + volume integrals), b) DNS reference solution.

a)   b)
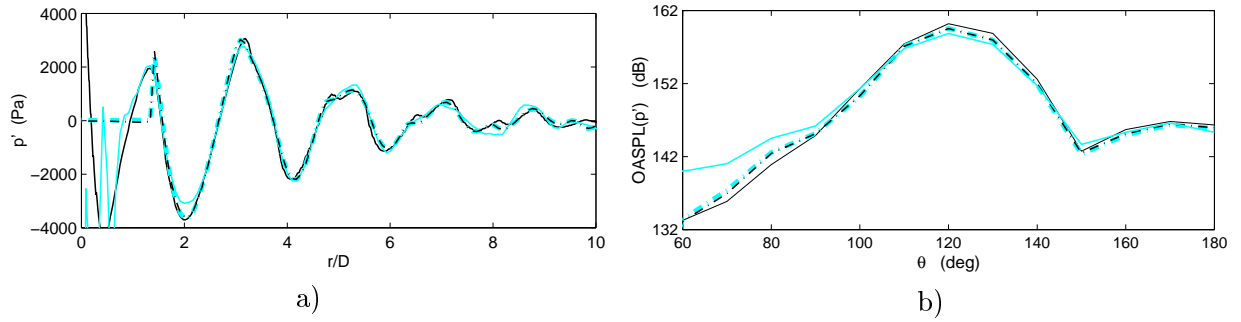
Figure 7: a), Pressure profile along the line $x_1 + x_2 = 2D$ $(r = \sqrt{x_1^2 + x_2^2})$ b), Overall sound pressure level as function of θ measured from streamwise axis with center at the downstream edge of the cavity. (— · — ·) Kirchhoff's method from L_1, (— · — ·) FW-H WEM from L_1, (——) FW-H analogy, (——) DNS.

However, FW-H analogy allows a better understanding of the structure of the radiated field than WEM since the direct and reflected sound field can be separated. Following reflection's theorem of Powell,[24] we can indeed argue that the volume integral (fig. 8a) represents the direct radiated field, and the surface integrals (fig. 8b) show essentially the reflected part of the field due to the cavity walls. These two fields at the same frequency give an interference figure where the two waves patterns are still distinguishable in our case because the cavity is not compact at the oscillation frequency $(L/\lambda = 0.47)$.

The FW-H analogy provides more informations than the WEM but is more expensive in CPU time because of the evaluation of volume integral (surface integral in 2-D) whereas wave extrapolation methods need only surface integral (line integral in 2-D). For example, the computation time needed by the FW-H WEM is around 13 minutes, whereas the FW-H analogy requires 17 hours, on a Dec α computer. For the purpose of comparison, the DNS would take 320 hours on this machine.

10
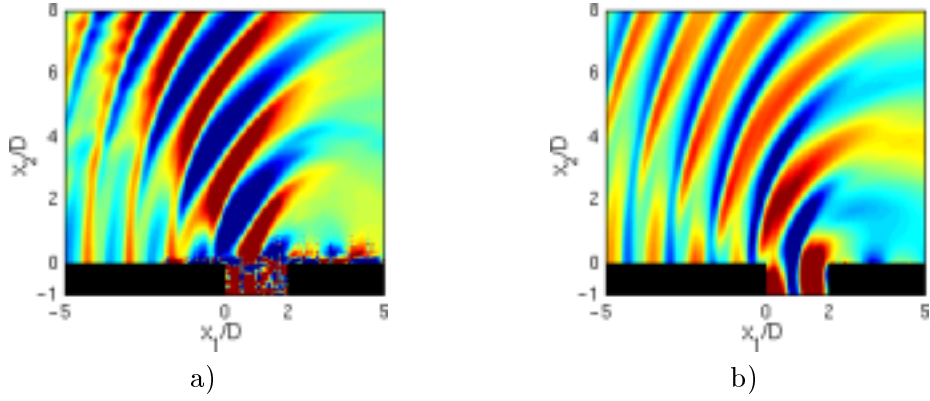
Figure 8: Pressure field obtained corresponding to: a) volume integral part of FW-H analogy, and b) surface integral part of FW-H analogy.

4. Conclusion

In a first part, a direct calculation of the sound radiated by a flow over a 2-D rectangular cavity is carried out. To this end, a DNS is performed using CAA numerical methods. This approach is expensive but is able to give all the interactions between flow and acoustic, and provides a powerful tool to determine noise generation mechanisms. The directly computed sound field is qualitatively and quantitatively consistent with Karamcheti's measurements in the same configuration.

The results of DNS are then successfully compared to three hybrid methods which use the DNS aerodynamic quantities to solve integral formulations. The wave extrapolation methods, like Kirchhoff's or porous FW-H methods, are relatively unaffected by the location of the control surface and constitute interesting complementary tools to extend CAA near-field to the far-field. Acoustic analogy is less efficient because volume integrations are costly and sensible to truncature effects. Nevertheless, it allows a separation between direct and reflected sound fields, which is useful for an analysis of radiation patterns.

To extend the present investigation, a 3-D simulation should be carried out. The recirculation zone inside the cavity is indeed characterized by a three-dimensional turbulent mixing, even if the development of the shear layer is almost two-dimensional. Such a study is under way.

Acknowledgments

References

[1]ROCKWELL, D., 1983, Oscillations of impinging shear layers, *AIAA Journal*, **21**(5), p. 645–664.

[2]ROSSITER, J.E. Wind-tunnel experiments on the flow over rectangular cavities at subsonic and transonic speeds. Technical Report 3438, Aeronautical Research Council Reports and Memoranda, 1964.

[3]KARAMCHETI, K. Acoustic radiation from two-dimensional rectangular cutouts in aerodynamic surfaces. *Tech. Note* 3487, N.A.C.A., 1955.

[4]HANKEY, W.L. & SHANG, J.S., 1980, Analyses of pressure oscillations in an open cavity, *AIAA Journal*, **18**(8), p. 892–898.

[5]ZHANG, X., RONA, A. & LILLEY, G.M., 1995, Far-field noise radiation from an unsteady supersonic cavity, *AIAA Paper 95-040*.

[6]COLONIUS, T., BASU, A.J. & ROWLEY, C.W., 1999, Numerical investigation of the flow past a cavity, *AIAA Paper 99-1912*.

[7]SHIEH, C.M. & MORRIS, P.J., 1999, Parallel numerical simulation of subsonic cavity noise, *AIAA Paper 99-1891*.

[8]SHIEH, C.M. & MORRIS, P.J., 2000, Parallel computational aeroacoustic simulation of turbulent subsonic cavity flow, *AIAA Paper 2000-1914*.

[9]GLOERFELT, X., BAILLY, C. & JUVÉ, D., 2001, Computation of the noise radiated by a subsonic cavity using direct simulation and acoustic analogy, *AIAA Paper 2001-2226*.

[10]BOGEY, C., BAILLY, C. & JUVÉ, D., 2000, Numerical simulation of sound generated by vortex pairing in a mixing layer, *AIAA Journal*, **38**(12), p. 2210–2218.

[11]TAM, C.K.W. & DONG, Z., 1996, Radiation and outflow boundary conditions for direct computation of acoustic and flow disturbances in a nonuniform mean flow, *J. Comput. Acous.*, **4**(2), p. 175–201.

[12]BRENTNER, K.S., 2000, Modeling aerodynamically generated sound: Recent advances in rotor noise prediction, *AIAA Paper 2000-0345*.

[13]COLONIUS, T. & FREUND, J.B., 2000, Application of Lighthill equation to a Mach 1.92 turbulent jet, *AIAA Journal*, **38**(2), p. 368–370.

[14]BOGEY, C., BAILLY, C. & JUVÉ, D., 2001, Noise computation using Lighthill's equation with inclusion of mean flow - acoustics interactions, *AIAA Paper 2001-2255*.

[15]LIGHTHILL, M.J., 1952, On sound generated aerodynamically I. General theory, *Proc. of the Royal Society of London*, **A 211**, p. 564–587.

[16]FFOWCS WILLIAMS, J.E. & HAWKINGS, D.L., 1969, Sound generated by turbulence and surfaces in arbitrary motion, *Philosophical Transactions of the Royal Society*, **A264**(1151), p. 321–342.

[17]GOLDSTEIN, M.E., 1976, *Aeroacoustics*, McGraw-Hill, New York.

[18]LOCKARD, D.P., 2000, An efficient, two-dimensional implementation of the Ffowcs Williams and Hawkings equation, *J. Sound Vib.*, **229**(4), p. 897–911.

[19]DI FRANCESCANTONIO, P., 1997, A new boundary integral formulation for the prediction of sound radiation, *J. Sound Vib.*, **202**(4), p. 491–509.

[20]FARASSAT, F. & MYERS, M.K., 1988, Extension of Kirchhoff's formula to radiation from moving surfaces, *J. Sound Vib.*, **123**(3), p. 451–460.

[21]BRENTNER, K.S. & FARASSAT, F., 1998, An analytical comparison of the acoustic analogy and Kirchhoff formulation for moving surfaces, *AIAA Journal*, **36**(8), p. 1379–1386.

[22]SINGER, B.A., BRENTNER, K.S., LOCKARD, D.P. & LILLEY, G.M., 2000, Simulation of acoustic scattering from a trailing edge, *J. Sound Vib.*, **230**(3), p. 541–560.

[23]PRIEUR, J. & RAHIER, G., 1998, Comparison of Ffowcs Williams-Hawkings and Kirchhoff rotor noise calculations, *AIAA Paper 98-2376*.

[24]POWELL, A., 1960, Aerodynamic noise and the plane boundary, *J. Acoust. Soc. Am.*, **32**(8), p. 982–990.

Low Frequency Noise:
A Major Risk Factor in Military Operations

Col. Nuno A.A. Castelo Branco, MD (PoAF, res.)
Center for Human Performance
Estrada Nacional No. 10, Edifício Cinema, Sala 109
2615 Alverca, Portugal
email: cph@mail.telepac.pt

Background. Noise is a major factor in many military environments. Usually the concern is with the higher frequency bands (> 500 Hz) that cause hearing damage or interfere with speech. Protection against noise is thus focused on these higher frequencies, while the bands of lower frequencies (< 500 Hz) are neglected, and non-audible bands, infrasound (< 20Hz) are ignored. In reality, long-term exposure to low frequency noise (<500 Hz, including infrasound) (LFN) can be quite detrimental to one's health. **LFN-Induced Pathology.** The disorders associated with occupational exposure to LFN have been described for aeronautical technicians and pilots. Diagnostic tools and methodologies for monitoring and controlling the development of LFN-induced pathology, have already been outlined. Immediate effects of LFN-exposure can include a) decreased capacity for cognitive functions, which implies a decline in performance, the consequences of which can be minor to devastating; b) sudden onset of acute respiratory problems, neurological disturbances, and mood alterations, such as, rage reactions. Cumulative effects of LFN-exposure can include triggering of early aging processes, and the development of vibroacoustic disease in susceptible (70%) individuals. Early compulsory retirement is a frequent situation.

Costs. Almost all military equipment require training programs for the operator. Long-term exposure to LFN can severely decrease the cost-return ratio for these operators, i.e., investment in training programs has little or no return. Accident/incidents can also damage the equipment itself, potentially jeopardizing missions. Waste of ammunition and other resources is another consequence of unmonitored LFN-exposed operators. The cost of ignoring LFN as an agent of disease is ultimately more expensive than the prevention, protection and, above all, selection of personnel for noise-environment positions.

INTRODUCTION

Noise is a major risk factor in many military environments. Noise is treated as a pollutant that can cause hearing damage and speech interference within the various vehicles and manned-stations. Thus, when protection against noise becomes an issue, the audible frequency bands (which coincide with those where speech occurs) are the focus of regulation and minimization.

Protection against noise is thus focused on these higher frequencies (>500 Hz), while the bands of lower frequencies (< 500 Hz) are neglected, and non-audible bands, infrasound (< 20Hz) are ignored [1]. This decades-old policy is based on an erroneous assumption: "Noise only affects the ear." This assumption pervades standard noise assessment procedures, the most blatant example of which is the use of the A-weighting system. This filtering system imitates human hearing, i.e., it de-emphasizes the lower frequencies and, naturally, ignores the non-audible infrasonic bands of acoustic phenomena [1].

In effect, when an acoustic environment is described merely in terms of dB(A), only the acoustic phenomena that can be perceived by the human auditory system is being evaluated. The acoustic environment may have significant components within the lower frequency

bands, including the infrasonic range, and yet the acoustic energy contained within these bands is not taken into account. Why? Because they are not a major contributor to hearing impairment and speech interference.

On the basis of our 20 years of research on the effects of low frequency noise (LFN - ≤500 Hz, including infrasound), our team has learnt to regard LFN as an agent of disease (not just a pollutant), and to search for objective clinical indicators of LFN-exposure. LFN impinges upon an individual and it is irrelevant whether or not such acoustic phenomena is heard, or even perceived by the individual. X-rays are a perfect analogy: merely at a different frequency of electromagnetic radiation (or light), x-rays are not seen or perceived by the individual. Yet undue exposure to x-rays is a well-known health hazard. We propose that LFN be treated as x-rays, and thus human perception, i.e., annoyance, loudness, etc, are given the import of subjective measures.

VIBROACOUSTIC DISEASE

Long-term exposure to LFN can cause Vibroacoustic Disease (VAD): a systemic pathology, characterized by whole-body proliferation of the extra-cellular matrix [2-4]. VAD has been identified in military [5,6] and civilian pilots and aircrews [7], aeronautical mechanics and technicians [8,9], and, more recently, in a civilian population exposed to military training exercises for over five decades [10]. VAD is a whole-body pathology, simultaneously compromising several organ systems.

Decreased Cognitive Abilities and NeuroPsychiatric Pathology

In 1985, our group was awarded the first prize of the National Institute for Public Health, for the mathematical treatment of brainstem auditory evoked potentials (BAEP's) in a population of LFN-exposed workers [11]. Using clustering algorithms and multivariate analysis of the distribution of action currents, we successfully demonstrated that statistically significant differences existed in the P300 (longer latencies and lower amplitudes) and N2 (longer latencies) components of LFN-exposed personnel, when compared to controls [12]. These abnormalities are associated with cognitive deterioration. Brainmapping showed wave displacement that changed the potentials topography into frontal, often asymmetric, with multipeaked patterns, consistent with degenerative processes, and usually seen in the elderly. The average age of the LFN-exposed population was 42.7 years (range 31-57) [12].

In a subsequent MRI study of the same population, the following brain abnormalities were correlated with the existence of abnormal BAEP's: hyperintense foci in T2 of the subcortical and periventricular white matter, basal ganglia and brain stem – usually seen in Alzheimer's disease before signs of cortical atrophy; and cerebral atrophy and dilation of the perivascular Virchow-Robin spaces – also seen in dementia [12,13].

The memory quotient of individuals occupationally exposed to LFN, evaluated with the Weschler Memory Scale test, is significantly lower than that of the control population, although attention span, evaluated with the Toulouse-Piéron test, was not altered [14]. PACT – performance assurance computerized test, developed by ARCO, California, EUA after the Exxon Valdez accident, confirmed the cognitive deterioration in these individual [15,16].

Other neurological signs and disorders are frequently present in LFN-exposed individuals. Late-onset epilepsy was diagnosed in 10% of a group of LFN-exposed workers in an aeronautical plant in Portugal [17,2]. The expected rate in the general population is 0.2%. Epilepsy has also been seen in flight attendants [7] and in a automobile sales-clerk, whose office was housed in an unusual LFN environment [4]. A unique case among the literature of

vibration-induced reflex epilepsy has also been identified in an aeronautical technician [18,19] and now again in a flight attendant [in press].

Some LFN-exposed workers exhibit automatisms – non-purposeful movements reminiscent of an epileptic nature. Reports abound on aircraft technicians who walk in front of the turbine, thus being sucked in by the engines [2], or personnel on aircraft carriers who suddenly decide to walk off the deck into the water [20]. Our group believes this phenomena may be related to reported rage-reactions and unusual suicide attempts seen in LFN-exposed populations [4]. Mood disorders are among the first signs of VAD, and begin to appear after the first 1-5 years of LFN exposure [3]. These later progress into severe mood disorders such as depression, increased aggressiveness and irritation, especially when exposed to daily, urban noise [3,4]. Noise intolerance is a very frequent finding in LFN-exposed personnel and VAD patients [3]. Addiction-like phenomena can also be observed among these individuals. Frequently, retirees return to engine test sites to "be near the noise" that they "can't stand". Retired pilots, even those who retired with VAD-associated disabilities, move to urban locations directly in the pathway of approaching aircraft, to "hear the noise that they miss". This phenomena is most easily observable in the music and entertainment selections of the younger populations, which later may become candidates for military or civilian jobs involving additional exposure to LFN.

Balance disorders are also a common finding among LFN-exposed personnel. In 140 LFN workers, 80 complained of balance disorders [21], and in a group of 30 female flight attendants, 6 were on sick leave for severe balance disorders, among other, co-existing VAD-associated pathology [7]. In a group of 60 aeronautical technicians, 30 exhibited the palmo-mental reflex, an archaic reflex [22]. The existence of this reflex is an indication of diffuse cerebral dysfunction, and is normally seen in Parkinson's disease, multiple sclerosis and AIDS. The average age of this group of aeronautical technicians was, as above, 42.7 years, (range 31-57) [22].

Other VAD-Associated Pathology

In 1992, our group initiated studies with animal models, exposing rats to occupationally-simulated LFN exposure (8hrs/day, 5days/week, weekends in silence). As a result of electron microscopy studies, it was discovered that the respiratory system is a major target for LFN [23-28] (Fig.1,2,3). In LFN-exposed human populations, repeated infections of the oropharynx, bronchitis (even in non-smokers), and atypical cases of pleural effusion were frequently observed [29]. Focal lung fibrosis was identified in the LFN-exposed animal models, and later confirmed through high resolution CT Scan in LFN-exposed, non-smoker workers [30].
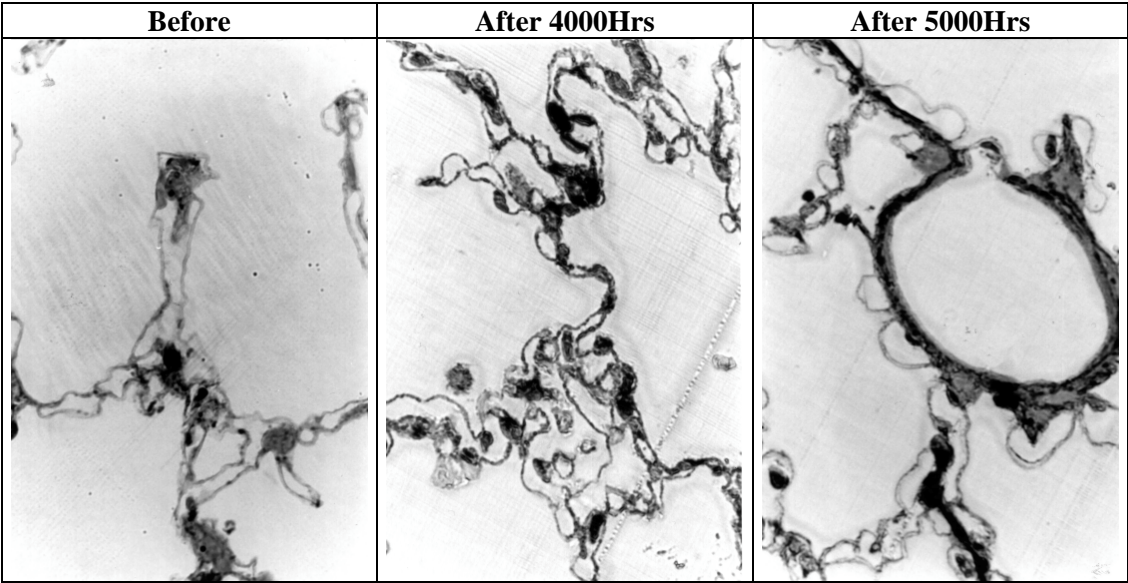
Before	After 4000Hrs	After 5000Hrs

FIG 1 - Histology of rat lung: normal (left), LFN-exposed for 4000h (center), and LF N-exposed for 5000h (right). (Orig. mag. x800)

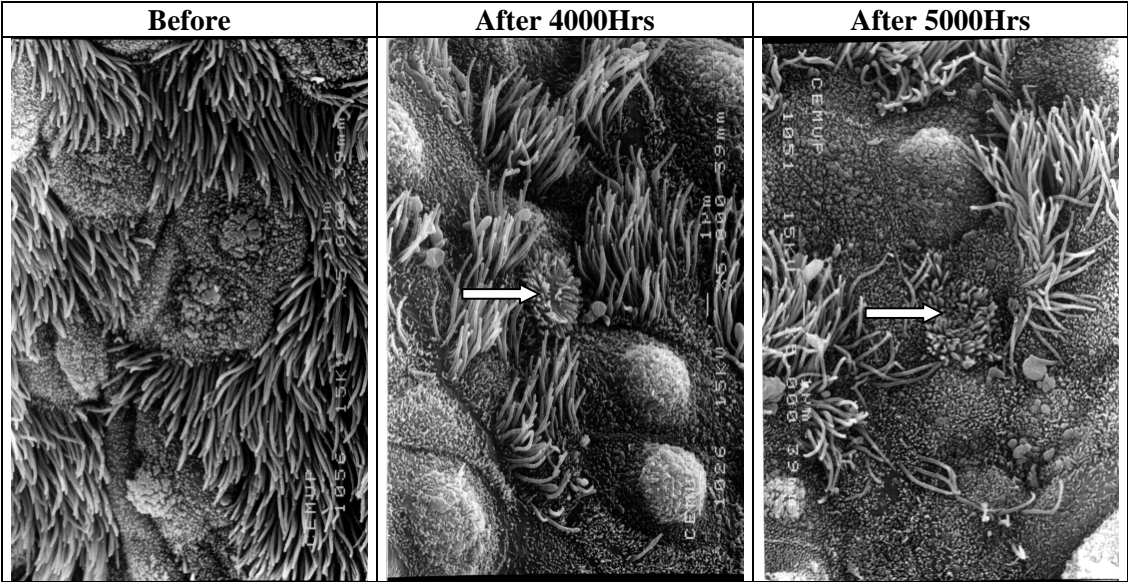| Before	After 4000Hrs	After 5000Hrs

Fig 2 - SEM of small brochioli: normal (left), LFN-exposed for 4000h (center), LFN-exposed for 5000h (right). Arrows indicate indentations in brush cells. (Orig. mag. x5000)
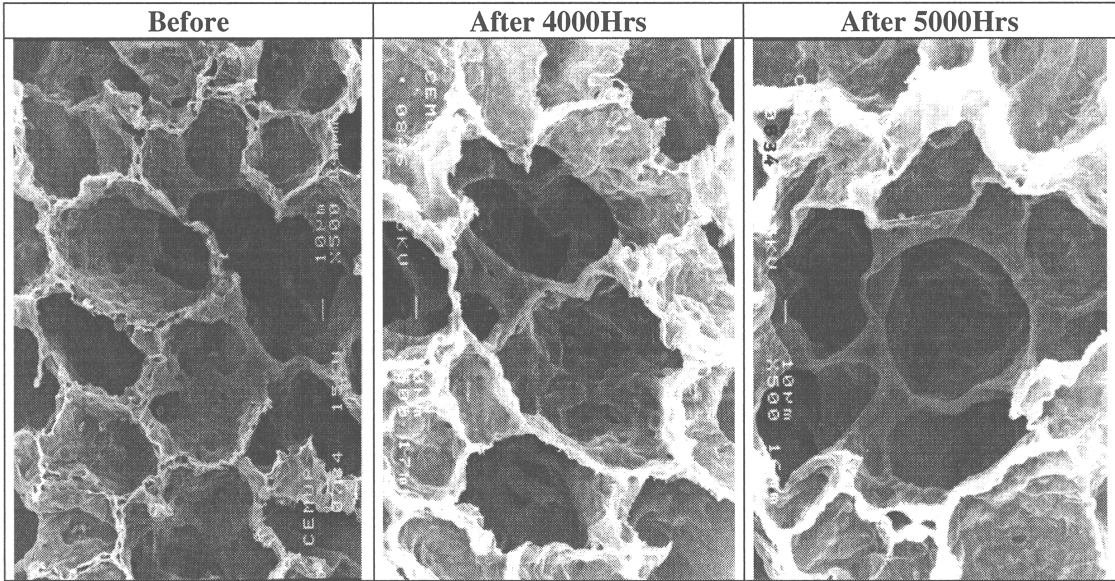
Fig 3 - SEM of lung parenchyma: normal (left), noise-exposed for 4000h (center), noise-exposed for 5000h (right). (Orig. mag. X500)

Cardiovascular pathology has been one of the most significant LFN-induced situations. Thickening of the pericardium is the hallmark of VAD and LFN-exposure [31, 32], although a generalized cardiovascular thickening exists throughout the LFN-exposed organism (Fig 4). It should be noted that unlike the typical thickening due to atherosclerotic plaques, LFN-induced cardiovascular thickening is like a continuous blanket, covering the walls of the vessel [6,33,36]. Echo-imaging of thickened pericardia, aortic and mitral valves, and carotid arteries are readily visible, and have made the echocardiogram the method of choice for screening for previous LFN exposure [7-10].

Normal	18 Years of occupational exposure
Fig 4 - Light microscopy of a normal pericardium from a 51-year-old male (Orig. mag. x100).	Light microscopy of the pericardium of a 39-year-old VAD patient (Orig. mag. X100).

The genotoxic component of LFN has already been demonstrated in both animal [37] and human models [38,39] through the increased frequency of sister chromatid exchanges in LFN-exposed populations. Malignancy among VAD patients has been increasingly well characterized. LFN-induced lung tumors are only of one type: squamous cell carcinoma. In the central nervous system, only glial tumors have been found. Other tumors are all located in hollow organs: bladder, colon, larynx and kidney [2].

Immunological studies have also been conducted on both human and animal models, and have shown that LFN modulated the immune system. In LFN-exposed workers, the amount of circulating CD8+ and CD4+ T lymphocytes was significantly altered [40]. In mice prone to developing lupus erythematosus, LFN-exposure accelerated the autoimmune kidney disease [41] and changed the lymphocyte subpopulation in the spleen [42]. Lupus is a common observation among LFN flight attendants [7] and other LFN-exposed populations [10].

Cumulative Effects, Recovery Periods and Individual Susceptibility

The effects of LFN-exposure are cumulative, and do not discriminate between sources. Acoustic phenomena within the lower frequency bands, including infrasound, can be generated by a variety of sources: ship or aircraft engines, weapons systems, manned vehicles, by jetskis, rock concerts, motorbikes, danceclubs, car audio systems, public transportation, high volume highways, etc. By being exposed to one or more of these sources, daily, cumulative effects of LFN exposure settle in and pathology is established.

Adequate recovery periods are fundamental to minimize LFN-induced damage. However, as should be expected, recovery periods are not linear. The silence-period required for reversibility of tracheal lesions induced by 48 hrs of continuous LFN exposure is 7 days [43]. Recovery periods for other LFN exposure patterns are under study.

Throughout all the studies with human populations, a consistent 30% of the individuals did not develop severe cases of VAD. Instead, discrete VAD-associated pathology would appear, however none would evolve to severe stages [3]. In a study conducted on airline pilots, the older pilots had less pericardial thickening than many of the younger pilots [7]. It is believed that this is due to survivorship bias: the older pilots are less susceptible to LFN. Studies are underway to confirm this hypothesis. Possible physiological indicators of individual susceptibility are also understudy. Early disability retirement is a frequent occurrence among LFN-exposed personnel [4].

Other Studies

Our group is not the first to describe this set of signs and symptoms in noise-exposed workers. In the Detroit Ford aircraft engine plant, in the 1940's, Dr. Dart was the first to identify an extra-aural, noise-induced pathology [44].

In the 1960's, the effects of LFN on the human respiratory system, suggesting that this system is very sensitive to noise, inducing severe coughing, gagging sensation and chest pressure after exposure of minutes to frequencies < 100 Hz, at > 100 dB [45, 46]. Dogs were used in another study which also showed the lungs to be particular susceptible to LFN: 3 mm pulmonary lesions, that do not increase in size with increased exposure, but instead increase in number [47]. Rumancev also in the 1960's studied workers in factories producing reinforced concrete, and described many of the symptoms today associated with VAD [48]. In the 1970's Cohen and Anticaglia published 2 studies that strongly supported the notion of a noise-induced, extra-aural pathology [49,50], and the inefficacy of hearing conservation programs on extra-aural pathology. Again, the symptomatology today associated with VAD is described in boiler plant workers [49].

In 1983, Matoba *et al.* was the first to describe pericardial thickening in noise-exposed workers [51]. Currently, Drs. Nekhoroshev and Glinchikov in St. Petersberg, Russia conduct microscopy animal studies, after exposure to single tones of LFN [52,53], verifying much of the same cellular pathology that our group has also seen.

COSTS

Most military equipment and weapons-systems require extensive and costly training programs for the operator. Most often, the work environment of the operator is pervaded by LFN, which is not assessed during standard noise measuring procedures for the reasons given in the beginning of this report. By not monitoring for LFN-induced pathology, the operator can develop severe stages of VAD without being diagnosed. The consequent risk is not trivial and should not continue to be ignored.

In addition to the possibility of human casualties, accident/incidents can damage the equipment itself, potentially jeopardizing missions. Waste of ammunition and other resources is another consequence of unmonitored LFN-exposed operators. Incorrect operation of weapons-systems can lead to a decreased operational lifetime, or even to very premature retirement of the entire unit. The possibility of rage-reactions, increased aggressiveness and irritability, all in added to noise intolerance, are hardly desirable conditions for military operators. Epileptic seizures and automatisms are also quite undesirable, especially within a military scenario. Long-term exposure to LFN can severely decrease the cost-return ratio for these operators, i.e., investment in training programs has little or no return, because operators' operational lifetime is severely decreased.

Screening and monitoring procedures for LFN-exposed personnel are cost-effective. Screening young candidates to LFN positions for pre-existing LFN exposure proved successful in an aeronautical plant. By excluding young men who already exhibited thickening of cardiac structures (due to previous LFN exposure) from LFN jobs, and by removing workers who exhibited severe stages of VAD from their LFN work environments, the number of early disability retirements dropped from 21 (1980-1989) to zero (1989-1996) [54].

The cost of ignoring LFN as an agent of disease is ultimately much more expensive than implementing prevention, protection, and selection procedures among personnel working in noise-environment positions. Monitoring LFN-exposed personnel could halt the cognitive deterioration in these individuals, prolonging their time on active duty, and avoiding the possibility of early disability retirement.

The most serious situations occur where LFN generation is continuous, and no possibility of "quiet" time (or recovery period) exists. Such is the case of ships, submarines, tanks, space vehicles, and long-haul aircraft. Often, personnel must remain within a LFN environment, usually an already confined space, for months at a time. Considering that mood disorders, increased aggressiveness and irritability, in addition to cognitive deterioration, are initial signs of VAD, there should be a vigorous effort to afford LFN-exposed personnel some protection. The most dramatic situation of LFN environments is in Space. Here there is no external damping to dissipate the LFN generated by life-support systems and other such equipment, onboard space vehicles. More importantly, in the case of an accident/incident, return to a "quiet" location may not be immediate. The importance of selection procedures for individuals who will be exposed to LFN is crucial for the success of long-term missions.

Auricle protectors will aggravate the effects caused by impinging LFN. Referring back to the x-ray analogy, auricle protectors for LFN is analogous to dark glasses for x-ray protection – they are inadequate. The problem with protection against LFN is the long wavelength of acoustic phenomena within the lower frequency bands. As a rule of thumb, the size of audible noise protectors are proportional to the acoustic phenomenon's wavelength. For example, the

wavelength of a pure tone at 4000 Hz (frequency at which professional deafness is decided) is 8.5 cm, at 1000 Hz it is 34.3 cm, at 500 Hz it is 68.6 cm, at 100 Hz it is 3.43 meters, at 20 Hz it is 17.1 meters, and at 5 Hz it is 68.6 meters. Clearly, physical protection against LFN is not yet feasible. In Pensacola, Florida, the U.S. Department of the Navy is researching new materials that can reduce LFN. They have achieved an impressive 30 dB reduction at 80 Hz, however implementation of this material in real-world scenarios is still not underway. Nevertheless, protection can be afforded, today, to LFN-exposed personnel by monitoring the progression of VAD using echocardiography. It is important to note that among aeronautical mechanics and technicians, those who regularly wore their auricle protectors suffered worse cases of VAD [S]. This is because the auricle protectors allowed them to remain within the LFN environment for much longer periods of time than their non-auricle-user co-workers.

It is not surprising that LFN, including infrasound, was investigated in order to develop weapons. LFN is an ubiquitous agent of disease, especially in the military. Our group urges physicians in charge of LFN-exposed personnel to establish and implement prevention and protections programs against LFN exposure and the development of VAD. It will be worth the fight!

BIBLIOGRAPHY

1. Alves-Pereira M. Extra-aural noise-induced pathology. A review and commentary. *Aviation, Space & Environmental Medicine* 1999; 70 (March, Suppl): A7-21.

2. Castelo Branco NAA, Rodriguez Lopez E. The vibroacoustic disease – An emerging pathology. *Aviation, Space & Environmental Medicine* 1999; 70 (3, Suppl): A1-6.

3. Castelo Branco NAA. The clinical stages of vibroacoustic disease. *Aviation, Space & Environmental Medicine* 1999; 70 (3, Suppl): A32-9.

4. Castelo Branco NAA, Rodriguez Lopez E, Alves-Pereira M, Jones DR. Vibroacoustic disease: some forensic aspects. *Aviation, Space & Environmental Medicine* 1999; 70 (3, Suppl): A145-51.

5. Canas J, Martinho Pimenta AJF, Castelo Branco NAA, ERP P300 and MRI Studies of the CNS in military pilots: A comparative study of early degenerative brain process. *Aviation, Space & Environmental Medicine* 1993; 64: 451.

6. Carmo G, Albuquerque e Sousa J, Dinis da Gama A, Castelo Branco NAA. Carotid Angiodynographic Studies in Helicopter Pilots. *Aviation, Space & Environmental Medicine* 1992; 63: 385

7. Araujo A, Pais F, Lopo Tuna JMC, Alves-Pereira M, Castelo Branco NAA. Echocardiography in noise-exposed flight crew. *Proceed. Internoise 2001*, The Hague, Holland 2001: 1007-10.

8. Araujo A, Ribeiro CS, Correia MJF, Pais F, Castelo Branco NAA. Echocardiographic appearances in patients with the Whole-Body Noise and Vibration Disease. *MEDICEF-Direct Information* 1989; 2: 101-2.

9. Marciniak W, Rodriguez E, Olsowska K, Botvin I, et al. Echocardiography in in 485 aeronautical workers exposed to different noise environments. *Aviation, Space & Environmental Medicine* 1999; 70 (3, Suppl): A46-53.

10. Torres R, Tirado G, Roman A, Ramirez R, Colon H, Araujo A, Pais F, *et al.* Vibroacoustic disease induced by long-term exposure to sonic booms. *Proceed. Internoise 2001*, August 2001, The Hague, Holland: 1095-98.

11. Castelo Branco MS, Castelo Branco NAA, Entrudo A, Marvão J. Padronização dos valores dos potenciais evocados precoces da via auditiva. [A standardization method of the brainstem auditory evoked potentials.] *Jornal da Sociedade das Ciências Médicas de Lisboa* 1985; 149: 214-20.

12. Pimenta MG, Martinho Pimenta AJF, Castelo Branco MSN, Castelo Branco NAA. ERP P300 and brain magnetic resonance imaging in patients with vibroacoustic disease. *Aviation, Space & Environmental Medicine* 1999; 70 (3, Suppl): A107-114.

13. Maurício JC, Branco G, Pimenta AJFM, Castelo Branco MSNA, Castelo Branco NAA. Noise and vibration exposure effects on the CNS - MRI study. *Medicine Aeronautique & Spatial* 1991; 119: 363-7.

14. Gomes L, Martinho Pimenta AJF, Castelo Branco NAA. Effects of occupational exposure to low frequency noise on cognition. *Aviation, Space & Environmental Medicine* 1999; 70 (3, Suppl): A115-8.

15. Gomes LMP, Rodriguez E, Castelo Branco NAA. Performance assurance computerized test – PACT. *Revista Portuguesa de Medicina Militar* 1993; 41 (1-4): 21-27.

16. Rodriguez E, Greenberg HL, Pimenta AM, Castelo Branco MSNAA, Castelo Branco NAA. Relationship of P300 and logged flight time in military pilots. *Revista Portuguesa de Medicina Militar* 1992: 40(1-4): 41-45.

17. GIMOGMA. Epilepsia sintomática de etiologia vascular, manifestação da síndrome das vibrações? (Epilepsy of vascular etiology, a clinical picture of vibration disease?) *Revista Portuguesa de Medicina Militar* 1984; 32: 5-9.

18. Martinho Pimenta AJF, Castelo Branco NAA. Epilepsy in vibroacoustic disease - A case report. *Aviation, Space & Environmental Medicine* 1999; 70 (3, Suppl): A122-7.

19. Martinho Pimenta AJF, Castelo Branco NAA. The vibroacoustic syndrome: a case of partial seizure by handling vibratory tools. *Proceed. XXX International Congress on Mililatry Medicine*, Ausgburg, Germany 1994; Lfd No 29.

20. Billings BP. Feeling the music can be dangerous to your health. A comprehensive review. http://www.omnisonic.com/bbillings.html.

21. Martinho Pimenta AJF, Castelo Branco MSNA, Castelo Branco NAA. Balance disturbances in individuals with vibroacoustic disease. *Aviation, Space & Environmental Medicine* 1999; 70 (3, Suppl): A96-9.

22. Martinho Pimenta AJF, Castelo Branco MSNA, Castelo Branco NAA.The palmo-mental reflex in vibroacoustic disease. *Aviation, Space & Environmental Medicine* 1999; 70 (3, Suppl): A100-6.

23. Grande N, Águas AP, Sousa Pereira A, Monteiro E, Castelo Branco NAA. Morphological changes in the rat lung parenchyma exposed to low frequency noise. *Aviation, Space & Environmental Medicine* 1999; 70 (3, Suppl): A70-7.

24. Oliveira MJR, Sousa Pereira A, Águas AP, Monteiro E, Grande NR, Castelo Branco NAA. Effects of low frequency noise upon the reaction of pleural milky spots to mycobacterial infection. *Aviation, Space & Environmental Medicine* 1999; 70 (March, Suppl): A137-40.

25. Sousa Pereira A, Lousã N, Águas AP, Grande NLR, Monteiro E, Alves-Pereira M, Castelo Branco NAA. Morphological changes in the cochlear cilia of Wistar rats exposed to low frequency noise. *Aviation, Space & Environmental Medicine* 2000; 71 (3): 301

26. Sousa Pereira A, Grande NR, Castelo Branco MSNAA, Castelo Branco NAA. Morphofunctional study of rat pleural mesothelial cells exposed to low frequency noise. *Aviation, Space & Environmental Medicine* 1999; 70 (3, Suppl): A78-85.

27. Sousa Pereira A, Águas A, Grande NR, Castelo Branco NAA. The effect of low frequency noise on rat tracheal epithelium. *Aviation, Space & Environmental Medicine* 1999; 70 (3, Suppl): A86-90.

28. Zagalo C, Águas AP, Sousa Pereira A, Monteiro E, Grande NR, Castelo Branco NAA. Bronchial reactivity in VAD patients and morphological changes in rodent brush cells. *Aviation, Space & Environmental Medicine* 2001; 72(3): 253.

29. Castelo Branco NAA. The respiratory system as a target of low frequency noise. Reports on human and animal models. *Proceed. 8th International Congress on Sound & Vibration*, Hong Kong, P.-R. China, July 2001: 1501-8.

30. Reis Ferreira JM, Couto AR, Jalles-Tavares N, Castelo Branco MSN, Castelo Branco NAA. Airflow limitations in patients with vibroacoustic disease. *Aviation, Space & Environmental Medicine* 1999; 70 (3, Suppl): A63-9.

31. Holt BD. The pericardium. In: Furster V, Wayne Alexander R, Alexander F, eds. *Hurst's The Heart*. 10th ed. New Yok: McGraw-Hill Professional Publishing, 2000: 2061-82.

32. Castelo Branco NAA, Águas AP, Sousa Pereira A, Monteiro E, Fragata JIG, Tavares F, Grande NR. The human pericardium in vibroacoustic disease. *Aviation, Space & Environmental Medicine* 1999; 70 (3, Suppl): A54-62.

33. Castelo Branco NAA. A unique case of vibroacoustic disease. A tribute to an extraordinary patient. *Aviation, Space & Environmental Medicine* 1999; 70 (3, Suppl): A27-31

34. Albuquerque e Sousa J, Martinho Pimenta AJF, Castelo Branco NAA. Three cases of the vibroacoustic syndrome with significant carotid stenosis. *Aviation, Space & Environmental Medicine* 1995; 66: 494.

35. Albuquerque e Sousa J, Dinis da Gama A, Macedo MV, Cassio I, et al. Carotid angiodynographic studies in individuals occupationally exposed to noise and vibration. *Aviation, Space & Environmental Medicine* 1991; 62: 134.

36. Carmo G, Albuquerque e Sousa J, Dinis da Gama A, Castelo Branco NAA. Carotid angiodynographic studies in helicopter pilots. *Aviation, Space & Environmental Medicine* 1992; 63: 385.

37. Boavida MG, Dias A, Castelo Branco NAA, Silva MJ. Analysis of sister chromatid exchanges in splenocytes of mice exposed to noise and vibration. *Aviation, Space & Environmental Medicine* 1999; 70(4): 376.

38. Silva MJ, Carothers A, Castelo Branco NAA, Dias A, Boavida MG. Increased levels of sister chromatid exchanges in military aircraft pilots. *Mutation Research - Genetic Toxicology and Environmental Mutagenesis* 1999; 44(1): 129-34.

39. Silva MJ, Carothers A, Castelo Branco NAA, Dias A, Boavida MG. Sister chromatid exchanges in workers exposed to noise and vibration. *Aviation, Space and Environmental Medicine* 1999; 70 (3, Suppl): A40-5.

40. Castro AP, Aguas AP, Grande NR, Monteiro E, Castelo Branco NAA. Increase in CD8+ and CD4+ T lymphocytes in patients with vibroacoustic disease. *Aviation, Space & Environmental Medicine* 1999; 70 (3, Suppl): A141-4.

41. Águas AP, Esaguy N, Castro AP, Grande NR, Castelo Branco NAA. Acceleration of lupus erythematosus-like processes by low frequency noise in the hybrid NZB/W mouse model. *Aviation, Space & Environmental Medicine* 1999; 70 (March, Suppl): A132-6.

42. Águas AP, Esaguy N, Castro AP, Grande NR, Castelo Branco NAA. Effect low frequency noise exposure on BALB/C mice splenic lymphocytes. *Aviation, Space & Environmental Medicine* 1999; 70 (March, Suppl): A128-31.

43. Gomes-Ferreira P, Mirones J, Sousa Pereira A, Águas AP, Monteiro E, Grande NR, Castelo Branco NAA. Prolonged and continuous low frequency noise stress on the tracheae of Wistar rats. *Aviation, Space & Environmental Medicine* 2001; 72(3): 253-4.

44. Dart, EE. Effects of high speed vibrating tools on operators engaged in airplane industry. *Occupational Medicine* 1946; 1: 515-50.

45. Mohr GC, Cole JN, Guild E, von Gierke HE. Effects of low-frequency and infrasonic noise on man. *Aerospace Medicine* 1965; 36: 817-24.

46. Cole JN, Mohr GC, Guild EG, von Gierke HE. The effects of low frequency noise on man as related to the Apollo Space Program. AMRL Memorandum B-66.

47. Ponomar'kov VI, Tysik Ayu, Kudryavtseva VI, Barer AS, et al. Biological action of intense wide-band noise on animals. *Problems of Space Biology* NASA TT F-529 1969; 7(May): 307-9.

48. Rumancev GI. Issledovania po qiqieniceskoj ocenke vibracil na zavodah sbornogo zelezobetona. [Investigations concerning the hygienic evaluation of vibration in factories producing reinforced concrete.] *Gigiena Truda Profissional Zabol* 1961; 5: 6-12.

49. Cohen A. The influence of a company hearing conservation program on extra-auditory problems in workers. *Journal of Safety Research* 1976; 8: 146-62.

50. Anticaglia JR, Cohen A. Extra-auditory effects of noise as a health hazard. *American Industrial Hygiene Association Journal* 1970; 31: 277-81.

51. Matoba T. et al. Increased left ventricular function as an adaptative response in vibration disease. *American Journal Cardiology* 1983; 15: 1223-6.

52. Nekhoroshev AS, Glinchikov VV. Morphological research on the liver structures of experimental animals under the action of infrasound. *Aviakosm Ekologie Medizin* 1992; 26: 56-9.

53. Nekhoroshev AS, Glinchikov VV. Effect of infrasound on morphofunctional changes in myocardium exposed to infrasound. *Gigiena Sanitariya* 1991; 12: 56-8.

54. Alvarez M, Taborda F, Gomes L, Marçal C, Soutenho A, Marmelo J, Castelo Branco NAA. Epidemiologia dos acidentes em serviço nas OGMA [Epidemiology of on-the-job accidents at OGMA]. *Revista Portuguesa de Medicina Militar* 1993; 4: 35-40.

Reference # of Paper: Invited Lecture # 3
Discusser's Name: Dr. D. G. Zimcik
Author's Name: Col. Nuno A. A. Castelo Branco, MD
Question:

Results presented on the human effect of low frequency noise (LFN) are startling and seem to be missed by current standards for acceptable noise used in many countries. What changes are planned or underway in regulations to include these effects?

Answer:

As far as we know, no changes to current legislation are planned or underway with two exceptions: Puerto Rico, where a Jan 2001 law limits the emission of LFN; and Mozambique, where preparations for a new law includes LFN. Permissible exposure levels for LFN, the necessary recovery times for each type of exposure period, and dose-response data are unknown. These are necessary for human exposure legislation. Individual susceptibility indicators are under study by our group: but, as yet, there is insufficient data.

Development of Discontinuous Galerkin method
for the Linearized Euler equations

Carl Blom,
Phd. student, Department of Mechanical Engineering, University of Twente,
P.O. Box 217, 7500 AE, Enschede, The Netherlands, c.p.a.blom@wb.utwente.nl

Rob Hagmeijer,
Associate Professor, Department of Mechanical Engineering, University of Twente,
P.O. Box 217, 7500 AE, Enschede, The Netherlands, r.hagmeijer@wb.utwente.nl

Eric Védy,
Phd, Acoustics Division, TNO Institute of Applied Physics,
P.O. Box 155, 2600 AD, Delft, The Netherlands, vedy@tpd.tno.nl

1   Introduction

The propagation of sound waves, defined as an oscillatory motion with small amplitude in a compressible fluid [1], can be described by the linearized Euler equations (LEE), under the assumptions that there is no feedback to the mean-flow and that effects of viscosity and heat conduction can be neglected.

In the field of Computational Aeroacoustics (CAA), it is widely recognized that the numerical algorithms applied to solve the governing equations must have sufficiently low numerical dispersion and dissipation in order to accurately simulate the propagation of aeroacoustic information. To this end, higher-order schemes can be used. The Discontinuous Galerkin (DG) [2, 3] method is an ultimately compact finite-element method which can be applied efficiently on unstructured meshes, thus allowing geometrically complex problems to be handled. Higher-order (higher than second-order) accuracy can be obtained relatively easily because of the compactness of the method, at the penalty, however, of an increasing number of unknowns per element. An extensive description of the application of the Discontinuous Galerkin method in the field of CAA is given by Atkins *et al.* [4, 5, 6, 7].

The results presented in the present paper are obtained with the computer code DIGS3D, which is based on a numerical algorithm developed to solve the LEE in three dimensions. For the spatial discretization of the LEE the Quadrature-free Discontinuous Galerkin method has been applied, while the time integration is performed by a four-step, low-storage Runge-Kutta algorithm. At present the algorithm is second-order accurate in both space and time. The numerical algorithm has already been applied to a three-dimensional broadband cavity-noise prediction problem [8], where it is part of a three-step method. In the three-step method, the first step provides the time-averaged RANS-solution from which, in the second step, turbulent aeroacoustic source terms for the LEE are obtained. In the third step DIGS3D is used to simulate the propagation of the aeroacoustic disturbances produced by the source field.

The work presented in this paper can be regarded as a continuation of the work presented in [9]. In [9] two verification problems, the convection of a 2D compact acoustic disturbance and the radiation from a three-dimensional harmonic monopole source, were presented. One of the conclusions drawn in that paper is that acceleration of the algorithm to relax requirements on computational effort was needed. Here we present results obtained for the first of the two

---

aforementioned verification problems, obtained with a parallelized version of the code. The algorithm is parallelized employing MPI (Message Passing Interface) and the code is run on a 1024-CPU platform (TERAS [10]). A more thorough description of parallelizing a DG-based CAA-algorithm, employing MPI, is presented in [11]. The main objectives of the work presented in the present paper are (continuation of) the verification of the numerical algorithm and conducting a performance test of the parallelized algorithm on TERAS.

The outline of the paper is as follows: In the first section the governing equations, i.e. the Linearized Euler equations (LEE), are presented. In the second section the Quadrature-free Discontinuous Galerkin method is briefly described. The next section describes the convection of a two-dimensional compact acoustic disturbance in a uniform mean flow. The analytical solution of the problem is presented and the obtained numerical results are compared with the analytical solution. Furthermore results of a performance test on TERAS are presented. Subsequently, concluding remarks and suggestions for further research are given.

2 Linearized Euler Equations

Consider the dimensionless linearized Euler equations (LEE) in conservation form in three spatial dimensions

$$\mathbf{L}(\mathbf{U}) \equiv \frac{\partial}{\partial t}\mathbf{U} + \frac{\partial}{\partial x_j}\mathbf{F}_j(\mathbf{U}) = \mathbf{S}, \qquad \mathbf{U}(\mathbf{x},t), \quad (\mathbf{x},t) \in \Omega \times (0,T), \tag{1}$$

where

$$\mathbf{F}_j(\mathbf{U}) = \mathbf{A}_j(\mathbf{U}_0)\mathbf{U}, \quad \mathbf{A}_j \in I\!\!R^5 \times I\!\!R^5, \tag{2}$$

with initial and boundary conditions. Here $\mathbf{S}$ ($\in I\!\!R^5$) is the source term for the LEE, $\Omega \in I\!\!R^3$ is an open domain with boundary $\partial\Omega$ and $t \in (0,T)$ denotes time. The summation convention is used on the repeated index j, where $j = 1, 2, 3$. $\mathbf{U} = (\rho', u_1', u_2', u_3', p')^T$, where the components of the vector denote the dimensionless aeroacoustic density perturbation, the three velocity perturbation components and the pressure perturbation, respectively. The components of vector $\mathbf{U}_0$ denote the dimensionless quantities related to the mean flow density, the three components of the mean flow velocity and the mean flow pressure. The matrices $\mathbf{A}_j$ are defined as:

$$\mathbf{A}_j(\mathbf{U}_0) = \begin{bmatrix} M_j & \delta_{j1} & \delta_{j2} & \delta_{j3} & 0 \\ 0 & M_j & 0 & 0 & \delta_{1j} \\ 0 & 0 & M_j & 0 & \delta_{2j} \\ 0 & 0 & 0 & M_j & \delta_{3j} \\ 0 & \delta_{j1} & \delta_{j2} & \delta_{j3} & M_j \end{bmatrix}, \tag{3}$$

where M_1, M_2, M_3 are the components of the mean flow Mach-number in x, y and z-direction, respectively, and δ_{ij} denotes the Kronecker-delta symbol.

3 Quadrature-free Discontinuous Galerkin Method

In this section we briefly describe the Quadrature-free Discontinuous Galerkin spatial discretization. In [8] a more detailed description is presented. Throughout this section we have $i \in [1, N_e]$,

$k \in [0, M]$ and $l \in [0, M]$.

Let us define the solution space V defined on Ω, let $\mathbf{U} \in V$ and let the inner product on V be defined as:

$$\langle u, v \rangle \equiv \int_\Omega u(\mathbf{x})v(\mathbf{x})d\mathbf{x}, \tag{4}$$

from which we can define [12] the L^2-norm $\|u\| = \sqrt{\langle u, u \rangle}$.

The domain Ω is partitioned into non-overlapping elements Ω_i, $\Omega = \cup\Omega_i$. Let $V_h \subset V$ be a finite-dimensional subspace, spanned by the linearly independent basis functions b_{ik}, and let $\mathbf{U}_h \in V_h$. $\mathbf{U}_h$ is obtained by the projection of $\mathbf{U}$ onto the subspace $V_h = span\{b_{ik}\}$:

$$\mathbf{U}_h = \sum_{i=1}^{N_e} \sum_{k=0}^{M} \mathbf{v}_{ik}(t)b_{ik}(\mathbf{x}). \tag{5}$$

In the Discontinuous Galerkin formulation the unknown coefficients $\mathbf{v}_{ik}$ are obtained by solving the system of equations given by:

$$\langle \mathbf{L}(\mathbf{U}_h), b_{il} \rangle = \langle \mathbf{S}, b_{il} \rangle, \quad \forall(i, l). \tag{6}$$

Partial integration of Eq.(6) yields:

$$\langle b_{il}, b_{ik} \rangle \frac{d\mathbf{v}_{ik}}{dt} - \langle \frac{\partial b_{il}}{\partial x_j}, \mathbf{A}_j b_{ik} \rangle \mathbf{v}_{ik} + \int_{\Gamma_i} b_{il}b_{ik}(\mathbf{A}_j n_j)\mathbf{v}_{ik}d\Gamma = \langle b_{il}, \mathbf{S} \rangle, \quad \forall(i, k, l), \tag{7}$$

where $\Gamma_i = \partial\Omega_i$ and $\mathbf{n}$ is the unit outward normal to boundary Γ_i.

Closer inspection of both Eq.(6) and Eq.(7) reveals that the solution within an element only depends on information within that element, i.e. there is no "communication" between elements. Furthermore the global solution is, in general, discontinuous over an element interface. To provide the crucial coupling and to handle the discontinuity at element interfaces, the boundary-normal flux, $\mathbf{F}_j(\mathbf{U}_h)n_j = \mathbf{A}_j n_j \mathbf{U}_h$, is modeled by means of an approximate Riemann flux $\mathbf{F}_j^R(\mathbf{U}_L, \mathbf{U}_R)n_j$, where $\mathbf{U}_L$ and $\mathbf{U}_R$ represent $\mathbf{U}_h$ on either side of the element interface. For the present implementation of the method we approximate the Riemann flux by the Lax-Friedrichs flux, which can be written as:

$$\mathbf{F}_j^R(\mathbf{U}_L, \mathbf{U}_R)n_j = \frac{1}{2}\{[\mathbf{F}_j(\mathbf{U}_L) + \mathbf{F}_j(\mathbf{U}_R)]n_j - \alpha(\mathbf{U}_R - \mathbf{U}_L)\}, \tag{8}$$

where $\mathbf{n}$ points from element L to element R and α is a positive quantity that is larger in magnitude than the eigenvalues of the Jacobian of $\frac{1}{2}[\mathbf{F}_j(\mathbf{U}_L) + \mathbf{F}_j(\mathbf{U}_R)]n_j$.

For a quadrature-free implementation [4] of Eq.(7) the source-term in the LEE (also) has to be projected onto V_h:

$$\mathbf{S}_h = \sum_{i=1}^{N_e} \sum_{k=0}^{M} \mathbf{s}_{ik}(t)b_{ik}(\mathbf{x}). \tag{9}$$

Since the LEE are linear, $\mathbf{F}_j(\mathbf{U}_h)$ is expanded in a natural way as can be seen from Eq.(7). Furthermore, Atkins and Lockard [5] report that for the simulation of the scattering of acoustic waves (where an assumption of linearity can be made) it is sufficient to represent the mean flow by a lower-order polynomial to ensure the formal order properties of the method.

Johnson and Pitkärata [2] prove that when the basis functions are polynomials of degree p, the order of accuracy is at least $p + \frac{1}{2}$. In most practical cases [4] the order of accuracy is observed

to be $p + 1$. With the relation between M, p and the number of space-time dimension d given by [4]:

$$M(p, d) = -1 + \frac{1}{d!} \prod_{k=1}^{d} (p + k), \tag{10}$$

this implies that in order to obtain second-order accuracy we must choose $p = 1$, resulting in $M = 3$ for $d = 3$.

Eq.(7) is conveniently evaluated through the introduction of computational coordinates. These coordinates are local to a reference element for which we choose an equal-sided tetrahedron. Within the reference element we define the basis set, consisting of monomials, as $b_k \in \{1, \xi, \eta, \zeta\}$. The time integration is performed by a second-order accurate, four-step, low-storage Runge-Kutta algorithm [13].

The Discontinuous Galerkin method, due to its local character, is very well suited for parallel calculations. The present parallel implementation is based on a domain decomposition of the unstructured mesh into several blocks where the calculation for each block is performed on a different processor. The MPI (Message Passing Interface) routines are used to communicate data between processors for the flux calculations at the interfaces of elements belonging to different partitions. The block partitioning itself, is based on the METIS ([14]) libraries, and is optimized in order to achieve both a quasi-uniform loading on the processors, and to lower the communication costs during computation (minimization of the number of interfaces).

4 Convection of a 2D Compact Acoustic Disturbance

4.1 Problem description

In this verification case the LEE (Eqs.(1) to (3)) are solved on a square domain in which a compact acoustic perturbation is imposed through the initial conditions. The two-dimensional domain has dimensions $x \in [-100, 100]$, $y \in [-100, 100]$ and the acoustic source is initially centered at $x = y = 0$. The mean flow is uniform with Mach-number components $M_1 = M = 0.5$ and $M_2 = 0$, there are no sources ($\mathbf{S} = \mathbf{0}$) and the initial condition for the 2D solution vector $\mathbf{U}(x, y, t) = (\rho', u', v', p')^T$ is given by:

$$\mathbf{U}(x, y, 0) = \begin{pmatrix} f(x, y) \\ \beta x f(x, y) \\ \beta y f(x, y) \\ f(x, y) \end{pmatrix}, \tag{11}$$

with

$$f(x, y) = e^{-\alpha(x^2 + y^2)}, \quad \alpha = \frac{ln(2)}{9}, \quad \beta = 0.04. \tag{12}$$

This test case has also been addressed by Atkins and Shu [4]. Together with a vorticity wave it is furthermore described as part of the ICASE/LaRC Workshop on Benchmark Problems in Computational Aeroacoustics [15]. Note, however, that in the benchmark-case the initial velocities, u' and v', are taken equal to zero.

4

4.2 Analytical solution

The LEE, together with the conditions described above, can be transformed into the wave equation:

$$\frac{D^2 q}{Dt^2} - \nabla^2 q = 0, \quad \text{with} \quad \frac{D}{Dt} = \frac{\partial}{\partial t} + M \frac{\partial}{\partial x}, \tag{13}$$

where q is either one of the primitive variables ρ', u', v' or p'.

Upon introducing a coordinate system moving with the mean flow: $\tau = t$, $\xi = x - M t$, $\eta = y$, the wave equation can be written as:

$$\frac{\partial^2 q}{\partial \tau^2} - \tilde{\nabla}^2 q = 0, \quad \tilde{\nabla} = (\frac{\partial}{\partial \xi}, \frac{\partial}{\partial \eta})^T. \tag{14}$$

Next we introduce polar coordinates (r, θ), where $\xi = r \cos(\theta)$ and $\eta = r \sin(\theta)$ and assume that q is independent of θ:

$$\frac{\partial^2 q}{\partial \tau^2} - \left(\frac{\partial^2 q}{\partial r^2} + \frac{1}{r} \frac{\partial q}{\partial r} \right) = 0. \tag{15}$$

Instead of solving Eq.(15) for one of the primitive variables we will solve it for the velocity potential $\phi(r, t)$, which also satisfies the wave equation. With $u' = \frac{\partial \phi}{\partial x}$ and $v' = \frac{\partial \phi}{\partial y}$ the primitive variables are related to the velocity potential by

$$\frac{\partial \phi}{\partial r} = u_r', \qquad \frac{\partial \phi}{\partial t} = -p', \tag{16}$$

where u_r' is the radial velocity component. The initial conditions can be obtained from these two relations

$$\phi(r, 0) = \int_\infty^r u_r'(r) dr = -\frac{\beta}{2\alpha} e^{-\alpha r^2}, \tag{17}$$

$$\frac{\partial \phi}{\partial \tau}(r, 0) = -p'(r, 0) = -e^{-\alpha r^2}. \tag{18}$$

The solution of Eq.(15) for $q = \phi$ with the initial conditions given by Eq.(17) and Eq.(18) can be obtained conveniently by employing the Hankel transform:

$$\phi(r, \tau) = \int_0^\infty \lambda J_0(\lambda r) \Phi(\lambda, \tau) \, d\lambda, \tag{19}$$

$$\Phi(\lambda, \tau) = \int_0^\infty r J_0(\lambda r) \phi(r, \tau) \, dr, \tag{20}$$

where J_0 is the zeroth-order Bessel function of the first kind. Upon applying the Hankel transform the problem reduces to solving

$$\frac{\partial^2 \Phi}{\partial \tau^2} + \lambda^2 \Phi = 0, \tag{21}$$

with

$$\Phi(\lambda, 0) = E(\lambda), \quad \frac{\partial \Phi}{\partial \tau}(\lambda, 0) = F(\lambda), \tag{22}$$

5

where $E(\lambda)$ and $F(\lambda)$ are given by:

$$E(\lambda) = -\frac{\beta}{2\alpha} \int_0^\infty r J_0(\lambda r) e^{-\alpha r^2} \, dr,$$

$$F(\lambda) = -\int_0^\infty r J_0(\lambda r) e^{-\alpha r^2} \, dr. \tag{23}$$

From Gradshteyn and Ryzhik [16] we obtain

$$\int_0^\infty r J_0(\lambda r) e^{-\alpha r^2} \, dr = \frac{1}{2\alpha} e^{-\frac{\lambda^2}{4\alpha}}. \tag{24}$$

The solution of Eq.(21) can be written as:

$$\Phi(\lambda, \tau) = E(\lambda) \cos(\lambda \tau) + \frac{F(\lambda)}{\lambda} \sin(\lambda \tau). \tag{25}$$

Using Eq.(19) to transform back from λ to r we obtain for the velocity potential:

$$\phi(r, \tau) = -\frac{1}{2\alpha} \left\{ \frac{\beta}{2\alpha} \int_0^\infty \lambda J_0(\lambda r) \cos(\lambda \tau) e^{-\frac{\lambda^2}{4\alpha}} \, d\lambda + \int_0^\infty J_0(\lambda r) \sin(\lambda \tau) e^{-\frac{\lambda^2}{4\alpha}} \, d\lambda \right\}. \tag{26}$$

The general solution, as function of r and t, finally becomes:

$$p'(r, t) = \frac{1}{2\alpha} \left\{ \int_0^\infty \lambda J_0(\lambda r) \cos(\lambda t) e^{-\frac{\lambda^2}{4\alpha}} \, d\lambda - \frac{\beta}{2\alpha} \int_0^\infty \lambda^2 J_0(\lambda r) \sin(\lambda t) e^{-\frac{\lambda^2}{4\alpha}} \, d\lambda \right\}, \tag{27}$$

$$u'(r, t) = \frac{x - Mt}{2\alpha r} \left\{ \int_0^\infty \lambda J_1(\lambda r) \sin(\lambda t) e^{-\frac{\lambda^2}{4\alpha}} \, d\lambda + \frac{\beta}{2\alpha} \int_0^\infty \lambda^2 J_1(\lambda r) \cos(\lambda t) e^{-\frac{\lambda^2}{4\alpha}} \, d\lambda \right\}, \tag{28}$$

$$v'(r, t) = \frac{y}{2\alpha r} \left\{ \int_0^\infty \lambda J_1(\lambda r) \sin(\lambda t) e^{-\frac{\lambda^2}{4\alpha}} \, d\lambda + \frac{\beta}{2\alpha} \int_0^\infty \lambda^2 J_1(\lambda r) \cos(\lambda t) e^{-\frac{\lambda^2}{4\alpha}} \, d\lambda \right\}, \tag{29}$$

where

$$r = \sqrt{(x - Mt)^2 + y^2}, \tag{30}$$

and $\rho' = p'$. In the above expressions J_1 is the first-order Bessel function of the first kind.

4.3 Numerical result

For a correct implementation of the initial condition we have to project $\mathbf{U}(x, y, 0)$, given by Eq.(11), onto the basis functions. The integrations which then have to be performed are not straightforward. Alternatively, we will approximate the initial solution by a second-order accurate Taylor-series expansion around the centroid of each element as was also done by Atkins and Shu [4].

In order to perform this 2D calculation with the present 3D method all derivatives in the z-direction are taken equal to zero. Furthermore symmetry-plane boundary conditions are used for the upper and lower boundary in the z-direction. On all the other boundaries of the computational domain characteristic-based non-reflecting boundary conditions are used. Both boundary conditions are described in [7]. We take for the 2D solution the result in the plane z=0.

The simulations have been carried out on different tetrahedral meshes. The physical domain,

Ω, is partitioned into N_e identical tetrahedrons obtained by dividing Ω into equally sized cubes, which provides us with a background mesh, and then dividing each cube into 12 identical tetrahedrons. In table 1, specifications of the different meshes are given. The background mesh dimensions are given by N_x, N_y and N_z, while np denotes the number of processors used in the computation. h denotes a characteristic mesh-size, and is given by $h = \frac{1}{N_x}$. All simulations have been carried out with a CFL-number of 0.15.

Case	N_x	N_y	N_z	Tetrahedrons	faces $z = 0$	h	np
II	40	40	2	38,400	3,200	$\frac{1}{40}$	2/4/8/16/32
III	80	80	4	307,200	12,800	$\frac{1}{80}$	*
IV	100	100	5	600,000	20,000†	$\frac{1}{100}$	2/4/8/16/32/64/128
V	120	120	6	1,036,800	28,800	$\frac{1}{120}$	64
VI	160	160	8	2,457,600	51,200	$\frac{1}{160}$	128

* result taken from reference [9]
† 2D result taken in $z = 1$-plane

Table 1: *Mesh specifications and number of processors used for the computations for the different cases*

Verification and accuracy
In [9] case IV was already considered with the non-parallel code. The results obtained with the current version of the code showes no differences with the results obtained with this previous version of the code.

Fig.(1) presents the results obtained for p', along the line $x = 10$ for $t = 20$, for the cases V and VI as well as the analytical solution. The location of the disturbance is accurately resolved in both cases. The magnification of the region $-30 < r < -10$, presented in Fig.(1.b), shows that the result obtained for case VI shows a slightly better comparison with the analytical solution, than the result obtained for case V, as one might have expected.

Fig.(2) presents the results obtained for p', along the line $x = 20$ for $t = 40$, for the cases IV and VI as well as the analytical solution. The results obtained for case VI show a better agreement with the analytical solution than those of case IV.

In Figures (1) and (2) the graph of the analytical solution is obtained by approximating the integrals in Eq.(27) by means of a composite Simpson's rule. The number of quadrature points is chosen sufficiently high, so that further increasing the number of quadrature points will not be visible in the figures.

For $r = 0$ Eq.(27) can be evaluated exactly, without any numerical approximation. For the pressure perturbation we obtain the analytical solution $p'(0, 20) = -0.016624864$. We denote the numerical approximation of $p'(0, 20)$, computed on a mesh with characteristic size h, by $\tilde{p}'_h$. In Fig.(3.a) we have plotted $\epsilon = |\tilde{p}'_h - p'(0, 20)|$ vs. h^{-1} on logaritmic scales. The values of the characteristic mesh size h related to the various cases are presented in table (1). The results of case III, V and VI almost lie on a straight line. The result obtained on the coarse mesh of case II only deviates a little from this line. (Note that the result obtained for case IV is not taken into consideration, since the result is not measured in the plane $z = 0$.) The slope of the line gives us the order of the method in the point $(r, t) = (0, 20)$. The slope suggests 5th-order accuracy in the specific point $(r, t) = (0, 20)$. In [17] Hu and Atkins present results of a detailed study of spatially propagating waves in a DG sheme applied to a 1D system of linear hyperbolic equations. They report that the phase error (of the physical mode) decays like h^{2p+2}, where p
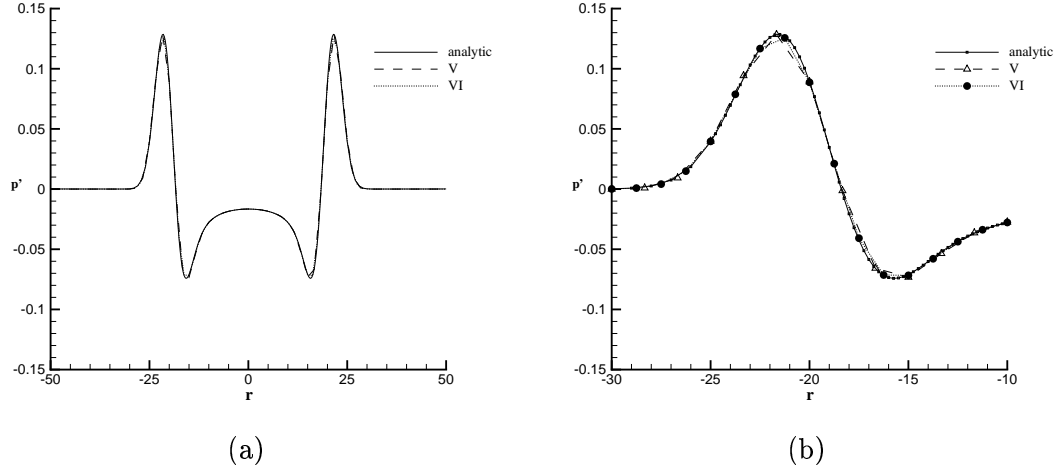
Figure 1: *Comparison of numerical results, obtained for case V and VI for $x = 10$ and $t = 20$, with the analytical solution $p'(r, 20)$. b: Magnification of the region $-30 < r < -10$.*
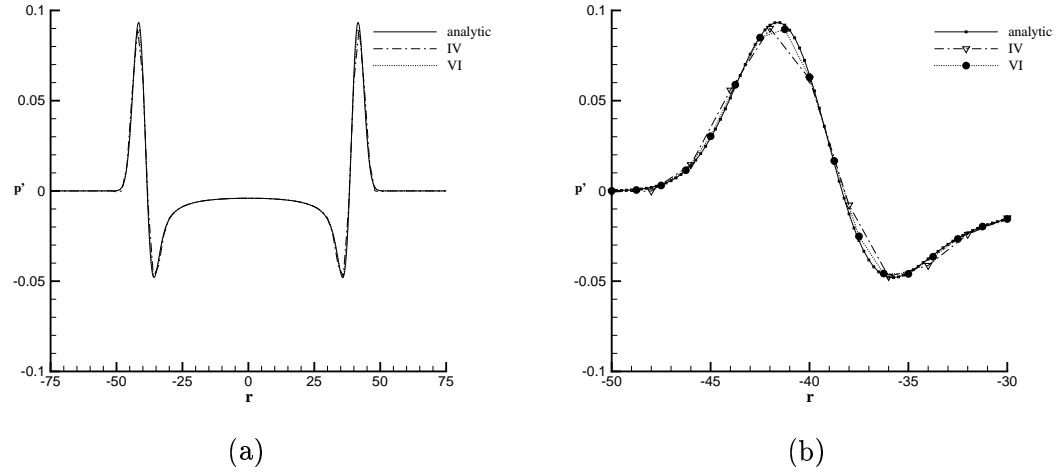
Figure 2: *Comparison of numerical results, obtained for case IV and VI for $x = 20$ and $t = 40$, with the analytical solution $p'(r, 40)$. b: Magnification of the region $-50 < r < -30$.*

is the degree of the polynomials which are used as basis functions. They also report that the global error measure (for the definition see [17]) reduces at order $2p + 1$. We use basis functions of degree $p = 1$ which would result in a decay of the phase error like h^4 and a decay of the global error measure like h^3, assuming that the results obtained by Hu and Atkins in 1D would apply to 3D. However, this still does not explain why we observe a decay of the error like h^{2p+3}. Clearly, further research on this topic is necessary.

Assuming that our method is 5th-order accurate in $(r, t) = (0, 20)$, we can apply Richardson extrapolation ([18]) to obtain a prediction of the exact solution. Employing Richardson
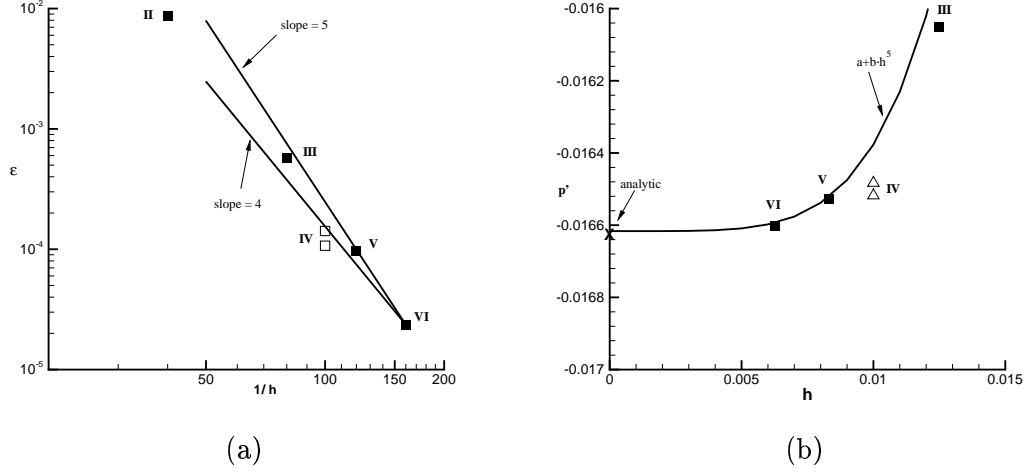
Figure 3: *Grid convergence study for the pressure perturbation in* $(r,t) = (0,20)$.

extrapolation we assume that the following holds:

$$\tilde{p}'_h = a + b\, h^5. \tag{31}$$

Using the numerical results of cases V and VI we can obtain the coefficients a and b. Coefficient a gives the prediction of the exact solution $p'(0,20)$, we obtain $a = -0.016616442$. The relative error $\left|\frac{a-p'(0,20)}{p'(0,20)}\right|$ is approximately 0.05 %. Fig.(3.b) shows the polynomial of Eq.(31) together with the numerical results of the different cases.

Speed-up
A performance test has been carried out for case II and IV on TERAS, which is a 1024-CPU platform ([10]) consisting of two 512-CPU SGI Origin 3800 systems. It has a peak performance of 1 TFlops (10^{12} floating point operations per second), it is fitted with 500Mhz R14000 CPU's organized in 256 4-CPU nodes and possesses 1 TByte of total memory. The speed-up is measured in terms of the ratio of the user CPU-times, where the two processor-job serves as reference. From Fig.(4.a) it can be seen that near-linear speed-up is obtained for case IV. Slightly superlinear speed-up is obtained on 4 processors for both case II and IV, which is probably caused by a more efficient cache performance. Fig.(4.a) shows furthermore that by dividing the domain of case II over more than 8 processors, the number of elements assigned to each processor becomes too small and the communication overhead becomes apparent. From Fig.(4.b) we observe that for case IV we have a near-linear speed-up, up to 64 processors. On 128 processors the relative speed-up (relative to $np = 2$) has dropped to 60%.

On 128 processors approximately 8.10^9 floating point operations were performed per second (8 Gflops). For the performance test for case IV, the computation involved 1000 time steps. The computation took less than 8 minutes on 128 processors (elapsed time). TERAS has a peak-performance of 1 Gflops per processor, for case IV the code was observed to operate, on average, at 10 % of this peak when up to 8 processors were used. Using increasingly more processors (more than 8) resulted in a gradual drop in performance to approximately 6% of the peak-performance, when 128 processors were used, which is thought to be due to the increased

9
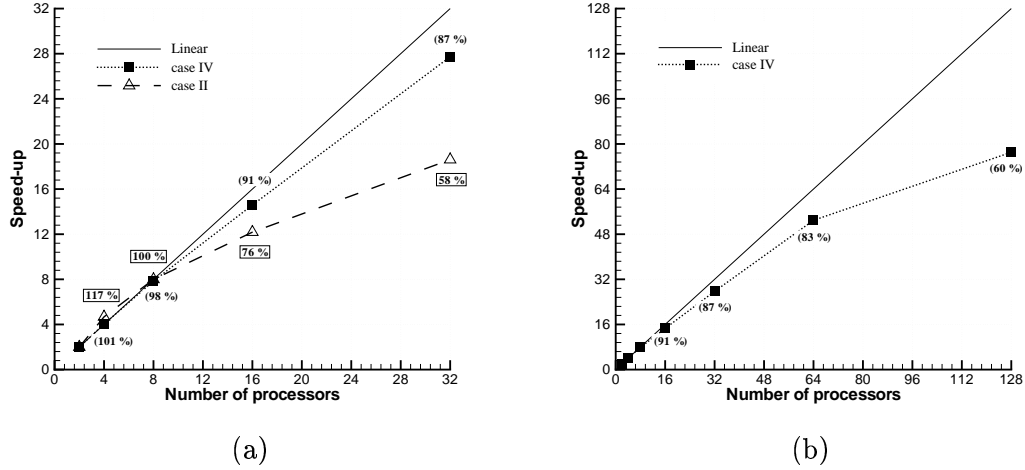
Figure 4: *Speed-up measured for case II (100 time steps) and case IV (1000 time steps) on Origin 3800. a: Result for case II and IV for up to 32 processors. b: Result for case IV for up to 128 processors.*

communication overhead.

5 Concluding Remarks

The results presented in the present paper are obtained with the computer code DIGS3D, which is based on a numerical algorithm, developed to solve the Linearized Euler equations (LEE) in three dimensions. For the spatial discretization of the LEE the Quadrature-free Discontinuous Galerkin method has been applied, while the time integration is performed by a four-step, low-storage Runge-Kutta algorithm. The algorithm is second-order accurate in both space and time. The main objectives of the work presented in the present paper are (continuation of) the verification of the numerical algorithm and conducting a performance test of the parallelized algorithm on TERAS.

As a verification problem, the convection of a 2D compact acoustic disturbance has been considered on different meshes employing different numbers of processors on TERAS, a 1024-CPU platform consisting of two 512-CPU SGI Origin 3800 systems. The obtained numerical solutions show very good agreement with the analytical solution. A grid convergence study for the pressure perturbation in the centre of the decayed and convected 2D Gaussian pulse at dimensionless time $t = 20$, suggests that the numerical result in that point is 5th-order accurate in the characteristic mesh size. The reason for this unexpected high accuracy, obtained in that specific point with the second order accurate algorithm, is unknown at present and needs further investigation.

The conducted performance test showes, that for a medium-sized mesh ($600,000$ elements), near-linear speed-up is obtained when up to 64 processors are used. Using 128 processors (for the same problem), showes that a computational speed of approximately 8.10^9 floating point operations per second (8 Gflops) is obtained.

In addition to further verification and validation, future activities will probably include optimization of the algorithm and extension of the algorithm towards higher-order accuracy.

Acknowledgement

References

[1] L.D. Landau and E.M. Lifshitz, *Fluid Mechanics, Course of Theoretical Physics, Volume 6*, Butterworth-Heinemann, reprint 2000.

[2] C. Johnson and J. Pitkärata, *An Analysis of the Discontinuous Galerkin method for a Scalar Hyperbolic Equation*, Mathematics of Computation, Vol. 46, No 176, pp. 1-26, 1986.

[3] B. Cockburn, B. Hou and C.W. Shu, *TVB Runge-Kutta Local Projection Discontinuous Galerkin Finite Element Method for Conservation Laws IV: The MultiDimensional Case*, Mathematics of Computation, Vol. 54(190), 1990, pp. 545-581.

[4] H.L. Atkins and C.W. Shu, *Quadrature-Free Implementation of Discontinuous Galerkin method for Hyperbolic Equations*, AIAA Journal, Vol. 36, pp. 775-782, 1998.

[5] H.L. Atkins and D.P. Lockard, *A High-Order Method using Unstructured Grids for the Aeroacoustic Analysis of Realistic Aircraft Configurations*, AIAA-Paper 99-1945, 1999, Fifth AIAA/CAES Aeroacoustics Conference, May 10-12.

[6] H.L. Atkins and C.W. Shu, *Quadrature-Free Implementation of Discontinuous Galerkin method for Hyperbolic Equations*, AIAA-Paper 96-1683, 1996.

[7] H.L. Atkins, *Continued Development of the Discontinuous Galerkin Method for Computational Aeroacoustic Applications*, AIAA-Paper 97-1581, 1997.

[8] C.P.A. Blom, B.T. Verhaar, J.C. van der Heijden and B.I. Soemarwoto, *A Linearized Euler Method Based Prediction of Turbulence Induced Noise using Time-averaged Flow Properties*, AIAA-Paper 2001-1100, 39th AIAA Aerospace Sciences Meeting and Exhibit, Reno, Jan. 2001.

[9] C.P.A. Blom, R. Hagmeijer, A. Biesheuvel and H.W.M. Hoeijmakers, *Three-dimensional Quadrature-free Discontinuous Galerkin Method for Computational Aeroacoustics*, AIAA-Paper 2001-2198, 7th AIAA/CEAS Aeroacoustics Conference, Maastricht, May 2001.

[10] www.sara.nl/Customer/systems/sgi3800.

[11] A. Baggag, H.L. Atkins, C. Özturan, D. Keyes, *Parallelization of an Object-oriented Unstructured Aeroacoustic Solver*, NASA/CR-1999-209098, ICASE Report No. 99-11, February 1999.

[12] E. Kreyszig, *Introductory Functional Analysis With Applications*, John Wiley & Sons, 1978.

11

[13] C. Bailly and D. Juvé, *Numerical Solution of Acoustic Propagation Problems Using Linearized Euler Equations*, AIAA Journal, Vol. 38, Nr. 1, pp. 22-29, Jan. 2000.

[14] G. Karypis, V. Kumar, *Multilevel k-way partitioning scheme for irregular graphs*, Journal of parallel and distributed computing, Volume 48, No. 1, pp96-129, Jan. 1998.

[15] H.L. Atkins, *Application of Essentially Nonoscillatory Methods to Aeroacoustic Flow Problems*, Proceedings of ICASE/LaRC Workshop on Benchmark Problems in Computational Aeroacoustics, Edited by J.C. Hardin, J.R. Ristorcelli and C.K.W. Tam, NASA CP-3300, pp. 15-26, 1995.

[16] I.S. Gradshteyn, I.M. Ryzhik, *Table of Integrals, Series, and Products*, Academic Press, inc. 1980.

[17] F.Q. Hu and H.L. Atkins, *Eigensolution Analysis of the Discontinuous Galerkin Method with Non-Uniform Grids*, AIAA-Paper 2001-2195, 7th AIAA/CEAS Aeroacoustics Conference, Maastricht, May 2001.

[18] L. Råde, *Mathematics Handbook*, for Science and Engineering, Fourth Edition, Springer-Verlag Berlin Heidelberg, 1999.

Reference # of Paper: 24
Discusser's Name: Dr. Bastiaan Oskam
Author's Name: Mr. Carl P. A. Blom
Question:
　　　　How great is the computational complexity of the DG method in comparison with the DRP scheme on the same finite element mesh? Is it larger than a factor of four?
Answer:
　　　　That will depend on the actual wave propagation properties of one method in relation to the other. I can't give a number at this stage because we don't have analytic values for the dispersion and dissipation errors in three dimensions. (I also don't know if these numbers are available for the DRP scheme in three dimensions.) However, on structured meshes the DRP scheme would be expected to be more efficient.

Discusser's Name: Prof. Ir. Joop Slooff
Author's Name: Mr. Carl P. A. Blom
Question:
　　　　Apparently you do not know precisely, on an analytical basis, what the order of accuracy is of your scheme. You had to do a numerical mesh convergence experiment to find out. Then, how do you intend to improve the order of accuracy of your method?
Answer:
　　　　We did a one dimensional wave propagation analysis that does give us that kind of information. The one dimensional analysis is on a structured mesh. We do not know if we can apply the results obtained in one dimension to three dimensional problems. We also don't know if, and how, it applies to unstructured meshes. Dr Hu [Hu, F. Q., Hussaini, M. Y., and Raestarinera, P., "An analysis of the discontinuous Galerkin method for wave propagation problems," Journal of Computational Physics, 141, 1998, pp. 921-946] has presented results of his one-dimensional analysis of wave propagation and showed very promising results. We also did this grid study to enable us to compare with analytical results that might be obtained at a later stage.

This page has been deliberately left blank

Page intentionnellement blanche

Advances in High-Resolution Schemes for Computational Acoustics on General Geometries

Miguel R. Visbal
Computational Sciences Branch
Air Vehicles Directorate
Air Force Research Laboratory
Wright-Patterson AFB, OH 45433
USA

ABSTRACT

A high-order compact-differencing and Pade-type filtering algorithm, coupled with either the standard fourth-order Runge-Kutta scheme or with a sub-iterative implicit method is developed and implemented to simulate aeroacoustic phenomena on curvilinear geometries. Several issues pertinent to the use of such schemes are addressed. The impact of mesh stretching in the generation of high-frequency spurious modes is examined and the need for a discriminating higher-order spatial filter procedure is established and resolved. The incorporation of these filtering techniques also permits a robust treatment of outflow radiation condition by taking advantage of energy transfer to high frequencies caused by rapid mesh stretching. Computations demonstrate that these algorithmic components are also suitable for interface treatments created in domain-decomposition strategies. For three-dimensional computations, special metric relations are employed to assure the fidelity of the scheme in curvilinear and dynamic meshes. Application to several benchmark 2D and 3D problems demonstrates the success of the overall computational approach.

INTRODUCTION

An important aspect of both civilian and military aircraft operation is the impact of aerodynamically generated sound on communities and structures. Examples of applications of current interest include weapon cavity acoustics, jet screech, sonic boom, cabin noise, and sound generated by blade/vortex interactions. The relatively new field of time-domain computational aeroacoustics (CAA) focuses on the accurate prediction of aerodynamic sound generated by airframe components and propulsion systems, as well as on its propagation and far-field characteristics. Both aspects of the problem (*i.e.* sound generation and propagation) are extremely demanding from a time-domain computational standpoint due to the large number of grid points and small time-steps that are typically required. Therefore, for realistic aeroacoustic simulations to become more feasible, higher-order accurate and optimized numerical schemes are sought in order to reduce the required number of grid points per wavelength while still ensuring tolerable levels of numerically-induced dissipation and dispersion. These strict simulation requirements are shared by other time-domain wave propagation applications such as computational electromagnetics.

Recent reviews of computational aeroacoustics have been given by Tam[1] and Wells and Renaut[2] who discuss various numerical schemes currently popular in CAA. These include among others the dispersion-relation-preserving (DRP) scheme of Tam and Webb[3], the family of high-order compact differencing schemes of Lele[4] and Essentially Non-Oscillatory (ENO) schemes[5]. The DRP and compact schemes are centered non-dissipative schemes, a property which is desirable for linear wave propagation. However, their inherent lack of numerical dissipation results in spurious numerical oscillations and instability in practical applications involving general geometries, approximate boundary conditions or non-linear features. In the DRP approach for instance, artificial selective damping must be employed under these conditions[1]. While quite robust, standard upwind and upwind-biased formulations are undesirable for situations involving linear wave propagation due to their excessive dissipation. To overcome this difficulty, higher-order upwind or ENO approaches must be employed. The above spatial semi-discretizations are typically combined with high-order explicit time-integration methods such as the multi-stage Runge-Kutta procedure. In addition to the spatial and temporal discretizations, another critical aspect in CAA simulations is the accurate treatment of the physical and computational boundary conditions. A recent review of radiation, outflow and wall boundary treatments has been provided in Ref. 6.

This paper focuses on the development and evaluation of a high-order computational methodology for aeroacoustic simulation on general geometries. There are two primary components to the algorithm chosen in the present work. The

first is the spatial differencing scheme, for which the choice rests primarily on Pade-type tridiagonal-based fourth- and sixth-order compact-difference formulas[4]. As compared to explicit schemes, this approach incurs an increase in computational cost but lowers the dispersion error and reduces the number of points near the boundary where special formulations are required. As noted earlier, the non-dissipative nature of centered schemes makes them susceptible to the unrestricted growth of spurious perturbations. This issue is resolved through the incorporation of high-order spatial low-pass filters. The filters are based on Pade-type formulas requiring the solution of tridiagonal systems of equations. The expressions are taken from Ref. 7, where up to 10th-order filters were employed to stabilize finite-volume electromagnetics calculations, and have been successfully extended to solve the Navier-Stokes equations[8]. Time integration is achieved through the use of a either the standard 4th-order Runge-Kutta algorithm or an implicit sub-iterative third-order method. The solver is written in general curvilinear coordinates in order to handle non-trivial geometries. The various components of the numerical procedure are described below with particular emphasis on metric evaluation for 3-D and dynamic meshes, multi-domain interface treatment and the extension of the filtering scheme to treat outflow radiation boundaries. The accuracy properties of the scheme, and the efficacy of the high-order low-pass filter approach, are highlighted by considering several benchmark test-cases on single and multiple domains.

METHODOLOGY

GOVERNING EQUATIONS

In order to develop a procedure suitable for nonlinear fluid dynamic, aeroacoustic and aeroelastic applications over complex configurations, the full Navier-Stokes equations are selected and are cast in strong conservative form introducing a general time-dependent curvilinear coordinate transformation (x,y,z,t) -> (ξ, η, ζ, t). In vector notation, and employing non-dimensional variables, these equations can be written as:

$$\partial(\vec{U}/J)/\partial t + \partial\hat{F}/\partial\xi + \partial\hat{G}/\partial\eta + \partial\hat{H}/\partial\zeta = (1/\text{Re})[\partial\hat{F}v/\partial\xi + \partial\hat{G}v/\partial\eta + \partial\hat{H}v/\partial\zeta] + \vec{S}/J \qquad (1)$$

where F, G, H, F_v, G_v, H_v are the fluxes, S denotes an imposed acoustic source, and J is the coordinate transformation Jacobian, which for dynamic meshes, is also a function of time. The specific form the fluxes appearing in Eq. (1) can be found for instance in Ref. 9.

SPATIAL DISCRETIZATION

A finite-difference approach is employed to discretize the above equations. This choice is motivated by the relative ease of formal extension to higher-order accuracy. For any scalar quantity, f, such as a metric, flux component or flow variable, the spatial derivative f' is obtained in the transformed plane by solving the tridiagonal system:

$$\alpha f'_{i-1} + f'_i + \alpha f'_{i+1} = b\frac{f_{i+2} - f_{i-2}}{4} + a\frac{f_{i+1} - f_{i-1}}{2} \qquad (2)$$

where α, a and b determine the spatial properties of the algorithm. The formula yields the compact five-point, sixth-order (C6) and three-point fourth-order (C4) schemes with $\alpha=1/3$, $a=14/9$, $b=1/9$ and $\alpha=1/4$, $a=3/2$, $b=0$ respectively. Equation (2) also incorporates the standard explicit fourth-order (E4) and second-order (E2) approaches for which the coefficients are ($\alpha=0$, $a=4/3$, $b=-1/3$) and ($\alpha=0$, $a=1$, $b=0$) respectively. The dispersion characteristics and truncation error of the above schemes can be found in Refs. 4 and 10. It should be noted that for a given order of accuracy, the compact schemes are significantly superior to their explicit (non-compact) counterparts.

FILTERING SCHEME

Compact-difference discretizations, like other centered schemes, are non-dissipative, and therefore susceptible to numerical instabilities due to the unrestricted growth of high-frequency modes. These difficulties originate from several sources including mesh non-uniformity, approximate boundary conditions and nonlinear flow features. In order to extend the present solver to practical simulations, while retaining the improved accuracy of the spatial compact discretization, a high-order implicit filtering technique [7,8] is incorporated. If a typical component of the solution vector is denoted by f, filtered values $\bar{f}$ satisfy,

$$\alpha_f \bar{f}_{i-1} + \bar{f}_i + \alpha_f \bar{f}_{i+1} = \sum_{n=0}^{N} \frac{a_n}{2}(f_{i+n} + f_{i-n}) \qquad (3)$$

Equation (3) is based on templates proposed in Ref. 4 and with proper choice of coefficients, provides a *2N*th-order formula on a *2N+1* point stencil. The *N+1* coefficients, $a_o, a_1, ..., a_N$, are derived in terms of α_f with Taylor- and Fourier-series analyses and are found in Refs. 8, 10 and 11, along with the corresponding spectral filter responses. The adjustable parameter α_f satisfies the inequality $-0.5 < \alpha_f < 0.5$, with higher values of α_f corresponding to a less

dissipative filter. In multi-dimensional problems, the filter operator is applied sequentially in each coordinate direction. The specified interior filter formula is denoted by appending its designation to that of the scheme. For example, *C6F10* designates the sixth-order compact scheme combined with a tenth-order filter. For the near-boundary points, the filtering strategies described in Refs. 8 and 11 are employed.

METRIC EVALUATION

The extension of high-order schemes to non-trivial 3-D geometries demands that issues of freestream preservation and metric cancellation be carefully addressed. These errors, which arise in finite-difference discretizations of governing equations written in strong-conservation form, can catastrophically degrade the fidelity of standard second-order as well as higher-order approaches[8,12]. In deriving the flow equations in strong-conservation form, the following metric identities have been implicitly invoked,

$$I_1 = (\xi_x/J)_\xi + (\eta_x/J)_\eta + (\zeta_x/J)_\zeta = 0$$

$$I_2 = (\xi_y/J)_\xi + (\eta_y/J)_\eta + (\zeta_y/J)_\zeta = 0 \tag{4}$$

$$I_3 = (\xi_z/J)_\xi + (\eta_z/J)_\eta + (\zeta_z/J)_\zeta = 0$$

$$I_4 = (1/J)_\tau + (\xi_t/J)_\xi + (\eta_t/J)_\eta + (\zeta_t/J)_\zeta = 0$$

In Ref. 8 it was shown that on highly distorted (static) curvilinear 2-D meshes, the compact scheme exhibits freestream preservation when the metrics are evaluated with the same finite-difference expressions as those employed for the fluxes. It was also demonstrated that the practice of prescribing *analytic* metrics on stretched curvilinear grids can lead to unacceptable errors and therefore should in general be avoided. The previous straightforward approach of calculating the metrics, although effective in 2-D, fails to provide metric cancellation for general 3-D curvilinear configurations. To illustrate this point, consider the standard metric relations:

$$\xi_x/J = y_\eta z_\zeta - y_\zeta z_\eta$$
$$\eta_x/J = y_\zeta z_\xi - y_\xi z_\zeta \tag{5}$$
$$\zeta_x/J = y_\xi z_\eta - y_\eta z_\xi$$

associated with the identity I_1. Evaluation of the *y* and *z* derivatives in the previous expressions using explicit or compact centered schemes does not satisfy I_1, and as a result, significant grid-induced errors may appear[12,13]. In order to extend the high-order compact scheme to general geometries, the metric terms are rewritten prior to discretization in the equivalent (conservative) form[14]:

$$\xi_x/J = (y_\eta z)_\zeta - (y_\zeta z)_\eta$$
$$\eta_x/J = (y_\zeta z)_\xi - (y_\xi z)_\zeta \tag{6}$$
$$\zeta_x/J = (y_\xi z)_\eta - (y_\eta z)_\xi$$

Similar expressions are employed for the remaining metric terms in order to satisfy the identities I_2 and I_3 above. When the transformation metrics are recast in this manner, and the derivatives are evaluated with the same high-order formulas employed for the fluxes, freestream preservation is again recovered in general time-invariant 3-D curvilinear geometries[12].

For deforming and moving meshes, the identity I_4 must be also satisfied to eliminate metric cancellation errors and to ensure freestream preservation. This metric identity is referred to in the literature[14] as the Geometric Conservation Law (*GCL*). For the time-integration methods employed in this work, the time-derivative term in Eq. (1) is split using chain-rule differentiation as follows:

$$(\vec{U}/J)_\tau = (1/J)\vec{U}_\tau + \vec{U}(1/J)_\tau \tag{7}$$

Rather than attempting to compute the time derivative of the inverse Jacobian directly from the grid coordinates at various time levels (either analytically or numerically), we simply invoke the *GCL* identity I_4 to evaluate $(1/J)_\tau$, *i.e.*

$$(1/J)_\tau = -[(\xi_t/J)_\xi + (\eta_t/J)_\eta + (\zeta_t/J)_\zeta] \tag{8}$$

where

$$\xi_t/J = -[x_\tau(\xi_x/J) + y_\tau(\xi_y/J) + z_\tau(\xi_z/J)]$$
$$\eta_t/J = -[x_\tau(\eta_x/J) + y_\tau(\eta_y/J) + z_\tau(\eta_z/J)] \tag{9}$$
$$\zeta_t/J = -[x_\tau(\zeta_x/J) + y_\tau(\zeta_y/J) + z_\tau(\zeta_z/J)]$$

For the case of an analytically prescribed dynamic mesh transformation, the grid speeds (x_τ, y_τ, z_τ) are obtained from the corresponding analytic expressions. An example in which the grid speeds are known analytically corresponds to the

case of a maneuvering wing when the entire mesh is rotated in a rigid fashion. In many practical applications involving deforming meshes (*e.g.* dynamic aeroelastic simulations), the grid speeds are not known *a priori*, and must therefore be approximated to the desired degree of accuracy employing the evolving grid coordinates at several time levels. As demonstrated in Ref. 15, the high-order method retains its superior accuracy on rapidly distorting meshes when the procedure outlined above is incorporated for the time metrics.

TIME-INTEGRATION SCHEME

Two different time-integration approaches are incorporated in the present family of solvers. For wave propagation applications, the equations are integrated in time with the classical fourth-order four-stage Runge-Kutta method (*RK4*). The scheme is implemented in low storage form requiring three levels of storage. For highly stretched grids exhibiting very small volumes, the stability constraint of the explicit time-marching scheme is found to render the approach too restrictive and inefficient. Therefore, the implicit, approximately-factored method of Beam and Warming[16] is also incorporated and augmented through the use of Newton-like subiterations in order to achieve high-order time accuracy. In delta form, the second-order form of the scheme (denoted as *BW2*) may be written as:

$$
\left[I + \left(\frac{2\Delta t}{3} \right) \delta_\xi \left(\frac{\partial F^p}{\partial Q} - \frac{1}{Re} \frac{\partial F_v^p}{\partial Q} \right) \right] \times \left[I + \left(\frac{2\Delta t}{3} \right) \delta_\eta \left(\frac{\partial G^p}{\partial Q} - \frac{1}{Re} \frac{\partial G_v^p}{\partial Q} \right) \right] \times \left[I + \left(\frac{2\Delta t}{3} \right) \delta_\zeta \left(\frac{\partial H^p}{\partial Q} - \frac{1}{Re} \frac{\partial H_v^p}{\partial Q} \right) \right] \Delta Q
$$
$$
= -\left(\frac{2\Delta t}{3} \right) \left[\left(\frac{1}{2\Delta t} \right) \left(3Q^p - 4Q^n + Q^{n-1} \right) + \delta_\xi \left(F^p - \frac{1}{Re} F_v^p \right) + \delta_\eta \left(G^p - \frac{1}{Re} G_v^p \right) + \delta_\zeta \left(H^p - \frac{1}{Re} H_v^p \right) + S^p \right]
$$

(10)

The spatial derivatives in the implicit operators are represented using standard second-order centered approximations whereas high-order discretizations are employed for the explicit side. Nonlinear artificial dissipation terms[17] are also appended to the implicit operator to enhance stability. In addition, for improved efficiency, the approximately-factored scheme is recast in diagonalized form[18]. Any degradation in solution accuracy caused by the spatial second-order implicit operators, artificial dissipation and the diagonal form is eliminated through the use of sub-iterations (typically, three sub-iterations are used per time step). By changing the number of time levels employed to evaluate the time-derivative term appearing in the *RHS* of Eq. (10), first (*BW1*) and third (*BW3*) order accurate forms of the implicit algorithm can be constructed.

MULTI-DOMAIN STRATEGY

Domain-decomposition techniques constitute an important component of modern computational strategy. Due to their spatially implicit nature, Pade-type schemes are more difficult to utilize in a multi-domain environment than explicit methods. However, a finite-size overlap can be employed with the present compact/filtering methodology to generate a powerful approach applicable to complicated curvilinear meshes[11,12]. Figure 1 depicts schematically the case of a simulation employing two sub-domains. The original domain of computation is divided into two parts to be distributed to different processors. Each sub-domain is supplemented with several points from the adjacent sub-domain to form an overlap region, whose details for a five-point vertical overlap are also shown in Fig. 1. Although the overlap points are collocated, they have been shown slightly staggered for clarity. Each vertical line is denoted by its *i*-index. Data is exchanged between adjacent sub-domains at the end of each sub-iteration of the implicit scheme (or each stage of *RK4*), as well as after each application of the filter. The values at points *1* and *2* of Mesh 2 are set to be identically equal to the corresponding updated values at points *IL-4* and *IL-3* of Mesh 1. Similarly, reciprocal information is transferred through points *4* and *5* of Mesh 2 which "donate" values to points *IL-1* and *IL* of Mesh 1. More details on the accuracy and robustness of the present multi-domain approach can be found in Ref. 11.

RESULTS

IMPACT OF SPATIAL FILTERING ON STRETCHED MESHES

In practical scattering simulations, grid stretching is usually employed in order to reduce required computational resources, as well as to permit the use of approximate farfield boundary conditions. Therefore, the performance of high-order schemes on general stretched meshes must be carefully examined.

An enlightening analysis of the behavior of a smooth solution as it passes through a sudden mesh coarsening has been presented by Vichnevetsky[19] for the 1-D advection equation semi-discretized with the standard second-order centered scheme. This analysis indicates that although total energy is preserved, at the grid coarsening interface, a significant portion of the energy is deposited on a *reflected* solution composed primarily of odd-even modes and modulated by a smooth envelope. This reflected energy propagates upstream (*i.e.* with negative group velocity) and in most circumstances if left unchecked has the potential of ultimately contaminating the genuine solution. However, since reflections due to grid stretching are characterized by high-frequency modes, they can be easily removed by the

high-order low-pass spatial filter. The effectiveness of the low-pass filter in controlling spurious reflections without degrading the fidelity of the solution was demonstrated previously in Ref. 12.

The combination of grid stretching with a discriminating low-pass filter may be exploited as an alternative procedure for outflow boundary treatment. By employing a large rate of stretching, a significant amount of energy can be reflected at the grid coarsening interfaces. Provided this *reflected* energy is deposited into high-frequency modes (in the fine mesh region), it can then be subsequently eliminated by the baseline low-pass filter without contaminating the genuine solution. Furthermore, the *transmitted* energy is also quickly dissipated by the high-order filter, as the transmitted solution features are represented by a diminishing number of points per wave in the stretching mesh. This proposed method eliminates the need for more sophisticated (and perhaps more restrictive) boundary conditions at the expense of extending the computational domain. Although the proposed approach has a mathematical foundation (at least based on the 1-D analysis of Ref. 19), its implementation is highly empirical, and therefore its utility must be evaluated in the context of practical applications.

As a severe test case, consider the propagation of acoustic waves in the grid of Fig. 2a. This mesh is uniform ($\Delta x = \Delta y = 0.05$) in the center of the computational domain ($-3 < x, y < 3$). Outside of this resolved region, Δx and Δy are increased abruptly. An acoustic source is specified according to the expression

$$S(x,y,t) = exp\{(ln2) \ [(x-x_c)^2+(y-y_c)^2 / b^2]\} \ sin(\omega t) \ f(t) \qquad (11)$$

$$f(t) = min\{ \ 1.0, \ (t/t_o)^3\}$$

with $x_c = y_c = 0$, $\omega = 5\pi$, $b = 0.2$ and $t_o = 4$. A snapshot of the pressure is displayed in Fig. 2b. It is apparent that the acoustic energy reflected at the grid-coarsening interface is almost completely annihilated by the high-order filter. The corresponding plot of the instantaneous pressure along the diagonal ($x = y$) is shown in Fig. 2c and indicates that the transmitted energy diffuses rapidly in the coarse mesh region. For this square grid, the circular waves cross the grid interface at a varying angle of incidence without apparent anisotropies being introduced. More quantitative tests demonstrating the suitability of the present far field radiation treatment can be found in Ref. 13 for a transient acoustic pulse and a convective vortical disturbance.

SCATTERING OF AN ACOUSTIC PULSE
In order to validate the present approach for curvilinear geometries, we select as a test case the benchmark problem denoted as Category I, Problem 2 in the 2nd CAA Workshop of Ref. 20. This configuration (Fig. 3) describes the scattering off a circular cylinder of a prescribed initial pressure pulse. The pulse at $t = 0$ is given by the expression

$$p = p_o + \varepsilon \, exp\{(ln2) \ [(x-x_c)^2+(y-y_c)^2 / b^2]\} \qquad (12)$$

with $x_c = 4$, $y_c = 0$, $\varepsilon = 0.01$, $b = 0.2$.

Along the cylinder surface, standard inviscid wall boundary conditions are employed. Since the configuration is symmetric, only the upper half of the domain is considered, and symmetry conditions are invoked along $\theta = 0^o, 180^o$. As indicated in Fig. 3a, the grid is stretched for $r/D > 7$ using a constant stretching factor of 1.1. Since in this coarse-mesh region the outgoing pulse is dissipated by the baseline filter, a simple extrapolation condition is suitable along the far field boundary. A polar-type grid of size 156X175 is employed, and the solution is advanced in time with a non-dimensional time step $\Delta t = 0.004$.

Pressure contours depicting pulse propagation and reflection off the cylinder surface are shown in Fig. 3 at several instants in time for the *C6F10-RK4* scheme. The history of the pressure at a selected point ($r/D=5$, $\theta=90^o$) and for several computations is presented in Fig. 4. On this relatively coarse mesh, the *C6F10-RK4* and *C4F8-RK4* schemes with a filter coefficient $\alpha_f = 0.4$ are observed to be in good agreement with the exact solution[20]. However, on this mesh, the *C4* scheme combined with an 8th-order *explicit* filter (*i.e.* $\alpha_f = 0$) displays appreciable error. This highlights the improved accuracy of the implicit filter formulation.

Results computed using the implicit sub-iterative time-marching scheme are provided in Fig. 5. These results were obtained with a non-dimensional time step $\Delta t = 0.004$ and employing two sub-iterations. The first order time advancement method (*BW1*) is found to be highly dissipative. However, significant improvement is achieved by

employing the second-order implicit approach (*BW2*). Finally, the third-order iterative implicit method (*BW3*) is in very close agreement with the fourth-order explicit (*RK4)* solution (see figure inset).

In order to demonstrate the advantages of the implicit time-marching scheme, we consider the previous pulse scattering example for the case of an elliptic cylinder of aspect ratio 10 (Fig. 6). As Fig. 6a indicates, the grid is highly clustered near the small radius of curvature at the edge of the ellipse. This results in small grid cells and consequently in a significant reduction of the allowable time step for the explicit method. Calculations employing the *RK4* scheme were found to be unstable even for a non-dimensional time step as low as $\Delta t = 0.000125$ which correspond to a maximum *CFL* number of approximately 0.96. Therefore it becomes apparent that the explicit time-marching method is very inefficient for general geometries wherein highly clustered meshes are necessary (*e.g.* sharp edges). By contrast, the third-order implicit iterative scheme was found to remain stable for the baseline time step ($\Delta t = 0.004$) which corresponds to $CFL_{max} \sim 31$. The corresponding instantaneous pressure contours obtained with the implicit method at $t = 1.5$ are displayed in Fig. 6b.

MULTI-DOMAIN SCATTERING SIMULATION
This case corresponds to Category I, Problem 1 in Ref. 20, and considers the scattering from a circular cylinder of a periodic acoustic source (Fig. 7a). This example constitutes a more stringent test of the algorithm and boundary conditions since an asymptotic periodic solution must be attained, and long-term numerical stability demonstrated. In addition, in order to highlight the capability of the present numerical approach to treat a multiple-domain situation, the single-domain grid, consisting of 361 X 321 points, is split along $\theta = 90^o$, where extra ξ-lines are added to form a five-point overlap as in Fig. 1. Solutions are advanced separately on each sub-domain, and information is exchanged at the overlap points in the manner previously discussed. The *C6* scheme is employed for interior points along with fourth- and fifth-order compact operators at the boundary and next-to-boundary points respectively whereas *RK4* is utilized for time-integration. In the interior of each sub-domain, a 10th-order filter is utilized whereas high-order one-sided techniques, are invoked near boundaries. For all filter operators, the coefficient $\alpha_f = 0.45$ is specified.

Figure 7b displays instantaneous pressure contours in the vicinity of the cylinder. It is apparent that the pressure waves cross the grid interface without producing any noticeable disruptions of the interference pattern even though pressure waves generated by the source propagate through the overlap region in an oblique direction to the zonal interface. A quantitative comparison of the single-domain, multiple-domain and analytic solutions is given in Fig. 7c in terms of the directivity of the radiated sound at $r/D = 5$. The directivity obtained with a 6th-order near-boundary filter in the overlap region is essentially the same as the corresponding single-domain baseline solution, and both results are in excellent agreement with the theoretical solution. These results highlight the potential of the present high-order methodology for domain-decomposition applications on parallel computers.

ACOUSTIC PROPAGATION ON 3-D CURVILINEAR MESHES
This validation case considers the propagation of a 3-D spherical pulse in a curvilinear mesh in order to examine metric cancellation errors. A three-dimensional curvilinear 61X61X61 mesh is generated using the equations given in Ref. 13, providing a grid in which the metric identities (Eq. (4)) are not trivially satisfied. A constant ζ-plane of the mesh at the location of maximum deformation is shown in Fig. 8a. The imposed grid undulations are resolved with approximately 15 points per wave. An initial pressure pulse is prescribed by

$$p = po + \varepsilon\, exp\{ \,(-ln2)\, (x^2+y^2+z^2)\,/\,9\}$$

where $\varepsilon = 0.01$.

The pulse propagation problem is computed with a $\Delta t = 0.004$ using the *C4F10-RK4* algorithm with $\alpha_f = 0.49$. Figure 8b displays the calculated pressure contours on a plane through the center of the spherical pulse at $t=10$ for the case when the metrics are evaluated in the standard fashion of Eq. (5). It is apparent that significant distortion of the wave front occurs due to the lack of freestream preservation (*i.e.* metric cancellation errors). The perturbation pressure along the grid line $i=j=31$, (Fig. 8d) indicates gross departure from the theoretical solution. The results obtained with the metric evaluation procedure of Eq. (6) exhibit no distortions of the spherical front (Fig. 8c) and are in excellent agreement with the exact solution (Fig. 8d). Calculations with *C6F10* (not shown) displayed reduced sensitivity to the choice of metric evaluation procedure. This is in agreement with the results of Ref. 12, wherein metric cancellation errors were shown to decrease with increasing order of accuracy. Nonetheless, without the incorporation of Eq. (6) in the calculation of the metric relations, all solutions on this distorted mesh were found to be of poor quality. Hence, even for relatively benign 3-D curvilinear grids, freestream preservation errors may swamp acoustic pressure levels unless proper metric evaluation procedures are employed. It should be noted that analytic metric evaluation (even if available)

does not remedy the situation [8,12]. The present results clearly demonstrate that the superior performance of the high-order method can be extended to the realm of general curvilinear grids including moving/deforming meshes as highlighted in the fluid/structure interaction described next.

ACOUSTO-STRUCTURAL-FLUID INTERACTION OVER A FLEXIBLE PANEL

As a final example of a simulation of multi-disciplinary physics with the present methodology, consider a transitional boundary-layer flow over a flexible finite panel embedded in a rigid surface as shown schematically in Fig. 9a. This problem is closely related to classic panel flutter phenomena, as well as to viscous flow over compliant surfaces. The panel of length *a* and thickness *h* extends over the region *0.5 < x/a < 1.5*. The leading-edge region of the plate (-*0.5 < x/a < 0.0*) is formed by an ellipse of half-thickness *0.05h* (*i.e.* aspect ratio 10). An additional challenge posed by this aeroelastic simulation is the need to accomodate the surface deflection with a dynamically deforming mesh. The problem has been examined in great detail in Ref. 21, which should be consulted for details regarding boundary condition implementation and mesh resolution studies. For brevity, only select results obtained at a freestream Mach number $M = 0.8$ and $Re_a = 10^5$ are summarized here to highlight the ability of the method to capture the complicated unsteady phenomena under the influence of flow-induced surface deformation. This case was computed employing the *C6F10-BW2* scheme.

At low values of the dynamic pressure, a steady flow is obtained despite the adverse pressure gradient induced by the downward deflection of the panel. At higher dynamic pressures, however, a traveling-wave-flutter phenomenon is observed as summarized in Fig. 9b, c. The instantaneous panel shapes (not shown) display a seventh-mode oscillation with a dominant non-dimensional frequency *St = fa/U = 1.52* which is substantially higher than the fundamental frequency of the elastic plate. The high-mode flexural deflections are observed to travel along the panel and to reflect at the panel edges. These high-frequency fluctuations result in a pronounced acoustic radiation pattern above the vibrating plate, shown in Fig. 9b in terms of the instantaneous pressure field. Downstream of the flexible surface, a regular train of vortical disturbances is observed (Fig. 9c) with characteristic wavelength and frequency compatible with those of Tollmien-Schlichting (T-S) instability. The traveling wave flutter appeared to originate from the coupling of the T-S waves with the panel high-mode transverse fluctuations, and this convective instability ceases below a critical value of Reynolds number.

SUMMARY

A high-order finite-difference method has been adapted to simulate aeroacoustic phenomena on curvilinear geometries. The scheme is based on 4th- and 6th-order compact differencing formulas coupled with up to 10th-order Pade-type low-pass spatial filters. Both explicit and iterative implicit time-marching schemes are considered. The high-order spatial filtering procedure is required in order to maintain stability in the presence of mesh stretching and approximate boundary conditions while ensuring high fidelity for wave propagation. The incorporation of these filtering techniques also permit a robust treatment of outflow radiation condition by taking advantage of energy transfer to high-frequencies caused by rapid mesh stretching. The potential of the procedure for parallel implementation is demonstrated by successful application to multi-domain scattering cases. Special metric procedures are also shown to be essential in the simulation of acoustic phenomena in general curvilinear three-dimensional meshes.

REFERENCES

1. Tam, C.K.W., "Computational Aeroacoustics: Issues and Methods, *AIAA J.*, Vol. 33 No. 10, 1995
2. Wells, V. L. and Renaut, "Computing Aerodynamically Generated Noise", *Annual Review of Fluid Mechanics*, Vol. 29, 1997.
3. Tam, C.K.W. and Webb, J.C., "Dispersion-Relation-Preserving Finite Difference Schemes for Computational Acoustics, *J. Comp. Phys.*, Vol. 107, 1993.
4. Lele, S.K., "Compact Finite Difference Schemes with Spectral-Like Resolution", *J. Comp. Phys.*, Vol 103, No. 1, Nov, 1992.
5. Casper, J., "Using High-Order Accurate Essentially Nonoscillatory Schemes for Aeroacoustic Application", *AIAA J.*, Vol. 34, 1994.
6. Tam, C.K.W., "Advances in Numerical Boundary Conditions for Computational Aeroacoustics", AIAA Paper 97-1774, 1997.
7. Gaitonde, D.V., Shang, J.S. and Young, J.L., "Practical Aspects of Higher-Order Numerical Schemes for Wave Propagation Phenomena", *Int. Jnl. Of Num. Methods in Eng.*, Vol. 45, 1999.
8. Visbal, M. and Gaitonde, D. "High-Order Accurate Methods for Complex Unsteady Subsonic Flows", *AIAA J.*, Vol. 37, No. 10, 1999.
9. Anderson, D., Tannehill, J. and Pletcher, R., *Computational Fluid Dynamics and Heat Transfer*, McGraw-Hill Book Co., 1984.

10. Gaitonde, D. and Visbal, M., "High-Order Schemes for Navier-Stokes Equations: Algorithm and Implementation into FDL3DI", Technical Report AFRL-VA-WP-TR-1998-3060, Air Force Research Lab., Wright-Patterson AFB, 1998.

11. Gaitonde, D. and Visbal, M., "Pade-Type High-Order Boundary Filters for the Navier-Stokes Equations", *AIAA J.*, Vol. 38, No. 11, 2000.

12. Gaitonde, D. and Visbal, M., "Further Development of a Navier-Stokes Solution Procedure Based on Higher-Order Formulas", AIAA Paper 99-0557, 1999.

13. Visbal, M. and Gaitonde, D., "Very High-Order Spatially Implicit Schemes for Computational Acoustics on Curvilinear Meshes", *J. Comp. Acoustics*, in press, 2001.

14. Thomas, P. and Lombard, C., "Geometric Conservation Law and its Application to Flow Computations on Moving Grids", *AIAA J.*, Vol. 17, No. 10, Oct. 1979.

15. Visbal, M. and Gordnier, R., "A High-Order Flow Solver for Deforming and Moving Meshes", AIAA Paper 2000-2619, June 2000.

16. Beam, R. and Warming, R., "An Implicit Factored Scheme for the Compressible Navier-Stokes Equations," *AIAA J.*, Vol. 16, No. 4, 1978.

17. Pulliam, T., "Artificial Dissipation Models for the Euler Equations", *AIAA J.*, Vol. 24, No. 12, Dec. 1986.

18. Pulliam, T. and Chaussee, D., "A Diagonal Form of an Implicit Approximate-Factorization Algorithm", *J. Comp. Phys.*, Vol. 39, No. 2, 1981.

19. Vichnevetsky, R., "Propagation Through Numerical Mesh Refinement for Hyperbolic Equations", *Math. and Comp. in Simulation*, XXIII, 1981.

20. Proceedings of the Second Computational Aeroacoustics (CAA) Workshop on Benchmark Problems. NASA Langley Research Center, Hampton, Virginia.

21. Visbal, M. and Gordnier, R., "Direct Numerical Simulation of the Interaction of a Boundary layer with a Flexible Panel", AIAA Paper 2001-2721, 2001.
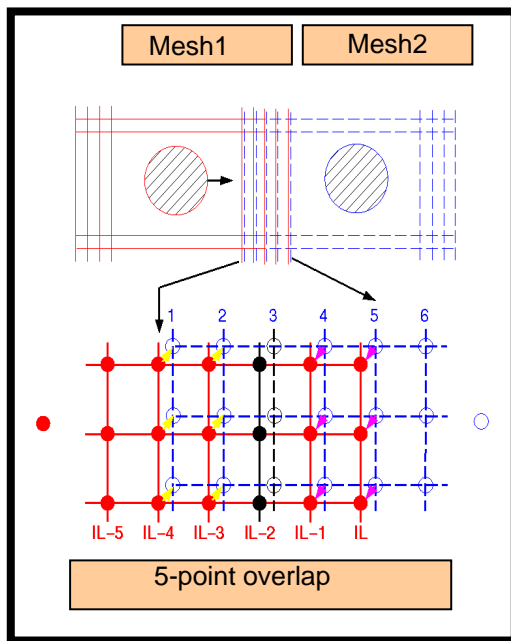
Fig. 1. Schematic of overlap strategy in high-order domain decomposition.
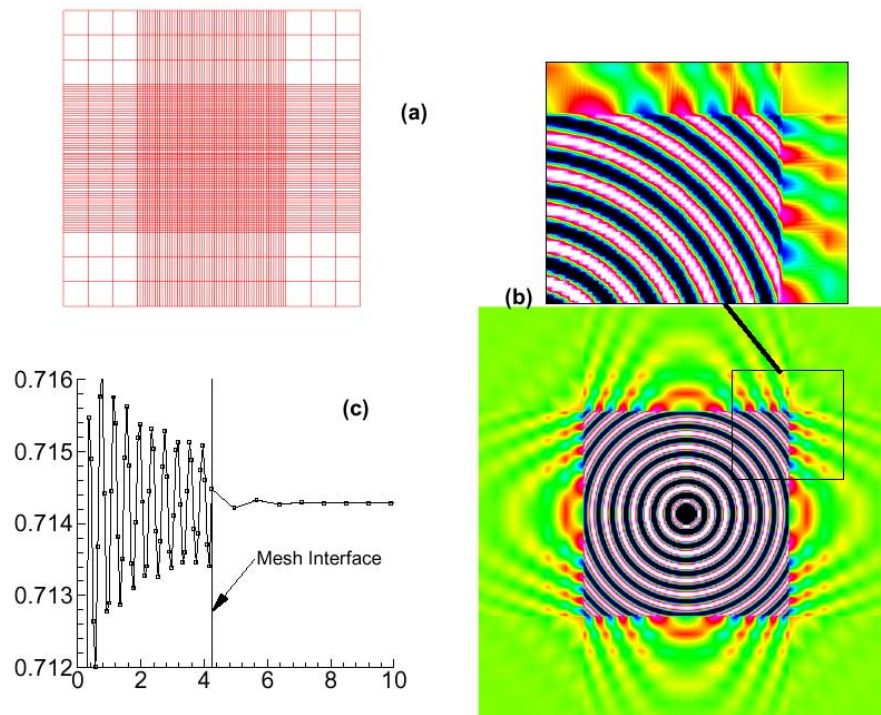
Fig. 2. Computation of 2-D acoustic source on mesh with abrupt stretching. (a) Grid, (b) Pressure contours, (c) Pressure along diagonal.
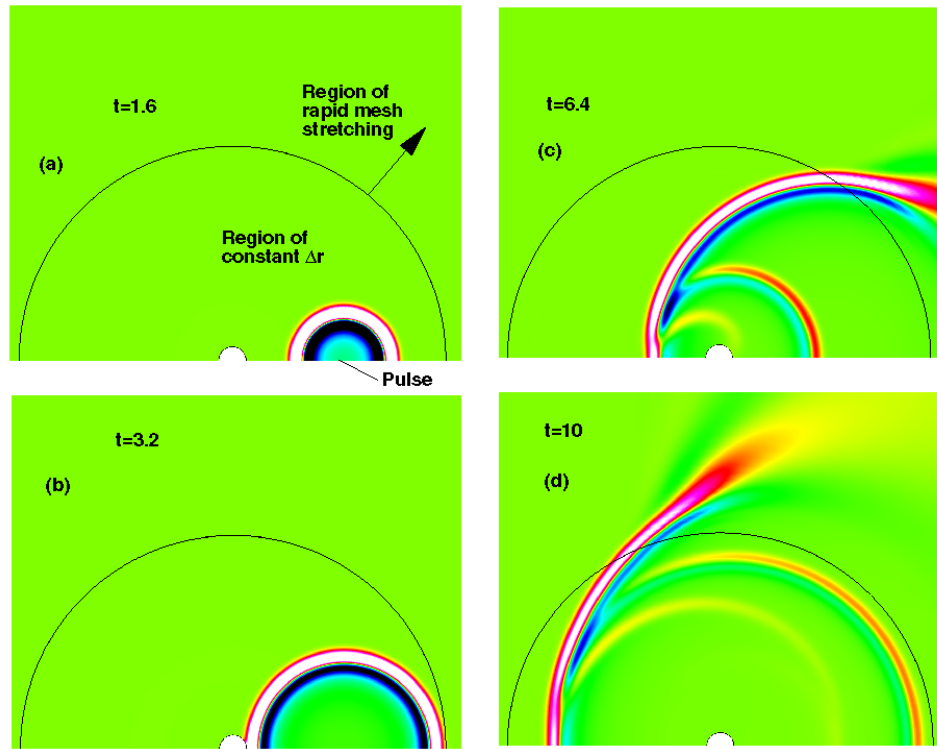
Fig. 3. Pressure contours at various instants for acoustic pulse scattered by a circular cylinder.
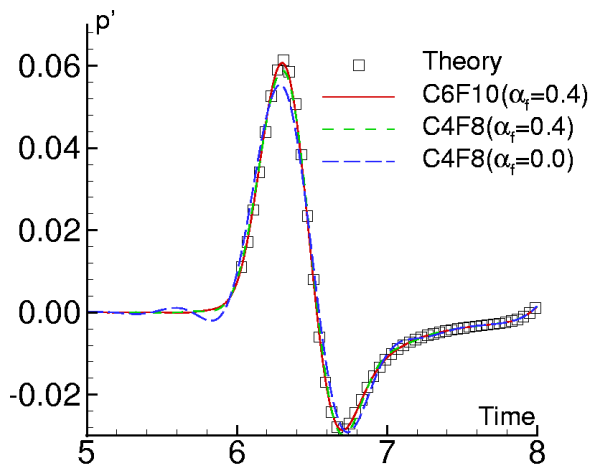
Fig. 4. Computed pressure history at select point for several spatial discretizations and the *RK4* scheme.
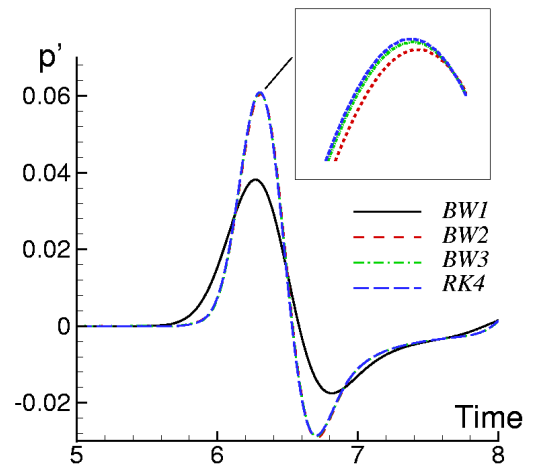
Fig. 5. Comparison of implicit and explicit time-marching schemes.
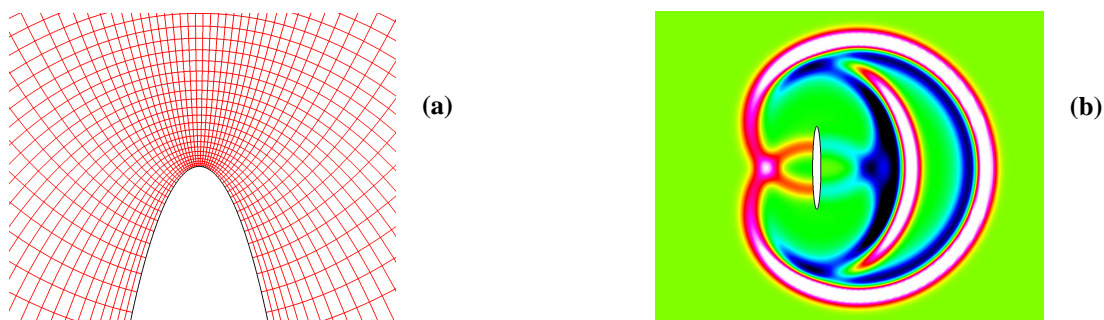
Fig. 6. Acoustic pulse scattered by elliptic cylinder. (a) Mesh , (b) Instantaneous pressure contours at *t = 1.5* for *C6F10-BW3* scheme.
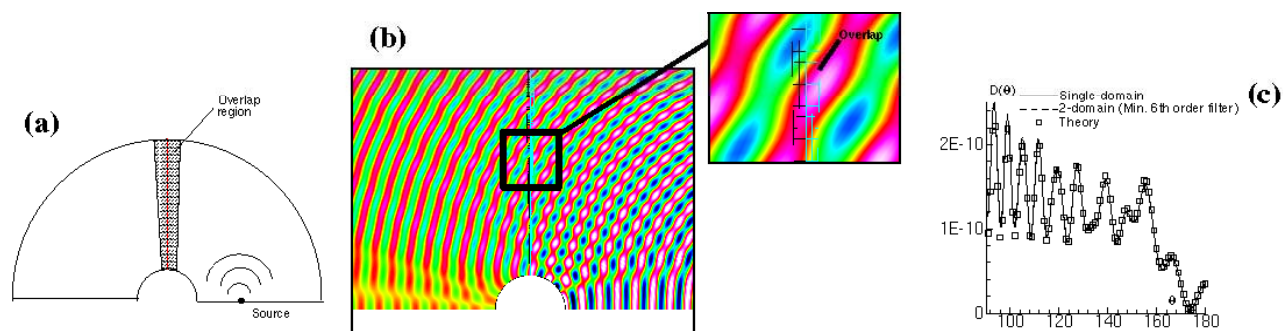
Fig. 7. Multi-domain scattering simulation. (a) Configuration, (b) pressure contours near mesh overlap, (c) Directivity at *r/D = 5*.
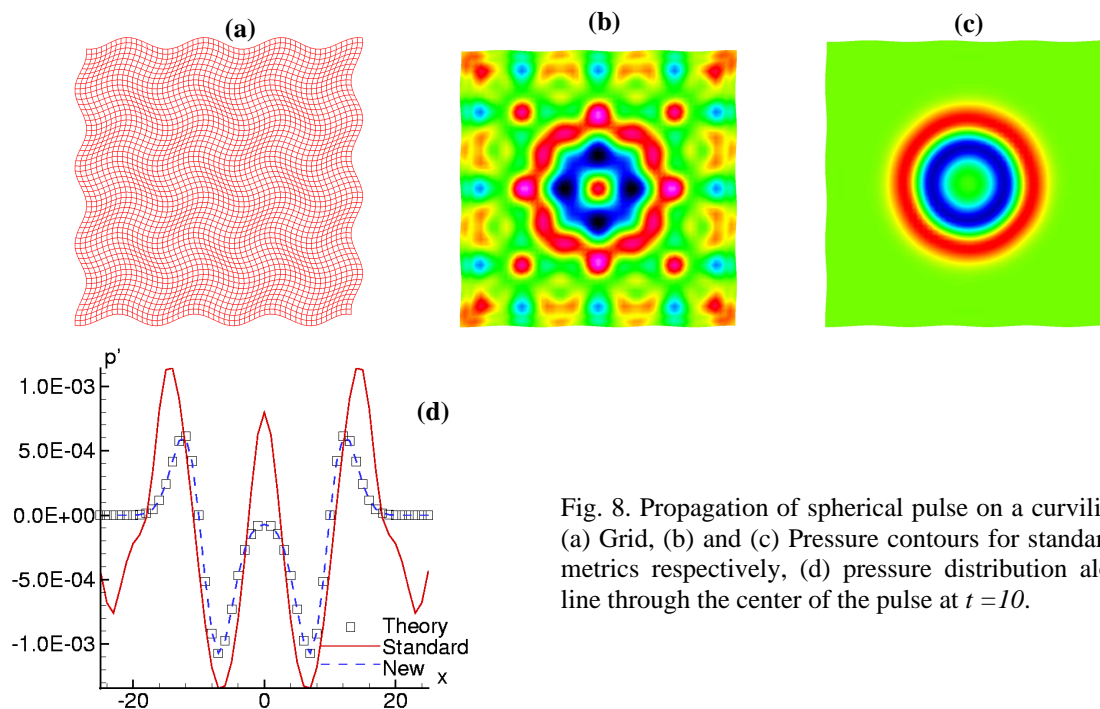
Fig. 8. Propagation of spherical pulse on a curvilinear mesh. (a) Grid, (b) and (c) Pressure contours for standard and new metrics respectively, (d) pressure distribution along a grid line through the center of the pulse at *t =10*.
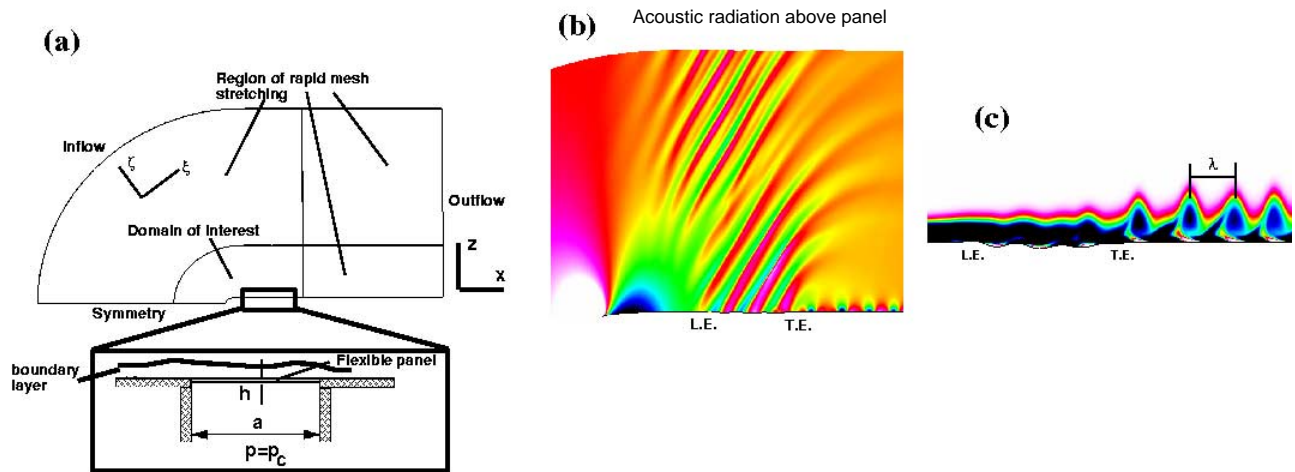
Fig. 9. Transitional boundary-layer flow over a fluttering elastic panel. (a) Configuration, (b) Instantaneous pressure, (c) Vorticity.

Numerical Analysis of Stochastic Dynamical Systems in the Medium-Frequency Range

Roger Ghanem
201 Latrobe Hall, The Johns Hopkins University, MD 21218, USA

Abhijit Sarkar
817 Sherbrooke St. W., McGill University, Montreal, Quebec, H3A 2K6 Canada

ABSTRACT

A stochastic finite element method (SFEM) has been applied to the mid-frequency vibration analysis of complex structural systems. A frequency domain model reduction strategy is devised using the energy operator approach. The dominant eigen-subspace of the energy operator adapted to a specified frequency band allows the construction of a reduced model using the Ritz-Galerkin procedure. Once an efficient reduced model is constructed, the system parameter uncertainty is performed using SFEM approach. The approach allows significant computational efficiency in performing system parameter uncertainty analysis. The SFEM approach utilized is based on an integration of the Karhunen-Loeve and the Polynomial Chaos expansions with the energy operator methodology. The approach presented avoids the combination of disparate approaches for the mid-frequency vibration analysis such as the statistical energy analysis (SEA), the traditional modal analysis (well-suited for high and low frequency vibration analysis respectively) and thus appears to provide a general framework for mid-frequency vibration analysis. The emphasis in the paper is on investigating the effect of system parameter uncertainty on the dynamical response. Firstly, a simple example involving a coupled uncertain rod system is studied to provide a better understanding of the formulation. Secondly, the examples of a capsule and a shell-plate assembly with random joint parameters are investigated using an existing FEM software.

INTRODUCTION

The traditional modal analysis technique in association with the finite element method (FEM) has been successfully applied for the linear dynamic analysis in the low frequency range. The success of the method relies on the fact that the first few structural normal modes primarily constitute the total response. In the higher frequency range, the statistical energy analysis (SEA) is a popular tool where a large number of resonant modes contributes to the total response. In this approach, the entire structural system is divided into a number of subsystems. In the state of dynamic equilibrium, the energy balance equations relate the responses in terms of total average energy for each subsystem. The parameter sensitivity of the high frequency vibration to minor deviations is accounted for by modeling the subsystem natural frequencies as Poisson random points along the frequency axis. However, the applicability of SEA is restricted only to the cases where each subsystem exhibits uniformly high modal density.

In the medium-frequency range, the situation is complicated by a number of facts: The modal superposition technique is computationally expensive as a large number of structural mode contributes to the total response, and various subsystems of the structure display high and low frequency behavior simultaneously not justifying the application of SEA.

The presence of imperfections and discontinuities significantly influences the response in the mid-frequency band due to short wavelength vibration features. Furthermore, uncertainty of the coupling parameters among the subsystems, lack of the precise model of the structure due to incomplete knowledge of the secondary systems complicate the analysis. As a result, the confidence level in the response prediction becomes questionable even with very detailed mathematical models based on nominal system parameters in the mid-frequency band.

A number of recent studies have addressed the higher frequency vibration problem including the effect of system parameter uncertainty. Manohar & Adhikari (1998) and Adhikari & Manohar (1999) formulated a frequency-domain dynamic analysis procedure for a randomly-parametered beam assembly using a frequency dependent FEM shape functions (see, Fergusson & Pilkey 1993a,b). The random system parameters modeled as independent Gaussian stochastic processes result in a set of weighted integrals as random variables in the FEM formulations. Adhikari & Manohar described numerous approaches based on the random eigen-function expansion method. Vlahopoulos & Zhao (1999) presented a hybrid procedure based on FEM and SEA for the mid-frequency range vibration analysis. They used SEA to model the subsystems having high modal density (having several wavelengths of vibration in the frequency band of interest). The subsystems exhibiting only a few wavelengths of vibration in the excitation frequency band are analyzed using FEM. Langley & Bremner (1998) recently presented perhaps a similar hybrid methodology based on dividing the total degrees of freedom into a global set and a local set. In their approach, SEA is used to solve the local degrees of freedom accounting for the effect of system parameter uncertainty. The solutions of the global degrees of freedom are sought deterministically accounting for the presence of the local degrees of freedom in terms of an approach similar to fuzzy structure theory (Ohayon & Soize 1998). Soize (1998a,b) presented an approach to construct a reduced model for linear structural systems by describing the mid-frequency structural dynamics by an energy operator. Using only the dominant eigen-subspace of the energy operator (symmetric positive definite) adapted to a fixed frequency band, the reduced model in that specific frequency band is thus constructed. The modifications of the method to consider the case of a linear structure coupled with internal acoustic cavities are also reported by Soize (1999) when the structure and the internal acoustic cavity exhibit the mid-frequency and the low-frequency behavior respectively. The proposed method appears to offer a flexible framework of analysis by avoiding the hybridization of disparate approaches such as FEM, SEA or fuzzy structure theory for mid-frequency dynamic analysis. Soize (2000) also proposed a nonparametric model of random uncertainties for the reduced system using the principle of entropy optimization. Only the knowledge of the global mean mass, stiffness and damping matrices are considered to obtain the complete probabilistic information of these matrices using the maximum entropy principle.

The present paper develops a general purpose probabilistic framework that is applicable to large scale built-up systems. A frequency-domain model reduction strategy is adopted to minimize the computational effort in the mid-frequency band. First introduced by C. Soize, an energy operator adapted to a fixed medium frequency band whose dominant eigen-subspace allows the construction of a reduced model using a Ritz-Galerkin method. Consequently, the effect of parameter uncertainties is investigated on the reduced model in the framework of SFEM. The approach, essentially based on dynamic stiffness methodology, overcomes the need of determination of the joint statistics of natural frequencies and mode shapes by avoiding the modal superposition approach. The uncertain system parameters are described by Gaussian random fields. The well-known Karhunen-Loeve expansion is used to decompose the random fields by a set of Gaussian random variables. Consequently, a typical response quantity is expanded using a generalized random series known as Polynomial Chaos expansion. The deterministic matrix equations governing the unknown coefficients of the Polynomial Chaos expansion is derived and solved. The approach is exemplified through its application to complex structural systems with parameter uncertainties.

MID-FREQUENCY STRUCTURAL DYNAMICS: DETERMINISTIC CASE

A finite element approximation of the response of a linear time invariant distributed parameter system is given by,

$$u_n(\mathbf{x}, \boldsymbol{w}) = \sum_{i=1}^{n} q_i(\boldsymbol{w}) N_i(\mathbf{x}) \tag{1}$$

with $N_i(\mathbf{x})$ being the finite element shape functions and q_i is the i-th nodal response quantity. Consequently, the governing equation of motion can be expressed as

$$\mathbf{A}_n \mathbf{q} = \mathbf{F}_n \tag{2}$$

where the dynamic stiffness matrix, $\mathbf{A}_n$ is given by

$$\mathbf{A}_n = -\omega^2 \mathbf{M}_n + i\omega \mathbf{D}_n + \mathbf{K}_n \qquad (3)$$

where $\mathbf{M}_n, \mathbf{D}_n, \mathbf{K}_n$ are the mass, damping, stiffness matrices and force vector respectively.

A brief description of the energy operator methodology for the mid-frequency vibration analysis is next presented (Soize, 1998a,b). The approach is adopted to construct a computationally efficient reduced model in the mid-frequency range. In this section, only the case of deterministic system parameters is considered. Subsequently, the extension of the procedure to consider the case of randomly parametered systems will be discussed.

ENERGY OPERATOR APPROACH

Definition of an Energy Operator

For the continuously parametered linear system under consideration, let $\mathbf{M}$ be the mass operator and the operator valued frequency response function $\mathbf{T}$ be defined as $\mathbf{A}^{-1}$. The energy operator over frequency band B, $\mathbf{E}_B$ is defined as

$$\mathbf{E}_B = \frac{1}{\pi} \int_B \omega^2 \, \text{Re}[\mathbf{T}^*(\omega)\mathbf{M}\mathbf{T}(\omega)]d\omega \qquad (4)$$

Its eigenfunctions satisfies the following equation

$$\mathbf{E}_B \mathbf{e}_i = \lambda_i \mathbf{e}_i \qquad (5)$$

The energy operator is a positive-definite symmetric operator which possesses a countable set of decreasing positive eigenvalues. Consequently, its eigenfunctions form a complete basis by which a finite element displacement field can be approximated. Thus, the dominant eigen-subspace of this operator can be effectively used to construct a reduced model using a Ritz-Galerkin method.

Finite Dimensional Approximation

As the analytical expressions of the eigenfunctions are not generally available, $\mathbf{E}_B$ is approximated as $\mathbf{E}_{B,n}$ in n-dimensional subspace with its eigenfunctions represented by $\mathbf{e}^n_i$. Thus, $\mathbf{E}_{B,n}$ the projection on the n-dimensional subspace spanned by the shape functions $N_i(\mathbf{x})$, is expressed as (Soize, 1998)

$$\mathbf{E}_{B,n} = \sum_{i,j=1}^{n} \left[E_n\right]_{ij} (.,N_j)_H N_i \qquad (6)$$

which means that for all $\mathbf{g}$,

$$\mathbf{E}_{B,n}\mathbf{g} = \sum_{i,j=1}^{n} \left[E_n\right]_{ij} (\mathbf{g},N_j)_H N_i \qquad (7)$$

with inner product operation defined over domain Ω as

$$(\mathbf{f},\mathbf{g})_H = \int_\Omega \mathbf{f}\mathbf{g}d\mathbf{x} \qquad (8)$$

where

$$E_n(\omega) = \frac{1}{\pi} \int_B \omega^2 \, \text{Re}[\mathbf{A}_n^{*-1}\mathbf{M}_n\mathbf{A}_n^{-1}]d\omega \qquad (9)$$

In an FEM framework, these eigenfunctions are approximated as,

$$\mathbf{e}_i^n = \sum_{j=1}^n P_j^i N_j \qquad (10)$$

Consequently, the standard eigenvalue problem is shown to be transformed into a generalized eigenvalue problem as given by (Soize 1998a,b)

$$GE_nG\mathbf{P} = \lambda_nG\mathbf{P} \qquad (11)$$

where

$$G_{ij} = (N_{i,}N_j)_H \qquad (12)$$

Representation of the Solution in the Mid-Frequency Range

As previously mentioned, the eigenvalues of the energy operator span the functional space in which the solution exists. Furthermore, only the first few eigenvectors of the energy operator, adapted to the frequency band B can effectively represent the solution vectors in that frequency band. Thus, the solution vector can be approximated by using the first N such eigenvectors as

$$u^N{}_n(\mathbf{x},\omega) = \sum_{i=1}^n U_i(\omega)\mathbf{e}_i^n(\mathbf{x}) \qquad (13)$$

Consequently, equation (2) reduces to

$$\mathbf{A}_N\mathbf{U} = \mathbf{F}_N \qquad (14)$$

and

$$\mathbf{F}_N = P^T\mathbf{F}_n \qquad (15)$$

The new coordinates $\mathbf{U}$ relate to the coordinates $\mathbf{q}$ as

$$\mathbf{q} = P^T\mathbf{U} \qquad (16)$$

where $[P]$ is the $(n{\times}N)$ real matrix whose columns are the N eigenvectors corresponding to the N highest eigenvalues in equation (11). The operator $\mathbf{A}_n$ reduces to $\mathbf{A}_N$ as

$$\mathbf{A}_N(\omega) = P^T\mathbf{A}_n(\omega)P \qquad (17)$$

In general, N is much smaller than the original system dimension n, thus demonstrating the efficiency of the reduced model.

MID-FREQUENCY STRUCTURAL DYNAMICS: STOCHASTIC CASE

For randomly parametered system, the energy operator becomes a random quantity leading to a random eigenvalue problem stated in equation (5). In case of such systems, the eigensolution computed in equation (11) can be viewed as a first order approximation to the mean eigenproblem of the energy operator. As the energy operator is obtained by a frequency averaging process, it should show milder fluctuations than the underlying material properties. Furthermore, only the higher order eigenvalues and eigenvectors are expected to be susceptible to the system randomness. However, we are only interested in the dominant eigen-subspace of the energy operator. The higher order eigenvalues and eigenvectors are not of interest for the purpose of the present analysis. These facts justify the approximation made for the eigenvalue analysis. However, once these eigenvectors have been calculated, the coordinates of the solution with respect to this basis can be expressed as a random quantity. In the present study, the variability of the system parameters are modeled as stochastic processes.

Mathematical Characterization of Random Processes

A stochastic process, α, is a function of $n+1$ variables with n being the physical dimension and θ identifies its probabilistic dimension. Thus, a typical system parameter modeled as random process is characterized by a set of basis functions ξ in Hilbert space H_G. Consequently, the state of the system modeled also as random process represented by a set of basis ψ in Hilbert space H_L. Identification of the basis ξ and ψ is accomplished by the Karhunen-Loeve and Polynomial Chaos expansions, which are presented next.

Karhunen-Loeve Expansion

The Karhunen-Loeve expansion of a random process α takes the following form (Ghanem & Spanos 1991)

$$\alpha(\mathbf{x},\theta) = \overline{\alpha}(\mathbf{x}) + \sum_{i=1}^{\infty} \sqrt{\lambda_i}\, \xi_i(\theta)\phi_i(\mathbf{x}) \qquad (18)$$

Here $\overline{\alpha}$ denotes the mean process and $\{\xi_i\}$ is a set of orthogonal random variable. $\{\phi_i(\mathbf{x})\}$ and $\{\lambda_i\}$ are the eigenvectors and eigenvalues of the covariance function $R_{\alpha\alpha}(\mathbf{x},\mathbf{y})$ of the random process and evaluated as the solution of the following integral equation (Ghanem & Spanos 1991)

$$\int_D R_{\alpha\alpha}(\mathbf{x},\mathbf{y})\phi_i(\mathbf{y})d\mathbf{y} = \lambda_i\phi_i(\mathbf{x}) \qquad (19)$$

where D defines the spatial dimension over which the process α is defined. If the random process α is Gaussian, then $\{\xi_i\}$ form an orthonormal Gaussian vector. The Karhunen-Loeve expansion is mean-square convergent irrespective of the probabilistic structure of the stochastic process provided it has finite variance.

Polynomial Chaos Expansion

As the covariance function of a solution process is not known *a-priori*, the Karhunen-Loeve expansion cannot be used to expand the solution quantity $S(\theta)$. Consequently, a typical solution quantity $S(\theta)$ is expressed by the Polynomial Chaos expansion (Ghanem & Spanos 1991)

$$S(\theta) = \sum_{j=0}^{\infty} S_j \Psi_j(\theta) \qquad (20)$$

where $\Psi_j(\theta)$ are the multidimensional Hermite polynomials of $\{\xi_i\}$, known as the Polynomial Chaos which form a complete basis in the space of second order random variables. Thus, the complete probabilistic description of the solution process $S(\theta)$ is obtained once the deterministic coefficients S_j are calculated. In

addition to the representation of the solution process, the Polynomial Chaos expansion can also be used to characterize non-Gaussian material properties.

Representation of the Stochastic System Equation

Expanding $\mathbf{A}_N$ in its Karhunen-Loeve expansion (obtained from the stiffness, mass and damping matrices, see Ghanem & Spanos 1991), the following expressions for the equilibrium equation is obtained,

$$[\sum_{k=0}^{nkl} \xi_k \mathbf{A}_N^k] \hat{\mathbf{U}} = \mathbf{F}_N \qquad (21)$$

where

$$\mathbf{A}_N^k = P^T \mathbf{A}_n^k(\omega) P \qquad (22)$$

Here *nkl* represents the number of terms retained in the Karhunen-Loeve expansions; ξ_i are the random variables obtained from the Karhunen-Loeve expansion, and are Gaussian whenever the material properties are modeled as Gaussian processes. Consequently, the solution process is approximated by the Polynomial Chaos expansion as

$$\hat{\mathbf{U}} = \sum_{j=0}^{npc} \Psi_j(\theta) \hat{U}_j(\theta) \qquad (23)$$

Here *npc* is the number of terms retained in the Polynomial Chaos expansions. Substituting the above expansion into the reduced model equation and performing a Galerkin error minimization procedure leads to,

$$\sum_{i=0}^{npc} \sum_{j=0}^{npc} < \xi_i \Psi_j \Psi_k > \mathbf{A}_N^i \hat{U}_j = < \Psi_k \mathbf{F}_N > \qquad (24)$$

where the deterministic coefficients U_j are computed as the solution of the aforementioned matrix equation. It is worthwhile to mention at this point that the frequency response curve for a fixed value of frequency is a random variable when the system parameters are modeled as random fields. Furthermore, it becomes a complex valued random process in its frequency evolution due to presence of damping. The presence of discrete natural frequencies induces strong non-stationary characteristics of the frequency response functions with the standard deviation peaking up significantly near the resonance points even with small random deviations of system parameters. This may potentially affect the extremes of the frequency response curves and thus the dynamic response.

NUMERICAL RESULTS

As an example of the foregoing analysis, firstly the dynamical response of a coupled rod system is investigated. The equation of motion of the rods is described by,

$$\frac{\partial}{\partial x}[EA(x)\frac{\partial u}{\partial x} + C_1(x)\frac{\partial^2 u}{\partial t \partial x}] = m(x)\frac{\partial^2 u}{\partial t^2} + C_2(x)\frac{\partial u}{\partial t} \qquad (25)$$

with appropriate initial and boundary conditions. Here *EA*, *m*, C_1 and C_2 are the stiffness, mass, strain-rate dependent and velocity dependent damping per unit length of a typical rod. The choice of this simple system is intended to provide a better understanding of the system behavior from the viewpoint of the energy operator approach. The schematic diagram of the system is shown in Figure 1. The free end of the bar B is excited externally. In this study, Young's moduli of the rods are assumed to be identical independent Gaussian random fields with a coefficient of variation equal to 0.05. The autocovariance function of each of the processes is taken to be of the following form: $R(x,y)=\exp^{-|x-y|/b}$; where *b* is the correlation length, assumed to be half of the

length of each rod. Only two terms in the Karhunen-Loeve expansion are used corresponding to the first Karhunen-Loeve mode for each rod. In the Polynomial Chaos expansion, the first six terms corresponding to a complete second order expansion, are considered. In the numerical investigation, the following parameters are assumed: for rod A, the mean $EA_A = 405284.0$ N; m_A=200.0 kg; $C_{1A} = 30.0$ Ns and C_{2A} =30.0 Ns/m^2, L_A = 100 m; for rod B, the mean $EA_B = EA_A /20$; $m_{B=} m_A$; $C_{1B} = C_{1A}/20$, $C_{2B} = C_{2A}/20$ and L_A = 100 m. The number of the finite elements is taken to be 350 for each rod. Figure 2(a) shows the eigenvalue spectrum of the energy operator for the frequency band 13-15 rad/s. Figure 2(b) presents the first few eigenvectors of the energy operator. Note that the eigenvectors fluctuate more rapidly in rod B than in rod A, identifying relatively higher frequency vibrations in rod B. Figure 2(c) presents the frequency response function at the free end of the rod. Only the eigenvectors corresponding to the first ten eigenvalues of the energy operator are used to construct the reduced model. In Figure 2 (c), the top and bottom solid lines represent the mean and standard deviation of the frequency response curve. The results of the direct Monte Carlo simulations with 100 realizations performed on the full-scale system is represented by point plots. The results from the Polynomial Chaos expansion performed on the reduced model are in very good agreement with the Monte Carlo simulations. Interestingly, only 10 degrees-of-freedom system can now effectively captures the original system behavior produced by a 700 degrees-of-freedom model.

Next, we consider the example of a capsule which includes two joints. The FEM mesh of the structure is shown in Figure 3. The total number of elements in the system is 128 with each joint having 16 elements. The cylindrical section of the capsule has a length of 60 m with radius of 7 m. The capsule and the joints are modeled as thin shell elements having six degrees-of-freedom in each node. The total number of degree-of-freedom of the system is 780. The effect of joint stiffness uncertainties on the frequency response function of the structure is investigated. The following properties of the shell elements are considered: Young's modulus E = 2×10^{11} N/m^2, Poisson ratio $\nu = 0.3$, density $\rho = 7500$ kg/m^2, shell thickness $t = 0.05$ m. In all cases, a proportional damping model for the global matrix is adopted as: $D_n = \alpha M_n + \beta K_n$. Young's moduli of both the joints are modeled as independent Gaussian random fields with exponential correlation function as: $R(x_1,x_2; y_1, y_2)$=exp$^{-|x_1 - x_2|/b_1 --|y_1 - y_2|/b_2}$ where b_1 and b_2 are the correlation lengths of the two dimensional random fields with coefficient of variation equal to .05. For both the joints, the correlation length in both circumferential and longitudinal directions are taken to be 20 m. The integral eigenvalue problem resulting from the Karhunen-Loeve expansion was solved using a standard eigen-analysis software package. Only two terms in the Karhunen-Loeve expansion and first six term Polynomial Chaos expansion are considered. The damping coefficients are arbitrarily taken as: α=10^{-2} Ns/Kg-m and β= 10^{-5} s. Figures 4(a) shows the dominant eigen-subspace of the energy operator in the frequency band (260-330) rad/s. Figure 4(b) shows the direct frequency response function (along the outer normal direction) of the node on the junction of the cylinder and the hemispherical cap (referred to as Case A) as highlighted in Figure 3. In Figure 4(b), the top and bottom solid lines represent the mean and standard deviation of the frequency response curve obtained using SFEM performed on the reduced model. The results generated from the direct Monte Carlo simulations (with 100 realizations) performed on the full-scale system is represented by point plots. Again it should be noted that uncertainty analysis performed on the 10 degree-of-freedom system (being the dominant eigen-subspace) using SFEM shows excellent agreement with Monte Carlo simulations. The similar results for a node on the top joint, referred to as Case B (highlighted on Figure 3) is presented in Figures 4(c) and 4(d) for the frequency band (910-970) rad/s. From Figure 4(c), the dominant eigenspace of the energy operator is characterized by first 15 eigenvectors. In Figure 4(d), the top and bottom solid lines show the mean and standard deviation of the frequency response function generated using SFEM. The point plots represent the direct Monte Carlo simulation results for 100 realizations for the full-scale system. Note that the reduced model SFEM results show very good agreement with the Monte Carlo simulations.

Finally, the example of a shell-plate assembly with random connection properties at the junctions between the shell and plate is considered. Figure 5 shows the FEM mesh of the system. The total number of elements is 114 with each connection having 12 elements. The total assembly is modeled with thin shell elements having six-degrees of freedom for each node. The total number of degrees of freedom is 756. The cylindrical section has an outer radius of 2.4 m and a length of 10 m. Both the shell and plate are assumed to have a thickness of 0.05m. The system is assumed to have $E = 2\times10^{11}$ N/m^2, Poisson ratio $\nu = 0.3$, density $\rho = 7500$ kg/m^2. The same proportional damping models as in the case of the capsule is considered. The uncertainty in the connections is modeled assuming a stochastic variation of Young's modulus as in the case of the previous example involving the capsule. Again, only two terms in the Karhunen-Loeve expansion and the first six terms

in the Polynomial Chaos expansion are considered for the SFEM analysis. In Figure 6(a), the dominant eigen-space of the energy operator for the frequency band (553-559) rad/s is shown for the case of damping coefficients: $\alpha=10^{-3}$ Ns/Kg-m and $\beta= 7\times10^{-7}$ s and a coefficients of variation of Young's modulus equal to 0.05. A typical frequency response function (for the response along the normal direction) for the node marked in Figure 5 is presented in Figure 6(b). Similar results are shown in Figure 6(c) and 6(d) for the case with $\alpha=2\times10^{-3}$ Ns/Kg-m and $\beta= 10^{-5}$ s and coefficients of variation of Young's modulus equal to 0.02. From both Figures 6(a) and 6(c), it is evident that the reduced model can be constructed using only the first 5 eigenvectors of the energy operator for the specified frequency band. In Figures 6(b) and 6(d), the top and bottom solid lines present the mean and standard deviation of the frequency response curve using SFEM. The results of Monte Carlo simulations performed on the full-scale system with 100 realizations are represented by point plots. Evidently, the Monte Carlo simulations show excellent agreement with the SFEM results.

CONCLUDING REMARKS

The paper integrates a SFEM approach based on the Karhunen-Loeve and the Polynomial Chaos expansions with an energy operator-based formalism for the mid-frequency vibration analysis of complex structural systems with parameter uncertainty. The uncertainties of the system parameters are modeled as Gaussian random fields. The well-known Karhunen-Loeve expansion is used to decompose the Gaussian random fields into a set of Gaussian random variables. Consequently, typical response quantities are expanded as Polynomial Chaos expansions. The use of the reduced model remarkably enhances the computational efficiency of the SFEM. The formulation presented has been implemented using existing finite element software. Thus, the approach is particularly useful for the mid-frequency vibration analysis of large scale structural systems in order to investigate the effect of parameter uncertainty on their responses.

REFERENCES

Adhikari, S. & Manohar C. S. 1999. Dynamic Analysis of Framed Structures with statistical uncertainties. *Int. J. Numerical Methods in Engineering*. 44: 1157-1178.

Fergusson, N. J. & Pilkey W. D. 1993a. Literature review of variants of dynamic stiffness method, Part 1: The dynamic element method. *The Shock and Vibration Digest*. 25 (2): 3-12.

Fergusson, N. J. & Pilkey W. D. 1993b. Literature review of variants of dynamic stiffness method, Part 2: Frequency dependent matrix and other corrective methods. *The Shock and Vibration Digest*. 25 (4): 3-10.

Ghanem, R. & Sarkar, A. 2000. The Medium-Frequency Range Vibration of Coupled Fluid-Structure Assembly with System Uncertainty, *The 14th ASCE Specialty Conference on Engineering Mechanics,* The University of Texas, Austin, May 22-24.

Ghanem, R. & Spanos, P. 1991. *Stochastic Finite Elements: A Spectral Approach*. Springer Verlag.

Langley, R. S. & Bremner P. 1998. A hybrid method for the vibration analysis of complex structural-acoustic systems. *Journal of the Acoustical Society of America*.105(3): 1657-1671.

Manohar, C. S. & Adhikari S. 1998. Dynamic stiffness of randomly parametered beams. *Probabilistic Engineering Mechanics*. 13 (1): 39-49.

Ohayon, R. & Soize C. 1998. *Structural Acoustics and Vibration*. Academic: San Diego.

Soize, C. 1998a. Reduced models in the medium frequency range for general dissipative structural-dynamics systems. *European Journal of Mechanics: A-Solids*. 17(4): 657-685.

Soize C. 1998b. Reduced models in the medium-frequency range for general external structural-acoustic systems. *Journal of the Acoustical Society of America*. 103 (6): 3393-3406.

Soize C. 1999. Reduced models for structures in the medium-frequency range coupled with internal acoustic cavities. *Journal of the Acoustical Society of America*. 106 (6): 3362-3374.

Soize C. 2000. A nonparametric model of random uncertainties for reduced matrix models in structural dynamics. *Probabilistic Engineering Mechanics*. 15: 277-294.

Vlahopoulos, N. & Zhao, X. 1999. Basic development of hybrid finite element method for midfrequency structural vibrations, *AIAA Journal.* 37 (11): 1495-1505.
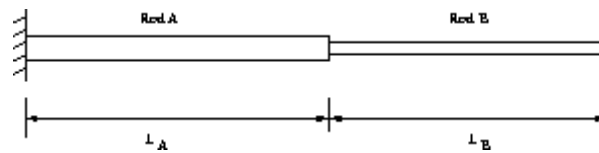
Figure 1. Schematic diagram for the coupled rod system.
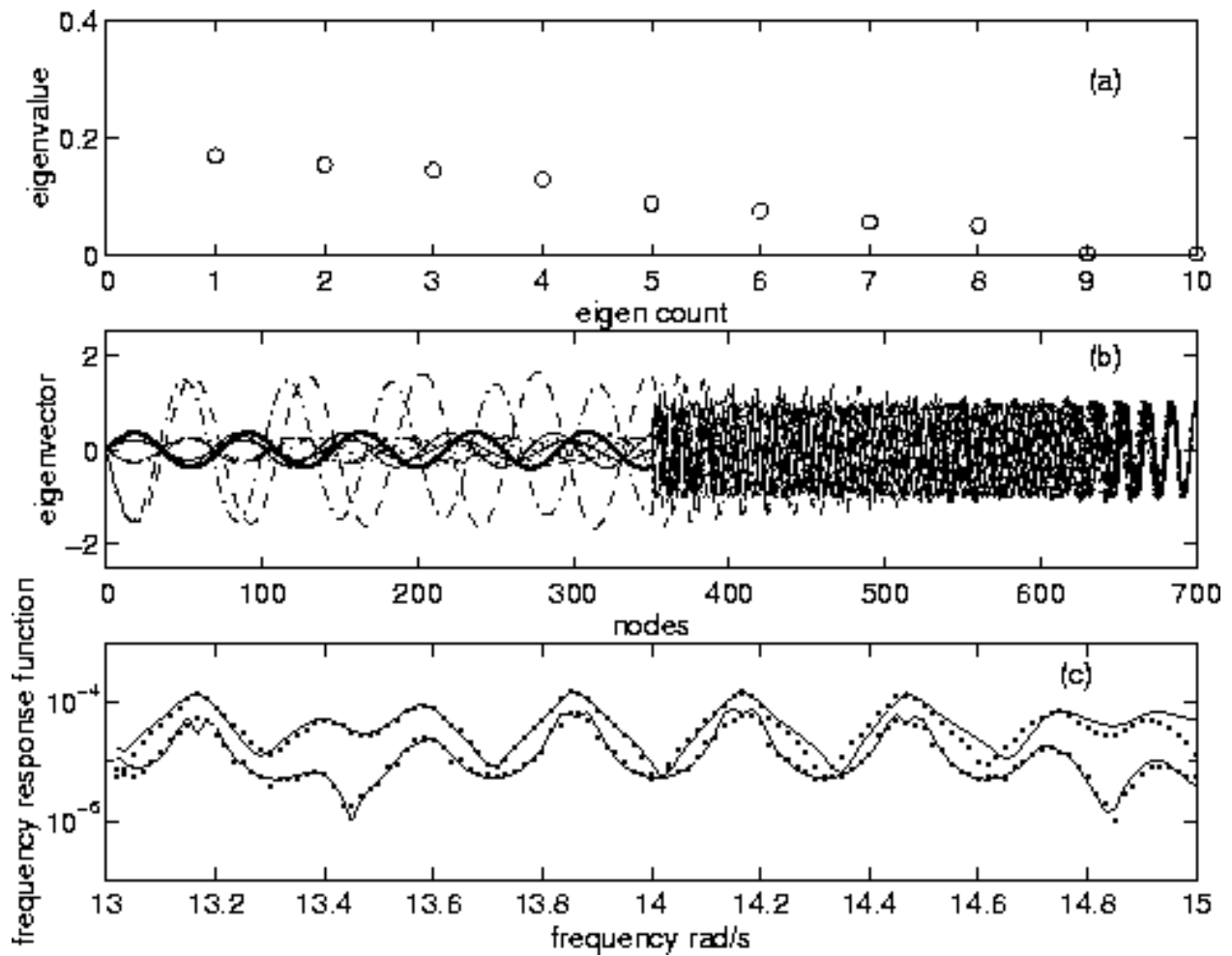
Figure 2. For the rod system: (a) The distribution of eigenvalues of the energy operator, (b) First few eigenvectors of the energy operator, (c) The frequency response function of the system at the free end.
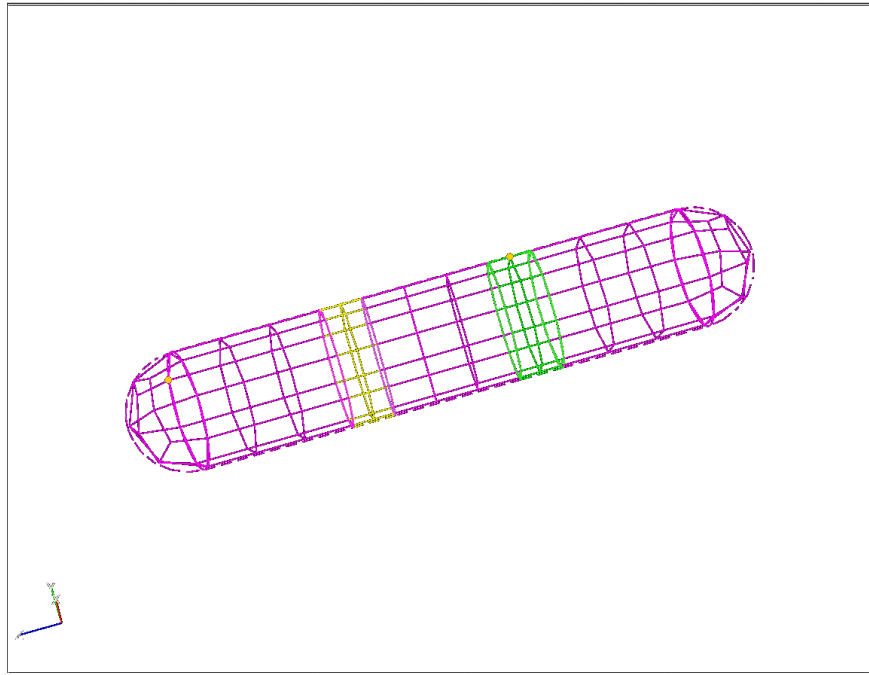
Figure 3. Finite element mesh for a capsule.
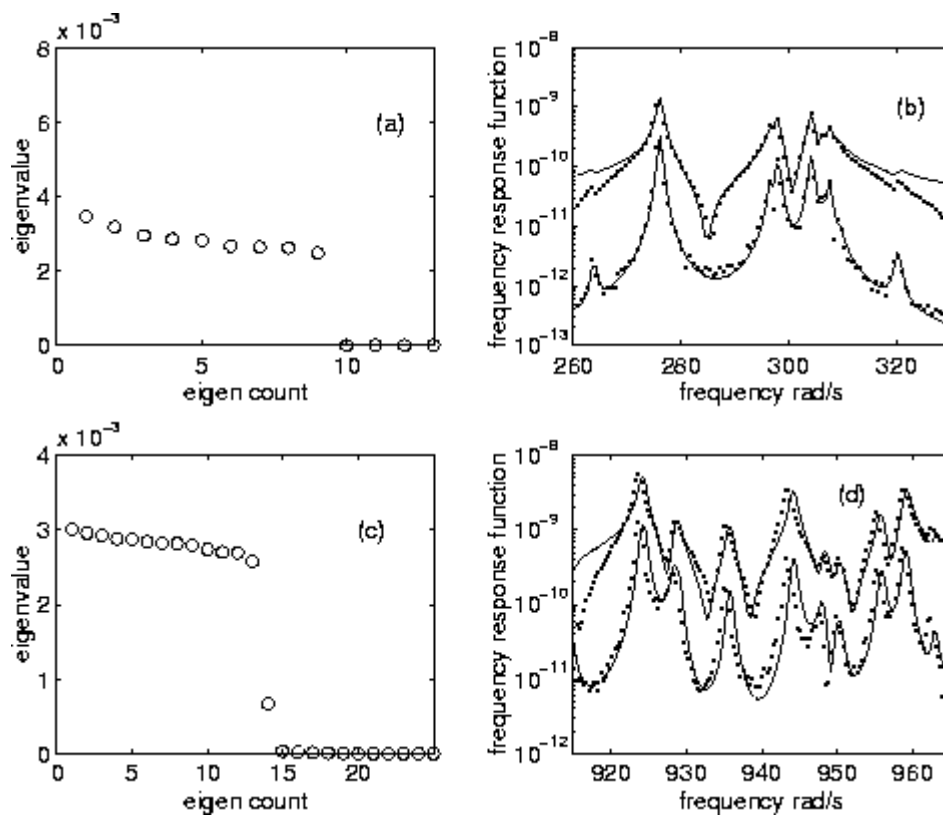
Figure 4. For the capsule: (a) The distribution of eigenvalues of energy operator in the frequency band (260-330) rad/s, (b) The frequency response function for Case A, (c) The distribution of eigenvalues of energy operator in the frequency band (910-970) rad/s, (d) The frequency response function for Case B.
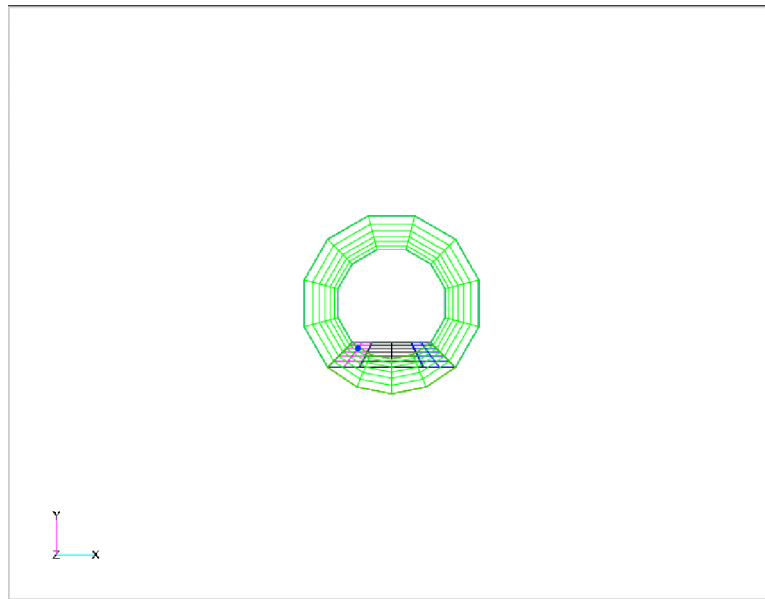
Figure 5. Finite element mesh for a shell-plate assembly.
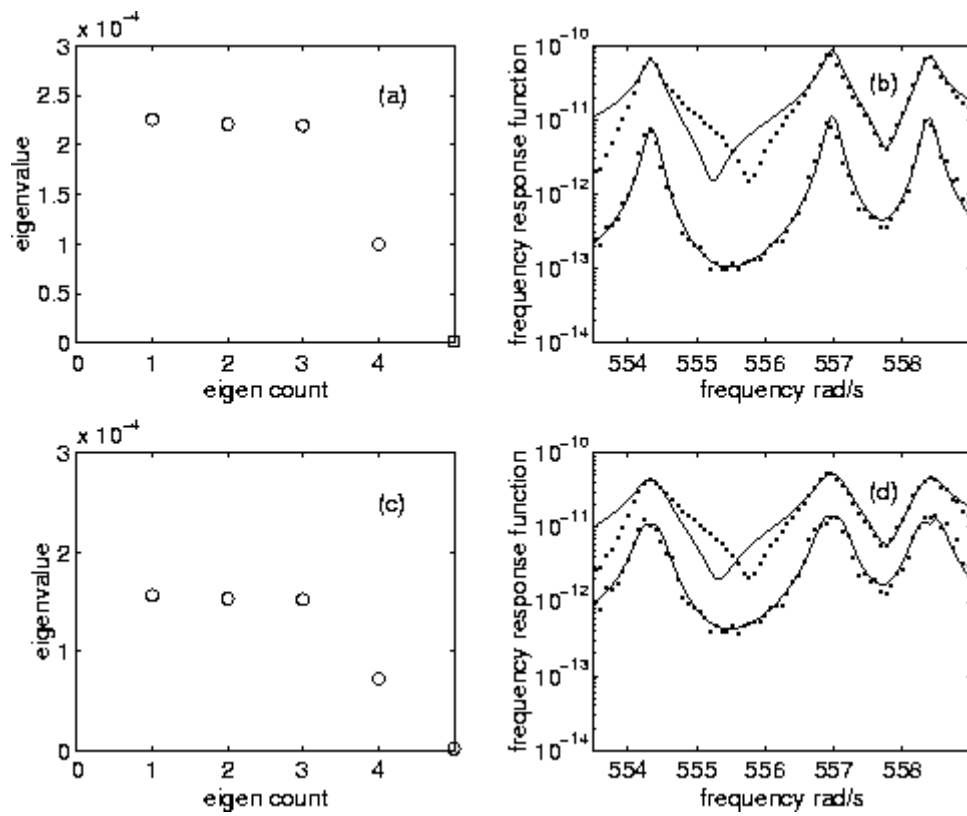
Figure 6. For the shell plate assembly: (a) The distribution of eigenvalues of energy operator for Case A, (b) The frequency response function for Case A, (c) The distribution of eigenvalues of energy operator for Case B, (d) The frequency response function for Case B.

This page has been deliberately left blank

_____

Page intentionnellement blanche

High Frequency Acoustic Suppression – Experimental & Computational Overview

Michael J. Stanek
Air Force Research Laboratory
AFRL/VAAI Bldg 45
2130 8th Street, Suite 1
Wright-Patterson AFB, OH 45433-7541, USA
Michael.Stanek@wpafb.af.mil

John A. Ross and Ian Wrisdale
Defence Evaluation and Research Agency
Bedford, MK41 6AE
United Kingdom
Jaross@dera.gov.uk

I. Abstract

The recent history of the relatively new field of high frequency acoustic suppression is outlined. Key experiments, actuator developments, and obvious applications are described. Differences between low frequency forcing and high frequency forcing are outlined, and definitions for the two regimes are offered. Preliminary first steps toward numerical simulation of the high frequency acoustic suppression are critiqued and compared to existing experimental evidence. Future research directions are briefly described.

II. Introduction

In fighter / bomber weapons bays, experience has shown that an open cavity at moderately high speeds can have a profound effect on internally carried weapons, their suspension equipment, separation characteristics, and the structural loads on the parent aircraft. Acoustic resonance causes high amplitude fluctuating acoustic loads in and near the bay, high enough to very quickly fatigue metal parts, and to damage sensitive electronics on "smart" weapons.

Vertical Take Off & Landing (VTOL), or Short Take Off, Vertical Landing (STOVL) systems (such as Harrier, or the new Marine variant Joint Strike Fighter (JSF)) suffer from a very similar sort of resonant acoustic situation as the weapons bay. Acoustic levels due to jet exhaust impingement resonance in the region between the ground plane and underside of the aircraft (during vertical takeoff or landing) are also (as in the weapons bay) potentially large enough to cause structural damage. For most of the discussions in this paper we will focus on the high–speed cavity resonance problem, because this serves well as a canonical resonance problem, and because the bulk of the exploration into high frequency acoustic suppression has been in this application.

Active flow control has been touted as a means to efficient suppression of resonant acoustic behavior in these various aerospace systems. Interest in active control methods centers around the promise of adjustable, optimal suppression for changing flight conditions. Acoustic suppression utilizing active flow control is traditionally achieved by seeding the unstable free shear layer traversing the cavity (weapons bay) with small amplitude disturbances (vortical, acoustic or otherwise). These "planted" disturbances grow and in successful cases, compete with and overwhelm the more dangerous naturally occurring disturbances (the ones which lead to acoustic resonance).

Most documented attempts in the literature to apply active flow control to high speed cavities have focussed on perturbing the shear layer traversing the bay at frequencies near the dominant Rossiter modes. We will refer to that type of forcing as "low frequency" forcing. We will offer a more formal definition of both low frequency and high frequency later in the discussion. These "low frequency" (LF) active flow control attempts have met with some moderate success, but in most cases there are still significant, energetic tones remaining in the acoustic spectra (after active suppression) which could be further reduced. References 1 through 7 display representative examples of this type of LF active cavity flow control. Overall suppression (reduction of the peak sound pressure level (SPL) across all frequencies) using these low frequency techniques are typically on the order of 5 to 10 dB reduction.

One must keep in mind that this is the same level of performance that might be expected from no-moving-parts, zero complexity, passive leading edge spoilers (which these new active flow control techniques are in competition with) found on today's strike aircraft with weapons bays. All of this changed in 1997, when the first attempt was made to explore active flow control in cavities at frequencies orders of magnitude higher than the dominant Rossiter modes.

III. Groundbreaking Early Work

For the purposes of this discussion, we will define ACTIVE suppression as any technique which attempts to control the cavity shear layer by inputting a time-dependent disturbance of KNOWN frequency. The first tangible example of an active suppression technique capable of **simultaneously** suppressing multiple acoustic modes (not due to excessive leading edge mass injection) was published by McGrath and Shaw in 1997 [Ref. 2]. Figure 1 from Ref. 2 shows an acoustic spectra from a Mach .6 cavity case with no suppression invoked. Figure 2 shows the same case with one type of high frequency suppression device in use (a rod in crossflow). The technique yielded dramatic results, suppressing all tones simultaneously, and giving a tone reduction across all frequencies of over 30 dB! The same cavity was tested at Mach .8, and the results were very good, if not quite as dramatic. There was no hint or suggestion in this early work that there was any fundamental difference between low frequency and high frequency flow control. Unfortunately, research resources were shifted into so-called "low frequency" suppression techniques when McGrath and Shaw found that their particular rod in crossflow device failed to produce suppression of any significance above Mach 1. See experimental data marked "Shaw 94" and "Shaw 95" in Figures 3 and 4 (Ref. 8).

Meanwhile, in non-cavity related high frequency work, Wiltse and Glezer [Ref. 9] were focussed on attempting to show that very small scales within a shear layer could be directly excited, instead of relying on the so-called "energy cascade" to move excitation energy from "large scale / low frequency " forcing to the small scales. They cited the work of Yeung et. al. [Ref. 10] as a source of insight in this respect. Wiltse and Glezer perturbed a small-scale rectangular subsonic jet shear layer with an aluminum wedge excited by a piezoceramic material, shown in Figure 5. Figure 6 shows a velocity spectra taken from that experiment. Two observations of note in that experiment were the fact that forcing at very high frequency affected ALL frequencies within the spectra, and the fact that below a certain transition frequency, energy was being taken OUT of the low frequency portion of the spectra due to this high frequency forcing (See Figure 6).

Cain [Ref. 12] describes the results of the Wiltse and Glezer's experiment as "startling", because they convincingly demonstrated a flow control concept which was completely foreign to the established fluid dynamics technical community. The status quo opinion of how free shear flows CAN be controlled was until now represented by the 1984 review article of Ho and Huerre [Ref 13]. Ho and Huerre [Ref. 13] characterizes the perspectives of the 1070's and 1980's, demonstrating the link between large-scale structures and linear stability theory [Ref 12]. In essence, the Wiltse and Glezer experiment was "startling" because it seemed to violate the time-honored principles established by the Ho and Huerre review.

In 1997, Alan Cain [Ref. 14] first proposed the notion that very high frequency active forcing (within several orders of magnitude of the so-called Kolmogorov frequency) of the shear layer spanning the weapons bay could be very effective at suppressing resonant cavity tones, citing the earlier work of Wiltse and Glezer [Ref. 9] in free shear layers. Cain suggested that the likely cause of the suppression in the earlier McGrath and Shaw [Ref. 2] rod-in-crossflow experiments was the same high frequency mechanism studied in detail and described by Wiltse and Glezer.

Based upon Alan Cain's recommendation, and under sponsorship from Air Force Research Laboratory (AFRL), Boeing took steps toward applying HF forcing to the high-speed cavity problem. The first step was to use the same actuator as in the Wiltse & Glezer experiment (Figure 5) and to modify the original free-jet experiment by creating resonance (i.e. to "simulate" a cavity flow). This was accomplished by inserting a scattering "wedge" downstream of the jet exit in order to set up edge tones [Ref. 15].

Figure 7 shows two views of the Boeing rectangular nozzle, with the wedge actuators mounted to supply forcing near the nozzle lip. Figure 8 shows schlieren images of the experiment from the side, with the nozzle exit and scattering wedge visible. This figure also shows the tip of the wedge actuator just touching the edge of the jet shear layer. The left inset figure shows jet flow without excitation- the right inset shows it with excitation. Figure 9 shows the clearly evident edgetones in the unsuppressed spectra, and the resulting suppression with HF excitation. The forcing frequency (near 5 khz) is clearly visible in the spectra. Even though the forcing in this experiment is not at a very "high" frequency, relative to the naturally occurring edge tones, the results were encouraging. They at least showed the prospect for simultaneously reducing all the resonant tones by forcing at a single high frequency. Boeing also demonstrated in this experiment that forcing at a high relative frequency affected ALL frequencies below it (the same result which Wiltse and Glezer [Ref 9] showed for a non-resonant free shear flow several years earlier – see Figure 6).

The decision was made, based upon these encouraging results, to take several so-called high frequency devices into a 1/10th scale cavity facility at DERA in Bedford, under a joint U.S. / U.K. cavity flow control testing program.

IV. 1st Supersonic High Frequency Acoustic Suppression

Stanek et. al. [Ref. 11] were the first to present a comprehensive evaluation of several high frequency devices, demonstrating the thesis of Cain, i.e. that the mechanism described in Wiltse and Glezer [Ref. 9] could indeed be used as a very effective cavity

acoustic suppression technique. This was accomplished by testing several "high frequency" devices, and then examining their performance for hints of behavior similar to that seen in Wiltse and Glezer's experiment. In Ref. 11, Stanek et. al. argued that high frequency acoustic suppression is based upon a fundamentally different physical mechanism than low frequency acoustic suppression, and that it is this physically based difference that allows for radically higher rates of acoustic suppression.

Ref. 11 is perhaps most important, because it presented the first example of successful use of HF acoustic suppression at realistic SUPERSONIC conditions. The primary driver for research into active flow control techniques in weapons bays is the inability of passive leading edge spoilers to provide reliable acoustic suppression above Mach 1. Ref 11 was significant, because it provided practical impetus for a host of new experimental and computational work, aimed at understanding the high frequency forcing effect in shear layers. Figures 3 and 4 [Ref. 8] show the superior supersonic performance of the "rod" devices described in Ref 11 (rod in crossflow, labeled "DERA 99") relative to other historical rod-in-crossflow data.

 Reference 11 describes the four devices designed to generate high frequency pulses (relative to the dominant Rossiter cavity modes) which were tested at various Mach numbers in a 1/10th scale DERA cavity model. Effective HF devices consistently outperformed a typical "effective" LF device (spoiler), usually producing suppression on the order of 10 to 15 dB in excess of their traditional non-HF counterpart.

Effective HF devices all produced similar effects on the Rossiter tones (**simultaneous** reduction) and produced profound changes to broadband levels and slopes consistent with the early benchmark HF free shear layer experiments of Wiltse and Glezer [Ref. 9].

The high frequency devices tested in the DERA cavity model were; a powered resonance tube, an unpowered resonance tube, a piezoceramic-driven vibrating wedge, and a rod in cross-flow. We will start by showing the cast of devices, and follow this with some representative results from the best performing devices, the powered resonance tube, and the rod in cross-flow.

Figure 5 shows a close-up of the by now familiar piezo-ceramic driven wedge actuator (used in the original Wiltse and Glezer [Ref. 9] experiment) – this was the first of the four devices. Figure 10 shows a view of the second device tested, a rod-in-cross-flow, as it appeared installed in the DERA 1/10th scale cavity model. Figure 11 shows a schematic of the third device, a powered version of a resonance tube. Figure 12 shows a bank of powered resonance tubes as they were installed in the DERA cavity model. A fourth device, a passive resonance tube concept (not shown) was also included in the DERA / AFRL test matrix. Interested readers are referred to Refs. 16-18 for descriptions of the resonance tube concept, and are referred to Ref. 15 for a detailed description of the development of the resonance tube "packages" used in the DERA/ AFRL experiments.

The highest suppression levels in these tests were delivered by the powered resonance tube device. It delivered suppression across all frequencies of roughly 26 dB at Mach .85, and about 29 dB at Mach 1.19. See Figures 13 and 14 (curves labeled ".411 lbm/sec").

The performance of the rod-in-crossflow was also very impressive. It produced suppression across all frequencies of roughly 14 dB at Mach .85, and roughly 21 dB at Mach 1.19. See Figures 13 and 14 (curves labeled "rod in xflow").

The unpowered resonance tube and powered piezo-wedge proved to be essentially ineffective for acoustic suppression in these particular tests.

Interested readers are referred to Refs. 11 and 19 for details concerning the DERA wind tunnel setup, the cavity model, data acquisition, or data reduction.

Having described highlights of the performance of these new high frequency devices, we will now examine the behavior of these devices more closely, and contrast their performance with more conventional types of flow control.

V.   Useful Suppression Categories

For the purpose of contrasting the different physical mechanisms responsible for cavity acoustic suppression, we find it convenient to define three categories of suppression; low frequency, high frequency, and zero frequency. It is also convenient to define two different classes of flow control; active and passive.

We define ACTIVE flow control (or active acoustic suppression) as any technique which produces its manipulation of the flowfield mainly through the introduction of time-dependent perturbations of a known frequency. Conversely, we define PASSIVE flow control (or in this case passive acoustic suppression) as any technique which derives the majority of its effect by manipulating gross, time-averaged (i.e. steady) quantities, without purposely inputting a perturbation of known frequency (recognizing, of course, that every flow control technique produces some unsteadiness – i.e. all real flows present or display varying degrees of unsteadiness).

Steady leading edge blowing, leading edge spoilers, and cavity rear wall sloping, are all good examples of zero frequency suppression techniques. They appear to derive MOST of their effect by decreasing the impact of vortex impingement on the rear wall of the cavity (Spoilers also seem to derive some of their suppression behavior from shed vorticity, which shows up as a

redistribution of energy among modes, and a shift in mode frequency). Low and high frequency suppression will be defined in subsequent sections.

VI.   Representative Low Frequency Suppression Results

Analysts interested in the stability of a particular fluid state usually develop stability "maps" which outline the range of frequencies (at a particular Reynolds number, and for a particular mode of instability) over which disturbances are amplified. Stability analysis also yields growth rates as a function of instability frequency. The frequency of maximal instability growth rate is frequently coined the most "dangerous" frequency. Low frequency (LF) shear layer excitation (and consequently low frequency acoustic suppression) methods work by exciting a shear layer in the frequency range of its most "dangerous" instability mode. This corresponds to the "classic" view of shear layer flow control described in Ho and Huerre [Ref. 13]. The Rossiter modes in the self-sustained cavity resonance problem fall in this range of most "dangerous" shear layer excitation frequencies.

The acoustic source for the cavity resonance problem (which "forces" the shear layer at the cavity front wall) is the impingement of coherent vortical structures on the cavity back wall. If you eliminate coherent vortical structures, you eliminate the source of the forcing, and the cavity resonance disappears. One of the problems with low frequency forcing of the cavity shear layer (for acoustic suppression) is that YOU ARE STILL FORCING IN THE RANGE OF MOST AMPLIFIED DISTURBANCES. You may reduce acoustic levels by making the production of coherent structures less efficient (by detuning the cavity), but YOUR forcing frequency is still being amplified, still generating large scale coherent structures, and STILL impinging on the back wall of the cavity (producing noise). The most effective flow control strategy in the cavity problem would be to ELIMINATE large coherent structures, not replace one noise producing set with another at a slightly different frequency. We will see in the low frequency acoustic suppression data to follow evidence of the growth of undesirable modes in LF forcing which lead to lower than optimal levels of acoustic suppression.

In coining the term "high frequency", we are begging the question "what constitutes low frequency?". We will attempt to answer that question by presenting representative examples of low frequency cavity suppression. We will begin with "zero mass addition" perturbation techniques. The common theme among these devices is that they typically are able to produce only small perturbations, are reasonably effective at low (less than .5) Mach numbers, and are shown to lose their effectiveness when applied to cavity flows at realistic Mach numbers (Mach .8 to Mach 1.5).

We will then proceed to examine LF devices capable of providing suppression in the "military" Mach range of interest (Mach .8 to 1.5). Since pulsed air is a popular form of suppression technique, we will begin by first describing the effect of steady (zero frequency) leading edge blowing. We will then look at the additional benefit derived from pulsing (in positive mass addition pulsed blowing).

VI.1 Cavity Acoustic Control Using Low Frequency, Zero Mass Addition Forcing

Figure 15 [Ref 20, Cattafesta et. al.] is a pressure spectra demonstrating the suppression of resonant cavity acoustics in a Mach .74 cavity flow. The device used in this case is similar to the earlier "piezo-wedge" – in this case it is a cantilevered metal flap (like a diving board), driven into first bending mode by a piezoceramic patch. The first thing to observe in this figure is that the forcing frequency is in the vicinity of the dominant Rossiter modes (just to the right of the first mode at about 550 hz), i.e. "low frequency", and that this forcing takes about 8 dB off the first mode. The second thing to notice is that it does this while having little or no effect on the broadband level. We will continue to see this same theme in subsequent experimental data – no evidence that low frequency forcing has any significant effect on broadband acoustic levels. Figure 16 [Ref. 21] shows that this same device achieved its highest levels of suppression (approximately 21 db) in a very low speed (roughly Mach .15) cavity flow.

Figure 17 [Ref. 22, Williams et. al.] shows acoustic suppression results for a Mach .48 cavity flow. In this case the zero mass addition, low frequency device is an acoustic driver, which forces a chamber connected to a slot near the leading edge of the cavity (a type of "synthetic jet"). The slot forces the cavity shear layer with a low speed inflow / outflow (zero net mass) in response to the movement of the driver. Similar remarks apply in this case. Forcing is in the "range" of Rossiter tones. This case is promising in that it shows the ability of a controller to simultaneously suppress multiple tones, but the level of suppression is not dramatic (less than 10 db). Figure 18 shows the best reported performance of this actuation technique, 18 dB at Mach .34. As before in the case of the low frequency piezo-flap, this "synthetic jet" zero mass addition device also leads to no appreciable change in the broadband sound pressure level, and also loses effectiveness as the Mach number increases.

Figure 19 [Ref. 23, Lamp and Chokani] shows best suppression results from another very low speed cavity experiment (Mach .15), using another version of a zero mass addition "synthetic jet". In this case the zero mass addition was managed using alternating positive outflow and powered suction (vacuum). Some "suppression" of the Rossiter cavity modes is evident, but with the presence of the strong forcing peaks, the net resulting suppression is only several dB. Two of the three forcing frequencies actually increased the peak level in the spectra. Consistent with the two other zero mass addition cases already discussed, no effect on the broadband level is present.

VI.2 Cavity Acoustic Control Using Steady Mass Addition

Figure 20 [Ref. 7] shows the effect of steady leading edge blowing on a Mach .8 cavity flow, as a function of mass flow rate. As can be discerned from the figure, increasing mass flow rates lead to both suppression of the tones, as well as a significant drop in the broadband level. Figure 21 [Ref. 24] shows the same type of suppression behavior from cavity leading edge blowing at Mach 1.5. The acoustic suppression in these cases is attributed mainly to displacement of the unstable free shear layer away from the cavity, leading to reduced impingement of vortical structures (and through feedback, subsequent reduced initial strength of those same vortical structures) on the rear wall of the cavity.

VI.3 Cavity Acoustic Control Using Positive Leading Edge Mass Addition With Low Frequency Pulsing

Pulsed blowing at the cavity leading edge has been popular as a candidate for cavity acoustic flow control, primarily because the more energy-frugal zero mass addition devices have proven to be largely unsuccessful in the range of realistic combat flight Mach numbers (Mach .8 to 1.5). Higher level perturbations from "positive mass addition" pulsed blowing devices, however, come at the expense of much higher mass flow rates.

Shaw and co-investigators [Refs. 1, 7, 25, 26, 27] have consistently pursued pulsed blowing as an acoustic suppression concept since 1995. Ref. 25 describes implementation of a low frequency pulsed blowing system in the leading edge of a weapons bay cavity within a 10% generic fighter model. Tests at Mach .85, and at various mass injection levels (.01 lbm/sec to 0.5 lbm/sec), show maximum suppression results of about 14 dB across all frequencies, occurring at a mass flow rate of .05 lbm/sec. (See Figs. 22 and 23). Later attempts to implement closed-loop control in the same model and wind tunnel (Fig. 24, Ref. 7) yielded no additional benefit. So-called "tonal" suppression in Ref 7 is quoted as high as 20 dB, but this measure of suppression is obviously very misleading, in that it ignores the rather large tone in the spectra created by the forcing itself (See Figure 24, and also the earlier explanation at the beginning of Section VI on undesirable mode growth in low frequency forcing).

Shaw, in collaboration with Lockheed Martin Corp., has also studied low frequency pulsed blowing in larger scale (20%) cavity models. Fig. 25 [Ref. 26] shows suppression due to pulsed blowing in a generic 20% scale cavity at Mach 0.85 . Three separate spectra with suppression (using different forcing frequencies) are plotted against a baseline (no suppression). There is no apparent effect of the pulsing on the spectra. Changing the frequency merely changes where the forcing peak appears, and has no effect on the dominant change in the broadband due to steady blowing. Fig 26 [Ref. 28] shows low frequency pulsed blowing suppression results on a 20% scale F-111 weapons bay cavity at Mach .9. The same result ensues. Varying the pulsing frequency resulted in no additional suppression over steady blowing. Even after redesigning the mass injection nozzles to provide enhanced pulse strengths (peak to peak amplitude) of roughly a FACTOR OF FOUR higher [see Ref. 27], this same technique yielded, at best, only 1-2 dB additional suppression over steady blowing.

It is now obvious, both from the results of section VI.1, and from the results of this section, that a significant portion (sometimes ALL) of the suppression from low frequency pulsed leading-edge blowing is due solely to the steady mass addition effect. This dominance of steady blowing over the pulse effect is seen at realistic Mach numbers (M > .8), where the naturally existing disturbance levels are quite high, and weak, low amplitude (low mass flow) pulsing would be fruitless. Pulsing the mass addition IS seen to be effective (approx. 20 dB suppression) for very low speed (M < .3) cavity flows, and marginally effective (approx. 10 dB suppression) up to M = .5.

VI.4 Low Frequency Acoustic Suppression Summary

In section VI.2, we showed that steady blowing at the cavity leading edge is a powerful suppression technique at relevant Mach numbers (up to **30 dB**), provided you can afford the relatively high mass flow rates (.3 lbm/sec at 1/10 scale – see Fig 20). We also saw in sections VI.1 and VI.3 that in the absence of steady blowing, one could achieve on the order of **10 dB** suppression with a low frequency forcing technique, provided the Mach number was low enough (< .5). If steady mass blowing was present (and serves as the dominant suppression effect) additional pulsing yielded at best only several (1-2) dB additional suppression. A telltale sign of the steady mass addition being the "dominant effect" is a significant drop in the entire broadband level (up to 10 dB). So, the state of affairs for low frequency acoustic suppression at relevant (> M = .5) Mach numbers is that there are currently NO unpowered, and NO zero mass flow powered devices capable of providing suppression levels better than a passive spoiler (on the order of **10 dB**). Higher levels of suppression are possible with mass addition, but several different experiments point to the conclusion that pulsing the flow is unnecessary. **So there are no low frequency pulsing techniques which have proven to be more effective than spoilers in the Mach range of interest (.8 < M < 1.5).**

Let us contrast this state of affairs with some of the high frequency suppression results quoted in section IV. The rod in crossflow (an **unpowered**, zero mass addition device) delivered **14 dB** suppression at Mach .85, and **21 dB** suppression at Mach 1.19. If one were willing to consider a **powered** high frequency device, the resonance tube delivered **26 dB** at Mach .85, and an impressive **29 dB** suppression at Mach 1.19 (See Figures 13 and 14). Unfortunately, the powered resonance tube produces, in a very loose sense, a high frequency pulsed jet, and so some portion of its suppression must also be attributed solely to mass addition.

In spite of the ambiguity as to the cause of the suppression with the HF resonance tube, it should be obvious to even the casual observer that the suppression levels of the high frequency rod-in-crossflow at **supersonic conditions** are impressive. The dominant questions remaining are:

1) Do the rod in crossflow and resonance tube share a common "high frequency" suppression mechanism?
2) What is the nature of this mechanism? How is it different from low frequency suppression?
3) What percentage of the suppression in the case of the resonance tube is due to mass flow alone?

VII.   Preliminary Theories / High vs Low Frequency Forcing

Stanek et. al. in References 11 and 19 provide several clues to the novel mechanism behind HF suppression. Figure 27 shows a schlieren image of a horizontal subsonic rectangular jet impinging upon a vertical wall. This "impinging jet" problem serves as a convenient analogue to the resonant cavity problem. Alternating light and dark round "blobs" reveal the presence of large scale coherent structures (and acoustic resonance). Figure 28 shows the same flow situation after the application of high frequency forcing from a resonance tube actuator. This flow shows no sign of large scale structures, and no evidence of acoustic resonance. Figure 32 shows a similar impinging round jet experiment where the high frequency forcing is accomplished using a bank of piezo wedges (see Figure 5). A similar destruction of the large scale coherent structures ensues. As shown in these schlieren photos, one possible explanation for the drop in the acoustic levels is the absence of large-scale vortical structures after the application of HF forcing. Figure 29 caricatures this first obvious difference between low frequency suppression and high frequency suppression in cavities, where LF forcing is described as a "detuning" mechanism (with large-scale structures still resident as evidenced by the acoustic spectra), and HF forcing is described as a "large-vortex" destroying operation.

The interesting question, of course, is what is causing the disappearance of the large-scale vortical structures? Is their disappearance simply a sign of suppression and not a cause? If we go back to the early non-resonant experiment by Glezer et. al., we see that the HF forcing in that experiment was accompanied by a substantial increase in the viscous dissipation (by at least an order of magnitude), and a fairly dramatic change in the broadband slope in the so-called inertial subrange (See Fig. 6). The first evidence of this type of change in a resonant flow is offered by Stanek et. al. [Ref. 11] in Figure 30 (compare to Fig. 6). There it is seen that the slope of the broadband spectra changes, depending upon whether one is forcing at low frequencies or high frequencies, implying that the RATE of energy flowing from low frequencies to high frequencies increases under HF forcing.

This evidence frames the argument over the source of the mysterious HF effect. A fundamental question is as follows: Is the HF mechanism similar to the rather obvious LF mechanism, where you are simply introducing a very small structure and this mode is "out-competing" it's neighbors? Or is the HF forcing different, perhaps somehow just "charging up" the viscous dissipation by increasing the flow of energy into the inertial subrange, and therefore, damping the growth of ALL instability modes? Put plainly, is HF forcing encouraging the growth of one HF mode or discouraging the growth of all LF modes?

Stanek et. al. [Ref. 11] surmised that the mechanism might be related to the fact that the forcing is occurring in the CONSERVATIVE (energy conserving) portion of the shear layer turbulence spectrum known as the inertial subrange. If the shear layer is receptive to accepting energy input in the inertial subrange, and the forcing frequency is still within the inertial subrange AFTER modification from forcing, then the rate of energy transfer from large to small scales MUST increase (since the energy cascade is conservative – what comes in must go out). It is possible that through HF forcing, the entire nature of the energy cascade is being redefined. Instead of the turbulence production range dictating the rate of energy dissipation (and feeding the smaller scales at **it's** own determined rate), perhaps now the inertial subrange is actually dictating the rate of turbulent energy production. This implies that the inertial subrange scales are actually DEMANDING more energy than the NORMAL turbulence production mechanisms can handle, with the net result being that the normally dominant large-scale cavity modes are literally being "starved" for energy (to feed the increased DEMAND of the inertial subrange).

Figure 31 lends some credence to the argument that it is forcing within the inertial subrange which produces the HF effect. In this figure, the "signature" of three high frequency devices are displayed for the same operating condition. Two of the **successful** devices (which produce the change in broadband and pronounced acoustic suppression), the rod in crossflow, and the resonance tube (mdot = .411) produce broad peaks, separated by roughly 1500 hz. Another unsuccessful HF device (which does not produce the characteristic HF slope change in the broadband), the piezo wedge, is represented by a very narrow peak, of similar amplitude to the first two devices. The message implied in this figure is twofold. First, the two devices which "worked" excited a mechanism which was not sensitive to forcing frequency. As long as the forcing was within the inertial subrange, the successful devices seemed to excite the HF mechanism. This bolsters the "accelerated conservative energy cascade" argument above. The other point is that the energy cascade is not "receptive" to all types of HF forcing. A device which produces a thin narrow spectral peak, even though it is of the right approximate amplitude and frequency, will not necessarily excite the mechanism. There may be some sort of "receptivity" or "minimum power" requirement somehow related to the breath (in frequency) of the forcing peak. It also hints at the notion that it may be a certain form of vorticity production (and not simply acoustic forcing) which is required to invoke the "high frequency" effect.

There is, of course, some danger in speculating along these lines. Both "successful" HF devices, in Figure 31, produce obviously similar effects on the broadband, but this is not proof that this is the cause of the bulk of the suppression. Both successful HF devices

also have some sort of "zero frequency" effect, and until that effect is separated from the high frequency signal effect, we can ONLY speculate as to cause and effect.

In light of our earlier discussion on low frequency pulsed blowing, and the fact that most of the suppression (at relevant Mach numbers) was due to STEADY mass flow, we must take pains to point out that this could also be the case with the HF resonance tube. In addition, in spite of the fact that the rod in crossflow eliminates the mass flow issue, there is also the "zero" frequency blockage effect of the rod which might be responsible for some or all of the suppression. Further testing is planned to attempt to resolve or clarify both these issues. What we CAN say at this time is that the rod in crossflow has already proven itself to be superior to the spoiler, at both subsonic and supersonic conditions [See Ref. 11], for comparable weight, size, and power (i.e. zero) input. The rod will be a serious contender for any future cavity suppression designs (and possibly as a retrofit to current cavity suppression systems).

It is also dangerous at the present time to declare "the destruction of large coherent vortical structures" as the CAUSE of the suppression of resonance in HF acoustic suppression systems. The disappearance of large coherent structures is at best right now, a *symptom* of the suppression of resonance. In fact, ANY technique (low frequency, high frequency, zero frequency) which successfully suppresses resonance should result in weakening of the large, dominant, coherent structures, which would be reflected in the flow visualization. The fact that we cannot settle this question now is a compelling statement for the need of high quality flow visualization in ALL resonant flow suppression experiments. Almost all of the cavity suppression experiments at realistic conditions provide only static and dynamic pressure data on the cavity walls and surrounding structure.

So far, the ONLY quantifiable "signal" proving whether suppression in a given situation is *possibly* due to HF forcing is the characteristic "shift" in the broadband (Figures 6 and 30). We have already seen that the existence of a clearly defined forcing peak (in the case of the piezo-wedge) at high frequency is not sufficient to cause this broadband slope "shift" which is the hallmark of the HF "effect". It may also be possible that one could produce this change in the broadband slope (indicative of an increase of energy in the high frequencies) without producing a characteristic forcing peak.

The essence of the argument for what might be high frequency acoustic suppression is captured in the original Wiltse and Glezer figure (Fig. 6). High frequency acoustic suppression does not necessarily require a peak at high frequencies which competes with other peaks. High frequency acoustic suppression derives its effect by raising the BROADBAND (not simply a single peak) over a RANGE of high frequencies. Forcing at a SINGLE high frequency raises the BROADBAND of the surrounding high frequencies. The key to this unique suppression is that the single frequency high frequency forcing somehow stimulates a mechanism where the BROADBAND high frequency range extracts energy from the BROADBAND low frequency range. The "change in slope" of the high frequency range broadband (Fig. 6) is direct evidence of the enrichment of the high frequencies at the expense of the low.

This characteristic shift in the broadband frequency could be used in the future as an acid test for the other supposition, that HF forcing can only be "engaged" within the inertial subrange. If this theory is true, then by lowering the forcing frequency, one should eventually hit the "crossover point", where you switch from HF to LF "physics". This should then be accompanied by the characteristic "jump" from one broadband slope to another (as seen in Figure 30). If all the speculations are on the mark, this crossover point will be at the point where the inertial subrange begins. This theory can only be tested experimentally by devising an actuator which does not change its physical characteristics (like size) as the operating frequency changes, and which can operate in a frequency band surrounding the expected crossover frequency.

The "high frequency effect" appears to be driven or triggered by raising the level of energy over an entire range of high frequencies (raising the broadband in the inertial subrange lowers the broadband in the turbulence production regime). This is why this type of suppression is independent of the forcing frequency, and what allows for a host of simplifications, such as optimization of actuators (for max amplitude) at a single frequency, forcing at a single frequency over a wide range of flight conditions, actuator simplicity (no moving parts), and no need for formal control systems (with or without feedback).

VIII.   Summary – Major Differences Between LF Cavity Suppression and HF Cavity Suppression

We now summarize the perceived differences between LF and HF forcing in resonant cavity flows:

In Low Frequency forcing:

1)   The energy addition takes place at frequencies near the dominate tones in a resonant cavity (turbulence production portion of the spectra).
2)   The energy addition occurs in a non-conservative region of the frequency spectra where turbulence exchanges energy with the mean flow (turbulence production portion of spectra). The forcing mode ITSELF grows, and generates turbulence (large coherent vortical structures).
3)   Strong resonant tones remain in the low frequency portion of the spectra after suppression (no simultaneous reduction of the Rossiter tones).

4) The candidate frequency (mode) supplied by the forcing is itself a significant source of unwanted noise, due to the fact that the largest structures (lowest frequencies) in the turbulent shear flow already contain the highest levels of energy in the spectra – and you are adding to that already high existing broadband SPL.

5) The resonant cavity is "detuned" (the feedback is out of phase with the forcing), but large coherent structures remain and serve as significant acoustic sources as they impinge upon the rear cavity wall.

6) The forcing frequency must adjust with changing Mach number, and must avoid coming too near the resonant Rossiter tones (to avoid <u>reinforcing</u> resonance). This requires the use of a control system. This also complicates the job of the actuator designer, who must sacrifice high amplitude at a single frequency for adequate performance over a prescribed bandwidth.

<u>In High Frequency forcing:</u>

1) The energy addition takes place at frequencies significantly higher (sometimes an order of magnitude or more higher) than the dominant tones in a resonant cavity (in the inertial subrange).

2) The energy addition occurs in a conservative region of the frequency spectra where turbulence does not exchange energy with the mean flow, and most energy flows from lower to higher frequencies (the inertial subrange).

3) All tones are suppressed in the low frequency portion of the spectra **simultaneously**, and <u>no strong tones remain</u>.

4) The energy supplied by the HF forcing does not become a problem itself, because the energy is added to that part of the spectra which has the least amount naturally – you are adding energy to a portion of the spectra with a naturally LOW broadband SPL.

5) All large coherent structures are minimized. This offers the lowest possible acoustic levels, because you have BOTH "detuned" the cavity flow, AND eliminated all significant acoustic sources due to impingement on the cavity rear wall – YOU HAVE ELIMINATED THE SOURCE FOR TONES.

6) The forcing frequency can remain constant (as long as changing conditions keeps the forcing within the inertial subrange). This eliminates the need for any control system. This also allows designers to make zero moving parts actuators with emphasis on maximum forcing level.

The terse defining statement of the philosophical difference between high and low frequency forcing is that high frequency forcing attempts to achieve suppression by directly manipulating the broadband at high frequency, causing a drain on the low frequencies, whereas low frequency forcing seeks to input a single dominant low frequency which will "out compete" the more dangerous natural (Rossiter) low frequency modes. Superimposed upon these basic mechanisms, in most cases, are zero frequency effects (like steady mass addition) which add to overall suppression levels, and complicate data interpretation. Zero frequency suppression causes a drop in the entire broadband level, **without** causing a change in the SLOPE of the HF range broadband, as seen in high frequency broadband manipulation.

Research is currently in progress to attempt to codify or eliminate from consideration individual perceived differences between HF and LF forcing from our list of possible suspects.

IX. Enter the Microjet / High Frequency Suppression of Impinging Jet Resonance?

During the same time frame as the cavity experiments at DERA, NASA was sponsoring research at Boeing focusing on acoustic suppression in impinging jet flows [Ref. 30]. Small-scale experiments using round jets forced by piezo wedges demonstrated suppression behavior similar to that seen in the Boeing rectangular nozzle work described earlier. Figure 32 shows "before" and "after" shots clearly demonstrating that the reduction in acoustic levels produced by HF forcing was accompanied by destruction of the large scale vortical structures in the flow.

Following the NASA work, AFRL (AFOSR – Air Force Office of Scientific Research) supported a very unique concept for the suppression of impinging jet resonance. Krothapalli et.al. [Ref 31] at Florida State University (FSU) produced dramatic acoustic suppression results in these impinging jet flows with a technique called the microjet.

To combat the resonance, Krothapalli et. al. installed a series of extremely small converging-diverging nozzles in the lip of the nozzle exit of a round jet. Figure 33 displays proof of the supersonic exit conditions for these nozzles (with diameters of .4 mm, relative to a main nozzle diameter of 28 mm.). When operated, the micronozzles consumed less than ½ percent of the core massflow of the main nozzle. The results were astounding. Figure 34 shows the spectra of the impinging round jet before and after activation of the microjets. The peak overall level drops by almost 50 dB! In addition, the broadband drops consistently by 10 dB across all frequencies.

The suspicion early on was that this suppression might be related to the suppression seen in the HF forcing cavity experiments. Due to the very small scale of the energetic small jets, and the fact that the presence of shock cells allowed for the presence of very small scale jet screech, it was postulated by several researchers that the mechanisms were the same.

One of the drawbacks to the microjet impinging jet experiments was, however, that there was no obvious forcing frequency present in the spectra [Fig. 34]. This might lead one to suspect that HF forcing is NOT responsible for the impinging jet acoustic suppression. To test this hypothesis, microjet leading edge inserts for the DERA cavity model were fabricated by the University of Florida under contract to Boeing, and Air Force Research Laboratory, and tested in February 2001. Preliminary analysis of the data

leads to the conclusion that steady blowing (not a HF effect) is most likely the dominant, if not the only cause of suppression in the case of microjets applied to cavity acoustic suppression, but further analysis is still underway.

Several other devices (in addition to the microjet) were tested in the Feb. 2001 DERA / AFRL test entry. These include two different "low mass flow" powered resonance tubes, a modified version of the original resonance tube bank (Figure 12) designed to kill the "resonance tube forcing" resonance and pass the same mass flow, and several rod / spoiler combinations. The data from that test is currently being analyzed and will be published in the near future.

X. Preliminary Numerical Simulations of High Frequency Forcing Behavior in Shear Layers

The first attempt to directly simulate the effect of high frequency forcing (high in the sense described in this review) in a shear layer was described in Cain and Rogers [Ref. 32, 2000. See also Ref 12, Cain et. al., 2001]. In this work, the pseudospectral free shear layer code used by Rogers and Moser [Ref. 33] and Moser, Rogers, and Ewing [Ref. 34] was applied to a plane wake under the influence of HF forcing. The intention was to attempt to simulate a situation similar to that seen in the Wiltse and Glezer experiments [Ref. 9]. In lieu of a more formal grid resolution study, Cain and Rogers use past simulations using this code as guidance for choice of mesh density. Fig. 35 shows a turbulent velocity spectra after HF forcing (simulated), and comparison with Figure 6 (experimental) demonstrates that the simulation resolution is adequate.

Cain and Rogers [Ref. 32] examines the effect of HF forcing on both fully turbulent and transitional wake flows. They find that HF excitation of a fully turbulent plane wake shows only a weak transient effect. In contrast, HF excitation applied to a transitional plane wake has a significant lasting impact. Figure 36 shows a plot of integrated turbulent kinetic energy vs time for the transitional simulation, with and without forcing. The simulation shows a reduction in this quantity by 20 % at the time the simulation was stopped (with more reduction possible). Figure 37 shows that integrated turbulence dissipation rate is increased by 14 %.   This figure also shows that if the HF perturbation is applied "late" in the life of the transition process, that it has no lasting effect. In addition to the dissipation being enhanced, Figure 38 shows the integrated rate of turbulent kinetic energy production is also diminished by 24%. Cain et. al. [Ref. 12] speculate that these effects may be due to nonlinear interactions between high amplitude high frequencies and the production scales, with the net effect being a reduction of the correlation coefficient between components of the Reynolds stress tensor. Further analysis is required to substantiate this claim.

While not directly applicable to the case of high-speed cavity flow, these results are intriguing. Certainly, the cavity flow shear layers are "transitional" in the same sense as Cain's plane wake flow is – evolving from boundary layer type turbulence to a "free shear layer" variety. Obviously, more high fidelity simulations (in high speed cavites) are required to enable a direct comparison to be made.

XI. Conclusions & Future Work

Over the relevant Mach range of interest for military high-speed cavities (.8 < M < 1.5), an "average" rule-of-thumb value for expected suppression using a passive spoiler is roughly 10dB. Steady leading edge blowing (relatively high mass flow rates) has been shown in numerous tests (including flight test) to be very effective in this Mach range of interest (max suppression on the order of 20 dB). Superimposing pulsing over high levels of steady blowing has no significant additional suppression effect (1-2 dB OASPL). A review of all low frequency pulsing techniques reveals that there is no experimental data demonstrating that pulsing is more effective than the standard leading edge spoiler in the relevant Mach range of interest.

Two high frequency devices (a rod in crossflow, and HF resonance tube) have demonstrated significant suppression improvements over spoilers (from 14 to 29 dB) in the .8 to 1.5 Mach range. The resonance tube device emits significant amounts of mass flow, and the percentage of suppression due to steady mass addition is currently under investigation.

Unique attributes of high frequency flow control (vs conventional, low frequency control) have been convincingly established in low speed flows (Ref. 9). Similar detailed measurements still need to be taken and interpreted for high-speed flows. Numerical studies have produced interesting insights into the nature of the high frequency flow control mechanism, but the expense of high fidelity simulations have limited the depth (extent) of these simulations. Conclusions at this time must be considered preliminary.

In spite of the obvious power of the emerging class of HF actuators, and their impact on resonant acoustic problems, several important matters of research remain. Attempts to scale these devices to flight conditions will likely depend upon a clearer understanding of the basic physics involved. Listed below are a limited selection of questions and issues remaining.

What constitutes sufficient "frequency or spectral breadth" of forcing signal for a HF device appears to be a function of experiment scale and Mach number. The piezo wedge devices (which eliminate the sticky question of the effect of mass flow) which are completely ineffective in the experiments described in this paper (and in Ref. 11), were shown to evoke the desired effect in a smaller scale, lower speed "bench" experiment described in Ref. 16.

Future studies will focus on answering some of the following questions:

What percentage of the suppression due to the powered resonance tube can be attributed solely to mass injection effects?

What is the range of effective HF forcing frequencies (the inertial subrange?)? Is there an optimum? Why?

Is it possible to force at too high a frequency?

How do these model-sized demonstrations scale-up to full scale?

Do other LF devices show changes to the broadband similar to the spoiler (and therefore dissimilar to the HF devices)?

Can we quantify the " frequency breadth" requirement evident in the experimental data?

Is the microjet mechanism the same as that produced by the rod and powered resonance tube devices? What percentage of the suppression for that device is due solely to mass flow?

XI. References

1. Shaw, L. , "Active Control For Cavity Acoustics", AIAA-98-2347.
2. McGrath, S. & Shaw, L. 1996 Active Control of Shallow Cavity Acoustic Resonance, AIAA-96-1949.
3. Williams, D. R., Fabris, D., Iwanski, K., and Morrow, J., "Closed-Loop Control In Cavities With Unsteady Bleed Forcing", AIAA-2000-0470.
4. Raman, G., Raghu, S., and Bencic, T., "Cavity Resonance Suppression Using Miniature Fluidic Oscillators", AIAA-99-1900.
5. Cattafesta, L. N. III, Shukla, D., Garg, S. & Ross, J. A. 1999 Development of an adaptive weapons-bay suppression system. AIAA-99-1901.
6. Mongeau, L., Kook, H., Franchek, M. A., "Active Control Of Flow-Induced Cavity Resonance", AIAA/CEAS AeroAcoustics Meeting, Toulouse, France, June 1998.
7. Shaw, L. and Northcraft, S., "Closed-Loop Active Control For Cavity Acoustics", AIAA-99-1902.
8. Maines, B. H., Robarge, J. E., Welterlen, T. J., and Smith, B. R., "Weapons Bay Acoustic Suppression From A Rod in Crossflow", Active Robust ConTrol of Internal Cavities (ARCTIC) Workshop Presentation, AIAA Aerospace Sciences Meeting, January, 2001.
9. Wiltse, J.M., and Glezer, A., "Direct Excitation of Small-Scale Motions in Free Shear Flows, Phys. Fluids, Vol. 10, No. 8, pp2026-2036, 1998.
10. Yeung, P.K., Brasseur, J. G., and Wang, Q., "Dynamics of Direct Large-Scale Couplings in Coherently Forced Turbulence: Concurrent Physical-Space and Fourier-Space Views", J. Fluid Mech., 1995, Vol. 283, pp 43-95.
11. Stanek, M. J., Raman, G., Kibens, V., Ross, J. A., Odedra, J., and Peto, J. W., "Control of Cavity Resonance Through Very High Frequency Forcing", AIAA/CEAS Aeroacoustics Meeting, Lahaina, Hawaii, AIAA 2000-1905.
12. Cain, A. B., Rogers, M. M., Kibens, V., and Raman, G., "Simulations of High-Frequency Excitation of a Plane Wake", AIAA-2001-0514.
13. Ho, C. M. and Huerre, P., "Perturbed Free Shear Layers", Annual Review of Fluid Mechanics, Vol. 16, p. 365, 1984.
14. Cain, Alan. Private Communication, 1997.
15. Raman, G., Kibens, V., Cain, A., and Lepicovsky, J., "Advanced Actuator Concepts For Aeroacoustic Control", AIAA-2000-1930.
16. Brocher, E., Maresca, C., and Bournay, M. H., "Fluid Dynamics of the Resonance Tube", J. Fluid Mech. (1970), Vol. 43, Part 2, pp 369-384.
17. Thompson, M.C., Hourigan, K., Welsh, M.C., and Brocher, E., "Acoustic Sources in a Tripped Flow Past a Resonator Tube", AIAA Journal, Vol. 30, No. 6, June, 1992.
18. Brocher, E., and Duport, E., "Resonance Tubes in a Subsonic Flowfield", AIAA Journal, Vol. 26., No. 5, 1987.
19. Stanek, M.J., Raman, G., Kibens, V., Ross, J. A., Odedra, J., and Peto, J.W., "Suppression of Cavity Resonance Using High Frequency Forcing – The Characteristic Signature of Effective Devices", 7th AIAA/CEAS Aeroacoustics Conference, 28-30 May, 2001.
20. Cattafesta, L. N. III, Shukla, D., Garg, S., and Ross, J. A., "Development of an Adaptive Weapons-Bay Suppression System", AIAA-99-1901.
21. Cattafesta, L. N., Garg, S., and Washburn, A. E., "Piezoelectric Actuators For Fluid-Flow Control", Proceedings of the S.P.I.E., 3044:147-157, 1997a.
22. Williams, D. R., Fabris, D., Iwanski, K., and Morrow, J., "Closed-Loop Control In Cavities With Unsteady Bleed Forcing", AIAA 2000-0470.
23. Lamp, A. M., and Chokani, N., "Control Of Cavity Resonance Using Steady and Oscillatory Blowing", AIAA 99-0999.
24. Grove, J. E., Birkbeck, R. M., and Kreher, J. M., "Acoustic and Separation Characteristics with Bay Leading Edge Blowing", AIAA 2000-1904.
25. Shaw, L., "Wind Tunnel Test Results For Active Suppression of Weapons Bay Acoustics", WL-TM-97-3109, Nov. 1997.
26. Shaw, L., "High Speed Application of Active Flow Control For Cavity Acoustics", AIAA-2000-1926.

27. Shaw, L., Smith, B., and Welterlen, T., "Actuator Optimization For Active Flow Control Of Cavity Acousics", AIAA-2001-2217.

28. Welterlen, T. J., "Active Weapons Bay Noise Suppression", FZM-8723, Final Report, Prepared by Lockheed Martin Aeronautics, for U. S. Air Force under Contract No. F33615-99-C-3218.

29. Raman, G., and Kibens, V., "Active Flow Control Using Integrated Powered Resonance Tube Actuators", AIAA-2001-3024.

30. Kibens, V., Wat, J.K., and Alvi, F.S., "High Frequency Excitation For Jet Noise Reduction", NASA Report CRAD-9310-TR-6155, October 1999.

31. Krothapalli, A, Elavarasan, R., Alvi, F., and Shih, C., "Active Control of Supersonic Impinging Jets", NATO RTO Symposium On Active Control Technology, Braunschweig, Germany, 8-10 May, 2000.

32. Cain, A. B. and Rogers, M. M., "High Frequency Excitation of a Plane Wake", Stanford Center For Turbulence Research, Annual Research Briefs, 2000.

33. Rogers, M. M., and Moser, R. D., "Direct Simulation of a Self-Similar Turbulent Mixing Layer", Physics. Of Fluids, Vol. 6, pp 903-923, 1994.

34. Moser, R.D., Rogers, M. M., and Ewing, D. W., "Self-Similarity of Time-Evolving Plane Wakes", Vol. 367, pp 255-289, 1998.
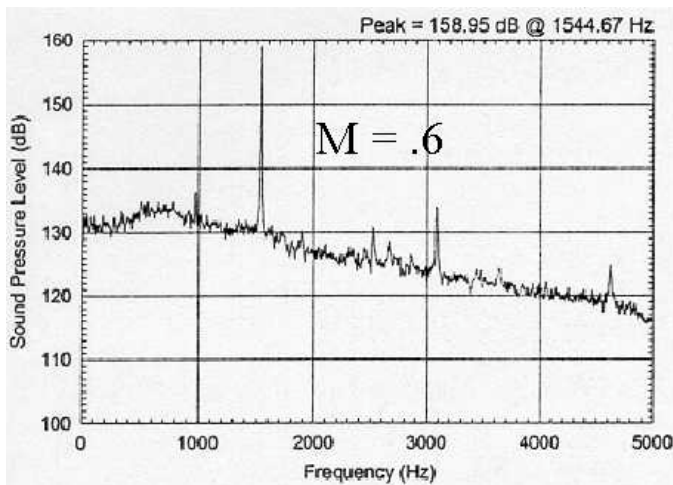
Figure 1.   1/10th Scale Cavity Spectra at Mach .6 – Before High Frequency Suppression (Ref. 2)
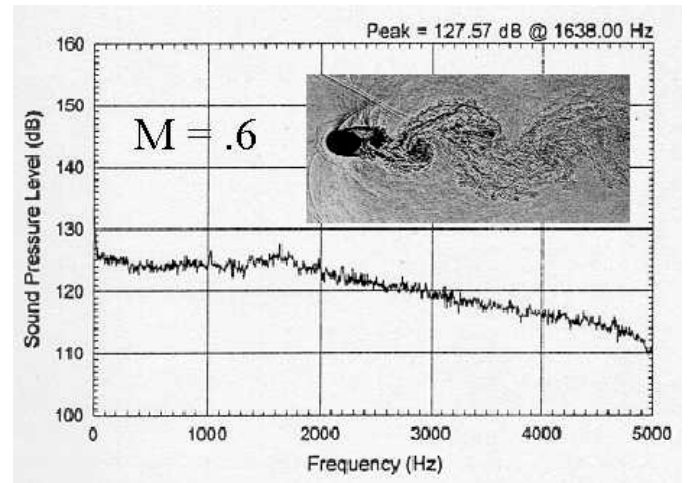
Figure 2.   1/10th Scale Cavity Spectra at Mach .6 – After High Frequency Suppression (Ref. 2)
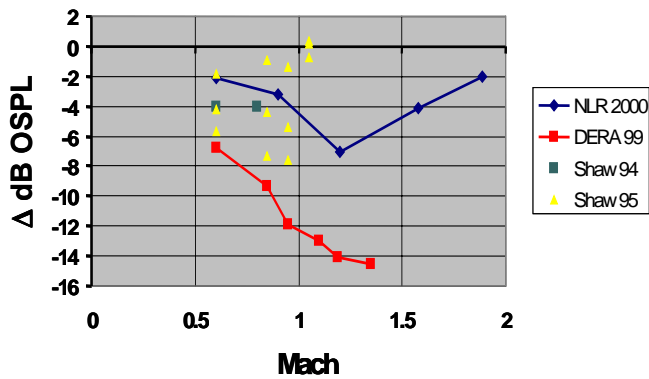
Figure 3. Historical "Rod in Crossflow" Acoustic Suppression Data (Ref. 8). Numbers in legend correspond to year of experiment.
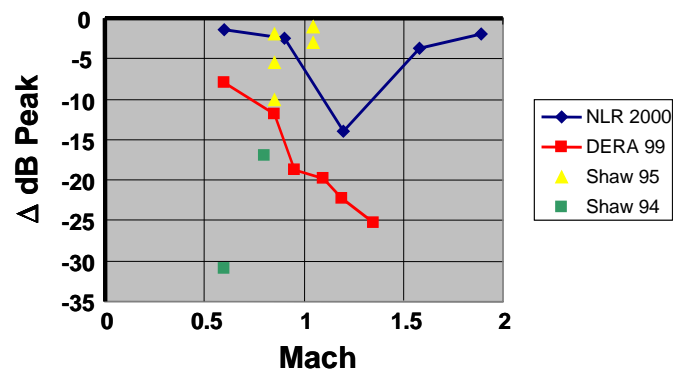
Figure 4. Historical "Rod in Crossflow" Acoustic Suppression Data (Ref. 8). Numbers in legend correspond to year of experiment.

Figure 5.   Close-up of a Single PiezoCeramic Driven Wedge (Ref. 11)
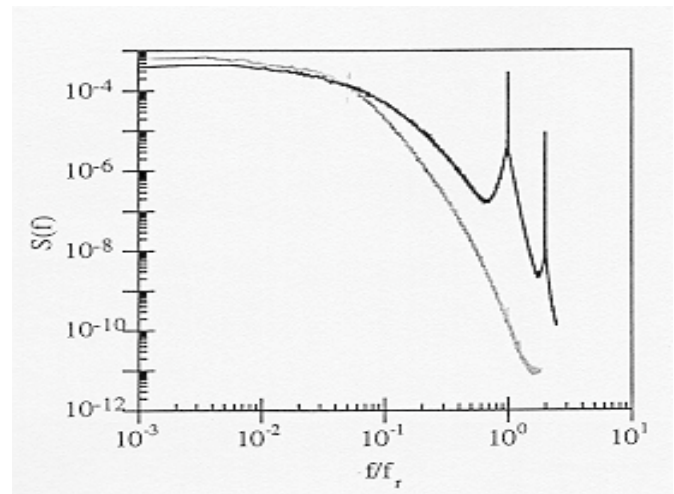
Figure 6.   Effect of High Frequency Forcing On A Laboratory-Scale Free Shear Layer (Ref. 9)
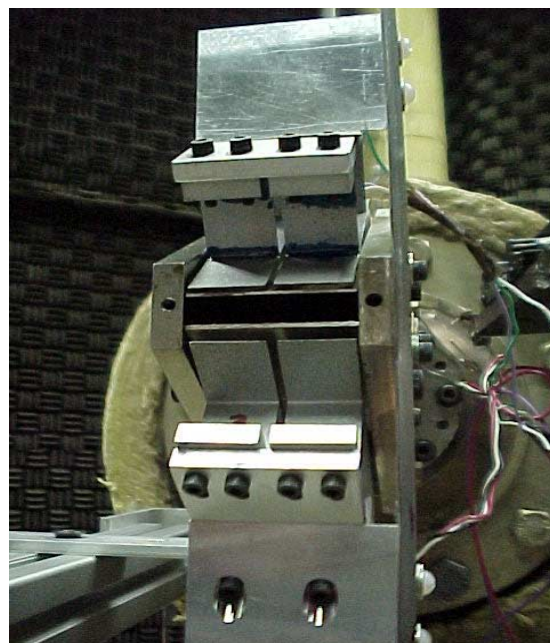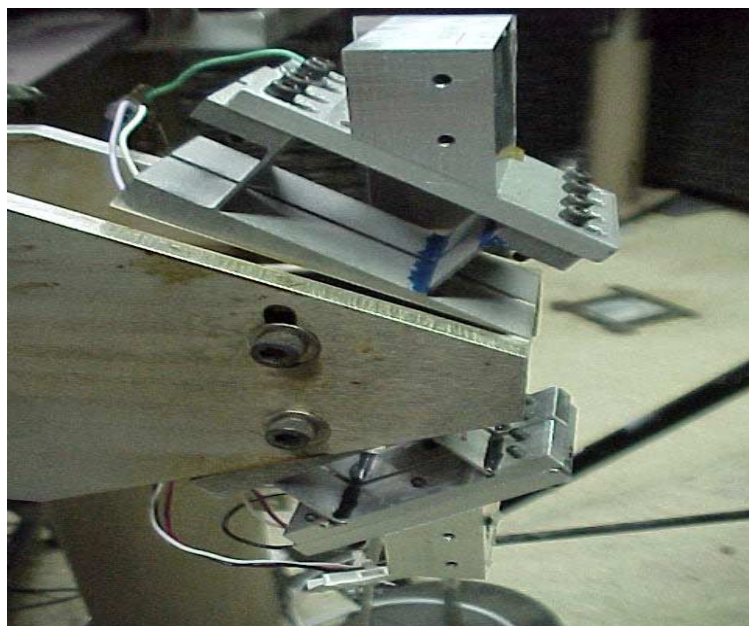
Figure 7.   Side and Front View of Boeing "High" Frequency Excitation Jet Edge-Tone Reduction Experiment (Simulated Cavity) Ref. 15.
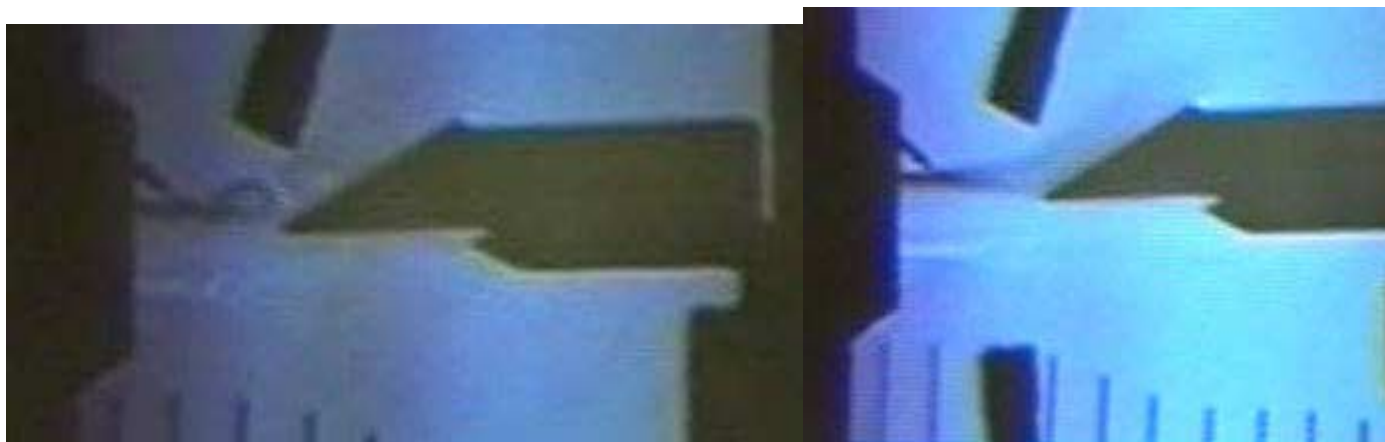
Figure 8. Side View Of Jet Edge Tone Experiment. Left inset Without HF Excitation. Right Inset With HF Excitation (Ref. 15).
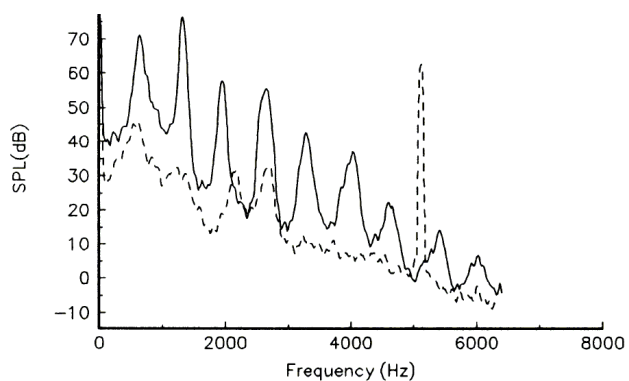
Figure 9. Acoustic Spectra in Jet Edgetone Experiment, Before and After HF Excitation. (Ref. 15)
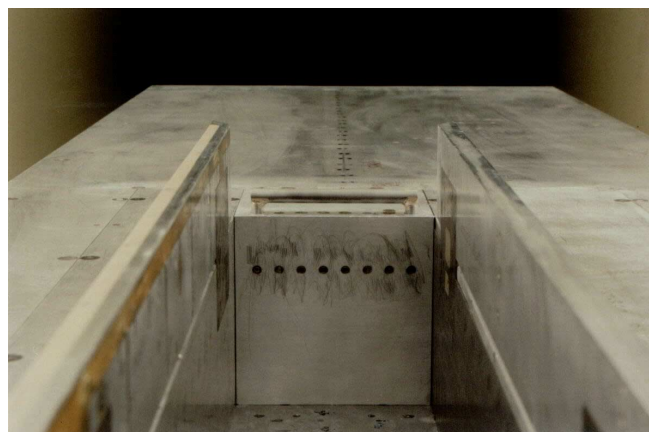
Figure 10. View (from rear of cavity) of Rod-in-Crossflow Device Installed in the DERA 1/10th scale cavity model. Vertical doors and surrounding flat plate visible in photo. (Ref. 11)
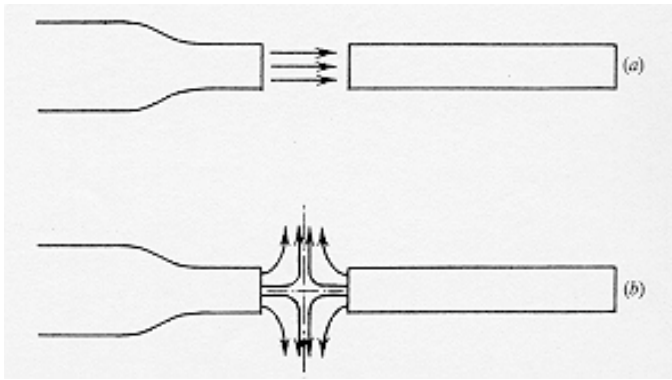
Figure 11. Schematic of Powered Resonance Tube Concept (Ref. 16)
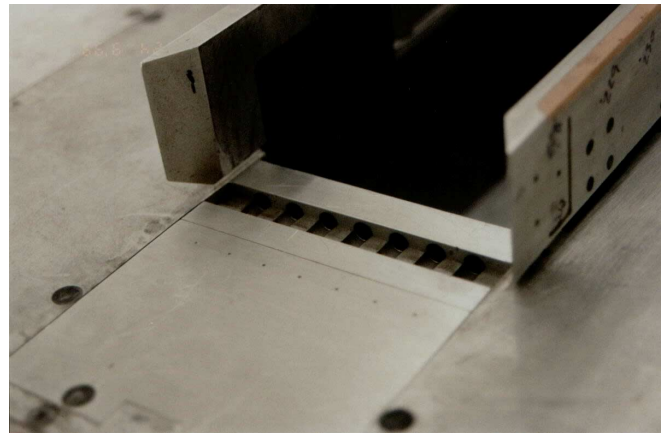
Figure 12. Close-up of Powered Resonance Tube Installation (Ref. 11).
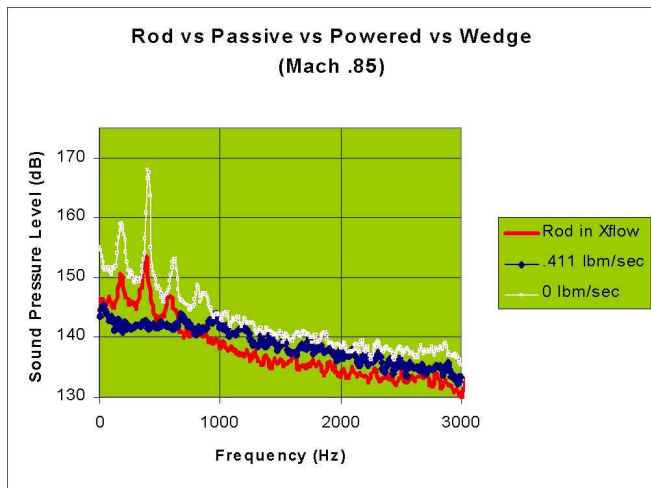
Figure 13. Suppression Effectiveness of Rod vs Powered Resonance Tube at Mach .85 (31 kHz sampling rate) Ref. 11.
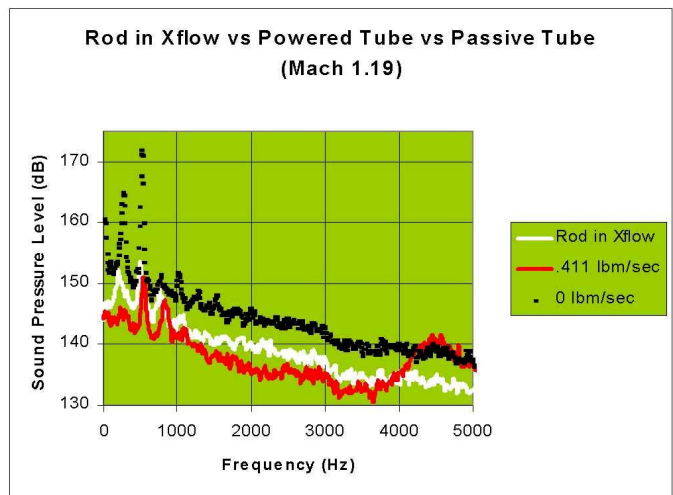
Figure 14. Suppression Effectiveness of Rod vs Powered Resonance Tube at Mach 1.19. (31 kHz sampling rate) Ref. 11.
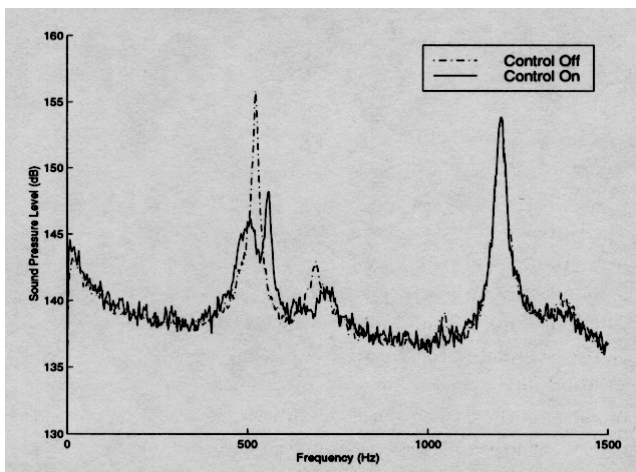
Figure 15. Reduction of 1st Mode SPL at Mach 0.74 in the PCT at NASA Langley Research Center (Ref. 20).
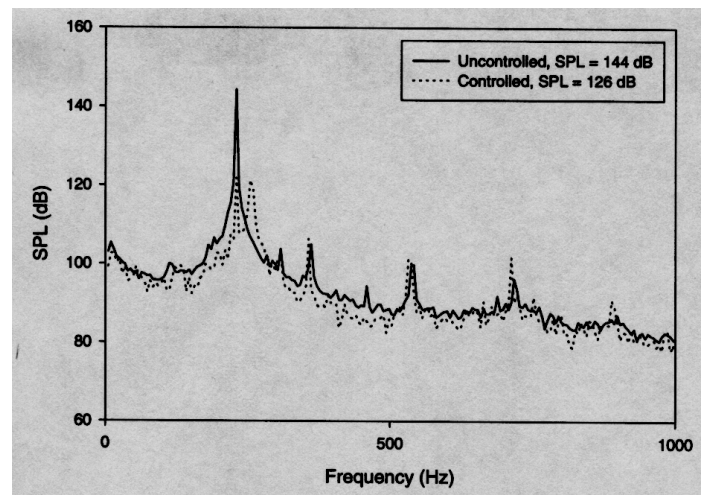
Figure 16. Measured Sound Pressure Level On Cavity Floor With and Without Piezo Flap Control (Ref. 21).
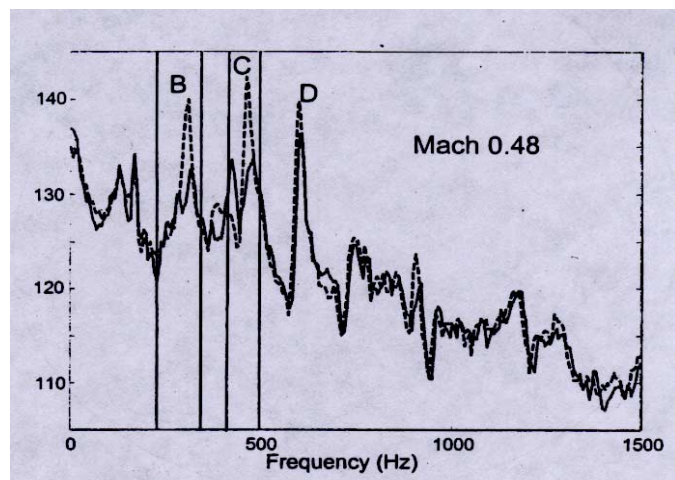
Figure 17. Acoustic Suppression Using Speaker-Driven Synthetic Jet. Multiple Pass Bands in feedback allow multimode suppression (Ref. 22)
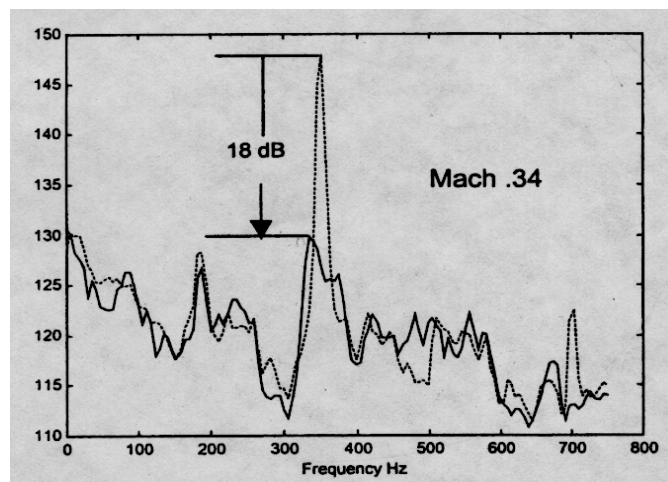
Figure 18. Acoustic Suppression Using Speaker-Driven Synthetic Jet. Closed-Loop Control, L/D = 5.0, M= .34 (Ref. 22)
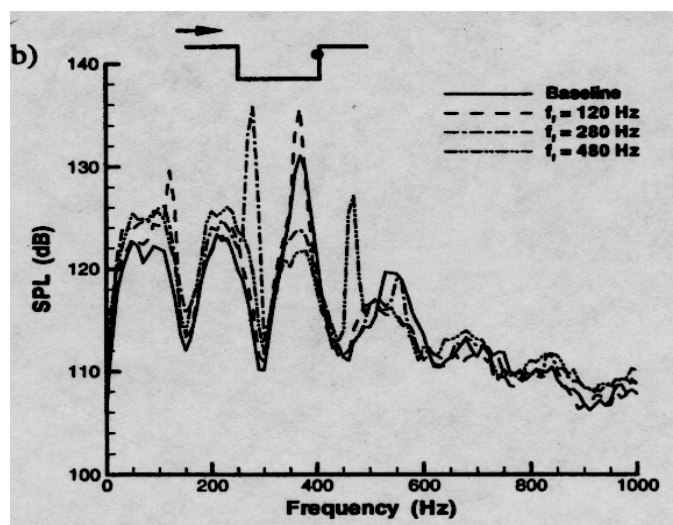
Figure 19. Spectra For Oscillatory Blowing (Zero Net Mass Addition). Rear Wall Location (Ref. 23).
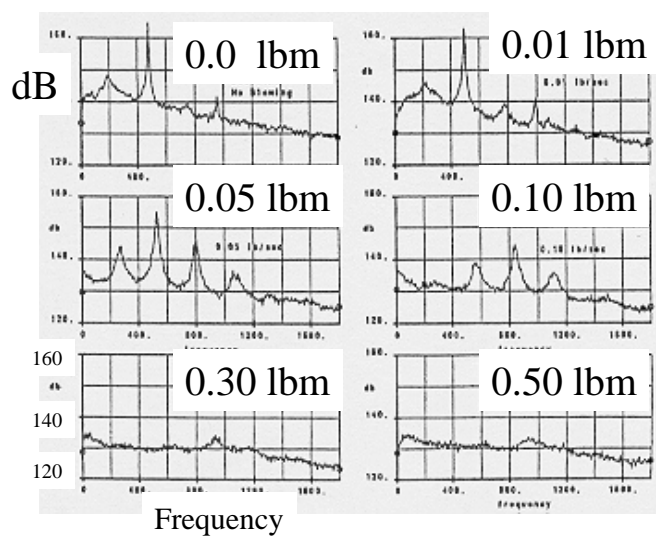
Figure 20. Suppression of Cavity Acoustic Levels With Steady Leading Edge Blowing at Mach .8 (1/10th scale – Ref. 7).
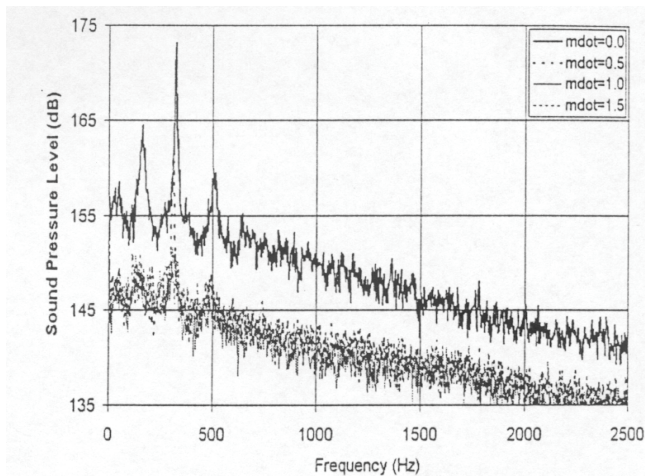
Figure 13. Mach 1.5 mass flow comparison, "full" bay.

Figure 21. Cavity Acoustic Suppression Due To Steady Leading Edge Blowing. 1/5th Scale, Mach 1.5 (Ref. 24).
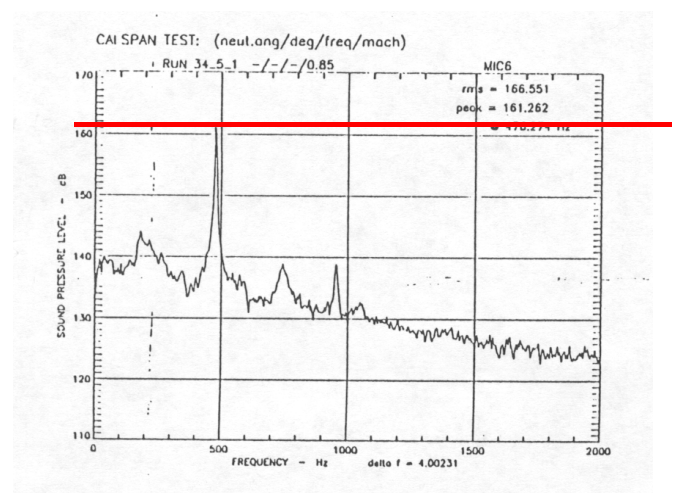
Figure 22. Baseline, Unsuppressed Spectra at Mach .85 (Ref. 25).
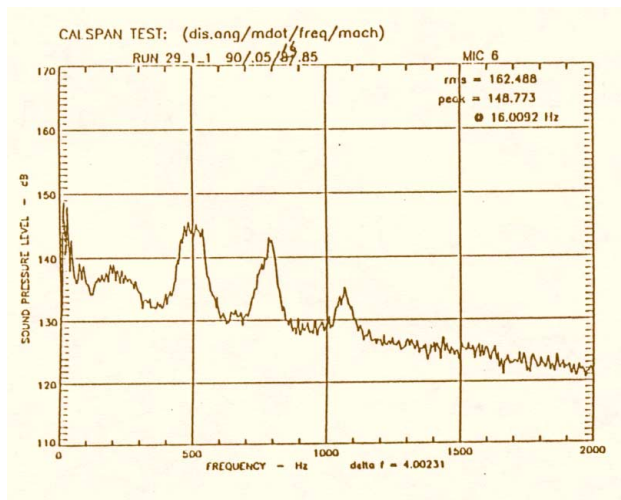
Figure 23. Suppressed Spectra. Pulsed Blowing @ 16 Hz, 0.05 lbm / sec (Ref. 25).
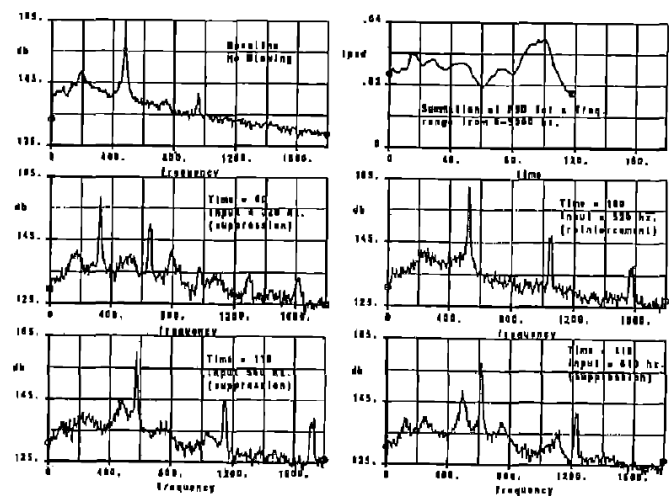
Figure 24. Suppression At Various Times Due To Pulsed Blowing. Continuous Sweep In Frequency(0 to 2000 Hz.), Mach 0.85 (Ref. 7).
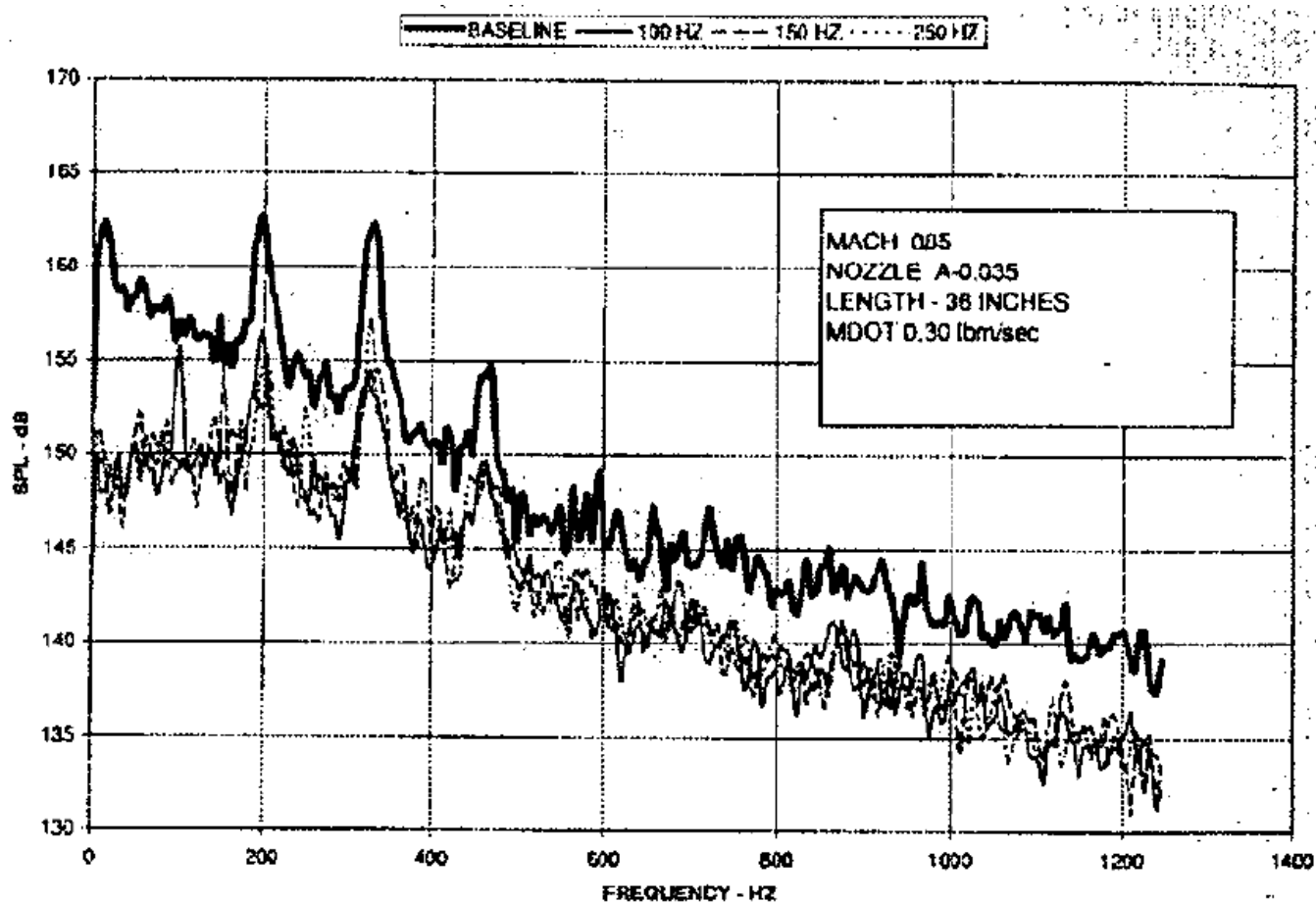
Figure 25. Figure Indicating That Change in Pulsing Frequency Has No Effect On Acoustic Suppression. Pulsed Blowing, 1/5th Scale, Mach .85, Forcing @ 100-250 hz (Ref. 26.).
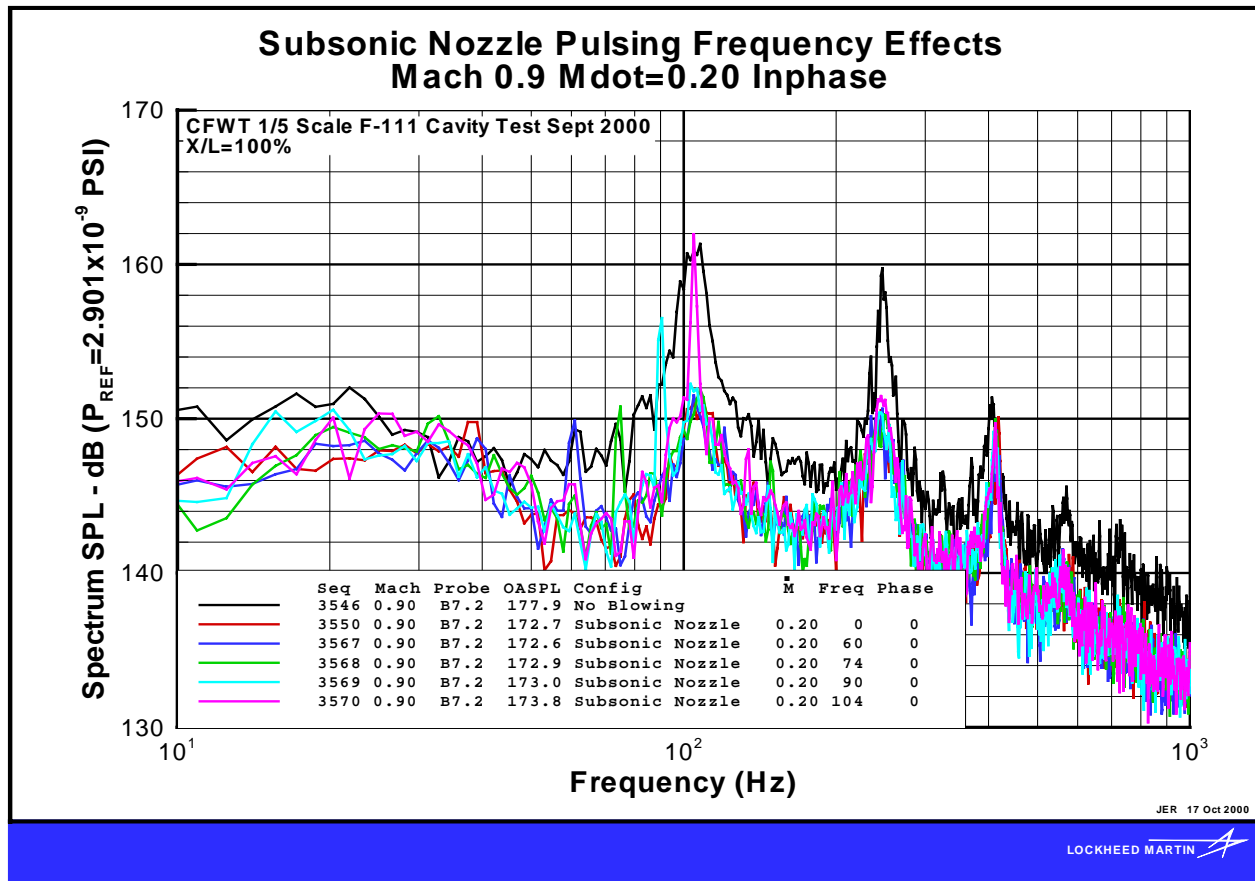
Figure 26. 20% Scale Test of Rotary Valve / Subsonic Nozzle Combination. No Additional Suppression Observed Over Steady Blowing (Ref. 28).

Figure 27. Integration of High Frequency Resonance Tube Near Lip Of Rectangular Jet Nozzle. Resonance Tube Turned Off (Ref. 29).
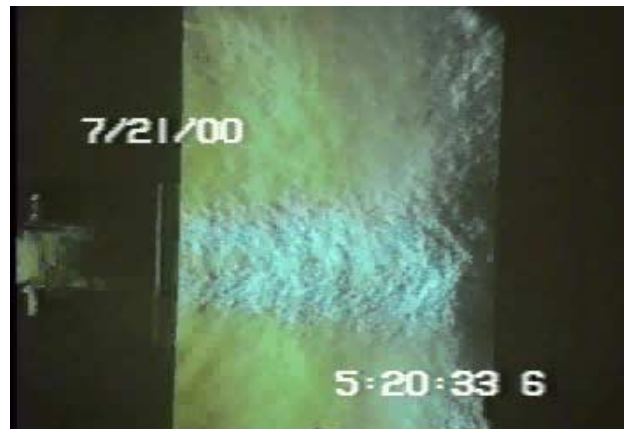
Figure 28. . Integration of High Frequency Resonance Tube Near Lip Of Rectangular Jet Nozzle. Resonance Tube Turned On (Ref. 29).
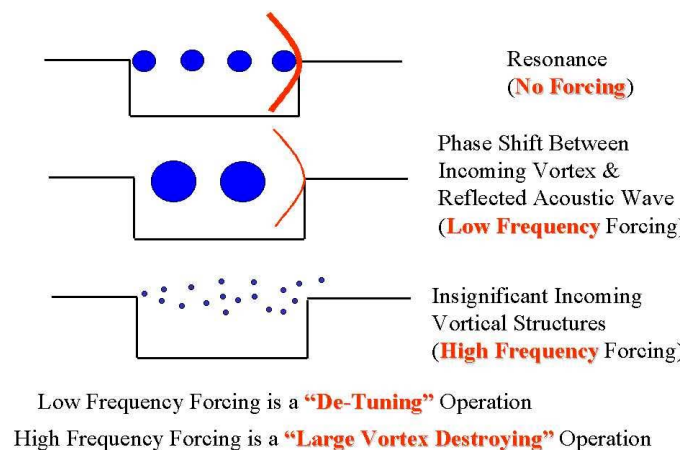
Figure 29. Schematic Illustrating Conceptual Differences Between No Forcing (Top), Low Frequency Forcing (Middle), and High Frequency Forcing (Bottom). (Ref. 11)
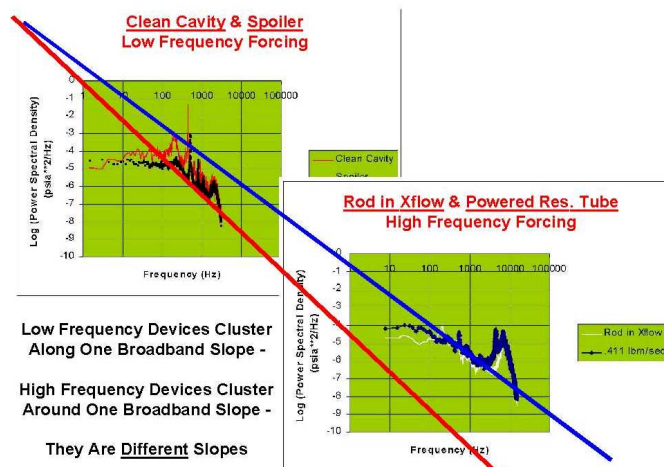
Figure 30. High Frequency Forcing Effect on Slope of Broadband Level (Ref. 11).
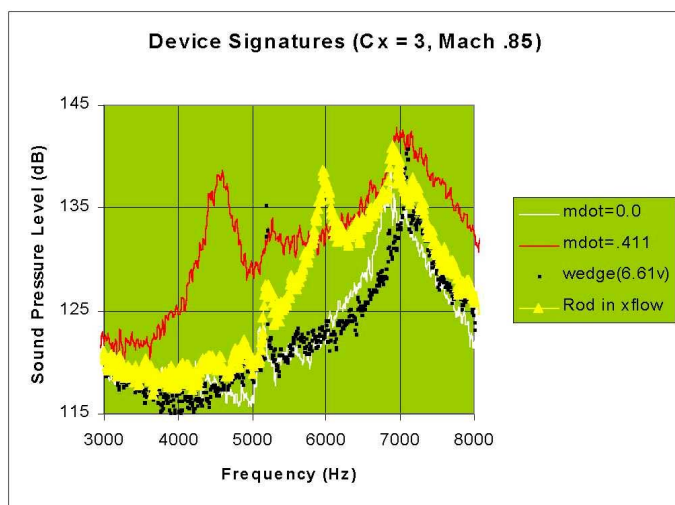
Figure 31. Spectral Signatures of Various Acoustic Suppression Devices. (Ref. 19)
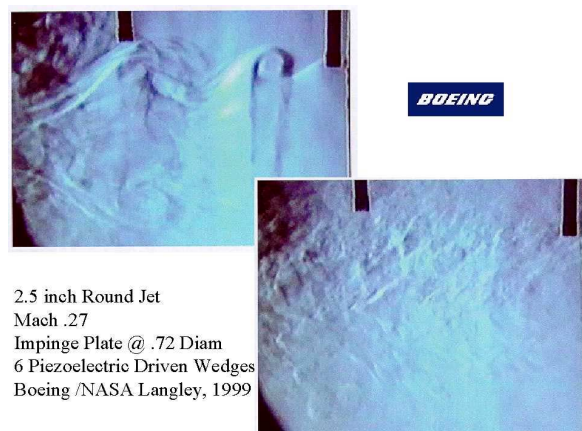
Figure 32. Schlieren Image of Jet Impinging on a Perpendicular Flat Plate. Top Image (With Large Coherent Structures) Before Suppression. Bottom Image (With No Visible Coherent Structures) After High Frequency Suppression (Ref. 30)
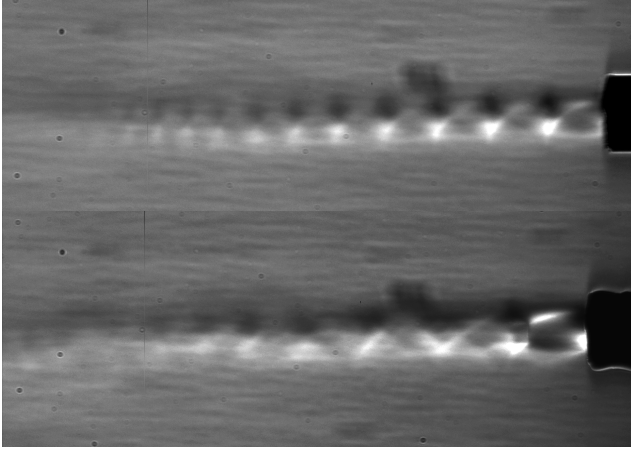
Figure 33. Schlieren Showing Periodic Shock Cells in 400 micron diameter Microjets, Top @ Po= 68 psi, Bottom @Po = 110 psi (Ref. 31)
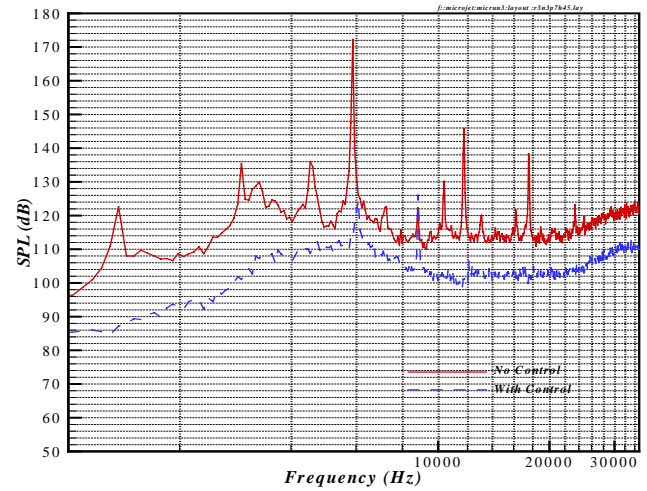
Figure 34. Spectra Showing Peak & Broadband Levels Significantly Reduced In Impinging Jet Problem With Application of Supersonic Microjets (Ref. 31).
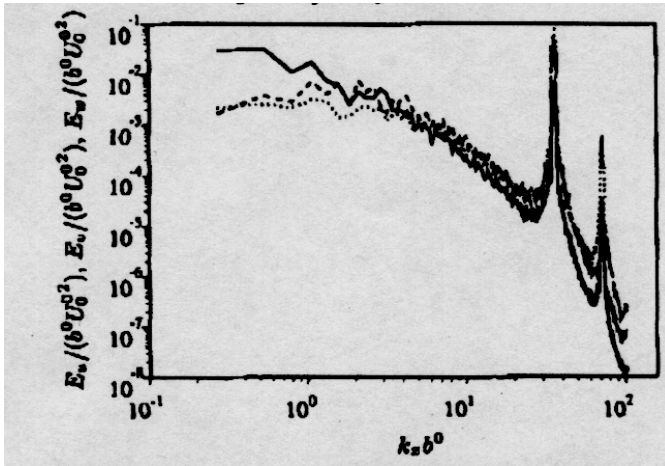
Figure 35. Spectra From Simulation of High Frequency Forcing Experiment (Ref. 32). Compare With Behavior Shown in Figure 6.
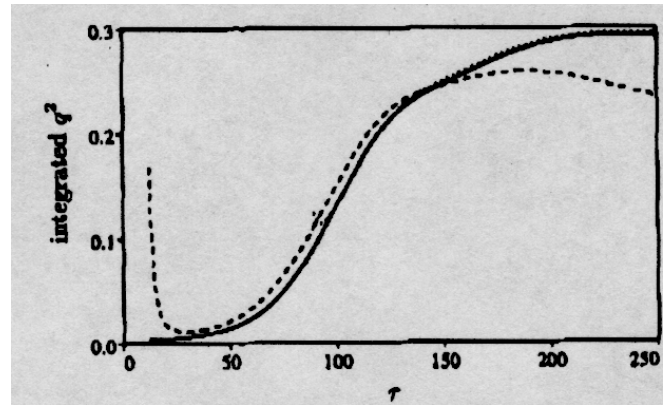
Figure 36. Integrated Turbulent Kinetic Energy As A Function Of Time (Ref. 32).
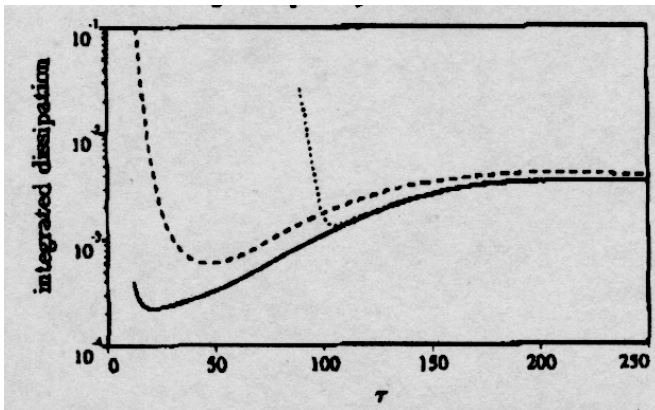
Figure 37. Integrated Dissipation Rate As A Function of Time (Ref. 32).
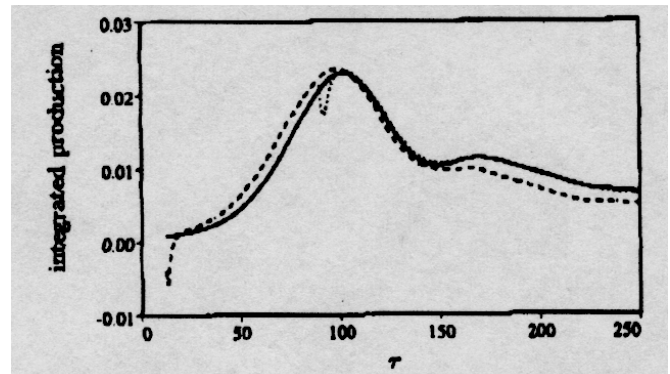
Figure 38. Integrated Rate Of Production Of Turbulent Kinetic Energy As Function of Time (Ref. 32).

Technical Evaluation Report

C.J. Eady
Chief Powerplant Engineer
British Airways
H3, TBA, S263, Heathrow, TW6 2JL
United Kingdom

OBJECTIVES

The goal of the NATO-RTO is to conduct and promote cooperative research and information exchange within NATO and with its Partners. To achieve this goal, the RTO has set out three key objectives:

- To support the development and effective use of national defence R&T and thus maintain a technological lead within the alliance.

- To meet the military needs of the alliance.

- To provide advice to NATO and national decision-makers.

The requirement for the RTO-AVT-075 Symposium on Monitoring and Management of Gas Turbine Fleets for Extended Life and Reduced Costs grew out of the activities of the RTO Working Group 28. The objective of the symposium was to facilitate additional information exchange to provide professionals responsible for monitoring and management of gas turbine fleets with guidance on existing and proven techniques, and an insight into new technologies and practices planned for future systems. Therefore, the objective of the symposium was assessed as effectively supporting the achievement of RTO's key objectives. The symposium addressed gas turbine life management issues under four session headings:

- Maintenance and Logistics Practices – knowledge of methodologies for forecasting spares requirements, parts tracking and determination of service levels.

- General Design Practices – defining the impact of component deterioration, performance sensitivities to component changes made to improve life, and performance levels required by new or different roles or mission profiles.

- Usage Data and Mission Analysis – information on monitoring systems, translation algorithms, sampling methodologies, design practices, and methodologies for assessing unforeseen in-service usage.

- Life Determination Methodologies – understanding of design models, failure modes, material properties, and life assessment methodologies.

The quality of the written papers and delivery of the presentations conveyed an enormous quantity of valuable information concerning research and development efforts in this area of specific military interest. The benefit of RTO's ability to bring together operators, logisticians, designers, scientists and academics in such highly focused symposia was evident in the lively and thought provoking discussions. In informing those who attended, provoking thought and promoting discussion, and in bringing together this collection of papers for publication and wider distribution, the RTO-AVT-075 Symposium successfully met its objective and contributed to the satisfaction of RTO's key objectives and the achievement of its goal.

CONCLUSIONS

The symposium reaffirmed and raised a number of conclusions on the subject of monitoring and management of gas turbines:

- Replacement of Life Limited Parts (LLPs) constitutes a strong cost of support driver.

- There is scope for life extension of LLPs, especially of older components under the safe-life philosophy.

- Self-reliance in lifing capabilities is important in enabling military gas turbine operators to manage in-service issues.

- Full fleet monitoring is the optimal solution for effective fleet management.

- There is a poor correlation between flight duration and component life usage

- Whilst large quantities of operational and maintenance data are collected and stored, many of the databases have severe limitations that impact on their usage and ability to support data manipulation and extraction of information on which to base fleet management decision-making.

- Data variability hinders analysis and imposes expensive conservatism in lifing methodologies.

- Greater understanding of crack propagation is urgently required and enhanced NDI techniques are essential to support life extension initiatives.

- In considering engine modification or upgrade, the whole of the engine system, including the monitoring functions, has to be considered to ensure that the probability of successful improvements and payback is necessarily high. The monitoring system requires a continuous improvement programme to ensure that fleet management is adequately supported and to realise the benefits of technology insertion.

- Life Cycle Cost (LCC) modelling is essential in supporting the business cases for modification or upgrade and for evaluating the ensuing impact of the investment. This support should be extended to inform decision making on fleet out-of-service dates to ensure that the appropriate level of logistic support is budgeted for.

RECOMMENDATIONS

To enhance monitoring and management of gas turbine fleets for extended life and reduced costs, the RTO's influence may be effectively applied to the promotion of cooperative research and information exchange in the following areas:

- Crack propagation – encourage research into this safety-related, non-competitive area.

- NDT – generate a symposium on critical component specific inspection techniques and residual stress measurement.

- Data transfer/exchange translation methods – research targeting materials and usage/damage databases.

- LCC modelling - generate a symposium.

INTRODUCTION

The continual downward pressure on defence expenditure has resulted in affordability being recognised as a key driver in future air equipment capability strategies and Life Cycle Costs (LCC) being considered with equal weight as performance in modern equipment procurement programmes. The acquisition of an engine and its associated components requires substantial financial outlay, however, it is the operating and support costs that drive the propulsion system to account for large proportions of weapon system LCC, typically 20% to 40% for air weapon platforms.

NATO armed forces specifically require:

- Highly capable forces, exploiting the operational benefits of advanced technology to enable them to make high quality contributions to multinational operations.

- Rapidly deployable forces, able to effectively project power quickly into theatre to prevent crises escalating into conflict.

- Sustainable forces, able to conduct simultaneous or prolonged operations in inhospitable environments.

- Flexible forces, able to fight and win intensive war-fighting operations, yet capable of effectively undertaking operations across the remainder of the crisis spectrum.

Financial constraint ensures that it is not possible to modernise or re-equip across all capability areas and raises the requirement for ageing systems to be retained in service for longer and possibly operated in a more flexible manner than had originally been anticipated. Sustainability of these ageing systems presents a major logistics challenge for fleet managers; they are required to ensure that operational availability remains acceptably high whilst driving support costs to necessarily low levels. With the vast majority of propulsion system LCC being consumed by operation and support activities, it is in the in-service portion of the life cycle where the benefits of advanced technology should yield significant affordability benefits. The motivation for the RTO-AVT-075 Symposium grew out of the activities of the RTO Working Group 28 and its publication of the RTO-TR-28, Recommended Practices for Monitoring Gas Turbine Engine Life Consumption. The aim of this meeting was to promote additional exchange of information on gas turbine life management techniques for improved support of existing in-service systems. Although the meeting was not focused on the development of new gas turbines, reviews of emerging systems were valuable in illustrating how previous monitoring shortfalls are being addressed for next generation equipment and highlighting technological advances that may become available for modification and upgrade programmes.

EVALUATION

The symposium comprised 24 technical papers, presented in 10 sessions under four major session headings. Although three papers were withdrawn, three additional papers were offered to restore the programme and, indeed, make a significant contribution to it. The breadth of the contributor-base, with papers submitted from a wide cross-section of NATO and her allies (Chart 1) and an even wider audience participation, awarded the symposium much credibility in its aim to promote, at a multi-national level, the exchange of research and development information on gas turbine life management techniques.
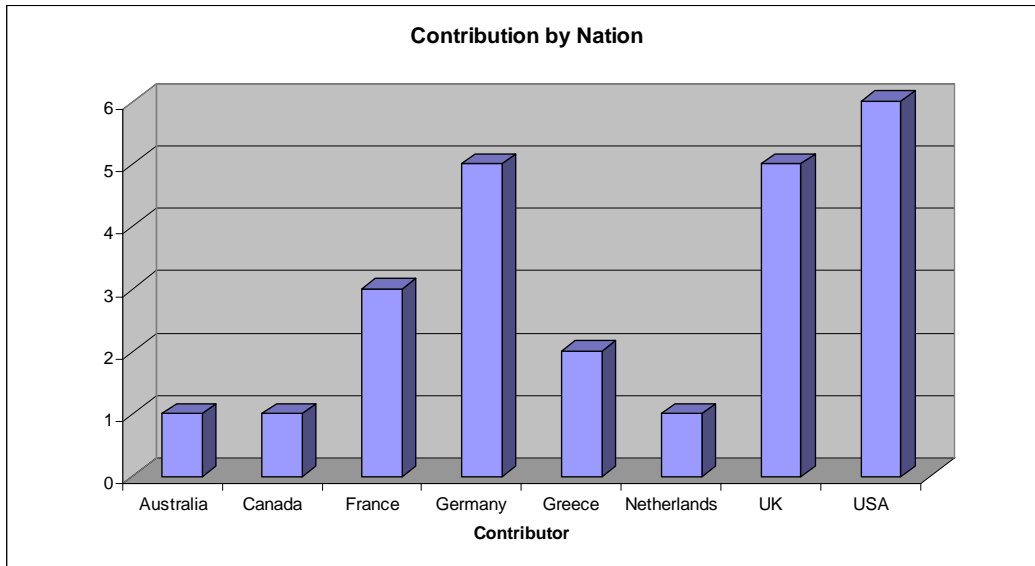
Chart 1

The 'contribution by sector' analysis (Chart 2) confirmed that the customer focus had been strongly represented and that all areas of research and development were able to contribute to the topic. The significant presence of 'independent' organisations was considered to be indicative not only of the openness of this topic to non-military and non-OEM technologies but also of the privatisation of government RTOs
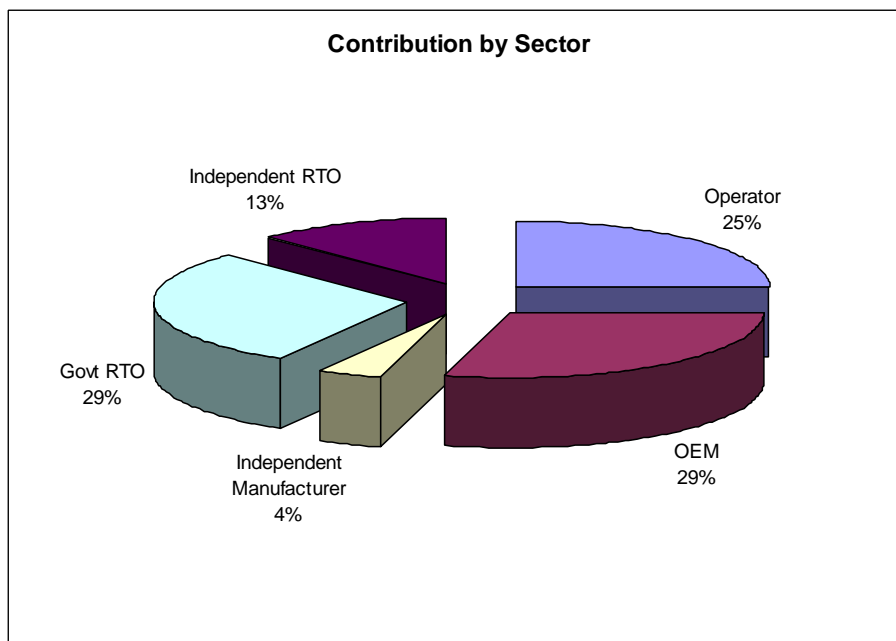

Chart 2.

The symposium content had been arranged to flow from the higher level objectives of maintenance and logistics practice, through general design practices, various approaches to usage data and mission analysis, into the intricacies of component life determination. The desired effect was achieved although the absence of some abstracts and papers for review in advance of the meeting resulted in allocation based only on the title of the paper. For the purposes of evaluation, a slightly revised allocation of papers to that followed by the symposium programme will be applied.

The Meeting was opened with a Plenary Keynote Address that set the scene for the symposium by discussing the management challenge posed by ageing aircraft fleets. This theme was strongly continued in the Keynote Addresses with Mike Botley clearly illustrating the strengths of functional collocation brought about by the

formation of the Warship Support Agency and the move to Integrated Project Teams. He discussed the impact of repair and overhaul studies and the detailed process management that has enabled significant cost and Turn Round Time (TRT) reductions. Inventory, or cost of stock-holding, reductions had also been achieved without reducing the level of operational support. Within this climate of cost reduction and competition, contrary to what might be expected, the relationship with industry had actually been improved through the application of incentivised contracts and partnering principles. Otha Davenport stated that ageing engine programmes always struggle to secure funding for new technology insertion and that, although new roles and manoeuvres and continued demand for performance may impose additional cost, engine support budgets were not factored for any increases during old age. This was contrasted against the many modification programmes, such as retrofitting of modern digital engine control systems, that had demonstrated significant financial and operational benefit. He described how the USAF had embraced the use of an Engine Life Management Plan to provide a comprehensive picture of component life, usage, maintenance, upgrades, wear patterns, deterioration rates etc. The plan is updated on a two-year cycle and is used by skilled engineers and logisticians to produce detailed workscopes for engines passing through overhaul, to achieve build standards matched to the operational requirement. The approach was described as RCM rather than OCM-based and claimed to have doubled engine on-wing life for the C5 fleet.

Maintenance and Logistics Practices

The fleet management practices highlighted in the Keynote Addresses are aimed at developing and concentrating the capabilities for forecasting spares requirements, parts-life tracking and determination of service levels. However, the studies and methodologies necessary to support them require data to fuel the analyses and generate the information upon which appropriate management decisions can be made. Paper 1 provides an insight into the amount of data that is available for the RAF Tornado fleet but also illustrates the difficulties faced in trying to manipulate data for a purpose other than that intended. It was found that data had not been generated and stored with the integrity and granularity necessary for the new purpose and, with it embedded in a multitude of separate databases not designed for the type of interrogation necessary, that the analysis was, at best, arduous and, at worst, unrealistic and misleading; an issue highlighted in a number of other papers.

It is shown that the bulk of RB199 engine support costs for RAF Tornado fleet operations are attributable to the in-service phase. Difficulties in securing full predicted benefits from modification action designed to address durability shortfalls are used to illustrate the importance of adopting a systems approach to the development of any life extension project; the application of skilled engineers and logisticians supported by data from monitoring and trending of both operational and maintenance performance considering the whole engine. This theme was continued in Paper 6, which described the evolution of SNECMA monitoring capabilities in concert with operational maintenance policies, and in Paper 19, in which the reliability-centred approach employed by Turbomeca in developing helicopter engine maintenance strategies was described. Paper 4 expands on the systems approach theme in describing the operation and benefits of a fleet support environment based on pooling of engine assets, utilising a closed-loop management system that confirms the interdependence of engine fleet management and monitoring system performance.

The paper, 'Risk Assessment Methodologies for Fracture Critical Components', discusses the different approaches that must be adopted, depending on the nature of the issue, in quantifying the risk to in-service components from unforeseen damage mechanisms or failure modes. Drawing upon risk analysis experience, the paper introduces a modified decision matrix that offers the flexibility to present the results in the most appropriate format for fleet management decision-making.

General Design Practices

The design and implementation of engine monitoring systems are daunting tasks; Paper 3 draws upon the past 15 years of experience in the introduction and operation of the OLMOS system to discuss the challenge. The paper strongly states that monitoring systems are not one-off improvements. Not only is the system required to respond to changes in the engine, the effects of ageing, modification, and changes in use, but the monitoring system itself requires a development programme to ensure that it is able to meet the increasing demands of the fleet management task. Technology insertion and modifications to improve monitoring capabilities are notoriously

difficult to justify, the payback periods may be extensive and the benefits may be viewed as intangible. However, unless the systems approach to engine modifications is extended to include the monitoring functionality, it is likely that project timescales will be extended and perceived benefits will remain beyond reach; component improvements operated under old lifing methods will never yield the return on investment that justified them. Similarly, advances in monitoring technology or data analysis techniques may be able to eliminate conservatism in the lifing methodology and make significant savings on critical parts replacement costs. This is illustrated by the application of plausibility boundaries to manage usage data scatter; the paper describes how major savings are made possible through realistic correction of outliers, often due to human data handling, rather than applying a worst case assumption.

The forecasting of engine support costs and justification of system modification and upgrade programmes demand the support of credible and effective LCC studies. The MTU LCC simulation model for maintenance, repair and operation is discussed in Paper 2 and clearly identifies the interdependence of various cost parameters impacting on the engine fleet. LCC calculations present similar multivariate optimisation challenges to those experienced in component design. Paper 5 discusses a formal method of coupling multi-disciplinary analysis with probabilistic methods and optimisation of design; a method that not only offers an exciting design route but also provides valuable experience of integrating established tools into an effective multi-level analysis suite.

Paper 11 provides a detailed briefing on the EJ200 engine monitoring and diagnosis system architecture and functionality; the discussion of lessons learned throughout the project is of particular value. As might be expected, the drive for increased functionality features strongly in potential development plans, however, the most significant recommendations are for a streamlined development process, with earlier EHM development and the inclusion of units in engine development and testing, and for greatly simplified system architectures and standardised interfaces.

Usage Data and Mission Analysis

Effective fleet management depends upon the timely receipt of accurate information on the state of health and usable life of the components throughout the system. Papers 7 and 8 focus on the health monitoring functions of vibration and wear debris analysis, and illustrate the benefits of applying new technology and advanced data processing to these established tasks. The vibration monitoring system claims to be achieving high quality results and has been designed with strong attention to reliability issues; a spurious indication has almost the same operational impact as a true fault but degrades confidence in the monitoring capability. The application of pattern recognition algorithms to wear debris analysis is being used to develop a consistent and reliable method of interpreting SEM/EDX results; such techniques are essential in minimising manual operator errors and provide insulation from experience gaps caused by changes in staff. However, it is interesting to note a point made during the presentation, that an operator guided system is necessary to overcome spot analysis errors and to manipulate debris to identify coating materials, ie the need to test each side of the particle.

Papers 9 and 10 discuss the optimisation and simplification of Gas Path Analysis (GPA); the first extends the singular value decomposition of the Jacobian matrix in an attempt to optimise the sensor suite necessary for health monitoring, and the second investigates the accuracy of multiple handle GPA as a method of both simplifying and speeding analysis routines. The integration of control and monitoring systems will undoubtedly lead to sensor selection being driven by both requirements and studies such as these are important to inform both the monitoring system retrofit community and the designers of new systems.

In Paper 12, discussion of the NASA Intelligent Life Extending Control (ILEC) programme applies the integration of control and monitoring to the mitigation of component damage during engine acceleration and cruise. The use of a control 'buffer' to lessen the impact of a demanded input is an emotive topic, however, through both theoretical and hardware in the loop simulation this project has shown significant reductions in engine damage in exchange for minor reductions in acceleration response or cruise Mach number. The philosophical arguments over placing a buffer between the pilot's demand and the engine's response will remain but this paper will contribute to the debate by quantifying what can be achieved from extending the role of on-board damage estimation to supervisory control of the engine.

Life Determination Methodologies

Papers 14 and 22 discuss genuine in-service lifing issues and illustrate both the latitudes and the limitations involved in the safe-life philosophy, on the one hand, the conservative analysis and large safety factors providing scope for life extension, and on the other the requirement for regular lifing reviews to ensure that the validity of assumptions has not been eroded by actual material, manufacturing and usage factors. The ability to address these particular cases depended on a significant understanding of design models, failure modes, material properties, and life assessment methodologies, and therefore, both papers demonstrate the importance of a degree of self-reliance in lifing capabilities to the management of military gas turbine fleets.

Whilst material properties, surface condition and operational exposure may detrimentally affect the usable life of a component, the ability to accurately monitor and record the life consumption rate is also imperative in achieving cost-effective utilisation of that life. Paper 15 and the paper entitled, 'The Assessment of Engine Usage Data', consider how to bridge data gaps to avoid the imposition of an expensive 'worst case' exchange rate filler. No monitoring system is successful in capturing 100% of the cycle counts, failures may be due to monitoring system faults, storage media damage and data corruption during transfer and, especially in the case where only a sample of the engine fleet is monitored, data loss can be significant. Large variability exists within usage data and there is often a poor correlation between mission duration and cycles counted, and between SPC and cycles counted. These papers provide guidance on the statistical methods that may be effective in extrapolating limited monitoring results.

A significant amount of work is being sponsored by the US Air Force in a programme designed to reduce the anticipated replacement cost of LLPs. Paper 16 considers crack propagation life extension, without increasing risk, by taking credit for residual stresses. Residual stress relaxation under operational exposure is discussed and the influence of various levels of retained residual stress on crack propagation is assessed. Development of this approach into a practical lifing methodology depends upon the availability of advanced NDI techniques capable of monitoring residual stresses. Papers 17 and 21 consider the influence of loading on crack propagation, the first assessing the effect of overload on subsequent damage accumulation, and the second assessing the influence of underloads on damage accumulation. These three papers should be read in conjunction to gain benefit from their contribution to the understanding of fatigue crack growth behaviour and their comment on the conservatism of current lifing methodologies.

Modern, high temperature, metallic materials present significant lifing challenges that demand advanced methodologies. Paper 20 describes the demonstration of an integrated analysis tool for the lifing of turbine components. The tool is capable of accepting data from on-board monitoring systems and comprises an engine gas path model, FEA for thermal distribution and mechanical loading, life modelling (LCF, creep, oxidation and crack growth) and has been applied to the lifing analysis of a film-cooled turbine blade. The results exhibited large uncertainty due to the inaccuracy of the life prediction model, especially in crack initiation and creep, caused by scatter in the material data. However, the tool has shown itself to be useful for relative life predictions and offers the potential to input to on-condition maintenance by tracking the life consumption of individual components and enabling optimisation of aircraft operational use through determination of life consumed in specific operational manoeuvres/sortie profiles; a feature that may contribute significantly to LCC calculations and 'what if' analyses for aircraft role change or fleet management of run-down to retirement.

The paper entitled, 'New Lifing Methodology for Engine Fracture Critical Parts,' states that the safe-life methodology is increasingly unable to cope with modern design complexities. A methodology employing non-linear 3-D FEA to calculate actual component stresses, modelling of both crack initiation and propagation phases, and accounting for the effect of material volume (size effect) is described. Prediction accuracy was seen to fall off at 600°C, prompting the need for a review of the fracture mechanics model, however, predictions show good agreement with a large proportion of the materials database and component predictions are encouraging. This work represents a significant achievement and will yield a valuable tool once a residual stress model has been incorporated and validation against other materials has been completed.

Paper 24 presents the results from development tests of a fatigue-creep-oxidation interaction model that shows much promise for the prediction of crack propagation in high temperature alloys. The crack propagation rate was over-predicted from simulated mission profile due to effect of minor cycles. The fatigue-creep-oxidation model

has been extended to account for complex loads in non–isothermal conditions but will also need some development to account for a wider temperature range.

DISCUSSION

The symposium sought to discuss monitoring and management of gas turbine fleets for extended life AND reduced costs, thereby setting a significant challenge to the contributors. It is without doubt that military gas turbine systems are required to remain in service for extended periods and the content of the papers has graphically illustrated that the replacement of LLPs constitutes a strong cost of support driver; over the next 20 years, disk replacement costs to for the US Air Force are expected to rise to $3bn.

It is recognised that the management of engine fleets demanded large quantities of operational and maintenance data to support decision-making. Whilst large quantities of data are collected and stored, many of the databases have severe limitations that impact on their usage and ability to support data manipulation and extraction of relevant information. Material and usage data variability also hinders analysis and imposes expensive conservatism in lifing methodologies. More effort should be made in developing interfaces between databases and releasing the potential stored by the NATO member nations.

In monitoring for engine life management, there is a consensus view that full fleet monitoring is the optimal solution. The meeting drew out the importance of Thermal Transient Algorithms in realising life extension benefits and support cost reductions, a point strongly made in the RTO Technical Report 28. However, modifications to extend component life or to insert additional monitoring functionality can be very difficult to justify unless safety related. Life cycle cost modelling is essential in supporting the business cases for modification or upgrade and for evaluating the performance of the system following introduction. It would be of great benefit to increase the exchange of information on LCC analysis techniques and to develop common approaches to modelling.

It is also stressed that a modification often has much wider impact on the system than just at the point of application. The important conclusion is that the engine system, and that includes its monitoring functions, both airborne and ground-based, has to be considered as a whole system in assessing the potential impact of modifications and upgrades. The single largest monitoring system improvement desired was to simplify both the airborne and ground-based system architectures to eliminate the impact of multiple interfaces and obviate the need for human intervention in data handling, as this always carries an inherent error rate. The subject of storage capacity was considered to be one of development time versus technology risk and fell into the category of obsolescence management.

It is important to note that due to high non-linearity of usage data, extrapolation of results is difficult and can be dangerous, similarly, applying a worst case exchange rate to data gaps is overly conservative and consequently expensive. The application of plausibility ranges to identify nonsensical outliers and statistical processes to bridge the gap, relocate the outlier or quantify the risk is viewed as an essential feature of the monitoring system to minimise the risk of overruns and promote airworthiness.

It is considered that due to conservatism in the safe-life philosophy design and the simpler design and materials processing routes, there is much scope for component life extension for older, conventionally forged LLPs. To support life extension initiatives, there is an urgent need to develop greater understanding of crack propagation and there is a specific need for improvements in NDI techniques for both crack detection and for residual stress measurement. The symposium brought out the importance of self-reliance in lifing capabilities in enabling military gas turbine operators to manage in-service issues, this type of expertise may be difficult to preserve in a climate of cost reduction and privatisation of government laboratories.

Forecasting of the Effect of Potential Aero Engine Modifications on Life Cycle Cost

F. Heitmeir, H. Summerer, E. Fendt
MTU Aero Engines
Dachauer Strasse 665
D-80995 Muenchen
Germany

1) Introduction

The life-time of an engine normally extends to over 50 years. During this long period engine technology moves on. New materials, new calculation procedures and new design features become available.

Introducing new technological elements is relatively easy during the early engine design phase.
The more mature the engine design becomes, the more difficult it is to introduce new features, because they affect numerous other components or design parameters.

It is not possible to incorporate a great number of new features into an engine which is already being operated by customers for financial reasons as well as from a logistical point of view.

During the operation phase the benefit of introducing modifications must be thoroughly weighed with respect to quite a number of parameters.

However, some modifications are important to be implemented due to flight safety reasons or due to cost saving aspects. The latter aspect will be discussed in this paper.

2) Basics of the Life Cycle Cost analysis

To find out, if a modification saves money during the rest of the operational life of the engine a business case has to be established.

Due to the existing interdependencies of the relevant parameters, cost estimation is a complex task.

For proper calculation of the business case, information such as
- number of aircraft
- existing engine standards
- maintenance, repair and overhaul procedures
- spare parts supply

          - documentation
          - etc.

must be available and considered very carefully. This is done by means of the so-called Life Cycle Cost Studies (LCC Studies).

The Life Cycle Cost calculation covers all phases of an engine life, starting from the beginning of its development until its retirement from the service, i.e. the cost of the
          - development phase,
          - procurement phase
          - and operation phase.

Of major importance for an LCC analysis is the operation phase.

Furthermore, it is important to consider how introduction of a modification into the fleet is to be performed. The two extreme positions are on the one hand to introduce a modification during natural arisings. In this case introduction of the modification will take a long time. On the other hand a quick retrofit campaign could be run. And, of course, in between there are many different ways with different implications concerning cost and introduction time of a modification.

Three different phases have to be taken into account for changing an engine standard:
       - operation with the current standard,
       - conversion phase,
       - operation with the new standard.

These phases are overlapping and dependent on the embodiment procedure chosen.

Each phase has its specific cost parameters and of course these parameters depend on each other .

3) Life Cycle Cost analysis

To calculate life cycle costs with respect to the above mentioned influencing parameters, a computer-based programme was developed at MTU which is capable of incorporating maintenance, repair and operation parameters.
The computer code has no restrictions as to the number of aircraft.

The required input parameters are as follows :

-    Engine delivery rate - squadron/fleet
-    Flight hours/years of operation
-    Component life characteristics
  - Failure mode distribution function
  - Probability of secondary damage
  - Life limitations - remaining issue service lives

- Maintenance strategies (concepts)
  - Various maintenance concepts
  - Inspection intervals (borescope inspection)
  - Preventive maintenance
    - Maintenance levels
    - Maintenance turnaround times, transportation
    - Maintenance capacities
    - Man hours per event
- Engine, module and component prices

- The possible output parameters are :

- Engine, module, component and accessory arisings
- Failure rates depicted by removal reason
  - scheduled/unscheduled
  - secondary damage
  - random or time-dependent failure
- Repairs shown by maintenance level and reasons for removal
- Maintenance/repair man hours
  - by maintenance level
  - by scheduled/unscheduled maintenance action
- Material costs of major components (quantity and DM/EFH)
- Spares requirements (engines/modules(components))

4) Results

The results are shown in a typical graph of a LCC Study.

5) Summary

The evaluation of the cost effectiveness of an engine modification is affected by a lot of parameters which depend on each other in many different ways. Due to the great amount of variables to be considered, a computer-based simulation model is necessary for the calculation.

One computer model was described in this paper. A number of possible results were discussed based on typical examples. Depending on the input parameters and the philosophy chosen, the results are varying.

This clearly indicates that the computer programme, although being a very powerful tool, does not show correct results, if there is no understanding of the calculation philosophy and if there is not a correct set of input parameters available.

However, if operated by specialists, the programme is a very helpful tool for both the engine manufacturer and the operator. The benefit of a modification will show up very clearly.

Overview of the mainpoints for the presentation

- The life-time of an aero engine extends to over 50 years.
- Example : Fuel consumption has been significantly reduced over the years.
- Modifications are necessary due to flight safety and cost reasons.
- Life cycle cost (LCC) analyses of modifications result in invaluable contributions to the Business Case.
- Life-cycle cost cover all phases of an engine life.
- Of major importance for an LCC analysis is the operation phase.
- Each modification is carried out in three phases.
- Each phase has its specific relevant cost parameters.
- The various cost parameters are inter-dependent.
- MTU has developed a computer-based LCC simulation model for maintenance, repair and operation.
- The required input parameters vary for technical and service-related modifications.
- The output parameters can be selected individually and the output used for further processing.
- The results are graphs and diagrams for easy comparison of various options.

Paper 2: Discussion

<u>Question from R Bolwell – UK MoD</u>

How much does safety cost?

<u>Presenter's Reply</u>

It depends on the special case, of course. Safety must be ensured at any time during the operational phase of an engine life cycle. If a flight safety case occurs, immediate actions are necessary to solve the problem. Different solutions are possible, one way may be to introduce a modification.

In the case of a flight safety issue, it is not necessary to base the decision on a detailed business case and to perform intensive Life Cycle Cost (LCC) studies because, to avoid the fleet being grounded, action must be taken in all circumstances.

On the other hand, a non-flight safety related modification could be offered to the customer. In which case, the customer should be provided with an understanding of the benefits to enable him to decide whether or not to procure the modification.

This second case is the main field for LCC calculations.

<u>Question from D K Hennecke - Germany</u>

How sensitive is your prediction to the accuracy of the input data? Which parameters are the most critical?

<u>Presenter's Reply</u>

As presented in the paper, all cost parameters are strongly interdependent. The main challenge is in setting up a correct set of input data; the results depend strongly on this input data.

The following factors would exert major influence over the LCC results:

- The way in which the modification was introduced, ie through a campaign or on natural attrition arisings.
- The residual value of the old parts, ie whether they could be reused or not.
- The cost of the affected components.
- The subsequent reduction in maintenance activity.

Due to the large number of parameters exerting influence over the LCC forecast, it is not possible to identify critical drivers; the relative importance depends upon the case in question.

This page has been deliberately left blank

Page intentionnellement blanche

Long-Term Operation and Maintenance of Engine Monitoring Systems - Recommendations Derived from 15 Years of OLMOS Use by the GAF

Hugo Pfoertner
MTU Aero Engines GmbH
Dept. TPM
P.O. Box 500640
80976 Munich
Germany
E-mail: hugo.pfoertner@muc.mtu.de

Abstract

Some aspects of the operation of a monitoring system over a time of several decades are discussed. It is shown, that the classical system design approach with well-defined definition, development, introduction and operation phases has to be replaced by a network of parallel activities. These activities are driven by the requirements to maintain fleet readiness and safe operation under the constraints of shrinking budgets and personnel reduction. Other factors driving the need for adaptations and enhancements are the obsolescence problems caused by the significantly different time scales for IT system components used in commercial or consumer oriented applications and for military applications.

The most important source for modifications in an engine monitoring system is the engine itself. A well-coordinated approach is necessary to match the introduction of new engine hardware with the required consequential changes in all components of the monitoring system. High quality of the monitoring results produced during operation can only be maintained by well-designed data handling procedures, user interfaces and appropriate documentation and training. There remains a practically unavoidable small percentage of data errors introduced by human data handling. Due to the potentially severe consequences of undetected errors in the life usage data of fracture critical engine components, it is necessary to apply suitable plausibility checks that are derived from statistical models of the life usage process in a fleet of engines.

Overview

It is very likely, that in-service times will exceed 40 years for existing and newly designed military jet or helicopter engines. One prerequisite for an achievable and safe extension of engine usage times is the application of engine fatigue life usage monitoring. The German Air Force decided to introduce fleet-wide on-board engine monitoring for the RB199 engines 15 years ago [BP97]. The application of the OLMOS system has made available comprehensive life usage data for all fracture critical parts to the fleet managers of the Tornado aircraft.

The operation of the OLMOS system has revealed that monitoring systems themselves need a considerable amount of maintenance and adjustment. Monitoring systems have a lot of internal and external interfaces, as shown in *Figure 1* [BPR98]. Both hardware and software cannot be kept unaltered over decades. The supposedly cost-saving use of COTS components causes a continuous need for adaptation with a frequency given by typical life times of operating systems, software development tools, database systems and of course also of computer hardware. The typical mismatch in time scales between commercial IT systems and their military derivatives is illustrated in *Figure 2* (Source: [Al00]). Strategies are known how to mitigate both hardware and

software related obsolescence problems [CT98, NRC01]. Implementing these strategies will require sufficient budgetary support. If this support is not available, equipment and methods have to be used beyond their planned replacement dates, which may cause data quality problems and frustration of personnel. Updates in the IT systems will also affect user interfaces with consequential requirements for documentation and training. Due to personnel reduction, system operators often are assigned their duties as secondary or even tertiary tasks. These changing skills of available personnel have also to be addressed in appropriate adaptations of the user interfaces.
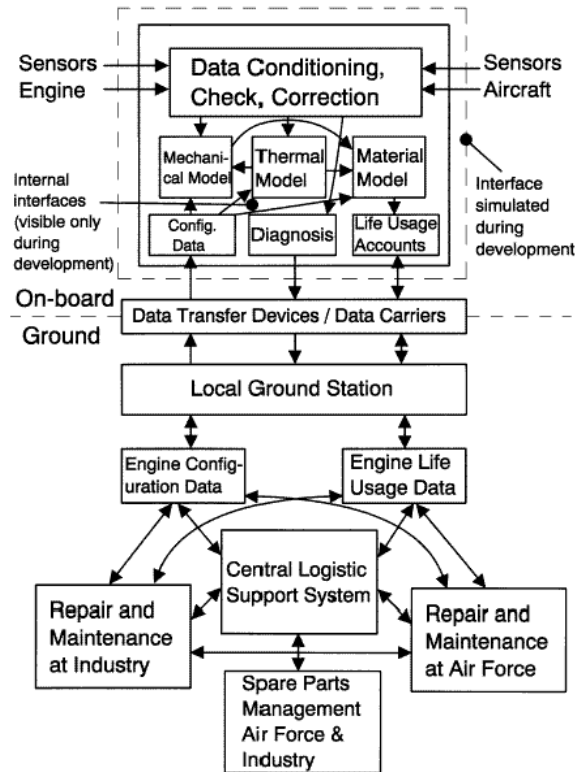
Figure 1: *Interfaces of a Life Usage Monitoring System (from [BPR98])*
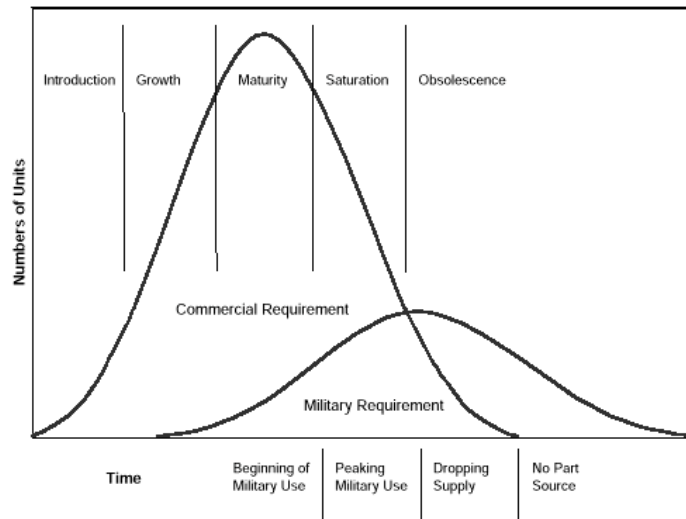
Figure 2: Commercial and Military Time Scales for IT Equipment (from [Al00])

Figure 3 shows the hardware components and interfaces of OLMOS. Together with the high complexity of data handling in the connected logistic systems of the air force and of industry the need for well-organized and coordinated procedures in the maintenance of this system is self-evident. A failure to address data management challenges properly would waist many of the system's potential benefits [HM98].
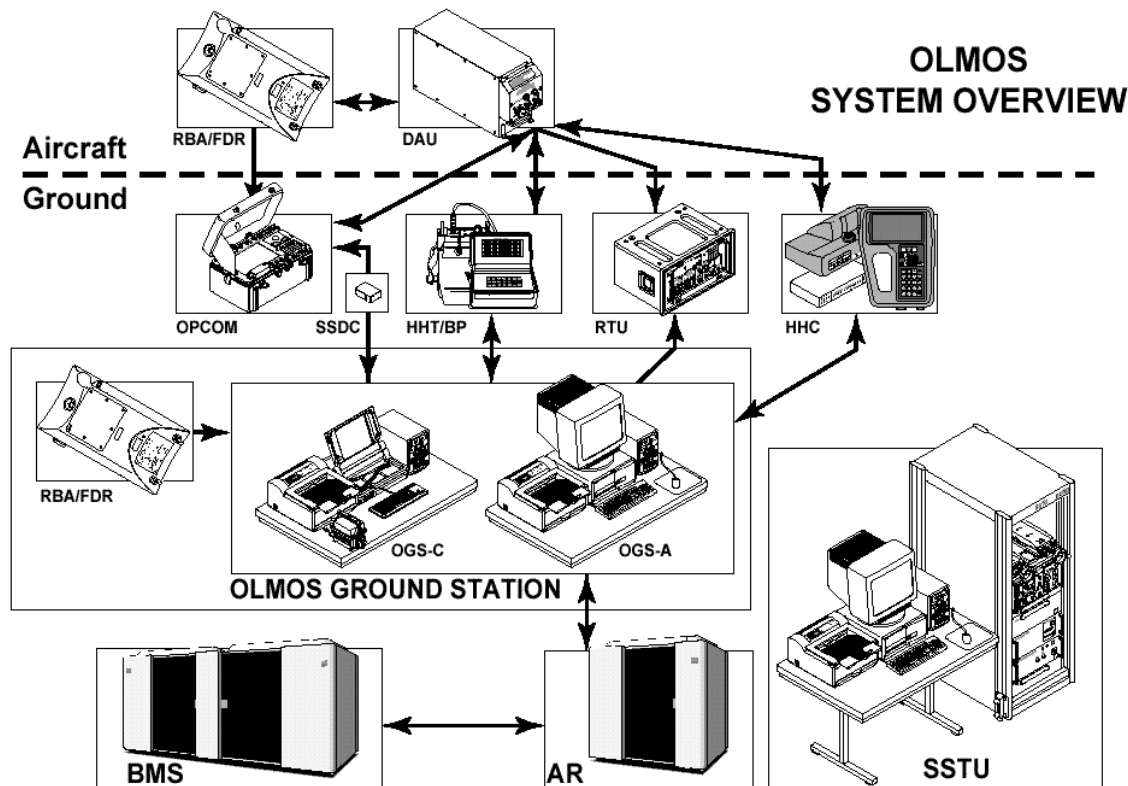
Figure 3: *OLMOS System Overview (Source EADS Dornier)*

The main source of change requirements is the engine itself. Even after 20 years of operation, the frequency of changes influencing the monitoring algorithms does not approach zero. Typical mid-life upgrades (e.g. improved air seals, new materials for disks or blades, optimised blade profiles) may require substantial modifications or even complete re-programming of parts of the life usage algorithms. There have been various partially still ongoing modifications of the RB199 engine, where the influence on the life usage had to be checked. Not all of them required changes of the previously used algorithms, and sometimes minor changes of some constants may be sufficient to take into account the changes in engine or component behaviour.

Relation between Engine Modifications and Monitoring Algorithms

Whenever a modification of an engine component is planned, developed and introduced, the consequences of this modification on engine life have to be assessed. Quite often, it is not sufficient to check those consequences for the changed component itself. As shown in the following examples, seemingly small modifications may influence adjacent components or even the behavior of the whole engine, thus requiring an adaptation of life usage algorithms.

•After some years of operation it turned out, that a certain vibration mode could occur in one of the compressor blade rows within a narrow speed band. To avoid a limitation of the operating envelope a redesign of the blade was performed. The redesigned blade was heavier than the previous one. This leads to higher centrifugal loads on the disk, which have to be considered in the stress model of the monitoring algorithm. Although the required modification would have

been rather simple, there was no means to transfer the blade type information to the onboard system without expensive modifications of the configuration data sets. Fortunately it was found, that the critical areas influenced by the centrifugal loads of the blades would normally not become life limiting, even when the heavier blade type was used. The final decision was to assume the presence of the heavier redesigned blade even in those cases, when the old blade type was retained.

•As a major part of the engine modification for life cycle cost optimization a redesign of the high pressure compressor blades was performed to achieve an increased mass flow and an improved surge margin. The design constraint was that no modifications of the rotor disks were allowed. Besides from minor changes in blade weights, the most important consequence was a shift of the thermodynamic cycle leading to changed boundary conditions for heat transfer to disks. A switch in the gas temperature calculation model that is dependent on the configuration data set treats this. The model for the heat transfer and heat conduction within the rotor itself remains unchanged. Nevertheless, a considerable software adaptation is required to insert the necessary control flow into the monitoring algorithms and to extract the compressor type information from the configuration data.

•A change in the manufacturing method of a disk can lead to a modification of residual stresses with consequences on the stress level and damage calculation. Therefore it is sometimes necessary to introduce different configuration codes dependent on the applied manufacturing methods, even if the geometry of the parts remains identical.

•Modified seal clearances that are introduced together with wear resistant coatings will have an influence on secondary air mass flows. It has to be checked if boundary conditions for the temperature calculation of disks are affected.

•A redesign of HP turbine nozzle guide vanes was performed to improve their cooling and durability. As a consequence of the redistribution of the airflows a shift of work distribution between turbine stages occurs. This in turn affects the spool speed ratios between HP, IP, and LP spools. Whereas the LP and HP spool speed are measured parameters, the IP spool speed is calculated from a mathematical model. This model has now to be adapted to include the influence of the new guide vane standard.

•The introduction of single crystal turbine blades is considered to be a major cost saving factor due to their superior material properties (e.g. creep life) at high temperatures. Unfortunately those blades tend to have higher weight than their conventional predecessors. As long as both blade types are used in parallel, the blade type has to be transferred to the disk stress computation via a blade type code to take into account the change in centrifugal loads. It even turned out, that blades from different manufacturers systematically used the limits of admissible weight tolerance bands, thus requiring another distinction within the stress computation.

•A change in control system schedules, e.g. a modification of the idle schedule will require an adaptation of criteria for execution flow of monitoring algorithms. To avoid the necessity for a software update, a so-called monitoring control parameter set is used, that contains constants of the algorithms, for which a dependency on external influences is known or suspected. It is then sufficient to introduce an update of the monitoring control parameters that has of course to be synchronized with the introduction of the related changes of other hardware or with changes of handling procedures.

Changes of the monitoring algorithms become also inevitable, if damage mechanisms or critical areas not considered so far turn out to be life limiting. This topic is discussed in [PB01].

Retrofits of improved engine components are nearly never performed in one "big bang" action, maybe excluding emergency fixes caused by flight safety concerns. A more realistic scenario is described in [HC99] with long times of overlapping mixed use of old and new configurations, including both engine hardware and different versions of the monitoring algorithms.

Development History

OLMOS has its roots in the early 1980's, starting from the idea, that most of the data required for monitoring the engines and the aircraft structure were already available in the existing data acquisition box DAU-1B for the tape based crash recorder, that is located in a deployable airfoil (RBA, see *Figure 3*) on top of the rear fuselage.
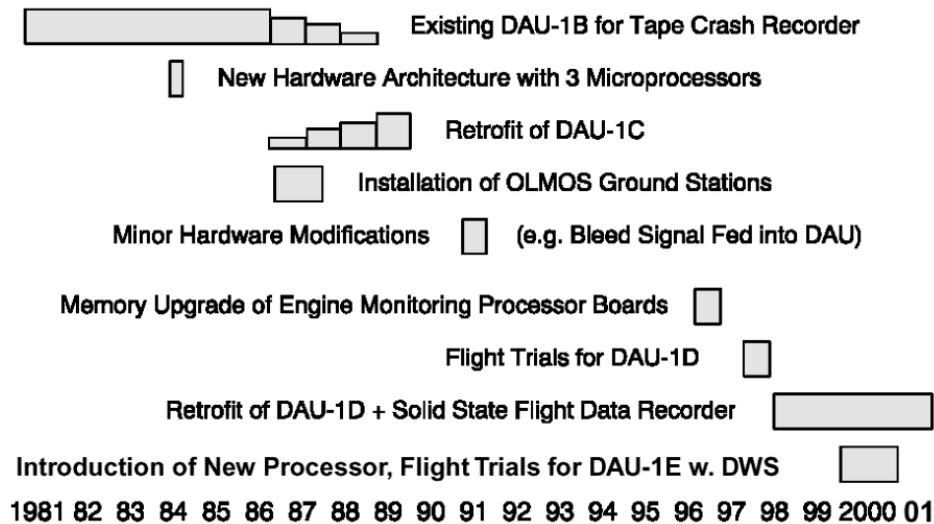

Figure 4: *Time Scales of OLMOS Hardware Development*

Figure 4 shows the development steps of the hardware configuration starting with the introduction of 3 new processor boards, two of which were dedicated to the engine monitoring functions. There was an incremental approach in both hardware and software development. Major development steps occurred with the introduction of the new engine standard Mk105, that is used to power the ECR Tornado and with the replacement of the obsolete tape based crash recorder by a solid state flight data recorder. The FDR replacement is now in its final phase. On the engine monitoring side, the FDR introduction was used to implement a memory upgrade and a software loading function that will simplify the process of software changes for the engine monitoring algorithms. Currently another upgrade of OLMOS is in its final phase of qualification. By replacing an obsolete data acquisition board by a state of the art microprocessor board it was possible to implement a warning function for aircraft instability (departure warning system). The next upgrade step in the engine monitoring functions will be the inclusion of the life usage algorithms for the so-called life cycle cost optimized engine that includes several improvements, e.g. an HP compressor with increased mass flow.

Figure 5 shows an overview of the development history of the engine life consumption-monitoring program ELCMP. Each change at this complex system requires an inspection and a consideration of numerous existing mutual dependencies, which are partly so serious that actually meaningful extensions or adjustments can either not be introduced at all or only with very long temporal delay. The continued use of LUM algorithms known to be outdated indicated at the end of the time scale in *Figure 5* is caused by the mutual dependence between availability of the software loading function for ELCMP into the onboard DAU and the necessity to have only one version of life consumption data in the data base of the logistic system BMS.
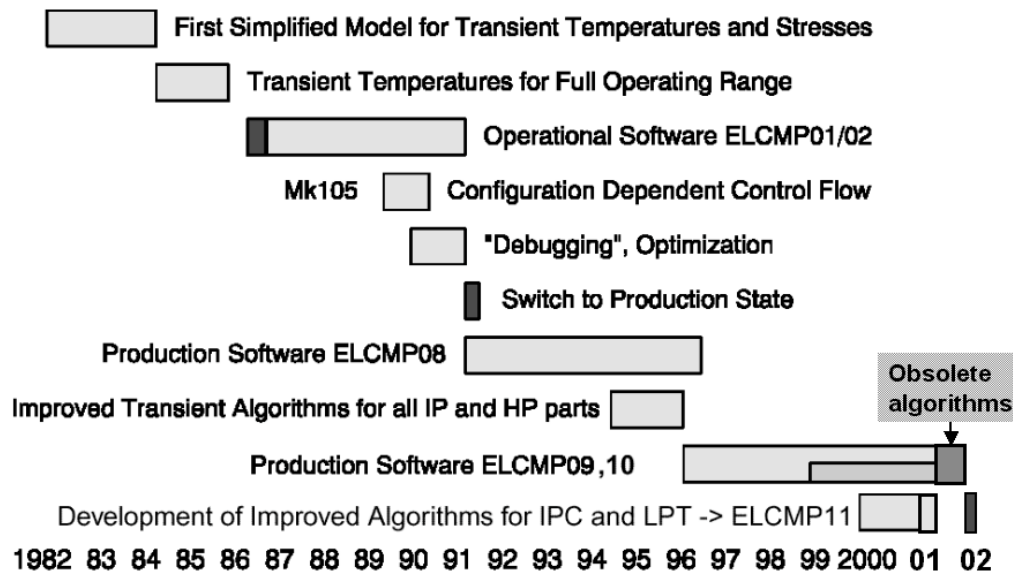
Figure 5: *Time Scales of Algorithm Development for Life Usage Monitoring*

Problem Tracking

A very important tool to maintain a high quality of a monitoring system is a reasonable procedure for problem data gathering and tracking. In the OLMOS system there exists one central query list, where all known problems are collected. Entries come from all parties in the development, management and planning, but the focus is on reports from the end users. This list is the basis for regular system reviews and for the planning of correction and update packages. Currently there are some 150 entries in the list. 70 of these queries have their origin in the introduction phase of major system changes, dealing mainly with requirements that were set aside during the specification phase (low priority, financial constraints), whereas the remaining larger part deals with problems detected during system operation.

The list is maintained at the technical training center of the GAF, which acts as an advisor to the GAF material command. This choice has proven to be rather beneficial, because the air force personnel assigned to the OLMOS system visits training courses before they start to work with the system. When problems show up, that can't be solved by using the documentation or the system's help functions, in many cases the first address to consult is the training center. As the query list contains also recommendations for a solution of known problems, it is sometimes possible to give hints how a problem may be solved manually or be circumvented until it is solved by a system patch or update.

User Training Environment

The environment of the training center is also used during tests of new features to be incorporated into the monitoring system. A very useful feature is the presence of virtual aircraft and engine data in the productive database of the BMS system operated by the material support command. All data records used for training purposes have unique, easily recognizable serial numbers that have no correspondence in the form of existing engine hardware. It is of course necessary to exclude those parts during statistical analyses or during productive database queries by means of suitably defined import filters. By means of this construction it is possible for the OLMOS personnel to practice all occurring handling procedures, including also the data transfers to and from the central logistic system.

To simulate the consequences of flight operations on the onboard data acquisition unit, the DAU can be fed with aircraft and engine data via two different interfaces. It is either possible to use the serial link for the HHT in a special transfer mode to send digital engine data or to stimulate the

analog and digital interfaces using a dedicated test rig (SSTU) with the same data the DAU would see in the aircraft. In both cases synthetic or real recorded engine runs can be used as input. This function has proved to be extremely valuable to verify the correct operation of the onboard components of OLMOS.

Plausibility Checks for Life Usage Data

Another area of improvement is the elimination of manual handling of life usage data. Human interaction always produces some low, but nearly unavoidable percentage of errors in the data. Besides from trying to eliminate the need for non-automatic processing steps (e.g. by a better integration of the data processing systems of the air force and of industry), methods have been developed to detect and correct inconsistencies in the logistic data by using suitable checks.

The life consumption data accumulated in the onboard systems are transferred via the processing chain indicated in *Figure 1* and finally collected in the BMS database at the GAF central computer facilities. Every month the life usage data of all monitored parts are extracted from this database and are sent to industry for statistical analysis. The results of the statistical assessment are summarized in a monthly status report. Currently a system for plausibility checks of those data is being introduced. The basis for the plausibility checks is a statistical analysis [PB01], which is based on simulation runs using recorded engine data together with the accumulated life usage data available in the logistic system BMS of the German air force. The planned application of those checks will allow an early detection of errors and thus avoid potential risks of hidden data errors on flight safety.
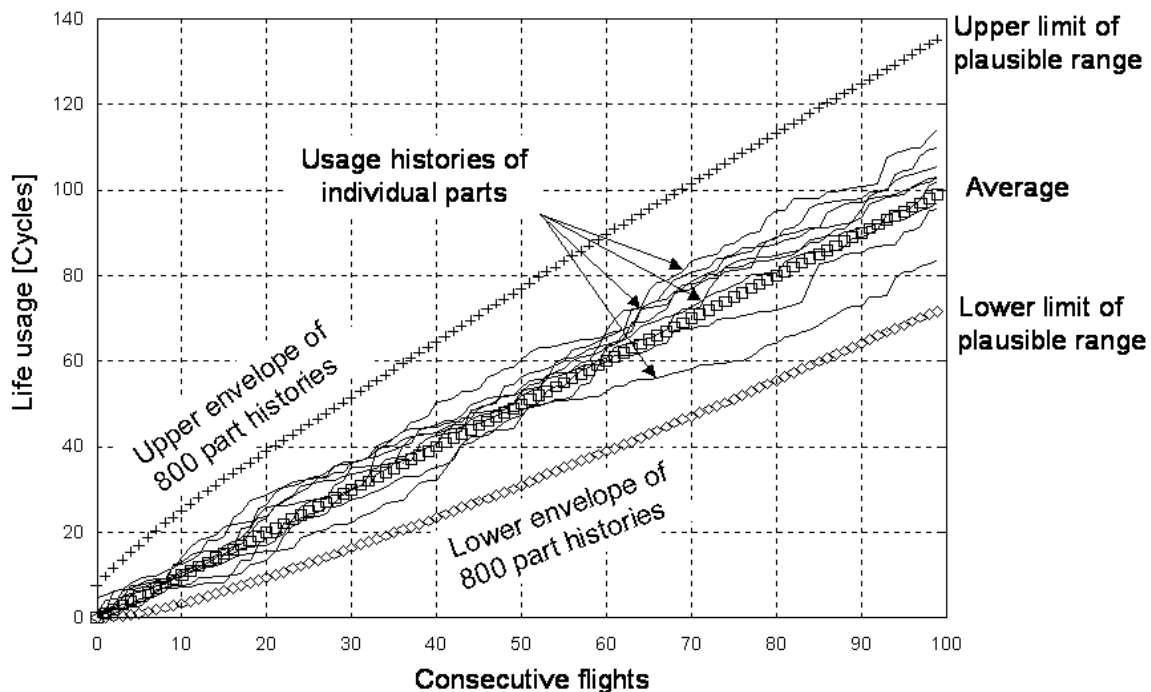
Figure 6: Scatter in accumulated life usage

Figure 6 illustrates the basic idea of the plausibility check. The relation between numbers of flights and accumulated life usage is acceptable, when the relation falls into the envelope of the simulation results. The results of the simulation are tables of upper and lower limit values as a function of the number of engine runs. There is one table per critical area, thus leading to more than 40 such tables for the whole engine. To convert those tables into the more usual dependence

on accumulated flight time, an average flight time per flight is used, that is either a value for the whole fleet or a specific value determined for a certain aircraft variant or for an air base with known mission types significantly different from the fleet average.

The data handling of many tables with several thousands of entries has been considered as impractical and therefore an alternative representation of the limit curves was required. By analysis and numerical experimentation a set of formulas was found, by which all occurring limit curves could be represented with very good accuracy. The idea is to use a weighted mean of two straight lines together with an expansion function that is used to widen the curve for lower times. The following formulas are used:

- 2 straight lines:

$$g_1(t) = s_1 \cdot t + d_1$$
$$g_2(t) = s_2 \cdot t + d_2$$

- Weighting function:

$$u(t) = \frac{1}{2} \cdot \left[\frac{1 - e^{\frac{t-a}{w}}}{1 + e^{\frac{t-a}{w}}} + 1 \right]$$

   For $t \to -\infty$ u(t) approaches 1, for $t \to \infty$ u(t) approaches 0. $u(a) = 1/2$, w is the width of a transition zone.

- Expansion function:

$$wd(t) = d \cdot \left(\frac{t}{b}\right)^{c-1} \cdot \exp\left(-\left(\frac{t}{b}\right)^c\right)$$

The final dependence is determined by a weighted combination of the two linear relations by means of the "sigmoid" function u plus an expansion with the 2-parametric Weibull density function wd.

$$z(t) = u(t) \cdot g_1(t) + (1 - u(t)) \cdot g_2(t) + wd(t).$$

These formulas can be used to represent both the lower and the upper limit curves, of course with different sets of coefficients. The coefficients $d_1, s_1, d_2, s_2, a, w, d, b, c$ are determined by means of a non-linear least squares fit of z(t) to the individual lower and upper limit curve tables. *Figure 7* shows an example of the construction of the combined upper limit curve, plotted versus the number of flights. The topmost line is g_1, whereas the lowest line is g_2. The coefficient s_2 is the slope of the limit curve for a large number of flights, because $u(t), wd(t) \to 0$ for large t. This makes s_2 equivalent to a long-term β-factor, i.e. it gives an asymptotic life consumption for large number of accumulated flights.
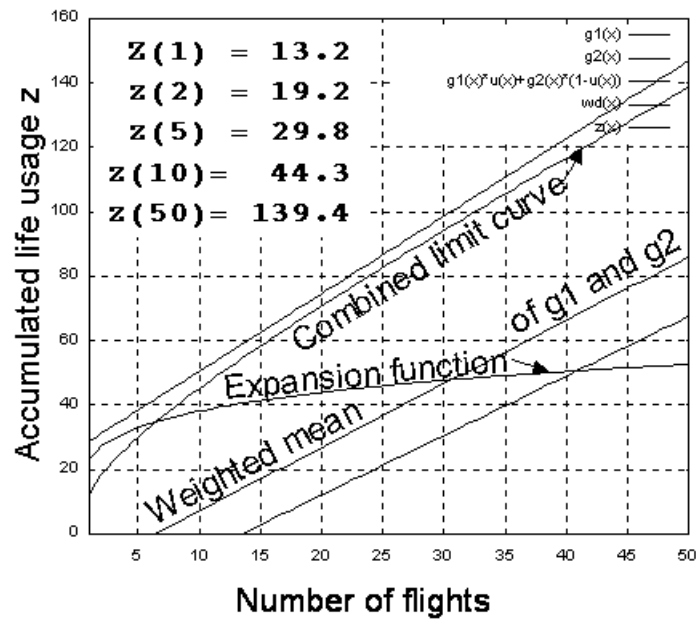
Figure 7: Construction of upper limit curve for small number of flights
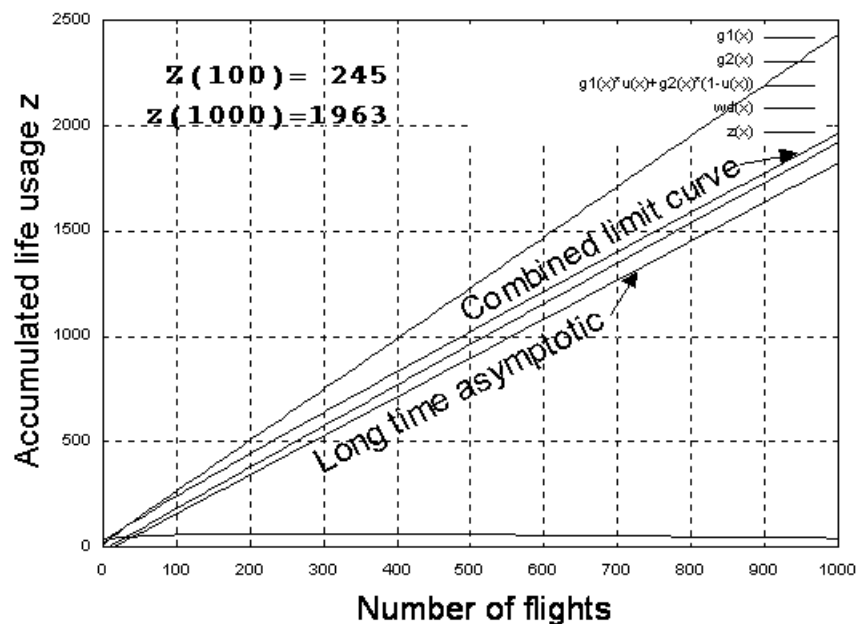
Figure 8: Construction of limit curve continued

The example in *Figure 8* shows the same (upper) limit curve as in *Figure 7*, but for a larger numbers of flights. The influence of g1 has diminishes at 1000 flights, but there is still some offset caused by the expansion function shown as near horizontal curve near the flight number axis. The numerical cycle values z(t) shown in both figures give a good impression, how the plausible range may vary for short and long time cycle accumulation. Whereas a life consumption of 44.3 cycles is plausible for 10 accumulated flights, a corresponding life consumption of 443 cycles for 100 accumulated flights has a nearly vanishing probability, at least if the assumption of random mission assignment is not severely violated.

The limit curves derived from the simulations were used in a first step to check all Group-A part data in the BMS database for a plausible relation between accumulated flight time and accumulated cyclic life usage. *Figure 9* shows a comparison of the limit curves predicted by the

fleet simulation with accumulated life usage data, for a component that has been monitored by OLMOS from its entry into service. The scatter of the actual data is slightly higher than the predicted scatter. This is caused by the comparatively small number of recorded flights that were available to determine the distribution parameters for the underlying "damage per flight" distribution.
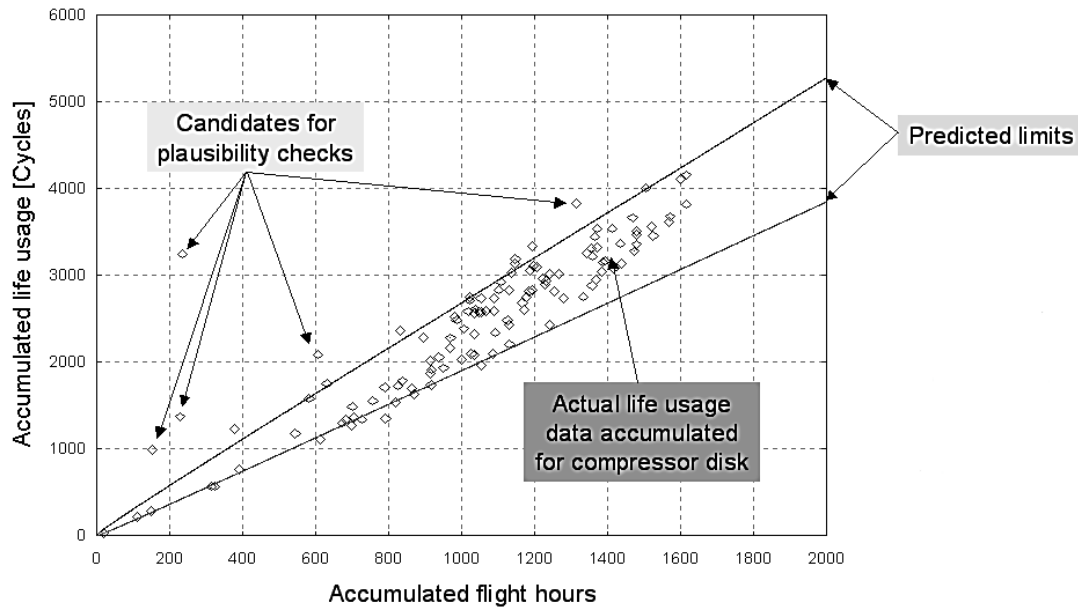
Figure 9*: Comparison of simulation results with actual life usage data*

A significant difference in data quality was found between parts that were actually used in flying engines and spare parts. Due to the system philosophy, that only parts used in an engine are checked for consistency, the frequency of data errors was higher in the spare parts inventory, than it was for the actively used parts. Especially those parts, where changes of the monitoring algorithms had been performed in the past, showed a higher percentage of inconsistent usage data. This was at least partially caused by incomplete conversions of data after the introduction of new life usage algorithms. Whereas the conversion of LUM data between subsequent versions is designed as an automatic process, the conversion of results from earlier versions usually requires some manual interference.

We found a significant connection between the accessibility of parts and the frequency of implausible data records in the BMS inventory. It was not very surprising, that a correlation existed between the required maintenance level to access a part and the frequency of data inconsistencies. Parts that were only accessible at industry or in the central repair facilities of the air force (e.g. disks of the HP compressor) had fewer data errors than parts that were changed at squadron level (e.g. HP turbine cover plates). For frequently changed or easily accessible parts it may be therefore be worthwhile to increase also the frequency of the plausibility checks.

Correction of implausible life usage data

Figures 10 and *11* illustrate the method to be applied, when the number or accumulated cycles is found outside the plausibility band. It is assumed, that the accumulated flight time could be confirmed to be correct. Whereas the conservative correction in *Figure 10* assumes, that no historical data are available, *Figure 11* reflects the situation currently found in the handling of the data from the OLMOS system, where monthly snapshots of all life usage data are stored and kept within a database maintained at industry. The availability of historical data turns out to be quite

beneficial and avoids the necessity for worst-case assumptions for the whole life in case of data errors.
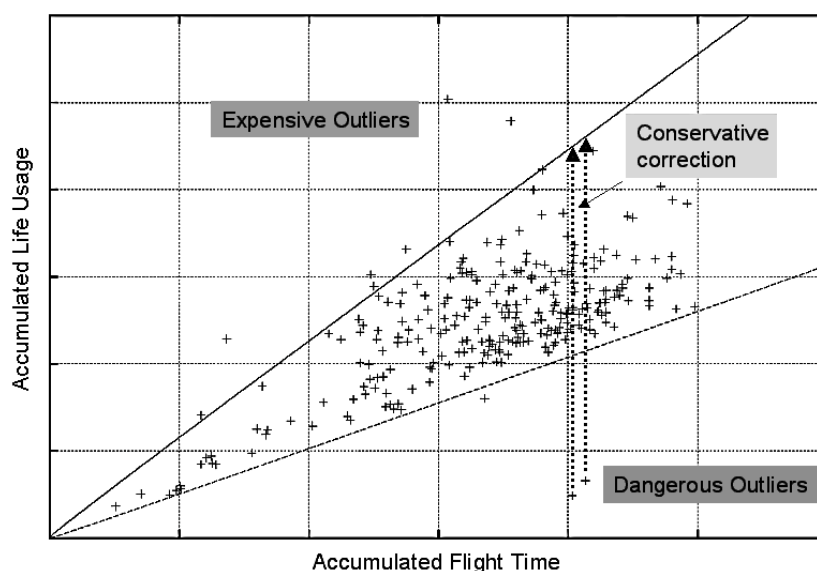
Figure 10*: Conservative Correction of Outliers*
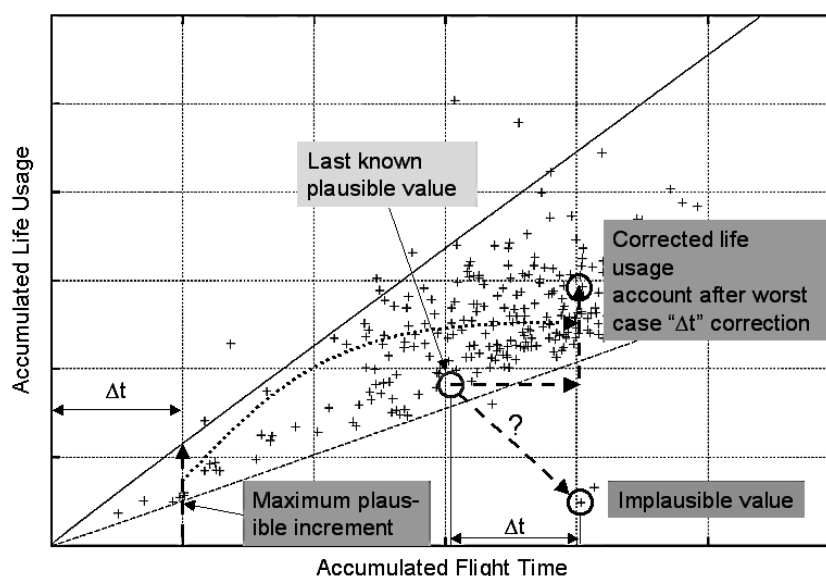
Figure 11*: Correction Using Stored Historical Data*

Influence of Usage Monitoring on Life Cycle Costs

Within the engine monitoring functions the computation of the life consumption of the fracture critical group A components represents the most extensive and also most substantial part regarding its effects on the total costs of the weapon system. The accurate information on the state of life usage in the whole fleet provides an excellent basis for the planning of workload in overhaul facilities, spare parts manufacturing, fleet management and financial requirements. A typical distribution of life usage determined by OLMOS is shown in *Figure 12.*
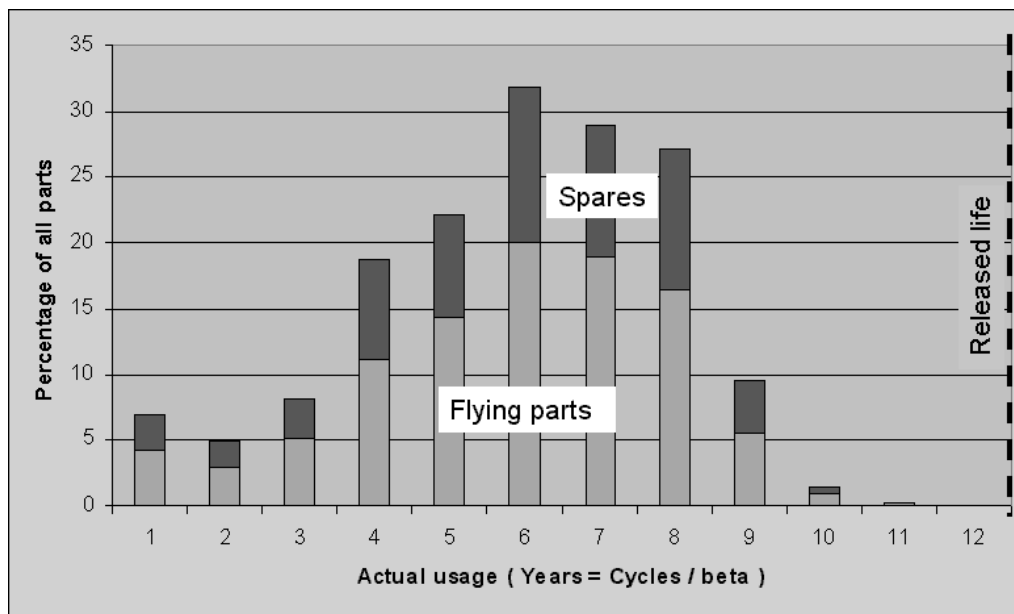
Figure 12: *Typical distribution of life consumption at half nominal life*

Using such data enables predictions of expected replacement costs as shown in *Figure 13*. Included in this figure is an expected trend of disk replacement costs for the USAF, that is characteristic for aging fleets without application of individual life usage monitoring (Source: [Blo01]). One of the benefits of individual life usage monitoring is the identification of components with low life usage that permits to limit the rising of costs, which would occur if replacement were only based on accumulated flight time. A comprehensive discussion of these benefits is found in [RTOTR28].
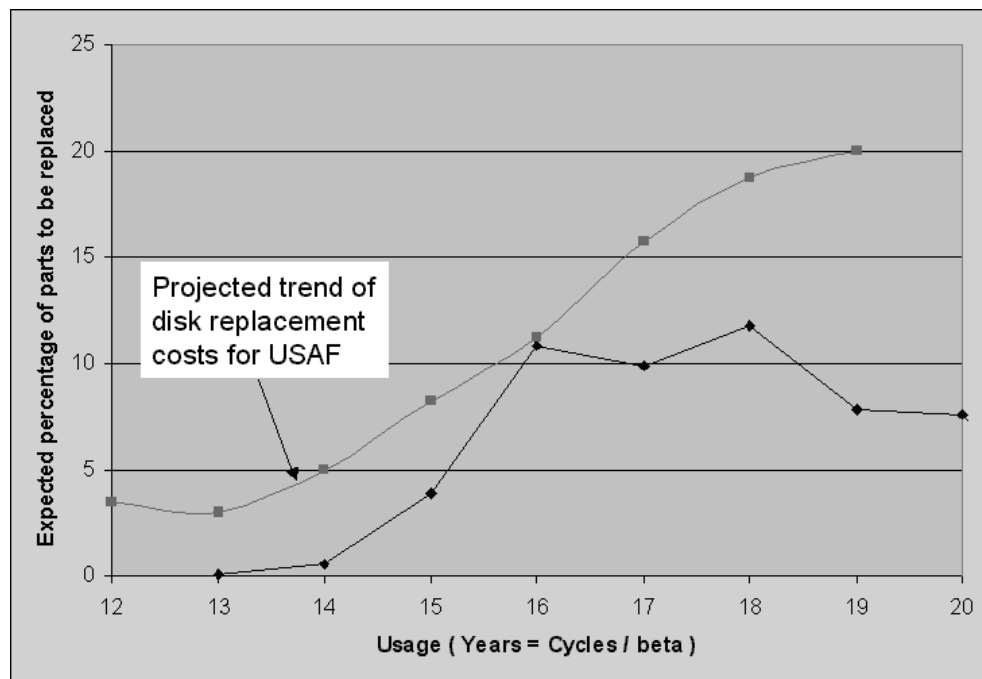
Figure 13: *Predicted replacement needs for a compressor disk*

On the other hand the maintenance of a sophisticated monitoring system also is a not negligible cost factor. Improvements in engine hardware have to be modeled in updated monitoring algorithms. Some benefits will not become visible until an update of the whole monitoring processing chain has been performed. A reasonable balance has to be found between the additional effort of updating the monitoring system and the cost reductions expected from application of the best available algorithms. Each attempt to reduce the development and investment costs for monitoring should take into account the well-known cost relation shown in the following *Figure 14* (Source: [Al00]).
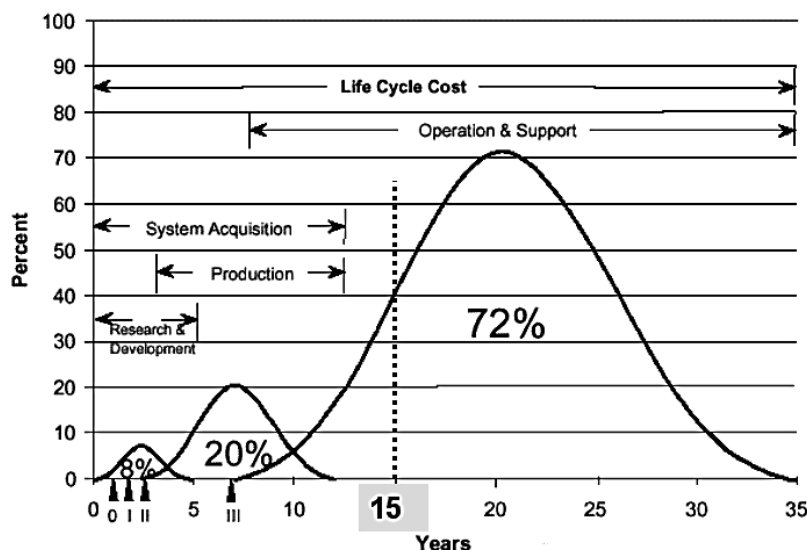
Figure 14: *Typical timescales and cost distribution of military IT systems*

Conclusions

This presentation is based on the experiences that were made in the last one and a half decades during the introduction and the operation of the OLMOS system. These findings can be used on the one hand during a still ongoing improvement and optimization of this system. On the other hand they form a wealth of experience that can and should help to design and implement new monitoring systems as efficiently as possible.

References

[Al00] Alford L.D.: Supporting Commercial Software. CROSSTALK, The Journal of Defense Software Engineering, Vol.13, No.9, pp.13-16, September 2000

[Blo01] M.Blodgett et al.: Residual Stress Measurement Needs for Component Life Extension: An Air Force NDE Perspective.
28th Annual Review of Progress in Quantitative Nondestructive Evaluation.
Bowdoin College, Brunswick Maine, July 29 - August 3, 2001

[BP97] Broede J., Pfoertner H.: OLMOS in GAF MRCA Tornado - 10 Years of Experience with On-Board Life Usage Monitoring.
Paper AIAA 97-2905, 33rd AIAA/ASME/SAE/ASEE Joint Propulsion Conference, Seattle, 1997

[BPR98] Broede J., Pfoertner H., Richter K.: The importance of testing for successful life usage monitoring systems. In: Proceedings of the 19th Symposium Aircraft Integrated Monitoring Systems (AIMS98), Garmisch-Partenkirchen, 1998, pp. 387-406

[CT98] Clapp J.A., Traub A.E.: A Management Guide to Software Maintenance
In: COTS-Based Systems. Guidebook MP98B0000069, Electronic Systems Center,
The MITRE Corporation, Bedford MA, 1998

[HM98] Hall S.R., Miner J.W.R.: Technical Data Management: An Essential Tool for Effective
Life-Cycle Management.
Proc. of the NATO/RTO-MP-7 Specialists Meeting, Exploitation of Structural Loads/Health Data
for Reduced Life Cycle Costs. Brussels 1998

[HC99] Hall S.R., Conquest T.J.: The Total Data Integrity Initiative (TDI^2) - Structural Health
Monitoring, The Next Generation!!
USAF 1999 ASIP Conference, San Antonio, TX 1999

[NRC01] National Research Council Committee: Aging Avionics in Military Aircraft.
Air Force Science and Technology Board Division on Engineering and Physical Sciences.
National Academy Press, Washington D.C., 2001

[PB01] Pfoertner H., Broede J.: Statistical Correlations for Analysis and Prediction of Turbine
Engine Component Life Usage.
Paper AIAA 2001-3754, 37th AIAA/ASME/SAE/ASEE Joint Propulsion Conference,
Salt Lake City, UT 2001

[RTOTR28] RTO AVT Panel Task Group AVT-017: Recommended Practices for Monitoring
Gas Turbine Engine Life Consumption.
RTO-TR-28 AC/323(AVT)TP/22, RTO/NATO April 2000.

List of Acronyms

BMS	Logistics system for configuration, material tracking and management
COTS	Commercial Off the Shelf
DAU	Data Acquisition Unit
DWS	Departure Warning System
ELCMP	Engine Life Consumption Monitoring Program
FDR	(Solid State) Flight Data Recorder
GAF	German Air Force
HHC	Hand Held Computer
HHT	Hand Held Terminal
HP	High Pressure
IP	Intermediate Pressure
LP	Low Pressure
LUM	Life Usage Monitoring
OGS	OLMOS Ground Station
OLMOS	Onboard Life (Consumption) Monitoring System
OPCOM	Operator Control and Measurement Computer
RBA	Recorder Beacon Airfoil
SSTU	Signal Stimulation Unit

Paper 3: Discussion

Question from D Shepherd - QinetiQ, UK

Were the data outliers simply identified on the basis of being outside of the predicted range or were you able to go back and positively confirm a problem with the actual data?

Presenter's Reply

The margins used to detect outliers are chosen to be very conservative and we were always able to confirm data handling problems that generated the implausible results. If an engine, or aircraft, is constantly operated in an extreme role, then the assumptions used in the plausibility checks are violated and an outlier may turn out to be a valid result. However, we have never identified such a situation but if it were to occur, an analysis of the results for single flights (raw flight data) or the downloaded data after every flight would be necessary.

This page has been deliberately left blank

————————————

Page intentionnellement blanche

Through Life Management of Naval Gas Turbines for Extended Service Lives and Reduced Lifetime Costs

Richard Bolwell
Warship Support Agency
Marine Propulsion Systems Integrated Project Team
MPS214, Room 130, Block J
MOD Foxhill
Bath BA1 5AB
United Kingdom

INTRODUCTION

Marine gas turbines have been used for many decades in a diverse range of commercial and naval marine vessels, almost exclusively for main propulsion duties in a number of different configurations. As well as providing an outline of the scope of operation, this paper aims to discuss the key Life Extension Programmes and Cost Reduction Strategies developed by the UK Ministry of Defence in support of the two international collaborative Memoranda of Understanding (MoU) for the marine Olympus, Tyne and Spey gas turbines. Where available, discussion is supported with evidence from emerging equipment maintenance policies, equipment modifications and data collected from components and engines returned from the fleet for repair or overhaul. In addition, and in terms of the economy of scale advantages that the arrangements offer, an assessment of accumulated savings and projected financial return is provided with an insight into the operational benefits and improved capability that the programmes realise.

The UK Warship Support Agency (WSA) provides overarching in-service gas turbine support and cooperation through two Memoranda of Understanding (MoU) involving 4 European nations, 21 years of collaboration and 3 million shared running hours of operation. The membership of the Olympus TM3B and Tyne RM1C MoU, in place since 1980, comprises of the UK, The Netherlands, France and Belgium. The MoU for the Spey SM1A, signed in 1989, is between the UK and The Netherlands. In addition, the Royal Navy (RN) also operates the Rolls Royce Spey SM1C and, from 2002, will be accompanied by The Royal Netherlands Navy (RNLN) under an extended Spey MoU to encompass the engines installed in their new class of Logistic Command Frigates.

Engines within the MOU's						
Engine Variant	Fleet Seats				Spare Engines	Total
	RN	RNLN	BN	FN		
Olympus	43	12	3	14	17	89
Tyne	35	12	-	-	23	70
Spey SM1A	25	16	-	-	9	50
Spey SM1C	16	6	-	-	6	28

BACKGROUND

Engine configurations :

Olympus engines are rated at 18 MW and Tyne at 4 MW. Generally both engines are used in a Combined Gas or Gas configuration (COGOG), however, in French and Belgian Navies, the Olympus operates in combination with direct acting diesel engines under a Combined Diesel or Gas (CODOG) arrangement. Depending on the class of vessel, the Spey is used at ratings of either 12.75 MW or 18 MW in combination either with the Tyne in a COGOG arrangement or with diesel engines either in a Combined Diesel Electric and Gas (CODLAG) mode of operation (Figure 1) or in a Combined Diesel and Gas (CODAG) configuration.
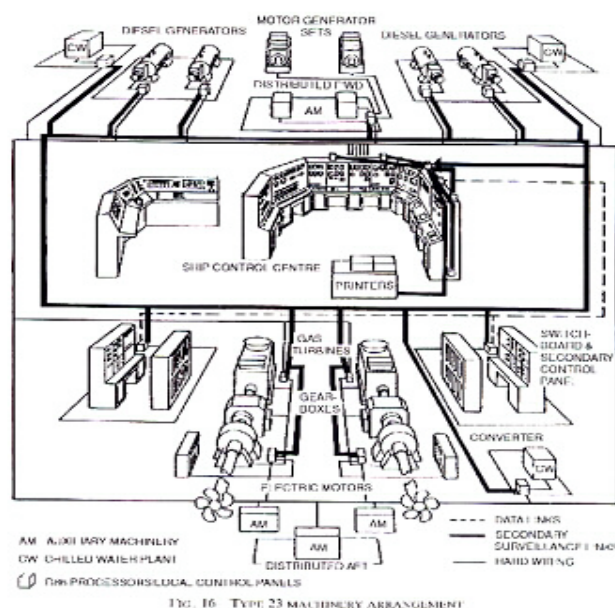
Figure 1 - Type 23 Frigate CODLAG Propulsion Machinery Layout.

Despite many permutations of operation this presents no real problems in terms of support, however, careful attention is required in considering and then managing the effects of

different mission profiles on component lives, in particular the effects of Low Cycle Fatigue (LCF).

All MoU partner navies operate using the principle of cruise and boost. In the case of a Tyne and Spey configuration as used in the last batch of Type 22 Frigates, the smaller Tyne unit is used as the cruise engine while the Spey is used for sprinting when operational commitment necessitates. The reason this configuration was chosen is due to the initial projected operational speed profile combined with the necessary utilisation of ship propulsive power and the relatively high fuel consumption of the Spey at low powers (Figure 2).
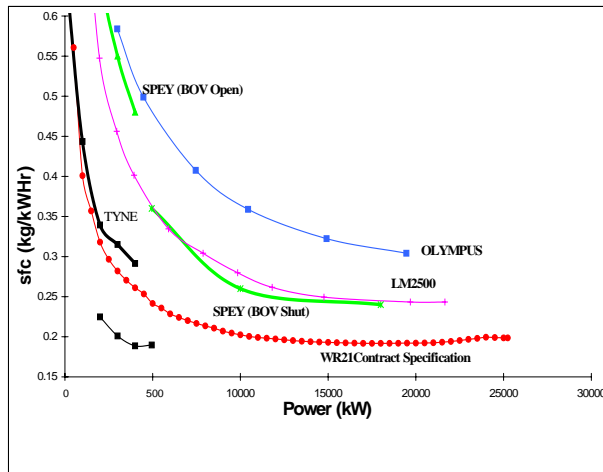
Figure 2 - Comparison of prime mover Specific Fuel Consumption.

In Frigates and Destroyers of the RN and RNLN, 25 % of the total available propulsion power is sufficient for 80 % of all operations (Figure 3).
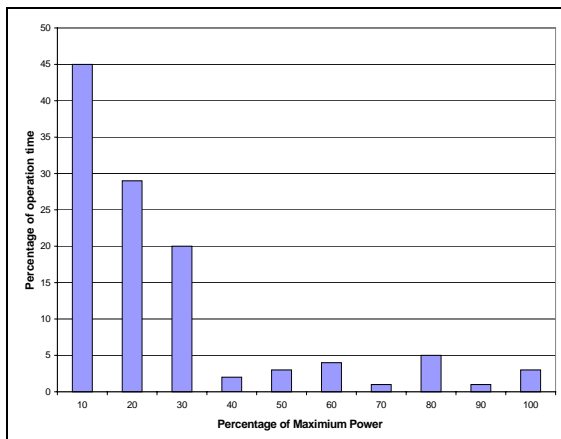
Figure 3 - FF/DD engine power band distribution.

The larger boost engines have relatively high fuel consumption at lower powers, and prolonged running at this condition is clearly undesirable.

This configuration allows for reasonable fuel economy to be obtained: at moderate to low ship speeds, by using the smaller cruise gas turbines; for higher ship speeds, the boost gas turbine is used. The arrangement enables a higher degree of ship operation at the relatively flat portion of the selected engine's SFC (Specific Fuel Consumption) curve, which for the simple cycle gas turbines being operated generally occurs above 80 % of rated power output.

This installation facilitates operational flexibility, but at the penalty of a relatively large number of installed propulsion prime movers, some of which will spend a large percentage of ship operational time not in use.

This is particularly the case in the post cold war era, where naval ship operating profiles have changed, and more specifically the demand for greater fuel economy has led to a situation where the boost gas turbines accumulate sometimes less than 300 hours per year, with the majority of running on cruise engines.

Objective of the MoU agreements :

A prime objective of each agreement is to minimise in-service support costs for all partners through the principle of economy of scale of common items using a pool of Gas Turbine Change Units and engine spares and the provision of mutual engineering, logistic and financial support. This reduces any single nation's commitment significantly below that required if it were solely a national programme. It also provides the flexibility to react to the unpredicted enabling tauter contracts and reduced turn around times for repair and overhaul. A largely identical hardware standard and similar utilisation means it is also possible to apply common logistic, maintenance and engineering procedures.

Overarching the above is the requirement to maintain design standards and ensure safe operation within the RN and other MoU fleets. Whilst the Design Authority, Rolls Royce, is supportive, each participating navy is responsible for its own 'day to day' fleet support activities whether this is in the form of gas turbine operational problem solving, condition monitoring, performance trending or predictive maintenance. The role in the UK rests with MPS214, a sub division within the Marine Propulsion System Integrated Project Team (MPS IPT) currently based in Bath but relocating to Bristol in 2002.

In addition to aforementioned activities, other key interests lay in :

- managing technical and financial Post Design Support activities on Rolls Royce,
- maintaining and operating the in-house Logistic Support Model (LSM) for the prediction of R&O arisings and the generation of costed management data (Figure 4),
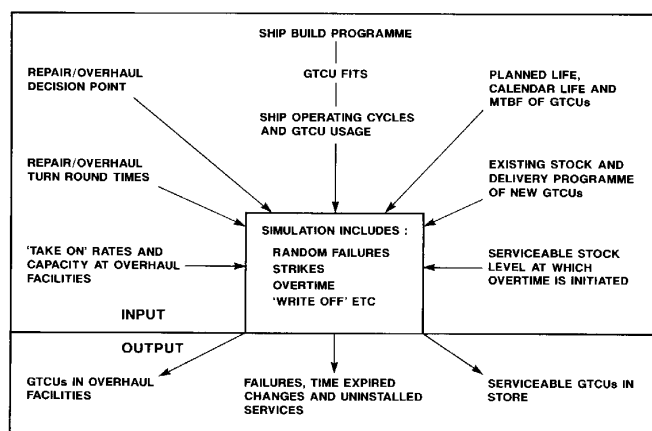
Figure 4 - The Gas Turbine Logistic Support Model .

- monitoring reliability, overhaul costs and technical information, reporting output to the partners through the mechanism of a Management Information System,
- liaising with the Design Authority and MoU partners in developing component and engine life assessment and extension strategies, taking into account any 'MoU rundown' implications,
- generating and implementing through life cost reduction initiatives and developing novel support mechanisms and gainshare initiatives with contractors,
- keeping abreast of technology with a view to its acceptability into service to solve discrete engineering issues,
- promoting information exchange internally (with the Royal Air Force Propulsion Support Group) and externally to foreign nations, future UK projects and industry.

The decision on UK management of the MoU's was made at the outset and was based on the fact that the UK MoD already had, at that time, considerable experience of in-service support and the necessary organisation in place. This was coupled with the fact that the RN was, and remains, the major stakeholder in having the largest number of engines in operation.

Problems faced in marine gas turbine operation :

Naval marine gas turbines have served well in the last four decades as main propulsion prime movers, enabling many of the original benefits to be realised. Derived almost exclusively from aero-engine parentage and having a good deal of operational experience, their use, however, in a harsh marine domain is somewhat demanding, with dissimilar operating profiles and environments ;

- highly variable mission profile, the majority of which historically has been at part-load with sudden load changes,
- salt and sand laden intake air, necessitating careful selection of intake filtration, corrosion resistant coatings and materials,
- the consequence of reducing vulnerability and increasing sea going stability now means that operating location presents longer intake and exhaust ducting than equivalent aero or industrial applications,
- variation in fuel quality and calorific value, due to embarkation from various global sources and standards,
- variable ambient conditions experienced during unrestricted global operation (Arctic to Middle East).

All of these issues place varying degrees of risk on reliability, durability and performance and as such must be overcome in order to reduce premature failures and increase the intervals between overhaul (IBO).

STRATEGIES IN REDUCING THROUGH LIFE COSTS

Current strategy :

As a strategy in the reduction of through life investment, the principal objective is to reduce overall Life Cycle Costs for all engines and to this end real improvements in component and engine reliability and availability are being sought by reducing the number of premature removals; where they are safety related, where they threaten operational effectiveness and where significant savings can be achieved over remaining life through cost effective investment. Other key factors are the application of a successful through life management programme to increase IBO's combined with the successful application of risk management in arriving at availability / capability tradeoffs.

Early engine life extension initiatives were based solely on endoscope inspections of gas path components. Understandably, these were not well received by the Design Authority who felt uncomfortable in basing advice to their customer on a limited understanding of component condition rather than being in a position of monitoring trends in performance and gradual deterioration. The additional argument was that specialist advice and experience from using other engines was also not being taken into account when arriving at conclusions.

Following discussions in 1996 between Rolls Royce and MPS214, a dedicated programme aimed at extending the IBOs for the Olympus and Tyne engines were defined and agreed between the two parties. A similar programme for the modular Spey SM1A engine was derived and in place by 1997 but this did not include the SM1C currently in RN operation as the declared overhaul lives for the modules are generally far superior to those in SM1A reflecting a number of material and performance improvements the SM1C embodies over the SM1A.

On reflection, it could be argued that as a Design and Overhaul Authority, Rolls Royce (or in fact any OEM) have no operator experience of their own, relying entirely on their customers for feedback on performance, defects and running issues in order for new generation products to evolve. Whilst it could be surmised that there is also a financial disincentive for any authority as an overhaul facility to extend engine lives, the programmes finally negotiated with the company are now both relevant and appropriate in scale to both parties. Working with a limited resource and a highly motivated team within MPS214, these strategies continue to provide very significant returns in increasing reliability and reducing the overall cost of operation of the engines.

However, not all returns are generated from the drive to increase overhaul lives, some are reflected in the group's wish to retain it's intelligent customer status. MPS214 employs a mix of service personnel and qualified civilian staff, some with many years of experience whether in gas turbine operation or equipment / project management. This allows the group to frequently take the first step in any initiative to extend condition based performance, however, this necessitates an inherent

degree of risk which must firstly be qualified and analysed prior to making any decision which may impact on engine and operator safety, platform availability or operational commitment.

ACHIEVING VALUE FOR MONEY IN PRACTICE :

The following details provide a summary of the key initiatives in place to achieve the overall aims of; increased engine reliability, increased availability and time on platform, reduced operator maintenance, reduced turnover of spares and reduced costs attributable to R&O. An assessment of some of the accumulated savings and projected financial return is provided alongside an insight into the operational benefits and improved capability that each of the initiatives has, and will, realise.

Engine Life Assessment and Extension Programmes :

For each gas turbine variant, the core of each managed programme consists of a number of well planned and documented in-service inspections on a small number of nominated engines at specified intervals. Upon removal, these engines also undergo an additional conditional assessment during overhaul, however, Critical Component Lives remain independent of the Interval Between Overhaul and this aspect of the lifing policy is managed alongside the three extension programmes.

In terms of the immediate objectives, initial stages of each programme have proved to be both realistic and achievable demonstrating the benefits of undertaking a strategy developed through close relationship between the Design Authority and the customer, Table 2 refers.

In addition to the operational benefits and flexibility to the Command from the increased installed lives, the extended IBOs are already resulting in very significant reductions in MOU engine overhaul bills. A direct collective saving between all three engines of approximately £ 3.0 M per year is currently being made. One could debate the actual value, however, in perspective, this represents a 28 % reduction in the marine gas turbine overhaul budget and the analysis does not include the increase in operational capability that arises.

MOU Gas Turbine Intervals Between Overhaul			
Engine Variant	RR Declared Overhaul Life	New Declared Overhaul Life	Remarks
Olympus	5000 hours or 10 year Calendar Life	Calendar Life 16 years	Subject to 2 yearly inspection after 10 years
		Frigates & Destroyers : 5500 hours	Subject to periodic inspection
		Carriers : 7000 hours	
Tyne	5000 hours	6500 hours	
Spey SM1A	3000 hours (12.75MW)	6000 hours	
Spey SM1C	9000 hours (12.75MW)	9000 hours	Lead engine currently at 2500 hours

Table 2 - MOU Gas Turbine Intervals Between Overhaul

The Tyne Life Extension Programme :

The Tyne engine in its 'cruise' role accumulates by far the most running hours of the three variants. By concentrating maintenance and improvement efforts on this engine, the highest returns on investments are being achieved.

The strategy of the Life Extension Programme is to conduct a series of detailed in-service inspections and performance condition assessments commencing on each engine at around 75 % of the IBO. This is then followed by an inspection at around 4800 hours of operation and if engine health is satisfactory then release life is extended incrementally, usually in stages of 500 or 1000 hours, to 6500 hours. Inspections are repeated until the engine is sentenced as unfit for further running.

Where possible, further engine operation is granted by exception, usually to undertake discrete operational requirements. That said, successes so far include an RNLN engine that had accrued 8000 hours prior to life expiry, an increase in IBO of 60 % over the original declared overhaul life.

The limitations of a gas path component inspection are, however, fully recognised. High risk areas such as bearings, oil seals and labyrinth elements are not immediately visible but may have potentially threatening consequences in terms of safety of engine operation and performance if they are allowed to degrade without being monitored. For this reason, decisions regarding life extension are strengthened with evidence from component analysis undertaken on high life engines during overhaul thereby allowing ratification of a formal life extension for the engines fleetwide.

The drive to improve performance and reliability of the engine was made from as far back as 1985 when sufficient time remained to make modifications cost effective. Furthermore, the Tyne engine overhaul policy was changed in 1986 to introduce what was called the 'Hot End Overhaul' at alternate 5,000 hour intervals, with little or no other work on remaining parts of the engine, the intention being that the engine would effectively achieve 10,000 hours between full reconditions as a cost savings measure. However the results of the introduction of this policy were to :

- increase the number of pass off test bed rejections mainly due to LP compressor vibration,
- increase the number of rejections of in-service engines at low running hours due to cracked LP compressor vanes, vibration and bearing problems in the compressor section.

During this time the overhaul bases were also having problems in maintaining their normally high standard of quality. The net result was that in the years 1987 and 1988 the Premature Removal Rate increased (Figure 5).
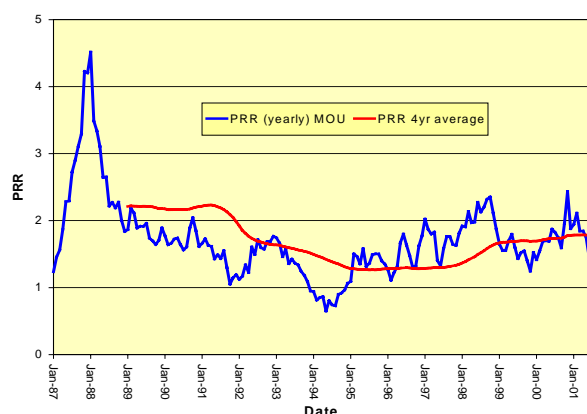
Figure 5 - Tyne Premature Removal Rate (PRR) since 1987.

The above situation was made somewhat worse by increased military tension in the Iraq-Iran war with the numbers of engines in ships with both navies reaching the maximum. Firstly, this had an increase in the number of Policy removals to the overhaul lines and secondly, this caused a demand for production engines that had hitherto been used in support of the pool of engines. This severely reduced the level of serviceable engines in the common pool.

Recovery actions commenced from late 1987 with a review of test bed rejections and overhaul procedures carried out with the full co-operation of the two engine overhaul bases at Rolls Royce and the Naval Aircraft Repair Organisation. This identified the main areas which needed attention in the cold end of the engine and resulted in an improved work package called 'Hot End Overhaul and Cold End Repair', which was subsequently re-termed the 'Mini-Overhaul' which has proven to be a successful policy.

Being a mature engine with a reducing fleet size and noting that changes can be expensive, the Tyne engine now uses a much stricter modification policy than preceding years. Modifications are now approved only if they relate to safety, obsolescence or operational reasons with the development of the engine constrained to improvements with an assured and short payback time.

Emphasis has been placed on the completion of the embodiment of existing modifications, particularly where these are known to improve reliability. The relaxation, where possible, of in service acceptance limits has been adopted in preference to modification action and in this respect it was agreed to adopt a fairly conservative approach with the Design Authority. Recent years have showed a steady increase in engine life, pushed by increased confidence in improved in-service inspection techniques and pulled by the wish to reduce cost. The PRR during this period moved upwards as a consequence of the significant increase in planed life but in general reliability for the engine still improves.

In 1998, a total of 5 engines ran in excess of 6000 hours prior to removal (7246 hours being the highest) as did a further 9 engines in 1999 (7898 hours being the highest) increasing to 10 engines in 2000 (6587 hours being the highest). Compare these figures with 1987 where no engines achieved anything greater than 5500 hours operation.

The Olympus Life Extension Programme :

The above detail of the Tyne life extension programme is provided by way of example. In addition, a similar programme is in place for the Olympus in MOU operation where they are used in naval Frigates as sprint engines and in aircraft carriers (CVS) as main propulsion prime movers. As such, the operational profiles and fueling considerations between the two roles differs significantly with the carriers undertaking as least six times the amount of usage (approximately 1800 hours per year per engine) as the rest of the DD/FF fleet (averaging 300 hours per year per engine). With all engines fundamentally 'interchangeable', it has been necessary to undertake a degree of tailoring of the overall Life Extension Programme for the Olympus.

The original IBO is 5000 hours but with such low usage for the majority of the fleet there is a Calendar Life condition attached which effectively means an engine must be returned for overhaul after 10 years, regardless of whether it has seen service or not.

Through a similar program to the Tyne in which a number of defined internal endoscope inspections are undertaken alongside condition assessments, the MOU have yet to remove an engine based on Calendar Life. Indeed, the lead engine in service is now approaching 17 years since installation and will be removed in 2002 to undertake a detailed assessment at overhaul in order to confirm acceptability of the current practice.

In addition , the other element of the programme is the drive to increase the IBO for engines installed in the carriers where, in terms of their higher running hours, the engines have proven themselves to be very reliable. Following a detailed life management plan, the programme currently allows CVS engines to operate up to 7000 hours prior to removal.

Compared with the Tyne engine, modification and maintenance efforts have been much lower with only two failure modes serious enough to justify modification action (discounting the improvements made to Combustion Cans which are covered later in the text) :

HP Turbine blade failures : During 1985, 9 premature removals were experienced due to HP Turbine blade failure all at varying hours run with the symptom of excessive vibration and resonant frequency excited by combustion defects. To reduce the vibration induced high cycle fatigue (HCF) a number of key measures were taken; a) improvements were made in the combustion area - a high number of combustion cans showed production deficiencies and a number of burners were partially blocked necessitating a burner calibration campaign, b) the vibrational sensitivity of the HP turbine blade was designed out by introducing an interlocked shroud and cast Inconel blade thereby helping to damp out the first flexible mode of vibration. Recent HPT failures on 3 engines are under investigation.

Starter motor drive bracket failures : There has been a lengthy history of low numbers of engine rejections caused by starter bracket cracking, rising to 11 such failures in 1988. During the period 1989 to 1992, for reasons unknown, the number of failures increased to 19. The main failure mechanism was identified as a high torque loading during the first phase of the start-up operation and a number of high stress areas in the starter motor bracket, therefore two modifications have been embodied in the fleet to overcome the problem : a) a 'soft start mechanism' allows a reduction in the initial torque by applying a much slower pressure rise during the first phase of the start and b) a more robust design of bracket is fitted. The

number of failures has reduced significantly, however, we are monitoring operation.

The effect of the improvements is clearly visible in the Premature Removal Rate (PRR) graph (Figure 6) where there is a marked increase in removal rate due to starter bracket failures and HP turbine blade cracking from 1990 to 1994. The effects of the burner campaign and 'soft start' modifications during the later years are also clear, however, a general decline in Olympus operation accompanied by a steady trickle of engine failures has lead to reduced reliability which is again being addressed. The PRR is currently low with a number of recent failures (other than HPT) being caused by incidents which are not engine related.
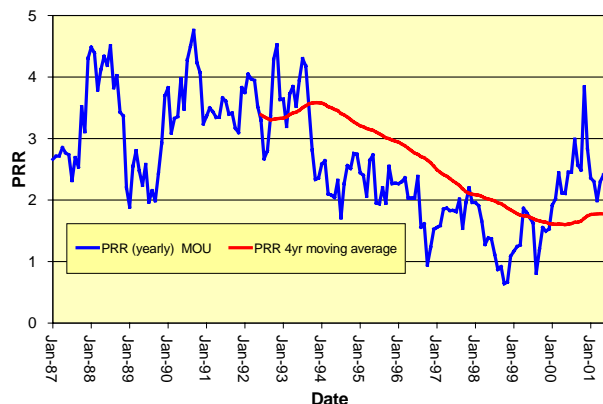
Figure 6 - Olympus Premature Removal Rate (PRR) since 1987.

The Spey SM1A Life Extension Programme :

The Design Authority has set planned lives for individual modules of the engine (MACU's) from the onset. From a user perspective with many years of experience, the MOU requires that the IBO's are extended (where service experience allows) in a similar manner to the programmes in place for the Olympus and Tyne. Being a modular engine, the low life MACU's are being targeted first; the objective for the Spey SM1A programme is to extend minimum MACU life in stages from the baseline of 3000 hours up to 6000 hours, 7500 hours and (longer term) to 9000 hours.

Again, Life Extension Programmes consist of a series of in-service inspections on a small number of engines at specified intervals. Opportunities are also taken to inspect engines returned for MACU repair if it is felt that there is some value to be gained towards the programme.

From the recent completion of life assessment rebuilds on three high life units (two at 5500 hours and one at 6500 hours of operation), it is clear that the first phase has been successful. Ratification of an increase in Turbine MACU life is expected shortly with an increase from 3000 to 6000 hours. Whilst a modification may be required, we shall be looking to go beyond this. Furthermore, other MACU's have already been extended to 7500 hours, the intention being that these MACU's will be subjected to abridged examination of the critical components identified from previous work conducted during life assessment activities. This self imposed, self regulated extension programme has meant an increasing degree of risk and engine management on MOU operators. Of note, is the protracted timescale for events with a general decline in annual operating hours. The current highest life SM1A in service is operating at 6182 hours. Even at

toady's usage rate this will take nearly 4 years to reach 7500 hours subject to passing strict inspection routines and performance assessments. Spey SM1A Mean Time Between Removals is portrayed graphically in Figure 7.

In terms of savings, this is dependant on increasing discreet MACU lives which may well evolve into a 'mix and match' basis as engines are returned back to service from repair or overhaul. For example, the additional 3000 hours extension in planned life of an 04 Turbine MACU represents one less engine removal and replacement operation, one less MACU exchange and one less Turbine overhaul, a saving of approximately £ 450 K through life. Increasing this life further to 7500 hours in line with the programme for two other MACU's on the engine represents two less engine removals, three less MACU exchanges and three less MACU overhauls, a saving in the region of £ 650 K per engine through life.
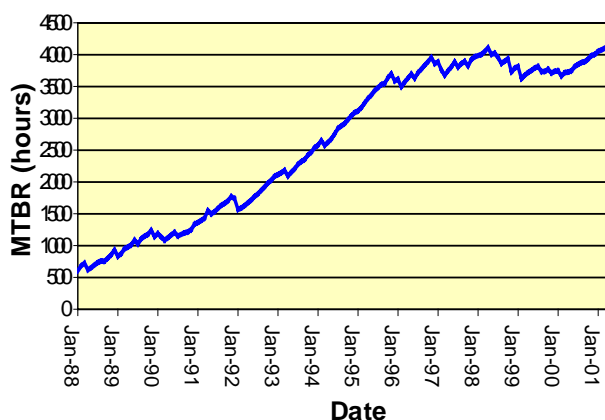
Figure 7 - Spey SM1A Mean Time Between Removals.

Component Life Assessment and Extension Programmes :

Tyne Fuel Pump Life Extension Programme :

Tyne Fuel Pumps are currently lifed by the OEM at 2500 hours of operation based on the reliability of the pump's Piston Spring. Whilst MOU partners have previously conducted spring changes in service to allow further life extension, this practice has recently ceased due to Health and Safety implications with the presence of asbestos parts until replacements are embodied across the fleet. The RN have traditionally followed this policy by replacing units on achieving life and on the basis that the Tyne fleet achieves approximately 77,000 hours average annual usage, this equates to a baseline arising of 31 units per annum. Following a review of the modes of failure, a decision was made by the RN to extend Tyne fuel pump life to 3500 hours, approximately 2 years engine usage. Prior to replacement with a springless design, similar Olympus springed fuel pumps could remain in service for 8 years prior to removal so this track record has been exploited.

Fleet experience shows that the majority of Tyne Fuel pumps are now achieving beyond 2500 hours without degradation in engine performance, however a formal Life Extension Programme which tracks the characteristics and wear mechanisms of selected units passed the 3500 hour point has been set up with the Design Authority with OEM support and advice.

Proposed savings : Increasing Tyne fuel pump life from 2500 hours to 3500 hours reduces the number of repair arisings from 31 units to 22 units per year representing a direct repair cost saving of £ 305 K per year. Additional benefits also include the reduction in ship staff activity to remove items, less engine down time and a reduction in the number of spare assets required.

Subject to the outcome of the lifing investigation the plan is to drive fuel pump life further, initially to 4000 hours, thereby reducing the number of repair arisings to 19 units per year (attracting a repair cost saving of £ 406 K per annum) and then on to 4500 hours (with a reduction in repair arisings to 17 units pre year with an associated saving of £ 474 K per year). With such a phased approach and the potential to life 'on-condition', the programme should mature within two to three years with many years remaining to run.

'On Condition' Component Lifing Policies :

At the request of the RN and in addition to discrete studies on all engines, a recent review of Spey accessory Critical Component Lives imposed during operation proved that sufficient running evidence was now available to explore a transition to 'on condition' maintenance policies for a large number of on engine components. The items selected for study were effectively minor components that ship staff have access to replace during the application of prescribed maintenance, whether on a cyclic or calendar basis. Such items include the Spey HP and LP Compressor Bleed Off Valves (HP and LP BOVs) and the Spey combustor Low Pressure Atomisers (LPA's). The principle applied was to review the reliability, probability and consequence of failure for the components selected and then, on the basis of successful operational experience, re-classify those items whose failure now presented a tolerable (or lower) hazard to ship staff or to the safe operation of the vessel. A number of real improvements have been made. In addition to the savings in part repair and overhaul, other benefits have included better component life management, reduced operator maintenance and a reduction in the CAL ('carried on board' allowance).

Tyne Power Turbine Metastream Coupling Life Extension :

The Tyne primary gearbox Metastream flexible coupling is currently lifed by Rolls Royce at 21,200 hours of operation (approximately 12 years service), however, a review undertaken recently suggests that the OEM has never applied a finite life to the coupling and that it should be possible to extend the imposed limitation by as much as 50 % or more.

With the exception of one particular RN ship, instances of Metastream coupling failure in service are rare with many units now approaching their current life of 21,200 hours.

Of the 22 issues since 1996, only 2 have been made to operational vessels. The remaining couplings have been used to support prescribed maintenance activities during ship refits, possibly unnecessarily, as replacement has routinely been included in the work package irrespective of remaining life on the unit, or if the balance of life is insufficient prior to the next Refit.

With this in mind, we are proposing that a life extension from 21,200 to 26,000 engine running hours is adopted for the Tyne power turbine Metastream coupling, subject to ship staff inspection every 1000 hours from the Current Planned Life. This is the first phase in a programme to validate an 'on condition' lifing policy,

reflecting a shift from prescribed calendar based exchange to Condition Based Maintenance. Current indications are that this will provide a saving of £ 75K per annum based on evidence from refit work package cost analysis.

Olympus Air Starter Motor (ASM) Life Extension Programme :

With an overhaul cost of £ 12.5 K per unit, a fleet arising of 22 units per year and a lengthy turn around time, Olympus air start motors are a high value annual investment in terms of R&O activity. There are, however, a number of critical issues which must be born in mind when forming a Life Extension Programme for this accessory as there are cyclic fatigue issues with their rotative components which must be considered.

The rotor disks are lifed by the OEM at 7,500 cycles, however, the current IBO for Olympus air start motors is defined by the Design Authority as 1,250 cycles, each cycle representing one operation. That said, a Special Reporting programme shows a high number of ASM's achieving in excess of 2,500 operations over a number of years. Analysis of the removal data, combined with a drive to reduce the burden of managing a lengthy and somewhat unrealistic overhaul programme, suggests that the majority of Olympus air start motors achieve their full overhaul life before removal and can therefore be formally life extended past their current IBO.

Through a managed programme the aim will be to extend the overhaul life initially to a revised life of 2,500 operations and, following successful overhaul assessments and in increments of 750 operations to the rotor disc life of 7,500 operations.

Doubling the current IBO to 2,500 operations represents an R&O saving of £ 135 K per year. Based on rotor disc life, this saving rises to £ 225 K per year.

Combustion Can Life Extension Programmes :

Olympus : Introduction of improved standard OLG301 combustionware has lead to an increase in life from 2000 to 4000 hours of operation. Through further in-service running and inspections, the life of the non igniter combustors has been increased to an 'on condition' basis with further potential to achieve 8000 hours of operation, thereby halving the arisings and associated expenditure on overhaul.

Proposed savings; at a current rate of arisings of 36 combustors per year and an associated overhaul cost of £2.7 K per combustor, this represents a direct annual cost saving of £ 49 K per year not including the projected maintenance and engine availability benefits.

Tyne : In a 'cruise' role, Tyne engines accumulate by far the largest proportion of annual usage, sometimes remaining on-line for periods of 24 hours or more during any one period of operation. The demands on the engine and its ancillaries in terms of reliability and availability are therefore very real, with a mission profile closely approaching that of a commercial ferry during operation.

The combustionware aspects of the engine have proved to be generally acceptable and through discrete inspection programmes lives have gradually increased to the current position where, following a review of service experience at the

request of the RN, Rolls Royce have recently re-classified Tyne combustion chambers to an 'on condition' lifing policy.

Current inspection requirements alternate the use of ship staff and in-service support desk officers at periods of 2000, 4000, 5000, 6000 and 6500 hours but, in comparison to the service offered by the support desk, it could be debated that ship staff inspections rarely unearth defects as the level of expertise is low and there are limitations to on-board inspection equipment. We are proposing that ship staff inspections are discontinued in favour of a 'mid life' inspection by support desk staff at 4000 hours followed by further inspections at an inspection frequency set by the officer based on the results of the inspection through to 6500 hours of operation.

A review of results will be undertaken prior to relaxing all current programmed inspections up to full combustor life of 6500 hours. Clearly, this programme does not fully support the Rolls Royce recommendations but shows the benefits of user experience and enables other possible factors which may also have a significant impact on combustor life to be considered, such as burner degradation and engine optimisation procedures.

Further, the majority of burner changes are still conducted as a direct result of programmed inspection requirements. Reducing the number of inspections has financial advantages in terms of reducing burner overhaul arisings. Based on the proposed revision to inspection frequency, Tyne burner overhaul costs could be reduced by as much as £ 50 K per year from implementation of the programme.

Spey : Spey gas turbines introduced into RN service in 1986 were originally fitted with 'VZ' combustion cans which tended to form brittle flakes of carbon on the Reflex Airspray Burner (RAB). Fleet experience up to 1991 showed that carbon shedding could lead to damage occurring on the leading edges of the HP turbine blades and Nozzle Guide Vanes so the Improved Reflex Airspray Burner (IRAB) was introduced to eliminate the problems of erosion on hot end components. Set against a can life of 3000 hours, experience has, until now, been disappointing with the 'boost' profile of the engine placing a significant demand on combustionware. Early IRAB are prone to cracking accompanied by material loss, holing and 'green rot' (fluxing sulphidation). The life of this standard of can is currently about 2200 hours depending on where fuel has been embarked and significantly, the level of sulphur.

Of note is the fact that the Japanese Navy operate Olympus, Tyne and Spey on low sulphur fuel (typically 0.05 to 0.15 % Sulphur). Their running hour experience is extremely high and they have, reportedly, no associated problems as a result, typically achieving combustion can lives in excess of 4500 hours.

The current in-service IRAB design, SPG 711, introduced by modification campaign in 1996, is presently the preferred standard with in-service lives now just past 3000 hours. It is clear that increased combustion temperatures have a debilitating effect on can life so every effort has been made to reduce skin temperatures by using an additional row of angled effusion holes in the vicinity of the 'Y' ring. Other enhancements include full coverage bond and thermal barrier coatings (TBC), a single piece pressed flare combustor head instead of the welded two piece design and Nimonic 86 transply in the RAB end cap which increases flow of cooling air to the cold face of the RAB. Improvements have lead to real reductions in the levels of carbon and smoke, particularly at part load. IRAB have also all but eliminated 'hot end' erosion and holing so profound with earlier 'VZ' combustors.

It is now feasible to run past 3000 hours with SPG 711. There are significant savings to be made in this area, a recent study showing that over £ 1.5 M can be saved in repair costs over the remaining life of the RN Frigates through combustor life extension and through re-use of combustor discharge nozzles.

Operation and maintenance :

Maintenance methodology :

Considerable differences in operation and maintenance exits between a naval gas turbine and its aero counterpart. Personnel involved with aircraft are trained to work in a strictly regulated manner, however, the naval environment requires a more pragmatic approach but there are limitations in that ships staff do not gain sufficient experience to become specialists while on board. A number of mechanisms are in place to overcome these restrictions :

- Experienced engine specialist teams have been formed - the RN unit is currently based at MPS214 in Bath to assist ships on demand. Corporate knowledge is maintained through a mix of civilians and uniformed personnel.
- 'Upkeep by Exchange' (UxE) is the base philosophy for repair of the gas turbine onboard ship, thereby reducing the amount of specialist fault finding required and hence the skill requirement.
- Defect communication between ships and the specialist teams is maintained using the latest techniques including image transmission equipment ('Photo Phone'), which recently acquired a stereo tip measuring head to detect the size of cracks and depths of pitting visible through the endoscope eye piece.
- Onboard repair techniques have been developed and retained by the waterfront repair and specialist technical groups.
- Specialist dockyard teams have been created to carry out engine replacements.

Tyne Power Reduction :

In an early attempt to discover why large differences existed between RN and RNLN Tyne Demonstrated Mean Achieved Life (DMAL – Figure 8), the records of engines at overhaul bases were interrogated in the late 1980's to establish whether any trends were evident.
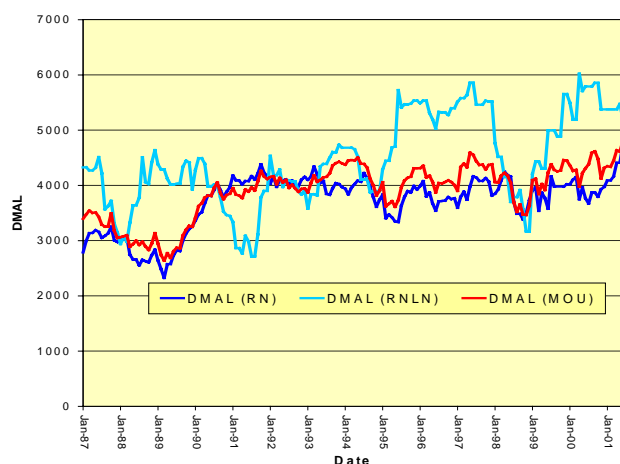
Figure 8 - Tyne Demonstrated Mean Achieved Life (DMAL).

Two families of engine were established through evidence of the condition of hot end components; scrap levels were high overall, but the components from the RN engines were significantly worse. The combustionware, NGV's and rotor blades on all engines showed signs of high or excessive temperature operation. A study of operational usage indicated the RN spent a slightly higher proportion of it's time at higher power levels although at the time this was thought not to be significant. The RNLN undertook a trial of two Tyne engines at 90 % power to establish the effects of lower running temperatures and the impact on operational capability. One of the engines became available at overhaul and was found to be in excellent condition. Furthermore, the RNLN identified that most of their operational requirements could be met using the 90 % power level despite the figures that had been drawn up in the original Staff Requirement. In the middle of 1989 both Navies adopted the practice of operating their Tyne engines at the reduced power level of 90 % (Figure 9).
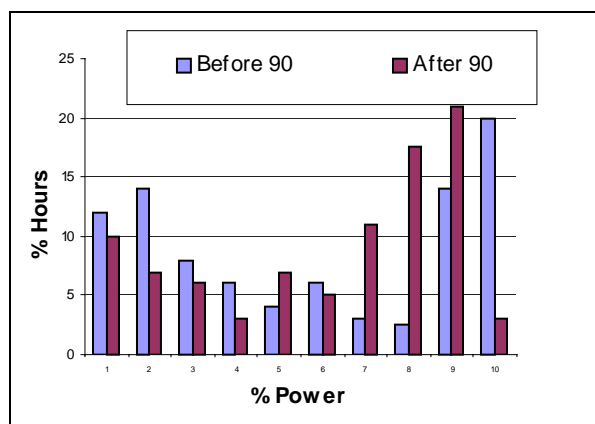
Figure 9 - Tyne engine powerbands showing 90 % rescheduling.

Tyne Engine Optimisation Procedure :

Today's DMAL for RN Tyne engines typically averages 4000 hours but this is 20 % lower than the figure for the RNLN at an average of 5000 hours achieved.

Clearly, analysis has been ongoing to fully understand the reasons surrounding the difference including investigations into bearing failures and oil hygiene standards, however, these have all proved somewhat inconclusive. A separate study by the RN, with much

liaison and assistance from the RNLN, recently compared engine operation, operator training and setting to work aspects with surprising results.

Observations concluded that somewhat unknowingly, the operating procedures in place routinely allowed the RN to over power it's engines. This was evident through ;

- the use of the LP RPM method of engine optimisation in an attempt to maintain original 'pass-off' compressor speeds without taking into account that higher lives can significantly degrade cycle efficiency leading to over fueling of engines and increased thermal degradation of hot end components,
- an inability (or misinterpretation) in applying the 90 % fuel flow limitation in service as discussed in previous text.

With the recent fitment of more accurate fuel flow meters in RN service (now within the $\pm$ 1.2 % accuracy demanded by the Design Authority), a recommendation is currently being drafted for the Command to adopt the fuel flow method of optimisation across the MoU fleet, to prevent 'over optimisation' of engines.

By increasing RN Tyne DMAL from 4000 to 5000 hours in line with the RNLN figure, the potential cost savings to the MOU are represented in the reduction of premature engine removals by as much as 2.7 engines per year, equivalent to a support cost of £ 900 K. If the proposed DMAL target is achieved then the reduction in fired hour cost could be by as much as 14 %.

Similarly, by striving to increase both RN and RNLN DMAL from 5000 hours to 6000 hours, a further predicted saving approaching £ 1.0 M per year could be made, potentially reducing hourly running costs by as much as 20 % from today's figures (Figure 10).
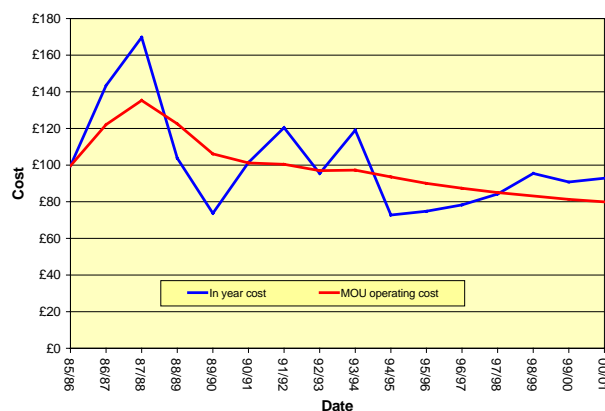
Figure 10 - Tyne hourly operating cost.

Improvements to Spey HP Bleed Valves (HP BOVs) :

Unlike their aero cousins, failure of the HP BOV (and associated Shutdown Control Valve) is a predominant early feature of unreliability for the SM1A and SM1C where the valves were found to be intolerant to fluid carry over into the air bleed system from compressor washing. Problems were experienced with gumming of the carbon seals accompanied by pitting corrosion of sliding surfaces.

In the short term, interim procedures for in-service valve reclamation were introduced followed by a requirement to prove operation of each unit after shut down for long periods. This, however, was somewhat tedious and presented operational difficulties. In addition, and to overcome the burden of additional maintenance, a long term solution was identified :

- A valve improvement campaign has begun. This entails chrome plating internal sliding surfaces accompanied by a new chemically nitrided centre bush which resists the galvanic couple when used with other materials in the valve. Two valves are in service on RNLN SM1A ships with very satisfactory performance so far.
- The timing point for injection of washing and inhibiting fluids has been re-scheduled to occur 15 seconds after starter cut off. This has had the effect of dropping spool speeds sufficiently enough to allow compressor cleaning but more significantly, in terms of BOV operation, has prevented wash fluid escaping up into the bleed ducting.
- A 'back to back' engine trial is underway to evaluate whether there is actually a need to undertake compressor cleaning (see text below).

RN trial aimed at deletion of compressor washing and inhibiting :

Original Spey washing and inhibiting routines traditionally carried out to restore engine performance and prevent corrosion were originally derived from the aero Spey which used untreated steel components in the compressor although the marine Spey uses high grade titanium and sacrificial coatings. As such it could be argued that the marine engine is not as susceptible to corrosion.

A ship trial which began in 1999 and is almost complete, is being run to monitor and assess the effect on performance when compressor cleaning and inhibiting are discontinued. This has required a 'back to back' approach with one engine acting as a baseline receiving water washing and inhibiting routines in the normal manner and the other engine receiving no activity at all.

There are many anticipated benefits available through deletion of washing and inhibiting :

- in terms of operability: reduced maintenance penalty and greater engine availability through less disruption to the ships propulsion configuration,
- in terms of performance: increased reliability of LP and HP BOVs, better anti fouling resistance of compressor blades (less gumming), increased starter motor lives through reduced operations and a reduced risk of downstream effects,
- in terms of health and safety: less operational and maintenance risk to ship staff through a reduction in HAZMAT fluids and the disposal of such fluids,
- in terms of materials and stores: a reduction in compressor cleaning fluid purchases and onboard stores and a reduced demand for compressed air required for engine washing and drying out operations.

Results to date indicate that with the unwashed engines in both trial ships engine health and performance has not suffered any discernable amount that could give rise to problems with a lack of power, high temperature operation or early governor interaction. Furthermore, salt fouling of compressors has been tolerable which brings the frequency of water washing into question. It is suspected that the oily film which has been identified on LP compressor blades is as a result of exhaust gasses from the diesels or the gas turbines themselves being drawn into the engine air intake. It is unlikely that airborne pollution is to blame especially in the marine environment.

Without wishing to pre-empt the final study report, and despite some initial scepticism, it is clear that there is little benefit to be gained by water washing and inhibiting engines in a marine environment. Furthermore, indications are that as a minimum a significant reduction in the frequency of washing will be possible, perhaps even culminating with a 'once per year' routine rather than the current 48 hour operation on the Spey. In conducting a routine at such a reduced frequency, there is also a need to address the quality and effectiveness of the actual procedure and chemicals used if a much increased periodicity between washes is recommended.

No attempt has been made to quantify the extent of the benefits which can be made, sufficient to say that it is understood there are a number of very interested parties in the results, a presentation of which is planned for ASME 2002. However, prior to this time, discussions to adopt a similar practice for Olympus and Tyne operation are already underway.

Periods of engine inactivity :

Ships are often inactive for prolonged periods because of leave or maintenance periods. As the engines are not used during these periods, fuel system components become sticky, oil coolers degrade and oil wetted internal surfaces and bearings are prone to corrosion due to humidity and drain down. The last point in particular has lead to an increased incidence of bearing rejections at overhaul due to surface corrosion. Measures in place to address these issues include :

- Introduction of OX22 lub oil: lubricating oil has been replaced by a specially developed synthetic marine gas turbine oil (OX22) that includes a better anti-corrosion additive package to reduce internal corrosion and attracts reduced cost,
- On-engine fuel systems: engine fuel systems are kept primed and closed during major maintenance activities and then 'exercised' before engine run up,
- Dehumidification: conservation measures are in place to protect engine gas paths against corrosion during maintenance periods,
- Introduction of Titanium SW/LO Coolers: A study in 1999 revealed that 21 Spey and Tyne engines (mainly in RN service) had been removed due to bearing failure which could be attributed to seawater lub oil cooler (SW/LO) tube perforation. Despite specialist assistance, however, the reason for failure had gone largely unresolved until the RN conducted a study of the sources of contamination at the time of failure and combined this with the dates of any maintenance conducted and with work that was underway with fuel tank corrosion. Tube failures were found to have been caused through the presence of 'Sulphate Reducing Bacteria' which attacked the oxide film on the inside of the tubes leading to Microbial Induced Corrosion. The phenomenon was most evident in estuarial waters when coolers had been shut down for maintenance. In these conditions the microbes thrive on the sulphate rich water in low levels of oxygen. From this discovery, the WSA embarked on a programme to replace existing

Copper Nickel cooler tubestacks with items manufactured from Titanium. This activity was combined with increased ships husbandry to drain cooler bodies if periods of inactivity were going to be longer than two weeks. Replacement by a titanium tubestack will ensure 100 % integrity under all operating and dormant conditions. Inspections to date indicate the tubestacks in service are in an excellent condition with no indications of any electrochemical or galvanic action. Furthermore, there have been no new failures in service.

As previous failures were unwittingly taken as 'the norm' over the fifteen year reign of bearing problems, implementing a strategy to resolve the cooler problem directly reduces the premature removal rate whilst providing a significant financial return of at least £ 0.5 M per year in reduced R&O activity.

Steel exhaust gaskets as a replacement for fibre items :

Asbestos free gaskets were introduced into the Tyne and Olympus inventory in 1994 to eliminate asbestos from main propulsion uptake systems. Whilst these meet Health & Safety legislation, they were proving unreliable averaging 25 RN Tyne and 30 RN Olympus gasket failures per year. As a replacement for asbestos, in 1991 the RNLN introduced a re-usable stainless steel gasket using Silkoset high temperature sealant. This was subsequently introduced as a standard fit across the RNLN fleet in Tyne, Olympus and Spey uptake systems proving to be both reliable and cost effective. A similar programme is now underway to embody this modification on all other MOU gas turbine vessels. A phased implementation is envisaged during Upkeep Periods or lightly loaded Maintenance Periods, however, there will an offset in potential savings against procurement and installation costs and replacement of previously good gaskets.

For Olympus and Tyne, the steel gaskets are low cost items at around £300 each, however, by preventing failures from occurring with fibre gaskets, the steel replacements being a 'one-time' investment represent a typical saving of approximately £ 340 K per year with a consequential increase in engine availability to the command.

Leaving engines installed during major maintenance periods :

In terms of engines removed during maintenance, 'Policy' removals concern the removal of serviceable engines when, for example, a ship enters a Refit Period or there are insufficient hours to undertake the next deployment. In terms of Tyne operation prior to 1989 a large number of these engines would go to the overhaul base for overhaul (sometimes both engines from the same ship if running hours were equal). Between them, the Navies agreed that engine hours needed to be managed such that there was a difference in running hours between the two propeller shafts, basically designating a preferred engine with the objective of ensuring that when a ship entered a period of maintenance requiring both engines to be removed, one engine should have useful life remaining thereby allowing it to remain in-situ, rather than both having insufficient life for deployment.

The minimum engine hours allocated for all regular deployments were also reviewed. A study of the historical records revealed that a strong case could be made for reducing the number of engine hours required for deployment providing that one engine met minimum criteria in terms of remaining hours. These two actions reduced policy removals by as much as 5 Tyne engines per year. Similar policies to leave engines in-situ during maintenance have also been accepted for Olympus and Spey unless specific issues with the hot

end mean the engines must be removed for inspection, repair or overhaul. With an average of 10 policy removals per year between ship classes, this initiative delivers a saving of approximately £ 200 K per year.

Photo-Phone inspection diagnostics :

Recent technological advances in digital processing and the ongoing development of e-mail now allows the RN support desk and other MOU operators the capability of offering a sophisticated imaging and analysis service when conducting planned life engine inspections or during fault finding procedures. Accompanying this initiative has been the fleet wide introduction (to gas turbine powered ships) of the 'Photo-Phone' system which allows ships on deployment an opportunity to communicate endoscope inspection images and written text by modem in real time to a fixed land line for analysis and / or in seeking advice by specialist or Design Authority staff.

This allows a very high degree of flexibility in terms of resource allocation whilst reducing response times thereby allowing better programme management and improved decision making.

Hardware is fully supported by Olympus Industrial and ImageBase Technology Ltd., both of which strive to retain close links with the RN support staff in order to incorporate any new technology as and when it becomes available into the suite of inspection equipment held by the desk officers. Recent advances include the provision of endoscope probe tips incorporating a stereo measurement facility allowing increased accuracy in classification and size of defects. Typical examples where this has been an advantage have been during the measurement of crack lengths in Spey transply combustion cans and during the classification of Tyne HP nozzle guide vane (NGV) leading edge perforations. The equipment also provides a reliable source of high quality data in which to base engine Life Assessment and Life Extension recommendations.

Reliability Centered Maintenance (RCM) :

As a Condition Based Maintenance tool, RCM is not new. However, it has only recently been introduced on the Spey engine in operation with the RN Type 23 Frigate as an alternative to the previously prescribed Planned Maintenance Programme. Whilst the level of maintenance required has been reduced, the emphasis is now on better placement of the maintenance resource with much more consideration for undertaking maintenance when performance deteriorates rather than on an autocratic basis. Following a Failure Modes, Effects and Criticality (FMECA) review and with the full support of the Design Authority, the first ship is due to receive the revised maintenance methodology in trial format later this year with full platform RCM roll-out occurring in early 2002. It is somewhat early to draw conclusions as to its effectiveness, however, RCM has been successfully adopted in the RN Hunt Class Mine Counter Measure Vessels.

<u>**Component rejection criteria and acceptance limits:**</u>

Interpretation of limits :

Late in 1989 and in the early part of 1990 a sudden occurrence of Tyne rejections due to internal failures of an external

gearbox was noted, some of these occurring at relatively low running hours. As engine removals were assessed, it soon became clear that one of the two overhaul bases was responsible (at the time) and following investigation was found to be misinterpreting the requirements of the overhaul specification. With the problem now corrected, the premature overhaul of Tyne gearboxes, and hence support costs, reduced significantly. This is an early example of the need to carefully monitor the acceptability and effectiveness of in service acceptance criteria.

Relaxation of component rejection criteria :

Clearly, there are gains to be made through relaxing rejection limits.   For this reason collaborative programmes have been established with the Design Authority to extend the in-service rejection criteria of a number of components where feasible. Real successes have been achieved in the areas of combustion can limitations, NGV erosion / cracking limits and defects associated with turbine blades.   However, human nature being what it is, overarching the criteria is the need for clear and responsible guidance in correctly interpreting any limitations imposed.

Technology de-risking for new ship projects :

WR21 Neptune high velocity intake filter project :

In order to safeguard marine gas turbines principally from foreign object damage (FOD) and salt ingestion there is a high degree of importance placed on the intake system, a principal element within which is the intake filtration equipment.

Since the introduction of marine gas turbines the RN have witnessed and participated in the development of intake filtration systems from knitmesh filters to highly efficient 3 stage separators (spray eliminators).   Conventional layouts have provided many years of successful operation, however, not only do the systems themselves require a large amount of space (which is already at a premium), but they also introduce areas of weakness into the ship's structure resulting in a number of cracking problems currently evident on several classes of ship.

A design and development study is currently underway between the RN and Altair Filters Ltd., one of the principle MOU intake filter manufacturers. The project has been established to look into the possibility of moving away from conventional separators to the use of new generation high velocity spray eliminators with a view to both commercial use and, at this time, confirming the suitability of the equipment for the intakes of the WR21 Intercooled Recuperated gas turbine chosen for the new RN Type 45 Frigate, the challenge being to build a compact, faster spray eliminator using a much smaller plenum chamber.   This, however, necessitates an increase in the velocity of the air to be processed, the problem being to ensure there is no relaxation in the efficiency of the salt particulate and water separation.   Advantages being explored include reduced procurement costs, reduced maintenance costs and reduced radar cross section.

With a clear aim of de-risking the technology and using the data to calculate intake sizes prior to incorporation into the Type 45, the design route chosen uses a hardware demonstration and evaluation phase (Figure 11) followed by back to back testing of a 'Neptune' system with a conventional unit onboard an RN Type 22 Frigate (Figure 12).

Figure 11 - Neptune high velocity filter during development testing.

Figure 12 - Neptune high velocity filter trial - HMS Coventry (Neptune filter left, conventional spray eliminator right).

HMS Coventry was chosen because the ship operates with rear facing intakes that are not sheltered thereby providing a harsher filtration environment than on many other vessels and also because there was a convenient fitting opportunity in the ships programme followed by operation in UK waters before going further afield.

At the time of writing, initial results indicate that the trial, which is due to end in November) is progressing well, with the Neptune unit performing as good as, if not better than, the conventional system.   It is the intention that a further insight into the results and conclusions of the trial will be presented at the next ASME Conference in Amsterdam 2002.

Improvements in in-service support administration :

Formation of Integrated Project Teams (IPT's) :

In   recent   years,   improvements   in   customer   supplier relationships have been made through the collocation of all the RN's marine propulsion support staff. Driving this challenge has been the formation of multi disciplinary groups which has lead, over the last two years, to a move in the Defence Logistics Organisation to the creation of IPT's. This has brought many benefits in the way we conduct business; in reducing operating costs, in achievement of key performance indicators and, ultimately, maintaining vessels at sea with zero defects. The main overarching improvement within the group has been in terms of communication and the increased teamwork of staff to achieve business goals.   Furthermore, IPT formation has increased both internal and external customer liaison and

decision taking, even if this is achieved during a simple fleet enquiry such as in the team's ability to question a stores demand.

Revised methods of support :

The RN is exploring, wherever practical, the possibility of revised methods of Through Life Support. Where it represents value for money and makes operational sense, the transfer of responsibility for risk and support to contractors is being evaluated accompanied by incentivisation and gainshare techniques. As well as an inherent need for the contractor to provide a positive track record if they are to be considered in such an approach, there will always be a need to retain intelligent customer status, a characteristic which is extremely difficult to nurture and develop but all too easy to lose if due consideration is not given to all of the issues highlighted during the decision making process in any move to Contractor Logistic Support (CLS).

Management of operational data and performance trend monitoring :

During operation of marine gas turbines a generic approach towards maintenance has been established. To benefit from the accumulating knowledge, extensive data bases maintained by support officers collate information gathered during engine operation as well as accumulated during repair and overhaul activities. The information is processed and displayed in graphical form thereby enabling effective trend monitoring and allowing changes in procedures and equipment modifications to be evaluated in terms of reliability. Graphs used in this paper are based on the Premature Removal Rate (PRR) and Mean Time Between Removals (MTBR), trending techniques maintained for all engines.

<u>**Compliance with Environmental Legislation :**</u>

Current topics being addressed include :

- <u>Replacement of parts containing Asbestos:</u> Modifications to introduce alternatives to parts that contain Asbestos have been generated on all three engine variants and a replacement programme is currently underway for carried onboard spares and those required during repair and overhaul.

- <u>Replacement of Halon fire fighting gas:</u> As a potentially ozone depleting fire fighting gas, a Statement of Requirements for a replacement fire fighting medium has been generated and dialogue is in place with contractors to identify and develop suitable alternatives to the halon based systems in MOU operation. With the potential for increased risk of thermal shock from a water mist based system and the increased storage volumes and pressures of a CO_2 solution, the use of novel techniques such as pyrotechnically generated aerosols and inert gas generators are also being considered both for retrofit into MOU ships and for adoption in the RN Type 45 Destroyer.

- <u>Replacement of parts containing Cadmium :</u> Following the format for Asbestos replacement, modifications to introduce alternative parts to those that contain Cadmium are also being generated on all three engine variants and will be followed by a phased programme of replacement

<u>**Managing obsolescence :**</u>

Various strategies are being used to address obsolescence issues as and when they arise either ;

- through the purchase of 'one-off life time buys',
- by cannibalising assets that are considered surplus,
- by development of unique alternatives with manufacturers.

Rolls Royce support in providing Design Authority guidance is preferred, however, in terms of customer support and experience, there is a move to the formation of direct partnership arrangements with original manufacturers. Components currently being addressed include the future support arrangements for turbine entry temperature amplifiers, igniters, vibration transducers and the Spey Analogue Fuel System Controller (FSC). It is worthy of note that Rolls Royce have approached the FSC issue by developing their own SM1C Digital Engine Control Unit (DECU) in collaboration with CAE Ltd. of Montreal, Canada. This design is being installed in the new RNLN LCF Frigate for which RN training facility assets were employed during DECU testing. Despite the improved availability aspects that a DECU allows in terms of a replacement for the analogue system in MOU service, it is, without doubt, a high value investment which in the current climate cannot be justified as cost effective.

<u>**The Future :**</u>

In terms of reducing Through Life Costs for aging prime movers, we see the way ahead as being one of continued vigilance and assessment of in service experience, searching out the drivers that decrease safety and increase operating costs and applying a no nonsense approach to achieve cost effective solutions.

In brief the following is our continuing approach :

- regard the Planned Life of an engine as being a target which may be exceeded in a controlled manner. Areas of risk will be further investigated and cost effective solutions found to allow increased running hours and lower removal rates to be achieved. The life of critical components will be respected,

- continue to develop, on a priority basis, improved in-service acceptance limits allowing extended running whilst managing risk,

- change, whether in configuration, maintenance or policy, nearly always involves expense, budgets have become tighter and therefore 'Financial Appraisals' have become a necessary discipline. The solutions adopted will have to pass the "How much ... ?" question, and if the answer is not "..... a saving", then a very good technical case will be required,

- the maintenance policy for engines in service will continue to be 'Upkeep by Exchange' (UxE), rather than repair in-situ. This policy has advantages for the smaller navies of the MOU,

- the continued support of the engines in later years when numbers become fewer, will need to be carefully managed with the method of disposal of the ships clearly defined and respected. If ships are sold complete with gas turbines and a spares package, a balance between the requirements of the MOU partners and their customer's interests will have to be made. Should the ships be scrapped then the support position will be somewhat simpler but will be lead by operational requirements and ever present financial considerations,

- the future years will be approached with some confidence in that we can maintain existing performance and, preferably, improve on it in most areas.

In conclusion, the DLO has a testing strategic goal which aims to improve the overall cost effectiveness of support. We have recognised that there will still need to be a managed risk programme and that we will still need to produce solutions to 'in- service hurts' that are both cost effective and technically acceptable.

Most of the advantages predicted for a continuing gas turbine operation policy are being realised in practice, indeed, some of the anticipated disadvantages have not been as serious as expected. Warship availability has improved; it is proving possible to increase the intervals between overhaul to double those originally prescribed with significant benefits to the defence budgets; and marine engineering complements have reduced significantly, yielding further benefits in operating costs.

Finally; any views expressed are those of the author and do not necessarily represent those of the Department / Agency.

BIBLIOGRAPHY :

Lt.Cdr. A.Schaap (RNLN) / Mr. R. Bolwell (UK MoD MPS214); Experience with Aero-Derivative Gas Turbines as Marine Propulsion Machinery, NATO RTO Paper, Symposium on Gas Turbine Operation and Technology for Land, Sea and Air, Ottawa 1999.

Mr. P.A.Denton, DLO MPS214; RN Gas Turbine Life Assessment and Extension Programme, RNE extract 51(4), 1998.

Mr. R. K. Mudge (UK MoD MPS214) / Mr. S. D. Hiner (Altair Filter Technology Ltd.); Gas Turbine Intake Systems - High Velocity Filtration For Marine GT Installations, ASME Paper, April 2001.

Paper 4: Discussion

<u>Question from D Shepherd – QinetiQ, UK</u>

Are the planned lives of your naval gas turbines the same as the component lives?

<u>Presenter's Reply</u>

No, the planned lives represent the Interval Between Overhaul (IBO). Critical component lives are the lives of those components within the engine that, if failures were to occur, represent a hazard to operator or engine safety. These lives are usually much greater than the IBO. An example of life extension of the IBO for the Spey SM1A turbine is that life between overhauls, the planned life, has been extended from 3000 to 6000 hours, however, we still respect the critical component lives. We are currently in the process of validating exchange rates and operating profiles to support us in assessing whether we are actually able to progress further IBO extensions or, indeed, whether we have got the original assumptions wildly wrong, either to our advantage or disadvantage.

This page has been deliberately left blank

———————————

Page intentionnellement blanche

Coupled Multi-Disciplinary Optimization for Structural Reliability and Affordability

Galib H. Abumeri[1]
QSS Group Inc.
21000 Brookpark Road
Cleveland, OH 44135, USA

And

Christos C. Chamis[2]
NASA Glenn Research Center
21000 Brookpark Road
Cleveland, OH 44135, USA

Abstract

A computational simulation method is presented for Non-Deterministic Multidisciplinary Optimization of engine composite materials and structures. A hypothetical engine duct made with ceramic matrix composites (CMC) is evaluated probabilistically in the presence of combined thermo-mechanical loading. The structure is tailored by quantifying the uncertainties in all relevant design variables such as fabrication, material, and loading parameters. The probabilistic sensitivities are used to select critical design variables for optimization. In this paper, two approaches for non-deterministic optimization are presented. The non-deterministic minimization of combined failure stress criterion is carried out by: (1) performing probabilistic evaluation first and then optimization and (2) performing optimization first and then probabilistic evaluation. The first approach shows that the optimization feasible region can be bounded by a set of prescribed probability limits and that the optimization follows the cumulative distribution function between those limits. The second approach shows that the optimization feasible region is bounded by 0.50 and 0.999 probabilities.

Introduction

Aircraft engines are assemblies of dynamically interacting components. Engine updates are required to keep aircrafts flying safely. In addition, engines for new aircrafts are progressively required to operate in a more demanding technological and environmental constraints. Designs to effectively meet those requirements are collections of multi-scale, multi-level, multidisciplinary analysis and optimization methods and probabilistic methods. These types of methods are necessary to quantify respective uncertainties and are the   only ones that can formally evaluate advanced composite designs, which satisfy those progressively demanding requirements while assuring minimum cost, maximum reliability and maximum durability.

Recent research activities at NASA Glenn Research Center have focused on developing multi-scale, multi-level, multi-disciplinary analysis and optimization methods. Multi-scale refers to formal methods which describe complex material behavior; multi-level refers to integration of participating disciplines to describe a structural response at the scale of interest; multi-disciplinary refers to open-ended for various existing and yet to be developed disciplines. For example, these include but are not limited to: multi-factor models for material behavior, multi-scale composite mechanics, general purpose structural analysis, progressive structural fracture for evaluating durability and integrity, noise and acoustic fatigue, emission requirements, hot fluid mechanics, heat-transfer and probabilistic simulations. Many of these, as well as others, are encompassed in an integrated computer code identified as Engine Structures Technology Benefits Estimator (EST/BEST[1]). The discipline modules integrated in EST/BEST include: engine cycle (thermodynamics), engine weights, internal fluid mechanics, cost, mission and coupled structural\thermal, various composite property simulators and probabilistic methods to evaluate uncertainty effects (scatter ranges) in all the design parameters.

---

[1]Senior Research Engineer
[2]Senior Aerospace Scientist

The objective of the paper is to present methods\codes for simulating computationally the process of tailoring a hot composite engine structure in the presence of uncertainties in material fabrication, material thermo-mechanical properties, and loading. An internally pressurized CMC duct subjected to forced convection loading condition on its inner walls is used to illustrate its application to non-deterministic optimization. The respective variables are defined as primitive variables.

The EST/BEST (Engine Structures Technology Benefits Estimator) software, shown in figure 1, is used to carryout the investigative study presented in this paper. Component as well as system evaluations are performed within a single software. The modules included are integrated computer codes with multiple functional capabilities. The ones that were used for the results to be presented later are (1) Cosmo for finite element generation; (2) Material Library - for composite mechanics simulation; (3) IPACS[2] for composite structures probabilistic evaluation and (4) CSTEM[3] for coupled structural/thermal analysis and Optimization

Deterministic Coupled Structural/Thermal Analysis

A hypothetical engine duct made from woven fabric (Nextel 720 fiber and Aluminosilicate matrix) is modeled as a tube with a uniform wall thickness of 0.1" and mean height of 1.0".   The Material Library in EST/BEST is used to estimate the balanced weave/thermal/mechanical properties of the composite system based on a fiber volume ratio of 0.45 and a void volume ratio of 0.1. The layup of the tube consists of 10 plies oriented as follows: $[2(0,90),0]_s$. The considered composite system is cured at a temperature of 300 F.

The coupled structural/thermal analysis of the CMC duct is carried out using the CSTEM code in EST/BEST. The duct is subjected to an internal pressure of 50 psig and forced convection on its inner walls. The forced convection is based on the flow of hot air through the duct at a velocity of 0.2 MACH and a convection temperature of 3000 F. On the outside of the duct, free convection at 70 F is considered. The structural deformation of the duct with internal pressure only is shown in Figure 2-a. The addition of the forced convection and its effect on the deformation of the duct is displayed in Figure 2-b. Note that the maximum displacement obtained with the application of combined thermo-mechanical loading is about eight times higher than that obtained with internal pressure only. The temperature distribution obtained for the composite duct from the coupled structural/thermal analysis is shown in figure 3. The temperature varied from 2935 F on the inner walls of the duct to 2821 F on the outside.

In CSTEM, the combined stress failure criterion is evaluated. The combined failure stress criterion is computed by summing various ply stresses to strength ratios. A failure function less than 1 indicates no failure, that equal to 1 indicates failure and greater than 1 indicates imminent failure.

Non-Deterministic Coupled Structural/Thermal Analysis

In EST/BEST, the IPACS module is used to perform probabilistic assessment of the composite structure.   With the direct coupling of composite mechanics, structural analysis and probabilistic methods, IPACS is capable of simulating uncertainties in all inherent scales of the composite, from constituent materials to the composite structure and its loading conditions.

Figure 4 shows the probabilistic evaluation of the CMC duct under combined thermo-mechanical loading. The effects of uncertainties in composite material properties, composite fabrication parameters, and combined thermo-mechanical loading are assessed. The combined stress failure criterion is evaluated probabilistically based on the following scatter in primitive variables: ±5% in fiber and matrix moduli, and convection temperature; ± 10% in fiber and matrix thermal conductivity, matrix thermal expansion coefficient, matrix strength, fiber volume ratio and heat transfer convection coefficient; and ± 15% in fiber thermal expansion coefficient and fiber strength, void volume ratio, and internal pressure.   The scatter ranges considered here are typical for the primitive variables selected in the study.

The results from the probabilistic evaluation are presented in Figure 4. Note that for a probability higher than 0.92, failure is imminent. The probabilistic sensitivities of the combined stress failure criterion to the scatter range of the primitive variables are presented in figure 5. The objective of this particular evaluation is to identify the primitive variables critical to the failure of the CMC duct.   Based on the probabilistic sensitivity analysis, the list of critical

primitive variables can now be reduced to include matrix modulus, matrix thermal expansion coefficient, matrix conductivity, matrix strength, fiber volume ratios, and void volume ratio. These set of primitive variables are used as design variables in the optimization. Although the primitive variables for loading show significant effects on the combined stress failure criterion, they are not included in optimization. These are assumed to be constant with values of their respective means.

Non-Deterministic Multi-disciplinary Optimization

Non-deterministic optimization may be defined as follows:

Find a set of primitive variables (those that describe the physics and can be varied by the designer such that some combined objective (merit) function is simultaneously minimized/maximized subject to probabilistically described variability in the primitive variables and in the constraints of the behavior (response) variables. In equation form the above statement is expressed thus:

Optimize: $\Im$ (P.V.) $\ni$ max (P_d) min (P_c) max (P_s) min (P_f) And $\ni$ $P_{lb} \le$ (P.V.) $\le P_{ub}$

Where $\Im$ is the function to be optimized; P.V. are a set of primitive variables; the symbol $\ni$ denotes such that; P_d is the probability of durability; P_c is the probability of cost; P_s is the probability of survivability and P_f is the probability of failure. The non-deterministic evaluation pursuit consists of three different parts. Part one is probabilistic evaluation followed by optimization. Part two is optimization followed by probabilistic evaluation. Part three is the simultaneous evaluations as defined above. The work presented in this paper does not include the three-part evaluation study.

Note that the non-deterministic optimization is carried out based on a design (feasible) region that is constrained by the limits that are determined in the probabilistic evaluation. As indicated in figure 6, the feasible region bounds are represented by the limits set at high and low probability levels. Results for probabilistic evaluation followed by optimization and for optimization followed by probabilistic evaluation are discussed in the next two sections.

Probabilistic Evaluation of Failure Stress
Followed by Optimization

It is instructive to illustrate non-deterministic multidisciplinary optimization by minimizing the maximum combined stress failure criterion of the CMC duct. First a probabilistic analysis of the structure is carried based on the following scatter in primitive design variables: ±5% in matrix modulus; ±10% in matrix thermal expansion coefficient, matrix thermal conductivity, matrix strength, and fiber volume ratio; and ±15% in void volume ratio.

Results from the probabilistic evaluation of the combined stress failure criterion based the aforementioned uncertainties are shown in figure 7. For probability value of 0.001 (1 occurrence in one thousand trials) the combined stress failure criterion of the composite duct would be under 0.357 (No ply failure). For probability value of 0.95, the failure function would be under 1.05 (ply failure has occurred). Optimization is than carried out to minimize the maximum combined failure stress criterion while constraining the first natural frequency of the structure. The design bounds lower and upper limits for optimization are set equivalent to the most probable design at probability levels of 0.001 and 0.95 respectively. Limits for the frequency constraint are set to those obtained probabilistically at the probability levels 0.001 and 0.95 (6517 to 8412 cps).

As shown in Figure 7, the optimization process that starts at 0.95 probability, follows the cumulative distribution function and reduces the objective function (maximum combined stress failure criterion) from 1.05 to 0.48. The actual frequency constraint at the end of optimization is about 7179 cps. Table I lists a summary of initial and optimum design variables and constraints, initial and optimum objective function, and the most probable design at 0.001 and 0.95 probability levels. Note that the largest variation is in the void volume ratio where it is reduced by more than 60% followed by the matrix strength which is lowered by more than 25%.

Optimization Followed by Probabilistic Evaluation

The maximum combined stress failure criterion of the CMC duct is minimized subject to frequency constraint. As shown in Table II, an initial design vector is selected and the optimization process is initiated according to the bounds prescribed in the Table. The upper and lower design bounds are computed based on the scatter in the design primitive variables. For example and as described in the previous section, the scatter in the matrix modulus is $\pm 5\%$ with a mean of 4.4 results in low and high bounds of 4.18 and 4.62 respectively. Note that the optimization reduced the objective function (combined stress failure criterion) from 0.910 to 0.563.

Results from probabilistic evaluation after the minimization of the combined stress failure criterion are shown in Figure 8. The feasible design region is bounded between 0.50 and 0.999 probabilities. In that region, the primitive variables are within the high and low bounds that defined in Table II. The probability of having a combined stress failure criterion less or equal to 0.55 is 0.50. Also, the probability of having a combined stress failure criterion less or equal to 0.89 is 0.999.

Concluding Comments

Important concluding comments from non-deterministic optimization results are:

1. The use of a collective multi-scale, multi-level, multi-disciplinary analysis and optimization and probabilistic methods shows that non-deterministic optimization can be done by performing probabilistic evaluation first then optimization or optimization first then probabilistic evaluation.

2. Performing probabilistic evaluation then optimization shows that the optimization follows the cumulative distribution function. The probabilistic evaluation is computationally more efficient than optimization. If the accuracy of the probabilistic response at extreme probabilities is improved, the use of optimization is not necessary.

3. Performing optimization then probabilistic evaluation shows that the optimization feasible region is bounded by 0.50 and 0.999 probabilities.

4. The probabilistic sensitivities can be used to select a reduced set of design variables for subsequent optimization.

References

1. Abumeri, G.H. and Chamis, C.C.: T/BEST a computer code for assessing the benefits of advanced aerospace technologies, published in the Advances in Engineering Software journal, pp. 231-238, 1997 Elsevier Science Limited, Printed in Great Britain.

2. Chamis, C.C.; and Shiao, M.C.: IPACS – Integrated Probabilistic Assessment of Composite Structures: Code Development and Applications. Third NASA Advanced Composite Technology Conference, Vol. 1, Pt. 2, NASA CP-3178-VOL-1-PT-2, 1993, pp. 987-999.

3. Hartle, M.; and McKnight, R.L: CSTEM User Manual, NASA CR-2000-209308, January 2000.

**Table I. Summary of Results From Probabilistic
Evaluation Followed by Optimization**

Design Variables	0.001 Prob	0.50 Prob	0.95 Prob	*Initial Design*	Optimum Design
Matrix modulus (Msi)	4.314	4.4	4.44	4.44	4.314
Matrix thermal expansion coeff. (x 1.0E-06 in/in/F)	3.059	3.25	3.35	3.35	3.059
Matrix thermal conductivity (BTU/hr-ft-F)	3.097	3.0	2.94	2.94	3.097
Matrix tensile strength (ksi)	15.81	13.0	11.84	11.84	15.81
Fiber volume ratio	0.399	0.45	0.479	0.479	0.399
Void volume ratio	0.071	0.100	0.116	0.1168	0.071
Objective					
Combined Stress Failure Criterion	0.3577	0.781	1.00	1.058	0.482
Constraint					
1st Natural Frequency (cps)	Limit set between 6517 and 8412			8116	7179

Table II. Summary of Results From Optimization Followed by Probabilistic Evaluation

Design Variables	Lower Bound	Upper Bound	Initial Design	Optimum Design
Matrix modulus (Msi)	4.18	4.62	4.62	4.18
Matrix thermal expansion coeff. (x 1.0E-06 in/in/F)	2.925	3.575	3.575	2.925
Matrix thermal conductivity (BTU/hr-ft-F)	2.70	3.3	3.30	3.30
Matrix tensile strength (ksi)	11.70	14.30	14.30	14.30
Fiber volume ratio	0.405	0.495	0.495	0.405
Void volume ratio	0.085	0.115	0.115	0.085
Objective				
Combined Stress Failure Criterion	0.712	0.910	0.910	0.563
Constraint				
1st Natural Frequency (cps)	Limit set between 6590 and 8357		8357	7187
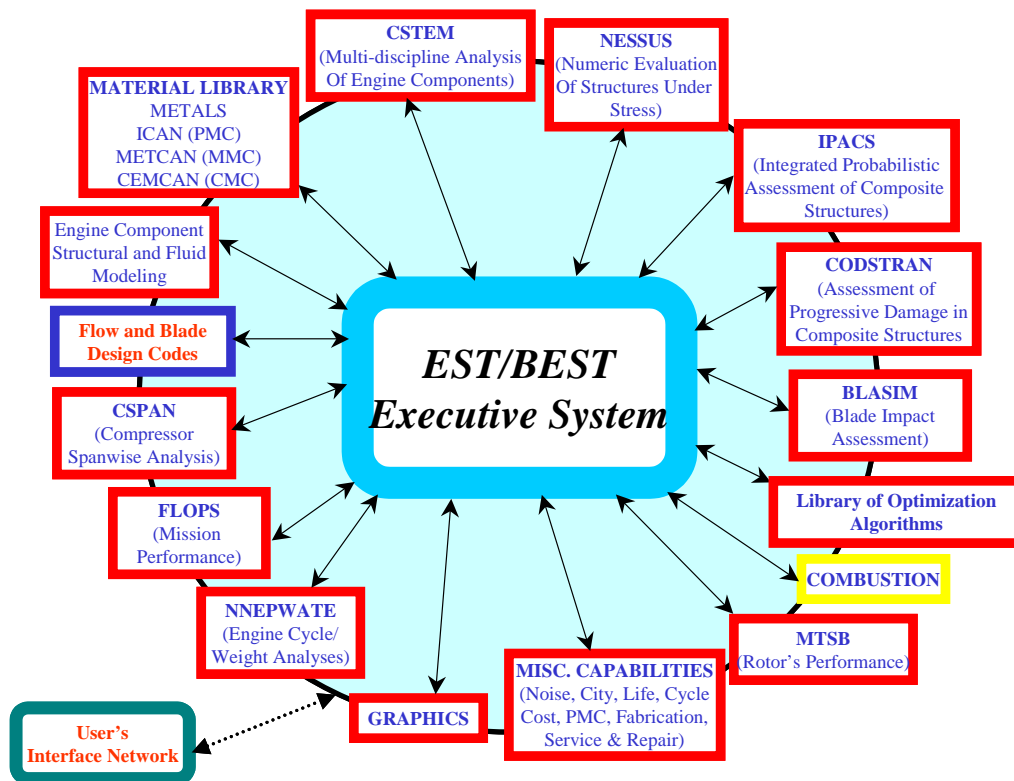
Figure 1. EST/BEST: Engine Structures Technology Benefit Estimator

a) With 50 psi Internal Pressure

b) With 50 psi Internal Pressure and Forced Convection
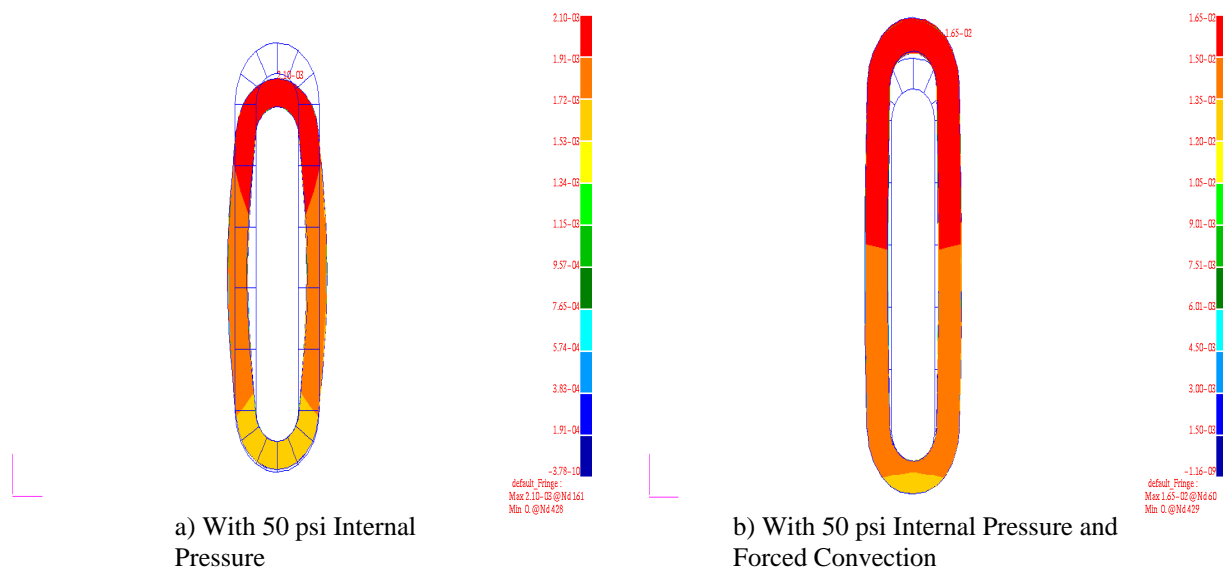
Figure 2. Displacement Fringe and Deformed Body Plots of CMC Duct
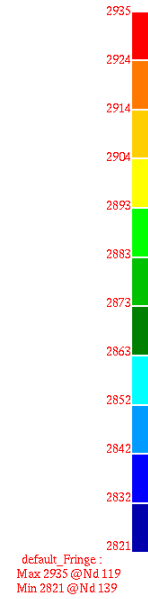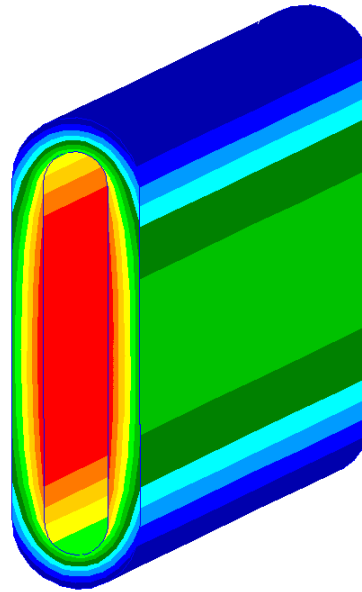
Figure 3. Temperature Plot of CMC Duct with Combined 50 psi Internal Pressure and Internal Forced Convection

Primitive Variables	Scatter (-/+%)
Fiber modulus (Ef11)	5
Fiber thermal expansion coefficient	15
Fiber thermal conductivity	10
Fiber strength (tension/compression)	15
Matrix modulus	5
Matrix thermal expansion coefficient	10
Matrix thermal conductivity	10
Matrix strength (tension/compression)	10
Fiber volume ratio	10
Void volume ratio	15
Internal pressure	15
Convection temperature	5
Heat transfer onvection coeffficient	10

Figure 4. Probabilistic Evaluation of Combined Stress Failure Criterion of CMC Duct – With Combined Internal Pressure and Forced Convection
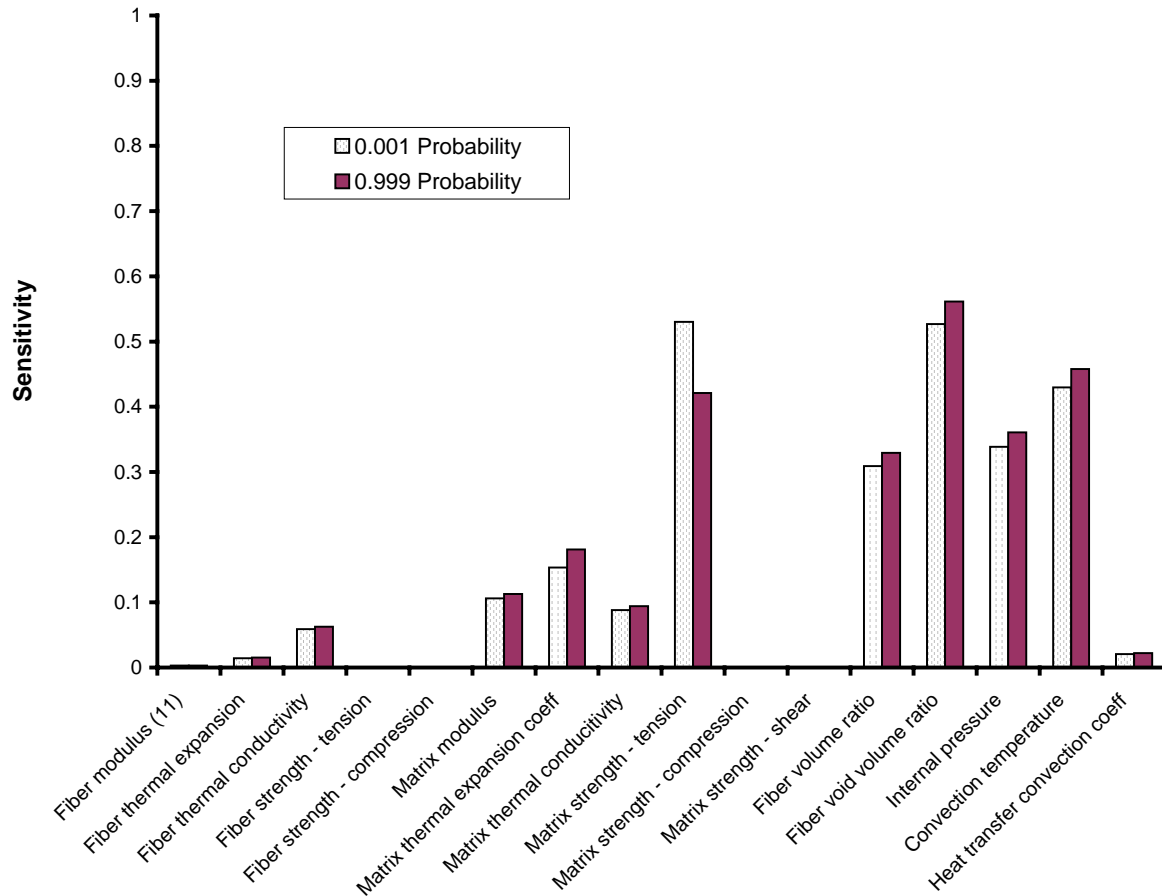
Figure 5. Sensitivity of Combined Stress Failure Criterion of CMC Duct to the Scatter Range - With Combined Internal Pressure and Forced Convection
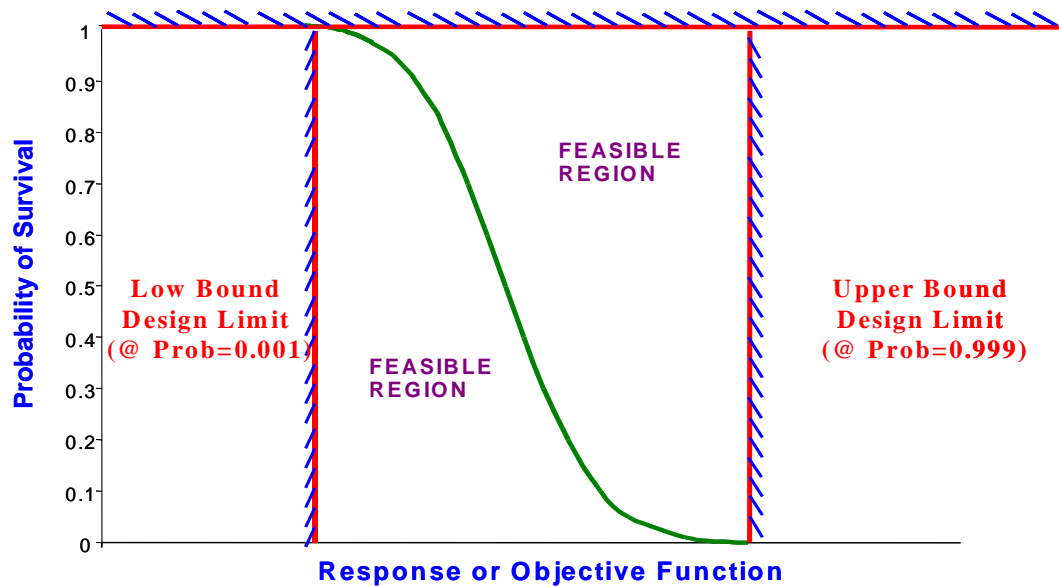
Figure 6. Optimization Feasible Region Based on Probabilistic Evaluation
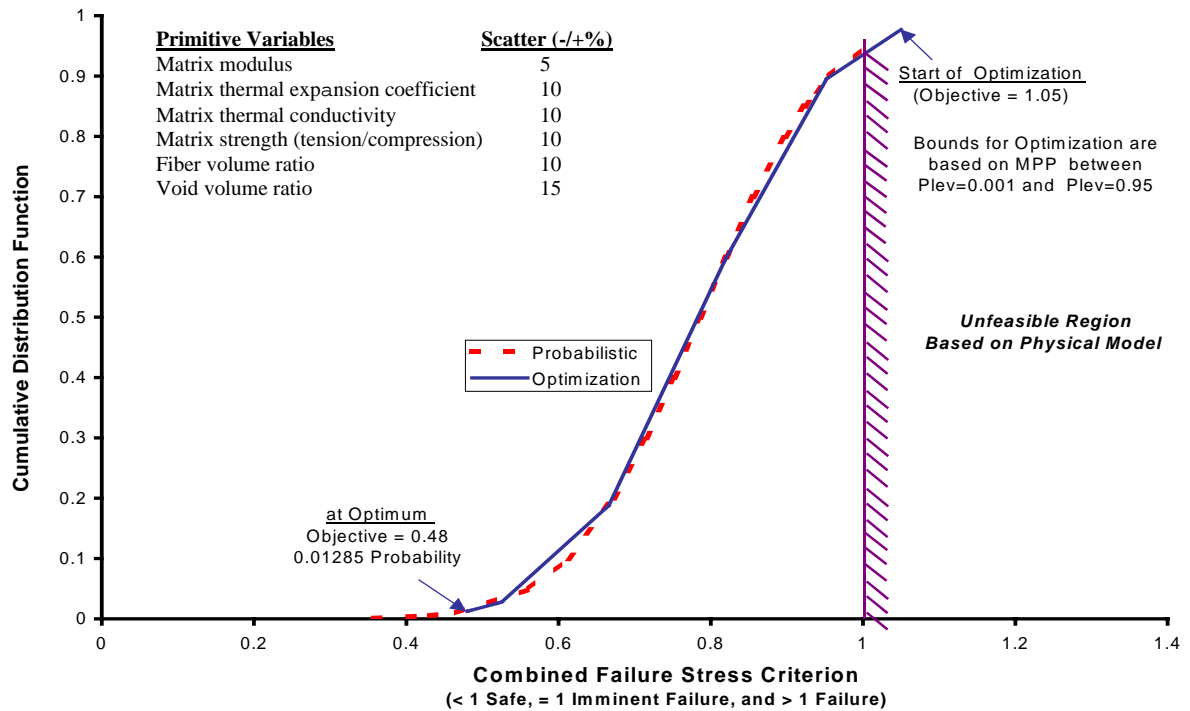
Figure 7. Probabilistic Evaluation of Combined Stress Failure Criterion Followed by Optimization (With Reduced Design Variables list)
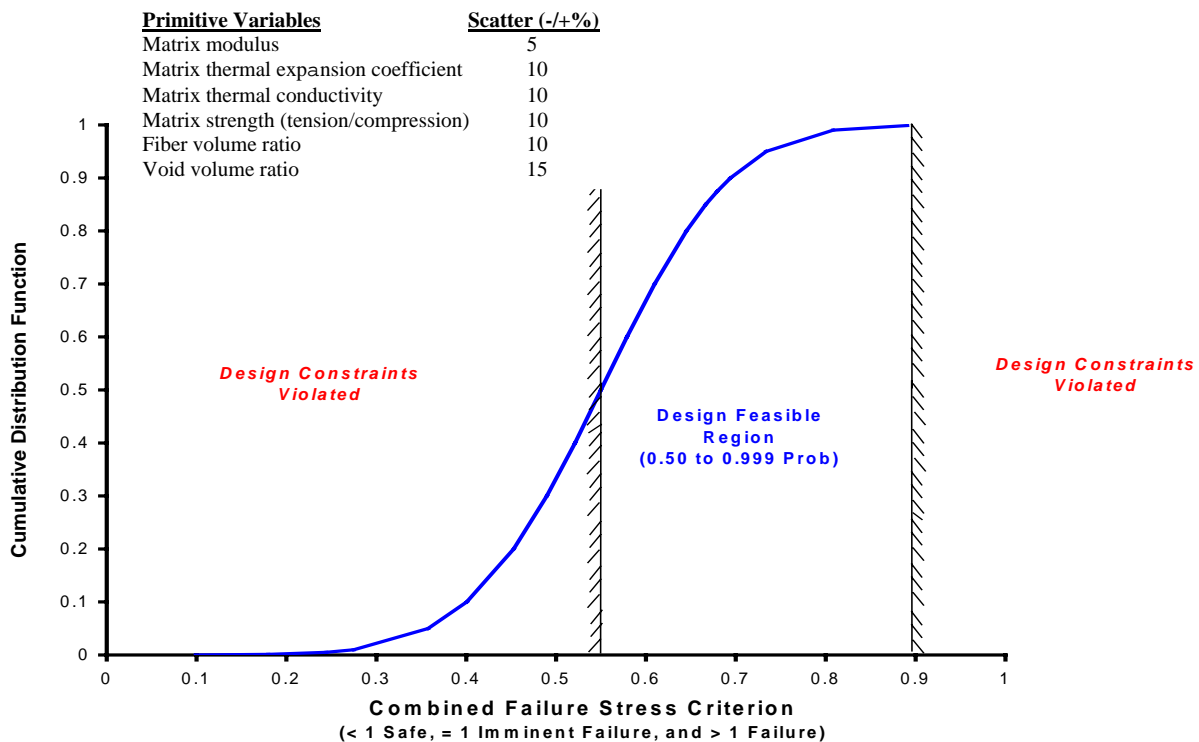
Figure 8. Probabilistic Evaluation After Minimization of Combined Stress Failure Criterion (Mean is Set Equal to Optimum Design)

Paper 5: Discussion

<u>Question from H Pfoertner – MTU, Germany</u>

What was the variation in loading and which optimisation method was used?

<u>Presenter's Reply</u>

In the probabilistic analysis, with the full set of primitive variables, variation in the internal pressure was +/-15% and variation of the convection temperature was +/-5% from their respective mean values. In the reduced set of primitive variables, only variations in the significant material and fabrication parameters were considered.

For the optimisation, a standard constrained minimisation code was utilised.

<u>Question from M Botley – UK MoD</u>

How were the data and the predictions of the model validated and how mature do you consider the technique to be?

<u>Presenter's Reply</u>

Computational simulation packages comprising the EST/BEST system, in particular the CSTEM and IPACS codes described in this paper, have been extensively validated with test cases over the last twelve years. The particular CMC duct structure presented here is a hypothetical example that was used to demonstrate the probabilistic optimisation methods.

Cost Reduction and Engine Life Extension Through Engine Life Monitoring at SNECMA

Frédéric Genot
SNECMA MOTEURS
Centre de Villaroche - Réau
77550 Moissy Cramayel, France

I - SUMMARY

The current market of the military Aircraft Gas Turbine Engines imposes reductions in the support costs. It has now become necessary to adapt our maintenance policy to comply with the new requirements. The present tendency focuses on a better knowledge of the real engine operation conditions to better relate damage to mission types. Our former maintenance policies for military engines were too expensive. SNECMA adopted the damage tracking on the ATAR, the flight recorder for the LARZAC and a life monitoring system for the M53 and the M88. It has become necessary to be more aware of the importance of feedback information on real engine operation conditions in order to specify design missions. After the control of engine parts life, it is now necessary to control the consumed life of fracture-critical rotating components in operation. Finally, the use of life monitoring system for the damage parts tracking in association with an adequate maintenance plan lead reduced support costs and improved engine parts life.

II - INTRODUCTION

Today, engine manufacturers are under heavy customer pressure to find a compromise between performance, mass and cost. The development of new contributes to an optimized performance/mass ratio but this often results in increased production cost. An engine is sold for a certain number of flying hours. The total support cost is calculated mainly according to the maintenance plan, the flying hours and the prices of spare parts. It is therefore easy to understand why long service lives combined with a good maintenance policy contribute towards reduced costs. SNECMA Moteurs develops an Engine Life Monitoring System (ELMS) called Damage Counter which makes it possible to comply with the latter requirements.

We should perhaps first illustrate various maintenance policies in order to better understand our customers' motives. Several examples will be presented as regards the maintenance policy adopted by SNECMA for its military engines ATAR, LARZAC, M53 and M88. An analysis will demonstrate the advantages and disadvantages of each policy. We will then present the Engine Life Monitoring System developed by SNECMA. Finally, we will explain the combined advantages of Engine Life Monitoring and optimized maintenance to reduce engine support costs and to improve engine life.

III - MAINTENANCE POLICY

Several maintenance policies have been developed by Aircraft Gas Turbine Engine Manufacturers. Two parameters were essential: design engines in a conservative way and control damaged parts to avoid rupture in service. It was therefore necessary to develop and set up a maintenance policy. The two primary criteria to be considered for the success of a maintenance policy for fracture-critical rotating engine parts are aircraft airworthiness

(parts removed in time) and combat readiness. An engine manufacturer must provid the customer with an optimized damage tracking system.

In maintenance, all parts must be capable of being traced to an engine. To simplify our description, we have identified two categories of parts. In the first, we have gathered those critical parts which do not ensure aircraft integrity in the event of rupture (disks for example) while the second category includes all other parts. Every engine is sold with usage hour limits for each one of its individual parts. As soon as a part life limit is reached, the maintenance service must carry out a maintenance operation called shopvisit.

At SNECMA maintenance policies have varied with the various military engines developed over the years such as the ATAR, the LARZAC, the M53 and finally the M88.

The ATAR is an engine developed in the 50's and 60's. The various versions of this family powered the Mirage F1, 3, 4 and 5, the Etandard, the Super Etandard, the Cheetah and Panthera. The tracking unit for engine parts such as discs and blades was the number of Engine Flying Hours (EFH). An inspection schedule was determined according to part ageing tests and the analysis of missions carried out on several engines. The pilots of several aircraft of the fleet had to declare their flight profiles to SNECMA. A data base consisting of theoretical reference flights provided for each tracked part a conversion factor between the EFH and Low Cycle Fatigue damage. Damage to parts could thus be assessed for a number of engines. Assessment of damage for the whole fleet was done by a conservative extrapolation. In many cases, the only way to extend life limits consisted in carrying out statistical ageing tests to evaluate the residual life of critical parts.

The LARZAC entered service in 1979 on the twin-engine Alpha Jet. Engine parts monitoring was also based on the number of EFH. The LARZAC maintenance policy principle was similar to that of the ATAR except for a major technological development: a few aircraft operated by the French Air Force were equipped with flight tape recorders to record, for each engine, the evolution of engine parameters (time, Low Pressure Rotational Speed, High Pressure Rotational Speed) which were measured every second. Periodically, the magnetic tape was retrieved and downloaded in a microcomputer to calculate life consumption for the recorded flights. The life algorithms implemented were very simple and they reduced computation times to a few hours with accuracy rates within ±10%. These models were composed of the following algorithmic blocks: thermodynamic, thermical, mechanical and damage. Inspection dates were set on the basis of simplified Engine Life Monitoring of damage for seven parts on selected engines. To ensure flight safety and the representativeness of all the engine parts, it was necessary to extrapolate the results in a conservative way for the whole fleet.

The M53 powers the Mirage 2000. Monitoring of parts service lives is based on Mixed Mission Units (MMU). A mixed mission is a mix of representative missions for a given engine, a so-called "average mission". The maintenance policy for the M53 is based on the LARZAC policy. The guiding principle is damage tracking by mission calculations using recorded engine parameters. For the M53, all engines are monitored and a special electronic unit is integrated into the on-board electronic systems. This unit calculates in real time damage consumption for 17 first-category critical parts in MMU. At ground level, an operator uses a microcomputer to download and retrieve consumption data. All parts are then monitored by conservatively extrapolating the results for the 17 parts. Maintenance operators can therefore manage all engine parts by cumulating MMU damage. When a part reaches its MMU limit, the ground operators must consider a maintenance operation. The damage algorithm hardware implemented includes four algorithmic blocks: thermodynamic, thermical, mechanical and damage. These blocks consist of reduced models which ensure an accuracy of ±10% compared with complete complex calculations.

IV - ANALYSIS

All the cases presented share a basic architecture. A complete maintenance policy shall include an analysis of parts life to process life limits for a specific unit, calculations of service times for critical parts and a life managing unit providing information on parts service lives to support decisions on aircraft deployment, component retirement, engine removal and engine and spare parts management.

As to the developments in life calculation methods, two approaches have emerged. The first development is related to the damage calculation mehtod while the second concerns the service life monitoring unit.

The various maintenance policies feature major changes in calculations for service life control. Compared with the highly conservative methods based on correlations calculation/ageing tests, the complex numerical models used by design offices to compute parts life have become higly predictive. The first ultra conservative calculation integrated important safety margins while the EFH monitoring method provided accurate measurements unit. Current life limit detemination takes into account fully modelized parts behaviour using 3-D numerical calculations and complex damage models. Crack propagation, multi-axial low cycle fatigue, creep, creep-fatigue interaction and crack probability are all considered by the designers. Critical components are identified in a very predictive way and the same part can have more than one critical location. Damage also depends on mission types. Therefore, life monitoring becomes very difficult for these parts.

Life design methods change whenever a further step in the understanding of engine operating conditions is reached in the design process. And customer pressure is equally important. To avoid losing our advantages, we must reconsider and adapt service life monitoring procedures in operation. Life monitoring calculations must be capable of being changed. This is why SNECMA has developed a modular structure for its simplified life models.

The easiest life monitoring unit is the Engine Flying Hours. An engine manufacturer sells its engine and ensures it reaches a number of flying hours. This damage unit does not provide for differences in mission severity and imposes a very strong conservatism through the use of penalizing design missions (Figure 1). This is why SNECMA decided to launch an analysis of missions in order to define missions more representative of real operating conditions. As safety margins in design life calculations and in mission definition became increasingly limited, it was necessary to develop a maintenance procedure using a life monitoring system taking real damage parts into account. Consequently the life monitoring unit logically became a Mixed Mission Unit. But this must still be translated into flying hours to be consistent with the number of hours sold to the customer.

Figure 1 : Difference between Flying Hours tracking and Engine Usage Monitoring
tracking after several flying hours

Service life management is at the core of a maintenance policy. A key element is undoubtedly the number of engines monitored since the control of only one or of several engines requires a conservative redistribution of the damage calculated on those parts which are not controlled. Differences in mission profiles observed between a leader and a follower in a patrol of interceptors or discrepancies in damage consumption between two air bases show that an individual monitoring method avoids taking excessively conservative safety margins to translate individual damage into fleet damage. The adoption of a systematic individual monitoring system has been an essential feature in the maintenance policy developed by SNECMA.

However, even if all the engines of the fleet are monitored, not all engine parts are tracked. Apart from the parts monitored in EFH, only the locations indicated as critical by the Design Offices have simplified algorithms to calculate their damage in operation. A procedure is required to redistribute damage on all the other parts. This problem especially affects blades: as only one algorithm is specified, the M53 ELM unit calculates the damage of only one blade. The problem becomes complex when there are several blades of different ages on the same disc. To preserve flight safety on the M53, we always monitor the oldest blade to redistribute its damage on the other blades. The solution is to apply a conservative policy.

V – THE M88 ENGINE LIFE MONITORING

The maintenance policy worked out for the M88 integrates the important points stated above. It is based on the use of a Life Monitoring System (Figure 2) developed by SNECMA. All the M88 engines powering the twin-engine RAFALE are monitored. The ELM structure is based on a data acquisition system equipping all engines and recording specific data on each mission, i.e. 10 thermodynamic parameters and 10 control values. The system tape is retrieved and downloaded in the ground station data processing system. The ELM Life Monitoring System is the software used for transient thermo-mechanical analyses on recorded flights and for damage assessement on thirty engine parts. Finally a ground maintenance software manages service life for components and residual engine lives for the engine. This maintenance software is capable of monitoring several engines. Only thirty parts are tracked and the maintenance system must manage all the parts of the engine by distributing the calculated damage to all the parts in an optimized way.

Figure 2: The Life Monitoring Software

SNECMA has identified significant engine parameters and aircraft parameters to define a mission in terms of damage. A data storage system has been developed. The engine control system transfers all the parameters to the ELM data acquisition. The system has a sufficient data capacity to record 10 thermodynamic parameters sampled every second on every engine. These parameters are pressure, temperature, flow and rotational speed. After each flight, the data acquisition system has a file for each engine. This file not only includes records for the 10 thermodynamic parameters but also for 10 additional values. These values are specific operating counters such as total engine operating time, after-burner operation time, x% over nominal values, number of engine starts, number of flights, number of take-offs. The latter is required for degraded damage calculations in the event of problems affecting the transmission of parameters to the acquisition system. The data recording system has a recording capacity for several missions so that maintenance operators do not have to download the files after each flight.

The ELMS is initialised with the engine identification informations, the residual life and damage continuous variable of the monitored components. The damage calculator works independently of the ground system. Life consumption is computed for thirty parts: each is individually monitored for Low cycle fatigue, Crack Propagation, Creep and Creep-Fatigue Interaction. This is performed using a conventional computing system. The software is divided into four main units: thermodynamic, thermal, mechanical and damage. The thermodynamic unit measures pressures, air temperatures and air flows. The thermal unit computes temperature for solid parts with the following inputs: air flow temperature, pressure and rotational speed. The mechanical unit determines local stress based on local temperature and rotational speed. Each critical localisation is defined by a thermo-mechanical background. Finally, damage computation is based on reduced damage models. Damage results are computed in an appropriate engineering unit such as LCF cycles and damage variables. For homogeneity reasons, damage is translated into authorised life units using exchange rates.

The maintenance system cumulates life consumption to determine the residual life of each component. The life management system is able to provide suitable outputs for maintenance and logistics. The system provides the operator with data such as flight clearance or flight ban, engine shop visit, statistic information. This information is required by the maintenance policy in order to plan maintenance operations and manage the stock of spare parts.

As mentioned previously, the Life Monitoring System is initialised with continuous damage variables of the monitored components. The problem is related to non-linear damage such as crack propagation or creep-fatigue interaction. The cumulative linear method cannot take non-linear damage behaviour into account. The non-linear models are implemented in the ELM and the required inputs are crack size for the parts tracked in Crack Propagation and engineering damage variables for the parts tracked in Creep-Fatigue Interaction damage. This additional information is stored for these parts by the ground system which restores them following ELM calculations.

An additional extrapolation method is implemented for blade damage consumption calculation in the life management system. Input data for the blades are life consumption and damage variables of the least damaged blade and the most damaged blade. In this way, all the blades can be tracked by interpolating damage consumption results. This optimized redistribution of life damage helps reduce conservatism.

VI - REDUCTION OF COST AND EXTENSION OF LIFE

The development of the Life Monitoring System is part of a programme of cost reductions and extended life. The cost reduction considered here applies to both development costs and ownership costs which are approximately the same. Several issues have emerged: mission analysis, design process, probabilistic approach and the reduction of safety margins.

This article focussed attention to the importance of a good knowledge of real engine use by defining design missions. The closer the design missions will be to the real missions, the more the sold Hours will be consistent with the consumed hours calculated by the ELM, reducing the margin between estimated and actual life consumed. Before the ELM was developed, mission analysis were too expensive. Without ELM data recording, the methods used to obtain required input data were: asking the pilots for their flight profiles and equipping an aircraft with a data recording device. The design missions established by the pilots were simply described in terms of sequences of throttle, altitude and speed and mission definitions were too theoretical. Only on aircraft equipped is not representative. The only way to be more representative is to equip more than one aircraft with a data recording system and operate them in standard use. The latter method is expensive in terms of human resources, hardware system and it must be accepted by the customer. Without a continuous mission analysis process, the gap between design life predictions and real life consumption is widening. One of the advantages of an ELM such as the Life Monitoring System is the possibility to create a huge engine mission data base. Operation feed-back becomes systematic and less costly.

The Life Monitoring algorithm is composed of different blocks. The life design is divided into the same blocks: thermodynamic, thermal, mechanical and damage. The ELM is a reduced model which allows rapid design life evaluation. SNECMA has decided to develop for its Design Offices a special Life Monitoring software version. This Design Version (Figure 3) will help the designers take decisions for advanced studies through optimization studies. The designer will regulate missions, thermodynamic behaviour, thermal behaviour, mechanical behaviour and the active damaging mechanisms to determine life design. This design tool will be extended to other engines and the constitution of a database for results

will allow the designer to extrapolate future developments. This complete ELM version will make work easier for the Design Offices while reducing considerably computation time for developments: it will thus contribute to reduced development costs.

Figure 3 : The Design Version of the Life Monitoring Software

As part of the maintenance policy, an in-service life limit is imposed for all the critical parts to control potential risks of failure. Life consumption estimation are used to define a maintenance plan. The maintenance plan needs to be updated periodically as significant new life consumption data becomes available. The number of tracked parts and the different damage mechanisms lead to different levels in mission severity factors. All parts do not reach their life limits at the same time. Since a maintenance operation is expensive, inspection intervals must be optimized to avoid too many overhauls, especially for the parts with damage tolerances. Optimizing inspection intervals consists in offering flexible inspection dates for the customer. Authorized margins are associated with risk evaluation. For example, an operator will take the risk to do only one inspection instead of two inspections with few operating hours in-between. As the Life Monitoring Software is integrated into a probabilistic system (Figure 4), it allows random calculations to evaluate risk. Its algorithmic structure can be easily integrated in a probabilistic environment. All the in-service limits will be announced with a margin and an associated risk. Optimizing inspection intervals using the Life Monitoring Software contributes to reduced support costs.

Figure 4 : The Probabilistic Version of the Life Monitoring Software

In the abscence of Engine Life Monitoring, a maintenance operator should monitor engine parts using Engine Flying Hours for example. Figure 1 demonstrates that damage can be twice as important as the damage calculated by an Engine Life Monitoring. Life limits would be reached twice as quikly and customers would have the impression that life are too limited. With the development of the ELM, the design calculator reduces the conservative margins integrated in the mixed mission definition. Moreover the quality of the reduced model implemented in the ELM system reduces the safety margins used in life consumption calculations. Finally, individual engine monitoring avoids conservative damage extrapolation to the fleet. In general, the individual ELM recommended by SNECMA contributes to improving life by reducing conservative margins.

VII - CONCLUSION

A survey of SNECMA's Engine Life Monitoring approach demonstrates the advantages provided by a systematic use of Engine Life Monitoring to reduce costs and extend life. The Life Monitoring System software implemented in the M88 Engine Life Monitoring System contributes towards reduced costs through Mission Analyses and the development of Design and Probabilistic Versions. It also improves engine part life through reduced conservative margins. The conditions for success are systematic individual monitoring, the quality of reduced damage models, the variety of the damage mechanisms implemented, the representativity in operation of the Mixed Mission, change capacity in the algorithmic structure, the quality of critical components identification and a good understanding of engine damage behaviour.

Cost Reduction and Engine Life Extension Through Engine Life Monitoring at SNECMA

Frédéric Genot
SNECMA MOTEURS
Centre de Villaroche - Réau
77550 Moissy Cramayel, France

I - SUMMARY

The current market of the military Aircraft Gas Turbine Engines imposes reductions in the support costs. It has now become necessary to adapt our maintenance policy to comply with the new requirements. The present tendency focuses on a better knowledge of the real engine operation conditions to better relate damage to mission types. Our former maintenance policies for military engines were too expensive. SNECMA adopted the damage tracking on the ATAR, the flight recorder for the LARZAC and a life monitoring system for the M53 and the M88. It has become necessary to be more aware of the importance of feedback information on real engine operation conditions in order to specify design missions. After the control of engine parts life, it is now necessary to control the consumed life of fracture-critical rotating components in operation. Finally, the use of life monitoring system for the damage parts tracking in association with an adequate maintenance plan lead reduced support costs and improved engine parts life.

II - INTRODUCTION

Today, engine manufacturers are under heavy customer pressure to find a compromise between performance, mass and cost. The development of new contributes to an optimized performance/mass ratio but this often results in increased production cost. An engine is sold for a certain number of flying hours. The total support cost is calculated mainly according to the maintenance plan, the flying hours and the prices of spare parts. It is therefore easy to understand why long service lives combined with a good maintenance policy contribute towards reduced costs. SNECMA Moteurs develops an Engine Life Monitoring System (ELMS) called Damage Counter which makes it possible to comply with the latter requirements.

We should perhaps first illustrate various maintenance policies in order to better understand our customers' motives. Several examples will be presented as regards the maintenance policy adopted by SNECMA for its military engines ATAR, LARZAC, M53 and M88. An analysis will demonstrate the advantages and disadvantages of each policy. We will then present the Engine Life Monitoring System developed by SNECMA. Finally, we will explain the combined advantages of Engine Life Monitoring and optimized maintenance to reduce engine support costs and to improve engine life.

III - MAINTENANCE POLICY

Several maintenance policies have been developed by Aircraft Gas Turbine Engine Manufacturers. Two parameters were essential: design engines in a conservative way and control damaged parts to avoid rupture in service. It was therefore necessary to develop and set up a maintenance policy. The two primary criteria to be considered for the success of a maintenance policy for fracture-critical rotating engine parts are aircraft airworthiness

(parts removed in time) and combat readiness. An engine manufacturer must provid the customer with an optimized damage tracking system.

In maintenance, all parts must be capable of being traced to an engine. To simplify our description, we have identified two categories of parts. In the first, we have gathered those critical parts which do not ensure aircraft integrity in the event of rupture (disks for example) while the second category includes all other parts. Every engine is sold with usage hour limits for each one of its individual parts. As soon as a part life limit is reached, the maintenance service must carry out a maintenance operation called shopvisit.

At SNECMA maintenance policies have varied with the various military engines developed over the years such as the ATAR, the LARZAC, the M53 and finally the M88.

The ATAR is an engine developed in the 50's and 60's. The various versions of this family powered the Mirage F1, 3, 4 and 5, the Etandard, the Super Etandard, the Cheetah and Panthera. The tracking unit for engine parts such as discs and blades was the number of Engine Flying Hours (EFH). An inspection schedule was determined according to part ageing tests and the analysis of missions carried out on several engines. The pilots of several aircraft of the fleet had to declare their flight profiles to SNECMA. A data base consisting of theoretical reference flights provided for each tracked part a conversion factor between the EFH and Low Cycle Fatigue damage. Damage to parts could thus be assessed for a number of engines. Assessment of damage for the whole fleet was done by a conservative extrapolation. In many cases, the only way to extend life limits consisted in carrying out statistical ageing tests to evaluate the residual life of critical parts.

The LARZAC entered service in 1979 on the twin-engine Alpha Jet. Engine parts monitoring was also based on the number of EFH. The LARZAC maintenance policy principle was similar to that of the ATAR except for a major technological development: a few aircraft operated by the French Air Force were equipped with flight tape recorders to record, for each engine, the evolution of engine parameters (time, Low Pressure Rotational Speed, High Pressure Rotational Speed) which were measured every second. Periodically, the magnetic tape was retrieved and downloaded in a microcomputer to calculate life consumption for the recorded flights. The life algorithms implemented were very simple and they reduced computation times to a few hours with accuracy rates within ±10%. These models were composed of the following algorithmic blocks: thermodynamic, thermical, mechanical and damage. Inspection dates were set on the basis of simplified Engine Life Monitoring of damage for seven parts on selected engines. To ensure flight safety and the representativeness of all the engine parts, it was necessary to extrapolate the results in a conservative way for the whole fleet.

The M53 powers the Mirage 2000. Monitoring of parts service lives is based on Mixed Mission Units (MMU). A mixed mission is a mix of representative missions for a given engine, a so-called "average mission". The maintenance policy for the M53 is based on the LARZAC policy. The guiding principle is damage tracking by mission calculations using recorded engine parameters. For the M53, all engines are monitored and a special electronic unit is integrated into the on-board electronic systems. This unit calculates in real time damage consumption for 17 first-category critical parts in MMU. At ground level, an operator uses a microcomputer to download and retrieve consumption data. All parts are then monitored by conservatively extrapolating the results for the 17 parts. Maintenance operators can therefore manage all engine parts by cumulating MMU damage. When a part reaches its MMU limit, the ground operators must consider a maintenance operation. The damage algorithm hardware implemented includes four algorithmic blocks: thermodynamic, thermical, mechanical and damage. These blocks consist of reduced models which ensure an accuracy of ±10% compared with complete complex calculations.

IV - ANALYSIS

All the cases presented share a basic architecture. A complete maintenance policy shall include an analysis of parts life to process life limits for a specific unit, calculations of service times for critical parts and a life managing unit providing information on parts service lives to support decisions on aircraft deployment, component retirement, engine removal and engine and spare parts management.

As to the developments in life calculation methods, two approaches have emerged. The first development is related to the damage calculation mehtod while the second concerns the service life monitoring unit.

The various maintenance policies feature major changes in calculations for service life control. Compared with the highly conservative methods based on correlations calculation/ageing tests, the complex numerical models used by design offices to compute parts life have become higly predictive. The first ultra conservative calculation integrated important safety margins while the EFH monitoring method provided accurate measurements unit. Current life limit detemination takes into account fully modelized parts behaviour using 3-D numerical calculations and complex damage models. Crack propagation, multi-axial low cycle fatigue, creep, creep-fatigue interaction and crack probability are all considered by the designers. Critical components are identified in a very predictive way and the same part can have more than one critical location. Damage also depends on mission types. Therefore, life monitoring becomes very difficult for these parts.

Life design methods change whenever a further step in the understanding of engine operating conditions is reached in the design process. And customer pressure is equally important. To avoid losing our advantages, we must reconsider and adapt service life monitoring procedures in operation. Life monitoring calculations must be capable of being changed. This is why SNECMA has developed a modular structure for its simplified life models.

The easiest life monitoring unit is the Engine Flying Hours. An engine manufacturer sells its engine and ensures it reaches a number of flying hours. This damage unit does not provide for differences in mission severity and imposes a very strong conservatism through the use of penalizing design missions (Figure 1). This is why SNECMA decided to launch an analysis of missions in order to define missions more representative of real operating conditions. As safety margins in design life calculations and in mission definition became increasingly limited, it was necessary to develop a maintenance procedure using a life monitoring system taking real damage parts into account. Consequently the life monitoring unit logically became a Mixed Mission Unit. But this must still be translated into flying hours to be consistent with the number of hours sold to the customer.

Figure 1 : Difference between Flying Hours tracking and Engine Usage Monitoring
tracking after several flying hours

Service life management is at the core of a maintenance policy. A key element is undoubtedly the number of engines monitored since the control of only one or of several engines requires a conservative redistribution of the damage calculated on those parts which are not controlled. Differences in mission profiles observed between a leader and a follower in a patrol of interceptors or discrepancies in damage consumption between two air bases show that an individual monitoring method avoids taking excessively conservative safety margins to translate individual damage into fleet damage. The adoption of a systematic individual monitoring system has been an essential feature in the maintenance policy developed by SNECMA.

However, even if all the engines of the fleet are monitored, not all engine parts are tracked. Apart from the parts monitored in EFH, only the locations indicated as critical by the Design Offices have simplified algorithms to calculate their damage in operation. A procedure is required to redistribute damage on all the other parts. This problem especially affects blades: as only one algorithm is specified, the M53 ELM unit calculates the damage of only one blade. The problem becomes complex when there are several blades of different ages on the same disc. To preserve flight safety on the M53, we always monitor the oldest blade to redistribute its damage on the other blades. The solution is to apply a conservative policy.

V – THE M88 ENGINE LIFE MONITORING

The maintenance policy worked out for the M88 integrates the important points stated above. It is based on the use of a Life Monitoring System (Figure 2) developed by SNECMA. All the M88 engines powering the twin-engine RAFALE are monitored. The ELM structure is based on a data acquisition system equipping all engines and recording specific data on each mission, i.e. 10 thermodynamic parameters and 10 control values. The system tape is retrieved and downloaded in the ground station data processing system. The ELM Life Monitoring System is the software used for transient thermo-mechanical analyses on recorded flights and for damage assessement on thirty engine parts. Finally a ground maintenance software manages service life for components and residual engine lives for the engine. This maintenance software is capable of monitoring several engines. Only thirty parts are tracked and the maintenance system must manage all the parts of the engine by distributing the calculated damage to all the parts in an optimized way.

Figure 2: The Life Monitoring Software

SNECMA has identified significant engine parameters and aircraft parameters to define a mission in terms of damage. A data storage system has been developed. The engine control system transfers all the parameters to the ELM data acquisition. The system has a sufficient data capacity to record 10 thermodynamic parameters sampled every second on every engine. These parameters are pressure, temperature, flow and rotational speed. After each flight, the data acquisition system has a file for each engine. This file not only includes records for the 10 thermodynamic parameters but also for 10 additional values. These values are specific operating counters such as total engine operating time, after-burner operation time, x% over nominal values, number of engine starts, number of flights, number of take-offs. The latter is required for degraded damage calculations in the event of problems affecting the transmission of parameters to the acquisition system. The data recording system has a recording capacity for several missions so that maintenance operators do not have to download the files after each flight.

The ELMS is initialised with the engine identification informations, the residual life and damage continuous variable of the monitored components. The damage calculator works independently of the ground system. Life consumption is computed for thirty parts: each is individually monitored for Low cycle fatigue, Crack Propagation, Creep and Creep-Fatigue Interaction. This is performed using a conventional computing system. The software is divided into four main units: thermodynamic, thermal, mechanical and damage. The thermodynamic unit measures pressures, air temperatures and air flows. The thermal unit computes temperature for solid parts with the following inputs: air flow temperature, pressure and rotational speed. The mechanical unit determines local stress based on local temperature and rotational speed. Each critical localisation is defined by a thermo-mechanical background. Finally, damage computation is based on reduced damage models. Damage results are computed in an appropriate engineering unit such as LCF cycles and damage variables. For homogeneity reasons, damage is translated into authorised life units using exchange rates.

The maintenance system cumulates life consumption to determine the residual life of each component. The life management system is able to provide suitable outputs for maintenance and logistics. The system provides the operator with data such as flight clearance or flight ban, engine shop visit, statistic information. This information is required by the maintenance policy in order to plan maintenance operations and manage the stock of spare parts.

As mentioned previously, the Life Monitoring System is initialised with continuous damage variables of the monitored components. The problem is related to non-linear damage such as crack propagation or creep-fatigue interaction. The cumulative linear method cannot take non-linear damage behaviour into account. The non-linear models are implemented in the ELM and the required inputs are crack size for the parts tracked in Crack Propagation and engineering damage variables for the parts tracked in Creep-Fatigue Interaction damage. This additional information is stored for these parts by the ground system which restores them following ELM calculations.

An additional extrapolation method is implemented for blade damage consumption calculation in the life management system. Input data for the blades are life consumption and damage variables of the least damaged blade and the most damaged blade. In this way, all the blades can be tracked by interpolating damage consumption results. This optimized redistribution of life damage helps reduce conservatism.

VI - REDUCTION OF COST AND EXTENSION OF LIFE

The development of the Life Monitoring System is part of a programme of cost reductions and extended life. The cost reduction considered here applies to both development costs and ownership costs which are approximately the same. Several issues have emerged: mission analysis, design process, probabilistic approach and the reduction of safety margins.

This article focussed attention to the importance of a good knowledge of real engine use by defining design missions. The closer the design missions will be to the real missions, the more the sold Hours will be consistent with the consumed hours calculated by the ELM, reducing the margin between estimated and actual life consumed. Before the ELM was developed, mission analysis were too expensive. Without ELM data recording, the methods used to obtain required input data were: asking the pilots for their flight profiles and equipping an aircraft with a data recording device. The design missions established by the pilots were simply described in terms of sequences of throttle, altitude and speed and mission definitions were too theoretical. Only on aircraft equipped is not representative. The only way to be more representative is to equip more than one aircraft with a data recording system and operate them in standard use. The latter method is expensive in terms of human resources, hardware system and it must be accepted by the customer. Without a continuous mission analysis process, the gap between design life predictions and real life consumption is widening. One of the advantages of an ELM such as the Life Monitoring System is the possibility to create a huge engine mission data base. Operation feed-back becomes systematic and less costly.

The Life Monitoring algorithm is composed of different blocks. The life design is divided into the same blocks: thermodynamic, thermal, mechanical and damage. The ELM is a reduced model which allows rapid design life evaluation. SNECMA has decided to develop for its Design Offices a special Life Monitoring software version. This Design Version (Figure 3) will help the designers take decisions for advanced studies through optimization studies. The designer will regulate missions, thermodynamic behaviour, thermal behaviour, mechanical behaviour and the active damaging mechanisms to determine life design. This design tool will be extended to other engines and the constitution of a database for results

will allow the designer to extrapolate future developments. This complete ELM version will make work easier for the Design Offices while reducing considerably computation time for developments: it will thus contribute to reduced development costs.

Figure 3 : The Design Version of the Life Monitoring Software

As part of the maintenance policy, an in-service life limit is imposed for all the critical parts to control potential risks of failure. Life consumption estimation are used to define a maintenance plan. The maintenance plan needs to be updated periodically as significant new life consumption data becomes available. The number of tracked parts and the different damage mechanisms lead to different levels in mission severity factors. All parts do not reach their life limits at the same time. Since a maintenance operation is expensive, inspection intervals must be optimized to avoid too many overhauls, especially for the parts with damage tolerances. Optimizing inspection intervals consists in offering flexible inspection dates for the customer. Authorized margins are associated with risk evaluation. For example, an operator will take the risk to do only one inspection instead of two inspections with few operating hours in-between. As the Life Monitoring Software is integrated into a probabilistic system (Figure 4), it allows random calculations to evaluate risk. Its algorithmic structure can be easily integrated in a probabilistic environment. All the in-service limits will be announced with a margin and an associated risk. Optimizing inspection intervals using the Life Monitoring Software contributes to reduced support costs.

Figure 4 : The Probabilistic Version of the Life Monitoring Software

In the abscence of Engine Life Monitoring, a maintenance operator should monitor engine parts using Engine Flying Hours for example. Figure 1 demonstrates that damage can be twice as important as the damage calculated by an Engine Life Monitoring. Life limits would be reached twice as quikly and customers would have the impression that life are too limited. With the development of the ELM, the design calculator reduces the conservative margins integrated in the mixed mission definition. Moreover the quality of the reduced model implemented in the ELM system reduces the safety margins used in life consumption calculations. Finally, individual engine monitoring avoids conservative damage extrapolation to the fleet. In general, the individual ELM recommended by SNECMA contributes to improving life by reducing conservative margins.

VII - CONCLUSION

A survey of SNECMA's Engine Life Monitoring approach demonstrates the advantages provided by a systematic use of Engine Life Monitoring to reduce costs and extend life. The Life Monitoring System software implemented in the M88 Engine Life Monitoring System contributes towards reduced costs through Mission Analyses and the development of Design and Probabilistic Versions. It also improves engine part life through reduced conservative margins. The conditions for success are systematic individual monitoring, the quality of reduced damage models, the variety of the damage mechanisms implemented, the representativity in operation of the Mixed Mission, change capacity in the algorithmic structure, the quality of critical components identification and a good understanding of engine damage behaviour.

Engine Vibration Monitoring and Diagnosis Based on On-Board Captured Data

Dr. Jorge Moreno Barragán
MTU Aero Engines GmbH
Engine Dynamics
Dachauer Strasse 665
D-80995 Munich
phone: ++49 89 1489 4191
fax: ++49 89 1489 99902
email: J.Moreno-Barragan@muc.mtu.de

ABSTRACT

An advanced vibration monitoring system (VMS) consisting of on-board and on-ground tasks is presented in this paper. The on-board part of the VMS includes the detection of vibration incidents by monitoring of defined vibration amplitude values and comparison with prescribed absolute and relative vibration limits, where the relative vibration limits are specific for each particular engine. Exceedence of defined vibration alarm limits trigger a cockpit warning. The processing and acquisition of different vibration data sets using several algorithms are additional tasks of the on-board vibration monitoring function. The on-ground part of the VMS comprises the trend analysis of vibration signals as well as sophisticated methods based on artificial intelligence for the diagnosis of vibration events which includes data generated on wing, test-bed and the results of numerical simulations performed using extensive structural Finite Element whole engine models.

In this paper the vibration data sets which are necessary to carry out the vibration monitoring function are described in detail. Finally experience gained during the application of the presented VMS to EJ200, the engine of the Eurofighter EF2000, are reported and discussed.

Key words: vibration, signal processing, trend analysis, incident detection, mechanical diagnosis

1   LIST OF ABBREVIATIONS

BSD	Bulk Storage Device	LP	Low pressure (rotor/system)
CSMU	Crash Survivable Memory Unit	MAS	Vibration Maximal Amplitudes Store
DECU	Digital Engine Control Unit	MDP	Maintenance Data Panel
ECMS	Engine Condition Monitoring System	MPR	Vibration Max Per Run
EF	Eurofighter	OOB	Out of balance
EF2000	European Fighter Aircraft	PMDS	Portable Maintenance Data Store
EHM	Engine Health Monitoring		
EJ-PC	Eurojet Partner Company	RMS	Root Mean Square
EMS	Engine Monitoring System	RPM	Revolutions Per Minute
EMU	Engine Monitoring Unit	RVE	Residual Vibration Energy.
EO	Engine Order (spool speed harmonic frequency)	THS	Vibration Time History Store
GSS	Ground Support System	VMS	Vibration Monitoring System
HP	High pressure (rotor/system)		
IPU	Interface Processor Unit		

2   INTRODUCTION

One of the most sensitive parameters for continuos monitoring of the condition of aero-engines are engine vibrations. These vibrations are captured by one or more accelerometers mounted at carefully selected casing positions. With these in-service gained signals and additional operational parameters, used for aircraft and engine control, it is possible to reliably monitor engine health and, if necessary, to diagnose the reason for the engine malfunction.

The main objectives of engine vibration monitoring can be summarised as:
- increased safety through identification of dangerous vibration conditions at all engine speeds and thrusts, including steady state and transient operation, and through generation of the corresponding cockpit warning,
- avoidance of major secondary damage by way of early failure identification,
- reduction of maintenance expenditure through isolation, localisation and diagnosis of the vibration causes and
- optimisation of maintenance by means of consideration of the current engine condition.

In the current paper an advanced vibration monitoring system will be presented which aims to satisfy the above requirements.

3   DATA ACQUISITION AND PROCESSING

Vibration monitoring is a substantial part of the Engine Monitoring System (EMS) of EJ200, the engine of the EF2000. The tasks of the vibration monitoring function are distributed over airborne and ground equipment, where the airborne equipment comprises vibration transducers and the Engine Monitoring Unit (EMU) and the ground equipment comprises the Engine Health Monitoring system (EHM) as an element of the Ground Support System (GSS).

As shown in Figure 1, this data is transferred to GSS using several devices - Interface Processor Unit (IPU) , the Bulk Storage Device (BSD) and the Portable Maintenance Data Store (PMDS) - and stored in the corresponding data base within the GSS.
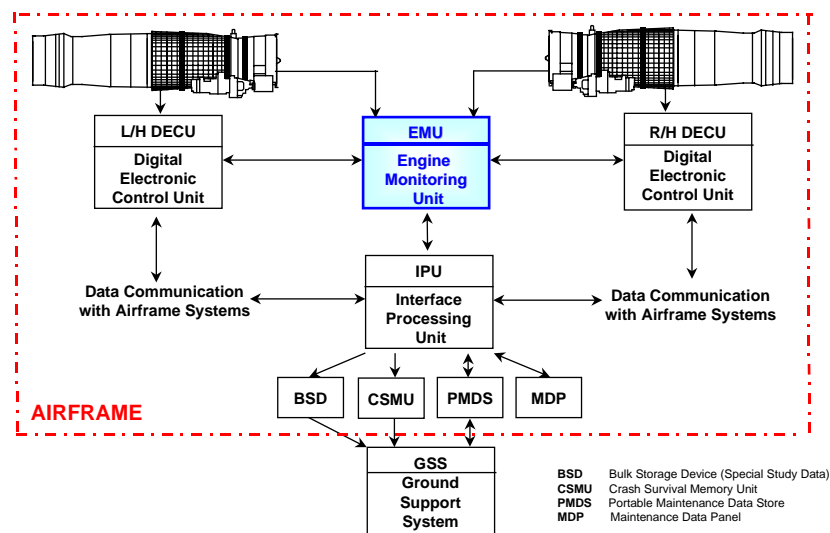
Figure 1: Data flow of the engine monitoring system

The location of the two engine vibration transducers is shown in Figure 2. The transducers are attached to the engine casings at carefully selected positions which allow monitoring of the dynamics of the rotors in the frequency range below 1 kHz. The vibration transducers are hardwired to the EMU and also positioned to ensure simple maintenance.
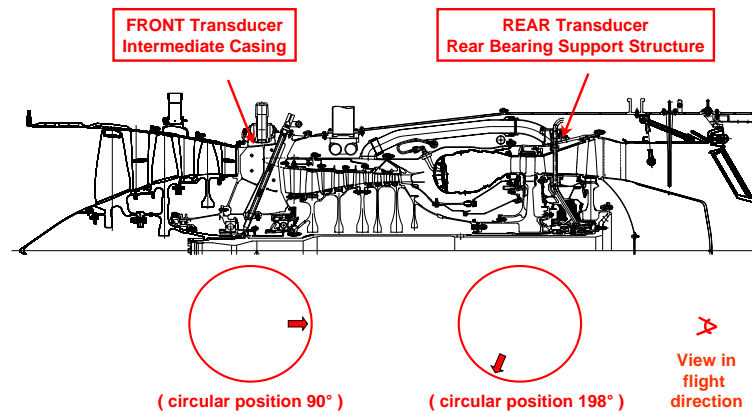
Figure 2: Vibration transducers attached to the EJ200 engine

The transducer signals are conditioned by the EMU to produce filtered velocity analogue signals. The health of the vibration transducers and of the EMU signal conditioning interfaces is continuously monitored and status information is stored together with the sampled and derived data. The resulting velocity signals are continuously sampled by EMU for analysis and storage.

Additionally, hardwired engine speed signals are provided from the Digital Engine Control Unit (DECU) to the EMU, see Figure 1. They are also conditioned by the EMU hardware. A number of values, like the current time for one revolution of the different spools, are generated, describing the rotor dynamics characteristics of the low pressure spool (NL) and the high pressure spool (NH). These values are then used for the generation of the vibration monitoring parameters.

The analysis of vibration related data is performed by the EMU during engine operation based upon a periodic time cycle of 0.5 s to collect and analyse the data. During each of these cycles two vibration sample sets in time domain are produced simultaneously, one for each vibration transducer. These vibration sample sets correspond to individual speed bands (SB), characterised by defined NL speeds and NL speed changes with respect to the time, and are the basis of the vibration monitoring function as illustrated in Figure 3. There are 100 SB which are derived from the NL spool speed. SB 0 covers NL spool speeds up to 30% of the nominal NL speed, SB 99 covers NL spool speeds higher then 103% of the nominal NL speed, SB 1 to 98 are evenly distributed between these two limits. The SB corresponding to acceleration and deceleration conditions are processed and stored separately.
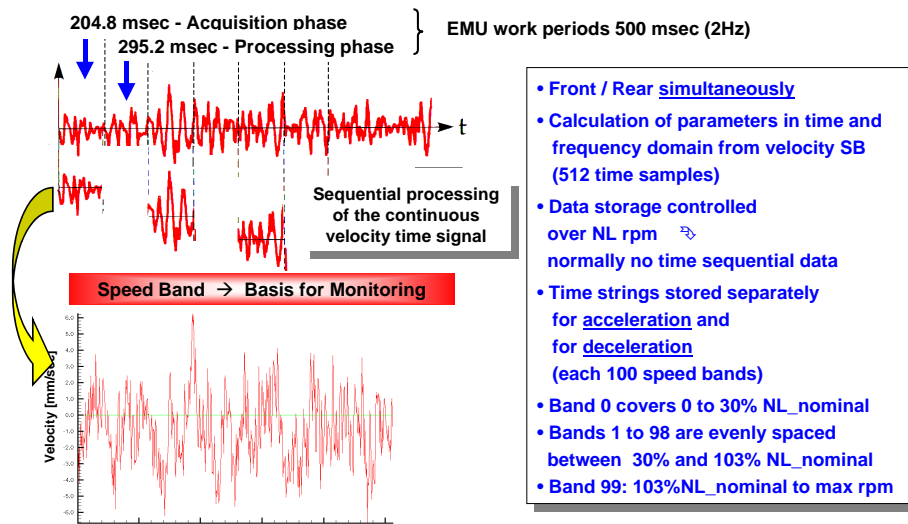
Figure 3: EMU work periods and data capture

The following vibration monitoring parameters (**derived amplitude values**) are generated from these sample sets for the FRONT and REAR transducers:

- Amplitude values corresponding to the first order of the NL fundamental spool frequency, identified as **1EO NL**. The amplitude values are derived via Discrete Fourier transform (DFT) using a subset of the sample sets that corresponds to 10 complete revolutions of the NL spool.

- Amplitude values corresponding to the first order of the NH fundamental spool frequency, identified as **1EO NH**. The amplitude values are derived via DFT using a subset of the sample sets that corresponds to the number of completed revolutions of the NH spool for 10 NL spool revolutions during the recording of the sample set.

- Amplitude values corresponding to a programmable frequency, that is calculated from a programmable order of the NL spool frequency plus a programmable order of the NH spool frequency plus a fixed frequency, identified as **PROG.** The amplitudes are derived via DFT using the same subset as used for the calculation of the amplitude value for 1 EO NL.

- Overall broadband energy amplitudes for the front and rear transducers are calculated via a Root Mean Square (**RMS**) extraction algorithm using the complete sample set.

- Residual Vibration Energy (**RVE**) amplitudes are calculated by subtracting the DFT amplitudes for 1 EO NH, 1 EO NL and PROG from the corresponding RMS amplitudes (separately for FRONT and REAR). This amplitude describes the energy content of the vibration signal in the observed time interval excluding the contribution of the 1 EO NL, 1 EO NH and PROG vibration components.

The measured and derived vibration data are continuously monitored and cumulatively stored to different data set stores for download to the Ground Support System.

Using these monitoring parameters and associated data, the following tasks can be performed within the vibration monitoring system:

- vibration incident detection with subsequent indications and warnings
- vibration trend analysis and
- vibration diagnosis.

The following data sets are available within the EMU for the vibration monitoring functions:

- Vibration **Datum** store (Datum)
  This data set contains the reference vibration signature of the engine, describing the reference vibration characteristics of the engine captured, for instance, during the corresponding pass-off test. It consists of all derived amplitude values (1 EO NL, 1 EO NH, PROG, RVE and RMS) for both FRONT/REAR transducers and for each speed band under ACCEL/DECEL conditions. This data set is used for the generation of relative limits for vibration incident detection.

- Vibration **Maximum Amplitude Per Run** store (MPR)
  The MPR store contains the derived amplitude values for FRONT and REAR transducers for acceleration and deceleration for all speed bands that have been detected during a single engine run. This data set includes the following additional parameters -Ambient static pressure, aircraft acceleration along normal axis (g_z), aircraft angular velocity about normal axis (r), Mach number (Ma) and intake temperature (T2)- which describe the corresponding operational conditions. The structure of this data set is illustrated in Figure 4. The store is reset at the start of each engine run. During engine operation, the data for the different speed bands are overwritten and the MPR store records the highest achieved vibration levels for each speed band.
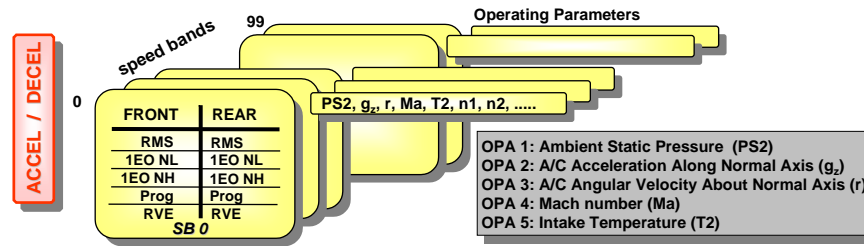
Figure 4: Max Per Run (MPR) → Incident detection and trend analysis

- Vibration **Maximum Amplitude Store** (MAS) in conjunction with
  Vibration **Time History Store** (THS).

  The MAS data set contains the maximal amplitudes of the different derived vibration parameters for the time interval since last EMU reset (data generated over several engine runs). The data for the different speed bands are overwritten, if no data have already been recorded for the corresponding speed band or if a weighting algorithm for the different amplitudes stored in the MAS indicates a higher vibration level for the new data than the previously stored data. Additional conditions for data overwrite are, that no surge is detected simultaneously and that the changing rate of the spool speeds related to the time (%NL/s) is within a defined range. This data set will be stored separately for accelerating and decelerating conditions.

  The THS contain measured velocity data sample sets for FRONT and REAR transducers in time domain for the different speed bands. The overwrite of these data sets is controlled by the overwrite criterion of the MAS data sets as described above. Figure 5 shows the structure of these data sets including the corresponding operational parameters.
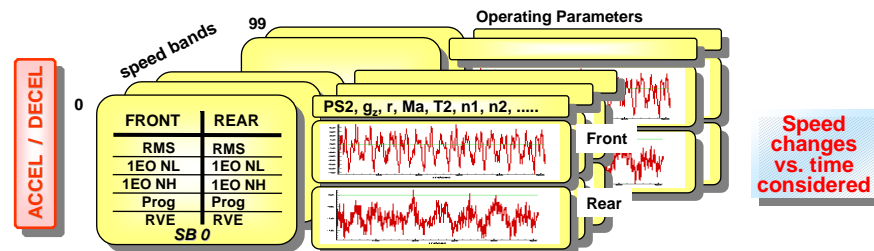
Figure 5: Max Amplitude Store (MAS) + Time Histories Store (THS) → Diagnosis

- **Vibration Incident Time History Store (VITHS)**
  VITHS contains continuously sampled, time based vibration velocity data for a specified period of time before and after a vibration incident has been detected. There are two VITHS in the data set. VITHS 1 is overwritten after the first vibration incident has been detected during engine operation. VITHS 2 is overwritten if a subsequent vibration incident has been detected, that is more severe than the first vibration incident and either the VITHS 2 is empty or the detected vibration incident is more severe than the incident already stored in VITHS 2.

- Vibration **Special Study Data (SSD)**
  SSD contains all the derived vibration parameters for the FRONT and REAR transducers stored continuously with respect to time at a frequency of 2 Hz. The corresponding operational parameters, stored partially with frequencies higher as 2 Hz, are also included in this data set.

With exception of VITHS and SSD, each of these data sets contains areas to store data for 100 speed bands separately for front and rear transducer data measured during acceleration and deceleration of the engine. A complete store therefore consists of data for 400 speed bands.

All of the data sets are tagged with status information (store status, transducer status, status of signal conditioning interfaces) and with operational parameters.

Vibration incident detection

In order to detect vibration incidents, each of the derived amplitude values is compared with a set of predetermined limits as shown in Figure 6. Incidents of different types are generated, depending on the limit exceeded:

- Cockpit warning (warning to the pilot due to exceedance of an absolute vibration limit)
- Maintenance warning (warning to the ground crew due to exceedance of an absolute vibration limit, which is lower than the cockpit limit)
- Relative maintenance warning (warning to the ground crew because the ratio between current vibration amplitudes and the Datum store engine vibration signature (specific current engine) exceeds a defined limit)

Each of these warnings can be generated according to its duration in two different types:

- steady state warning (limit exceedance longer than a defined time interval)
- transient warning (limit exceedance shorter than a defined time interval).

Different limit values are used for both, transient and steady state warnings. Additionally, each vibration warning (incident) is classified according to the actual flight manoeuvres (normal flight conditions or high g and/or gyro-loads). The cockpit warning signals are relayed via the DECU to the aircraft systems.
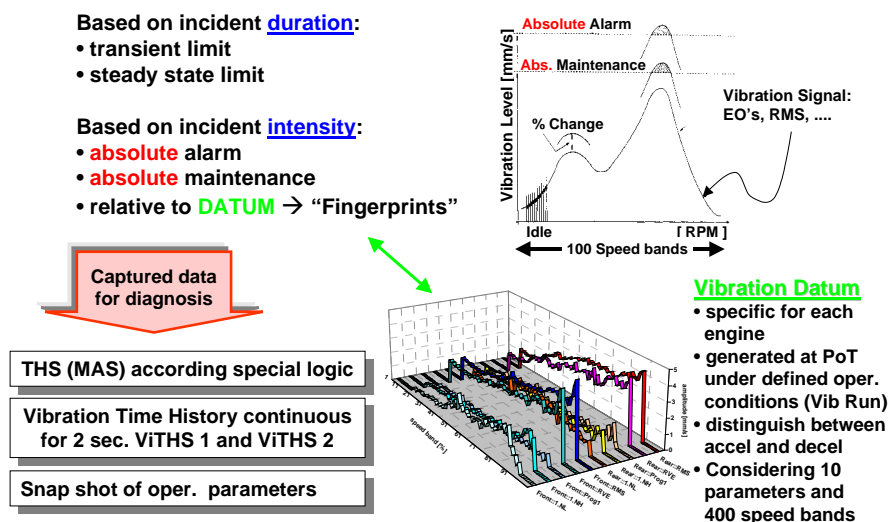
Figure 6: Concept for incident detection → Exceedence of vibration limits

Vibration trend analysis

Trend evaluations are performed to predict problems, preventing engine failure. The purpose of this analysis is to derive prognoses from downloaded data sets from a number of engine runs. The trending is carried out based on the observation of an overall increase or decrease of engine vibration levels. The data sets on which vibration trending is based are the Max Per Run (MPR), Maximum Amplitude Store (MAS) and Time History Store (THS). The current data is compared with the reference data and deviations are evaluated. A trending curve can be generated with regression techniques to predict when the engine will exceed allowable limits. The consideration of the associate operational parameters which describe the flight conditions is mandatory for vibration trend analysis, as the corresponding amplitudes depend on these parameters.

Vibration diagnosis

The vibration data are transfer into the frequency domain using Discrete Fourier Transform, for tracked orders of engine spool speeds, and Fast Fourier Transform to obtain amplitude spectra in the frequency domain. For diagnosis purposes the use of waterfall plots is very useful. These diagrams are generated by arrangement of the different spectra with respect to the spool speed as shown in Figure 7.

Selected indicators, as for example changing of the engine orders, sub-harmonics, side-bands, fixed frequencies, resonances, jump ups / kick downs and noise floor, will be generated based on waterfall diagrams in order to create vibration patterns.

These vibration patterns are compared with a library of known vibration induced patterns obtained from typical engine fault situations. Therefore, identification of the cause of certain engine vibrations (i.e. a defect source) is supported.

Semi-automatic analysis is provided for pattern recognition by the vibration monitoring function presented here. This means, that the current vibration characteristics (pattern) is derived automatically from download data. A correlation analysis between the current pattern and the patterns in the library is performed, leading to a proposal of the most probable matching pattern.

The vibration data necessary for generation of patterns library are collected mainly on wing, at the different operating flight test centres, but also on the test-beds of the diverse companies of the EuroJet consortium (EJ-PC). 3D simulations of the mechanical engine response due to different excitations are also a substantial source of data for generation of vibration patterns, in particular by extreme or catastrophic situations.
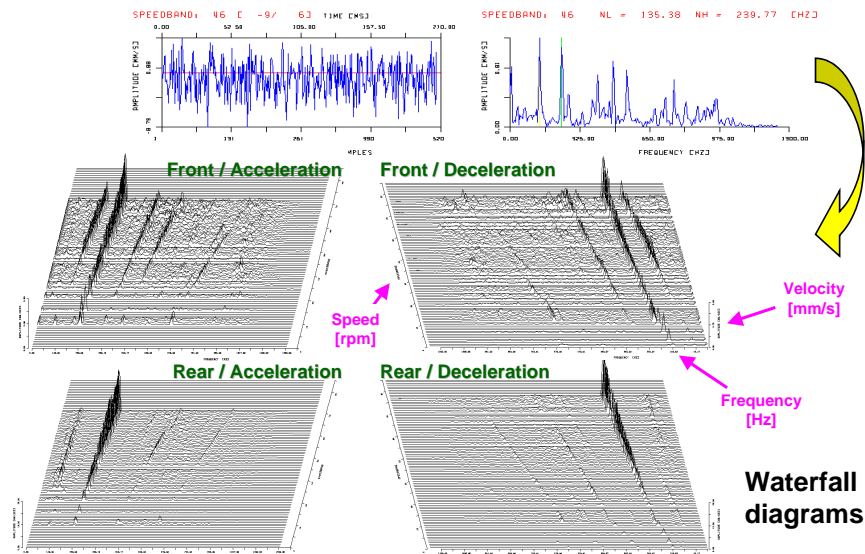
Figure 7: Transformation of the THS in the Frequency Domain Using FFT

Some mechanical faults which can be detected and diagnosed by this vibration monitoring system are:
- increased out of balance due to "normal" deterioration
- ice build up LP compressor blades under icing conditions
- high pressure rotor bow
- aircraft buffeting
- excessive out of balance due to FOD, bird strike, blade loss
- instabilities due to malfunction of squeeze-films, rub, loose joints
- low bearing thrust
- misalignment due to internal distortions broken bearing support / mounting links

In particular the vibration monitoring system combined with an extensive 3D structural Finite Element Model of the whole engine is a very powerful tool for the evaluation and interpretation of the impact of vibration events on the mechanical integrity of the engine.

4   APPLICATIONS

In this section experience gained during the application of the presented vibration monitoring system on the EF2000 engine EJ200 will be presented and discussed. Only a sample of selected cases will be reported giving an impression of the flexibility and reliability of the system.

The initial set of three examples concentrates investigations related to the high pressure turbine (HPT). That means, it can be expected that high vibration parameters amplitudes mainly associated with the HPT (1.EO NH / REAR and RMS / REAR) will be detected, the remaining vibration parameters amplitudes will be within the usual boundaries.

For the first two investigations the evolution of the vibration amplitudes signals with respect to time were analysed. Using this representation it was possible to identify and diagnose the vibration causes considering continuous changes of the amplitudes after reaching defined operational conditions.

Figure 8 shows an out of balance (OOB) occurrence on the HP turbine which can be identified by an increase of the amplitudes of the vibration parameters 1 EO NH and RMS captured with the rear transducer. It was noted that the vibration level started to increase at about 80% NH during acceleration from idle to max dry. At max dry the amplitude of the 1 EO NH is approx. 10 mm/s and increases continuously to a maximum value of 18 mm/s during an engine stabilisation period of 1-2 min. This cycle was repeated two times.
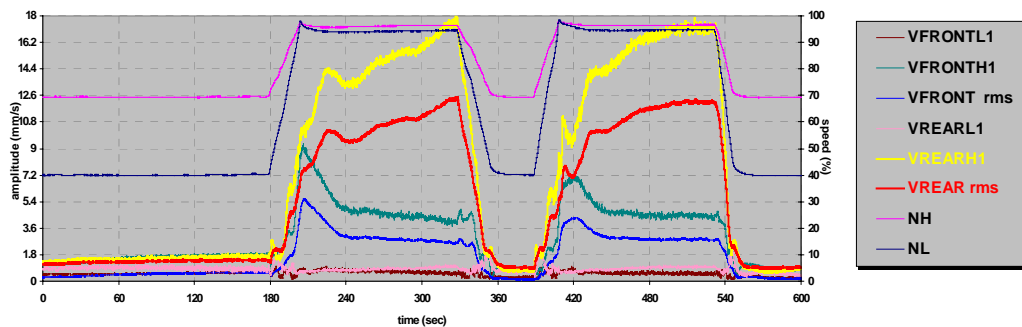
Figure 8: HPT out of balance – Case (a)

Analysis of the manufactured tolerances of the involved parts, shown in Figure 9, identified the cause of the vibrations to be as follows:

> A heavy interference (top limit) on pos. 1 combined with a loose interference on pos. 2 (bottom limit) leads to loss of interference on pos. 2 during engine operation causing high unbalance, which increases with time at constant speed.
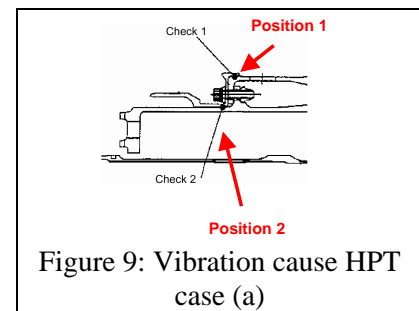
Figure 9: Vibration cause HPT case (a)

A similar investigation, case (b), was performed using a modified design of the involved parts shown in Figure 9 in order to compensate out of balance effects. The signals of the relevant vibration parameters in Figure 10 show also an increasing of the amplitudes. Reaching the rotor speed of about 80%NH the amplitudes of the 1 EO NH are about 7 mm/s in the first run and about 9 mm/s in the second run. The vibration level increases continuously up to max dry, 1 EO NH amplitudes of about 29 mm/s and 34 mm/s for the first respectively second run were achieved. A vibration step change is visible, the maximal amplitudes difference is approx. 17%. After reaching max dry the vibration level decreases continuously in contrast to the case above, and reaches values of about 18 mm/s respectively 21 mm/s after about 2 minutes of engine stabilisation.
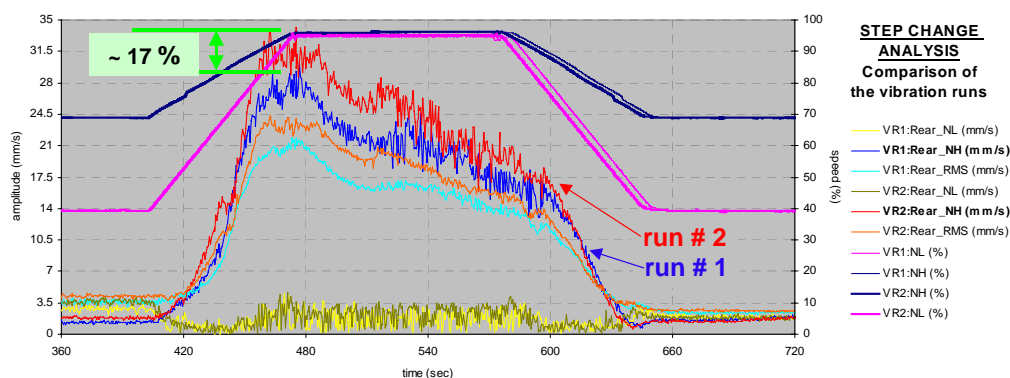
Figure 10: HPT out of balance – Case (b)

In this situation the cause of high vibration was identified as follows:

Similar to case (a), high unbalance resulting of loss of interference on pos. 2 is detected, but here other thermal effects related to additional masses (resulting of a balancing procedure) according to Figure 11 are identified. These effects compensate the high unbalance resulting of the loss of interference after some seconds of engine operation and the vibration level decreases continuously at constant speed.
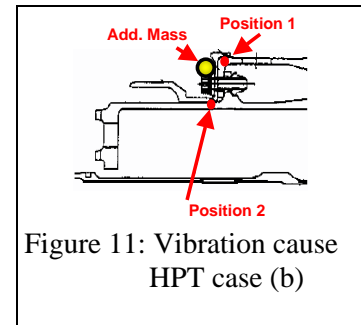
Figure 11: Vibration cause HPT case (b)

HP turbine blade deterioration also has a significant effect on vibration levels. Figure 12 shows max per run (MPR) data stored during vibration runs (slow acceleration – stabilisation – slow deceleration) over several engine runs. During early runs the amplitudes of the 1 EO NH / REAR reach maximum values of approx. 26 mm/s. During later runs the maximum amplitudes achieve approx. 37 mm/s, showing a vibration level increase of some 40%.
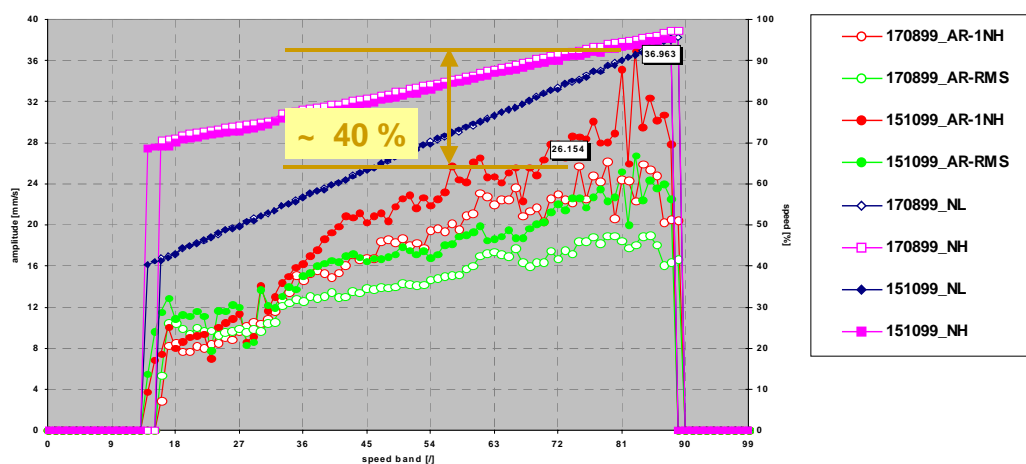
Figure 12: HPT out of balance – Case (c)

In this case the cause of high vibration levels was identified as follows:
Incremental deterioration of the tip of HPT blades due to a malfunction of the blade cooling system progressively increasing out of balance (and consequently vibration amplitudes) with time, see Figure 13.
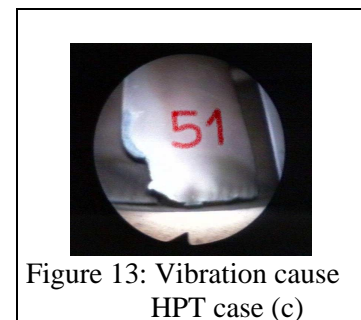
Figure 13: Vibration cause HPT case (c)

Vibration monitoring and investigation during icing tests showed high out of balance effects on the LP compressor rotor.

Figure 14 shows waterfall diagrams generated from the acceleration and deceleration vibration signals recorded during icing tests. The corresponding four first engine orders (EO) associated with the LP rotor are exposed in the right hand part of the figure.

The amplitudes of the 1 EO NL near idle reach abnormally high values for both acceleration and deceleration conditions. These dominating amplitudes can be easily identified in the waterfall diagrams.
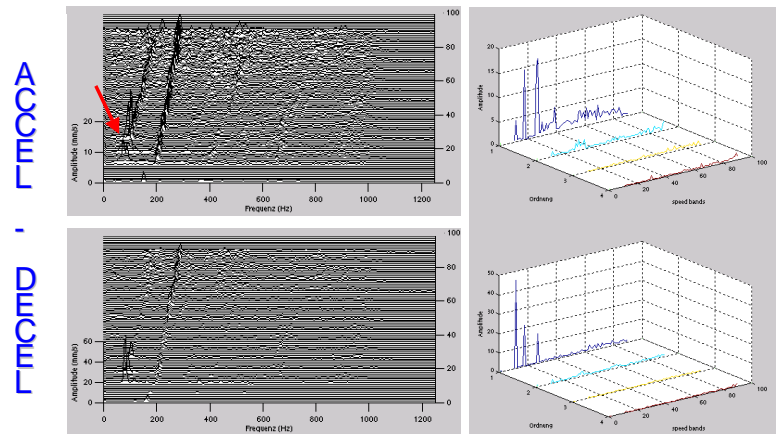
Figure 14: LPC out of balance due to ice build up

The THS corresponding to a selected acceleration speed band captured simultaneously for the FRONT and REAR transducers are plotted in Figure 15. The left hand side of the figure in the time domain and the right hand side in frequency domain.
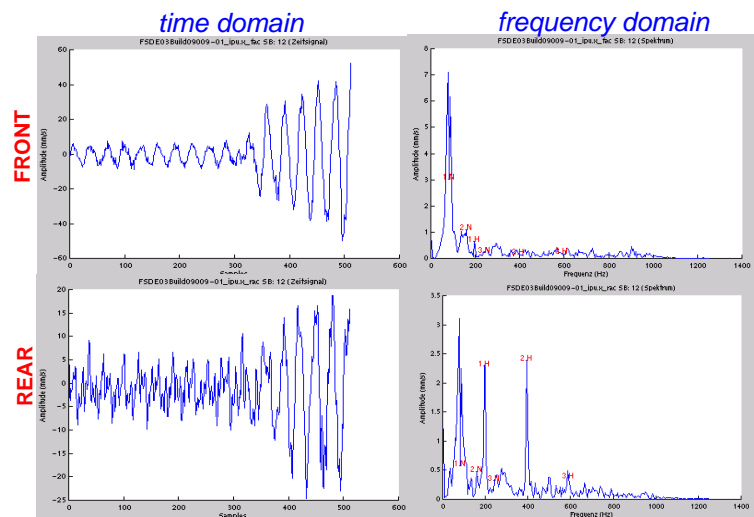
Figure 15: THS acceleration speed band 11 / FRONT and REAR transducers

The increase of the vibration level at a certain time results from the build up of a non-symmetric ice layer in the front stages of the LP rotor and consequently generates a high level of unbalance. After shedding of the ice layer the engine resumes a stable condition and the vibration levels of engine return to normal values.

Another significant application of the vibration monitoring system is for the identification of high vibration levels due to thermal rotor bow. This temporary deformation of the HP rotor can generate very high vibration amplitudes due to the excitation of different primary modes of the rotor. As a consequence of these high vibration levels, significant damage to HP compressor blading and seals can occur causing considerable premature engine deterioration.
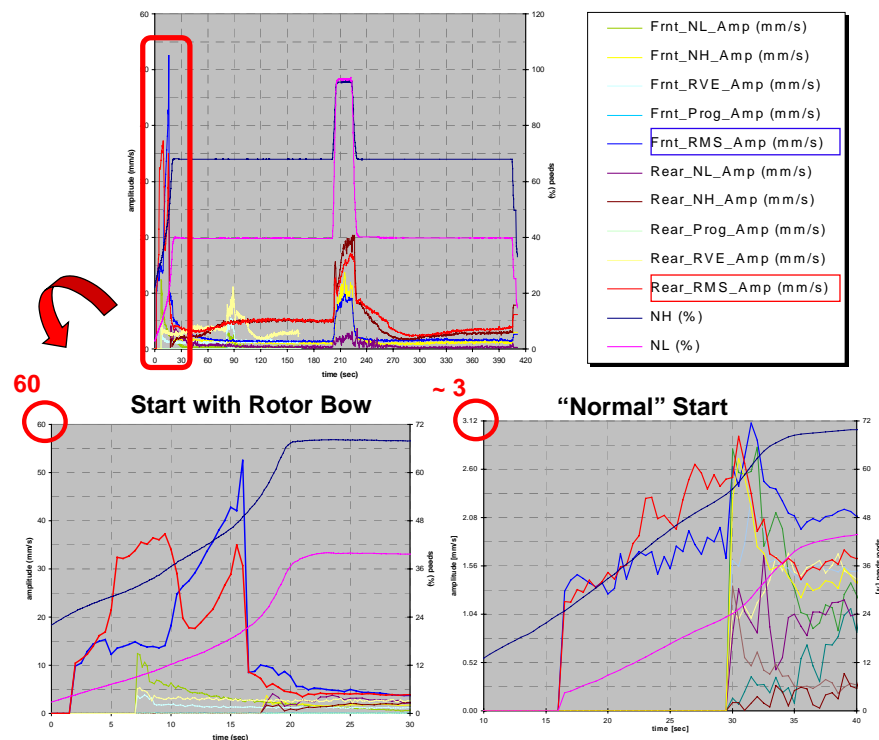
Figure 16: Engine start with HP rotor bow

The upper part of Figure 16 shows a typical engine run including the start phase to idle. The amplitudes of the different vibration parameters are related to the left hand axis whereas the rotor speeds in % of the nominal speeds are related to the right hand axis. Maximum vibration levels up to 55 mm/s for RMS/FRONT were reached. After a short time period the rotor returns to the nominal shape and the high vibrations resume normal levels. In the left hand lower part of Figure 16 an expansion of the vibration signals during the start phase is shown, including the rapid decline of vibration amplitudes to normal values. The start phase of a normal start is shown on the right hand lower part of the figure to compare the amplitudes with the amplitudes of the start with rotor bow. The ratio of the maximal amplitudes is approx. 20.

To illustrate the use of the vibration time histories (VITHS) an example of surge investigation is shown. Figure 17 shows different parameters versus time. At a selected operational condition (constant spool speeds), the nozzle throat area is continuously reduced in order to generate an engine surge with the corresponding increase of the vibration level and subsequent vibration incident detection.
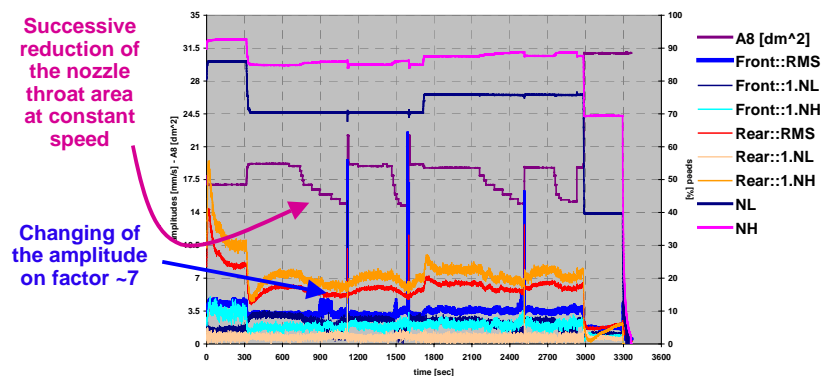
Figure 17: Engine surge due to continuous reduction of the nozzle throat area

Figure 18: Surge analysis / Vibration Time History

The evaluation of the VITHS in Figure 18 shows maximal vibration velocities of approx. 95 mm/s p-p at the FRONT transducer. Moreover in a time period shorter then 1 second three events can be clearly identified.

The vibration monitoring system presented in this report also enables engine external excitations to be detected and analysed. The Aircraft buffeting resulting of the application of the air brake is one such case. The engines are excited with a vibration component with a constant frequency of about 35 Hz independent on the speed of the rotors. The upper part of Figure 19 shows a waterfall diagram generated using the vibration time histories captured at the REAR transducer during decelerating conditions. In particular the first two EO of the HP rotor can be identified as well as high vibration amplitudes at a constant frequency band between 30 and 40 Hz. The same conclusions can be observed using an order analysis as shown in the left hand lower part of Figure 19 for the LP orders and in the right hand lower part of the figure for the HP orders. Also here the constant vibration components are readily identifiable.

Due to air brake buffeting in the rear section of the core engine, high vibrations with amplitudes up to 3 mm p-p can be induced which, depending on the duration of the excitation, can be detrimental to the engine or to its parts.

The use of the vibration monitoring system presented in this report in combination with an extensive 3D structural Finite Element Model of the whole engine represents a powerful tool for a detailed analysis and evaluation of the mechanical impact of vibrations to the condition of the engine and its components in terms of displacements and stresses as well as for diagnosis of the causes of vibration.

Engine Order Analysis - NL -   Engine Order Analysis - NH -
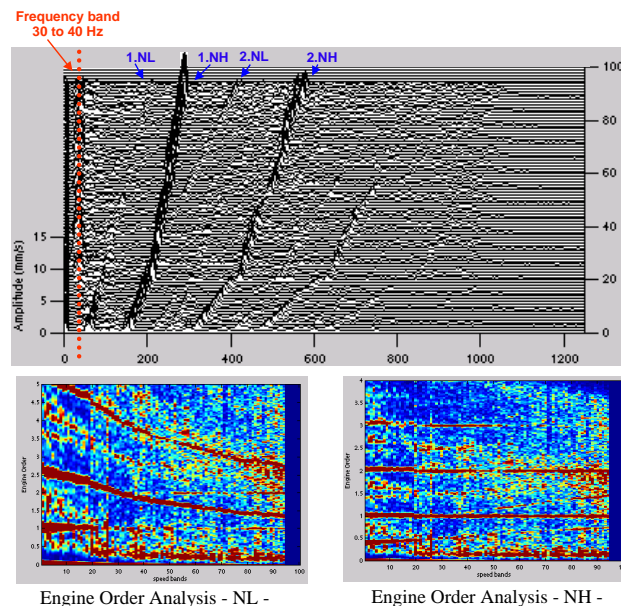
Figure 19: Waterfall diagrams – Excitation due to air brake buffeting

5   CONCLUSIONS AND OUTLOOK

The capabilities of the vibration monitoring and diagnosis system presented in this report to satisfy the requirements:

- increased safety by identification of dangerous vibration conditions at all engine speeds and thrusts, including steady state and transient operation and through the generation of the corresponding cockpit warning,

- avoidance of major secondary damage by way of early failure identification,
- reduction of maintenance expenditure through isolation, localisation and diagnosis of the vibration causes and
- optimisation of maintenance by means of consideration of the current engine condition.

are being demonstrated during the first phase of application.

The initial findings are favourable with respect to the quality of the signals, the philosophy for vibration incidents detection and the logic for storage of the different vibration data sets. The diagnostics and prognostics facilities currently developed will be extended, improved and automated by the use of artificial intelligence for pattern recognition. Additional data will be collected during further applications of the VMS to continue these efforts and to determine the cost and performance benefits.

Paper 7: Discussion

<u>Question from H Pfoertner – MTU, Germany</u>

Why is the vibration not measured in the axial direction when, with respect to gas turbines, this may be more relevant to bearing defects?

<u>Presenter's Reply</u>

All vibration measurements will be captured using accelerometers on the casing of the engine. As the bearing support structures, upon which the accelerometers are located, are very stiff in the radial direction, it can be assumed that the rotor vibrations will be transmitted, unchanged, to the sensors.

In the case of vibration in the axial direction, measurements are only reliable if the sensors are located directly in contact with the bearing chambers. Such locations are generally not considered for accelerometers due to the maintenance implications and, moreover, because of confidence in detecting bearing defects from vibration measurements in the radial direction.

<u>Question from Dr R Szczepanik – Instytut Techniczny Wojsk Lotniczych, Poland</u>

What was the reason for the increased level of engine vibration during the engine icing test?

<u>Presenter's Reply</u>

The vibration was due to a non-symmetrical ice layer that developed on part of the first stage of the fan.

Mathematical Pattern Recognition Techniques Applied to Wear Debris Characterisation for Condition Monitoring of Gas Turbine Engines

J. Ortner, J.v. Czarnecki, A. Laufer, P. Gauly, D. Oley
Wehrwissenschaftliches Institut für Werk-, Explosiv- und Betriebsstoffe
Institutsweg 1, D-85435 Erding, Germany

Abstract

The automation of wear debris characterisation by SEM / EDX analysis using mathematical pattern recognition techniques offers a reliable identification of particle alloy composition. It is less time consuming than an individual check for the best fitting material. Another advantage is the full automatic generated Word report, which can be easily distributed by LAN or email.

Introduction

A standard tool for condition monitoring and early failure detection of jet engines and other tribological systems are magnetic plugs in combination with the characterisation of the collected wear debris by SEM / EDX analysis. The quantitative analysis of the elemental composition of individual wear particles is used to indicate and localise a damage in its early stages and in general before a critical phase occurs.

In our institute about 3700 jet engines and other tribological systems of 86 different types are under early failure detection control. About 50% of the units are equipped with magnetic plugs. The percentage increases steadily and so does the number of wear particles to identify. Additionally depending on the system up to 30 different relevant alloys are used of which wear particles are found in the debris.

Due to the importance for operational safety of jet engines and other tribological systems wear debris analysis is used for years and was described in several articles. To optimise the identification process and to reduce the time and manpower effort, different attempts for automation were taken in the past. In most cases automation focuses on sample handling and on an automatic (mostly unattended) scanning of the debris sample with subsequent alloy identification and statistical interpretation. Particle analysis is in general done by x-ray fluorescence or SEM/EDX analysis with the sample mounted on a xy-scanning stage.

It is unquestioned that the quality of the analytical data about particle composition is directly related to an unambiguous alloy identification. But alloy identification is made complicated because debris samples removed from magnetic plugs in most cases are present as agglomerates of particles of different origin. So unattended analysis in general does not separate contaminant particles sticking to the debris particle of interest. The result is an increasing number of unidentified or questionable alloys. Moreover, due to alloy inhomogenity small spot analysis has to be avoided for particle identification. For improved results spot size has to be optimised to particle size, while excluding attached agglomerates. Additionally particle geometry and orientation is of influence on the analytical results. Excluding simple cases, from our experience debris analysis has to be done by an operator guided analysis. But automation is possible and very effective by using mathematical pattern recognition techniques to reduce the boring and time consuming alloy identification process. Unrenounceable requirement is the quality of the analytical data.

It is expected, that wear debris characterisation by SEM/EDX will continue to be of high importance in the future and for modern tribological systems equipped with chip detectors. Chip detectors only reduce the number of inspections and the determination of the amount of debris. In the case of excessive debris production debris analysis and alloy identification is still of interest.

As an example, the need for a reliable alloy identification can also be made clear by the number of samples to identify in the case of the RB 199 engine. The Bundeswehr operates about 800 RB 199 jet engines. Each engine is equipped with 5 or 6 magnetic plugs. On the average, each engine is operated 150 hours per year. Magnetic plugs are inspected after 19 hours of operation. This results to 32000 inspections per year. Only in about 100 cases (0.3%) excessive wear is found and send in for debris analysis. In 20% of these 100 questionable cases the engines could be directly operated again, because normal debris due to run in period or uncritical foreign matter sources was detected. In 55 cases (0.15%) a recommendation for oil change an test operation was given. Only in 25 cases (0.07%) the change of an engine was recommended. Taking into account the costs for recommended service, the need for reliable and precise debris identification becomes clear. Widely automated systems tend to fail this goal.

So having both capabilities (automated scanning and operator controlled analysis) we favour the second way while optimising the identification process by mathematical pattern recognition techniques because better results are obtained. Identification can be done by principal component analysis (PCA) or hierarchical cluster analysis (HCA) applied to quantitative EDX results on a routine basis. We use a modified HCA technique.

A data set of reference alloys, depending on the tribological system, is automatically extended by the composition of wear particles analysed. The mathematical pattern recognition techniques aid the analyst to see clustering of the multivariate data in higher dimensional spaces. Instead of a time consuming comparison of scattering quantitative results for individual elements of the alloys, the pattern recognition procedure determines the similarity of a complete data set with reference data. It looks for a similarity in element composition and not for individual element concentrations. Thus scattering of the quantitative results for individual element concentrations, which can not be ruled out in SEM/EDX analysis of microscopic particles, is less critical. The techniques can be implemented in an expert system which makes the identification of wear particle alloys less time consuming and which helps to reduce the misinterpretation of the data. Though the whole diagnostic routine is very reliable, fast and cost-saving, it may be improved. Depending on the system, up to 30 different relevant alloys are used of which wear particles are found in the debris.

EDX-Analysis

With scanning electron microscopy (SEM), combined with energy dispersive x-ray analysis (EDX), the interesting particles are analysed. Typically, 14 elements (V, Cr, Mn, Fe, Co, Ni, Cu, Zn, Mo, Ag, Cd, W, Al, Si) are quantified. Depending on the tribological system, additional elements can be taken into account if required. The accuracy of the EDX-analysis is shown in fig. 1:

After all particles are analysed, the data sets are transferred from the EDX-computer (PDP 11) to a expert system based on a PC via the serial interfaces and stored in a text file.

Fig. 1 *Accuracy of EDX-analysis*
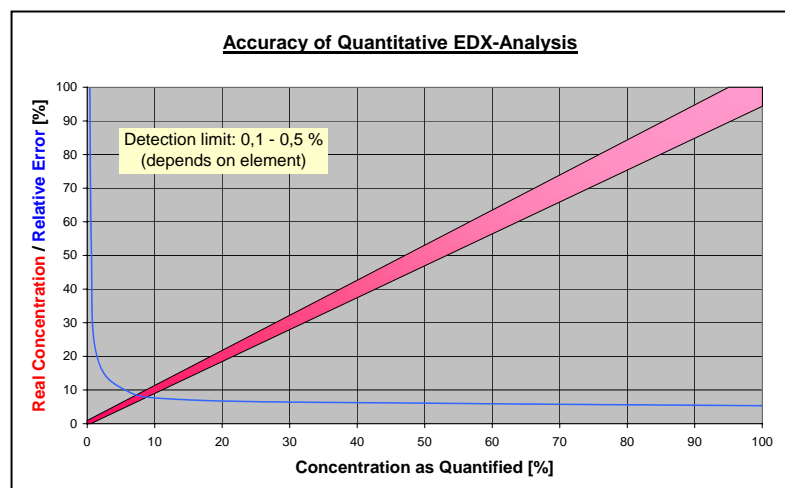
Data Base

As shown in fig. 2, the user has to select a certain tribological system. Implemented are the RB 199 and APU engine of the Tornado, the Tornado gearbox and the engines of three different helicopters (UH-1 D, BO 105 and Sea King). The RB 199 and the Sea King engine data sets are divided in 5 (see fig. 3) respectively 3 magnetic plugs.

Fig. 2: *The Tornado and 3 different helicopters are checked by SEM / EDX analysis*
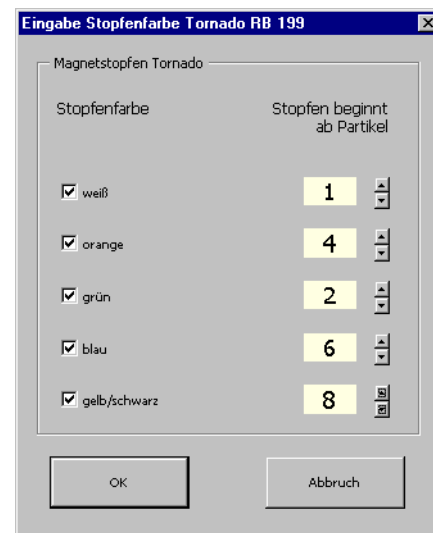
Fig. 3: *The RB 199 consists of 5 different tribological systems, monitored by magnetic plugs*

Each tribological system contains specific alloys and related parts. This information is stored in Excel worksheets, which can be changed or supplemented without problems (fig. 4).

	A	B	C
1	**Triebwerk**	**Bauteil, Komponente**	**Werkstoff**
2	RB 199, weiß	Lager 1 + 2: Innenring	MV 1172
3	RB 199, weiß	Lager 1 + 2: Außenring, Wälzkörper	MV 1174
4	RB 199, weiß	Rollenlager 1 + 2: Käfig	100Cr6
5	RB 199, weiß	vord. Lagerkammer: Labyrinthdichtung S3, Öldichtring, IPC S7	MV 1211
6	RB 199, weiß	Gehäuse: Dichtgehäuse, Dichtungsgehäuse	MV 1211
7	RB 199, weiß	Beschichtungen, Leitschaufelgehäuse St 3: Verschleißschicht	MSRR 9507/1
8	RB 199, weiß	Beschichtungen, Dichtungsgehäuse: Einlaufbelag	MSRR 9507/5
9	RB 199, weiß	Beschichtungen, Dichtungsgehäuse: Einlaufbelag	MSRR 9507/6
10	RB 199, weiß	Ag-Beschichtung	Ag-Beschichtung
11	RB 199, weiß	Cu-Beschichtung	Cu-Beschichtung
12	RB 199, weiß	Zn-Beschichtung	Zn-Beschichtung
13	RB 199, weiß	Ni-Beschichtung	Ni-Beschichtung
14	RB 199, weiß	Al-Beschichtung	Al-Beschichtung
15	RB 199, blau	Lager 3: Innenring, Außenring, Wälzkörper	MV 1174
16	RB 199, blau	Lager 3: Käfig	100Cr6
17	RB 199, blau	Lager 4: Innenring, Wälzkörper	MV 1174
18	RB 199, blau	Lager 4: Außenring	MV 1172
19	RB 199, blau	Lager 4: Käfig	100Cr6
20	RB 199, blau	Lager 4a: Innenring, Außenring, Wälzkörper	MV 1174
21	RB 199, blau	Lager 4a: Käfig	100Cr6

Tornado / UH-1D / Sea King / Bo-105 / Werkstoffe / EDX_Konz / W_Konz / Ergebnis / Bauteile / Fiktive Bauteiltabelle / Fehler /

Fig. 4: *Part of Tornado's component table. For each part, the alloy name is given.*

In another Excel worksheet, the composition of all alloys is summarised (see fig. 5).

Fig. 5: *The composition of all materials involved in the above mentioned tribological systems.*

Visual Basic Program

The EDX-data of the debris wear particles are compared with the materials of the specific tribological system. With a pattern recognition algorithm the best fitting material is selected and all components, made out of this alloy are determined. Finally an automatic report is generated.

The program consists of the following procedures:

1) Selection of the tribological system (see fig. 2). To section the data set for Tornado RB 199 and Sea King Gnome engines, the number of the analysed particles have to be assigned to the plugs (fig. 3).

2) Generation of an Excel worksheet with the data of the EDX-analysis text file.

3) Depending on the tribological system, the software selects a reference data base including parts and alloys.

Fig. 6: First page of the Word report with the data of the EDX-analysis.

4) Pattern recognition algorithm:

   a) Determination of the optimised reference concentration for alloys where a concentration range is defined instead of a single value. In this case the best fitting value has to be determined.

   b) For each particle, the similarity value relative to possible alloys is calculated. The similarity is determined by the differences in the elemental concentrations between a particle and all possible materials. To improve selectivity the pattern recognition algorithm is optimised for specific elements and concentration ranges. This is necessary because the element concentrations significant for the identification range between 1% and 20 %. This may be explained by the following examples:

   ➢ If the difference is calculated by formula 1 (absolute error), the main element is dominant and wrong materials are identified.
   ➢ If the difference is calculated by formula 2 (relative error), the elements with very low concentrations ($< 1\%$) get dominant.

$$D = \sqrt{\sum_{i=1}^{E} (P_i - M_i)^2} \qquad (1); \qquad\qquad D = \sqrt{\sum_{i=1}^{E} \left(\frac{P_i - M_i}{M_i} \right)^2} \qquad (2)$$

$D = Difference$

$E = Number\ of\ elements$

$P_i = Concentration\ of\ element\ i\ in\ the\ particle$

$M_i = Concentration\ of\ element\ i\ in\ a\ material$

If a coating is present, the particle has to be identified as a coating. Therefor a different algorithm has to be used for particles with significant concentration of Ag, Cd, Cu, Zn, Ni or Al.

   c) Determination of the best fitting alloy for each particle. If more materials are similar, they all have to be listed including a ranking.

5) For all alloys identified, the relating parts are determined.

6) Generation of a Word report (see fig. 6 - 7).

7) Data exchange by the institute's LAN.

<u>Results</u>

Particle	Material (best fit)	Similarity	Alternative Materials	Similarity
1	MV 1175	69.63%	-	
2	MV 1175	75.81%	-	
3	MV 1175	73.36%	-	
4	MV 1175	76.04%	-	
5	MV 1175	73.71%	-	
6	MV 1175	68.82%	-	
7	MV 1175	62.56%	MV 1137	58.72%
8	MV 1171	56.71%	MV 1175	53.15%
9	MV 1175	82.84%	-	
10	MV 1175	66.40%	-	
11	MV 1175	71.41%	-	
12	Ni-coating	52.59%	-	
13	Ni-coating	42.44%	-	

<u>Parts</u>

Plug	Material	Parts
RB 199, gelb / schwarz	MV 1171	Außengetriebe: Wälzlager, Innenring;
	MV 1175	Außengetriebe: Wälzlager, Wälzkörper; Doppelschulterkugellager: Wälzkörper;
	MV 1137	Getriebe: Welle Innengetriebe, Verzahnung;
	Ni-coating	Ni-Beschichtung;

<u>Comments</u>

Fig. 7: Last page of the Word report with the results of mathematical pattern recognition.

Summary:

The automation of wear debris characterisation by SEM / EDX analyses using mathematical pattern recognition offers a reproducible and reliable technique and is less time consuming than an individual check for the best fitting material. Another advantage is the full automatic generated Word report, which can be easily distributed by LAN or email.

This page has been deliberately left blank

_____

Page intentionnellement blanche

Optimizing Diagnostic Effectiveness of Mixed Turbofans by Means of Adaptive Modelling and Choice of Appropriate Monitoring Parameters

Ph. Kamboukos
Research Assistant

P. Oikonomou
Student

A. Stamatis
Research Associate

K. Mathioudakis
Associate Professor

Laboratory of Thermal Turbomachines
National Technical University of Athens
PO Box 64069, Athens 157 10, Greece

ABSTRACT

Methods for the optimal selection of measurements and health parameters used for diagnostic purposes in aircraft gas turbine engines are presented. Principles of aerothermodynamic diagnostic techniques are first briefly reviewed. The problem of optimal selection of measurements and health parameters is examined from two different standpoints. (a) How to select out of all available measurements the minimum set that will be capable to provide sufficient information to assess engine health condition. (b) When a set of measurable quantities from an operating engine is given, how to select the combination of health parameters, in order to provide in an optimal way the information about the condition of the engine. The present paper concentrates mainly on the second type of problem since it is related to the handling of an existing fleet. Methods based on sensitivity analysis are discussed, but it is shown that the most substantial information is produced by analyzing the properties of the Jacobian matrix, interrelating parameters and measurement deviations. Finally, results of condition estimation for a number of turbofans in service are presented.

Nomenclature

a_{ij}	Element of Jacobian matrix, eq (A9),(A10)
CN	Condition number of Jacobian matrix, eq(A14)
$EPR=P_7/P_2$	Engine Pressure Ratio
$\boldsymbol{F}$	Prediction algorithm, eq(1)
$\boldsymbol{f}$	(nx1) Vector of health parameters Eq. (13, 14)
$\boldsymbol{J}$	Jacobian matrix
m	Number of measurements
N	Number of health parameters
N_1	Low pressure rotational speed
N_2	High pressure rotational speed
P	Total pressure along the gas path
$S\Delta$	Overall sensitivity operator, Eq (11)
T	Total temperature along the gas path
$\boldsymbol{u}$	(3x1) Vector of variables defining the operating point, Eq. (1)
$\boldsymbol{V}$	Matrix containing the singular vectors of $\boldsymbol{J}$ Eq(A13)
$\boldsymbol{W}$	Diagonal matrix containing the singular values of $\boldsymbol{J}$, Eq(A13)
WFB	Fuel Flow
$\frac{w\sqrt{}}{\vartheta}$	Corrected flow rate
$\bar{Y}$	(mx1) Vector of measurable quantities, Eq(1,2)
Δf	Health parameter deviation from reference value, Eq(4)
ΔY	Measurement deviation from reference value, Eq(5)
η	Efficiency

Superscript

ref	Reference State

Subscripts

actual	Actual value of parameter on component performance map
reference	Reference value of parameter on component performance map
s	Static Pressure or Temperature
2, 13, 23, 3, 41, 5, 7	Numbering of aerothermodynamic stations along the gas path, fig. 1

1. INTRODUCTION

The optimal exploitation of an existing fleet of engines is highly related with the ability to assess the health condition of each engine during operation or after overhaul. A large number of techniques for this purpose have been proposed in the past by several authors. A significant part of them uses aerothermodynamic measurement data in order to estimate the condition of each component and to assess the overall condition of the engine. Such techniques are characterized as gas path analysis techniques and are divided in two main groups.

The first group of techniques is referred to linear methods and comprises Least squares methods, Kalman filters and their derivatives. Health assessment is based on the formation of an appropriate matrix called Influence Coefficient Matrix, which relates deviations on measurable quantities from the reference state to deviations of health parameters under estimation. The fundamentals of Linear Gas Path Analysis have been posed by Urban (1972). Least Squares Techniques coupled with gas path analysis have been presented by Doel (1992, 1993). Techniques based on Kalman filters, have been presented by Provost (1994) and Volponi (1994), giving the possibility to distinguish between sensor fault and component fault. Stamatis and al. (1991) have proposed the linear gas path analysis in discrete operating points, a way to overcome the obstacle of limited available information from an operating engine.

The second group comprises the non-Linear methods. The estimation of the parameters describing the health condition of the engine is achieved using a non-linear model capable to simulate the engine behavior. These methods have been introduced by Stamatis and al. (1990a).

A common feature of both linear and non-linear techniques is the use of measurable quantities from an operating engine in order to estimate a set of diagnostic indices that reflect the health of the engine. Such indices can be the deviations in component performance parameter values, introduced by Urban (1972) or the component modification factors of Stamatis (1990a). Another common feature is the need of a performance model for the considered engine type. The derivation of health indices using linear or non-linear formulation can be achieved with the help of the model.

An issue of major importance is the selection of appropriate measurements and parameters, which will be used in the diagnostic procedure. Stamatis and al. (1992) have presented the method of sensitivity analysis for the optimal selection of measurements and health parameters with application to an industrial gas turbine. Provost (1994) has presented a method, which is capable to evaluate the correlation level among measurements or health parameters used on a diagnostic system. Tsalavoutas and al. (1999) have presented the implementation of the method based on sensitivity analysis for measurements and health parameters selection to the case of a twin spool, two-shaft gas turbine.

In the present paper measurement and parameter selection methods are presented, focusing on the case of a mixed, low by-pass ratio, turbofan. The implementation of the method presented in the past (Stamatis et al 1992) on this particular type of engine is examined, while some new ways of selection are introduced.

2. FUNDAMENTALS OF DIAGNOSTICS

For the purpose of the present analysis an engine is considered as a system, whose operating point is defined by means of a set of variables, denoted as u. The health condition of its components is assumed to be represented through the values of a set of appropriate "health parameters", denoted as f. The system is observed through measured variables, denoted as Y. In symbolic form we can write:

$$Y = F(u, f) \qquad (1)$$

For a given operating point u the measurement values depend only on the health condition of engine components.

$$Y = F(f) \qquad (2)$$

When an engine is in intact condition the health parameters have the reference values and the measurements have also reference values:

$$Y^{ref} = F(f^{ref}) \qquad (3)$$

Occurrence of particular faults can be expressed through deviations of health parameters from the reference state. These deviations are defined for any health parameter as:

$$\Delta f_j = \frac{f_j - f_j^{ref}}{f_j^{ref}} \times 100 \qquad (4)$$

Any mechanical or other alteration, which can be classified as engine fault, initially affects the performance of the damaged component and finally the overall performance of the engine, resulting to deviations on measured quantities:

$$\Delta Y_i = \frac{Y_i - Y_i^{ref}}{Y_i^{ref}} \times 100 \qquad (5)$$

The relation between ΔY_i and Δf_j is, in general, non-linear. If deviations are small, however, a linear relation can be used as shown in APPENDIX 1, which can be written in a matrix form:

$$\begin{pmatrix} \Delta Y_1 \\ \Delta Y_2 \\ \Delta Y_i \\ \Delta Y_m \end{pmatrix} = \begin{pmatrix} a_{11} & a_{12} & a_{1j} & a_{1n} \\ a_{21} & a_{22} & a_{2j} & a_{2n} \\ a_{i1} & a_{i2} & a_{ij} & a_{in} \\ a_{m1} & a_{m2} & a_{mj} & a_{mn} \end{pmatrix} \cdot \begin{pmatrix} \Delta f_1 \\ \Delta f_2 \\ \Delta f_j \\ \Delta f_n \end{pmatrix} \qquad (6)$$

or in symbolic form:

$$Y = J \cdot f \qquad (7)$$

where J is the Jacobian matrix.

The problem that has to be solved when an engine condition diagnosis is to be performed, is the determination of f when Y are known. In mathematical terms this means that eq. (2) has to be solved for f when Y is given:

$$f = F^{-1}(Y) \qquad (8)$$

For this solution to be possible, it is essential that the number of equations must be equal to the number of unknowns, which translates to the fact that we must have as many different measured quantities as the number of unknown health indices. This is not sufficient however. To be able to solve the system of equations, this system must have a unique solution, namely the system representing the engine must be observable.

An equivalent approach is to determine Δf from ΔY if deviations are small. In this case eq. (7) gives:

$$\Delta f = J^{-1} \cdot \Delta Y \qquad (9)$$

Of course derivation of f through eq. (8), or (9) would be reliable for noise free measurements. For actual measurements with noise, appropriate estimation techniques have to be used. The previous equations can nevertheless be used for the purposes of the present analysis, as they express the fundamental relation between measurements and health parameters.

Two questions can be stated at this point.

a) For an engine represented through given set of health parameters, which is the best combination of measurements taken from an operating engine that is going to provide sufficient diagnostic information?

b) For an available set of measurements taken from an operating engine, which is the best combination of health parameters to be estimated?

Methods for addressing these two questions are presented in the following.

3. MEASUREMENTS SELECTION

Information collected along the engine gas path determines the state of the working fluid inside the engine, reflecting any alteration, which happens to the engine. The amount of collected information depends on the number of sensors placed along the gas path. In order to have information for the condition of each component a large number of sensors would be necessary. These sensors should be placed in the inlet and the outlet sections of the components in order to have the full picture of the change that the components operation causes to working fluid. For example, in the case of a twin spool turbofan engine with 5 rotating components, a number of 12 sensors must be placed in the engine. That is not acceptable for an operating engine for several reasons: In general sensors and related systems are very expensive, increasing the complexity of the engine. Another important issue is that the addition of wall taps, pitot probe, and thermocouples causes disturbances on the flow. Also they are not always possible, because of harsh local conditions (for example measuring the TIT at combustion chamber outlet section). Not even on the phase of designing and testing a new engine such detailed methods are adopted.

It is thus desirable to have a minimum number of sensors placed on an engine. The choice of this minimum set has to be done without sacrificing diagnostic capability. In the following we will present methods, which allow selection of such measurements. It can be commented here that this part of the analysis is mainly addressed to engine manufacturers who want to select the instruments that must be placed on an engine under design, in order to ensure a good diagnostic ability in the engine. It can be also useful to the engine user, who wants to modify an existing instrumentation set.

3.1 Sensitivity of measurements

A first means of examining which measurements are suitable for monitoring purposes is their sensitivity to component condition changes. It is shown by Stamatis et al (1991) that sensitivity of measurements can be used to select the most appropriate measurements to estimate a given set of health parameters. The sensitivity of measurement Y_i to health parameter f_j is defined as follows:

$$\Delta Y_i^j = \frac{Y_i^j - Y_i^{ref}}{Y_i^{ref}} \times 100 \qquad (10)$$

when f_j deviates by a given amount from its reference value (typically 1%).

For a set of health parameters under estimation, the most appropriate measurements to be used are these, which exhibit the greater sensitivities on individual change of each parameter. Individual measurements are suitable for monitoring the condition of specific component. The way each measurement reflects the overall condition can be expressed through an overall sensitivity measure, defined as:

$$S\Delta Y_i = \left[\frac{1}{n} \cdot \sum_{j=1}^{n} \left[\Delta Y_i^j \right]^2 \right]^{1/2} \qquad (11)$$

Large overall sensitivity of a measurement indicates that at least one health parameter influences the examined measurement. The most sensitive measurements with respect to overall sensitivity can be selected in order to form the set to be used for a diagnostic system.

Although the most sensitive measurements should be included in the monitoring set, one additional condition has to be fulfilled: the measurements chosen have to be linearly independent with respect to parameters deviations. This means that the vectors of the influence coefficients for the measurements to be selected have to be linearly independent. A method to examine the degree of interdependence of measurements has been proposed by Provost (1994). Angles between the vectors are calculated and when found sufficiently large, they indicate a very small interdependence. The criterion proposed in the following subsection is another alternative method to select measurements, which are not linearly dependent.

3.2 Condition number of Jacobian. Examination of rows

The condition to have a unique solution is the sufficient observability of the diagnostic system. That issue is very common in control theory (Stengel 1993).

There is a well-known method to find out if a system is observable. This method is mainly related to the solution of linear system equations. When n health parameters have to be estimated and m measurements are possible ($m>n$), we can select n out of these measurements to form a closed (nxn) system. The ones that will be chosen have to ensure (a) that that system has a solution (b) that the solution of the system gives the minimum amplification to the measurement noise. For a linear system of equations these conditions translate to the requirement for a small condition number for the matrix of the system. In APPENDIX 2 the relevant theorem and the principles of the method to determine matrix condition number are given. The criterion thus introduced is that the set of measurements that will be chosen will have to be such that the condition number of the system expressed by eq. (7) is the minimum possible. The procedure for materializing this criterion is described below.

We can form a number of squares sub-matrices of the Jacobian. The number of these sub-matrices is given from the number of possible combinations of m available measurements taken n each time (n health parameters under estimation).

$$Ncombi = \binom{m}{n} = \frac{m!}{n!(m-n)!} \qquad (12)$$

Using the above described formulation we can investigate all the possible combinations of measurements for the given set of health parameters. The procedure to be followed is: (1)Using a performance model for the engine a mxn Jacobian is formed., (2)All the possible square sub-matrices of Jacobian are formed, (3) The condition number of each sub-matrix is evaluated, (4)Results are sorted in ascending order of condition number.

At this point it must be said that the results must be judged from an engineering point of view as well. Common practices, which are in use, such as the desire to measure in the cold section of an engine, must be taken in to account, when the resulting combinations are inspected in order to select the most appropriate one.

4. HEALTH PARAMETERS SELECTION

A common feature of engines in service is the availability of minimum instrumentation, which accompanies the engine. This instrumentation is used primarily by the control of the engine, which ensures safe operation within its operating envelope. It is thus desirable to exploit the information provided from the sensors along the gas path in a way deriving the maximum diagnostic information about its state.

4.1 Singular Value Decomposition analysis of Jacobian matrix

In the general case we can form a Jacobian matrix, which has m rows corresponding to measurements and n columns ($n>m$) corresponding to health parameters. Stamatis and al. (1991) have proposed the use of Singular Value Decomposition method in order to select m health parameters among n to form the most observable system for diagnosis of the state of the engine. According to that method the Jacobian matrix is decomposed as explained in APPENDIX 2.

Using the following lemma of linear algebra we can choose combinations of health parameters in order to form a well observable diagnostic system: *Linear combinations of elements of health parameters that correspond to the direction of the greater singular values vectors are estimated with the greater accuracy*. This implies that health parameters with the greater projections in the direction of the greater singular vectors are estimated with greater accuracy and must be preferred among all possible.

The procedure to be followed is: (1)Using a performance model for the engine considered, a mxn Jacobian is formed, (2)Jacobian is decomposed using SVD analysis, (3)The singular values of Jacobian are shorted in descending order and the singular vectors are properly rearranged, (4)Results are inspected in order to select the best combination of parameters.

4.2 Condition number of Jacobian. Examination of columns

The approach presented above for measurement selection using the condition number of Jacobian can also be used for parameter selection. In this case sub-matrices are formed by combining columns, which correspond to health parameters.
1. Using a performance model for the engine type considered, a mxn Jacobian is formed.
2. All possible square sub-matrices of Jacobian are formed.
3. Each one of the sub-matrices is decomposed using SDV analysis and the condition number is evaluated.
4. Results are sorted in ascending order of condition number.

The combinations, which exhibit the smaller condition numbers, are more suitable to be estimated from the diagnostic system.

Engineering judgment should also be applied. Since the problem is not just mathematical but also physical, the chosen combination must supply the diagnostic procedure with substantial information. For example, existing experience may indicate that certain parts of the engine are more prone to damage than others. This means that some health indices should be included in the set to be defined while some others could be kept constant. This means that the combination to be selected, must rank high in the list (small condition number) but should not necessarily be the first.

5. APPLICATION OF PRESENTED METHODS

Application of the methods presented above is demonstrated for a twin spool mixed turbofan engine. The layout of the engine is shown in figure 1.
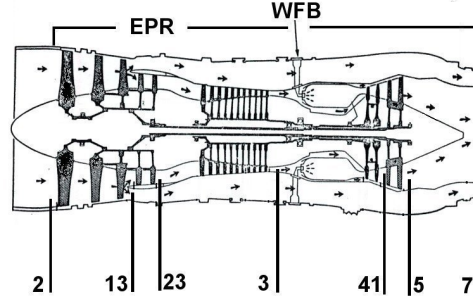
Figure 1: Layout of twin spool mixed turbofan

The data for the particular engine simulated are chosen to represent the Allison TF-41 engine. This particular engine was chosen because test cell test data were available, and are used later in the paper.

The model created simulates engine behavior for a wide range of operating conditions. The simulation is done using the operating point definition variables and the health parameters. The operating point u is defined using the desired value for net thrust and the total conditions P2, T2, at fan inlet section (station 2). A diagnostic ability is incorporated in the model through the use of appropriate component health parameters. In the present study the considered health parameters are these introduced by Stamatis (1989). For each rotating component, two health parameters are defined:

Flow capacity: $f_j = \left(\dfrac{W\sqrt{\vartheta}}{\delta}\right)_{actual} \Big/ \left(\dfrac{W\sqrt{\vartheta}}{\delta}\right)_{reference}$ j=1,3,5,7,9   (13)

Efficiency: $f_j = \eta_{actual} / \eta_{reference}$ j=2,4,6,8,10   (14)

The set of parameters is shown in Table 1.

Table 1: Health parameters for the engine components

	Considered Health Parameters for mixed turbofan	
	Symbol	Description
1	f_1	Flow capacity factor at FAN
2	f_2	Efficiency factor at FAN
3	f_3	Flow capacity factor at IPC
4	f_4	Efficiency factor at IPC
5	f_5	Flow capacity factor at HPC
6	f_6	Efficiency factor at HPC
7	f_7	Flow capacity factor at HPT
8	f_8	Efficiency factor at HPT
9	f_9	Flow capacity factor at LPT
10	f_{10}	Efficiency factor at LPT

5.1 Measurements Selection

The objective is to select ten measurements in order to estimate ten health parameters. For that set a sensitivity analysis has been performed. Each health parameter has been disturbed by -1% from reference and measurement sensitivity is derived. The procedure is repeated for all health parameters under consideration. In figure 2 the overall sensitivity of each measurement to all health parameters is shown.
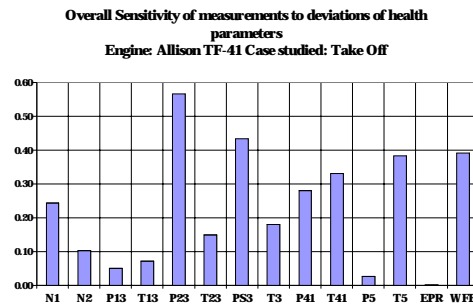
Figure 2: Measurements overall sensitivity

For the examined case we can easily see that the most sensitive measurements in an order of descending overall sensitivity are: P_{23}, P_{S3}, WFB, T_5, T_{41}, P_{41}, N_1, T_3, T_{23} and N_2. With the use of these ten measurements we can proceed to the estimation of the ten considered health parameters. In this point we must say that if two measurements exhibit large sensitivity but they are also correlated between them, then the one must be removed from the diagnostic set.

It is worth observing that *EPR* exhibits practically zero sensitivity. This is an immediate consequence to the fact that *EPR* is related to thrust in an almost one-to-one relationship, irrespective of components condition. Since deviations were calculated for a constant thrust, *EPR* practically did not change either. P_5 is a quantity with a value very close to the value of P_7, which sets the *EPR*. That's why it shows a very small sensitivity too.

In order to have a more precise image for the sensitivity of each measurement we can inspect the result of measurement sensitivities to individual changes of health parameters. In figure 3 the sensitivity of measurements to deviation of factor f_1 (flow capacity of Fan) is shown. Inspection of the figure shows that some measurements exhibit a large degree of sensitivity in comparison with others. These measurements should be included in order to form a diagnostic system for the estimation of f_1. For the case studied ($\Delta f_1 = -1\%$) the most sensitive measurements are P_{23}, N_1, P_{41}, P_{S3}, T_{23} and *WFB*. Measurements like P_5, T_{41}, which are insensitive to change of f_1, are not suitable for the estimation of that parameter.

Sensitivity of measurements when health parameter f1 deviates -1% from reference
Engine: Allison TF-41 Case studied: Take Off
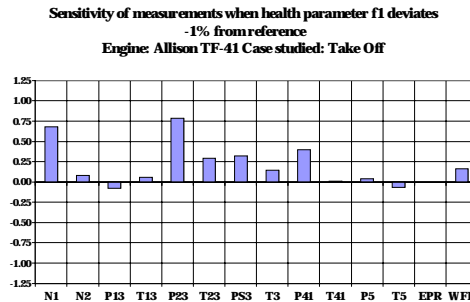
Figure 3: Measurements sensitivity to deviation of f1 from reference

We proceed now by applying the method based on the condition number of the linear system. A 14x10 Jacobian has been generated and 1001 square sub-Jacobians are examined. The condition number of each one is derived and results are shorted in ascending order. Figure 4 shows the Condition Number values for all combinations. There is a fast rise of condition number in the first hundred combinations. This rise of condition number corresponds to a progressive degradation of the quality of the examined combinations of measurements for the given set of health parameters. In Figure 5 we can see in detail the rise of condition number and also the first fifteen combinations. It is worth noting that *EPR* is not contained in the first fifteen combinations. Actually, the first combination containing *EPR* has a condition number about two orders of magnitude larger than the smallest one.

At this point it should be mentioned that the method of Provost (1994) has also been applied to the present data. Angles between the measurement vectors were calculated in all possible combinations. The measurement pairs whose vectors were found to form small angles were P_5, P_{13} and T_5, T_{41}. It should therefore be desirable to avoid having both measurement of each one of those pairs in a measurement set. This observation is in agreement with the analysis using the condition number, as combinations containing those pairs are only found for set with higher condition numbers.

Condition number of Jacobians which are formed using all the possible combinations of 14 measurements taken 10 at time
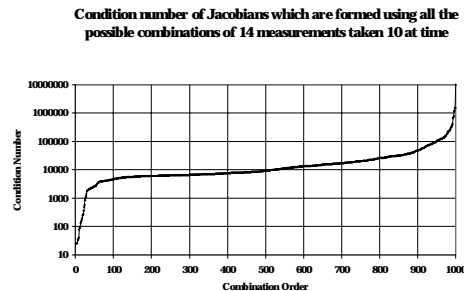
Figure 4: Condition Number of measurements sets in ascending order

Figure 5: The lowest condition numbers and corresponding measurement sets

5.2 Health parameters Selection

In the actual TF-41 engine installed in a test cell seven measurements are available: N_1, N_2, P_{S3}, T_3, T_5, P_5 and WFB. It is obvious that the estimation of the full set of health parameters is not possible and a limited set of those must be chosen. Thus we must choose seven health parameters in order to form a square diagnostic system.

First the 7x10 Jacobian matrix is formed. The 7x10 Jacobian is given on table 2. Operating point is set defining the total inlet conditions $P2$, $T2$ for a given level of thrust. For these settings following the procedure described at APPENDIX 1, the Jacobian obtained is shown in table 2.

Table 2: Jacobian matrix for 7 measurements and 10 parameters

	f_1	f_2	f_3	f_4	f_5	f_6	F_7	f_8	f_9	f_{10}
N_1	-0.68	0.18	0.00	0.06	0.05	0.13	-0.05	0.16	-0.07	0.21
N_2	-0.08	-0.13	0.03	-0.06	-0.18	0.11	-0.08	0.13	0.10	0.00
P_{S3}	-0.32	-0.05	0.33	-0.04	0.04	0.14	-1.23	0.21	0.29	-0.12
T_3	-0.14	-0.24	0.04	-0.12	-0.10	-0.25	-0.30	0.18	0.17	-0.03
P_5	-0.04	-0.01	0.04	-0.01	0.00	0.01	0.00	0.01	0.04	-0.04
T_5	0.07	-0.49	-0.27	-0.16	-0.21	-0.54	0.22	-0.67	-0.02	-0.55
WFB	-0.16	-0.61	-0.05	-0.18	-0.18	-0.46	0.19	-0.57	0.19	-0.68

Before proceeding to selecting parameters we observe that that the elements on the row that is referred to P_5, have very small magnitude in comparison to the elements of the other rows. This means that the measurement P_5 is insensitive to deviations of all considered parameters under estimation and the presence of P_5 on the diagnostic system do not supply us with extra information to be used in the estimation. Inspection of figure 5 shows also that P_5 is not contained simultaneously with the remaining six measurements, for any of the sets with low condition number. Thus another problem appears. If we decide to keep P_5 then we introduce a singularity on the diagnostic system. If we decide to remove it then we should decrease the number of health parameters under estimation from seven to six.

We have applied the method of SVD analysis for health parameters selection for both cases and the projections of the singular vectors in the direction of the greatest Singular Value are given in figure 6. It is very clear that if we take in to account the matrix containing 7 rows (P_5 is included) or the matrix containing 6 rows (P_5 is removed), the results are almost exactly the same, which means that the inclusion of P_5 in the diagnostic system does not offer significant information and for this reason the number of health parameters under estimation must be decreased.

Inspecting figure 6 we can perform a selection for health parameters using the criteria of section 4.1. Placing the projections of singular vectors in descending order with absolute norm we see that the first six projections correspond to the following health parameters: f_8, f_{10}, f_2, f_6, f_7, f_3.

Comparison of the projections of the Singulars Vectors in the
direction of first singular value
Case studied: 1. Use of 7 measurements
Case studied: 2. Use of 6 measurements
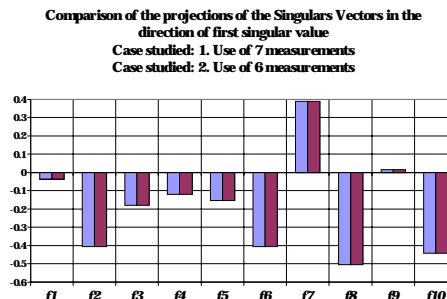
Figure 6: Projections of Singular vectors in the direction of first singular value

We come now to the selection of parameters using Jacobian condition number. Two cases have been examined and results have been derived. First a selection of seven health parameters is performed. Next P_5 has been removed from the set of measurements and calculations for the selection of six health parameters are repeated.

Figure 7 shows the condition number of all square matrices, which can be formed using all possible combinations of 10 health parameters taken 7 at time. Figure 8 give the lowest Condition numbers and corresponding measurement. The resulting combination of health parameters is f_1, f_2, f_5, f_6, f_7, f_9, f_{10}.

Condition Number of Jacobians which are formed using all the possible combinations of 10 health parameters taken 7 at time
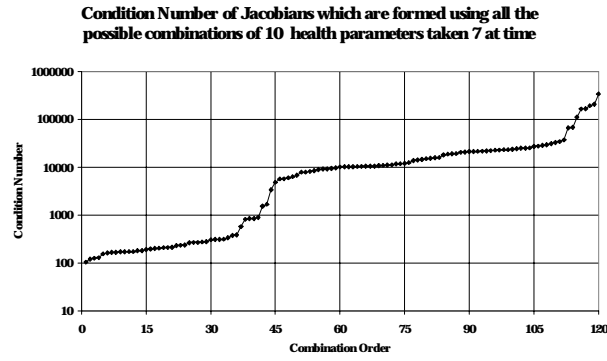
Figure 7: Ascending order of CN for parameters selection. Case of 7 available measurements

	1	2	3	4	5	6	7	8	9	10	11	12	13	14	15
f_1															
f_2															
f_3															
f_4															
f_5															
f_6															
f_7															
f_8															
f_9															
f_{10}															
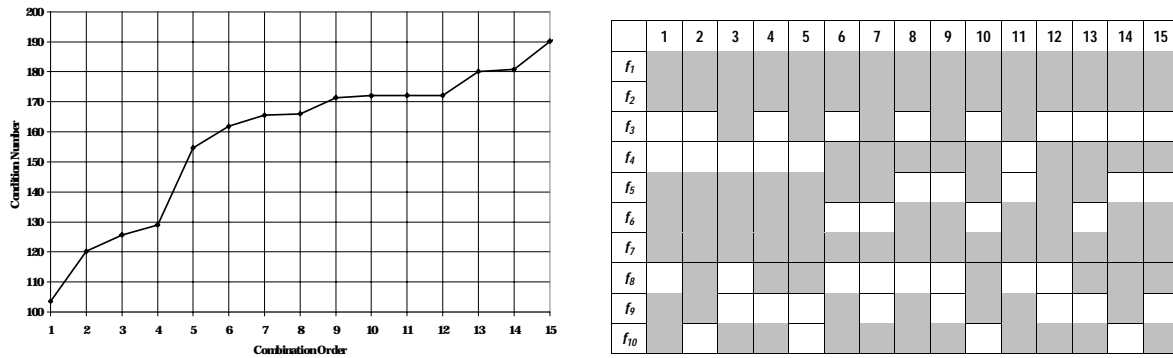
Figure 8: The lowest Condition numbers and corresponding measurement set. Case: 7 measurements and 10 parameters

As discussed above P_5 can be removed from the diagnostic system because is insensitive in the changes of health parameters under estimation. In order to find out the influence that such a decision has on parameters estimation a study for the selection of six parameters has been performed. Figure 9 shows the condition number of square Jacobians formed using all possible combinations of ten health parameters taken six at time. A first observation is that the combinations appearing at the higher positions of the ascending order have condition numbers, which are one order of magnitude lower than the previous case. We can see now that the amelioration of diagnostic system with the removal of $P5$ has an immediate consequence on the condition number of Jacobians. Figure 10 gives the condition numbers for the first fifteen positions and also the actual combinations of parameters. For this studied case the best combination is: f_1, f_5, f_6, f_7, f_9, f_{10}.

The method of Provost has also been applied to the parameters and it was found that with the particular measurement set, the pair of parameters f_2, f_4 have a high degree of correlation.

Condition Number of Jacobians which are formed using all the possible combinations of 10 health parameters taken 6 at time
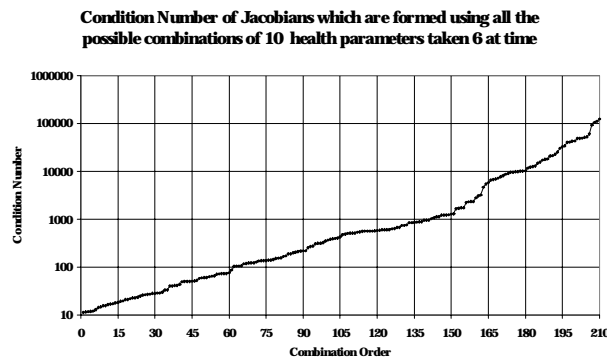
Figure 9: Ascending order of CN for parameters selection. Case of 6 available measurements
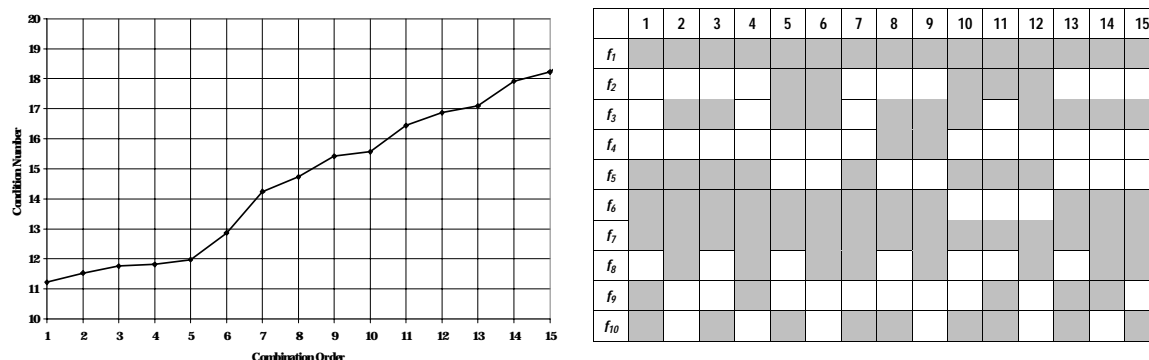
Figure 10: The lowest condition numbers and corresponding measurement set. Case: 6 measurements and 10 parameters

6. CONDITION ASSESSMENT OF A TURBOFAN, FROM TEST CELL DATA

The conclusions drawn from the parameter selection approach have served as a guide for pursuing a diagnostic study on the basis of a number of test reports from test cell runs of TF41 engines. The method of adaptive modeling (Stamatis et al 1990a) has been used.

First issue on the setup of the system is the adaptation of the general model to the performances of the considered engine type. This adaptation is related with the ability of the model to assess the health condition of the engine. When a model is adapted to the performance of a particular engine and a reference state has been established then it is ready to assess the health condition of the engine. The combination of health parameters that is used for adaptation and diagnosis is the sixth one of figure 10 namely f_1, f_2, f_3, f_6, f_7, f_8. We have selected that combination because it contains parameters expressing the full state (flow capacity and efficiency) of two components of the engine namely fan and HPT, which are more inclined to faults.

Test data were available from a "calibration" engine. These data have been used to calibrate the model, namely to produce the values of the health parameters that will be used as reference. For the data coming from this engine the adaptation procedure is performed and the results are given in figure 11. Each one of the runs of this figure corresponds to a different level of thrust.
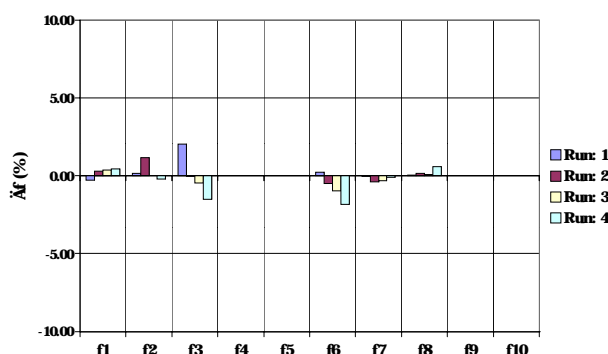
Figure 11: Results of adaptation procedure for the reference engine

Health parameters representing the reference state of TF-41 have very small values. Their values change with thrust level, a fact that is taken in to account in later exploitation of the model. These values are going to be considered as initial ones (reference) for the health parameters under estimation.

After establishing the reference state of TF-41 using the reference engine we have used a series of data coming form tests of different engines in order to see what the range of variation of the different parameters is.

In figure 12 results of applying adaptive modeling are presented. Results are presented for the six health parameters and are given for all examined engines without any classification according to engine or thrust level. For these reasons the results exhibit a large scattering. A close look at results can provide a better insight on the significance of the values produced by adaptive modeling.
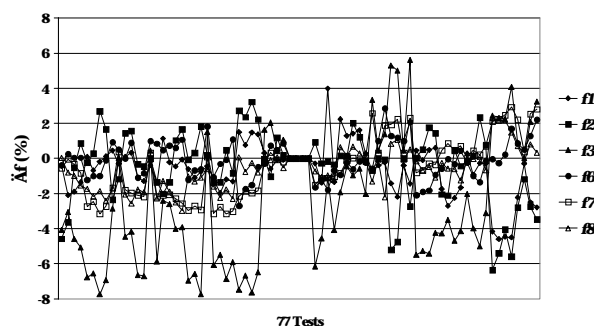
Figure 12: Results of diagnostic procedure from 77 tests

In figure 13 (a) and (b) results for the same engine before and after maintenance are shown. We see that the health parameter f_1, f_2, f_7, f_8 come closer to the reference value after maintenance.

| (a) before | (b) after |
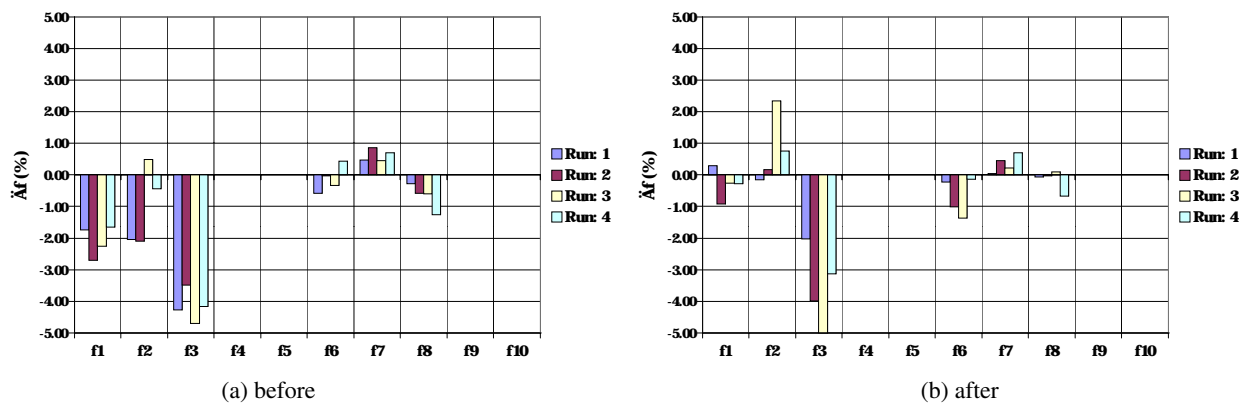
Figure 13: Results of diagnostic procedure before and after maintenance

An important issue, which is related with the handling of an existing fleet, is the degradation of operating engines with time. The health parameters employed by the present method give the possibility to assess the level of deterioration in individual engine components. We will show some indicative results supporting this point, coming from the data sets, which were available. Unfortunately no consistent data sets for one particular engine were available at successive instants in time. Nevertheless, data from tests of engine with different life spans were available. Health parameters from three different engines, each one having a different time operating hours, are shown in figures 14. Although engine-to-engine differences do not permit a strict comparison of values, it is evident that performances deteriorate as the 'age' of the engine increases.
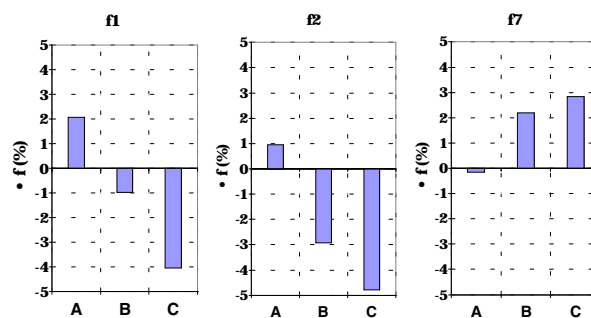
Figure 14: health parameters for three different engines
(A: "New" Engine, B: 1200 hours of operation, C: 5000 hours of operation)

7. CONCLUSIONS

Methods for the optimal selection of measurements and health parameters for diagnostic purposes in aircraft gas turbines have been presented. First, method based on sensitivity analysis and singular values decomposition of the Jacobian, have been used. A method adding significant information was then introduced, based on the condition number of the Jacobian.

The method of indices selection was then applied to the case of a given turbofan, to select a set of parameters that can be estimated, to describe engine condition. These parameters were then evaluated from data sets coming from test cell runs.

It was found that if the overall set of engines is looked at, an apparent scattering of values exists, indicating that each individual engine has to be followed separately. It was shown that the effect of engine overhaul can be assessed using the chosen set and method.

REFERENCES

Doel D., 1992, TEMPER A gas path analysis tool for commercial jet engines ASME 92-GT-315.

Doel D., 1993, An assessment of weighted-least-squares based gas path analysis. ASME 93-GT-119.

Lancaster P., Tismenetsky M., 1985, The theory of matrices. Computer science and applied mathematics. Second edition with applications. San Diego Academic Press.

Press W., Teukolsky S., Vetterling W., Flannery B., 1992, Numerical recipes in FORTRAN 77. The art of scientific computing. Second Edition. Cambridge University Press.

Provost M.J., 1994, The use of optimal estimation techniques in the analysis of gas turbines. Phd Thesis. Cranfield Univercity.

Stamatis A., Mathioudakis K., Papailiou K.D., 1990a, Adaptive simulation of gas turbine performance. Journal of Engineering for Gas Turbines and Power. Vol 112. April 1990. pp 168-176. ASME 89-GT-205.

Stamatis A., Mathioudakis K., Smith M., Papailiou K.D., 1990b, Gas turbine component fault identification by means of adaptive performance modeling. ASME 90-GT-376.

Stamatis A., Mathioudakis K., Berios G., Papailiou K.D., 1991, Jet engine fault detection with discrete operating point gas path analysis. Journal of Propulsion. Vol. 7 No 6. Nov.-Dec. 1991. ISABE 89-7133.

Stamatis A., Mathioudakis K., Papailiou K.D., 1992, Optimal measurement and health index selection for gas turbine performance status and fault diagnosis. Journal of Engineering for Gas Turbines and Power. Vol. 114. April 1992. pp 209-216. ASME 91-GT-294.

Stengel. R.F., 1993, Optimal control and estimation. Dover Publications Inc.

Tsalavoutas A., Pothos S., Mathioudakis K., Stamatis A., 1999, Monitoring the performance of a twin spool ship propulsion turbine by means of adaptive modeling. RTO MP-34: "Gas Turbine Operation and technology for Land, Sea and Air Propulsion and Power Systems". Ottawa, Canada 18-21 October 1999, paper 26.

Urban L.A., 1972, Gas path analysis of commercial engines.

Volponi A., 1994, Sensor error compensation in engine performance diagnostics. ASME 94-GT-58.

APPENDIX 1: Linear and Non-Linear approaches of parameters estimation

Estimation of health parameters can be achieved using the inverse algorithm of F, eq (1).

$$f = F^{-1}(Y) \qquad (A1)$$

Since in general faults are expressed with small changes of health parameters from the reference state, a simplification of above presented algorithm can be performed. When all considered health parameters are in the state of reference engine response will be:

$$Y^{ref} = F(f^{ref}) \qquad (A2)$$

When a fault occurs some health parameters modify their values from reference with the following form.

$$f_j = f_j^{ref} + \delta f_j \qquad (A3)$$

Where δf_j is a small quantity (magnitude in the range 0.01 to 0.03). The response of the engine to these changes will be:

$$Y = F(f) \qquad (A4)$$

Since the changes δf_j are very small, using the Taylor's theorem for each Y_i we can write:

$$Y_i = Y_i^{ref} + \sum_{j=1}^{n} \frac{\partial F_i}{\partial f_j} \cdot \left(f_j - f_j^{ref} \right) + H.O.T. \qquad (A5)$$

Where H.O.T. are the higher order terms that have a very small influence on the sum because the change $f_j - f_j^{ref}$ is considered very small. We can thus write:

$$Y_i - Y_i^{ref} = \sum_{j=1}^{n} \frac{\partial F_i}{\partial f_j} \cdot \left(f_j - f_j^{ref} \right) \qquad (A6)$$

and taking the percentage changes we can have:

$$\frac{Y_i - Y_i^{ref}}{Y_i^{ref}} = \sum_{j=1}^{n} \frac{\partial F_i}{\partial f_j} \cdot \frac{f_j^{ref}}{Y_i^{ref}} \cdot \frac{f_j - f_j^{ref}}{f_j^{ref}} \qquad (A7)$$

or

$$\Delta Y_i = \sum_{j=1}^{n} a_{ij} \cdot \Delta f_j \qquad (A8)$$

where $a_{ij} = \dfrac{\partial F_i}{\partial f_j} \cdot \dfrac{f_j^{ref}}{Y_i^{ref}} \qquad (A9)$

This relation is written in a matrix form as eq. (6) of the main text.

Under these conditions the non-linear model can be replaced by a linear relation between deviations on measurements and deviation on health parameters. Matrix $\mathbf{J}$ (Jacobian) contains the elements a_{ij} and can be created using a performance model. Each element is derived by the following formula:

$$a_{ij} \cong \frac{\dfrac{Y_i^j - Y_i^{ref}}{Y_i^{ref}}}{\dfrac{f_j - f_j^{ref}}{f_j^{ref}}} = \frac{\Delta Y_i^j}{\Delta f_j} \qquad (A10), \text{ where: } Y_i^{ref} = F_i(f^{ref}) \text{ and } Y_i^j = F_i(f_1^{ref}, f_2^{ref}, ..., f_j, ..., f_n^{ref})$$

or in symbolic form:

$$Y^j = F(f^{ref} + e_k \cdot \delta f_j) \qquad (A11)$$

where δf_j small quantity and

$$\begin{cases} e_k = 0, \text{ for } k \neq j \\ e_k = 1, \text{ for } k = j \end{cases} \qquad (A12)$$

APPENDIX 2: Condition number of matrices.

A norm of matrix condition is the condition number. In the open literature there are several definitions about the condition number of a matrix. A very convenient definition for the purpose of the present task is the one using the singular values of the matrix under consideration (Press et al 1992). We have based our effort to that definition since it is very easy and quick to be performed and also it is capable to demonstrate the level of linear independence between the rows or the columns of the matrix. The method consists in applying singular values decomposition of the matrix, using the well-known theorem in the following form (Lancaster et al 1985):

$$J = U \cdot W \cdot V^T \qquad (A13)$$

Where W is diagonal containing the singular values of matrix J and V is the matrix whose columns contain the singular vectors of J. Each column of matrix V can be considered as a separate vector that corresponds to each derived singular value. The coordinates of these vectors are referred to each health parameter.

The condition number of matrix J is defined as the ratio of greatest singular value to the smallest.

$$CN = \frac{max\{W_j\}}{min\{W_j\}} \qquad (A14)$$

It is known that well-conditioned matrices will have small condition numbers. As condition number increases, matrix condition deteriorates.

Paper 9: Discussion

<u>Question from Dr R Szczepanik – Instytut Techniczny Wojsk Lotniczych, Poland</u>

According to your experience and presented methodology, which parameters can be defined as the most effective and valuable for fault diagnostics and health monitoring purposes?

<u>Presenter's Reply</u>

For the particular engine we analysed (TF41), the most effective parameters are the ones given in the paper. For another engine type, the methodology would have to be applied in order to generate a specific answer.

<u>Question from W P J Visser – NLR, Netherlands</u>

Is the methodology equally applicable to non-mixing turbofans, and is N1 suitable, instead of EPR, as a thrust setting parameter for the reference operating point?

<u>Presenter's Reply</u>

The methodology is applicable to any gas turbine engine, provided there is a performance model available; so a non-mixing turbofan can also be analysed.

For the particular engine we considered, we found that EPR has an advantage over N1 as a thrust setting parameter, in that its correlation with thrust is influenced less by changes in engine condition caused by faults and deterioration.

<u>Question from H G Cook</u>

You have discussed the optimisation of measurements and parameters but, traditionally, some of these are not measured on the installed engine. Can current/traditional measurements be optimised to the same effectiveness or is there a case, possibly in life cycle cost, to move to the use of new parameters/measurements?

<u>Presenter's Reply</u>

The measurements for the test case presented in the paper come from a test cell and are more comprehensive than those available on an installed engine. The procedure presented, however, is generic and can be applied to the measurement set of an installed engine. Effectiveness will be reduced in the case of fewer measurements. The optimisation can, nevertheless, provide new parameters that will improve effectiveness over current practice.

This page has been deliberately left blank

_____

Page intentionnellement blanche

Application of Multiple Handle Gas Path Analysis
on a Twin Spool Turbofan Engine

Eftychios Kleinakis
Hellenic Air Force Applied Technology and Research Centre (KETA)
Ano Glyfada, 16501, Athens, Greece

Petros Kotsiopoulos
Hellenic Air Force Academy
Dekeleia Attikis, Athens, Greece

Pericles Pilidis
School of Mechanical Engineering, Cranfield University
Cranfield, Bedfordshire MK43 0AL, U.K.

ABSTRACT

In this paper the development of multiple handle gas path analysis, an analytical approach that has two advantages over linear gas path analysis is described. Firstly, it allows all instruments to be used for diagnostics purposes, without having to use one to determine the baseline. The other advantage is that diagnostics can be crosschecked against one another to allow greater faith in the result.

A conclusion that can be drawn regarding multiple handle gas path analysis is that it appears to be a promising technique. For some faults it appears to give better diagnostics than linear gas path analysis, without going to the complexity of non-linear gas path analysis. The latter is however more accurate.

The analysis of a high performance twin spool turbofan engine, gave rise to a very useful diagnostic. Several fault sets were analysed and several instrumentation sets were examined, ranging from the minimum available in the cockpit to a much more comprehensive one.

NOMENCLATURE

DOD	domestic object damage	LPT	low pressure turbine
FOD	foreign object damage	HPT	high pressure turbine
GPA	gas path analysis	MH GPA	multiple handle GPA
HPC	high pressure compressor	HAF	Hellenic Air Force
LPC	low pressure compressor	PCN	rotational speed
W	air mass flow (flow capacity)	HOT	high order terms
n_c	compressor isentropic efficiency		
n_T	turbine isentropic efficiency		
n_{CC}	combustion efficiency		
RMS	root mean square		
TET	turbine entry temperature		

INTRODUCTION

Faults like fouling, erosion, corrosion, worn seals, excessive tip clearances and damage from various objects entering the engine (FOD-DOD) affect the performance of each of the gas path components and results in performance deterioration. The need for identifying the effects of faults in the gas turbines led to the study of gas path analysis (GPA) methods, which would give the operator a sign of what's happening inside the engine (Volponi, 1982).

The performance of the gas path components is characterized by parameters like flow capacity and efficiency, which are called 'independent parameters' and degrade because of the effects of the physical faults. These parameters although fundamental in nature are not readily or practically measurable. However changes in independent parameters produce deviations in parameters such as pressures, temperatures, fuel flow and rotational speed throughout the engine, these can be measured; they are called 'dependent parameters' and any difference from their baseline values can be used for the determination and detection of the independent parameters.

Urban conceived a technique (1969, 1974) to assess the independent engine parameter (flow capacity, efficiency) deviation by using the relationship between them and the dependent parameters (pressures, temperatures) based on customized baseline data. Later, more studies were published that focused on either civil (Doel 1994) or military aero-engines (Zedda and Singh, 1996).

The technique of gas path analysis outlined above was based on the assumption of a linear relationship between the dependent and independent parameters. Recognising that the larger faults may invalidate this assumption, complex non-linear gas path analysis techniques were developed in PYTHIA (Escher 1995). Furthermore a major uncertainty is introduced by measurement error in the diagnostics capability of GPA. A large amount of effort is being devoted to this problem (Zedda and Singh, 1999).

The objective of the research described here was the performance analysis of the engine model and the investigation of the fault detection capability using GPA methods. Moreover a new concept, multiple handle gas path analysis (MH GPA), is examined. It is based on the selection of more than one handle and the results are compared to those obtained using the "traditional" method using one handle. The interest in this method arises from the simplicity of the technique, which hopefully addresses the drawbacks of linear GPA without going to the complexity of non-linear one.

For the purposes of the present study the engine selected is a high performance twin-spool turbofan engine, as shown in figure 1.
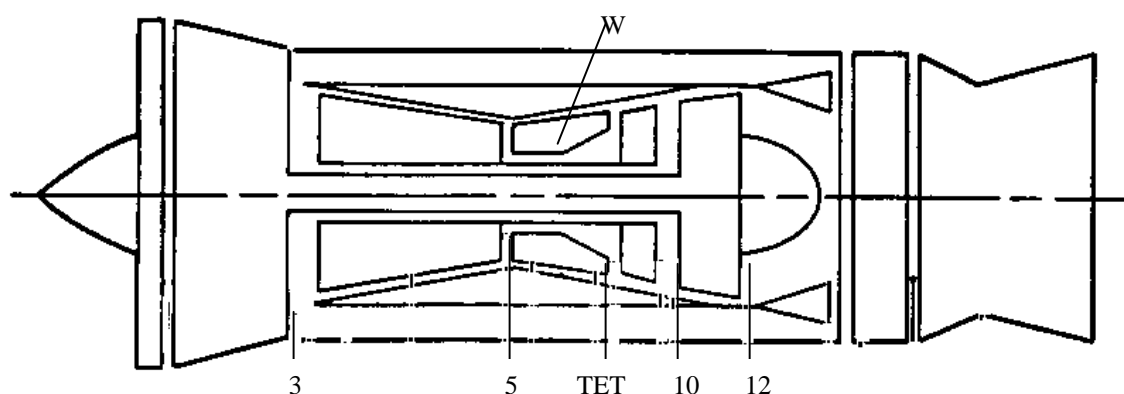
Figure 1: Engine Schematic with station numbers

The standard engine was simulated using the TURBOMATCH Scheme (Palmer 1983), a code developed at Cranfield University to facilitate design point and off-design performance calculations for gas turbine engines using a digital computer. After obtaining the results, the PYTHIA Scheme was used to assess the analysis of the deterioration on the gas path components.

These facilities allowed a meaningful comparison between linear GPA, multiple handle GPA and non-linear GPA. Given that the focus is on the thermodynamic analysis technique, the instrumentation error analysis is not described here. It is assumed that the interested user would apply suitable techniques, (Zedda and Singh 1996) to allow for this very important factor.

MULTIPLE HANDLE GAS PATH ANALYSIS

Principles of GPA

The relationship between dependent and independent parameters can be expressed by:

$$Z_e = H_e \cdot X_e$$

where Ze is the column matrix of monitored dependent parameters deltas, He is the Influence Coefficient Matrix (ICM) and Xe is the column matrix of the independent parameters (gas path component characteristics) deltas. Inverting the ICM, a new matrix the Fault Coefficient Matrix (FCM) is obtained which gives a new relationship between the independent and dependent parameters.

Each row of the ICM is a differential equation wherein the net change in the dependent variable corresponding to that row is the arithmetic sum of the product of the coefficients times the change in the variable specified at the head of each column.

The non-linear concept (Echer, 1995) tries to solve the non-linear relationship between dependent and independent parameters with an iterative method such as Newton – Raphson method. Using this method, the basic assumption is that the noise errors as well as instrumentation errors are not taken into account. The method uses the mathematical model that is described in the following paragraph.

Assuming that $\underline{x}$ stands for the independent variable vector matrix and $\underline{y}$ stands for the dependent one, the relationship between them may be represented as

$$F(\underline{x}) = \underline{y}$$

Then for small changes in the independent variable vector matrix $\underline{x}$

$$F(\underline{x} + \delta\underline{x}) = \underline{y} + \delta\underline{y} \quad \text{or} \quad F(\underline{x} + \delta\underline{x}) = F(\underline{x}) + \delta\underline{y} \quad (1)$$

Using the Taylor series expansion of $\delta\underline{x}$ about $\underline{x}$

$$g(\alpha + \beta) = g(a) + \beta \cdot g'(a) + \frac{\beta^2}{2!} \cdot g''(a) + \dots$$

In order to express the first derivative in the Taylor series expansion of the matrix function F(x) times the small change in the independent variable δ$\underline{x}$, the following Jacobean matrix notation is used as follows:

$$J \equiv \begin{pmatrix} \frac{\partial f_1(\underline{x})}{\partial x_1} & \frac{\partial f_1(\underline{x})}{\partial x_2} & \cdots & \frac{\partial f_1(\underline{x})}{\partial x_n} \\ \frac{\partial f_2(\underline{x})}{\partial x_1} & \frac{\partial f_2(\underline{x})}{\partial x_2} & & \frac{\partial f_2(\underline{x})}{\partial x_n} \\ & \vdots & & \\ \frac{\partial f_m(\underline{x})}{\partial x_1} & \frac{\partial f_m(\underline{x})}{\partial x_2} & & \frac{\partial f_m(\underline{x})}{\partial x_n} \end{pmatrix} \quad \text{and} \quad \delta\underline{x} = \begin{pmatrix} \delta x_1 \\ \delta x_2 \\ \vdots \\ \delta x_n \end{pmatrix}$$

Given that $\underline{y} = \begin{pmatrix} y_1 \\ y_2 \\ \vdots \\ y_n \end{pmatrix}$ $\quad \begin{aligned} y_1 &= f_1(\underline{x}) \\ y_2 &= f_2(\underline{x}) \\ &\vdots \\ y_n &= f_n(\underline{x}) \end{aligned}$ where $\underline{x} = \begin{pmatrix} x_1 \\ x_2 \\ \vdots \\ x_n \end{pmatrix}$ and

Therefore the Taylor series expansion can be expressed as follows:

$$F(\underline{x} + \delta\underline{x}) = F(\underline{x}) + J \cdot \delta\underline{x} + HOT$$

since the changes in x are expected to be small and therefore we may make the assumption that the HOT (High Order Terms) are negligible, that is to say, the relationship is considered linear, the above equation is expressed as follows:

$$F(\underline{x} + \delta\underline{x}) = F(\underline{x}) + J \cdot \delta\underline{x} \qquad (2)$$

From equation (1) and (2), by rearranging

$$F(\underline{x} + \delta\underline{x}) - F(\underline{x}) = \delta\underline{y} \Rightarrow \delta\underline{y} = J \cdot \delta\underline{x}$$

$$\Rightarrow J^{-1} \cdot \delta\underline{y} = \delta\underline{x} \qquad\qquad (3)$$

The corrections $\delta\underline{x}$ are then added to the solution vector

$$x_{new} = x_{old} + \delta\underline{x}$$

The above process is iterated to convergence. For each linear GPA calculation an appropriate baseline is required. In the first iteration the actual measured baseline is used. The second iteration uses a calculate baseline that is derived by implanting faults that are detected in the iteration. The same applies to the following iterations where the implanted faults are taken from the previous iteration.

Equation (3) gives the relationship between the independent and dependent parameters. In fact any change in the depended parameter can be related with a change in the independent parameter using the inverse matrix of J, which is referred to as "Fault Coefficient Matrix" (FCM). The J matrix is referred to as "Influence Coefficient Matrix" (ICM). The primary objective of GPA technique is the calculation of the ICM so that by obtaining the FCM after inverting the former, the detection of the implanted faults (independent parameters) becomes feasible.

The concept of MH GPA

An important issue in the GPA technique is the selection of the appropriate baseline to establish the reference conditions with which to compare the measured parameters. The applicable baseline is called the handle, which in this case, the parameter that establishes the matching conditions of the engine. Once selected, it is normally held constant.

The accuracy of GPA is normally tested by implanting a fault, in the engine or model, and using the diagnostic technique to detect it. In linear GPA it is assumed that a change in the independent parameter results in an analogous change of the dependent parameter. In reality gas turbine engines are highly non-linear systems, so the assumption of linear behaviour applies only to small departures (deltas) from the baseline.

Given the unsuitability of linear GPA and the complexity of non-linear GPA, the concept of multiple handle GPA is examined here. The philosophy of the method is to employ the basic linear GPA technique, but to apply it several times for each analysis. So the clean engine baseline is established and then the degraded engine is modelled over a relatively narrow operating range. This will, probably, ensure a uniform influence of each fault.

Then the analysis is carried out several times, each time matching the engine with a different operating parameter (or handle). So, for example, the analysis is carried out once matching the engine on rotational speed, a second time matching the engine on fuel flow, a third time matching the engine on turbine pressure ratio. This analysis can be carried out as many times as pertinent instruments are available. The results can then be collated and a comprehensive analysis carried out.

It is worth noting that once the handle has been selected, it is excluded from the instrumentation set since the deviation of its measurement is by definition zero. The instrumentation set, then, includes the

rest of the instruments so that the number of them must be at least equal to the number of implanted faults.

This method presents several advantages. Firstly it is based on linear assumptions. It also extracts as much information as possible from the instrumentation, because, as explained above, when one measured item is used as handle, some diagnostic capability is lost. The most important question is if it can match the results of non-linear GPA, which is recognised as a superior technique to linear GPA.

CASES ANALYSED

When carrying out gas path analysis, the choice of baseline parameter and the instrumentation available will determine the faults that can be successfully diagnosed. Naturally the need to use a measurement as baseline limits the diagnostics that can be carried out. Multiple handle gas path analysis allows the use of all instruments for diagnostic purposes because different baselines are used in each prediction.

One of he objective of the investigation described here is to examine the viability of multiple gas path analysis in lean and rich instrumentation sets and to compare it with linear and nonlinear gas path analysis.

Selection of the faults

Much work has been published about performance degradation on gas turbines, however, the magnitude of the applied deterioration in most cases is arbitrary or it is based on published experimental results, which are been used as background (Aker 1989, Seddigh 1991, Lakshminarasimha, 1994) . This happens mainly because the degree of deterioration, the rating and effect of physical faults on engine performance depend upon the design, the environment condition in which the engine operates and the quality of the applied maintenance on the plant. It is well understood that many non-measurable factors have to be taken into account for the calculation of engine characteristics degradation.

Due to the lack of specific magnitudes for the faults, a general guideline that was presented by Echer (1995) was used in which the physical faults are been expressed as independent parameter changes. The selected magnitudes of the implanted faults are given in Table 1.

	W_c	n_c	W_T	n_T	n_{CC}
Compressor fouling	-5%	-2.5%	-	-	-
Turbine fouling	-	-	-5%	-2.5%	-
Poor combustion	-	-	-	-	-2.5%
Turbine erosion	-	-	+3%	-1%	-

Table 1: Magnitudes of the implanted faults

Selected Instrumentation

The instrumentation selected has been divided into 7 Sets as it is shown in table 2. It varies from a lean to a rich instrumentation set.

	A	B	C	D	E	F	G
P_3			x		x		x
T_3			x		x		x
P_5			x			x	x
T_5			x			x	x
W_f	x	x					x
P_{10}				x		x	x
T_{10}				x		x	x
P_{12}		x		x	x		x
T_{12}	x	x		x	x		x
PCN	x	x					x

Table 2: Instrumentation sets

Set A: Consists of the standard instrumentation provided in a typical aircraft's cockpit.

Set B: Includes the instruments of set A plus the measurement of the pressure at the turbine exit (P_{12}). The main reason for selecting this instrument is that the pressure at the exit of the turbine would be less difficult to implement because the temperature at that position (T_{12}) is already available.

Set C: Includes the instrumentation for the measurement of the parameters in the compressor section. The measured parameters are LPC exit pressure and temperature (T_3, P_3) and HPC exit pressure and temperature (T_5, P_5).

Set D: Includes the instrumentation for the measurement of the parameters in the turbine section. The measured parameters are HPT exit pressure and temperature (T_{10}, P_{10}) and LPT exit pressure and temperature (T_{12}, P_{12}).

Set E: Includes the instrumentation for the measurement of the parameters in the low pressure section. The measured parameters are LPC exit pressure and temperature (T_3, P_3) and LPT exit pressure and temperature (T_{12}, P_{12}).

Set F: Includes the instrumentation for the measurement of the parameters in the high pressure section. The measured parameters are HPC exit pressure and temperature (T_5, P_5) and HPT exit pressure and temperature (T_{10}, P_{10}).

Set G: Consists of all measurement parameters in the engine.

Fault sets

PYTHIA simulates engine's deterioration using ten parameters;

- LPC mass flow and efficiency (W_{LPC} , n_{LPC})
- HPC mass flow and efficiency (W_{HPC}, n_{HPC})
- Combustion chamber efficiency (n_{CC})
- LPT mass flow and efficiency (W_{LPT}, n_{LPT})
- HPT mass flow and efficiency (W_{HPT}, n_{HPT})
- Pressure drop in the exhaust nozzle (ΔP_n)

The pressure drop in the exhaust nozzle is not used for this study because the main interest for gas path analysis in this study is the gas turbine itself and not the components of the Quick Engine Change kit (QEC kit). Therefore the maximum number of independent parameters is nine.

The full set of implanted faults, from the single ones up to maximum number is shown in table 3, which consists of 30 approaches. Because the number of instruments has to be at least equal to number of faults the whole set of 30 approaches is applied only to instrumentation set G. For the rest of them,

the number of approaches is smaller and depends upon the number of monitored parameters (instruments).

Fault	1	2	3	4	5	6	7	8	9	10	11	12	13	14	15
W_{LPC}	x									x				x	
n_{LPC}		x								x				x	
W_{HPC}			x								x			x	
n_{HPC}				x							x			x	
n_{CC}					x										
W_{LPT}						x						x			x
n_{LPT}							x					x			x
W_{HPT}								x					x		x
n_{HPT}									x				x		x

Fault	16	17	18	19	20	21	22	23	24	25	26	27	28	29	30
W_{LPC}	x					x		x		x		x	x	x	x
n_{LPC}	x					x		x		x		x	x	x	x
W_{HPC}		x			x		x		x		x		x	x	x
n_{HPC}		x			x		x		x		x		x	x	x
n_{CC}	x	x	x	x					x	x	x	x			x
W_{LPT}			x			x	x			x	x		x	x	x
n_{LPT}			x			x	x			x	x		x	x	x
W_{HPT}				x	x			x	x			x	x		x
n_{HPT}				x	x			x	x			x	x		x

Table 3: Fault sets

Faults 1 to 9 represent single faults including mass flows and efficiencies for the gas path components. Reduction in compressor isentropic efficiency, represents FOD or blade tip rubs. Similarly, decreased turbine efficiency is the result of FOD, blade tip rubbing or worn seals inside the turbine. For the combustion chamber, drop in combustion efficiency is caused by poor combustion, carbon deposits in the chamber and goggled fuel nozzles.

Faults 10 to 13 are double faults and simulate compressor and turbine fouling. The faults are included within all instrumentation sets.

Faults 16 to 19 are triple faults, which are similar to double faults and include the combustion chamber efficiency as the third fault. They represent fouling in combination with combustion efficiency degradation. The prescribed faults are applied for detection by all instrumentation sets.

Faults 14, 15, 20 to 23 comprise four simultaneous faults as a combination of LPC or HPC fouling, with LPT or HPT fouling.

Faults 24 to 27 consist of 5 faults. In fact, they are similar to the faults in the above paragraph with the addition of combustion chamber deterioration. Detection of these faults will not be attempted with the instrumentation sets A, B, C, D, E and F.

Faults 28 to 30 include LPC, HPC fouling and LPT or HPT fouling. Detection of these faults will be attempted only with the instrumentation set G.

For the purposes of the present study, the name "Case" will be given to the combination of the instrument set with the fault set. For example instrument set G with the 30 approaches make up the "Case G".

LINEAR & NON LINEAR GPA

Obtaining the results from GPA method, the Root Mean Square (RMS) error is deployed for the evaluation of the technique. The RMS error is defined as follows:

$$RMS = \sqrt{\frac{\sum\limits_{i=1}^{n}(\delta x_{implanted} - \delta x_{detected})^2}{n}}$$

Where n is the number of independent parameters measured, $\delta x_{implanted}$ is the implanted fault and $\delta x_{detected}$ stands for the observed fault or detected one from the diagnostics technique.

Approach 5. Combustion chamber efficiency deterioration is well detected using any one of the instrumentation set since all the measurements are below 0.05 for the linear GPA. Therefore there is no need for calculating the non linear RMS error.
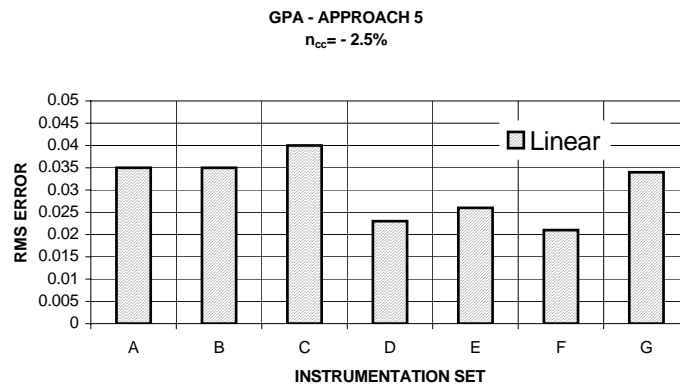
Figure 2: Approach 5, Linear and Non Linear Error

PYTHIA gave great results for all Cases and especially for Set D (figure 2) which contains the turbine area instrumentation. In addition, although Set G includes all instruments, there is no benefit using it for the detection of the combustion fault.

Approach 12. Turbine fouling is represented by a 5% reduction in mass flow and a 2.5% reduction in efficiency. Accurate detection is achieved using any one of the Sets, since all RMS errors are well below 2.0 (figure 3). Case D seems to give better accuracy whilst Case B gives the worst one but the error is still below 2.0. The primary reason for the increased inaccuracy of Case D is the location of the instruments; All of them are installed in the turbine section therefore the detection of turbine faults is accurate.

GPA - APPROACH 12

$W_{LPT} = -5\%, n_{LPT} = -2.5\%$
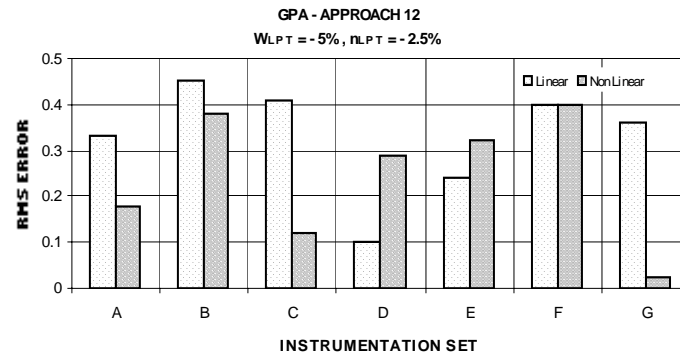
Figure 3: Approach 12, Linear and Non Linear Error

Approach 15. The implanted faults represent fouling of the same magnitude in both turbines. Sets A and B are not diagnosed because the number of implanted faults is higher than the number of instruments (figure 4). It should be noticed that using C, E and F instrumentation sets, the linear error is greater than 2.0, and therefore it is unacceptable. On the other hand, Sets D and G gave the best acceptable results. The latter is obvious since Set D includes instruments from the faulty region and Set G includes all the available instruments.

GPA - APPROACH 15

LPT & HPT FOULING
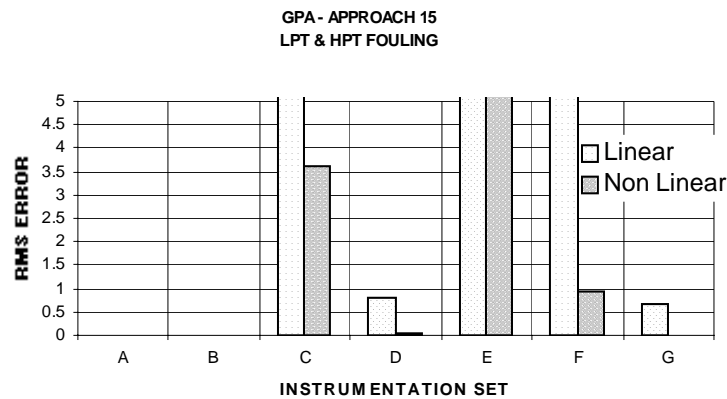
Figure 4: Approach 15, Linear and Non Linear Error

Selected Approaches for MH GPA

As it was shown in the previous paragraphs, most of the implanted single faults were detected successfully using both linear and non-linear GPA. In contrast, less accurate was the detection of the multiple faults like combined LPT and HPT fouling.

The selection of the fault sets and instrumentation for the implementation of the MH GPA is based on the above conclusion. Fault sets representing compressor or turbine fouling are being studied. The selected instrumentation sets are taken from Case G with ten instruments providing full instrumentation for the engine. Additionally, for the evaluation of the new technique, additional approaches have been selected from Case G involving single faults.

For each selected approach employing 10 instruments (as it happens in Case G) the total runs in PYTHIA are 20 (10 for linear and 10 for non-linear). Obviously the number of available approaches, which have been studied with the previous technique, increases under the concept of MH GPA. For

that reason the number of the selected approaches under study is limited. The selected fault sets and instrumentation is given below

Appr	5	6	8	9	10	12	13
P_3	x	x	x	x	x	x	x
T_3	x	x	x	x	x	x	x
P_5	x	x	x	x	x	x	x
T_5	x	x	x	x	x	x	x
W_f	x	x	x	x	x	x	x
P_{10}	x	x	x	x	x	x	x
T_{10}	x	x	x	x	x	x	x
P_{12}	x	x	x	x	x	x	x
T_{12}	x	x	x	x	x	x	x
PCN	x	x	x	x	x	x	x
W_{LPC}					x		
n_{LPC}					x		
W_{HPC}							
n_{HPC}							
n_{CC}	x						
W_{LPT}		x				x	
n_{LPT}						x	
W_{HPT}			x				x
n_{HPT}				x			x

Table 4: Selected approaches from Case G

Results for MH GPA

After the study of each approach, it is important to determine the parameter, which gives the best diagnostic when it is used as the engine's handle. An indication is obtained of the most appropriate handle by calculating the error resulting from each handle for all the approaches. Using the RMS error as a statistical calculation tool, the error of each approach for the same handle is determined (figure 5).

The RMS error for each handle has been calculated for all approaches of Case G that have been studied with the MH GPA method. That is to say, the RMS error for the PCN is calculated by the respective RMS errors, which are given by approaches 5, 6, 8, 9, 10 and 13. The comparison between the different handles, including the TET, which was used in the previous sections, highlights the following interesting points:

- All the handles used in MH GPA method give worse accuracy than the TET, except T_5 and P_3.

- The best accuracy is achieved when P_3 is used as the engine's handle.

By the same way, the detection accuracy that is provided by multiple handles for each approach would be an indication of how effective the technique of MH GPA is, as a diagnostic tool. A high RMS also gives an interesting message. It means that the diagnostics do not agree, therefore the instrumentation set is unsuitable for detecting the faults sought.

Using more than one handle for each approach, the user can crosscheck the results. The combined results would be more credible than the single ones in terms of reliability. Using only one parameter as a handle, the risk of failure of the instrument measuring it is a real possibility. The handle is one of the dependent parameters and operates under the same "laws" as the rest of instruments do. Wear and failures make their presence felt through the operational life of the engine and its systems.

MH GPA
RMS ERROR PER HANDLE
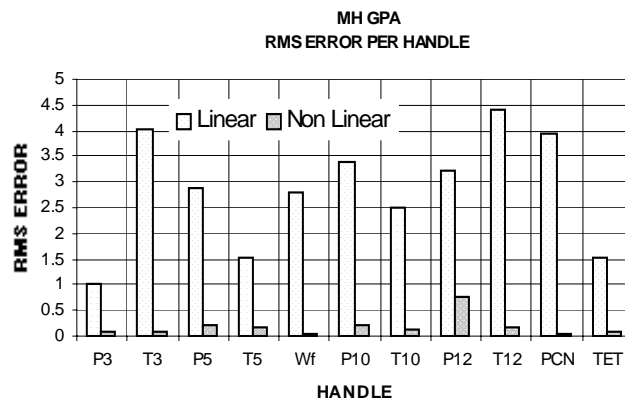
Figure 5: RMS Error for each parameter that serves as the engine's
handle for Instrumentation Set (Case) G

In these cases, the baseline would not be the same for all the measurements and therefore the detection accuracy would be poor. The measured parameter deviations would assist the detection of the implanted faults, which, in these circumstances, be based on inaccurate baseline data. For example, using only TET as a handle the risk of failure is higher than using TET and T_{10} in combination in a MH GPA method. Thus many combinations of different handles would give more confidence and a measure of redundancy.

MH GPA vs TET
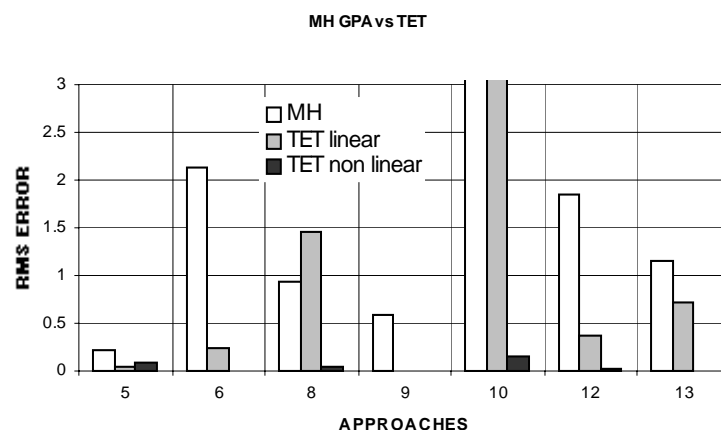
Figure 6: Comparison between multiple handle GPA
and single-handle GPA for selected approaches

Using traditional GPA with the TET as the engine's handle, the results shown in figure 6 have been obtained. Obviously for approach 8, MH GPA gave better results than the traditional GPA with TET as the handle. Instead, for the rest of them, although MH GPA accurately detected the faults (except for approach 10) the error is higher than the one from the traditional GPA. Nevertheless, it seems that using the MH GPA there are some benefits especially when the approach under examination includes multiple faults (approaches 10, 12 and 13).

CONCLUSIONS

The application of GPA methods for fault detection on a single spool low bypass turbofan engine revealed the following:

(1). Non Linear Gas Path Analysis was able to detect the implanted faults more accurately than linear GPA.

(2). The optimum detection capability is achieved when the instruments are installed in the region where the fault occurs. Detecting compressor faults accurately presumes that the utilized

instrumentation is located inside the compressor section. Similarly, instrumentation that includes instruments in the hot section gives better results in detecting combustor and turbine degradation.

(3). Hot section degradation (i.e poor combustion) is well detectable using any one of the available instrumentation sets.

(4). Although set G involves full instrumentation, there is no benefit of using it for the detection of the single faults (changes in only one dependent parameter). In contrast, the accuracy is better when the deterioration is due to combined faults in the compressor and the hot section of the engine.

(5). The utilisation of P_{12} as instrument gives better results for the detection of multiple faults. In contrast, the accuracy becomes poor when the above instrument is involved for the detection of single faults.

Multiple Handle GPA (MH GPA) is a new technique which is based on the selection of multiple handles. The selection of the handle is related to the capability of accurately using it as the baseline's controlling parameter. The use of multiple handles on the engine model revealed the following interesting points:

(1). The use of other than the TET handle may improve the detection accuracy of linear GPA. Best results are obtained when P_3 serves as the engine's handle. In contrast the accuracy of the method is poor when the handle is T_{12}. This outcome is interesting because T_{12} is already measured.

(2). Although the detection capability is improved, the diagnostic message remains the same. Careful study of figure 6 shows that approaches 5 and 9 are detectable with better accuracy than approaches 10 or 13 for both methods.

REFERENCES

Aker, G.F., Saravanamuttoo H.I.H,'Predicting Gas Turbine Performance Degradation Due to Compressor Fouling Using Computer Simulation Techniques', ASME 88-GT-206

Doel, D.L., 'TEMPER4: Gas Path Analysis Tool for Commercial Jet Engines', ASME 92-GT-315, Transactions of the ASME, Journal of Engineering for Gas Turbines and Power. Vol 116, No1 January 1994

Escher, P.C., 1995, PYTHIA: An Object Oriented Gas Path Analysis Computer Program for General Applications, PhD Thesis, Cranfield University.

Kleinakis, E., 1999, Application of Gas Path Analysis on a Military Turbofan Engine, MSc Thesis, Cranfield University.

Lakshminarasimha, A.N., Boyce, M.P., Mehel-Homji, C. B., 'Modeling and Analysis of Gas Turbine Performance Deterioration'. Transactions of ASME Vol 116, January 1994.

Palmer, J.R., 1983, "The Turbomatch Scheme for Aero/Industrial Gas Turbine Engine Design Point/Off Design Performance Calculation". Cranfield University, School of Mechanical Engineering.

Paschos, D.I, 1994, Turbojet Engines Performance Analysis and Deterioration Modeling, Cranfield University.

Seddigh, F., Saravanamuttoo H.I.H, 'A proposed Method for Assessing the Susceptibility of Axial Compressors to Fouling' Journal of Gas Turbines and Power, vol 113, October 1991

Urban, L.A., 1969, Gas Turbine Engine Parameter Interrelationships, 2nd edition, HS UAC, Windsor Locks, CT

Urban, L.A., 1972, Gas Path Analysis Applied to Turbine Engine Condition Monitoring, AIAAISAE 8th Joint Propulsion Specialist Conference, December 1972, AIAA paper 72-1082

Urban, L.A., 1974, Parameter Selection for Multiple Fault Diagnostics of Gas Turbine Engines, ASME Paper 74-GT-62

Volponi, A.J. 1982 'Gas Path Analysis: An Approach to Engine Diagnostics' 35th Symposium Mechanical Failures Prevention Group, 20-22 April 1982, Gaitherburg, MD, USA

Zedda, M., Singh, R., 'Gas Turbine Engine and Sensor Diagnostics.' IS10/UNK010, XIV International Symposium on Air-Breathing Engines (ISABE), 5-10 Sept 1999, Florence, Italy

Zedda, M., Singh, R., 'Fault Diagnosis of a Turbofan Engine using Neural Networks: a quantitative approach', AIAA 98-3062, AIAA, SAE, ASME, ASEE 34 Joint Propulsion Conference and Exhibit, July 1996, Cleveland, Ohio, USA.

Advanced Engine Monitoring and Diagnosis Systems: Actual System for the EJ200 Engine of the EuroFighter 2000 Aircraft and Future Trends

Thomas Zoller
MTU Aero Engines GmbH
Dept.: TKRS
Dachauer Straße 665
80976 Munich, Germany
Thomas.Zoller@muc.mtu.de

Table of Contents

1   Introduction

The EJ200 engine for the EuroFighter 2000 military aircraft will, like other modern military jet engines, operate in usage scenarios characterised by increased complexity and reduced turn-around times. Additionally, the limited defense budgets force the need for a continuous reduction of maintenance effort and cost and for methods for reducing the engine life cycle costs.
These requirements and the increased complexity of the engine system stimulate the continuous improvement of the associated control and monitoring systems.

Ground based Engine Health Monitoring (EHM) Systems in conjunction with on-board monitoring systems form an essential part of the whole system to aid the fulfilment of the above requirements.
Key areas for the ground-based systems to better contribute to the fulfilment of these requirements are a better automation of the monitoring tasks, improved fault diagnosis and localisation and a better guidance of maintenance personnel.

The new and comprehensive Engine Health Monitoring System, which is planned to be used for the EJ200 engine of the EuroFighter 2000 aircraft, is described. This system will provide engine health monitoring and diagnosis for areas like life usage monitoring, engine performance monitoring, supervisory and diagnosis of engine vibration and an advanced fault detection and location system. Engine related logistics and maintenance tasks will also be supported. The EHM will be part of the EuroFighter Ground Support System (GSS), which will be shortly described.

Critical areas and possible improvements of actual engine monitoring systems are described and their potentials to better fulfil the requirements are discussed. This includes the extension of the monitoring functionality as well as improvements of the EHM architecture related to the inclusion of the EHM into the overall Ground Support System of the aircraft and the development process for future engine monitoring, diagnosis and logistic support systems.

2   The EuroFighter Ground Support System

The Ground Support System for the EuroFighter is currently developed by Partner Companies of the four EuroFighter partner nations United Kingdom, Italy, Spain and Germany.

The system will cover all logistic support tasks at the flight-line of the EF2000 on main operating bases as well as on forward operating bases and during deployment.

In accordance with the major support tasks at the flight-line, the GSS is structured into the following main components:

- Mission Support System
- Engineering Support System
- Ground Loading and Data Transfer Unit

The mission support system is the part of the GSS that is mainly responsible for the operational support of the aircraft weapon system. It will cover all tasks related to mission planning and preparation, briefing, debriefing, mission analysis, reporting and statistics.

All engineering and logistics support for the EF2000 is performed via the Engineering Support System (ESS). The ESS comprises of a number of sub-systems:

- EuroFighter Logistics Software (Asset Management, Forms and Records, Maintenance Management Status Monitoring, Reports/Statistics/Analysis)
- Engine Health Monitoring (EHM; engine monitoring and diagnosis, configuration of the on-board engine monitoring system)
- Structural Health Monitoring (SHM; airframe monitoring and diagnosis)
- Secondary Power System Monitoring (SPS; monitoring of the secondary power system)
- Aircraft System Health Software (ASH; initial processing of downloaded data)
- IETP-Browser (Display of technical documentation)
- Experience Capturing System (ExCS; build-up of an experience database from maintenance information)
- System Services Software (basic functions such as interfaces to the operating system, database management, external interfaces, user management, audit logging for all sub-systems)

The ground loading and data transfer unit is responsible for all tasks related to the upload of aircraft application software and of multi-mission data and for the download of aircraft configuration data and of the data from the Crash Survivable Memory Unit (CSMU) in the case of an aircraft incident.

The GSS will be fully integrated into the National logistic support infrastructure of the different EuroFighter nations.

This paper will concentrate on the Engine Health Monitoring System, this being part of the Engineering Support System.

Engine Health Monitoring System of the EJ200 Engine

The Engine Health Monitoring System (EHM) as an essential part of the Engineering Support System is responsible for all ground based engine condition monitoring and failure diagnosis tasks for the EJ200 engine at the flight line. Maintenance management and the support of the maintenance personnel via technical publications and repair instructions are not in the responsibility of the EHM. These facilities are covered by other sub-systems of the ESS

The EHM is seamlessly integrated into the ESS. It is no separate software application. Instead of this it is realised as a number of software components which are included into the ESS application. There are no direct interfaces between the EHM and systems outside the ESS. All interfaces to the outside world, e.g. for the data transfer to and from the aircraft, with other logistic support systems or with the national IT systems of the airforces are implemented using common facilities of the ESS. All basic services such as database access, user authorisation, security features, audit logging, file access or printing are also provided by the system services part of the ESS.

3   The Engine Monitoring, Diagnosis and Logistic Support System for the EJ200 Engine

The following figure gives an overview about the architecture of the monitoring and ground support system for theEJ200 engine. The system comprises of

- an on-board system for engine control, monitoring and diagnosis,
- the data transfer devices that are used to transfer engine related data
- the Engine Health Monitoring System as part of the Engineering Support System of the GSS.

The figure also shows the data paths for engine data transfer.
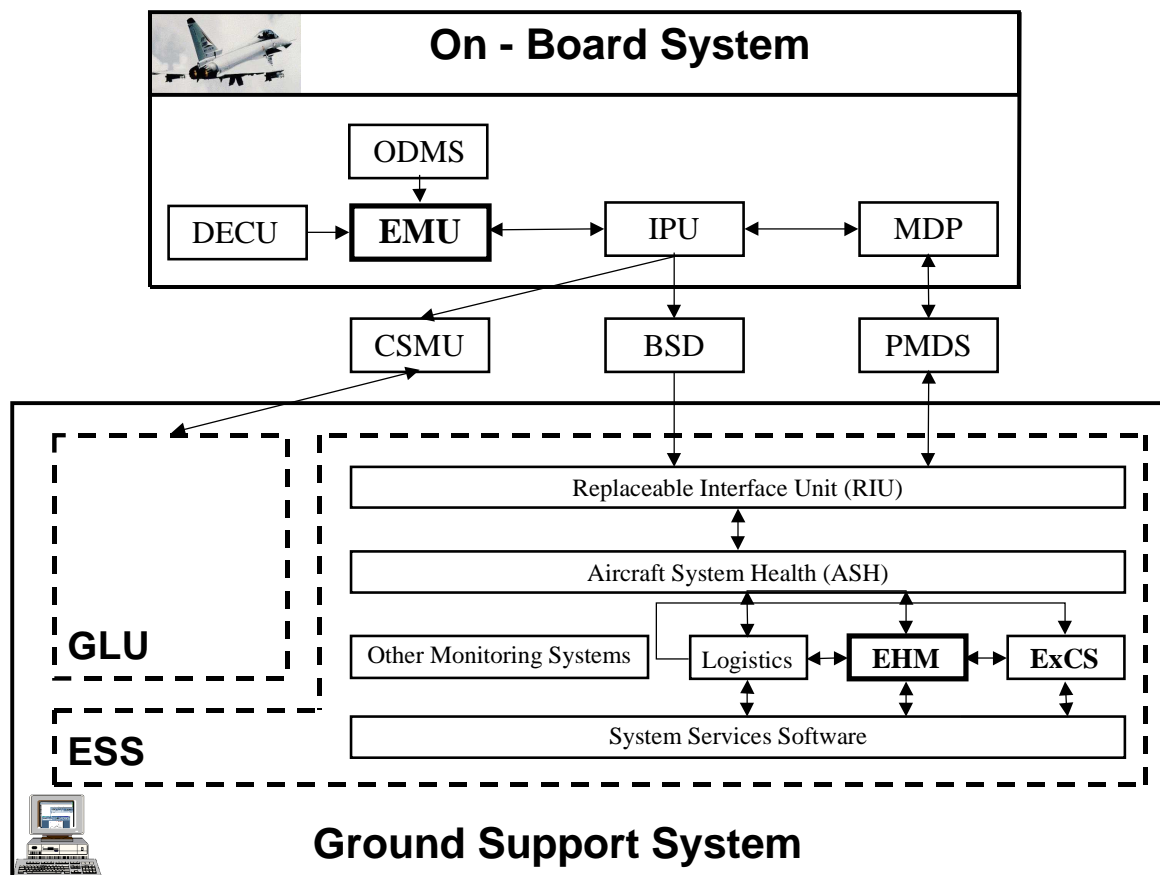
Figure 1: Architecture of the Engine Monitoring and Ground Support Systems of the EuroFighter

Abbreviations used on the figure:

DECU:	Digital Electronic Control Unit	EMU:	Engine Monitoring Unit
ODMS:	Oil Debris Monitoring System	IPU:	Interface Processing Unit
MDP:	Maintenance Data Panel	PMDS:	Portable Maintenance Data Store
BSD:	Bulk Storage Device	CSMU:	Crash Survivable Memory Unit
EHM:	Engine Health Monitoring	ExCS:	Experience Capturing System
ESS:	Engineering Support System	GLU:	Ground Loading (and Data Transfer) Unit

For a description of the system parts refer to sections 2, 3.1, 3.2 and 3.3 of this paper.

3.1   On-board System

The data used for monitoring and diagnosis of the engine are recorded and initially analysed by the on-board systems during flight and immediately after engine shutdown. On-board analysis covers the detection of all engine system failures, which prevent or significantly decrease the operational capabilities of the engine.

The on-board system comprises of the following control and monitoring devices, that are involved in engine related data collection and transfer:

- The Engine Monitoring Unit (EMU)
  The EMU is the key system for the on-board monitoring of the whole engine system including the engine accessories.
  The EMU directly supervises the engine configuration, the life usage of critical engine parts and the actual level of engine vibrations.
  The results of these supervisory tasks and the supervisory results delivered from other engine accessories (DECU, ODMS) are stored and analysed to allow a continuous real-time classification of the condition of the engine system and immediate detection of engine defects during operation.
  The supervisory and analysis functions of the EMU can be widely adapted to the configuration of the engine and to changed monitoring and diagnosis requirements. For this purpose configuration data sets can be transferred from the Ground Support System to the EMU.
  The analysis results, including information about detected engine errors and parameters describing the actual condition of the engine are transferred to the Interface Processing Unit (IPU) for distribution to the data transfer devices and to the Maintenance Data Panel (MDP).

- The Digital Electronic Control Unit (DECU)
  The DECU is the engine control device of the EJ200 engine system. As part of this task, all sensors and actuators of the engine are continuously supervised. The results of this supervisory logic and information about the actual status and condition of the engine such as engine parameters and information about critical events (engine surge, flame out etc.) are continuously transferred to the EMU for storage and inclusion into engine condition monitoring and failure diagnosis. Additionally, in the case of detected failures of the engine or its accessories, detailed information about the failure found and actual engine parameters are stored by the DECU for detailed analysis in non-volatile memory.

- The Oil Debris Monitoring System (ODMS).
  This device is responsible the supervisory of oil debris. Information about actual oil debris and the exceedance of debris limits are reported to the EMU.

- The Interface Processing Unit (IPU)
  With respect to engine related data the IPU acts as a data transmission and distribution system.

- The Maintenance Data Panel (MDP)
  The MDP is a display device that is directly attached to the aircraft. Information about failures and special events that have been detected by the different on-board systems are displayed on the MDP after flight. So the MDP is an initial point for aircraft and engine maintenance by providing a first overview about the aircraft and engine condition to the maintenance personnel.

3.2   Data Transfer Devices

The engine related data that have been collected by the on-board systems are transferred after flight to the Ground Support System via the following data transfer devices:

- The Portable Maintenance Data Store (PMDS).
  All regular maintenance data for all sub-systems of the aircraft, including the engine related data, are transferred between the on-board systems and the Ground Support System via this device.

Due to the limited capacity of the PMDS, the continuous storage of engine parameters or other aircraft data for a whole flight is not possible. Instead of this only information about detected failures/events, small snapshots of characteristic engine parameters at the time when the failures/events have been detected and limited information about the actual condition of the engine (e.g. life accounts, vibration signature) can be recorded on this device.

In addition to the downloaded flight data, the data-sets to configure the monitoring and diagnosis functions of the on-board system are uploaded from the GSS to the EMU via the PMDS.

The PMDS is installed during each flight or ground run. The capacity of this device allows the storage of maintenance data from up to 5 aircraft cycles (flights or ground test runs).

- The Bulk Storage Device (BSD)
  The purpose of this mass storage device is to allow the continuous recording of characteristic engine or aircraft parameters during a whole flight to support special investigations on ground. The BSD is attached to the aircraft only in the case of such investigations. Predefined data-sets can be recorded for one flight to support different types of investigations about engine or aircraft aspects. Examples are the engine performance, vibration or the stress to the aircraft structure.
  The BSD data are downloaded to the GSS for display and for transfer to other systems (e.g. analysis systems in the National Support Centre or at Industry). An automated analysis of these data by the GSS or the EHM is currently not foreseen.

- The Crash Survivable Memory Unit (CSMU)
  This device stores aircraft and engine data to support investigations after serious incidents or accidents. The CSMU is always attached to the aircraft. The data stored by this device are not read on a regular basis.
  In the case of events the CSMU data can be read and displayed by the Ground Support System. The data are then transferred to the authorities performing the investigations of these data. An automated analysis of these data by the Ground Support System is currently not planned.

3.3 Engine Health Monitoring System as Part of the EuroFighter ESS

The following figure gives an overview about the fundamental architecture of the Engine Health Monitoring System:
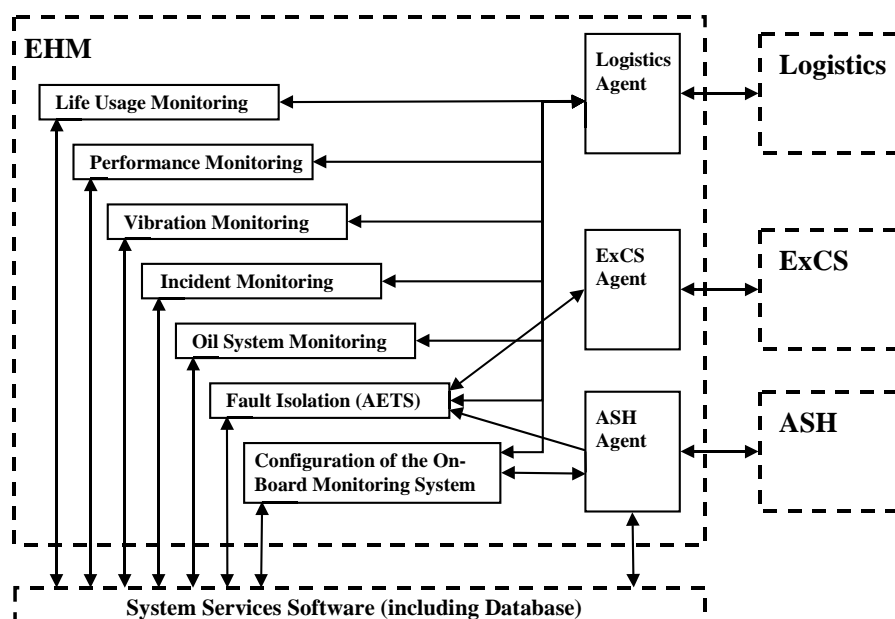
Figure 2: Structure of the EHM System

The different monitoring functions of the EHM system are described in the next section.

As previously shown, the monitoring and diagnosis functions of the Engine Health Monitoring system are mainly built on data that have been recorded by the EMU, DECU and ODMS during flight and transferred to the GSS via the PMDS. In the GSS these data are read by an interface unit and transferred to the EHM.

After reception by the EHM, the data are checked for completeness, consistence and plausibility and stored to the EHM partition of the ESS database. Engine defects that have been detected by the on-board systems are reported to the Logistics sub-system of the ESS to initiate the necessary maintenance actions.

The downloaded data are displayed on user request to allow their manual analysis.

The EHM will implement a number of automated analyses of the downloaded data, such as long term trend analyses or pattern recognition that extend the limited analyses of the on-board systems. These sophisticated analyses cannot be performed by the on-board systems due to the limited computational capacity of the these systems and due to the non-availability of data from more than one engine run.

Engine defects or changes in trends that are manually or automatically detected within the EHM are also reported to the Logistics sub-system of the ESS to initiate the necessary maintenance activities.

The EHM is also responsible for the handling of the configuration data sets that are needed to adapt the monitoring functions of the on-board system to the engine configuration and to the actual monitoring requirements. For this purpose preconfigured, authorised data sets delivered from Industry or national authorities are imported into the EHM and prepared for upload to the EMU.
Only a limited number of parameters in the configuration data sets such as information about the configuration of the engine or the (de)activation of certain monitoring functions can be manipulated within the EHM.

3.4   Functionality of the Engine Monitoring and Diagnosis

The monitoring and diagnosis functions for the EJ200 engine are split into a number of functional areas that are presented in the following sub-sections.

Life Usage Monitoring

It is a common requirement to todays engine systems to optimise the usage time of all parts of the system to extend the life of those parts and the maintenance-free periods to reduce the system and maintenance costs. The Life Usage Monitoring function for the EJ200 engine is responsible for the supervisory of the life span of a number of critical parts. The length of life of these parts strongly depends on their usage profile (strain).
The actual life accounts of these parts are updated by the on-board system depending from the usage profile.
The EHM retrieves the actual life accounts after each flight and supervises the update of these accounts by performing plausibility checks. Fill-in factors are used within the EHM to correct the life accounts in the case of errors due to defects of the on-board system (e.g. sensor defects or defects of the memory storing the accounts). It is planned to automatically adapt these fill-in factors to the real usage profile. The corrected life accounts are uploaded to the EMU before next engine run.
Additionally, the EHM will provide trend analyses of the life accounts to predict the expected remaining life of the supervised parts. This improves predictability and planning of maintenance actions due to life limit exceedance.

Performance Monitoring

The task of the Performance Monitoring function is to provide a constant thrust level over the life of the engine.

For this purpose characteristic engine parameters are recorded at "stabilised" engine conditions. These recorded parameters are used within the EMU to supervise the actual thrust level and to calculate correction factors that are used by the engine control system to adapt engine control to guarantee the required thrust level.

The EHM supervises this functionality of the on-board system and performs a thrust level trend analysis in order to detect engine problems that result in a rapid deterioration of the engine and to forecast the exceedance of thrust correction limits requiring maintenance activities or the replacement of an engine.

Vibration Monitoring

The Vibration Monitoring function continuously supervises the vibration level of the engine. Two sensors are attached to the engine for this purpose. The measured sensor signals are continuously supervised for limit exceedance or sudden changes of the vibration level that could be caused by impending engine defects. Additionally, characteristical parameters and vibration signatures are recorded during flight for transfer to the EHM.

Within the EHM these data will be used to perform engine vibration trend analyses in order to allow the early detection of impending defects. Information about the vibrational characteristics of an engine will be used by pattern comparison algorithms in order to detect engine defects before the vibration levels are exceeded and to support the localisation of defects.

Fault Isolation (AETS)

The whole engine system including sensors, actuators, engine accessories and the behaviour of the engine are continuously supervised by the on-board devices. The defect information delivered from the different supervisory functions is combined by the on-board Advanced Engine Testability System (AETS). Failures are localised at the level of (Flight)Line-Replaceable-Items (LRIs) to give an indication to the maintenance personnel about the source of a defect and the necessary maintenance activities to fix it.

This information is displayed on the MDP after the flight in the form of 'Maintenance Messages'.

Not all defects can be localised completely and reliably by automated analyses. In these cases the EHM will support the isolation of a failure by guiding the maintenance personnel through a manual fault isolation process. The system will propose manual inspections. The results of these inspections will be recorded and used by the EHM to further isolate the failure.

Oil System Monitoring

The task of the Oil System Monitoring function is to supervise the oil consumption of the engine and the oil debris level. A limit exceedance will be reported in both cases. Additionally long term trend analyses will be performed to detect impending engine defects.

Incident Monitoring

In the engine monitoring and diagnosis system, an Incident means each event or occurrence of a failure, that affects the usability or safety of the engine. Single defects of redundant systems are not considered as Incidents.

The Incident Monitoring function collects and records information about all defects or events that are detected by the other parts of the on-board monitoring system. Weighting factors are calculated for the different events, depending from their duration and severity. Additionally, for most incident types characteristic engine parameters are recorded for a short period of time before and after the failure or event have been detected in order to support the failure investigation on-ground.

All Incidents are displayed on the MDP after the flight.

The EHM reports all detected incidents to the Logistics sub-system of the EHM in order to initiate the necessary maintenance actions. Facilities will be provided by the EHM to support the investigation of incidents by showing information about similar events and performing statistical analyses.

4   Future Trends in EHM Systems

The development of future EHM systems will face a number of challenges that are mainly driven by the following two contrary trends:
- Stagnating or decreasing military budgets in most countries.
  Resulting from this a substantial reduction of the development costs as well as of the operational costs of aircraft weapon systems is necessary. The development of these systems must become more effective than today, the development times must be significantly reduced and the multiple development of similar functionality, e.g. for engine monitoring at testbed and at customer sites must be avoided.
  The maintenance costs for future military jet engines must be reduced via a better support and guidance of the maintenance personnel for all maintenance tasks and via an enhanced automation of monitoring and diagnosis functions in order to reduce the workload to the ground crews.
- Ever increasing customer requirements to the aircraft and engine systems related to utilisation capabilities, flexibility of usage, extension of system life, reduction of turn-around times, simplification of maintenance and other criteria.

Future EHM systems will have to cope with those requirements. Additionally, the increased requirements to the aircraft systems will lead to the introduction of new technologies into and to a higher technical complexity of the jet engines, their accessories and of the engine control and monitoring systems. This causes also increasing demands to the EHM systems.

4.1   Improvement Potentials for Future EHM Systems

The effects of the aforementioned trends on future engine monitoring and diagnosis systems including the engine health monitoring and logistic support systems have been analysed in MTU during a technology study. The goal of this study was the definition of an optimum concept for future control, monitoring and engine ground support systems which allows the fulfilment of the aforementioned increasing requirements and a considerable reduction of costs. The results of this study with respect to EHM systems will be summarised in the following sections. Although a complete differentiation between on-board and ground-based systems is not possible, this paper concentrates on the EHM related improvement potentials.

In addition to the analysis of future requirements, experiences from existing engine programs, namely the RB199 of the Tornado aircraft and the GSS/EHM for the EJ200 engine of the EuroFighter have been analysed to identify areas of problems and possible improvements of future systems.

Resulting from the analysis of increased requirements, technological trends and experiences from existing and productive engine systems, the following areas for potential improvements of the EHM systems in the future have been identified:
- Extension and optimisation of the monitoring and diagnosis functionality
- System architecture
- Development of monitoring and diagnosis systems

4.2   Extension and Optimisation of the Monitoring and Diagnosis Functionality

To cope with the aforementioned increasing demands to aircraft weapon systems and their jet engines at lower costs, a considerable number of technological improvements are expected to be introduced into future engine systems and thus will influence the development of future EHM systems.
Examples are
- Vectorisation of thrust with vector nozzles, requiring the implementation of thrust vector control and related monitoring tasks into the engine control system
- Optimisation of the engine control algorithms. Examples are performance seeking control, surge control or active oil systems. Resulting from this, increased monitoring and

diagnosis requirements are to be fulfilled to ensure the safety and reliability of those functions
- Closer integration of engine control and monitoring, supported by the integration of multiple on-board systems into one device. An example is the planned integration of todays DECU and EMU devices of the EJ200 engine into one device, with the option to integrate also the ODMS in the future.

The following list gives an overview about possible improvements of the monitoring and diagnosis functionality that should be considered for future systems:
- Introduction of expert systems for diagnosis. With these systems the specific knowledge of engine experts from industry or customer can be made available to all maintenance personnel at very low cost. Experiences made during engine development and during solution of problems in the past are automatically used for the solution of actual problems, reducing time and cost of maintenance and increasing the trustworthiness and understandability of diagnoses.
  It should be noted, that expert systems, due to their non-deterministic nature, are not suited for on-board monitoring tasks.
- Usage of modern analysis methods such as Bayesian (probabilistic) Networks to identify failures sources and neural networks to recognise characteristical patterns within aircraft signals (e.g. recorded vibration signatures)
- Thrust Monitoring (in conjunction with performance seeking control)
- Surge detection and control
- Detection of FOD and bird strike via inlet sensors or engine distress monitoring
- Detection of cable defects
- Active oil systems
- Re-calculation of life accounts after changes of lifing algorithms or of their parameters
- Earlier detection of defects via improved trend analyses

Many of these functions are built on very complex algorithms and large amounts of data and must be widely configurable. Therefore most of these algorithms can be executed on ground only. This requires the storage and transmission of large amounts of data by the on-board systems. Future systems will therefore have to support the continuous storage of relevant parameters during the whole flight and the transmission of these data to the GSS/EHM, where they will be stored for the whole life of an engine.

4.3 System Architecture (Integrated Monitoring and Ground Support System)

The flexibility and commonality of the actual EHM system is limited due to the following problems:
- The EHM is inseparably integrated into the health monitoring system of the aircraft. Parts of the engine related functionality and all basic functions and interfaces to the outside world are implemented by other ESS sub-systems.
  Thus a further development of the EHM strongly depends from modifications of other ESS sub-systems, resulting to high modification costs. Porting of on-board and off-board parts of the engine monitoring and diagnosis system due to the usage of the same engine in other aircraft systems requires a redevelopment of the EHM system.
  Another problem resulting from the distribution of the engine related functionality over a number of ESS sub-systems is, that the ensuring of the fulfilment of all requirements related to engine monitoring, diagnosis and maintenance is very complicated. There is a considerable risk, that functionality will be missed or duplicated in the completed ESS system, because the responsibilities for these functions are unclear.
- The complexity of the on-board system is too high.
  In the EuroFighter five on-board devices contribute to the collection and transfer of engine related data, which are distributed over 3 transfer devices. This causes high technical effort, high expenses and complicated co-ordination. Modifications and extensions of the on-board system affect a lot of devices. This and the technical complexity of the system make modifications complicated, expensive and risky due to possible side-effects.

- Engine data are transferred using the same transfer devices as aircraft data.
  The capacity of those systems is limited, all on-board systems compete for the storage space.
  The number of devices involved in engine data transfer is too high. Thus adaptations of transferred engine data to future requirements are nearly impossible, again expensive and time consuming.

All off these hindrances prevent the development of a really flexible, fully integrated engine monitoring, diagnosis and ground support system, that is easily adaptable to the ever-changing technological needs and customer requirements. The fulfilment of the requirements is significantly complicated, expensive and time consuming with the current system architecture and concepts.

Therefore the following improvements should be considered for future systems:
- Thorough integration of all engine related monitoring and diagnosis tasks into the EHM
- Standardised interfaces to the logistic system
- Usage of a dedicated engine data transfer medium

4.3.1   Thorough Integration of all Engine Monitoring and Diagnosis Tasks into the EHM

An essential condition to ensure the flexibility of future EHM systems and their adaptability to different requirements and aircrafts is the integration of all engine related monitoring and diagnosis tasks into the EHM.

There is a number of engine related functions in the ESS for the EuroFighter, that are not in the responsibility of the EHM:

- The Maintenance messages that are created on-board by the AETS function of the EMU are initially handled by the Aircraft System Health (ASH) sub-system of the ESS. The corresponding maintenance activities are initiated by the ASH system before the messages are passed to the EHM for further handling and analysis.
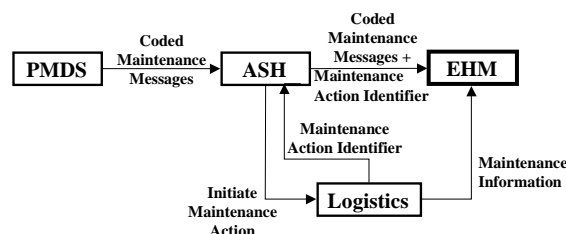
Figure 3: Transfer of Information related to AETS Maintenance Messages in the ESS

- The handling of the life accounts of engine parts is split between the EHM and the logistics sub-system. The EHM handles the life accounts of the critical parts that are supervised by the EMU, the accounts for all other life limited parts are handled by the logistics sub-system.
- Experience capturing functionality will be provided by the Experience Capturing system of the ESS. Although this functionality requires an in depth knowledge about the engine system, it is planned to implement this into another sub-system.

  The aforementioned examples of a problematic distribution of engine related functionalities over different sub-systems result to the following weaknesses during development and advancement of EHM systems:
  - The system design becomes unnecessarily complex.
  - A number of additional interfaces have to be introduced between sub-systems.
  - The development of the whole ESS is considerably complicated due to the high co-ordination effort that is needed to ensure, that all related functionality is provided and that no functionality is implemented twice.

- The development of distributed functionalities cannot be started before the last involved party starts with the development, resulting in a high program risk to the other parties.
- A porting of EHM systems with this distribution of functionality means in fact a complete re-development.

4.3.2   Standardised Interfaces to the Logistic System

From customers point of view only an integrated monitoring, diagnosis and logistic support system for the whole aircraft weapon system is thinkable, a differentiation between different systems for aircraft related tasks and engine related tasks is not acceptable.

There must be a common, uniform and consistent user interface. Therefore the integration of maintenance management tasks into the EHM is not possible since it would lead to two different user interfaces for aircraft and engine maintenance. Instead of this the EHM must be seamlessly integrated into the aircraft maintenance system. All engine defects must be reported to the central maintenance management system for the whole aircraft system, all EHM functionalities must be callable from the logistics sub-system.

This can be ensured in an effective and flexible way only, if there is a standardised interface to the logistics system. The specification of this interface must include features that allow the EHM to
- initiate maintenance activities after engine defects have been detected
- handle call-backs from the logistics sub-system to support the fault investigation and to provide engine specific maintenance guidance
- to get back information about completed maintenance activities
- get information about the aircraft configuration.

The development of such an interface, that allows flexible adaptations to special needs of a concrete system is supported by todays software component architectures.

4.3.3   Usage of a dedicated engine data transfer medium

A dedicated engine data transfer module (Portable Engine Data Store – PEDS) should be used for engine data instead of sharing the same transfer media for engine and aircraft data

A number of problems resulting from this shared usage of the data transfer devices for engine and aircraft data could be solved by the usage of such a device:
- The on-board system would become significantly less complex due the avoidance of additional interfaces for engine data transfer and of engine data processing capabilities that must be implemented otherwise into a number of devices just to handle the transfer of engine related data.
- Within the ESS, the engine data could be read directly by the EHM instead of their reading and decoding by another ESS system, splitting them from the aircraft data and transmission to the EHM, where they can be handled.
- The development of the engine transfer medium in the responsibility of the engine manufacturer would ensure, that the needs of the engine system related to data transfer are fully met.
- The development of engine data transfer mechanisms could be undertaken independently from the development of the mechanisms for aircraft data transfer.
- Changes in the transferred data would be significantly less complicated due to the smaller number of involved systems and manufacturers.
- A porting of the engine monitoring, diagnosis and ground support system would be significantly easier, because the same PEDS module could be used for different aircraft types. Additionally, a PEDS would allow the design of a complete fully integrated system of on-board devices, transfer media and ground support components

To avoid the implementation of an additional data transfer device into the aircraft, the PEDS should not be realised as a separate device. Instead of this, it should be a memory module that can easily be integrated into the aircraft data transfer devices.

The storage capacity of the PEDS should be large enough to allow the continuous recording of engine parameters with a resolution that is sufficient for ground based monitoring and diagnosis functionalities. In this case the BSD would no longer be needed for engine data recording, another device and a set of interfaces would become obsolete. Additionally, a complete data recording and archiving over the whole life of the engine would be possible. This is not the case today, because the BSD must be shared between aircraft and engine data.

4.3.4   Comparison of Actual and Optimised Architecture

The following figure shows the optimised architecture of the engine monitoring, diagnosis and ground support system, to be compared with the actual architecture as shown on Figure 1.
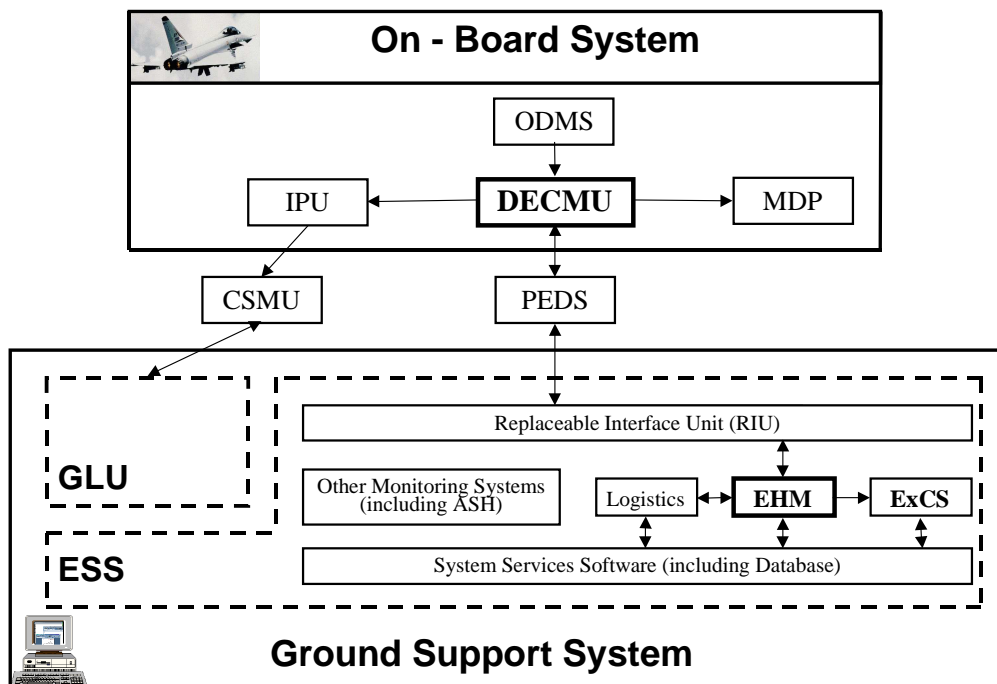
Figure 4: Optimised Architecture of the Engine Monitoring and Ground Support Systems of the EuroFighter

The optimised architecture includes all improvements that have been proposed and the introduction of an integrated control and monitoring on-board device (DECMU).

The optimum architecture represents an engine monitoring, diagnosis and ground support system with the following benefits in comparison to the actual system:
- Optimum integration between the on-board system, the engine data transfer media and the ground support system
- The distribution of functionality within such a system is very flexible.
- The system is considerably less complex. The number of devices and interfaces is substantially reduced.
- The system can be fully developed in the responsibility of the engine manufacturer, with less dependencies from the aircraft manufacturer.
- The development can be done at lower cost and shorter times.
- The fulfilment of engine related requirements can be ensured.
- Changes can be implemented faster and easier.
- The system is easily portable to other aircraft types.

4.4   Development of Monitoring and Diagnosis Systems

Beside the extension of the monitoring and diagnosis functionality and a better structured system architecture, potential for improvements of future EHM systems and for cost and development time reductions also lies in the development process of the system.

A better integration with development support systems and with other logistic support systems for other maintenance tasks beside the flight line maintenance should be aspired to provide a better reuse potential for developed system parts.

A number of systems with similar tasks as the EHM is needed for development, production and repair of the engine:

- Monitoring and set-up units to support the development of the control and monitoring system hard- and software
- Systems for monitoring, diagnosis and engineering data transfer and analysis at the engine testbed during development, certification and production pass-off tests
- Data transfer and analysis systems to be used at higher maintenance levels, e.g. engine repair&overhaul at customer and industry sites.

Currently, separate systems with similar functionalities are developed for the different stages of the product lifecycle.

An earlier design and development of the EHM, parallel with the on-board and data transfer parts of the engine monitoring and diagnosis system would significantly reduce the development risk.

Todays EHM systems are usually developed after the design of the on-board monitoring, control and diagnosis system and of the data transfer devices has been finalised.

So the EHM system has to deal with and to make the best use of the realities of the given systems, an optimisation of the on-board and transfer components to the needs of the ground based system is either not possible or requires a huge effort to modify these systems.

This causes additional effort in EHM system development as well as limitations to the functionalities of the ground based system.

To solve both problems, the development of future EHM systems should be done in parallel to the development of the on-board and of the data transfer systems. Parts developed for the EHM should be used already during development to support similar tasks. This would avoid the multiple development of similar systems for the different stages of the development cycle and for the operational phase of the system.

Additionally, really integrated and coherent engine monitoring, diagnosis and ground support systems could be developed. The usage of identical systems would improve the compatibility between customer and industry systems, i.e. between the EHM and the industry systems for repair&overhaul.

Integration and coherence could be fully validated during the different development phases, the EHM would be validated together with the other parts of the system. This would significantly improve the maturity of the whole system before the operational phase.

5   Summary and Conclusions

The EJ200 EHM will be a modern, state-of-the-art engine health monitoring system with a comprehensive and sophisticated monitoring and diagnosis functionality that provides extensive engine maintenance support and guidance to the ground crew. The EHM system will be seamlessly integrated into the overall Ground Support System for the EuroFighter.

However, continuous improvements of EHM systems are required to ensure that future EHM systems will meet the challenges resulting from the ever-increasing complexity of the engine system and due to continuously rising customer requirements that are to be fulfilled at lower cost.

Improvement potential has been identified in the following areas:
- Extension and optimisation of the monitoring and diagnosis functionality
- EHM System architecture
  - Thorough integration of all engine related monitoring and diagnosis tasks into the EHM
  - Standardised interfaces to the logistic system
  - Usage of a dedicated engine data transfer medium
- Development of monitoring and diagnosis systems
  - A better integration with development support systems and with other logistic support systems outside the flight line maintenance
  - Earlier development of the EHM, parallel with the on-board and data transfer parts of the engine monitoring and diagnosis system.

These improvements result to a number of benefits:
- Improved monitoring and diagnosis of engine defects
- Reduced complexity of the engine monitoring, diagnosis and ground support system
- Improved portability and modifiability of EHM systems
- Reduced development time and cost.

Paper 11: Discussion

<u>Question from L Jaw – Scientific Monitoring Inc, USA</u>

Can you describe what you meant by an 'active oil system'?

<u>Presenter's Reply</u>

Preliminary thought on this is to utilise valves to control oil temperature and quantity, in order to match them to the requirements of specific engine operating conditions.

This page has been deliberately left blank

————————————

Page intentionnellement blanche

Tracking and Control of Gas Turbine Engine Component Damage/Life

Dr. Link C. Jaw, Dr. Dong. N. Wu, Dr. David J. Bryg
Scientific Monitoring, Inc., 4801 S. Lakeshore Dr., Tempe, Arizona 85282, U. S. A.
link@scientificmonitoring.com, http://www.scientificmonitoring.com

ABSTRACT

This paper describes damage mechanisms and the methods of controlling damages to extend the on-wing life of critical gas turbine engine components. Particularly, two types of damage mechanisms are discussed: creep/rupture and thermo-mechanical fatigue. To control these damages and extend the life of engine hot-section components, we have investigated two methodologies to be implemented as additional control logic for the on-board electronic control unit. This new logic, the life-extending control (LEC), interacts with the engine control and monitoring unit and modifies the fuel flow to reduce component damages in a flight mission. The LEC methodologies were demonstrated in a real-time, hardware-in-the-loop simulation. The results show that LEC is not only a new paradigm for engine control design, but also a promising technology for extending the service life of engine components, hence reducing the life cycle cost of the engine.

1. Introduction

Gas turbine engines consist of primarily rotating components. These rotating components operate under cyclic loading condition and harsh environment (i.e., under high temperature, pressure, corrosion condition) such that the deterioration of these components is accelerated. Deterioration is generally tracked by damages, or damage rates, for different damage mechanisms. The most common damage mechanisms for a gas turbine engine include: low cycle fatigue (LCF), thermo-mechanical fatigue (TMF), high cycle fatigue (HCF), creep, rupture, corrosion, and foreign object-induced damages (FOD). Of these common damage mechanisms, LCF and HCF are primarily design issues; FOD and corrosion are ambient-condition driven; hence TMF, creep, and rupture are the prime candidates for damage control and life extension on a continuous-operation basis.

TMF, creep, and rupture have similar damage patters. The simplest patter is where the damage rate (d) is geometrically proportional to a key engine operating parameter (x), sometimes called a damage driver, as shown in Figure 1. To analyze damage mechanisms more accurately, we often consider additional damage drivers. Additional damage drivers reveal more complex damage patterns as shown in Figures 2 and 3.
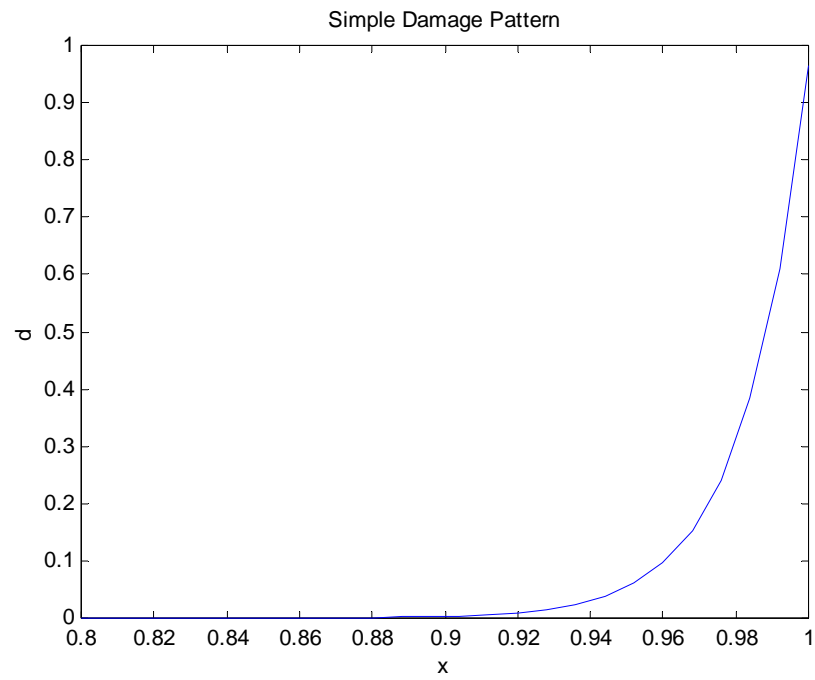
Figure 1: A simple damage pattern
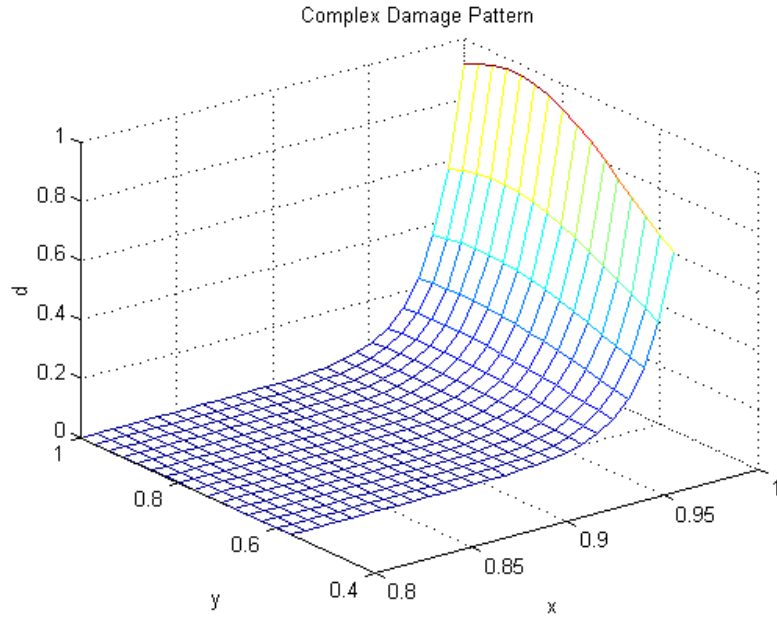
Figure 2: A complex damage patterns
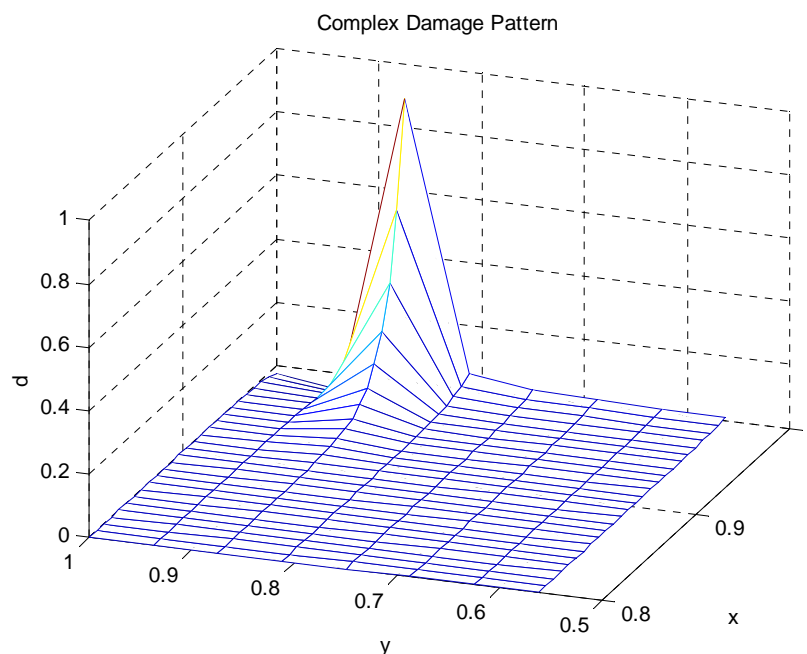
Figure 3: Another damage pattern

Generally speaking, the approaches to controlling the damage and extending component life fall into two categories:

- *Active* control: changing the operating procedures pertaining to mission planning or engine control, and tracking the damage concurrently[1].
- *Passive* control: tracking damages and adjusting maintenance practices to maximize the utilization of the service life of a component.

This paper concerns with the active control approach, specifically, extending the life of hot-section components through active engine control of TMF, creep, and rupture damages. This approach is called life-extending control (LEC). The LEC concept originates from damage mitigating control research for rocket engines [1-5]. It controls engine fuel flow rate by including damage-reduction as an active objective. The differences between a liquid-fueled rocket engine and a gas turbine engine are summarized as follows: 1) a rocket engine has a narrow operating envelope, its mission profile is mostly fixed; 2) a rocket engine has much shorter firing durations; 3) a rocket engine has much longer down time for each mission cycle; 4) a rocket engine has no air breathing provision, hence, not susceptible to contamination and corrosion.

The challenge of LEC is to maintain satisfactory levels of performance and operability while reducing component damages. To meet this challenge, LEC is preferably designed to trim the standard engine control logic with a limited authority.

This paper describes two methodologies to reduce the life cycle cost of gas turbine engines. The first methodology reduces stress rupture/creep damage to turbine blades and stators by optimizing damage accumulation concurrently with the flight mission. This methodology is

---

[1] By concurrent tracking of damages we mean the time from feeding damage information back to mission planning or engine control is much shorter compared with this feedback process in the passive control approach.

described in Section 2. The second methodology modifies the baseline control logic of an engine to reduce the TMF damage of cooled stators during acceleration. This methodology is described in Section 3. These methodologies have also been implemented in an actual full-authority digital electronic control (FADEC) unit of a small gas turbine engine to demonstrate the feasibility of LEC. A real-time, hardware-in-the-loop (HITL) simulation has also been conducted as a part of the feasibility demonstration. Section 4 describes the HITL simulation.

2. Stress Rupture/Creep Damage Reduction

A typical flight mission of an aircraft consists of taxi, take-off, climb, cruise, descent and landing. In this section, we describe the reduction of rupture damage during a specific portion of a flight mission: cruise. Since a civil airplane flies most of the time at the cruise condition, reducing engine component damages during cruise will directly increase the service life of the engine components.

Generally speaking, increasing cruise speed reduces flight time but increases the thrust requirement. This implies higher engine speed and temperature hence high damage rate to the turbine blades and stators.   Therefore, there is trade-off among flight time, fuel cost, and accumulated component damages during cruise. An optimization to perform this trade-off among flight time, fuel cost, and accumulated engine component damages during cruise was formulated and is shown in the Figure 4 below.
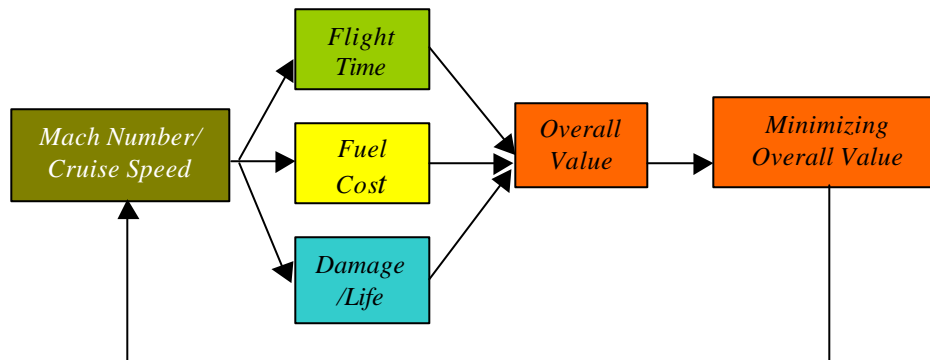
Figure 4: A trade-off between performance and rupture/creep damage in cruise conditions

Flight Mission

A business jet is used to demonstrate this trade-off optimization concept. A typical flight mission of this type of airplane is shown in Figure 5. There are three cruise segments in the flight mission. The first cruise segment is at altitude 41000ft, the second cruise segment is at altitude 43,000ft, and the third cruise segment is at altitude 45,000ft. The Mach number for all three cruise segments is 0.8.
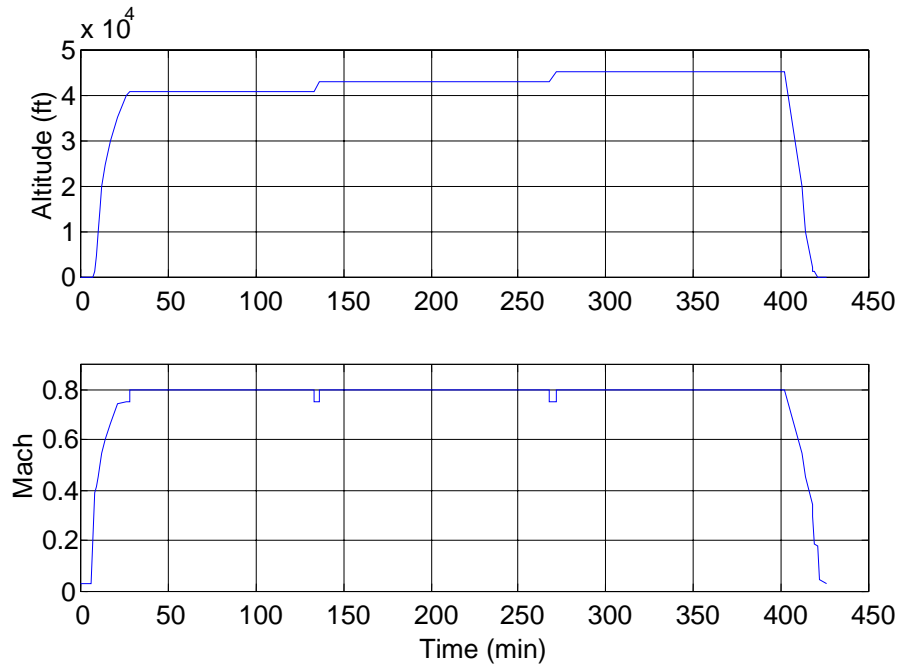
Figure 5: A typical flight mission of the business jet

Aircraft Model

From the equations of motion of an aircraft in level flight, the required engine thrust in cruise condition can be determined from the following two equations:

$$T = \tfrac{1}{2}\rho S C_d V^2 \tag{1}$$

$$mg = \tfrac{1}{2}\rho S C_l V^2 \tag{2}$$

where ρ the density of the air, S the reference area of the aircraft, C_d the drag coefficient, C_l the lift coefficient, V is the cruise speed.

The relationship between C_d and C_l is described by the drag-polar equation:

$$C_d = C_{d0} + \beta C_l^2 \tag{3}$$

where the zero-lift drag coefficient C_{d0} and the induce drag factor β are functions of Mach number only.

The thrust T, as a function of cruise speed and mass of aircraft, can be written as

$$T = \tfrac{1}{2}\rho S C_{d0} V^2 + 2\beta \frac{m^2 g^2}{\rho S V^2} \tag{4}$$

Cumulative Damage In Cruise

Based on the required thrust determined by Eq. (4), cumulative component damages during cruise are determined by using the damage model. For the first cruise segment of the mission profile (altitude 41000ft, cruise speed 0.8 Mach, cruise time 105 min), Figures 6 to Figure 8

show the cumulative damages for blades and stators. Figure 9 shows the total fuel consumption as a function of cruise Mach number and initial weight with respect to a reference initial weight $m_0 g$.

It can be seen from these figures that the cumulative component damage during cruise increases exponentially with respect to the Mach number. Large damage reduction can be achieved with very small sacrifice in flight time. Total fuel consumption during cruise.
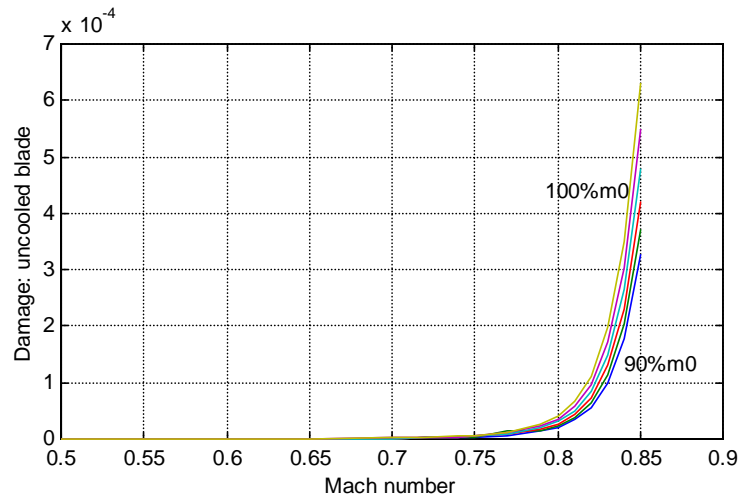
Figure 6: Cumulative damage of un-cooled blade during cruise
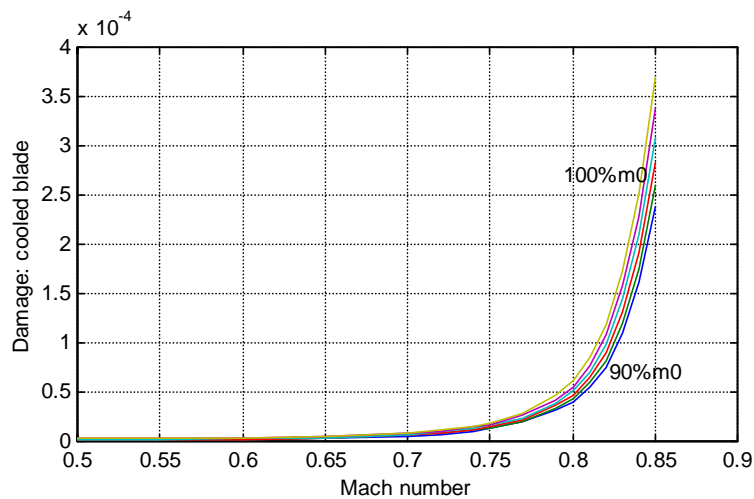
Figure 7: Cumulative damage of cooled blade during cruise
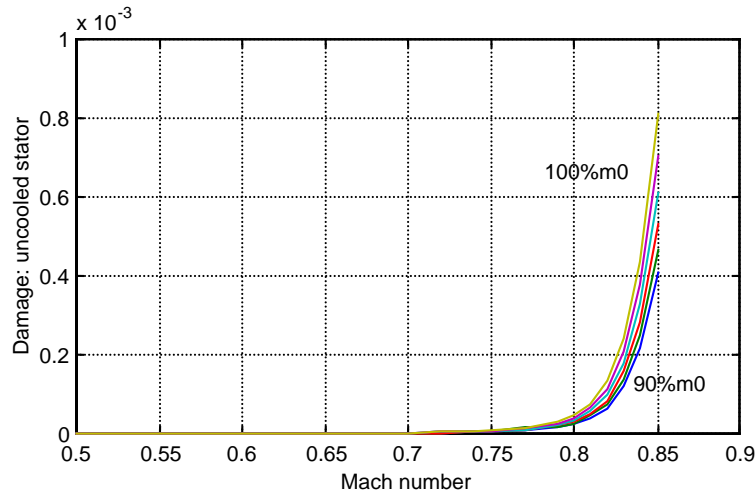
Figure 8: Cumulative damage of un-cooled stator during cruise
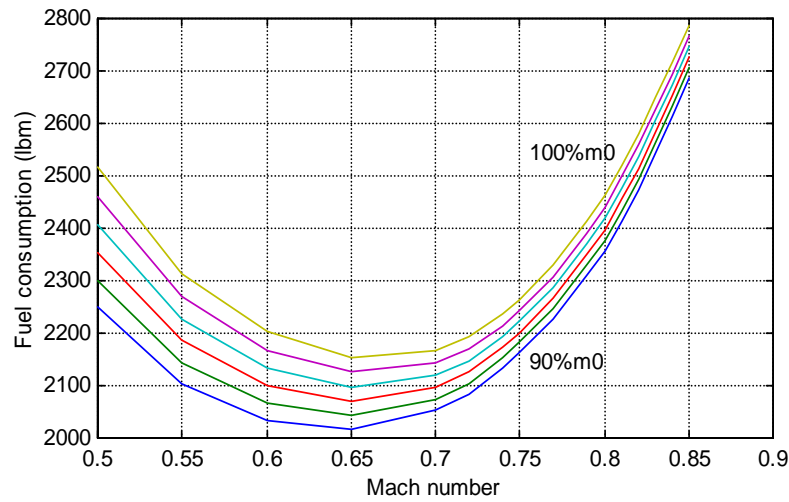
Figure 9: Fuel consumption during cruise

Trade-off Optimization

To demonstrate this optimization approach, a linear objective function of flight time, fuel consumption and cumulative damage is formulated as follows:

$$J = \alpha_1 \frac{t_f}{t_{f\_ref}} + \alpha_2 \frac{D_1}{D_{1\_ref}} + \alpha_3 \frac{D_2}{D_{2\_ref}} + \alpha_4 \frac{D_3}{D_{3\_ref}} + \alpha_5 \frac{WF}{WF_{ref}} \qquad (5)$$

where

t_f : Cruise time

t_{f_ref} : Cruise time at a nominal cruise Mach number

D_1 : Cumulative damage for uncooled blade

D_{1_ref} : Cumulative damage for uncooled blade at a nominal cruise Mach number

D_2 : Cumulative damage for cooled blade

D_{2_ref} : Cumulative damage for uncooled blade at a nominal cruise Mach number

D_3 :   Cumulative damage for cooled stator

D_{3_ref} : Cumulative damage for uncooled stator at a nominal cruise Mach number

WF :   Total fuel consumption during cruise

WF_{ref} : Total fuel consumption during cruise at a nominal cruise Mach number

α_i :   Weighting coefficients

Assume $\alpha_1 = 10$, $\alpha_2 = \alpha_3 = \alpha_4 = \frac{1}{3}$, $\alpha_5 = 1$. For different reference cruise Mach number 0.70, 0.75, 0.80, Table 1 below lists the optimal Mach number, the damages at the optimal cruise Mach number divided by the damages at the reference cruise Mach number, and the fuel consumption at the optimal cruise Mach number divided by the fuel consumption at the reference cruise Mach number, for three reference Mach numbers.

Note that the objective function reaches its minimum at the reference cruise Mach number for the reference Mach number below 0.70. This is caused by the large weighting on the cruise time in the objective function. The objective function at different Mach number for the reference Mach number 0.8 is shown in Figure 10. For the Mach numbers greater than 0.75, more reduction in Cumulative damages can be achieved with small reduction in cruise speed.

Table 1: Optimization results

Ref. Mach	Optimal Mach	D_1/D_{1_ref}	D_2/D_{2_ref}	D_3/D_{3_ref}	F/F_{ref}
0.70	0.70	1.0	1.0	1.0	1.0
0.75	0.72	0.43	0.58	0.41	0.96
0.80	0.77	0.32	0.48	0.30	0.94
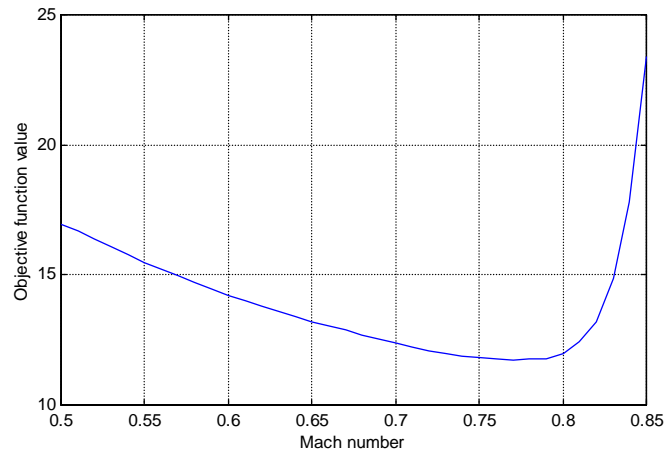
Figure 10: Objective function value at different cruise Mach number

3. TMF Damage Reduction

The actual engine control logic has been modified to reduce the TMF damage during engine acceleration from ground idle to maximum power. The goal is to reduce the TMF damage while maintaining fast engine acceleration. Several approaches to modifying engine control logic have been investigated including: target speed offset, control gain increase/decrease and acceleration schedule reduction. It was found from engine simulation that acceleration schedule reduction is the most effective.

In a typical turbine engine control, engine acceleration follows an acceleration schedule; specifically, the engine speed is controlled to follow the acceleration schedule. To reduce TMF damage, the acceleration schedule was reduced by a certain percentage once the difference between the controlled speed, high pressure spool speed (NH) and the target speed is less than a threshold. This is illustrated in Figure 11 below.
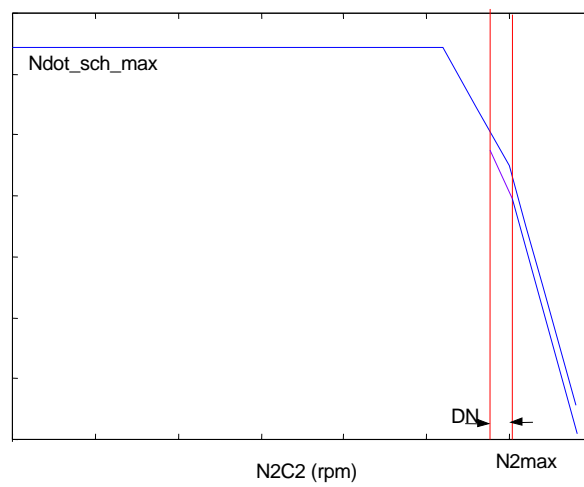
Figure 11: Illustration of acceleration schedule reduction logic

For the threshold values (DN) of 800 rpm, 1000 rpm, and 1200 rpm, the reductions in TMF damage (in percentage) and the increase of rise time of fan speed (N1) (an indicator of engine thrust) during the engine acceleration from ground idle to maximum power are shown in Tables 2 to Table 4, and in Figure 12 and Figure 13 for 50% to 90% reduction of the acceleration schedule. It can be seen that the greater the reduction of TMF damage, the greater the increase in rise time. It is also found that the relationship between the TMF damage reduction and increase in rise time is not sensitive to the threshold values. For all three cases, significant reductions in TMF damage can be achieved with only a very small increase in rise time for N1 and thrust.

Table 2: TMF damage reduction for DN=800 rpm

%, reduction	TMF reduction (%)	Extra rise time (sec)
10%	13.7	0.06
20%	24.5	0.12
30%	35.3	0.22
40%	45.6	0.32
50%	49.0	0.58

Table 4: TMF damage reduction for DN=1000 rpm

%, reduction	TMF reduction (%)	Extra rise time (sec)
10%	14.7	0.06
20%	26.4	0.16
30%	37.7	0.28
40%	47.5	0.40
50%	54.3	0.74

Table 5: TMF damage reduction for DN=1200 rpm

%, reduction	TMF reduction (%)	Extra rise time (sec)
10%	14.7	0.08
20%	27.5	0.18
30%	39.2	0.32
40%	49.0	0.50
50%	56.9	0.86
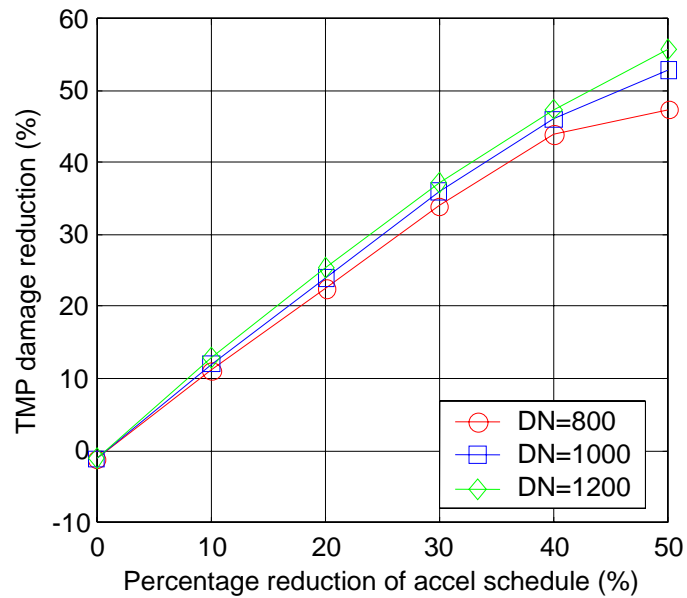
Figure 12: TMF reduction vs. reduction of acceleration schedule vs. speed threshold

Figure 13: TMF reduction vs. increase in rise time vs. speed threshold

4. Hardware-in-the-loop Simulation

The methodologies have been implemented in an actual full-authority digital electronic control (FADEC) unit of a small gas turbine engine to demonstrate the feasibility of LEC. Real-time, hardware-in-the-loop simulations have been conducted and verified the LEC concept through the two life extension methodologies. Figure 14 shows the simulation environment and a data screen.

Figure 14a: HITL simulation setup

Figure 14b: real-time data display

5. Conclusions

This paper describes two methodologies to extend the service life of hot-section components, particularly, turbine blades and stators, by reducing the damages incurred on these components. One methodology has been designed to reduce the creep damage in cruise. The other methodology has been designed to reduce the thermo-mechanical fatigue damage in rapid transients. These methodologies for damage reduction and life extension have been evaluated for a small commercial turbine engine for a general aviation aircraft. Evaluation was performed by hardware-in-the-loop simulations where an actual engine full-authority digital electronic control (FADEC) unit was modified with the LEC, and it interacted with an engine simulator in real time. The results of this evaluation show that significant reductions in these damages are promising and the design for life extension could be considered in engine control systems. The team anticipates to substantiate the analytical results by carefully designed experiments and engine testing in the next phase of the program.

6. Acknowledgment

7. References

1. Ray A, Dai, X, Wu M-K, Carpino M., Lorenzo C., "Damage-mitigating Control of a Resusable Rocket Engine", AIAA Journal of Propulsion and Power, vol. 10, pp:225-233, 1994.
2. Ray A, Wu M.K., Carpino M., Lorenzo C., "Damage-mitigating Control of Mechanical Systems: "Part I:-Concept Development and Model Formulation", Journal of Dynamic Systems, Measurement, and Control, vol. 116, pp.347-447, 1994.
3. Ray A, Wu M.K., Carpino M., Lorenzo C., "Damage-mitigating Control of Mechanical Systems: "Part II:-Formulation of an Optimal Policy and Simulation", Journal of Dynamic Systems, Measurement, and Control, vol. 116, pp.448-455, 1994.
4. Dai X., Ray A., "Damage-mitigating Control of a Resusable Rocket Engine: Part I-Life Prediction of the Main Thrust Chamber Wall", Journal of Dynamic Systems, Measurement, and Control, vol.118, pp.401-408, 1996.
5. Dai X., Ray A., "Damage-mitigating Control of a Resusable Rocket Engine: Part II-Formulation of an Optimal Policy", Journal of Dynamic Systems, Measurement, and Control, vol.118, pp.409-415, 1996.

Dr. Link Jaw
President and CEO
Link@scientificmonitoring.com

Link Jaw founded Scientific Monitoring, Inc. (SMI) in 1993. He has been involved in all aspects of corporate management including projects, strategies and resources.   Link has over 25 years of experience in engineering, software, and management. Prior to starting SMI, he worked for AlliedSignal Aerospace, Link Flight Simulation, and FlightSafety Simulation. Link is the inventor of five U.S. patents. He holds an M. S. degree from the University of Michigan and a Ph. D. degree from Stanford University. He also completed executive management training at the Tuck School of Business Administration of Dartmouth College.
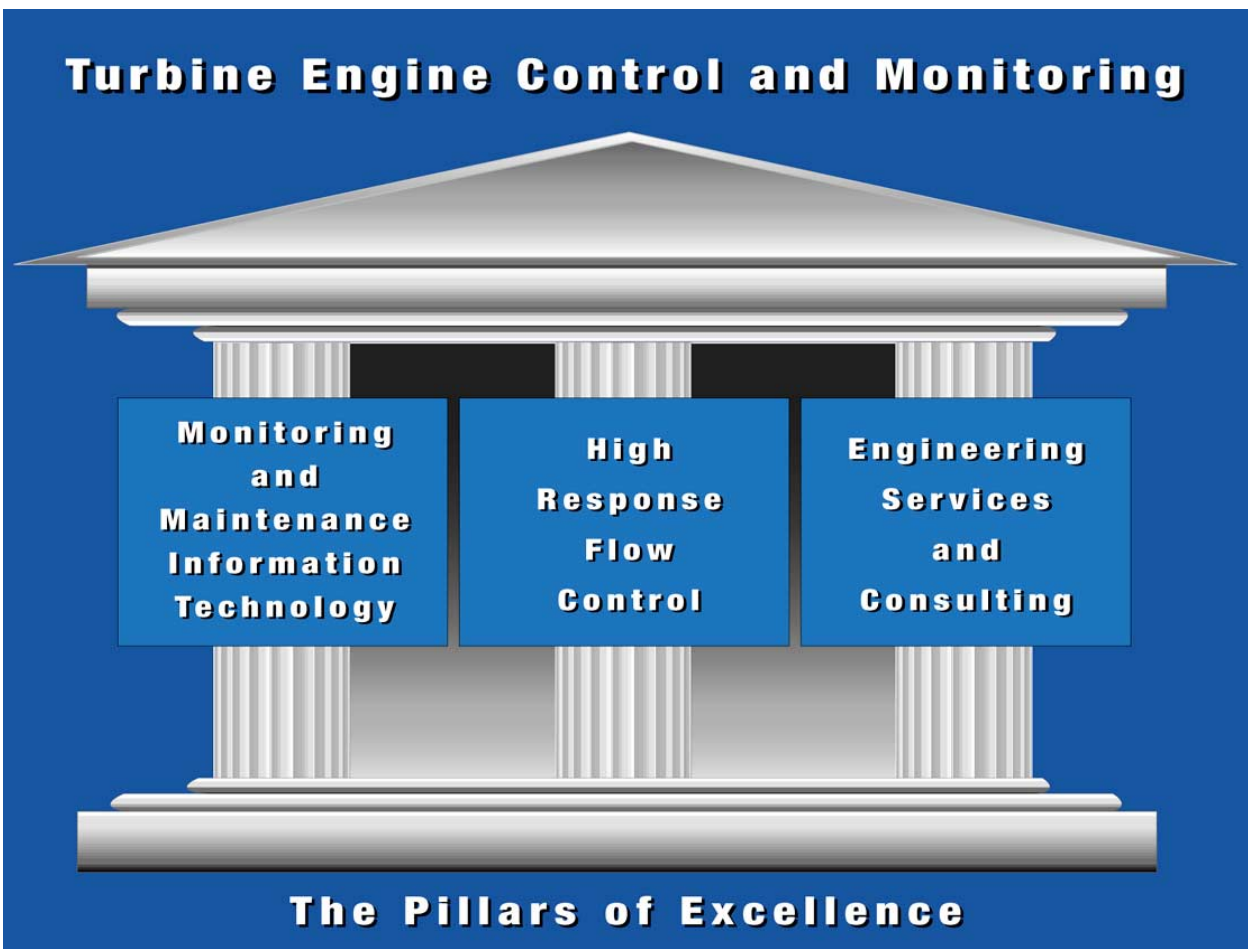
Paper 12: Discussion

Question from H Pfoertner – MTU, Germany

Creep life usage is heavily dependent on temperature. Does the cruise segment, as considered in your analysis, really contribute a significant percentage of total creep damage?

Is it necessary to change the control laws to change cruise speeds, surely that could be readily achieved by the pilot?

Presenter's Reply

Your comment on cycle-independence for creep and rupture damage is correct; these types of damage depend mostly on temperature and pressure.

Of course, it is possible for the pilot to set the cruise speed but the pilot requires some instructions from a flight management or mission computer to know the required setting. To make optimised recommendations, such computers require inputs of usage tracking information from a controller or diagnostic unit like the one described.

Damage Tolerance Assessment of Aging Nene X Turbine Discs

W. Beres
National Research Council of Canada
1500 Montreal Road
Building M-7
Ottawa, Ontario K1A 0R6
Canada

A.K. Koul
Life Prediction Technologies Inc.
P.O. Box 46125
2339 Ogilvie Road
Ottawa, Ontario K1J 8M0
Canada

ABSTRACT

The paper describes the application of the damage tolerance methodology to predict a safe inspection interval (SII) for the Nene-X engine turbine disc. The fracture critical location was established on the basis of stress analyses performed using 2D and 3D finite element models. To establish the stress intensity factor dependence on crack size in the fracture critical location of the disc, finite element based fracture mechanics analyses were conducted for both through-thickness and thumbnail cracks with different surface-length to depth ratios. Fatigue crack growth rate data were generated on compact tension (CT) specimens machined from a high time disc. Deterministic fracture mechanics (DFM) and probabilistic fracture mechanics (PFM) calculations were performed to compute a safe inspection interval for the disc.

1. INTRODUCTION

NATO countries are currently faced with the need to operate fleets of mature gas turbine engines. Because of diminishing resources for new equipment, the prospects of replacing these engines with new ones are not good at present. How long such engines can be kept in service safely, without replacing a significant portion of their aging structural components, has become a growing concern to engine life-cycle managers, due to uncertainties in residual lives. Another concern is the high maintenance cost associated with the replacement of durability-critical components, such as blades and vanes. The need to balance risk and escalating maintenance costs explains the growing interest in the application of life extension technologies for safely extracting maximum usage out of life-limited parts, [1], [2]. This paper describes the application of a damage tolerance approach to predict a safe inspection interval (SII) for the Nene-X engine turbine disc.

Nene-X engines power the Canadian Forces (CF) CT-133 aircraft. The original low cycle fatigue (LCF) life limits, also called the safe life (SL), for critical rotating components of Nene-X engines were calculated by the engine manufacturer, Rolls-Royce Ltd, Bristol, UK (RR) in the 1970s. At that time, RR had recommended a SL expressed in number of cycles, which when converted to flight hours, using a then specified number of LCF cycles per typical flight hour, yielded a 10,000 hours Nene-X turbine safe life. However, on the basis of the results of a more recent pilot survey conducted by the Canadian Forces (CF) and an analysis of this survey by RR, the factored exchange rates were revised. As a result of this revision, the safe lives of critical Nene-X components, expressed in hours, were reduced substantially. One of the most severely affected components of the engine was the turbine disc since approximately 25% of the discs in CF operation had exceeded the revised safe life limit. These parts needed to be replaced, however no spares were available. To maintain operations, it was decided to investigate the use of a damage tolerance based, safety by inspection, life cycle management scheme for this critical Nene-X engine components.

To implement this approach, development work was needed to quantify the component damage tolerance in terms of fatigue crack growth rates, at the temperatures representative of the fracture critical locations of the disc, and to predict a fracture mechanics based safe inspection interval (SII). A key requirement of this analysis was the determination of the SII that would assure that an initially undetected crack growing in a component in service would be detected before it reached a critical length. This paper describes the SII prediction methods used for the Nene-X turbine disc and discusses the application of the damage tolerance based fleet management concept in the field.

2. DAMAGE TOLERANCE APPROACH

Under the safe life approach to life cycle management of turbine discs, the goal is to assure that only 1 in 1000 components likely develops a small fatigue crack at the end of a safe life period, Figure 1. The remaining 999 components clearly have some structural capability at the end of their safe design life. Continued safety of these components can be assured through a damage tolerance based safety by inspection life cycle management approach which relies on nondestructive inspection of components at overhaul.

Damage tolerance based life cycle management procedures assume that the fracture critical locations of a component contain cracks of a size just below the detection limit of the non-destructive inspection (NDI) technique used to inspect the discs at overhaul. The crack is then assumed to grow during service in a manner that can be predicted by linear elastic fracture mechanics or other acceptable methods, until a predetermined dysfunction limit is reached, beyond which the risk of failure due to rapid crack growth becomes excessive. The rates of crack growth and the dysfunction crack sizes are established analytically, based on the best estimates of service loads and material properties. The time or number of fatigue cycles required to grow the assumed crack (a_i) to its dysfunction size (a_d) is then used to define a Safe Inspection Interval (SII), usually by dividing the life to dysfunction by a safety factor. Probability of Detection information is also considered in the analysis.

This life cycle management concept is illustrated in Figure 2, which shows that at the end of one SII, all components are inspected and crack-free components are returned to service for another SII. This procedure can be repeated until a crack is found. In this manner the components are retired on an individual basis when their condition warrants such action. Usually deterministic fracture mechanics calculations are used to predict SII and probabilistic fracture mechanics methodologies are used to quantify risk. The US ENSIP damage tolerance approach uses some quantitative measures of the maximum crack size that may be missed during depot level inspection as the starting point for damage tolerance analysis.

Some assumptions have to be made in the damage tolerance assessment of old hardware due to a lack of availability of the detailed technical data. In the approach reported here it was assumed that

- cracks in the component are large enough to grow according to the Paris law,
- growth of the three-dimensional cracks is governed by the stress intensity factor at the deepest point,
- the effect of minor cycles can be neglected,
- only a one dimensional stress state is driving the crack,
- the temperature distribution in the disc can be inferred from the temperature values at the disc rim and the disc bore locations,
- the effect of compressive residual surface stresses can be neglected.

Conservative safety coefficients were used during the analysis to compensate for these simplifying assumptions.

3. STRESS ANALYSIS

Both two and three-dimensional (2D and 3D) finite element (FE) models of the disc were built. MSC.PATRAN and MSC.NASTRAN were used to perform modelling and numerical calculations. Thermal and mechanical loads were considered in the analysis. The disc operating temperature was determined from the data provided by Rolls-Royce Canada (RRC). The centrifugal force and fir-tree pressures were calculated using the Nene-X engine maximum operating rotational speed value.

A 2D simplified model of the turbine disc was analysed first. The results showed that the von Mises stress in the center of the disc was 53% of the UTS, a level which closely matched the data obtained from the engine manufacturer.

Ten different mesh patterns for FE analysis were generated in 3D to establish an optimum balance between numerical accuracy and available computational capacity. The 3D FE model used represented a disc segment of 13.33° angular section comprising two fir-trees with a fine mesh in one fir-tree and a coarser mesh in others as shown in Figure 3. Solid elements with 20 and 15 nodes were used to construct the model. The 3D disc model had 228,825 degrees of freedom (DOF).

Symmetrical boundary conditions were added at the isolated surface of the FE model. The blade centrifugal force was applied as an external load. The interaction of the blade and the disc was simulated as a uniform pressure applied to the lower surfaces of the fir-tree serration of the disc. The calculated pressure corresponded to the disc maximal rotational speed. In addition to mechanical loading, a thermal gradient was applied to the disc. This gradient was calculated on the basis of the boundary temperature values of 200°C at the disc center and 430°C at the rim using the heat transfer analysis capabilities of MSC.NASTRAN. Since the engine is primarily used in a cyclic mode, no hold time effects were considered in this study.

A submodelling approach [3] was used to increase the calculation accuracy in the critical area of the disc. In this approach, the global model used a 13.33° angular section that had already been analysed to identify an area with the highest stress level. This area was then isolated to build a local model for subsequent detailed analysis. The mesh pattern for this local model comprised one fir-tree only with a considerably refined mesh when compared to the global model. The displacements at the separation boundaries, the temperature distribution at the FE nodes as well as the pressures on the fir-tree serration derived from the global model were transferred to the local-model. To assess solution convergence, the model was further refined by increasing the number of finite elements in the disc thickness direction. This approach increased the numerical accuracy for the available computer resources.

The disc center and the bottom serration of the fir-tree were identified as two areas of high stresses in the 3D FE analyses. In the disc center, the highest von Mises stress reached 53% of the material UTS. In Figure 4, which shows the geometry of one fir-tree, Curves A and B are located at the root of the fir-tree and connect the front and back faces of the disc. Curves C and D are located at the center of fir-tree thickness along the circumferential direction. The highest von Mises stress is present at the intersection of curves B and D. Figures 5 and 6 provide details of the von Mises stress distributions at the highest stress location in the fracture critical area of the disc [4].

The 3D FE analysis confirmed that the root of the bottom fir-tree is the primary fracture critical location of the disc. These findings were further confirmed upon examining the

engine operational logs where it was indicated that in the early 1970's, cracks had been found in the bottom serration region of Nene X disc.

4. FRACTURE MECHANICS ANALYSIS

The quantitative dependence of the stress intensity factor (SIF) on the crack depth is an important factor in the application of deterministic and probabilistic fracture mechanics (DFM/PFM) analyses for predicting a SII for the component.

Taking into account the length of the crack that can be missed during depot level inspection using the liquid penetrant inspection (LPI) technique, and utilising the results of a previous demonstration program performed on stainless steel compressor discs [5, 6], through-thickness and thumbnail cracks that were 4 mm and 8 mm in depth were studied. These crack depths corresponded to surface crack length in the range of 12 to 32 mm depending on the assumed semi-elliptical crack shape expressed by 2c/a ratio. In the analysis, the crack growth plane was assumed to be perpendicular to the lowest serration of the fir-tree as well as the disc radial line. This was based on previous operational experience with the engine and the stress analysis results that showed that the maximum von Mises stress direction at this fracture critical location lay in the radial direction.

In the FE based fracture mechanics modeling of the turbine disc, cracks were embedded at the fracture critical location. To properly model the stress field singularity in the crack vicinity, 3D singular elements were used around the crack front in the 3D finite element models. These elements were arranged by moving finite element middle nodes to the quarter point positions along element edges for wedge (PENTA) elements. The singular elements must be small enough to be fully included in the entire singularity dominated region in the vicinity of the crack front. Therefore, their sizes were carefully chosen to assure accuracy and convergence to obtain a finite element model that could be solved using available computer facilities.

The extraction of SIF from the finite element results can be done using field extrapolation near the crack tip or utilizing the energy release rate when a crack propagates. The methods based on stress field approximation require a finer mesh to produce a stress gradient around the crack tip, but recent findings [7] suggest that the displacement extrapolation technique can give very accurate predictions, even for a course mesh, if a good angular discretization is made around the crack tip region. This method was thus used for SIF recovery from the finite element results. The choice was mainly dictated by the features of the commercial software package (MSC.NASTRAN) that was available to the authors. The displacement approximation method uses nodal displacements, which are a primary output of the FE program. Three variations of the displacement field approximations in the SIF extraction process were used for comparison. They were: the method described by Shih *et al.* [8], the method presented by Chen and Kuang [9], and the method proposed by Chan *et al.* [10], which is the original formulation of the displacement approximation method. All three methods consider displacements at different nodes. A disadvantage of all three methods is that the user has to decide whether plane stress or plane strain conditions are operative ahead of the crack front. In the 3D FE calculations, plane strain conditions were assumed because of the large thickness of the disc in the fir-tree as compared to the crack sizes analysed. In addition, Newman *et al.* [11] have shown that, in the 3D case, the state of stress around the crack front is nearly plane strain, while the global deformation is accurately modelled by plane stress conditions.

For thumbnail cracks, surface crack length (2c) to crack depth (a) ratios of 3:1 and 4:1 were assumed. The aspect ratio 2c/a of 3:1 is often observed in aero engine discs, whereas a 2c/a ratio of 4:1 represents the worst case assumption. The relationships between the stress intensity factor K_I and the surface crack length (2c) for thumbnail surface cracks, embedded

in the disc fracture critical location, with aspect ratios 2c/a of 4:1 and 3:1 are shown in Figure 7.

Using our past operational experience with gas turbine critical engines parts and the FE calculation results, an 8 mm deep thumbnail crack was selected as the dysfunction crack size for the disc. This is because the K_I value at the crack tip for a 2c/a ratio of 3:1 was approximately 45 MPam$^{1/2}$, which corresponds to 50% of the experimentally obtained fracture toughness (K_{IC}) value of 90 MPam$^{1/2}$ for the disc material.

5. FATIGUE CRACK GROWTH RATE

Upon reviewing the mission profile and the engine usage data, it was concluded that cyclic usage was the primary driver for crack initiation and growth processes in the Nene-X disc. Since the component is operating at a homologous temperature less than 0.4 under predominantly cyclic usage, the contribution of creep towards transgranular crack propagation was neglected. Therefore, fatigue crack growth rate (FCGR) data as a function of ΔK were generated on compact tension (CT) specimens machined from the high time disc and these data were used in the damage tolerance analyses. The turbine disc is made out of Rolls Royce modified Type 409 stainless steel. The high time disc was selected to account for any service-induced microstructural degradation effects on crack growth. The CT specimens, conforming to ASTM E-647 specifications, were machined from the material located close to the disc bottom rim serration. A CT specimen thickness of 13 mm was used to ensure that plane strain conditions prevailed ahead of the crack tip in all cases.

The CT specimens were pre-cracked in fatigue at room temperature to develop a sharp crack prior to cyclic loading using servo-controlled hydraulic test machines. All FCGR tests were performed in air at 430°C, which is representative of the disc rim temperature. Crack growth as a function of the number of cycles (N) was monitored using an automated DC-PD technique [12]. The crack length versus the number of cycles data, together with calibration curves, were used to plot FCGR as a function of ΔK.

The data show the existence of two crack growth regimes, the Paris regime at lower ΔK values up to 55 MPa√m, and the tertiary regime at higher ΔK values of the order of 55 to 65 MPa√m. The least squares method of linear regression was used to obtain the FCGR versus ΔK relationship in the Paris regime:

$$\frac{da}{dN} = C(\Delta K)^n$$

The parameters for the mean line was found to be C=1.29x10^{-7} mm/cycle, n=2.28 whith ΔK expressed in MPa√m . The conditional standard deviation was calculated to account for the scatter in the FCGR results. The parameter of the upper bound line of the scatter band was estimated as C=1.50x10^{-7} mm/cycle.

A power exponent of 2.28 in the Paris regime obtained from experiments is well within the typical range (2–4) observed for most stainless steels and superalloys under intragranular fracture conditions. The final crack lengths at specimen rupture were also measured at 430 ºC to compute the fracture toughness for the material. The measured K_{IC} values were in the range of 87 to 95 MPam$^{1/2}$.

The fracture surfaces of all failed CT specimens were examined by scanning electron microscopy. All specimens revealed classical flat, occasionally striated, intragranular fracture characteristics. Such features are typically observed in most stainless steel materials.

6. DAMAGE-TOLERANCE BASED LIFE-CYCLE ANALYSIS

6.1 METHODOLOGY

Both, deterministic fracture mechanics (DFM) and probabilistic fracture mechanics (PFM) methodologies were used to predict the safe inspection interval for the Nene-X turbine disc. DFM methods are used to assess the damage tolerance of a part containing a crack at the detection limit of the inspection technique and using material data conforming to minimum assured material properties while PFM methods are used for assessment of the risks associated with various inspection strategies for engine component maintenance and life cycle management. The initial surface crack size used in DFM analyses corresponded to the 90% probability of detection (POD) with 95% confidence (90/95 POD) for the LPI techniques shown in Figure 8. A flow diagram of the DFM/PFM methodology is presented in Figure 9, while the basics and details of the both DFM and PFM methods are described elsewhere [5, 6].

Each set of simulated failure data obtained in PFM analyses was evaluated statistically. Two or three parameter Weibull, lognormal or gamma distributions were used as probability distribution functions (PDF) candidates which fit the simulated data [13]. Probability-plot-correlation-coefficient plots were used to initially estimate shape parameters for Weibull or gamma distributions. This determined which specified distribution family provides the best fit to the simulated disc failure data. Next, the three distributions were fitted to the data using both, the least square and the maximum likelihood methods. Finally, the Anderson-Darling goodness of fit test was performed for fitted PDF curves. This test is a modification of the Kolmogorov-Smirnov (K-S) test which gives more weight to the tails than the K-S test [14]. Sensitivity analysis was also performed to find the effect of the various input parameters on the calculated SII.

In-house PFM and DFM software packages were used to perform disc failure simulations, while MATLAB®, DATAPLOT [15] and in-house statistical analysis software were used to analyse the simulation results.

6.2. SAFE INSPECTION INTERVAL (SII) PREDICTIONS

The DFM calculation was performed to compute the surface crack length versus the number of cycles curves for the Nene X turbine disc [16]. A typical crack propagation curve for the disc, covering a surface crack length range of 6.0 mm to 32.0 mm, as a function of the number of cycles, is shown in Figure 10. The effect of the sensitivity and reliability of an NDI technique on SII predictions is clearly demonstrated in this figure because the crack propagation interval (CPI) value changes significantly with the initial surface crack length. For example, for a surface crack length of 6 mm, the CPI is 22,300 cycles while the CPI reduces to approximately 8,300 cycles for the initial crack length value of 16 mm.

A scatter factor (safety factor) must be defined. This safety factor is based on confidence in the analysis, material property data, usage and inspection capability. Typically this safety factor is between 2 and 5 based on representative testing, hence the SII would be between 4,400 and 11,000 cycles.

PFM analysis was used to simulate the consequences of missing a crack during inspection. The PFM approach uses the same linear elastic fracture mechanics (LEFM) principles for calculating a SII but input parameters such as initial crack size, crack size dysfunction, constants of Paris equation are treated as random variables. A range of SII was calculated and appropriate values were selected to maintain a sufficiently low but cost-effective probability of failure. The distribution of surface crack size missed was used randomly as the starting condition for each simulation. PFM simulation using 5000 point and assuming using

the worst case scatter in the FCGR data, was carried out. In the case analysed, it was found that a log-normal distribution fits the simulated data better than either a Weibull or a gamma distribution. Typical cumulative probability distribution function (F) of cycles to dysfunction is presented in Figure 11 where normal deviate refers to the standard deviations of underlying normal probability distribution function. The 0.1%F which yields the number of cycles for which 1 in 1000 probability exists of a crack reaching dysfunction size were extracted from such plots. For the assumed scatter condition in the FCGR data, it was found that 0.1%F corresponds to 26,000 cycles.

Applying a safety factor of 2, the SII value of 13,000 cycles was calculated. Furthermore, assuming a usage of 5 cycles/hour for the engine, a SII of 2,600 engine operating hours is predicted.

7. EXPERIMENTAL VERIFICATION

Predicted SII are verified experimentally under simulated service conditions using a spin rig facility installed at the Institute for Aerospace Research of NRC. A damage tolerance test is being performed with this facility. For this test an artificial notch of 4 mm surface length and 1 mm deep was embedded in the Nene X turbine disc lowest firtree serration using the EDM technique. The disc was thoroughly inspected prior to the test using LPI and eddy current techniques. A custom made eddy current probe was used for inspections of the disc firtree serrations. No flaws were found in the disc during these initial inspections. The disc containing the artificial notch and undergoing spin testing is removed from the spin rig facility periodically and inspected using visual and eddy current based techniques. At the time of writing of this paper the disc has accumulated approximately 3000 cycles without any signs of a propagation of the embedded flaw. Spin rig testing of the disc is continuing.

8. CONCLUSIONS

The bottom serration region was determined to be the fracture critical location in the Nene-X turbine disc. The dysfunction surface crack length crack for the disc is estimated to be 32 mm using a range of assumptions for the 2c/a ratios in a crack of a semi-elliptical crack shape. This dysfunction crack size value was based on experimentally determined fracture toughness values of the rim material at an operating temperature of 430 ºC. The SII was computed on the basis of FCGR data alone, and no creep effects were considered in the analysis.

PFM calculations revealed that if the scatter in material properties is represented by the experimental scatter in FCGR data, a 1 in 1000 chance exists for a crack to reach the dysfunction size in 26,000 cycles, if the LPI technique alone is used to inspect the discs.

DFM calculations showed that the crack propagation interval for the Nene-X disc is of the order of 22,000 cycles.

The results presented in this paper, along with other data, permitted the CF fleet managers to make a decision regarding life cycle management of the Nene X engine fleet. Significant saving can be achieved by using the damage tolerance approach, because discs can be used beyond their OEM assigned safe life limit.

ACKNOWLEDGEMENTS

the finite element calculations performed by Dr. S.M. Cheng, the crack growth testing done by Ms. R. He and also contributions made by Dr. X. J. Wu.

REFERENCES

1. Recommended Practices for Monitoring Gas Turbine Engine Life Consumption, NATO RTO Working Group AVT-017 Report , RTO Technical Report 28, April 2000.

2. Immarigeon, J-P., *et al.*, Life Cycle Management Strategies For Aging Engines, NATO RTO Specialist's Meeting on Life Management Techniques for Aging Air Vehicles, Manchester, UK, Oct 8-11, 2001, Paper No. 17.

3. Cormier, N.G., et al., Aggressive submodelling of stress concentrations, International Journal for Numerical Methods in Engineering, 1999, 46(6), pp. 889–909.

4. Cheng S. and Beres W. Stress and Fracture Mechanics Analysis of a Turbine Disc of Nene-X Engine,**,** *Report of the Institute for Aerospace Research, National Research Council Canada*, LTR-ST-2139, 1998.

5. Koul, A.K., Bellinger, N.C. and Fahr, A., Damage-tolerance-based life prediction of aeroengine compressor discs: I. A deterministic fracture mechanics approach, International Journal of Fatigue, 1990, 12(5), pp. 379–387.

6. Koul, A.K., N.C. Bellinger and Gould, G., Damage-tolerance-based life prediction of aeroengine compressor discs: II. A probabilistic fracture mechanics approach, International Journal of Fatigue, 1990, 12(5), pp. 388–396.

7. Guinea, G.V. *at al.*, K_I evaluation by the displacement approximation technique, Engineering Fracture Mechanics, 2000, 66(3), pp. 243–255.

8. Shih, C.F., deLorenzi, H.G. and German, M.D., Crack extension modelling with singular quadratic isoparametric elements, International Journal of Fracture, 1976, 12, pp. 647–651.

9. Chen, L.S. and Kuang, J.H., A modified linear extrapolation formula for determination of stress intensity factors, International Journal of Fracture, 1992, 57, pp. R51–R58.

10. Chan, S.K. Tuba, I.S., and Wilson, W.K., On the finite element method in linear fracture mechanics, Engineering Fracture Mechanics, 1970, **2**, pp. 1–17.

11. Newman, J.C., Jr., Booth, B.C., and Shivakumar, K.N., A elastic-plastic finite element analysis of the J-resistance curve using a CTOD criterion, *Fracture Mechanics: Eighteen Symposium, ASTM STP-945, D.T. Reed and D. Reed, Eds., ASTM*, Philadelphia, 1988, pp. 665–685.

12. Pishva, R. *et al.*, DC-PD technique for crack length measurements at elevated temperatures, *Report of the Institute for Aerospace Research, National Research Council Canada*, LTR-ST-1635, 1987.

13. Lawless, J.F., Statistical Models and Methods for Lifetime Data, Wiley, 1982.

14. MIL-HDBK-17-1E, Vol 1, Guidelines for Characterization of Structural Materials, Chapter 8 Statistical methods. 1997.

15. DATAPLOT On-line Documentation. National Institute of Standards and Technology, U.S.A., 2001.

16. Koul, A.K., Beres, W., Cheng, S.M., He, R. and Wu, X.J., Predictions of safe inspection intervals for the Nene-X turbine disc, *Report of the Institute for Aerospace Research, National Research Council Canada,* LTR-ST-2142, 1998.
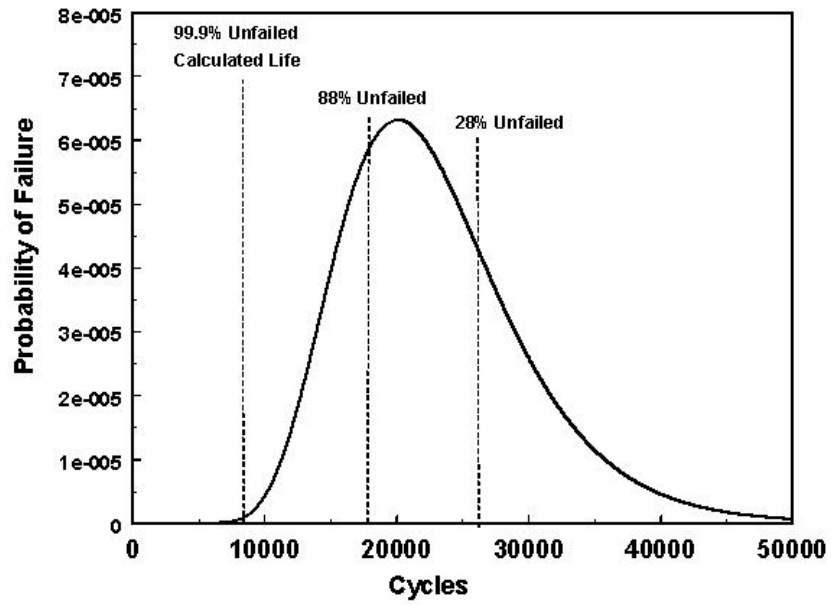
Figure 1. Probability of failure in the safe life approach.
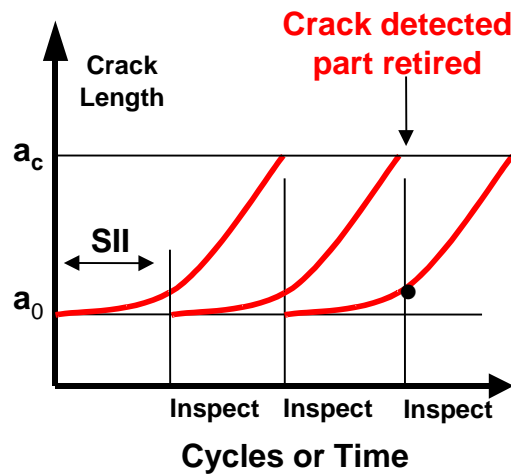
Figure 2. Schematic representation of the damage tolerance based life cycle management approach.
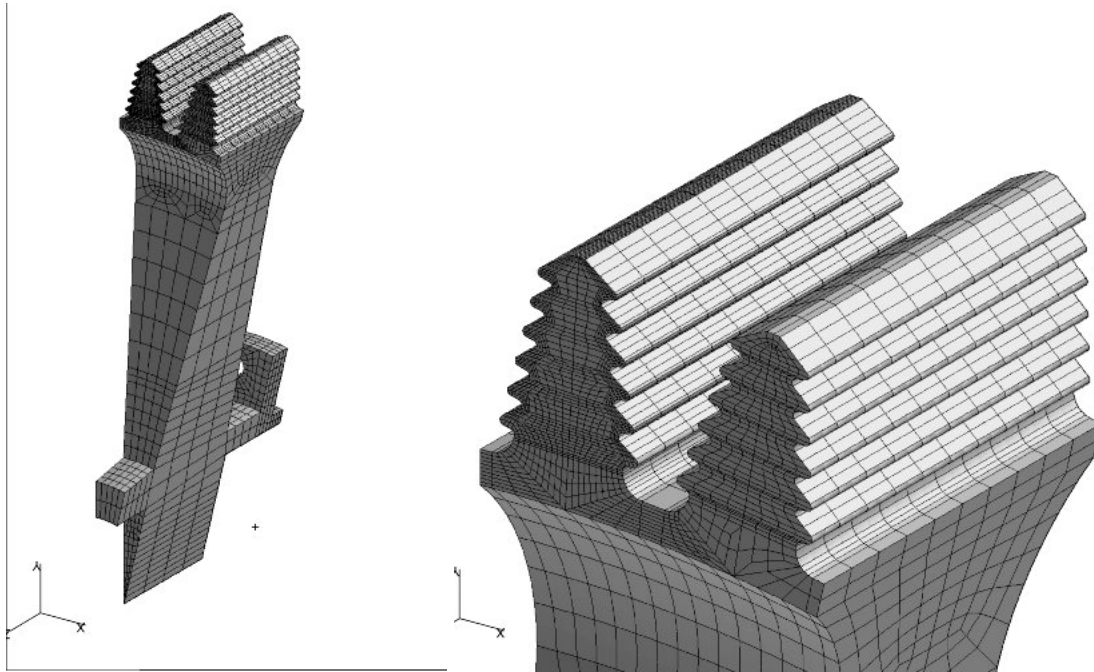
Figure 3 FE model for the turbine disc
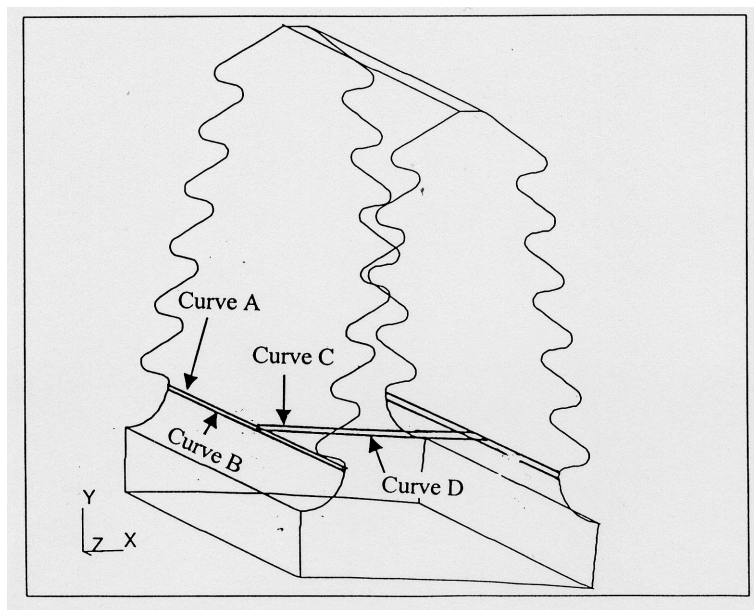
Figure 4. Geometrical configuration of the fir-tree.
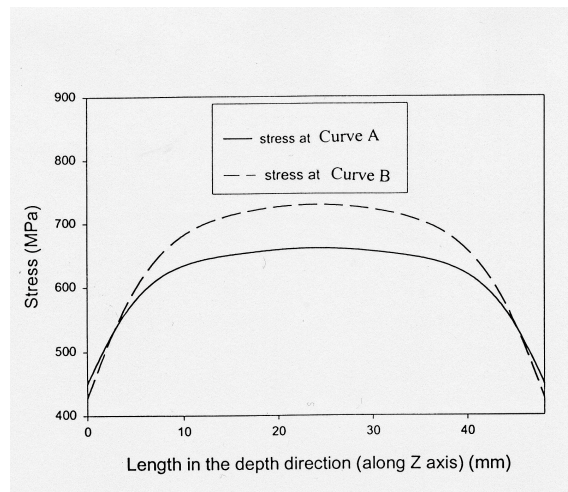
Figure 5. Von Mises stress distribution in the disc thickness direction below the innermost serration of the disc. This is the highest stress region.
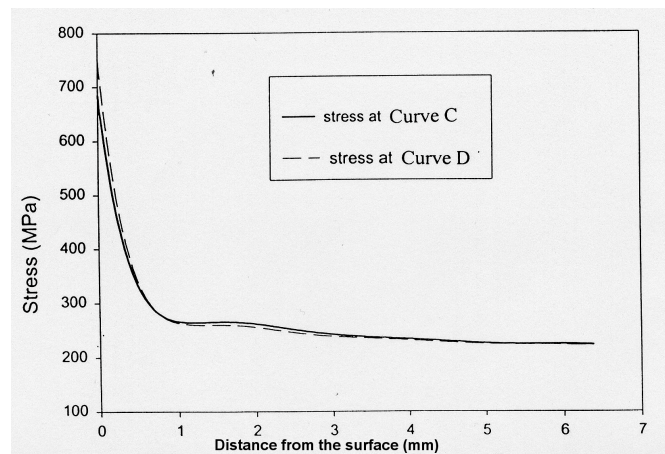
Figure 6. Von Mises stress distribution in the depth of the material starting from the centre of the lowest serration.
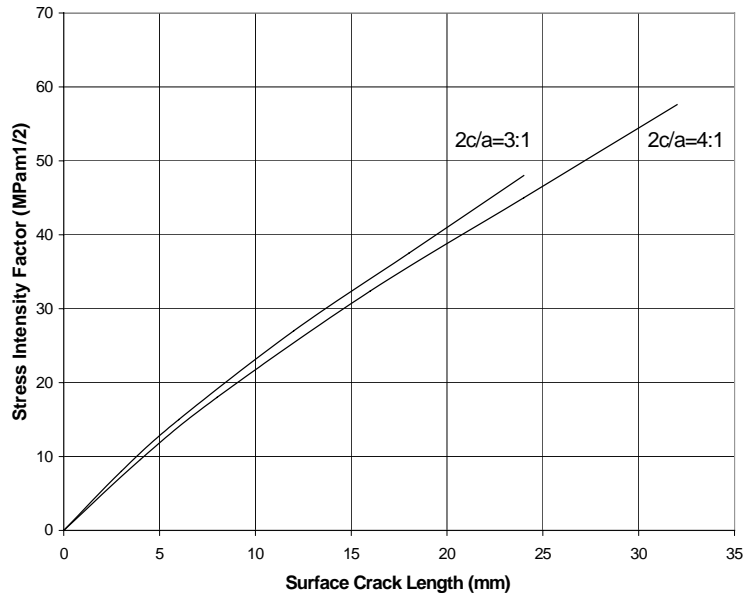
Figure 7. Stress intensity factors for two semi-elliptical cracks embedded in the lowest serration of the firtree.
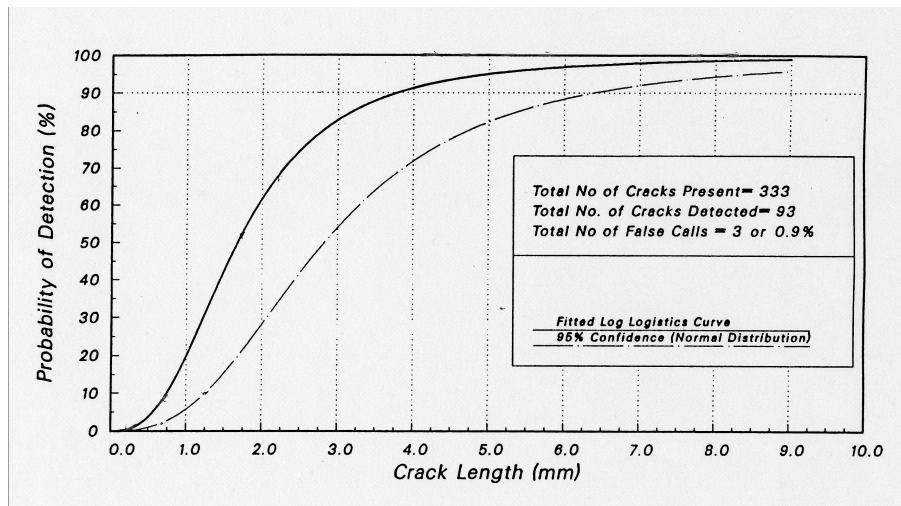
Figure 8. POD for natural cracks in Fe-Ni-Cr alloy turbine disc using the LPI technique 9 (after Koul et al. [5], [6]).
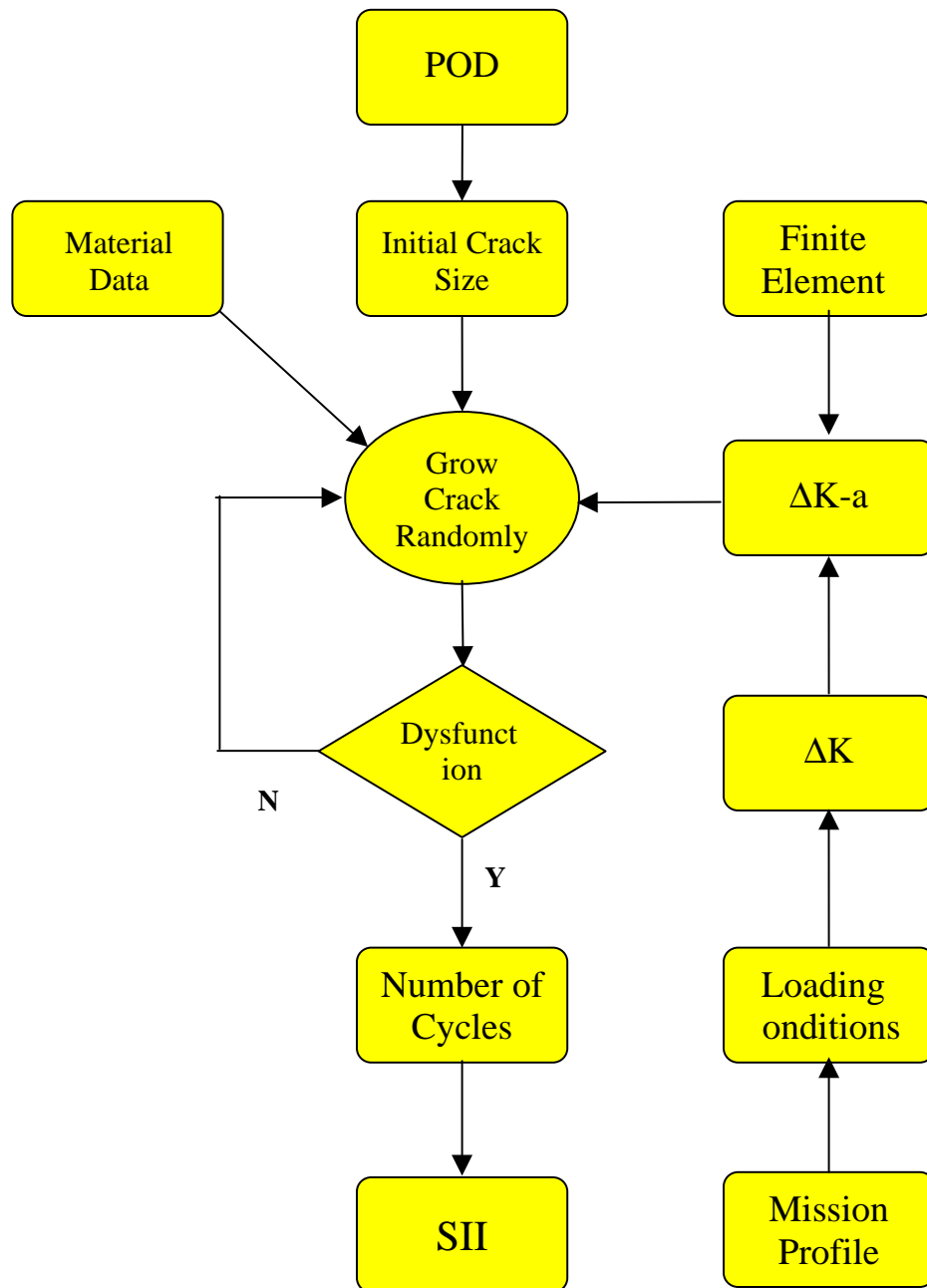
Figure 9 A flow diagram of the DFM and PFM program used to calculate SII for the Nene-X disc.
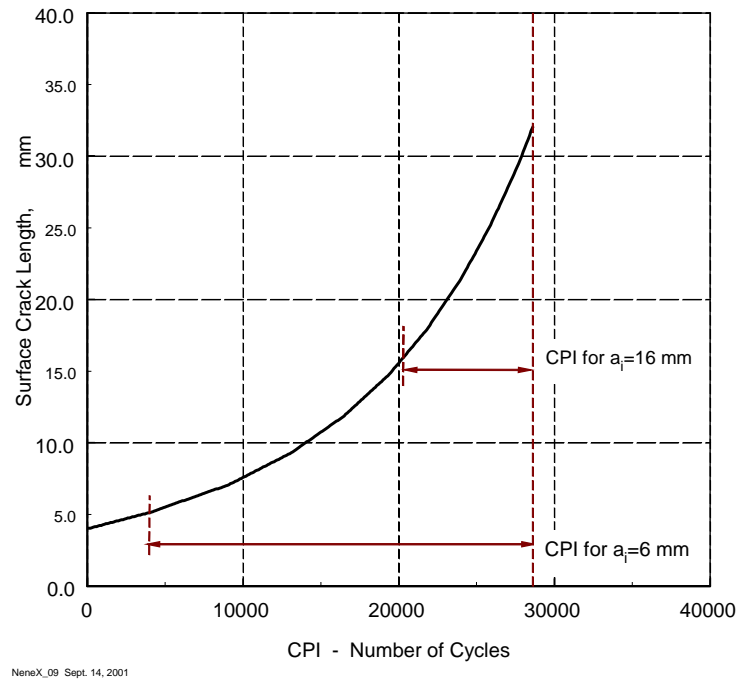
Figure 10. Damage tolerance based life cycle management curve for Nene-X turbine discs using 90/95 POD value of the LPI technique as the detection limit.

No. of Disks = 4821
Median = 42000.62 Cycles
0.100 % F = 26294.79 Cycles
Lambda = 10.65
dzeta = 0.15
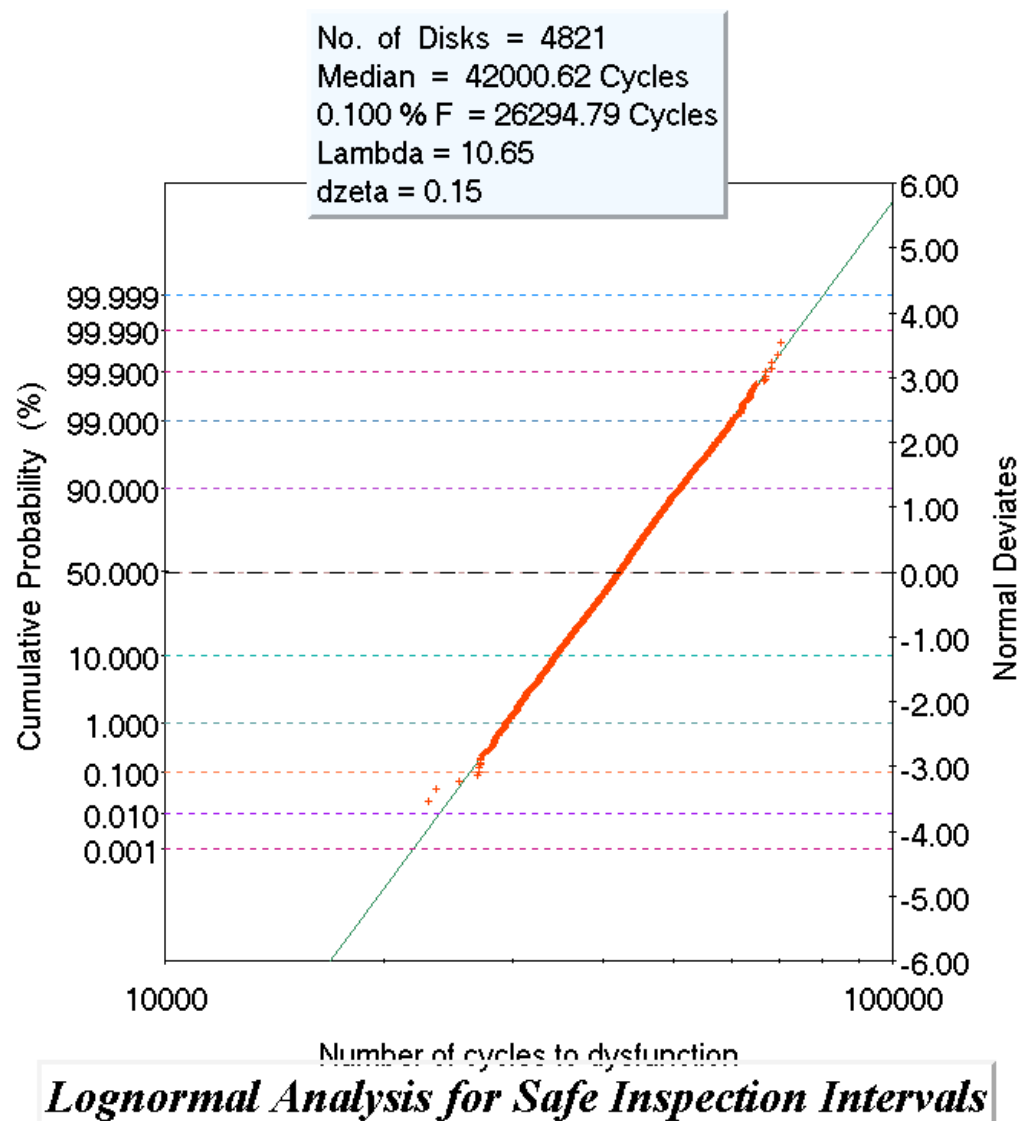
Figure 11. Lognormal analysis of PFM generated data for Nene-X turbine discs simulating the effect of worst possible scatter in FCGR data and uncertainties associated with the LPI technique.

Paper 14: Discussion

Question from P R Parolo – DGTA, Australia

How did you determine the Probability Of Detection (POD) for your eddy current inspection procedures?

Presenter's Reply

We utilised an extensive in-house database of POD on a wide variety of materials and crack data.

Question from Dr B Wicks – DSTO, Australia

In this case, you have looked at the critical location for crack initiation. How can you be assured that there is not another critical location for crack propagation that has a faster rate of crack growth than the one you have analysed?

Have you carried out this analysis for all critical locations on the disc?

Presenter's Reply

Spin rig testing was used to validate our assessment. Possible cracks initiating from other locations would be detected through NDI of the entire disc after rig testing.

Question from D Shepherd - QinetiQ, UK

You have put a lot of effort and time into developing a damage tolerance approach for this component. In view of the long crack-growth life available, would it not have been simpler and more cost-effective to implement a crack-growth based safe-life extension?

Presenter's Reply

Safe life is determined on the basis of a surface crack length of 0.8mm which, assuming that a surface crack length to crack depth ratio of 4 to 1 is observed in service induced cracks, corresponds to a crack depth of 200 microns. Assuming that most wrought disc materials possess an average grain size of 100 microns, the safe-life criteria then essentially considers time or cycles to metallurgical crack nucleation (between 1 and 3 grain diameters) in a disc. Crack-growth based safe-life extension is only possible if a crack, nucleated at the fracture critical location, is allowed to propagate beyond the 200 micron depth range to, say, 1000 microns, corresponding to 10 grain diameters. Within this range of crack depth, a typical disc material would be expected to exhibit short-crack growth behaviour, a phenomenon that is poorly understood at this time. Particular difficulties have been encountered in measuring short-crack growth rates and developing reliable empirical or metallurgical models for describing the short-crack growth behaviour. These limitations would impose unnecessary uncertainties on the predicted life-extension interval. It is, therefore, advisable to extend usable life on the basis of long-crack growth behaviour using damage tolerance concepts, since empirical as well as mechanistic models for describing the long-crack growth phenomenon, along with experimental techniques for measuring coupon and component level long-crack growth data are well established. In our opinion, crack-growth based safe-life extension should only be used in situations where it is not possible to implement a damage tolerance based safe inspection interval in the field.

Critical Part Life Extension Efforts
in a Military Engine

Robert L. Kiang
Naval Air Systems Command
Air-4.4.7.2
38142 Shaw Road
Patuxent River, MD 20670
United States

Abstract

Three specific schemes aimed at increasing critical part lives of a
military engine are described. Quantitative life extensions, as a result
of implementing these schemes, are given when appropriate. Any of
these schemes could be applicable to other engines when sufficient
field usage data are available.

1.0 Introduction

A critical part is defined as a part whose failure will result in a catastrophic loss of the
engine, the aircraft, and possibly human lives. Every gas turbine engine, with its inherent
high pressure, high temperature, and high rotational speed operation, contains a number of
such parts. When a new engine is first introduced for fleet use, various uncertainties ranging
from material characteristics to the type of missions that will be flown prudently dictate that a
rather conservative low cycle fatigue (LCF) life is released for each critical part. Life
extension becomes possible as field experience and technological advancements are
incorporated.

This turbofan engine was originally developed in the 1970s. It was upgraded for US Navy
use and was fielded in 1993. Since then, as part of the component improvement effort, the
lives of many critical parts have been re-evaluated and extended. For instance, the life of the
high pressure turbine (HPT) disc was originally released at 8,900 LCF cycles. The
performance of several spin tests, guided by refined 3-D finite element analyses, allowed the
life to be increased first to 10,300 then to 15,400 cycles.

In addition to spin tests and state-of-the-art analyses, a variety of other schemes have been
employed to specifically improve the lives of the critical parts in this engine. Three of these
schemes are summarized in this paper. They are (1) Statistics Based Fill-in Exchange Rates,
(2) Mission Specific Exchange Rates, and (3) High Resolution Airborne Data Recorder.

2.0 Statistics Based Fill-in Exchange Rates

The Navy aircraft under discussion is equipped with an Airborne Data Recorder (ADR).
It records among other airframe and engine parameters, engine operating hours and LCF
cycles consumed in each flight. A critical part in the engine is retired before its LCF damage
accumulation exceeds the established limits. For various reasons from subsystem
malfunction to memory overflow, the ADR does not always capture 100% of the cycle

counts. The missing information, essentially the difference between the pilot reported flight hours and the ADR registered hours, have to be filled in with a fill-in exchange rate defined as the number of cycles per hour.

Figure 1 is a plot of the exchange rate data over time from a high pressure turbine disk segregated by engine builds. Each point on the graph is an exchange rate calculated from the ADR data, namely, cycles used and accumulated flight hours over several flights. As noted on the top margin of this graph, this engine has gone through two builds in the 3-1/2 year period shown. Build 1 has also been installed in two different aircraft resulting in three data sets. In data set 1, there are 18 data points. Missing are 13 data points, inferred from pilots reported data, due to either ADR malfunction or other types of errors. This translates to a data capture rate of 58%. In set 2, no data were captured. In set 3, the capture rate was 62%.
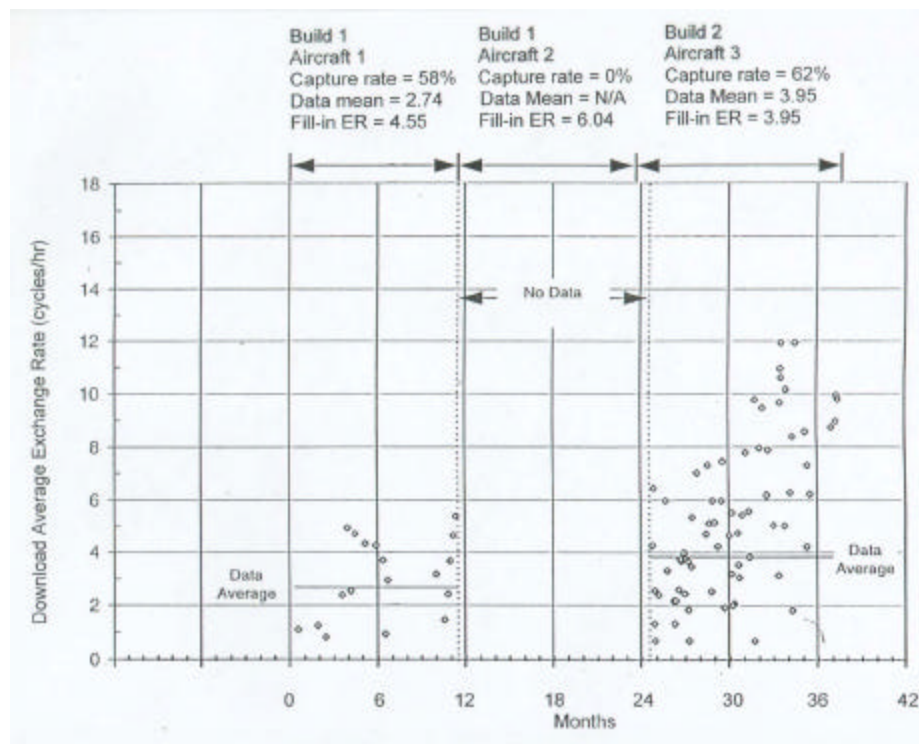
Figure 1 Exchange Rate Data of an HP Turbine Disk

Prior to 1998, the missing data were filled in with a set of "worst case" exchange rates derived from Weibull analyses. Using the example in Figure 1, the 13 missing data points in set 1 would each be assigned a fill-in exchange rate of 4.55 cycles/hour, significantly higher than the data average of 2.74 cycles/hour. Any flight in set 2 would be assigned an exchange rate of 6.04 cycles/hour, and the 38% missing data in set 3 would be assigned an exchange rate of 6.6 cycles/hour. This high degree of conservatism means a large number of critical parts are retired prematurely. An ad hoc procedure was adopted in 1998 to reduce conservatism. It was decided, based on a limited data analysis, that the worst case fill-in values would still be used if the capture rate in any particular engine build is below 60% (such as sets 1 and 2 in Figure 1). When the capture rate is above 60%, the average exchange rate from the captured data would be used as the fill-in value (as shown in Figure 1). The rationale for introducing such a threshold capture rate is of course the law of averages. Namely, one would not expect the missing data to be radically different from the vast majority of the captured data.

A statistically more rigorous methodology has since been developed to provide fill-in exchange rates. It owes its concept to the Student's t-law which can be found in most statistics books. The Student's t-law allows one to ascertain the value of the population mean from a given sample of data with known sample mean and standard deviation. In the case of the incomplete ADR data, the sample is the number of captured data points in a given engine build. The "population" is the larger set of data if all flights were captured. There are two important distinctions that preclude direct application of the Student's t-law. The first one being that the "population" referred to in the t-law is a sample of infinite size. The total number of data points, captured and missing, in a particular engine build is far from infinite. Thus using the Student's t-law would not be theoretically correct. The second distinction, a more troublesome one, is that the Student's t-function has only one independent parameter, namely, the number of samples, n. In the missing ADR data problem, there are two independent parameters: the number of captured data points in an engine build, n, and the capture rate, n/N, where N is the total "population" had there been no missing data. The methodology described below involves generation of an equivalent t-function with two independent parameters using available ADR data. More details of this methodology can be found in Ref 1. Use of this method can minimize premature retirement of expensive engine components while maintaining safe operation.

2.1 Methodology

The data available to us are contained in 282 data sets, each corresponding to either an engine build or an aircraft installation. That means for each of the four critical components (LP compressor drum, HP compressor drum, HP turbine disk, and LP turbine disk) that the ADR records their cyclic usages, there are 282 sets of exchange rate values or data points. Within each data set, there can be as few as two exchange rate values and as many as 130. The average number of points in a set is about 40.

In this exercise, we assume the number of points in a data set is the full "population" and denote that number by N. Random removal of points from this set will generate many subsets each has n points and a corresponding capture rate (n/N). Note that even though N is far less than infinite, we still define the full set as the population for ease of identification. The corresponding average of all N points will hence be denoted as the population mean, μ. The average of a subset is the sample mean, X. By this process of random removal, a (μ - X)/X versus n plot can be generated for a given N.

Figure 2 is such a plot for N = 80 (HPT data are used in this illustration). Within the 282 data sets, there are 36 sets that have 80 points or more. For sets that contain more than 80 points, excess points are removed by a random selection process so that each of the 36 sets starts with exactly 80 points, and a μ is calculated for each of these sets. Next, a point is removed, randomly, from each of these sets. Thirty six sample means with n = 79 are then obtained, from which 36 values of (μ - X)/X can be readily calculated. All 36 of these values are plotted along the abscissa value of n = 79. The process is repeated by randomly removing two points from each set resulting in further spreading of points at n = 78. As expected, the spread becomes wider and wider as n, or equivalently n/N, gets smaller. Assuming the vertical scatter seen along any value of n is Gaussian distributed, one can calculate the standard deviation of these 36 (μ - X)/X values. Two curves corresponding to +/- twice that standard deviation are plotted in this diagram. Since 2-sigma encompasses 95% of the area under a bell shaped curve, this means 95% of the points should lie between the two curves.
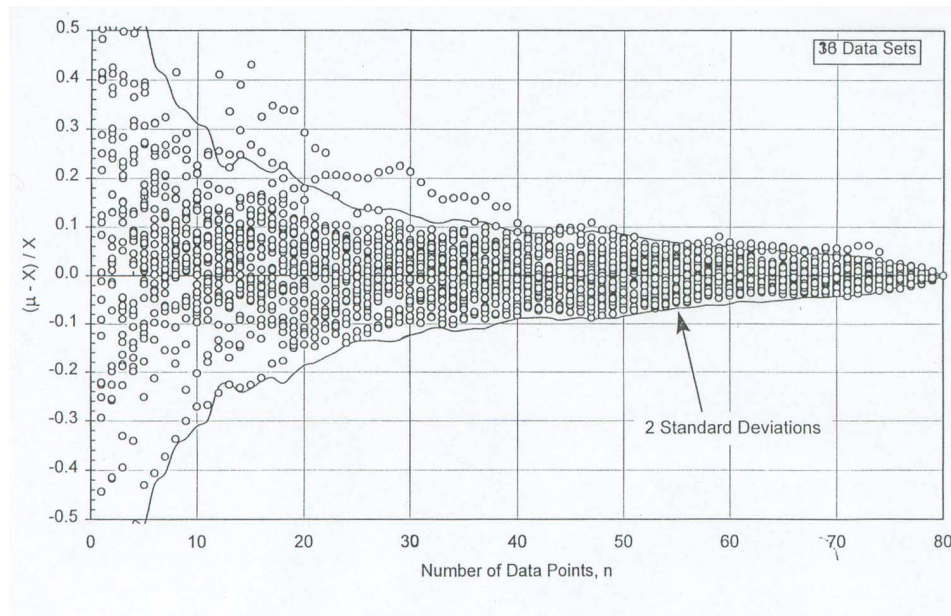
Figure 2
Effect of Capture Rate on Relative HPT Exchange Rate Means
(80 points per data set, i.e., N = 80)

As far as the exchange rate is concerned, the upper curve, along which μ > X, is of interest. Since the Gaussian distribution is symmetrical about its mean, the probability that a point lies above the upper curve is only 2.5%. In other words, the upper curve marks the boundary at which one has 97.5% confidence that the sample mean X will not be greater than the population mean μ and gives the quantitative value of μ - X. For instance, at N = 80 (that is the basis of Figure 2) and n = 40, or equivalently a capture rate of n/N = 50%, μ - X is expected (with 97.5% confidence) to be 0.1X. This upper curve, without the underlying points, is re-plotted in Figure 3.

Plots similar to Figure 3 have been generated for N = 90, 65, 50, 30, 20 and 10. From each of these 2-sigma plots, (μ - X)/X as a function of n and the capture rate can be determined. For example, in the case of N = 80 (see Figure 3), (μ -X)/X = 0.2 for n = 18 and a capture rate of 23%. Table 1 summarizes these relationships for all N including this example of N = 80. For N = 50, three random reduction exercises were performed resulting in three slightly different two-standard deviation curves, hence three sets of values. These were done to get a measure of the scatter from different random reduction exercises.

Number of points n versus capture rate from Table 1 are plotted as squares, along with a linear regression, in Figure 4. Area to the upper right of this linear fit marks the region where (μ - X)/X < 0.2, whereas that to the lower left marks the region where (μ - X)/X > 0.2. Also shown in Figure 4 are points and lines for (μ - X)/X = 0.05, 0.10, 0.15, and 0.25.

Table 1 Threshold n and Capture Rate for (μ - X)/X = 0.2 with 97.5% Confidence

N	90	80	65	50	30	20	10
n	21	18	16	13, 16, 17	13	10	7
Cap. Rate	0.23	0.23	0.25	.26, .32, .34	0.43	0.50	0.70
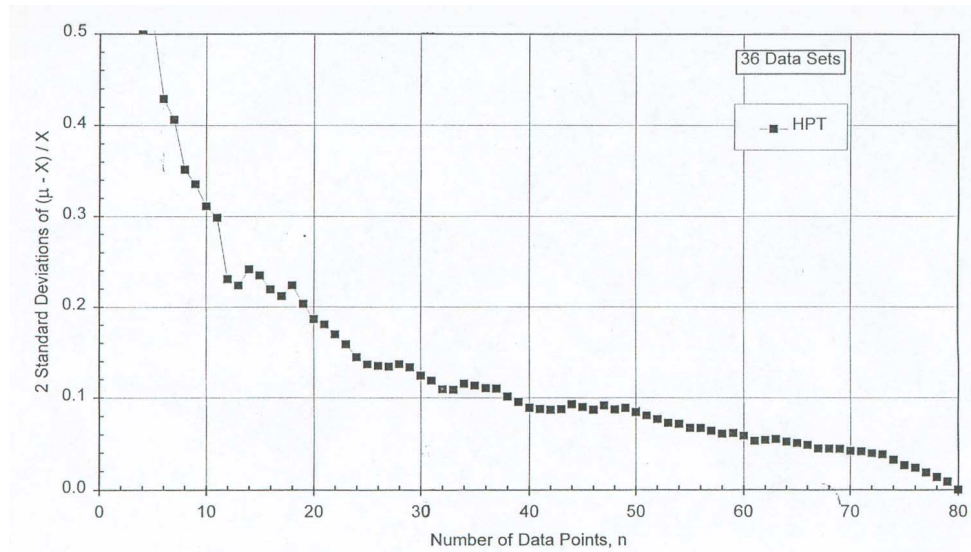
Figure 3
Two-Sigma of the Relative Exchange Rate Means
(80 points per data set, i.e., N = 80)
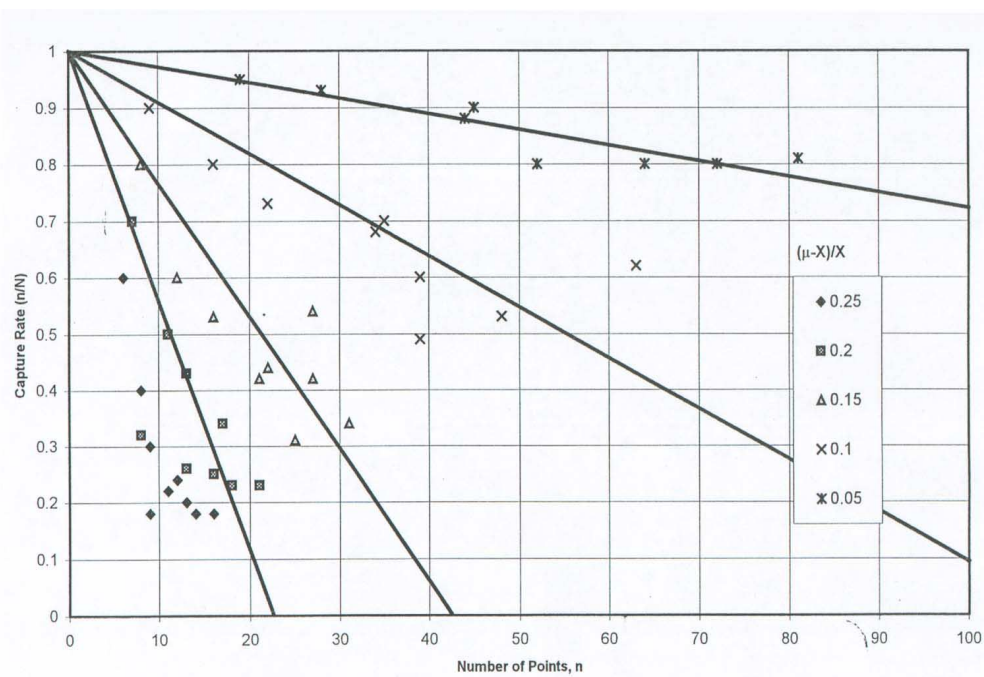
Figure 4 HPT Fill-in Exchange Rate Factor, (μ - X)/X

Figure 4 is the desired "t-function" with two independent variables n and n/N. This function is used to determine the fill-in exchange rate as follows.

1. Assemble an exchange rate data set for a specific engine build.
2. Determine the number of data points captured, n, and the number missing, N-n.
3. Calculate the average exchange rate X of the captured data.
4. Determine, from Figure 4, the value of (μ - X)/X corresponding to the n and n/N obtained in item 2. Interpolate if necessary.
5. Calculate the value of μ and use it to fill in all the missing data.

The linear regression lines in Figure 4 are made to converge at capture rate equals 1.0 and n = 0 because these values represent the physical limits of these two parameters. The lines' intersects with the x-axis, corresponding to a capture rate of zero, are equivalent to the Student's t-law. Indeed, Student's t predictions of (μ - X)/X from the individual 282 data sets (with a 97.5% confidence) are close to the results of Figure 4 at very small capture rates. (Note: A direct comparison to the Student's t prediction at n/N = 0 is not possible because for n = 0, i.e., no data captured, there is no standard deviation. Neither the Student's t-law nor the "t-function" for two variables derived above is meaningful.)

Even though we have illustrated our methodology using only the HPT data, similar data analyses have been done for the HPC, LPT, and LPC data.   Provided that sufficient exchange rate, or equivalently, cyclic usage data exist on any engine, the same methodology can be used to derive the "t-function" for a specific critical part.

2.2 A Critical Part Usage Example

As an example of how different fill-in methods would affect the cyclic usage of a critical part, we have chosen a low pressure turbine disk example. This disk has been installed in five different engine builds over its service life. The data capture rates by the ADR range from 0 to 91% as seen in Table 2. Thus, fill-in is needed in every one of the five builds. All three fill-in methods are applied for comparisons. In the worst-case fill-in scenario, it has also been determined that the fill-in value should be 11.9 cycles/hour. This value is used to calculate the fill-in cycles based on the missing flight hours. The resulting total usage is calculated to be 22,876 cycles. If on the other hand, the 60% capture rate cutoff method is used, the total usage is slightly less, at 22,768 cycles. Finally the "t-function" method is used to calculate the usage. As can be seen in Table 2, the worst case exchange rate is still used for build 3 because it has zero capture rate. The fill-in exchange rates for all other builds are determined by an n versus capture rate plot similar to that shown in Figure 4. Not only the subjectivity is removed, but in this case, the usage is reduced by 10% to 20,579 cycles.

To date, the lives of scores of critical parts in this engine are being tracked using this Student's t-function equivalent method and resulting in life extension of hundreds of flights hours for each part.

3.0 Mission Specific Exchange Rates

It is common knowledge within the engine lifing communities that part usage, or equivalently the exchange rate, depends upon the mission profile. Certain missions are inherently more damaging to a part than others. The fill-in methodology described in Section 2.0 is component specific but not mission specific. That is, when we have missing ADR data, statistically corrected fill-in exchange rates are used for each of the critical parts but the type

Table 2 Fill-in Comparisons

Build No.	1	2	3	4	5	
No. of Dnload, n	13	6	0	99	97	
Pilot Hrs	116	81	337	896	828	
ADR Hrs	93	74	0	526	446	
ADR Cycles	779	592	0	4374	3815	
Cap. Rate	0.80	0.91	0.00	0.59	0.54	
Fill-in Hrs	23	7	337	370	382	
Av. ER, X	8.4	8.0	N/A	8.3	8.6	
Worst Case Fill-in						
Fill-in ER	11.9	11.9	11.9	11.9	11.9	
Fill-in Cycles	274	83	4010	4403	4546	
Total Cycles	1053	675	4010	8777	8361	$\Sigma = 22876$
60% CR Cutoff						
Fill-in ER	8.4	8.0	11.9	11.9	11.9	
Fill-in Cycles	193	56	4010	4403	4546	
Total Cycles	972	648	4010	8777	8361	$\Sigma = 22768$
"t-function" Method						
Fill-in ER	9.3	8.9	11.9	8.8	9.1	
Fill-in Cycles	214	62	4010	3256	3476	
Total Cycles	993	654	4010	7630	7291	$\Sigma = 20579$

of missions flown by these missing "flights" is not taken into account. Exchange rates, however, are mission dependent. The analysis, summarized below, can be combined with the equivalent t-law methodology to provide mission specific fill-in exchange rates for the missing ADR data. Once that is implemented, fidelity of parts usage tracking will be further enhanced.

3.1 Missions and Exchange Rates

The military aircraft under study performs 17 stated missions as listed in Table 3.

Exchange rates within a mission type are by no means uniform. In fact, they vary by a wide margin as seen in Figure 5. Plotted in Figure 5 are the ACM exchange rates (for an HP compressor drum) from 1604 flights over a one year period. Despite large variations, one can see that the vast majority of flights accumulate about 4 cycles/hour. These same 1604 exchange rates are plotted on a Weibull chart (Figure 6). The more or less straight line distribution seen on that plot means that exchange rates can be considered a Weibull distribution. The minimum and the maximum exchange rates are seen to be 0.3 and 11 cycles/hr. Their Weibull mean, Eta + t_O, is 4.69 cycles/hr, agreeing with the eye-ball estimate of 4 cycle/hr.

Similar Weibull plots for all the other mission types were produced, and their Weibull means noted. These mean exchange rates are plotted in Figure 7 in an ascending order. Considering the large amount of overlap in exchange rates from one mission to another, it is obvious that one does not need to treat each mission individually. For example, the slight difference in the means between the ACM and the OCF flights is really insignificant. On the

Table 3
Mission Names and Abbreviations

	Mission Name	Abbrv.
1	Air Combat Maneuver	ACM
2	Airway Navigation	AN
3	Basic Instruments	BI
4	Carrier Qualification	CQ
5	Familiarity	FAM
6	Formation	FORM
7	Gunnery	GUN
8	Instruments Rating	IR
9	"Not Applicable" (miscellaneous)	NA
10	Night Familiarization	NFAM
11	Night Formation	NFORM
12	Out-of-Control Flight	OCF
13	Operational Navigation	ON
14	Radio Instruments	RI
15	Tactical Formation	TACF
16	Target Towing	TOW
17	Weapon Delivery	WEP
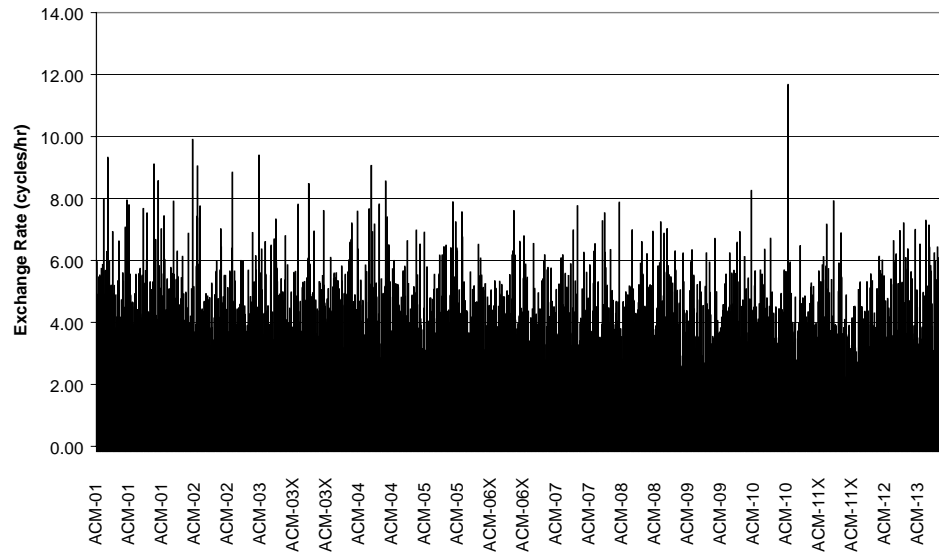
Figure 5 Variations in ER of the ACM Flights
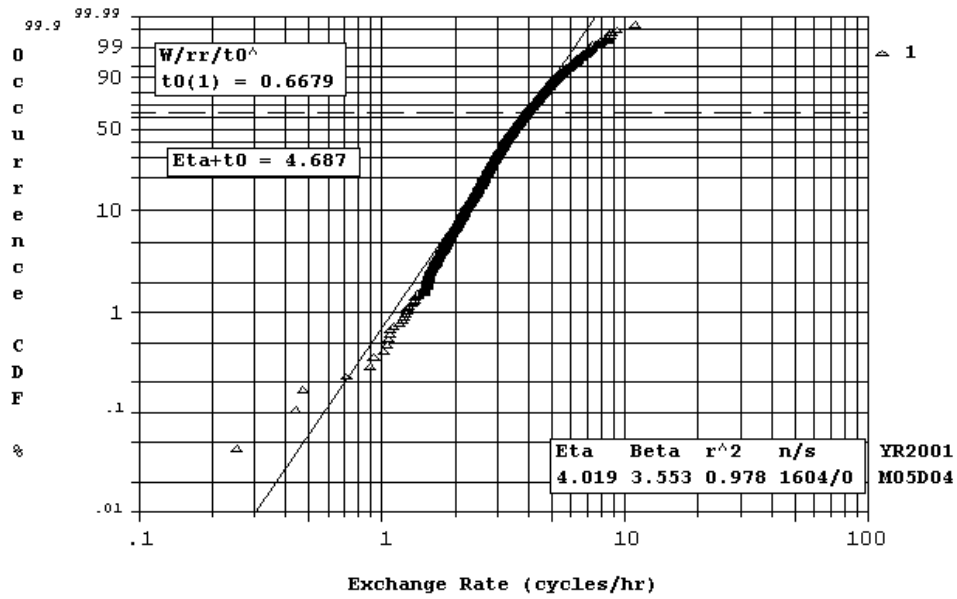
Figure 6
Weibull ER Distribution of ACM Flights
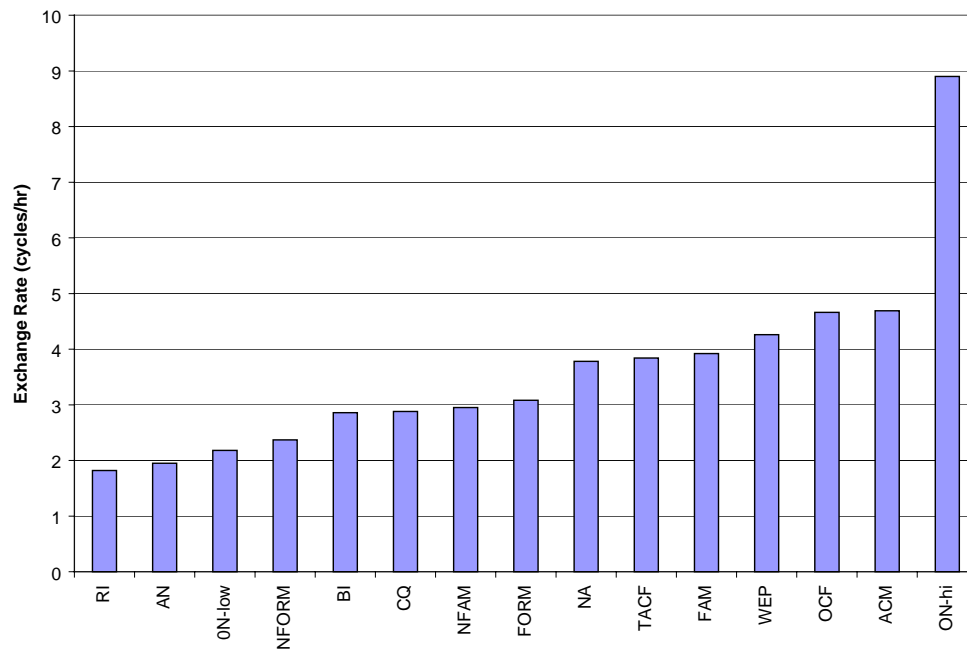
Figure 7
Weibull Mean ERs for Different Missions

other hand, an AN flight is definitely a low exchange rate mission compared with an ACM flight. We thus propose to group the missions into four categories:

> low ER missions: AN, IR, RI, TOW
> medium ER missions: BI, CQ, GUN, FORM, NFAM, NFORM, ON-low
> high ER missions: ACM, FAM, NA, OCF, TACF, WEP
> ultra hi ER mission: ON-hi

It is noted that the ON flights are divided into two sub-categories, low and high. The high ON flights are special missions in which the pilots are to reach check points along the way within specified time intervals. The extra throttle maneuvers needed to accomplish such a mission is the reason for the ultra high exchange rates. It is also noted that three of the 17 missions in Table 3 (IR, GUN, and TOW) do not appear in Figure 7, but their mean exchange rates are known and have been incorporated into the four categories.

Similar statistical analyses need to be done for the LP compressor, HP turbine, and LP turbine - the other three major critical parts in this engine.

3.2 Implementation of Mission Specific Fill-in Exchange Rates

When all the work is done, it is expected that flights with missing exchange rates will be filled in with one of 16 Weibull mean exchange rates. For low ADR capture rates, it would be desirable to devise 16 "t-functions" similar to that of Figure 4. However, the ADR capture rates in recent years have been well above 95%, making fill-in with mean exchange rates justifiable.

4.0 High Resolution Airborne Data Recorder

The existing ADR on this aircraft is of 1980s vintage. It does have sufficient processing power to calculate, in real time, the cumulative cycle counts of the four major critical parts in the engine from the 1 Hz engine performance data. However, its limited data storage dictates that the 1 Hz data cannot be saved for posterior analysis (Filtered 1/8 Hz data are saved but insufficient for critical parts lifing analysis).

In recent years, as Finite Element Modeling (FEM) becomes more sophisticated and accurate, a number of critical parts in this engine have been subjected to the much refined Thermal Transient Analyses (TTA). Complemented by additional spin tests and other appropriate tests, LCF lives of some of these parts have been increased. One component, on the other hand, had its life reduced (TTA promises more accurate stress predictions but not necessarily a reduction in stress. This also illustrates an important fact that TTA may extend the lives; but it certainly does not compromise safety). As we extend the TTA to cover more components, it became apparent that a real time TTA is highly desirable as it would extend the lives of majority of the components, thus saving both acquisition and maintenance costs in the long run.

A comprehensive cost benefit analysis was performed which showed that developing and fielding an advanced ADR with real time TTA capability would give a return on investment in 7 years. A contract is now in place to develop such an advanced ADR. It will incorporate a much more powerful processor to perform the complex TTA calculations in real time, and expanded memory to allow storage of all 1 Hz data.

5.0 Summary

Three specific schemes aimed at increasing critical part lives of a military engine are described. Quantitative life extensions, as a result of implementing these schemes, are given when appropriate. Any of these schemes could be applicable to other engines when sufficient field usage data are available.

Reference

Kiang, R.L., "A New Statistical Approach for Cyclic Life Tracking of Engine Critical Parts," Int. Soc. for Air Breathing Engines Conf., paper No. 99-7022 (1999)

This page has been deliberately left blank

———————————

Page intentionnellement blanche

The Assessment of Engine Usage Data

D.P. Shepherd
Structures and Materials Centre, QinetiQ
Farnborough, Hants, GU14, 0LX, UK
Phone +44-1252-392000
Fax +44-1252-397298
Email: dpshepherd@qinetiq.com

1   INTRODUCTION

Within aero gas turbine engines, fracture critical parts are defines as those whose failure could hazard the entire aircraft. Because of the potentially catastrophic impact of such a failure, a fundamental airworthiness requirement on all aero gas turbine engines is that the operational life of these parts is managed to ensure this does not happen. Consequently, considerable effort is devoted to deriving methods for estimating the usable life of such components, to ensure that the probability of in-service failure is acceptable low. Such methods must accurately account for the basic material properties, the impact of the various manufacturing processes employed, and the operational loads the components will be subjected to during service usage. In general terms, the lives are derived on the basis of laboratory specimen test and/or full scale component rig tests, finite element stress analyses, together with appropriate statistical models of fatigue behaviour. A vigorous and ongoing research activity is devoted to developing and refining these methods, and to ensure that they are kept up to date with changes in the basic engine technology.

From the available information, these estimation procedures will produce component lives quoted in terms of some reference stress cycle. Once this has been done, however, there remains the problem of relating these reference cycle lives to operationally measured parameters. For civil applications, there is only minor throttle movement once the aircraft has reached cruise conditions, and the engines see a standard, relatively simple operational cycle. For this reason, reference cycles can fairly accurately be related to flights on a one-to-one basis. However, for military operation, the problem is considerably more complex. In many military sorties, the output from the engines requires constant adjustment, which inflicts considerable amounts of minor cycle damage on the engine components. Moreover, the level of this minor cycle damage will itself vary considerably from mission to mission, even for the same type of sortie. Thus, it is essential to account for these fluctuations in usage to ensure adequate life consumption tracking.

The issue of relating complex mission profiles to the consumption of reference cycles involves two separate technical problems. The first of these is the physical monitoring of how the engine is being used in practice, and the recording of this information. This is achieved by fitting the engines with instrumentation that measures a number of important parameters, such as spool speeds, gas temperatures and so on, which are recorded on data logging equipment. The second problem involves the development of engine usage algorithms, which interpret the recorded data and provide an assessment of the resulting usage. These algorithms translate the recorded parameters into mechanical and thermal loads, which are then converted to reference cycles through damage accumulation models. Using these techniques, it is possible to provide an equivalent reference cycle count for any mission, no matter what the complexity of the manoeuvres undertaken.

However, the instrumentation of the engines, together with the collection and management of the data generated, represent considerable costs to the operator. For this reason, it has traditionally been the case (at least in the UK), that only a sample of engines from the fleet have been monitored in this way. Whilst this approach clearly represents an immediate cost benefit, it introduces a third element in the life tracking process; namely, that of relating the data on life consumption from the monitored aircraft to that of the rest of the fleet. To do this, it is necessary to exploit the fact that a number of parameters relating to the operation of the aircraft, such as sortie type and duration, are routinely recorded for all missions part of the fleet management process. By developing a relationship for the monitored engines between cycles

recorded and flight parameters, cycle count predictions can be estimated for all unmonitored situations. However, this introduces a further difficulty, due to the fact that the damage recorded from individual flights can vary significantly, even under nominally identical conditions. Thus, the relationship between the cycles consumed and the flight parameters is probabilistic in nature, and a statistical model must be developed to represent this relationship. Moreover, the manner in which this model is related to the rest of the fleet must also, therefore, be statistical in nature.

In this paper, a statistical model for the analysis of engine usage data generated from a sample of monitored aircraft is developed, and its application to a set of cycle counts is described. In section 2, the UK experience in military aircraft monitoring is described, and the calculation methods used in the application of these data are discussed. Next, a set of usage data, taken from a current UK military engine programme, is introduced, and the results from an initial analysis are illustrated. An appropriate statistical model describing the relationship between consumed cycles and relevant operational parameters is then developed, and fitted to the data. Current and future practice with regard to the prediction of life consumption for unmonitored aircraft is considered in the light of this. Finally, areas where further work is required are highlighted.

2   HISTORICAL BACKGROUND AND CURRENT PRACTICE IN THE CALCULATION OF EXCHANGE RATES

For the situation in which only a subset of engines from a particular fleet are instrumented to record accumulated damage, the fundamental problem in tracking component life is to provide an estimate of cycles consumed for those engines which are not monitored. This requires that a prediction of consumed cycles be derived solely on the basis of the available information which describes the unmonitored missions. The purpose of developing a model from the monitored missions, therefore, which describes the relationship between these measured parameters (referred to below as explanatory variables) and the actual cycles consumed, is to provide this predictive capability. However, to provide reliable and accurate predictions, it is necessary to account for any relationships which may exist between the measured values and the descriptive parameters. For example, suppose that a particular mission flown from one operational base results in higher average levels of accumulated damage than the nominally identical mission flown from a second base. If the two different averages can be successfully identified, then these can be used separately to provide predictions of the behaviour for future missions flown from these two bases. However, if a simple average of the total set of missions from both bases were used to provide the predictions, usage at the first base would be systematically underestimated, and that at the second overestimated. Such systematic discrepancies in cycle count predictions could lead to significant errors over the lifetime of a component, and in the worst case could result in a serious underestimation of life consumed. From an airworthiness point of view, therefore, it is important to identify any underlying relationships between the explanatory variables and the measured cycle counts, so that these can properly be taken into account. The problems to be overcome in fulfilling this task are, firstly, that such trends can be difficult to identify where several influencing variables are acting simultaneously, and secondly, the statistical scatter inherent in the data will tend to mask further these underlying trends.

In the UK, it has traditionally been considered that the dominant explanatory variable influencing the accumulation of cycles is mission duration, and that usage is assumed to be a direct multiple of the flight time. This dependence has been expressed in terms of 'cyclic exchange rates' (also referred to as 'β' factors), which are calculated for any mission simply by dividing the cycles consumed by the duration. The required relationship is defined by identifying a representative exchange rate, based on the individual exchange rates calculated from each monitored mission. In very early exchange rate calculation exercises, the representative β factor was often calculated simply as a gross average of measured exchange rates. The influence of other systematic variables on the exchange rate was accounted for by adding various 'safety factors' to this average, with little or no attempt to directly quantify the underlying relationships. Moreover, the means by which these additional safety factors were calculated varied between the different engine projects (ref 1). However, as time progressed, either role or sortie pattern code were introduced as additional explanatory variables. In these cases, the data was broken down according to the variable being used, and individual averages were established for each case. A fleetwide exchange rate was then established by estimating the (average) time spent in each role/SPC, and using this to calculate a weighted average of the individual β's (ref 2).

In practice, these methods were found to give acceptable results, as long as the type of flying undertaken by any particular engine application was reasonably simple and stable. However, as operational requirements became more complex, particularly with the introduction of multi-role aircraft, some doubt as to the adequacy of this approach was raised. As a result, in the mid 1970's, the RAF enlisted the aid of the MoD's statistical branch, Stats (S) 3, to provide a more robust solution to the problem. Over the next several years, a detailed statistical model of the then available data was developed, and a series of computer programmes were written to automate the exchange rate calculation process (ref 3). This approach, which became known as the 'Baillie method' after the author, made a direct attempt to assess which operational variables had a significant impact on the overall consumption. The statistical model proposed by Baillie (in the single engined case), was expressed by the equation

$$y_{jkr} = A + E_j S_k t_{jkr} \varepsilon_{jkr}.$$

In this equation, A is a factor representing the cycle consumed during take off and landing within each flight, E_j is a multiplicative factor representing the effect of the jth engine, S_k accounts for the effect of the kth Sortie Pattern Code/role combination, t_{jkr} is the duration of the rth sortie flown within the particular engine/SPC combination, and ε_{jkr} is a lognormally distributed random variable, which accounts for the random variation. From this equation, it can clearly be seen that usage is not assumed to be a simple multiple f the flight time. Rather, the two are related according to a straight line which is offset by a constant factor (A), and hence does not pass through the origin. Moreover, engine and SPC are explicitly included as explanatory variables in the model. Estimates for the required constants were obtained from the data through a maximum likelihood approach. A safe exchange rate for the fleet was then derived from this analysis, incorporating an additional factor to account for the worst likely engine in the fleet. This was obtained from the individual engine effects, E_j, by fitting a lognormal distribution to them and taking an upper percentage point appropriate to the number of engines in the fleet. This method was used to derive cycle count predictions for the Spey engines powering the RAF's fleet of Phantom aircraft.

However, the application of this method on one particular project led to further concerns regarding the lack of commonality between engines, and attempts were made to derive a common method suitable for all applications (ref 2). Despite (or perhaps because of) its statistical rigour, the Baillie method was rejected as being too complex, and a simpler alternative was proposed (ref 5). This was based on fitting a linear regression line to plots of cumulative cycles against cumulative flying hours, and computing a suitable upper confidence bound. Unfortunately, this too failed to produce the desired commonality, and different methods continued to be used on a number of programmes. In the early 1990's, the Weibull distribution was adopted within some engine projects as offering a superior description of exchange rate distributions to the lognormal. However, the analysis still consisted of breaking the data down into individual SPC's, fitting distributions and deducing representative rates (by going to an upper percentile to account for systematic variability), and calculating a weighted average. Despite the enormous advances that have been made with regard to damage counting algorithms, and the sophistication of modern data logging systems, it remains the case that the exchange rate calculation procedure itself is based on a very simplified representation.

3   DATASET AND INITIAL DATA ANALYSIS

To investigate the assumptions which form the basis of the various exchange rate calculation procedures discussed above, a set of cycle counts for a particular engine have been examined. To do this, the data have been subjected to an initial visual inspection, to try and assess whether any clear relationships can be identified. A statistical model has then been constructed and fitted to the data, so that these assumptions can be examined in more detail. This leads to a number of conclusions regarding current exchange rate calculation practice, and suggestions for areas in which further analysis may provide significant improvements.

The data used in the current analysis are taken from a current UK military engine programme. The total dataset consists of nearly 3000 individual engine recordings, taken over a period of 14 years. The aircraft is twin engined, and data are recorded[1] for both engines separately, so the actual number of flights from which the data are taken is considerably less than this. (It is greater than half, though, since there are a

---

[1] The sampling rate used is 8 Hertz

significant number of cases where data from one or other of the engines is missing). For each flight, 9 parameters relating to the flight are manually recorded, in addition to the cycles consumed. These are aircraft tail number, sortie number, engine number, mark of engine, whether equiaxed or single crystal turbine blades were fitted, the base from which the mission was flown, the date, duration of the flight and sortie pattern code. The cyclic damage consumption for a single component within the engine is considered, though it is strongly anticipated that the structure of the data will be very much the same for all other components.

As with any statistical model fitting exercise, the first step is to have an initial look at the data using knowledge of the situation and simple graphing techniques. The first point to establish is which variables are likely to be the important ones in developing an adequate statistical model. Common sense plus a knowledge of previous exchange rate models clearly indicate that SPC, base and duration are likely to be the primary correlating variables. Whilst tail number, sortie number and engine number may be of use in exploring detailed structure within the data, they clearly play little or no role in determining cyclic consumption in themselves. Similarly, whilst it may be of interest for some purposes to consider whether there are any trends in the data with respect to time, this is not considered within the present study. Within the sample, all engines are of the same mark, so this is clearly irrelevant from the point of view of statistical modelling. For the type of turbine blade, it is known that this does have an effect, since an allowance for the extra load induced by the heavier single crystal blades is built into the damage calculation algorithm. However, the effect is small (5-10%) and predictable, so it is considered to be very much a second order effect.

A cursory inspection of data immediately reveals that it is very uneven in terms of the number of recorded flights within any particular category. For example, the data contains recorded flights from 40 different bases, of which 29 have less than 10 recorded flights. Similarly, there are 34 different sortie pattern codes recorded in the data, of which 23 contain less than 20 flights. Since it will be virtually impossible to deduce anything of value regarding the main effects or there interactions with so little data, these very weakly populated factors have been removed from the analysis. This leaves 11 sortie pattern codes and 11 bases to consider. Even within this reduced dataset, however, the number of flights in each base/SPC combinations is highly variable, and there are a number which do not contain any data at all (see Figure 6). Clearly, this will have a influence on the information which can be derived regarding engine usage in these particular situations, and in practice it makes the statistical modelling process considerably more complex (see below).

Using this reduced dataset, one of the first points to consider is whether the distribution of cycles per hour (or cycles) is best described using a Weibull or lognormal model. The easiest and most reliable way to do this is to look at the quantile-quantile[2] plots for different SPC's and bases. Figures 1-4 clearly show that a lognormal distribution provides a superior description of the data. Indeed, points that appear as outliers in the Weibull plot of Figure 3 are seen to fall into the body of the distribution in the lognormal plot of Figure 4. Consequently, in the following analysis, the random element in the model is assumed to follow a lognormal distribution, (as was used in the Baillie approach). This means that, by taking a log transformation of the data, the normal distribution becomes the basis for the model. This has interesting consequences from the statistical point of view, since it means that the classical least squares regression and analysis of variance techniques can be used. The consequences of this are discussed in the next section.

A further point that can usefully be addressed at this stage is the regression of the cyclic damage counts against the mission duration. Figure 5 show multiple plots of the log cycles per hour and log cycles, broken down by both SPC and base. It can be seen that the regression against log cycles is somewhat variable in nature, in some situations appearing to be virtually flat[3]. This suggests that the current practice of calculating cycles consumed as a multiple of flight duration is somewhat unrepresentative of actual experience, and could lead to a significant underestimation of the consumed damage for short duration flights. Moreover, it suggests that the approach adopted by Baillie is much more representative in this respect also, since it allows for regression lines which do not pass through the origin. Notice also that the very flat nature of the regression response in certain situations suggests mission duration has

---

[2] A quantile-quantile plot (or Q-Q plot), is a plot of the ordered values against the corresponding quantiles of the respective distribution
[3] This observation is also confirmed by other studies of cycle count data (see ref 8)

virtually no influence on accumulated damage in these cases. However, the plots still suggest that at least some of the regression coefficients will be non-zero, indicating that it will still be necessary to include mission duration as an explanatory variable.

4   MODEL FITTING

Once a preliminary visual examination of the data has been conducted, the next step in any statistical analysis is to examine the basic observations already established, and to explore any further relationships which may not be so immediately obvious. This is achieved by fitting statistical models to the data, which allows for multiple causal relationships to be explored, and which ensures that the random variation present in the data to be properly accounted for. The process involves constructing statistical models containing multiple variables, and assessing their validity by examining the extent of the random variation still present once the fit has been achieved. More specifically, in the presence of random variability in the raw data, the influence of any particular variable will be revealed through the extent to which this variability is partitioned. For example, suppose that missions flown from a particular base consumed significantly more damage, on average, than the equivalent missions at another base. Whilst the data from the two bases may well overlap, the scatter associated with each individually will be significantly less than that that produced by both combined. Thus, the greater the extent to which the variability is reduced in fitting a model containing that variable, the more significant the variable is in 'explaining' the data. The aim of the statistical analysis is to reduce the extent of the scatter as far as possible, by accurately identifying the systematic relationships within the data.

It is in this sense that the ability to assume a normal description for the underlying variability is significant. It was mentioned in section 3 that this assumption allows the classical methods associated with least squares analysis to be employed, and in particular techniques generally referred to as the Analysis of Variance. This is significant, because this is the branch of statistics which was developed specifically to investigate problems involving the partitioning of variability (as the name implies). It is also significant, because potentially it represents a distinct advance over the methods used in the Baillie analysis. One reason for this it that it allows for the construction of specific hypothesis tests, which can be used to assess the relative significance of the different variables. The reason Baillie himself did not take advantage of these techniques is probably due, at least in part, to the limitations in computer power available at the time. The basic solution techniques, when applied to datasets of the size considered here, requires the inversion of very large matrices which would have swamped most computer systems available in the 1970's. However, given that todays computers can perform such tasks as a matter of routine, the very powerful techniques developed to examine this type of problem can now be applied to the analysis of cycle count data.

In spite of the advances in computer technology, however, there are still significant difficulties involved in applying this type of analysis. The most important of these is the fact that the data points are distributed very unevenly amongst the cells of the SPC/base categorisation, as observed in section 2. This is unfortunate, because it severely affects the type of hypothesis tests which can be conducted, and under the regular form of analysis it renders them largely meaningless. More sophisticated methods for dealing specifically with this type of data do exist (see ref 8), but require a significant effort to employ because they are not generally available within commercial statistical analysis packages[4]. Since this was not possible within the scope of the present study, such test have not been used. A further consequence of the unbalanced nature of the data, and particularly the fact that some cells are empty, is that there are certain quantities within the model which cannot be estimated. This should not be surprising, since it is clearly impossible to derive meaningful conclusions concerning a physical phenomenon with no available data. However, is does illustrate the importance of increasing the available sample size to ensure that all operational situations are being appropriately accounted for.

The model fitted to the data in the current analysis is of the form

$$\log C_{ijk} = \alpha + S_i + B_j + S_i * B_j + Dx + \varepsilon_{ijk}$$

---

[4] This may have been another reason why Baillie did not use these techniques, since the methods required to analyse this type of data were in the process of being developed at the time.

where S is SPC, B is base and D denotes log mission duration. Moreover, the same model has been fitted repeatedly, but with some of the terms removed, to examine the influence of each term separately. An example of the output from the fitting programme is shown in figure 7, displaying the calculated constants. From the statistical modelling point of view, the important number in figure 7 is the sum of squares due to the residuals, which is given as 141.7. This is important, because it represents the amount of random variability left after the model has been fitted. By examining this figure as the different terms from the model are removed, the effectiveness of each term in reducing this variability can be assessed. This process reveals that this figure does not vary by large amounts, as shown in the following table[5].

Terms included in model	Residual sum of squares
Base, Hours, SPC, Base*SPC	141.7
Base, Hours, SPC	153.5
SPC, Hours	160.0
Base, Hours	175.9
Hours	187.5
None	192.9

The conclusion to be drawn from this is that effect the explanatory variables employed in the model is largely swamped by the residual variability, which confirms the visual analysis given in Figure 5. The remaining plots in Figure 8 to Figure 10 show the residuals (that is, the difference between the model and the observed values at any point) plotted in various ways, and are diagnostic in nature. They show that, essentially, none of these assumptions used in constructing the model are violated. In particular, the histogram in Figure 8 shows hat the assumption of underlying normality is well justified. The conclusion from these plots is that the model fits extremely well, and provides a more than adequate representation of the data.

5   DISCUSSION

Before moving on to consider the implications of this analysis for cycle count prediction methods, some features of the analysis warrant further discussion. For example, the fact that the mission duration shows little or no effect on the cyclic damage accumulation in under certain sortie and base combinations may at first appear surprising. However, for many types of flying undertaken by the RAF, there are severe limits imposed on how this can be carried out. For example, there are relatively few places in Britain where low level flying activities can be undertaken. Consequently, aircraft from different bases will need to use the same airspace for this activity, and the transit times to and from these locations to the bases themselves will vary significantly. Consequently, whilst the mission times will be very different depending on which base they are flown from, it is reasonable to suppose that the actual level of damage will be more or less the same. Thus, when one considers the constraints under which many of the missions are flown, it starts to appear that this is to be expected after all.

A natural consideration which immediately arises from the relative lack of success in partitioning the variability, is whether better correlating factors can be found. In fact, there are a number of other operational parameters routinely recorded against flights of these engines, which may perform this function. Such factors include number of landings, number of in-flight refuellings and role. Whilst these may allow for a better description of the variability, it seems likely that they will only partially explain the observed scatter. Previous studies have indicated strongly that there is a large variability in the way that different pilots fly combat aircraft, and without explicitly including this effect into the analysis, it is unlikely that the observed scatter in consumed cycles can be reduced much beyond that achieved in the

---

[5] It is important to remember that these figures represent the sums of squares of residuals, so the percentage change is much smaller than represented here.

current analysis. Consequently, it appears likely that this feature of the data will remain a dominant influence in determining overall exchange rates.

Next, there is a further feature of the data presented here which, if modelled correctly, could provide very significant benefits in terms of both exchange rate calculation and general fleet management. Figure 11 shows a plot of a series of cycles counts, taken over consecutive sorties flown by a single aircraft between engine removals. It shows that the right hand engine consistently accumulates greater amounts of damage than the left, irrespective of the severity of the sortie. The reason for this discrepancy is the variation of build between the two engines, which leads to a differential between the spool speeds and temperatures required to provide the same amount of thrust. It is well known that such differences exist in service engines, and it is not itself suprising to observe such differences being recorded in practice. However, there would be many advantages to be gained if these variations could be quantified in such a way that they could be compared between tail numbers. For example, this would allow for a general distribution of engine variability to be derived, which would quantify the overall spread in build standard. Moreover, by the process of extracting this information would effectively remove the contribution made by build quality to the overall variability. Finally, provided enough raw information was available, it could be used as a diagnostics tool to assess trends in build quality over time, and ensure that common standards were being maintained. The difficulty with Figure 11 as it stands is that it only allows for the variation in these two engines to be assessed relative to each other. In order to provide a comparison between engines in different aircraft, they would need to be assessed relative to the mean damage rate for that particular combination of explanatory variables, taking into account the residual scatter. This would require a more sophisticated model, which would included the effect of engine in an appropriate way. Notice also, that this is precisely the purpose of the parameter E_j in the Baillie model. This emphasises further the comprehensive nature of the Baillie analysis, given the constraints that were operating at the time. Finally, it is important to reflect on the implications of the analysis on current usage prediction and life consumption monitoring practice. Whilst the introduction (or, more accurately, re-introduction) of the lognormal distribution for describing the underlying variability in the data has a very significant impact in terms of the models used, in itself it is unlikely to have a large effect on the numerical estimates obtained. The relative flatness of the regression lines when plotting log cycles against mission, on the other hand, suggest that the current practice of multiplying the number of cycles consumed per hour by the mission duration could introduce significant errors into the life management process. The importance of this error, however, can only be assessed against the extent to which the engines experience a random sample from the population of consumed cycles. Indeed, if engines really do sample at random from the distribution, then it is unlikely to have a significant impact overall, since the underestimation at low mission durations will be compensated for by a parallel overestimation for long missions. But if this really is the case, then the current practice of taking an upper percentage point on the distribution as defining a safe exchange rate for the fleet would appear to be overconservative. This is because if the sampling is actually random, the large number of sorties flown by an engine during its service lifetime will mean that its cyclic life consumption per mission, averaged over its life, will be very close to the mean. Consequently, the whole question of the most appropriate means of estimating fleetwide exchange rates depends on the investigation of this problem. Thus, the work following on from the current analysis will be to investigate this problem, so that the most accurate and cost effective means of exchange rate calculation can be determined.

6   CONCLUSIONS

The analysis of low cycle fatigue cyclic consumption data for military aircraft has been reviewed, for the situation in which only a sample of engines are monitored. In particular, the analysis developed by D H Baillie has been described, and contrasted with past and present methodology. Moreover, the problems to be addressed in this type of analysis have been identified, and some assumptions underlying current practice are described. To investigate the validity or otherwise of these assumptions, a set of cycle count data from a modern UK military aircraft has been analysed. Initial investigation of the data reveals that previous assumptions concerning the probability model describing the scatter in the data are not optimal, and a lognormal distribution appears preferable to the commonly used Weibull. This has a distinct advantage form the statistical point of view, since it means that the classical methods relating to the analysis of linear models can be applied directly to the problem. Consequently, a regression model has been derived and fitted to the data, which includes two factors in addition to mission duration. The

analysis, however, is complicated by the unstructured nature of the data, and particularly the fact that the observations are very unevenly distributed through the classification scheme. The results indicate that whilst the model fits the data perfectly adequately, the explanatory variables employed in the analysis only provide a relatively weak description of the data. In the course of the analysis, however, three areas of further work are identified, which may allow substantially stronger results to be derived. These are,

1) The development of an analysis capability which can fully account for the unbalanced nature of the data, resulting in the full power of the available techniques being applied.

2) The introduction of additional explanatory variables into the model, which could potentially provide a much improved description of the data.

3) The development of techniques which could quantify the effect of variation in build quality on the consumption rate, which could provide substantial benefits to both cyclic consumption prediction and fleet management.

Finally, the problem of applying this type of analysis to the problem of fleetwide usage calculation has been addressed, and the need for a comprehensive analysis of the operational data for the fleet is emphasised.

7   REFERENCES

1) J A Lang, 'Towards an Agreed Method of Estimating a Safe Cyclic Exchange Rate From EUMS/EDR data', D/D Eng D(PE)/19/61/2, 28 Sept 1982.

2) 'Minutes of a Meeting Held to Discuss the derivation of Military Engine Low Cycle Fatigue Exchange Rates', D/D Eng T(PE)/4/33/9, 6 Dec 1982

3) D H Baillie and G J Knightley, 'Rederivation of Aero-Engine Low Cycle Fatigue Consumption Rates', Defence Statistics report, Nov 1976

4) D H Baillie, 'A Statistical Model of Low Cycle fatigue Consumption in Single Engined Aircraft', Defence Statistics report, Oct 1980

5) R H Jenkins, 'The Derivation of Cyclic Exchange Rates Calculated From Flight Recorded Data', Rols-Royce report BSR 4789, 9 Dec 1983

6) T M Edmunds, 'Derivation of Exchange Rates From Flight Recorded Data', Rolls-Royce report BSN/D/1039, 6 Jun 1984

7) H Pfoertner and J Broede, 'Statistical Correlations for Analysis and Prediction of Turbine Engine Component Life Usage', 37th AIAA/ASME/SAE/ASEE Joint Propulsion Conference, Salt Lake City, Utah, July 2001

8) G A Milliken & D E Johnson, 'Analysis of Messy Data: Volume 1, Designed Experiments', Van Nostrand Reinhold, 1984

8   FIGURES
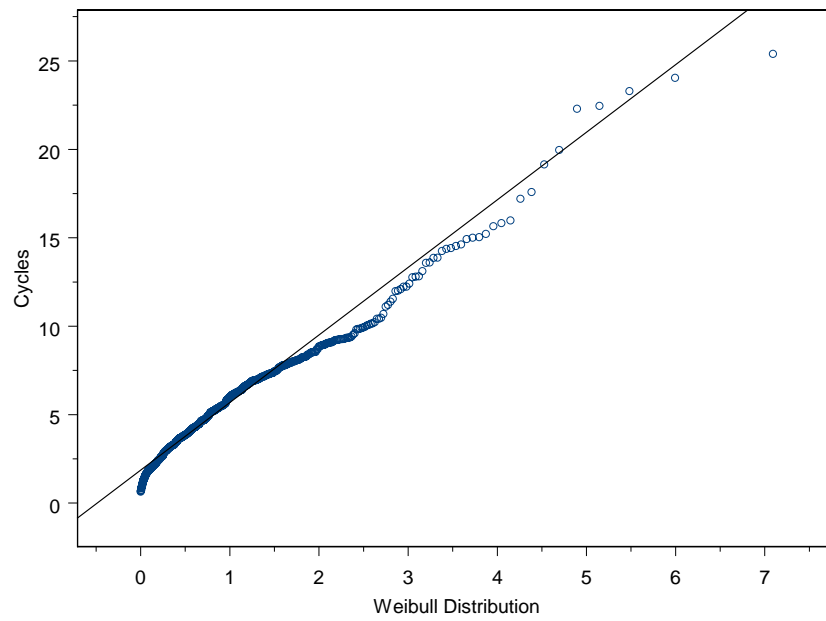
Figure 1 Fit of Weibull distribution to SPC data
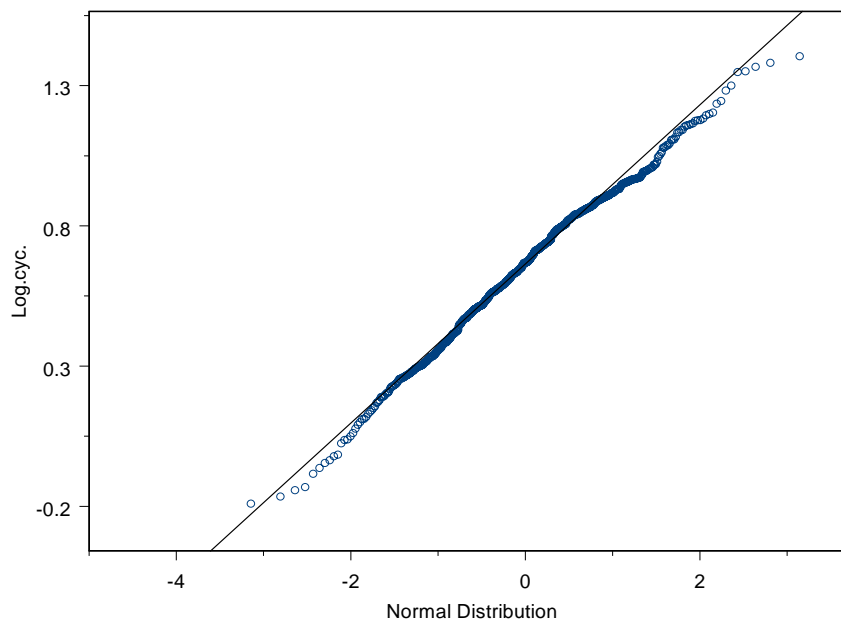
Figure 2 Fit of lognormal distribution to SPC data
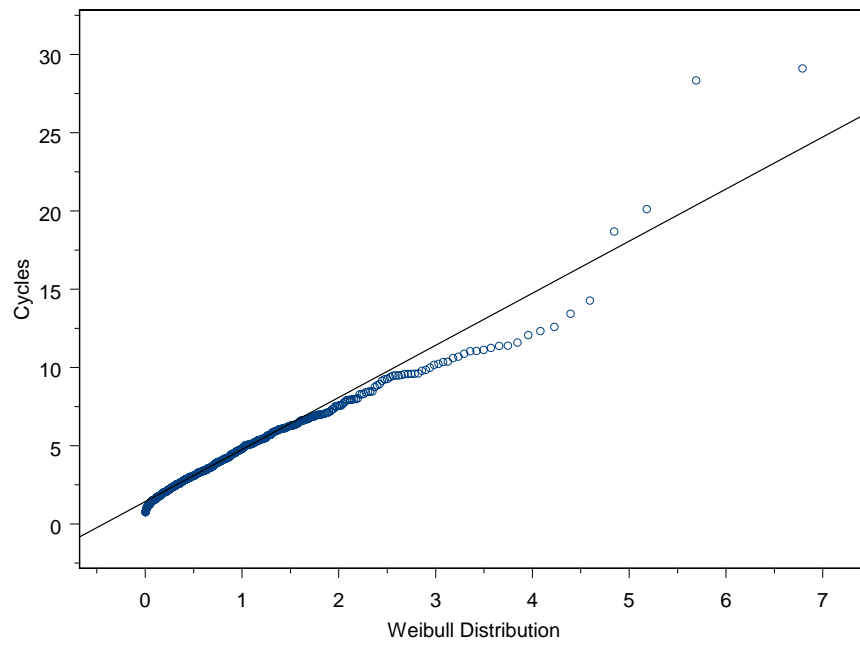
Figure 3 Fit of Weibull distribution to SPC data
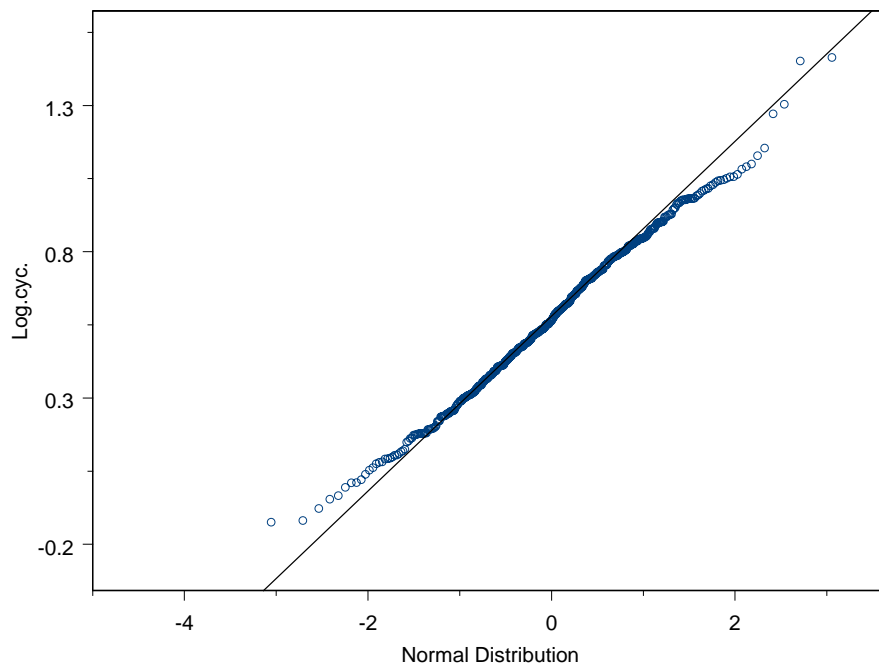
Figure 4 Fit of lognormal distribution to SPC data
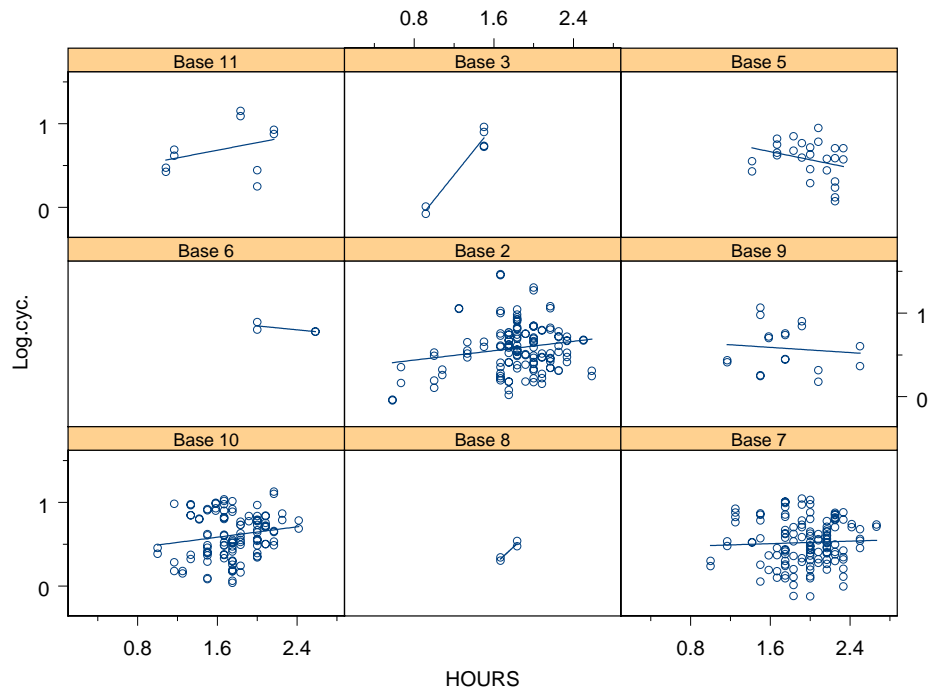
Figure 5 Regression slope of mission duration against log cycles for individual bases
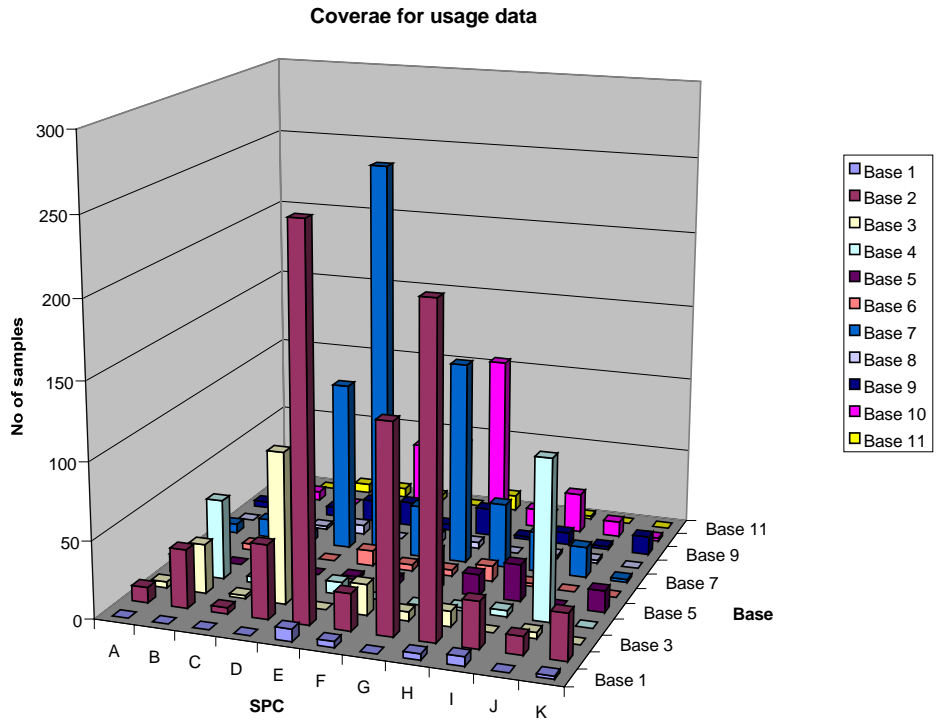
Figure 6 Coverage of data across classification

```
              Df  Sum of Sq  Mean Sq   F Value
    LOCATION  10     9.3294  0.932936  14.86182
         SPC  10    23.9976  2.399761  38.22860
       HOURS   1     6.0223  6.022310  95.93643
LOCATION:SPC  64    11.7982  0.184347   2.93668
   Residuals 2258  141.7436  0.062774

                    Pr(F)
    LOCATION 0.000000e+000
         SPC 0.000000e+000
       HOURS 0.000000e+000
LOCATION:SPC 2.131628e-013
   Residuals

Call: lm(formula = Log.cyc. ~ LOCATION + SPC + HOURS + LOCATION * SPC, singular.ok
 = T)
Residuals:
    Min    1Q   Median    3Q     Max
 -0.8069 -0.163 0.001212 0.1607 0.9077
```

Figure 7 Output from statistical fitting routine
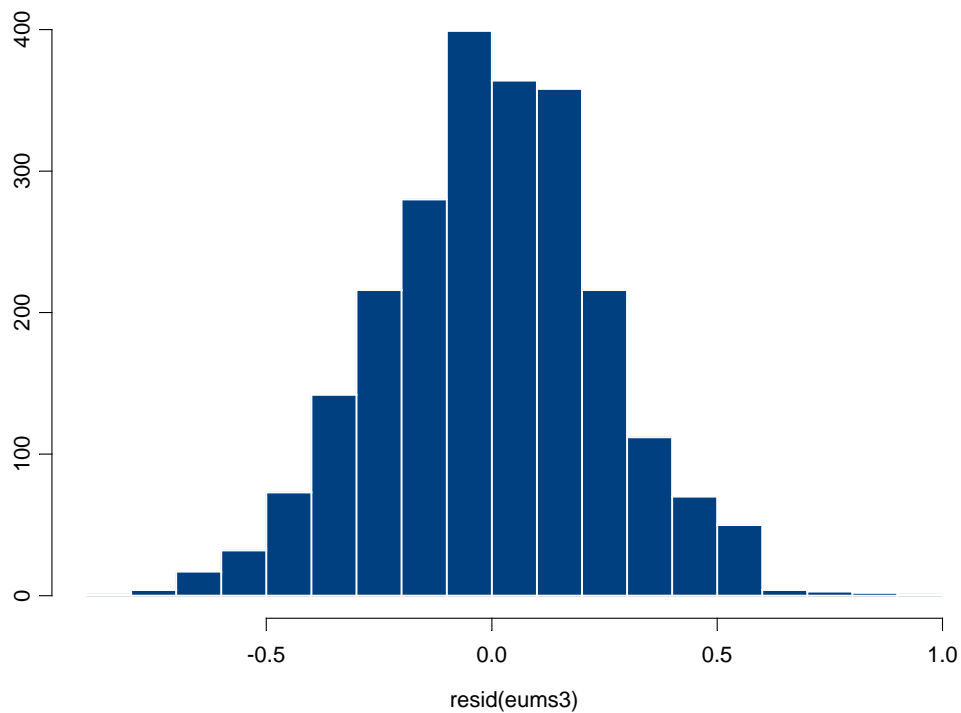
Figure 8 Histogram of residuals
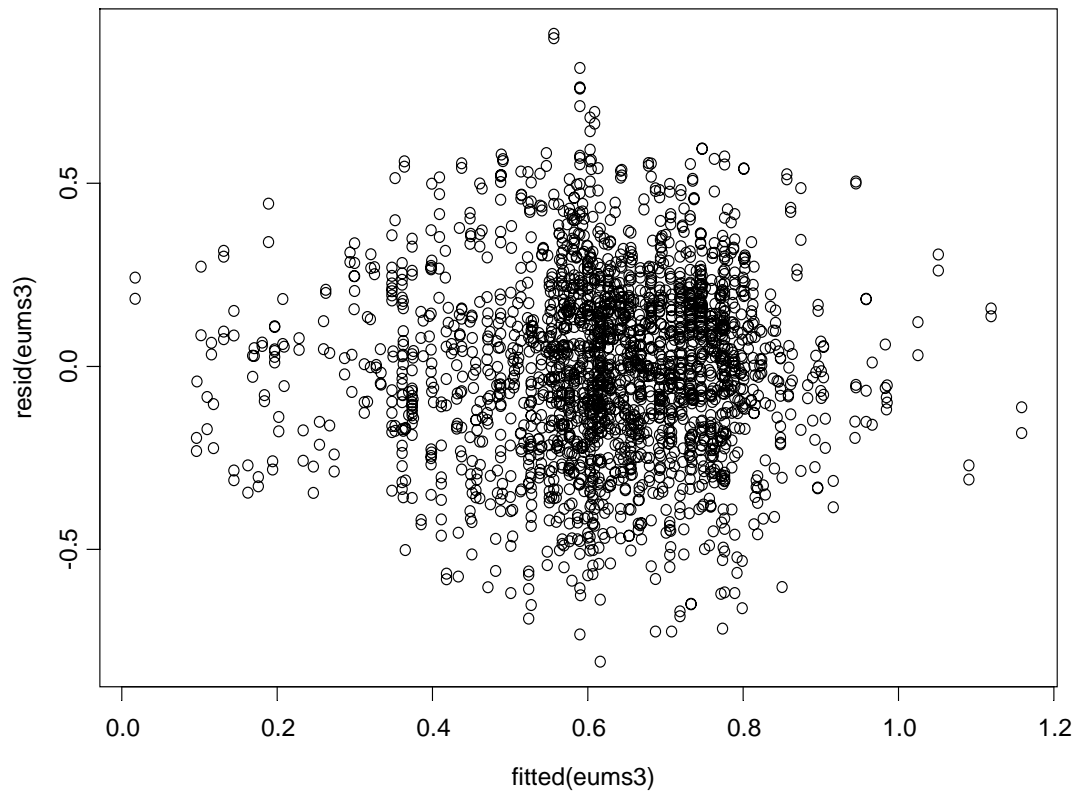
Figure 9 Plot of residuals
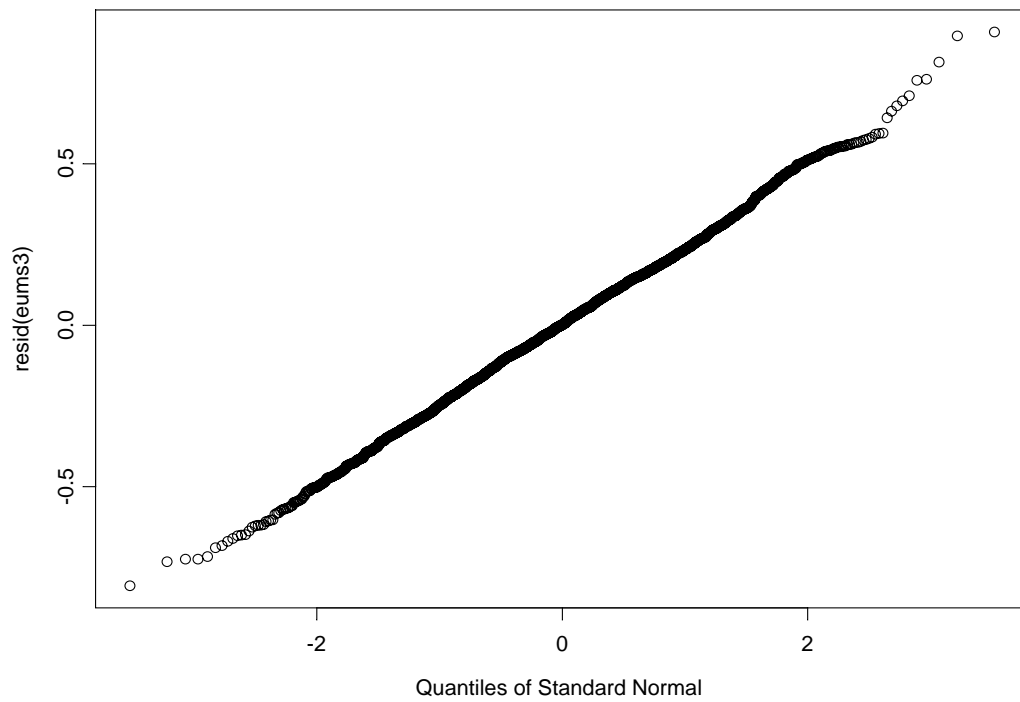
Figure 10 Quantile-quantile plot of residuals
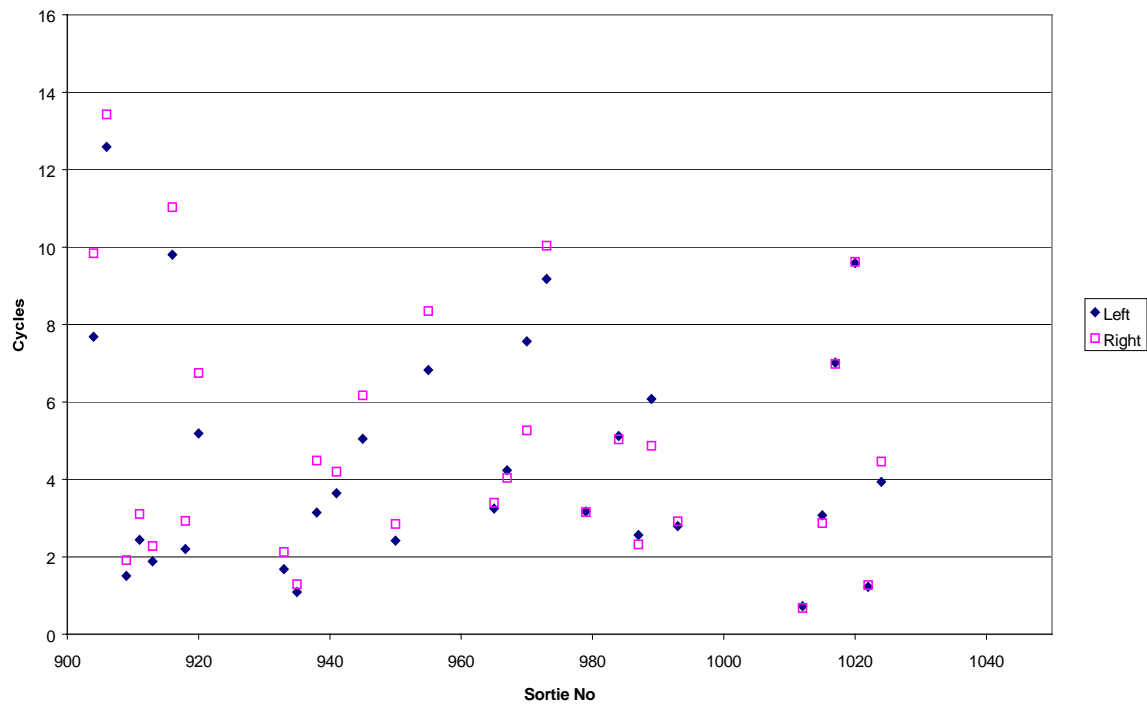
Figure 11 Relative damage of left and right engines

Paper, 'The Assessment of Engine Usage Data': Discussion

<u>Question from S Mosset – SNECMA, France</u>

What is the sortie pattern code and how does the cycle counting operate?

<u>Presenter's Reply</u>

The sortie pattern code is a numerical index that refers to a categorisation of mission types. The cycle counting is done using damage algorithms run post-flight on ground-based computers.

<u>Question from H Pfoertner – MTU, Germany</u>

I would like to make the following observations, based on our experience of GAF operations, in support of your paper:

- The correlation between the duration of a single flight and life usage at a selected critical area is, in most cases, weak. We prefer to use damage per flight instead of damage per flight hour.

- There are known reasons for systematically different life usage between the left and right engines in one aircraft. One reason may be due to differences in engine health, requiring different spool speeds to achieve equal thrust. Another may be caused by different operating procedures between the two engines, such as one engine always being started first, introducing additional thermal stresses.

- Mission type/sortie pattern code may translate into quite different usage. Even if the same pilot flies the same mission, with the same aircraft, on two different days, a factor of two in life usage figures has been observed for certain critical areas.

<u>Presenter's Reply</u>

Agreed.

This page has been deliberately left blank

————————————

Page intentionnellement blanche

Incorporating Residual Stresses in Life Prediction of Turbine Engine Disks

Reji John, James M. Larsen
Air Force Research Laboratory
Materials and Manufacturing Directorate
AFRL/MLLMN, 2230 Tenth Street, Suite No. 1
Wright-Patterson Air Force Base, Ohio 45433-7817, U.S.A.

Dennis J. Buchanan, Noel E. Ashbaugh
University of Dayton Research Institute
300 College Park, Dayton, Ohio 45469, U.S.A.

ABSTRACT

The U.S. Air Force has initiated a technology development initiative known as Engine Rotor Life Extension (ERLE), which has the goal of extending the useful lifetime of major, fracture-critical components in currently fielded gas turbine engines, without increasing the risk of component failure. Full achievement of this goal will require improvements in a broad range of technologies, including life prediction and fracture mechanics, nondestructive evaluation, engine usage and health monitoring, and component repair. This paper focuses on a key aspect of the life prediction process – the incorporation of residual stress effects. The benefits of compressive residual stresses in improving fatigue life, retardation of crack growth and resistance to foreign object damage have been demonstrated. Hence, these beneficial surface treatments are extensively employed in the turbine engine components. However, current damage-tolerance-based life management practices do not explicitly account for the residual stresses induced by surface enhancement procedures. Significant increase in predicted damage tolerance can be obtained if residual stresses are included in the life prediction methodology. This paper provides an assessment of the role of residual stresses in the durability of the component and identifies critical issues to be addressed during implementation in life prediction methods.

INTRODUCTION

The U.S. Air Force has initiated a technology development initiative known as Engine Rotor Life Extension (ERLE) [1], which has the goal of extending the useful lifetime of major, fracture-critical components in currently fielded gas turbine engines, without increasing the risk of component failure. A broad range of related technologies such as life prediction and fracture mechanics, nondestructive evaluation, engine usage and health monitoring, and component repair have been targeted for achievement of this goal. The total life of an engine component can be determined as the sum of crack initiation life and crack propagation life. Crack propagation life typically includes the short and long crack growth regimes. Current life management practice (Engine Structural Integrity Program, ENSIP) [2,3] by the U.S. Air Force uses a damage-tolerance-based method for managing the life of safety-critical components. This approach is based on systematic inspections of critical life-limiting locations in components. The inspection intervals are determined as 50% of the predicted crack growth life from an assumed initial crack growth size. Using nondestructive inspection (NDI) techniques, the components are inspected for location-specific crack sizes. The

component design lifetime is based on a crack initiation criterion, but if a crack is detected prior to this mandatory component retirement lifetime, then the component is retired immediately.

The prediction of the crack length versus cycles behavior at critical locations in a component is based on the expected thermo-mechanical loading conditions and the assumed crack growth behavior of material. Prior to insertion in service, most critical locations, such as holes, stress concentration sites, etc., are subjected to surface enhancement procedures such as shot peening. Most of the legacy engines used shot-peening to retard crack growth at critical locations. Shot-peening introduces significant near-surface (within 150-200 μm) compressive stresses. The benefits of these compressive residual stresses in improving fatigue life, retardation of crack growth and resistance to foreign object damage have been extensively demonstrated. However, current damage-tolerance-based life management practices, i.e. predictions of crack initiation life and crack propagation life, do not explicitly account for the residual stresses induced by surface enhancement procedures. In current engines, shot-peening is used as a bonus factor of safety, resulting in potentially excessive conservatism in the component life prediction. Hence, incorporating residual stresses in crack growth life prediction is a key life extension technology. This paper provides an assessment of the role of residual stresses in the durability of the component and identifies critical issues to be addressed during implementation in life prediction methods.

MATERIAL

One of the materials used in components under consideration for life extension is Ti-6Al-2Sn-4Zr-6Mo (weight %) (Ti-6246). This material was forged and heat treated to produce a fine duplex microstructure of equiaxed primary α phase (hexagonal close packed) in a matrix of Widmanstatten α + β (body-centered cubic) phase as shown in Figure 1.

The analysis of crack growth in the presence of residual stresses requires characterization of baseline crack growth behavior of the material over a wide range of stress ratios, R. Hence, fatigue crack growth experiments were conducted using standard compact tension, C(T) geometry and single edge cracked geometry with clamped ends, CSE(T). The C(T) specimen was used for R = 0.1, 0.2, 0.3, 0.5, 0.6, 0.7, 0.8 and 0.9, and the CSE(T) specimen was used for R=-0.5 and –1.0. The crack growth data were acquired under decreasing stress-intensity-factor-range, ΔK, fatigue followed by constant-load amplitude fatigue. The resulting fatigue crack growth rate data were fit using Eqn. (1).

$$\log\left(\frac{da}{dN}\right) = C_1 \left\{\arctan h \left(C_2\left[\log(\Delta K) + C_3\right]\right)\right\} + C_4 \tag{1}$$

in which,

$$C_i = A_{0i} + A_{1i} \log(1 - R) + A_{2i} \left[\log(1 - R)\right]^2 . \tag{2}$$

The baseline crack growth behavior of Ti-6246, as described by Eqn. (1), is shown in Figure 2 for the range $-1 \leq R \leq 0.8$. In obtaining the constants A_{0i}, A_{1i} and A_{2i}, the fracture toughness of Ti-6246 was set equal to 28 MPa√m, based on the data. Note that, in Figure 2, $\Delta K = K_{max} - K_{min}$ for all R. The threshold stress intensity factor range, ΔK_{th}, is $\approx 1.5 - 4$ for all R. Hence, the near-threshold crack growth response of materials with such low values of ΔK_{th} can be expected to be influenced significantly by residual stresses, even if the magnitude of residual stress is low.

SHOT PEEN INDUCED RESIDUAL STRESSES

Shot peening induced residual stress (σ_{res}) distributions for Ti-6246 were unavailable in the open literature. Hence, we estimated the residual stress distribution as a function of depth based on available data on similar materials such as Ti-6Al-4V. The magnitude of the residual stress distribution was estimated using the ratio of the yield stresses of the materials ($\approx$1170 MPa for Ti-6246 and $\approx$950 MPa for Ti-6Al-4V). The estimated σ_{res} for Ti-6246 is shown in Figure 3 for four shot peening intensities. Extensive data for various materials available in the literature show that the surface residual stress is typically lower than the sub-surface peak value. The magnitude of the surface residual stress depends on many factors such as shot-peening intensity, shot-peening coverage, surface finish prior to shot peening, material hardening behavior, etc. Hence, based on available data, the surface stress was conservatively assumed to be 50% of the sub-surface peak value.

Using the weight function method, the stress intensity factor due to residual stresses, K_{res} was determined for a semi-elliptical surface with surface crack length = 2c (tip-to-tip), crack depth = a, and aspect ratio, a/c=1. K_{res} at the surface crack tip (c), $K_{res,c}$, and at the deepest point in the depth direction (a), $K_{res,a}$, is shown in Figure 4 corresponding to the σ_{res} distributions shown in Figure 3. Since residual stresses are compressive, the computed K_{res} is mathematically negative. While the authors recognize that a negative K_{res} has no formal meaning, negative K_{res} is used to describe the relative magnitude of the compressive stress across the crack surfaces. K_{res} is always added to the applied K, and the total K = applied K + K_{res} should be positive for crack growth to occur. The magnitude of $K_{res,c}$ and $K_{res,a}$ are in the same range or higher than ΔK_{th} for a = 50 – 300 μm. Hence, in this regime of crack growth, significant influence of σ_{res} on the crack length versus cycles response can be expected. $K_{res,c}$ reaches a maximum at c $\approx$ 200 μm and remains constant up to c = 1000 μm. In contrast, $K_{res,a}$ reaches a maximum at c = a $\approx$ 100 μm and decreases to $\approx$0 at c = a $\approx$ 600-1000 μm. This difference between $K_{res,c}$ and $K_{res,a}$ implies that, in the presence of residual stresses, minimal crack extension might be observed on the surface while the crack is growing inside the specimen.

During service, the turbine engine components are subjected to complex thermal and mechanical loading conditions. Numerous studies using coupon-type specimens have shown that residual stresses relax during thermal exposure and fatigue loading [for example, 4-9]. Most of the data available are based on surface residual stress measurements. However, accurate prediction of crack growth requires the knowledge of residual stress distribution as a function of depth. Recent work by Cao et al. [6] and Prevey et al. [7,8] report residual stress distributions as a function of exposure time. Figure 5(a) shows the relaxation of residual stresses in Ti-6Al-4V at 325°C [7]. Rapid and significant relaxation ($\approx$50%) is observed near the surface during the first ten minutes and the distribution remains relatively stable beyond 10 minutes. Similar results were also reported by Cao et al. [6] for a Ni-base superalloy (Astroloy) at 650°C. An important feature to be noted is that most of the relaxation of the residual stresses is confined to $\approx$ 100 μm below the surface.

Recently, Vukelich et al. [10] reported the results of residual stress measurements at various locations in Ni base superalloy engine disks, as shown in Figure 5(b). These disks had been subjected to complex thermal and mechanical loading conditions during service. These data are a compilation of measurements from numerous disks. Hence, the initial residual stresses (post shot-peen, pre-service) and the subsequent relaxation during service were not tracked at the same location and on the same component. Although there is significant scatter in the results, the data clearly show that, even after 8000 TACs (Total Accumulated Cycles), the minimum retained surface residual stress is $\approx$30-50% of the initial level.

The above results show that a wide variation in the magnitude of retained residual stresses can be expected during service. Hence, this paper is directed towards an assessment of the influence of residual stresses on the remaining crack propagation life and the effect of various degrees of retention of residual stresses. Incorporation of residual stresses in prediction of crack growth life requires accurate models to predict the relaxation of residual stresses during service. A few relaxation models [6,9] have been developed for a limited range of temperatures and mechanical loading. Additional extensive testing and modeling are required for accurate prediction of the true rate of decrease in the residual stresses under a wide range of thermal and mechanical loading conditions. Available data indicate that the most substantial residual stress relaxation occurs during the initial cycles. Hence, during this study, crack growth analysis was conducted for various levels of retained residual stresses as a percentage of the original stress distribution, as shown in Figure 6(a). This approach will result in conservative predictions for surface initiated cracks because as shown in Figure 5(a) most of the measured residual stress relaxation is restricted to the initial $\approx 100\mu m$ beneath the surface. The corresponding $K_{res,c}$ and $K_{res,a}$ are shown in Figure 6(b). Note that even an assumption of 50% retention of residual stresses results in K_{res} of $\approx$ -4 to –8 MPa$\sqrt{m}$ for crack sizes of $\approx$ 50 to 200 μm. These K_{res} values are of the same order of magnitude as ΔK_{th}, and hence, the retained residual stresses are sufficient for significant crack growth retardation. The influence of retained residual stresses on fatigue limits and crack propagation life is discussed next. In the following sections, the long-crack growth behavior shown in Figure 2 was used for analysis of small cracks. For cracks greater than $\approx$ 25μm, this assumption was previously shown to be valid based on experiments on naturally initiated small surface cracks in Ti-6246 [11,12].

RESIDUAL STRESS EFFECTS ON THRESHOLD STRESS AND FLAW SIZE

The influence of residual stresses on the threshold crack size corresponding to no-growth conditions was studied by utilizing a Kitagawa-Takahashi [13] type plot of maximum stress versus flaw size. Such a plot corresponding to R=0.1 and R=0.8 is shown in Figure 7(a) and 7(b), respectively. These stress ratios bound the typical stress ratios experienced by some of the life extension candidate components. The maximum stress is bounded by the fatigue limit (typically 10^7-cycle fatigue limit) [14] and the stress-crack length relationship defined by the threshold stress intensity factor range, ΔK_{th}. A similar approach was used by Larsen et al. [14,15] to generate fatigue life maps and to assess the influence of residual stresses on threshold crack sizes. At R=0.1 and 0.8, if the assumed initial flaw depth exceeds 10 and 30 μm, respectively, the threshold stress (fatigue limit) decreases with increasing flaw size per LEFM equations. Figure 7 also shows the predictions for threshold stress in the presence of residual stresses corresponding to intensities of ~ 4A and ~16A. The predictions for the two shot peening intensities are nearly similar and clearly shows the substantial increase in the fatigue limit for a given flaw size. For a flaw size $\approx$ 100 μm, at R=0.1 and 0.8, the threshold stress $\approx$ 200 and 500 MPa, respectively, in the absence of residual stresses. These threshold-stresses increase to the respective upper bound fatigue limit in the presence of the residual stress. For a stress level of $\approx$ 200 MPa, the threshold flaw size increases from $\approx$ 100 μm to $\approx$ 400 μm. Thus, the safe region for the no-growth condition is increased substantially by the residual stresses. Although, the threshold flaw size at R=0.8 is higher than that at R=0.1 for a given stress, the subsequent benefit of the residual stresses is significantly lower than that at R=0.1. Figure 7 also shows that the benefits of the residual stresses vanish for flaw size greater than 600-700 μm. This result is consistent with the predicted near-zero $K_{res,a}$ for flaw sizes greater than 600-700 μm, as shown in Figure 4(b).

As discussed earlier, shot-peening induced residual stresses relax during service. Hence, the threshold stress for two flaw sizes were determined for various levels (0 to 100%) of the residual stress corresponding to ~8A intensity, as shown in Figure 8(a). The corresponding residual stress

distribution was shown in Figure 6. Under LCF conditions (R=0.1), for a flaw size of 120 μm, the threshold stress is ≈ 150% higher than the baseline stress even at residual stress retention of only 50%. For a flaw size of 25 μm, the threshold stress at R=0.1 is ≈ 40% higher than the baseline. Therefore, the larger flaw size exhibits a higher increase of threshold stress. At R=0.8, even though the relative increase is lower than that for R=0.1, the retained threshold stress is still higher than the baseline value. The sensitivity of the threshold flaw size corresponding to stress = 500 MPa to the level of residual stress is shown in Figure 8(b). Corresponding to the baseline value, at 100% of residual stress, the threshold flaw is ≈ 10X and 2X higher at R=0.1 and 0.8, respectively. Even with only 50% retention of the residual stress, the threshold flaw size is still greater than the current NDE limit (≈ 125 μm) for some components. The results in Figure 8 clearly show that 50% retention of residual stresses is sufficient to generate substantial increases in threshold stress and flaw size. In this calculation, the entire residual stress distribution was assumed to decrease by the same percentage. As discussed earlier, Figure 5(a), the bulk of the relaxation occurs near the surface. Hence, the actual retained residual stress benefits can be expected to be higher than that predicted in Figure 8. The benefits of residual stresses on the crack propagation life are discussed next.

RESIDUAL STRESS EFFECTS ON CRACK GROWTH BEHAVIOR

The ENSIP design philosophy assumes that a 794 μm (=1/32 in.) flaw could initiate during service in 1 out of 1000 components. In addition, ENSIP requires that the remaining crack propagation life from an inspectable crack size be equal to the component design life. This life management practice relies on accurate prediction of the crack growth behavior at critical locations and the ability to define safe inspection intervals based on this prediction. Current crack growth predictions exclude the influence of beneficial compressive residual stresses. Extensive data and analyses are available in the literature highlighting the significant increase in crack propagation life due to residual stresses. As discussed earlier, residual stresses relax, and significant scatter exists in the retained residual stresses. Hence, prior to implementation of the residual stresses in component lifing, the sensitivity of crack propagation life to various levels of residual stresses should be assessed. Extensive crack growth analyses were conducted for a semi-elliptical surface crack in an infinite geometry. The crack growth analysis code AFGROW [16] was used during this study. Equations (1) and (2) were used to generate a tabular database to represent the crack growth behavior of the material in AFGROW.

Figures 9(a) to 9(c) show the predicted maximum stresses versus crack propagation life, N_p, for two initial flaw sizes (25 and 120 μm) and residual stress levels corresponding to 20 and 50% of 8A. In actual components, the amount of retained residual stresses can be expected to be dependent on the applied stresses. The relaxation occurring at locations with high stresses (close to yield) will be the maximum. In this analysis, we assumed that the extent of relaxation is independent of stress level. The results from Figures 9(a) to 9(c) are summarized in Figure 9(d), which shows the ratio of N_p to N_p corresponding to $\sigma_{res}=0$ as a function of maximum applied stress. At R=0.1, this ratio ranges from 2 to 50 depending on the stress level and initial flaw size. The smaller the initial crack size, the higher is the relative gain in N_p. For initial flaw size of 25 μm, under LCF conditions (R = 0.1), 20% retention of the residual stress was sufficient to retain 5X to 50X increase in N_p compared to the baseline. Relative life gain higher than 2X at the high stress level for flaw size of 120 μm required 50% retention of the residual stresses. Under HCF conditions (R=0.8), the relative gain at high stress levels is less than 2X for residual stress retention of 50%. The lower gain in N_p at R=0.8 is consistent with similar observations of crack growth in residual stress fields in the literature [17]. The data shown in Figure 5(b) exhibited residual stress retention of ≈ 30-50%, based on surface measurement. The calculations were conducted assuming that the entire stress distribution decreased by the same percentage, in contrast to the data. Hence, the predictions shown in Figure 9 may be considered conservative, considering observations similar to those in Figure 5(a).

The crack growth response (surface crack length and crack depth versus cycles) at 600 MPa / R=0.1 corresponding to $\sigma_{res} = 0$ and 50% 8A is shown in Figure 10(a) and 10(b), respectively. The initial flaw size was $c_i = 120$ μm and the initial aspect ratio was $a_i/c_i = 1.0$. In the absence of residual stresses, this surface crack grows such that the aspect ratio nearly remains the same. In addition, at half-life, c has increased from 120 μm to ≈ 210 μm. Hence, the detectability of this crack has increased significantly at the end of the half-life period. In contrast, in the presence of residual stresses, the surface crack shows negligible crack growth almost up to 90% of total life. This response is similar to the response under HCF loading conditions. In the depth direction, there is marked increase in the rate of crack growth at ≈ 67% of life. This distinct difference in the crack growth response in the presence of σ_{res} compared to that in the absence of σ_{res} identifies a critical need for a more accurate and reliable NDI technique, which is sensitive to the crack extension in the surface <u>and</u> depth directions.

The influence of retained residual stresses on crack growth in the presence of combined LCF-type and HCF-type cycles is shown in Figure 11. Crack propagation life for an initial crack size of 120 μm subjected to maximum stress = 625 MPa was predicted for various ratios of number of cycles at R=0.8 to number of cycles at R=0.1. The retained residual stress distribution was assumed to be 30% of 8A. Also shown in Figure 11 is the baseline prediction (σ_{res}=0) and the trend-line corresponding to two times the baseline predictions. The crack propagation life in the presence of σ_{res} was always greater than twice that of the baseline, even for the case with high number of HCF-type cycles. Note that at stress levels close to the yield stress, the retained residual stresses may be significantly lower than 50%. In this case, the higher number of HCF-type cycles result in significantly reduced residual stress benefits on crack propagation life.

REMARKS

The properties used during this study are based on the original material prior to insertion in service. During service, the *in situ* properties of the material could change. Hence, analysis conducted to predict the remaining life should account for the current material behavior and the anticipated changes in these properties. Fractographic examinations of post-service components are in progress to assess the changes in the microstructure during service. Following these examinations, crack growth behavior will be characterized on specimens extracted from these components.

Successful incorporation of residual stresses in life management will require a good understanding of the surface <u>and</u> sub-surface residual stress changes. As mentioned earlier, only limited data [e.g. 6-8] are available documenting sub-surface residual stress changes. Vuckelich et al. [10] reported the first work documenting surface residual stress changes from detailed measurements on actual components. This work provided an idea of the range of relaxation of residual stresses that can be expected during service. However, accurate prediction of crack growth life requires sub-surface residual stress distributions also. Hence, additional data from destructive sub-surface measurements need to be collected.

The results of this study show that even retention of only 30% of the original residual stress distribution can yield greater than 2X increase in crack growth life, compared to the current baseline predictions, which exclude residual stresses. Data from laboratory coupon specimens and recent field inspection studies have shown that residual stresses can be expected to relax in most components. Thus, combining data from the field with detailed laboratory experiments and analysis, a reduced level of residual stress can be established and implemented in life management practice. Monitoring residual stresses at critical locations during service can help reduce the potential increase in risk associated with disk life extension. Life management based on such threshold residual stress level

will require NDI-based accurate monitoring of residual stress at critical locations. Recent depth measurements have shown that the most substantial residual stress relaxation occurs close to the surface. Sub-surface residual stress relaxation is not as severe as that observed on the surface. Hence, the NDI techniques should be capable of sub-surface residual stress measurement, preferably up to 150 μm deep. Note that such residual stress inspections are in addition to current crack inspections being conducted under the ENSIP program. Therefore, successful implementation of a life prediction methodology using residual stresses requires two critical NDI technology developments. These are: (1) accurate and reliable NDI techniques sensitive to crack extension in the surface <u>and</u> depth directions, and (2) NDI techniques to monitor surface <u>and</u> subsurface changes in residual stresses in components.

Surface enhancement procedures, such as shot peening, retard or prevent surface crack growth. Hence, if the lives of some of the components are extended, at certain locations, the chances of sub-surface crack initiation and growth are increased. Additional testing and analysis are required to characterize and model this behavior. New NDE techniques for detecting sub-surface crack initiation and growth may also be required to mitigate the increased risk of failure at these locations.

The results from this study show that substantial gains in crack propagation life can be realized if residual stresses are included in the life prediction methodology. This would require: (1) adequate quality control during the surface enhancement procedure, (2) understanding of changes in the residual stress distribution (surface <u>and</u> depth) during service, (3) accurate life prediction with residual stresses, and (4) monitoring of surface <u>and</u> depth residual stress periodically during service, similar to current crack inspection procedures. The utilization of residual stresses in the engine life management practice is also a key technology necessary for developing longer life and durable engines. Introduction of residual stresses via newer procedures such as low plasticity burnishing (LPB) [18] and laser shock peening (LSP) [19] are being explored. The retention of residual stresses generated by LPB and LSP have been reported to be significantly better than that generated by shot peening because of the reduced cold work [7,8]. Hence, re-introduction of residual stresses in legacy engine components using LPB and LSP should also be explored.

SUMMARY

Life extension of fracture critical parts is under consideration by the US Air Force. This technology development initiative is expected to significantly reduce the sustainment burden and to enable future long-life durable engines. Data from legacy engines indicate that shot-peen induced residual stresses at critical locations are retained only partially during service. This paper assessed the influence of various levels of retained residual stresses on the threshold stresses, threshold crack sizes and crack propagation in Ti-6Al-2Sn-4Zr-6Mo. The results show that even retention of only 30% of the original residual stress distribution can yield greater than 2X increase in crack growth life compared to the baseline predictions excluding residual stresses. Thus, combining data from the field with detailed experiments and analysis, a threshold level of location-specific residual stress can be established and implemented in the life management practice. The inclusion of residual stresses in life prediction of the component will require NDI-based accurate monitoring of residual stress at life-limiting critical locations, in addition to crack inspections being conducted under the ENSIP program. The NDI techniques should enable monitoring of surface <u>and</u> sub-surface residual stresses. Improved NDI techniques, sensitive to surface <u>and</u> depth crack growth, are also required.

ACKNOWLEDGMENTS

REFERENCES

1. Larsen, J.M. et al., "The Engine Rotor Life Extension (ERLE) Initiative and It's Opportunities to Increase Life and Reduce Maintenance Costs," presented at AeroMat 2001, Long Beach, CA, 12 June 2001.
2. Harris, J.A., "Engine Component Retirement for Cause, Vol. I - Executive Summary," AFWAL-TR-87-4069, Vol. I., Air Force Wright Aeronautical Laboratories," Wright-Patterson AFB, OH, 1987.
3. Engine Structural Integrity Program (ENSIP), MIL-STD-1783 (USAF), 30 November 2001.
4. Holzapel, H., Schulze, V., Vohringer, O., and Macherauch, E., "Residual Stress Relaxation in an AISI 4140 Stell due to Quasi-static and Cyclic Loading at Higher Temperatures," Materials Science & Engineering, Vol. A248, pp. 9-18, 1998.
5. Berger, M.-C and Gregory, J.K., "Residual Stress Relaxation in Shot Peened Timetal®21S," Materials Science and Engineering, Vol. A263, pp. 200-204, 1999.
6. Cao, W., Khadhraoui, M., Brenier, B., Guedou, J.Y., and Castex, L., "Thermomechanical Relaxation of Residual Stress in Shot Peened Nickel Base Superalloy," Material Science and Technology, Vol. 10, pp. 947-954, November 1994.
7. Prevey, P., Hornbach, D., and Mason, P., "Thermal Residual Stress Relaxation and Distortion in Surface Enhanced Gas Turbine Engine Components," Proceedings of the 17th Heat Treating Society Conference and Exposition and the 1st International Induction Heat Treating Symposium, D.L. Milam et al., Eds., ASM, Materials Park, OH, pp. 3-12, 1998.
8. Prevey, P., "The Effect of Cold Work on the Thermal Stability of Residual Compression in Surface Enhanced IN718," Proceedings, 20th ASM Materials Solutions Conference & Exposition, St. Louis, Missouri, Oct. 10-12, 2000.
9. Ahmad, J., Chandu, S., and Prevey, P., "An Analysis of Redistribution of Surface Treatment Induced Residual Stresses", To be submitted for publication, 2001.
10. Vukelich, S., Russ, S.M., Berkley, S., and Bradley, E.F., "Residual Stress Measurement and it's Application to Achieve Predicted Full Life Potential of Low Cycle Fatigue (LCF) Limited Engine Disks," The 9th International Symposium on Transport Phenomena and Dynamics of Rotating Machinery, Honolulu, Hawaii, February 10-14, 2002.
11. Larsen, J.M. and Jira, J.R., Experimental Mechanics, pp. 82-87, 1991.
12. Jira, J.R., Nicholas, T., and Larsen, J.M., Fatigue 87, Vol. IV, E. Starke and R.O. Ritchie, Eds., Engineering Materials Advisory Services, Ltd., West Midlands, U.K., pp. 1851-1860, 1987.
13. Kitagawa, H. and Takahashi, S., Proceedings of the Second International Conference on Mechanical Behavior of Materials, Boston, MA, pp. 627-631, 1976.
14. Larsen, J.M., Russ, S.M., John, R., and Maxwell, D.C., "The Role of Threshold Fatigue Crack Growth in Life Prediction of Two Titanium Alloys Under High Cycle Fatigue Spectra," To be submitted for publication, 2001.
15. Larsen, J.M., John, R., Russ, S.M., Maxwell, D.C., Worth, B.D., Rosenberger, A.H., Li, K. and Porter, W.J., "The Role of Near-Threshold Small-Crack Behavior in Life Prediction of Titanium Alloys For Use in Advanced Turbine Engines," Small Fatigue Cracks: Mechanics and Mechanisms, K.S. Ravichandran, R.O. Ritchie, and Murakami, Y., Eds., Elsevier Science, Oxford, UK, 1999.
16. AFGROW, Harter, J., US Air Force Research Laboratory, AFRL/VASM, Wright-Patterson Air Force Base, OH, USA. Available at http://fibec.flight.wpafb.af.mil/fibec/afgrow.html.
17. Ruschau, J.J., John, R., Thompson, S.R., and Nicholas, T., "Fatigue Crack Growth Characteristics of Laser Shock Peened Ti-6Al-4V" Journal of Engineering Materials and Technology, Vol. 121, No.3, pp. 321-329, 1999.
18. Prevey, P.S. and Cammett, J., "Low Cost Corrosion Mitigation and Improved Fatigue Performance of Low Plasticity Burnished 7075-T6," Proceedings, 4th International Aircraft Corrosion Workshop, Solomons, MD, Aug 22-25, 2000.
19. Clauer, A.H., "Laser Shock Peening for Fatigue Resistance," Surface Performance of Titanium, J.K. Gregory et al., Eds., TMS, Warrendale, PA, pp. 217-230, 1996.
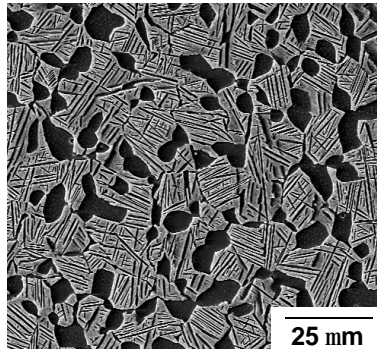
Figure 1. *Fine, equiaxed **a** + **b** microstructure of Ti-6Al-2Sn-4Zr-6Mo after heat treatment.*
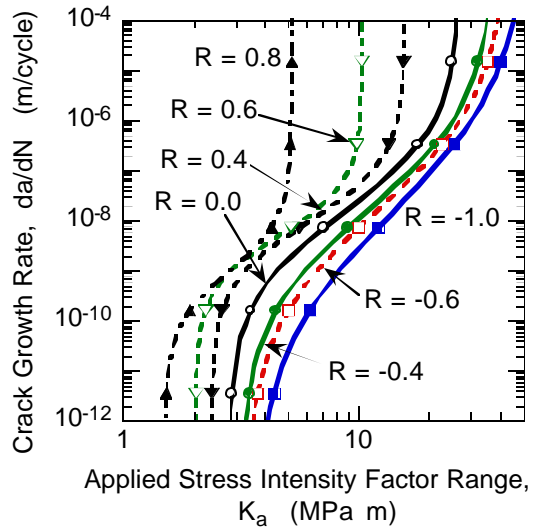
Figure 2. *Baseline long crack growth behavior of Ti-6Al-2Sn-4Zr-6Mo. These curves are from Equation (1).*
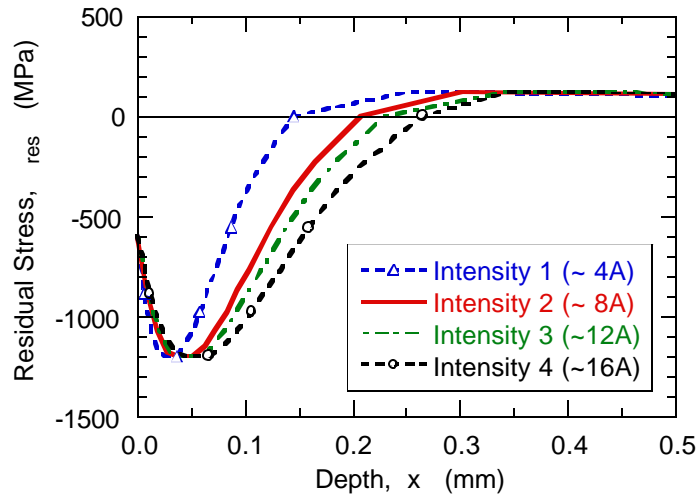
Figure 3. *Estimated residual stress, s_{res}, distributions in Ti-6Al-2Sn-4Zr-6Mo due to shot-peening.*

(a)

(b)
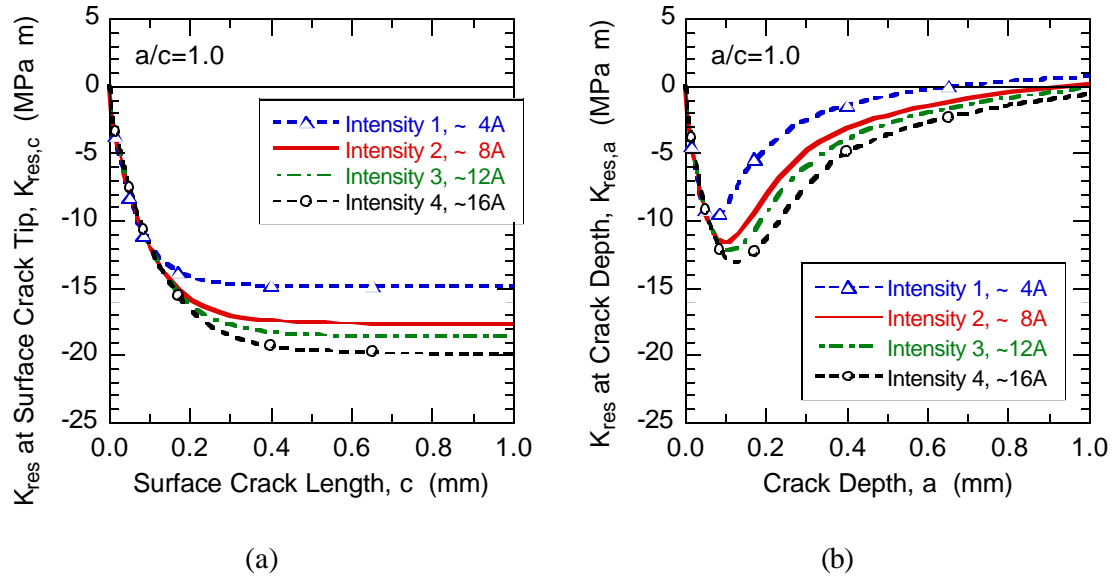
Figure 4.   Residual stress intensity factor, K_{res}, for a semi-elliptical surface crack with aspect ratio (a/c) = 1, due to the residual stress distributions shown in Figure 3. (a) K_{res} at surface crack tip,c, and (b) K_{res} at crack depth, a.

(a)

(b)
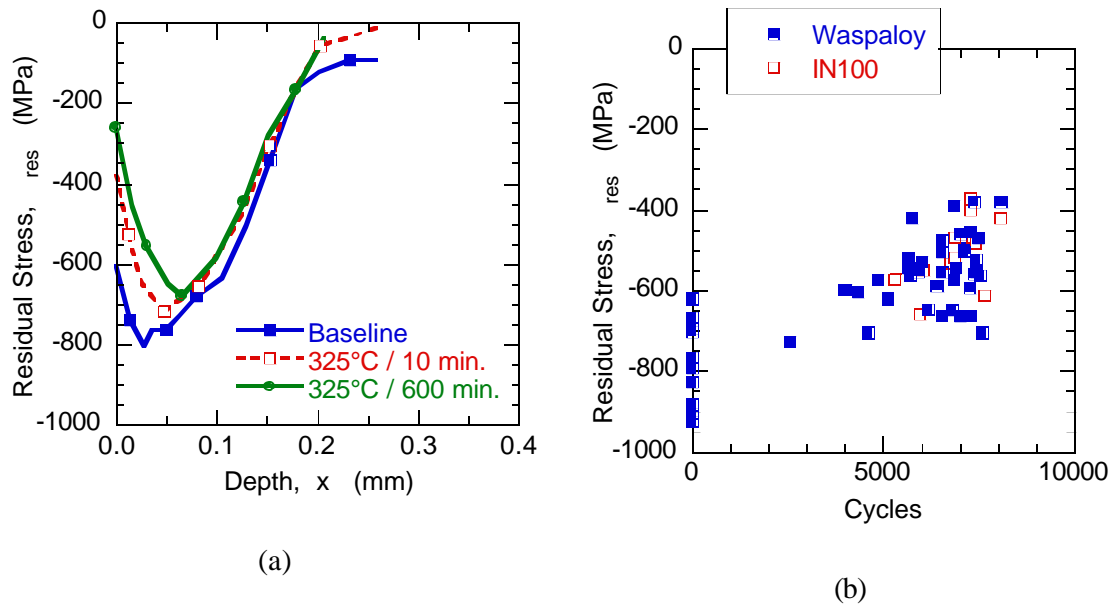
Figure 5.   (a) Residual stress relaxation in Ti-6Al-4V at 325 °C [Prevey et al., 1998], and (b) Surface residual stress relaxation at notches in Ni-base superalloy engine disks [Vukelich et al., 2002].
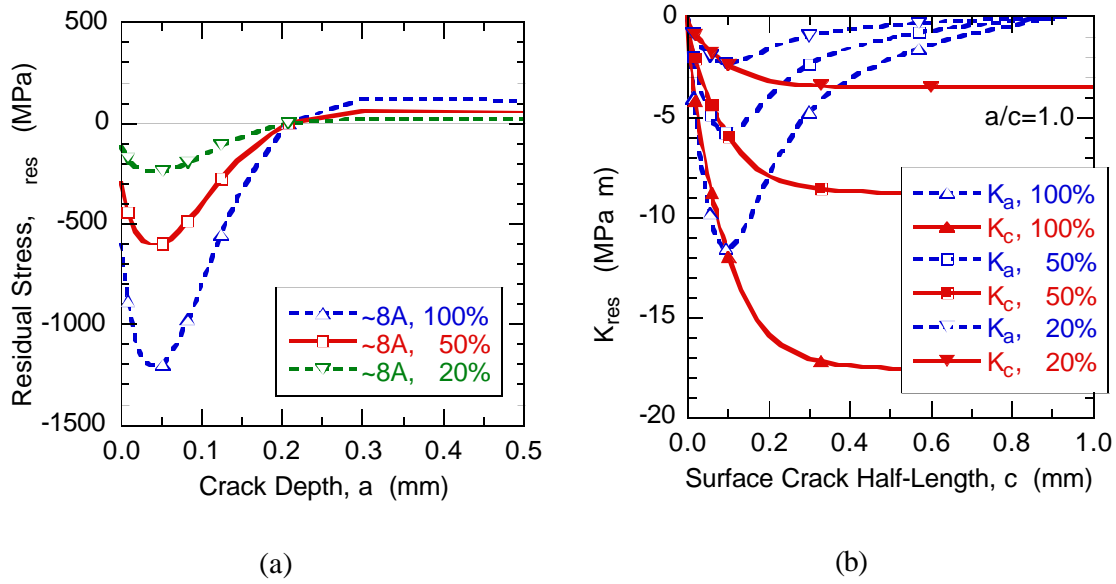
Figure 6.   *(a) Assumed residual stress distributions to simulate relaxation during service.*
        (b) Corresponding $K_{res,c}$ and $K_{res,a}$ for aspect ratio, a/c=1.
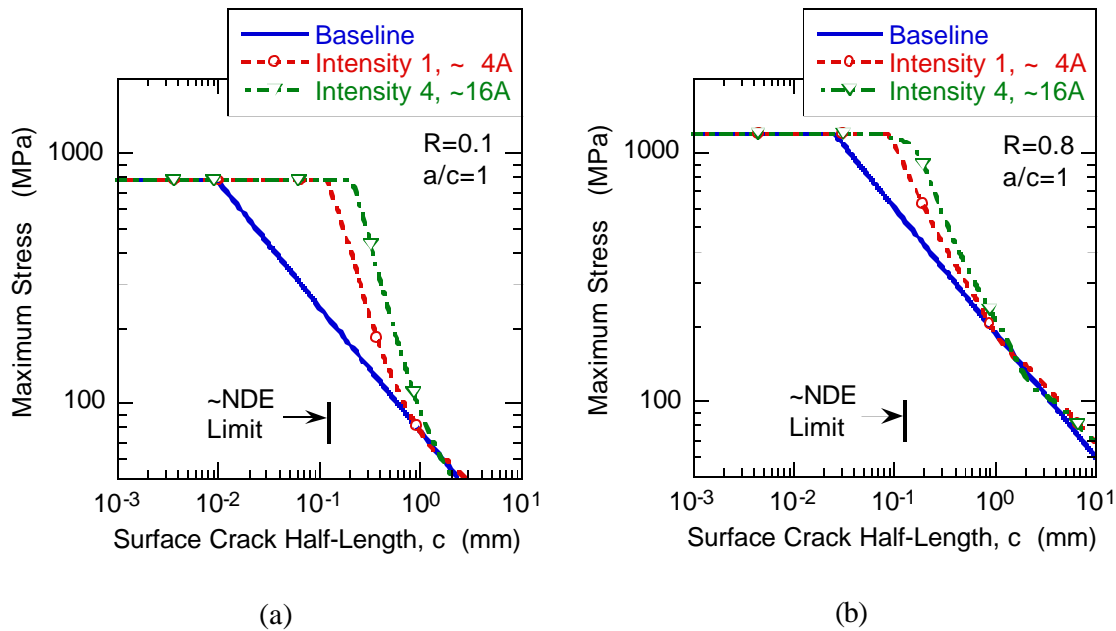
Figure 7.   *Predicted influence of shot-peen residual stresses on fatigue limit of Ti-6Al-2Sn-4Zr-6Mo at (a) R=0.1 and (b) R=0.8. Aspect ratio, a/c=1.*
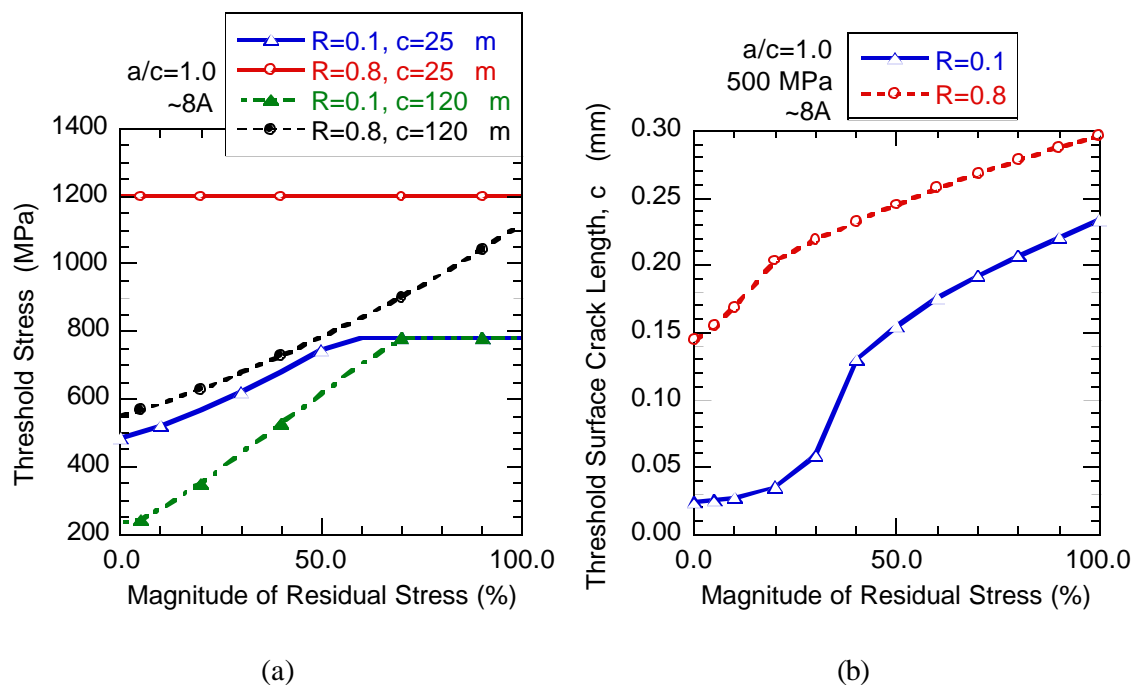
Figure 8.   Influence of varying levels of residual stresses (0-100% of Intensity 2, ~8A) on (a) Threshold stress corresponding to c=25 and 120 mm, and (b) Threshold surface crack length corresponding to maximum applied stress = 500 MPa for a/c=1.0.
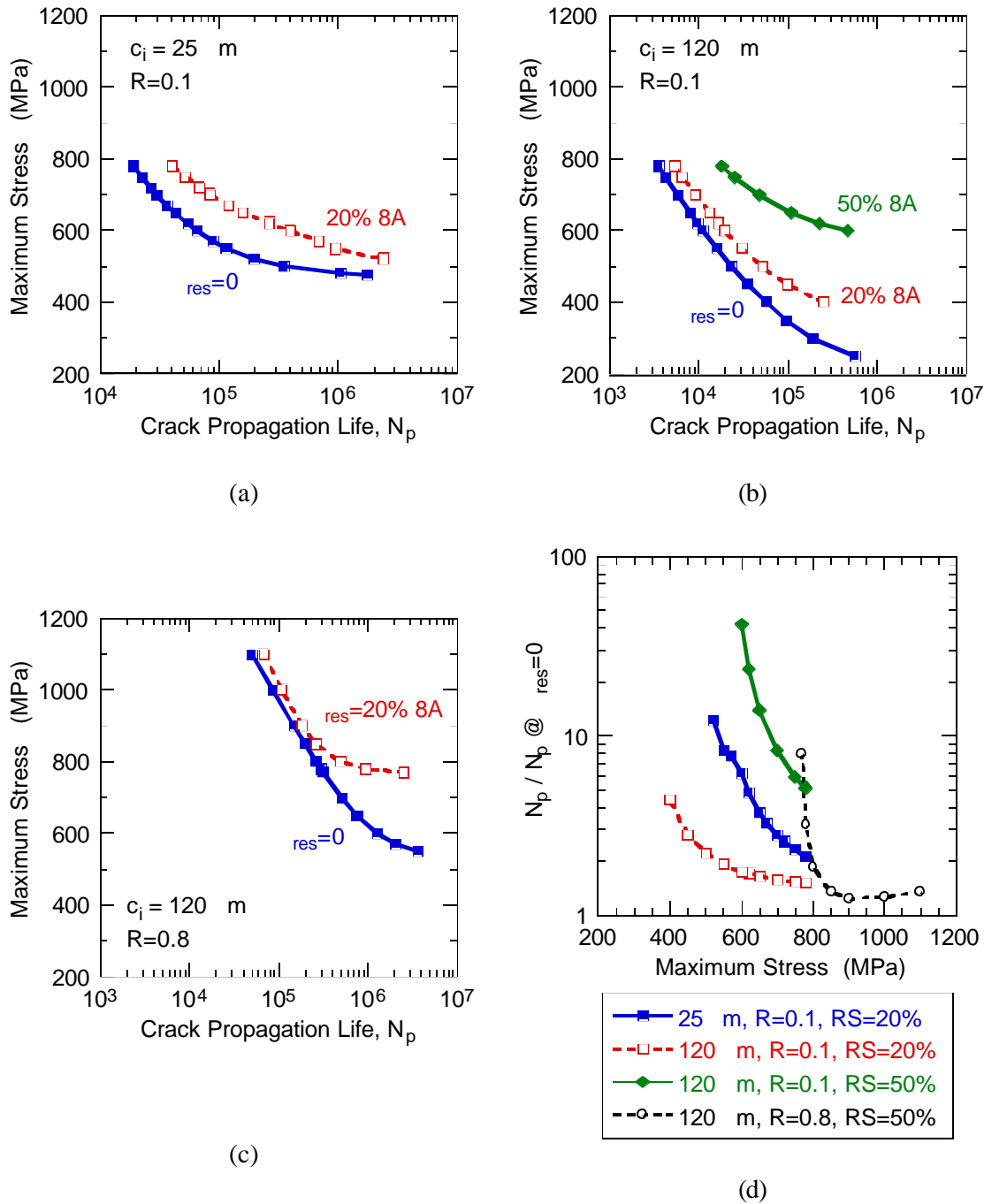
Figure 9.   *Predicted influence of retained residual stresses on crack propagation life (N_p). (a) Maximum stress versus propagation life (S-N_p) behavior at $R=0.1$ for $c_{initial}=25$ mm and $a/c=1$. (b) S-N_p behavior at $R=0.1$ for $c_{initial}=120$ mm and $a/c=1$. (c) S-N_p behavior at $R=0.8$ for $c_{initial}=120$ mm and $a/c=1$. (d) Ratio of N_p to baseline ($s_{res}=0$) N_p as a function of maximum stress.*
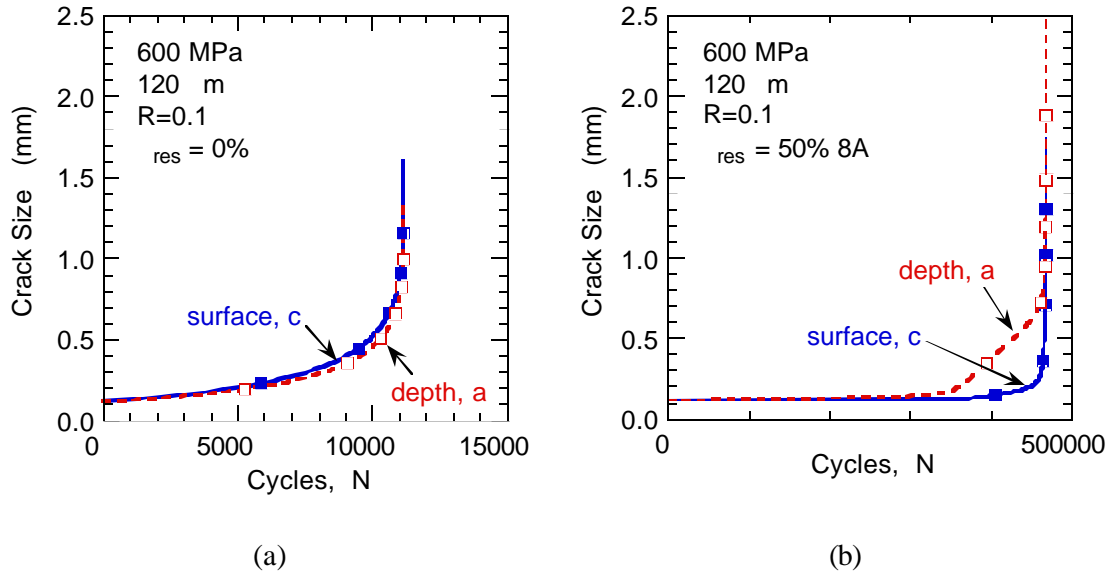
Figure 10. Crack growth behavior in the presence of residual stresses at R=0.1.
(a) s_{res} = 0, and (b) s_{res} = 50% of 8A. Assumed initial crack size = 120 mm and initial a/c = 1.0.
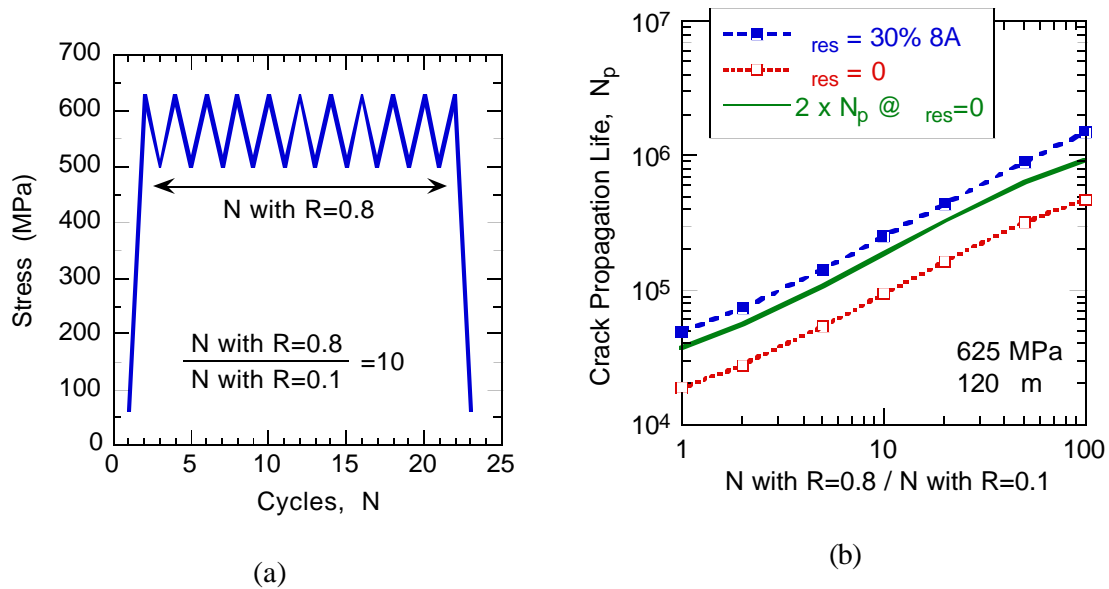
Figure 11. (a) Assumed simple mission loading sequence containing 1 R=0.1 cycle and multiple R=0.8 cycles. (b) Predicted crack propagation life, N_p. Assumed maximum stress = 625 MPa and initial crack size = 120 mm.

The Role of Spectrum Loading
in Damage-Tolerance Life-Management
of Fracture Critical Turbine Engine Components

James M. Larsen[1], Andrew H. Rosenberger[1], George A. Hartman[2]
Stephan M. Russ[1] and Reji John[1]

[1] Air Force Research Laboratory, Materials and Manufacturing Directorate
AFRL/MLLMN, 2230 Tenth Street, Ste 1
Wright-Patterson Air Force Base, Ohio 45433-7817, U.S.A.

[2] University of Dayton Research Institute
Structural Integrity Division
300 College Park, Dayton, Ohio 45469-0128, U.S.A.

ABSTRACT

Recent developments in experimental and computational capabilities suggest an opportunity to develop improved models of crack growth for use in life management of materials and components in advanced gas turbine engines. Improvements in such models have potential benefits in the sustainment of aging engines, as well as the design of more durable future engines. Current approaches for life management of engine components tend to ignore potential increases in crack propagation lifetime that may occur as the result of load interaction phenomena under variable amplitude spectrum loading. In effort to quantify these potential benefits, a study of updated mission profiles was performed. A variety of engine usage spectra were surveyed to document their cycle content statistically, including characterization of the fundamental load sequence events and the expected severity of damage produced by these events, using data from the advanced nickel-base superalloy IN100.

INTRODUCTION

Current deployment plans by U.S. Air Force dictate that most aircraft be used well beyond their original design lifetimes [1,2]. It has been estimated that replacing the Air Force's existing fleet of aircraft would cost approximately $290B in 1995 dollars [3], while the budget for acquisition of new aircraft is approximately $2-3B per year. Since significant increases in the acquisition budget are unlikely in the foreseeable future, the need for, and cost of, aircraft sustainment will continue to be a major Air Force expense. Moreover, sustainment costs will almost certainly grow substantially over the next few years, as the large number of aircraft acquired in the 1980's continue to age. The National Materials Advisory Board (NMAB) report on Aging of U.S Air Force Aircraft [2] clearly defined this problem and identified technology needs to support sustainment of aircraft structures. To make the NMAB study tractable, the issue of aging turbine engines was excluded from consideration, although the board's chairman, C. F. Tiffany, noted that aging engines were a major concern and should be the subject of a future study.

Aging turbine engines are traditionally viewed as being more easily maintained than aging aircraft, since engines are disassembled during periodic overhauls, making replacement of aging engine components a comparably straightforward process. However, the current cost of engine maintenance represents over 60% of the Air Force's annual budget for turbine engines. This budget also includes

engine development, acquisition, and about 2.6% for science and technology. A key aspect of the engine maintenance process is the life management of fracture critical components, such as engine disks and spacers, as specified by the Engine Structural Integrity Program (ENSIP) [4]. Such components are most critical in single-engine fighter aircraft, since component failure normally results in loss of the aircraft. The cyclic safe-life of such components is typically defined as the point at which the probability of initiating a 0.79-mm surface crack is predicted to be 1/1000. In addition, to preclude effects of possible rogue flaws, the crack propagation lifetime from a possible initial material defect must equal or exceed the design life. When the component service life reaches the design life, the component is to be replaced. Unfortunately, the 0.79-mm crack-initiation requirement necessitates that 99.9% of the components be retired prematurely in order to assure removal of the remaining 0.1% of components that are predicted to contain such a crack. Although this life-management approach has been effective in assuring flight safety, evidence suggests that it may be highly conservative in many instances. This conservatism contributes to high maintenance costs and may limit readiness, if the necessary spare parts are unavailable.

An alternative approach, known as inspection-based life management or retirement for cause, relies on nondestructive evaluation (NDE) to identify crack-like damage, which is then used as the primary basis for component retirement. To assure safety, the minimum remaining crack propagation lifetime should be at least twice the inspection interval. Typical fighter aircraft engines are designed for a nominal life limit of 8000 total accumulated cycles (TACs), which equates to a lifetime of approximately 10 to 14 years at current rates of aircraft usage. These engines undergo an overhaul and safety inspection at their half-life.

Many of the engines in the Air Force's fleet of F15 and F16 aircraft will soon reach their design lifetimes, which is expected to result in a major wave of increased engine sustainment costs as the aging components are replaced. However, it has been estimated [5] that extending the operational life of 60% of the disks in F16 and F15 aircraft by one inspection interval, nominally from 8000 to 12000 TACs, would result in a cost avoidance on the order of $600M over the period of 2005-2010, and substantially more in the long run. Such a life extension might be expected to produce an accompanying increase in the risk of catastrophic failure. However, current projections indicate that it should be possible to extend the lives of many components in today's engines without increasing overall risk, if key improvements in life management technology are developed and implemented. Many of these technologies would also apply to life management of future engines, which could be designed to optimize durability and affordability.

To address these issues, the U.S. Air Force is embarking on a technology development and implementation initiative, known as the Engine Rotor Life Extension (ERLE) program, which is organized to reduce the cost of sustainment of its current fleet of advanced turbine engines. The ERLE program, which is part the larger Versatile Affordable Advanced Turbine Engine (VAATE) program [6] and its National Turbine Engine Durability initiative, has the goal of extending the useful lifetime of major, fracture-critical components in currently fielded gas turbine engines, while maintaining or improving overall engine safety and reliability. Full achievement of the ERLE objectives will require improvements in a broad range of technologies, including nondestructive evaluation, engine usage and health monitoring, life prediction and fracture mechanics, data fusion, and component repair. The current paper highlights some of the background and opportunities for improvement in the area of life prediction and life management based on fatigue crack growth, with a specific focus on effects of engine operating spectra on fatigue crack growth under cycle- and time-dependent conditions.

ENGINE MISSION LOADING

It is well known that loading spectra of major rotating components in engines typically exhibit less variability than spectra experienced by aircraft structures [7,8,9]. The major cycles in mission spectra for these rotating components result from variations in engine speed produced by throttle excursions for take-off, in-flight maneuvers, and landing.   For components exposed to elevated temperatures there is additional stress imposed by thermal gradients and thermal transients produced by variations is operating conditions and heat transfer within the engine. A schematic of a flight profile showing the simplified elements of a typical flight is illustrated in Fig. 1 [7]. This figure shows normalized spectra for routine engine operating speeds and associated temperatures for a given location on a generic component. As shown, the maximum loading tends to occur at takeoff, although additional, but infrequent, full-power excursions may occasionally reach this maximum level.   Hold periods of constant stress occur at moderate stress (60 to 65% of maximum) representative of cruise or transit portions of the mission. Major rotating components, such as disks and spacers, are typically designed such that their maximum stresses at full power are only slightly below the component burst stress at the operation temperature.

The engine-component design practices, combined with the relatively controlled nature of the mission spectra, tend to obviate the large effects of load sequence, or load interaction, on crack growth that are often common in fatigue spectra of airframe structures. Depending on the nature of the load sequence, such load interaction effects can produce either crack acceleration or crack retardation [10], although the latter is far more common. Crack retardation tends to occur in fatigue cycles that follow an overload, and this effect can be extremely significant, particularly as the overload ratio (OLR) increases. Here we define the OLR to be σ_{max} of the overload divided by σ_{max} of the subsequent cycles. Airframe spectra may contain cycles with OLRs well in excess of 2 or 3, while experience with engine spectra has suggested that a limiting OLR of 1.25 is common. Such conclusions were drawn by a NATO AGARD task group established in the early 1980s to develop a loading standard for fighter aircraft engine disk usage [11].   This task group developed TURBISTAN, a test spectrum applicable for titanium alloys operating at or near ambient temperature. Noteworthy from analysis of the TURBISTAN load spectrum was that the spectrum tended to approximate a simple sequence containing a high stress ratio baseline with periodic underloads, where the underloads in this case were at loads near zero – but not compressive.

Typical Loading Spectra for Major Rotating Components

Data on engine usage profiles are continually collected and used to update the life analyses. Figures 2a and 2b present recently obtained examples of loading and temperature histories for a specific location on a titanium-alloy rotor component during a single flight. These spectra correspond to a single ground-air-ground cycle and indicate the low-cycle-fatigue (LCF) nature of the loading and the extent of stress and temperature variability for this modest-temperature component location. Figure 2c plots the relationship between stress ratio (R = $\sigma_{min}/\sigma_{max}$) and normalized maximum stress for each of the individual loading cycles depicted in Fig. 2a. The data indicate that almost all of the cyclic loading occurs under a relatively high stress ratio, combined with a correspondingly high normalized stress. These loading conditions are the result of the combined effects of changes in engine speed, coupled with the effects of thermally induced stresses. The relationship between stress and temperature is illustrated in Fig. 2d, where normalized stress is plotted versus temperature for each reversal point in the stress spectrum. This figure also shows that stress and temperature are negatively correlated, that is, stress and temperature tend to be out-of-phase for the majority of the fatigue cycles. The loading may be further quantified by plotting a histogram of the normalized stress, as illustrated in Fig. 2e, which shows that a majority of the cycles have maximum stress levels greater than 70% of the maximum mission stress. Alternatively, one can calculate the ratio of the maximum cyclic stress to the maximum mission stress - the OLR. Defining the maximum stress in Fig 2a as an overload, the OLR of the remaining cycles was calculated, and a histogram of the results in plotted in Fig 2e. This figure shows that many of the cycles experience OLRs in the range of 1.25, consistent with the earlier reports. Notably absent in the spectrum is any significant hold time near a constant load of appreciable magnitude.

A second stress spectrum for a higher-temperature, nickel-base-superalloy component is show in Fig. 3a, and the corresponding temperature spectrum is shown in Fig. 3b. In this case the fatigue stress cycles have a larger relative amplitude, and a significant compression cycle occurs when the engine is powered down and cools slowly to ambient temperature. The relationship between stress ratio and temperature is plotted in Fig. 2c, and a stress versus temperature plot is presented in Fig. 3d. As shown in the latter figure, this mission and component location also exhibits an out-of-phase stress-temperature relationship for most fatigue cycles. Figures 3d and 3e, respectively, show histograms of the cyclic maximum load data and the corresponding OLRs. The majority of the maximum loads in cycles with high values of maximum load are centered on a value of approximately 0.7 times the maximum mission load. As shown in Fig. 3e, in terms of overload ratio, this corresponds to values of OLR approximately centered about a value of 1.4, with a substantial number of cycles above this level. This trend is in contrast to the data of Fig. 2e from the lower-temperature titanium-alloy component, wherein the OLRs more commonly fell around 1.25. Like the earlier spectrum, the spectrum in Fig. 3 does not exhibit significant periods of sustained loading.

HIGH-TEMPERATURE LOAD SEQUENCE EFFECTS IN IN100

The powder metallurgy, nickel-base alloy IN100 was chosen as a representative material for assessment of the role of turbine engine load sequence effects on crack growth. This material was selected for several reasons: (1) as noted above, the more extreme mission stress spectrum was observed in the higher-temperature, nickel-base-alloy component, (2) IN100 is in widespread use in advanced engines, (3) a substantial database for this alloy was already available, and (4) this material is representative of other high performance, powder-metallurgy, nickel-base alloys used throughout the turbine engine industry. The specific material chosen was superplastically forged and heat treated by Pratt & Whitney according to their alloy specification PWA 1073. This produced the fine uniform microstructure of primary gamma-prime grains in gamma-gamma prime matrix shown in Fig. 4.

A U.S. Air Force contract report by Pratt & Whitney served as the primary reference for data on this material [7]. This report demonstrated that the main parameters controlling high-temperature fatigue crack growth in this alloy were temperature, frequency, and stress ratio. These data were obtained from tests of compact tension, C(T), specimens in accordance with ASTM standard E-647. For most cases, the range in ΔK over which the tests were performed was limited by the relatively low fatigue frequencies used and the resulting long test times.

Figure 5 plots the effect of temperature on fatigue crack growth for temperatures ranging from 538 to 732 °C, at a frequency of 0.167 Hz, or 10 cycles/minute. For the data shown, the crack growth rate increased by a factor of approximately 3 to 4 as the temperature increased from 538 to 732 °C. The curves shown in the figure and the subsequent plots represent the correlation provided by an interpolative hyperbolic-sine regression model originally developed by Annis et al [12,13,14]. This model provides a mathematical representation of effects of temperature, frequency, stress ratio, and load-sequence effects.

Figure 6 shows crack growth data for tests of IN100 at a temperature of 649 °C as a function of frequency, ranging from 0.00833 to 20 Hz. Over this range in increasing frequency, the crack growth rate decreased by a factor of approximately 5 to 7, depending on the applied ΔK. Figure 7 shows data collected at 649 °C, a frequency of 0.167 Hz, and stress ratios ranging from 0.1 to 0.8. For a given value of ΔK, this range in stress ratio resulted in an increase in crack growth rate by a factor of approximately 3 with increasing R.

When considering effects of variable-amplitude loading, it is convenient to define loading parameters in terms of the stress ratio of the baseline fatigue cycle, the OLR, and the number of baseline cycles between overloads (CBO). These parameters are depicted schematically in Fig. 8, which shows

blocks of constant-load-amplitude fatigue interrupted by periodic overloads. By testing under repeated blocks of such cycles, one can quantify the effects of load interactions that simulate the key elements comprising a typical engine mission. Figure 9 shows effects of applying one cycle at an OLR of 1.5, followed by 40 cycles of baseline fatigue loading at an R of 0.5. As shown, increasing from no overload (OLR = 1.0) to a relatively modest overload (OLR = 1.5) results in a reduction in the crack growth rate of approximately a factor of 4 due to the action of the overload. This effect is further revealed in Fig. 10, which shows the effect of increasing the number of CBO from 5 to 40 with an OLR of 1.5. As shown, this increase in the number of CBO produced a reduction in crack growth rate by a factor of 5 or more. This effect was particularly accentuated at lower values of ΔK.

To extend the understanding of load-sequence effects in IN100, a focused study of crack growth rates was conducted under repeated mission-element cycle blocks of the type shown in Fig. 8. In this study, spectra were applied under constant-K-controlled conditions, rather than constant-load-controlled conditions. This specialized testing method incorporates a greatly improved direct-current potential-difference technique for measurement of crack length. This improved technique results in substantial improvements in the accuracy and precision of corresponding calculations of da/dN, and the time required to perform key experiments is greatly reduced. Tests were performed on C(T) specimens using repetitive fatigue blocks composed of a single overload followed by a block of constant-ΔK cycles. In each case the crack was extended until it became clear that a macroscopic steady state crack growth rate had been achieved, which was indicated by a linear crack-length vs. cycles (a vs. N) response. In this manner any transient behavior due to changes in the type of spectrum being applied was clearly identified and excluded from the valid data.

These tests were performed under a variety of loading conditions, which are exemplified by the data presented in the lower region of Fig. 11. This graph plots crack growth rate as a function of the number of CBO for OLRs of 1.125, 1.25, 1.375, and 1.5, and the experimental results are indicated by solid symbols and connected by dotted lines. The tests were performed in air at 649 °C, a frequency of 0.167 Hz, R = 0.5, and K_{max} of the baseline cycles = 30 MPa√m. The horizontal line represents the crack growth rate observed under this baseline constant-K-amplitude condition. The upper region of this plot also shows calculations of crack growth rate obtained by a linear summation of the contribution from one overload cycle plus the given number of CBO, ignoring any possible load interaction effects. This simple approximation shows that the expected growth rate approaches the baseline value as CBO increases.

In contrast to the simple approximation, the data for the overload tests show that the crack growth rate quickly drops below the baseline growth rate as CBO increases. When CBO is zero, the crack growth rate corresponds to constant amplitude cycling under the overload condition. As CBO is increased, the resulting average crack growth rate soon drops below the baseline rate. At a CBO of 40, the growth rates for the higher OLR experiments fell substantially below the baseline. To further examine the influence of OLR, a number of additional experiments were performed as a function of OLR with CBO held constant at 40, Fig. 12. This figure shows a continually reducing growth rate as OLR was increased from 1.0 (no overload) to 1.6. As shown, relatively minor overloads produced a reduction in crack growth rate, and the greatest reduction in crack growth rate occurred in the approximate range of 1.0 < OLR < 1.3.

To further reveal the behavior of the observed load-interaction effect, the procedure depicted in Fig. 13 was performed, wherein the results for a given OLR were used to deduce the instantaneous crack growth rate following an overload. Under this procedure, the local crack growth rate following an overload is deduced by subtracting effects of successive cycle blocks. For example, subtracting the crack growth during a 20-CBO block from the growth observed during a 40-CBO block gives the apparent average growth rate contribution from cycles 21 through 40, which eliminated the apparent effect of the initial portion of the block, including the overload. By performing this procedure on successively smaller blocks, the data shown in Fig. 14 were obtained. These data indicate that the local crack growth rate

following an overload is reduced almost immediately, and that continued crack growth retardation is almost constant until the subsequent overload interrupts and restarts the process. For example, the apparent growth rate for an OLR of 1.5 drops after one cycle to a value that is approximately an order of magnitude below the baseline rate.

SUMMARY AND CONCLUSIONS

To address the growing financial and logistical costs of sustainment of turbine engines, the U. S. Air Force is investing in a range of science and technology initiatives to improve and extend capabilities for component life management. Recent advances in computational and experimental capabilities present important opportunities for development of more accurate and robust life-management technologies. In support of models of damage tolerance and fatigue crack growth, the current study surveyed a number of updated turbine-engine mission-usage histories. From these data it appears that the combination of loading and thermal histories may produce appreciable variations in stress, particularly in some of the higher temperature components that experience significant thermally induced stresses. As produced by variations in engine speed, the majority of the engine duty cycles occur at relatively high stresses, presenting the opportunity for load sequence effects.

The potential magnitudes of the effects of key mission usage variables were assessed using data from the superalloy IN100 from the literature, plus data generated using a newly developed constant-K-controlled experimental capability. This method, which also used a much improved direct current potential difference technique for measurement of crack length, provided a unique capability to perform highly specialized load-sequence experiments quickly. It was shown that the role of mission load sequence events can produce variations in crack growth rate that are as significant as those produced by the more common primary variables of temperature, frequency, and stress ratio. In tests of simplified mission elements containing relatively modest overloads, reductions of crack growth rate of a factor of four were observed, and the greatest sensitivity in crack-retardation occurred over the interval of overload ratios from 1.05 to 1.3. These findings suggest that a potentially significant beneficial effect of load sequences may be expected under typical mission loading.
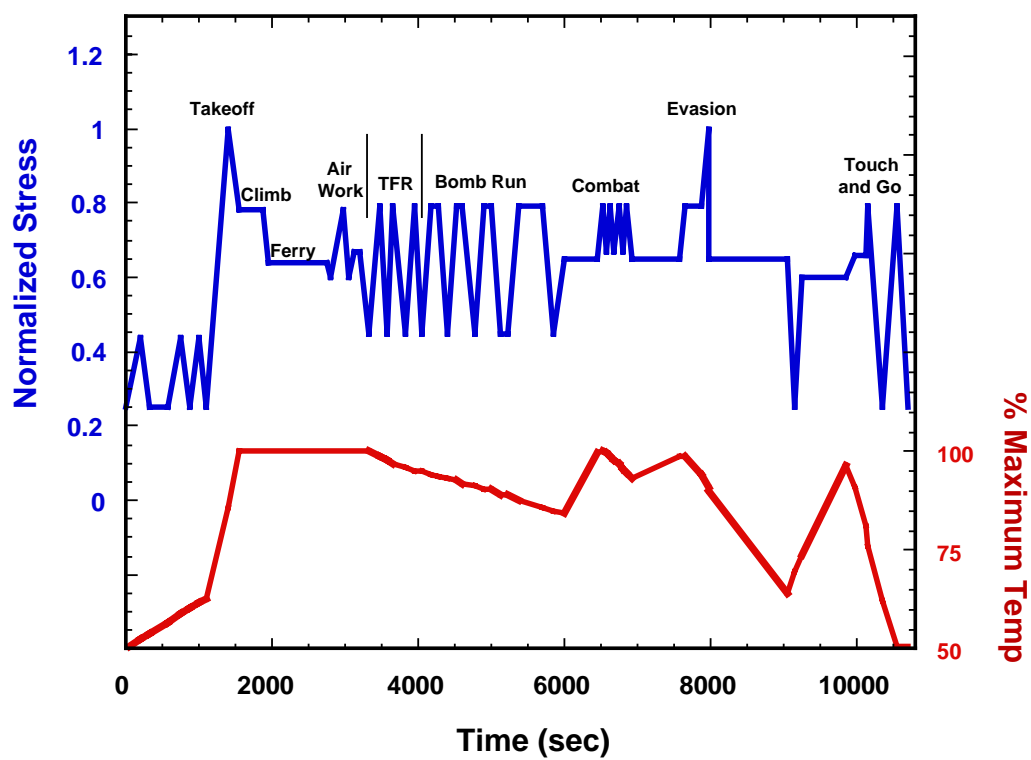
Figure 1. Schematic of typical mission loading and temperature spectra for high temperature military turbine engine rotor components, such as disks.
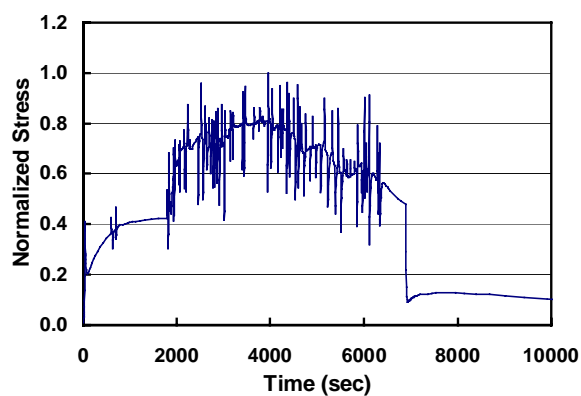
(a) Stress-time mission history
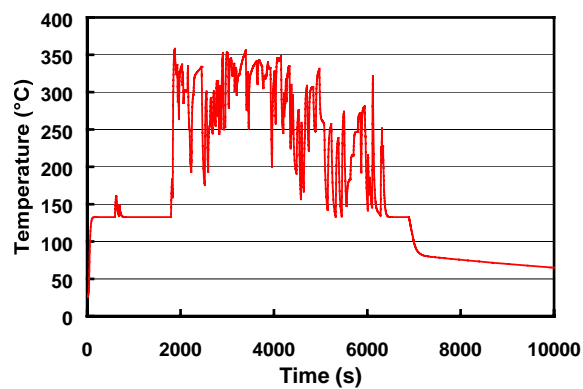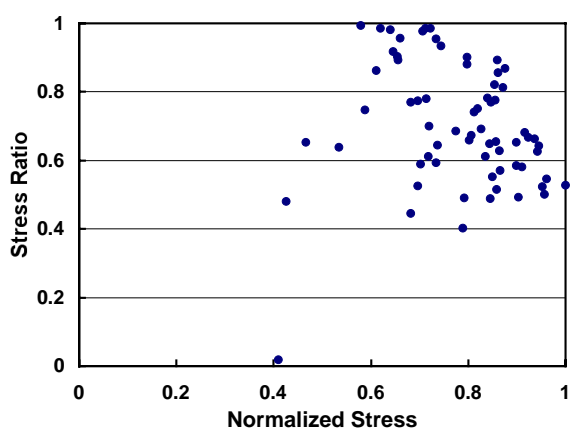
(b) Temperature-time mission history

(c) Stress ratio vs. normalized stress
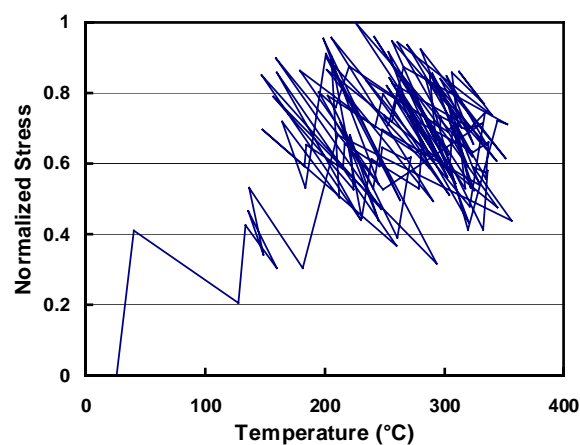
(d) Stress-temperature mission history
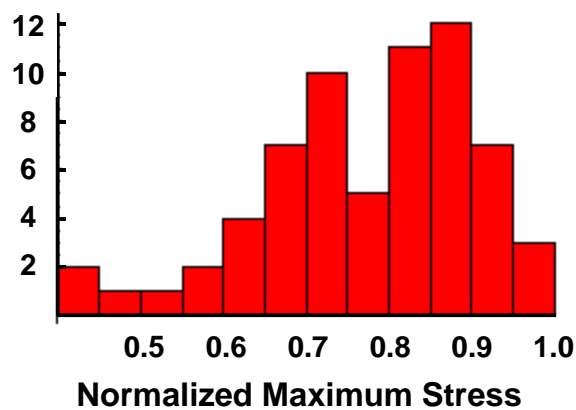
(e) Histogram of maximum stresses
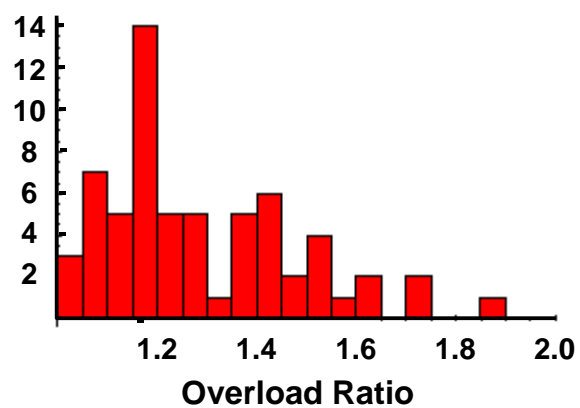
(f) Histogram of overload ratios (OLRs)

Figure 2. Typical engine mission data for a titanium alloy component.
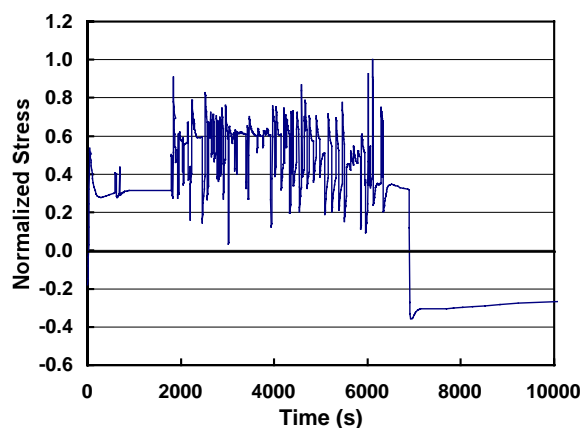
(a) Stress-time mission history
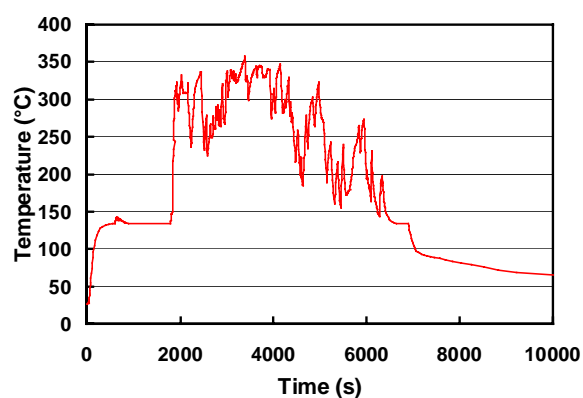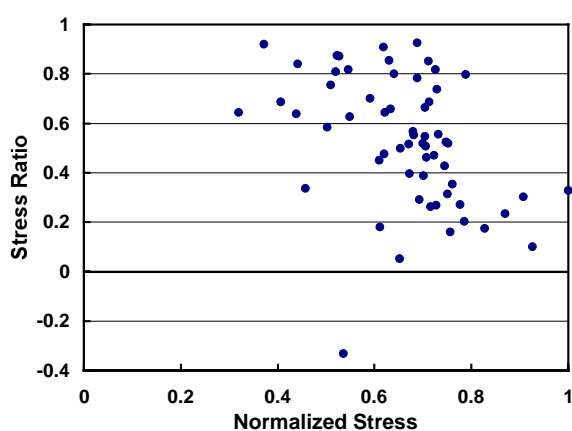
(b) Temperature-time mission history

(c) Stress ratio vs. normalized stress
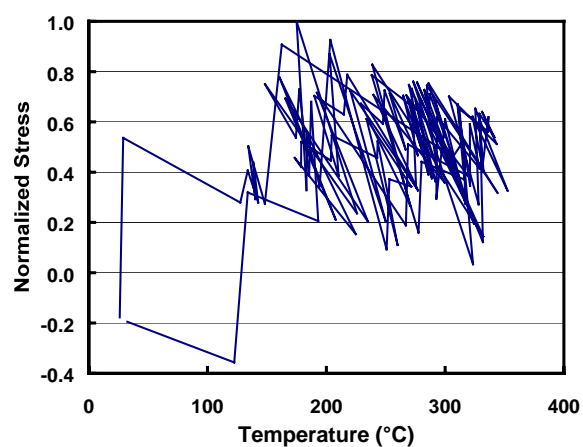
(d) Stress-temperature mission history
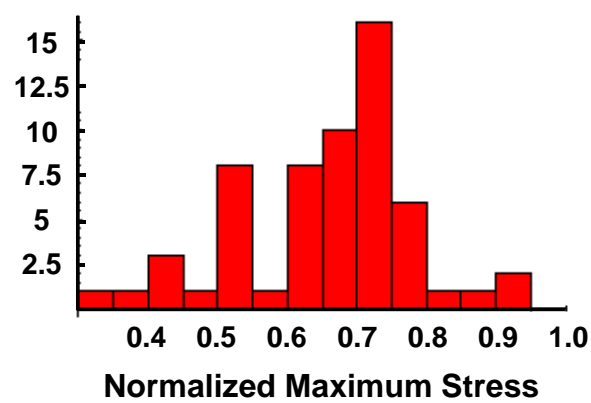
(e) Histogram of maximum stresses
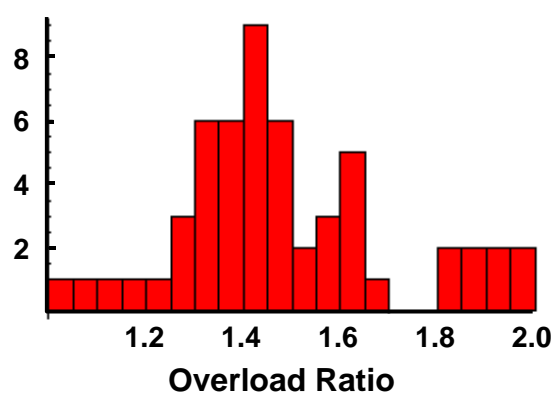
(f) Histogram of overload ratios

Figure 3. Typical engine mission data for a nickel-base superalloy component.
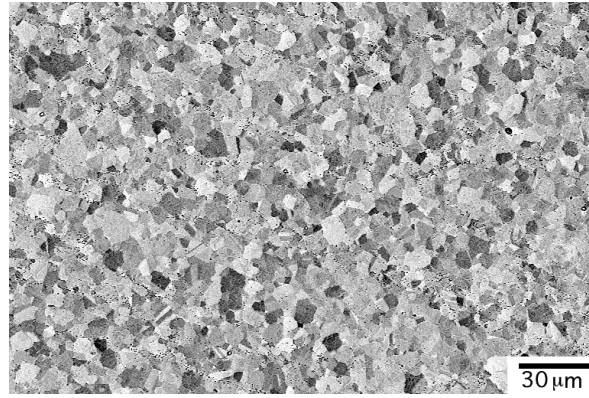
Figure 4. Microstructure of IN100
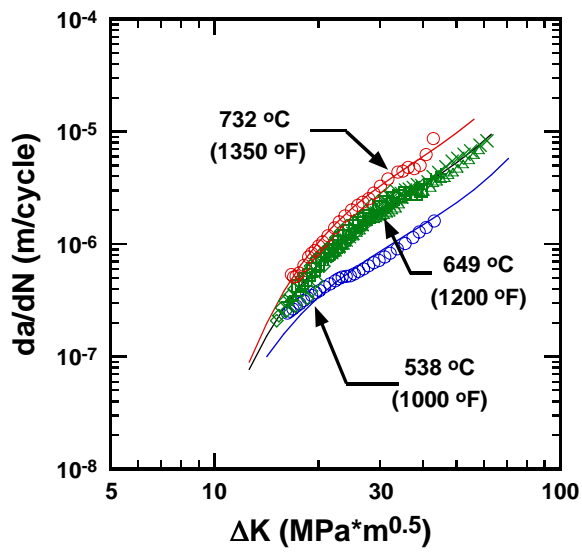
Figure 5. Effect of temperature on crack growth in IN100; R = 0.1, Freq. = 0.167 Hz.
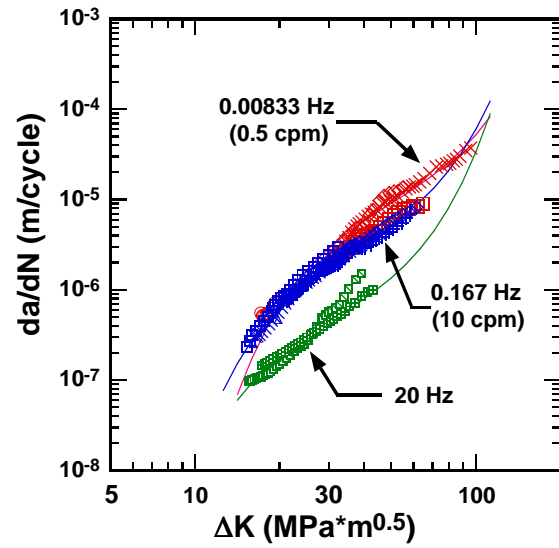
Figure 6. Effect of frequency on crack growth in IN100; T = 649°C, R = 0.1.
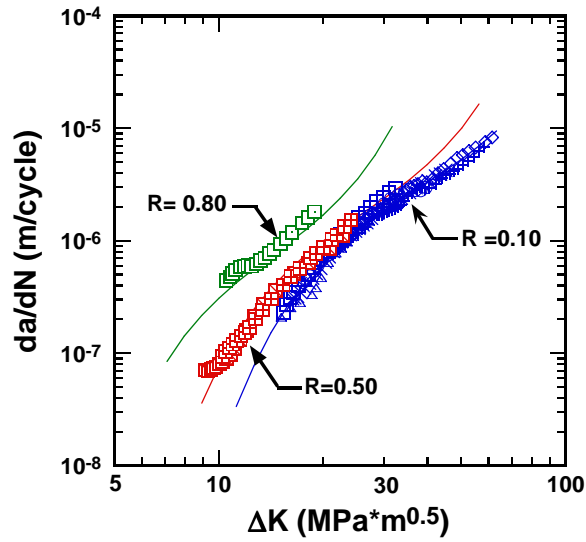
Figure 7. Effect of stress ratio on crack growth in IN100; T = 649°C; Freq. = 0.167 Hz.
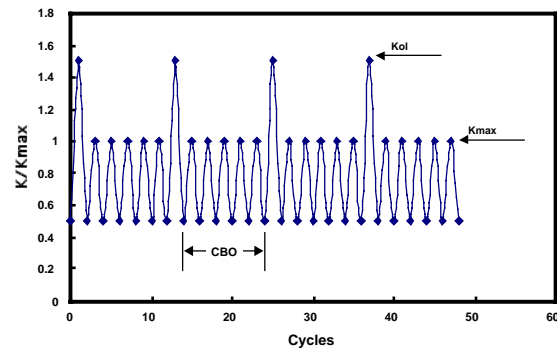
Figure 8. Schematic of simplified mission element containing repeated overloads and a fixed number of cycles between overloads (CBO).
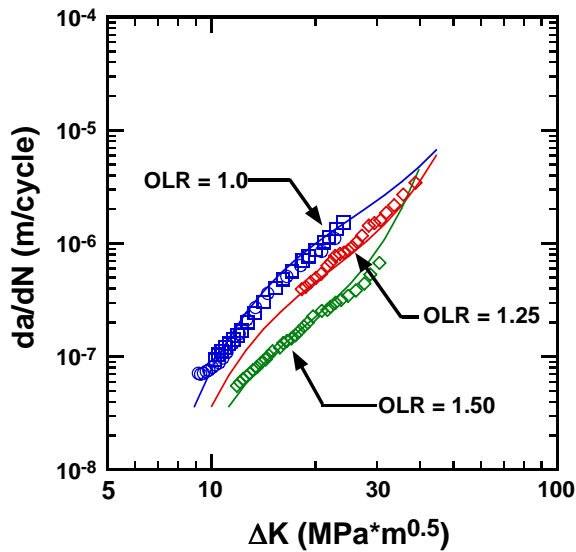
Figure 9. Effect of overload ratio (OLR) on crack growth in IN100; T = 649°C; R = 0.5, Freq. = 0.167 Hz, CBO = 40.
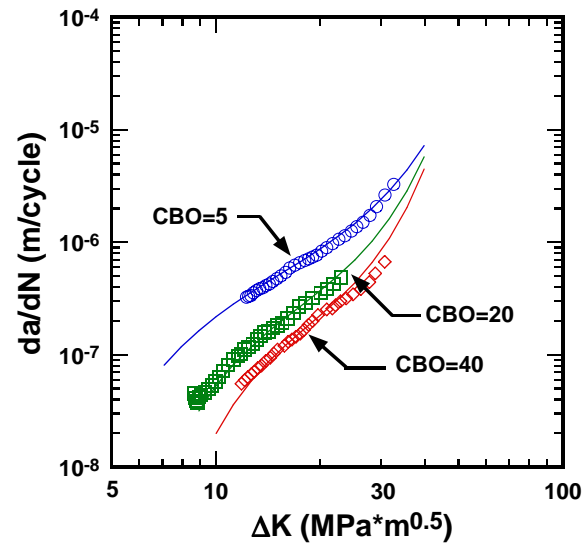
Figure 10. Effect of number of cycles between overloads (CBO) on crack growth in IN100; T = 649°C; R = 0.5, Freq. = 0.167 Hz, OLR = 1.5.
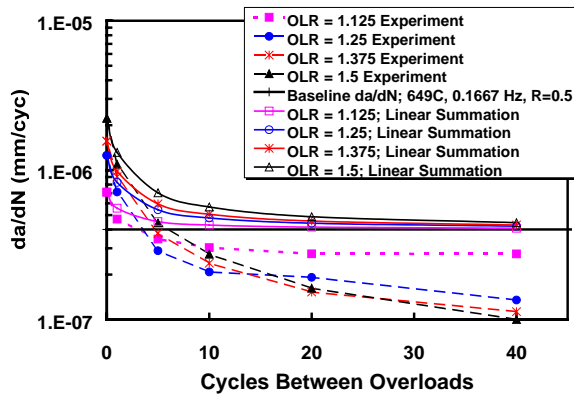
Figure 11. Crack growth behavior plotted as a function of the number of cycles between overloads (CBO) for K-controlled block loading illustrated in Fig. 8. T=649°C, Frequency = 0.167 Hz, R = 0.5, K_{max} = 30 MPa*m$^{0.5}$. Also shown are the baseline growth rate under the same conditions and the growth rates predicted by a linear summation technique.
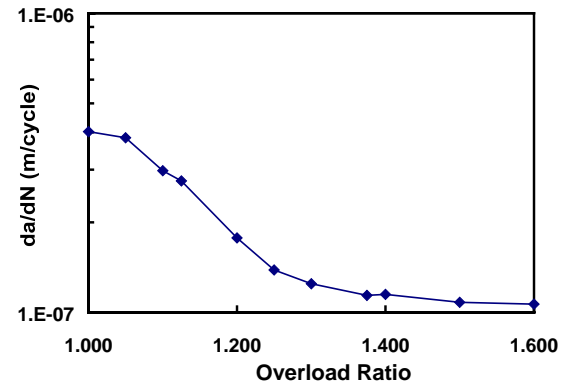
Figure 12. Crack growth behavior plotted as a function of the overload ratio with CBO = 40. T=649°C, Frequency = 0.167 Hz, R = 0.5, K_{max} = 30 MPa*m$^{0.5}$.
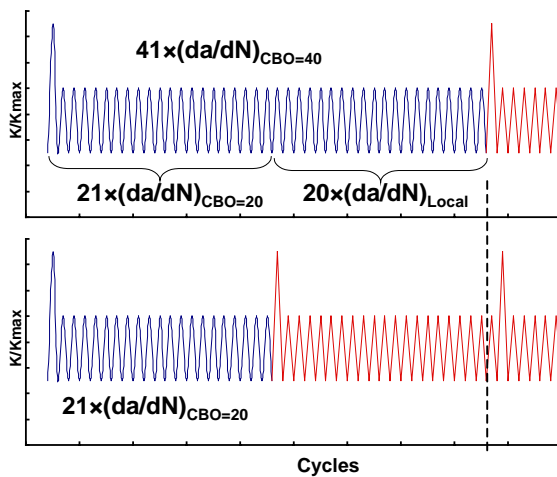
Figure 13. Schematic illustrating how the local crack growth in the baseline cycling following an overload block is determined.
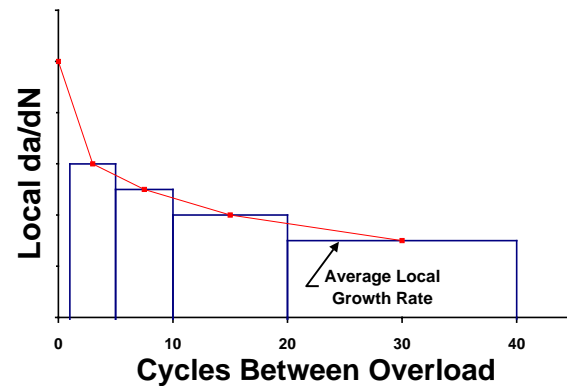
Figure 14. Schematic of the average local crack growth rate in the baseline cycling following an overload block.
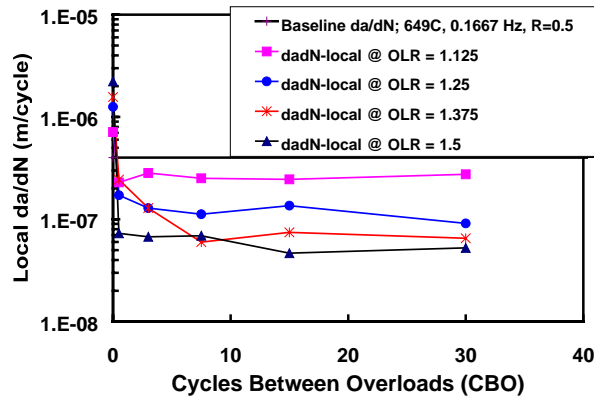
Figure 15. Local crack growth in the baseline cycles following an overload block behavior plotted as a function of the average number of cycles between overload following the schema in Figs 13 and 14. T=649°C, Frequency = 0.167 Hz, R = 0.5, K_{max} = 30 MPa*m$^{0.5}$.

REFERENCES

1. SAB (Scientific Advisory Board), Report of the Ad Hoc Committee on Life Extension and Mission Enhancement for Air Force Aircraft, U.S Air Force Scientific Advisory Board, Washington, D. C., Department of the Air Force, Report TR-94-01, 1994.
2. NMAB (National Materials Advisory Board), Aging of U.S. Air Force Aircraft, National Research Council, National Academy Press, Washington, D.C., Publication NMAB-488-2, 1997.
3. Hadcock, R. N., "Aging Airframe Structural Life Enhancement: An Overview," presented at The First Joint DOD/FAA/NASA Conference on Aging Aircraft, Ogden, Utah, July, 1997.
4. U.S. Air Force, Engine Structural Integrity Program, Military Standard 1783, Aeronautical Systems Division, Wright-Patterson Air Force Base, OH, 1984.
5. Reimann, W. H., "U.S. Air Force Turbine Engine Maintenance Practices", Air Force subcontract report, 1997.
6. Stricker, J., "Advanced Turbine Engines – A Strategic Vision", presented at the World Aviation Conference, San Diego CA, Nov., 1999.
7. J. M. Larsen, B. J. Schwartz, and C. G. Annis, Jr., "Cumulative Damage Fracture Mechanics Under Engine Spectra," Air Force Materials Laboratory Report AFML-TR-79-4159, Wright-Patterson AFB, OH, 1979.
8. Larsen, J. M. and Nicholas, T., "Cumulative Damage Modeling of Fatigue Crack Growth," AGARD Conference Proceedings No. 368, Engine Cyclic Durability by Analysis and Testing, Advisory Group for Aerospace Research and Development, Neuilly sur Seine, France, 1984, pp. 9-1 – 9-15.
9. Larsen, J. M. and Nicholas, T., "Cumulative-Damage Modeling of Fatigue Crack Growth in Turbine Engine Materials," Engineering Fracture Mechanics, Vol. 22, No. 4, 1985, pp. 713-730.
10. Russ, S. M., Rosenberger, A. H., Larsen, J. M., and Johnson, W. S., "Fatigue Crack Growth Predictions for Simplified Spectrum Loading: Influence of Major Cycles on Minor-Cycle Damage Rates," in this proceedings, 2001.
11. Mom, A. J. A, Evans, W. J., and ten Have, A. A., "TURBISTAN, a Standard Load Sequence for Aircraft Engine Discs," AGARD Conference Proceedings No. 393, Damage Tolerant Concepts for Critical Engine Components, Advisory Group for Aerospace Research and Development, Neuilly sur Seine, France, 1985, pp. 20-1 - 20-11.

12. C. G. Annis, Jr., R. M. Wallace, and D. L. Sims, "An Interpolative Model for Elevated Temperature Fatigue Crack Propagation," Air Force Materials Laboratory Report AFML-TR-76-176, Part I, Wright-Patterson Air Force Base, OH, 1976.
13. R. M. Wallace, C. G. Annis, Jr., and D. L. Sims, "Application of Fracture Mechanics at Elevated Temperature," Air Force Materials Laboratory Report AFML-TR-76-176, Part II, Wright-Patterson Air Force Base, OH, 1976.
14. D. L. Sims, C. G. Annis, Jr., and R. M. Wallace, "Cumulative Damage Fracture Mechanics at Elevated Temperature," Air Force Materials Laboratory Report AFML-TR-76-176, Part III, Wright-Patterson AFB, OH, 1976.

Risk Assessment Methodologies for Fracture-Critical Components

A.D. Boyd-Lee and D.P. Shepherd
Structures and Materials Centre, QinetiQ, Farnborough, Hants, GU14, 0LX, UK
Phone +44-1252-392000
Fax +44-1252-397298
Email: adblee@qinetiq.com, dpshepherd@qinetiq.com

1   INTRODUCTION

Within gas-turbine aeroengines, fracture-critical components are defined as those whose in-service failure would hazard the entire aircraft. For these components, airworthiness regulations require that a maximum permitted service life be identified, such that the probability of failure occurring before this life is reached is extremely remote. However, although the intent behind the derivation of these lives is to minimise the possibility of in-service failure, the procedures used to establish them are not usually specified in terms of this probability of dysfunction itself. For example, under the conventional 'safe life' methodology, it is the probability of a component exceeding some identifiable fraction of its total life, rather than of the total life, which is used as a fundamental criterion. The portion of the life remaining beyond this point is regarded as an additional, unspecified, safety factor, which ensures the probability of actual failure is acceptably small. Similar considerations apply to most other methods of component life determination.

There are, however, many instances that can arise during the service life of an engine fleet, in which it becomes very desirable to ascertain the actual probability of a service component failure. This is often prompted by the occurrence of some unforeseen or unpredictable event, which indicates that the actual failure probabilities are higher than those that should be achieved under the normal airworthiness procedures. In such circumstances, informed decisions concerning the appropriate action can only be made if accurate estimates of the resulting failure probability (usually referred to as the risk) are estimated. For example, if the safe life for a certain component is cut during the service life of an engine (which can happen for a variety of reasons) a situation may result where over life components are being operated in service. Since the immediate rejection of these components may present severe operational difficulties, the question as to how fast they must be removed whilst maintaining acceptable safety levels becomes extremely important. Similarly, very occasionally, components belonging to a particular set or batch are discovered subsequent to entry into service to be substandard. Again, the affected components should be dealt with as quickly as possible, but how this process should be managed depends heavily on how seriously they impact on safety. For these and other cases of risk exposure, the required action can only be properly assessed if the reduction in the level of safety is estimated in terms of effective measures of the probability of actual failure over specified time periods.

To illustrate, some of the considerations associated with estimation of probabilities of failure, the next section discusses several scenarios associated with engine service operation for which such assessments become desirable. Aspects commonly encountered in deriving the appropriate estimates are described, and solution methods are discussed briefly. These are illustrated by examples of actual risk assessment exercises, which have been conducted in support of UK military engine operation. Subsequent sections analyse how judgements of the significance of airworthiness risks are made. Particularly, the manner in which the risks are to be related to the RAF Hazard Risk Index (HRI) are discussed. It is emphasised that these may be vary significantly depending on the situation being addressed. Finally, these issues are related to UK current and future safety requirements at the aircraft platform level and the implications discussed.

2   RISK ASSESSMENT METHODOLOGIES

There are diverse factors that can cause the risk of engine failure to exceed normal levels, thus requiring the explicit calculation of failure probabilities to become necessary. These include but are not limited to: foreign object damage (FOD), problems arising in the critical parts lifing process itself, problems

associated with production and manufacturing process, errors in maintenance, hazards associated with extreme operating conditions. From the viewpoint of the methods needed to assess the risks that arise, these factors fall into a number of different categories. At the simplest level, there are hazards that are ever present, and unaffected by parameters associated with the engine itself. Examples of this type may include those attributable to FOD (foreign object damage) or extreme weather conditions. The calculations for the associated risks can be simple in such cases, for example, obtained by dividing the number of occurrences across the fleet by an appropriate measure of exposure time (usually engine flying hours). However, for other cases, the calculation procedure is more complex. For example, to address potential failure modes associated with life-limiting mechanisms, account must be taken of the dependence of the risk of failure upon the life consumed, which in turn could be dependent on a variety of other factors such as component tolerances and the severity of service usage. Moreover, in situations where some subset of the population of components is below standard in some sense, difficulties arise in identifying and characterising the degree of non-conformance. This also occurs in problems associated with a lapse in maintenance standards, or some difficulty with build, or the use of contaminated fuels or lubricants. Finally, problems associated with operational factors may require special methods. Each of these latter cases will be considered in more detail below.

In any risk assessment associated with fracture-critical parts, the method used in deriving the risk estimates will depend significantly on the procedure used in deriving the original component service lives. This is because the form of the available data for calculating the estimates will be determined to a large extent by the particular lifing methodology employed. In this paper, discussion of problems associated directly with components will concern those lifed according to the 'safe life' methodology, whereby lives are directly inferred from suitable test data using representative statistical models. In these situations, the statistical models required for the risk estimation procedure can be derived from those which underlie the procedures themselves. The reason for this focus on 'safe life' procedures is that, for the most part, risk assessment exercises are required for engine fleets which have reached some degree of maturity, and it is only relatively recently that alternative methodologies have been incorporated within UK airworthiness regulations. However, it is important to note that risk calculation exercises conducted for parts lifed using alternative methods may require quite different models and methods.

2.1 Risk assessment associated with Low Cycle Fatigue life shortfall

It is a normal part of aeroengine certification procedures that acceptable safe service lives for the fracture-critical components are identified prior to engine entry into service. Particularly for the larger fleets, it is highly likely that some lives will be revised during the operational life of the fleet. For UK military engines in particular, such a life progression is normally a required part of the life management procedure. This is in recognition of the fact that the true nature of component degradation can be better quantified and understood by taking account of service experience. Thus, it has been the case that when a new aeroengine design enters service, the service lives declared for its fracture-critical components have been set at half of the respective 'safe lives' calculated from the component rig tests. The remainder is only released on completion of additional tests of components that have been exposed to significant service usage. Moreover, there are several other factors not specified by the airworthiness procedures, which ensure that component safe service lives are continuously evolving as the engine progresses through its life cycle. For example, the stress analysis techniques on which all life declaration is based are themselves subject to an ongoing process of development, and it is common practice for these stress analyses to be recalculated. Indeed, when improved methods have been applied to service components, very large life revisions have sometimes resulted. Also, the calculation of the exchange rates, used to convert from engine flying hours to cycles, are periodically recalculated as the available data sets of sampled flights increase over time.

Since life revisions occur more often when the fleet is at a mature age, a sufficiently large downward revision can cause some of the respective service components to become immediately life expired. In such situations, the task of managing the withdrawal of these components is a question of minimising the operational impact, whilst keeping the risks below acceptable limits. This can only properly be undertaken if the risks themselves have been estimated using the most effective available methods.

In order to perform such a risk assessment, the fundamental task (as in most situations) is to identify the relevant failure distribution. For the case of straight low cycle fatigue life shortfall, this process is assisted by the fact that a standard statistical model for describing the life distribution of fracture-critical

parts already exists. That is the model from which the lifing procedures given in current UK airworthiness regulations are derived. These procedures specify that the distribution of life to crack initiation (defined as the appearance of a crack of 0.75mm surface length) is lognormal, with known log standard deviation[1]. All that is required to fully specify the model is to identify the log mean, which is obtained from appropriate test data. There is then the problem of identification of the dysfunction distribution. It is thus necessary to obtain the ratio of the life to dysfunction versus the life to crack initiation (for typical components the ratio is equal to1.5). If it is further assumed that the dysfunction distribution is itself lognormal with the same given log standard deviation, it follows that the failure log mean is equal to this ratio times the known initiation log mean. This allows the dysfunction distribution to be completely specified, thus giving the probability of failure for any particular component lifetime.

Whilst these properties form the basis of most risk models describing low-cycle fatigue situations, there are a number of complicating features which must necessarily be addressed if meaningful risk estimates are to be derived. Detailed descriptions of the models which result from these considerations have been give elsewhere (ref.1), so the paper will only give a brief outline of some of the problems which arise and how they are addressed. Firstly, it has often been observed that the variability in crack initiation data is greater than that in crack propagation. This suggests that the assumption of equal variance between the initiation and failure distributions is unrealistic, and that in practice the variance on the failure distribution will be smaller than that specified for initiation. Consequently, an appropriate means of calculating the failure variance, given the variabilities in initiation and propagation, must be derived.

Particularly for fixed wing military aircraft and helicopters, minor cycles have a much greater relative effect on the rate of damage accumulation once a crack has initiated. Consequently, the exchange rates (that convert between engine flying hours and reference cycles) are several times larger during the crack propagation phase of component life than during crack initiation. This impacts on lifing models in two ways. Firstly, it means that, for all significant applications, the model is best expressed specifically in terms of hours (missions) rather than cycles. The reason for this is that a component lifetime is generally expressed in terms of hours, and the aim of the model is to evaluate the risk of failure. Further, suppose that the lifetime is large enough to have reached some significant percentile on the initiation distribution. If we want to convert this lifetime into cycles, we are forced to consider the possibility that the component might already have an initiated crack. Moreover, since the exchange rates for initiation and propagation are different, it is necessary to address when this event occurs in order to calculate the equivalent cycles. However, since the life to initiation is itself a random quantity, we have no idea when this will have occurred for a particular component. Consequently, we have no information, for a specific component, about what the equivalent lifetime in reference cycles is once the life gets large enough. The second impact of this inequality of exchange rates is that the relationship between the log means for the initiation and failure distributions will be very different, depending on whether they are specified in terms of cycles or hours. Indeed, the ratio between the means when considered in hours is very much less than 1.5; typically, it will be between 1.15 and 1.2 depending on the exact ratio of the exchange rates. A significant implication is that, the risk of failure rises very much more rapidly when considered in terms of actual flight hours than it appears to when expressed in terms of reference cycles.

An example of a more complex situation is one where fatigue cracks are initiated by corrosion. In terms of probability distributions, the degradation processes associated with corrosion differ from that of conventional low-cycle fatigue crack initiation. Whilst a component susceptible to corrosion may sustain numerous corrosion pits, the vast majority of these will not usually result in a propagating crack. However, occasionally, corrosion can continue beneath the surface, leading to the accelerated initiation of a large crack. Moreover, it is almost impossible to detect, from surface inspection, which of the corrosion features will result in this type of behaviour. In this situation, the conventional fatigue model of initiation and propagation is inappropriate, and if an accurate assessment of the worst case is used as the basis of the calculation, the life obtained will be unrealistically short. To model this situation, it is necessary to take account of both of the distribution in properties of the initiation mechanism, its probability of occurrence and its location. Thus, the calculated safe life will contain an expression describing the minimum life resulting from this mechanism, multiplied by an expression describing the probability that

---

[1] The log standard deviation of a lognormal distribution is the standard deviation of the associated normal distribution, obtained by taking the logarithm of the component lifetime. Similarly, the log mean is the mean of this distribution.

it will occur at all. Only by combining these elements can a realistic estimate of the overall risk be obtained.

2.2   Risk assessment for batch problems

A risk management situation that requires a different approach can be illustrated by an investigation prompted by the discovery of service components that are either inferior or substandard in some way. Manufacture of fracture-critical components involves detailed checking of the dimensions and surface profiles of new major components. More costly inspection techniques, such as microanalysis, X-ray analysis, SEM etc. are usually limited to batch sampling. Also, manufacturing quality control of aeroengine fasteners is usually based on sample inspection of batches. Hence, the possibility of a manufacturing basic inspection error should be extremely rare by virtue of the many pairs of quality controller hands that aeroengine components must go through. When a poor quality component has entered service, in most cases there appears to have been a factor that made the defect difficult to detect, such as:

1.   very small inner radii (e.g. Helical spline case discussed below);

2.   inaccessibility (e.g. threads, hidden interfaces, interior geometry, etc.);

3.   critical dimensions (e.g. those that affect running clearances or component assembly); or

4.   manufacture over 20 years ago when quality control was less stringent; or

5.   inconsistencies that have been associated with the materials processing (e.g. large grains with twins in Ni-base superalloys, Waspaloy inclusions, soft alpha in Ti, plucking, etc).

Should such a feature or processing complication affect the performance of the component, the consequences can sometimes be such that high levels of risk result. An example of such a case was encountered in connection with the inner radii (at either side of the bottom of the teeth) of a helical spline on a shaft within a military aeroengine. Theoretical predictions and testing confirm that the expected life of this spline depends critically on these inner radii. Consequently, the design specification is that the inner radii should not be less than 0.3mm. Unfortunately, one of these splines was found in service having teeth with significantly smaller inner radii. The primary lifing issue was to estimate how the radius affected the life of the component. From this, the risk of shaft failure could be assessed and it was established that the minimum acceptable inner radius was in region of 0.15mm. This provided a safe criterion for acceptance or rejection of components.

It was also necessary to characterise the extent of the deviance within the population, so that the severity of the problem could be estimated. Characterisation of the distribution of radius sizes, in conjunction with the life estimation calculations, ensured that appropriate risk estimates were derived, and the offending batches of splines were identified and removed from service.

A second example of problems associated with production batches arises in connection with material that had been subject to inadequate process control. In one case, several cracks and materials defects were found in Waspaloy service discs and shafts manufactured about 30 years ago. The cracks were found to have initiated from extremely large inclusions that were the result of substandard materials processing. Since identification of the higher risk components could not be achieved by inspection, a process modelling approach was used instead. The plastic-flow forging process for the disc was predicted to identify where the inclusion had come from in the original casting. It was established that the oxide had fallen into the melt from the wall of the crucible. Having established this, the process model was then used to predict that the defects were more likely to be present in the rim and outer web than in the bore of the disc, which was consistent with the observations. A conservative probability of this event occurring was estimated, and from this the risk of in-service failure as a function of component life was evaluated.

In general, risk assessments involving batches of substandard components tend to be highly case dependent and the more complex cases demand a wide range of expertise to reach an acceptable solution. However, in any situation, it will almost certainly be necessary to characterise the severity of the problem. From this, the impact on the component lives can be estimated, and then the associated risks can be derived. Also, a significant issue can be deciding what, if any, inspections are needed to ensure that the problem is adequately characterised.

2.3   Risk assessment connected with operational usage

When a hazard associated with operational usage is in some sense exceptional, a risk analysis may be required. Typically, this will involve an interaction between an existing, identified hazard, and a particular operational situation or manoeuvre. An example is given by a power surge problem associated with a certain aeroengine. It was found that a voltage spike in the fuel system could result in a sudden uncontrollable rise in thrust. The probability of occurrence was remote (of the order of 10^{-5} per engine flying hour) and in most stages of flight it should not result in an air accident. However, if it were to occur during manoeuvres with little margin for error, it could result in the loss of the aircraft. For this problem, the available evidence indicated that occurrence of surge was independent of any normally measurable parameter (such as altitude, age of engine, etc) and in particular of the type of flying being undertaken. Thus, the estimated probability of aircraft loss per aircraft flying hour is the multiple of the probability of surge and the proportion of time spent in the critical manoeuvres. Simplifying slightly, the cumulative risk of a catastrophe was thus obtained by multiplying this probability by the time taken to rectify the fuel circuit problem.

The critical elements in this situation are the assessment of the operational usage, and the assumption of 'randomness' of the underlying event. The latter factor is particularly important, because deviations from this assumption could radically alter the predictions. Thus, in the above example, if it transpired that the fault could only arise under a particular condition or combination of conditions, then the underlying probability of aircraft loss could be zero if this could not occur in conjunction with the critical modes of flight. Alternatively, if it transpired that surge is more commonly associated with the critical flight modes then risk of catastrophe would be many times higher.

3   RISK MANAGEMENT USING THE RAF HAZARD RISK INDEX

3.1   Background

Once a particular risk has been estimated or updated, the next consideration is to assess the acceptability of this risk with respect to prioritisation of maintenance or technical actions.

For UK military aeroengines, the RAF Hazard Risk Index (HRI) controls the management of technical risks (ref. 2). The current HRI procedure is based around two matrices: one for fighter aircraft (figure 1) and the other for military transport or passenger aircraft (figure 2).

The primary purpose of the HRI is to ensure common standards of safety are applied across the RAF fleets. It is also used to prioritise technical actions, given limited resources. The associated HRI probability criteria have actively driven current risks of failure for at least the last 5 years, and consequently they have become a minimal requirement to support current RAF safety levels.

	PROBABILITY PER AIRCRAFT FLIGHT HOUR				
	(A) FREQUENT >10^{-3}	(B) PROBABLE 10^{-3} to 10^{-4}	(C) OCCASIONAL 10^{-4} to 10^{-5}	(D) REMOTE 10^{-5} to 10^{-6}	(E) IMPROBABLE < 10^{-6}
(1) CATASTROPHIC Death or system loss	1	2	4	8	12
(2) CRITICAL Severe injury, severe occupational illness, or major system damage	3	5	6	10	15
(3) MARGINAL Minor injury, minor occupat-ional illnes, or minor system damage	7	9	11	14	17
(4) NEGLIGIBLE Less than minor injury, occupational illness or system damage	13	16	18	19	20

CRITERIA

🟥 UNACCEPTABLE
🟧 UNDESIRABLE
🟩 ACCEPTABLE WITHOUT REVIEW

Figure 1: RAF Hazard Risk Index – Combat aircraft

	PROBABILITY PER AIRCRAFT FLIGHT HOUR				
	(A) **FREQUENT** $>10^{-3}$	**(B)** **PROBABLE** 10^{-3} to 10^{-5}	**(C)** **OCCASIONAL** 10^{-5} to 10^{-7}	**(D)** **REMOTE** 10^{-7} to 10^{-9}	**(E)** **IMPROBABLE** $< 10^{-9}$
(1) CATASTROPHIC Death or system loss	1	2	4	8	12
(2) CRITICAL Jeopardised flight, severe injury, major system damage	3	5	6	10	15
(3) MARGINAL Minor injury, minor system damage, or precautionary mission abort	7	9	11	14	17
(4) NEGLIGIBLE Mission safety unaffected	13	16	18	19	20

CRITERIA

UNACCEPTABLE
UNDESIRABLE
ACCEPTABLE WITHOUT REVIEW

*Figure 2: RAF **Hazard Risk Index – Military transport aircraft***

Each significant failure mode or other hazard is assigned to an HRI category. Red categories risks are deemed unacceptable, the amber ones require management action (undesirable) and the green ones require no action. The 'amber' band is there to provide a degree of flexibility in the management, and avoid unnecessary groundings and engine removals. A management objective is to reduce the risk associated with 'amber/red HRI category' failure modes to the extent that they become 'green HRI category' failure modes.

An aeroengine has numerous potential failure modes, and if all of these were allowed to exceed a risk of 10^{-6}/afh, (i.e. per aircraft flight hour) the aircraft would be unsafe to fly. Thus, design standards such as Def. Stan. 00-971 specify a requirement for even lower probabilities of failure than those allowed by the HRI matrix. Typically, the effect is that only a few dozen of the failure modes of a particular engine type belong to the amber HRI category.

3.2   Interpretation of the current HRI matrix

3.2.1   Measures of risk

As originally defined, the HRI matrices have axes of fleet average risk per aircraft flying hour versus severity of the hazard. The fleet average is calculated simply by summing the risks over an entire engine fleet, and dividing by the number of aircraft. Many past life management exercises have been based upon this measure of risk.

In situations where a given risk is constant, (in other words, unaffected by other parameters associated with the operation of the engines such as component life or flight envelope), fleet average is an adequate measure of the significance of the risk. It is worth noting that, under these circumstances, the fleet average risk is the same as the maximum risk per aircraft flying hour in the fleet. When the severity of the risk is low, and the rate of arising is high, the average risk is particularly useful to assess trends in the fleet.

However, a major problem with using this risk measure as the default to decide levels of management action is that airworthiness risks are more often than not highly non-uniformly distributed. As a result, in some cases, the seriousness of a given situation is not indicated by the fleet average risk. To illustrate this, consider a situation in which the life of the fleet-leading component (of a given type) is just 15% higher than the declared safe life. Then the associated risks would typically be an order of magnitude higher than that at the declared life, and the vast majority of the risk could be confined to a life-leading component in a service aeroengine. Suppose further that the fleet average risk /afh is marginally below 10^{-6}/afh and there are 500 engines in service. Assuming that 90% of the risk is being incurred by the life leading

component, then it would be incurring a risk of 4.5×10^{-4}/afh (= $0.9 \times 500 \times 10^{-6}$), that is HRI category 2 and clearly unacceptable.

In view of such considerations, it is suggested that no single measure of hazard exposure is appropriate to all situations, and in practice different measures are relevant to different circumstances. Moreover, sometimes multiple measures of risk are required to properly quantify a life management situation. In what follows, two alternative probability measures of incident arisings are described, and their use in various situations discussed.

3.2.2   Peak risk

The peak risk per aircraft flying hour is defined as the peak risk with respect to the parameters that cause a risk in question to be non-uniformly distributed. For example, in situations involving over life components, the peak risk will be the maximum with respect to the different components (i.e. the highest percentage over life component). Alternatively, if a risk were driven with respect to a particular operational manoeuvre or sortie type, then the peak risk would be the maximum amongst the risks for the different activities. Peak risks are important in situations where the risks (or the vast majority of the risks) are confined to a few components or engines, or a limited set of circumstances. In these situations, it is the peak risk that should be used in conjunction with the HRI, and not the fleet average risk. The advantage of using the peak risk in this way is that it clearly highlights the source of the problem, and will direct the management action to address those risks, which constitute the majority of the total. This ensures that no service component incurs unacceptable risk.

3.2.3   Expected cumulative arisings

The expected cumulative arisings per annum (or other relevant operational period) is defined as the cumulative risk over that period, summed over the entire fleet. When the risk is more evenly distributed, the expected cumulative arisings may be a more useful measure than peak risk, for two main reasons. Firstly, it takes account of the duration of risk exposure (usually associated with the time required to implement a maintenance action). This is very important when the risks under investigation are changing with time, and it allows for an assessment of how quickly problems need to be addressed. Secondly, it takes account of the number of aircraft affected. This is important in assessing priorities when different numbers of aircraft are affected by different problems. The expected cumulative arisings has the additional advantage that it is the measure that can most accurately related to observed failure rates. This is because it takes into account all aspects of the service situation including fleet size, observation period, engine mark and so on[2].

To illustrate the use of these risk measures, consider again the example discussed on page 3, whereby a component was subject to a life cut which resulted in a number of installed parts having exceeded their safe life. In this example, the peak risk for the fleet leading component was calculated, which, when compared to the HRI matrix resulted in an amber reading. Consequently, a programme of component withdrawals was derived, which required the components to be removed over a period of 2 years. However, it was also recognised that the risks associated with the installed components would be increasing whilst they were still in service, and it was important to ensure that these risks would not become unacceptable during this period. For this reason, an upper bound on the expected cumulative arisings over the period of the management plan was introduced, and the risk curves were integrated to ensure that the management plan conformed to this criterion.

4   TOWARDS AN IMPROVED HRI MATRIX

Given that several different measures of risk are used in practice to make appropriate aeroengine fleet managerial decisions, users of the HRI matrix have had difficulty interpreting airworthiness risk in relation to this decision matrix. Furthermore, difficulties of interpretation have also been encountered with the severity axis of the HRI matrix. It is suggested that the HRI matrix could be improved by using stronger inputs. These issues are discussed in turn.

---

[2]Note that for small fleets, the resources might not be available to revise component life and exchange rate calculations as frequently as for larger fleets. Thus, the uncertainty in estimates of the peak risk may be significantly higher, and so it may be necessary to introduce additional safety margins to account for this.

4.1 Risk criteria

Of the three measures of risk discussed, the peak risk and the expected cumulative arisings are the most critical with respect to safety. A solution would therefore be to use a dual risk axis for the HRI columns (figure 3). One axis gives the risk criteria in terms of peak risk (see section 3.2.2) , the other in terms of expected cumulative arisings (section 3.3.3). The user would then select the lowest letter column associated with either risk. For example, if for a certain hazard the estimated peak risk is 2×10^{-7}/afh and the expected cumulative arisings per annum is 10^{-4} then risk band (E) would be selected.

	(A)	(B)	(C)	(D)	(E)	(F)	(G)	(H)	(J)
INDIVIDUAL AIRCRAFT PEAK RISK /AFH	10^{-3}	10^{-4}	10^{-5}	10^{-6}	10^{-7}	10^{-8}	10^{-9}	10^{-10}	
EXPECTED CUMULATIVE ARISINGS / ANNUM	10	1	10^{-1}	10^{-2}	10^{-3}	10^{-4}	10^{-5}	10^{-6}	
(1) CIVIL DISASTROUS Uncontrolled flight into highly populated building, crowd or civilian passenger aircraft	Red	Red	Red	Red	Red	Red	Yellow	Yellow	Green
(2) CATASTROPHIC FOR MILITARY TRANSPORT Multiple military or a civilian death or multi-engine aircraft loss	Red	Red	Red	Red	Yellow	Yellow	Green	Green	Green
(3) CRITICAL FOR MILITARY TRANSPORT Jeopardised flight, severe injury, major system damage	Red	Red	Red	Yellow	Yellow	Yellow	Green	Green	Green
(4) CATASTROPHIC FOR COMBAT AIRCRAFT Loss of pilot or loss of single/twin aircraft or severe injury to civilian passenger	Red	Red	Red	Yellow	Green	Green	Green	Green	Green
(5) ATTRITION/CRITICAL FOR COMBAT AIRCRAFT Severe injury, severe occupational illness or major system damage or technically caused loss in combat	Red	Red	Yellow	Yellow	Green	Green	Green	Green	Green
(6) MARGINAL Minor injury, minor occupat-ional illnes, or minor system damage	Yellow	Yellow	Yellow	Cyan	Cyan	Green	Green	Green	Green
(7) NEGLIGIBLE Less than minor injury, occupational illness or system damage	Green	Green	Green	Green	Green	Green	Green	Green	Green

Green — ACCEPTABLE WITHOUT REVIEW
Cyan — UNDESIRABLE IF MILITARY TRANSPORT
Yellow — UNDESIRABLE
Red — UNACCEPTABLE

Figure 3: Improved HRI matrix that overcomes the difficulties highlighted by the examples.

4.2 Severity criteria

A problem we have encountered with the severity axis, is with respect to the higher accepted risk of a catastrophe due to technical causes during military active service compared to other flight activities. For example, in a combat situation a pilot might judge it to be necessary to take his aircraft slightly outside the normal flight-control envelope. The issue is that the HRI matrix should identify how much higher a technical risk is then accepted. Assuming a factor of 10 higher risk is accepted, this issue is addressed by broadening the definition of 'critical' (see severity category (5)) to include attrition due to engineering causes (i.e. loss of aircraft during active service), as shown in figure 3.

Secondly, there is a concern that the current definition of the 'catastrophic' category (given in figure 1) is too broad. For example, loss of flight control during a display flight could be far more hazardous than a fuel pump failure of a single engine aircraft (where there is a good chance of being able to glide the aircraft to an unpopulated region before the pilot ejects). There is also public and political pressure to distinguish between the risk of an air accident involving large numbers of civilian casualties and a flight into the ground where the pilot has good chance of being able to eject. To address, this an additional 'civil disastrous' category could be added ('(1) 'in figure 3). In addition to hazards associated with flight displays, loss of flight control during take-off, landing or over flight of highly populated areas and buildings could fall into the proposed highest severity category.

Thirdly, there is the option that the two HRI matrices could be subsumed into one table, so that the potential confusion of reading the wrong table is discouraged (as they look very similar). In the proposed matrix, the risk criteria of the current two HRI matrices are preserved so that using the new matrix does not affect the status of risks for which the current matrices work well.

In summary, the proposed developments to the HRI matrix are to use stronger inputs so that it copes better with the wide variety risks that occur in service. The new risk criteria introduced in figure 3, are only intended for suggestion and further discussion. As yet, they are neither implemented in any current analysis nor form part of any operational procedure.

5 OTHER RISK MANAGEMENT CONSIDERATIONS

Application of the HRI matrix is a reactive management approach in so far as it prompts a change in action when there is a change in risk. It is also proactive to the limited extent that risk estimation concerns prediction of the likely exposure to potential hazards. However, another vital proactive aspect of risk management apart from that addressed by the HRI is to minimise of the impact the unforeseeable. A further fundamental issue is that the quality of the statistical methods used can have a very significant impact on the risk values obtained and hence on the HRI category of a risk. These two aspects are discussed in turn.

5.1 Minimisation of the impact of the unforeseeable

Despite conscientious implementations of design standards and service life management procedures, unexpected failures both in the civil and military aircraft fleets have still occurred. Such incidents and particularly in cases where there is a repeat occurrence after a component modification aimed to rectify the problem, can sometimes raise complex questions about whether the level of technical effort invested in lifing such components was adequate. From a technical viewpoint, the complexity of the life limiting behaviour of components combined with the high scatter in their dysfunction life distributions has several implications. Firstly, even using state-of-art analysis there can still be significant error in the estimated service component lives. Secondly, advances over the last decade in: stress analysis standards, lifing methods and revisions of (service usage) exchange rates have brought substantial revisions to a number of military aeroengine component lives. The rapid pace of such progress being made is such that it is likely to continue for the foreseeable future and it is important that fleet managers exploit the resulting benefits.

One of the most important elements of a safe life management procedure for an aeroengine (or indeed for the entire aircraft) is periodic revision of the lives of its critical components. In the immediate term this tends to reduce the severity of costly downward revisions of component lives. In the longer term, experience from the management of large fleets shows that it stops the potential incidence of catastrophic failures rising grossly as the fleet reaches maturity. It also greatly diminishes the likelihood of discovery of cracks in service and subsequent potential grounding of a fleet.

When the reanalysis of a component life has resulted in a significant downward revision, the development of component life extension methods has often played a very significant role in alleviation of the situation (ref. 1). This field concerns enhanced life prediction methods, development of advanced materials, better surface treatments and repair.

Another source of uncertainty is associated with the estimation of the severity of service usage when only a small sample of the fleet in monitored. Recent analyses have shown that much higher (than previously thought) percentage samples of service usage have to obtained to measure service usage to a certain level of accuracy and thus to support a certain component life.

5.2   Statistical accuracy

As discussed above, estimates of airworthiness risk associated with a particular hazard can be prone to large errors, partly arising from the limited available data upon which a risk model can be based. Lack of data can force assumptions to be made that are highly conservative. However, it normally makes a very significant difference to the quality of risk estimate when it is based on a rigorous statistical analysis, including accounting for sampling error.

To illustrate the sensitivity of some risk estimates, a 3% error in stress, might equate to a 15% error in component life (assuming an SN slope of 5), which in turn might equate to an order of magnitude difference in risk of fatigue failure. If the stress is dependent on a tolerance distribution that has been sampled, then the associated sampling error will have a significant effect on the risk estimate.

6   TRENDS IN MILITARY AIRCRAFT SAFETY AND FUTURE IMPLICATIONS

6.1   Mature aircraft

Using Tornado as an example of an aircraft that has benefited from life management techniques such as those described above the situation is broadly as follows. There has been a fairly large improvement in safety mainly associated with non-technical causes. Although, the improvement in safety associated with technical causes is smaller, this is still a significant technical achievement. Regular revision of aeroengine component lives has resulted in significant changes, and catastrophic failures have been avoided as a result.

For a typical UK military combat aeroengine the estimated total (of the green and amber category) risks might typically be $>3\times10^{-5}$ flight hour. That is, up to a factor of 2 greater than the observed rate of technical failures for the whole aircraft. The reason why the estimated total risk of engine failure typically comes out higher than the observed risk of a catastrophic engineering/technical failure of the aircraft is because it is standard practice to calculate risks conservatively.

Based on risk models that QinetiQ has developed, the probability of a fatigue failure per flight hour of a given component occurring at its full life should lie between 2×10^{-8} and 2×10^{-7}. In practice there are typically many complex factors (such as those discussed earlier in the paper) that cause the risks of failure of a few of the components to be sufficiently high to enter the amber or upper green categories of the HRI matrix.

6.2   New aircraft

Essentially the same fatigue lifing design probabilities are used for EFA (the Eurofighter engine) as for mature aeroengines such as RB199 and Pegasus. The current requirement is that the Eurofighter should achieve a failure rate (due to technical causes) of not more than half of that of a mature aircraft (such as Tornado). This requirement can be met with the current risk criteria in the RAF HRI matrices, if fewer risks are allowed into the amber and upper green HRI categories than is typical for current mature RAF combat aircraft.

6.3   Future aircraft

The relatively low fatalities associated with recent wars involving the RAF and media attention to transport accidents have raised safety expectations. In reference (3), Adelard notes that the UK Health and Safety Executive (HSE) has set military airworthiness targets of reduction of the incidence of fatal and major injury accidents by 5% by 2004 and by 10% by 2010. In the longer term, the stated intent is to

achieve aircrew survival levels of greater than 999 in 1000 per annum by 2050. For future military aircraft, the UK MOD safety document JSP318b (ref. 4) defines the airworthiness criteria as being that:

"The cumulative probability of the loss of an aircraft due to a technical fault and the cumulative probability of a technical failure of the aircraft (inclusive of its systems, structures and stores) which could result in the death of any air crew or its passengers, should both be assessed to be of the order of 1 in a million per flight hour, when operated within the conditions used for the airworthiness system".

The precise magnitude of safety improvement that would be required to meet this criterion should become clear in the fullness of time. Broadly, it indicates that future aircraft design will require the risk of aircraft loss (due to technical causes) to be reduced by in the region of 4 to 20 fold (relative to current mature RAF fighter aircraft). It seems to not be an impossible goal because civil passenger aircraft exceed this safety level. However, military aeroengines are taken frequently to more extreme regions of the flight envelope than a civil aircraft and this can be more severe on the aeroengine components. Achievement of up to a 4 to 20-fold improvement in safety could therefore pose a demanding technical challenge in practice. The lifing standard EJ400 (5) for the EJ200 engine exceeds Def. Stan 00-971 (6) and thus should work to probabilities of component failure that are less than or equal to those specified by lifing standard TU346 for the RB199 engine (7) in Tornado.

High-level safety requirements can only achieved in practice if their quantitative implications are percolated down to the component-level design standards and HRI procedures. There are two basic options. The option to limit the number of amber category risks to one or two does not seem to be viable, since it could result in grounding of fleets each time more than a couple of risks enter the amber and upper green categories. A more realistic option therefore seems to be to allow revision downwards of the probabilities in the HRI tables according to the required improvement factor over current safety levels. This option would result in proliferation of HRI matrices, which is an additional reason why it is suggested that the two current matrices should be merged into one.

Realisation of a large improvement factor in safety (relative to current mature aircraft) would also require downward revision of the probabilities of failure in Def. Stan. 00-971 (shortly to be absorbed into Def. Stan. 00-970). Based on current risk models, a 20-fold reduction in the risk of fatigue at full life equates to approximately a 15% reduction in component life.

For completeness, a brief mention should be made of the risk management implications for UAV aircraft. Clearly, UAV technology has considerable development potential in terms of flight platforms that: reduce pilot workload, operate more effectively in remote and hazardous environments, allow greater manoeuvrability than a manned aircraft, etc.. Any associated reduction in the need for pilot training could reduce component life requirements and thus alter the optimum lifing tradeoffs between risk, affordability and aeroengine performance.

7 CONCLUSIONS

1. A variety of examples were given to illustrate some of the issues that arise in the risk assessment of aeroengine component failure modes and other potential hazards.

2. The RAF Hazard Risk Index (HRI) management procedure was also critically reviewed.

3. It is suggested that this HRI matrix could be improved using stronger inputs:

   a. using probabilities of failure of:

      - Peak risk per flight hour   (defined in section 3.2.2)

      - Expected cumulative arisings   (defined in section 3.2.3)

   b. and using additional severity criteria that:

      - discrimate risks of technical causes of attrition from other risks;

      - discriminate the risks of more serious catastrophic accidents involving numerous civilian fatalities from those that are limited to flight into the ground and pilot ejection; and

      - enable the two matrices (for fighter aircraft and military transport) to be merged into a unified matrix.

4. A brief review of trends in RAF air safety is given to show why future requirements to improve safety could at some future point necessitate design and risk management standards to be shifted to lower probabilities of failure.

8   REFERENCES

1. A D Boyd-Lee and G F Harrison, 'The development of life extension methods for fracture-critical aero-engine components', in *Qualification if life extension schemes for engine components,* RTO-MP-17, 1999.

2. Gp. Capt. J.K. Meagher and Sqn. Ldr. L. Jones, 'The challenge of managing the logistic support of combat engines in the Royal Air Force', in *Gas turbine operation and technology for land, sea and air propulsion and power systems,* RTO-MP-34, 2000.

3. Validation of Airworthiness Target by the ALARP Principle, Adelard Report Reference D/188/5601/8v1.0,1 February 2001

4. Regulation of the Airworthiness of Ministry of Defence Aircraft, JSP 318B.

5. Specification for the EJ200-01 R-A1 engine, EJ400, Issue 5, July 1995.

6. UK Military Defence Standards, Def, Stan. 00-971, General Specification for aircraft gas-turbine engines, 1986.

7. Lifing procedures for RB199 group A parts, TU346, issue 3, amendment 4, May 1999.

Paper, 'Risk Assessment Methodologies for Fracture Critical Components' : Discussion

<u>Question from P R Parolo – DGTA, Australia</u>

Given the size of the newly proposed risk/decision matrix, how practical is it to use and how practical is it to quantify a case in so much detail? Based on experiences involving reduced LCF lives in the RAAF, I think that a smaller matrix is more practical for an operator to use.

<u>Presenter's Reply</u>

The matrix in the paper is only a proposal to the RAF.

This page has been deliberately left blank

_____

Page intentionnellement blanche

Coût de Maintenance et Durée de Vie des Turbomoteurs

Charles Claveau
TURBOMECA
SNECMA Group
64511 Bordes Cedex
France

1. Les Composantes du DMC

Le coût de maintenance des Turbomoteurs s'exprime familièrement sous la forme du DMC (Direct Maintenance Cost).
Le DMC peut être décomposé en deux parties principales :

> ➢ *Maintenance programmée*
> ➢ *Maintenance non programmée*

Typiquement, sur un turbomoteur d'hélicoptère, la maintenance programmée représente 80% du DMC contre 20% pour la maintenance non programmée.
Réduire le coût de maintenance d'un turbomoteur c'est donc, avant tout, réduire le coût de la Maintenance Programmée.

2. La Maintenance Programmée

La Maintenance Programmée comprend les inspections périodiques chez l'utilisateur final, les Révisions et remplacements de pièces à vie-limite qui se font en atelier spécialisé. Typiquement, pour un turbomoteur d'hélicoptère, le poids de ces différents postes est le suivant :

> ➢ *Révision moteur et accessoires* : *80 %*
> ➢ *Pièces à vie-limite* : *17 %*
> ➢ *Inspections périodiques* : *3 %*

Révisions et pièces à vie-limite constituent finalement l'essentiel du DMC.

3. La Méthode Classique de Maintenance Programmée

La Maintenance Classique de Maintenance Programmée repose sur la définition d'un potentiel moteur (TBO) quantifié en heures au bout duquel le moteur subit une intervention en atelier, dite Révision Générale.
L'objectif de cette Révision Générale est de remettre le moteur et ses accessoires dans une configuration lui permettant d'effectuer un nouveau potentiel complet.

Le TBO est complété des vies-limites pour les pièces critiques en termes de Navigabilité.

4. Inconvénients de la Maintenance Programmée classique

Dans la méthode classique le but de la Révision Générale est de reconditionner le moteur pour un potentiel complet.
Si un tel objectif est simple et évident en termes opérationnels et de gestion de flotte moteurs en service, il est coûteux.

Reconditionner un moteur pour un potentiel complet nécessite un contrôle approfondi de toutes les pièces et des critères sévères afin d'être sûr que le potentiel suivant pourra être tenu. Il impose également de déposer les pièces à vie-limite dont la vie arriverait à échéance durant le TBO suivant.

L'objectif de reconditionnement pour un potentiel complet génère une intervention lourde, des actions de nature conservative et des déposes ou réparations prématurées de pièces. Beaucoup de pièces déposées ou réparées en Révision Générale pourraient continuer de fonctionner en l'état pour une durée intéressante opérationnellement avant d'être réparées ou rebutées.

Or l'essentiel du coût d'une Révision Générale se trouve dans le remplacement et la réparation des pièces.

Réduire le DMC revient donc à prolonger, à optimiser la durée de vie effective en service des pièces du moteur. Les pièces ne doivent pas être déposées "par précaution" afin d'être certain de tenir le prochain potentiel, mais parce qu'elles ont effectivement atteint leur limite de vie. Il faut consommer tout le potentiel des pièces.

5. Les différentes catégories de pièces

On peut définir différentes catégories de pièces pour un moteur donné :

> ➢ **Les pièces à vie-limite qui sont relatives à la Navigabilité et qui doivent impérativement être déposées à l'issue de leur vie certifiée.**

> ➢ **Les pièces, non critiques en termes de Navigabilité, mais dont la défaillance peut générer un arrêt de fonctionnement du moteur.**

> ➢ **Les pièces dont l'usure ou la défaillance génère une dépose moteur à l'occasion d'une visite programmée de Maintenance.**

6. Optimiser la durée de vie de ces pièces

La durée de vie des pièces à vie-limite est optimisée de fait.
Elles sont déclarées en certification. Leur évolution est possible et se fait selon des règles formalisées avec les Autorités.

Pour les pièces dont la défaillance peut générer un arrêt de fonctionnement, Turboméca a défini le concept de PLU : Pièce à Limite d'Utilisation. Cette limite d'utilisation peut être en heures, en cycles, calendaire ou une combinaison de ces trois paramètres.

La définition de ces pièces et de leurs limites est faite par un groupe de techniciens comprenant des représentants du Support, de la Réparation, des Etudes et des Programmes. Elles prennent en considération les risques d'arrêt de fonctionnement, leur taux, la réparabilité des pièces et son aspect économique, l'expérience sur le moteur considéré mais aussi les autres types de turbomoteurs et enfin l'accessibilité des pièces en maintenance courante ou en atelier. La liste des Pièces à Limite d'Utilisation et leurs limites évoluent avec l'expérience.
Les PLU sont mentionnées dans la documentation d'entretien et inscrites dans le Livret-Moteur afin d'en assurer la traçabilité. Arrivées au terme de leur limite d'Utilisation, les PLU doivent être remplacées. On notera qu'au cours de leur vie, ces pièces peuvent subir des opérations de réparation ou reconditionnement.

Les autres pièces, sans vie-limite ni limitation d'utilisation, sont "selon état", la maintenance programmée niveau 1 et 2 suffisant à en assurer la surveillance.
La définition des pièces à vie-limite, des PLU et de la maintenance de niveaux 1 et 2 permet d'éliminer la notion de potentiel ou de TBO. Plus exactement, le concept de potentiel demeure, mais attaché aux pièces individuelles et non plus aux ensembles, modules ou moteurs.

7. Gérer opérationnellement les pièces

Vivre avec des potentiels modules ou moteurs et des vie-limites est confortable opérationnellement. Il est vrai qu'individualiser les potentiels au niveau des pièces augmente la difficulté de gestion.

Mais cette difficulté est source de grandes économies. Pour faciliter la vie opérationnelle et réduire encore les coûts, les principes suivants sont appliqués par Turboméca :

> ➢ **Aligner, autant que possible, vies-limites et limites d'utilisation pour grouper les remplacements de pièces.**

> ➢ **Modulariser les turbomoteurs pour regrouper les pièces de manière homogène et ne renvoyer en atelier qu'une partie du moteur.**

> ➢ **Développer la Maintenance Profonde, niveau 3, pour être capable de remplacer pièces à vies-limites et PLU sans retour en atelier de réparation.**

> ➢ **Automatiser le suivi des pièces grâce aux calculateurs moteurs, aux calculateurs hélicoptère, aux dispositifs HUMS et aux stations-sol correspondantes.**

8. Une nouvelle façon de maintenir les turbomoteurs

Réduire le coût de maintenance des turbomoteurs c'est, avant tout, éviter de les renvoyer en atelier de réparation.
C'est, idéalement, faire la totalité de la Maintenance chez l'Utilisateur final. Pour ce faire, deux concepts doivent être mis en place :

> ➢ **Les potentiels par pièces**
> ➢ **La Maintenance Profonde**

Le premier concept cible l'intervention au "juste nécessaire" tandis que le deuxième améliore la disponibilité du matériel.
La combinaison des deux réduit significativement le coût de Maintenance.
Ce déplacement de ces activités chez l'utilisateur final accroît évidemment la charge de travail de celui-ci, nécessite du personnel formé et un minimum d'outillage. Mais au global l'économie et la souplesse opérationnelle sont au rendez-vous.

<div style="background-color:orange; color:white; text-align:center;">

Trois catégories de pièces

</div>

❍ **Les Pièces à Vie-Limite**

- *Vies-Limites*

❍ **Les Pièces dont la Défaillance entraîne un Arrêt de Fonctionnement**
- *Limites d'Utilisation*

❍ **Les Pièces dont la Défaillance entraîne une Dépose lors d'une Opération de Maintenance Programmée**

- *Selon Etat*

Gérer opérationnellement les pièces

○ **Aligner, autant que faire se peut, Vies-limites et Limites d'Utilisation**

○ **Concevoir des Moteurs Modulaires**

○ **Développer la Maintenance Profonde**

○ **Automatiser le Suivi des Pièces**

Les Composantes du DMC

Maintenance Programmée .... *80 %*

Maintenance Non Programmée .... *20 %*

Les Composantes de la Maintenance Programmée

Révision Moteur et Accessoires .... *80 %*

Pièces à Vie-Limite .... *17 %*

Inspections Périodiques .... *3 %*

Réduire le DMC

=

Optimiser la durée de vie en service des pièces

Integrated Lifing Analysis of a Film-Cooled Turbine Blade

Tiedo Tinga, Wim B. de Wolf, Wilfried P.J. Visser and Sandor Woldendorp
National Aerospace Laboratory
P.O. Box 153, 8300 AD Emmeloord, The Netherlands
Tel. +31 527 248727, Fax. +31 527 248210, email: tinga@nlr.nl

Abstract
A method to predict gas turbine component life based on engine performance analysis is demonstrated on a hot section gas turbine component. The mechanical and thermal loading of the first stage high pressure turbine rotor blade of the F100-PW-220 engine, one of the most severely loaded components in the engine, is analyzed and a life assessment is performed. For this analysis, engine performance history is obtained from in-flight monitored engine parameters and flight conditions and downloaded for processing by a tool integrating a number of software tools and models. Data acquisition is performed by the FACE system installed in a large number of RNLAF F-16 fighter aircraft. Data then is processed by a thermodynamical engine system model, calculating gas properties like pressure and temperature at the required station in the engine. A computational fluid dynamics model, including the blade film cooling, is used to calculate the heat transfer to the blade. A thermal finite element model calculates the temperature distribution in the component and the stress distribution is obtained with a structural finite element analysis. Finally a life consumption model is used to determine the creep and fatigue damage accumulation in the component. The tool has significant potential to enhance on-condition maintenance and optimize aircraft operational use.

Acronyms

NLR	National Aerospace Laboratory
RNLAF	Royal Netherlands Airforce
FACE	Fatigue and Autonomous Combat Evaluation
GSP	Gas Turbine Simulation Program
CFD	Computational Fluid Dynamics
FE	Finite Element
FMU	Flight Monitoring Unit
DRU	Data Recording Unit
LDS	Logistic Debriefing Station
SCF	Set-up Configuration File
DEEC	Digital Electronic Engine Control
PLA	Power Lever Angle
HPT	High Pressure Turbine
TIT	Turbine Inlet Temperature
LCF	Low Cycle Fatigue

Symbols

Q	heat flux [W/m^2]
h	heat transfer coefficient [W/m^{2}K]
T_{aw}	adiabatic wall temperature [K]
T_w	wall temperature [K]
η	film cooling efficiency
ω	rotational frequency [rad/s]
L	characteristic length [m]
C_p	specific heat [J/kgK]
T_t	total temperature [K]
p_t	total pressure [bar]
$\tilde{\omega}$	dim.less rotational frequency
$\tilde{\mu}$	dim.less fluid viscosity
$\tilde{p}$	HPT pressure ratio

1. Introduction
Maintenance costs form a major part of total aircraft engine operating costs. A significant reduction in these costs would be obtained if inspection intervals could be extended and component service life increased. Inspection intervals and service life are commonly based on statistical analysis, requiring a limited probability of failure (a certain level of safety) during operation. However in many cases this approach leads to conservative inspection intervals and life limits for the majority of parts or components. The analysis tool developed at the NLR [1],[2] offers a way to attempt to reduce maintenance costs and improve safety by applying usage monitoring to predict operational component condition and lifetime consumption and thereby facilitating "on-condition maintenance".

The next section will describe the several constituents of the analysis tool. The third section then describes the gas turbine component that is analyzed, a first stage turbine rotor blade of the F100-PW-220 engine of a Royal Netherlands Airforce (RNLAF) F-16 fighter aircraft. In section four the tool is demonstrated and evaluated on this component and in the final section some conclusions are drawn and the potential of the tool to support a gas turbine operator is shown

2.   Description of the integrated analysis tool

The integrated analysis tool consists of a sequence of software tools and models. An overview of this sequence is given in Fig. 1. The algorithms and system models incorporated in this tool represent the relation between operational usage of the engine and component condition. Optimally, the system is able to accurately determine component condition and predict life consumption based on operational data obtained from a number of sensors.

The developed analysis tool predicts engine component (or part) life based on analysis of engine performance. Engine performance history is obtained from in-flight monitored engine control parameters and flight conditions and downloaded for processing by a number of software tools and models. Most of the models and tools used to determine engine performance, component usage and condition (health) and to predict life consumption were already commonly applied at the National Aerospace Laboratory (NLR) as stand-alone. The benefit of the integrated tool is the direct relation between engine performance and component life. The following tools must subsequently be applied to process the data:

FACE	Fatigue and Air Combat Evaluation (FACE) system for monitoring flight / engine data.
GSP	Gas turbine Simulation Program (GSP) for calculating engine system performance data.
CFD model	Computational Fluid Dynamics (CFD) model for calculating the heat transfer to hot section components.
FE model	Finite Element (FE) model for calculating temperature and thermal and mechanical stress in hot section components.
Lifing model	for deriving life consumption data from the stress history data.

Flight data acquisition (FACE)

The FACE system used to measure flight data is based on the Autonomous Combat Evaluation (ACE) system of RADA Electronic Industries, which is used for pilot debriefing purposes. The NLR has developed a fatigue analysis system that has been combined with ACE to form the FACE system [3]. The FACE system consists of both on-board and ground-based hardware. In the aircraft two electronic boxes are installed: the Flight Monitoring Unit (FMU) and the Data Recording Unit (DRU). The ground-based hardware relevant for maintenance purposes is the Logistic Debriefing Station (LDS).

The FMU is a programmable unit that determines which signals are stored and how they are stored. By generating a Set-up Configuration File (SCF) and uploading it into the FMU, the data collection process can be adapted to all requirements. In this way several data reduction algorithms (e.g. peak and through, time at level) can be selected and the sampling frequency can be adapted. The relevant signals stored by the DRU are engine parameters from the engine's Digital Electronic Engine Control (DEEC) and avionics data. The DEEC signals can be sampled at a maximum frequency of 4 Hz. The following signals, which together fully describe engine usage, are stored:
- Fuel flow to the combustor
- Fuel flow to the afterburner
- Exhaust nozzle position
- Flight conditions: Mach, altitude and air temperature

These parameters, as functions of time, are used as input for the GSP model, which is the next tool in the sequence. The first three parameters could also be substituted by the Power Lever Angle (PLA) signal, provided that the GSP model contains a control unit, which translates the PLA to the appropriate fuel flows and nozzle area. A data reduction algorithm is applied to reduce the amount of operational data before it is used as input for GSP.

Engine system performance (GSP)

The Gas Turbine Simulation Program (GSP) is a tool for gas turbine engine performance analysis, which has been developed at the NLR [4],[5]. This program enables both steady state and transient simulations for any kind of gas turbine configuration. A specific gas turbine configuration is created by arranging different predefined components (like fans, compressors, and combustors) in a configuration similar to the gas turbine type to be simulated. An example of a model for a twin spool turbofan engine like the Pratt & Whitney F100-PW-220 is given in Fig. 2. The simulation is based on one-dimensional modeling of the processes in the different gas turbine components with thermodynamic relations and steady-state characteristics ("component maps").

For implementation in the integrated analysis tool, GSP can be used to calculate gas temperatures, pressures, velocities and composition at relevant engine stations from measured engine data. This particularly applies to stations for which no measured data is available such as the critical high-pressure turbine entry temperature. Also, GSP is able to accurately calculate dynamic responses of these parameters (critical to engine life) where measured data is not available or has unacceptable high time lags or low update frequencies.

The GSP model input obtained from FACE includes all measured flight conditions and engine power setting data. With GSP, the entire engine transient (usually an entire mission) is calculated with an integration step size of 0.05 seconds. With a smallest input step size of 0.2 seconds, this is sufficient to accurately calculate the critical effects such as typical severe acceleration / deceleration temperature transients in the hot section. A GSP report (ASCII format) is used to output data for further processing by the fluid dynamics (CFD) and finite element (FE) models.

Computational Fluid Dynamics analysis (CFD)

The Computational Fluid Dynamics (CFD) model is used to accurately calculate the heat transfer from the hot gas stream to the component. The FINE/Turbo code of Numeca is used to construct the model and perform the calculations, solving the Reynolds-averaged Navier-Stokes equations. For these calculations it is important to have detailed information on the geometry of both the flow channel and the different components (blades, vanes). Real components have been measured with a scanning device and this information is combined with information from drawings and other technical documents to define the model geometry. From CFD analysis of the gas flow through the gas turbine values for the heat transfer coefficient h and adiabatic wall temperature T_{aw} ($\approx$ gas temperature) are obtained along the surface of the component. Values of h and T_{aw} are used to calculate the heat flow Q from the fluid to the structure (with a wall temperature T_w).

$$Q = h \, (T_{aw} - T_w)$$

It is hereby assumed that the heat transfer coefficient is not dependent on the blade temperature. The blade temperature is calculated with the thermal FE model and is still unknown when the CFD analysis is performed. Assuming no dependence of h on blade temperature allows for decoupling of the CFD and FE analysis. For every condition two CFD analyses have to be performed: firstly a calculation with adiabatic conditions (no heat flow from fluid to structure) is performed, yielding the adiabatic wall temperature (T_w) distribution. After that a calculation is done with either a constant heat flux Q or a constant wall temperature T_w. In combination with the known adiabatic wall temperature this yields the heat transfer coefficient (h) distribution. Note that the h value varies significantly along the flow path, due to variations in the flow conditions (gas velocity, type of flow (laminar, turbulent), viscous effects, etc).

Finite element analysis (FE)

The Finite Element (FE) model consists of two interrelated models. The thermal model calculates the temperature distribution in the component, based on the heat input from the hot gas stream. The mechanical model calculates the stresses and strains in the component, caused by the varying temperature distribution and the externally applied loads. The finite element code used is MSC.Marc, which is a commercially available, multipurpose finite element package. Definition of the geometry and mesh generation is performed with the pre-processor MSC.Patran. MSC.Patran is also used as postprocessor to view and analyze the results.

In the mechanical model, there are two sources for stress in a rotating component: centrifugal forces due to rotation of the component and temperature gradients in the material. The gas bending forces are in most blade designs counterbalanced by geometric measures like blade leaning. The resulting stresses are therefore much smaller than the stress due to the other two sources, and are thus not considered here.

Lifing analysis
A lifing model defines the relation between loading level and lifetime. It generally calculates either total time to failure or number of cycles to failure for a certain component subjected to a specific load sequence. A large number of specific life prediction models have been developed over the last forty years, where each model is appropriate for a specific application. The major division in lifing models is between total life models and crack growth models. Total life models, like the Palmgren-Miner model [6],[7], only calculate the time to failure, not considering the way failure is reached. These models are representative for the Safe Life philosophy, aiming to retire a component before a crack originates. On the other hand, crack growth models represent the Damage Tolerance philosophy, which accepts the presence of material defects and aims to monitor crack growth and remove the component before the crack becomes unstable. In addition, several different mechanisms can cause the failure of a component, for example fatigue, creep or oxidation. Every failure mechanism requires a specific lifing model. In the end, the actual choice of the lifing model(s) depends on the expected failure mechanism of the component under consideration.

3. Description of the turbine blade
The component under consideration is the first stage high pressure turbine blade of the Pratt & Whitney F100-PW-220 engine (Fig. 3). This blade operates in very severe conditions due to its location just behind the combustion chamber. Because of the severe loading, much effort is put in measures to keep the blade from degrading. The blade is fabricated as a single crystal, having a relatively low elastic modulus in radial direction and having good creep properties due to the absence of grain boundaries. Furthermore several cooling mechanisms are applied to keep the blade temperature acceptably low. Firstly the blade is cooled internally by cooling gas flowing through a number of cooling channels inside the blade (see figure 4). Inside the cooling channels turbulators are positioned to increase the heat transfer. The cooling gas is obtained from one of the last stages of the high-pressure compressor and enters the blade through a number of entries in the root of the blade. Secondly the blade is film-cooled which means that cooling gas is injected into the hot gas stream from orifices in the airfoil. This cooling air forms a relatively cool film between the blade surface and the hot gas, resulting in a decreased blade heating.

4. Integrated analysis of 1st stage turbine blade
This section describes how the integrated tool is applied to the real component described in the previous section.

FACE / GSP
The FACE system is used to measure the flight data for a number of missions flown with F-16 fighter aircraft of the Royal Netherlands Airforce (RNLAF). One arbitrary mission has been selected to be used for the current lifing analysis. The gas turbine simulation program GSP is used to translate the flight data to appropriate gas flow properties, which can be used as input for the fluid dynamics and finite element analyses.

CFD analysis
During the transient analysis of a mission it is impossible to do a separate CFD analysis for every occurring engine operating condition. The following simplification is therefore used. By carefully analyzing the fluid dynamics equations, it is observed that under certain assumptions only three dimensionless groups are needed to characterize any dimensionless flow property in the engine for any operating condition. These dimensionless groups are:

$$\tilde{\omega} \equiv \frac{\omega L}{\sqrt{c_p T_t}}, \qquad \tilde{\mu} \equiv \frac{\mu(T_t)\sqrt{c_p T_t}}{p_t L}, \qquad \tilde{p} \equiv \frac{p}{p_t}$$

where $\tilde{\omega}$ can be seen as a dimensionless rotational frequency, $\tilde{\mu}$ as a dimensionless fluid viscosity and $\tilde{p}$ expresses the pressure ratio over the high pressure turbine (HPT). With GSP the variation of these three groups during a representative mission is analyzed. This results in the definition of seven operating points which cover the complete operating envelope of the engine: one center point and two more points in each dimension are defined. Then for each of the seven points CFD analyses are performed and a tri-linear interpolation function is used to obtain the results for any other condition. In this way only CFD analyses for seven conditions have to be performed to obtain the results for any arbitrary condition. During the transient mission analysis the values of the dimensionless groups for every time step are calculated by GSP, and the corresponding heat transfer and gas temperature values are obtained from the interpolation function.

The CFD model also allows for incorporating the effects of blade film cooling on heat transfer. Cold air is injected through cooling orifices into the outer flow to provide a cooling air layer with effective temperature T_{film} between the blade surface and the outer hot gas flow. The film temperature T_{film} depends on the film cooling efficiency η and the injection temperature T_{inj} in the following way:

$$T_{film} = T_{gas} - \eta(T_{gas} - T_{inj})$$

Modeling all separate cooling orifices in the airfoil would require a very fine computational grid, resulting in very long calculation times. Therefore a row of orifices is simulated by a cooling slot with the same width as the local grid and covering the blade from root to tip. The cooling efficiency of such a slot is much higher than that of an orifice row (0.8 compared to 0.15 [8]), so a correction is made by increasing the injection temperature, resulting in a more realistic film temperature and heat transfer.

Finite Element analysis

The thermal analysis for the current component is quite complex. The blade is heated from outside by the hot gas and at the same time cooled from inside by the cooling gas. Moreover, the cooling gas is eventually injected into the hot gas stream through cooling orifices to establish film cooling. The blade temperature is therefore dependent on hot gas temperature and cooling gas temperature, but on the other hand the cooling gas temperature is dependent on the blade temperature. Such a coupled fluid-structure problem must be solved in an iterative way. Because it would take too much computation time to solve the complete transient problem in an iterative way, a simple model is used to derive an approximation. This model, which is shown in figure 5, is used to derive a relation between the blade temperature distribution and the turbine inlet temperature (TIT). During the transient analysis this approximated blade temperature distribution is used to calculate the cooling gas temperature distribution, which together with the hot gas temperature distribution is used as input for the thermal analysis. This eliminates the coupling between fluid and structure.

The thermal model is thus used to calculate the temperature distribution in the component. For each finite element on the airfoil of the turbine blade, the heat transfer coefficient and the local gas temperature follow from interpolation in the CFD results. In the cooling channels inside the blade, the heat transfer coefficient is assumed to be constant. The cooling gas is heated while it flows through the hot blade and the local gas temperature is calculated from an approximated blade temperature distribution as explained above. With the thermal conductivity α of the material, the temperature distribution in the component can be calculated. A transient thermal analysis is performed for the complete flight under consideration with the time-varying dimensionless groups (used to determine h and T_{aw}), cooling gas inlet temperature and turbine inlet temperature (used to approximate the cooling gas temperature rise) obtained from GSP as input. An example of the temperature distribution in an internally cooled turbine blade at some point during a flight is shown in Fig. 6. A limited number of CFD packages, having the ability to incorporate fluid-structure interaction, can perform both the heat transfer coefficient and temperature distribution calculation. This would make the MARC thermal model calculation redundant and would allow for a coupled fluid-structure analysis.

The mechanical model calculates the stress and strain distribution in a component. Again a transient analysis is performed for the complete mission. In this case the rotational frequency and the temperature distribution, both as function of time, are the input for the model and the stress and strain

distributions in time appear as output. The temperature distribution is obtained from the results of the thermal analysis and the values of the rotational frequency are read from the GSP report file. An example of the stress variation at 3 different locations on a turbine blade is shown in Fig. 7.

<u>Lifing model</u>
For the first stage turbine blade both creep and Low Cycle Fatigue (LCF) are important damage mechanisms. Therefore a combined creep / fatigue lifing model is applied. The strain history of the mission, calculated with the mechanical FE model, is used to determine the fatigue damage. The fatigue damage according to Miner's rule is given by

$$D_{fatigue} = \sum_i \frac{n_i}{N_{f,i}}$$

where n_i is the number of cycles at a certain load level and $N_{f,i}$ is the number of cycles to failure at that load level. End of life is reached when the damage becomes 1. This rule is applied to the maximum principal strain sequence for every node in the FE model, yielding the fatigue damage distribution in the blade after one mission. The result is in Figure 8. The creep damage is calculated with Robinson's rule:

$$D_{creep} = \sum_i \frac{t_i}{t_{r,i}}$$

Equivalent to Miner's rule t_i is the time at a certain stress and temperature and $t_{r,i}$ is the corresponding rupture time. This rule is applied to the equivalent stress and temperature sequence for every node. The calculated creep damage is shown in figure 9. Combining these two results yields the total life time distribution (Fig. 10). This number is obtained by adding the creep and fatigue damage contributions and inverting the number. As the damage in Figs 8 and 9 is calculated for one mission, the total life in Fig. 10 is also given in number of missions. As can be seen in these figures, the shortest life is located at the spots with the highest creep damage, indicating that creep is the critical failure mechanism for this component.

5. Discussion
An important point of discussion for this tool is the accuracy of the calculated results. The accuracy of the integrated tool is obviously dependent on the accuracy of the separate tools and models. The measurements of the FACE system combined with the data reduction algorithm introduce a maximum error of about 1%. The GSP model inaccuracy is considered to be less than 2%, provided that a suitable integration time step has been chosen. The accuracy of the temperatures calculated with the thermal FE model is mainly determined by the accuracy of the heat transfer coefficient and adiabatic wall temperature obtained from the CFD analysis. It must be noted that the problem under consideration is at the edge of the capabilities of current CFD codes and a number of assumptions and approximations must be made to even get a solution. Firstly slot cooling is used in stead of orifice cooling and h is assumed to be independent on wall temperature (decoupling of CFD and FE). Furthermore tri-linear interpolation between 7 standard conditions is used to obtain results for any arbitrary condition and finally the thermal interaction between (internal) cooling gas and blade material is removed by approximating the cooling gas heating (no iterative solution of FE problem). Off coarse, these assumptions decrease the accuracy, but still the adiabatic wall temperature can be calculated within about 10% and the heat transfer within a factor 2. The uncertainty in heat transfer coefficient will cause uncertainty in the temperatures during transients. However, the steady state temperatures are unaffected by the heat transfer rates. This means that for creep life calculations the value of the heat transfer coefficient is not very important, but for fatigue life calculations it is of much more importance. The mechanical FE model has an inaccuracy of less than 2%, provided that the right and accurate material data is used. For the 1st stage turbine blade analysis, the single crystal material data were not available, and data for an isotropic superalloy were used. Obviously the inaccuracy of the FE calculations will be larger when an inaccurate geometry or a course mesh is used, but this can be improved rather easily and is therefore not considered to be a limitation of the tool. Note however that refining the FE mesh rapidly increases the computation time and the required memory.

All together this means that the loading of a component can be calculated with an inaccuracy of about 10%, provided that sufficient (aerodynamic) information about the specific component is available. However, performing the actual life prediction will introduce an additional inaccuracy of 20 to even 50%. This large inaccuracy is due to the large scatter in experimentally determined material data used for the life prediction. The actual inaccuracy depends on the type of material data used by the model. For example S,N-curves representing the relation between number of cycles to failure and applied stress level, show a higher scatter than crack growth curves and creep rupture curves. It is therefore a fundamental material property phenomenon, which has its effect on the lifing model inaccuracy. Development of lifing models must be focussed on model types, which are based on material data with little scatter (like crack growth data). Another problem is the strong sensitivity of calculated life on deviations in stress and temperature, especially for creep life (see figure 11). A small deviation in stress and especially temperature is therefore amplified in the life prediction.

Due to the assumptions in the CFD analysis and the unavoidable inaccuracy in the life prediction, the tool is not yet suitable to do absolute life predictions. However, the tool is very useful for relative life predictions or sensitivity studies.

6. Conclusions and Potential

An integrated lifing analysis on a complex gas turbine component has been demonstrated. The internally and film-cooled turbine blade has been analyzed with a sequence of software tools and models. Especially the CFD model used is state-of-the-art for current CFD codes, using a slot-cooling model to represent the blade film cooling. It has been demonstrated that the mechanical and thermal loads of the turbine blade can be calculated from operational flight data, and that subsequently a combined creep and fatigue life prediction can be performed. As the overall life prediction inaccuracy of the tool is dominated by the relatively high inaccuracy of lifing models and the large scatter in the associated material behavior, future work must be focussed on improving those models. A more accurate CFD model, having the possibility to model orifice cooling, can improve the accuracy further. The present tool, with its limited accuracy can be used to perform relative life assessments and sensitivity studies.

The potential of the analysis tool presented here is twofold. Firstly the tool can be used to apply *on-condition maintenance*. The load history of every individual component could be tracked and could be used to determine the inspection interval or actual life limit of that specific component. The general and mostly very conservative life limits supplied by the manufacturer are based on a certain assumed usage, on top of which a safety factor has been applied to account for heavier usage. This safety factor can now be quantified and probably decreased, which leads to a huge saving in spare parts and inspection costs.

Secondly, the tool can be used to compare different missions with respect to life consumption. The results can for example be used to optimize the planning of operational deployment of the aircraft.

7. Acknowledgements

8. References

[1] Tinga, T., Visser, W.P.J., Wolf, W.B. de, Broomhead, M.J., *Integrated Lifing Analysis Tool for Gas Turbine Components*, ASME-2000-GT-646, 2000, NLR TP 2000-049.

[2] Tinga, T.; Visser, W.P.J.; Wolf, W.B. de; *Integrated lifing analysis for gas turbine components,* presented at USAF Aircraft Structural Integrity Program Congress, San Antonio, Texas, USA, 5-7 December, 2000, NLR TP 2000-632.

[3] Spiekhout, D.J., *F-16 loads / usage monitoring,* NLR TP 98172, National Aerospace Laboratory, 1998, Amsterdam.

[4] Visser, W.P.J., *Gas turbine Simulation Program - GSP – Description and Status*, NLR CR 91022 L, National Aerospace Laboratory, 1991, Amsterdam.

[5] Visser, W.P.J., *Gas turbine Simulation at NLR*, NLR TP 95574 L, National Aerospace Laboratory, 1995, Amsterdam. Paper presented at the CEAS Symposium on Simulation Technology, October 30, 31 and November 1, 1995, Delft, the Netherlands.

[6] Miner, M.A., *Cumulative Damage in Fatigue*, ASME Journal of Applied Mechanics, Vol. 67 (1945), pp. 159-164.

[7] Palmgren, A., *Die Lebensdauer von Kugellagern*, Verfahrenstechnik, Vol.68 (1924), pp. 339-341.

[8] Wolf, W.B. de; Woldendorp, S.; Tinga, T.; *Analysis of combined convective and film cooling on an existing turbine blade;* presented at RTO-AVT Symposium Heat Transfer and Cooling in Propulsion and Power Systems, Loen, Norway, May 2001, NLR TP 2001-148.
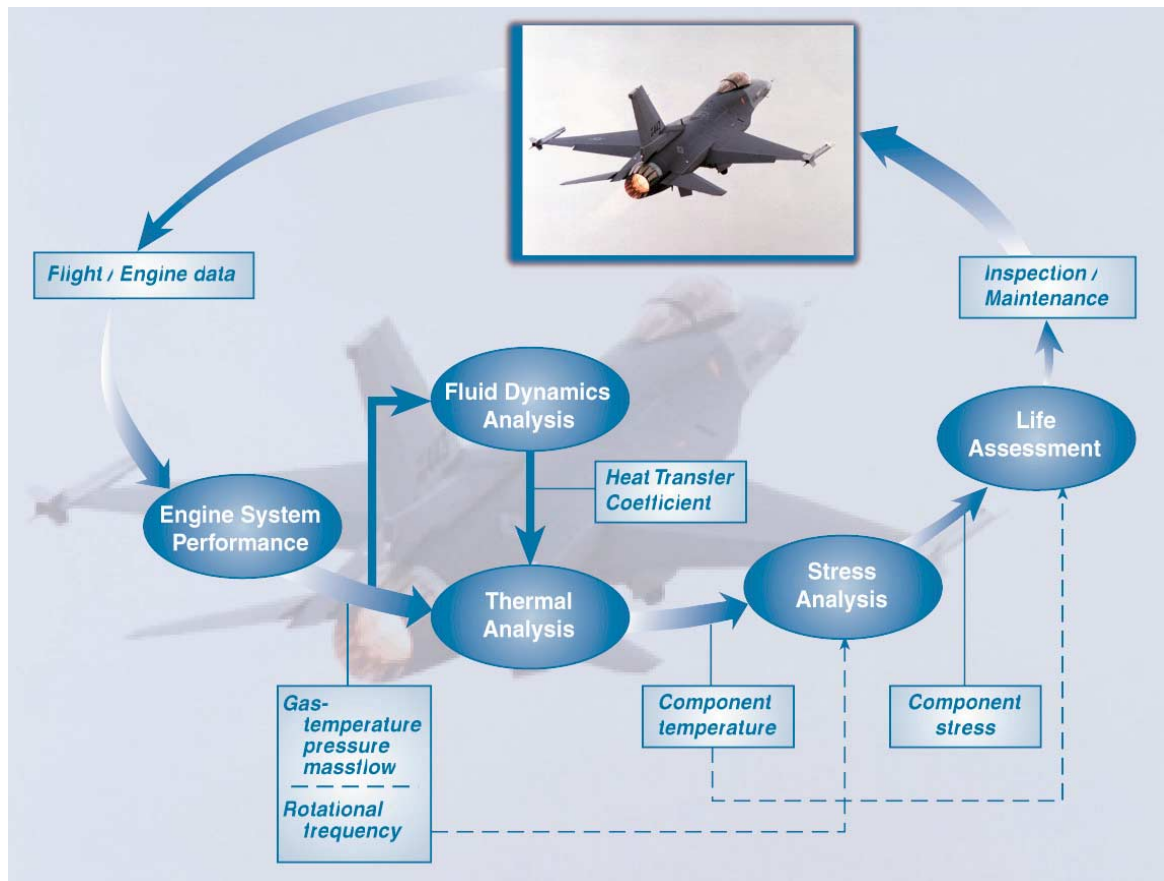
Figure 1: Overview of the integrated analysis tool.
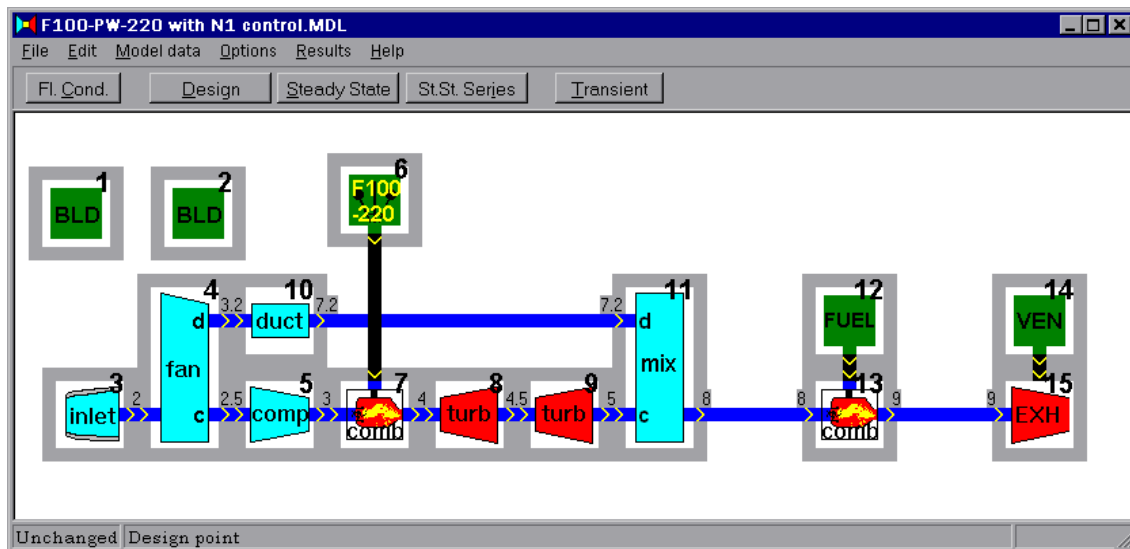
Figure 2: GSP model of the Pratt & Whitney F100-PW-220 turbofan engine.

Figure 3: 1st stage turbine blade
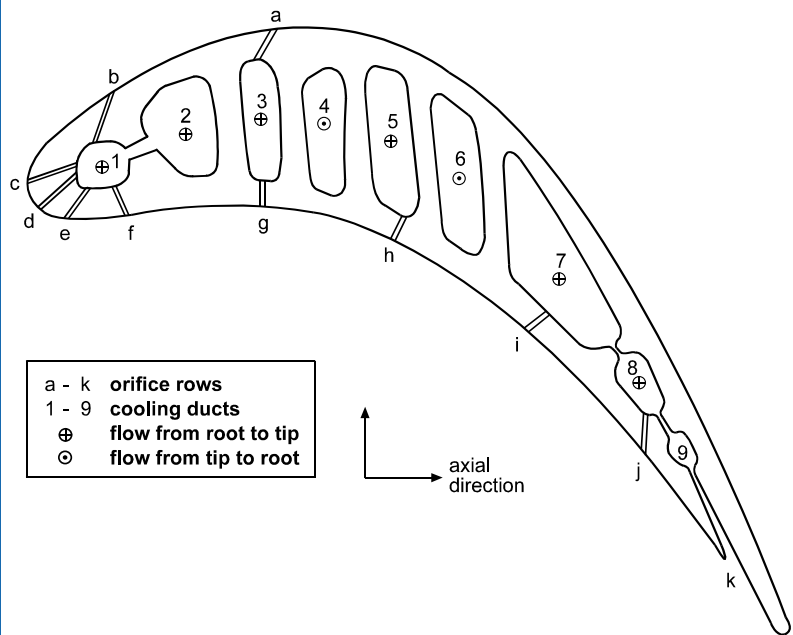
Figure 4: Overview cooling ducts and orifice rows

a - k   orifice rows
1 - 9   cooling ducts
⊕   flow from root to tip
⊙   flow from tip to root

axial direction
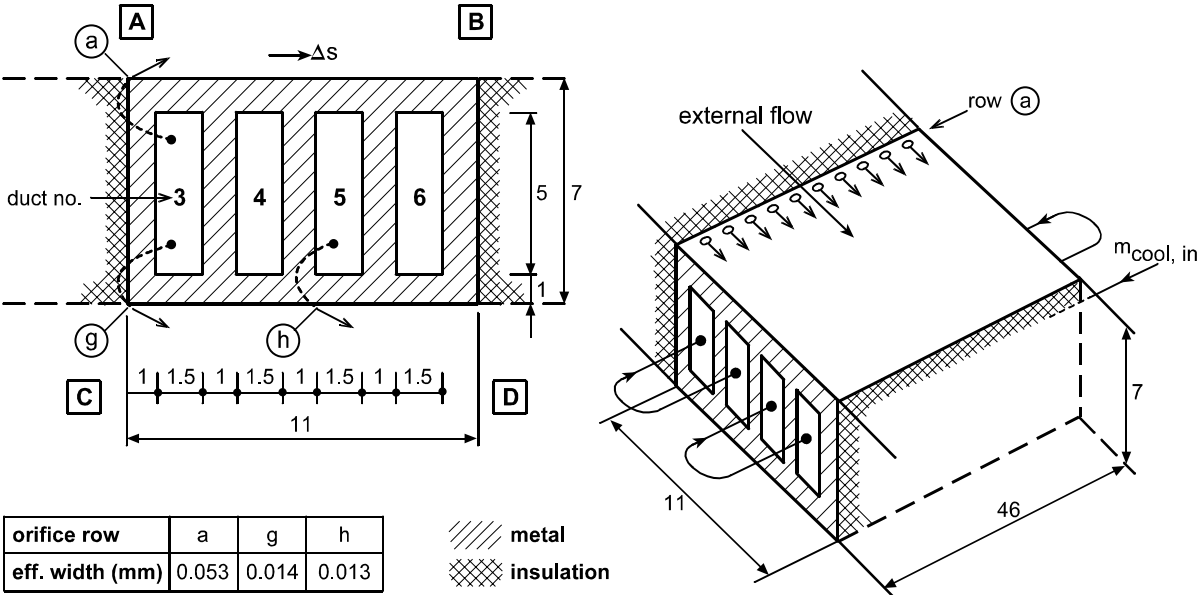
orifice row	a	g	h
eff. width (mm)	0.053	0.014	0.013

metal

insulation

external flow

row (a)

$m_{cool, in}$

Figure 5: Model to approximate cooling gas temperature increase
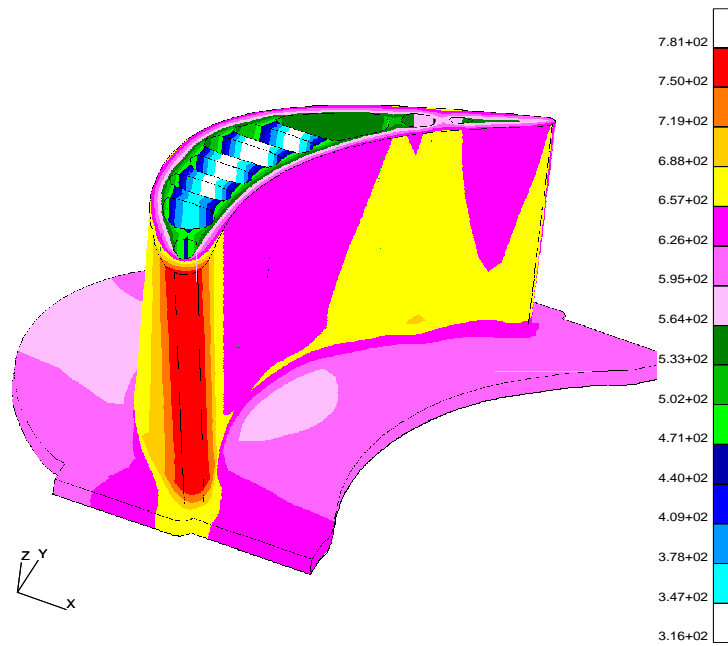
Figure 6: Temperature distribution (^{o}C) in the lower half of an internally cooled turbine blade.
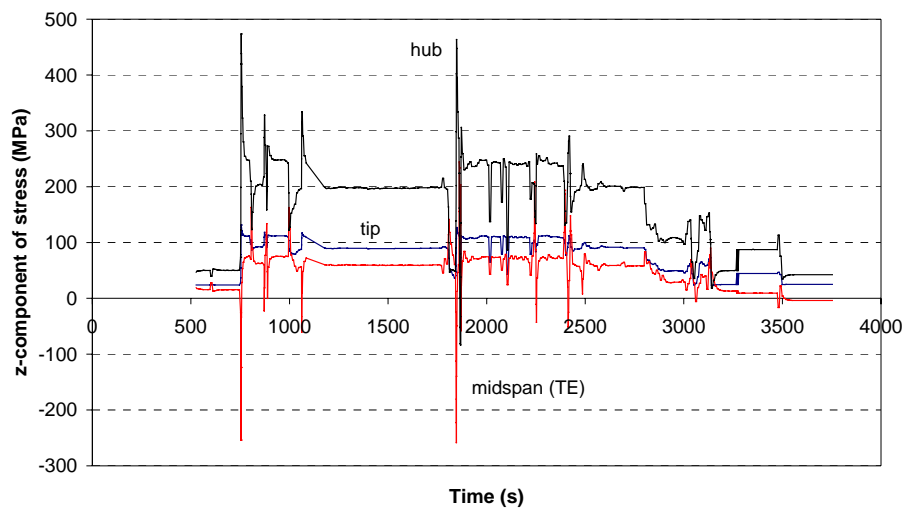
Figure 7: Variation of stress in time for three different locations on the blade.
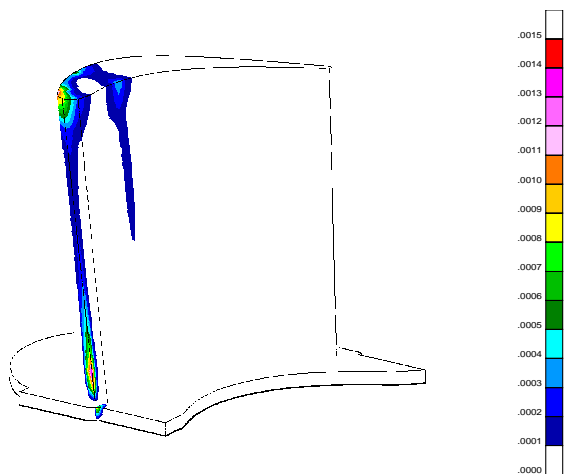
Figure 8: Fatigue damage distribution.
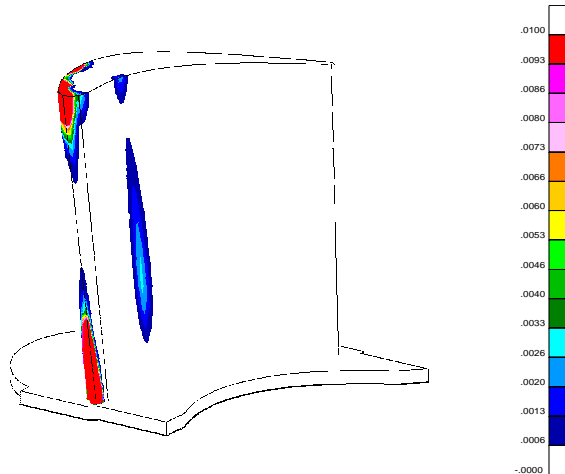
Figure 9: Creep damage distribution.
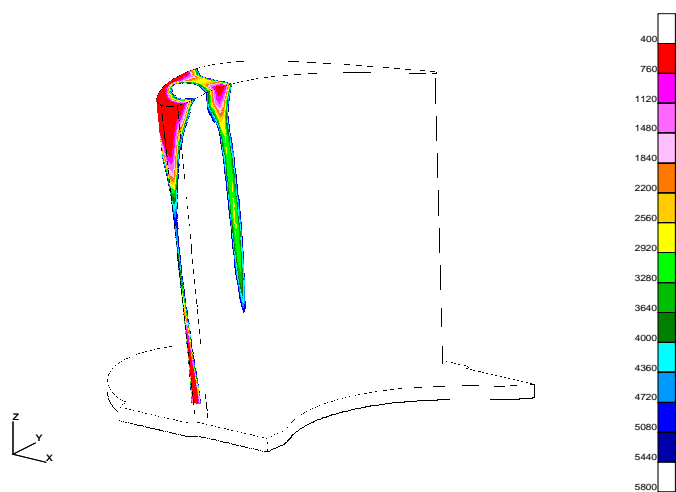
Figure 10: Predicted total life distribution.
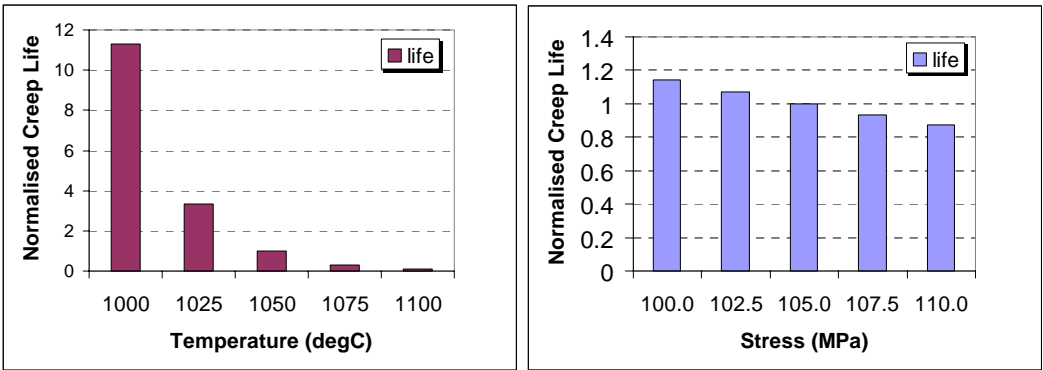
Figure 11: Temperature and stress sensitivity of creep life.

Paper 20: Discussion

<u>Question from Dr B Wicks – DSTO, Australia</u>

I am puzzled as to why you have used such a complex problem as a first stage turbine blade analysis to demonstrate your modelling tool. Have you considered applying the tool to lifing a disc?

<u>Presenter's Reply</u>

We did start our analysis with a simpler component, the third stage turbine blade. However, the Royal Netherlands Air Force was interested to see whether a complicated component could also be modelled.

<u>Question from H Pfoertner – MTU, Germany</u>

Is your complicated model suitable for processing a large amount of flight data?

<u>Presenter's Reply</u>

No, we are in discussion with the OEM (P&W) to see how the operational data collection can be of use.

This page has been deliberately left blank

_____

Page intentionnellement blanche

Fatigue Crack Growth Predictions for Simplified Spectrum Loading: Influence of Major Cycles on Minor-Cycle Damage Rates

Stephan M. Russ,[1] Andrew H. Rosenberger,[1] James M. Larsen,[1] and W. Steven Johnson[2]

[1]U.S. Air Force, Air Force Research Laboratory
Materials and Manufacturing Directorate
AFRL/MLLMN, 2230 Tenth Street, Ste 1
Wright-Patterson Air Force Base, Ohio 45433-7817, U.S.A.

[2]Georgia Institute of Technology
School of Materials Science and Engineering
Atlanta, GA 30332-0245, USA

ABSTRACT

As part of the Engine Structural Integrity Program, USAF turbine-engine components are subject to a damage tolerance or crack-growth assessment. This assessment involves the prediction of crack-growth lifetimes from an initial flaw size under simulated mission loading. The accuracy of the prediction is dependent upon numerous assumptions and inputs: how well the actual mission is simulated by the simpler load spectrum, the accuracy of the component temperature and stress analysis, the ability to account for load-history effects and time dependency using steady-state crack-growth data, and accounting for thermomechanical fatigue crack growth using isothermal data, to name just a few. It is evident that the life prediction is a very complex problem, and numerous effects are accounted for with empirical factors based on experience and laboratory observations. However, understanding the damage mechanisms and their controlling variables is essential in improving the accuracy of crack-growth predictions, given the complex nature of the problem.

Based on reported engine mission spectra, some missions can, in their most simple form, be represented by a major cycle, representing an engine start-up and shut-down, bracketing numerous minor cycles, resulting from in-flight throttle excursions. The major cycle has a stress ratio near zero, and the minor cycles have stress ratios on the order of 0.4 and above. Depending on the number and severity of the minor cycles, the damage, as predicted by available linear damage summation rules, can be dominated by either the minor or major cycle or these may be more evenly partitioned. Thus, there is a need to quantify the effect of tensile underloads, represented by the major cycle, on the minor cycle and vice versa.

Data have been generated on a titanium compressor-disk alloy (Ti-17) utilizing a stress ratio of 0.4 or 0.7 to represent the minor cycles and 0.1 to represent a major cycle. Results indicate that simple linear-damage rules can over predict crack propagation life, depending on the ratio of minor to major cycles. Several tests were performed in the vicinity of the fatigue crack growth threshold to scrutinize the effect. It is shown that the crack-growth predictions can be enhanced by slight modifications of the stress intensity range. A relatively new load-sequence method was evaluated to determine its merits relative to inveterate approaches. The method is based on a measure of the crack propagation resistance of the system.

INTRODUCTION

Fatigue crack growth predictions have been an essential element of the life-management system for turbine engine components since the mid 1980's. The United States Air Force's (USAF) *Retirement for Cause* (RFC) program [1] demonstrated the potential as well as the benefits, from a sustainment-cost perspective, of managing fracture-critical components based on fatigue crack growth behavior and nondestructive inspections. Today, USAF engines are designed and managed under the *Engine Structural Integrity Program* (ENSIP) [2], which mandates both crack-growth and crack-initiation predictions for all key locations on fracture-critical components. A cornerstone of both RFC

and ENSIP is the ability to predict fatigue crack growth, and to do so under realistic load-temperature-time spectra.

The bulk of fatigue crack growth (FCG) studies available in the literature have been performed under constant amplitude loading, otherwise known as steady-state conditions. However, the problem of predicting FCG lives becomes incresingly more difficult under *variable amplitude* or *spectrum loading*, when the steady-state assumptions are violated. Under spectrum loading, results can vary significantly with respect to steady-state predictions depending on the significance of load-interaction effects. It has been demonstaratd by Skorupa [3,4] that the effects can vary depending on the application. Models, like those developed by Newman and Fleck [5-8], based on plasticity-induced closure have enabled an interpretation of significant portions of experimental results. "Some observations, however, which cannot be understood in terms of plasticity-induced crack closure, or which are even in contradiction with the crack closure approach, indicate a possible role of other factors. A general conclusion is that conditions under which various phenomena can affect variable amplitude fatigue crack growth and interactions between them are insufficiently recognized."[4] The lack of a fundamental understanding of the FCG process under variable amplitude loading can lead to excessive safety factors in design and/or inordinate testing to characterize the material response to a limitless number of possible load scenarios.

A majority of load-interaction studies in the literature involve the application of periodic overloads and/or overload - compressive underload cycles which for the turbine engine industry are of academic interest but applicability is questionable. For starters, major, fracture-critical components are not subjected to significant overloads or compressive load excursions. A typical load-temperature-time history for a cooled turbine disk was shown by Larsen and Nicholas [9] to contain only mild overloads, and they occur on such a routine basis that it limits any crack retardation effect. In fact, the overloads were found to " . . . account for much of the crack propagation produced by a fatigue spectrum."[9] Similar conclusions were drawn by an AGARD working group established in the early 1980s to develop a loading standard for fighter aircraft engine disk usage. The working group developed TURBISTAN (TURBIne loading STANdard) [10], a test spectrum applicable for titanium alloys operating at or near ambient temperature. From a breakdown of the TURBISTAN load spectrum, it begins to approximate a simple sequence containing a high stress-ratio baseline with periodic underloads at or near zero. The AGARD study provided further evidence that for rotating turbine-engine components the applicable load spectrum consists of high-R minor cycles and periodic major cycles with minimum loads near zero. Overloads were determined to be of less importance than for airframe structures. However, based on experimental results presented by Raizenne [11], effects of underloads should be taken into account. Also, Jany and Renne [12] demonstrated, through comparisons with life prediction models, that the minor cycles contributed to the fatigue crack growth process and, therefore, could not be neglected.

Relative to research involving overloads, a much smaller number of studies have investigated the effect of underloads in the absence of overloads, and the attention of most of these was on compressive underloads. A general conclusion was that compressive load excursions cannot be neglected during crack growth analysis, and that the underloads can produce FCG rate acceleration and/or a reduction in threshold. [13-18] However, there are cases, such as the study by Yang [19], where no significant load interactions were oserved. In general, increased growth rates were attributed to decreases in closure. Of notable interest is that Yu et.al. [14] demonstrated acceleration of high-R FCG rates, yet the closure models do not predict closure under these high-R conditions. Therefore, the observed FCG acceleration cannot be explained based on closure arguments. This suggests that other phenomena have a prominent role under these load scenerios.

Sehitoglu and colleagues [20-22] have performed finite element analyses of closure, deformation, and residual stresses ahead of a crack. Their recommendations include development of crack propagation models that capture the residual stresses, both in the wake and at the crack tip, and determination of S_{tt}, an estimate of when the stresses ahead of a crack first become tensile. They warned that under variable amplitude loading, the difference between the opening load, S_{open}, and S_{tt} could become significant. Thus, even in the absence of closure; stress ratio, overload, and underload effects would be expected. These recommendations are consistent with the experimental observations

of Yu et.al. [14] as well as the recent work on load-interaction effects on threshold by Moshier et.al. [23] and Lang [24,25].

The goal of this study was to investigate the effect of tensile underload cycles on the high stress-ratio, fatigue crack-growth response of beta-forged Ti-17, and to guide development of an appropriate lifing methodology to account for observed load-interaction effects. To accomplish these objectives a modified description of the crack driving force, ΔK_{eff}, is proposed from which crack growth rates can be determined on a cycle-by-cycle basis. The modified description of ΔK_{eff} is based on a measure of an instantaneous propagation resistance of the material.

TEST PROCEDURE

Material and Specimen Geometry

Ti-17 is the commercial name for Ti-5Al-2Sn-2Zr-4Mo-4Cr (wt%), an alpha-beta titanium alloy designed for applications at temperatures below 427°C. Redden [26] demonstrated the advantages over Ti-6Al-4V in strength, hardenability, fracture toughness, fatigue crack initiation, and crack growth resistance. However, the property improvements come at an expense of a five-percent increase in density. For this study, specimens were machined from a laboratory-scale pancake forging. The starting billet was forged above the beta transus, with a final reduction ratio of 3.5:1, resulting in a "pancake" with a nominal thickness of 77 mm and diameter of 330 mm. The pancake was solution heat treated and aged to produce a Widmanstatten microstructure, Figure 1. The microstructure consisted of approximately 45% acicular alpha (dark phase) and 55% transformed beta (light phase).

Compact tension, C(T), specimens were machined with the notch oriented in the radial direction of the forging. The C(T) specimens had a thickness of 10 mm, which satisfied plane-strain conditions established by ASTM E399-90 [27]. All other specimen dimensions are shown in Figure 2. The specimens were mechanically polished to a one-micron finish, providing a mirror-like surface to facilitate optical crack-length measurements.
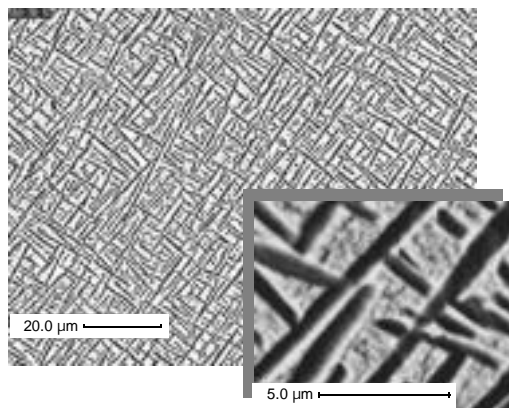
Figure 1. Widmanstatten microstructure of beta-forged Ti-17.
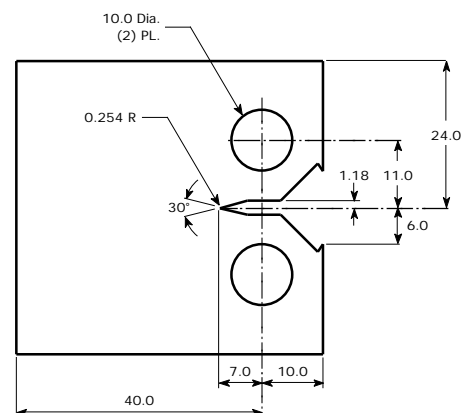
Figure 2. C(T) specimen geometry, dimensions in mm, 10 mm thickness.

Steady-State Fatigue Crack Growth

Baseline, steady-state FCG behavior was evaluated at stress ratios of 0.1, 0.4, and 0.7. All tests were conducted on an MTS servo-hydraulic test frame, and were performed in general accordance with ASTM test specification E647-95a [28]. The C(T) specimens were instrumented with a clip gage at the mouth of the machined notch for measuring crack opening displacements and a direct-current electric potential (DCEP) system for continuous monitoring of crack length. The DCEP technique is described in detail by Hartman and Johnson [29]. A DCEP lead half-spacing of 7 mm was used, and a constant supply current of 2.5 amps was introduced at the top and bottom of the front face of the specimens. Ceramic loading pins and teflon washers were used to electrically isolate the specimen from the load frame. Two traveling microscopes, one on each side of the specimen, were

used to periodically obtain optical, surface, crack-length measurements for comparison to, and post-test correction of, the DCEP measurements. Periodically throughout each test, load-displacement traces were acquired for post-test closure analysis.

Prior to testing, specimens were precracked at a frequency of 5 Hz, R of 0.1, and initial and final K_{max} of 14 and 6 MPa m, respectively, to a final crack length of approximately 10 mm. Actual FCG tests were performed at a frequency of 40 Hz. Fatigue crack growth response was determined from two separate test-control procedures. Immediately following precracking, a K-decreasing test, with a normalized K-gradient of approximately –0.079 mm^{-1}, was performed until crack arrest - defined as less than 0.1 mm crack growth after greater than 5 x 10^6 cycles, i.e. growth rate less than 2 x 10^{-11} m/cycle. This test was followed by a P_{max}-constant test. Fatigue crack growth rates, da/dN, were determined from the crack length versus cycles data utilizing a sliding least squares fit as outlined in ASTM E647-95a, Appendix X1.2 [28].

Propagation Resistance (K_{PR})

Tests similar to those outlined by Lang [24] were performed to determine the propagation resistance, K_{PR}, of the material as a function of stress ratio under constant amplitude conditions. The term propagation resistance refers to an experimentally determined load below which the crack will not propagate, even at stress ranges greater than steady-state threshold. The test set-up was nearly identical to that described for the baseline steady-state FCG tests, with the exception of two modifications to the DCEP system in order to enhance the sensitivity to the onset of crack growth. First, the constant supply current was increased from 2.5 to 9 amps. Second, the DCEP leads were placed just above and below the tip of the machined notch, one on each side of the specimen, as opposed to 7 mm above and below the machined notch along the midline of the front face.

Table 1. Steady-state K_{PR} test matrix and initial results.

PreCrack							
R	$K_{max, PC}$	a_{PC} (mm)	K	K_{NG}	K_{CG}	K_{PR}	K_{PR} / K_{max}
0.3	13	10.51	2.5	9.42	9.53	7.95	0.61
0.5	18	11.53	2.5	14.03	14.13	12.55	0.70
0.1	10	13.77	2.5	7.42	7.51	5.94	0.59
0.2	11	14.75	2.5	7.98	8.08	6.50	0.59
0.6	20	15.53	2.5	16.64	16.73	15.16	0.76
0.4	15	16.52	2.5	11.43	11.52	9.95	0.66
0.7	22	18.25	2.5	19.08	19.18	17.60	0.80
0.2	12	19.51	2.5	8.59	8.75	7.14	0.60
0.8	25	22	2.36	22.34	22.41	20.85	0.83

All stress intensities (K) have the units MPa m

To characterize K_{PR} after steady-state FCG as a function of R, a series of tests was conducted as shown in Table 1. The sequence of R was randomly selected, with the exception of R equal 0.7 and 0.8. Due to maximum load restrictions of the ceramic pins, these latter two tests had to occur when the crack was longer, when lower applied loads could achieve the desired K_{max} values. For a given R the crack was first grown under constant K_{max} for a minimum of 0.5 mm to ensure that steady-state crack growth conditions were achieved. Following the precrack, K_{PR} was measured using the load-step technique depicted schematically in Figure 3. A series of load blocks was applied with each successive block being stepped by nominally 0.1 MPa m. Each block consisted of 400,000 cycles at 40 Hz, and K was held constant at 2.5 MPa m. Note that the K of the blocks was decreased for the R of 0.8 condition in order to keep the minimum load of the first block from being less than the precrack minimum load. The load steps continued until the crack began to grow, resolved by an increase in the DCEP voltage. A "snapshot" of the test - consisting of the load, DCEP voltage, and temperature - was recorded once every 20 seconds. An example is shown in Figure 4, where the DCEP voltage is overlaid on the recorded loads. Precracking and the onset of crack growth during block 11 are apparent, characterized by a positive slope of the DCEP voltage. Post test analysis was performed to determine K_{CG} and K_{NG}, the stress intensities of the load blocks when the crack began to grow and the last one where the crack did not grow, respectively. K_{PR} was then

calculated using Equation 1, where K_T equal to 1.53 MPa $\sqrt{m}$ was used as the intrinsic threshold for this material.

$$K_{PR} = \frac{\left(K_{NG} + K_{CG}\right)}{2} - K_T \qquad (1)$$
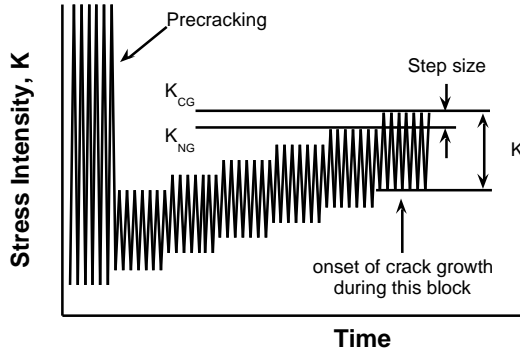
Figure 3. Schematic of loading sequence for measurement of K_{PR}.
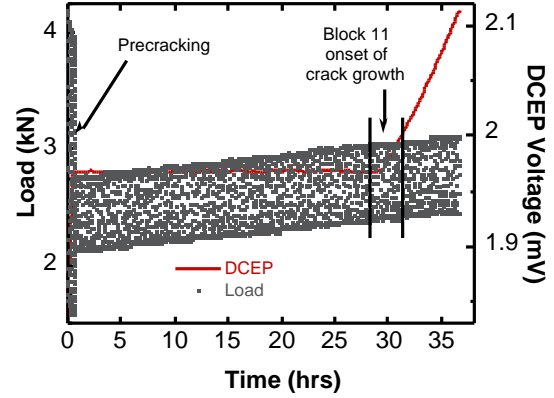
Figure 4. DCEP voltage and load versus time for determination of K_{PR} for precrack conditions $K_{max} = 15$ MPa $\sqrt{m}$ and R = 0.4.

Simple-Sequence Load-Interaction Tests

To investigate load-interaction effects, a simple sequence spectrum (SSS) was created consisting of a number of high-R baseline cycles with periodic tensile underloads. The high-R baseline ($R_{BL} = P_{min,BL}/P_{max}$) was applied at R of either 0.7 or 0.4, and the underload consisted of an R of 0.1 cycle ($R_{UL} = P_{min,UL}/P_{max}$). A schematic is shown in Figure 5. The number of baseline cycles, N_{BL}, was varied from 10 to 100 to 1000 to examine acceleration / deceleration of the FCG response relative to the baseline cycles. As suggested previously, due to the relative growth rates of the high and low R cycles, it would be difficult, if not impossible, to discern any change in FCG rates without ensuring the baseline cycles contribute a significant percentage of the crack growth. The test matrix executed is presented in Table 2.
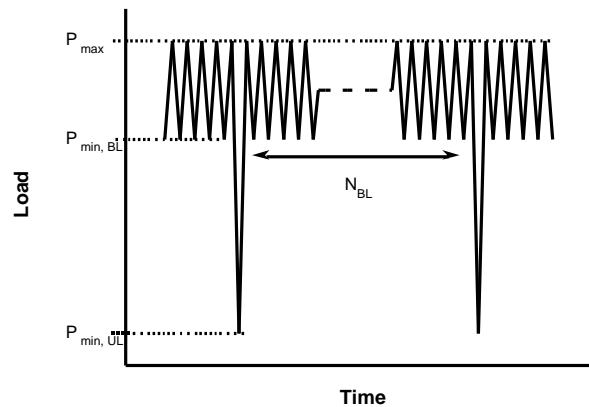
Figure 5. Schematic of simple sequence spectrum (SSS).

For the eight simple-sequence tests the specimen set-up was identical to that used for the steady-state FCG tests described previously. Prior to application of the spectrum loading, specimens were precracked at R of 0.1 and a frequency of 5 Hz under K-decreasing conditions. A minimum of 0.33 mm of crack extension was produced during precracking to ensure the crack was removed from history effects from any previous tests on the same specimen. The final load during precrack was

approximately equal to the maximum load of the subsequent simple-sequence test. Tests were performed under P_{max}-constant conditions at a frequency of 15 Hz, and P_{max} was selected to establish the initial ΔK of the baseline cycles at or near ΔK_{th}. The applied load, initial conditions, the number of blocks (i.e. the times the load sequence was applied), and final conditions are provided in Table 2. Test nomenclature is provided in the left-hand column to facilitate later reference to specific tests.

Table 2. Simple-sequence spectrum (SSS) test matrix and initial results.

Test Nomenclature	Spectrum Definition				Initial		Blocks	Final	
	R_{BL}	N_{BL}	R_{UL}	Load (kN)	a_i (mm)	$K_{max,i}$ (MPa√m)		a_f (mm)	$K_{max,f}$ (MPa√m)
SSS07-10	0.7	10	0.1	2.82	10.39	7.17	349,050	17.29	11.24
SSS07-10	0.7	10	0.1	1.46	20.02	7.06	264,450	23.98	9.95
SSS07-100	0.7	100	0.1	2.00	15.71	7.15	65,390	19.49	9.30
SSS07-1000	0.7	1000	0.1	2.85	10.21	7.14	9,500	14.00	9.13
SSS04-10	0.4	10	0.1	1.15	18.41	4.95	323,860	25.31	9.00
SSS04-10	0.4	10	0.1	0.61	24.32	4.30	488,090	27.52	6.17
SSS04-100	0.4	100	0.1	1.47	11.78	4.44	54,940	15.05	5.48
SSS04-1000	0.4	1000	0.1	1.26	14.66	4.21	15,050	17.81	5.20

RESULTS / DISCUSSION

A straightforward technique, the linear-damage summation model, was concluded to be adequate in predicting simple-sequence tests in both the AGARD study [12] and the work by Yang [19] without including interaction effects. The latter study was based on a comparison of FCG rates, and the former was based on cycles to grow a crack a prescribed amount. The AGARD results are of especial interest, since this study also represents the foremost FCG study published on Ti-17.

Steady-State Fatigue Crack Growth

A hyperbolic arctangent model, Equation 2, was used to fit the experimental growth rate data.

$$\log \frac{da}{dN} = C_1 \arctan h\{C_2[\log(\Delta K) + C_3\} + C_4 \tag{2}$$

where ΔK is the applied stress intensity range, $\frac{da}{dN}$ is the FCG rate, and C_1 through C_4 are constants manipulated to best represent the data. In the curve-fitting practice, the near-threshold data were weighted to give as good a fit as possible to the very low crack growth regime - since life predictions for gas turbine engines are most sensitive to this portion of the FCG curve.

The experimental FCG rate data and hyperbolic arctangent fits for all three stress ratios are shown in Figure 6. There is very good agreement between the K-decreasing and P_{max}-constant portions of the data sets. The fits from Equation 2 represent the data very well, especially in the difficult-to-fit near-threshold regime which is a strength of the hyperbolic arctangent model. [30] Figure 6 also displays the expected stress ratio dependence. The data layer as a function of R; as R increases, growth rates increase (for the same applied ΔK) and ΔK_{th} decreases.

A common methodology to collapse FCG rate curves as a function of stress ratio is to plot the rates versus ΔK_{eff} instead of $\Delta K_{applied}$, where $\Delta K_{eff} = K_{max} - K_{op}$, and K_{op} is the stress intensity when the crack opens during the loading cycle. Figure 7 shows representative load-displacement traces as the crack extends for the R of 0.1 test. The loads have been normalized with respect to P_{max}, and displacements have been adjusted based on the range and sequentially incremented for ease of presentation. The load-displacement traces exhibited an extended linear upper range, and a line was fit through this upper portion to facilitate closure analysis. For this test closure was negligible immediately following precracking and increased continuously to a level of approximately 0.25 as indicated in the figure. Similar load-displacement traces for the R of 0.4 and 0.7 tests were completely linear, therefore, no closure was detected, and attempts to collapse the FCG curves using closure analysis of this type would be fruitless.
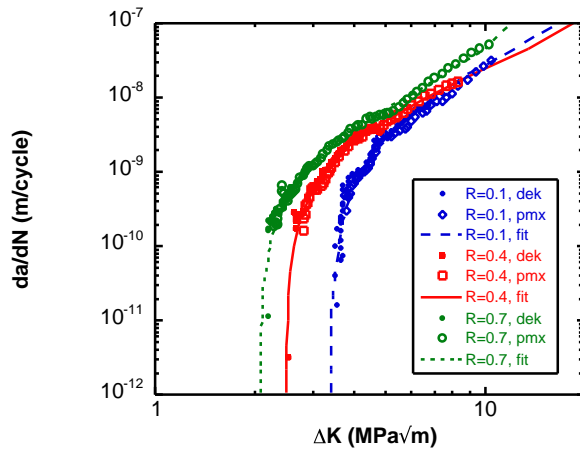
Figure 6. Steady-state, FCG rate data and hyperbolic arctangent fits. Note that in the legend *dek* refers to K-decreasing and *pmx* refers to P_{max}-constant test data.
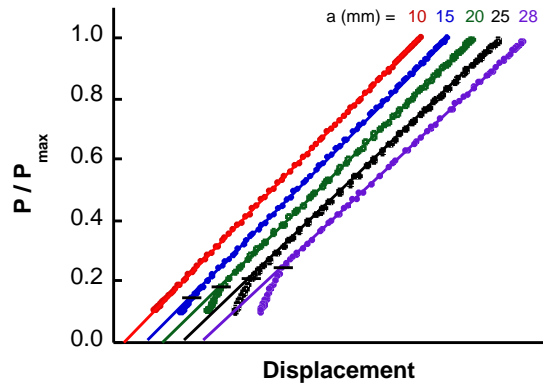
Figure 7. Representative load-displacement traces for R = 0.1 FCG test.

Propagation Resistance (K_{PR})

The results from the tests outlined in Table 1, K_{PR} normalized with respect to K_{max} of the precrack as a function of R during precracking, are graphically shown in Figure 8. A polynomial fit to the data is also displayed based on Equation 3,

$$\frac{K_{PR}}{K_{max,pc}} = A_1 + A_2 R + A_3 R^2 \tag{3}$$

where A_1, A_2, and A_3 are constants having values of 0.572, 0.066, and 0.361, respectively, and adequately represented the data. It is envisioned that K_{PR}, calculated from Equation 3, can be used in establishing a ΔK_{eff} which sufficiently accounts for stress-ratio dependence of steady-state FCG behavior and ultimately can be used in load-interaction FCG algorithms. For the case of modeling load-interactions, the attraction of using K_{PR}, and ΔK_{eff} as defined by Equation 4, is that ΔK_{eff} is less than $\Delta K_{applied}$ even at R greater than 0.7.

$$K_{eff} = K_{max} - K_{PR} \tag{4}$$

However, prior to suggesting K_{PR} be used to model load-interaction effects, it must be demonstrated that it can collapse the stress-ratio dependence of FCG behavior. In other words, there should be a characteristic curve of growth rate described by ΔK_{eff}. To demonstrate, the steady-state data were used along with K_{PR} calculated using Equation 3. A hyperbolic arctangent fit, Equation 5, was fit to all three data sets, R of 0.1, 0.4, and 0.7. Equation 5 is similar to Equation 2 with ΔK_{eff} substituted for ΔK.

$$\log \frac{da}{dN} = C_1 \arctan h \left\{ C_2 \left[\log\left(K_{eff} \right) + C_3 \right] \right\} + C_4 \tag{5}$$

The results are shown in Figure 9. The three data sets collapsed to one curve described effectively by Equation 5 with C_1 of 1.28, C_2 of 1.94, C_3 of –0.70, and C_4 of –7.61. The constants in Equations 3 and 5, along with ΔK_T of 1.53 MPa m used in Equation 1, were arrived at through an iterative process to minimize the variance between the hyperbolic arctangent fit and the steady-state FCG data.

Simple-Sequence Load-Interaction Tests

Figures 10 and 11 present growth rates as a function of K_{max} for the SSS07 (R_{BL} = 0.7) and SSS04 (R_{BL} = 0.4) series of tests, respectively. K_{max} was selected as the abscissa, because for a given spectrum there is no unique K. Growth rates, da/dB, are displayed in meters per block of cycles.

Repeatability was demonstrated by the proximity of the two tests with 10 baseline cycles. The growth rates contained a larger amount of scatter than the steady-state tests due to an unexplained increase in the noise of the DCEP signal. Notable was that the growth rates did not increase by a simple factor of 10 as the number of baseline cycles increased from 10 to 100 to 1000. This can be attributed to the relative contribution between the baseline and underload cycles to the overall growth.
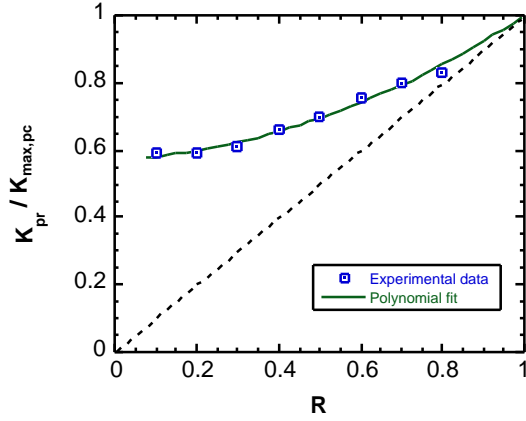
Figure 8. K_{PR} normalized with respect to the precrack K_{max} a function of R during precracking under steady-state conditions.
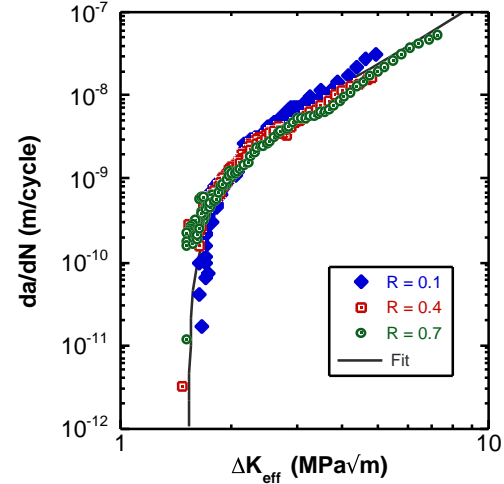
Figure 9. Stress ratio dependence of steady-state FCG behavior described by $\Delta K_{eff} = K_{max} - K_{PR}$.
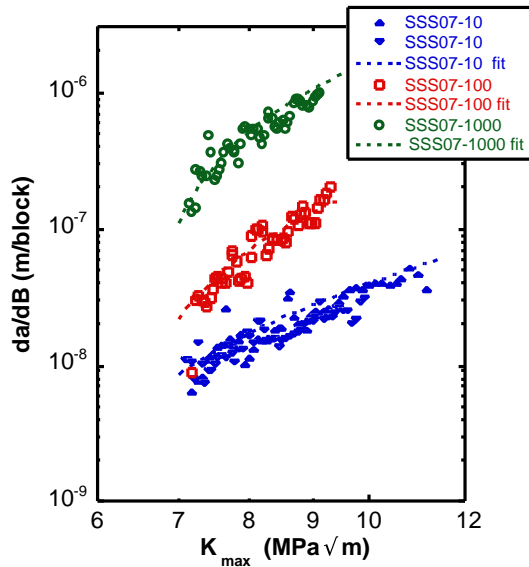
Figure 10. Comparison of predicted and actual FCG rates for SSS07 simple sequence tests.
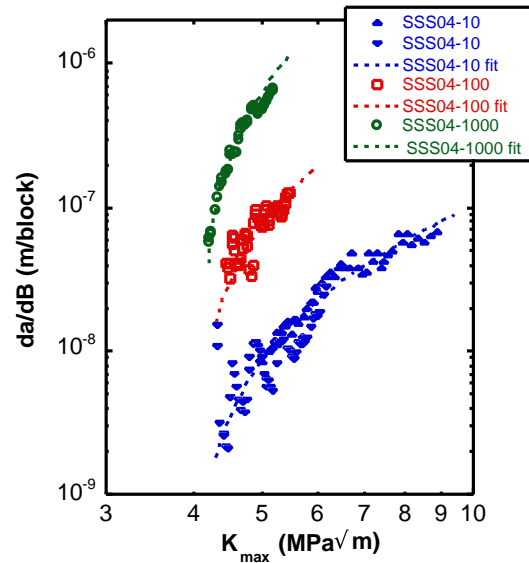
Figure 11. Comparison of predicted and actual FCG rates for SSS04 simple sequence tests.

Linear-Damage Summation Model Without Load-Interaction Effects

Based on success claimed under the AGARD study [12] and Yang [19] in predicting the FCG response for simple-sequence spectra, the linear-damage summation model, ignoring any potential load-interaction effects, was employed to predict the crack growth response from the SSS tests. Linear-damage summation models are simply a summation of predicted crack extension for individual cycles within a block. For the SSS spectra, Equation 6 represented the crack growth for a given block of cycles,

$$\frac{da}{dN}\bigg|_{Block} = N_{BL}\frac{da}{dN}\bigg|_{BL} + \frac{da}{dN}\bigg|_{UL} \qquad (6)$$

where N_{BL} is the number of baseline cycles per block, and $\frac{da}{dN}\big|_{BL}$ and $\frac{da}{dN}\big|_{UL}$ are the growth rate per cycle for baseline and underload cycles, respectively. When assuming no load-interaction effects, the steady-state FCG curves were used to represent the growth rates under variable amplitude loading. Thus, $\frac{da}{dN}\big|_{BL}$ and $\frac{da}{dN}\big|_{UL}$ were calculated using the hyperbolic arctangent fits to the steady-state FCG data and the applied ΔK, Equation 2 and Figure 6.

For the tests with R_{BL} of 0.7, the predictions of the no-interaction, linear-damage summation model are presented in column 5 of Table 3. The table displays the results in the form of the ratio of the predicted number of cycles with respect to the experimental, N_{pred} / N_{exp}. Also included is the percent of crack extension attributed to the baseline cycles. For the SSS07-10 tests the predictions were amazingly accurate, within five percent. Noteworthy is that the percent of crack extension attributed to the baseline cycles was less than 30 percent. Therefore, the majority of damage was predicted to be a consequence of the less frequent underload cycles. Hence, if an interaction was occurring, and the baseline cycles were more damaging than assumed, it would not necessarily be apparent within the scatter of FCG data. This is perhaps why both the AGARD study and Yang concluded no interaction was present. As N_{BL} increased from 10 to 100 to 1000, the predictions became increasingly worse. This was interpreted as a true indication that a load-interaction effect was present. Since the underload cycles have a less dominant role as the number of baseline cycles increased, the effect must be manifested as an acceleration of the growth rate of the baseline cycles. As mentioned earlier, other researchers have attributed acceleration of growth rates due to underloads to reductions in closure, and the corresponding increase in K_{eff}. However, in the absence of closure, K_{eff} equals $K_{applied}$, and K_{eff} can not be increased in this manner. Therefore, a different methodology needs to be devised to allow an increase in the effective crack-growth driving force in the absence of closure.

Table 3. Linear-damage summation model predictions for simple sequence spectrum FCG tests both with and without a load interaction effect.

Test Nomenclature	Spectrum Definition			NO Interaction		With interaction			
	R_{BL}	N_{BL}	Load (kN)	N_{pred} / N_{exp}	% from BL	N_{pred} / N_{exp}	% from BL	BLMF	ULMF
SSS07-10	0.7	10	2.82	1.04	29.6	0.99	65.8	1.17	0.90
SSS07-10	0.7	10	1.46	1.01	23.9	0.99	62.4	1.17	0.90
SSS07-100	0.7	100	2.00	1.67	70.7	1.00	90.9	1.09	0.90
SSS07-1000	0.7	1000	2.85	1.93	95.4	1.00	98.7	1.06	0.90
SSS04-10	0.4	10	1.15	1.16	80.3	1.01	86.4	1.045	0.94
SSS04-10	0.4	10	0.61	1.38	77.5	0.98	89.2	1.045	0.94
SSS04-100	0.4	100	1.47	1.47	97.2	1.01	98.8	1.040	0.94
SSS04-1000	0.4	1000	1.26	1.45	99.6	0.99	99.9	1.015	0.94

For the tests with R_{BL} of 0.4, the predictions of the no-interaction, linear-damage summation model are also found in column 5 of Table 3. A load-interaction effect was not as obvious for this series of tests. This was attributed to the less severe underload relative to the minimum load of the baseline cycle. Noteworthy was that the predictions for the SSS04-10 tests were not as accurate as the SSS07-10 tests. For the SSS04-10, in the absence of any load-interaction effect, the percent of crack growth attributed to the baseline cycles was approximately 80 percent, versus less than 30 percent for the SSS07-10 tests. Intuitively, an R of 0.4 cycle is more damaging than an R of 0.7 cycle relative to an R of 0.1 cycle with the same K_{max}. Therefore, if load-interaction effects were occurring, since the R of 0.4 cycles are expected to contribute a significant percentage of the overall crack extension, the effect may be detectable even at a 10-to-1 ratio of baseline-to-underload cycles. The less accurate predictions of the SSS04-10 may then in fact be an indication of the presence of a load-interaction effect. The prediction of the SSS04-100 was worse still. However, when N_{BL} increased to 1000

(SSS04-1000) the prediction relative to the experimental results had about the same accuracy as the SSS04-100. It has been observed by Fleck [31] that interactions, in the form of crack growth rate accelerations, reach a maximum and decay for both very high and very low values of N_{BL}. This suggests that the maximum deviation from a prediction not including interaction effects could be somewhere between N_{BL} of 100 and 1000 for the spectra with R_{BL} of 0.4.

Linear-Damage Summation Model With Load-Interaction Effects Included

As pointed out previously, including an interaction effect using closure techniques is not possible for the SSS07 and SSS04 spectra, since closure was not present at the high-R load conditions. What is needed to better estimate FCG lives under these conditions is a methodology to increase the effective driving force even in the absence of closure. Lang[24] proposed the modified definition of ΔK_{eff} of Equation 4. He attributed K_{PR} to compressive residual stresses ahead of the crack tip, although not necessarily quantifiably. Sehitoglu and colleagues [20-22] have attempted to calculate residual stresses in the process zone ahead of a crack tip, and even suggested they likely play a significant role in controlling the fatigue crack growth process. It would not be difficult to envision K_{PR}, if truly governed by residual stresses ahead of the crack tip, as being affected by load excursions, and Lang [24] has observed such phenomemon.

Based on the success demonstrated utilizing K_{PR} to collapse the stress-ratio dependence of FCG rates, and the attraction that K_{PR} defines a K_{eff} smaller than $K_{applied}$, even in the absence of closure, it is proposed to utilize K_{PR} to model the load-interaction effects suspected in the SSS tests. Application of this approach acknowledges that for high-R cycles the stresses in the process zone ahead of the crack tip influence the propagation resistance of the material, as characterized by K_{PR}. It is assumed that the occurrence of an underload disturbs the steady-state conditions, lowering the propagation resistance, and allowing accelerated crack growth rates until the steady-state conditions are reestablished.

To accomplish this, K_{PR} must be defined as a transient variable affected by non steady-state conditions. A schematic of how a "transient" K_{PR} could fluctuate from measured steady-state values is depicted in Figure 12. In this figure K_{PR} is initially shown to be equal the steady-state, R of 0.7 condition, as determined from Equation 3 and Figure 8. As a result of the underload, K_{PR} drops below the high-R steady-state value, and the cycles immediately following the underload are more damaging, i.e. larger K_{eff} and higher growth rate. After some number of cycles the steady-state value is again achieved, and the FCG rate equals the steady state. It is also depicted that the R_{UL} of 0.1 underload cycle would be slightly less damaging than predicted from steady-state behavior. A prediction of the crack growth due to the simple-sequence spectra would be accomplished with the following set of equations:

$$\frac{da}{dN}\bigg|_{Block} = \sum_n \frac{da}{dN} \tag{7}$$

$$\log\frac{da}{dN} = C_1 \operatorname{arctanh}\left\{C_2\left[\log\left(K_{eff}\right) + C_3\right]\right\} + C_4 \tag{8}$$

$$K_{eff} = K_{max} - K_{PR(n)} \tag{9}$$

where Equation 7 is the crack growth for a block of n cycles, and the growth increment for each individual cycle within the block would be determined from Equations 8 and 9. The constants for Equation 8 would be those provided from the steady-state data of Figure 9, and $K_{PR(n)}$ would represent the "transient" K_{PR} depicted in Figure 12. Also, ΔK_{eff} would be set equal $K_{applied}$, in the event $K_{PR(n)}$ was less than K_{min}. What is required is a representation of K_{PR} as a function of the cycle count, n, within a given block.

To evaluate the merit of this approach, the sensitivity of the linear-damage summation model to slight adjustments of ΔK was assessed. Using the hyperbolic arctangent fits to the steady-state data, shown in Figure 6, a ΔK_{eff} was utilized based on multiplication factors applied to the baseline and underload cycles, *BLMF* and *ULMF*, respectively. The linear-damage summation model,

Equation 6, was used with the growth rates and effective stress-intensity factor ranges determined from Equations 10 through 13.

$$\log \left(\frac{da}{dN} \right)_{BL} = C_1 \operatorname{arctanh}\left\{ C_2 \left[\log \left(K_{eff,BL} \right) + C_3 \right] \right\} + C_4 \tag{10}$$

$$K_{eff,BL} = BLMF\left(1 - R_{BL}\right)K_{max} \tag{11}$$

$$\log \left(\frac{da}{dN} \right)_{UL} = C_1 \operatorname{arctanh}\left\{ C_2 \left[\log \left(K_{eff,UL} \right) + C_3 \right] \right\} + C_4 \tag{12}$$

$$K_{eff,UL} = ULMF\left(1 - R_{UL}\right)K_{max} \tag{13}$$

Using the multiplication factors, ΔK_{eff} can be adjusted to evaluate the effect of a transient K_{PR}. A schematic is shown in Figure 13 depicting the effect of setting the BLMF equal to 1.17 for N_{BL} of 10 and 1.09 for N_{BL} of 100, given R_{BL} of 0.7, and $K_{PR,steady-state}$ equal 0.795. It was acknowledged a priori that the following constraints and/or conditions would have to be met if this sensitivity analysis were to demonstrate capability likely described by the approach utilizing $K_{PR(n)}$.

1. For the predictions of the SSS07 tests, *BLMF* must be less than 1.46. Otherwise ΔK_{eff} would be predicted greater than $K_{applied}$.
2. For the predictions of the SSS04 tests, *BLMF* must be less than 1.215. Otherwise it would be equivalent to K_{PR} for the baseline cycle dropping below the steady-state K_{PR} for R of 0.1.
3. *ULMF* must be less than or equal to one. This assumes that the underload cycle should be less damaging than the R of 0.1 steady-state condition.
4. *ULMF* was maintained constant for a given R_{BL} (not a function of N_{BL}).
5. For the same R_{BL}, *BLMF* should decrease with increasing N_{BL}. This indicates that K_{PR} would move toward the steady-state value with additional fatigue cycles.
6. The *ULMF* for SSS07 series should be less than *ULMF* for SSS04 series. This assumes that the further away from the steady-state value the longer it should take to achieve it.

Of this list, first four were constraints on the sensitivity analysis, and last two were consequences that needed to be demonstrated.
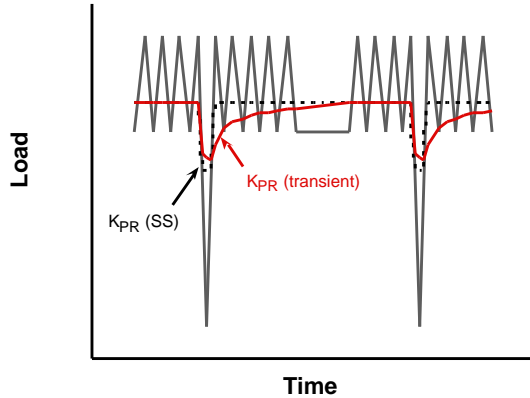
Figure 12. Schematic of a transient K_{PR} to be used in modeling load-interaction effects.
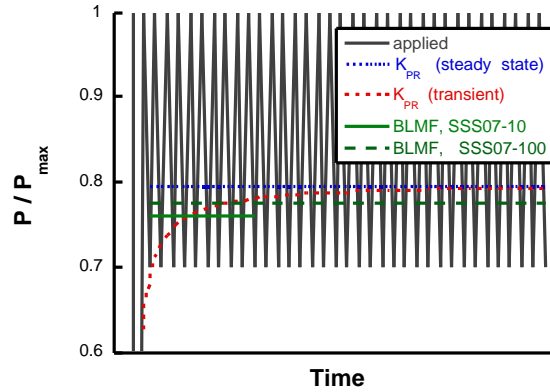
Figure 13. Schematic of how BLMF can simulate the effect of a dynamic K_{PR}.

Values of *BLMF* and *ULMF* were adjusted to best simulate the experimental crack growth data from the simple-sequence spectra. First, the data from the two SSS07-10 tests were used, and a minimization routine was used to best fit the final crack lengths. Both tests could be predicted within one percent by setting *BLMF* to 1.17 and *ULMF* to 0.90. Next the SSS07-100 test was best emulated by decreasing *BLMF* to 1.09 while maintaining *ULMF* at 0.90. Finally, the SSS07-1000 test was emulated while again holding *ULMF* equal 0.90 and decreasing *BLMF* to 1.06. A similar exercise

was accomplished in modeling a load-interaction of the SSS04 series of tests. To best represent these tests lower *BLMFs* and a higher *ULMF* were required. The predictions of the SSS07 and SSS04 series of tests are compared to the experimental data in column 7 of Table 3. Figures 14 and 15 present graphically the predictions with and without the load-interaction incorporated for the SSS07-100 and SSS04-100 tests, respectively. The "fits" of the FCG rates shown in Figures 10 and 11 represent Equation 7 assuming the load interaction effect described. The FCG rates from the model closely resemble the experimental results for all cases tested.

In modeling the test results using this methodology all the constraints previously listed were maintained, and the expected trends observed: *BLMF* decreased with increasing N_{BL}, and *ULMF* was lower for the SSS07 series versus the SSS04 series. The model was made to mimic the data, and does so within two percent of the total blocks to grow the cracks the prescribed amounts. In order to better simulate the crack growth, the percent of crack extension due to the baseline cycles increased significantly, with a corresponding decrease in the relative damage of the underload cycles. This implied that there indeed was a load-interaction effect, and that it manifested itself as an acceleration of the high-R baseline cycles and deceleration of the R of 0.1 underload cycle, relative to steady-state.
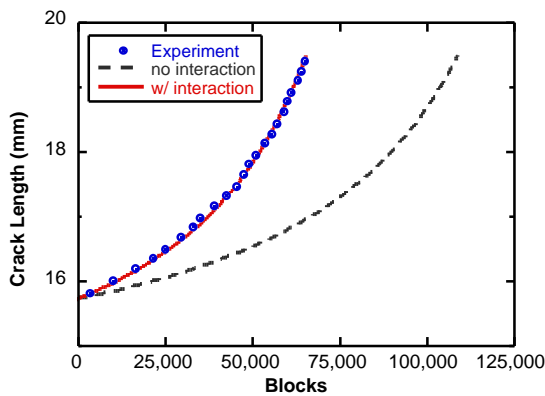
Figure 14. SSS07-100 ($R_{BL} = 0.7$, $N_{BL} = 100$) crack growth data compared with predictive models.
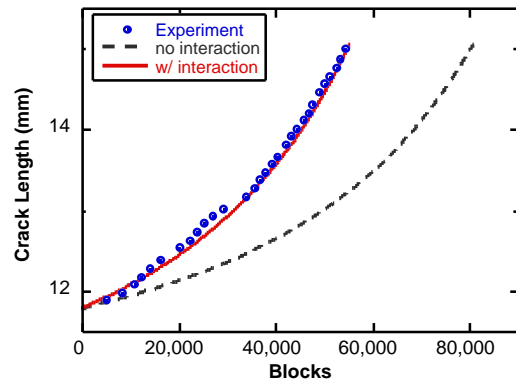
Figure 15. SSS04-100 ($R_{BL} = 0.4$, $N_{BL} = 100$) crack growth data compared with predictive models.

CONCLUSIONS

It was demonstrated that underloads, even in tension, can accelerate the crack growth process of high-R baseline cycles for Ti-17. This load-interaction effect was not immediately discernable until the high-R baseline cycles provided the bulk of the crack extension. The data also supported other researcher's observations that load-interactions reach a maximum at an intermittent number of baseline cylces and decay for both high and low values of N_{BL}.

A load-interaction model was proposed that involved the application of a propagation resistance, K_{PR}, in the definition of the effective driving force, K_{eff}, for crack propagation. The merit of the approach was assessed through a simple modification to a linear-damage summation model, which simulated anticipated phenomena. The output from the model incorporating a simple load-interaction effect was made to mimic experimental data of several simple-spectrum tests. In doing so, all a priori constraints were maintained, and anticipated relationships were observed. Thus, it substantiated the hypothesis that a load-interaction effect occurred, and that it was manifested as an acceleration of the high-R baseline cycles and deceleration of the R of 0.1 underload cycle.

K_{PR} is suspected of being a function of the load history and, for high stress ratios, controlled by the stress state ahead of the crack tip. K_{PR} was characterized as a function of stress ratio under steady-state FCG, and successfully demonstrated the capability to collapse the stress-ratio dependence of fatigue crack growth rates. It was hypothesized that the occurrence of an underload disturbs the steady-state conditions ahead of the crack tip, thus, reducing the propagation resistance of the system and accelerating the FCG rate of high-R baseline cycles.

ACKNOWLEDGEMENTS

REFERENCES

1 Harris, J. A., *Engine Component Retirement For Cause, Volume I – Executive Summary*, AFWAL-TR-87-4069, Volume I, AFWAL, Wright-Patterson AFB, OH, 1987.
2 Engine Structural Integrity Program (ENSIP), MIL-STD-1783 (USAF), 30 November 1984.
3 Skorupa, M., *Fatigue and Fracture of Eng Matls and Str*, Vol. 21, No. 8, 1998, pp. 987-1006.
4 Skorupa, M., *Fatigue and Fracture of Eng Matls and Str*, Vol. 22, No. 10, 1999, pp. 905-926.
5 Newman, J. C., Jr., *Methods and Models for Predicting Fatigue Crack Growth under Random Loading, ASTM STP 748*, ASTM, Philadelphia, PA, 1981, pp. 53-84.
6 Newman, J. C., Jr., *Design of Fatigue and Fracture Resistant Structures, ASTM STP 761*, American Society for Testing and Materials, Philadelphia, PA, 1982, pp. 255-277.
7 Fleck, N. A., and Newman, J. C., Jr., *Mechanics of Fatigue Crack Closure, ASTM STP 982*, J. C. Newman, Jr. and W. Elber, Eds., ASTM, Philadelphia, PA, 1988, pp. 319-341.
8 Newman, J. C., Jr., *Int J of Fracture*, Vol. 80, 1996, pp. 193-218.
9 Larsen, J. M. and Nicholas, T., *Eng Fracture Mechanics*, Vol. 22, No. 4, 1985, pp. 713-730.
10 Mom, A. J. A, Evans, W. J., and ten Have, A. A., *AGARD Conference Proceedings No. 393, Damage Tolerant Concepts for Critical Engine Components*, AGARD, Neuilly sur Seine, France, 1985, pp. 20-1 - 20-11.
11 Raizenne, M. D., *AGARD Engine Disc Cooperative Test Programme, AGARD Report 766 (Addendum)*, AGARD, Neuilly sur Seine, France, 1993, pp. 4-1 - 4-33.
12 Jany, E. and Renne, O., *AGARD Engine Disc Cooperative Test Programme, AGARD Report 766 (Addendum)*, AGARD, Neuilly sur Seine, France, 1993, pp. 6-1 - 6-83.
13 Topper, T. H. and Yu, M. T., *Int J of Fatigue*, Vol. 7, No. 3, 1985, pp. 159-164.
14 Yu, M. T., Hopper, T. H., and Au, P., *Fatigue 84*, C. J. Beevers, Ed., Engineering Materials Advisory Services Ltd., United Kingdom, Vol. I, 1984, pp. 179-189.
15 Zaiken, E. and Ritchie, R. O., *Engr Fracture Mechanics*, Vol. 22, No. 1, 1985, pp. 35-48.
16 Kardomateas, G. A. and Carlson, R. L., *J of App Mechanics*, Vol. 62, No. 1, 1995, pp. 240-243.
17 Kardomateas, G. A. and Carlson, R. L., *Int J of Fracture*, Vol. 70, No. 2, 1995, pp. 99-115.
18 McClung, R. C. and Sehitoglu, H., *Mechanics of Fatigue Crack Closure, ASTM STP 982*, J. C. Newman, Jr. and W. Elber, Eds., ASTM, Philadelphia, 1988, pp. 279-299.
19 Yang, R., *Int J of Fatigue*, Vol 19, 1994, p.397-402.
20 Sehitoglu, H., Gall, K., and Garcia, A. M., *Int J of Fracture*, Vol. 80, 1996, pp. 165-192.
21 Sun, W. and Sehitoglu, H., *Fatigue and Fracture of Eng Matls and Str*, Vol. 15, No. 2, 1992, pp. 115-128.
22 Sehitoglu, H. and Sun, W., *J of Eng Materials and Tech*, Vol. 113, January 1991, pp. 31-40.
23 Moshier, M.A., Nicholas,T., and Hillberry, B.M., *Int J of Fatigue*, submitted Oct 2000.
24 Lang, M., *Fatigue and Fracture of Eng Matls and Str*, Vol. 23, 2000, pp. 587-601.
25 Lang, M., *Fatigue and Fracture of Eng Matls and Str*, Vol. 23, 2000, pp. 603-617.
26 Redden, T. K., *Beta Titanium Alloys in the 80's*, R. R. Boyer and H. W. Rosenberg, Eds., The Metallurgical Society of AIME, Warrendale, PA, 1984, pp 239-253.
27 E399-90, *Annual Book of ASTM Standards*, American Society of Testing and Materials, Philadelphia, PA, Vol. 03.01, 1999, pp. 422-431.
28 E647-95a, *Annual Book of ASTM Standards*, American Society of Testing and Materials, Philadelphia, PA, Vol. 03.01, 1999, pp. 577-602.
29 Hartman, G. A. and Johnson, D. A., *Experimental Mechanics*, March 1987, pp. 175-229.
30 Larsen, J. M., Worth, B. D., Annis, C. G., Jr., and Haake, F. K., *Int J of Fracture*, Vol. 80, 1996, pp. 237-255.
31 Fleck, N. A., *Acta Metallurgica*, Vol. 33, 1985, pp. 1339-1354.

Paper 21: Discussion

Question from H Pfoertner – MTU, Germany

Do you think that your load interaction method can be generalised to arbitrary load sequences as they occur during real engine operation?

Presenter's Reply

The simple method used for demonstration purposes in this paper would require substantial data generation - testing under all envisioned load interaction scenarios to create the desired multiplication factors - and thus, is probably not suited from the arbitrary case. It was created to quickly emulate, for this specific case, the more general approach of using a K_{pr}-type methodology. This latter approach, I believe, can be generalized for arbitrary load sequences. We are working toward that goal in this and other load-interaction research efforts at the Air Force Research Laboratory. Currently the other co-authors and I are evaluating the appropriateness of K_{pr} for periodic overloads and simple mission spectra as well as periodic underloads. We are striving to better understand the physics of the problem so more general models can be developed with broader applicability.

Question from Dr M Winstone – DSTL, UK

The recovery of K_{pr} was presented in terms of cycles; for Ti alloys, deformation is also time dependent. Would you expect to see a frequency/ramp rate effect? Were the tests done at ramp rates consistent with compressor acceleration and deceleration?

Presenter's Reply

Actually I believe the recovery may be dependent upon the extent of crack propagation for this simple case of periodic underloads. I am presently performing finite element simulations to evaluate the effect of the underload on the stresses/strains/displacements ahead of and behind the crack tip. Immediately after the underload, the simulation suggests some drastic increases in strains a small distance ahead of the crack tip. The recovery may require the crack to grow through this affected region until the steady-state conditions are re-established. Obviously, the accuracy and relevance of this approach is dependent upon the ability to predict the materials constitutive behaviour. Regarding expectations of a frequency effect, the tests were run at nominally 15 Hz, which is much faster than ramp rates experienced under compressor acceleration/deceleration. Interestingly, I have compared my baseline crack growth results (40 Hz) with crack growth rates reported in the AGARD #766 Addendum from 1993 (0.25 Hz). Comparing the two data sets, no frequency effect was noted for Ti-17 from the range of 0.25 to 40 Hz.

The Inadequacy of Safe-Life Prediction:
Aero-Engine Fan and Compressor Disk Cracking

B.J. Wicks, R.A. Antoniou, S.L. Slater and J. Hou
Aeronautical and Maritime Research Laboratory
Defence Science and Technology Organisation
Department of Defence
Box 4331 GPO
Melbourne 3001
Australia

Abstract

The use of a safe-life methodology to ascribe a replacement interval to gas turbine engine components has been used extensively for over 40 years. However there are inherent limitations in the methodology, resulting in significant under-utilisation of component lives, and an inability to account for rogue flaws and other non-representative factors. This paper will present three examples where the safe-life approach was inadequate in predicting the safe working life of critical engine components. These examples illustrate the complexity of the processes that have to be taken into account to produce realistic life estimates.

1. Introduction

Critical gas turbine rotating components, such as compressor disks, spacers, cooling plates and turbine disks, are subjected to cyclic stresses caused by engine start-up and shutdown, as well as by major throttle excursions during flight manoeuvres. These cyclic stresses can exceed the yield strength of the material at stress-concentration sites, such as bolt holes, bores, blade dovetail slots and rim serrations and can thus lead to low cycle fatigue cracking.

A safe life method is conventionally used to determine the in-service life of rotating gas turbine components subject to low cycle fatigue. In this procedure a safe service life for the component is obtained from component and specimen tests of the appropriate material under representative loading conditions. The component life is calculated by fitting a statistical model to the fatigue results, and the life is determined based upon the probability of crack initiation after a period of engine usage, calculated using mathematical models that take into consideration mission profiles and mission mixes. Component usage is then normally restricted to the number of flight hours which are calculated to produce a 0.8mm surface crack in one component out of an assumed population of 1000 identical parts under the same usage. This represents approximately three standard deviations from the mean (-3σ). This crack size is considered detectable with high reliability by the most commonly used inspection technique - liquid penetrant inspection.

The consequence of this criterion is that the bulk of component lives lie above the -3σ limit and all of these lives are discarded. Furthermore, when a component contains a rogue flaw, the safe-life procedure cannot accurately predict the life, as the flaw is not considered in the original probability distribution function of the LCF database.

This paper will present three examples where the safe-life approach was inadequate in predicting the working life, and illustrate the inability of the safe life methodology to take account of defects not considered in the original probability distribution.

In the first example a severely deformed surface microstructure was caused by abusive machining of a tie-bolt hole in a fan disk. As a consequence the life of this component fell outside the original probability distribution function (PDF) upon which the safe-life predictions were made, resulting in premature cracking. Cracks formed within this microstructure around the perimeter of the hole and once the component was placed in service those cracks perpendicular to the hoop stress began to grow as low cycle fatigue cracks.

In the second case, the manufacture of a disk with an abnormal microstructure resulted in cracks emanating from a tie bolt hole when that disk was placed in service. Once again the PDF upon which the original safe-life estimates was based is not applicable and consequently an erroneous life prediction was made. However in this case an appropriate PDF can be determined retrospectively so that other uncracked disks with this abnormal microstructure could be appropriately lifed.

In the third case the life of a low-pressure compressor disk was based on the stresses at a particular circumferential structural feature with an acute radius of curvature. As the safe-life is defined as the time to initiation of a 0.8 mm flaw size, no consideration is given to the behaviour of the crack after initiation. Detailed modelling and simple experiments indicated that in this case the crack is expected to grow in an orientation such that it would not affect the performance of the component nor compromise safety for a considerable period of time after initiation.

The paper presents the view that safe-life analysis alone represents only a partial view of all the processes that should be taken into account in determining overall component replacement intervals.

In this paper the prediction of remanent life was based on the use of stress, thermal, metallographic and fractographic analyses, as well as risk assessments using probabilistic rather than deterministic parameters to achieve more realistic life assessments. Mission profile analyses were also carried out to assess the severity of engine usage.

2.   An Abusively Machined Tie-Bolt Hole

Following the detection of a crack emanating from a bolt-hole in an engine disk, an investigation was undertaken to determine the subsequent crack growth behaviour. The disk geometry and observed crack direction are shown in Figure 1. The radial crack emanating from the bolt-hole was cut from the disk and opened, revealing the crack face shown in Figure. 2. The cracking was found to be due to fatigue which had started within the bore of the hole and away from the corner. The crack markings were examined using both optical and scanning microscopy and the crack growth rate was predicted using both numerical and analytical methods and compared to the measured growth rate.

The metallographic studies indicated the presence of a surface deformed layer, with a depth of approximately 0.6 mm, and the crack growth progression measurements on the fracture surface showed rapid crack growth through the deformed layer from multiple surface cracks all around perimeter of the hole. Furthermore the presence of tungsten carbide was detected at the surface, presumably from a piece of tooling.

The fatigue cracks originated in alpha case particles in the microstructure of the hole surface, indicative of localised overheating. It was concluded from these observations that an abusive hole drilling or reaming operation caused overheating and localised damage.
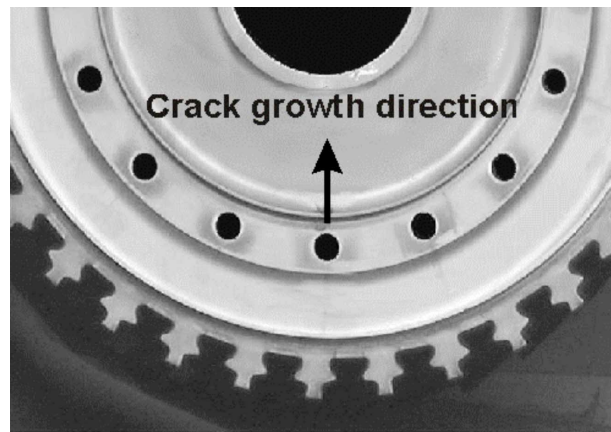
Figure 1: Disk geometry and crack growth direction.
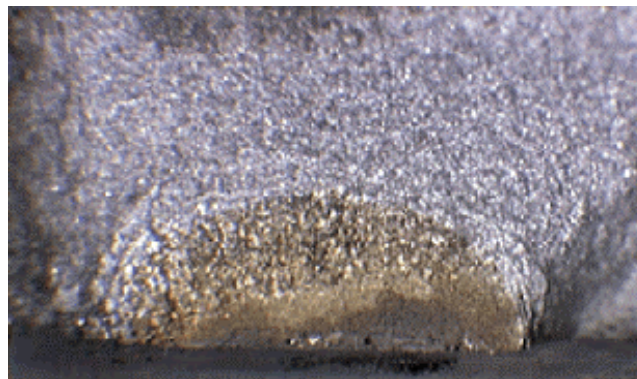
Figure 2: Radial bolt-hole crack using optical microscopy.

The material of the disk and adjacent components was Ti-8Al-1Mo-1V. The nominal operating temperature at the bolt-hole region of the disk was determined by analysis and measurement to be approximately 200°C. Crack growth data for various stress ratios was obtained from the published literature and interpolated to the operating temperature.

A 3D cyclic FE assembly model (22.5° sector) was created, consisting of three fan disks, spacers and air seals to determine the global behaviour, as shown in Figure. 3. These components were meshed using 20-noded brick elements. The applied loading includes the centrifugal and thermal loads at maximum power setting (1, 2) Appropriate boundary conditions were applied to the end surfaces of the assembly model. Stress analysis was carried out using ABAQUS software (3) and displacement solutions were obtained.
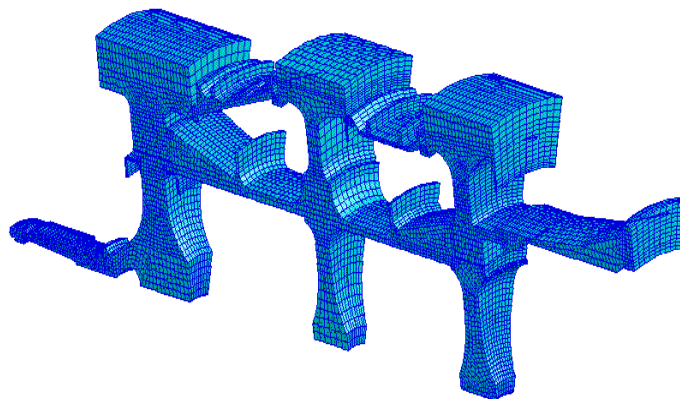
Figure 3: 3D FE model of the assembly.

A 3D FE sub-model (22.5° sector), including all the local geometry features, was created for the disk. The solutions from the 3D FE assembly model were transferred to the cutting boundaries in the sub-model and the stress distribution of the disk were determined, as shown in Figure. 4. The maximum principle stress of 435 MPa occurs under maximum power settings at the bore-side of the bolt-hole, indicating the region where a crack is most likely to form, and in fact where it was observed.

Furthermore, from fractographic analysis it was determined that crack propagation rates through the deformed microstructure were twice as fast as through the non deformed microstructures, with the cracks perpendicular to the maximum principal stress becoming propagating cracks. The crack growth analyses carried out as part of the FE analysis corresponded very closely with the fractographic measurements, indicating that failure of the disk was likely within the scheduled safe life.
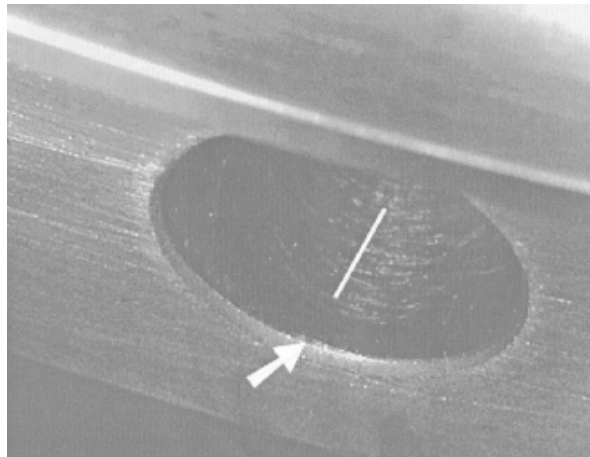
Figure 5. Indication of the crack direction in the bolt hole

It was concluded that machining of the tie-bolt holes was done in such a way that a deformed surface layer of approximate depth 0.6mm was produced. This layer either had micro-cracks form all around the perimeter of the hole during the machining operation or shortly thereafter. Once in service the cracks were readily propagated due to the stresses caused by start stop start cycling, leading to premature cracking and a life considerably shorter than the safe life predicted from the standard database.
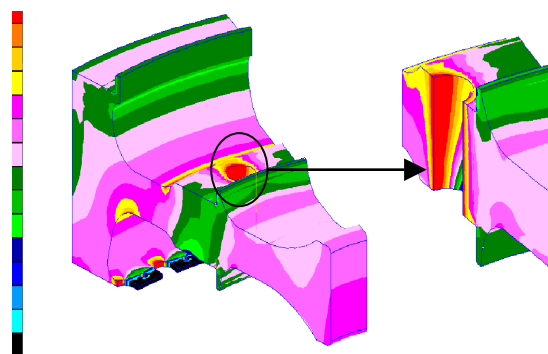
Figure 4: Maximum principal stress distribution for the disk with detailed view of the critical location.

3. A Disk With An Abnormal Microstructure

A crack was found in the tie-rod hole of a second stage compressor disk. No other cracks of this type had been seen previously. This hole was believed to experience relatively low stresses, and hence was not expected to be life-limiting in terms of low cycle fatigue. An indication of the orientation of the crack is shown in Figure 5.

The single longitudinal crack on the inner surface of the tie rod hole showed extremely faint markings consistent with fatigue progression marks. The crack was very deep with a short surface length and is shown schematically in Figure 6. The material of the disk and adjacent components was Ti-8Al-1Mo-1V.
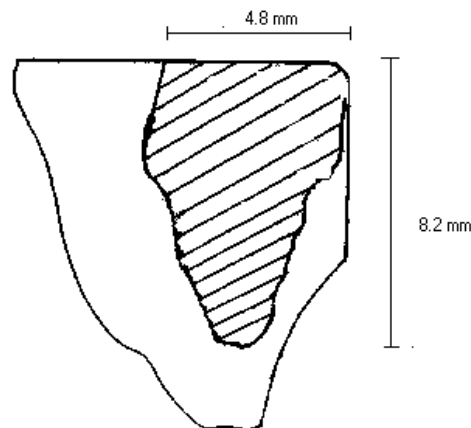
Figure 6. Schematic of the shape of the crack

The crack was difficult to observe visually as it did not extend to the outer edge of the hole, appearing to start about 0.8 mm inside the bore of the hole from the front face of the disk.

The crack was noted to be very deep and narrow in relation to its length on the bore surface with a length of about 4.8 mm and a depth of about 8.2 mm.

The microstructure of this disk was found to contain significant banding of the α phase. This was probably due to incorrect processing or perhaps segregation in the original ingot. This microstructure has been described previously for this alloy (4)

SEM examination of the crack fracture face revealed that fracture appeared to have occurred transgranularly. The nature of the fracture changed within different bands of the material. Some bands displayed elongated facets with a fairly consistent direction of crack propagation evident from the markings on the facets. Other bands displayed more equiaxed facets in which the crack direction as indicated on each facet appeared to be almost random. In all cases faint markings could be observed consistent with fatigue at low stress intensities.

The crack initiated within the hole at a location coincident with the maximum principal stress (σ_{hoop}). The propagation behaviour of the crack was determined by the presence of α-phase bands which tended to constrain the crack growth in the through-disk direction, as a result of preferential crack growth along the α-bands compared to growth in the normal titanium $\alpha + (\alpha+\beta)$ microstructure (5).

In this case the prediction of a safe life analysis is possible if the probability density functions were to be based upon a data base derived from LCF properties of the α-rich banded material. The promulgated safe life was in fact based on an inadequate database and hence cracking

occurred in service much earlier in the life than expected. The promulgated safe life for this type of microstructure is thus very un-conservative.

4. Benign Crack Growth

A finite element (FE) method was utilised to analyse the mechanical and thermal stress in a 4th stage Low Pressure Compressor (4th LPC) disk assembly in an aircraft gas turbine engine(6). This FE analysis indicated that the critical region for fatigue is at a front snap radius. The geometry of the disk is shown in Figure 7.

It was found that the maximum principal stress at the front snap radius dropped rapidly from 800 MPa at the free surface to 350 MPa at a depth of 0.5 mm.
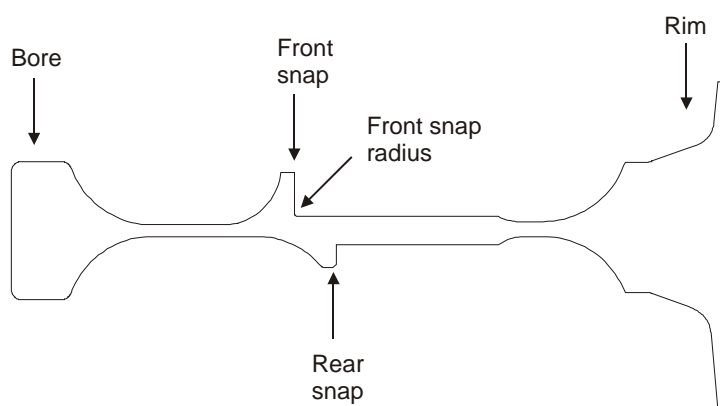
Figure 7: Schematic cross-section of a compressor disk.

Based on the calculated stresses and the available mechanical property data it was possible to determine a safe life for this location which was consistent with the safe life derived by the OEM. However further analyses and experiment were carried out to determine the consequences of cracking in order to assess the significance of the safe life concept.

Traditionally a FE crack profile has to be created manually and this can be very time consuming, especially for the 3D case (7). The process involves the collapse of normal elements to crack tip elements and the translation of the mid-side nodes of the crack tip elements to quarter points towards the crack tip. These features have been automated in the code ZENCRACK (8), which is interfaced with the FE code ABAQUS. A crack block can be re-meshed so that this block is replaced with a crack front comprising of crack tip elements. The crack front can be either semi-circular/semi-elliptical or straight, within a crack block. Therefore, by combining blocks with various embedded crack fronts, both surface and through-thickness cracks can be generated easily.

In ZENCRACK, the direction of crack growth is governed by the direction of the maximum strain energy release rate. The amount of crack growth is determined by the magnitude of the energy release rate (9, 10).

The crack growth procedure starts with the generation of an initial crack and the calculation of the stress intensity factors. The crack growth direction and the amount of growth are then determined by the virtual extension method and the crack front is updated after a nominated increment of crack growth. This process is repeated until the required crack size or number of cycles is reached.

Semi-circular and semi-elliptical surface cracks with a depth of 0.2 mm were inserted perpendicular to the front snap radius at the peak stress location, 25 degrees from the radius

runout (Figure 8). Stress intensity factors (SIF's) were then calculated using the J-integral method. The SIF values at the both free surface ends increase with crack length whilst the crack depth remains constant (Figure 9). Therefore, a crack initiated at the front snap radius is expected to grow preferentially in the circumferential direction and to grow at a slower rate in the radial direction.
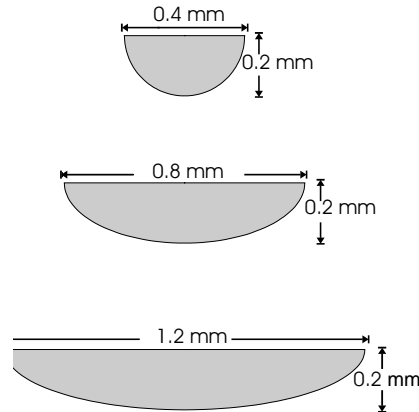
Figure 8 Initial crack profiles used in the analysis
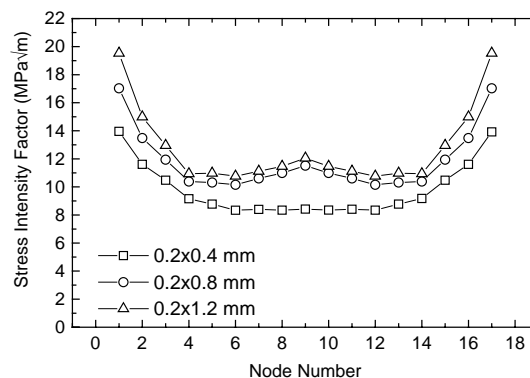
Figure 9: Stress Intensity Function distributions for initial crack profiles.

A typical load spectrum was obtained for the disk and ZENCRACK was used to transform the spectrum into an equivalent constant amplitude spectrum using a weighting function (defined by the occurrence of each load pair), and a scaling factor was used in order to convert the number of cycles to engine flight hours.

The crack profile derived from this crack growth procedure changed from a planar semi-circular to a non-planar elliptical shape with a 12° deviation from the original crack plane. The amount of crack growth in the circumferential direction was more than twice that in the radial direction, resulting in a reduction of the aspect ratio of depth to length from 1 to 0.6. It is therefore expected that a crack starting from semi-circular shape will grow in both circumferential and radial directions, evolving into an elliptical crack and becoming more elliptical with time

These analyses showed that a planar semi-circular crack could be expected to evolve into a non-planar semi-elliptical crack because propagation is predicted to be faster in the circumferential than in the radial direction. The extreme case of radial propagation from a 360° circumferential crack produces the shortest propagation life and hence provides the most

conservative disk life prediction. With this very conservative assumption the crack growth life is indicated to be in excess of 5500 hours beyond the 6000 hours initiation life, and is very likely to be very considerably longer.

The results of these analyses have been confirmed by experimental studies which have found that cracks generated in the front snap radius of samples cut from the parent disk grow preferentially in the circumferential direction. The tests in these studies produced a stress-state in the front snap radius that was similar to, but not fully representative of, the service conditions. The shape of the crack obtained in these test conditions is shown in Figure 10.

Since no in-service cracks have been seen to-date this prediction has not been fully validated. It is intended to carry out full-scale spin pit tests of 4th LPC engine disks with implanted flaws in the front snap radius to fully validate these predictions.
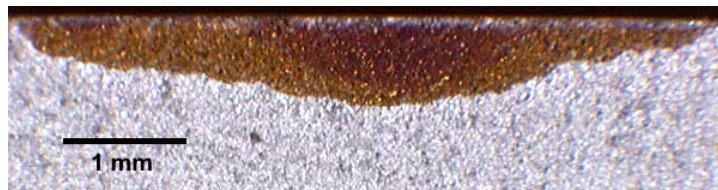
Figure 10 Crack Configuration in an experimental test replicating the engine conditions

5. Conclusions

The cases presented here indicate that the traditional LCF safe life analysis represents only a partial view of all the processes that contribute to defining and determining component replacement intervals. The fact that the LCF statistical data base omits to include other contributing factors such as the ones described in this paper, i.e. non-representative microstructures and the possibility of manufacturing and re-work flaws, leads to a non-conservative estimate of component replacement intervals. However, if no account is taken of the behaviour of cracks subsequent to reaching the assumed size of 0.8mm the assessment of replacement intervals may be excessively conservative.

The cases presented here illustrate the complex processes which have to be taken into account in determining replacement and overhaul intervals for critical components. The LCF analysis carried out by the OEM is only part of the analysis. A more detailed analysis, including a risk analysis needs often to be carried out retrospectively, including all the possible failure mechanisms.

The use of a 0.8 mm detectable crack as the criterion for a safe life was originally based on what could be reliably detected with NDI equipment at the time of the development of safe-life methodology. Modern automated NDI equipment can detect much smaller crack sizes with a very high degree of confidence, and safe-life estimates could therefore be adjusted to take advantage of this extra sensitivity without a commensurate increase in risk.

Conventional safe life methodology is founded on the assumption of nominal material and manufacturing conditions, and under these conditions the methodology provides a structured process for design and life management of high energy rotors. However undetected material and manufacturing anomalies represent a departure from the assumed nominal conditions and have resulted in the service incidents described in this paper.

References

1. Hou, J. Stocks, G. and Wicks, B., "Finite Element Analysis Of A Low-Pressure Compressor Assembly", pp.253-258, Proceedings of The Second Australasian Congress on Applied Mechanics, Canberra, February 1999.

2. Hou, J, Slater, S., Goldsmith, N. and Wicks, B.J., "Fatigue Crack Growth Prediction In A Turbine Fan Disc," Symposium 2000 on Structural Integrity and Fracture on 29-30 June, 2000 at University of Technology, Sydney Australia

3. Habbit, Karlsson and Sorensen Inc. "ABAQUS User's Manual", Ver 5.8 1998

4. Beyer, J.B., Sims, D. L., Sims and Wallace, R., AFMRL-TR-77-101 Titanium Damage Tolerant Design Data For Propulsion Systems June 1977

5. Yoder, G.R. ,Cooley, L.A. and Crooker, T.W., Quantitative Analysis of Microstructural Effects of Fatigue Crack Growth in Widmanstatten Ti-6Al-4V and Tio-8Al-1Mo-1V, Engineering Fracture Mechanics, Vol 11, pp805-816, 1979

6. Hou, J., Slater, S and R. Antoniou, "3D Fatigue Crack Growth Prediction of Snap Radius In A Compressor Disc", Symposium 2000 on Structural Integrity and Fracture on 29-30 June, 2000 at University of Technology, Sydney Australia

7. Fawkes, A.J., Owen, D.R.J., and Luxmore, A.R., An Assessment Of Crack Tip Singularity Models For Use With Isoparameteric Elements, Engineering Fracture Mechanics, Vol. 11, 1979, pp. 143-159.

8. Zentech Inc., "ZENCRACK User Manual", Issue 6, 1999.

9. Hou, J. and Wicks, B.J., Fatigue Life Prediction of a Low-pressure Compressor Disk, Compumod Users Conference Oct. 1999, pp20.1-20.7.

10. Billardon, R. Adam, C. and Lemaitre, J., Study Of The Non-Uniform Growth Of A Plane Crack In A Three-Dimensional Body Subjected To Non-Proportional Loadings, Int. J. Solids Structures, Vol 22, 1986, pp. 677-692.

Paper 22: Discussion

<u>Question from H Pfoertner – MTU, Germany</u>

Would you comment on the relationship between numerical crack-growth predictions and the necessity to perform spin testing?

<u>Presenter's Reply</u>

Each case has to be taken on its merits. In probably a few cases with simple geometries, an analytical solution alone may be sufficient. However, most cases will involve a combination of analytical solutions and tailored validation tests, ranging from simple tests, through multi-axial loading tests, up to full-scale component tests and spin tests. Each method has strengths and weaknesses, and these need to be understood.

New Lifing Methodology for Engine Fracture Critical Parts

D.P. Shepherd
Structures and Materials Centre, QinetiQ, Farnborough, Hants, GU14, 0LX, UK
Phone +44-1252-392000, Fax +44-1252-397298, Email: dpshepherd@qinetiq.com

S.J. Williams
Mechanical Methods and Design Technology, Rolls-Royce PLC, PO Box 31, Derby, DE24 8BJ, UK
Phone +44-1332-240-648, Fax +1332-240-327, Email: steve.williams@rolls-royce.com

1   INTRODUCTION

Within gas turbine aeroengines, fracture critical parts are defined as those whose failure would hazard the entire aircraft. Consequently, it is of central importance to the airworthiness of these engines that the probability of such a component suffering an in-service failure is kept below acceptable levels. In order to achieve this, lifing methodologies have been devised which provide a means for calculating the required limits. These methodologies consist of a material test requirement, together with a calculation process based on a statistical characterisation of the material/component behaviour. The outstanding safety record achieved by commercial and military aeroengines is in large part due to the success of these lifing methods.

Over the last 30 years or more, considerable research activity has been devoted to developing these methodologies, and the models and assumptions that underlie them. This has ensured that the methods have kept pace with the developments in gas turbine technology, and provide safe lives which fully reflect the characteristics of the relevant components. However, the commercial pressure on engine manufacturers to produce engines with improved performance and reliability at lower cost is at least as great today as at any previous time. Consequently, the rate of development of the technologies on which engine design and manufacture is based is, if anything, increasing. The introduction of new techniques in materials development and processing, component manufacture and design analysis is ongoing and rapid. In view of these developments, the lifing methods themselves must constantly be re-evaluated and updated if the safety record achieved to date is to be maintained and improved.

Recently, the trends in aero gas turbine design have raised questions with regard to the applicability of the lifing methods used previously within the UK. The fact that engine temperatures and speeds continue to rise has meant that the components, and the materials from which they are manufactured, have been operating closer to the limit of their capability than ever before. One result of this has been that certain parameters, previously seen to have little effect on the fatigue life, are now observed to play a significant role. Moreover, the interactions between these parameters are observed to be increasingly important, and must be characterised an understood if accuracy is to be ensured. Furthermore, since these effects are also observed to have differing characteristics during the initiation and propagation phases of fatigue life, it is becoming increasingly important to distinguish between the two. All of these effects mean that significant developments in lifing methodology are required if the required accuracy of estimation is to be ensured.

In this paper, a new lifing methodology is described, which combines several features of lifing analysis in a novel way. The main elements of this methodology are, firstly, a 3-D non-linear finite element stress analysis, which is used to estimate the actual stresses experienced in service by the component. Secondly, both the crack initiation and propagation phases of life consumption are modelled explicitly, so that the most appropriate behaviour models can be used throughout the fatigue process. Finally, it explicitly includes a statistical model for the size effect in fatigue, so that any component feature can be assessed from plain specimen data alone. The methodology has been extensively validated against a database of fatigue results for a typical engine alloy, and has been demonstrated to provide accurate estimates of specimen and component life under extreme combinations of both stress and volume.

2   THE HISTORICAL DEVELOPMENT OF LIFING METHODOLOGIES

In order to appreciate clearly the requirement for improved lifing methods, and the problems that they are attempting to tackle, it is important to understand the evolution of the currently available philosophies. This allows the issues currently facing the lifing community to be seen in context, and allows the new methodology to be understood as a response to the issues that stimulated its development. Consequently, this section is devoted to a description of this development.

In the very early days of gas turbine development, fracture critical parts lifing was a relatively unimportant issue. This was because the performance of the hot end parts was so poor, and engine strips so frequent, that discs were very rarely subjected to sufficient exposure for fatigue to be a problem. Moreover, any problems that did arise were picked up by inspection. Consequently, there was little or no need to formally declare lives for these components. However, as the hot part technology began to develop, and reliability began to improve, so disc failure began to be appreciated as an issue requiring closer attention. Put simply, failures of the components began to occur in-service, and there was clearly a need to address the matter in an alternative fashion.

The response to this issue was the development of what is known today as the 'safe life' approach to engine component lifing. The basis of this method was the estimation of component life through the construction and use of empirical stress-life (S-N) curves, for the relevant materials. In order to account for the different features on an engine disc, for example, it was necessary to obtain these curves at different temperatures and for a variety of stress concentrations. Safety was built into the process by basing the design and lifing calculations not on the curves themselves, but on some curve lying below the mean line which represented a suitable statistical safety factor. In the UK, such methods were always supplemented by full scale component rig tests, which were used as the basis of service life release. However, whilst these methods generally worked well, the development of materials with superior high temperature properties, better design methods and the introduction of novel manufacturing techniques pushed back the limits of what components were expected to endure in service. As a result, it became increasingly apparent that several additional factors such as mean stress and surface finish also play an important role in determining component life. Unfortunately, the empirical nature of the traditional safe life approach meant that additional design curves had to be generated to account for these different factors. The ever-increasing amount of experimental data required to sustain this approach eventually led to the search for alternative methods.

The success of stress intensity factor based fracture mechanics in combining the effects of these different factors into a unified physical model, appeared to offer a solution to the difficulties experienced in the safe life method. Different attempts were made to utilise this theory for calculating engine component lives, each of which revolves around the establishment of an initial flaw size from which the crack growth process proceeds. One of these is the 'damage tolerance' approach, whereby the initial crack size is established on the basis of the minimum detectable by non-destructive inspection methods. Another is the 'databank' method, which back calculates from known test data to establish an effective initial flaw size, this being the initial flaw that would have caused failure in the observed time under linear elastic fracture mechanics. From a set of test results, a distribution of flaw sizes is developed, and a maximum is established on the basis of a statistical analysis. Fracture mechanics is then used again to grow the flaw to failure, this being taken as the minimum life achievable. Much research work has been devoted to developing these methods, and they have been approved for use by regulatory authorities on both sides of the Atlantic. However, the ongoing developments in gas turbine technology have once again led to a situation in which the ability of the existing methods to account adequately for all relevant effects has been questioned. In particular, disc materials are now being subjected to operating temperatures at which creep plays a significant role both in determining stabilised component stresses and as a potential failure mechanism. The improvement in fatigue resistance achieved in new materials is also usually through a longer initiation period, crack growth rates being similar or even slightly worse. In short, it is now recognised that there are inherent difficulties in deriving engine component lives from a purely linear elastic fracture mechanics based approach.

3   THE NEW LIFING METHODOLOGY

The lifing methodology described in this paper attempts to overcome the shortcomings of the philosophies previously used in the UK, in order to meet the challenges presented by modern gas turbine design. It seeks to do this by directly addressing the problems with the existing methods, and by drawing on the latest developments in the technologies underlying lifing calculations. There are three basic features which combine to create the new method, and which differentiate it from those it seeks to supersede.

The first feature of the philosophy behind this approach is that the stressing carried out for each component attempts to calculate the full stress field actually experienced in service. This contrasts to, say, the data bank method, whereby the results of the elastic analysis are known to be a simplified representation of the actual stresses. The possibility of calculating actual component stresses has only been made possible by the rapid development, in recent years, both of improved numerical analysis techniques and of the hardware on which the algorithms are run. The result of this is that non-linear 3-D stress analysis of complex component shapes can now be used as a general purpose tool. Moreover, such stress analysis techniques must include the calculation of time dependent behaviour, for the reasons discussed above. Thus, in component assessment, both plastic and creep stresses must be calculated, so that an important part of introducing of the methodology has been the development of suitable methods for doing this.

The second feature of this approach, is that the crack initiation and crack propagation phases of component life consumption are modelled separately. This is in direct response to the difficulties with purely initiation or purely propagation based models discussed above. The way that this is achieved within the framework of the method is that firstly, an engineering model for total life is fitted to the available data. Then, a model for the propagation phase is used to estimate the proportion of the total life due to this phase, and a model for crack initiation is obtained by subtracting one from the other. A significant advantage of this approach is that factors which predominantly influence initiation can be included in an appropriate way, and can be treated completely separately from those which primarily influence propagation. It also means that recent developments in materials modelling can be utilised and integrated in a straightforward manner.

The third feature of the methodology is the inclusion of a model for the size effect in fatigue.   This is included as the final link which allows laboratory specimen data, generated to aid and validate materials modelling, to be included in the assessment of component behaviour. It is also in recognition of the fact that materials model development relies almost exclusively on specimen data. Whilst these specimens are designed to reflect the service loadings as closely as possible, they are typically a fraction of the size of full scale components. It has long been recognised that material volume itself plays a very significant role in determining fatigue life, and hence that specimen tests alone cannot fully describe component behaviour. Moreover, this effect is not restricted to the mean behaviour of the material; rather, the distribution of fatigue lives as a whole is dependant on volume. Thus, a further modelling step is required, which allows for the so-called size effect to be incorporated into the overall life prediction scheme.

In the subsections that follow, each of these three major features is discussed in some detail.

3.1   Stress analysis

A fundemantal concept of the current approach is that the stress and strain fields causing fatigue in any particular situation are estimated as accurately as possible. To this end, a plasticity model based on the Mroz multilayer kinematic hardening rule (ref 1) has been developed. This model extends the Prager linear hardening rule by the superposition of several yield surfaces of different sizes, each exhibiting linear behaviour with a different gradient.

To model the shakedown behaviour accurately, a technique has been developed whereby the material is allowed to relax over several cycles. The model shakedown is controlled as a linear function of the total plastic strain, and is stabilised according to certain preset limits. The model is combined with standard creep algorithms, assuming that the two phenomena are uncoupled.

3.2 Fatigue and crack propagation models

As described above, the new lifing methodology requires that suitable models for both the total life and the crack propagation behaviour are identified. Both must be capable of describing the phenomena relevant to the material behaviour under each regime, under the conditions experienced within the engine.

The fatigue life model chosen for the current analysis is that commonly referred to as the Walker strain parameter. The parameter itself has the form

$$\varepsilon_W = \frac{\sigma_{max}}{E}\left(\frac{E\Delta\varepsilon}{\sigma_{max}}\right)^m,$$

where E is the material modulus, $\Delta\varepsilon$ denotes the strain range, and m is an empirical factor to account for the effects of mean stress (ref 2). The effect of temperature is included through the use of a temperature dependant modulus.

The fracture mechanics model utilised within the study uses the elementary equations of LEFM, implemented using the finite element derived geometry and stress correction factors described in (ref 3)). The particular stress intensity solutions describe the growth of surface and corner cracks in rectangular blocks, with the advantage that user defined stress fields can be applied. This is particularly important in studying the growth of cracks in notches and around other stress concentration features. However, in view of the fact that the plain specimens tests analysed within the validation exercise were conducted on circular specimens, it was decided that more appropriate stress intensity solutions were readily available and should be used. For this purpose, the handbook solutions for elliptical surface cracks in round bars under tension were chosen as being more suitable (ref 4).

In addition to these models, it is necessary to account for the fact that, under certain conditions, mechanisms other than fatigue can be the primary cause of specimen and component failure. In particular, for specimen test designed to reproduce material behaviour relating to fracture critical components, it is necessary to account for the fact that some of the failures may be due to creep rupture. For this purpose, the Rolls-Royce internal creep rupture law was used, and all specimen tests were checked for this type of failure mode before being included in the database of results.

3.3 Size effect model

Existing models for the size effect in fatigue are almost invariably based on the so-called 'weak link' hypothesis, which assumes that bulk material failure will be triggered by the failure of the weakest sub-element within the material. This is related to general material behaviour by first developing a description of the material behaviour under constant load. For non-uniform loads and arbitrary geometries, the material is broken down into much smaller volumetric units, (the size of which will depend on the stress gradients involved), and the uniform stress behaviour is applied to these small volumes. The probability distribution for bulk failure is then derived by integrating individual probability distributions associated with the volume units over the body. The resulting expression is generally quoted in the form

$$F_\Sigma(\sigma;V) = 1 - \exp\left(-\frac{1}{V_0}\int_V\left(\frac{\sigma}{\eta(x)}\right)^\beta dx\right),$$

where V_0 is the reference volume at which the parameters η and β are defined (ref 5). The expression is essentially a Weibull distribution, with the appropriately normalised integral included inside the exponential. The expression as it stands applies to fatigue strength rather than life. However, it can be applied to the latter case by simply inverting the S-N relationship appropriate to the material or situation, and using this to express the characteristic life η as a function of stress (or Walker strain).

Examination of the test data made available for the validation, however, revealed that this relationship would not be sufficient for the model. In particular, there appeared to be a linear threshold, below which no failure were observed to occur. For this reason, an expression of the form

$$F_\Sigma(N; V, \varepsilon_W(x)) = 1 - \exp\left(-\frac{1}{V_0} \int_V \left(\frac{N - N_0(\varepsilon_W(x))}{N_\eta(\varepsilon_W(x))}\right)^\beta dx\right)$$

was selected as the basis of the model. This is equivalent to the choice of a 3-parameter Weibull model to describe the failure distribution at the volume element level.

Given a suitable database of test results, the manner in which the different elements of this framework are combined to produce life estimates is illustrated in Figure 1. The database of test results should contain enough plain specimen tests to represent the behaviour of the material under all conditions of interest, and should ideally include a variety of other test results for validation purposes. The calculation procedure itself involves four main stages. In the first stage, the non-linear stress analysis is used to calculate estimates of both the plastic and creep strain accumulated for each of the tests considered. The second stage involves analysing the plain specimen data,. A creep rupture analysis is performed, to determine whether the observed failures are attributable to creep or fatigue, and those which are creep induced are then eliminated from the analysis. A statistical model is then fitted to the remaining data, to provide a description of total life. Finally, a crack propagation analysis is performed, which is then subtracted from the original test result in a suitable manner, to give the required initiation model. In the third stage, the size effect model is employed to calculate an initiation life for the particular test piece under investigation. This is achieved by substituting the expression for the position dependent stress field, together with the model for initiation life, into the size effect equation and integrating. In the final stage, a crack propagation analysis is performed for the new geometry/stress field, and added to the initiation life already calculated to provide the final life estimate.

4   VALIDATION OF THE MODEL

In order to test and validate the model as a means of predicting component life, it is necessary to acquire a suitable database of fatigue test results. This database must include sufficient plain specimen results to allow the behaviour of the material to be characterised under all conditions of interest, and some other form of test result against which the predictions of the model can be compared. For this purpose, part of the Rolls-Royce database on Waspaloy was identified as an ideal vehicle for this purpose, and it was subsequently made available for this purpose by the company. The database itself consists of 2053 fatigue test lives, together with another 224 unfailed results. The 2053 finite lives consists of 1527 plain specimen results, 454 rotating bend tests, 33 notched specimen tests (Kt 1.66 and 2.29), 10 component rig tests and 29 washer specimen results. Not all of the data have been used in the study; thus far, only the notched specimen results and some of the component results have been included in the validation studies. It is anticipated that the remaining component results and the washer specimens will be included at a later date.

Once the stress analyses have been completed, and the data checked for possible non-fatigue failures (41 tests were rejected as being due to creep rupture), the next step in analysing the data is to fit the fatigue model to the plain specimen data. The data itself is shown in Figure 2. Given the linear appearance of the data overall, a linear S-N curve of the form

$$\varepsilon_W = (cN)^{-1/\alpha}$$

was selected as the basis for the model. This was inverted and substituted into the expression for the total probability of failure to give this equation in an explicit form. However, before the analysis could proceed, a further decision had to be made concerning the geometry over which the integral should be evaluated. Conventionally, the integral in the expression is regarded as a pure surface integral over the entire body, or, it is taken over the whole of the volume. In view of the surface sensitive nature of Waspaloy, it was initially decided that the integral should be evaluated over the surface, rather than through the volume. Unfortunately, this was found to give very poor results. However, rather than revert to evaluating the integral over the entire volume, which appeared to be somewhat unrealistic in physical

terms, it was decided that the integral should be evaluated over a surface layer of the material. This appeared to be the option that makes sense physically, since in any crack initiation process it will be the layer of material at and just below the surface which will be actively influencing the process. This created two difficulties; one was to choose the depth to which the integral should be taken, and the other was to develop the capability to be able to extract the relevant information from the stress analysis output files. The latter problem was solved by developing some software to convert FE node numbers into geometrical locations, thereby providing the means to extract them, if desired. The former problem was solved by selecting a value of 0.4mm, initially for no reason other than this was convenient in terms of the meshes under investigation. (In fact, later studies established that the results of the model are rather insensitive to this parameter anyway, at least for the notched specimen results). The results obtained by this method were very much better, indicating that this approach is actually representing the real physical process.

Initially, a single line was fitted through the plain specimen data, to give the fit of the fatigue life failure model. Once this was done, the next step was to subtract the crack propagation results to give he initiation model. However, this raises a further question, namely at what crack depth does the change from crack initiation to propagation take place? This is clearly critical in determining the success of the model, and so it was decided to optimise the model with respect to this parameter. The answer obtained was 0.3mm, which was close to the conventional definition of an 'engineering crack' used to define the boundary between initiation and propagation in current UK lifing proceedures. It is also close to the surface depth parameter identified as the layer over which the integral is taken. This suggests that it may be possible to treat these two criteria as a single parameter, thus reducing the number of input parameters required.

The fatigue life model for the plain specimen data, together with the crack propagation predictions and the resulting initiation life model are shown in Figure 2. The predictions for the notched specimen results calculated using this model are shown in Figure 3 to Figure 9, and the prediction for three of the component test results are shown in Figure 11. It can be seen from these figures that the results for the notched specimens is very good, with the exception of the Kt 1.66 tests at 200C and the Kt 2.29 tests at 600C which are discussed below. Moreover, the predictions for the component tests are also very accurate. Taken together, these two sets of results are extremely important, since notched specimens and component bores represent opposite extremes in terms of both strain and volume of material. The results therefore represent a strong validation of the basic concepts, since the model is seen to produce accurate results across the entire scale of likely application.

5   Discussion

As can be seen, the results are either good or very good for all the temperatures and notch types shown, apart from two. These are the Kt 1.66 tests at 200C which overestimate the results, and the Kt 2.29 tests at 600C, which underestimate the results. Considering the first of these, a further look at the data in figure 2 reveals that the data at 500C and at 200C do not really lie on top of one another. Rather, the 200 data are somewhat below the rest, and offset from the mean line. This means that the current position of the mean line tends to overestimate the initiation life at this temperature, explaining why the results are in error in this way. To correct this, it is a simple task to fit a separate line to the 200C data, derive a temperature specific initiation model and recalculate the predictions using these new results. The result of this exercise are shown in Figure 10, where it can be seen that the overprediction has been removed. In fact, the calculations now tend to underpredict the lives, although the error is considerably smaller than in the previous calculations.

The fact that a separate fatigue life model is required to resolve specific prediction errors raises a significant question regarding the use of engineering parameters in predictive work of this kind. Namely, would it be preferable to fit a multiple regression model to the data at the outset, rather than trying to derive laws which describe the behaviour of materials under very general circumstances? Although an approach of this kind would introduce additional empirical parameters, limiting the use of the resulting model, accuracy of the kind needed in the current exercise would be easier to achieve. Whilst the desirability of obtaining universally applicable (or even generally applicable) material laws is very clear, if the law is not sufficiently accurate to allow appropriate validation of models against experimental results, then their value seems to diminish somewhat.

The discrepancies encountered in the Kt 2.29 results at 600C are somewhat more difficult to resolve. Initially, it was thought that the underprediction could be related to the fact that the Walker strain values for these results lie above the point at which the crack propagation line in figure 1 crosses the total life regressions line. In other words, the initiation life for these results is zero. Moreover, checks revealed that, at these very high Walker strain values, the plain specimens would fail in tension before reaching the critical crack size. Thus, the crack propagation life would be overpredicted, potentially leading to an underprediction of the initiation life. However, given that the specimens are failing in tension, the failure point of the plain specimens will depend on the UTS for the material. The difficulty is that the UTS is itself a random quantity, and so it is necessary to establish the statistical relationship between the UTS and the initiation and propagation lives before this type of effect can be included in the calculations. Work to establish the nature of the relationship between these quantities at very high strain values is continuing.

To develop the method further, several issues need to be addressed. Firstly, the stress analysis methodology developed thus far does not include the ability to incorporate residual stresses. This is particularly important in view of the finishing techniques applied to modern components, which deliberately introduced compressive surface residual stresses in an attempt to prolong the fatigue life. Secondly, the fracture mechanics methods currently employed are based on linear elastic fracture mechanics methodology, and do not necessarily capture all the features of crack growth at high temperatures which may significantly affect the life. Thirdly, the statistical relationship between crack initiation and propagation are not fully understood at present, and further work is required to develop suitable models to describe this. Finally, it is only when the methodology has been validated against a range of materials, that the ability to provide accurate predictions over the range of conditions of interest will have been fully demonstrated.

6   Conclusions

Modern aero engine fracture critical component design presents a number of challenges to the lifing methods which have been used previously to derive safe service lives. In particular, the rise in engine temperatures means that types of material behaviour not relevant to previous component designs are playing an increasingly important role. A New Lifing Methodology has been developed, which aims to overcome the limitations of lifing methodologies currently employed in the UK, with respect to these issues. The three main distinguishing features of this new methodology are, firstly, the advanced non-linear stress analysis techniques are employed to calculate the actual component stresses experienced in service, secondly, that explicit models of both crack initiation and crack propagation are employed, and finally, that a size effect model is incorporated, which explicitly accounts for the effect of volume on fatigue. These elements allow for the prediction of fatigue lives for arbitrary geometries and stress fields, based on the analysis of plain specimen data alone.

The model has been validated against an extensive database of fatigue results in a typical aeroengine disc material (Waspaloy). The model predictions display very good agreement with notched specimen results over a wide range of temperatures and loads. Significant discrepancy is observed at the very highest temperature/load combinations, and the source of this is still being investigated. However, the model is also observed to provide excellent agreement with component results. This is very important, because notched specimens and components represent opposite extremes in terms of both stress level and material volume. Thus, the fact that the model can provide accurate predictions in both these situations is a very strong validation of the basic concept and the implementation.

REFERENCES

1) Z Mroz, 'An attempt to describe the behaviour of metals under cyclic loads using a more general work-hardening model', Acta Mechanica, **7**, 199-212 (1969)

2) M Doner, K B Bain & J H Adams, 'Evaluation of methods for the treatment of mean stress effects on low-cycle fatigue', J. Eng. Power, **104**, p 411 (1982)

3) A C Pickard, 'The application of 3-dimensional finite element methods to fracture mechanics and fatigue life prediction', EMAS, Warley (1986)

4) H Nisintani & D Chen, 'Stress intensity factor for a semi-elliptical surface crack in a shaft under tension', Trans. Japan Soc. Mech. Engrs,. **50**, p1077-1082, referenced in '*Handbook of stress intensity factors*', Ed by Y Murakami, Pergamon press (1987)

5) G Schweiger & K Heckel, 'Size effect in randomly loaded specimens', Int J Fatigue, **4**, p 231-234 (1986)

6) FIGURES

New lifing methodology process
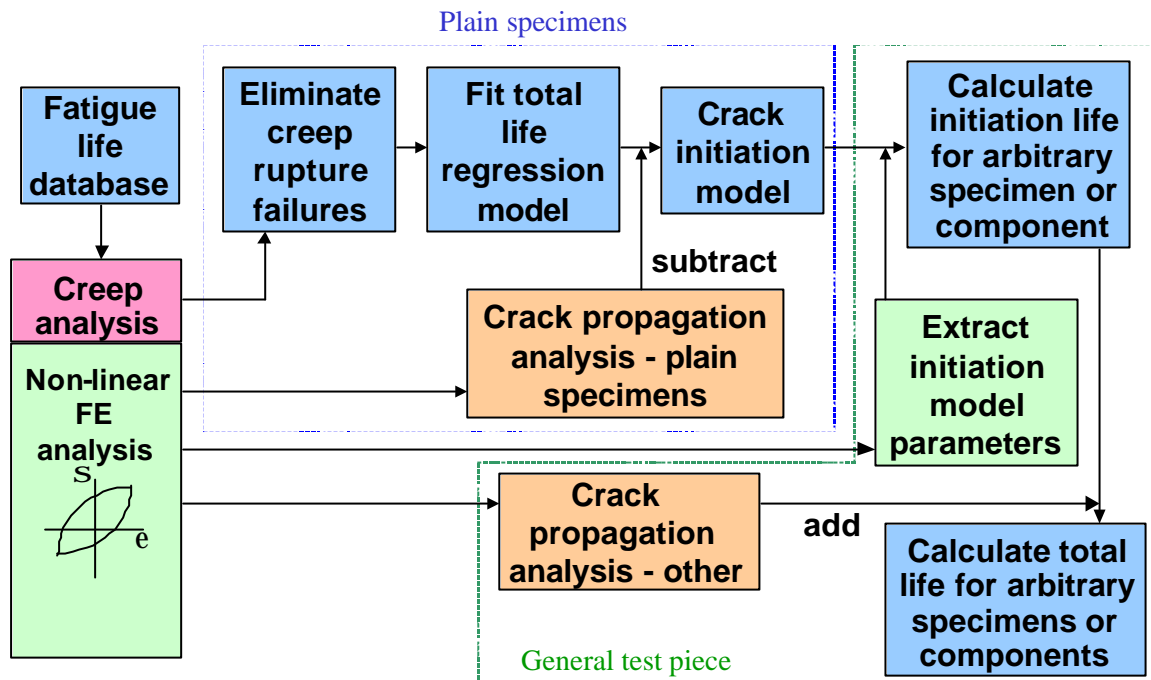
Figure 1: Framework for the new lifing methodology
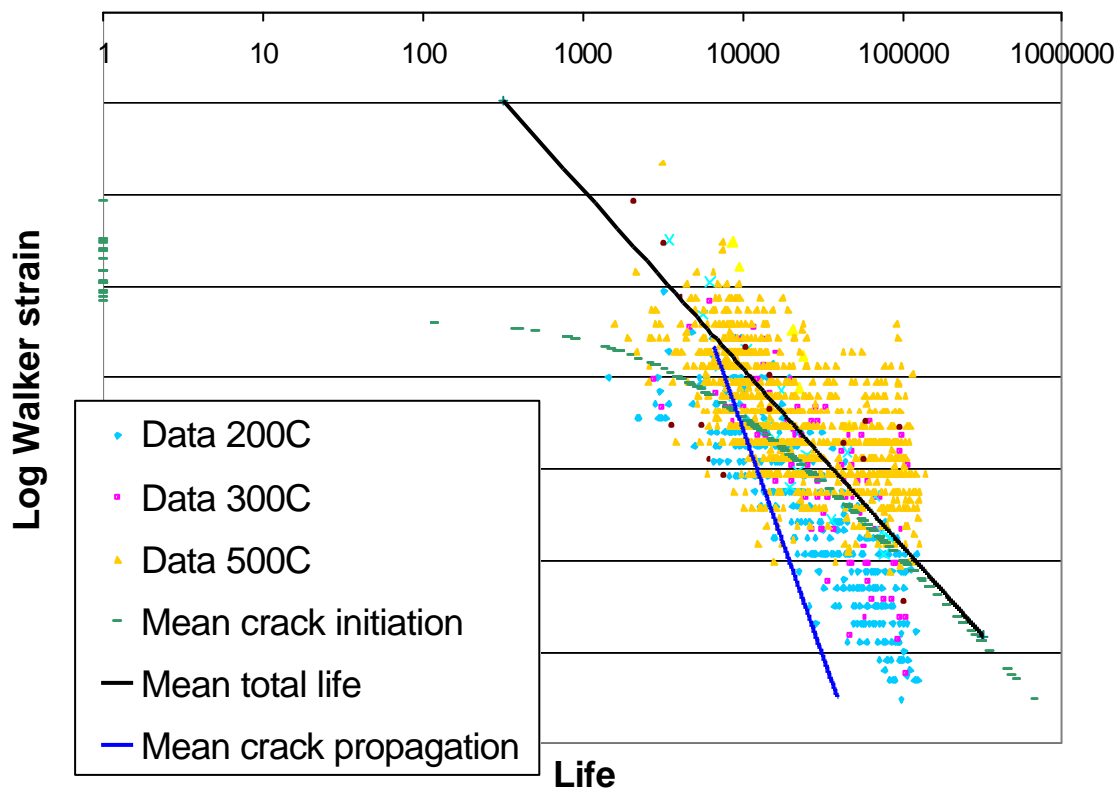
Figure 2: Derivation of the initiation model for the Waspaloy data
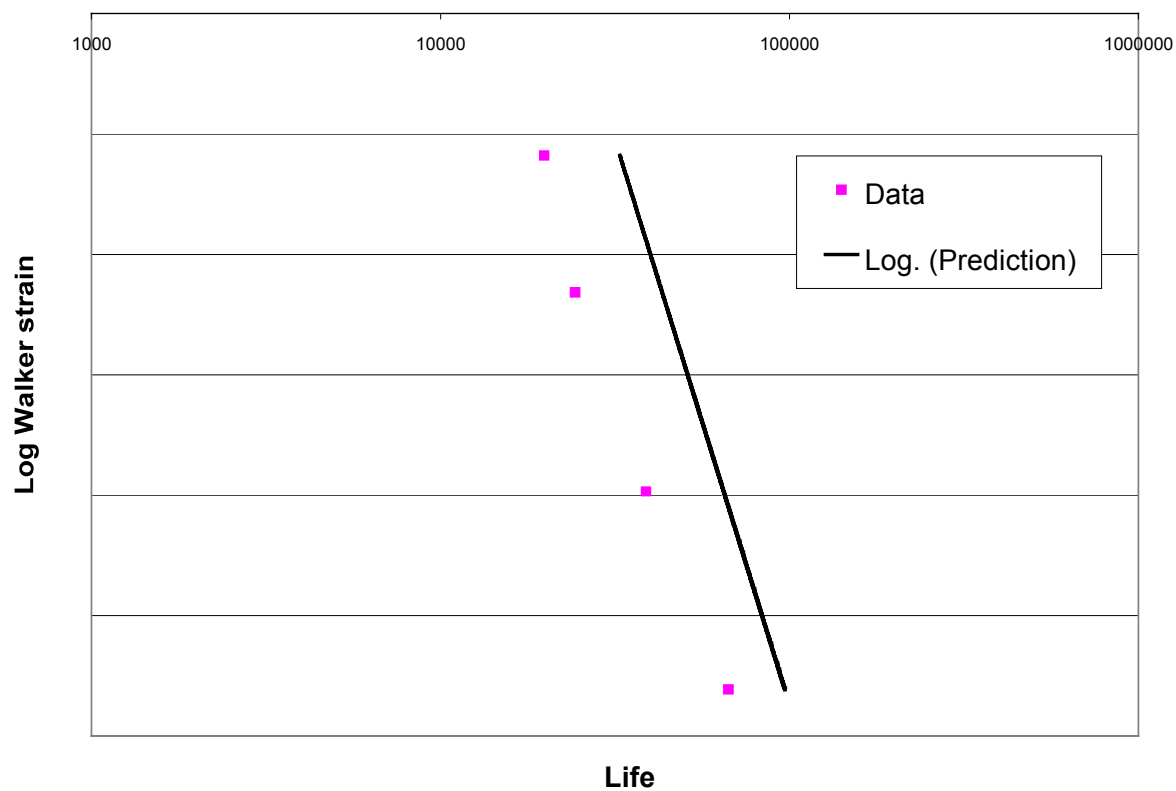
Figure 3: K$_t$ 1.66, 200C data against prediction
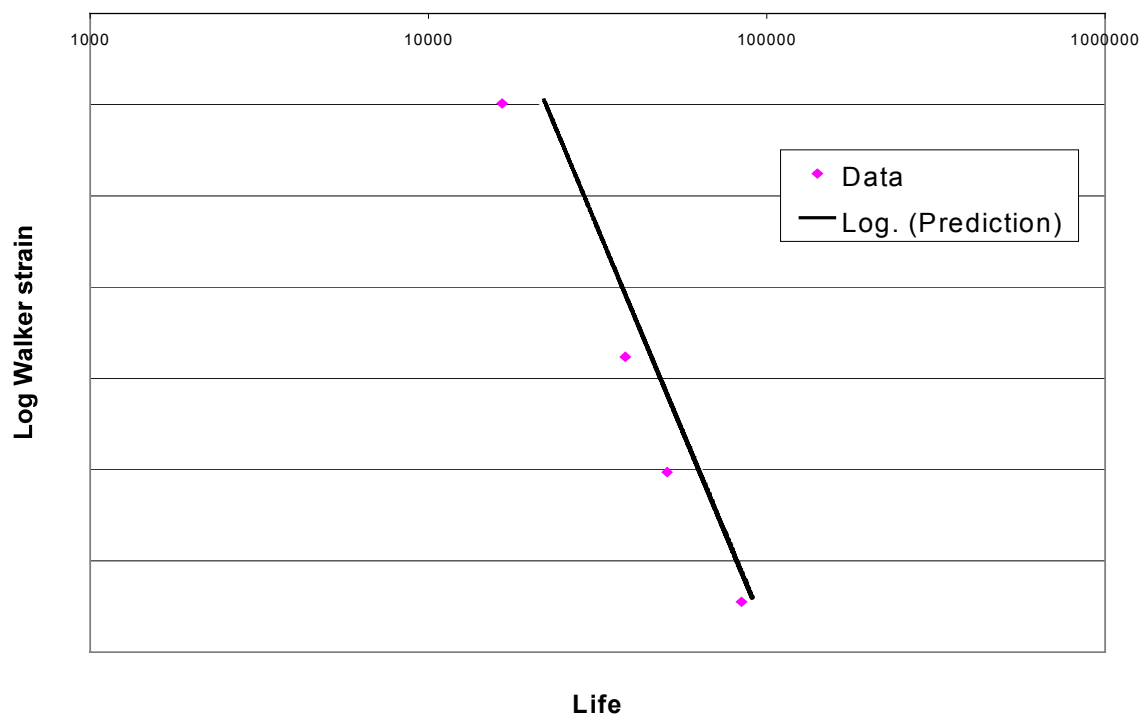
Figure 4: K$_t$ 1.66 400C, data against prediction
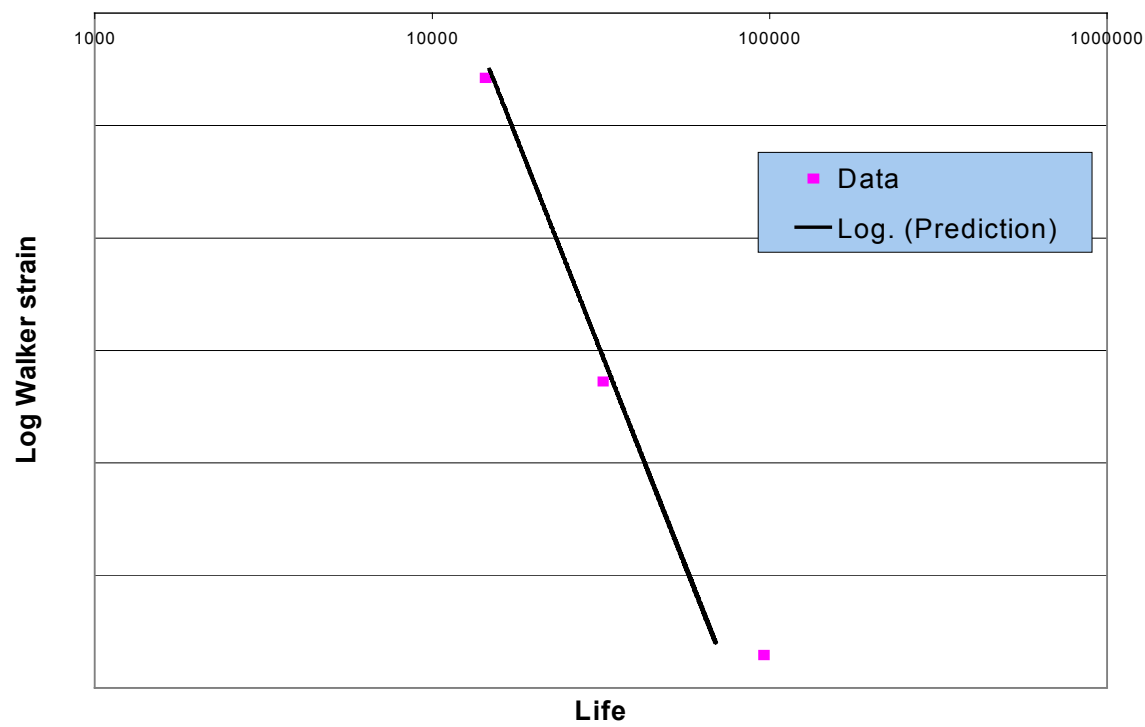
Figure 5: Kt 1.66 500C, data against prediction
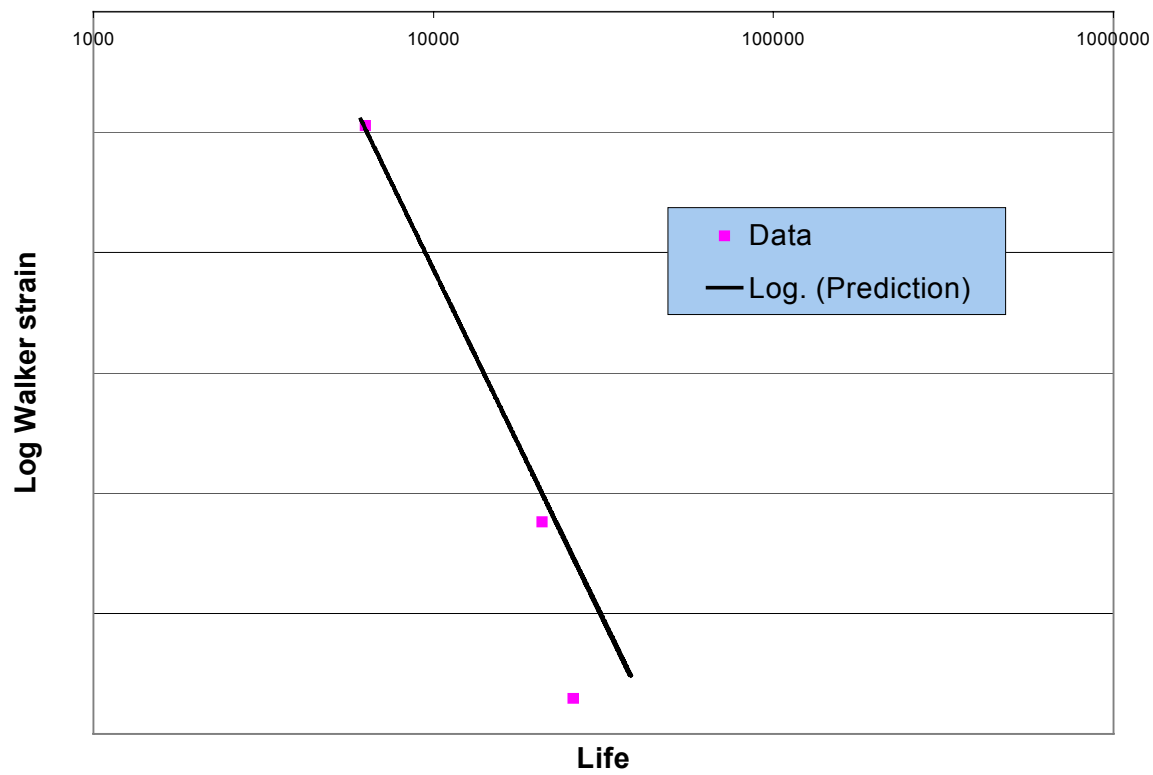
Figure 6: Kt 1.66 600C, data against prediction
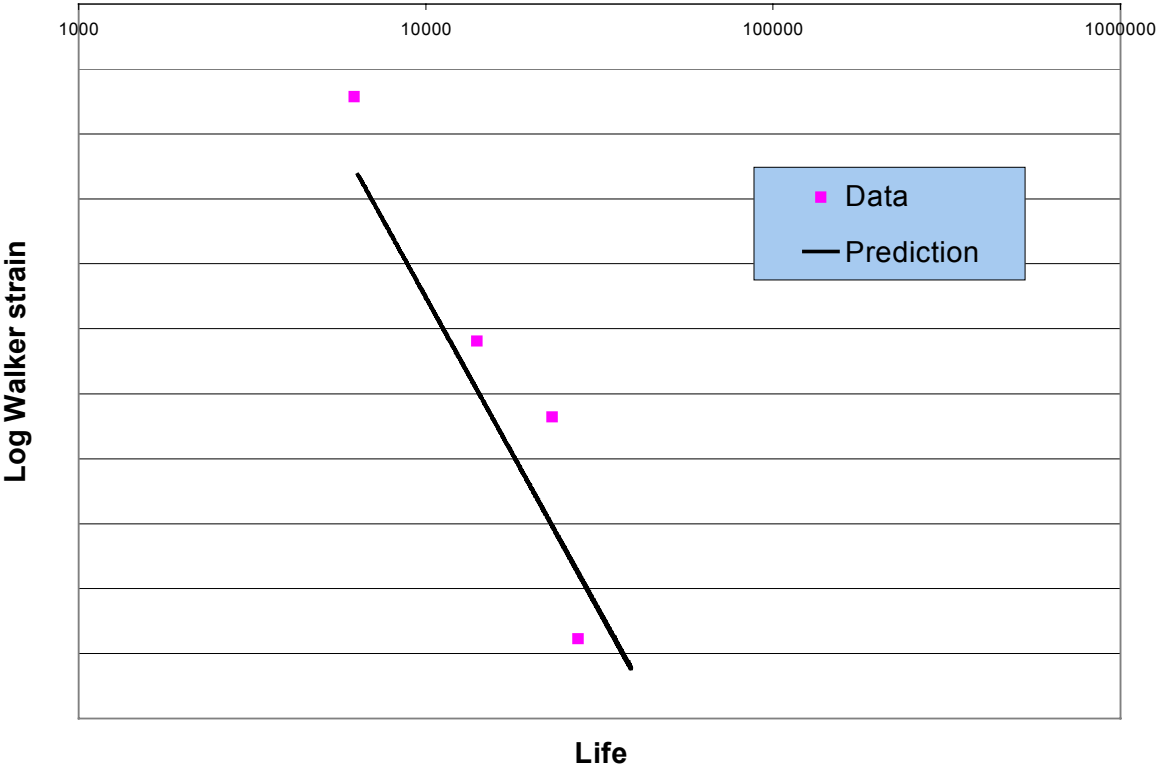
Figure 7: Kt 2.29 400C, data against prediction
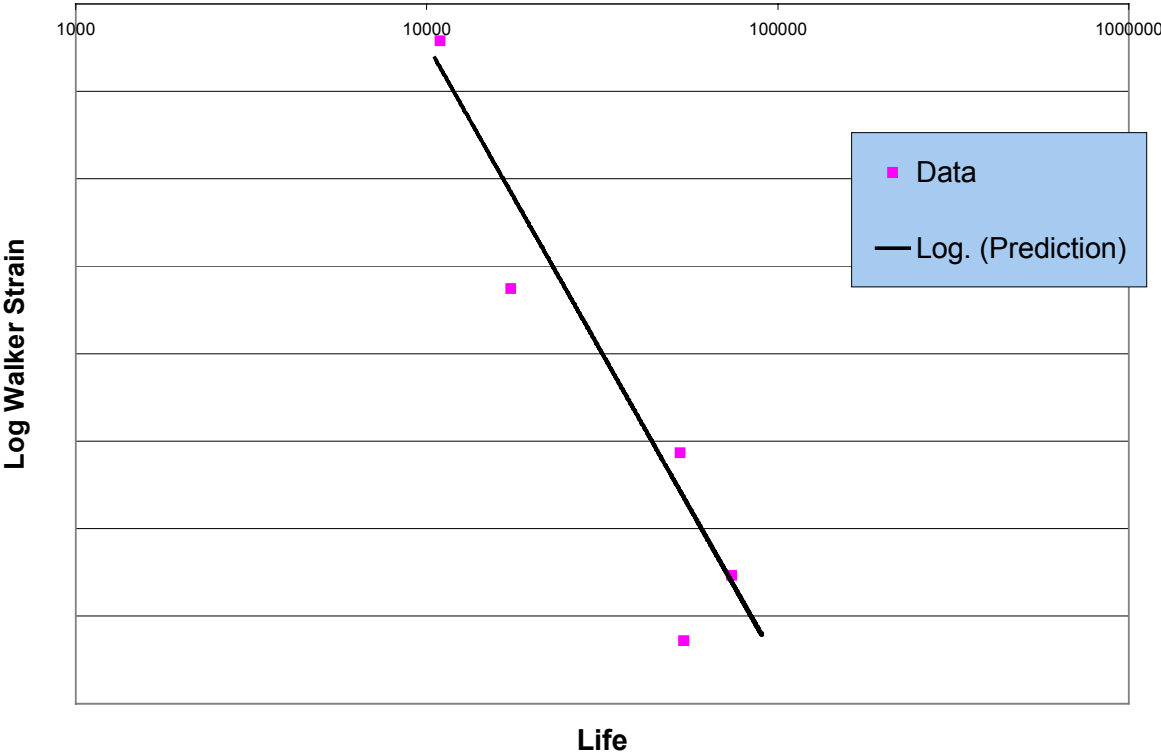
Figure 8: Kt2.29 500C, data against prediction
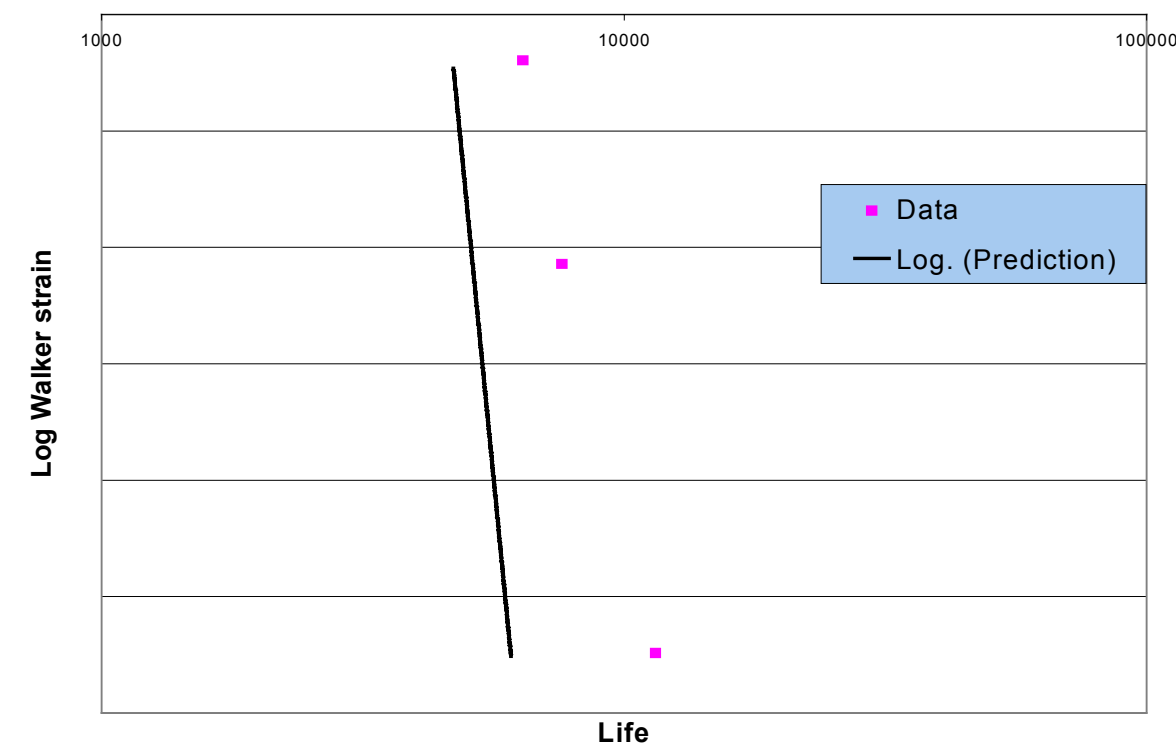
Figure 9: Kt 2.29 600C, data against prediction
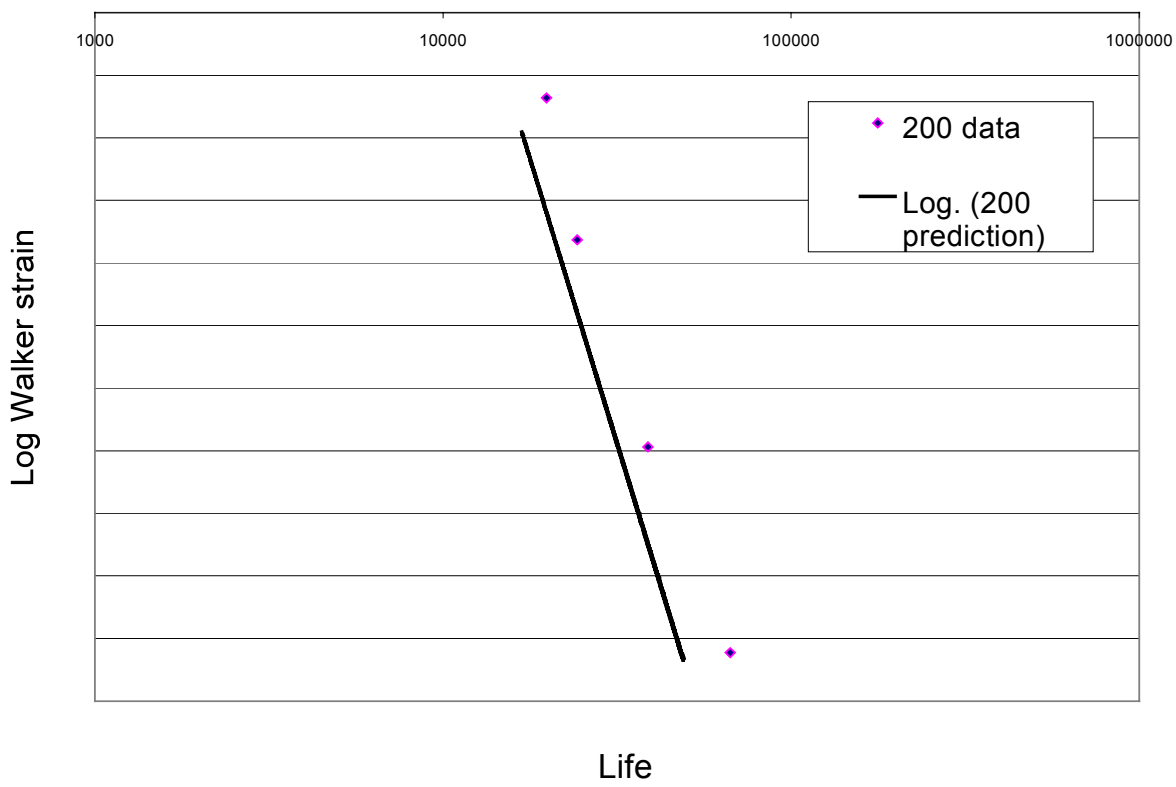
Figure 10: Kt 1.66 200C data with revised prediction
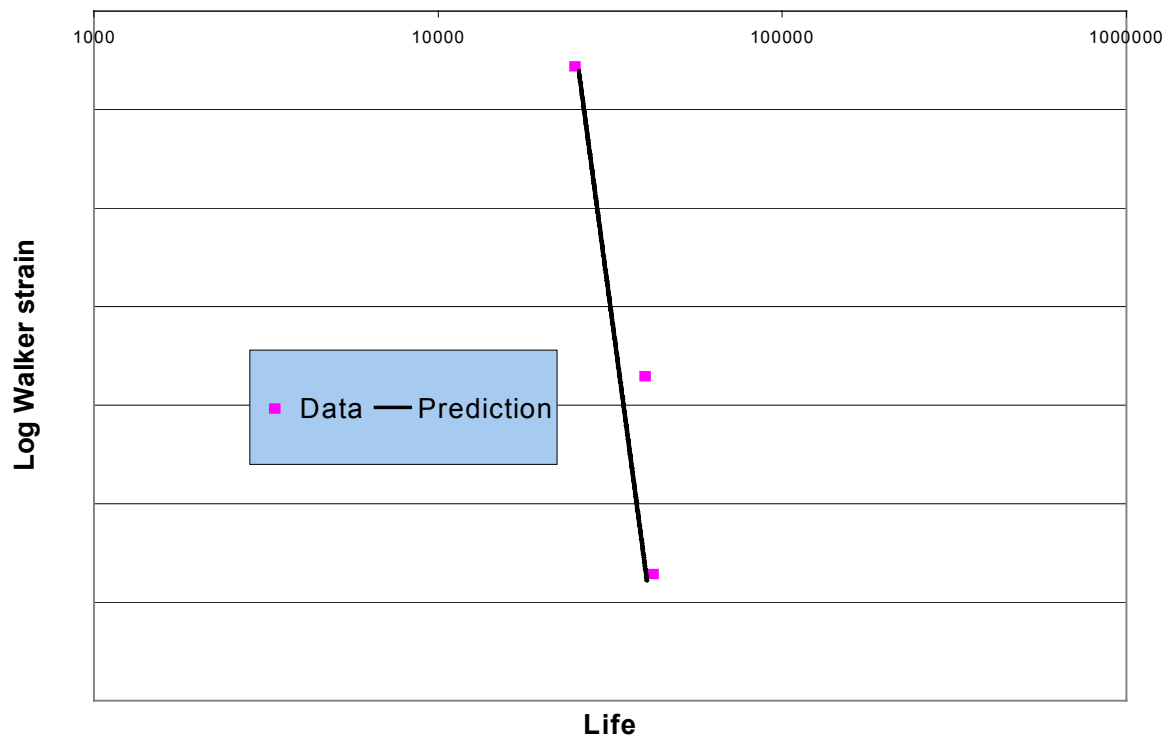
Figure 11: Component bore test data against prediction

Paper 23: Discussion

Question from Dr R Szczepanik – Instytut Techniczny Wojsk Lotniczych, Poland

Could we, in Poland, use this risk-regulated inspection methodology for engines of Soviet-origin, bearing in mind that they have a wide distribution of material properties relative to comparable western materials?

Presenter's Reply

It should be possible to apply risk-regulated inspection to the Polish fleet case. Assuming that the situation is that budgets are very small but labour is relatively inexpensive, then frequent disassembly and inspection might be the most effective option, depending on the effort required in removing and re-fitting the engines. One may be able to take account of the fact that the fleets may have already consumed significant life, as the basis for calculation of a safe inspection interval. That is, if many components have survived to a certain life, then this should say something about the crack propagation life capability of the components. However, a disadvantage of frequent inspections is that they increase the risk of handling damage and build errors.

A New Modelling of Crack Propagation with Fatigue-Creep-Oxidation Interaction under Non Isothermal Loading

F. Gallerneau, S. Kruch and P. Kanouté
Office National d'Etudes et de Recherches Aérospatiales
B.P. 72, 92322 Châtillon Cedex, France

B. Burgardt
SNECMA Moteurs, Centre de Villaroche
77550 Moissy Cramayel, France

This paper deals with the extension of a crack growth model to high temperature complex loading and application to turbine disc. The proposed model is based on an extensive experimental study performed by SNECMA Moteurs on N18 from 450ºC to 650ºC, in isothermal and also in non isothermal condition, which comprises fatigue with or without hold times and special sequence tests representative to the disc in service. The crack growth model is built up in the framework of classical linear elastic fracture mechanics. Time effects at high temperature are traduced by creep-fatigue and oxidation-fatigue interactions. The proposed writing in non isothermal condition is very attractive for easy model identification on a large temperature domain. Model predictions are shown for a large set of experimental data including complex loading in non isothermal condition.

1   INTRODUCTION

This paper presents a phenomenological model able to simulate the crack growth in a metallic material at high temperature and under complex cyclic loading condition. This one uses the actual stress intensity factor as the loading variable, but also several material parameters are introduced in order to describe the history of the various processes that operate near the crack tip during for instance an hold period at high temperature: the mechanical stress redistribution due to visco-plasticity, the creep damage process under tensile condition, the environmental driven brittle oxide at crap tip that increases the fatigue crack propagation and the interaction of overloads with both fatigue and creep crack growth.

After reminding and discussing the main features of the model, originally proposed by Prigent [1] and Kruch et al [2], we propose in a first section a model extension to account for non isothermal complex loading together with the functions describing the fatigue, creep and oxidation damages and the different interactions. We give then in the second section the results of the application made with N18 aeronautical superalloy, the model predictions of many isothermal tests performed at different temperatures and also of non isothermal tests more representative of real loading subjected to the component in service.

2   CRACK GROWTH MODEL

2.1 *Assumptions of the creep-fatigue-oxidation interaction under complex loading*

The proposed model is built up in the framework of classical linear elastic fracture mechanics. The main points the model must take into account are: the fatigue crack propagation, the creep crack propagation, the stress intensity factor relaxation during creep, the creep-fatigue interaction and the environment effects. The various state variables that store the post-loading events are as follows:

–   A threshold K_s^f for fatigue crack growth, similar to the opening stress intensity factor. Its evolution is influenced both, by fatigue overloads (and under-loads) as proposed by Baudin and Robert [3], and by the hold time or low loading rate during which a relaxation can occur. Built up in the basis of Onera's crack propagation model proposed to account for complex loading in fatigue, it can take into account the overload effects applied during a cycle through the plastic zone evolution in front of the crack and the value of the fatigue threshold K_s^f; that will not be developed in this paper.

–   This threshold is also introduced to describe the creep crack growth K_s^c in a time dependent expression.

–   The size of the oxidised zone at the crack tip l_p, from which is deduced an effective local toughness of the material K_C, that operates in the fatigue crack growth model through a Forman's expression.

To account for the creep-fatigue contribution for a given cycle, the crack growth is classically divided into two parts, the first one concerning the fatigue propagation, and the second one the creep:

$$da = \left(\frac{da}{dN} \right)_{Fatigue} dN + \left(\frac{da}{dt} \right)_{Creep} dt \qquad (1)$$

For the treatment of a general complex loading, for instance with hold time and overload as described in figure 1, we post the fatigue crack growth (the minimum value of the stress intensity factor is memorised) for the given loading at the next unloading. Only time dependent phenomena such as creep crack growth, threshold relaxation and oxidised zone increasing are computed during the loading. Let us precise that the threshold is supposed to be constant during the creep crack growth. It is only actualised just before to post the fatigue crack growth, and just after for instance to take into account an overload (or an under-load). The environment effects are also posted for the next cycle through decreasing of the material toughness.
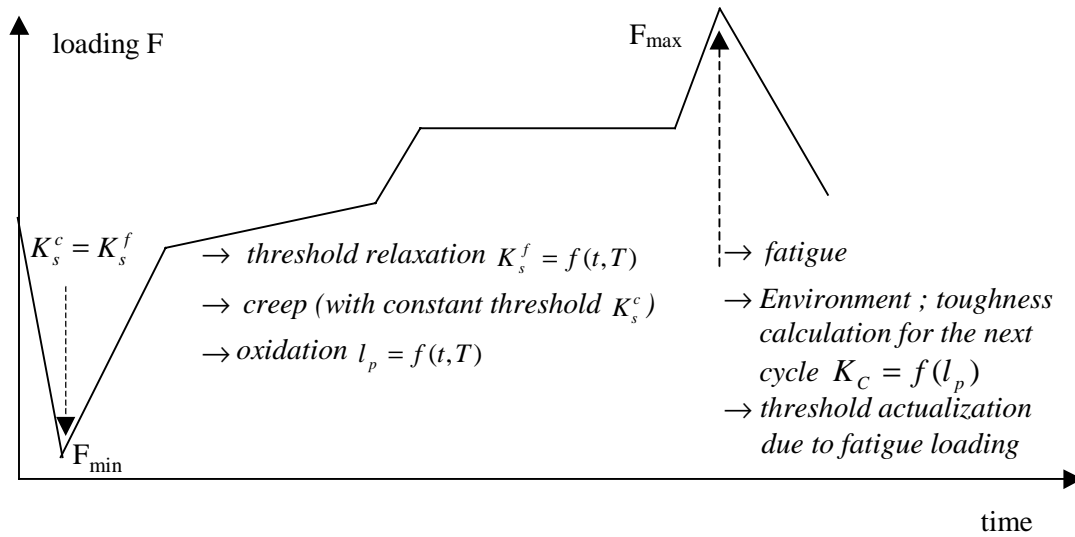
FIGURE 1. General scheme of the creep-fatigue-oxidation interaction model

2.2 Non isothermal writing

Let us consider a thermo-mechanical loading for which the temperature $T(t)$ can strongly vary during the force cycle $F(t)$ or the stress intensity factor $K(t)$ at the instant t. The difficulty for the model extension in non isothermal condition concerns the fatigue law which predicts a fatigue damage rate per cycle. Which temperature do we have to consider ? We can consider the maximum temperature over the cycle to be in the security way, or to define a mean temperature T^* as proposed by Taïra (4).

The way we propose here to account for the temperature dependency is to use a reduced stress $S = \dfrac{K(t)}{K_{cv}(T(t))}$ as parameter describing the thermo-mechanical fatigue cycle, where

$K_{cv}(T)$ is the material toughness (without oxidation effect) which is temperature dependent, the fatigue law can then be supposed temperature independent. In another words, this hypothesis requires that the fatigue material properties evolve with temperature only through the evolution of the material toughness supposed here to obey to an Arrhenius law:

$$K_{cv}(T) = K_{cv}^{o}\exp(\frac{Q}{RT}) \qquad (2)$$

where Q (the activation energy) and K_{cv}^{o} are material coefficients. We define then a fatigue law as a Forman [5] expression of S variable:

$$\left(\frac{da}{dN}\right)_{Fatigue} = \frac{C_f^*\left[S_M - S_s^{f*}\right]^{\eta_f^*}}{(1-R)\left[S_c - S_M\right]} \qquad (3)$$

where C_f^* and η_f^* are temperature independent material coefficients. S_s^{f*} is the fatigue threshold, also temperature independent. R is the loading ratio, S_c the normalised toughness equal to 1 without environment effect, and S_M the maximum value of S during the cycle. From tests results obtained in fatigue regime, without time effect such as creep or

environment effect, and for several temperatures, we have to find only one mistress curve if we report $\left(\dfrac{da}{dN}\right)$ as a function of $\Delta S = \dfrac{K_M}{K_{cv}(T(t))} - \dfrac{K_s^f}{K_{cv}(T(t))}$.

Tests performed by Bernede [6] on Astroloy superalloy in vacuum and in air at high temperature show a great influence of environment on the crack propagation process. The main environment effect is the material oxidation at the crack tip leading to a reduction of the mechanical properties. It is introduced in the model through the variation of the local normalised toughness induced by oxidation:

$$S_{c1}(t) = \frac{K_{cox}^o}{K_{cv}^o}\left[1 - u + u.\exp\left(\frac{mz^*}{l_p(t)}\right)\right]$$ (4)

$$S_c = Min(S_{c1}, 1)$$

where mz^* and u are material temperature independent coefficients. By considering the toughness $K_{cox}(T)$ of the completely embrittled material at the crack tip, necessarily lower than $K_{cv}(T)$ and also supposed to obey to the same Arrhenius law (same activation energy):

$$K_{cox}(T) = K_{cox}^o \exp(\frac{Q}{RT})$$ (5)

we assume then that the ratio $\dfrac{K_{cox}^o}{K_{cv}^o}$ is temperature independent. $l_p(t)$ is the penetration length of oxide inside the material as a function of time and temperature:

$$dl_p(t) = \frac{1}{4}(F(x)\alpha)^4 l_p^{-3} dt$$

$$\alpha = \alpha_o \exp(\frac{-Q_o}{RT})$$ (6)

α_o and the activation energy Q_o are material coefficients. This function traduces the material oxidation kinetics at the crack tip [7] and its temperature dependency. The function $F(x)$ accounts for the loading effect on the oxidation kinetics, for instance an hold time after an overload. x is the ratio between the actual load and the previous overload:

$$F(x) = cx^4 = c(\frac{F(t)}{F_M})^4$$ (7)

c is a constant. In the case of increasing load, x equals to 1 and the oxidation effect on fatigue process is completely operative.

As creep damage is concerned, the extension in non isothermal does not require supplementary development because the creep model is described by a temporal equation:

$$da = \int_{t_1}^{t_2} C_c(T(t))\left[K(t) - K_s^c\right]^{\eta_c(T(t))} dt$$ (8)

A given cycle (time, load, temperature) is treated by considering time steps sufficiently small to assure the calculation convergence, and by taking at each time step the corresponding parameters $C_c(T(t))$ and $\eta_c(T(t))$. Crack propagation by creep is posted

as soon as the actual stress intensity factor $K(t)$ is higher than the non propagation threshold K_s^c. We can remind here that this threshold is considered as a constant during the cycle and equals to the fatigue non propagation threshold K_s^f calculated at the previous cycle. On the other hand, we compute during creep the relaxation of this one, by a relaxation type equation deduced from the study of viscous behaviour of the material:

$$d(\frac{K_s^f}{K(t)}) = -A(T(t))(\frac{K_s^f}{K(t)})^{\omega(T(t))} dt \qquad (9)$$

As well as the creep model integration, we consider the instantaneous values of the parameters $A(T(t))$ and $\omega(T(t))$ at each time step of the calculation.

3   APPLICATION TO A NICKEL-BASE SUPERALLOY FOR TURBINE DISK

We present in this section the application made on N18 Nickel-base superalloy at high temperature. A wide experimental program has been conducted by SNECMA Moteurs [8] from 450°C to 650°C for various loading conditions. After showing the results of the identification, we give predictions of many isothermal and non isothermal tests.

3.1 Identification of the model parameters

The proposed formulation makes the model attractive for its identification on a large temperature domain. As a matter of fact, the fatigue law evolves with temperature through the variation of the material toughness $K_{cv}(T)$ supposed to be known. Fatigue tests results performed at high temperature but at high loading frequency in a pure fatigue regime, for which time effects such as creep and oxidation can be neglected, or at low temperature whatever the loading frequency (no time effect), are then used to identify the fatigue coefficients.
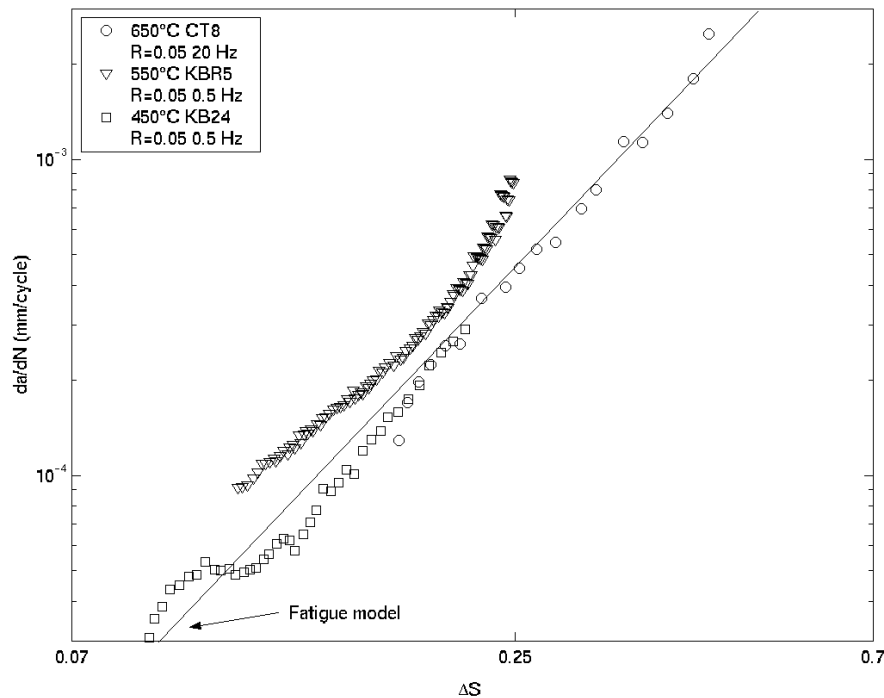
FIGURE 2. Identification of the pure fatigue model

The figure 2 gives the result of C_f^* and η_f^* identification (the initial non propagation threshold S_s^{f*} is taken equal to $0,5$) by reporting in a diagram ($\dfrac{da}{dN}, \Delta S$) tests results obtained at 450°C (we observed any time effect at this temperature), 550°C (we suppose to have a small time effect for those tests performed at 0,5 Hz) and 650°C (at 20 Hz in a pure fatigue regime) for the same loading ratio. At a given temperature, we can then calculate $C_f(T)$ and $K_s^f(T)$ parameters by the following relations:

$$C_f(T) = C_f^* \cdot K_{cv}^{1-\eta_f^*}(T)$$
$$K_s^f(T) = S_s^{f*} \cdot K_{cv}(T)$$

(10)

Pure creep tests at different temperatures are required to identify the creep model temperature dependent parameters $C_c(T)$ and $\eta_c(T)$ of equation 8. The initial non propagation threshold $\dfrac{K_s^c}{K_{max}}$ is also taken equal to $0,5$. We reported in figure 3 the results of the identification at 650°C.
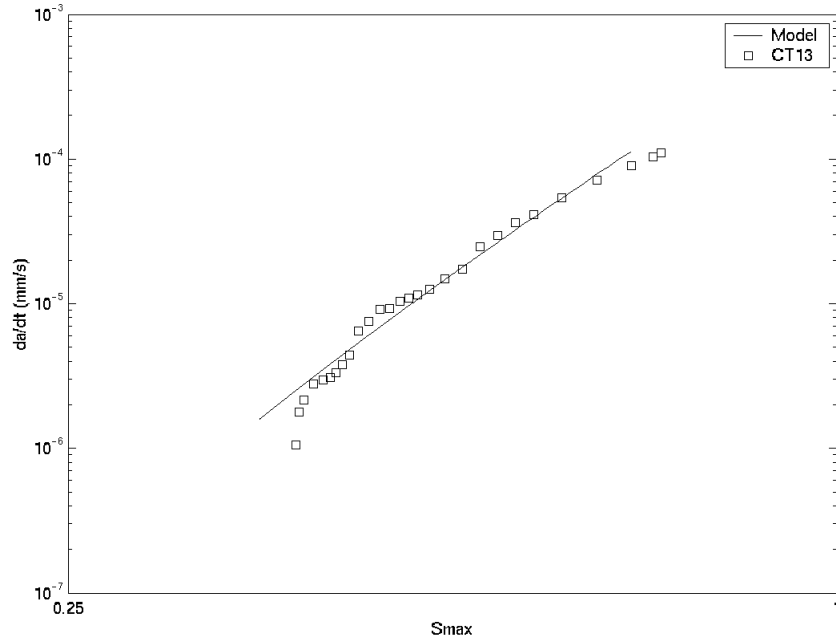
FIGURE 3. Identification of the pure creep model at 650°C

To complete the information obtained by tests, all the phenomena concerning the crack opening and closure and the stress redistribution at the crack tip induced by plasticity or visco-plasticity during the crack propagation can be obtained by a numerical analysis using a finite element method, as it has been made by Prigent (1) in the case of Astroloy superalloy. This numerical analysis conducts to the identification of $a(T)$ and $\omega(T)$ threshold relaxation parameters of equation 9 (the visco-plastic behaviour of the material at high temperature is of course supposed to be known and predicted by accurate constitutive models).

The oxidation kinetics of the material as well as its temperature dependency is (α_o and Q_o coefficients of equation 6) supposed to be known. The evolution of the material toughness ahead of the crack tip (K_{cox}^o and then the ratio $\dfrac{K_{cox}^o}{K_{cv}^o}$; mz^* and u coefficients of

equation 4) can be deduced from special tests performed on oxidised specimens. The coefficient c (equation 7) which traduces the loading effect on the oxidation kinetics is identified by one test result obtained in fatigue-creep regime, for instance by the simulation of a test with hold time.

3.2 Predictions of isothermal tests

We give in this section several comparisons model/prediction of tests performed on specimens with notches of different geometry (KB, KBR and FC).
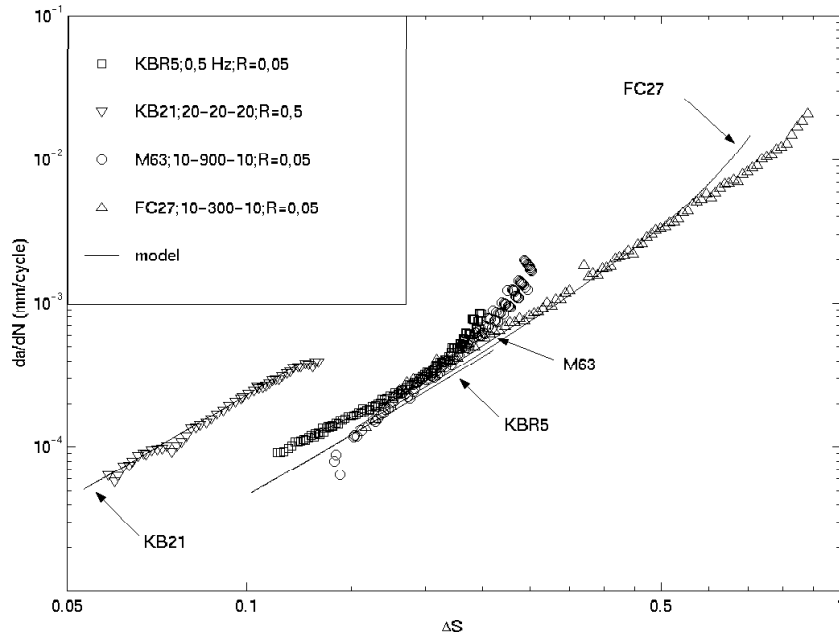
FIGURE 4. Prediction of time and load ratio effects at 550°C

In figure 4 are reported the model predictions at 550°C. As it can be seen, the model predicts almost any time effect at this temperature in agreement with the tests results. The load ratio effect is also correctly reproduced. Complex loading have been defined to simulate on a specimen what can be observed on the real component such as SF1, SF2 and A'20 cycles reported on figure 5.
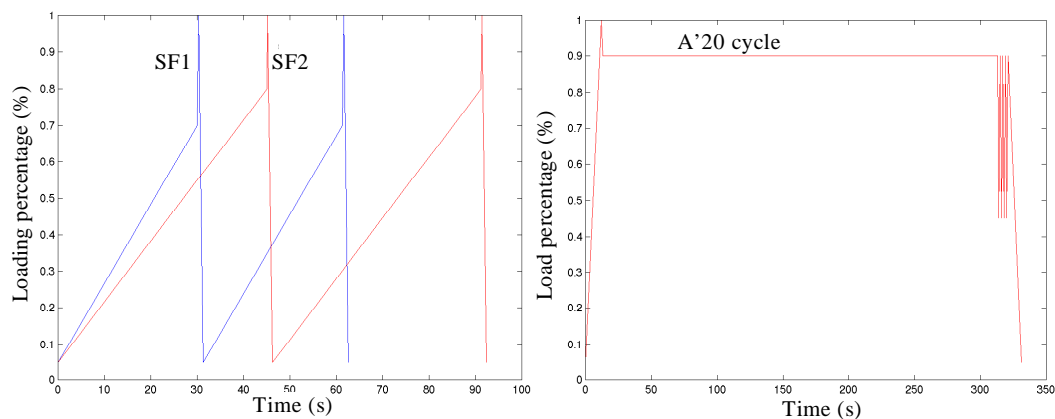
FIGURE 5. Complex cycles SF1, SF2 and A'20

The figure 6 gives the model predictions for these complex cycles. The loading rate effect is well reproduced as SF1 and SF2 cycles are concerned. The test reproducing A'20 mission is predicted with a little too high crack propagation rate.
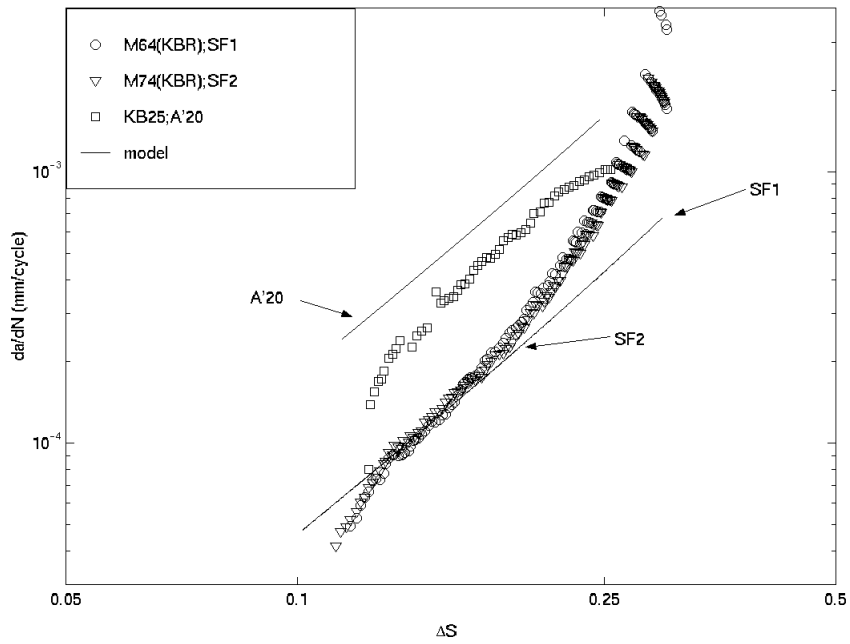
FIGURE 6. Predictions of complex tests SF1, SF2 and A'20 at 550°C

We present now tests predictions at 650°C for which time effects are important.
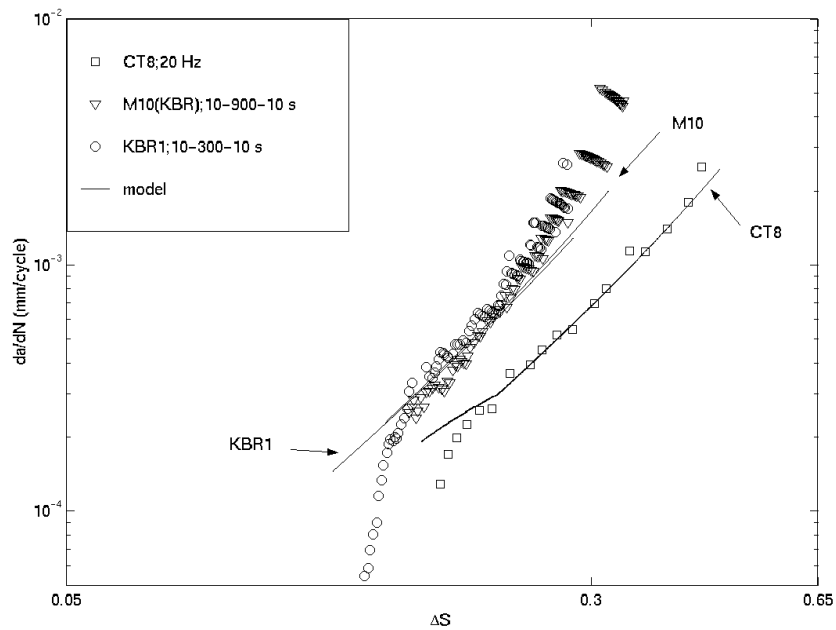
FIGURE 7. Predictions of tests with hold time at 650°C

In figure 7 are given the predicted curves for tests with different hold times. The model predictions are quite good whatever the hold time duration. It appears a small difference between the two predicted tests with hold times of 300 s and 900 s, in agreement with the tests results.
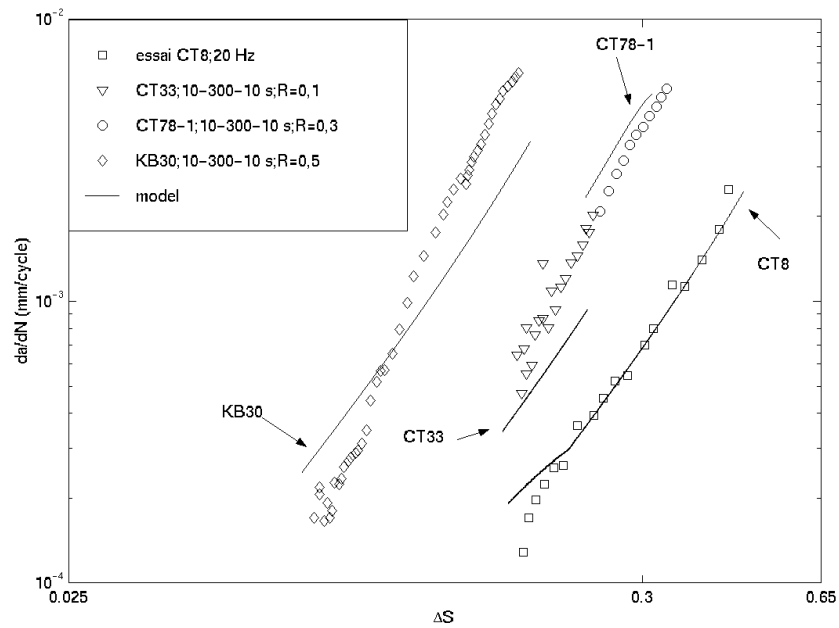
FIGURE 8. Predictions of tests with hold time for different load ratios at 650°C

The last predictions reported on figure 8 concern the loading ratio effects at 650°C for tests with the same hold time of 300 s. The loading ratio effects predicted by this crack propagation model reproduce quite correctly what it can be observed with N18 superalloy and for tests with consequent creep-fatigue-oxidation interaction.

3.3 Predictions of complex tests under non isothermal condition

Three different complex loading in non isothermal condition were studied [8] to simulate on specimens what can be subjected to critical zones of a turbine disc.
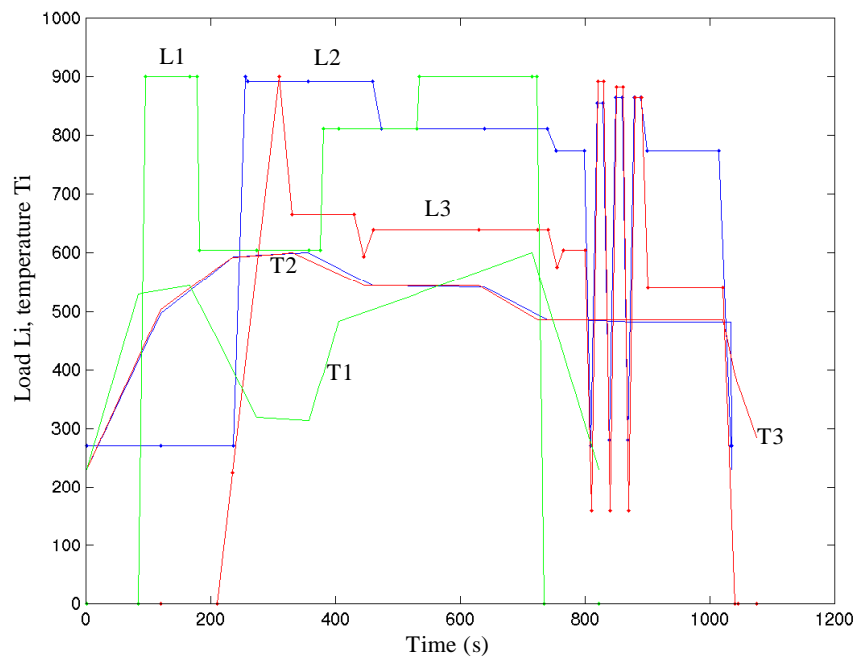
FIGURE 9. Thermo-mechanical fatigue cycles simulated in the laboratory
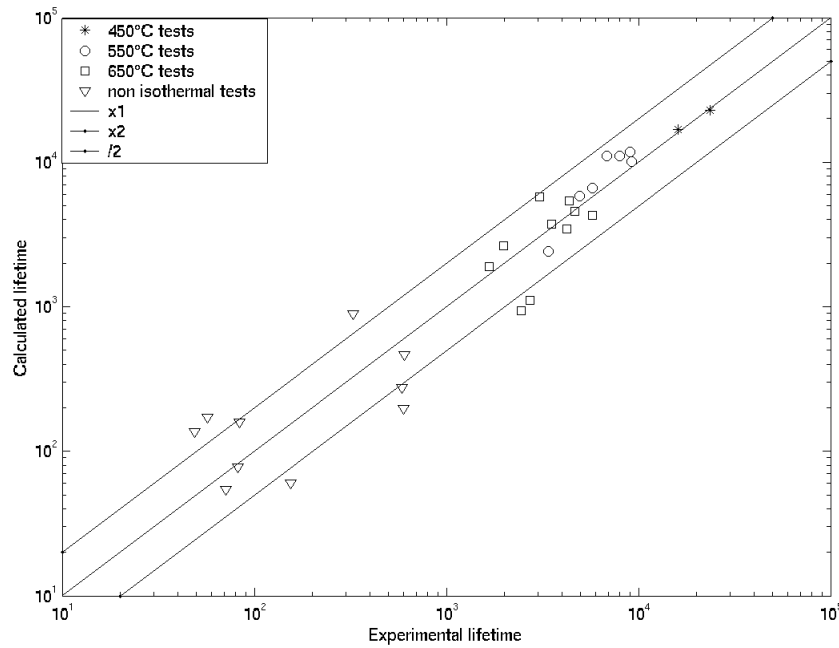
FIGURE 10. Comparisons between calculated and experimental lifetimes

The applied load to the specimen and the temperature loading are reported in figure 9. The temperature varies for each cycle from about 200°C to 600°C. The lifetime is the number of missions to reach a given crack length. We present in figure 10 the comparisons between the experimental and calculated lifetimes for isothermal and non isothermal tests. The model predictions are fairly good, as well as for many isothermal tests at several temperatures and loading conditions, and for the thermo-mechanical fatigue tests for which the lifetime is correctly predicted, even if the model parameters have not been identified at the maximum temperature of the cycles (600°C) but interpolated with results obtained at 550°C and 650°C.

4   CONCLUSION

The works summarised in this paper demonstrate actual possibilities to predict the crack propagation of metallic materials at high temperature such as Ni-base superalloy for turbine discs. The strong requirements in design procedures have led to the development of sophisticated crack propagation models to account for fatigue, creep and environment effects as well as theirs interactions on crack propagation rate. We proposed a phenomenological fatigue-creep-oxidation interaction model for an application in isothermal condition but also in non isothermal condition. We presented the lifetime prediction of many isothermal tests and of a few anisothermal tests. Predictions are fairly good for the set of experimental data and are very promising to make the model predictive under complex thermo-mechanical loading.

Acknowledgements

5   REFERENCES

(1) Prigent, P., *Modèle de propagation de fissure à haute température avec interaction fatigue-fluage-oxydation*, PhD thesis, Ecole Nationale des Ponts et Chaussées, Paris, France, 1993.

(2) Kruch, S., Prigent, P. and Chaboche, J.-L., *Int. J. Pres. Ves. & Piping*, Vol. 59, 1994, pp. 141-148.

(3) Baudin, G., and Robert, M., Crack growth life-time prediction under aeronautical loading, *Proceedings of ECF5*, Lisbon, Portugal, 1984.

(4) Taïra, S., *Creep in structures*, Academic Press, New-York, U.S.A, 1962.

(5) Forman, R., Kearney, V., and Engle, R., Trans ASME, *J. Basic Engng*, Vol. 89, 1967, pp. 459-464.

(6) Bernede, P., *Fissuration à chaud de l'Astroloy en métallurgie des poudres*, PhD thesis, Ecole des Mines, Paris, France, 1993.

(7) Reger, M., Rémy, L., Influence de l'oxydation sur le comportement à haute température d'un alliage à base de nickel, *Proceedings of the J. Printemps SFM*, Paris, France, 1986.

(8) Renevey, P., Desquines, J., *Base de données de l'alliage N18*, SNECMA Moteurs report, 1999.

This page has been deliberately left blank

_____

Page intentionnellement blanche

REPORT DOCUMENTATION PAGE

1. Recipient's Reference	2. Originator's References	3. Further Reference	4. Security Classification of Document
	RTO-MP-079(I) AC/323(AVT-074/075)TP/50	ISBN 92-837-0024-4	UNCLASSIFIED/ UNLIMITED

5. Originator	Research and Technology Organisation North Atlantic Treaty Organisation BP 25, F-92201 Neuilly-sur-Seine Cedex, France

6. Title	Ageing Mechanisms and Control Symposium Part A – Developments in Computational Aero- and Hydro-Acoustics Symposium Part B – Monitoring and Management of Gas Turbine Fleets for Extended Life and Reduced Costs

7. Presented at/sponsored by	the RTO Applied Vehicle Technology Panel (AVT) Symposium, held in Manchester, United Kingdom, 8-11 October 2001.

8. Author(s)/Editor(s)	9. Date
Multiple	February 2003

10. Author's/Editor's Address	11. Pages
Multiple	664 (text) 61 (slides)

12. Distribution Statement	There are no restrictions on the distribution of this document. Information about the availability of this and other RTO unclassified publications is given on the back cover.

13. Keywords/Descriptors

Acoustic emission	Aging (metallurgy)	Gas turbine engines	Methodology
Acoustic impedance	Aircraft	Human factors engineering	Models
Acoustic properties	Computational acoustics	Hydroacoustics	Noise (sound)
Acoustic signatures	Fatigue (materials)	Life (durability)	Sound waves
Acoustics	Fatigue life	Life cycle savings	Structural analysis
Aeroacoustics	Fatigue tests	Mechanical properties	Structural design
Ageing tests (materials)	Fluid flow noise	Mechanical tests	

14. Abstract

Part A:

The acoustic characteristics of air and sea vehicles are of increasing importance for war-time as well as peace-time operations. The meeting treated the potential of and results obtained with computational aero- and hydro-acoustics. It is a relatively new and rapidly expanding technical discipline with a large potential for (more) accurate prediction of the acoustic characteristics of air and sea vehicles. Examples are:

Acoustic signatures.

Acoustic fatigue loads and their consequences for the structural integrity.

Effects of inboard noise levels and the near-field acoustic environment including low frequency noise on the effective and efficient operation of the vehicle and its systems (human factors).

Community noise of air vehicles during peace-time operation.

Papers were presented on the following topics.

Propulsion & power noise: propellers, fans, jets, power systems.

Fluid flow noise: shear layers and vortex shedding/interaction, cavities.

Noise propagation.

Structural response and acoustic loads suppression.

Part B:

Financial constraints make it imperative to retain weapon systems for longer periods than originally planned and to operate them in ways not envisioned by the designers. Therefore technologies that extend the useful lives of weapon systems and their components are needed.

Twenty four papers from seven NATO nations and one allied nation (Australia) were presented threating the Monitoring and Management of Gas Turbine Fleets for Extended Life and Reduced Costs. Papers were presented in four major categories:

Maintenance and logistics practices,

General design practices,

Usage data and mission analysis, and

Life determination methodologies.

These categories provided material of interest to, respectively, the fleet manager, the equipment designer, the fleet operators, and the technical specialists responsible for fundamental technologies.

A consensus view emerged that full fleet monitoring is optimal for understanding fleet life. Further, limitations in existing data bases with regard to both content and ability to support appropriate data manipulation were identified as a significant concern. There is need for more research into the failure mechanisms such as crack growth in order to identify and safely use the remaining life in fielded systems. This originated from the work of the former AGARD/PEP WG28.

This page has been deliberately left blank

_____

Page intentionnellement blanche

NATO's Research and Technology Organisation (RTO) holds limited quantities of some of its recent publications and those of the former AGARD (Advisory Group for Aerospace Research & Development of NATO), and these may be available for purchase in hard copy form. For more information, write or send a telefax to the address given above. **Please do not telephone**.

Further copies are sometimes available from the National Distribution Centres listed below. If you wish to receive all RTO publications, or just those relating to one or more specific RTO Panels, they may be willing to include you (or your organisation) in their distribution.

RTO and AGARD publications may be purchased from the Sales Agencies listed below, in photocopy or microfiche form. Original copies of some publications may be available from CASI.

NATIONAL DISTRIBUTION CENTRES

SALES AGENCIES

Requests for RTO or AGARD documents should include the word 'RTO' or 'AGARD', as appropriate, followed by the serial number (for example AGARD-AG-315). Collateral information such as title and publication date is desirable. Full bibliographical references and abstracts of RTO and AGARD publications are given in the following journals: